FRACTURE MECHANICS OF CONCRETE STRUCTURES

Edited by Zdeněk P. Bažant

FRAMCOS 1

ELSEVIER APPLIED SCIENCE

FRACTURE MECHANICS OF CONCRETE STRUCTURES

Proceedings of the First International Conference on Fracture Mechanics of Concrete Structures (FraMCoS1) held at Beaver Run Resort, Breckenridge, Colorado, USA, 1–5 June 1992

organized by

Northwestern University

in collaboration with the

NSF Science and Technology Center for Advanced Cement-Based Materials (ACBM)

and the

ACI Committee 446 on Fracture Mechanics

under the auspices of the

International Association for Bridge and Structural Engineering (IABSE)

and the

American Concrete Institute (ACI)

and sponsored by the

US National Science Foundation (NSF)

FRACTURE MECHANICS OF CONCRETE STRUCTURES

Edited by

ZDENĚK P. BAŽANT

Walter P. Murphy Professor of Civil Engineering, Northwestern University, Evanston, Illinois, USA

ELSEVIER APPLIED SCIENCE
LONDON and NEW YORK

ELSEVIER SCIENCE PUBLISHERS LTD
Crown House, Linton Road, Barking, Essex IG11 8JU, England

WITH 103 TABLES AND 635 ILLUSTRATIONS

CIP Catalogue record for this book is available from the British Library

ISBN 1-85166-869-1

Library of Congress CIP data applied for

Printed and bound in Great Britain by Hartnolls Ltd

Dedicated to

Maurice F. Kaplan

(1917 – 1991) ,

Emeritus Professor of the University of Cape Town
and pioneering researcher in fracture mechanics of concrete.

PREFACE

Although fracture mechanics, originated by Griffith in 1921, is by now a mature discipline that has already found broad applications to metallic structures, the fracture mechanics of concrete structures is a young emerging theory. It will no doubt become very important for the design and evaluation of concrete structures, but has yet to be fully developed and verified. Research began with a pioneering experimental investigation of concrete fracture by M. F. Kaplan[1] and an equally pioneering finite element analysis of cracking in a concrete dam by R. W. Clough[2]. But the progress was relatively slow through the 1970's and the opinion that fracture mechanics was not really applicable to concrete structures prevailed. This opinion, of course, pertained to fracture mechanics in either its linear form or the form of small-scale yielding known at that time. The attitude changed radically around 1980. It was realized that the fracture mechanics of concrete must take into account the large size of the fracture process zone which causes a pronounced R-curve behavior and, most importantly, gives rise to a strong size effect which is transitional between plastic limit analysis (no size effect) and linear elastic fracture mechanics (the strongest possible size effect). Because of the coarse heterogeneous microstructure of the material, many concrete structures are at the lower limit of the size effect transition, which permits their analysis according to plasticity theory. However, many large structures, especially nuclear reactor vessels or dams, or special structures such as those made of high-strength concrete, are in upper part of the size effect transition, which in effect dictates the use of fracture mechanics.

The research activity suddenly exploded at the beginning of the 1980's. Various committees of international societies devoted to the advancement of the subject were formed, the earliest being the RILEM committee chaired by F. H. Wittmann. After the conference in Lausanne in 1983, sponsored by Wittmann's committee, the number of conferences on the subject grew rapidly. During each of the last several years, there were many major international meetings and conferences dealing with concrete fracture, and they often conflicted with each other. This created a confusing situation. An active researcher was unable to attend all of these conferences, and at the same time he did not know which would be the principal one to choose. Realizing this state of affairs firsthand with my initial attempt at the scheduling of the present conference, I decided to discuss the situation with the leading researchers around the world. In summer 1990, I circulated a letter to the members of the freshly organized International Scientific Advisory Committee of this conference, in which I suggested that the disorderly spectrum of conferences could be remedied by organizing an international association that would run a series of the main conferences dealing with the subject, such that every active researcher would know well ahead of time which conference not to miss and where to present his best results.

The response was overwhelmingly supportive. It thus became clear that discussions of the details of founding an association were appropriate. I have held such discussions with a number of leading researchers, with whom I got a chance to meet, including S. P. Shah, F. H. Wittmann, H. Reinhardt, A. Carpinteri, H. Mihashi, L.

---

[1] "Crack Propagation and the Fracture of Concrete," ACI Journal, 58, 1961, No. 11.

[2] "Stress Distribution in Norfolk Dam," Department of Civil Engineering Series 100, Issue 19, University of California, Berkeley, 1962.

Cedolin, J. Mazars, J. Planas, K. Willam, B. I. G. Barr, R. de Borst, V. E. Saouma, J. van Mier, and others. We talked about it at the international workshop on concrete fracture held in Locarno, Switzerland, in September, 1990 (organized by Wittmann and Dungar) and the international workshop on concrete fracture held in Torino in October 1991 (hosted by A. Carpinteri). As a result of our discussions at these most charming locations, the detailed concept crystallized.

An organizing meeting was called to hotel Oranje in Noordwijk, Netherlands, where it was held on June 19, 1991, during a conference organized by J. van Mier. The International Association of Fracture Mechanics of Concrete Structures (IA-FraMCoS) was created by unanimous consensus of the members of the International Scientific Advisory Committee of this conference who were present in Noordwijk. They became the founding members. The president, the secretary and the steering committee members were elected on that day. The steering committee, headed by F. H. Wittmann and with B. I. G. Barr as secretary, is preparing the bylaws of our new Association, which will be voted on at this conference. It was decided to incorporate our Association in the state of Illinois and have the headquarters in Evanston. Mr. Clement J. Caroll, Jr., an attorney with Gordon & Glickson, a Chicago law firm, was hired to take care of the legalities of the incorporation as a non-profit organization, with the initial Board of Directors consisting of F. H. Wittmann, H. Mihashi and myself, as representatives of three continents. The incorporation was obtained from the State of Illinois on December 16, 1991, which lent our new Association legal status. The principal goal of our Association, run democratically by its members, will be to organize at regular intervals (typically every three years) FraMCoS Conferences, dealing with all the aspects of fracture mechanics of concrete structures. The sites should alternate among various continents and countries, with no geographic or other bias, however, favoring the main centers of research. If desired, our Association might also sponsor or co-sponsor various other symposia or workshops focused on more specialized subjects. Furthermore, it could serve to coordinate a calendar of meetings and promote the advancement and applications of fracture mechanics of concrete structures by other means.

As is clear from the present proceedings volume, an exciting program lies ahead of us in Breckenridge. There are many thought-provoking papers on difficult subjects, and also many questions still to be answered. Let us hope that the discussions at the conference will be lively and stimulating, not only the formal discussions at the sessions but also the private discussions during the free time, which is plentiful at this conference. There are reasons to believe we will make a good start and create a favorable climate for the subsequent conferences. The applications of fracture mechanics are important enough to require our most dedicated efforts.

It is proper for me to acknowledge my gratitude to the U. S. National Science Foundation for providing partial financial support for this conference. I wish to thank all the members of the Organizing Committee, and especially Professors K. H. Gerstle, V. E. Saouma, S. Sture and K. Willam of the University of Colorado, Boulder, and visiting scholar I. Carol, for their valuable help. I am grateful to the members of the International Scientific Advisory Committee for their advice. Thanks are also due to Milan Jirásek, Graduate Research Assistant at Northwestern University, for his expert assistance in preparing the present proceedings volume, and to Martha Moser for her general secretarial assistance. Furthermore, thanks are due to (1) the NSF Science and Technology Center for Advanced Cement-Based Materials at Northwestern University, (2) ACI and its Committee 446, Fracture Mechanics, and (3) International Association for Bridge and Structural Engineering for agreeing to co-sponsor this conference. Finally, I wish to thank the authors of the conference papers for their excellent contributions.

Zdeněk P. Bažant
President, IA-FraMCoS
Conference Chairman

CONTENTS

CHAPTER 3 - Nonlinear Fracture Models with Softening Zone

CHAPTER 4 - Special Nonlinear Fracture Models Based on Adaptations of LEFM

CHAPTER 5 - Size Effect and Brittleness of Structures

CHAPTER 6 - Experimental or Analytical Determination of Material Fracture Parameters

CHAPTER 7 - Factors Influencing Fracture Parameters

CHAPTER 8 - Effect of Reinforcement

CHAPTER 9 - Crack Systems

PART II: CONFERENCE PAPERS

CHAPTER 1 - Material Models for Concrete Fracture

CHAPTER 3 - Numerical Analysis of Concrete Fracture

CHAPTER 4 - Experimental Methods and Determination of Fracture Characteristics

CHAPTER 5 - Measurements of Damage and Size Effect

CHAPTER 6 - Dynamic Fracture

CHAPTER 7 - Fracture Under Shear

CHAPTER 8 - Fracture of Reinforced Concrete

CHAPTER 9 - Interaction Between Concrete and Reinforcement

CHAPTER 10 - Fatigue and Rate Effects

CHAPTER 11 - Environmental Effects (Temperature, Shrinkage, Corrosion)

Part I
State-of-Art Report [1]

by

ACI Committee 446, Fracture Mechanics

[1]This report is being published by American Concrete Institute (ACI), Detroit, as ACI Special Publication, and is reprinted in the present conference volume with ACI permission. The highlights of this report are presented at the conference in the lecture by Z. P. Bažant and V. Gopalaratnam.

Principal Lecture

FRACTURE MECHANICS OF CONCRETE: AN APERÇU OF BASIC CONCEPTS AND MODELS

ZDENĚK P. BAŽANT[1] AND VELORE S. GOPALARATNAM[2]
[1]Walter P. Murphy Professor of Civil Engineering,
Northwestern University, Evanston, Illinois 60208;
Chairman,ACI Committee 446, Fracture Mechanics
[2]Associate Professor of Civil Engineering,
University of Missouri, Columbia, Missouri 65203;
Secretary, ACI Committee 446, Fracture Mechanics

ABSTRACT

The lecture presents an aperçu of some selected highlights of the state-of-art report of American Concrete Institute (ACI) Committee 446, Fracture Mechanics, *entitled "Fracture Mechanics of Concrete: Concepts Models and Determination of Material Parameters", which is published as ACI Special Publication [1] and is reprinted (with ACI permission) in this volume. The oral presentation also offers some comments on the second state-of-art report of the same committee, entitled "Fracture Mechanics Aspects of Structural Behavior and Potential Code Improvements", which is near completion. Attention is focused principally on the size effect on maximum loads caused by the release of stored energy, the implications for design codes as well as finite element analysis, and the nonlocal finite element models for quasibrittle materials such as concrete. Various examples of experimental results and their theoretical modeling are also presented.*

INTRODUCTION

Originated in 1921 by Griffith, fracture mechanics is a theory of failure which was for a long time applied only to metallic structures and ceramics. Concrete structures, on the other hand, have been successfully designed and built without any use of fracture mechanics, even though their failure process involves crack propagation. However, the proper type of fracture mechanics, which takes into account the growth of distributed cracking and its localization into major fractures, did not begin to emerge until about 1980. During the 1980's, however, such a type of fracture mechanics has emerged, as a result of a surge of research activity. Fracture specialists became convinced that introduction of fracture mechanics into the design of concrete structures, both reinforced and plain, is inevitable and will eventually bring about a revolution comparable to the introduction of plastic limit

analysis, which occurred during 1930-1970. It will significantly improve structural safety and economy. It will be particularly important for safe exploitation of the capabilities of high-strength and fiber-reinforced concretes. It might even make possible new structural forms, similarly as the research of creep and shrinkage made possible the development of prestressed concrete.

REASONS FOR ADOPTING FRACTURE MECHANICS

Fracture mechanics is a failure theory that

1. uses *energy* in the failure criterion, possibly in conjunction with strains and stresses, and
2. takes into account the nonsimultaneity of the failure process, i.e. failure *propagation*.

Five compelling reasons for introducing fracture mechanics are offered in the first chapter of the ACI report [1]:

- The physical fact that formation of a crack requires a certain amount of *energy* is one reason, which however suffices only to a physicists.
- A second reason arose from finite element analysis. If the mesh in the zone of cracking (characterized by strain softening) is refined, one finds that normally (depending on stability check) the cracking front must localize into a sharp fracture. This, in turn, causes that the stress in the finite element immediately in front of the fracture must tend to infinity no matter how small the load might be. Consequently, the finite element analysis of cracking on the basis of strength criteria is unobjective, with the results depending strongly on the analyst's choice of mesh size (spurious mesh sensitivity), and the calculated energy dissipated by cracking during failure is found to converge to zero as the element size tends to zero – a paradox. A remedy, that is *objectivity* with regard to mesh choice and proper *convergence* of finite element codes with cracking, is in general achieved only by deciding propagation of a fracture or cracking band on the basis of an energy criterion. Otherwise calculations can match the experimental data for only one element size (which is unfortunately unknown before the experiments are carried out).
- The third reason is the *nonexistence of yield plateau* on the observed stress-strain diagrams or load-deflection diagrams. The present code-sanctioned design approach, that is plastic limit analysis, is valid *only* if there is a prolonged yield plateau, both in the stress-strain and load-deflection diagrams. But yield plateaus are seen neither in the stress-strain tests of concrete nor in the load-deflection diagrams observed in the brittle types of failures of concrete structures (such as punching shear, Fig. 1a). As a result, the material strength is never attained simultaneously throughout the whole failure surface (as exemplified in Fig. 1b). The point at which the strength limit is attained propagates along the failure surface, leaving in its wake a stress drop (whose steepness, importantly, depends strongly on the structure size); Fig. 1c,d. Hence, considering failure propagation (Fig. 1e) is inevitable.
- The fourth reason, the *most compelling* one from the design viewpoint, is the *size effect* (or scale effect—effect of the characteristic dimension d) on the nominal strength

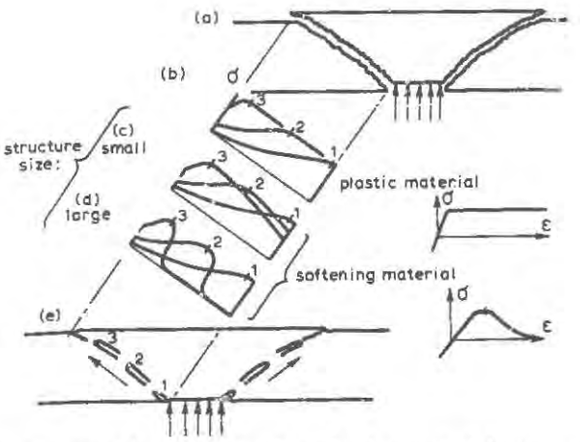

Figure 1: Difference, between plastic and strain-softening materials, in stress profiles along failure surface, and failure front propagation.

σ_N of geometrically similar structures, defined as $\sigma_N = P_u/bd$ or P_u/d^2 (for two- or three-dimensional similarity); P_u = maximum (ultimate) load and b = structure thickness. For all theories in which the failure criterion is written in terms of stresses and strains, for instance plastic limit analysis or elastic analysis with allowable stress (which include all the present code formulations), there is no size effect (see the dashed horizontal line in Fig. 2). But in fracture mechanics there is. In the idealized theory of linear elastic fracture mechanics (LEFM), in which all the fracture process is assumed to occur at one point—the crack tip, the size effect is the strongest possible; $\sigma_N \propto 1/\sqrt{d}$ or $\log \sigma_N = -\frac{1}{2}\log d +$ const., which is represented by the downward inclined dashed straight line of slope $-1/2$ in Fig. 2. In concrete structures, the process zone has a significant size, causing the size effect to follow the curve shown in Fig. 2 (right), which is approximately described by the size effect law $\sigma_N = Bf_t'[1 + (d/d_0)]^{-1/2}$ where d_0 and Bf_t' are two constants, to be determined by tests (and f_t' = tensile strength of concrete, which is introduced for convenience, to make B nondimensional).

This kind of size effect is exhibited not only by notched fracture specimens but also by brittle failures of concrete structures, provided that the length and shape of the fractures or cracking bands in structures of various sizes are geometrically similar. Experiments confirm that this is indeed so in most types of brittle failure. By extensive laboratory testing of reduced-scale geometrically similar laboratory structures made with reduced-size aggregate, the aforementioned size effect law has already been shown to apply quite closely (over a size range $d_{\max}/d_{\min} \approx 20$) to most types of brittle failures of concrete structures, including: (1) diagonal shear failure of longitudinally reinforced beams without stirrups (Fig. 3), (2) torsional failure of longitudinally reinforced beams, (3) punching shear failure of slabs, (4) pullout failures of bars and (5) of anchors, (6) failure of bar splices, (7) ring and beam failures of unreinforced pipes, and (8) double punch compression failure. Although verification and calibration on full-scale structures is mostly still lacking (except for

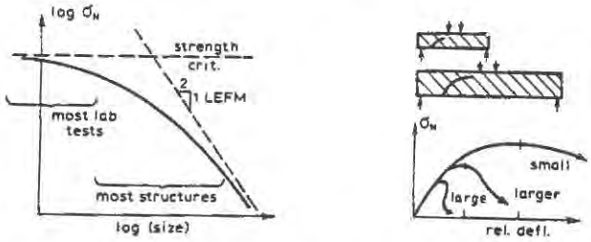

Figure 2: Size effect on nominal strength and post-peak response of structures failing in a brittle manner.

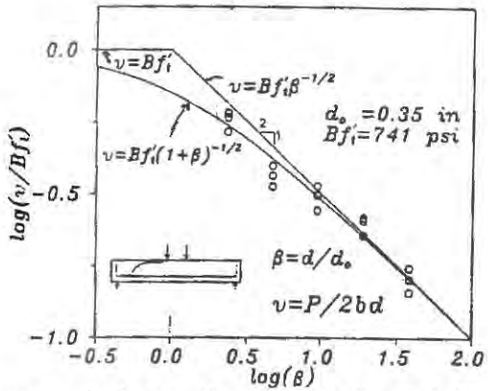

Figure 3: Size effect on nominal strength $\sigma_N = v$ in diagonal shear failure of geometrically similar longitudinally reinforced concrete beams without stirrups (tested in 1989 by Bažant and Kazemi) (size range 1:16, d_a = maximum aggregate size).

some latest results reported by Eligehausen et al. from Stuttgart University and Walraven from Delft University of Technology), it is already clear that the existing code formulas will have to be modified to include the size effect (this has already started in Germany and Japan).

The size effect is explained by *stress redistribution* due to fracture which causes a *release of the strain energy* stored in the structure into the front of fracture or crack band. This energy release is the driving force of fracture propagation (a basic concept in fracture mechanics). Now, in a larger structure, the energy is being released from a larger volume of material. Thus, if σ_N were the same as in a geometrically similar smaller structure, the energy release per unit fracture extension would be higher in a larger structure. But the amount of energy required to extend the fracture by a unit length is approximately independent of the structure size. Therefore, σ_N in a larger structure must be *less*, exactly so much less that the energy release per unit fracture extension be made the *same* as in a smaller structure. Hence the size effect.

Until about eight years ago, it used to be generally believed that the observed size effects are explained by Weibull-type statistical theory of random strength (we leave

aside the size effects due to hydration heat transport and moisture transport or the so-called wall effect, which were insignificant for the ultimate loads of the laboratory specimens tested). It has been demonstrated [2], however, that (except for a feeble effect in very small structures), the statistical size effect is completely overshadowed by the deterministic size effect due to energy release [2]. The statistical size effect characterizes only structures at which the maximum load is attained while the fracture is still very small compared to the structure dimensions, that is, at the beginning of crack propagation. This is normally the case for metallic structures, but not for concrete structures, because a good design practice needs (and in some cases the code dictates) that the maximum load be much larger than the crack initiation load. To put is briefly, the reason for the *negligibility of statistical size effect* is that a significant contribution to the probabilistic averaging integral comes only from the fracture process zone, the size of which is (except for very small structures) almost independent of the structure size; thus the strength randomness in structures of different sizes is being averaged over a zone of the *same* size, which causes the resulting statistics to be size-independent.

- The last, fifth reason is that the *energy absorption capability* of a structure, as well as the *ductility*, cannot be theoretically predicted without being able to calculate correctly the complete post-peak declining load-deflection curve of the structure. This cannot be accomplished without the use of fracture mechanics (note that plasticity implies the energy absorption capability to be infinite).

FRACTURE MODELS

In the idealized theory of linear elastic fracture mechanics (LEFM), reviewed in chapter 2 of the ACI report [1], all the fracture process is assumed to happen at one point—the crack tip, at which the stress tensor σ is singular (infinite, in theory). Near the tip, $\sigma = K_I r^{-1/2} f(\vartheta)$ where r is the distance from the tip, $f(\vartheta)$ is a function of polar coordinate ϑ, which is the same for any structure geometry, and K_I is called the stress intensity factor. The energy release rate, defined as $\mathcal{G} = -\partial\Pi/\partial a$ where a=crack length and Π= potential energy of the structure, is related to K_I; $\mathcal{G} = K_I^2/E$ where E = Young's elastic modulus. The central concept is that a crack propagates if and only if $\mathcal{G}$ reaches a certain critical value G_f called the fracture energy.

Realistic fracture models for concrete, described in chapters 3 and 4 of the ACI report [1], must be nonlinear, reflecting the fact that (1) the fracture process zone has a finite tensile strength f_t' and (2) is large, same as in ductile metals, but (3), due to distributed damage (cracking) and in contrast to metals, exhibits strain-softening (i.e. decline of stress with increasing strain) rather than plasticity. In the models developed for finite element analysis, the fracture process zone is treated either as a crack with bridging stresses (Fig. 4 top), characterized by a softening stress-displacement relation (Hillerborg's fictitious crack model) or a cracking band of finite width (Fig. 4 middle), characterized by an equivalent strain-softening stress-strain relation (Bažant's crack band model). The area under the stress-displacement curve (Fig. 4 top) divided by the crack area is taken to be approximately the fracture energy, G_f.

The most general continuum model is the so-called "nonlocal" damage model, in which the development of damage (cracking) depends on a certain weighted average of

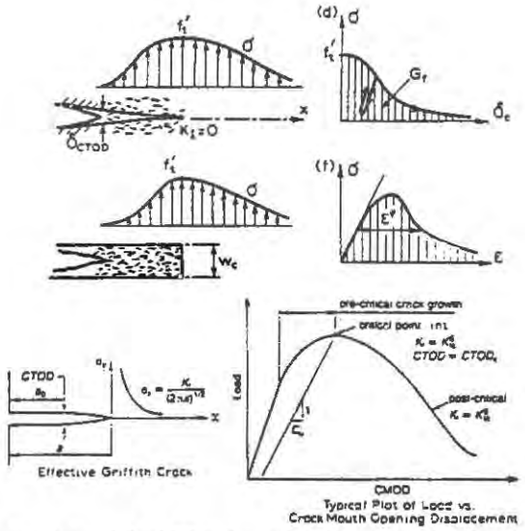

Figure 4: Fictitious crack model of Hillerborg (top), crack band model (middle) and Jenq and Shah's two parameter model (bottom).

the strains in a certain representative volume of the material surrounding the given point, rather than depending on the strain at that point. The size of this volume, called the characteristic length ℓ, is considered to be a material property. The weight function in the averaging integral may be understood as the crack influence function, describing the stress at a "frozen" microcrack at the given point that is caused by a pressure applied on a neighboring microcrack.

A very effective stress-strain law for damage is the novel "microplane" model, in which the damage is characterized separately on planes of various orientations in the microstructure (microplanes) and the contributions from all the microplanes are then superimposed. The nonlocal microplane model has been shown to match very well a broad range of test data, including all the types of concrete fracture tests as well as tests of nonlinear triaxial behavior under compression and shear. The most realistic fracture model probably is a randomly generated particle system simulating the microstructure, but its application to larger structures still poses forbidding demands for the computer.

There are also simpler, equivalent LEFM models, reviewed in chapter 4 of the ACI report [1]. They include: (1) Jenq and Shah's two-parameter model (Fig. 4 bottom), in which the material fracture properties are characterized by G_f, f'_t and the critical opening displacement at a certain distance behind the crack tip, and (2) the R-curve models, in which the energy release rate required for crack growth (called fracture resistance, R) is considered to depend on crack length a. Contrary to the initial view, the R-curve is not a material property but depends on structure geometry. As recently discovered, it may be easily determined from the aforementioned size effect law—as the envelope of the fracture equilibrium curves corresponding to the measured maximum loads of geometrically similar specimens of different sizes. The load-deflection curves calculated from such an R-curve are in good agreement with tests. It is also found that the R-curve is followed only up to the peak load, while during the post-peak response the energy release rate required for crack growth must be considered constant.

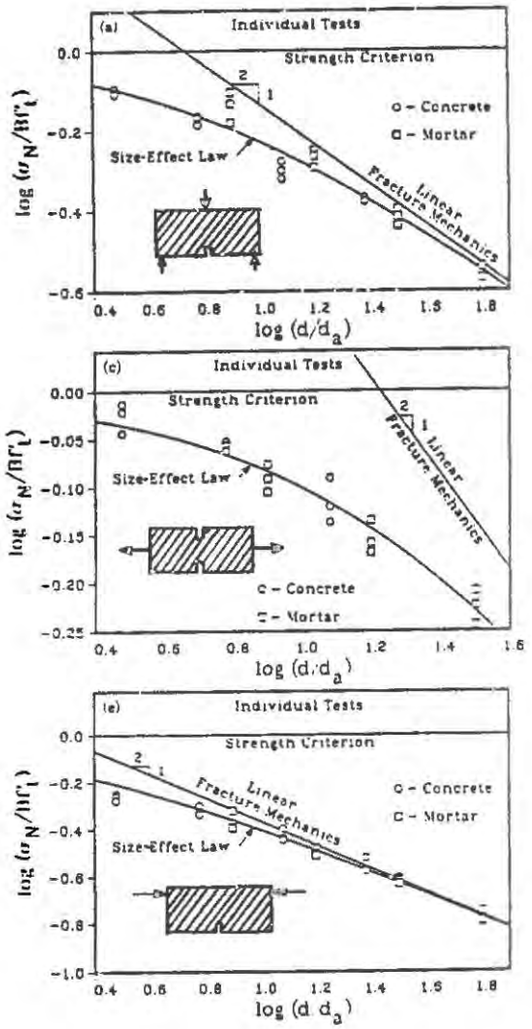

Figure 5: Measurements (by Bažant and Pfeiffer) of nominal strength of three types of notched specimens of various sizes, and fits by size effect law (each specimen type yielded nearly the same fracture energy).

The size effect law makes it further possible to characterize the structural response by a *universal* "brittleness number", $\beta = d/d_0$, such that for $\beta < 0.1$ the structure can be approximately analyzed according to plastic limit analysis (the case of existing codes for $\beta > 1$to dams), and for $0.1 < \beta < 10$ nonlinear fracture mechanics must be used (chapter 5 of the ACI report [1]). Adjustment of the existing code formulas by means of the brittleness number would be a simple way to introduce fracture mechanics into design, but the method to predict d_0 in absence of test data necessitates further research.

IDENTIFICATION OF FRACTURE CHARACTERISTICS

As discussed in chapter 6 of [1], the classical way to determine the fracture energy is from the measurements of the increment of the compliance of a notched specimen associated with an increment in the crack length a. In concrete, however, this is complicated by the fact that the precise location of the crack tip is hard to determine (and is probably quite different on the surface and in the interior of a specimen). Thus, a more refined approach is needed.

One such approach, in which the elastically equivalent crack length is estimated from measurements of the elastic part of the crack mouth opening displacement, was recently proposed by Jenq and Shah. Alternatively, G_f can be determined by the work-of-fracture method, whose application to concrete was proposed by Hillerborg; in this method, G_f is obtained as the area under the load-displacement curve of a notched beam, divided by the specimen thickness and the length of the complete crack. But the results have recently been found to depend significantly on the specimen size and shape, which may be due to energy dissipation outside the fracture process zone and the (suspected) size and shape dependence of the curve of the crack bridging stress vs. the opening displacement.

A third, recently invented and apparently very effective and simple method, is the size effect method: One needs to test the maximum loads of geometrically similar specimens of several sizes (with $d_{max}/d_{min} \geq 4$) and use the relation $G_f = g_\alpha/AE$, in which g_α is the nondimensionalized energy release rate, known or calculated for the chosen specimen shape according to LEFM, and A is the slope of the regression line of the plot of σ^{-2} vs. d for determining the parameters of the aforementioned size effect law. Although different specimen sizes are needed, this method can be implemented even with the most rudimentary laboratory equipment capable of measuring the maximum loads only, and the results are essentially independent of specimen shape, and of course size (which is proven by the size effect law fits of the data in Fig. 5). The problem of characterizing shear (mode II and III) fractures is also discussed in chapter 6 of the ACI report [1].

The characteristic length ℓ required for nonlocal models can be approximately determined as $\ell = G_f/W_s$ where W_s is the energy dissipated per unit volume measured in a test in which cracking is stabilized so as to remain uniformly distributed.

INFLUENCING FACTORS, REINFORCEMENT AND CRACK SYSTEMS

As reviewed in chapter 7 of [1], concrete fracture properties significantly depend on the the loading rate and load duration, the phenomenon being intertwined with creep. Recently the knowledge of ht loading rate effect was extended to static loadings with time to peak load ranging from 1s to 300,000s, which revealed an interesting new property: The size effect is affected by the loading rate, the response shifting in the size effect plot closer to

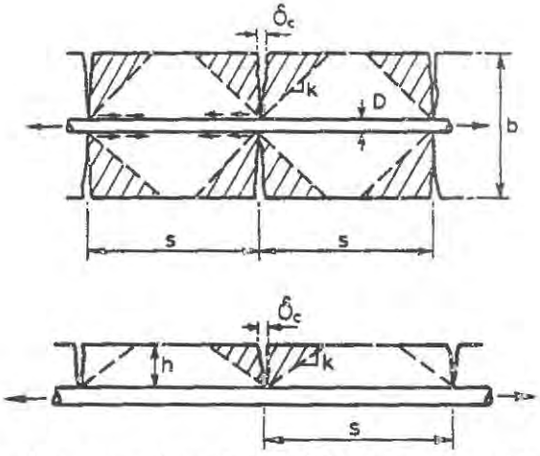

Figure 6: Energy release zones (cross-hatched) for determining the crack spacings.

LEFM as the loading rate decreases.

The fracture properties also significantly depend on temperature and moisture content. Under cyclic loading, the crack growth is adequately described by the Paris law, originally formulated for metals and ceramics, but a combination of this law with the aforementioned size effect law is needed to match fatigue fracture data for specimens of significantly different sizes.

The tendency to fracture is significantly reduced, and can even be eliminated, by steel bars as well as fibers crossing a developing crack (chapter 8). Their effect is to modify the effective curve of the crack bridging stress vs. the opening displacement, and augment the effective fracture energy of the composite due to energy dissipated by frictional slip of bars or fibers and to increase the size of the process zone. The overall result is a great increase of ductility of concrete, especially in the case of fiber reinforcement.

Prediction of crack spacing and width in reinforced concrete (chapter 9) needs to be also based on fracture mechanics. Attainment of the tensile strength limit only means that cracks can begin to form, but whether they actually form depends on whether sufficient energy can be released; see Fig. 6, in which the strain energy initially stored in the triangular cross-hatched areas must be equal to the energy required to form the cracks plus the energy dissipated by bond slip.

A difficult theoretical problem is the growth of a system of interacting cracks, which is the last subject reviewed. Crack interactions in terms of energy release influence the spacing and width of parallel shrinkage and thermal cracks, as well as of parallel cracks in tensile zones of reinforced concrete. To ensure stability of dense crack spacing can be regarded as a fundamental criterion for minimum reinforcement.

CONCLUDING REMARK

While only about a dozen years ago the applicability of fracture mechanics to concrete was doubted, the rapid development during the 1980's has led to the formulation of a realistic and adequate theory. It is probably no exaggeration to observe that fracture specialists are now convinced the time has become ripe for applying the new theory in design practice, both in codes and in computer methods of structural analysis.

ACKNOWLEDGMENT.—Partial financial support under AFOSR Grant 91-0140 to Northwestern University is gratefully acknowledged.

REFERENCES

1. ACI Committee 446 on Fracture Mechanics (Z.P. Bažant, chairman), Fracture mechanics of concrete: concepts, models and determination of material properties." *ACI Special Publication*, American Concrete Institute (ACI), Detroit, 1991.

2. Bažant, Z.P., and Xi, Y., Statistical size effect in quasi-brittle structures: II. Nonlocal theory. *Journal of Engineering Mechanics ASCE*, 1991, 117 (11), 2623–40.

Invited Paper

STABILITY OF A CRACK IN A LINEAR VISCOELASTIC TENSION-SOFTENING MATERIAL

CHUNYUAN ZHANG [1]
and
BHUSHAN L KARIHALOO
School of Civil and Mining Engineering,
The University of Sydney, NSW 2006, Australia

ABSTRACT

This paper deals with instantaneous, delayed and directional stability of a mode I crack in a tension-softening, linear viscoelastic material. It also calculates the velocity of sub-critical quasi-static crack growth, as well as the rupture lifetime. The results are applied to the analysis of stability of a vertical central crack in the upstream face of a diamond head buttressed concrete dam.

INTRODUCTION

This study is motivated by the need to ensure the safety of concrete dams. Such structures invariably contain large cracks almost from the moment they are constructed. These may however remain dormant for many years after the reservoir has been impounded. It is therefore necessary to investigate not only any instantaneous crack instability(ICI), but also the possibility of delayed crack instability(DCI) and of directional instability(DI). For this investigation the time-dependent response of concrete is modelled by a linear viscoelastic material and an allowance is made for its known tension-softening behaviour. The theory of linear viscoelastic fracture mechanics developed by Zhang [1–2] is generalized to take into account sub-critical crack growth. Another approach would be the viscoelastic-plastic fracture theory developed, among others, by Knauss [3], Schapery [4], McCartney [5], Kaminskii [6]. This theory does not however account for the tension-softening behaviour.

[1]Visiting Scholar from the Department of Mechanical Engineering, Xiangtan University, Hunan 411105, PR CHINA.

If an allowance is made for this behaviour, then the application of both theories permits one to calculate the critical crack lengths or critical stresses at which instantaneous or delayed instability can take place, as well as the velocity of sub-critical crack growth and the rupture lifetime. The results of these calculations are applied to the analysis of stability of a vertical central crack in the upstream face of Zhexi concrete dam. We will also comment upon the directional stability of the crack by following the arguments of Karihaloo [7].

Zhexi diamond head buttressed concrete dam is one of the largest dams in Hunan Province of China. Soon after the placement of concrete in December, 1959, hundreds of cracks appeared near the centre lines of the buttresses. The length of the longest vertical crack was about 20–30 m with a width of 0.1–0.2 mm (Fig.1). The depth of the crack was hard to estimate. Before the reservoir was impounded at the end of 1960, the cracks were filled with grout. In June 1969, the crack on buttress No. 1 propagated suddenly and water spurted through the crack into the inspection gallery. Core drilling indicated that the crack had extended about 43 m into the dam, and almost reached the foundation. The crack width was 2.5 mm, thus giving a cracked area of about 2000 m^2. Measures were taken to prevent further crack growth. It was subseqently found that the initial cracks in the other buttresses had also propagated to some extent, but the cracks had stopped to grow at the time of inspection (1979).

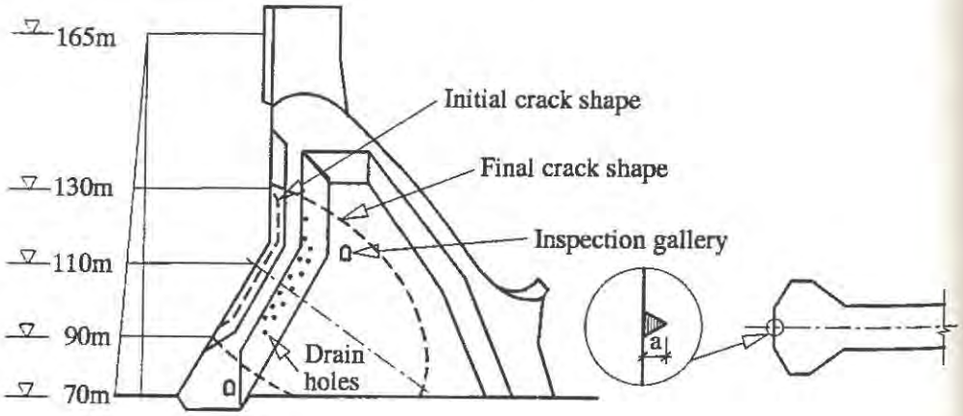

Figure 1. Cross-section of the dam through the diamond head buttress, showing the position of the crack before the reservoir was impounded and after 8 years.

INSTANTANEOUS AND DELAYED CRACK INSTABILITY

For a linear viscoelastic body there is no slow, stable subcritical crack growth under a constant load for cracks with $\partial K_I/\partial a > 0$, where K_I is the mode I stress intensity

factor. The critical crack sizes for ICI and DCI for mode I can be determined from the criterion of the theory of linear viscoelastic fracture mechanics (LVFM)

$$G_I(t) = G_I(0) f_{Ig}(t) = G_{Ic}, \qquad f_{Ig}(t) = f_{I\sigma}(t) f_{Iu}(t), \tag{1}$$

where $G_I(0) = K_I^2/E'$ is the instantaneous energy release rate, and $E' = E$ for plane stress, and $E' = E/(1-\nu^2)$ for plane strain. For a given material, G_{Ic} may be assumed to be a constant. $f_{Ig}(t)$, $f_{I\sigma}(t)$, $f_{Iu}(t)$ are the time factors for the energy release rate, stress intensity factor and displacement component, respectively. For cracks with $\partial K_I/\partial a > 0$, if the criterion $G_I(0) = G_{Ic}$, is met, instability will occur instantaneously. If at a certain time $t_c > 0$, $G_I(t_c) = G_I(0) f_{Ig}(t_c) = G_{Ic}$, delayed instability will take place at that instant. As $G_I(t)$ is a monotonically increasing function of t, the critical state for longterm delayed crack instability ($t_c \to \infty$) is determined by the condition $G_I(\infty) = G_{Ic}$

For the description of the viscoelastic behaviour of concrete, the Rabotnov fractional creep exponential kernel

$$\phi(t) = \frac{\lambda}{E} t^{-\alpha} \sum_{n=0}^{\infty} \frac{-\beta^n t^{n(1-\alpha)}}{\Gamma[(n+1)(1-\alpha)]} = \frac{\lambda}{E} \mathcal{E}_\alpha(-\beta, t), \tag{2}$$

is suitable in the uniaxial constitutive equation

$$\varepsilon(x,t) = D(0)\sigma(t) + \int_0^t \sigma(\tau)\phi(t-\tau)d\tau. \tag{3}$$

Here $\phi(t) = \partial D/\partial t$ is the uniaxial creep kernel, $\lambda > 0$, $\beta > 0$, $0 \le \alpha < 1$ are material constants, and $\Gamma(\ )$ is the gamma function. The creep compliance $D(t)$ corresponding to eqn (3) is

$$D(t) = D(0)\left[1 + E\int_0^t \phi(\tau)d\tau\right] = D(0)\left[1 + \lambda\int_0^t \mathcal{E}_\alpha(-\beta,\tau)d\tau\right], \tag{4}$$

such that the longterm compliance $D(\infty) = D(0)(1 + \lambda/\beta)$.

The material properties of the dam concrete used in subsequent calculations are as follows: fracture toughness K_{Ic}=1 MN/m$^{\frac{3}{2}}$, tensile strength f_t=1.2 MPa, α=0.65, β=0.0658 h$^{-0.35}$, λ=0.91 h$^{-0.35}$, instantaneous compliance $D(0)=\frac{1}{E}$ =4.69×10^{-5} MPa^{-1}, and longterm compliance $D(\infty)$=11.18×10^{-5} MPa^{-1}.

If it is assumed in eqn (1) that $f_{I\sigma}(t) = H(t)$ is a unit Heaviside step function and that Poisson's ratio does not vary with time, then $f_{I\sigma} = D(\infty)/D(0)$. The critical crack sizes a_{ci} for ICI and $a_{c\infty}$ for the longterm DCI are found to be $a_{ci} = K_{Ic}^2/(\pi k^2 \sigma^2)$, and $a_{c\infty} = a_{ci} D(0)/D(\infty)$.

In the Zhexi dam crack problem the water pressure σ (assuming linear distribution along the height) at the middle of the crack length (elevation 110 m, Fig. 1) is 0.55 MPa, so that $K_I = 0.44\sigma\sqrt{\pi a}$. For this problem a_{ci} =5.44 m, and $a_{c\infty}$ = 2.28 m. Since delayed crack instability occurred eight years after the reservoir was impounded, the above results imply that the initial crack depth a_i must have been in the range $a_{c\infty} \le a_i < a_{ci}$, and that it had grown by a stable, subcritical process.

SUBCRITICAL CRACK GROWTH

It is well known [6] that the time it takes for a crack to become unstable consists of incubation t_i and initial-growth Δt_1 periods, a principal period of slow subcritical crack growth Δt, and finally a brief period of rapid growth before rupture. For macroscopic cracks for which the size of the process zone d is significantly smaller than the length of the crack itself $a(t)$, which is true for the dam crack under consideration, the principal, slow growth period is considerably longer than the other periods and for all practical purposes determines the rupture lifetime T.

In order to calculate the subcritical crack growth velocity, we use Hillerborg's fictitious crack model [8] and approximate the tension-softening response by $f = \sigma_f/\sigma_m = (e^{-c\eta^2} - e^{-c})/(1 - e^{-c})$, where c is a material constant. σ_f denotes the reduced stress carrying capacity and σ_m is its maximum value, $\eta = \xi/d$, d is the length of the process zone, and ξ is the distance from the fictitious crack tip (Fig. 2).

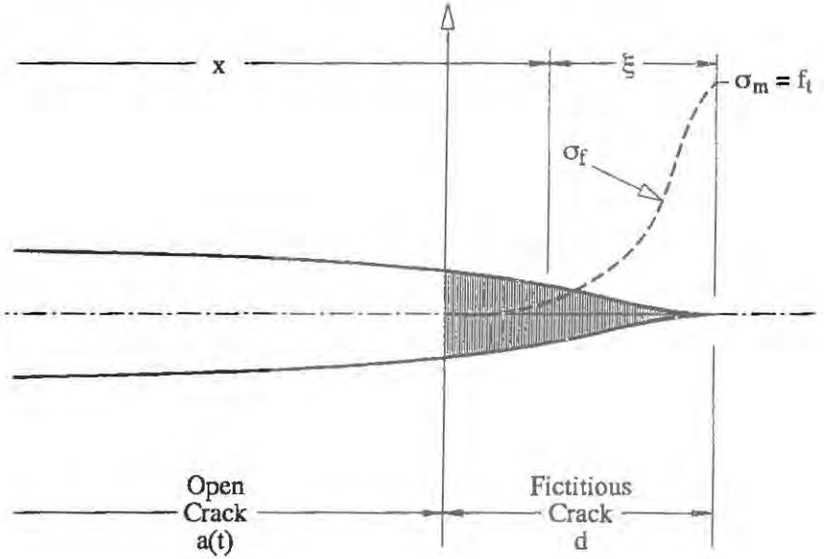

Figure 2. The fictitious crack model, showing the coordinate system and the assumed variation of the tensile carrying capacity in the process zone

We assume in the sequel that either d or σ_m does not vary with time, and for brevity denote this fact by subscript d or σ. Moreover, without loss of generality, it is assumed that the external applied stress does not vary with time. The elastic solution with a parameter t has the form $\delta_e[x, a(t)] = C' f[x, a(t)]$, where, following Schapery [4], it may be shown that

$$f_\sigma[x, a(t)] = \frac{4I_2}{\sigma}\left(\frac{K_I(t)}{I_1}\right)^2 F[s(t)] \tag{5}$$

$$f_d[x, a(t)] = \frac{8I_2\, K_I(t)}{I_1}\sqrt{\frac{d}{2\pi}}\, F[s(t)]; \tag{6}$$

$$F(s) = \sqrt{1-s} + \frac{s}{2}\ln\frac{1-\sqrt{1-s}}{1+\sqrt{1-s}}, \quad s(t) = 1-\eta. \tag{7}$$

Here, $C' = 1/E'$ is the elastic compliance for plane stress or plane strain, $I_1 = \int_0^1 f/\eta^{\frac{1}{2}}\, d\eta$, $I_2 = -\int_0^1 (df/d\eta)\eta^{\frac{1}{2}} d\eta$. Under the condition that $a(t)$ and/or $d(t)$ is a monotonic, non-decreasing function of t, the crack opening displacement of a growing crack in a viscoelastic body can be obtained by replacing the elastic constant C' in the corresponding elastic solution by Volterra's integral operator of the second kind [6].

The tip of the open crack is assumed to propagate when the following condition is fulfilled by the crack-tip opening displacement

$$\delta(x,t)|_{x=a(t)} = \delta_e[a(t)] + \int_{t'}^{t} E'\ \phi(t-\tau)\delta_e[a(t), a(\tau)]d\tau = \delta_c, \tag{8}$$

where t' is the time when the crack-tip first reaches the point x, and δ_c is the critical crack-tip opening displacement.

Principal Period of Slow Subcritical Crack Growth

After the initial growth period of unstable-type cracks, further crack growth under a constant external applied stress takes place slowly and almost at a constant rate. For Rabotnov kernels, the following approximations are valid for small time q

$$\int_0^q \mathcal{E}_\alpha(-\beta, \tau)d\tau \simeq \frac{Q}{1+Q\beta}, \quad Q\beta \ll 1,\ Q = \frac{q^{1-\alpha}}{\Gamma(2-\alpha)}, \tag{9}$$

$$\int_0^t \mathcal{E}_\alpha(-\beta, t-\tau)\delta[a(t), a(\tau)]d\tau \simeq k(\alpha)\delta[a(t)]\int_0^t \mathcal{E}_\alpha(-\beta, t-\tau)d\tau, \tag{10}$$

where $k(\alpha) = [\sqrt{\pi}\,\Gamma(2-\alpha)]/[2(2-\alpha)\,\Gamma(2.5-\alpha)]$. By changing the variables of integration through $q = t - t'$ and $\tau = \theta + t'$ in eqn (8), and substituting eqn (10) into this equation, we obtain

$$\frac{\delta_c}{\delta[a(t)]} = 1 + k(\alpha)\int_0^q \mathcal{E}_\alpha(-\beta, \tau)d\tau, \tag{11}$$

where q is the time needed for the crack to grow by d, and $q = d/\dot{a}$, when d=const; $q = (\pi K_I^2)/(2I_1^2 f_t^2 \dot{a})$, when σ=const. Substituting eqn (9) into eqn (11) and integrating the two sides of the resulting equation after separating the variables we obtain the following equations for determining Δt

$$\begin{aligned}(\Delta t)_\sigma &= \kappa_1 \int_1^{x_{ci}} \frac{1}{x}\left\{\frac{1 - x/x_{ci}}{\zeta(x/x_{ci}) - 1}\right\}^{1/(1-\alpha)} dx \\ (\Delta t)_d &= \kappa_2 \int_1^{x_{ci}} \left\{\frac{1 - (x/x_{ci})^{1/2}}{\zeta(x/x_{ci})^{1/2} - 1}\right\}^{1/(1-\alpha)} dx\end{aligned} \tag{12}$$

where $x = a/a_1, x_{ci} = a_{ci}/a_1, \kappa_1 = 2\,(I_1 f_t/k\sigma\pi)^2\,[\Gamma(2-\alpha)/\beta]^{\frac{1}{(1-\alpha)}}, \zeta = 1 + \frac{\lambda E\ k(\alpha)}{\beta}$, and $\kappa_2 = (a_1/d)\ [\Gamma(2-\alpha)/\beta]^{\frac{1}{(1-\alpha)}}$.

RUPTURE LIFETIME

As mentioned above, for macroscopic cracks the rupture lifetime T is approximately equal to the principal slow growth period Δt, so that the subcritical crack growth velocity in metres/hour is

$$\left(\frac{da}{dt}\right)_\sigma = \frac{\pi K_I^2(t)}{2I_1^2 f_t^2}\left(\frac{\beta}{\Gamma(2-\alpha)}\right)^{\frac{1}{1-\alpha}}\left\{\frac{(1+\frac{\lambda k(\alpha)}{\beta})\left(\frac{K_I(t)}{K_{Ii}}\right)^2-1}{1-\left(\frac{K_I(t)}{K_{Ii}}\right)^2}\right\}^{\frac{1}{1-\alpha}}$$

$$\left(\frac{da}{dt}\right)_d = \left(\frac{\beta}{\Gamma(2-\alpha)}\right)^{\frac{1}{1-\alpha}} d\left\{\frac{(1+\frac{\lambda k(\alpha)}{\beta})\frac{K_I(t)}{K_{Ii}}-1}{1-\frac{K_I(t)}{K_{Ii}}}\right\}^{\frac{1}{1-\alpha}} \qquad (13)$$

where K_{Ii} is the critical stress intensity factor for instantaneous crack initiation.

From the material properties of the Zhexi concrete dam, we have $k(\alpha) = 0.6186$, $\zeta = 1.857$, κ_1=12300 h, κ_2 = 12300 h, $1/(1-\alpha)$=2.857, I_1 = 1.2,d = $(\pi K_{Ic}^2)/(2f_t^2 I_1^2)$ =0.76 mm, $\sigma_m = f_t$=1.2 MPa.

Substituting the above parameters into eqns (12) gives in hours

$$(\Delta t)_\sigma = 12300\int_1^{x_{ci}} \frac{1}{x}\left\{\frac{1-x/x_{ci}}{1.857(x/x_{ci})-1}\right\}^{2.857} dx$$

$$(\Delta t)_d = 12300\int_1^{x_{ci}} \left\{\frac{1-(x/x_{ci})^{1/2}}{1.857(x/x_{ci})^{1/2}-1}\right\}^{2.857} dx, \qquad (14)$$

and into eqns (13) gives, after introduction of $y = a/a_{ci}$

$$\left(\frac{dy}{dt}\right)_\sigma = \frac{y}{12300}[(1.857y-1)/(1-y)]^{2.857}\ (h^{-1})$$

$$\left(\frac{dy}{dt}\right)_d = \frac{1}{12300}[(1.857y^{1/2}-1)/(1-y^{1/2})]^{2.857}\ (h^{-1}). \qquad (15)$$

From eqns (14)–(15) it is clear that if $a = a_{ci}$, then the crack growth velocity tends to infinity and $\Delta t \to 0$. If, on the other hand $a = a_{ci}/1.857$=2.93 m (σ_m=const), or $a = a_{ci}/1.857^2$=1.58 m (d=const), then the crack growth velocity tends to zero and the lifetime to infinity. It is evident from Fig. 3 that if the initial crack size $a_o = 0.58a_{ci}$=3.16 m (assuming $\sigma_m = f_t$ =const) or $a_o = 0.36a_{ci}$=1.95 m (assuming d =const), then the critical time T is approximately equal to eight years. This shows that a crack of depth between 1.95 m and 3.16 m must have been present in the buttress when the reservoir was impounded.

In diamond head buttressed concrete dams mode I cracks have been observed to grow stably more or less in their own plane. This may be explained by the presence of a compressive in-plane stress such that the T stress (not to be confused with the rupture lifetime T used above) defined in [7] is negative. It is known [7] that when $T < 0$, the quasi-static crack growth in mode I is directionally stable in the sense that if the

straight crack deviates from its path owing to some disturbance, it invariably tends to revert to its original straight path.

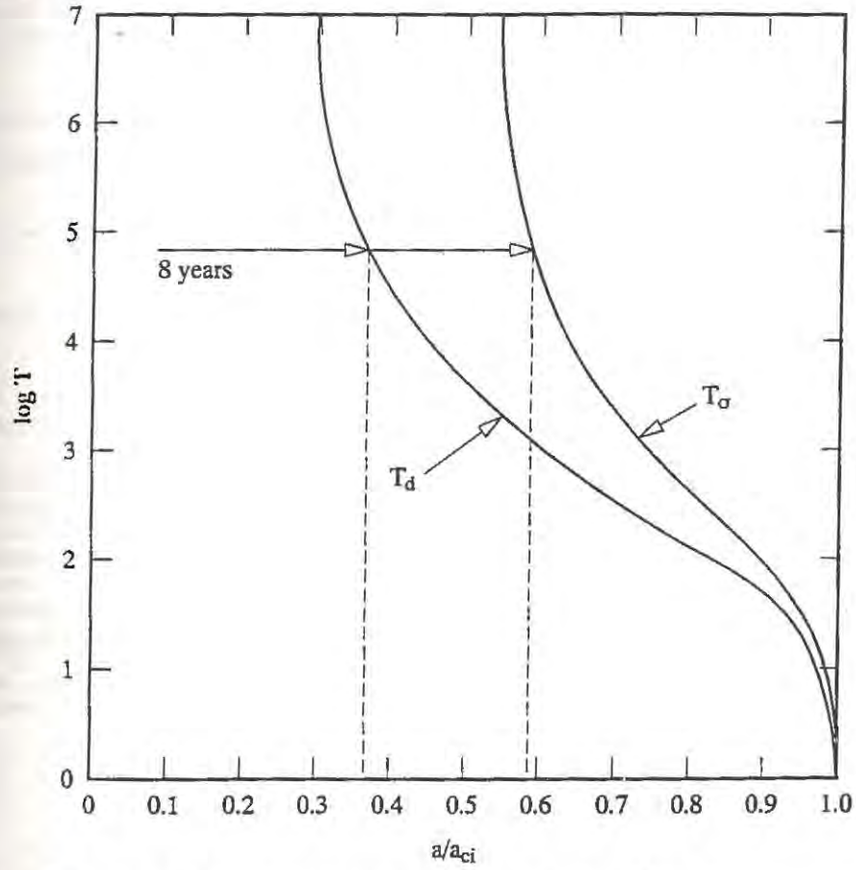

Figure 3. Rupture lifetime T (in hours) versus normalized crack length, indicating the initial crack size necessary for the onset of delayed instability in 8 years.

CONCLUSIONS

The theory of linear viscoelastic fracture mechanics is shown to predict the delayed response of a cracked concrete dam provided an allowance is made for the sub-critical crack growth. The latter is included through the fictitious crack model with an appropriate approximation to the known tension-softening response of concrete. The generalized theory is useful in predicting not only the slow crack growth rate but also the rupture lifetime. It is also possible to use the theory for forensic purposes, for instance for calculating the depth of an initially present crack that could not be originally measured or estimated.

REFERENCES

1. Zhang Chunyuan, Delayed Crack Instability of Concrete. In Fracture of Concrete and Rock, ed. S.P. Shah & S.E. Swartz, Springer-Verlag, New York, 1989, pp. 376–87.

2. Zhang Chunyuan, Viscoelastic Fracture Mechanics Analysis of a Strain-softening Concrete Dam. In Applied Mechanics, Proc. of Int. Conf. on Appl. Mech., ed. Zhen Zhemin. 1989, pp. 908–13.

3. Knauss, K.G., Delayed Fracture—The Griffith Problem for Linearly Viscoelastic Materials. Int. J. Frac. Mech., 1970, **6**, 7-20.

4. Schapery, R.A., A Theory of Crack Initiation and Growth in Viscoelastic Media I–III. Int. J. Frac., 1975, **11** 141–59; 369–88; 549–62.

5. McCartney, L.N., Crack Propagation, resulting from a Monotonic Increasing Applied Stress, in a Linear Viscoelastic Material. Int. J. Fract., 1977, **13**, 641–54.

6. Kaminskii, A.A., Fracture Mechanics of Viscoelastic Bodies, Naukova Dumka, Kiev, 1980. (in Russian)

7. Karihaloo, B.L., On Crack Kinking and Curving, Mech. Mater., 1982, **1**, 189-201.

8. Hillerborg, A., Modéer, M. and Petersson, P.E., Analysis of Crack Formation and Crack Growth in Concrete by means of Fracture Mechanics and Finite Elements, Cement and Concrete Research, 1976, **6**, 773–82.

INTERFACE FRACTURE MECHANICS OF CONCRETE COMPOSITES

ORAL BUYUKOZTURK and KWANG M. LEE
Dept. of Civil Engineering
Massachusetts Institute of Technology
Cambridge, MA 02139

ABSTRACT

Recently, the interest in the study of mortar-aggregate interfaces in concrete has increased, particularly, in view of the efforts to develop high performance concrete with improved mechanical properties, including strength, ductility, and durability. In this paper, we first discuss interface fracture mechanics concepts applicable to mortar-aggregate interfaces in concrete. Then, interface fracture toughness curves developed through novel fracture specimens with the effects of mixed mode loading conditions are presented. Finally, a study is presented on two-phase composite models of concrete, consisting of a mortar matrix and an aggregate inclusion, to investigate the crack propagation in the interface regions. A criterion based on energy release rate is considered to study the crack penetration vs. crack deflection scenarios.

INTRODUCTION

Concrete is a heterogeneous material, and its behavior is complicated by the interaction of many internal elements which constitute the material. Buyukozturk et al. [1] modelled concrete as a two phase composite consisting of mortar and aggregate inclusions and investigated the cracking problem through laboratory testing of the physical models and numerical analysis using the finite element method. Recently, following the work of Buyukozturk et al. [1], Yamaguchi and Chen [2] studied the propagation of microcracks in two-phase concrete models by the finite element analysis incorporating the smeared cracking model for mortar, and the interface finite elements for bond coupled with the generalized plasticity concept. In these studies a Mohr-Coulomb type failure criterion was employed for cracking at the interface regions. The approach developed by these previous studies led to some very useful information with respect to the understanding of global concrete behavior as affected by the bond cracking. However, the results obtained in this way are limited due to the phenomenological nature in which the interface bond property was assumed, and the bond cracking criterion was established. Hence, there is a need to develop rigorous methodologies and novel models for defining and quantifying explicitly the mortar-aggregate interface characteristics. Such a methodology, as will be described in this paper, would involve both testing of physical laboratory models and employment of interface fracture mechanics concepts.

BASICS OF INTERFACE FRACTURE MECHANICS

One objective of interface fracture mechanics is to define and assess a property, i.e. toughness, that characterizes the fracture resistance of interfaces. Recently, a number of studies on the interface fracture mechanics of bimaterial systems have been made [3,4]. A bimaterial is a composite of two homogeneous materials with continuity of traction and displacement across interfaces maintained. Consider a semi-infinite free crack lying along the interface between two homogeneous isotropic half planes, with material 1 above and material 2 below (see Fig. 1). Here, plane strain deformation in isotropic bimaterial is considered. In Fig. 1, E, μ, and ν are Young's modulus, shear modulus and Poisson's ratio, respectively. For plane strain the moduli mismatch parameters of Dundurs are

$$\alpha = \frac{\bar{E}_1 - \bar{E}_2}{\bar{E}_1 + \bar{E}_2} \quad , \qquad \beta = \frac{1}{2}\frac{\mu_1(1-2\nu_2) - \mu_2(1-2\nu_1)}{\mu_1(1-\nu_2) + \mu_2(1-\nu_1)} \tag{1}$$

where $\bar{E} = E/(1-\nu^2) = 2\mu/(1-\nu)$ is the plane strain tensile modulus. The parameter α measures the relative stiffness of the two materials. The parameter β causes the linear crack tip stress and displacement fields to oscillate [3], leading to surface interpenetration. Note that both α and β vanish when dissimilarity between the elastic properties of the materials is absent, and α and β change signs when the materials are switched.

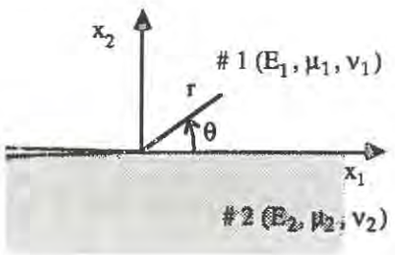

Figure 1. An Interface crack configuration

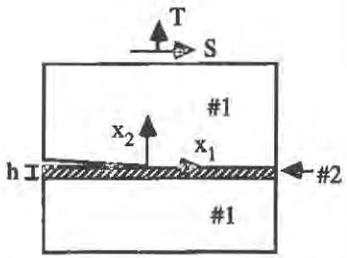

Figure 2. Interface crack problem in a sandwiched layer model

For the plane problems, the normal and shear stresses of the singular field acting on the interface a distance r ahead of the tip can be written in the compact "complex" form

$$\sigma_{22} + i\sigma_{12} = \frac{K}{\sqrt{2\pi r}} r^{i\varepsilon} \tag{2}$$

where $K = K_1 + iK_2$ is the stress intensity factor at an interface, $i = -1$, and the oscillation index ε depends on β according to

$$\varepsilon = \frac{1}{2\pi}\ln\left(\frac{1-\beta}{1+\beta}\right) \tag{3}$$

The parameter ε brings in some complications which are not present in the elastic fracture mechanics of homogeneous solids. The associated crack face displacements a distance r behind the crack tip, $\delta_i = u_i(r,\theta = \pi) - u_i(r,\theta = -\pi)$, are given by

$$\delta_1 + i\delta_2 = \frac{4K(1/\bar{E}_1 + 1/\bar{E}_2)}{(1+2i\varepsilon)\cosh(\pi\varepsilon)}\left(\sqrt{\frac{r}{2\pi}}\right) r^{i\varepsilon} \tag{4}$$

For any interfacial crack problem, the complex K will have the form of

$$KL^{i\varepsilon} = YT\sqrt{L}e^{i\psi} \tag{5}$$

where T is an applied traction on the structure, L is a characteristic length describing the geometry (e. g., crack length, layer thickness), Y is a dimensionless real positive quantity, and

ψ is the phase angle of $KL^{i\varepsilon}$. Both Y and ψ depend on the geometric and loading details of the structure. For a better characterization of loading phase, we may choose a fixed length $\hat{L}$. $\hat{L}$ can be selected as 1 mm, 1 cm, or 10 cm so long as a fixed length is used for reporting data in conjunction with the toughness curve. Then, the loading phase angle $\hat{\psi}$ of the complex quantity $K\hat{L}^{i\varepsilon}$ is given by

$$\hat{\psi} = \psi + \varepsilon\ln\left(\frac{\hat{L}}{L}\right) \tag{6}$$

However, it has been recognized that, for many bimaterial systems of interest, β is small, i.e., ε is small. With this hypothesis the square root singularity is retained at the tip. Thus, when $\beta = 0$, K_1 and K_2 measure the normal and shear traction singularities on the interface ahead of the crack tip with the standard definition for the stress intensity factors. With $\beta = 0$ the phase angle $\hat{\psi}$ is defined as $\tan^{-1}(K_2/K_1)$.

The energy release rate G per unit length of extension of the crack at an interface is related to the stress intensity factors with an Irwin-type relation

$$G = \frac{(1/\bar{E}_1 + 1/\bar{E}_2)}{2\cosh^2\pi\varepsilon}|K|^2 \tag{7}$$

where $|K|^2 = K_1^2 + K_2^2$ and $\cosh^2\pi\varepsilon = 1/(1-\beta^2)$. If both $\hat{\psi}$ and G are defined, one can establish a fracture toughness curve, called G_c-$\hat{\psi}$ curve, for an interface. In linear elastic fracture mechanics, G_c-$\hat{\psi}$ curve is the property of the given interface in the sense that, in principle, it is independent of the specimen geometry and the loading system.

ASSESSMENT OF INTERFACE FRACTURE TOUGHNESS

In the study of concrete fracture, characterization of the interfacial fracture toughness as a property of the mortar-aggregate interface is essential. An early experimental study on the measurement of the fracture toughness of mortar-aggregate interfaces in concrete was performed by Hillemeier and Hilsdorf [5]. They reported limited test results which involved mode I loading conditions only. Cracking of mortar-aggregate interfaces involves mixed mode fracture effects due to the differences in the properties of individual materials forming the concrete composites, and due to loading conditions. In what follows, we introduce the sandwich specimens as a physical model for fracture toughness assessment of the interfaces in concrete composite systems.

Sandwich Specimen

An interface crack model including a thin layer of material 2 sandwiched in a homogeneous body of material 1 is shown in Fig. 2. Each material is assumed to be isotropic and linearly elastic. Here, mortar and aggregate are referred to material 1 and 2, respectively. The crack lies along one of the interfaces coincident with the x_1-axis with the tip at the origin. If the thickness of the sandwich layer h is small compared to the crack length and to all other relevant in-plane length quantities, a universal asymptotic relation between the interface intensity factors, K_1 and K_2, and the stress intensity factors, K_I and K_{II}, for the homogeneous problem, is obtained [6]

$$Kh^{i\varepsilon} = \sqrt{\frac{1-\alpha}{1-\beta^2}}K^{\infty}e^{i\omega(\alpha,\beta)} \tag{8}$$

where $|h^{i\varepsilon}| = 1$, $K^{\infty} = K_I + iK_{II}$, and the real function $\omega(\alpha,\beta)$ represents the shift in "phase" of the interface stress intensity factors relative to the applied stress intensity factors. Here, one also defines

$$Kh^{i\varepsilon} = |K|e^{i\psi}, \quad K^{\infty} = |K^{\infty}|e^{i\phi} \tag{9}$$

where ψ is a real phase angle and $\phi = \tan^{-1}(K_{II}/K_I)$. Then, the universal relation shown in Eq. 8 can be expressed as

$$\psi = \phi + \omega(\alpha,\beta) \tag{10}$$

Now, by substituting Eq. 10 into Eq. 6, the loading phase angle $\hat{\Psi}$ is obtained.

The universal relation given in Eq. 8 may be applied to any sandwich specimen. Proper techniques are required to sandwich an aggregate layer into the specimen and ensure that the crack stays along one of the interface. Residual stresses in the layer do not contribute to K in the sandwich specimen and, in calibrating such a specimen, one needs to take account of the external loading only [6]. The proposed specimens for the study of mortar-aggregate interfaces include the sandwiched beam specimen shown in Fig. 3a and the sandwiched Brazilian disk specimen shown in Fig. 3b, from which the interface fracture toughness curves can be established in the full range of mixed mode effects [7].

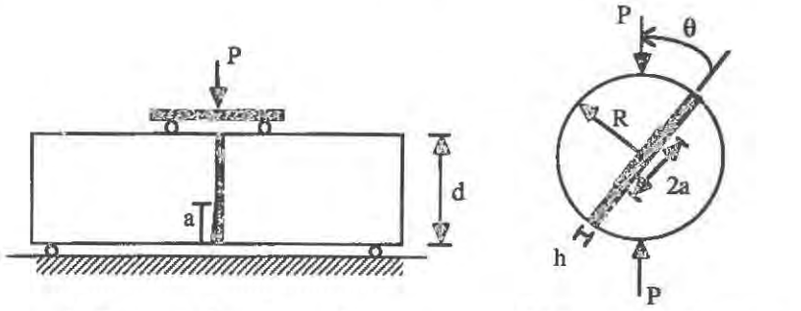

(a) Four-point bending specimen (b) Brazilian disk specimen

Figure 3. Sandwiched specimens

Testing of Sandwich Specimens

In order to generate the fracture toughness curves of the mortar-aggregate interfaces, two types of sandwich specimens proposed in the preceding section were used. The dimensions of the sandwiched beam specimen were 152.0 mm (length) x 50.8 mm (height) x 38.1 mm (thickness). Radius (R) and thickness (t) of the sandwiched Brazilian disk specimen were 38.1 mm and 25.4 mm, respectively. The thickness of the aggregate layer, h, was 2.54 mm for both specimens. The relative crack size (a/R) in the Brazilian disk specimen was fixed to be 0.25 and the relative crack size (a/d) in the beam specimen was 0.375. One mortar mix with 28-day compressive strength of 45.5 MPa, and granite was used as an aggregate. For mortar/granite combination, Dunders' parameters α and β are -0.323 and -0.105, respectively, the oscillation index ε is 0.033, and the total phase shift ω is about 2.8°, indicating that the effect of β is weak. The interfacial toughness values were determined from testing the specimens shown in Fig. 3 in conjunction with the use of Eqs. 7 and 8. The interfacial fracture toughness curve developed for the specimens with mortar/granite interfaces is shown in Fig. 4. It is observed from this curve that the interfacial fracture energy markedly increases as the loading phase increases.

CRACK PROPAGATION AT THE MORTAR-AGGREGATE INTERFACE

In elastically homogeneous brittle solids, cracks are generally found to follow a local trajectory for which $K_{II} = 0$. The above crack path criterion is clearly not valid when the crack advances at an interface because in this case the consideration of the relative magnitudes of the fracture toughness between the interface and aggregate or mortar, is also involved. In this section the problem of interfacial crack propagation is studied by considering a criterion based on energy release rate.

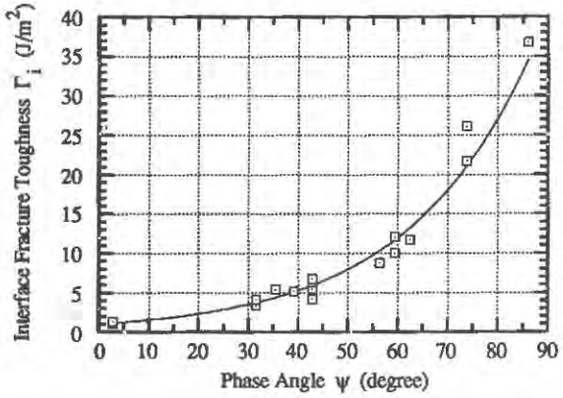

Figure 4. Fracture toughness curve for the mortar/granite interfaces

Crack Penetration vs. Deflection at an Interface

In concrete a crack impinging a mortar-aggregate interface may advance by either penetrating into the aggregate or deflecting along the interface. Let Γ_i be the toughness of the interface as a function of $\hat{\Psi}$ and let Γ_1 be the mode I toughness of material 1 ahead of the crack. The impinging crack is likely to be deflected if

$$\frac{\Gamma_i}{\Gamma_1} < \frac{G_d}{G_p^{max}} \tag{11}$$

where Γ_1 and Γ_i are material properties, which can be measured by fracture testing, and G_d is the energy release rate of the deflected crack and G_p^{max} is the maximum energy release rate of the penetrated crack. For complex geometries the ratio G_d/G_p^{max} can be calculated using a numerical analysis scheme [7]. He and Hutchinson [8] computed the ratio G_d/G_p^{max} by solving the semi-infinite crack problem.

Testing of Beam Type Composite Model

Model shown in Fig. 5 was tested to investigate the crack propagation at the mortar-aggregate interface. This specimen consisted of a mortar beam with an embedded aggregate inclusion. The dimensions of the beam were 228.6 mm (length) x 76.2 mm (height) x 38.1 mm (thickness). The dimensions of the aggregate inclusion were 63.5 mm (length) x 19.05 mm (height) x 38.1 mm (thickness). The mortar had the same properties as those for the mortar used in the sandwich specimen test, and granite was chosen for making the aggregate inclusion. Fig. 5 shows a failed specimen with a maximum load of 394 lb. It was observed that in the beam specimen embedded with a granite inclusion the crack went around the granite inclusions, i.e the interface cracking occurred.

When the hitting angle is 90° and α is 0.32, the phase angle $\hat{\Psi}$ for the deflected crack is predicted to be 30°. The interface fracture toughness, $\Gamma_i(30)$ can be semi-empirically estimated by the criterion in Eq. 11. The mode I fracture toughness of granite (material 1), Γ_g is 17.5 J/m^2. For the tested model, the ratio G_d/G_p^{max} is 0.29 as predicted by FE analysis. By substituting Γ_g and the G_d/G_p^{max} values into Eq. 11, $\Gamma_i(30)$ is estimated to be less than 5.075 J/m^2. From Fig. 4, $\Gamma_i(30)$ for the mortar-granite interface is approximately 3.5 J/m^2, and is less than 5.075 J/m^2 as stated by Eq. 11. Thus, it can be concluded that the semi-empirical method based on a criterion given in Eq. 11 is valid and it can provide a reasonable range of the

interface fracture toughness values.

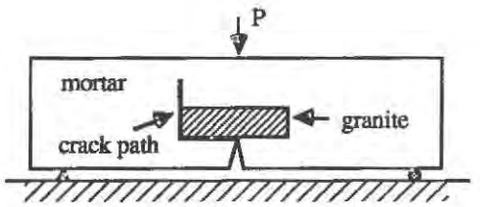

Figure 5. Failure of beam type concrete composite

CONCLUSION

In this paper, novel fracture models are presented to study the fracture of mortar-aggregate interfaces in concrete. Sandwich specimens are proposed and used to measure the fracture toughness of mortar-aggregate interfaces in concrete under mixed mode loading conditions involving tensile and shear loadings. A study is then presented on the two-phase composite models of concrete, consisting of a mortar matrix and an aggregate inclusion, to investigate the crack propagation in the interface regions. The present approach is based on a linear elastic interface fracture mechanics concepts, and is considered to be appropriate due to the linear elastic behavior and brittle failure of the interfaces. This aspect needs to be further studied. Furthermore, experimental work should be extended to study the effects of roughness variations of aggregate surfaces, the size effects of the test specimens, and the loading rate effects.

ACKNOWLEDGEMENT

Support of this work was provided by the National Science Foundation through Grant No. MSM-9016814. The cognizant NSF program official was Dr. K. P. Chong; his support is gratefully acknowledged. The authors would like to thank Professor J. W. Hutchinson of Harvard University, and Dr. C. K. Y. Leung of MIT for their valuable comments.

REFERENCES

1. Buyukozturk, O., Nilson, A. H., and Slate, F. O., "Deformation and Fracture of Particulate Composite," Journal of Engineering Mechanics, ASCE, 1972, **98**, June, pp. 581-593.
2. Yamaguchi, E., and Chen, W.-F., "Microcrack Propagation Study of Concrete under Compression," Journal of Engineering Mechanics, ASCE, 1991, **117**, No. 3, pp. 653-673.
3. Rice, J. R., "Elastic Fracture Concepts for Interfacial Cracks," J. Appl. Mech., 1988, **55**, pp. 98-103.
4. Hutchinson, J. W., "Mixed Mode Fracture Mechanics of Interfaces," In Metal-Ceramic Interfaces, Eds., M. Ruhle et al., Pergamon Press, New York, 1990, pp. 295-306.
5. Hillemeier, B., and Hilsdorf, H. K., "Fracture Mechanics Studies on Concrete Compounds," Cement and Concrete Research, 1977, **7**, pp. 523-535.
6. Suo, Z., and Hutchinson, J. W., "Sandwich Test Specimens for Measuring Interface Crack Toughness," Materials Sci. and Engrg., 1989, **A107**, pp. 135-143.
7. Lee, K. M., Buyukozturk, O., and Oumera, A., "Fracture Analysis of Mortar-aggregate Interfaces in Concrete," submitted to ASCE Journal of Engineering Mechanics, 1991.
8. He, M.-Y., and Hutchinson, J. W., "Crack Deflection at an Interface between Dissimilar Elastic Materials," Int. J. Solids Structures, 1989, **25**, pp. 1053-1067.

FRACTURE CRITERIA OF CONCRETE

SHERIF S. MORCOS
HDR Engineering, Inc.,
Pittsburgh, PA 15222

REIDAR BJORHOVDE
University of Pittsburgh
Pittsburgh, PA 15261

ABSTRACT

The relationship between the fracture energy of concrete and the ultimate crack width has been studied by considering the post cracking strength, or softening of concrete. Linear, power, and exponential models were used to describe the tensile softening. Excellent correlation has been established between the inelastic behavior of concrete and metals.

INTRODUCTION

The application of fracture mechanics to cementituous materials has opened up a new field for modeling of phenomena which often have been treated empirically in the past. Traditionally, strength parameters have been used to define the fracture initiation, specifically, the tensile and compressive strength of concrete. Bazant and Oh [1] concluded that such parameters are "inobjective", since the results of the analysis can be strongly affected by the size of the finite element mesh.

Other studies have aimed at extending the principles of linear elastic fracture mechanics and elasto-plastic fracture mechanics to cementituous materials by using the stress intensity factor approach. However, these have generally proved to be inadequate, since concrete cracks throughout the fracture zone, rather than in a specific location.

Recent studies have used a new set of material property parameters to describe the cracking process. These are the tensile strength of concrete, the fracture energy, and the shape of the tensile-strain softening diagram.

FRACTURE ENERGY AND TENSILE SOFTENING OF CONCRETE

Experiments have shown that the tensile response of concrete is primarily controlled by the formation of micro-cracks. Initially, a limited number of such cracks develop in the

concrete due to shrinkage, creep, and temperature effects. However, if, somewhere in the material, the tensile stress reaches the tensile strength, any additional deformation will increase the size of the micro-cracks within a so-called fracture zone, due to debonding between the coarse aggregates and the matrix. As the deformation increases, the stress-carrying capacity of the specimen decreases, since more micro-cracks are created. They eventually merge into a macro-crack that cannot transfer any load. This phenomenon is termed tensile-strain softening of concrete; it is represented by the descending portion of the stress-crack opening displacement curve in Fig. 1. The area under the curve represents the amount of energy required to create a crack of one unit of area, G_f.

The tensile-strain softening of concrete is defined by three parameters. These are the tensile strength of concrete, f_t, the area under the softening curve, G_f, and the shape of the descending branch, as shown in Fig 2. In early studies, linear and bilinear softening models were used to determine the stiffness of cracked concrete. However, tensile tests have shown that the concrete stress-strain softening diagram is highly nonlinear. Numerous mathematical models have been proposed for the nonlinear strain-softening phenomenon [2, 3, 4].

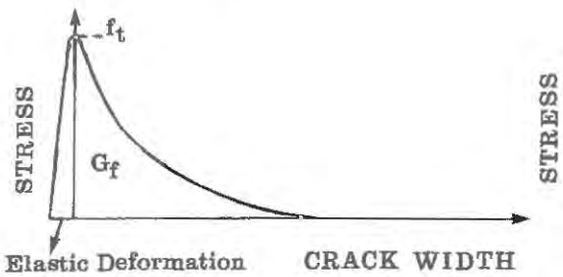

Figure 1. Stress-Crack Opening Displacement.

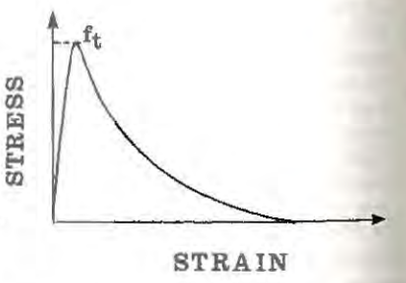

Figure 2. Tensile Stress-Strain.

FRACTURE ENERGY VS ULTIMATE CRACK WIDTH

For a smeared crack model, the crack opening displacement, w, is represented by a crack strain acting over the crack band width, h, within the finite element. Therefore, w is the accumulated crack displacement. By assuming that the micro-cracks are uniformly distributed over the crack band width, w can be expressed as:

$$w = h\,\epsilon \tag{1}$$

where ϵ is the crack normal strain in the direction of the maximum tensile stress.

The fracture energy of concrete, G_f, is equal to the area under the stress-crack opening softening diagram. It can therefore be expressed as:

$$G_f = h\,g_f = h \int_0^{\epsilon_o} \sigma\, d\epsilon \tag{2}$$

where g_f is the area under the stress-strain softening diagram.

Since the fracture energy and the tensile strength are material properties of the concrete, it is important to predict the relationship between these properties and the ultimate crack opening, w_o, at which stress can no longer be transferred (Morcos [5]). By using the

Reinhardt and Moelands [2] mathematical model, G_f is found by integration as

$$G_f = h\,f_t \int_0^{\epsilon_o} [\,1 - (\frac{\epsilon}{\epsilon_o})^{0.31}\,]\,d\epsilon = 0.23664\;\epsilon_o\,h\,f_t \tag{3}$$

and w_o, G_f, and f_t are related as

$$w_o = 4.226\,\frac{G_f}{f_t} \tag{4}$$

w_o is thus linearly related to the material properties of concrete.

The Reinhardt and Cornelissen [3] exponential model gives

$$G_f = h\,f_t \int_0^{\epsilon_o} [\,1 + c_1\,(\frac{\epsilon}{\epsilon_o})^4]\,\exp(-\,c_2\,\frac{\epsilon}{\epsilon_o})\,d\epsilon = 0.247\;\epsilon_o\,h\,f_t \tag{5}$$

$$w_o = 4.05\,\frac{G_f}{f_t} \tag{6}$$

Finally, another model [4] gives:

$$G_f = hf_t \int_0^{\epsilon_o} [[1+(\frac{\epsilon}{\epsilon_o})^3]\exp(-\,5.64\frac{\epsilon}{\epsilon_o})-7.106\times10^{-3}\,(\frac{\epsilon}{\epsilon_o})]\,d\epsilon = 0.178\epsilon_o hf_t \tag{7}$$

$$w_o = 5.618\,\frac{G_f}{f_t} \tag{8}$$

Equations (4), (6), and (8) show that G_f, f_t, and w_o are linearly related. Further, the relationship is independent of the mathematical expression that is used to describe the descending curve of the strain softening diagram. Analyses using other nonlinear models have given the same result (Morcos [5]). In a more general form, this can be expressed as:

$$w_o = C\,\frac{G_f}{f_t} \tag{9}$$

where C is a constant that depends on the mathematical model that is used to describe the descending branch of the tensile strain-softening diagram.

FRACTURE BEHAVIOR OF CONCRETE VS METALS

The form and parameters of Eq. (9) are similar to the expression that defines the crack characteristics of metallic materials. In elastic-plastic fracture mechanics analysis of metals, the crack-tip opening displacement is related to the material properties, as follows:

$$\delta_c = \frac{K_c^2}{m\,E\,\sigma_{flow}} \tag{10}$$

where δ_c is the critical crack-tip opening displacement at which fracture would be initiated; K_c is the critical stress intensity factor for static loading and plane stress conditions; E is the

modulus of elasticity; σ_{flow} is taken as the average of the ultimate strength and the yield stress of the material; and m is a constraint factor which is equal to 1.2 and 1.6 for plane stress and plane strain conditions, respectively (Barsom and Rolfe [6]).

The fracture energy is related to the critical stress intensity factor, K_c, by

$$G_c = \frac{K_c^2}{E} \tag{11}$$

where G_c is the critical-strain energy-release rate. Substituting Eq. (11) into Eq. (10) gives

$$\delta_c = \frac{G_c}{m\ \sigma_{flow}} \tag{12}$$

Although the shape, size, and behavior of the fracture zone in concrete is very different from those of steel and other metallic materials, Eqs. (9) and (12) demonstrate an excellent correlation between the inelastic behavior of metals and concrete. The critical crack widths of both are linearly related to the fracture energy and tensile strength, which are material properties.

CONCLUSIONS

It is found that the fracture energy and tensile strength of concrete are linearly related to the ultimate crack width. This relationship is independent of the model used to describe the softening curve. The fracture behavior of concrete and metals has been compared, and an excellent correlation has been established between the inelastic behavior of the two materials. The critical crack widths of both are linearly related to the material properties.

REFERENCES

1. Bazant, Z. P., and Oh, B. H., "Crack Band Theory For Fracture of Concrete," Materiaux et Constructions, Vol. 16, No. 94, July-August, 1983.
2. Reinhardt, H. W., "Fracture Mechanics of an Elastic Softening Material Like Concrete," HERON, Vol. 29, No. 2, 1984.
3. Reinhardt, H. W., and Cornelissen, H. A. W. "Strain-Softening Analysis of Concrete Fracture Specimens", in Fracture Toughness and Fracture Energy of Concrete, F. H. Wittmann (Ed.), Elsevier, Amsterdam 1986.
4. Cornelissen, H. A. W., Hordijk, D. A., and Reinhardt, H. W., "Experimental Determination of Crack Softening Characteristics of Normalweight and Lightweight Concrete," HERON, Vol. 31, No. 2, 1986.
5. Morcos, S. S., "Fracture in Continuous Composite Beams", Ph.D. Dissertation, University of Pittsburgh, Pittsburgh, Pennsylvania, 1991.
6. Barsom, J. M. and Rolfe, S. T., "Fracture and Fatigue Control in Structures Applications of Fracture Mechanics", 2nd Edition, Prentice-Hall, 1987.

INTERACTING FLAWS IN LINEAR ELASTIC MEDIA

C. FOND, J.-L. FLEJOU and Y. BERTHAUD
Laboratoire de Mécanique et Technologie
(E.N.S. CACHAN/C.N.R.S./Université Paris 6)
61, Avenue du Président Wilson
94235 CACHAN Cedex (France)

ABSTRACT

The aim of this work is to study both the local and the global responses of an elastic matrix in presence of many singularities such as cracks, pores or inclusions. Interactions between all these inhomogeneities are supposed to play a great rule on both the behavior of such a material and the damage process. In this case one has to take into account the effect of friction between the lips of the cracks. The first step of our work was to build a general scheme to solve this problem. The original method of Kachanov [10] and Beneveniste [2] has been extended to the case of various inhomogeneities.

INTRODUCTION

Bi-dimensionnal elastic linear media constitutes the matrix of our mesoscopic model. Three kinds of "element" are today implemented - straight line cracks - circular cavities and straight boundaries. The semi-analytical method we have chosen to solve elastic problems uses Airy's functions due to these particular geometries and the superposition principle. This method gives good accuracy for problems involving many singularities. Moreover, crack closure effect and friction between the crack lips can be easily taken into account. In fact, this method can be seen as a boundary element method where cracks do not need special treatment neither discretization.

METHOD

A method of influences can be applied to linear elastic media by using the superposition principle. To solve problems with the theory of linear elasticity we can superpose some well known stress fields since the boundary conditions are satisfied (see [2] and [6] and [10]).

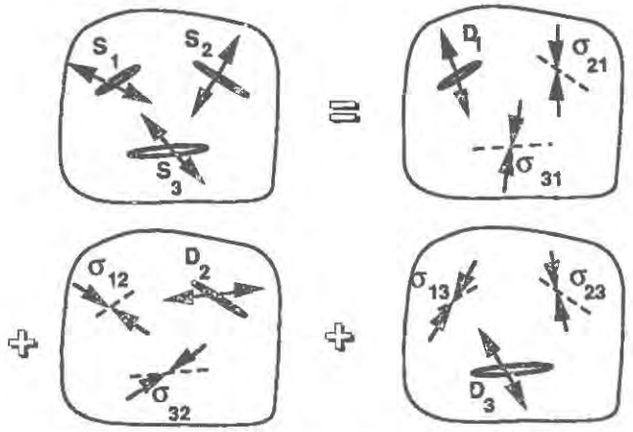

Figure 1. Superposition principle and effect of single cracks.

For this, we use the analytical solution of a single crack or a single circular cavity under any distribution of tangential or normal pressure in an infinite medium, or the solution of a semi infinite medium submitted to forces or displacements. We can obtain an approximated solution of any problem involving different kinds of geometries. In a same way as in a boundary element method, elastic inclusions can be added by the respect of the stresses and displacements compatibilities.

General formulation

Let us consider a finite bi-dimensionnal medium containing cracks with friction or not and circular cavities (see figure 1). If stress boundary conditions are considered one has to satisfy equation (1).

N_f is the number of elements (cracks or boundaries or pores). $S_i(x_i)$ is the stress repartition inside the alone element in an infinite medium caused by the external stresses . $D_j(x_j)$ is the unknown stress repartition to equilibrate the interactions and external stresses on the body .
By using the superposition principle several times , one can write for the i crack:

$$S_i(x_i) = \sum_{j=1}^{Nf} \mathcal{F}_{ij}\,(D_j(x_j)) \qquad (1)$$

$$\mathcal{F}_{ij}\,(D_j(x_j)) = -\,\sigma_{ij}(x_i) \quad \text{and} \quad \mathcal{F}_{jj} = Id$$

F_{ij} is a non-symmetric linear operator which gives the stress repartition $S_{ij}(x_i)$ at the i element location (inside an infinite or semi-infinite medium) for the D_j stress repartition on the j element .

By choosing a set of orthogonal functions as $D_j(x_i)$, the formulation is linearised and F_{ij} become a non-symetric matrix . One obtains :

$$[\,F_{ij}\,]\,D = S$$

where S is a known vector and D the calculated vector .

There are no restrictions for three dimensional media but the complexity of three dimension functions renders this extension quite difficult for non constant pressures [6].

For our applications we used polynomial expansions for cracks and boundaries and Fourier's expansions for cavities. The functions for boundaries are formed with the Boussinesq's solution for a concentrated force applied to a semi-infinite medium. This solution is integrated over an interval for polynomial distributions of tangential or normal stresses. (These analytical calculations have been done using a specific software). Anyway, problems can be solved in bounded media and also in infinite media (fig. 2). A good accuracy in presence of singularities and a small number of unknown values is coupled with the fact that inputs are easy and fast for users. It has to be noticed that this technic is ideal for parallel computers.

Friction

Moreover, according to some hypothesis, friction inside cracks is introduced and the history of loading can then be added. These hypothesis are the following : cracks are opened, closed or rubbing along its whole length because cracks are never discretized. Since the interactions are low and the stress tensor has a small gradient these hypothesis do not constitute any important restriction and the solution is then correctly approximated. The crack opening displacements and friction parameters are known for each step of loading and so the validity of the hypothesis can be estimated for each computation.

Accuracy

No proof of the convergence of this method has been given. Anyway a great number of comparisons between analytical solutions and our results has shown that our technique is efficient. The comparisons are dealing with the stress intensity factors for various geometry of cracking, with the interaction between cracks and cavities or between cavities (Figure 2). In the case of bounded media with stress (by now) boundary conditions, it is possible to compute the approximated solution of the problem on the boundaries. The comparison between this solution and the imposed conditions gives us an indication of the accuracy of the solution. In all the cases we have tested the difference between the approximated solution and the imposed condition has the shape of higher order terms in the expansion and their intensity is also less than a few percent of the intensity of the boundary condition.

APPLICATIONS

As an example, the case of a main crack passing through several small cracks has been computed for parallel cracks and random cracks of same length. These cases have ever been looked at by [6] for instance and no general conclusion for intensity factor could be given by any of us. Meanwhile, using a similar technic with crack closure effect and friction, we propose to see if this remark remains available. Results given in figures 3 and 4 show that it is possible to obtain results in these different cases - crack array or pore array. The evolution of the stress intensity factor of the main crack depends on the distribution of cracks or of pores in front of this crack. The case of ramdom array (table 1) illustrates the importance of the closure effect. We have computed for two different array the SIF for tension and tension combined with compression in the perpendicular direction. The presence of this compression tends to close some of the cracks and that reduces the SIF of the main crack.

It is also expected that interactions will have significant effects on the local stress and then on the failure map but not on the global responses. We have plotted the global responses for a cyclical loading in presence of friction in the case of a bounded medium (figure 5). The crack density and friction coefficient remain constant during the loading (cracks do not propagate).

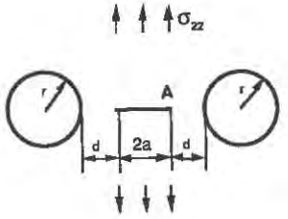

geometry		reference value [11]	our results	difference
a/r	d/r	K_{IA}	K_{IA}	(%)
0,8	0,2	3,33	3,3	1,0
2	0,25	2,48	2,47	0,5
1	0,5	2,59	2,64	1,9

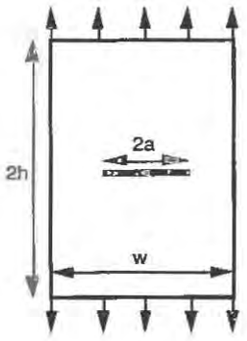

geometry			reference results [11]	our results
a	w	2h	K_{IA}	K_{IA}
3	15	24	3,44	3,43
1	4	2	3,49	3,49
1	2,857	2	3,88	3,88
1	2,857	1,143	6,50	6,50

Figure 2. Comparison between analytical solutions and our formulation.

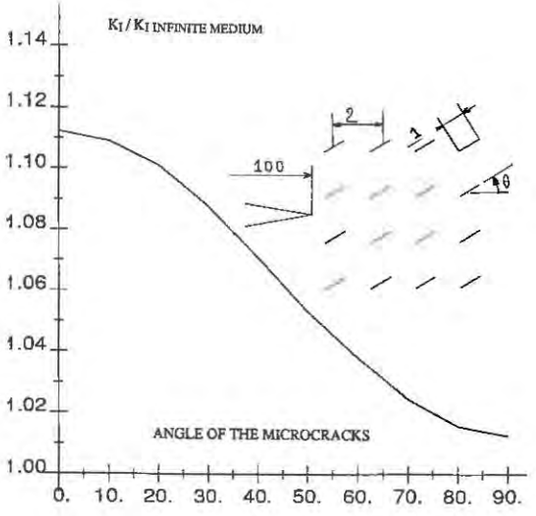

Figure 3. Evolution of the stress intensity factor in function of the angle of the crack array.

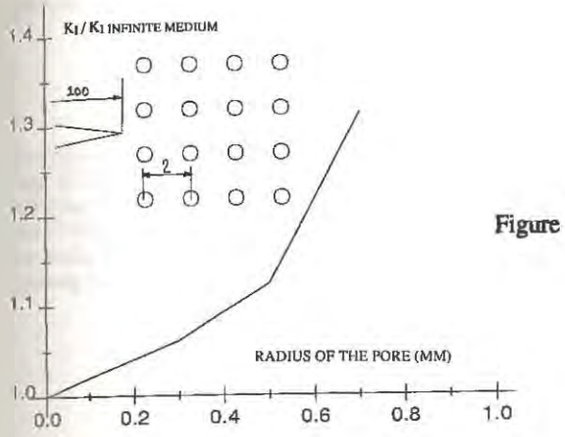

Figure 4. Evolution of the stress intensity factor in function of the radius of the pores.

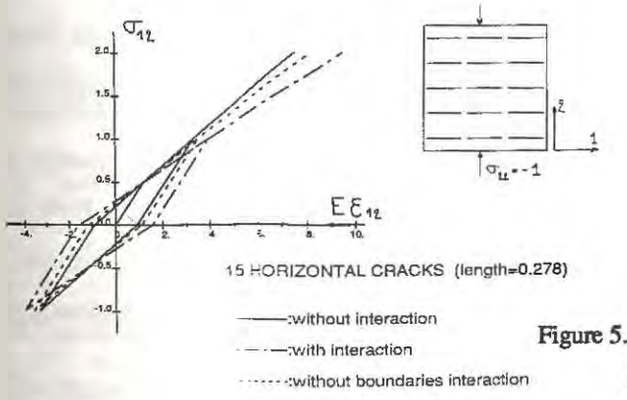

Figure 5. Behavior of a cracked medium under cyclic loading.

Lateral pressure σ_{22}(MPa) σ_{11} = constant = 1	SIF/SIF infinite medium Ramdom array n° 1	SIF/SIF infinite medium Ramdom array n° 2
0	1.078	1.069
-1	1.073	1.069
-3	1.064	1.069

Table 1. Effect of the crack closure on the stress intensity factor for two ramdom arrays.

We obtain a cycle with dissipated energy due to friction in the cracks and can also remark that the boundaries have a strong effect on the decrease of the stiffness of the medium.

CONCLUSION

Results are showing that the superposition technique is available to determine the effect of interactions. It is obvious that compressive failures involve interactions. Nothing really new has been now noticed but we are going to continue the development of the model for compressive response to point out how much the mode II is coupled with the mode I [14] when the rupture or localization is reached. Anyhow we have obtained accurate solutions even with strong interactions . The displacement conditions are introduced in the general formulation to impose mixed - stress and displacement - conditions.

REFERENCES

1. Belkacemi, Y., Méthode des discontinuités de déplacement en champ complexe, Thèse de doctorat de l'université de Lille Flandres Artois, 1987.
2. Benveniste,Y.,Dvorak, G.J., Zarzour, J. and Wung, E.C., On interacting cracks and complex configurations in linear elastic media, Department of Civil Engineering, Rensselaer Institute, Troy, NY 12180, USA, May 1988.
3. Berthaud, Y. et Pijaudier-Cabot, G., Nonlocal continuum and micromechanics of damage in quasi-brittle materials, "Micromechanics of failure of quasi-brittle materials", Ed. by S.P. Shah, S.E. Swartz and M.L. Wang, Elsevier Pub., Albuquerque, USA, 1990, pp. 125-134.
4. Brebbia, C.A., Telles, J.C.F.and Wrobel, L.C., Boundary Element Techniques - Theory and Applications in Engineering, Springer-Verlag, 1984.
5. Bouhaddane, A., Application de l'intégrale de Cauchy à la méthode des discontinuités de déplacement et autres méthodes de collocation, Thèse de doctorat de l'université de Lille Flandres Artois, 1987.
6. Chudnovsky, A. , Dolgopolsky, A. , Kachanov, M. , Elastic interaction of a crack with a microcrack array - I. Formulation of the problem and general form of the solution, International Journal of Solids and Structures, 1987, **23**, pp. 1-10.
7. Hallam, S.D. et Ashby, M.F., The failure of brittle solids containing small cracks under compressive Stress States, Acta Metallica, 1986, **34**, pp. 497-510.
8. Henry, J.P. and Parsy, F., Cours d'élasticité, Ed. Dunod Université, 1982.
9. Henry, J.P. and Caignaert,G., Exercices d'élasticité, Ed. Dunod Université, 1982.
10. Kachanov, M. , Elastic solids with many cracks - a simple analysis, Int. Journal of Solids and Strutures, 1987, **23**, pp. 23-43.
11. Murakami, Y., Stress intensity factors handbook, Pergamon Press, 1988.
12. Mazars, J., Prévision de la rupture des structures en béton par la mécanique de la rupture, Thèse de doctorat de 3ème cycle de l'université de Paris 6, 1976.
13. Nemat-Nasser, S. and Hoori, H., Compression induced non planar crack extension with application to splitting, exfoliation and rockburst, Journal of Geophysic, 1982, Res, **87**, pp. 6805-6821.
14. Ouyang, C. , Landis, E. and Shah, S. P. , Damage assessment in concrete using quantitative acoustic emission, Journal of Engineering Mechanics, 1991, **117**, pp 2681-2698.
15. Pijaudier-Cabot, G. and Berthaud, Y., Effet des intéractions dans l'endommagement d'un milieu fragile - formulation non locale, C.R.A.S., 1990, t. 310, série II, pp. 1577-1582.

MARKOV PROCESS MODEL FOR RANDOM GROWTH OF CRACK WITH R-CURVE

By Yunping Xi and Zdeněk P. Bažant
Department of Civil Engineering
Northwestern University
Evanston, Illinois 60208, U.S.A.

Due to the statistical nature of material properties, crack growth is a random process. This process may be described by the Markov chain model (see Fig. 1). However, model must exhibit R-curve behavior. The basic relation for the Markov chain model (Bogdanoff and Kozin, 1985) is

$$\underset{\sim}{p}_X = \underset{\sim}{p}_0 \, \underset{\sim}{P}^X \tag{1}$$

in which $\underset{\sim}{p}_0$ is the initial state probability vector, $\underset{\sim}{p}_0 = \{\pi_1, \pi_2, \cdots \pi_{B-1}, 0\}^T$, $\sum \pi_j = 1$, in which π_j = Prob(damage state j is initially occupied). We assume $\pi_1 = 1$, with other $\pi_j = 0$, which means the crack (or damage) always starts from state 1; $\underset{\sim}{p}_X$ is the damage state probability, $\underset{\sim}{p}_X = \{p_X(1), p_X(2), p_X(B)\}^T$, where $p_X(j)$ = Prob(damage state j is occupied at stress level X); $\underset{\sim}{P}$ is the probability transition matrix,

$$\underset{\sim}{P} = \begin{bmatrix} p_1 & q_1 & 0 & \cdots & 0 \\ 0 & p_2 & q_2 & \cdots & 0 \\ 0 & 0 & p_3 & \cdots & 0 \\ \cdots & \cdots & \cdots & \cdots & \\ 0 & 0 & 0 & \cdots p_{B-1} & q_{B-1} \\ 0 & 0 & 0 & \cdots 0 & 1 \end{bmatrix} \tag{2}$$

where p_i = probability of remaining in the state i during one loading step, and q_i = probability that in one loading step the damage moves from state i to state i+1. The present model is a unit-jump, discrete-variable and state-dependent stationary process. p_i and q_i can be determined from the deterministic relation of stress and crack length and the deviation of this relation. The deterministic relation for the nominal stress may generally be written in the form:

$$\bar{X} = \frac{\sqrt{R(a - a_0)E_c}}{\sqrt{\pi a}\, F(a/d)} \tag{3}$$

where $\bar{X}$ represents the mean nominal stress (which is proportional to the applied load), E_c is initial elastic modulus, $R(a - a_0)$ is the R-curve, $F(a/d)$ is a geometry dependent function, available in handbooks (e.g. Tada, 1983), a is the current crack length, and a_0 is the initial crack (or notch) length. The R-curve can be obtained from the size effect law proposed by Bažant (Bažant and Kazemi, 1990), calibrated by size effect measurements.

The variance at state j may be expressed approximately as a linear function of the crack length a,

$$\sigma_j^2 = \frac{(a_j - a_0)}{(a_{max} - a_0)} \sigma_{max}^2 \tag{4}$$

where a_{max} can be obtained from Eq. 3. σ_{max}^2, representing the variance of the peak load, may be considered to be size independent, because the random scatter is mainly related to the size of the fracture process zone during the loading process and at ultimate state the fracture process zone size is almost independent of the structure size.

The formula for any state j can be derived from Eqs. 3,4

$$B_j = \frac{(\bar{X}_j - \bar{X}_{j-1})^2}{(\bar{X}_j - \bar{X}_{j-1}) + (\sigma_j^2 - \sigma_{j-1}^2)} + B_{j-1} \tag{5}$$

$$r_j = \frac{\bar{X}_j - \bar{X}_{j-1}}{B_j - B_{j-1}} - 1$$

where $p_i = r_i/(1+r_i)$, and $q_i = 1/(1+r_i)$.

Consider, now, a notched three-point-bend beam specimen of high strengtconcrete as an example. The details of the test can be found in Gettu (1990). The R-curve obtained from the peak loads is shown in Fig. 2. Fig. 3 shows the probability at each damage state and nominal stress. One can see that, for example, at loading level 61 (almost the peak load) the probability for the occurrence of the damage state 61 (almost the failure state) is very high, more than 90%. On the other hand, the probabilities for the occurrence of the lower damage states, 1 - 50, at the same loading level are almost zero, which is true in reality.

An advantage of present model is that the sample curve can be easily simulated by the computer. In this manner, the scatter band and the trend of damage evolution can be seen. Fig. 4 shows the sample curves of the relation between the crack extension and the loading level. One can clearly see that the generated sample curves represent the observed test curves quite well. This means that the present model can characterize the probabilistic structure for the entire loading history from the initial state up to the failure load.

REFERENCES

1. Bažant, Z.P., and Kazemi, M.T., "Size Effect in Fracture of Ceramics and Its Use To Determine Fracture Energy and Effective Process Zone Length", J. Am. Ceram. Soc., 1990, 73(7) pp. 1841-1953.

2. Bogdanoff, J.L., and Kozin, F., "Probabilistic Models of Cumulative Damage", John Wiley & Sons, New York, 1985.

3. Gettu, R., Bažant, Z.P., and Karr, M.E., "Fracture Properties and Brittleness of High-Strength Concrete", ACI Material Journal, Nov.- Dec., 87, 1990, 608-618.

4. Tada, H., "The Stress Analysis of Cracks Handbook", Del Research Corp., St. Louis, MI 63105, 1983.

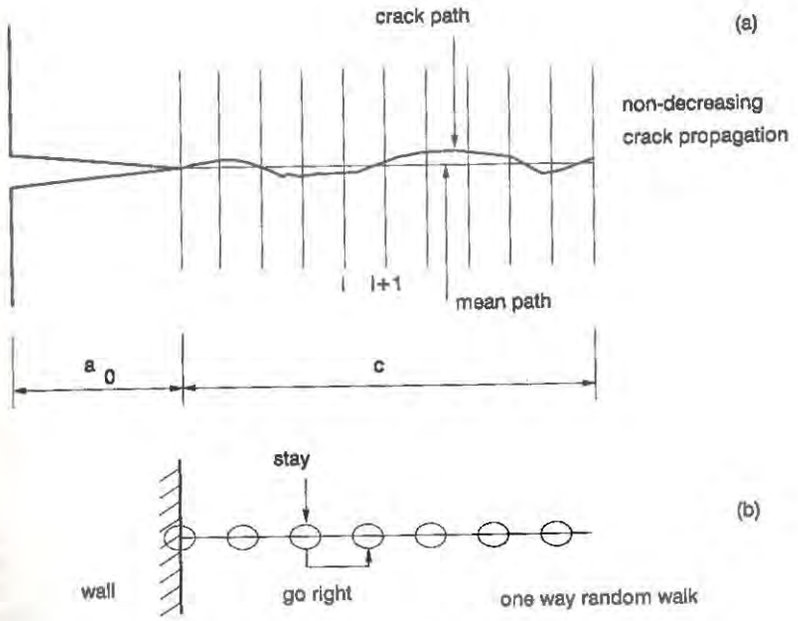

Fig. 1 One way random walk model

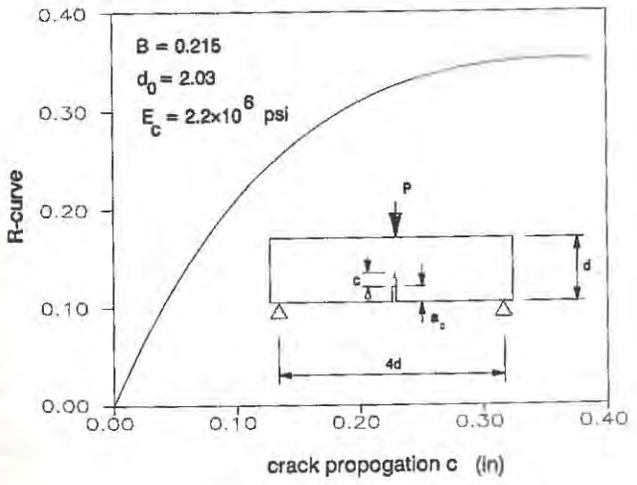

Fig. 2 R-curve

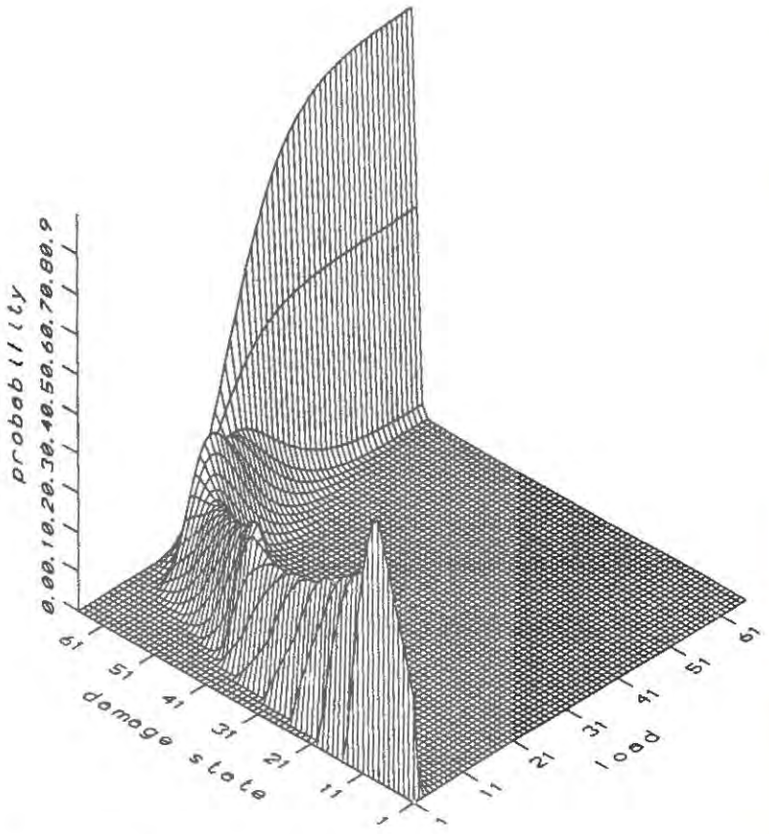

Fig. 3 Probability - loading level - damage state

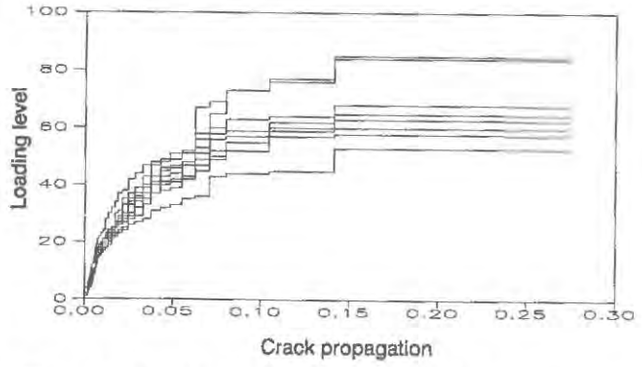

Fig. 4 Samples of load - crack propagation

THE EFFECT OF INITIAL CRACK DEPTH ON THE BEND SPECIMEN CRACK GROWTH RESISTANCE CURVE FOR A CONCRETE-TYPE MATERIAL

E. SMITH
Materials Science Centre, University of Manchester/UMIST
Grosvenor Street, Manchester M1 7HS, UK

ABSTRACT

Concrete-type materials have the characteristic that when a crack grows, a partially fractured ligament zone forms behind the crack tip, and the restraining stresses provided by the crack bridging elements within this zone are responsible for the crack tip stress intensity factor increasing during crack growth, thus leading to an effective toughening of the material. The edge crack-finite width bend specimen is frequently used to determine the stress intensity (K) - crack growth (R) curve, and this paper examines the effect of the initial crack depth on the shape of the K-R curve. A theoretical analysis shows that for a given specimen width, and as crack extension proceeds, the general level of the K-R curve is higher the greater is the initial crack depth.

INTRODUCTION

Several types of brittle material, and particularly concrete-type materials, exhibit a behaviour such that the fracture resistance, as manifested by the crack tip stress intensity K, increases with the amount R of crack extension. Upon loading a pre-cracked solid, the crack tip remains stationary until $K = K_{IC}$ when the material fractures at the crack tip. As loading continues, the crack extends, leaving behind ligaments which bridge the crack faces. The restraining stresses due to these ligaments are responsible for the stress intensity increase associated with crack growth. The opening, i.e. the relative displacement of the crack faces, at the original crack tip location, i.e. the trailing edge of the partially fractured ligament zone, increases as the crack grows until the opening becomes too large for any bridging to occur, and the ligament zone is then said to be fully developed.

The stress intensity-crack extension behaviour depends on a variety of factors: the crack/solid geometrical configuration, the mode of loading, the restraining stress-relative displacement law for the ligament material, and the magnitude of K_{IC}. Considerations of the K-R behaviour are simplified if it is assumed that the restraining stress has a constant value p_c within the ligament zone, and that there is a sharp cut-off to a zero restraining stress when the relative displacement of the crack faces attains a critical value δ_m; the Dugdale-Bilby-Cottrell-Swinden (DBCS) representation[1,2] is then used to describe the behaviour of the ligament material. From this basis and regarding the case (referred to as the small zone situation) of a semi-infinite crack in a remotely loaded infinite solid as a bench mark for comparison, it has been shown[3] that the K-R curve slope is particularly high for an edge crack in a finite width bend specimen, a geometry that is often used to experimentally determine the K-R curve. There are obvious advantages if credit can be taken for the enhanced toughness associated with an increasing K-R curve, and this is the

motivation for understanding the geometry dependence of the K-R curve, particularly in the context of the transferability of laboratory test data to the behaviour of actual engineering structures.

Majumdar and co-workers[4] study of the bend specimen geometry used finite element solutions for two specific cases: $a_o/w = 0.2$ and $a_o/w = 0.4$ (a_o = initial crack depth and w = solid width). The K-R curves were similar for these specific situations, and indeed Majumdar and co-workers inferred that the crack growth resistance behaviour was independent of the initial crack depth. This apparent independence of the K-R curve with respect to the initial crack depth for the bend configuration is not intuitively obvious, and it is against this background that the present paper provides further insight on the effect of initial crack depth on the K-R behaviour of a crack in a finite width bend specimen. A bounding procedure is used to show that, for a given specimen width, and as crack extension proceeds, the general level of the K-R curve is in fact higher the greater is the initial crack depth.

THEORETICAL ANALYSIS

Figure 1 shows the model of a bend specimen of width w, thickness B, which contains a crack with initial depth a_o, the specimen being subjected to a moment M; there is a ligament

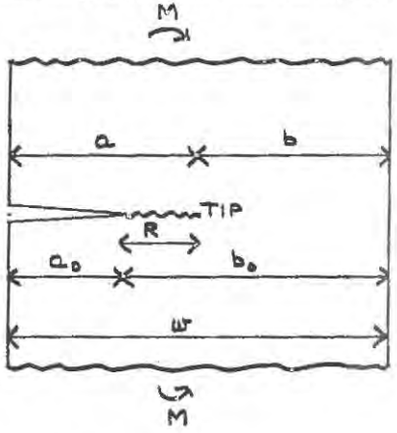

Figure 1. The model of the bend specimen.

zone of length R at the crack tip, which is therefore at a distance $a = a_o + R$ from the surface containing the crack. The restraining stress within the ligament zone is p_c, and the analysis is with regard to the case $K_{IC} = 0$; for non-zero K_{IC} the crack tip stress intensities referred to in this section are merely raised by an amount K_{IC}. The stress intensity at the tip of this crack of depth a is equal to the stress intensity due to the restraining stress p_c acting within the ligament zone.

This stress intensity is bounded (below) by the stress intensity for the situation where $a_o = 0$, and is bounded (above) by the stress intensity for the situation where $a_o = \infty$. As regards the lower bound case (a) where $a_o = 0$, the stress intensity is given by an expression of the form:

$$K = p_c \sqrt{\pi R}\, F(R/w) \qquad (1)$$

where F(R/w) is a function that has been given in graphical form[5]; K is shown in the Table, for values of R/b_o (b_o is initial ligament width) up to 0.4. As regards the upper bound case (b), by integrating the effect of line forces applied to the faces of a semi-infinite crack using known results[5], it is readily shown that the upper bound K value lies between the values K_1 and K_2, which are given by the relation

$$\frac{\begin{pmatrix}K_1\\K_2\end{pmatrix}}{p_c\sqrt{\pi b_o}} = \frac{\sqrt{8}}{\pi}\sqrt{x}\left\{\begin{pmatrix}1.0\\1.2\end{pmatrix}\sqrt{\frac{1-\frac{x}{2}}{1-x}} + 2.49\sqrt{\frac{x}{1-x}}\left[\frac{\left(1-\frac{x}{2}\right)}{(1-x)} - 0.736\right]\right\} \qquad (2)$$

with $x = R/b_o$. The values of K_1 and K_2 are shown in the Table for values of $x = R/b_o$

TABLE

Lower bound K values (second column); the upper bound K values lie between K_1 and K_2.

$\frac{R}{b_o}$	$\frac{K}{p_c\sqrt{\pi b_o}}$	$\frac{K_1}{p_c\sqrt{\pi b_o}}$	$\frac{K_2}{p_c\sqrt{\pi b_o}}$
0	0	0	0
0.1	0.381	0.368	0.427
0.2	0.612	0.622	0.707
0.3	0.906	0.928	1.036
0.4	1.333	1.348	1.479

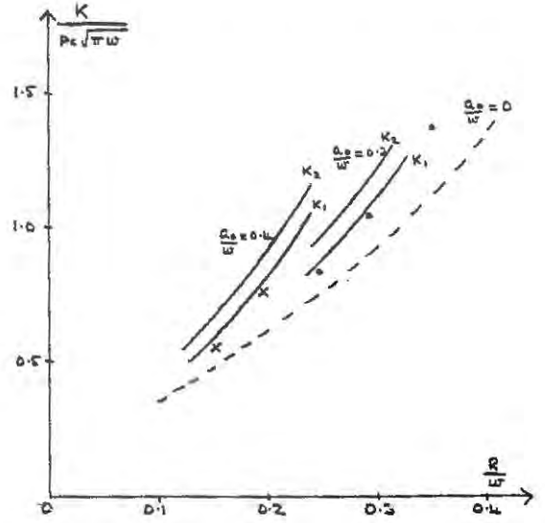

Figure 2. Lower bound (K_1) and upper bound (K_2) values of K expressed in terms of the specimen width w; R is the crack extension. Majumdar and co-workers' finite element results[4] are also shown; full circles are for $a_o/w = 0.2$ and crosses are for $a_o/w = 0.4$. The dotted curve represents the $a_o \to 0$ results.

up to 0.4; the upper bound K value will be close to K_1 at very small $x = R/b_o$. Comparison of the results in the Table clearly shows that the lower bound K value is within 2% of the K_1 value. This means that K_1 and K_2 can be regarded as being lower and upper bounds to K, recognizing that K will be very close to K_1 for very small $x = R/b_o$. The lower and upper bound results can be expressed in terms of specimen width w, and Figure 2 shows the relevant bounding curves for $a_o/w = 0.2$ and $a_o/w = 0.4$, together with the actual results for $a_o/w = 0$ (see Table) and Majumdar and co-workers' finite element results[4].

DISCUSSION

Recognizing that for each a_o/w, the actual K-R variation will be close to the lower bound (K_1) curve for small R, inspection of the results shows that there is very good agreement with the present paper's results and Majumdar and co-workers' results[4], which were obtained on the basis of finite element solutions. These workers recognized that the K-R variations for the two specific cases $a_o/w = 0.2$ and $a_o/w = 0.4$ were similar and, in fact, inferred that the crack growth resistance behaviour was independent of the initial crack depth. However, if one examines the behaviour trends in Figure 2, it is clear that, as crack extension proceeds, the general level of the K-R curve is higher the greater is the initial crack depth; indeed careful inspection of Majumdar and co-workers' results (see Figure 2) also shows this to be the case. Nevertheless, the K-R curve shape is not overly sensitive to the a_o/w ratio for $a_o/w < 0.4$.

In assessing the implications of the present paper's results, when coupled with Majumdar and co-workers' results, which in both cases have been obtained on the assumption of a constant stress within a ligament zone, it is important to emphasize that the results are for crack extensions less than that required for the full development of a ligament zone, i.e. they are valid until the crack extension is sufficient for the relative displacement of the crack faces at the initial crack tip to exceed the critical value δ_m at which the restraining stress becomes zero. Though the K-R curve is not overly sensitive to the a_o/w ratio for $a_o/w < 0.4$, and the K-R curve will be the same for both moment and tensile loading of a finite width solid containing an edge crack, the K and R values associated with the full development of a ligament zone are likely to be markedly dependent on the initial crack depth and, for a prescribed initial crack depth, will be different for moment and tensile loading. Subsequent to the full development of a ligament zone, the K-R curve shape may well show a marked dependence on the initial crack depth. A detailed consideration of these issues is beyond the scope of the present paper, whose objective has been to examine the effect of the initial crack depth on the shape of the K-R curve prior to the full development of a ligament zone. However, these issues are relevant with regard to the transferability of laboratory test data to the behaviour of actual engineering structures, and it is in this context that the present paper's results provide important input.

REFERENCES

1. Dugdale, D.S., J. Mech. Phys. Solids, 8 (1960) 100.
2. Bilby, B.A., Cottrell, A.H. and Swinden, K.H., Proc. Roy. Soc., 1963, A272, 304.
3. Smith, E., paper accepted for publication in Theoretical and Applied Fracture Mechanics.
4. Majumdar, B.S., Rosenfield, A.R. and Duckworth, W.H., Eng. Fract. Mechs, 1988, 31, 683.
5. Tada, H., Paris, P.C. and Irwin, G.R., The Stress Analysis of Cracks Handbook, Del Research Corporation, Hellertown, Pennsylvania, USA, 1973.

CRACK ANALYSIS IN HARDENING CONCRETE

OLA DAHLBLOM
Division of Structural Mechanics
Lund University
Box 118, S–221 00 Lund, Sweden

ABSTRACT

A material model for hardening concrete is presented. Tensile fracture is modelled using a smeared crack approach based on the fictitious crack model. The development of material properties like elastic modulus, tensile strength and fracture energy during hardening of the concrete is considered. The material model has been implemented in a finite element program and computational results obtained for the response of a concrete tension specimen are presented.

INTRODUCTION

Prediction of the behaviour of a hardening concrete structure in general requires computer simulation. A crucial point in such a simulation is the modelling of the material behaviour. The present paper is focussed on modelling of stiffness and fracture or hardening concrete.

ELASTIC STRAIN

Assuming isotropy, the elastic strain rate $\dot{\underset{\sim}{\epsilon}}^e$ is related to the stress rate $\dot{\underset{\sim}{\sigma}}$ by the expression

$$\dot{\epsilon}_{ij} = C^e_{ijkm}\ \dot{\sigma}_{km} \tag{1}$$

where $\underset{\sim}{C}^e$ is the compliance tensor, given by

$$C^{e}_{ijkm} = \rho_e \, \delta_{ij} \, \delta_{km} + \kappa_e(\delta_{ik} \, \delta_{jm} + \delta_{im} \, \delta_{jk}) \tag{2}$$

in which δ_{ij} is Kronecker's delta and ρ_e and κ_e are parameters related to the elastic modulus E and Poisson's ratio ν by the expressions

$$\rho_e = \frac{\nu}{E} \quad ; \quad \kappa_e = \frac{1+\nu}{2E} \tag{3}$$

The development of the elastic modulus E during hardening of the concrete may be described

$$E = \eta_E \, E_0 \tag{4}$$

where

$$\eta_E = \frac{\frac{a_{1E}}{(\frac{t_e}{t_r})^{b_{1E}}}}{1 + \frac{a_{1E}}{a_{2E}}\frac{t_e}{(\frac{t_e}{t_r})^{(b_{1E}-b_{2E})}}} \tag{5}$$

and E_0 is the elastic modulus at 28 days. In Eq. (5) t_e is the maturity time and $t_r = 28$ days. The parameters a_{1E}, b_{1E}, a_{2E} and b_{2E} depend on the cement type and the concrete composition.

According to experimental data by e.g. Byfors [1], Poisson's ratio decreases rapidly at a very early age and then increases. This may be described by the relation

$$\nu = \nu_1 \, e^{-\alpha_{1\nu}(\frac{t_e}{t_r})} + \nu_2 \, e^{-\alpha_{2\nu}(\frac{t_e}{t_r})} \tag{6}$$

where ν_1 and ν_2 is the initial and the final value of ν, respectively, and $\alpha_{1\nu}$ and $\alpha_{2\nu}$ are parameters which express the influence of hardening.

FRACTURING STRAIN

The fictituous crack model according to Hillerborg et al. [2] is based on the fact that fracture is localized to a thin zone. The fracture in that zone is modelled by a fictituous crack, whose width represents the total fracture in the zone. A smeared crack approach

based on the fictituous crack model has been proposed by Ottosen and Dahlblom [3], [4]. In the present model the concept is modified to consider development of properties during hardening of the concrete.

Crack development is assumed to start when the maximum principal stress reaches the tensile strength f_t, whose development is described as

$$f_t = \eta_t \, f_{t0} \tag{7}$$

where

$$\eta_t = \frac{\frac{a_{1t}}{(\frac{t_e}{t_r})^{b_{1E}}}}{1 + \frac{a_{1t}}{a_{2t}}\frac{t_e}{(\frac{t_e}{t_r})^{(b_{1t}-b_{2t})}}} \tag{8}$$

and f_{t0} is the tensile strength at 28 days.

The fracture energy G_F necessary to produce one unit area of crack is given by the integral

$$G_F = \int_0^{w_c} \bar{\sigma}_{11} \, dw_{11} \tag{9}$$

where $\bar{\sigma}_{11}$ is the stress normal to the crack plane, expressed in a local coordinate system, w_{11} is the crack width, and w_c is the crack width when $\bar{\sigma}_{11}$ has dropped to zero. According to experimental results by Petersson [5], the fracture energy G_F of hardening concrete develops proportional to the elastic modulus E. Thus, the fracture energy G_F may be described as

$$G_F = \eta_E \, G_{F0} \tag{10}$$

where G_{F0} is the fracture energy at 28 days.

In the present model a linear relation between $\bar{\sigma}_{11}$ and w_{11} is assumed, i.e.

$$\bar{\sigma}_{11} = f_t + \frac{f_t^2}{2G_F} \, w_{11} \tag{11}$$

The mean fracturing strain $\bar{\epsilon}^f_{11}$ in some region which includes the crack is defined

$$\bar{\epsilon}^f_{11} = \frac{w_{11}}{L_1} \tag{12}$$

where L_1 is an equivalent length related to the size and shape of the finite element where the crack develops. In the present work the equivalent length is defined as in Ref. [4].

Crack development will reduce the ability to transfer shear stresses across the crack plane. In the analysis of fracture it is important to use a reasonable expression for the shear behaviour. In Ref. [4], the shear displacement was assumed to be proportional to the shear stress and to the crack width. To avoid having a non–symmetric system of equations, it is in the present work instead assumed that the rate of the shear displacement is proportional to the rate of the shear stress and to the crack width, i.e.

$$\dot{w}_{12} = \frac{w_{11}}{G_S} \dot{\sigma}_{12} \tag{13}$$

where G_S is the so–called slip modulus, which may be assumed to develop during hardening in the same way as the elastic modulus, i.e.

$$G_S = \eta_E \, G_{S0} \tag{14}$$

where G_{S0} is the slip modulus at 28 days.

As in the case of fracture normal to the crack plane, a fracturing strain component is defined for shear displacement. The fracturing shear strain is defined by

$$\bar{\epsilon}^f_{12} = \frac{1}{2}\left(\frac{w_{12}}{L_1} + \frac{w_{21}}{L_2}\right) \tag{15}$$

STRESS–STRAIN RELATION

The strain rate $\dot{\underset{\sim}{\epsilon}}$ is assumed to be the sum of the elastic strain rate and the fracturing strain rate, as described above, i.e.

$$\dot{\epsilon}_{ij} = \dot{\epsilon}^e_{ij} + \dot{\epsilon}^f_{ij} \tag{16}$$

Substitution of the above expressions for $\dot{\underset{\sim}{\epsilon}}^e$ and $\dot{\underset{\sim}{\epsilon}}^f$, expressed in a global coordinate system, into Eq. (16) yields a relation between $\dot{\underset{\sim}{\sigma}}$ and $\dot{\underset{\sim}{\epsilon}}$ which can be expressed as

$$\dot{\sigma}_{ij} = D_{ijkm} \, \dot{\epsilon}_{km} \tag{17}$$

FINITE ELEMENT RESULTS

The theory proposed has been implemented into a finite element program. Results from simulations of the behaviour of the concrete tension specimen are shown in Fig. 1(a). The geometry of the specimen is the same as that of the specimens used in tests by Petersson [6]. Plane stress conditions are assumed and, owing to symmetry, only one quarter of the specimen is analysed. The specimen is analysed using an eight–node isoparametric element and the mesh shown in Fig. 1(b). The analysis simulates a tensile test where the specimen is subjected to an increasing vertical displacement. The following material parameters are adopted: $E_0 = 40.0$ GPa, $a_{1E} = 1.0 \cdot 10^7$, $b_{1E} = 4.0$, $a_{2E} = 1.0$, $b_{2E} = 0.1$, $\nu_1 = 0.5$, $\nu_2 = 0.25$, $\alpha_{1\nu} = 150.0$, $\alpha_{2\nu} = 40.0$, $f_{t0} = 4.0$ MPa, $a_{1t} = 1.0 \cdot 10^5$, $b_{1t} = 3.0$, $a_{2t} = 1.0$, $b_1 t = 0.14$, $G_{F0} = 100.0$ N/m and $G_{S0} = 4.0$ MPa.

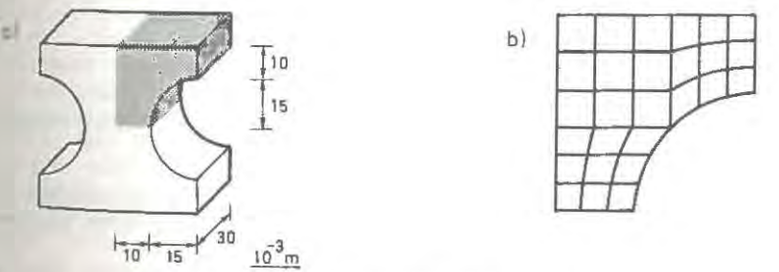

Figure 1.(a) Specimen studied; (b) finite element mesh

In Fig. 2 the total vertical force on the specimen is shown as a function of the vertical displacement for simulations at age 12 h and 672 h, respectively. The area under the curves divided by the cross sectional area at the crack plane is, for the two simulations, 40.1 N/m and 98.1 N/m, respectively, which is very close to the values of the fracture energy, i.e. 40.0 N/m and 100.0 N/m, respectively.

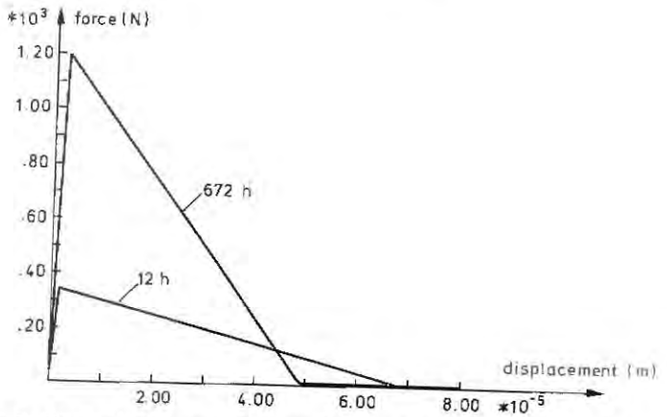

Figure 2. Force–displacement curves for simulations at 12 h and 672 h

CONCLUSIONS

A material model for hardening concrete is proposed. Fracture is modelled using a smeared approach based on the fictitious crack model of Hillerborg et al. [2]. The concept proposed by Ottosen and Dahlblom [3], [4] is modified to consider development of properties during hardening of the concrete. Finite element simulation of a concrete tension specimen demonstrates use of the theory.

REFERENCES

1. Byfors, J., Plain concrete at early ages, Swedish Cement and Concrete Research Institute, Fo3:80, Stockholm, 1980

2. Hillerborg, A., Modeer, M. and Petersson, P.–E., Analysis of crack formation and crack growth in concrete by means of fracture mechanics and finite elements, Cement and Concrete Research, Vol. 6, pp. 773–782, 1976

3. Ottosen, N.S. and Dahlblom, O., Smeared crack analysis using a nonlinear fracture model for concrete, In Numerical methods for non–linear problems, Vol. 3, Edited by C. Taylor et.al. Pineridge Press, Swansea, 1986, pp. 363–376

4. Dahlblom, O. and Ottosen, N.S., Smeared crack analysis using generalized fictitious crack model, Journal of Engineering Mechanics, Vol. 116, No. 1, January 1990, pp. 55–76

5. Petersson, P.–E., Crack growth and development of fracture zones in plain concrete and similar materials, Report TVBM–1006, Lund Institute of Technology, Division of Building Materials, Lund, 1981

INFLUENCE OF TRANSVERSE COMPRESSION ON MODE I FRACTURE OF CONCRETE

RAVINDRA GETTU, MARCEL O.F. OLIVEIRA*, IGNACIO CAROL and ANTONIO AGUADO

Technical University of Catalunya, ETSECCPB-UPC,
Campus Nord, Gran Capitán s/n, E-08034 Barcelona, SPAIN

ABSTRACT

Tensile strength and fracture resistance can be significantly reduced by transverse compression. Under compressive loads, considerable distributed cracking occurs almost parallel to the loading. An analysis using the microplane constitutive model also simulates this satisfactorily. The cracks induced by the previously applied transverse compression propagate and cause a decrease in tensile strength. Results of tests on high-strength concrete show losses of up to 25%. It is demonstrated that the loading history is important in fracture analysis. It also appears that damage distribution in structures can be deduced using multi-axial constitutive models and used in subsequent fracture analysis after the onset of localized cracking.

INTRODUCTION

The importance of damage (microcrack) orientation is significant in structures subjected to multi-axial loading [1]. In the present work, attention is drawn to the effect of transverse compression on tensile fracture. Several researchers have shown that compression results in progressive distributed microcracking in concrete. Shah and Sankar [2] concluded from a petrographical study that, with increase in load, microcracks initiate and grow with a bias towards the compression, and are oriented at about 10° with the loading direction near the peak load. Through scanning electron microscopy, Attiogbe and Darwin [3] obtained three-dimensional crack distributions in cement paste and mortar which also showed that cracking was skewed towards the direction of applied compression. This anisotropic microcracking under compression would obviously decrease the fracture resistance when tensile loading is later imposed. The critical case is when the cracks are transverse (or orthogonal) to the tensile loading.

Constitutive models of the triaxial behavior of concrete can provide information on the distribution of damage. Here, the microplane model is used to determine possible crack orientations under compression. Results of an investigation of the loss in tensile strength in high-strength concrete previously subjected to transverse compression are also presented.

---

*On leave from Universidade Federal de Espirito Santo, UFES/CAPES, Brazil

MICROMECHANICS OF COMPRESSION ACCORDING TO THE MICROPLANE MODEL

Bažant and co-workers [4,5,6] have proposed microplane models for the response of concrete and other quasi-brittle materials. Behavior under several types of loading, including compression, has been satisfactorily modeled. Stress-strain relations are prescribed for a general arbitrarily oriented plane within the material (called the microplane). By integrating over several such independent planes that are uniformly oriented spatially around a point, the constitutive (macroscopic) behavior of that point is obtained.

The model used in the present study [5,6] employs 56 microplanes distributed over the surface of a sphere. Also, a kinematic constraint is assumed whereby the microplane strains are the resolved components of the macro-strains. The state of each microplane is characterized by normal deviatoric, volumetric and shear strains. The form of the volumetric compression stress-strain relation on the microplane is shown in Fig. 1a. Relations for volumetric tension, deviatoric compression and tension, and tangential shear are of the form shown in Fig. 1b.

Using the model parameters obtained by Bažant and Prat [5] from fitting the uniaxial compression data of van Mier [1], the response of the microplanes were computed until just after the peak load. For axisymmetric loading such as this, the 5 microplanes that are independent are shown in Fig. 2a which represents one-eighth of the sphere containing the 56 microplanes. The angles ϑ (see Fig. 2b) between their normals and the loading direction (x-axis) are 21°(denoted A in Fig. 2a), 46°(B), 55°(C), 75°(D) and 79°(E). The computed normal strains (sum of the volumetric and deviatoric components) along these directions are shown in Fig. 3a, as a function of the compressive stress. Each circled point on the curves corresponds to a point on the uniaxial (macroscopic) compressive stress-strain diagram in Fig. 3b. Note that the compressive strength of the concrete is about 40 MPa, and the specimen is a 100 mm cube.

When the normal strain is tensile, it comprises contributions from the elastic strain and the widths of the cracks which are parallel to the microplane [4]. From Fig. 3a, it can be seen that the normal strains of D and E are always tensile. It appears, therefore, that the uniaxial compression produces considerable cracking even before the peak, and these cracks are generally oriented at 0° to 30° with the loading direction. This compares satisfactorily with the experimental results mentioned earlier.

EFFECT OF COMPRESSION ON SUBSEQUENT TENSILE FRACTURE

The microcracking caused by previously applied compressive loads ("pre-compression") significantly decreases the tensile strength. Tinić and Brühwiler [7] observed that direct tensile strength, measured in the same direction as the pre-compression, decreases by 10-25%. Delibes [8] determined that transverse, rather than uni-directional, pre-compression was more damaging to the tensile strength. He obtained losses of up to 40% in splitting strength, which increased with increase in magnitude and duration of the pre-compression. Both investigations were conducted on cylinders of normal strength concrete.

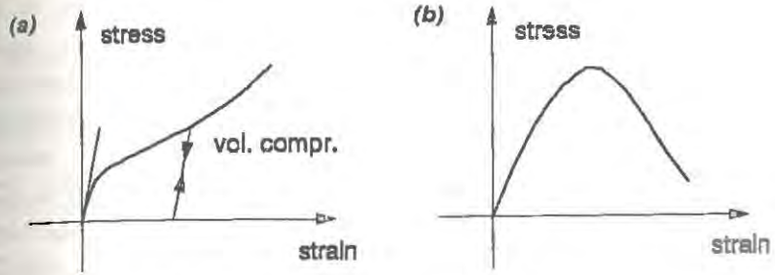

Figure 1. Forms of the microplane stress-strain relations

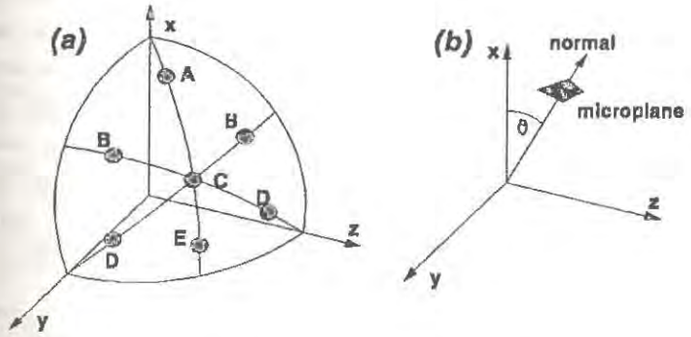

Figure 2. Microplane orientation

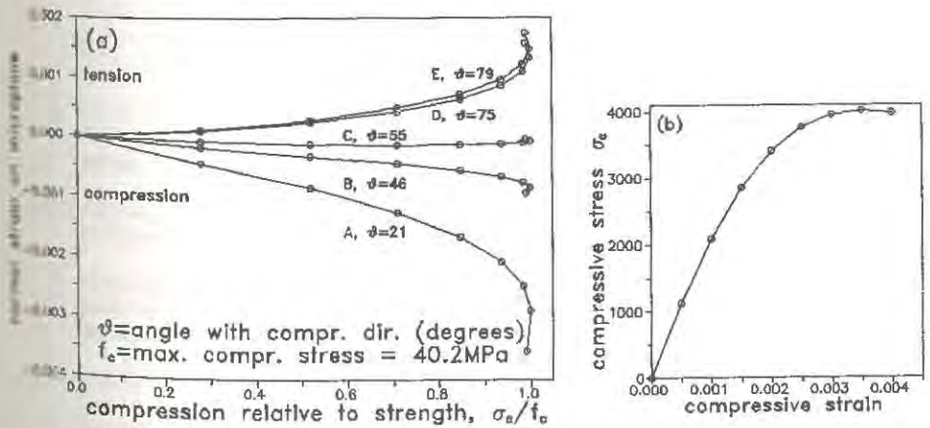

Figure 3. Micro- and macro-behavior under uniaxial compression

Recently Oliveira [9] performed tests on high-strength concrete at the Technical University of Catalunya to further study the loss in tensile strength due to pre-compression. The specimens were standard 100 mm cubes, and all tests were conducted 28 days after casting. The maximum compressive strength f_c was 78.4 MPa (the cylinder strength was 62.5 MPa). Uniform pre-compression (stress) σ_c ranging from $0.25f_c$ to $0.85f_c$ was applied on faces normal to the casting direction, and maintained for 900 seconds. After unloading, the specimen was rotated 90° about the casting direction, and split along a plane normal to the casting direction and passing through the center of the cube (see inset of Fig. 4). The splitting tensile strength σ_t was computed as $2P/\pi L^2$, where P = splitting load and L = side of cube. The tensile strength decreases significantly with σ_c (see Fig. 4; note that the line in the plot joins the average loss at each σ_c-level). The maximum loss is about 25%. The lower losses in high-strength concrete are probably due to the presence of fewer flaws in the "virgin" material. Also, it has been observed that the damage in high-strength concrete is characteristically less than in normal concrete [10]. Note that the virgin splitting strength f_t is 5.43 MPa ($f_t=\sigma_t$, when $\sigma_c=0$).

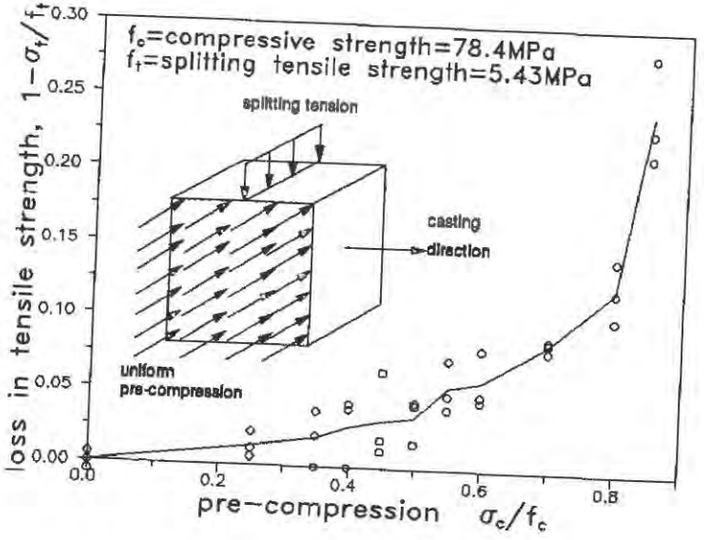

Figure 4. Loss in tensile strength due to transverse compression

CONCLUSIONS

A reasonable idea of the damage orientation can be obtained from general multi-axial constitutive models. The microplane analysis shows that tensile microcracking occurs almost parallel to the applied compression. When such damaged concrete is later subjected to tension in an orthogonal direction the fracture resistance decreases considerably. Tests of high-strength concrete show losses in tensile strength of up to 25%, which is, however, less than in normal concrete. It is concluded that the multi-axial loading history should be taken into account in fracture analysis. Until the onset of localized cracking, the material response can be simulated in structural analysis through constitutive models such as the microplane model. The resulting damage distribution, or in general the micromechanical state, can be used in the nonlinear fracture analysis that followed.

REFERENCES

1. van Mier, J.G.M., Influence of damage orientation distribution on the multiaxial stress strain behaviour of concrete. Cem. Concr. Res., 1985, 15, 849-862.

2. Shah, S.P. and Sankar, R., Internal cracking and strain-softening response of concrete under uniaxial compression. ACI Mater. J., 1987, 84, 200-212.

3. Attiogbe, E.K. and Darwin, D., Submicrocracking in cement paste and mortar. ACI Mater. J., 1987, 84, 491-500.

4. Bažant, Z.P. and Oh, B.H., Microplane model for progressive fracture of concrete and rock. J. Engng. Mech., 1985, 111, 559-582.

5. Bažant, Z.P. and Prat, P.C., Microplane model for brittle-plastic material: I. Theory, II. Verification. J. Engng. Mech., 1988, 114, 1672-1702.

6. Carol, I., Bažant, Z.P. and Prat, P.C., New explicit microplane model for concrete: Theoretical aspects and unified implementation for constitutive verification and FE analysis. Report GT015, School of Civil Engrg., Tech. Univ. of Catalunya, Barcelona, Spain, 1990; also Int. J. Solids Struct., 1992, in press.

7. Tiniç, C. and Brühwiler, E., Effect of compressive loads on the tensile strength of concrete at high strain rates. Int. J. Cem. Comp. Lightweight Concr., 1985, 7, 103-108.

8. Delibes Liniers, A., Microcracking of concrete under compression and its influence on tensile strength. Mater. Struc., 1987, 20, 111-116.

9. Oliveira, M.O.F., Fatigue and microcracking in high strength concretes. Doctoral Thesis, School of Civil Engrg., Tech. Univ. of Catalunya, Barcelona, Spain, 1992, in press.

10. Smadi, M.M. and Slate, F.O., Microcracking of high and normal strength concretes under short- and long-term loadings. ACI Mater. J., 1989, 86, 117-127.

APPLYING NONLOCAL SMEARED CRACK CONCEPTS TO MODELING CONCRETE FRACTURE

JOHN BOLANDER Jr. and HIROSHI HIKOSAKA
Department of Civil Engineering
Kyushu University, Fukuoka 812, Japan

ABSTRACT

A nonlocal smeared-cracking finite element model is used to simulate tensile fracture in mortar notched-beam specimens under three-point loading. In the presence of high strain concentrations (e.g. near the pre-notch tip), standard nonlocal averaging causes overstrength and excess energy consumption to occur at nearby sampling points. Such difficulties are treated using a variable weighting function for nonlocal spatial integration. The variance of the weighting function is prescribed in a manner which promotes natural process zone formation and proper energy consumption in the notch vicinity.

INTRODUCTION

A nonlocal smeared-cracking finite element model [1] is used to simulate tensile fracture in mortar notched-beam specimens under three-point loading. For a local smeared-cracking model, damage initiates at a sampling point when the maximum principal tensile strain violates a limiting value. Typically, a damage parameter ω would be used to control the softening of the material normal to the initial crack plane (Fig. 1). However, for the model utilized in this study, nonlocal strain is used to define nonlocal damage $\overline{\omega}$, which in turn controls material softening at the point in question. See [1, 2] for details and further references.

Experience shows this type of nonlocal model is able to represent the essential features of fracture through the center portion of the ligament [3]. This paper focuses upon complications which occur near the notch tip and proposes a first-aid treatment for obtaining both natural process zone formation and proper energy consumption in this vicinity.

TEST SPECIMENS AND FINITE ELEMENT MODEL

Several series of mortar notched-beam specimens were tested in a separate study, as reported in [4]. The specimens considered here are representative from the M1/8 series, which had dimensions and boundary conditions as shown in Fig. 2a.

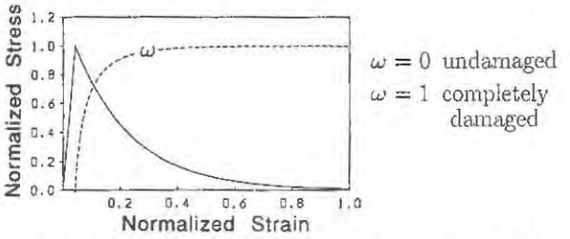

Figure 1. Stress-strain relation normal to crack plane.

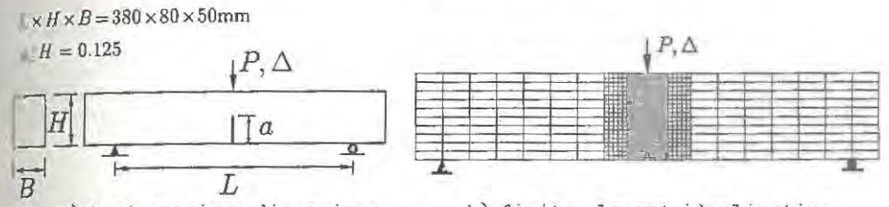

a) test specimen dimensions b) finite element idealization

Figure 2. Mortar notched-beam specimen under three-point loading.

The M1/8 series indicated an average fracture energy G_f = 53 J/m^2 for cracks propagating through the center portion of the ligament. The mortar used in the specimens had a maximum aggregate size $d_a \approx 3$mm. Other pertinent parameters were taken from direct tension testing of a similar mortar: direct tensile strength $f_t = 4.5 \pm 0.5$ MPa; and Young's modulus $E = 27800 \pm 600$ MPa.

The finite element idealization of the test specimen and boundary conditions is shown in Fig. 2b. Four-node elements composed of four CST elements are used. A rather fine mesh is required for capturing strain and damage variance within the fracture region. The pre-notch is modeled by a one-element wide (i.e. 2mm) gap at midspan. The dimension of the damage-representative volume is set as $l = 3d_a$.

STRESS-STRAIN RESPONSE LOCAL TO FRACTURE PROCESS

Typical behavior within the center portion of the ligament is shown in Fig. 3a. Sampling points incur varying degrees of damage depending on their location relative to the center of the process zone. Points near the center of the zone continue to load, consume the most energy, and eventually reach a completely damaged state modeling material separation. Points to the sides unload sooner and consume progressively less energy with increasing distance from the center of the zone. Sampling points E and F (responses not plotted) also become damaged and consume minor amounts of energy. These results [3] are supported, at least in a qualitative sense, by high-resolution measurements of strain variance over the fracture region [5].

Due to strain concentration near the notch tip, nonlocal strains computed for sampling point G (Fig. 3b) are significantly less than the corresponding local strain at the same point. Since nonlocal damage $\overline{\omega}$, and consequently stress release normal to the crack plane, is controlled by nonlocal strain, the resulting local stress-strain relation greatly overestimates strength and energy capacity (curve G). For sampling points H through L, closing stresses behind the damage front blunt this singularity.

By point J, local and nonlocal elastic strains are roughly equal and damage therefore initiates near f_t, which is typical throughout the center portion of the ligament.

IMPROVING THE RESPONSE NEAR THE NOTCH TIP

To promote proper energy consumption near the notch tip, one is tempted to modify the traditional fracture parameters, f_t and G_f, in this vicinity. However, such an approach by itself has limited physical basis. Alternatively, we choose to modify the weighting function $\alpha(x)$ for nonlocal spatial integration; x is a spatial coordinate relative to the point in question. Micromechanics arguements indicate that $\alpha(x)$ is not necessarily constant, but generally varies according to the surrounding stress tensor field and damage characteristics [2].

The approach presented here modifies $\alpha(x)$ *a priori* as shown in Fig. 3. The normal distribution (1-D case shown for simplicity) defined by characteristic length l is gradually transitioned to a normal distribution defined by length l^* as we approach the notch tip from a given radial direction.

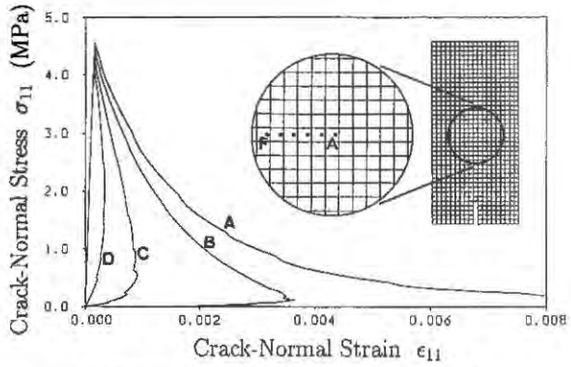

a) through mid-portion of ligament

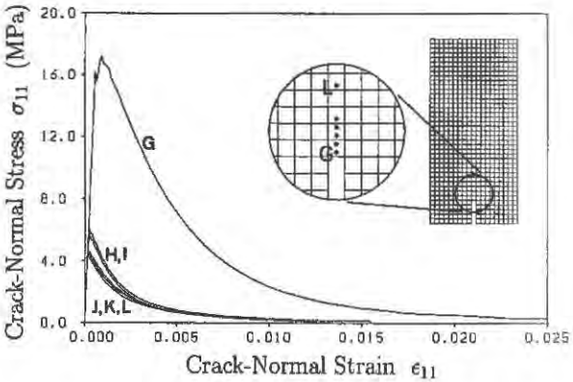

b) near notch tip

Figure 3. Local stress-strain response.

An elipse is used to define the limits within which the weighting function is contracted; the integration point just above the notch tip coincides with the elipse focal point as shown in the figure. The eliptical shape is chosen merely because of its simplicity and in order to bias the transition region in the direction of fracture propagation. Input to the analysis requires the dimension l^* and the transition length l_t, which were set to $l/3$ and l, respectively.

Since the material model assumes secant branch unloading, the incremental energy consumed at a given sampling point can be approximated in a simple manner [3]. Fig. 5 shows contours of energy consumption rate obtained by both standard and modified weighting near the notch tip. By standard weighting, we mean that $\alpha(x)$ does not vary between sampling points. Both planar contours are normalized within each load step) and perspective view contours (energy per unit displacement at the load point) are given. Load stages correspond to prescribed displacement values, as indicated along one of the response curves in Fig. 6.

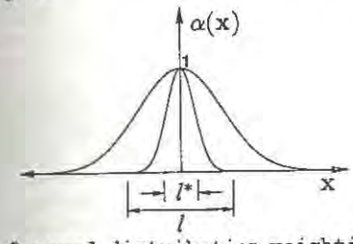

a) 1-D normal distribution weighting

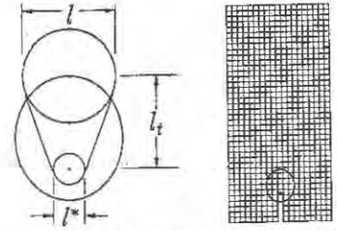

b) transition region around notch tip

Figure 4. Varying weighting function $\alpha(x)$ near the notch tip.

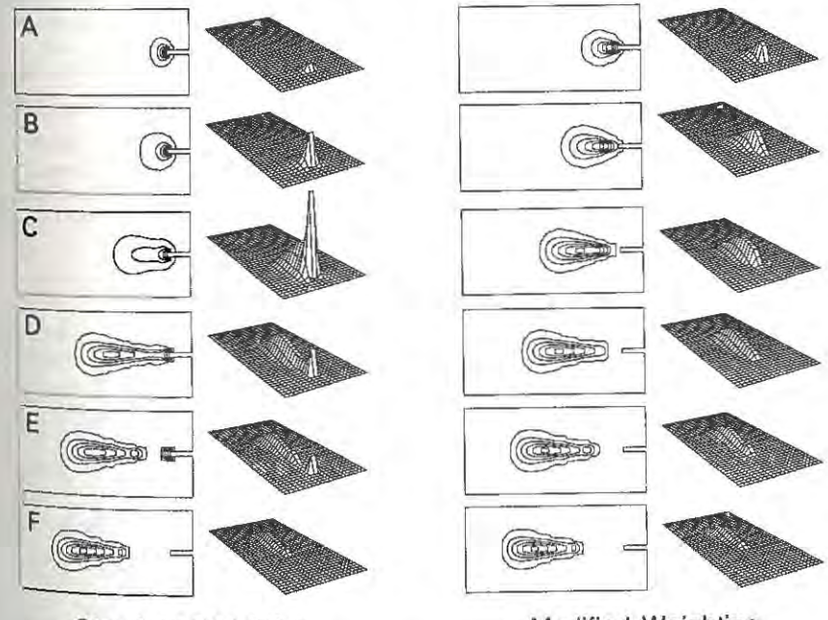

Figure 5. Smoothed energy consumption rate.

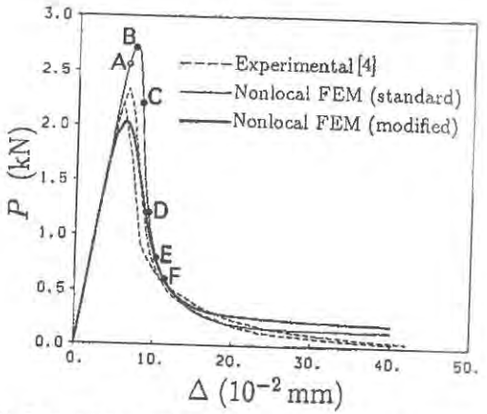

Figure 6. Reactive force versus controlled displacement.

Results from standard weighting show an excess amount of energy being consumed near the notch tip; this not only inhibits natural process zone formation, but also causes the global load-deflection response to be too strong. On the other hand, modified weighting promotes natural process zone formation. That is, after peak load the process zone detaches from the notch tip and thereafter becomes nearly constant in size. Peak stress at sampling point G is still rather high, reaching about $2f_t$, but this may be reasonable for a small volume under high strain gradient [7].

Modifying the weighting function near the notch-tip also improves the quantitative simulation of energy consumption during crack propagation. Fig. 7 compares the numerical results with the test results for the M1/8 series. Each • mark represents the results for one test specimen, as described in [4], and the dashed line indicates a sort of best fit to these test data points. The damage front associated with $\bar{\omega} = 0.99$ is used to define effective crack length in the numerical model.

The numerical results agree well with the experimental data, particularly with respect to: 1) initial energy consumed prior to crack formation, 2) lower energy consumption rate just after crack formation, and 3) nearly constant energy consumption rate over the ligament mid-length. Better fit

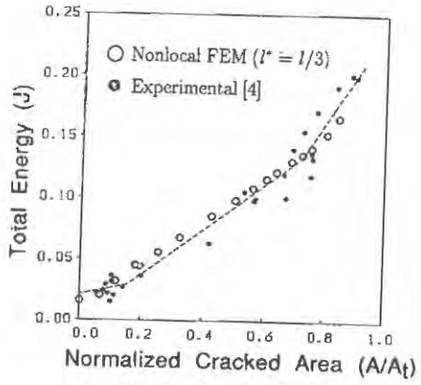

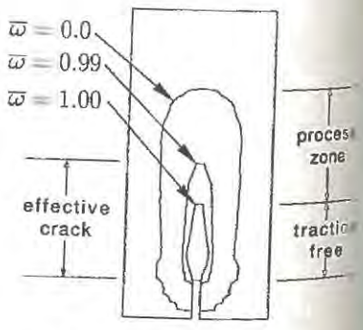

Figure 7. Energy rate variance during crack propagation.

the energy rate or global response can be achieved by adjusting the input parameters, l^* and l_t. However, obtaining a precise fit to the test results has not been pursued here due to numerous uncertainties in the analysis. Effective crack lengths defined by the traction free condition, $\bar{\omega} = 1.00$, provide results similar to those shown in Fig. 7, except displaced upward by about 0.015 J.

CONCLUDING REMARKS

A nonlocal smeared-cracking finite element model is used to simulate tensile fracture in mortar notched-beam specimens. The weighting function $\alpha(x)$ for nonlocal spatial integration is varied near the notch tip to promote natural process zone formation and proper energy consumption in that vicinity. Nice correlation has been obtained with respect to test results provided by other researchers. However, our phenomenological approach to modifying $\alpha(x)$, while helpful in illustrating certain aspects of the problem, is not adequate for general application (i.e. for situations of differing geometry, material properties, and finite element idealization.) Physical approaches, based on micromechanics considerations, appear necessary for modifying nonlocal weighting according to the surrounding stress tensor field and damage characteristics [2]. Finally, it remains to be seen what implications these concerns have towards practical analyses of larger, more complicated structures.

ACKNOWLEDGMENTS

Funding received by the first author through a fellowship from the Japan Society for the Promotion of Science is greatly appreciated. Financial support has also been received through a Grant-in-Aid for Scientific Research from the Japanese Ministry of Education, Science and Culture.

REFERENCES

[1] Bazant, Z P, and Lin, F B, Nonlocal Smeared Cracking Model for Concrete Fracture. J. Struct. Div., ASCE, 114(11), 1988, pp. 2493-2510.

[2] Bazant, Z P, Why Continuum Damage is Nonlocal: Micromechanics Arguements. J. Eng. Mech. Div., ASCE, 117(5), 1991, pp. 1070-1087.

[3] Bolander, J, and Hikosaka, H, Characterizing the Fracture Process in Concrete Using Nonlocal Continuum FE Modeling. In Theor. and Appl. Mech., Vol. 40, eds. Japan NCTAM, Science Council of Japan, Tokyo Univ. Press, Tokyo, 1991, pp. 319-326.

[4] Bascoul, A, Kharchi, F, and Maso, J C, Concerning the Measurement of the Fracture Energy of a Micro-Concrete According to the Crack Growth in a Three Point Bending Tests on Notched Beams. In SEM/RILEM Int. Conf. on Fracture of Concrete and Rock, eds. S P Shah and S E Swartz, Springer-Verlag, New York, 1987, pp. 396-408.

[5] Cedolin, L, Dei Poli, S, and Iori, I, Tensile Behavior of Concrete. J. Eng. Mech. Div., ASCE, 113(3), 1987, pp. 431-449.

[6] Bascoul, A, Ollivier, J P, and Poushanchi, M, Stable Microcracking of Concrete Subjected to Tensile Strain Gradient. Cem. and Conc. Res., Vol. 19, 1989, pp. 81-88.

[7] Bascoul, A, and Maso, J C, Microcracking and Cracking Limit State as Functions of Strain Gradients for Concrete. Cem. and Conc. Res., Vol. 17, 1987, pp. 661-672.

COHESIVE CRACK MODEL AND A TWO PARAMETER FRACTURE CRITERION

NAISONG WANG
Dept. of Civil Engineering, The Univ. of Calgary
Calgary, Alberta, T2N 1N4, CANADA

ABSTRACT

A cohesive crack model has been derived for describing the strain-softening behaviour of reinforced concrete structures, and a two-parameter fracture criterion has been suggested in defining the failure of the structures. In corporation the cohesive model with this criterion, the whole fracture process of concrete structures can be described. The criterion uses concrete tensile strength f_{ct} and a weighted total average crack width G^*_f as the two parameters. The parameters reflect both strength and energy. It has been found that the critical energy release rate G_f cannot correctly describe the fracture behaviour of concrete structures due to the initial flaws and micro-cracking features of the concrete material. While f_{ct} and G^*_f have been found to be good parameters in describing the fracture behaviour of concrete structures. The model has successfully been used in bond strength prediction of reinforced concrete members.

INTRODUCTION

The study of fracture of concrete structures has been very active due to its importance in concrete engineering. Since concrete is a compound product which is brittle in tension and tough in compression, the theory of fracture mechanics developed for metal cannot be directly used for concrete. Experimental studies have shown that after cracking, the tensile strength of the concrete will not be lost suddenly [1]. The behaviour of concrete after cracking is described by strain softening effect.

Recent experimental research has been directed to the study of the post-peak behaviour of cementitious materials, and new damage models have been proposed. Now it is believed that instead of stress-strain relation, the stress-crack width relation is a material property for cracked cementitious materials. A general representation of stress-crack width relation was derived by [2]. Our study shows that the stress-strain relation is related to a characteristic length and can be derived from stress-crack width relation.

Fracture of concrete in almost all cases is the direct result of the failure in tension. Larrard et al [3] used K_{1c} and G_{1c} as concrete fracture criterion. Shah mentioned in [4] that

a single parameter criterion was not suitable for concrete fracture, and he suggested a two parameter criterion by using K_{1c} and CTOCc (Critical Crack Tip Opening Displacement) as the two parameters. With the increase use of high strength concrete, a fracture criterion which can be used for both normal and high strength concrete is desired. A two parameter fracture criterion is development for this purpose in this paper.

COHESIVE MODEL AND THE FRACTURE CRITERION

It is found that after cracking, the tensile stress can still be transmitted cross the crack so long as the crack width is small. This crack is defined as a cohesive crack. The tensile stress-crack width relation is described by equation (1).

$$(\sigma_c + h)(w + k) = m \tag{1}$$

where, σ_c is the tensile stress, w is the average crack width, and h, k and m are constants which are determined from the experimental tests. The critical fracture energy release rate G_f can be obtained by the integral shown in equation (2).

$$G_f = \int_0^{w_c} \sigma_c \, dw \tag{2}$$

where, w_c is the critical average crack width. If the crack width is large, the tensile stress cannot be transmitted through the crack further. This crack is defined as an open crack in this study. Crack will initiate when the maximum principal tensile stress in concrete reaches its tensile strength f_{ct}, then the stress decreases following the descending branch of the stress-strain curve which can be derived from equation (1) incorporated with a characteristic length l_c (5). Since defining w_c, the critical average crack width, is difficult, an alternative parameter is used in the study. Fig.1 shows the tensile stress-average crack width curve normalized by concrete tensile strength.

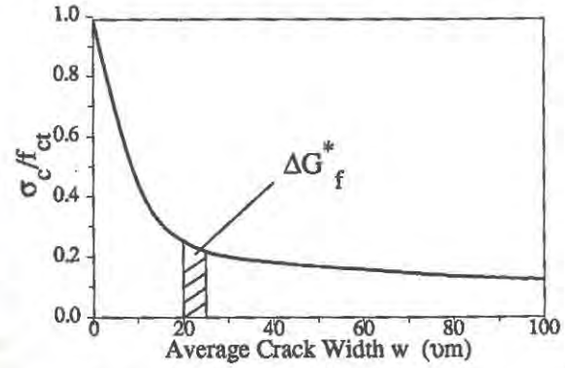

Fig.1 The relation of concrete tensile stress with average crack width

The area under the curve in Fig.1 represents the G_f multiplied by f_{ct}, defining as G^*_f here. The unit of G^*_f is the length, and its geometrical meaning is the area under the σ_c-w curve, and the physical meaning is the total average crack width weighted by the σ_c-w curve. If both G_{fc} and f_{ct} are determined from experimental tests, then a critical value of G^*_f defining as G^*_{fc} can be obtained. Once the G^*_f exceeds the G^*_{fc}, the tensile strength of that part of the crack will be lost and the crack is defined as an open crack. Thus with the f_{ct} and G^*_f the whole fracture process of concrete in tension can be described. This two-parameter criterion reflects both strength and energy and is a better one in concrete fracture prediction.

Fig.2 shows the G^*_f versus f'_c for the concrete compressive strength varying from 20 MPa to 100 MPa. The G^*_f decreases with the increase of f'_c indicating the higher the concrete compressive strength, the more brittle of the material. If G_f is used instead of G^*_f, an ascending curve will be obtained which indicates the wrong conclusion that the higher the f'_c is, the tougher the material will be. This graph also shows that the two-parameter fracture criterion suggested here is a general one which can be used for high strength concrete too.

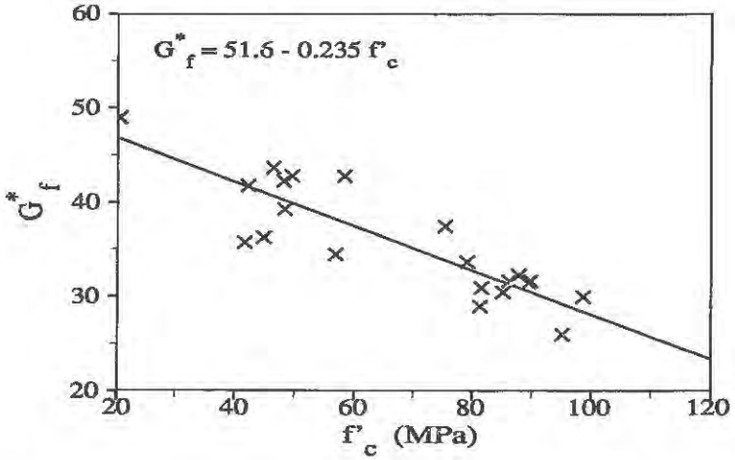

Figure 2. Normalized energy release rate G^*_f as a function of concrete compressive strength

APPLICATIONS

The cohesive model and the criterion developed above have been used in the bond strength prediction for the reinforced concrete members. The edge action of reinforcing bars on concrete is simulated by a uniform swollen of the bar. Tensile stress distributions are obtained for different fracture stages. Figure 3 shows the distribution in the -Y direction corresponding to three fracture stages. It shows that with the growth of the crack, the peak stress shifts from the interface at uncracked stage, to the outer edge of the concrete member at fully cracked stage. The bond strength can be obtained by the tensile stress volume along the development length.

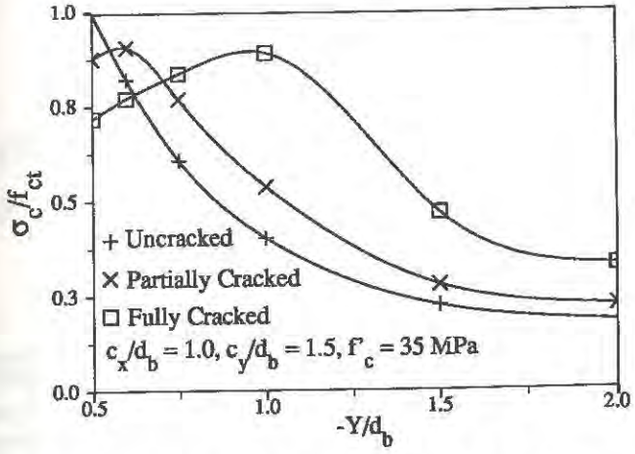

Figure 3. Tensile stress distribution corresponding to the three fracture stages

CONCLUSIONS

A cohesive model and a two parameter fracture criterion have been derived for concrete fracture prediction. The model has been used for bond strength prediction of reinforced concrete members. The criterion derived here is suitable for both normal and high strength concrete. As it reflects strength and energy, it seems to be a better criterion and can be used in the general fracture analysis of concrete structures.

REFERENCES

1. Gopalaratnam, V.S. and Shah, S.P., Softening response of plain concrete in direct tension. ACI Journal, 1985, 82, pp. 310-323.

2. Duda, H. and König, G, Rheological material model for the stress-crack width relation of concrete under monotonic and cyclic tension. ACI Material Journal, 1991, 88, pp. 278-287.

3. de Larrard, F., Boulay, C., and Rossi, P., Fracture toughness of high-strength concretes. Proceedings of the First International Symposium on Utilization of High-Strength Concrete, 1987, Norway, pp. 215-223.

4. Shah, P.S., Fracture toughness for high-strength concrete. ACI Material Journal, 1990, 87, pp. 260-265.

5. Loov, R.E and Wang, N, Bond strength and behaviour predicted by a cohesive crack model. Proceedings of CSCE Annual Conference, 1991, Vancouver, Canada, pp. 322-331.

S-FPZ MODEL FOR CONCRETE SEN SPECIMEN

Jung-Heum Yon and Neil M. Hawkins
Department of Civil Engineering, University of Illinois, Urbana, IL 61801
Albert S. Kobayashi
Department of Mechanical Engineering, University of Washington, Seattle, WA 98195

ABSTRACT

Material characteristics for a singular-fracture process zone (S-FPZ) model are determined from experimental results for a three-point bend test on a single-edge notched (SEN) specimen. That model is then used to predict the external load versus load-line displacement relationships of the same SEN specimen for crack-line and direct tensile loadings. A fully developed FPZ is predicted for three-point bend and crack-line loadings but unstable micro-crack propagation at the peak load is predicted for direct tensile loading. It is concluded that the optimum specimen for determining FPZ characteristics is an SEN specimen subjected to three-point bend loading and that boundary conditions affect significantly the validity of fracture results.

INTRODUCTION

The fracture criterion for the popular fictitious crack model (FCM) [1] is a maximum tensile stress at the crack tip equal to the tensile strength. For a direct tensile test that means failure occurs simultaneously with first cracking. That prediction is inconsistent with direct tension test results where careful measurements have shown significant stress concentrations at a crack tip, and slow crack growth, prior to the peak load [2]. With an S-FPZ model a behavior is predicted consistent with those direct tension test observations.

In this paper the physical meaning of the FPZ characteristics and procedures for calculating stress intensity factors (SIF) are explained first. Next, FPZ characteristics are determined from three-point bend results for an SEN specimen and then used to predict fracture behavior for the same SEN specimen for crack-line (wedge) and direct tensile loadings.

S-FPZ MODEL

Yon et al. [3] proposed an S-FPZ model for modelling the dynamic fracture behavior of concrete. The model has two parameters: a critical SIF (K_c) and an FPZ relationship. By contrast, the two-parameter model suggested by Jenq and Shah [4] involved a K_c at an effective crack tip and a critical crack tip opening displacement ($CTOD_c$).

In the S-FPZ model the micro-crack tip is defined as the average location, through the thickness, of the pre-existing bond cracks that start to propagate and the K_c is that for the average micro-crack tip location. Resistance behind the micro-crack tip is represented by a crack closure stress (CCS) which depends on the crack opening displacement (COD) as in customary nonsingular (NS-FPZ) model or the FCM.

If the material outside the FPZ is linear elastic and a discrete crack model is assumed for numerical analysis then, as shown in Figure 1, the effect of the singularity and the trailing FPZ can be treated theoretically using superposition. If the SIF of (a) is equal to or larger than zero, then it can be calculated by subtracting the SIF of (c) from that of (b). Thus, the NS-FPZ model is a special case of the S-FPZ model where the CCS on the micro-crack tip generates an SIF with the same magnitude but a negative value to that generated by the external load. An NS-FPZ model is appropriate for numerical analysis only if it has a plastic zone trailing the micro-crack tip as in the three-line segment model of Jeang et al. [5].

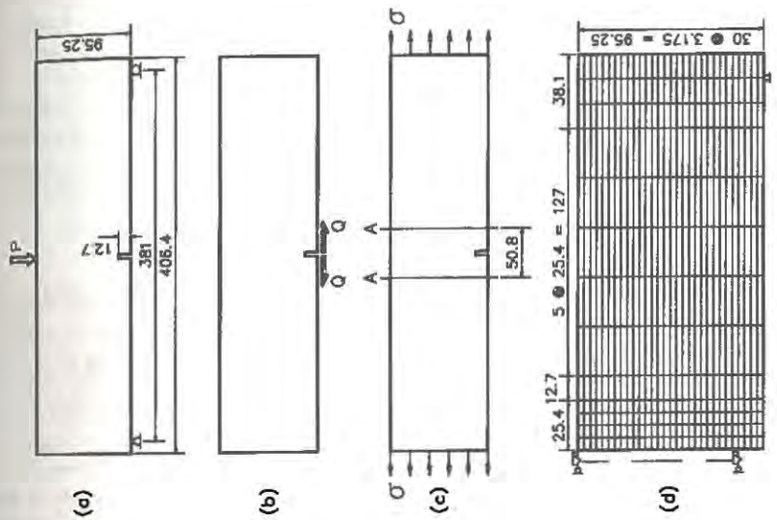

Figure 2. Specimen Geometry and Loading Conditions: (a) Three-Point Bend Loading; (b) Crack-Line Loading; (c) Direct Tensile Loading; and (d) Mesh Design

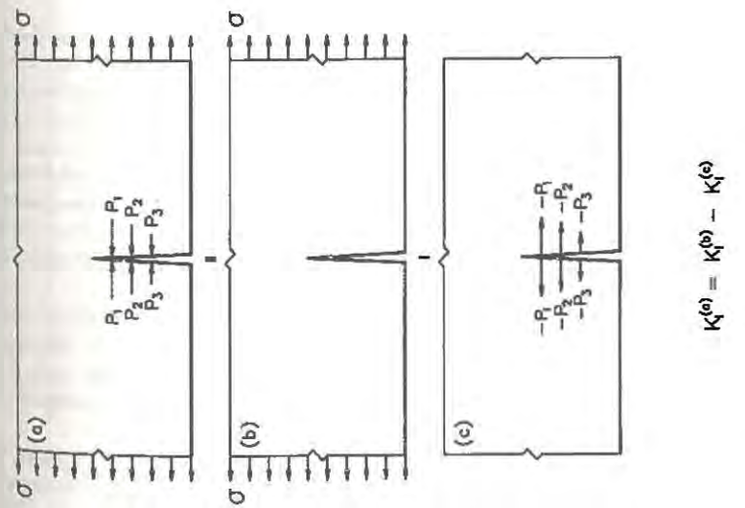

Figure 1. Illustration of Superposition Principle for Calculation of SIF in S-FPZ Model

DETERMINATION OF MATERIAL PROPERTIES

To determine appropriate material properties for a concrete SEN specimen, results for the three-point bend specimen shown in Figure 2 (a) [6] were analyzed using an S-FPZ model and the mesh shown in Figure 2 (d). The measured load versus load-line displacement relationship for that specimen is shown in Figure 3 with a solid line. The elastic modulus of the specimen was determined from the initial linearity of the load versus displacement relation. That relation deviated first from the measured relation at A. After A spring elements were inserted on the crack line to create non-linear behavior and the corresponding K_{Ic} was calculated using the superposition principle of Figure 1. The CCS-COD relationship was assumed to be bilinear and determined by trial-and-error matching of the predicted and experimental relations subsequent to A. The corresponding elastic modulus, K_{Ic}, fracture energy density (G_F) and CCS-COD relationship are shown in Figure 4.

ANALYTICAL RESULTS

Three-Point Bend Loading: The load versus displacement relation predicted using the computed material properties is shown in Figure 3 by solid points. At the maximum displacement of 0.20 *mm* (0.008 *in*) the micro-crack tip extended through 87 % of the beam depth. The load at the onset of micro-crack propagation was 69 % of the peak load (3.53 *kN* or 794 *lb*). Crack tip nodes were then released sequentially as the SIF at a node reached the critical value. The variations in micro- and macro-crack lengths with displacements are shown in Figure 5. At the peak load, B, the micro-crack extension was 31.75 *mm* (1.25 *in*) and between loads equal to 95 % of that load, the increase in micro-crack extension was 25.4 *mm* (1.0 *in*) or one third of the total micro-crack extension. Even though the peak load occurred at B, the fracture behavior, (crack extension rate and energy release rate), remained unchanged until C. However, after C and until D the load decreased rapidly with increasing displacements as the micro-crack extension rate also decreased. Then at a displacement of 0.11 *mm* (0.0043 *in*), D, the behavior again changed. The rate of decrease in external load with displacement decreased as the FPZ became fully developed. By contrast, for an NS-FPZ model there was no macro-cracking for this size of specimen [6].

Effectively the micro-crack extension rate increased continuously with increasing displacements until C. The micro-crack extension rate decreased significantly only after the external load also decreased markedly. At the onset of macro-crack (traction-free crack) propagation, the FPZ reached its maximum size of 57.2 *mm* (2.25 *in*). That size then decreased with increasing displacements because the macro-crack propagated faster than the micro-crack. The decreasing FPZ length resulted in decreasing stresses in both the tension and compression zones of the beam. The maximum stress at the top of the beam was always less than the concrete's compressive strength of 49.06 *MPa* (7,116 *psi*), consistent with the observation of no crushing at the loading point in the test. By contrast, the NS-FPZ model predicted a maximum stress greater than the concrete's compressive strength.

Crack-Line Loading: The load versus load-line displacement relationship predicted for the same SEN specimen for the crack-line loading, Figure 2 (b), is shown in Figure 6. Micro-crack propagation, A, started at 44 % of the peak load (4.39 *kN* or 988 *lb*). At the peak load, B, the micro-crack extension was 25.4 *mm* (1.0 *in*) and at the onset of macro-crack propagation, D, the maximum FPZ length was 63.5 *mm* (2.5 *in*).

Direct Tensile Loading: The predictions for direct tensile loading, Figure 2 (c), were very different to those for the other two analyses. As shown in Figure 6, at the onset of micro-crack propagation, A, the computed load was 85 % of the peak load (13.14 *kN* or 2,954 *lb*). In Figure 6, two relationships are shown, one for displacements input at the ends of the specimen and the other for displacements averaged over the 50.8 *mm* (2.0 *in*) length between sections A in Figure 2 (c). The peak load was 3.5 times, but the displacement was only 60 %, of those for three-point

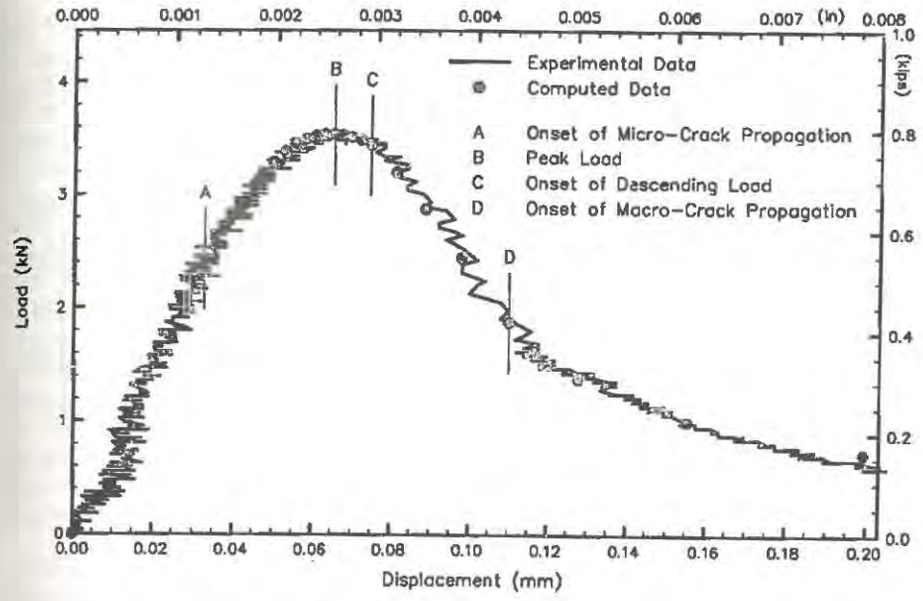

Figure 3. Measured and Computed Load versus Load-Line Displacement Relations for Three-Point Bend Loading

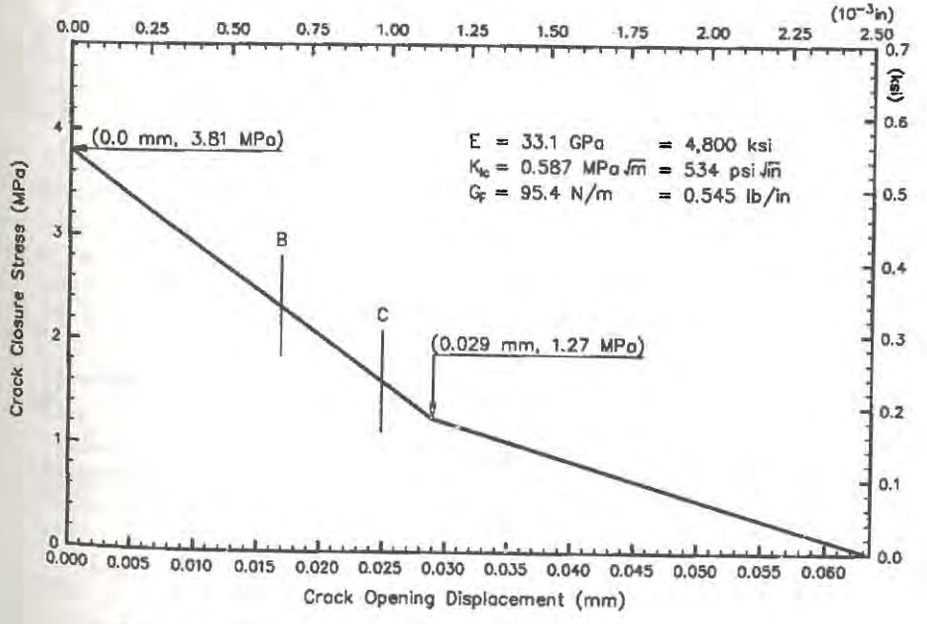

Figure 4. CCS versus COD Relation Used for Numerical Analysis

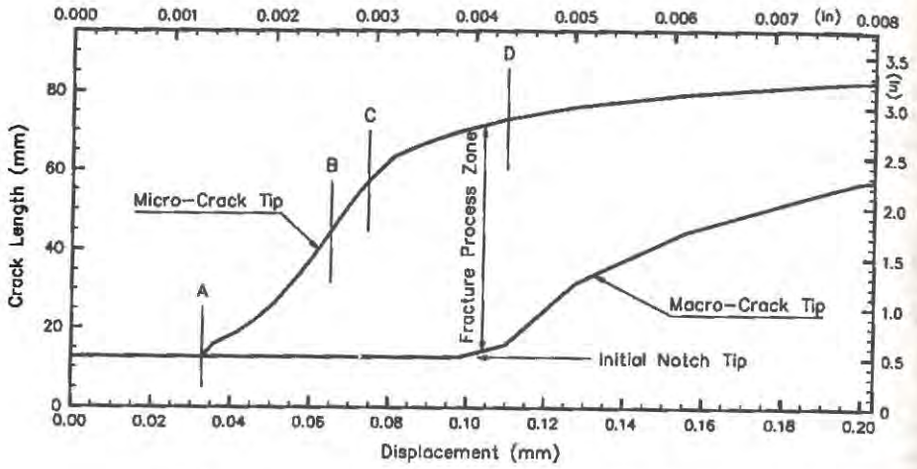

Figure 5. Computed Micro– and Macro–Crack Propagations for Three–Point Bend Loading

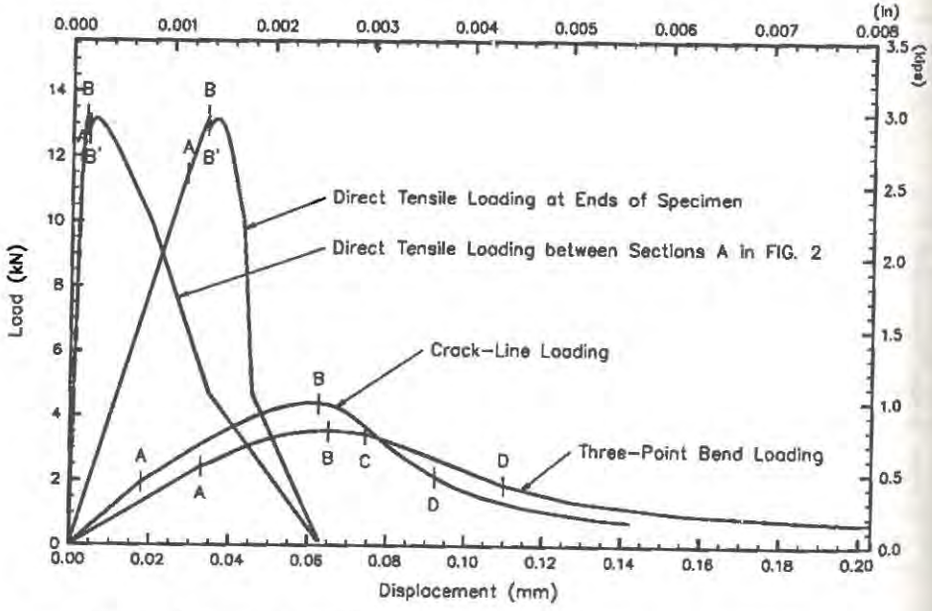

Figure 6. Computed Load versus Load–Line Displacement Relations for SEN Specimens

bend loading. At the peak load, the micro-crack extension was only 15.88 *mm* (0.625 *in*) and at that load unstable micro-crack growth occurred because the SIF at the micro-crack tip became larger than the critical value. When the displacement was held constant and crack tip nodes released sequentially, the external load dropped from B to B'. After 22.23 *mm* (0.875 *in*) of unstable micro-crack growth, there was no additional micro-crack extension and the load did not change even though all crack tip nodes were released. This arrest of unstable micro-cracking was caused by the constrained displacements of the ends of the specimen. Therefore, after B', a $CTOD_c$ criterion was used instead of K_{Ic} criterion. The COD for the last released crack tip node for B' was used as the $CTOD_c$ and for increasing boundary displacements the load again increased back up to the peak load before decreasing rapidly with increasing displacements. The decreasing load for increasing displacements at sections A was smoother than that for increasing displacements at the specimen's ends. This oscillation of the load versus displacement relation at the peak load has been observed by Van Mier [7]. When the micro-crack extended the full depth of the specimen, the average displacement between sections A was 5.60 times that at the peak load, while for end displacements the corresponding ratio was 1.27. These results shows that displacements measured near the critical section may appear to show stable cracking. However, the behavior of the entire specimen may be unstable due to the large strain energy stored in the uncracked ends.

CONCLUSIONS

The NS-FPZ model is a special case of the S-FPZ model and for which the SIF is zero. The SIF for an S-FPZ model can be calculated using superposition and with appropriate material properties determined from test results using the hybrid experimental-numerical technique. The optimum SEN specimen for determining FPZ characteristics is an SEN specimen subject to three-point bend loading. Crack-line loading is more difficult to apply and boundary constraints significantly affect direct tensile test results.

ACKNOWLEDGEMENT

The assistance of the College of Engineering, University of Illinois; the National Science Foundation through Grant No. MSM 8922877; and the Air Force Office of Scientific Research through Grant No. 91-0128, for support of this study is gratefully acknowledged.

REFERENCES

1. Hillerborg, A., Modeér, M., and Petersson, P.-E., Analysis of crack formation and crack growth in concrete by means of fracture mechanics and finite elements, Cem. Concr. Res., 6(6), 1976, 773–782.
2. Cornelissen, H. A. W., Hordijk, D. A., and Reinhardt, H. W., Experimental determination of crack softening characteristics of normalweight and lightweight concrete, Heron, 31(2), 1986, 45–56.
3. Yon, J.-H., Hawkins, N. M., and Kobayashi, A. S., Numerical simulation of Mode I dynamic fracture of concrete, J. Engrg. Mech., ASCE, 117(7), 1991, 1595–1610.
4. Jenq, Y.-S. and Shah, S. P., Two parameter fracture model for concrete, J. Engrg. Mech., ASCE, 111(10), 1985, 1227–1241.
5. Jeang, F. L. and Hawkins, N. M., Non-linear concrete fracture in CLWL-DCB specimens, Technical Report SM 85-2, Dept. of Civ. Engrg., Univ. of Washington, Seattle, WA., 1985.
6. Yon, J.-H., Hawkins, N. M., and Kobayashi, A. S., Dynamic fracture of concrete, Technical Report SM90-1, Dept. of Civ. Engrg, Univ. of Washington, Seattle, WA., 1990.
7. van Mier, J. G. M., Mode I behavior of concrete: influence of the rotational stiffness outside the crack-zone, In Analysis of Concrete Structure by Fracture Mechanics, ed. L. Elfgren and S. P. Shah, Chapman and Hall, London, U.K., 1991, 19–31.

SYMMETRIC AND NON-SYMMETRIC CRACK OPENING IN DIRECT TENSION TESTS FOR SOFTENING MATERIALS: A SIMPLE MECHANICAL MODEL

ALBERTO FRANCHI AND PAOLO RIVA
Civil Engineering Department, Universita' di Brescia
Via Valotti 9 - 25133 Brescia, Italy

FRANCESCO GENNA
Department of Structural Engineering, Politecnico di Milano
P.zza L. da Vinci 33 - 20133 Milano, Italy

ABSTRACT

A simple mechanical model is discussed in order to understand under what conditions the crack propagation is symmetric or non-symmetric in a direct tension test for softening materials. The incremental problem is formulated in terms of the standard tangent stiffness matrix K_T and of matrix A governing a Mathematical Programming description of the phenomenon. The merits of the latter over the former formulation are finally illustrated through a complete stability analysis example.

INTRODUCTION

Numerical experience [1,2] in simulating the uniaxial tensile behaviour of brittle plane-stress specimens modelled via an elastic-plastic softening cohesive model has posed the questions of (i) understanding under which conditions the response is symmetric or non-symmetric, and (ii) discussing the stability of the solutions [3]. Mechanically speaking, the problem is that of predicting if the crack propagates from one side only, or, alternatively, from both sides of the specimen at the same time, and if the two possibilities can exist at the same time.

An attempt of giving an answer to these questions is presented herein, adopting a simple structural model as a tool both for understanding some basic features of the problem and for suggesting some useful consideration.

A SIMPLE UNIAXIAL MODEL

The model in Figure 1 is studied in order to understand some aspects of the uniaxial test for elastic-plastic softening materials. The model consists of four parallel bars connected by a rigid element, so that the structural response is described by two generalized displacements, the rotation φ and the vertical translation v. Bars 1 and 4 are elastic up to the limit axial force $\bar{N}_{1,4}$, after which their

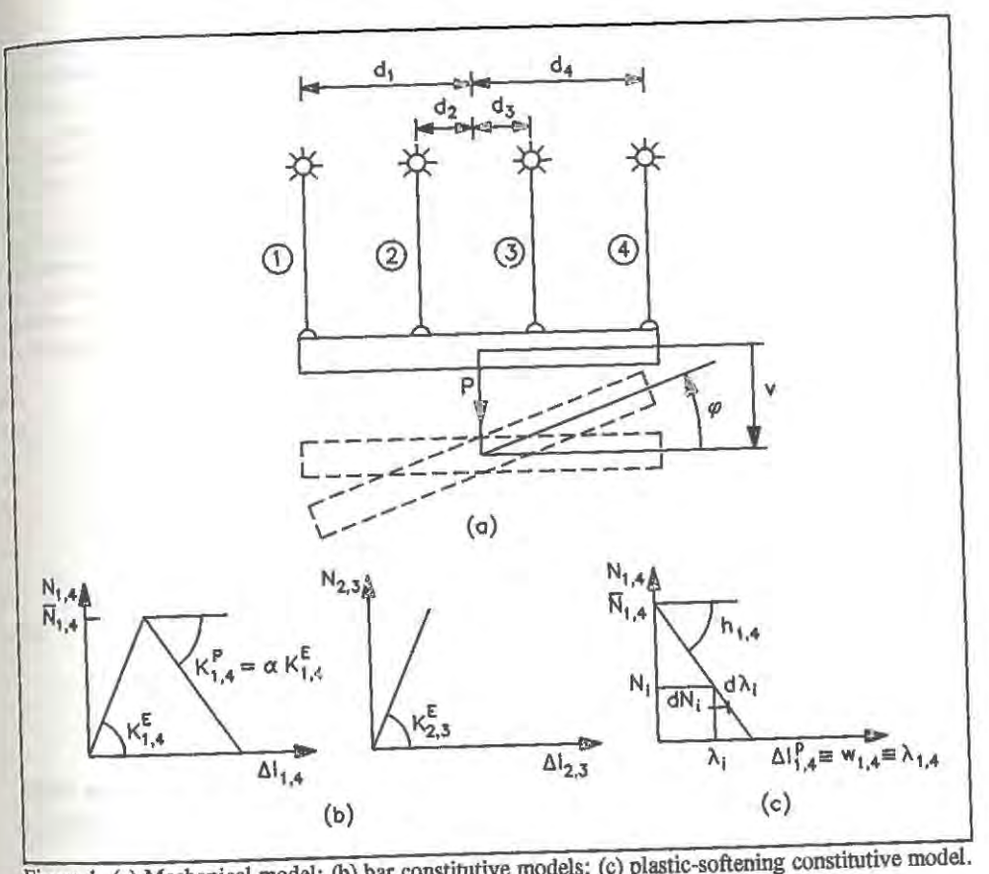

Figure 1. (a) Mechanical model; (b) bar constitutive models; (c) plastic-softening constitutive model.

behaviour becomes elastic-plastic softening, while bars 2 and 3 are considered indefinitely elastic. This assumption is justified by recalling that the analysis is restricted to the rate problem at the first activation of the limit axial force at bars 1 and 4. Finally, the section area of bars 2 and 3 is assumed twice the area of bars 1 and 4, and the external action is a symmetric vertical loading P.

THE INCREMENTAL PROBLEM AND THE TANGENT STIFFNESS MATRIX

The incremental constitutive law of the generic bar can be written as:

$$dN_i = K_{ri} d\Delta l_i \tag{1}$$

where $K_{ri} = K_i^E$, $i = 2,3$, and $K_{ri} = K_i^E$, $i = 1,4$, (elastic unloading), or $K_{ri} = K_i^P$, $i = 1,4$, (plastic-softening loading). The incremental small displacement equilibrium equation of the structure can then be written in the following form:

$$dF = \begin{bmatrix} dP \\ 0 \end{bmatrix} = \begin{bmatrix} \Sigma K_{ri} & \Sigma K_{ri} d_i \\ \Sigma K_{ri} d_i & \Sigma K_{ri} d_i^2 \end{bmatrix} = K_T du \tag{2}$$

This is the basic formulation adopted by the majority of computer codes for integrating the elastic-plastic hardening/softening structural response. Nevertheless, (2) is ambiguous and misleading in that the tangent modulus K_T is not known at the starting point but it depends on the plastic deformation rates, and through them on the rate of the generalized displacements dv and $d\varphi$.

The only way to correctly solve Eq. (2) is that of considering all possible combinations of loading/unloading configurations hoping to find the 'true' one (if the solution exists and is unique) before having tried all possible alternatives.

At the onset of cracking, i.e. when bars 1 and 4 reach the limit axial tensile force $\bar{N}_{1,4}$, two possibilities exist: (i) bars 1 and 4 enter the inelastic range (symmetric case), or (ii) bar 1 enters the inelastic range and bar 4 unloads elastically, or vice-versa (non-symmetric case). The trivial case of unloading of both bars (reverse loading) is not considered herein. It is convenient to define the plastic tangent modulus $K_1^P = \alpha K_1^E$ as function of a parameter α, positive if hardening and negative if softening. The tangent stiffness matrix can then be written as:

(i) Symmetric case:

$$\boldsymbol{K}_T = K_1^E \begin{bmatrix} 2(\alpha+2) & 0 \\ 0 & 2d_1^2(\alpha+\frac{2}{9}) \end{bmatrix}$$

(ii) Non-Symmetric case:

$$\boldsymbol{K}_T = K_1^E \begin{bmatrix} (5+\alpha) & d_1(\alpha-1) \\ d_1(\alpha-1) & d_1^2(\alpha+\frac{13}{9}) \end{bmatrix}$$

The equation $det|\boldsymbol{K}_T| = 0$ gives the following values of α:

(i) symmetric case: $\alpha_{III}^{\ S} = -2$; $\alpha_I^{\ S} = -2/9$

(ii) non-symmetric case: $\alpha_{II}^{\ A} = -14/19$

It can be concluded that for moderate softening, up to $\alpha = -2/9$, the tangent stiffness matrix is definite positive, the solution exists and it is unique.

THE INCREMENTAL FORMULATION WITH MATRIX A

In order to discuss the solution/s both in the stable and in the unstable range, it seems more convenient to abandon the tangent stiffness matrix $\boldsymbol{K}_T$ and the associated unknown displacement increments, dv and $d\varphi$, and solve the incremental problem by adopting the so called $\boldsymbol{A}$ matrix formulation [1,4,5] and the associated unknown vector $\dot{\lambda}$ of plastic multiplier rates.

The stress admissibility (figure 1(c)), i.e. the condition that for a given crack opening $w_i = \lambda_i$ the axial force N_i does not exceed the value prescribed by the softening line, can be expressed as:

$$\varphi_i = N_i - (\bar{N}_i + h_i\lambda_i) \le 0 \tag{3}$$

where the softening parameter h is related to the softening parameter α adopted in the tangent stiffness matrix approach by the relation $h = K_{EI}\alpha/(1-\alpha)$.

The rate of function φ_i is computed as:

$$\dot{\varphi}_i = \dot{N}_i - h_i\dot{\lambda}_i \tag{4}$$

Function λ_i must be always positive, $\lambda_i > 0$, and its rate $\dot{\lambda}_i$ is zero if the function φ_i is not zero, i.e. $\varphi_i\dot{\lambda}_i = 0$. Vice-versa, if the function φ_i is zero, its rate must be non positive; only in the case it is zero, $\dot{\lambda}_i$ might be positive, and in any case it can't be negative. Hence, the analytical model reads:

$$\text{if } \varphi_i = 0 \text{ then } \dot{\varphi}_i \le 0;\ \dot{\lambda}_i \ge 0;\ \dot{\varphi}_i\dot{\lambda}_i = 0 \tag{5}$$

which can be recognized as the structure of a Linear Complementarity Problem (LCP) in Mathematical Programming Theory.

Matrix $\boldsymbol{A}$ enters the picture when the axial force N_i is computed as the sum of an elastic term (as if the structure could have an indefinitely elastic behaviour) N_i^{el} and a term due to the plastic deformations λ_i, considered as distortions imposed on the elastic structure. Analytically this can be formalized by means of matrix $\boldsymbol{Z}$, relating the self stresses N_i^S to the plastic strains λ_i, as:

$$\begin{bmatrix} N_1 \\ N_4 \end{bmatrix} = \begin{bmatrix} N_1^{el} \\ N_4^{el} \end{bmatrix} + \begin{bmatrix} N_1^S \\ N_4^S \end{bmatrix} = \begin{bmatrix} N_1^{el} \\ N_4^{el} \end{bmatrix} + \begin{bmatrix} Z_{11} & Z_{12} \\ Z_{21} & Z_{22} \end{bmatrix} \begin{bmatrix} \lambda_1 \\ \lambda_4 \end{bmatrix} \tag{6}$$

Matrix $\boldsymbol{Z}$ is evaluated with simple elastic calculations as:

$$\boldsymbol{Z} = -K_1^E \begin{bmatrix} 14/33 & 8/33 \\ 8/33 & 14/33 \end{bmatrix}$$

Introducing (6) in (4), Eq.(4) may be rewritten as a function of the plastic multiplier rates $\dot{\lambda}_i$ as:

$$\begin{bmatrix} \dot{\varphi}_1 \\ \dot{\varphi}_4 \end{bmatrix} = \begin{bmatrix} \dot{N}_1^{el} \\ \dot{N}_4^{el} \end{bmatrix} + \begin{bmatrix} Z_{11} & Z_{12} \\ Z_{21} & Z_{22} \end{bmatrix} \begin{bmatrix} \dot{\lambda}_1 \\ \dot{\lambda}_4 \end{bmatrix} - \begin{bmatrix} h & 0 \\ 0 & h \end{bmatrix} \begin{bmatrix} \dot{\lambda}_1 \\ \dot{\lambda}_4 \end{bmatrix}$$

or in compact notation as:

$$\begin{cases} \dot{\boldsymbol{\varphi}} = \dot{\boldsymbol{N}}^{el} - \boldsymbol{A}\dot{\boldsymbol{\lambda}} \le \boldsymbol{0} \\ \dot{\boldsymbol{\lambda}} \ge \boldsymbol{0};\ \ \dot{\boldsymbol{\varphi}}^t\dot{\boldsymbol{\lambda}} = 0 \end{cases} \tag{7}$$

where matrix $\boldsymbol{A}$ is defined as:

$$\boldsymbol{A} = \boldsymbol{Z} + h\boldsymbol{I} = K_1^E \begin{bmatrix} \frac{14}{33} + \frac{h}{K_1^E} & \frac{8}{33} \\ \frac{8}{33} & \frac{14}{33} + \frac{h}{K_1^E} \end{bmatrix} = K_1^E \begin{bmatrix} \frac{14}{33} + \frac{\alpha}{1-\alpha} & \frac{8}{33} \\ \frac{8}{33} & \frac{14}{33} + \frac{\alpha}{1-\alpha} \end{bmatrix} \tag{8}$$

The condition $det|\boldsymbol{A}| = 0$ gives the critical values of α for the symmetric case:

$$\alpha_{III}^{\ S} = -2\ ;\ \alpha_I^{\ S} = -2/9$$

while the condition $det|\hat{\boldsymbol{A}}| = 0$, i.e. that the determinant of any principal minor is zero, gives the values corresponding to the non-symmetric propagation:

$$\alpha_{II}^{\ A} = -14/19$$

A first result is that *all* critical values of softening parameter α can be found by examining only one matrix A, which contains the information of all possible stiffness matrices K_T.

A second result consists in how easily and systematically all possible solutions can be found. Note that positive components of vector $\dot{N}^{el}$ means loading ($dP > 0$) and vice-versa unloading ($dP < 0$). The symmetric solution, if it exists, is found by imposing $\dot{\varphi}_1 = \dot{\varphi}_4 = 0$ and by computing $\dot{\lambda}_1$ and $\dot{\lambda}_4$ for a given vector $\dot{N}_1^{el} = \dot{N}_4^{el}$ and verifying that $\dot{\lambda}_1 = \dot{\lambda}_4 \geq 0$. The non-symmetric solution, if it exists, is found by imposing only one equality, i.e. $\dot{\varphi}_1 = 0$ with $\dot{\lambda}_4 = 0$, by computing $\dot{\lambda}_1$ for a given $\dot{N}_1^{el}$, and verifying the remaining inequalities $\dot{\varphi}_4 \leq 0$ and $\dot{\lambda}_1 \geq 0$. The rate problem is solved for different values of the parameter α and the results are summarized in the following, where the different solutions are qualitatively illustrated by load (P) - displacement (v) plots.

RESULTS

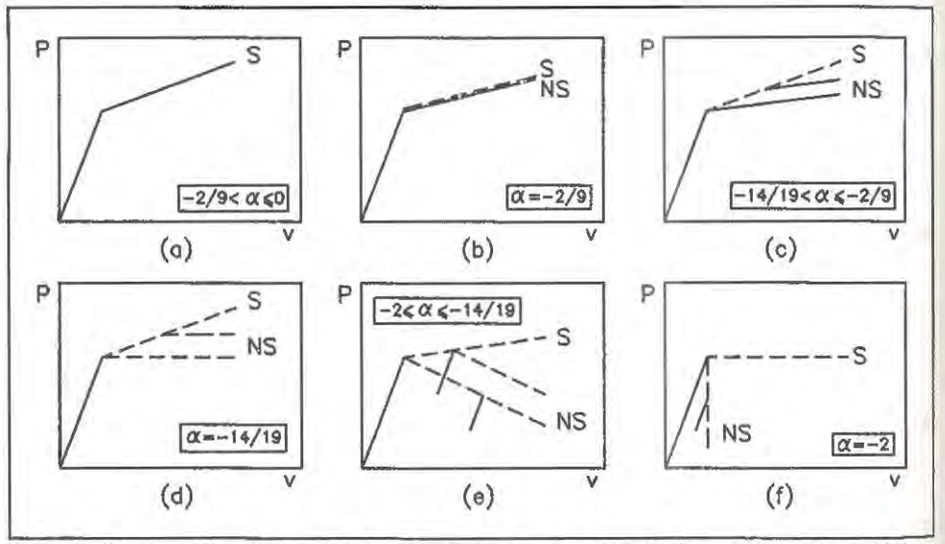

Figure 2. Summary of analysis results for softening paramater α varying between 0 and -2: solid lines = stable starting configuration; dashed lines = unstable starting configuration.

- $-2/9 < \alpha < 0$ (Figure 2(a)): only the symmetric solution exists and it is stable, i.e. it corresponds to a matrix A definite positive.
- $\alpha_I^S = -2/9$ (Figure 2(b)): both symmetric and non-symmetric solutions exist; the symmetric solution is unstable (matrix A(2x2) singular) while the non-symmetric solution is stable (matrix A(1x1) definite positive).
- $-14/19 < \alpha < -2/9$ (Figure 2(c)): as above, with the only difference that the unstable symmetric solution corresponds to an indefinite matrix A(2x2). This is shown graphically by the indication of the two possible solutions (S or NS) at each point of the symmetric path.
- $\alpha_{II}^A = -14/19$ (Figure 2(d)): both solutions exist, but the non-symmetric solution corresponds to a singular A(1x1) matrix.
- $-2 < \alpha < -14/19$ (Figure 2(e)): the unstable symmetric solution exists; the unstable non-symmetric solution exists only for decreasing load P, together with the stable unloading solution.
- $\alpha_{III}^S = -2$ (Figure 2(f)): the unstable symmetric solution does not exist any more for increasing load.

Analogous results can be obtained by examining the same model by prescribing the vertical displacement v and finding the force P as the resulting reaction. The corresponding analysis is omitted for brevity.

CONCLUSIONS

1. Both the symmetric and non-symmetric solutions may exist for softening materials.
2. The symmetric solution is stable for moderately low negative values of the softening parameter α while the non-symmetric solution can be stable for more negative values of α.
3. Within a particular range of α values, one solution is unstable (symmetric) and one is stable (antisymmetric). In other words, a stable equilibrium path may be reached starting from an unstable configuration.
4. Under some critical values of α the solution (stable or unstable, symmetric or non-symmetric) does not exist for increasing load P but it exists (and it is not unique) for reverse loading.
5. Matrix A formulation contains all information regarding both the algorithm for finding the solution/s and the qualification of the solution/s with regard to stability.

ACKNOWLEDGEMENTS

The financial contribution of the Italian Ministry of University and Scientific and Technological Research (MURST) is gratefully acknowledged.

REFERENCES

1. Franchi, A. and Genna, F., A Stable/Neutral Equilibrium Path for the Numerical Solution of Elastic-Plastic Softening Problems, Comp. Meth. Appl. Engrg., 90, 1991, 921-42.
2. Rots, J.G. and de Borst, R., Analysis of Concrete Fracture in 'Direct' Tension, Int. J. Solids Structures, 25, 12, 1989, 1381-94.
3. Bažant, Z.P. and Cedolin, L., Stability of Structures, Oxford University Press, New York, N.Y., 1991.
4. Franchi, A. and Genna, F., A 'Self Adaptive' Model for Structural Softening of Brittle Materials, ASCE J. Eng. Mech., 115, 7, 1989, 1543-58.
5. Maier, G., On Softening Flexural Behaviour in Elastic-Plastic Beams, Rend. Ist. Lomb.Scienze e Lettere, 102A, 1968, 648-677.

AN OVERVIEW OF NON-LINEAR EFFECTS AT CRACK TIPS

E. SMITH
Manchester Materials Science Centre, University of Manchester/UMIST,
Grosvenor Street, Manchester M1 7HS, U.K.

ABSTRACT

The paper provides a very brief overview of a general model describing the restraining effect of unfractured material in a partially fractured zone behind a crack tip. The model has a wide-ranging applicability, particularly with brittle and quasi-brittle materials, but there is also a similarity with the strip yield model of a crack in a ductile material. The overview has been prepared against the background of the author's research experience, which has been primarily with regard to fracture of ductile materials.

INTRODUCTION

Concrete is just one example of the several types of brittle and quasi-brittle material which are characterized by having a zone of partially-fractured material at a crack tip. Other examples are particulate reinforced ceramics, composites with brittle matrices, rubber-toughened brittle polymers and ceramics themselves, where the non-fracturing is provided by the untangling of interlocking crystals. Upon loading a pre-cracked solid, the crack tip remains stationary until the crack tip stress intensity attains a critical value K_{IC} when the material fractures at the crack tip. With continued loading, the crack extends, leaving behind a zone of partially fractured material, and the restraining stresses due to the ligaments which bridge the crack faces, are responsible for the stress intensity increasing during crack growth, and thereby introducing a desirable measure of toughness into the material. In order to take credit for this enhanced toughness behaviour, it is important in the context of transferring crack growth data from laboratory-type specimens to engineering structure behaviour, to quantify the crack growth behaviour, and in particular to understand how this growth behaviour is affected by geometrical parameters.

THE IDEALISED MODEL OF A SEMI-INFINITE CRACK IN A REMOTELY LOADED INFINITE SOLID

In modelling the restraining effect of the partially fractured material for plane strain deformation, the simplest way is to smear-out the effect of individual bridging ligaments and

represent the restraint by an effective stress that restricts the relative displacement of the opposite faces of the crack. The stress intensity (K)-crack extension (R) behaviour depends on a variety of factors: geometrical configuration, loading state (where and how the load is applied), restraining stress-relative displacement law and the magnitude of K_{IC}. However the considerations can be simplified by assuming that $K_{IC} = 0$, and that the restraining stress retains a constant value p_c within the ligament region. The model is then similar to the DBCS model[1,2] of a plastically relaxed crack in a ductile material, with the stress p_c being analogous to the yield stress of the material. Cottrell[3] in his 1963 Tewkesbury lecture recognized the generality of this model of a crack tip with its constant stress zone at the tip, but twenty five years later it is now evident that such a model has a far wider range of applicability than was envisaged in the mid 1960's.

For the idealised situation of a semi-infinite crack in a remotely loaded infinite solid, hereafter referred to as the "small zone" situation, Figure 1 shows a partially developed ligament zone of size R behind the crack tip, i.e. the crack has extended a distance R from

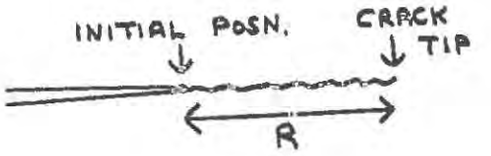

Figure 1. The model of a semi-infinite crack in a remotely loaded infinite solid.

its original position, the displacement at the trailing edge of this zone, i.e. at the initial crack tip, being δ. The stress intensity K due to the applied loadings, which is equal to the stress intensity due to the restraining ligament material, is then given by the expression

$$K = p_c[8R/\pi]^{1/2} \qquad (1)$$

this K-R relation being valid until the full development of the ligament zone, i.e. until δ attains a critical value δ_m. The critical K value associated with the attainment of a fully developed ligament zone is given by the expression

$$K_\infty = [E_o p_c \delta_m]^{1/2} \qquad (2)$$

where $E_o = E/(1-\nu^2)$, E being Young's modulus and ν being Poisson's ratio. The fully developed ligament zone size R_∞ is given by the expression

$$R_\infty = \frac{\pi E_o \delta_m}{8 p_c} \qquad (3)$$

Subsequent to the attainment of the critical fracture toughness K_∞, the crack continues to extend at the same applied stress intensity $K = K_\infty$ with a constant opening displacement δ_m being maintained at the trailing edge of the ligament zone, which retains a constant size.

The preceding considerations are with regard to the idealised case where there is a constant restraining stress p_c within the ligament region. When the restraining stress is a general function p(u) of the relative displacement u of the crack faces, relation (2) for K_∞ is replaced by the relation

$$K_\infty = \left[E_o \int_0^{\delta_m} p(u)\,du \right]^{1/2} \qquad (4)$$

and consequently K_∞ is markedly dependent on the details of the restraint force law. It is not possible to have such a simple relation for R_∞. However a detailed analysis has shown[4] that though R_∞ is very dependent on the maximum stress p_c and the maximum displacement δ_m, it is nevertheless not overly dependent on the precise force law relation except when there is a particularly long tail in the restraint force law; relation (3) provides an approximate working estimate for R_∞.

SIGNIFICANCE OF THE PARAMETERS K_∞ AND R_∞

The parameter K_∞ is important in that it provides an indication of the potential for toughening of the type of material, for which a crack is associated with a ligament zone. R_∞ is important because it provides an indication of the critical dimensions of a solid, e.g. initial crack size and initial width, below which geometrical effects are expected to become important and the behaviour pattern appropriate to the small zone situation cannot then be used to describe the solid's behaviour. It provides a very rough estimate of the dimensions, e.g. crack depth, below which failure conforms to a limiting stress (p_c) criterion.

As examples, Carpinteri[5], assuming a linear softening law for the restraining material, examined the behaviour of a concrete-like material with $E_o \sim 4 \times 10^4$ MPa, $p_c \sim 4$ MPa and $\delta_m = 5 \times 10^{-3}$ cm, whereupon relation (3) gives $R_\infty \sim 20$ cm while relation (4) gives $K_\infty \sim 3$ MPa$\sqrt{m}$. Foote, Mai and Cotterell[6] examined a cellulose/asbestos fibre reinforced mortar with $E_o \sim 6000$ MPa, $p_c \sim 6$ MPa and $\delta_m = 8 \times 10^{-2}$ cm, whereupon $R_\infty \sim 32$ cm and $K_\infty \sim 4$ MPa$\sqrt{m}$. With a ceramic (alumina) for which the restraining stress between the crack faces is provided by the untangling of interlocking crystals[7], typical input values are $E_o \sim 350 \times 10^3$ MPa, $p_c \sim 30$ MPa and $\delta_m = 2 \times 10^{-4}$ cm, whereupon $R_\infty \sim 1$ cm and $K_\infty \sim 3$ MPa$\sqrt{m}$. When developing materials with a high toughness, one should strive for a balanced contribution from E_o, p_c and $_m$ such that their product is maximised. As regards the magnitude of R_∞, a high value is favoured by high values of E_o and δ_m and a low p_c value; the relatively low R_∞ value for alumina is due in large part to a high p_c value and a low δ_m value. With alumina, for which $R_\infty \sim 1$ cm, in the light of this section's earlier comments, geometrical effects are important with small but not large laboratory specimens; another paper[8] at this conference focusses on geometrical effects in the bend specimen configuration. On the other hand with the concrete-like material[5] or the reinforced mortar[6] where R_∞ is of the order of tens of cms, geometrical effects are important even with large laboratory specimens. Materials of this type provide the greatest challenge in using fracture data from laboratory specimens to predict the behaviour of engineering structures. The large R_∞ value is an important reason why concrete-type materials are so interesting from a research perspective; a similar state of affairs exists with regard to many of the ductile materials, e.g. ferritic and austenitic

steels, used in engineering components fabricated from metallic alloys.

THE STABILITY OF CRACK GROWTH

The stability of crack growth for a particular loading state requires a comparison of the K-crack growth relation for the material and the applied K (K_{APP})-crack growth relation, with crack growth becoming unstable when $(\partial K_{APP}/\partial a)$ for a fixed value of the loading parameter (load or displacement) exceeds (dK/da) for the material. With a material that has a small R_∞ value in comparison with the specimen's or structure's characteristic dimensions, instability occurs upon attaining the fully developed ligament situation, i.e. when $K_{APP} = K_\infty$, provided that $(\partial K_{APP}/\partial a)$ is positive. However the situation becomes more complicated with a material having a high R_∞ value; this situation has been addressed, by Carpinteri[5], for a concrete-type material, and he showed that a cusp catastrophe type of displacement control crack growth instability can occur, i.e. one in which both load and displacement decrease during crack extension, with particular ranges of a configuration's geometrical parameters. There is a similarity here with the behaviour of a very ductile material, such as austenitic stainless steel, where such a phenomenon can occur when there is extensive plastic deformation, provided that the structure is sufficiently flexible; this situation has been examined extensively for the case of circumferentially cracked stainless steel piping with regard to the integrity of nuclear reactor piping systems.

REFERENCES

1. Dugdale, D.S. J. Mech. Phys. Solids, 1960, **8**, 100.
2. Bilby, B.A., Cottrell, A.H. and Swinden, K.H., Proc. Roy. Soc., 1963, **A272**, 304.
3. Cottrell, A.H., Proceedings of First Tewksbury Conference, Faculty of Engineering, University of Melbourne, Australia, 1963, p. 1.
4. Smith, E., Int. Jnl. Eng. Science, 1989, **27**, 301.
5. Carpinteri, A., J. Mech. Phys. Solids, 1989, **37**, 567.
6. Foote, R.M.L., Mai, Y.W. and Cotterell, B., J. Mech. Phys. Solids, 1986, **34**, 593.
7. Majumdar, B.S., Rosenfield, A.R. and Duckworth, W.H., Eng. Fract. Mechs., 1988, **31**, 683.
8. Smith, E., "The effect of initial crack depth on the bend specimen crack growth resistance curve for a concrete-type material" paper at this Conference.

Chapter 2

Damage Modeling

Principal Lecture

FUNDAMENTAL ASPECTS OF STRAIN-SOFTENING DESCRIPTIONS [1]

KASPAR WILLAM AND ANDREAS DIETSCHE
University of Colorado, Boulder, CO 80309-0428, USA
Institute of Mechanics, University of Karlsruhe, W-7500 Karlsruhe 1, FRG

ABSTRACT

The paper examines alternative continuum descriptions of the degradation of strength. In particular we study recent proposals to regularize local strain-softening descriptions which introduce both spatial as well as temporal discontinuities in the solution domain. The formation of spatial discontinuity surfaces is normally accompanied by loss of ellipticity, which in turn is responsible for ill-posedness of the underlying initial boundary value problem. This results in extreme sensitivity of numerical solutions with regard to mesh size, and especially with regard to mesh orientation. Three regularization concepts will be interrogated, whether or not the formation of discontinuity surfaces will be suppressed: (i) the fracture energy concept of equivalent softening, (ii) the second order gradient formulation, and (iii) the Cosserat theory of polar continua. All regularization concepts are essentially local in character in spite of their characteristic length measures. The implications of the three degradation descriptions will be discussed at the oral presentation of the uniaxial tension problem, for which appropriate extensions of the Rankine maximum stress hypothesis and the J_2-theory of maximum shear distortion will be examined.

CONTINUUM DESCRIPTIONS OF DEGRADATION

The traditional continuum description of progressive failure reveals a number of shortcomings which are mainly because of the narrow scope of local material descriptions, in particular when the traditional format of simple materials is utilized. Thereby the basic question is, whether a phenomenological degradation theory can be successful at all in describing the transition from a continuum into a discontinuum, if no recourse is taken to the microstructure of the material at hand. For this reason it is meritious to re-visit some of the underlying assumptions of continuum mechanics, and in particular the regularity of the mappings between the primary field variables, the displacements, strains and stresses.

Preliminaries of Continuum Mechanics

In continuum mechanics we normally start off by defining a continuous body $\mathcal{B}$ as a compact set of material particles and its configuration as a topological map of the material particles and their spatial location. The regularity of the topographical mapping, $\mathbf{x}=\boldsymbol{\phi}(\mathbf{X})$, infers continuity of the first partial derivatives $\mathbf{F}=\partial\mathbf{x}/\partial\mathbf{X}$. This assures that neighbouring material particles will always occupy neighbouring spatial locations. The non-vanishing determinant of this Jacobian map implies single-valuedness, i.e. one-to-one correspondence between the material particles and their spatial location. This homoeomorphism forms the basis for defining the motion of the body as a continuous sequence of configurations in the time domain, i.e. $\mathbf{x}=\boldsymbol{\phi}(\mathbf{X};t)$, whereby

[1] invited paper at FramCoS 1, Breckenridge, Colorado, June 1-5, 1992

the deformation gradient $\mathbf{F}_t(t) = \partial \mathbf{x}_t / \partial \mathbf{X}$ defines the mapping between the material particle and their spatial location in the current configuration.

'Non-local' material formulations define the stress at the material particle $\mathbf{X}$ and the time t in terms of a functional which accounts for far-reaching interaction both in space and time. Observer indifference, or inversely material objectivity, reduces the dependence of stress on the history of relative motions within the body, i.e. the difference history among all material particles within the configuration space,

$$\sigma(\mathbf{X},t) = \mathcal{F}_{s=0}^{\infty}\,[\mathbf{x}(\mathbf{Y},t-s) - \mathbf{x}(\mathbf{X},t-s); \mathbf{X}]; \quad \mathbf{Y} \in \mathcal{B} \tag{1}$$

This broad material statement encompasses far-reaching interaction among all material particles within the body through the entire history of particle motion. This non-local material description provides the framework for the recent integral representations by BAŽANT [1] and PIJAUDIER-CABOT AND BAŽANT [16].

The spatial interaction is normally approximated by truncated Taylor series which represents the history of relative motions of neighbouring particles in terms of *'local'* descriptors, i.e. the deformation gradients $\mathbf{F}_1, \mathbf{F}_2, ..\mathbf{F}_n$ of order one to n,

$$\mathbf{x}(\mathbf{Y},t-s) - \mathbf{x}(\mathbf{X},t-s) = \mathbf{F}_1(\mathbf{X},t-s)[\mathbf{Y}-\mathbf{X}] + \frac{1}{2}\mathbf{F}_2(\mathbf{X},t-s)[\mathbf{Y}-\mathbf{X}] + ... \frac{1}{n!}\mathbf{F}_n(\mathbf{X},t-s)[\mathbf{Y}-\mathbf{X}] \tag{2}$$

Obviously, the interaction reach diminishes rapidly with the distance between the material particles $\|\mathbf{Y}-\mathbf{X}\|$. Therefore, the stress functional reduces to the *'local'* description involving the histories of n'th-order deformation gradients at the material particles $\mathbf{X}$. Thus, materials of grade n are defined as

$$\sigma(\mathbf{X},t) = \mathcal{F}_{s=0}^{\infty}\,[\mathbf{F}_1(\mathbf{X},t-s), \mathbf{F}_2(\mathbf{X},t-s), ...\mathbf{F}_n(\mathbf{X},t-s) : \mathbf{X}] \tag{3}$$

This type of material description provides the framework for the so-called gradient models advocated recently by SCHREYER [19], VARDOULAKIS AND AIFANTIS [24], MÜHLHAUS AND VARDOULAKIS [13], and recently DE BORST AND MÜHLHAUS [5].

It remains to recall the limiting case of grade one materials which define the constitutive structure of *'simple materials'*.

$$\sigma(\mathbf{X},t) = \mathcal{F}_{s=0}^{\infty}\,[\mathbf{F}_1(\mathbf{X},t-s); \mathbf{X}] \tag{4}$$

This traditional constitutive structure is the repository of viscoelasticity, and in the limiting case of history independence, that of nonlinear elasticity. In this context, plasticity is recovered if the history effects are introduced in terms of internal variables rather than time integrals.

In sum, continuum mechanics introduces regularity requirements both in space and time, whereby the material description implies continuity of the history of relative motions among neighbouring material particles. As a result, localization due to the formation of discontinuity surfaces in the body is connected to bifucation of the deformation gradient. In the sequel we will focus on the regularization of these localization phenomena, and we will discuss various enrichment strategies for simple material descriptions which suppress or rather control the formation of discontinuity surfaces.

Micropolar Cosserat Continua

Independently of these non-local and higher grade extensions of the simple materials the micropolar formulation of Cosserat continua introduces additional material parameters in a natural manner, see COSSERAT [7]. The constitutive relationship of the non-symmetric components of stress and strain on one hand, and in particular the relationship between the couple-stress and

the curvature introduces a characteristic length measure. This latter length scale of Cosserat continua may be thought of as a measure of local flexural stiffness versus axial stiffness and classifies as a material of grade $n = 2$. In fact the Cosserat length scale lends itself to regularize the impending loss of ellipticity in the vincinity of localization. Further extensions of the linear elastic Cosserat-theory to elasto-plastic behavior are of particular interest, notably the generalized J_2-theory by LIPPMANN [12], BESDO [3] and recently by DE BORST AND MÜHLHAUS [5]. There the characteristic length of the elastic behavior is used in the extended yield condition in order to normalize the couple-stresses. This further tightens the coupling between the non-symmetric stress and couple-stress fields with the non-symmetric strain and curvature fields in the plastic response regime, and stiffens the constitutive operator when compared to the non-polar case. As a consequence of this additional *'flexural'* stiffness the Cosserat description regularizes the material formulation and eventually suppresses the formation of discontinuity surfaces, see STEINMANN AND WILLAM [21].

Scope of Study

In the following we interrogate various enriched softening constitutive operators, whether they exhibit localization in the form of discontinuous bifurcation, or whether they suppress the formation of discontinuity surfaces altogether. Three different variations of strain-softening models will be examined and compared with regard to their localization characteristics, the fracture energy-based formulation, the second order gradient as well as the micropolar Cosserat formulation of elasto-plasticity.

The background of our bifurcation study is the well-known formation of tensile failure mechanisms in brittle and ductile fracture, whereby the normals of the resulting discontinuities and cracks enclose an angle of ± 90 to ± 35 degrees with the load axis, when flat tension specimens made of brittle and ductile materials are subjected to uniaxial tension.

ALTERNATIVE SOFTENING FORMULATIONS

In the following we will resort to three material descriptions of strength degradation due to softening. The fist softening description is based on the traditional format of local strain-softening elasto plasticity of grade one materials, where the softening modulus is re-interpreted and related to the fracture energy release rate involving the characteristic fracture length ℓ_f. The second softening description follows the second order gradient extension of strain-softening elasto-plasticity, where the equivalent plastic strain is augmented by the curvature of plastic strain. This local softening description corresponds to a grade two material in which the characteristic length ℓ_g appears in the normalization of the curvature. The third softening description is based on the elasto-plastic Cosserat formulation of micropolar continua in which the characteristic length ℓ_c appears in a natural manner in the elastic moment-curvature relation, in addition to its role in plasticity.

Fracture Energy-Based Elasto-Plastic Description

For the sake of definiteness we will resort to the format of elasto-plastic constitutive operators. Thus for isotropic softening behavior the yield condition delimits the elastic response regime by

$$F(\sigma, \epsilon_p) = f(\sigma) - Y(\epsilon_p) = 0 \tag{5}$$

In the case of isotropic softening the state of internal material degradation is described either in terms of the scalar-valued equivalent plastic strain or in terms of plastic work for characterizing

the evolution of the degradation process.

$$\dot{\epsilon}_p = \sqrt{\dot{\epsilon}_p : \dot{\epsilon}_p} = \dot{\lambda}; \qquad \dot{w}_p = \boldsymbol{\sigma} : \dot{\epsilon}_p = \dot{\lambda} \tag{6}$$

The rate of change of degradation of the yield strength is controled by the plastic modulus $E_p = dY/d\epsilon_p$. The usual argument of linearized consistency leads to the elasto-plastic stress-strain relationship,

$$\dot{\sigma} = \mathbf{E}^f_{ep} : \dot{\epsilon}; \qquad \mathbf{E}^f_{ep} = \mathbf{E} - \frac{\mathbf{E} : \mathbf{n} \otimes \mathbf{n} : \mathbf{E}}{E^f_p + \mathbf{n} : \mathbf{E} : \mathbf{n}} \tag{7}$$

where the elasto-plastic operator above holds for the case of associated plastic flow and isotropic hardening/softening. We resort to *'normal'*, i.e. associated behavior for the sake of simplicity whereby the arguments of regularization are even more acute for non-associated flow, when the lack of symmetry destabilizes the constitutive operator and induces localization prematurely.
In the past several proposals have been advocated to regularize local strain-softening formulations. Among others the volume fraction concept of PIETRUSCZAK AND MROZ [15] is noteworthy, since it is based on the elementary hypothesis that strain-softening is confined to a plastic failure band which is embedded within the finite element. This leads essentially to the modification of the plastic modulus according to the volume fraction of the softening zone in the finite element domain, i.e.

$$E^f_p = \frac{1}{\eta} E_p; \qquad \eta = \frac{A_s \ell_s}{V_e} \tag{8}$$

This concept of a small volume fraction does not consider however the locking tendencies of finite elements when discontinuities are to be captured due to localized failure in shear. Consequently, the volume fraction for shear failure is definitely larger than one, $\eta > 1$, since the standard low order elements spread unduly the width of the failure zone to three to five times the element size when fixed meshes are used. In spite of this shortcoming of the original proposal the η-parameter introduces an independent length scale for the failure band.
The fracture energy-based softening concepts for tension and shear did re-interpret the plastic softening behavior in terms of the fracture energy release, see WILLAM ET AL. [25] and WILLAM AND MONTGOMERY [26]. In the case of strain softening, the degradation of strength down to the residual strength level is described in terms of an equivalent tensile fracture strain which extracts the tensile strain components from the plastic strain trajectory. The plastic modulus is in this case redefined in terms of the second rate of change of the fracture energy release. The characteristic fracture length translates the surface-dominated fracture process into an equivalent volume-dominated process, i.e.

$$E^f_p = \ell_f E_f; \qquad E_f = \frac{dY}{du_f} = \frac{d^2 G_f}{du_f^2} \tag{9}$$

In that case E_f designates the softening modulus in terms of relative displacement u_f rather than plastic strain, and ℓ_s specifies the width, i.e. the reach of the degradation zone. Clearly, for tensile cracking this corresponds to the original proposal of BAZANT AND OH [2]. For degradation in mixed mode fracture this concept was extended by PRAMOMO AND WILLAM [17] to mixed mode failure when plain concrete is failed in tension and low confined compression. In that context the work-softening formulation provides an attractive alternative to strain softening, since it relates directly to the fracture energy release rate, see CAROL AND PRAT [6]. Because of the local character of the fracture energy-based softening formulation this approach has to be connected to enhanced finite elements which are capable to capture the formation of discontinuity surfaces, see STEINMANN AND WILLAM [23]. Recently the important benefit

of enhanced spatial discretizations was demonstrated by ETSE ET AL. in the context of the fracture energy formulation of the extended Leon-model for plain concrete, see [9].

Second Order Gradient Elasto-Plastic Description

For the sake of argument we will focus here on the second order gradient formulation which was originally proposed for J_2-plasticity by VARDOULAKIS AND AIFANTIS [24], in order to regularize discontinuous bifurcation in the form of localization. In this case the extended yield condition depends not only on the equivalent plastic strain, but also on the Lapacian thereof, i.e.

$$F(\mathbf{s}, \bar{\epsilon}_p) = \sqrt{3J_2} - Y(\bar{\epsilon}_p) = 0; \qquad \dot{\bar{\epsilon}}_p = \dot{\epsilon}_p + \frac{1}{\ell_g^2} \nabla^2 \dot{\epsilon}_p = \dot{\lambda} \tag{10}$$

For isotropic strain softening the effective plastic strain is comprised of two contributions, thus the softening description of the yield strength involves now two plastic moduli, E_{p1} and E_{p2}

$$\dot{Y}(\bar{\epsilon}_p) = E_{p1} \dot{\epsilon}_p + \frac{E_{p2}}{\ell_g^2} \nabla^2 \dot{\epsilon}_p \tag{11}$$

The usual arguments of linearized consistency lead to the augmented elasto-plastic softening stress-strain relation below,

$$\dot{\sigma} = \mathbf{E}^g_{ep} : \dot{\epsilon} + \mathbf{L}^g_{ep} \nabla^2 \dot{\epsilon}_p \tag{12}$$

where the normal elasto-plastic operator for isotropic hardening/softening is complemented by a second order tensor associated with the second order gradient of equivalent plastic strain

$$\mathbf{E}^g_{ep} = \mathbf{E} - \frac{\mathbf{E} : \mathbf{n} \otimes \mathbf{n} : \mathbf{E}}{E_{p1} + \mathbf{n} : \mathbf{E} : \mathbf{n}}; \qquad \mathbf{L}^g_{ep} = \frac{E_{p2} - E_{p1}}{\ell_g^2} \frac{\mathbf{E} : \mathbf{n}}{E_{p1} + \mathbf{n} : \mathbf{E} : \mathbf{n}} \tag{13}$$

In sum, the second order gradient concept introduces an additional term into the differential elasto-plastic constitutive relations, which corresponds to the curvature of the plastic strain.

Micropolar Elasto-Plastic Description

For definiteness we will focus on the original proposals by LIPPMANN [12] and BESDO [3] for extending J_2-plasticity to micropolar continua. In that case the standard yield condition

$$F(\mathbf{s}, \mathbf{m}, \epsilon_p, \kappa_p) = \sqrt{3J_2} - Y(\epsilon_p, \kappa_p) = 0 \tag{14}$$

resorts to the generalized second invariant of deviatoric stress $\mathbf{s}$ and couple-stress $\mathbf{m}$

$$J_2 = \frac{1}{4}\mathbf{s} : \mathbf{s} + \frac{1}{4}\mathbf{s} : \mathbf{s}^t + \frac{1}{2\ell_c^2}\mathbf{m} : \mathbf{m} \tag{15}$$

The particular choice of 1/4 weighting for the symmetric and skew-symmetric contributions dates back to the recent proposal by DE BORST [4]. For granulates other weighting strategies were suggested earlier by MÜHLHAUS AND VARDOULAKIS [13] which were based on micromechanical considerations. For isotropic hardening/softening the scalar-valued yield strength $Y = Y(\epsilon_p, \kappa_p)$ is in general a function of both the equivalent plastic strain and the plastic curvature. We focus here on the strain softening formulation of J_2-plasticity, where the rate of change of the generalized von Mises stress $\sqrt{3J_2}$ is controled only by the equivalent plastic strain and not the curvature through the plastic modulus $E^c_p = dY/d\epsilon_p$.
In the elasto-plastic Cosserat theory the non-symmetric strain and curvature rates are decomposed additively into elastic and plastic components, $\dot{\epsilon} = \dot{\epsilon}_e + \dot{\epsilon}_p$; $\dot{\kappa} = \dot{\kappa}_e + \dot{\kappa}_p$ Using an

associated flow rule and resorting to the traditional argument of linearized consistency results in the compacted tangential format of STEINMANN AND WILLAM [21] relating the rates of stress and couple-stresses to the rates of strain and curvatures in terms of,

$$\begin{pmatrix} \dot{\sigma} \\ \dot{\mathbf{m}} \end{pmatrix} = \begin{pmatrix} \mathbf{E}_{ep} & \mathbf{D}_{ep} \\ \mathbf{D}^t_{ep} & \mathbf{C}_{ep} \end{pmatrix} : \begin{pmatrix} \dot{\epsilon} \\ \dot{\kappa} \end{pmatrix} \tag{18}$$

The quasi-linear suboperators for strain-softening plasticity define the relationships between the non-symmetric stress and the non-symmetric strain in terms of

$$\mathbf{E}_{ep} = \mathbf{E} - \frac{\mathbf{E} : \mathbf{n}^\sigma \otimes \mathbf{n}^\sigma : \mathbf{E}}{E^c_p + \mathbf{n}^\sigma : \mathbf{E} : \mathbf{n}^\sigma + \mathbf{n}^m : \mathbf{C} : \mathbf{n}^m} \tag{17}$$

and the coupling between the non-symmetric stress and the curvature as

$$\mathbf{D}_{ep} = - \frac{\mathbf{E} : \mathbf{n}^\sigma \otimes \mathbf{n}^m : \mathbf{C}}{E^c_p + \mathbf{n}^\sigma : \mathbf{E} : \mathbf{n}^\sigma + \mathbf{n}^m : \mathbf{C} : \mathbf{n}^m} \tag{19}$$

and the relationship between the couple-stress and the curvature as

$$\mathbf{C}_{ep} = \mathbf{C} - \frac{\mathbf{C} : \mathbf{n}^m \otimes \mathbf{n}^m : \mathbf{C}}{E^c_p + \mathbf{n}^\sigma : \mathbf{E} : \mathbf{n}^\sigma + \mathbf{n}^m : \mathbf{C} : \mathbf{n}^m} \tag{19}$$

In comparison to the classical non-polar formulation of $\mathbf{E}_{ep}$ the additional quadratic form $\mathbf{n}^m : \mathbf{C} : \mathbf{n}^m$ arises in the denominator. This supplement reduces the plastic contribution and shifts possible singularities of the elasto-plastic operator. The interaction of the strain rate field and the curvature rate field is controled by the coupling sub-operators $\mathbf{D}_{ep}$ and $\mathbf{D}^t_{ep}$ which depend in turn on the magnitude of the characteristic length ℓ_c and the occurrence of couple stresses. If ℓ_c is set to zero, or if the couple-stresses vanish, then $\mathbf{D}_{ep} = \mathbf{D}^t_{ep} = \mathbf{0}$ and the stress field is no longer coupled to the curvature field, and vice versa.

For the sake of comparison with the previous extensions of strain-softening elasto plasticity we further reduce the micropolar formulation via static condensation into,

$$\dot{\sigma} = \mathbf{E}^c_{ep} : \dot{\epsilon} + \mathbf{L}^c_{ep} : \dot{\mathbf{m}} \tag{20}$$

where the curvature rates were eliminated by $\dot{\kappa} = -\mathbf{C}^{-1}_{ep} : \mathbf{D}^t_{ep} : \dot{\epsilon} + \mathbf{C}^{-1}_{ep} : \dot{\mathbf{m}}$. Thereby the condensed tangential material stiffness tensors are defined as,

$$\mathbf{E}^c_{ep} = \mathbf{E}_{ep} - \mathbf{D}_{ep} : \mathbf{C}^{-1}_{ep} : \mathbf{D}^t_{ep}; \qquad \mathbf{L}^c_{ep} = \mathbf{D}_{ep} : \mathbf{C}^{-1}_{ep} \tag{21}$$

As postscript, the constitutive structure with two separate contributions of the condensed micropolar formulation exhibits the same structure as the second order gradient formulation.

CONSTITUTIVE BRANCHING OF DIFFUSE FAILURE

For the sake of terminology we distinguish among diffuse and localized failure modes according to the degree of continuity, or rather discontinuity, of the deformation field. Diffuse failure mechanisms are associated with material branching, i.e. singularities of the tangential material stiffness, without introducing discontinuities in the deformation field. In contrast localized failure mechanisms are associated with the formation of a discontinuity surface across which the deformation field bifurcates. It is noteworthy that diffuse failure mechanisms do not require special mesh provisions for transmission onto the element and system levels respectively, see STEINMANN AND WILLAM [22], since all standard element formulations reproduce constant

strain states because of the constant strain condition. In contrast, the localized failure mechanisms require either enrichment or alignment of finite element mesh lay-outs in order to capture the discontinuity, see ORTIZ AND QUIGLEY [14], and STEINMANN AND WILLAM [22].

Branching of Fracture Energy-Based Elasto Plasticity

Diffuse failure corresponds to stationary values of the stress rate,

$$\dot{\sigma} = \mathbf{E}^f_{ep} : \dot{\epsilon} = \mathbf{0}; \qquad \det(\mathbf{E}^f_{ep}) = 0 \quad \forall \quad \dot{\epsilon} = \dot{\epsilon}_{crit} \tag{22}$$

This singularity of the tangential material operator is traditionally expressed in terms of the uniqueness argument of material branching. On the other hand, the pointwise argument of material instability in the small furnishes another criterion for diffuse failure in terms of vanishing values of the second order work density,

$$d^2W = \frac{1}{2}\dot{\epsilon} : \dot{\sigma} = \frac{1}{2}\dot{\epsilon} : \mathbf{E}^f_{ep} : \dot{\epsilon} = 0 \quad \forall \quad \dot{\epsilon} = \dot{\epsilon}_{crit} \tag{23}$$

For associated plastic flow, the instability argument of vanishing second order work coincides with the singularity of the tangential material operator. Both indicators of diffuse failure reduce to the classic result that $d^2W = 0$ and $det(\mathbf{E}^f_{ep}) = 0$ if the plastic modulus, and thus if either the fracture modulus, or the characteristic fracture length go to zero $E^f_p = \ell_f\, E_f \to 0$. Thereby the critical eigendirection is governed by the plastic flow rule, i.e. $\dot{\epsilon}_{crit} = \mathbf{n}$.

For non-symmetric constitutive formulations of non-associated plastic flow the instability argument of vanishing second order work does not coincide with the singularity of the non-symmetric tangent material operator. In fact, the instability argument provides a lower bound since the quadratic form of the incremental energy functional only activates the symmetric content of the material operator, i.e.

$$d^2W = \frac{1}{2}(\dot{\epsilon} : \dot{\sigma}) = \frac{1}{4}\left(\dot{\epsilon} : (\mathbf{E}^f_{ep} + (\mathbf{E}^f_{ep})^t) : \dot{\epsilon}\right) = 0 \tag{24}$$

Because of the Bromwich limiters, the symmetrizing effect of the second order work functional provides a lower bound to the singularity of the non-symmetric operator, i.e. $d^2W \leq det(\mathbf{E}^f_{ep})$, see WILLAM AND ETSE [27]. In sum, the second order work indicator leads to premature instability diagnostics before the non-symmetric material operator experiences a singularity.

Branching of Second Order Gradient Elasto Plasticity

In the case of the second order gradient theory the arguments of constitutive branching yield conditions for the loss of uniqueness when both requirements

$$\det(\mathbf{E}^g_{ep}) = 0; \quad \mathbf{L}^g_{ep} = \mathbf{0} \tag{25}$$

are satisfied. This illustrates the stabilizing influence of the gradient term of plastic strain as long as the plastic moduli satisfy the constraint condition $E_{p2} > E_{p1}$. For the symmetric operator of the associated flow formulation above the instability argument of $d^2W = 0$ infers the same condition: the gradient effect vanishes if $E_{p2} = E_{p1}$. Hence perfect plasticity with $E_{p1} = 0$ is again a sufficient condition for instability in the small. In general the second order work condition infers,

$$d^2W = \frac{1}{2}\dot{\epsilon} : \dot{\sigma} = \frac{1}{2}\dot{\epsilon} : \mathbf{E}^g_{ep} : \dot{\epsilon} + \frac{1}{2}\dot{\epsilon} : \mathbf{L}^g_{ep}\nabla^2\dot{\epsilon}_p = 0 \quad \forall \quad \dot{\epsilon} = \dot{\epsilon}_{crit} = \mathbf{n} \tag{26}$$

which illustrates the stabilizing effect of the gradient term if the plastic moduli satisfy the restriction $E_{p2} - E_{p1} > 0$.

Branching of Micropolar Elasto Plasticity

In the case of micropolar elasto plasticity the branching argument reveals the further stabilization beyond that of the gradient formulation. Loss of uniqueness is now connected to two singularity conditions which have to be satisfied simultaneously,

$$\det(\mathbf{E}^c_{ep}) = 0; \quad \det(\mathbf{L}^c_{ep}) = 0 \tag{27}$$

The instability condition further illustrates the stabilizing effect as

$$d^2W = \frac{1}{2}\dot{\epsilon} : \dot{\sigma} = \frac{1}{2}\dot{\epsilon} : \mathbf{E}^c_{ep} : \dot{\epsilon} + \frac{1}{2}\dot{\epsilon} : \mathbf{L}^c_{ep} : \dot{\mathbf{m}} = 0 \quad \forall \quad \dot{\epsilon} = \dot{\epsilon}_{crit} = \mathbf{n} \tag{28}$$

In sum, the constitutive operators of the gradient and the micropolar formulations exhibit both a second auxiliary condition which removes, or at least delays the branching points of the tangential material operator.

LOCALIZATION ANALYSIS OF DISCONTINUITIES

The localized failure mechanism originates in a singularity of the localization tensor which signals discontinuous bifurcation of the velocity gradient field. This event is associated with the formation of a discontinuity surface of first order, i.e. a jump condition in the field of displacement, or rather velocity gradients.

Localization of Fracture Energy-Based Elasto Plasticity

Discontinuous bifurcation is manifested by a singularity of the localization or acoustic tensor, respectively, i.e. when

$$\det(\mathbf{Q}^f_{ep}) = \det(\mathbf{N} \cdot \mathbf{E}^f_{ep} \cdot \mathbf{N}) = 0 \tag{29}$$

In numerical computations, this corresponds to pointwise loss of ellipticity which causes severe mesh-dependence because of the underlying singularity of $\mathbf{Q}^f_{ep}$. Thereby predictions of the post-peak behaviour depend crucially on the mesh design and the choice of the element formulation. In the fixed mesh approach without mesh-adaption, the finite element grid has to transmit this singularity throughout the structural system in order to capture sharp localization. This requires either enrichment of the underlying finite element expansion in order to meet the weak localization condition of STEINMANN AND WILLAM [22], or adaptive re-alignment of the element boundaries along the discontinuity surface, see ORTIZ AND QUIGLEY [14].
The formation of discontinuities may also be expressed in terms of vanishing wave speeds $c \to 0$ because of the one-to-one analogy to the acoustic tensor,

$$\rho c^2 = \mathbf{M} \cdot \mathbf{Q}^f_{ep} \cdot \mathbf{M} \to 0 \tag{30}$$

whereby the vector $\mathbf{M}$ designates the polarization direction. This quadratic form symmetrizes the non-symmetric constitutive operator and thus leads to an indicator which signals premature loss of hyperbolicity in wave propagation. In sum, the loss of positive wave speeds is synonymous with the loss of strong ellipticity in quasistatic localization problems.

Localization of Second Order Gradient Elasto Plasticity

In the case of the second order gradient theory the localization argument follows the question of discontinuous bifurcation in analogy to the traditional local constitutive formulation. As the material operator is augmented by the gradient term, the localization condition is comprised of two contributions,

$$[\![\dot{\epsilon}]\!] = [\![\text{grad}\dot{u}]\!] = \dot{\gamma}^E(\mathbf{M} \otimes \mathbf{N} + \mathbf{N} \otimes \mathbf{M}) \tag{31}$$

$$[\![\nabla^2 \dot{\epsilon}_p]\!] = \dot{\gamma}^L \mathbf{M} \cdot \mathbf{N} \tag{32}$$

The two jump conditions determine entirely the character of the discontinuities in the strain rate and the second order gradient of the equivalent plastic strain. With the help of Maxwell's compatibility condition the jump conditions may be represented by a second order rank-one tensor and a scalar involving the polarization vector $\mathbf{M}$ and the normal vector $\mathbf{N}$ of the discontinuity surface.
The balance of linear momentum across the discontinuity surface requires that the traction vector $\mathbf{t}^\sigma$ remains continuous, i.e. the jumps of the traction field has to vanish:

$$[\![\dot{\mathbf{t}}^\sigma]\!] = \mathbf{N} \cdot [\![\dot{\sigma}]\!] = \mathbf{0} \tag{33}$$

Combining the equilibrium condition with the elasto-plastic constitutive equation

$$[\![\dot{\sigma}]\!] = \mathbf{E}^g_{ep} : [\![\dot{\epsilon}]\!] + \mathbf{L}^g_{ep}[\![\nabla^2 \dot{\epsilon}_p]\!] \tag{34}$$

leads to the localization condition for the second order gradient description,

$$[\![\dot{\mathbf{t}}^\sigma]\!] = \left(\dot{\gamma}^E \mathbf{Q}^{Eg}_{ep} + \dot{\gamma}^L \mathbf{Q}^{Lg}_{ep}\right) \cdot \mathbf{M} = \mathbf{0} \tag{35}$$

In other terms, discontinuous bifurcation can only take place when the combined localization tensor exhibits a singularity, i.e. $det(\mathbf{Q}^{Eg}_{ep} + \frac{\dot{\gamma}^L}{\dot{\gamma}^E}\mathbf{Q}^{Lg}_{ep}) = 0$. Thereby, the first term coincides with the previous localization condition for a jump in the velocity gradient, where $\mathbf{Q}^{Eg}_{ep} = \mathbf{N} \cdot \mathbf{E}^g_{ep} \cdot \mathbf{N}$. The second term introduces the additional jump condition of the second order gradient of the equivalent plastic strain rate, i.e. $\mathbf{Q}^{Lg}_{ep} = \mathbf{N} \cdot \mathbf{L}^g_{ep} \otimes \mathbf{N}$.
The first localization condition corresponds to that of the previous fracture energy description of the traditional local formulation. The second localization condition of the gradient contribution counteracts the destabilizing effect of the softening plasticity contribution and stabilizes the localization tensor.

Localization of Micropolar Elasto Plasticity

In the case of Cosserat continua the localization condition implies discontinuous bifurcation of both fields, the strain and the curvature rate fields,

$$\begin{pmatrix} \mathbf{Q}_{ee} & \mathbf{Q}_{ec} \\ \mathbf{Q}_{ce} & \mathbf{Q}_{cc} \end{pmatrix} \cdot \begin{pmatrix} \dot{\gamma}^u \mathbf{M}^u \\ \dot{\gamma}^\omega \mathbf{M}^\omega \end{pmatrix} = \begin{pmatrix} \mathbf{0} \\ \mathbf{0} \end{pmatrix} \tag{36}$$

where the suboperators of the localization tensor are defined as

$$\begin{aligned} \mathbf{Q}_{ee} &= \mathbf{N} \cdot \mathbf{E}^c_{ep} \cdot \mathbf{N} \\ \mathbf{Q}_{ec} &= \mathbf{N} \cdot \mathbf{D}^c_{ep} \cdot \mathbf{N} \\ \mathbf{Q}_{ce} &= \mathbf{N} \cdot \mathbf{D}^c_{pe} \cdot \mathbf{N} \\ \mathbf{Q}_{cc} &= \mathbf{N} \cdot \mathbf{C}^c_{ep} \cdot \mathbf{N} \end{aligned} \tag{37}$$

Again there are two localization conditions for the development of dicontinuities. Condition # 1 infers singularity of the augmented localization tensor which involves in the case of micropolar continua

$$\det\left(\mathbf{Q}^e_{ep}\right) = \det\begin{pmatrix} \mathbf{Q}_{ee} & \mathbf{Q}_{ec} \\ \mathbf{Q}_{ce} & \mathbf{Q}_{cc} \end{pmatrix} = 0 \tag{38}$$

A second condition derives from the balance of linear and angular momenta across the discontinuity surface: to this end the bifurcated stress and couple-stress field may be expressed in terms of the continuous fields $\dot{\boldsymbol{\sigma}}$ and $\dot{\mathbf{m}}$ and their jumps $[\![\dot{\boldsymbol{\sigma}}]\!]$ and $[\![\dot{\mathbf{m}}]\!]$.
The balance of linear and angular momentum for example at the '+' side of the discontinuity surface renders

$$\operatorname{div}(\dot{\boldsymbol{\sigma}}^+) = \operatorname{div}(\dot{\boldsymbol{\sigma}}) + \varsigma_\sigma \operatorname{div}[\![\dot{\boldsymbol{\sigma}}]\!] = 0 \tag{39}$$

$$\operatorname{div}(\dot{\mathbf{m}})^+ + \mathbf{e} : \dot{\boldsymbol{\sigma}}^+ = \operatorname{div}(\dot{\mathbf{m}}) + \mathbf{e} : \dot{\boldsymbol{\sigma}} + \varsigma_m \operatorname{div}[\![\dot{\mathbf{m}}]\!] + \varsigma_m \mathbf{e} : [\![\dot{\boldsymbol{\sigma}}]\!] = 0 \tag{40}$$

Since $\operatorname{div}(\dot{\mathbf{m}}) + \mathbf{e} : \dot{\boldsymbol{\sigma}} = 0$, a constant amplitude of the jump conditions along the discontinuity surface leads to the second localization condition for micropolar continua

$$\mathbf{e} : [\![\dot{\boldsymbol{\sigma}}]\!] = \underbrace{\mathbf{e} : [\dot{\gamma}^u \mathbf{E}^e_{ep} : [\mathbf{M}^u \otimes \mathbf{N}]]}_{\text{Condition \# 2a}} + \underbrace{\mathbf{e} : [\dot{\gamma}^\omega \mathbf{D}^e_{ep} : [\mathbf{M}^\omega \otimes \mathbf{N}]]}_{\text{Condition \# 2b}} = 0 \tag{41}$$

Condition # 2 is a symmetry restriction of the stress rate jump which is composed of two parts, the restriction on the strain rate field (Condition # 2a) and on the curvature rate field (Condition # 2b).
In sum, the two localization conditions permit discontinuous bifurcation only if the localization tensor is singular and, additionally, if the jump of the stress rate field is symmetric.

CONCLUDING REMARKS

The extension of the classical localization condition to gradient models and micropolar continua introduces auxiliary localization conditions which are mobilized as soon as jumps in the second order plastic gradients or the curvature field are admitted.
The direct tension experiment of DIETSCHE ET AL. [8] did demonstrate the stabilizing effects of both the gradient and the micropolar theories, when J_2-plasticity is used. On the other hand, localization was still possible for perfect plasticity when the gradient effect or the miropolar effect of couple-stresses remained negligible. In fact the likelihood of localization does increase with increasing softening in the plasticity formulation.
As a final note, the stabilizing effects of the micropolar theory did not retrofit the localization properties of the strain-softening Rankine condition, see DIETSCHE ET AL. [8], even when couple-stresses were introduced in its extended version. Thus the micropolar extension of the Rankine hypothesis does not regularize the tensile softening branch in the smeared crack approach.

ACKNOWLEDGEMENT

This work was partially supported by the National Science Foundation under Grant MSS-9121616 to the University of Colorado at Boulder.

References

[1] BAZANT, Z.P., "Why Continuum Damage is Nonlocal: Micromechanics Arguments", ASCE J. Eng. Mech., Vol. 117 (1988), pp. 1070-1087.

[2] BAZANT, Z.P. AND OH, B.H. "Crack Band Theory for Fracture of Concrete", RILEM Matl. Struct., Vol. 16 (1983), pp. 155-177.

[3] BESDO, D., "Ein Beitrag zur nichtlinearen Theorie des Cosserat-Kontinuums", Acta Mechanica, Vol. 20 (1974), p. 105

[4] DE BORST, R. , "Simulation of Localization Using Cosserat Theory", Proc. 2nd Intl. Conf. Comp. Aided Anal. Design Concrete Str., N. Bicanic and H.A. Mang eds., Pineridge Press, Swansea (1990), pp. 931-944.

[5] DE BORST, R. AND MÜHLHAUS, H.-B., "Continuum Models for Discontinuous Media", RILEM Proc. Fracture Processes in Concrete, Rock and Ceramics, J.G.M. van Mier, J.G. Rots and A. Bakker Eds., Chapman & Hall, London, (1991), pp. 601-618.

[6] CAROL, I. AND PRAT, P.C., "Smeared Analysis of Concrete Fracture Using Microplane-Based Multicrack Model with Static Constraint", RILEM Proc. Fracture Processes in Concrete, Rock and Ceramics, J.G.M. van Mier, J.G. Rots and A. Bakker Eds., Chapman & Hall, London, (1991), pp. 619-628.

[7] COSSERAT, E. AND F., "Théorie des corps déformables", Herman et fils, Paris (1909).

[8] DIETSCHE, A., STEINMANN, P. AND WILLAM, K. "Micropolar Elasto-Plasticity and its Role in Localization Analysis", submitted for publication in Intl. J. Plasticity, (1992).

[9] ETSE, G., STEINMANN, P. AND WILLAM, K. "Rechnerische Erfassung von lokalisiertem Betonversagen im Zug- und Druckbereich", Proc. Finite Elemente-Anwendungen in der Baupraxis, J. Eibl, H. Obrecht und P. Wriggers, Universität Karlsruhe, (1991).

[10] GÜNTHER, W., "Zur Statik und Kinematik des Cosserat'schen Kontinuums", Abh. Braunschweig. Wiss. Ges., (1958), pp. 195-213.

[11] GURTIN, M.E., " The Linear Theory of Elasticity", Mechanics of Solids, Vol. 2, C. Truesdell ed., Springer-Verlag, (1972).

[12] LIPPMANN, H., "Eine Cosserat-Theorie des plastischen Fließens", Acta Mechanica, Vol. 8 (1969), pp. 255-284.

[13] MÜHLHAUS, H.-B. AND VARDOULAKIS, I., "The Thickness of Shear Bands in Granular Materials", Géotechnique, Vol. 37 (1987), pp. 271-283.

[14] ORTIZ, M. AND QUIGLEY, IV, J.J., "Adaptive Mesh Refinement in Starin Localization Problems", Comp. Meth. Appl. Mech. Eng., Vol 90, (1991), pp. 781-804.

[15] PIETRUSCZAK, S.T. AND MROZ, Z., "Finite Element Analysis of Deformation of Strain-Softening Materials", Intl. J. Num. Meth. Eng., Vol. 17 (1981), pp. 327-334.

[16] PIJAUDIER-CABOT G. AND BAZANT, Z.P., "Nonlocal Damage Theory", ASCE J. Eng. Mech., Vol. 113 (1987), pp. 1512-1533.

[17] PRAMONO, E. AND WILLAM, K., "Fracture Energy-Based Plasticity Formulation of Plain Concrete",ASCE-EMD, Vol. 115, (1989), pp. 1183-1204.

[18] RUDNICKI, J.W. AND RICE, J.R., "Conditions for the Localization of Deformation in Pressure-Sensitive Dilatant Materials", Journal for Mechanics of Physics and Solids, Vol. 23 (1975), pp. 371-394.

[19] SCHREYER, H., "Analytical Solutions for Nonlinear Strain-Gradient Softening and Localization", ASME J. Appl. Mech., Vol. 57 (1990), pp. 522-528.

[20] STEINMANN, P. AND WILLAM, K., "Localization in Micropolar Elasto-Plasticity", Proc. 3rd Int. Conf. 'Constitutive Laws for Engineering Materials', C.S. Desai et al. eds., ASME-Press, New York, (1991), pp. 461-465.

[21] STEINMANN, P. AND WILLAM, K. "Localization within the Framework of Micropolar Elasto-Plasticity", V. Mannl, O. Brueller, J. Najar eds., 60th Anniversary Volume Horst Lippmann, Springer Verlag, Berlin, (1991), pp. 296-313.

[22] STEINMANN, P. AND WILLAM, K., "Finite Elements for Capturing Localized Failure", Archive of Appl. Mech., Vol. 61 (1991), pp. 259-275.

[23] STEINMANN, P. AND WILLAM, K., "Performance of Enhanced Finite Element Formulations in Localized Failure Computations", Comp. Meth. Appl. Mech. Eng., Vol. 90 (1991), pp. 845-867.

[24] VARDOULAKIS, I. AND AIFANTIS, E.C., "A Gradient Flow Theory of Plasticity for Granular Materials", to appear in Acta Mechanica, (1991).

[25] WILLAM, K., BIĆANIČ, N. AND STURE, S., "Constitutive and Computational Aspects of Strain-Softening and Localization in Solids", ASME-WAM'84 New Orleans, Symp. Vol. G00271, ASME New York, 1984, pp. 233-252.

[26] WILLAM, K. AND MONTGOMERY, K., "Fracture Energy-Based Softening Plasticity Model for Shear Failure", Proc. Intl. Symp. Inter. Convent. Munition and Protect. Struct., Vol II, Mannheim, March 9-13, 1987, pp. 679-691.

[27] WILLAM, K. AND ETSE, G., "Assessment of the Extended Leon Model for Plain Concrete", Proc. 2nd Intl. Conf. Comp. Aided Anal. Design Concrete Str., N. Bicanic and H.A. Mang eds., Vol. II, Pineridge Press, Swansea, (1990), pp. 851-870.

Principal Lecture

MATERIAL STRUCTURE AND TENSION SOFTENING PROPERTIES OF CONCRETE

HIROZO MIHASHI
Tohoku University, Faculty of Engineering,
Dept. of Architecture, Sendai 980, Japan.

ABSTRACT

Tension softening behavior of concrete is studied from the view point of the influence of material structure on toughening mechanism. On the basis of fracture energy test results of notched beams, toughening properties of concrete are discussed in relation to compressive strength and the maximum aggregate size. Moreover these test results are analyzed by means of the inverse analysis to obtain the tension softening diagram. The parameters of a bilinear tension softening diagram are determined and the relation of the tension softening diagram and the material structure is discussed.

The results indicate that the softening initiation stress and the first descending branch of the tension softening diagram is strongly related to the microstructure of the matrix and the softening tail including the critical crack width is attributed to the heterogeneity of the mesostructure.

INTRODUCTION

Mortar and concrete can be considered as two-phase composite materials in which hardened cement paste is binding together fine and coarse aggregate particles. The overall mechanical and physical properties of such composite systems are dependent on the volume fraction and properties of the constituents, as well as the mechanisms of interaction between phases.

The recent development of numerical analyses and design of reinforced concrete structures needs rational constitutive relations not only under compressive stress but also under tensile stress. As the constitutive relation under tensile stress, fracture mechanics has been expected to work. The tremendous progress in the field of fracture mechanics of concrete during the past decade has revealed that a large fracture process zone (FPZ) is created before the unstable crack propagation because of the composite system and that the fracture properties are strongly influenced by the behavior of the FPZ. Accordingly the conventional fracture mechanics parameters are not available to concrete. Instead of them, Hillerborg and his coworkers developed the fictitious crack model (FCM) to describe the nonlinear behavior of the FPZ and fracture energy G_F was proposed as a fracture mechanics parameter to represent the toughness of

concrete [1]. In this FCM, it is assumed that all sources of the nonlinearity under tensile stress are involved in a fictitious crack that is able to transfer stress as a function of the opening width [1]. The parameter G_F is defined as the energy absorbed to create a unit area of projected fracture surface and the concept is rather similar to the work of fracture.

Since RILEM recommendation on the experimental procedure to determine G_F was issued in 1985 [2], several papers have been published to show the relation between G_F and concrete engineering parameters such as compressive strength f_c, the maximum aggregate size d_{max} and so on. On the other hand, it was shown by Petersson [3] and also by Roelfstra and Wittmann [4] that a given value of G_F was not sufficient for a realistic prediction of the failure process. The load-displacement curve and the maximum load-bearing capacity of a notched beam can vary when the analysis is done with constant G_F but with varying the shape of the tension softening diagram.

Petersson [3] studied the effects of the following factors on G_F: type of aggregate, water-cement ratio: w/c, volume fraction of aggregates, d_{max} and age of concrete. He obtained the following results: G_F decreases when w/c increases; G_F seems to increase somewhat with increasing volume fraction of aggregate; G_F seems to be insensitive to d_{max}; stronger aggregates produce higher value of G_F than that produced by weaker aggregates . On the other hand, Kleinschrodt and Winkler [5] reported that the mean value of G_F for d_{max} of 16mm was about 25% higher than that for d_{max} of 8mm. Based on the round robin test results of 700 beam tests organized by RILEM-TC50, Hillerborg [6] concluded that there was no major

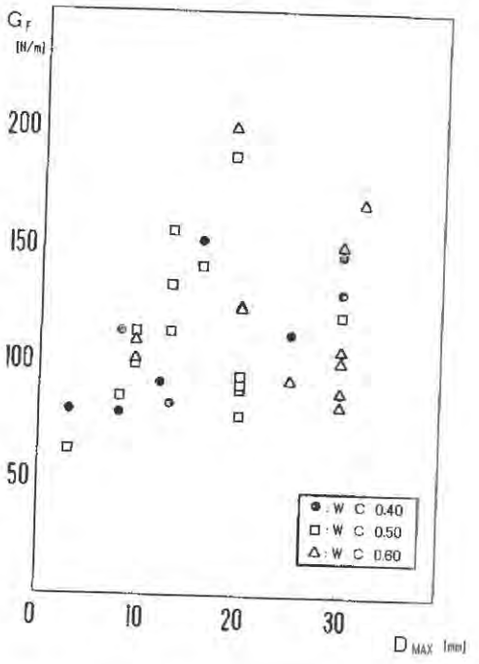

FIGURE 1. Variation of G_F with maximum aggregate size and water/cement ratio for standard beams according to RILEM recommendation [6].

influence of w/c but there was a tendency for G_F to increase with d_{max} increasing from 8mm to 20mm. However, there was a great scatter (FIG. 1) and this tendency was uncertain. Wittmann and his co-workers [7] studied the influence of age of loading, w/c and rate of loading on G_F and on the shape of the tension softening diagram with notched beams. They also tested compact tension specimens with the sufficient ligament length to study the influence of the specimen size, rate of loading, d_{max} and w/c on fracture mechanics parameters [8]. It was shown that larger specimens, higher rate of loading, larger d_{max} and smaller w/c gave larger values to G_F.

It should be noticed that a formula of G_F as a function of compressive strength and also a bilinear tension softening diagram are given in the CEB-FIP Model Code 1990 (MC 90) [9, 10]. The following relation has been formulated in the code:

$$G_F = a_d \cdot (f_{cm}/f_{cm0})^{0.7} \qquad (1)$$

where f_{cm} is the mean compressive strength, f_{cm0}=10MPa, and a_d is a coefficient dependent on d_{max}. The author and his co-workers indicated that G_F might not proportionally increase above 100 MPa of compressive strength [11]. Hordijk summarized the results of many previous experimental studies including their own data concerning several factors influencing G_F [12]. This compiled information may be useful to overlook how G_F is influenced by various factors.

On the basis of the inverse analysis, Roelfstra and Wittmann developed a numerical procedure to determine an optimum tension softening diagram from measured load displacement curves [4]. By means of this procedure, it was shown that the diameter of d_{max} had a strong influence on the critical crack width of the FCM. Wittmann and his co-workers also studied the influence of various factors on the shape of the tension softening diagram which was approximated with a bilinear model [7, 8]. These two series of experimental data [7, 8] were re-analyzed by the author and his co-workers [13] to conclude that the tension softening diagram might be potential to investigate the mechanism how material structures influence the tensile fracture behavior, though it is hardly possible to understand the mechanism directly from the relation between G_F and the material structure.

The aim of this contribution is to study the influence of the maximum aggregate size and compressive strength on G_F from the view point of changes in the tension softening diagram.

MATERIALS AND METHODS

Sample Preparation and Testing Procedure

Notched beams of concrete and mortar were tested in three-point bending mode. The length, width and height of the beam were 840mm, 100mm and 100mm, respectively. After demoulding, all specimens were cured in water of 20°C for 28 days. A notch with a length of half of the height was sawn at midspan. The mixproportions per unit volume of mortar and of two types of concrete used in these tests series are given in TABLE 1 together with compressive and splitting tensile strength. Normal Portland cement was used. Coarse aggregates of crushed hard rock and river sand from Miyagi Prefecture were used. The volume fraction of aggregates was kept constant for concrete, whose sand-aggregate weight ratio was 0.44. Three specimens were tested for each case.

All beams were loaded by a servo-controlled hydraulic jack with a rate

TABLE 1. Mix proportion and strength of concrete

Series	d_{max} (mm)	W/C	W/(C+Si)	W (kg)	C (kg)	Sand (kg)	Aggre. (kg)	Silica-fume(kg)	Superpl. (cc/CW)	Comp. Str. (Mpa)	Tens. St. (Mpa)
A	25	0.25	0.20	111	444	721	1006	111	35.5	96.4	6.42
B	25	0.24	0.20	111	472	721	1006	83	40.6	72.8	6.88
C	25	0.47	0.40	160	340	721	1006	60	12.1	64.5	4.95
D	25	0.60	0.60	188	313	721	1006	0	0.0	32.2	3.14
E	25	0.65	0.65	227	349	721	1006	0	0.0	21.4	2.88
F	5	0.25	0.20	111	444	721	1006	111	57.0	105.9	6.08
G	5	0.47	0.40	160	340	721	1006	60	28.0	58.8	3.82
H	5	0.65	0.65	227	349	721	1006	0	0.0	20.9	2.35
I	-	0.25	0.20	111	444	721	0	111	57.0	110.7	6.13
J	-	0.47	0.40	160	340	721	0	60	28.0	46.3	3.84
K	-	0.65	0.65	227	349	721	0	0	0.0	33.8	2.67

of deflection $\dot{\delta}$ = 0.07mm/min. The span length was 770mm. The load was measured by a load cell and the deflection with an displacement tranceducer. Both values were simultaneously recorded together with the crack mouth opening displacement measured with a clip gauge.

Numerical Evaluation of Tension Softening Diagrams

Previous experimental studies of tension softening diagrams by means of direct tension tests show that a bilinear model may be a good approximation [3, 14]. On the bases of the FCM with a bilinear tension softening diagram, the inverse analysis of mean load-deflection curves of each series was performed to determine the modulus of elasticity and essential four parameters of the bilinear tension softening diagram: F_t, S_1, w_1 and w_2 as shown in FIG. 2 by means of a special finite element code whose concept was originally developed by Roelfstra and Wittmann [4]. These determined parameters can lead to a good agreement between measured load-deflection curves and numerically simulated ones by finite element analysis. An analytical value of the fracture energy G_F' is calculated by eq. (2), which coincides with the area under the two lines of the tension softening diagram (FIG. 2).

$$G_F' = (F_t w_1 + S_1 w_2)/2 \qquad (2)$$

RESULTS

According to the RILEM recommendation [2], G_F was determined from the measured load-deflection curve considering the influence of the self-weight. FIG. 3 shows the relation between G_F and the compressive strength f_c. Recommended curves of MC 90 are also shown. While increasing the maximum aggregate size leads to a larger value of G_F, G_F does not simply increase as f_c increases. There is a large scatter in G_F especially in

of d_{max} = 25mm. Nevertheless, G_F of the weakest concrete (Series E) much higher than the predicted value by MC 90. Very rough fracture ces were observed in the specimens with higher values of G_F.

Determined four parameters to characterize the bilinear tension ening diagram are shown in FIG. 4 as a function of f_c for each case of . Although both of F_t and S_1 increase as f_c increases, the ratio of F_t is not constant. The ratio varies between 0.21 and 0.31 =25mm), 0.13 and 0.24 (d_{max}=5mm), and 0.13 and 0.18 (mortar). There tendency that the ratio decreases as f_c increases.

In case of d_{max}=25mm, a very large value was given to w_2 of the low ength concrete (f_c=21MPa). Then the value of w_2 decreases as f_c reases. In case of d_{max}=5mm, however, the largest value of w_2 was given a secondary high strength of concrete (f_c=60MPa). In these three cases, of very high strength concrete and mortar (about 100MPa) is much reduced comparison with that of the low strength concrete (about 20MPa). hough the difference among three values of w_2 in the low strength ncrete series (w/c=0.65) is very large, the influence of d_{max} on w_2 is most eliminated in the very high strength concrete series /(c+Si))=0.20). While there is a tendency that w_1 decreases as f_c reases, it is still difficult to evaluate quantitatively the relation w_1 and f_c. The ratio of w_1/w_2 is rather randomly distributed between 0.10 and 0.19.

DISCUSSION

scatter of G_F shown in FIG.3 seems to be much larger than that of ncrete using gravels [13], that may be due to the rather short ligament ngth in comparison with the aggregate size. Other possibilities to cause uch a large scatter in G_F may be the influence of the geometry f aggregates, volume fraction of large aggregates and the strain gradient. hile it has been recognized in the previous studies that the influence of terial structure of concrete on G_F has a large variety, it is essential study the mechanism that creates so large variation of G_F.

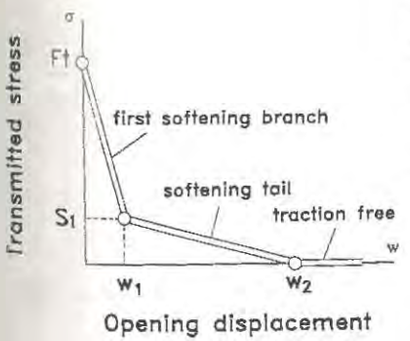

FIGURE 2
Tension softening diagram of fictitious crack model.

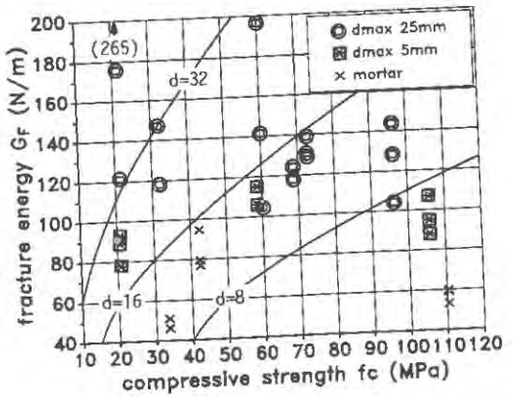

FIGURE 3
Relation between compressive strength and G_F.

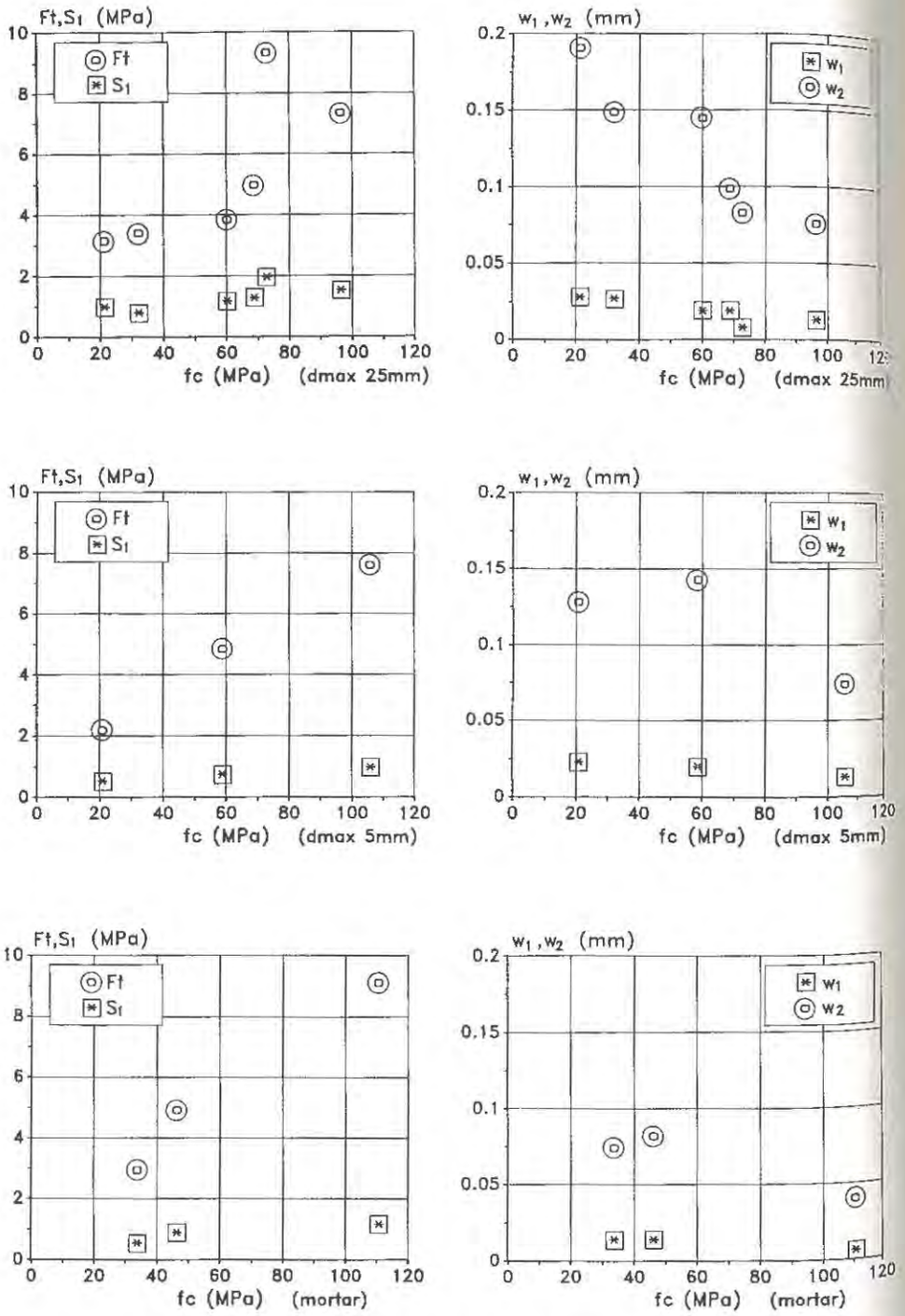

FIGURE 4. Parameters of the bilinear tension softening diagram.

Since G_F of concrete is defined by the area under the load-deflection curve, G_F would be highest when an optimum combination of strength and deformability is developed. In case of composite materials, the strength and the deformability are dominated by the composite structure. Consequently, the macroscopic fracture behaviour needs to be understood from the view point of mesolevel and microlevel fracture toughening mechanisms in the FPZ. Since it is hardly possible to separate the strength effect and the deformability effect directly from G_F, it may be essential to investigate the relation of physically measured material properties and the tension softening diagram. Moreover elastic modulus and the tension softening diagram of the FPZ are essential for numerical analyses of cracking process as the constitutive law.

On the basis of round robin test results organized by RILEM TC-50, Hillerborg [15] concluded that the modulus of elasticity and the tensile strength calculated from the notched beam tests were so different from those measured with cylinder specimens. Here the modulus of elasticity and the tensile strength are discussed first.

In FIG.5, the relation between the determined modulus of elasticity by the inverse analysis and the measured dynamic modulus of elasticity is shown. FIG. 5 indicates that modulus of elasticity calculated from the initial stiffness of the notched beam coincides well with E_d determined by a transverse vibration of cylinders (100 x200mm). The static modulus of elasticity was about 80% of E_d in these tests.

As shown in FIG. 2, the tension softening process of concrete can be subdivided into two stages. The first steep descending branch until the break point may characterize the interfaces of hydration products, whereas the second softening tail can be attributed to the bridging and pulling out behavior of large aggregates. In order to discuss the changes of the dominant mechanisms involved in the softening process, G_F' is tentatively subdivided into two parts as follows (FIG. 6):

$$G_{Fm} = (2F_t + S_1)w_1/4 \quad (3)$$

$$G_{Fb} = (2w_2 - w_1)s_1/4 \quad (4)$$

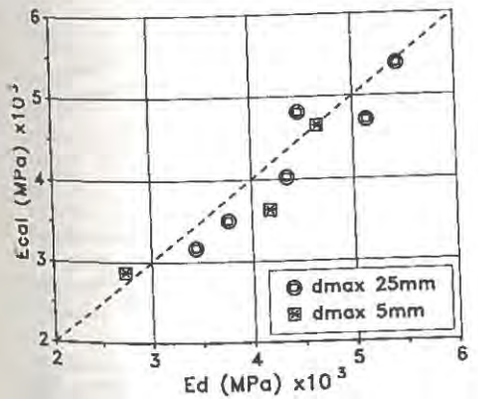

FIGURE 5
Relation of determined modulus of elasticity and measured dynamic one.

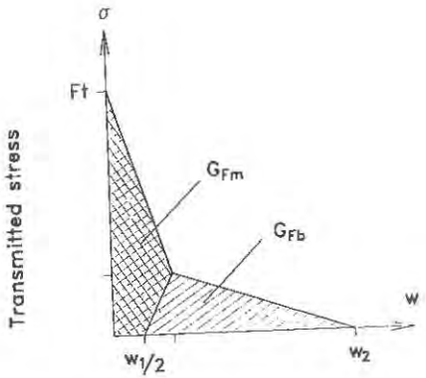

FIGURE 6
Two components in G_F'.

It is supposed that the first part G_{Fm} characterizes the strength effect and the second part G_{Fb} is corresponding to the deformability effect. FIG. 7 shows how the ratios of G_{Fm}/G_F' and G_{Fb}/G_F' change as a function of f_c. Although the results especially in case of d_{max}=25mm are widely scattered, there is a tendency that G_{Fm}/G_F' relatively increases and G_{Fb}/G_F' decreases as f_c increases. At least, the toughening mechanism below f_c=20MPa may be different from that above f_c=100MPa. In the FCM, it is assumed that the softening behavior in the FPZ initiates when the tensile stress reaches F_t. If it is possible to fix the critical stress F_t without any inverse analyses, the tension softening diagram would be more easily determined. FIG. 8 shows the relation between F_t determined by the inverse analysis and f_t that is the splitting tensile strength of cylinders (ϕ100 x200mm). It is obvious that F_t is in good agreement with f_t up to f_t=5MPa. It should be noticed, however, that F_t is about 30 % higher than f_t above f_t=6MPa. This result indicates that F_t may be approximated with f_t up to a certain strength of concrete, but that f_t may give an underestimation to

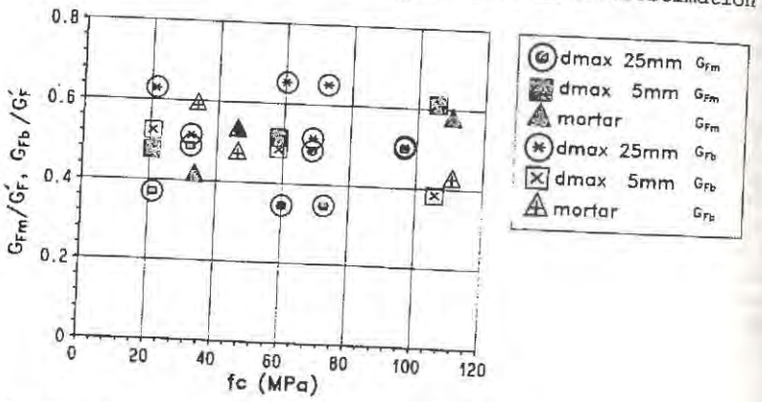

FIGURE 7. Relation of G_{Fm}/G_F' and G_{Fb}/G_F' vs. compressive strength.

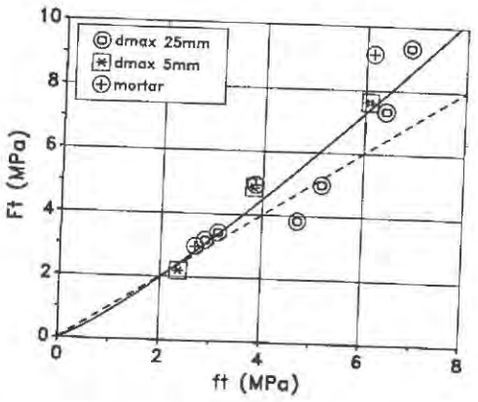

FIGURE 8
Relation between F_t and f_t.

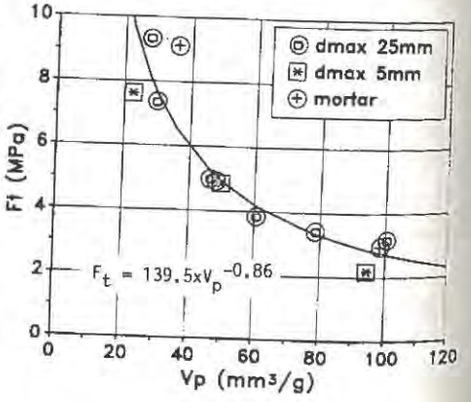

FIGURE 9
Relation of F_t and porosity.

case of very high strength concrete. While F_t is supposed to be the tensile strength in a local region near the crack tip, f_t is an averaged strength. It may be the reason why the discrepancy between F_t and f_t is enlarged in a high strength range.

It is expected that the tensile strength may be strongly dependent on the porosity. In FIG.9, the relation of F_t and the porosity V_p is shown. FIG. 9 indicates that hydration products may resist the initiation of loosening the microstructure. This results may support the assumption of Wiggins and Bailey [16] that crack starts from the weak boundary of hydration products and tortuously propagates along the boundaries. The same mechanism based on the microstructure in hydration products may explain the influence of water-cement ratio and age of loading on G_F and F_t.

Previous papers [7, 8] concluded that the influence of aggregates on G_F was related to the pull-out behavior of large aggregates during the fracture process and w_2 was characterized by the maximum aggregate size. RILEM [9, 10] gives the relation of w_2 and d_{max} in which w_2=0.12, 0.15 and 0.25 (mm) for d_{max}=8, 16 and 32 (mm), respectively. FIG. 4 shows, however, that w_2 is strongly dependent on f_c, too. In the lowest strength concrete of d_{max}=25mm (Series E), for example, the fracture surface is very tortuous and many holes have been created. There are quite few broken aggregates observed on the fracture surface. On the other hand, specimens of high strength concrete such as Series A and B have smooth fracture surfaces and most of aggregates are broken. Schlangen and van Mier simulated the failure process by a lattice model and concluded that a more ductile post peak behavior could be obtained and the width of the FPZ increased with decreasing bond strength [17]. During the mixed mode crack propagation to link bond cracks, a lot of energy should be absorbed in matrix and the angular geometry of the aggregates might perform a more remarkable function as bridging bars than that of round gravels.

By means of the acoustic emission technique, the author and his co-worker [18] showed that the width of the fracture process zone normal to the fracture surface was obviously influenced by the heterogeneity such as the maximum aggregate size. From the comparison with the tension softening properties evaluated by the inverse analysis, it was concluded that especially w_2 might have a strong relation to the width of the fracture process zone. The present results seem to have a same tendency because the highest value of w_2 has been obtained from the specimen with the most tortuous fracture surface.

FIG. 10 and FIG. 11 show the analyzed results [13] of compact tension (CT) tests carried out by Wittmann and his co-workers [8, 19]. The corresponding compressive strength is shown in TABLE 2. In these CT tests, round river gravels were used and the specimens had the ligament length of 100mm and the thickness of 120mm. In comparison with the present beam tests, CT specimens give slightly smaller values to F_t but much larger values to w_2. It is worthwhile to notice, however, that the tendency of relations of these parameters and the compressive strength is quite similar to that obtained from beam tests. Although w_2 of concrete with larger aggregates is remarkably increased as the compressive strength decreases, changes of w_2 become more gentle as the maximum aggregate size is reduced.

Since FIG. 4 and FIG. 11 show that w_2 cannot be simply described as a function only of the maximum aggregate size, some other means is necessary to be found for practical purposes. In plain concrete, the denser microstructure of matrix increases the tensile strength but makes the composite structure less heterogeneous. These structural changes influence the shape of the tension softening diagram. If there are any correlations between the slope of the first descending branch and the slope of the

TABLE 2
Compressive strength of concrete used in CT tests [8].

d_{max} \ w/c	0.43	0.50	0.60
mm 8	MPa 40.6	MPa 39.0	MPa 30.2
mm 16	MPa 42.9	MPa 37.7	MPa 24.4
mm 32	MPa 42.2	MPa 39.2	MPa 28.7

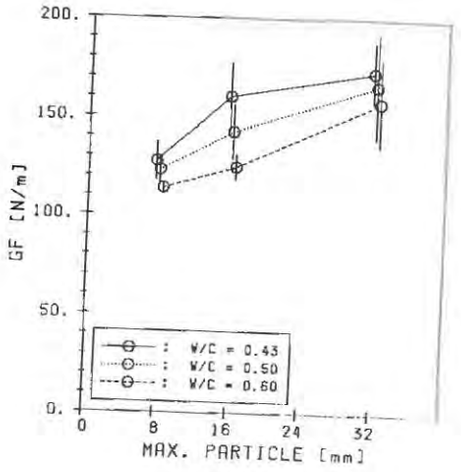

FIGURE 10
Influence of maximum aggregate size on G_F of concrete in CT tests [19].

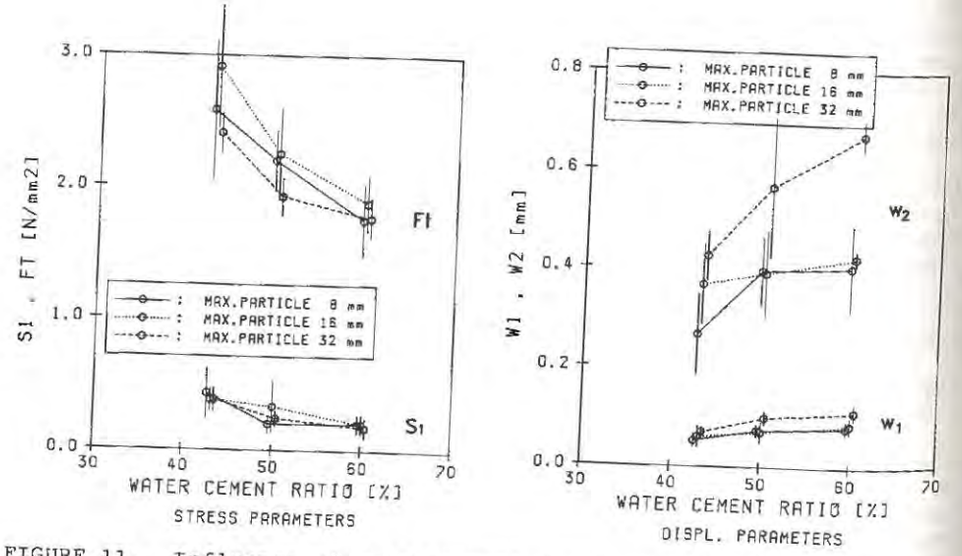

FIGURE 11. Influence of water-cement ratio on the bilinear tension softening diagram of concrete in CT tests [13].

softening tail, they may be useful to determination of the tension softening diagram. FIG. 12 shows the relation between the following two parameters:

$$T_1 = w_1/(F_t - S_1) \quad (5)$$

$$T_2 = S_1/(w_2 - w_1) \quad (6)$$

The relation shown in FIG. 12 is no more than an empirical formula but may not be generally valid. Further investigation is necessary.

CONCLUSIONS

The tension softening properties of concrete were studied from the view point of the relation of the tension softening diagram determined by the inverse analysis and physically measured material properties. The results indicate that the softening initiation stress F_t increases as the microstructure becomes denser but that the critical crack width w_2 decreases in a very high strength concrete whose fracture energy G_F is reduced. F_t may be approximated with the splitting tensile strength f_t up to 5MPa but that f_t may give an underestimation to F_t above 5MPa. Although w_2 increases as the maximum aggregate size increases, it is not true in a very high strength concrete.

ACKNOWLEDGEMENT

The author thanks Mr. K. Kirikoshi for help with the experiments and Dr. M. Nomura for analyzing the tension softening parameters.

REFERENCES

1. Hillerborg, A., Modeer, M. and Petersson, P-E., Analysis of crack formation and crack growth in concrete by means of fracture mechanics and finite element, Cement & Concrete Res., 1976, 6, 773-782.

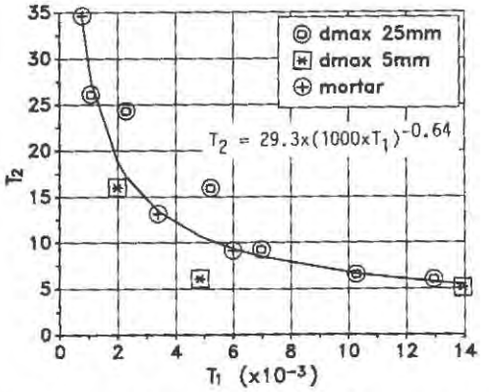

FIGURE 12. Relation between slopes of the bilinear tension softening diagram.

2. RILEM 50-FMC, Determination of the fracture energy of mortar and concrete by means of three-point bend tests on notched beams, Mater. Str., 1985, **18** (106), 45-48.
3. Petersson, P-E., Crack growth and development of fracture process zones in plain concrete and similar materials, Report TVBM-1006, Lund Inst. Tech., Sweden, 1981.
4. Roelfstra, P.E. and Wittmann, F.H., Numerical method to link strain softening with failure of concrete. In Fracture Toughness and Fracture Energy of Concrete, ed. F.H. Wittmann, Elsevier Science Publishers, Amsterdam, 1986, 163-175.
5. Kleinschrodt, H.D. and Winkler,H., The influence of the maximum aggregate size and the size of specimen on fracture mechanical parameters. In Fracture Toughness and Fracture Energy of Concrete, ed. F.H. Wittmann, Elsevier Science Publishers, Amsterdam, 1986, 391-402.
6. Hillerborg, A., Results of three comparative test series for determining the fracture energy G_f of concrete, Mater. Str., **18** (107), 407-413.
7. Wittmann, F.H., Roelfstra, P.E., Mihashi, H, Huang, Y.-Y., Zhang, X.-H., and Nomura,N., Influence of age of loading, water-cement ratio and rate of loading on fracture energy of concrete, Mater. Str., 1987, **20** (116), 103.
8. Wittmann, F.H., Rokugo, K., Bruhwiler, E., Mihashi, H. and Simonin, P., Fracture energy and strain softening of concrete as determined by means of compact tension specimens, Mater. Str., 1988, **21** (121), 21-32.
9. Comite Euro-International du Beton, CEB-FIP Model Code 1990 - Final Draft, Bulletin d'Information, 1991, **203**.
10. Hilsdorf, H.K. and Brameshuber, Code-type formulation of fracture mechanics concepts for concrete, Int. J. of Fracture, 1991, **51**, 61-72.
11. Mihashi, H., Nomura, N. and Izumi, M., Influence of matrix strength and gravel grain size on fracture properties of concrete. In Fracture of Concrete and Rock - Recent developments, ed. S.P. Shah, S.E. Swartz and B. Barr, Elsevier Applied Science, 1989, 503-512.
12. Hordijk, D.A., Local Approach to Fatigue of Concrete, Ph.D. Thesis, Delft University of Technology, 1991.
13. Mihashi, H., Nomura, N. and Izumi, M., Influence of internal structure on tension softening and fracture energy of concrete. In Fracture Toughness and Fracture Energy - Test methods for concrete and rock, A.A. Balkema, Rotterdam, 19989, 87-99.
14. Cornelissen, H.A.W., Hordijk, D.A. and Reinhardt, H.W., Experiments and theory for the application of fracture mechanics to normal and light weight concrete. In Fracture Toughness and Fracture Energy of Concrete, ed. F.H. Wittmann, Elsevier Science Publishers, Amsterdam, 1986, 565-575.
15. Hillerborg, A., Additional Concrete Fracture energy tests performed by 6 laboratories according to a draft RILEM recommendation, Report TVBM-3017, Lund Inst. Tech., Sweden, 1984.
16. Higgins, D.D. and Bailey, J.E., A microstructural investigation of the failure behaviour of cement paste, Proc. of a Conf. on Hydraulic Cement Paste: their structures and properties, Cement and Concrete Association, 1976, 283-296.
17. Schlangen, E. and van Mier, J.G.M., Experimental and Numerical Analysis of Micromechanisms of Fracture of Cementbased Composites, Report 25.5-91-1/VFC, Delft University of Technology, 1991.
18. Mihashi, H. and Nomura, N., Microcracking and tension softening properties of concrete, Cement and Concrete Composites, (in press).
19. Mihashi, H., Wittmann, F.H., Simonin, Ph. and Rokugo, K., Compact tension test to study several factors influencing fracture energy of concrete, Trans. of the Japan Concrete Institute, **9**, 1987, 503-508.

Invited Paper

A GRADIENT CONTINUUM MODEL FOR MODE-I FRACTURE IN CONCRETE AND ROCK

R. DE BORST

Delft University of Technology / TNO Building and Construction Research, Delft, Netherlands

H.-B. MUHLHAUS

CSIRO Division of Geomechanics, Mt. Waverley, Australia

J. PAMIN

Delft University of Technology, Delft, Netherlands

ABSTRACT

A gradient continuum theory is proposed to describe mode-I fracture in concrete and rock. The numerical implications of this theory are investigated as well as consequences for uniqueness, stability and ellipticity of the rate boundary value problem. The potential of the approach is demonstrated in numerical analyses of the direct tension test and the four-point bending test.

INTRODUCTION

The modelling of fracture processes in concrete and rock calls for refined continuum theories when the size of the structure is such that modelling every separate grain or every small crack is not feasible. The need for enhanced continuum theories especially becomes manifest in the post-peak regime, where the negative slope of the homogenized stress-strain curve results in a loss of ellipticity of the governing differential equations. Since such problems are not well-posed, their numerical solution gives answers that are completely determined by the discretization.

Several approaches have been pursued in the past to remedy this anomaly. Pijaudier-Cabot and Bazant [1] have suggested the use of non-local (integral) continuum models. A problem with these models is that their numerical implementation is only efficient if total stress-strain relations are employed. Alternative approaches, e.g., the use of rate dependence [2,3] or the use of Cosserat continua [4,5] also have drawbacks. The first strategy obviously only works for time-dependent problems, while the second procedure is basically limited to cases where the dominant carrier of the inelastic deformation is grain boundary sliding rather than decohesion. If the mode-I component is relatively high compared with the mode-II component the regularization mechanism appears to be too weak [6].

The approach that we shall explore in this paper is the introduction of higher-order deformation gradients into the constitutive model, that is the available tensile strength is made a function not only of the average fracturing strain, but also of the Laplacian of this internal state variable [7,8]. In conventional numerical schemes such an added dependence has a tremendous impact, because it is at odds with the normal flow of a finite element program. Therefore a novel strategy is described in which the inelastic part of the constitutive equation is satisfied only in a weak sense, instead of pointwise as is conventionally done.

The introduction of higher-order continuum models as the gradient model advocated here has a profound influence on the ellipticity, the uniqueness and stability of the rate boundary value problem at hand. Some of these issues will be elucidated at the end of this article, where we shall also consider some numerical examples of pure mode-I problems.

A GRADIENT CONTINUUM THEORY FOR MODE-I FRACTURE

We consider the following set of equations:

$$\mathbf{L}^{\mathrm{T}}\dot{\boldsymbol{\sigma}}=\mathbf{0}\,, \tag{1}$$

$$\dot{\boldsymbol{\sigma}}=\mathbf{D}[\dot{\boldsymbol{\varepsilon}}-\dot{\lambda}\mathbf{n}]\ ,\ \dot{\lambda}\geq 0\,, \tag{2}$$

$$f(\boldsymbol{\sigma},\boldsymbol{\varepsilon}^{\mathrm{f}},\nabla^2\boldsymbol{\varepsilon}^{\mathrm{f}})=0\,, \tag{3}$$

$$\dot{\boldsymbol{\varepsilon}}=\mathbf{L}\dot{\mathbf{u}}\,, \tag{4}$$

which define the elastic-fracture rate problem during progressive micro-cracking. In the equilibrium equation (1) $\boldsymbol{\sigma}$ is a vector that contains the stress components (Voigt's notation), $\mathbf{L}$ is a differential operator matrix and the superscript T is the transpose symbol. Stress and elastic strain, $\dot{\boldsymbol{\varepsilon}}^{\mathrm{e}}=\dot{\boldsymbol{\varepsilon}}-\dot{\lambda}\mathbf{n}$, are related through the elastic stiffness matrix $\mathbf{D}$. The superimposed dots denote differentiation with respect to time. $\dot{\lambda}$ is a non-negative scalar-valued quantity which is a measure of the inelastic flow intensity and $\mathbf{n}$ is the gradient to the fracture surface f, that is, $\mathbf{n}=\partial f/\partial\boldsymbol{\sigma}$.

The salient feature of the continuum theory adopted here is the functional dependence of the fracture function on the Laplacian of the equivalent fracture strain $\boldsymbol{\varepsilon}^{\mathrm{f}}$, in addition to the usual dependence of f on $\boldsymbol{\varepsilon}^{\mathrm{f}}$. In a continuum approach the gradient terms reflect the fact that below a certain size scale the interaction between the microstructural carriers of the deformation is non-local. For cementitious materials experimental evidence on the evolution of micro-structures during failure has been given by Van Mier [9]. His studies clearly show, on a micro-level, the existence of grain bridging in cracks. At the meso-level, at which we carry out the homogenization and constitutitive modelling, these micro-effects are accounted for by the inclusion of higher-order deformation gradients in the continuum description.

The dependence of the fracture function on spatial gradients of an invariant measure of the fracture strain $\boldsymbol{\varepsilon}^{\mathrm{f}}$ has a major impact when elaborating the condition that, during inelastic flow, the stress point must remain on the fracture surface:

$$\dot{f}(\boldsymbol{\sigma},\boldsymbol{\varepsilon}^{\mathrm{f}},\nabla^2\boldsymbol{\varepsilon}^{\mathrm{f}})=0\,. \tag{5}$$

Taking into account the above dependencies eq. (5) can be rewritten to give:

$$\mathbf{n}^{\mathrm{T}}\dot{\boldsymbol{\sigma}}-h\dot{\lambda}+c\nabla^2\dot{\varepsilon}^{\mathrm{f}}=0\,, \tag{6}$$

where h and c are defined as:

$$h=-\frac{1}{\dot{\lambda}}\frac{\partial f}{\partial\varepsilon^{\mathrm{f}}}\dot{\varepsilon}^{\mathrm{f}}\quad,\quad c=\frac{\partial f}{\partial\nabla^2\varepsilon^{\mathrm{f}}}\,. \tag{7}$$

In the examples we shall adopt a Rankine yield condition

$$f=\sigma_1-\bar{\sigma}(\varepsilon^{\mathrm{f}},\nabla^2\varepsilon^{\mathrm{f}}) \tag{8}$$

with σ_1 the major principal stress, and $\bar{\sigma}$ the tensile stress-carrying capacity at the current level of the equivalent fracture strain ε^{f}:

$$\dot{\varepsilon}^{\mathrm{f}}=|\,\dot{\varepsilon}_1^{\mathrm{f}}\,|\,, \tag{9}$$

with $\dot{\varepsilon}_1^{\mathrm{f}}$ the major principal fracture strain component. Substituting the fracture function (8) into the flow rule and this result subsequently into the hypothesis (9) gives $\dot{\varepsilon}^{\mathrm{f}}=\dot{\lambda}$. We now obtain in lieu of eq. (6):

$$\mathbf{n}^{\mathrm{T}}\dot{\boldsymbol{\sigma}}-h\dot{\lambda}+c\nabla^2\dot{\lambda}=0. \tag{10}$$

From eq. (10) we observe that the consistency condition results in a partial differential equation. This has the far-reaching consequence that an explicit expression for $\dot{\lambda}$ cannot be obtained at a local (integration point) level. To further investigate the implications thereof we substitute the elastic stress-strain relation (2) into eq. (10). Upon rearrangement we then have

$$c\nabla^2\dot{\lambda}-(h+\mathbf{n}^{\mathrm{T}}\mathbf{D}\mathbf{n})\dot{\lambda}=-\mathbf{n}^{\mathrm{T}}\mathbf{D}\dot{\boldsymbol{\varepsilon}}\,. \tag{11}$$

In an explicit Euler forward scheme eq. (11) can be replaced by

$$c\nabla^2\Delta\lambda-(h+\mathbf{n}^{\mathrm{T}}\mathbf{D}\mathbf{n})\Delta\lambda=-\mathbf{n}^{\mathrm{T}}\mathbf{D}\Delta\boldsymbol{\varepsilon}\,, \tag{12}$$

with $\Delta\lambda$ now the finite value of the multiplier within a load step. To solve this partial differential equation we can either

- set up a mesh that connects all integration points, or
- extrapolate the stresses $\boldsymbol{\sigma}$ (which are needed to compute the gradients to the fracture function $\mathbf{n}$) to the nodes and then use the same mesh as for the resolution of the displacements.

In both cases the solution of the partial differential equation (12) would be obtained by first recasting eq. (10) in a weak format:

$$\int_V\delta\dot{\lambda}\,[\mathbf{n}^{\mathrm{T}}\dot{\boldsymbol{\sigma}}-h\dot{\lambda}+c\nabla^2\dot{\lambda}]\,\mathrm{d}V=0\,, \tag{13}$$

with the δ-symbol denoting the variation of a quantity, and then carrying out the usual finite element computations.

A third alternative, that would obviate the need to explicitly formulate a stiffness matrix that derives from the contribution $c\nabla^2\Delta\lambda-(h+\mathbf{n}^{\mathrm{T}}\mathbf{D}\mathbf{n})\Delta\lambda$ is to bring the gradient part to the right-hand side:

$$\Delta\lambda=\Delta\lambda_{\mathrm{local}}+\frac{c}{h+\mathbf{n}^{\mathrm{T}}\mathbf{D}\mathbf{n}}\nabla^2\Delta\lambda\quad,\quad\Delta\lambda_{\mathrm{local}}=\frac{\mathbf{n}^{\mathrm{T}}\mathbf{D}\Delta\boldsymbol{\varepsilon}}{h+\mathbf{n}^{\mathrm{T}}\mathbf{D}\mathbf{n}}\,. \tag{14}$$

Now suppose for simplicity that we have a one-dimensional grid where the integration points are spaced at equal distances (practical situations will not be that beautiful of course). At integration point i we then have in a finite-difference approximation:

$$\Delta\lambda_i=(\Delta\lambda_{\mathrm{local}})_i+\frac{c}{h+\mathbf{n}^{\mathrm{T}}\mathbf{D}\mathbf{n}}\,\frac{\Delta\lambda_{i-1}-2\Delta\lambda_i+\Delta\lambda_{i+1}}{k^2} \tag{15}$$

if k is the distance between two neighbouring integration points. The problem is now that $\Delta\lambda_{i+1}$ is hitherto unknown. At best we can substitute $(\Delta\lambda_{\text{local}})_{i+1}$. This implies that we must carry out an iterative procedure within each global equilibrium iteration to properly calculate the multiplier $\Delta\lambda$:

$$\Delta\lambda_i^j = (\Delta\lambda_{\text{local}})_i^j + \frac{c}{h+\mathbf{n}^{\mathrm{T}}\mathbf{D}\mathbf{n}} \frac{\Delta\lambda_{i-1}^j - 2\Delta\lambda_i^j + \Delta\lambda_{i+1}^{j-1}}{k^2} , \tag{16}$$

where the superscript j is the iteration counter and $\Delta\lambda_{i+1}^0 = (\Delta\lambda_{\text{local}})_{i+1}$. A simple alternative to the iterative procedure defined by eq. (16) would be to just carry out one iteration where the non-local multipliers on the right-hand side of eq. (16), $\Delta\lambda_{i-1}$, $\Delta\lambda_i$ and $\Delta\lambda_{i+1}$, are approximated by their local values $(\Delta\lambda_{\text{local}})_{i-1}$, $(\Delta\lambda_{\text{local}})_i$ and $(\Delta\lambda_{\text{local}})_{i+1}$ respectively [10]. Unfortunately, this simple method does not satisfy the consistency requirement (5).

To connect as closely as possible with conventional elasto-plastic finite element procedures we prefer to devise an algorithm that is rooted in the second alternative, so that the scalar multiplier $\dot{\lambda}$ is interpolated for the same topology as the displacements. Indeed, eq. (13) together with the weak form of (1)

$$\int_V \delta\dot{\mathbf{u}}^{\mathrm{T}}[\mathbf{L}^{\mathrm{T}}\dot{\boldsymbol{\sigma}}]\,\mathrm{d}V = 0 , \tag{17}$$

the elastic stress-strain relation (2) and the kinematic relation (4), both of which are satisfied in a pointwise manner, completely define the rate boundary value problem. However, the fact that the consistency condition is no longer satisfied in a pointwise manner marks a major departure from conventional algorithms. Now, $\dot{\lambda}$ is considered as a *fundamental unknown* and has a role equal to that of the displacements. It is solved at global level simultaneously with the displacement degrees-of-freedom.

The displacement field $\mathbf{u}$ and the field of multipliers $\dot{\lambda}$ can now be discretized to nodal variables $\mathbf{a}$ and $\boldsymbol{\Lambda}$ in the usual way, leading to the following set of equations [8]:

$$\begin{bmatrix} \mathbf{K}_{\mathbf{aa}} & \mathbf{K}_{\mathbf{a}\lambda} \\ \mathbf{K}_{\mathbf{a}\lambda}^{\mathrm{T}} & \mathbf{K}_{\lambda\lambda} \end{bmatrix} \begin{bmatrix} \dot{\mathbf{a}} \\ \dot{\boldsymbol{\Lambda}} \end{bmatrix} = \begin{bmatrix} \dot{\mathbf{f}}_{\mathrm{e}} \\ \mathbf{0} \end{bmatrix} , \tag{18}$$

where

$$\mathbf{K}_{\mathbf{aa}} = \int_V \mathbf{B}^{\mathrm{T}}\mathbf{D}\mathbf{B}\,\mathrm{d}V , \tag{19}$$

$$\mathbf{K}_{\mathbf{a}\lambda} = -\int_V \mathbf{B}^{\mathrm{T}}\mathbf{D}\mathbf{n}\mathbf{h}^{\mathrm{T}}\,\mathrm{d}V , \tag{20}$$

$$\mathbf{K}_{\lambda\lambda} = \int_V [(h+\mathbf{n}^{\mathrm{T}}\mathbf{D}\mathbf{n})\mathbf{h}\mathbf{h}^{\mathrm{T}} - c\mathbf{h}\mathbf{p}^{\mathrm{T}}]\,\mathrm{d}V \tag{21}$$

and $\mathbf{f}_{\mathrm{e}}$ the external force vector. In eqs. (18)-(21) $\mathbf{B}$ is the strain-nodal displacement matrix, $\mathbf{h}$ is the vector that contains the interpolation polynomials for the multiplier $\dot{\lambda}$ and $\mathbf{p}$ contains the Laplacians of the latter functions. An unpleasant property of (18) is the unsymmetry that enters through $\mathbf{K}_{\lambda\lambda}$ as defined in (21). For the pure rate problem $\mathbf{K}_{\lambda\lambda}$ can be symmetrized. Introducing $\mathbf{q}$ which contains the gradients of the interpolation functions and using Green's theorem we obtain

$$\mathbf{K}_{\lambda\lambda} = \int_V [(h+\mathbf{n}^{\mathrm{T}}\mathbf{D}\mathbf{n})\mathbf{h}\mathbf{h}^{\mathrm{T}} + c\mathbf{q}\mathbf{q}^{\mathrm{T}}]\,\mathrm{d}V \tag{22}$$

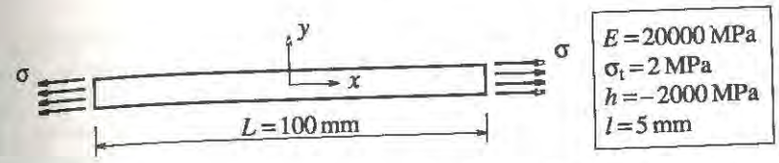

Figure 1. Tension bar with a length L subjected to an axial stress σ.

and the non-standard boundary conditions at the elasto-plastic boundary S_λ: $\dot{\lambda}=0$ or $(\nabla\dot{\lambda})^{\mathrm{T}}\mathbf{n}_\lambda = 0$ with $\mathbf{n}_\lambda$ the outward normal at S_λ. These results can also be derived directly from a variational principle [7,8]. Unfortunately, it seems that, when finitely sized loading steps are used, the symmetric form of $\mathbf{K}_{\lambda\lambda}$ does not give a proper convergence behaviour in an incremental-iterative procedure and that one then has to resort to the unsymmetric form of $\mathbf{K}_{\lambda\lambda}$ as in eq. (21).

STABILITY AND UNIQUENESS IN HIGHER-ORDER CONTINUUM THEORIES

We shall now investigate the issues of uniqueness and stability by consideration of the simple example of a tension bar (Figure 1). For such a uniaxial stress state the onset of fracturing is coincident with the vanishing of

$$f = \sigma - \bar{\sigma}(\varepsilon^{\mathrm{f}}, \mathrm{d}^2\varepsilon^{\mathrm{f}}/\mathrm{d}x^2) , \tag{23}$$

where, for linear softening, we have

$$\bar{\sigma} = \sigma_{\mathrm{t}} + h\varepsilon^{\mathrm{f}} - c\mathrm{d}^2\varepsilon^{\mathrm{f}}/\mathrm{d}x^2 . \tag{24}$$

The softening modulus h has a constant, negative value. Typically, higher-order continuum models have periodic solutions in the strain-softening regime. Introducing the characteristic length of the continuum as $l = \sqrt{-c/h}$, we can derive that inside the localization zone a solution for $\dot{\varepsilon}$ is given by

$$\dot{\varepsilon} = \dot{\sigma}/E + \dot{\sigma}/h\cdot[1 - \cos(x/l)/\cos(w/(2l))] . \tag{25}$$

Outside the localization zone we have: $\dot{\varepsilon} = \dot{\sigma}/E$.

Suppose now that we have a single localization zone with a width w. Then, the velocity at the right end of the bar is given by:

$$\dot{u}(L)/\dot{\sigma} = L/E + [w - 2l\tan(w/(2l))]/h . \tag{26}$$

We are now interested in the solution that results in the steepest descending branch, i.e., the most critical equilibrium path. This solution is obtained by requiring that

$$\mathrm{d}(\dot{u}(L)/\dot{\sigma})/\mathrm{d}w = 0 . \tag{27}$$

Imposing this requirement results in explicit expressions for the width of the localization zone, $w = 2\pi l$, and the slope of the load-displacement curve when the localization zone has developed fully:

$$\dot{u}/\dot{\sigma} = L/E + 2\pi l/h . \tag{28}$$

We can also analyse the case that we have two, non-overlapping localization zones. Such an analysis results in the same expression for w, but the slope of the load-displacement curve for a fully developed localization zone is now given by

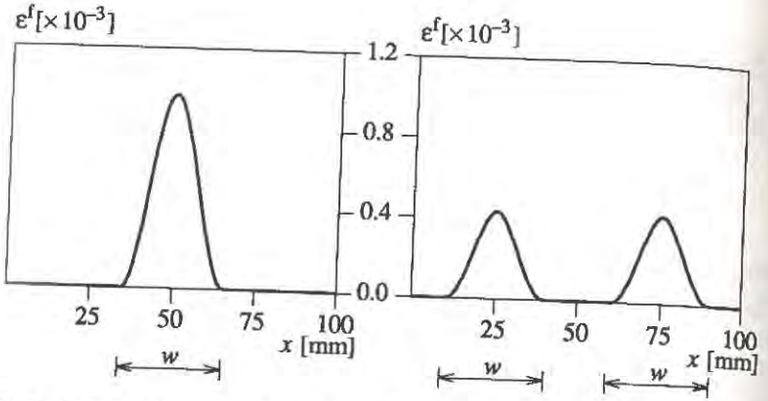

Figure 2. Inelastic strain distribution along the axis of a tension bar for one imperfection (left) and two imperfections (right) ($u/L=0.02$).

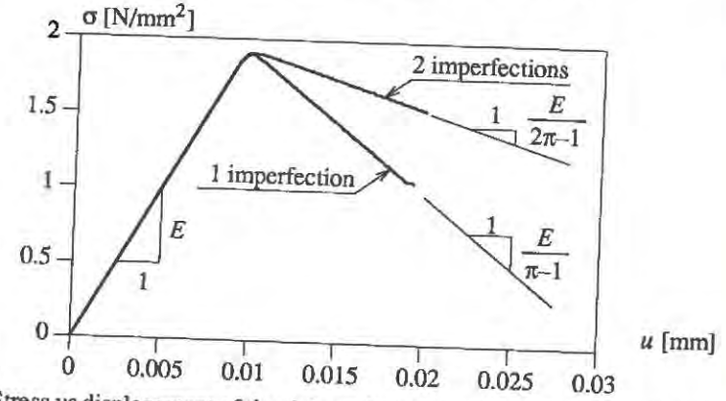

Figure 3. Stress *vs* displacement of the right end of the bar for different imperfection patterns.

$$\dot{u}/\dot{\sigma} = L/E + 4\pi l/h \,. \tag{29}$$

The above simple example shows that enrichment of the standard, rate-independent strain-softening continuum model does not normally result in uniqueness of the solution in the post-peak regime. Typically, there exist a *finite* number of periodic solutions. In fact, this number is bounded by the number of wave lengths of the periodic solutions that fit within the size of the structure. How many of these solutions will grow, depends on the number and the location of the imperfections. If there is only one imperfection or when two or more imperfections are located within the wave length of the periodic solution, just one localization zone will emerge. When the imperfection distribution is such that the localization zones do not interfere, several such zones will arise, at least initially. This is shown in Figures 2 and 3 where a numerical analysis has been carried out for the tension bar of Figure 1. Firstly, a single imperfection was inserted in the centre of the bar. Secondly, two imperfections were inserted at $x=0.25\,L$ and $x=0.75\,L$ respectively. Obviously, the solution for two imperfections gives, in accordance with the analytical prediction of eqs. (28) and (29), a shallower post-peak response, and two localization zones instead of one zone.

In a later stage of the loading process it may happen that only one localization zone persists, while the others are arrested. This is because a situation with several localization zones is always less stable - in the sense of Hill's definition of stability [11] - than a situation with only a single localization zone. This holds true for standard continuum models as well as for enhanced continuum descriptions. For the example considered here this is shown easily. For the case of one localization zone the second-order work reads

$$W_{\mathrm{I}} = \tfrac{1}{2}\dot{\sigma}\dot{u} = \tfrac{1}{2}\dot{u}^2 \frac{Eh}{Lh + 2\pi lE} \,. \tag{30}$$

This value is smaller than the value calculated from the solution for two localization bands,

$$W_{\mathrm{II}} = \tfrac{1}{2}\dot{\sigma}\dot{u} = \tfrac{1}{2}\dot{u}^2 \frac{Eh}{Lh + 4\pi lE} \,, \tag{31}$$

that is $W_{\mathrm{I}} < W_{\mathrm{II}}$. The path that corresponds to the smallest value of the second-order work is the most critical situation, and, if secondary imperfections allow it, will be followed ultimately.

Apparently, enhancing the continuum description does *not* result in uniqueness or stability of the solution. However, it can result in restoring *well-posedness* of the rate boundary value problem. This is most important, because it means that the rate boundary value problem admits a *finite* number of linearly independent solutions, which depend continuously on the data [12]. The standard, rate-independent continuum model does not satisfy this requirement. The solutions in the post-peak regime for the bar of Figure 1 are then given by

$$\dot{u}/\dot{\sigma} = L/E - nL/(mh) \,, \tag{32}$$

where n is the number of (linear) finite elements in which localization occurs and m is the number of elements into which the bar has been divided. If $m \to \infty$ the number of possible solutions becomes *infinite*, which violates well-posedness of the rate boundary value problem.

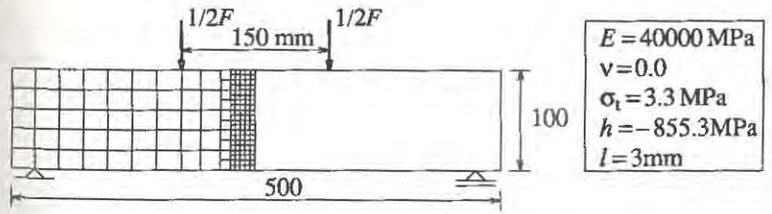

Figure 4. Four-point bending test on a plain concrete beam (geometry after Hordijk [13]).

APPLICATION TO MODE-I FRACTURE

For the one-dimensional bar of Figure 1 De Borst and Mühlhaus [8] have demonstrated that addition of the gradient term leads to convergence upon mesh refinement in the sense that a finite width of the localization zone is computed. Below we shall investigate whether this mesh-independent behaviour also results for two-dimensional configurations.

For this purpose a four-point bending test will be simulated. The geometry and material data come from experimental work by Hordijk [13], but in deviation from his work no notch was assumed in the centre of the beam. Instead an imperfect element (10% reduction in

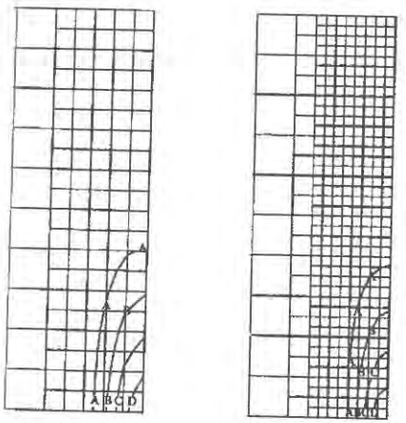

Figure 5. Contours of equivalent fracture strain at peak load for coarse and fine mesh.

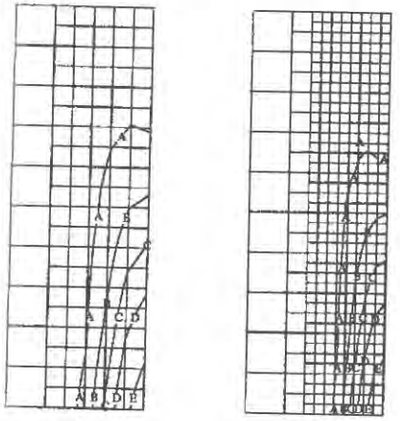

Figure 6. Contours of equivalent fracture strain beyond peak load for coarse and fine mesh.

tensile strength) was inserted. Therefore the results obtained here cannot directly be compared with his experimental results. Of interest is the estimation of the gradient parameter c. First the characteristic length l was estimated using $l = w/(2\pi) = 3$ mm. From the measured fracture energy $G_f = 120\,\mathrm{J/m^2}$ the softening modulus was computed using $h = -(w\sigma_t^2)/(2G_f) \approx -855.3$ MPa, which holds true for a linear softening diagram. Accordingly, the value $c = 7697.7$ kN was adopted in the analyses in which the effect of mesh refinement was investigated.

The discretization for the coarse mesh is shown in Figure 4. The fine mesh is identical to the coarse mesh except for the region in which localization occurs, where a uniform refinement was made. At locations where mesh densification occurs linear dependence relations have been added to ensure compatibility of the displacement field. Four-noded plane-strain

elements were used with a bilinear interpolation for the displacements and a bicubic Hermitian interpolation for the multiplier λ.

The results are shown in Figures 5 and 6 in terms of contours of the equivalent fracture strain ε^f for the coarse mesh and the fine mesh. We observe a good agreement between the contours of the coarse and fine mesh. This even holds true for the results beyond the peak load (Figure 6), despite the fact that these results do not correspond to completely converged equilibrium states. This is a defect of the algorithm we are using and currently much effort is put into replacing our numerical strategy by a more stable and robust approach.

CONCLUDING REMARKS

The use of higher-order continuum models is absolutely necessary for meaningful and realistic smeared crack simulations in concrete and rock. Yet, it seems that the present state-of-the-art is very immature. Much work is needed on the proper determination of material data for such models, efficient and robust numerical algorithms, assessment of issues like ellipticity, stability and uniqueness, mixed-mode behaviour and application to real structures.

ACKNOWLEDGEMENTS

Financial support by CUR-committee A30 and by the Commission of the European Communities through the Brite-Euram Programme (Project BE-3275) is gratefully acknowledged.

REFERENCES

1. Pijaudier-Cabot, G. and Bazant, Z.P., Nonlocal damage theory, *ASCE J. Eng. Mech.*, 1987, **113**, 1512-1533.
2. Needleman, A., Material rate dependence and mesh sensitivity in localization problems. *Comp. Meth. Appl. Mech. Eng.*, 1988, **67**, 69-86.
3. Sluys, L.J. and Borst, R. de, Rate-dependent modelling of concrete fracture, *Heron*, 1991, **36**, No. 2, 3-15.
4. Borst, R. de and Sluys L.J., Localisation in a Cosserat continuum under static and dynamic loading conditions. *Comp. Meth. Appl. Mech. Eng.*, 1991, **90**, 805-827.
5. Mühlhaus, H.-B., Borst, R. de and Aifantis, E.C., Constitutive models and numerical analyses for inelastic materials with microstructure. In *Computer Methods and Advances in Geomechanics*, eds. G. Beer, J.R. Booker and J.P. Carter, Balkema, Rotterdam, 1991, pp. 377-386.
6. Sluys, L.J., Wave propagation, localisation and dispersion in softening solids. Dissertation, Delft University of Technology, Delft, June 1992.
7. Mühlhaus, H.-B. and Aifantis, E.C., A variational principle for gradient plasticity. *Int. J. Solids Structures*, 1991, **28**, 845-857.
8. Borst, R. de and Mühlhaus, H.-B., Gradient-dependent plasticity: formulation and algorithmic aspects. *Int. J. Num. Meth. Eng.*, 1992, accepted for publication.
9. Mier J.G.M. van, Mode-I fracture of concrete: discontinuous crack growth and crack interface grain bridging. *Cement and Concrete Research*, 1991, **21**, 1-15.
10. Bazant, Z.P. and Lin, F.-B., Non-local yield limit degradation. *Int. J. Num. Meth. Eng.*, 1988, **26**, 1805-1823.
11. Hill, R., A general theory of uniqueness and stability in elastic-plastic solids. *J. Mech. Phys. Solids*, 1958, **6**, 236-249.
12. Benallal, A., Billardon, R. and Geymonat, G., Localization phenomena at the boundaries and interfaces of solids. In *Proc. Third Int. Conf. Constitutive Laws for Engineering Materials: Theory and Applications*, ed. C.S. Desai, Tucson, Arizona, 1991.
13. Hordijk, D.A., Local approach to fatigue of concrete. Dissertation, Delft University of Technology, Delft, October 1991.

Invited Paper

DAMAGE MODELS AND MODELLING STRATEGIES FOR CONCRETE STRUCTURES UNDER SEVERE LOADINGS

Jacky MAZARS, Jean François DUBE, Jean Pierre BOURNAZEL
Laboratoire de Mécanique et Technologie , Ecole Normale Supérieure
CNRS, Université Paris VI and GRECO Géomatériaux
94235 Cachan, France

ABSTRACT

This paper deals with the interest of the use of internal variables to the description of two different processes which can induce damage in concrete structures. One is linked to microcracking due to severe loadings, such as triaxial combination of stresses, dynamic loadings, the other concerns mechanical effects at early age due to hydration. The applications presented show the interest of the concepts used to simulate the evolutions of damage inside a structure, the interactions between concrete and steel and the resulting global behavior.

INTRODUCTION

At a given time the state of a structure depends on the whole history of this structure and of its components . For concrete this history begin with the construction, due to the processes induced by the cement hydration. During services, the occurence of loadings, severe or not, which can includes, triaxial combination of stresses, cyclic loadings or dynamic evolutions, induce micro- and macro-cracking processes which affected, in a non linear and irreversible way, the residual strength of the structure.

Focus on the works done by several authors at L.M.T. Cachan the aim of this paper is to present, in a synthetic way, the interest of the use of internal variables to describe the non linear evolution of the structural state of a construction. The number and the type of variables, which determine the sophistication of the model, depend on the processes which must be described.

Established within the framework of thermodynamics [1] these models are physically consistant and the corresponding structural computations need adequate strategies to give objective simulations. Different examples show the interest of the arguments presented.

INTERNAL VARIABLES : INTEREST AND CHOICE

1 - Basis

The starting postulate is that the thermodynamic state of a material medium , at a given point and instant, is completely defined by the knowledge of the values of the state variables at this point. This postulate implies that phenomena can be described with a precision which depends on the choice of the nature and the number of state variables [2].

The state variables are "observable", such as strain (ε) temperature (T) or humidity (H), or "internal", such as plastic strain (ε_p) or damage (D). Introduced in the constitutive equations they describe the actual state of the medium and automatically they adapt the behavior to this state.

We present hereafter the description of two major processes acting on concrete structures, one is microcracking, the other is the description of mechanical effects due to hydration.

2 - Microcracking process.

The main assumption is that microcracking affects the mechanical properties of the material in an irreversible manner. Therefore this process can be described using internal variables, the so-called damage variables, which act on the mechanical characteristics of the material.
Table 1 presents three levels for the representation of this process. From 1 to 3 the description is more and more complete and the domain cover larger.

2-1 First level - One scalar damage model [3] [4] :

This model couples elasticity and damage. Describe only with one variable D, damage is assumed isotropic, however the combination of two damage modes (tension Dt and compression Dc) allows to take into account the asymmetry of the uniaxial behavior but not the anisotropic response of the damaged material.
Such a description of microcracking is very easy because, D acting only on the Young modulus E, the description uses the classical linear elastic constitutive equations in which E evolves with the damage state (E=Eo(1-D), Eo initial value for E).
In this model D is piloted by the so-called "equivalent tensile strain" $\tilde{\varepsilon}$, which is an indicator of the tensile strain state, responsible of mode I microcracks, at a given point. The microcracks and heterogeneities interactions are introduced using a nonlocal formulation which consists in the definition of an adapted mean value of $\tilde{\varepsilon}$, calculated on a representative volume of the concrete used [5].
Consequenses are:
i) the 3D phenomena are taken into account in an isotropic way, however this model is useful for monotonic loadings and not for certain cases of reverse loadings,
ii) without tensile strain the behavior remains linear elastic.
Being a non linear elastic behavior, the implementation in a F.E.M. code of such a model is easy and the mesh objectivity is automatically solved by the nonlocal formulation [4].

2-2 Second level - Two scalars damage model [6] :

This model was established mainly to describe the case of reverse loadings. The two damage variables are needed to introduce the micro-crack closure effect. One variable (D_1) acts on the traction response and the other one (D_2) acts on the compression response, related respectively to the positive and the negative parts of the stress tensor ($\underline{\sigma} = \underline{\sigma}_+ + \underline{\sigma}_-$).

Kind of Model	Assumptions	Internal Variables	Evolutions	Effects described Constitutive equations
1st Level	. Isotropy . Traction - Comp - asymmetry	one Scalar D $D = a_t D_t + a_c D_c$	Piloted by the tensile strains : - variable : $\tilde{\varepsilon} = \sqrt{\Sigma \langle \varepsilon_i \rangle_+^2}$ - threshold : $\tilde{\varepsilon} - K(D) = 0$ - evolution : $D = f_D(\tilde{\varepsilon})$	. Decrease of stiffness $\underline{\underline{\varepsilon}} = \frac{\underline{\underline{\sigma}}(1+\nu)}{E_0(1-D)} - \frac{\nu}{E_0(1-D)}(t_r\underline{\underline{\sigma}})\underline{\underline{1}}$ or $\underline{\underline{\sigma}} = \mu_0(1-D)\underline{\underline{\varepsilon}} + \lambda_0(1-D)(t_r\underline{\underline{\varepsilon}})\underline{\underline{1}}$ $\langle X \rangle_+ = (\lvert X \rvert + X)/2$
2nd Level	. Isotropy . 2 damage modes	Two scalars : D_1 for traction D_2 for compression	Piloted by the strain energy, Y : - for traction $(\underline{\underline{\sigma}}_+) : Y_1(\underline{\underline{\sigma}}_+, D_1)$ - for compression $(\underline{\underline{\sigma}}_-) : Y_2(\underline{\underline{\sigma}}_-, D_2)$ - thresholds : $Y_i - Z(D_i) = 0$ - evolution : $D_i = f_i(Y_i)$ $(\underline{\underline{\sigma}} = \underline{\underline{\sigma}}_+ + \underline{\underline{\sigma}}_-)$	. Decrease of stiffness . Crack closure . Permanent strains $\underline{\underline{\varepsilon}} = \frac{\underline{\underline{\sigma}}_+}{E(1-D_1)} + \frac{\underline{\underline{\sigma}}_-}{E(1-D_2)} + \frac{\nu}{E}[\underline{\underline{\sigma}} - (t_r\underline{\underline{\sigma}})\underline{\underline{1}}] + \frac{\beta_1 D_1}{E(1-D_1)} f(\underline{\underline{\sigma}}) + \frac{\beta_2 D_2}{E(1-D_2)}\underline{\underline{1}}$
3rd Level	. Anisotropy . 2 modes of damage	A 2nd order tensor $\underline{\underline{d}}$ and a scalar Surfacic damage $\underline{\underline{d}}$ Volumic damage δ	Piloted by the elastic strain state : - for surfacic damage : . threshold : $\frac{1}{2}t_r(\underline{\underline{\varepsilon}})^e_+ \cdot \langle \underline{\underline{\varepsilon}} \rangle^e_+ - K(\underline{\underline{d}}) = 0$. evolution : $\underline{\underline{d}} = f_d(\langle \underline{\underline{\varepsilon}}^e \rangle_+)$ - for volumic damage : . threshold : $\frac{1}{2}\langle(\varepsilon^e_v)_+\rangle - K(\delta) = 0$. evolution : $\delta = f_\delta(\langle \varepsilon^e_v \rangle_+)$ with $\varepsilon^e_v = (t_r\underline{\underline{\varepsilon}}^e)_+$	. Anisotropic decrease of stiffness . Anisotropic permanent stresses $\underline{\underline{\sigma}} = 2\mu_0\left(1-\underline{\underline{d}}\right)^{1/2} \cdot \underline{\underline{\varepsilon}} \cdot \left(1-\underline{\underline{d}}\right)^{1/2} + \lambda_0\left(1-\delta\right)(t_r\underline{\underline{\varepsilon}})\underline{\underline{1}} + \frac{1}{2}\left(2\mu_0\,\beta\,\underline{\underline{d}} \cdot \underline{\underline{d}} + \lambda_0\,\gamma\,\delta^2\,\underline{\underline{1}}\right)$

Table 1 : Description of the Microcracking process using damage internal variables

Permanent strains, important for cyclic loadings, are also described and, as experiments shown, they are related to the evolution of damage. This evolution is piloted by the local strain energy release rate.

More efficient that the previous one, its implementation in a F.E.M. is also more difficult and the non local formulation as not yet been solved. But using specific precautions, in particular with the mesh, interesting results has been obtained [6].

2-3 Third level - Anisotropic damage model [7] :

It is well-knowned that oriented microcracking introduced a strong anisotropy. The analysis of such a phenomenon under high compressive loading shows that there are two different damage modes, one is due to the decohesion mainly at the interface paste-aggregate, and is responsible of the induced anisotropy, the other one affects the microporous matrix of the medium and acts on the volumic variations. Therefore the description of these two aspects needs two different kind of damage variables, one must be a tensor $\underline{\underline{d}}$ (choosen here of second order), the other one can be a scalar (δ).

3 - Hydratation processes.

The progressive crystallization of the cement paste induces 3 phases of evolution of the medium :

- the "suspension phase", the material can be consider as a liquid including grains and, from the mechanical point of view, quasi-nothing occurs ;
- the "setting phase", the progressive structuration of hydrates around the cement grains lead to the solidification of the medium ;
- the "hardening phase", after solidification and due to the fact that the reaction of hydration is still active, the medium hardens with aging.

To describe at any moment the state of the medium the maturity M is introduced as an internal variable from which one can deduce mechanical properties such as the Young modulus [8,9] :

$E = E_\infty M$ with E_∞ = value at long term and the Poisson ratio ν=0,5-aM, a is a constant.

Maturity pilots the evolution of autogeneous shrinkage, choosen in a first approach parabolic :

$$\varepsilon^{sh} = \varepsilon^{sh}_\infty M(2-M), \qquad \varepsilon_\infty \text{ shrinkage at infinity.}$$

Under stresses, creep-relaxation processes are activated. Considering only the case of mass concrete at constant humidity we assume for it a same kind of evolution than shrinkage :

$$\varepsilon^c(t,t_1) = \frac{\sigma_1}{E_1} k_1 M(2-M), \qquad \text{with } M = M(t).$$

Over a threshold of the "equivalent tensile strain" damage appears. Coupling damage and maturity in the simpliest way, the Young modulus is given by :

$$E = E_\infty M(1-D)$$

The damage evolution is the same given for the first level model described before. As used by other authors [10], the global strain is finally given by the addition of 4 specific strains, elastic strain, thermal strain, creep and shrinkage :

$$\varepsilon = \varepsilon^e(\sigma, M, D) + \varepsilon^c(\sigma, D, M, H) + \varepsilon^{sh}(M, H) + \varepsilon^{sh}(M, T)$$

The evolution of maturity is the major point of this modelling. It must be included the effect of time and the thermal activation using Arrhenius law as given in table 2. Time appears under the form $\langle t-t_0 \rangle_+$ which means that the beginning of mechanical evolution is at time t_0, when the medium is assumed to become a solid [11]. For more details on this model see ref. [8].

Internal Variables	Causes and Evolutions	Effects described
- Maturity **M** $M = 0$ when the medium becomes a solid $M = M_\infty$, close or equal to 1 at infinity	- Time and temperature : $M = M_\infty \frac{K(T)\langle t-t_0\rangle_+}{1+K(T)\langle t-t_0\rangle_+}$ $K(T) = A \exp\left(\frac{B}{T}\right)$ (Arrhenius law)	- Increase of the stiffness and decrease of the Poisson ratio : $E = E_\infty M$; $\nu = 0.5 - aM$
	- Stress, maturity and humidity : $\varepsilon^C(t,t_1) = \frac{\sigma_1}{E(M_1)} \varnothing_c(M,H)$	- Volumic variations $\varepsilon^{sh} = \varepsilon^{sh}_\infty f(M,H)$ $\varepsilon^{th} = \gamma \Delta T$
- Creep ε^C	- Loading over a threshold : $\tilde{\varepsilon}$ - K(D) = 0 with D=f(ε) and $E_D = E(1-D)$ (1st level damage model)	- Thermo-elastic-viscous damage response : $\underset{\sim}{\varepsilon} = \underset{\sim}{\varepsilon}^e(\sigma,M,D) + \underset{\sim}{\varepsilon}^c(\sigma,D,M,H) + \underset{\sim}{\varepsilon}^{sh}(M,H) + \underset{\sim}{\varepsilon}^{th}(T)$
- Damage **D**		

Table 2 : Description of the mechanical effects due to hydration processes using internal variables

PERFORMANCES OF THE MODELLING

We have chosen here to present applications linked with two different topics. One is the simulation of the response of structures under sismic loading. The other is the presentation of results linked to the behavior of concrete at early ages ; they show the interest of such a modelling to help the design and the elaboration of construction codes.

1 - Damage of concrete elements due to hydration processes

We propose here to discuss the problem of concrete slabs at early ages. Assumed to represent a building floor the slab considered is linked to the walls on its sides and supported by the mould. Therefore no gravity stress is considered but only the connections with the walls and the thermal exchanges with the environment (air and wall). Figure 1-a gives the details of the geometry and of the boundary conditions.
In order to demonstrate the interest of reinforcements to distribute the volumic effects of hydration, two calculations have been performed one on plain concrete (normal with 375 kg of Portland Cement/m^3), the other on reinforced concrete. R-bars (diameter 12 mm) are placed each 20 cm on the upper and lower parts of the slab which corresponds more or less to the reinforcement imposed to contain volumic variations (Cf. European Codes).
Calculation uses a F.E. code, 1d steel elements are superposed to the 2d concrete mesh to represent the reinforcements. Figure 1 shows the main results obtained. In the two cases, reinforced and plain, due to the conduction exchange, the increase of temperature (therefore the maturity) is lower near the walls. Then, due to the fact that temperature, and then maturity, are not homogeneous in the slab (thermal exchanges are greater with the walls) and due to the competition between dilation and shrinkage, the effect of volumic variations are

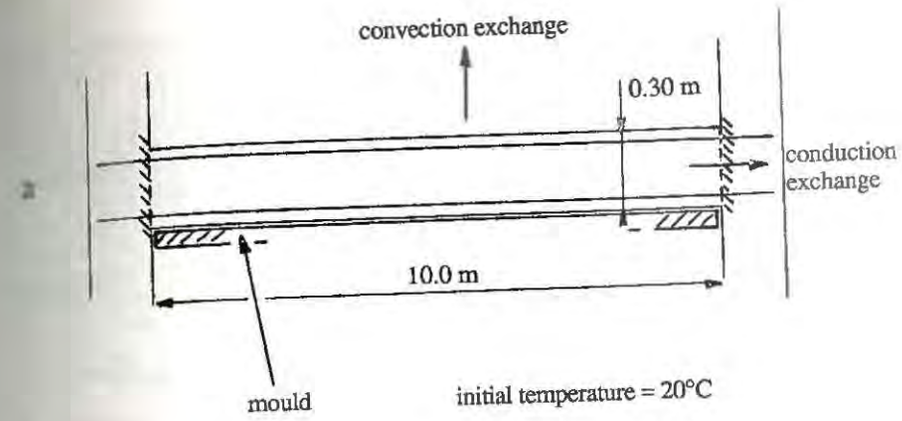

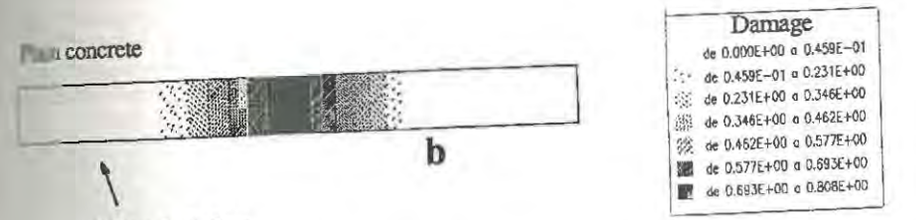

After 1.5 day

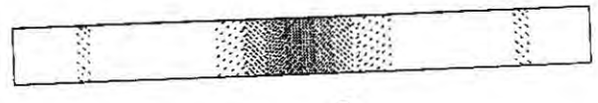

Reinforced concrete

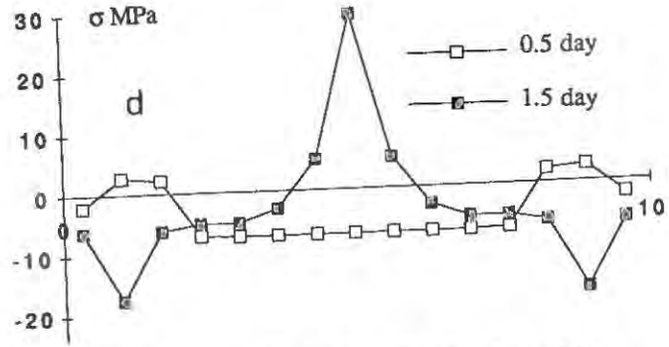

Figure 1 : Simulation of the hydration effects at early age on a slab

a - Geometry and boundary conditions
b - Failure of the plain concrete slab after 1.5 day
c - Damage inside the R.C. slab
d - Stress distribution along the reinforcements

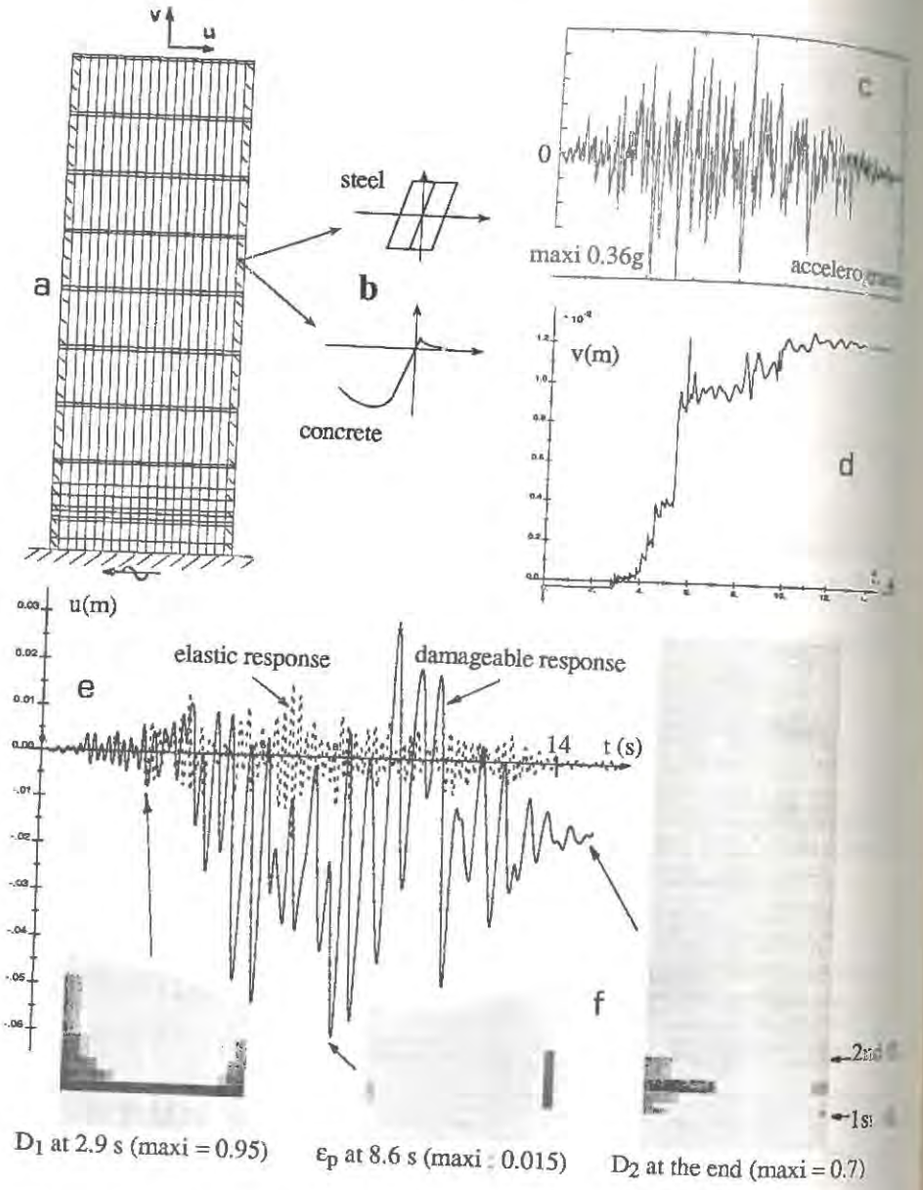

Figure 2 : Seismic response of a 8 storeys building

a - Mesh with layered elements
b - Local behaviors "mixed" to obtain R.C. behavior
c - Accelerogram
d - Relative horizontal displacement at the top
e - Vertical displacement at the top
f - Local evolution at different time

an homogeneous. After 1.5 day, a strongly damaged zone (D greater than 0.8) is located in the center part of the plain concrete slab which indicates the failure of the element (Figure 1-b). At the same time, the reinforced concrete slab (Figure 1-c) shows a large zone with distributed damage (from 0 to 0.5) in the center of the slab and two small zones close to the sides (D < 0.1).
The evolution of the stress in the reinforcement is consistent with these observations (Figure 1-d). Damage on the sides appears first (at 0.5 day) and the bars are under tension in these zones. After 1.5 day when damage is mainly in the center of the slab, reinforcement is in tension in this part (max. of the stress 30 MPa) and is in compression anywhere else with a stress peak in the previous damage zone where the mechanical properties of concrete are affected. This example shows how reinforcement acts to distribute stress along the specimen in order to reduce the localization of damage and therefore to avoid the failure.

3 - Seismic response of an 8 storeys building

To simulate the effect of loading when there are reverse loadings, which is the case during an earthquake, the description of the crack closure is fundamental. Therefore the use of the second level modelling is necessary.
The application presented here is the simulation of the response of an eight storeys building the structure of which is composed by concrete walls. We assumed that the seismic action is parallel to the wall and we consider the part of the building between two walls.
The foundation is connected to the ground (consider as a rock). The wall is reinforced vertically on each side (from 4 Ø 10 mm at the top up to 6 Ø 16 mm at the bottom) and the slabs are normaly reinforced. The finite element discretization used layered elements (Figure 3-a) [12]. The behavior of each layer is deduced from the response of the second level model under uniaxial stress and the elastoplastic behavior of steel is integrated at the corresponding layer using and homogenized technique (fig. 3-b) [6]. The association of the different layers (21 in this case) leads to the determination of the behavior of the corresponding section of the wall with global variables (M,N,T,θ,u,v). Therefore the behavior of this element includes the damage of concrete, the plasticity of steel and the association R-bar-concrete.
The seismic loading imposed, respects the accelerogram shown figure 3-c which includes a maximum equal to 0.36 g. The dynamic response is obtained using an implicit Newmark technique.
Results obtained concerned the history of displacements. Figure 3-d gives the evolution of the relative horizontal displacement at the top of the building compare to those obtained with a linear elastic behavior (dash line) ; damage and plasticity induce a great increase of the displacement and a decrease of the frequency. Figure 3-e gives the relative vertical displacement of the top, one can observe that from the beginning of damage the trend is an uprising of the building. On figure 3-f are shown three examples of local evolutions, traction damage D_1 at 2.9 seconds, showing the creation of a crack just above the first floor, plastic deformation of reinforcement ε_p at 8.6 seconds and compression damage D_2 at the end of the loading. In each case, the main effects appear at the first storey.
This work is in progress an experiment of a third scale building is planned on a shacking table in order to have a better understanding of the seismic response of that kind of structure and to validate our choices for the simulation.

CONCLUSION

Predicting the response of reinforced concrete structures requires three major ingredients. (1) Constitutive equations for steel and concrete which fit closely with experimental reality ; (2) an objective computational method which allows predictions up to the failure of structure ; and (3) a consistent model for the steel concrete association.

The first item has been extensively studied over the past years and many models for con... are available fracturing strain models [13], smeared cracks models [14] or micropl... models [15].We have worked at LMT Cachan on using internal variables to describe th... evolution of the mechanical state of the materials under two types of processes, one is link... to the hydration effects, the other to microcracking induce by severe loadings. The probl... linked to the second item need to be careful with the choice of the mesh which can be sol... using "localization limiters" [16] such as non local damage concepts [5].
About the third item we have used in this paper two kind of steel concrete association, on... the superposition of 1d steel elements to the 2d concrete mesh and the other is ... combination, using an homogenized technique, of the plastic behavior of the steel and ... damageable behavior of concrete [6].
The applications presented show the interest of the concepts used to simulate the evoluti... of damage inside a structure, the interactions between concrete and steel and the resulti... global behavior. These results allow to envisage the use of that kind of numerical modelli... as experiments to help the understanding of complex phenomenon such as hydration effe... or cyclic loadings and then to help the design of concrete structures.

Acknowledgements : Financial support from the french GRECO Géomatériaux and from th... french research program CASSBA are gratefully acknowledged.

REFERENCES

1. GERMAIN, P. and MULLER P., Introduction à la mécanique des milieux continus, Masson, Pari... 1980.
2. LEMAITRE, J. and CHABOCHE, J.L., Mechanics of Solid Materials, Cambridge University Pres... 1990, p. 57.
3. MAZARS, J., A Description of Micro- and Macroscale Damage of Concrete Structures, Engineering Fracture Mechanics, Vol 25, 5/6, 1986, p. 729-737.
4. SAOURIDIS, C. and MAZARS, J., Prediction of the Failure and Size Effect in Concret via a Bi-Scal... Damage Approach, Engineering Computations, Vol 9 (to be published 1992).
5. PIJAUDIER-CABOT, G. and BAZANT, Z.P., Nonlocal Damage Theory, J. Engrg. Mech., ASCE, 11... (10), p. 1512-1513.
6. LA BORDERIE, C., MAZARS, J. and PIJAUDIER-CABOT, G., Response of Plain and Reinforce... Concrete Structures under Cyclic Loadings, ACI Structural Journal (to be published 1992).
7. RAMTANI, S., BERTHAUD, Y.and MAZARS, J., Orthotropic Behavior of Concrete with Directiona... Aspects Modelling and Experiments, Nuclear Engrg and Design, (to be published 1992).
8. MAZARS, J., BOURNAZEL, J.P. and MORANVILLE REGOURD, M., Thermomechanical Damage due to Hydration in large Concrete Dams, Proc. of the First, Materials Engineering Congress, ASCE August 1991, Denver, Colorado, Vol 2, p. 1061-1070.
9. ACKER, P., EYMARD and R., PIAU, J.M., Ingénierie des ouvrages en béton : la prise en compte des effets thermiques et hydriques, Annales des Ponts et Chaussées, N° 60, 1er trimestre 1992, p. 3-15.
10. BAZANT, Z.P. and PRASANNAN, S., Solidification Theory for Concrete Creep, Part I : Formulation, Journal of Engineering Mechanics, ASCE Vol 115, N° 8, 1989, p. 1691-1725.
11. BOURNAZEL, J.P., MORANVILLE REGOURD, M. and HORNAIN, H., Early Age Concrete Strength - A Phenomenological Approach to Physico-Chemical Processes, Int. Workshop on Hydration and Setting, July 1991, Dijon - France.
12. BAZANT, Z.P., PAN, J.and PIJAUDIER-CABOT, G., Softening in Reinforced Concrete Beams and Frames, Journal of Structural Engineering, ASCE, Vol 113, 1987, p. 2233-2347.
13. DOUGILL, J.W., On Stable Progressively Fracturing Solids, J. Appl. Mathematics and Physics, 27 (3). 423-446.
14. BORST, R. de, Non Linear Analysis of Frictional Materials, Dissertation T.U. Delft, 1986.
15. BAZANT, Z.P. and PRAT, P.C., Microplane Model for Brittle Plastic Material, Part 1, J. Engrg Mech., ASCE, 114 (10), 1988, 1672-1702.
16. MAZARS, J. and BAZANT, Z.P., Strain Localization and Size Effect due to Cracking and Damage. Elsevier, London, G.B., 1989.

COMPOSITE ANALYSIS WITH DISCRETE AND SMEARED CRACK CONCEPTS

T. STANKOWSKI, G. ETSE, K. RUNESSON, S. STURE, K. WILLAM
CSZ - Consult, Darmstadt, FRG
Institute of Mechanics, University of Karlsruhe, FRG
Chalmers Technical University, Gothenburg, Sweden
University of Colorado, Boulder, Colorado, USA

ABSTRACT

Progressive failure analysis of cementitious composites requires realistic degradation mod... for both the cementitious matrix as well as the interface between individual aggregates and the matrix phase. In this paper we investigate the failure process of a random particle composite with and without interfacial debonding and two different constitutive models for the mortar matrix. On one hand, a simple decohesive *'Drucker-Prager'* model is employed to account for softening properties of the matrix. On the other hand, the evolution of failure is modeled by a more realistic elasto-plastic model for frictional materials. The so-called *'Extended Leon Model'* simulates the strength degradation with a fracture energy-based softening mechanism and features a *'characteristic length'* measure to assure mesh objectivity with respect to the fracture energy release. For illustration, the different failure predictions of the two matrix and interface models are compared on the composite level, when a representative composite specimen is loaded in tension and compression.

INTRODUCTION

The macroscopic failure characteristics of cementitious particle composites such as concrete depend strongly on the stress state and its history. Progressive failure is accompanied by the formation of distinct transverse cracks in tension, axial splitting in uniaxial compression, and formation of shear bands or diffuse microcracking as the confining stresses increase in triaxial compression. These macroscopic observations are tied to a variety of degradation mechanisms in the internal structure of the heterogeneous composite. In order to analyze the progressive failure, the cementitious material is considered as a two-phase composite consisting of individual aggregate particles embedded in a mortar matrix. The interaction between the two constituents is modeled by means of an interface model which accounts for coupling between debonding adhesion and the frictional shear slip between the two constituents in the presence of compressive and tensile normal tractions.

DESCRIPTION OF THE COMPOSITE

Topological Description of the Constituents

The composite material considered here is comprised of aggregates, cement paste and voids. Since it is unfeasible to include each separate particle explicitly in the topological description, the idealization is restricted to a two-phase matrix particle composite in which only the larger inclusions are accounted for. The aggregate phase is idealized by polygonal approximations of crushed angular particles, which are embedded in the mortar matrix. The distribution pattern of the aggregates particles as well as their shapes are randomly generated with the aid of Voronoi-polygonization. However, the aggregate area fraction and the size distribution are controlled at the same time by the procedure developed by Stankowski in ref. [1].

Material Properties of Aggregate and Mortar

In the case of normal strength concrete the mechanical properties of the aggregate are generally far higher than those of the mortar and the interface both with respect to strength as well as stiffness. It is therefore assumed that the (isotropic) aggregate particles remain in the linear elastic regime throughout the loading history.

The simplified model of the mortar matrix is based on an elementary bilinear hypoplastic *'Drucker-Prager'* (*DPM*) formulation with progressive degradation of the cohesion. Associated flow is assumed during softening, thus the friction angle Φ is constant and coincides with the dilatancy angle Ψ during the entire deformation process. Hence excessive inelastic dilatancy will ensue at relatively large shear strains. The model is implemented within the framework of the invariant response models of nonlinear hypoplasticity and does not contain an internal length or volume measure that reduces mesh size dependency of the softening computation.

A more realistic model for frictional materials is the *'Extended Leon Model'* (*ELM*) based on the original formulation by Pramono & Willam [2]. This hardening/softening elasto-plastic formulation was recently extended by Etse [3] in order to generate (i) a smooth C^1-continuous surface following the elliptic 5-parameter approximation by Willam & Warnke in the deviatoric section, and (ii) a transparent isotropic work hardening/softening formulation for the nonlinear response behavior in the pre- and post-peak regimes.

The encompassing loading surface in the hardening and softening regime is described by the *ELM* as follows:

$$F(p,\rho,\theta,k,c) = \left[(1-k)\left(\frac{p}{f_c'}+\frac{\rho g(\theta)}{\sqrt{6}f_c'}\right)^2 + \frac{\rho}{f_c'}g(\theta)\sqrt{\frac{3}{2}}\right]^2 + \frac{k^2 m}{f_c'}\left(p+\frac{\rho g(\theta)}{\sqrt{6}}\right) - k^2 c = 0$$

where p, ρ and θ denote the coordinates of the Haigh-Westergaard stress space, f_c' the

uniaxial compressive strength and the function $g = g(\theta)$ describes the variation of the deviatoric strength $\rho = \rho(\theta)$ as a function of the Lode angle. The different loading surfaces in the hardening regime are generated by a scalar parameter k which varies between 0.1 and 1.0, while c and m, which are the cohesion and friction parameters, remain constant. The strength parameter k depends on the work-hardening measure κ_h which accounts for the level of confining stress in the hardening behavior.

The softening stages below the transition point of brittle-ductile fracture are defined by the decohesion parameter c, which reflects the degradation of the tensile strength σ_t. The decrease of tensile strength is monitored by the equivalent fracture energy release rate measure κ_s in analogy to the work-softening hypothesis of isotropic plasticity. This scalar-valued softening measure is expressed in terms of the ratio between the fracture energy release rate in direct tension and that in shear, G_f^I/G_f^{II}. It also involves a geometric length scale, h_t, which accounts for the fracture energy concept of a surface- rather than a volume-dominated fracture process of tensile cracking. To reduce excessive dilatation a non-associated flow rule was introduced in the *ELM* which is based on a volumetric modification of the yield condition, $Q = F(p,\rho,\theta,k,c,m_Q)$.

Constitutive Model for the Interface

The constitutive model for the interface behavior it is based on the relative displacement v between the aggregate particles and the mortar matrix. Decomposition into reversible and irreversible parts, $\dot{\mathbf{v}} = \dot{\mathbf{v}}^e + \dot{\mathbf{v}}^p$, follows the elasto-plastic approach delineated in ref. [4], where the reversible component $\mathbf{v}^e$ is due to *adherence*, whereas the irreversible component $\mathbf{v}^p$ is due to *slip*. The relative displacement $\mathbf{v} = v_n\mathbf{e}_n + v_t\mathbf{e}_t$ is related to the contact traction $\mathbf{q} = q_n\mathbf{e}_n + q_t\mathbf{e}_t$ through the interface constitutive model. The adhesion between the constituents $\dot{\mathbf{v}}^e = \mathbf{C}^e\dot{\mathbf{q}}$ is a measure of the reversible elastic compliance, while the irreversible deformation is described in analogy to plasticity. In direct tension the strength is characterized by the tensile peak (or ultimate) strength $q_{n,fu}$. In combined normal and shear loading, the strength is comprised of both, adhesion as well as slip $q_{t,fu}$ between the two constituents depending on the mobilized friction. The two mechanisms of tensile debonding in the normal direction $\mathbf{e}_n$ and slip in the tangential direction $\mathbf{e}_t$ are interrelated, since both processes contribute to crack formation along the interface.

A simple *'Fracture Criterion'* in the (q_n, q_t)-space was developed by Stankowski et al.[4] in terms of three parameters

$$F = \mid q_{t,f} \mid^a - \frac{(q_{t,fu})^a}{q_{n,fu}}(q_{n,f} - q_n) = 0$$

where $q_{n,f}$ denotes the current value of the normal strength and $q_{t,f}$ the current value of the shear strength. The strength values at peak are denoted by $q_{n,fu}$ and $q_{t,fu}$ respectively.

The current position of the slip surface is defined by $q_{n,f}$ which is obtained by simply translating the initial surface along the q_n-axis using a kinematic shift strategy. In order to obtain realistic dilatancy characteristics it is necessary to employ a non-associated slip rule which offers the possibility to modulate normality and further suppress undesired dilatancy.

Continued deformation after the onset of fracture/slip is assumed to be accompanied by softening for any loading path. Thus, the behavior in direct tension as well as in pure shear governs the behavior for any combined loading via the fracture energy release rates G_f^I and G_f^{II}. For any load path defined by the surface tractions $q_n = q_n(v_n^p)$ and $q_t = q_t(v_t^p)$ the ratio of the fracture properties $k = G_f^I/G_f^{II}$ varies typically in the range $k \sim 0.01-0.1$. The characteristic relationship between $q_{n,f}$ and v_n^p determines the behavior in combined fracture and slip, since $q_{n,f}(v_n^p)$ is here assumed to describe the universal stress-strain relationship. The tensile strength is taken to degrade exponentially as

$$q_{n,f}(v_n^p) = q_{n,fu} e^{-\alpha v_n^p}, \quad \alpha = q_{n,fu} \,/\, G_f^I$$

For any loading path other than direct tension, slip will accompany the dilatant debonding process. A key assumption in the model is that this debonding process can be described via an *equivalent fracture energy release rate* measure $\dot{\kappa}$ in analogy to a *work-softening* hypothesis which is chosen according to the rate law

$$\dot{\kappa} = < q_n > \dot{v}_n^p + k(q_t - q_{t,r})\dot{v}_t^p$$

The $< \cdot >$-symbol designates the McAuley bracket, and $q_{t,r}$ denotes the residual shear strength that can still be mobilized even after maximum degradation has occurred.

COMPARISON OF FAILURE MODES

Figs.(1) and (2) illustrate the nominal stress-strain response of the composite specimens which were loaded in tension and compression together with their failure modes. The extent of failure in the mortar matrix is visualized in terms of active zones of plastic work. The load is applied in displacement control with full lateral restraint at top and bottom faces simulating rigid loading platens. For both load histories the composite specimen is modeled a) with the simplified *Drucker-Prager* model for the mortar matrix without interface elements, b) with the same model for the mortar matrix, but including interface elements, and c) with the *Extended Leon Model* without considering interface elements. All studies are based on the assumption of plane stress since the kinematic plane strain constraint leads to excessive strength predictions of the *Drucker-Prager* model which are totally unrealistic.

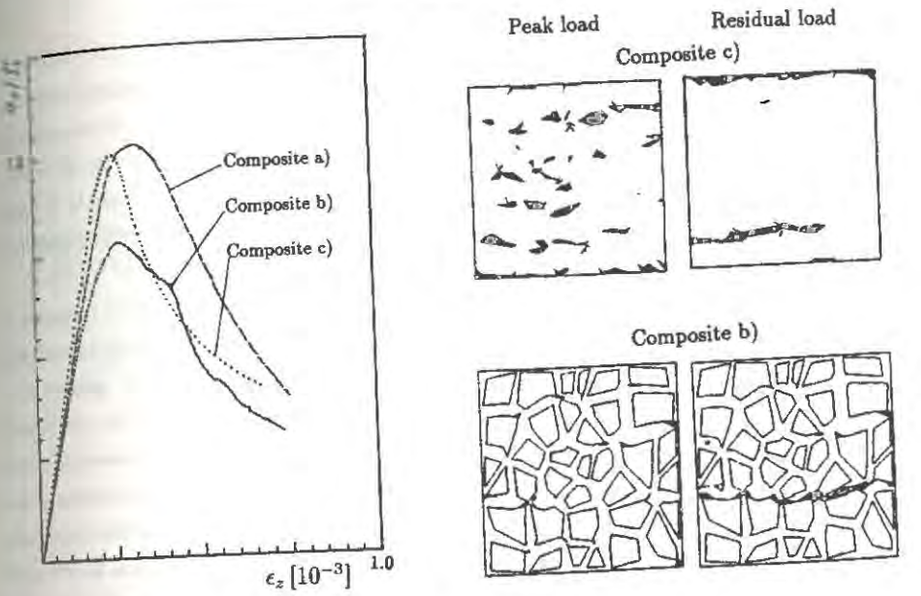

Fig. 1 Uniaxial Tension for Composite with a) *DPM*, b) *DPM* and Interface, c) *ELM*

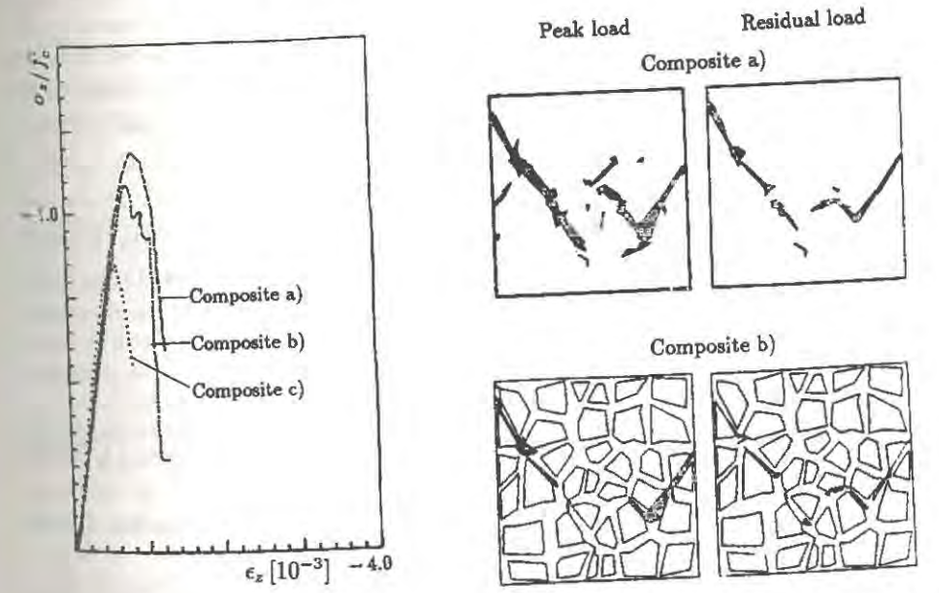

Fig. 2 Uniaxial Compression for Composite with a) *DPM*, b) *DPM* and Interface, c) *ELM*

For the tensile load histories, Fig. (1), the strength of the composite is directly related to the tensile strength of the constituents. In the composites a) and c) the tensile strength of the composite is identical to the tensile strength of the mortar matrix. In the composite b) the tensile strength is reduced by the 'weak' interfaces. For all three composite specimens a single discontinuity emerges through the cross section and failure is confined to a single layer of elements. The localization of displacements is enhanced by the inhomogeneous stress distribution and the spacing of the aggregate particles.

A significant variation in strength can be observed for the compressive load histories as shown in Fig. (2). While for the composites a) and b) the overall strength is larger than the compressive strength of the mortar matrix itself, this is not the case for specimen c). The results indicate that compressive softening of the composite depends on the tensile and shear strength as well as on the ductility, which are activated in the heterogeneous specimen in the form of splitting. Since the biaxial strength of the *ELM* is always lower than for the *DPM*, the *Extended Leon Model* predicts the lowest strength of the composite specimen. An accurate model for the mortar matrix with realistic prediction of strength and ductility is clearly a prerequisite for the analysis of compressive load histories.

CONCLUDING REMARKS

The composite failure analysis provides new insight into the failure mechanisms in heterogeneous matrix aggregate composites such as concrete. The computational results indicate that failure is very distributed throughout the specimen, either in terms of interface failure in tension or matrix failure. Only the final stages of failure are truly localized. The plane stress simulations of tensile load histories indicate that both, the failure mode as well as the tensile strength, are not sensitive and can be captured even with the simple *DPM* constitutive model for the mortar matrix. The plane stress analyses of compressive load histories, however, require accurate constitutive representation of the mortar matrix.

References

1. Stankowski,T., 'Numerical Simulation of Progressive Failure in Particle Composites', Ph.D. Thesis, C.E.A.E. Department, University of Colorado, Boulder, CO 80309-0428, USA, (1990)

2. Pramono, E., Willam, K., 'Fracture Energy-Based Plasticity Formulation of Plain Concrete', *ASCE J. Eng. Mech.*, Vol. 115, No. 6, 1989, pp. 1183-1203

3. Etse, G., 'Numerische Analyse von Versagensvorgängen in Beton', Dissertation, Institute of Mechanics, University of Karlsruhe, W-7500 Karlsruhe, FRG (1992)

4. Stankowski, T., Runesson, R., Sture, S., 'Fracture and Slip in Cementitious Composites', submitted for publication to *ASCE J. Eng. Mech.*, (1991)

A MICROMECHANICS-BASED CONTINUUM THEORY FOR STRAIN LOCALIZATION AND SOFTENING UNDER COMPRESSION

YOSHIAKI OKUI*, HIDEYUKI HORII** and NARIOKI AKIYAMA*

* Dept. of Foundation Eng., Univ. of Saitama
Shimo-ohkubo 255, Saitama, 338, Japan

** Dept. of Civil Eng., Univ. of Tokyo
Hongo 7-3-1, Bunkyo-ku, Tokyo, 113, Japan

ABSTRACT

The objective of this study is to establish a micromechanics-based continuum theory which can reproduce localization phenomena, such as shear failure of brittle materials under compression. A new field variable that characterizes the interaction effect between microstructures is introduced, and the governing integral equation for the interaction field is formulated. Numerical results are given that illustrate the difference between the proposed theory and the conventional continuum damage mechanics. It is confirmed that the proposed theory can describe the localization process of microcracking in shear failure of brittle materials under compression.

INTRODUCTION

To establish a theory for mechanical behaviors of engineering materials, it is important to take account of the influence of microstructures. However, the consideration of the interaction effect of individual microstructures with a discrete model is not feasible for analyses of general problems with arbitrary boundary and loading conditions. It is therefore necessary to establish a continuum theory that describes the overall behavior of materials containing microstructures.

One of the example of such a continuum theory is micromechanics-based Continuum Damage Mechanics (CDM) [1]. Although the micromechanics-based CDM does not fail for the reproduction of deformation behavior, the micromechanics-based CDM does not reproduce the localization phenomena. This disadvantage is caused by the following reason : when the evolution of damage is evaluated, the interaction effect is not directly considered. The evolution law is derived for uniform evolution of microstructures.

In this paper, a micromechanics-based continuum theory, named Interaction Field Theory (IFT), is presented. To reserve information on the interaction effect between microstructures in the homogenization process, we introduce an additional field variable (interaction field), and derive the governing integral equation for the interaction field. Although the theory is general and applicable to any material with microstructures, the present formulation is carried out for the behavior of brittle materials under compression.

A MODEL OF CRACK GROWTH UNDER COMPRESSION

The mechanical behaviors of brittle solids such as rock or concrete under compression are known to be governed by growth of cracks. To represent the behavior of crack growth under compression, the micromechanics model has been proposed as shown in Fig. 1(a). The initial defect PP' of length $2c_0$ undergoes frictional sliding under the action of far-field principal stresses σ_1^∞ and σ_2^∞ (positive in tension). The solution of the problem shown in Fig. 1(a) is obtained by the numerical method. The closed form solution of this problem, however, is not available.

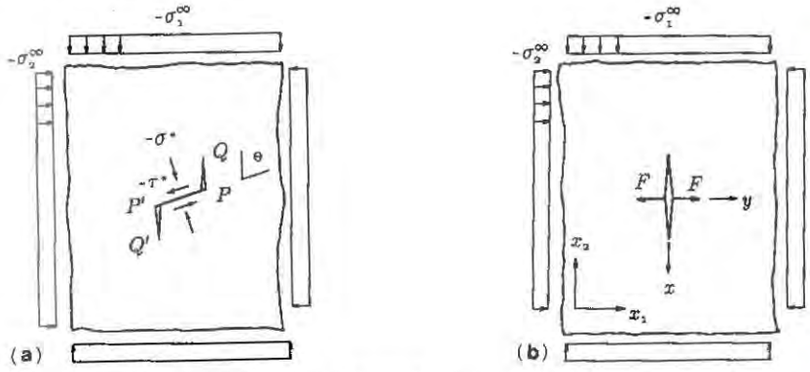

Figure 1: Microstructure of brittle material under compression.

A further simplified model is considered as shown in Fig. 1(b). The straight crack of length $2l$ is parallel to the direction of the maximum compressive stress σ_1^∞. The effect of the sliding of the initial defect is modeled as a pair of concentrated forces F at the center of the crack:

$$F = -c_0(\lambda_1\sigma_1^\infty - \lambda_2\sigma_2^\infty), \tag{1}$$

where $\lambda_1 = \sin\theta\{\sin 2\theta - \mu(1-\cos 2\theta)\}, \lambda_2 = \sin\theta\{\sin 2\theta + \mu(1+\cos 2\theta)\}$, μ is the coefficient of friction and θ is the angle of the initial defect.

INTERACTION EFFECTS OF DISCRETE MICROSTRUCTURES

The proposed theory is based on the homogenization of the method of pseudotractions [2]. Before IFT is introduced, we begin with the method of pseudotractions for the considered model. Consider an infinite plane with two microstructures defined in Fig. 1(b). We decompose the original problem into the homogeneous problem with no microstructures and the sub-problems each containing the single microstructures; see Fig. 2(b),(c),(d). Then, the superposition of the homogeneous problem and the subproblems leads to the following consistency equation that ensures the traction free condition on the crack surfaces;

$$\boldsymbol{\sigma}^{P\alpha} = \boldsymbol{\gamma}^{\alpha\beta}(\boldsymbol{\sigma}^{\infty\beta} + \boldsymbol{\sigma}^{P\beta}), \quad (\beta \text{ not summed}), \tag{2}$$

where $\boldsymbol{\sigma}^{P\alpha} = \{\sigma_{11}^{P\alpha}, \sigma_{22}^{P\alpha}, \sigma_{12}^{P\alpha}\}^T$ is pseudotraction, $\boldsymbol{\sigma}^{\infty\alpha} = \{\sigma_{11}^{\infty\alpha}, \sigma_{22}^{\infty\alpha}, \sigma_{12}^{\infty\alpha}\}^T$ and

$$[\gamma_{ij}^{\alpha\beta}] = \frac{1}{2}\left(\frac{l_\beta}{d}\right)^2 \begin{bmatrix} (1+\lambda_2 b/l_\beta)a_1 & -(\lambda_1 b/l_\beta)a_1 & a_4 \\ (1+\lambda_2 b/l_\beta)a_2 & -(\lambda_1 b/l_\beta)a_2 & a_5 \\ (1+\lambda_2 b/l_\beta)a_3 & -(\lambda_1 b/l_\beta)a_3 & a_6 \end{bmatrix} \tag{3}$$

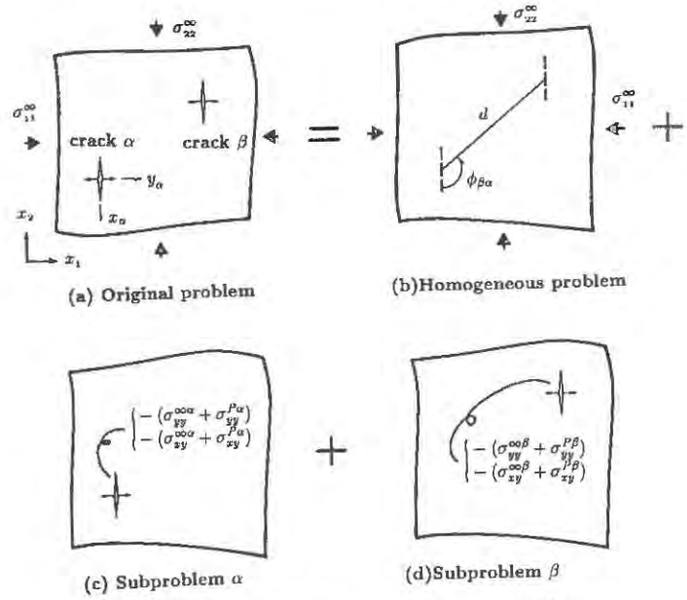

Figure 2: Decomposition of an original problem.

with $a_1 = 2\cos 2\phi_{\beta\alpha} - \cos 4\phi_{\beta\alpha}, a_2 = a_6 = \cos 4\phi_{\beta\alpha}, a_3 = a_4 = \sin 2\phi_{\beta\alpha} - \sin 4\phi_{\beta\alpha}, a_5 = \sin 2\phi_{\beta\alpha} + \sin 4\phi_{\beta\alpha}, b = 2c_0/\pi$.

Note that the Mode I stress intensity factor at the tips of the crack-α is given by

$$K_I^\alpha = \sqrt{\pi l_\alpha}(\sigma_{11}^{\infty\alpha} + \sigma_{11}^{P\alpha}) + \frac{c_0}{\sqrt{\pi l_\alpha}}(-\lambda_1(\sigma_{22}^{\infty\alpha} + \sigma_{22}^{P\alpha}) + \lambda_2(\sigma_{11}^{\infty\alpha} + \sigma_{11}^{P\alpha})). \tag{4}$$

HOMOGENIZATION AND GOVERNING EQUATIONS

In this Section we carry out the homogenization, and generalized the formulation for the discrete system shown above by considering the distributed microstructures. The stress and strain tensor $\hat{\boldsymbol{\sigma}}$ and $\hat{\boldsymbol{\varepsilon}}$ and displacement vector $\hat{\boldsymbol{u}}$ are understood as the averaged quantities over a representative volume element V_e. Similarly to the ordinary continuum theory, they satisfy the equilibrium equation and the strain–displacement relationship:

$$\nabla \cdot \hat{\boldsymbol{\sigma}} = 0, \quad \hat{\boldsymbol{\varepsilon}} = \frac{1}{2}(\nabla \otimes \hat{\boldsymbol{u}} + (\nabla \otimes \hat{\boldsymbol{u}})^T). \tag{5}$$

The constitutive equation consists of the stress–strain relationship for a certain state of microstructures and the evolution law of the microstructures. The former relationship is given by the relationship between the averaged stress $\hat{\boldsymbol{\sigma}}$ and the averaged strain $\hat{\boldsymbol{\varepsilon}}$ of the elastic solid containing many microstructures. It has been shown that,

$$\hat{\boldsymbol{\sigma}} = \boldsymbol{D}^e : (\hat{\boldsymbol{\varepsilon}} - \hat{\boldsymbol{\varepsilon}}^*), \qquad \hat{\boldsymbol{\varepsilon}}^* = \frac{1}{V_e}\int_S \frac{1}{2}([\boldsymbol{u}] \otimes \boldsymbol{n} + \boldsymbol{n} \otimes [\boldsymbol{u}])ds, \tag{6}$$

where $\boldsymbol{D}^e$ is elastic moduli of the matrix, $\hat{\boldsymbol{\varepsilon}}^*$ is the average strain due to the displacement gap $[\boldsymbol{u}] \equiv \boldsymbol{u}^+ - \boldsymbol{u}^-$ along crack surface with unit normal vector $\boldsymbol{n}$ and S being the crack surfaces contained in the representative volume V_e.

If the displacement gap $[\boldsymbol{u}]$ is expressed in terms of the averaged stress by solving the problem of many microstructures, the strain due to crack opening is given by $\hat{\boldsymbol{\varepsilon}}^* = \boldsymbol{C}^* : \hat{\boldsymbol{\sigma}}$. Then, the stress–strain relationship takes the following form :

$$\hat{\boldsymbol{\sigma}} = \boldsymbol{D}^e : (\boldsymbol{I} - \boldsymbol{H}) : \hat{\boldsymbol{\varepsilon}}, \tag{7}$$

where $\boldsymbol{H} = (\boldsymbol{I} + \boldsymbol{C}^* : \boldsymbol{D}^e)^{-1} : \boldsymbol{C}^* : \boldsymbol{D}^e$ and $\boldsymbol{I}$ is the forth-order identity tensor.

For the two-dimensional problem, we set $\hat{\boldsymbol{\sigma}} = \{\hat{\sigma}_{11}, \hat{\sigma}_{22}, \hat{\sigma}_{12}\}^T, \hat{\boldsymbol{\varepsilon}} = \{\hat{\varepsilon}_{11}, \hat{\varepsilon}_{22}, 2\hat{\varepsilon}_{12}\}^T$, and accordingly the tensors $\boldsymbol{C}^*, \boldsymbol{D}^e, \boldsymbol{I}, \boldsymbol{H}$ are reduced to 3×3 matrices. In general, it is difficult to obtain the explicit expression of the matrix $\boldsymbol{C}^*$ and accordingly $\boldsymbol{H}$. However, neglecting interaction effect of microstructures, the matrix $\boldsymbol{H}$ is given by

$$\begin{aligned} H_{1i} &= \frac{2\rho l\{(\pi l + 2\lambda_2 c_0) D^e_{1i} + 2\lambda_1 c_0 D^e_{2i}\}}{E' + 2\rho l\{(\pi l + 2\lambda_2 c_0) D^e_{11} + 2\lambda_1 c_0 D^e_{21}\}}, \qquad (i = 1, 2), \\ H_{33} &= \frac{2\rho l^2 \pi D^e_{33}}{E' + 2\rho l^2 \pi D^e_{33}}, \qquad \text{otherwise } H_{ij} = 0, \end{aligned} \tag{8}$$

where ρ is the crack density (the number of microstructures per unit area) and $E' = E$ for plane stress and $E' = E/(1-\nu^2)$ for plane strain.

The damage evolution in the present case is the increase in the crack length l with a constant crack density ρ. Hence, the crack length serves as the damage parameter. We employ linear elastic fracture mechanics for the crack extensions. We express the Griffith's criterion with a damage surface $f = K_I - K_c$ as

$$\begin{cases} f = 0 \ ; \ \delta l \geq 0 & \text{(possible growth)}, \\ f < 0 \ ; \ \delta l = 0 & \text{(no growth)}, \end{cases} \tag{9}$$

where K_c is a fracture toughness.

The evaluation of the interaction effect in the evolution law is the key point in the theory. To take account of the direct interaction effect, we apply and extend the method of pseudotractions for distributed microstructures. Similarly to the discrete system, we consider the decomposition of the problem. When we pay attention to the evolution of microstructure at a particular point, we consider a single microstructure located at the point. The number of other cracks is not finite, but they are distributed over the domain with certain distribution of the crack density $\rho(\boldsymbol{x})$ and the crack length $l(\boldsymbol{x})$. Hence the number of other sub-problems is understood to be infinite; see Fig. 2. In the subproblem with the crack under consideration, we apply pseudotractions which is calculated from the interaction field on the surface of the crack. Then, the damage surface is given by

$$f(\hat{\boldsymbol{\sigma}}, \boldsymbol{\sigma}^P, l) = \sqrt{\pi l}(\hat{\sigma}_{11} + \sigma^P_{11}) + \frac{c_0}{\sqrt{\pi l}}(-\lambda_1(\hat{\sigma}_{22} + \sigma^P_{22}) + \lambda_2(\hat{\sigma}_{11} + \sigma^P_{11})) - K_c. \tag{10}$$

Since the distributed cracks are considered and the number of the subproblems is infinite, the consistency condition, which ensures the traction free condition of the surface, takes the following form,

$$\boldsymbol{\sigma}^P(\boldsymbol{x}) = \int_V \rho \boldsymbol{\gamma}(\boldsymbol{x} \mid \boldsymbol{\xi})\{\hat{\boldsymbol{\sigma}}(\boldsymbol{\xi}) + \boldsymbol{\sigma}^P(\boldsymbol{\xi})\} d\boldsymbol{\xi}, \tag{11}$$

where $\boldsymbol{\gamma}(\boldsymbol{x} \mid \boldsymbol{\xi})$ is the same definition of $\gamma^{\alpha\beta}_{ij}$ in equation (3) except $d = \| \boldsymbol{x} - \boldsymbol{\xi} \|$, and l_β and $\phi_{\beta\alpha}$ being replaced by the half crack length at the point $\boldsymbol{\xi}$: $l(\boldsymbol{\xi})$ and $\phi = \tan^{-1}(x_2 - \xi_2)/(x_1 - \xi_1) + \pi/2$, respectively.

COMPARISON WITH CONTINUUM DAMAGE MECHANICS

To illustrate the feature of the proposed theory, we present the conventional CDM for the same problem and make a comparison with them. In CDM, the direct interaction effect between microstructures is not taken into account, and a single microstructure in an infinite body is considered. Then the damage surface becomes

$$f(\hat{\boldsymbol{\sigma}}, l) = \sqrt{\pi l}\hat{\sigma}_{11} + \frac{c_0}{\sqrt{\pi l}}(-\lambda_1\hat{\sigma}_{22} + \lambda_2\hat{\sigma}_{11}) - K_c. \tag{12}$$

The other governing equations, the equilibrium equation, the strain–displacement relationship and the stress–strain relationship, are the same as IFT. Note that the main feature that distinguishes IFT from CDM is the fact that the stress–strain relationship at a point depends on the stress and the crack length at all other points. Such a nonlocal constitutive relation is also discussed by Bažant [3].

NUMERICAL EXAMPLE

As an example, we consider a biaxial test of a block under plane strain condition; see Fig. 3(a). We employ the conventional three–node triangular element for the approximation of the displacement field $\hat{\boldsymbol{u}}$. The damage parameter l and the interaction field $\boldsymbol{\sigma}^P$ are approximated to be constant in an element. To simplify numerical calculation, the evolution law (9) is approximated by $f = 0$. This corresponds to make the irreversible variable l reversible, and hence to reduce the inelastic problem to the nonlinear elastic problem. The following values are used in all calculations: normalized Young's modulus $E/\sigma_0 = 1000$, Poisson's ratio $\nu = 0.3$, the normalized crack density $\rho c_0^2 = 0.3$, $\lambda_1 = 0.5$ and $\lambda_2 = 0$, where σ_0 is the reference stress defined by $\sigma_0 = K_c/\sqrt{\pi c_0}$.

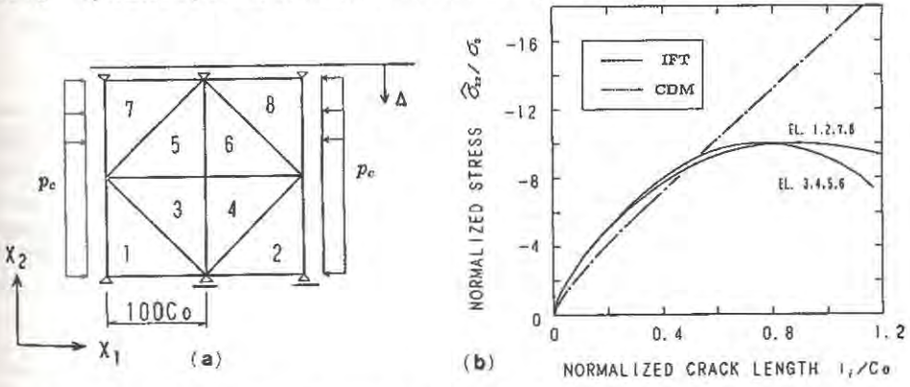

Figure 3: (a) Finite element mesh, (b) Axial stress versus crack length curve.

Figure 3(b) shows the evolution of the crack lengths (damage parameters) in every element with the normalized confining pressure $p_c/\sigma_0 = -2.0$ for the cases of both IFT and CDM. At initial loading stage, all crack lengths of IFT as well as CDM grow uniformly. In IFT, after the critical load is attained, all damage parameters still increase with the decreasing load. Moreover, the distribution of the damage becomes gradually not uniform in the specimen. In contrast to IFT, all damage parameters in CDM are identical in the specimen at all loading stages, and there is no critical load.

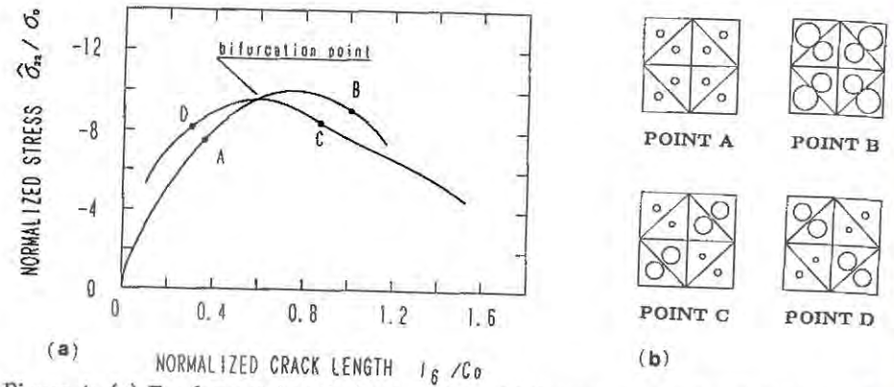

Figure 4: (a) Fundamental path (path AB) and bifurcating path (path CD), (b) Distribution of damage parameter at point A to D

To detect bifurcation points, an eigenvalue analysis is carried out at each incremental step. While the solution of CDM has no bifurcating paths, the solution of IFT is found to have possibility of bifurcation. In Fig.4(a), the bifurcation path (path C to D) as well as the fundamental path (path A to B) are plotted for the damage parameter of the element 6. Figure 4(b) shows the distribution of the damage parameters corresponding to the points A to D in Fig. 4(a). The radii of the circles denote the magnitude of the damage parameters. In post-bifurcation regime, the damage parameters of elements in the diagonal direction increase and the others decrease with the decreasing load. This shows the features observed in the localization of damage or the shear band formation in laboratory test. It is confirmed that IFT can simulate these localization phenomena as well as damage softening, while conventional CDM can not reproduce those features.

CONCLUSIONS

In this paper, a micromechanics-based continuum theory, named Interaction Field Theory (IFT), is proposed. The main feature that distinguishes IFT from micromechanics-based CDM is the direct evaluation of the interaction effect between microstructures distributed in materials. In IFT, the interaction tensors that are field variables characterizing the interaction effect between microstructures are introduced, and their governing integral equations are formulated. The numerical results presented here confirm that IFT can reproduce localization phenomena as well as softening behavior, which is not reproduced by the conventional CDM.

REFERENCES

1. Krajcinovic, D. and Sumarac, D., A Mesomechanical Model for Brittle Deformation Processes: Part I, J. Appl. Mech., Vol.56, 1989, pp.51–56.

2. Horii, H. and Nemat-Nasser, S., Elastic Fields of Interacting Inhomogeneities, Int. J. Solids Structures, Vol.21, No.7, 1985, pp.731–745.

3. Droz, P. and Bažant, Z.P. Nonlocal Analysis of Stable States and Stable Paths of Propagation of Damage Shear Bands, Cracking and Damage, (J. Mazars and Z.P. Bažant eds.), Elsevier, 1989 pp.415–425.

STRAIN LOCALIZATION IN CONCRETE LOADED IN COMPRESSION: THE INFLUENCE OF BOUNDARY CONDITIONS.

J.M. TORRENTI, E.H. BENAIJA and C.BOULAY
Laboratoire Central des Ponts et Chaussées.
58, bd Lefebvre. 75732 PARIS

ABSTRACT

This study concerns simple compressive tests on prismatic specimens of mortar. The blocking or non-blocking of rotation of the top platen of the press and the use or abscence of an anti-friction system have led us to consider four different boundary conditions. The onset of strain localization and its development in the course of loading are determined by the stereophotogrammetric method. The results obtained show that rotation (when it is permitted) always starts after the force peak. The post-peak portion of the force-deformation curve depends to a very large extent on the boundary conditions. On the other hand, the onset of strain localization occurs just before the peak. Finally, it seems that the onset of localization does not depend on the boundary conditions imposed.

INTRODUCTION

Since the beginning of the 1970s, stereophotogrammetry has been applied to the study of the flow of a few materials, in particular by BUTTERFIELD et al. (4), BEYNET and TRAMPZYNSKI (3), BENEFICE and BOEHLER (2), BERKA et al. (5), and by DAVIDSON (6). These different authors have in this way obtained the displacement fields resulting from the loadings of plane models and the corresponding isovalues by analog restitution with a resolution of the order of 0.01 millimetre.

Analytical restitution was used by J.DESRUES (7) in 1984. It makes it possible to use a numerical approach to determine the strain field associated with the stereoscopic measurements. J. DESRUES has shown that this method is especially well suited to study of the problem of strain localization in shear bands in granular media.

For our part, we have shown in a previous study that it could be applied successfully to the concrete (13). This study concerned simple compressive tests. In such tests, if the press is controlled with respect to the shortening of the specimen, the force first increases, passes through a maximum (force peak) then decreases (softening). The press used had a top plate fitted with a ball joint allowing all rotations. During all of these tests, we noted that the force peak, the onset of localization of strains, and the start of rotation of

the top plate of the press occurred at nearly the same stage of loading. The question then arises of learning the scenario leading up to these three phenomena and to failure. It was therefore important to know the couplings existing between boundary conditions and localization. This problem has already been dealt with partially by other authors. They found that the post-peak portion of the force-displacement curve is a function only of the boundary conditions imposed during the test (KOTSOVOS (10), VONK et al. (11)).

We accordingly thought it worthwhile to determine the influence of confinement and rotation on the behaviour of our specimens. This article begins by describing our experimental procedure together with all boundary conditions imposed. It then gives a summary of all results obtained. The main conclusions of this study are given in the final part.

EXPERIMENTAL INVESTIGATION

Description of tests:

The experimental investigation consists of simple compressive tests with a constant imposed displacement rate measured between the platens. The displacement is obtained taking the the mean of three sensors forming an equilateral triangle about the specimen tested.

Material and dimensions of the specimens chosen:

Because the stereophotogrammetric method is limited to the study of plane objects undergoing a plane transformation, our tests must satisfy the condition of plane stresses. This condition is easier to meet when the thickness of the specimen tested is negligible with respect the other two dimensions. The capacity of the press (10 tonnes) imposes maximum dimensions beyond which the test can no longer be performed. However, the specimen must remain representative of the material. A suitable choice of mortar enabled us to attain a compromise among these requirements. Finally, we selected the following dimensions: height 12 cm, width 6 cm, and thickness 2 cm.

Boundary conditions:

During the preliminary tests, several anticonfinement systems were tested. 5-mm squares of aluminium cut from a sheet 2 mm thick constituted the anticonfinement system adopted: it gives satisfactory results, at least up to the force peak (the ratio of Young's modulus to Poisson's ratio of aluminium is very close of that of the mortar). Because of their fragmentation, the squares are expected to follow the displacements even in the post-peak portion. The transverse strains measured in one of our tests with one gauge located at the middle of the specimen and the other under the support remain very close, proof of the effectiveness of this system.

Four boundary conditions were considered: rotation of the ball joint of the upper thrust plate free or locked, presence or absence of anticonfinement system. The notations are: N (rotation free, no anticonfinement system), A (rotation free, anticonfinement system), B (rotation locked, no anticonfinement system) and AB (rotation locked, anticonfinement system).

Results obtained:

a) Displacement transducers (LVDTs):

In the course of each of our tests, the displacements measured by the three LVDTs and the force exerted on the specimen were recorded. From these raw measurements, using numerical processing, we have access to other physical magnitudes such as the rotations affecting the top plate of the press.

b) Stereophotogrammetry:

This method consists, in our case, of taking photographs of the specimen tested at different loading stages. Stereocomparison of these photographs yields the incremental displacement field between two views. This field then undergoes numerical processing to obtain the associated strain field. A more detailed description of these operations can be found in the articles by DESRUES (7,9) and TORRENTI et al. (8,13).

RESULTS

LVDTs

The various force-displacement curves show an identical ascending portion. The behaviour of the specimens in this stage of loading depends only on the modulus of the mortar used for their production. On the other hand, the strength value at the force peak exhibits no simple correlation with the boundary conditions.

On the force-displacement curve, the rotation between plates is reflected in a change of slope. As table 1 indicates, the rotation occurs after the force peak (the displacement at the peak is of the order of 0.5 mm). In consequence, the post-peak portion of the force-displacement curve depends on the rotations allowed during the test in question. The origin of such rotations is probably local damage, in this loading stage, of the specimen tested. The rotation should therefore be a consequence of some localization of the strain.

If we look at the mean slope of the redescending part of the force-displacement curve we find, in agreement with KOTSOVOS, that the use of the anticonfinement system does increase the slope, in other words, that the "behaviour" becomes less "softening".

test	N1	N2	N3	A1	A2	A3
ddr/dp	1.30	1.00	1.34	1.08	1.12	1.14

ddr is the displacement at the start of the rotation an dp that at the peak.

Table 1: Start of rotation.

Stereophotogrammetry:

In the various stereocomparison results we have obtained (figures 1, 2, 3, and 4), we can detect the onset of localization and follow its development. We can also record the cracks existing in a given loading stage and so their mode of opening and of propagation between two successive photographs (8).

The onset of localization coincides with the appearance of a zone where the distorsions are clearly greater than those in the rest of the specimen. It corresponds, in general, to the appearance of a region where there is an increase of surface (dilatancy) and to some bunching of the displacement isovalues. The development of localization continues until the end of the test, when the specimen is split into two or more blocks. The strain field is practically uniform within each block. The recorded strains are caused in large part by the relative displacement of the blocks: the behaviour is that of a structure.

Table 2 situates the onset of localization with respect to the force peak. Displacement ddl corresponds to the photograph in which localization has just occurred. The onset of localization therefore occurs between this photograph and the one before it. We note then that localization occurs just before the force peak whatever the boundary conditions.The peak is therefore a consequence of the strain localization. It should be noted, on the one hand, that WANG (12), using X-ray measurements, has shown that localization can occur earlier, depending on the boundary conditions, and on the other hand, that BAZANT (1) has shown, by thermodynamic considerations, that as soon as the peak is reached there is necessarily strain localization.

test	N3	A3	AB1	B1
ddl / dp	1.0	1.0	0.93	1.0

ddl is the displacement at the onset of localization and dp that at the force peak.

Table 2: Onset of localization.

Confinement has some influence on the onset and growth of cracks. All tests with anti-confinement devices produced cracks that emerged on the bearing faces. On the other hand, cracking in the tests with confinement took the form of a "band", generally joining the two free sides of the specimens.

CONCLUSIONS:

From the analysis of our tests by stereophotogrammetry we can deduce the following: the force-displacement curve represents the behaviour of the concrete up to the vicinity of the force peak. Beyond it, it depends on the boundary conditions imposed during the test: rotations between plates of the press cause changes of slope, and confinement decreases the modulus of the decreasing slope of this curve.

The start of rotation of the top plate of the press always occurs after the force peak, itself a consequence of some strain localization. We can therefore state the following symbolic result:

localization -------> force peak -------> rotation (if any)

It is therefore never the rotation that causes the localization, the onset of which, observed by stereophotogrammetry, seems to be independent of the boundary conditions and always occurs just before the force peak.

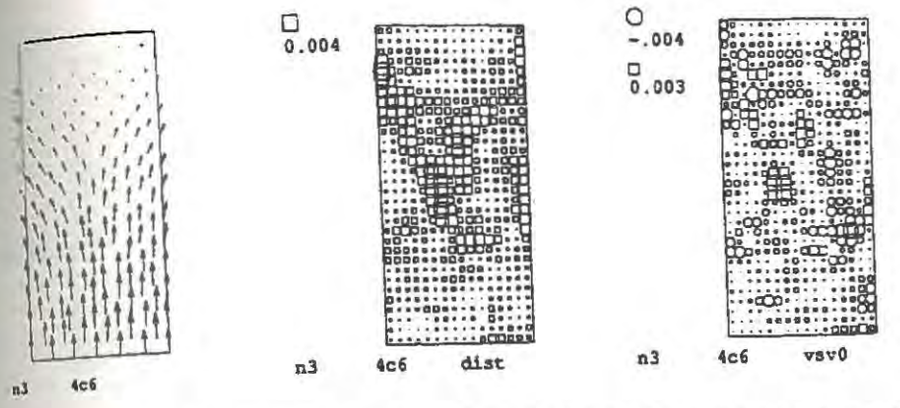

Figure 1: test N3; displacement, distorsion and surface variation maps around the stress peak.

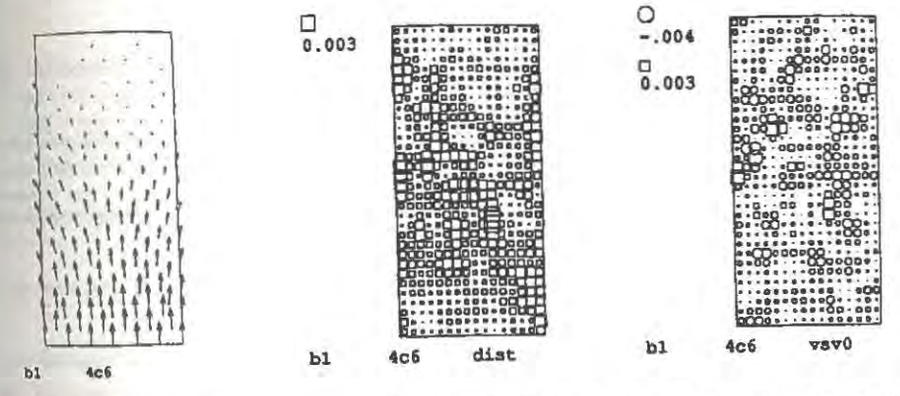

Figure 2: test B1; displacement, distorsion and surface variation maps around the stress peak.

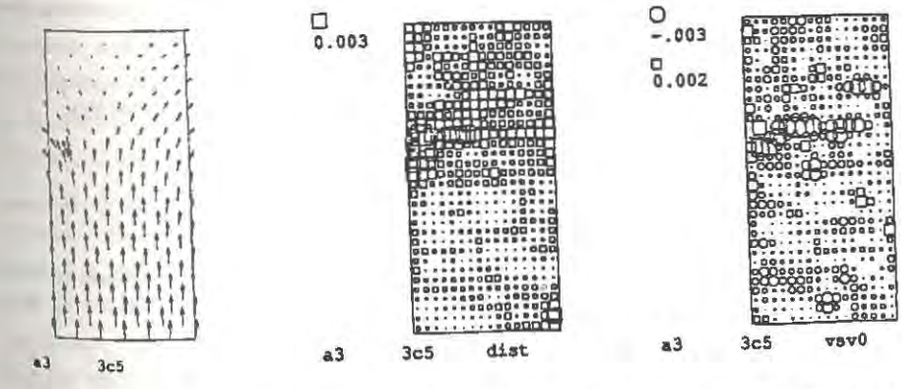

Figure 3: test A3; displacement, distorsion and surface variation maps around the stress peak.

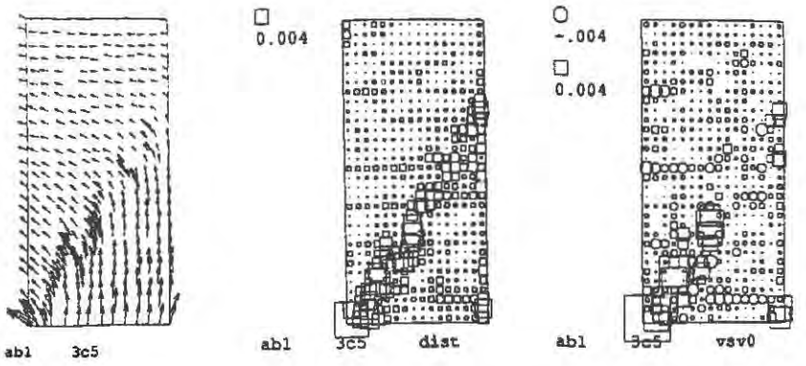

Figure 4: test AB1 ; displacement, distorsion and surface variation maps around the stress peak.

REFERENCES:

1. BAZANT (1988), "Stable states and paths of structures with plasticity or damage", J. Engineering Mech., ASCE, 114(12), pp. 2013-2034.

2. BENEFICE and BOEHLER (1979), "The application of stereophotogrammetry to the analysis of displacement fields in solid mechanics", in proc. of IUTAM, Symposium of Optical Methods in Mechanics of solids, Poitier.

3. BEYNET and TRAMPCZYNSKI, "Application of stereophotogrammetry to the measurement of displacements and study of the flow of materials", Matériaux et Constructions, vol.10, no. 59 (in French).

4. BUTTERFIELD, HARNESS and ANDRAWES (1979), "A stereophotogrammetric method for measuring displacement fields", Geotechnique 20, no. 3, pp. 308-314.

5. BERKA, RUZEK, SCHENK, SOVA and VASINA (1990), "A strain and stress analysis in microobjects", 9th International Conference on experimental Mechanics, Copenhagen, pp. 609-618.

6. DAVIDSON (1990), "Micromechanics of Brittle Materials at Ambient Temperature", Micro Mechanics of failure of quasi brittle materials, SHAH, SWARTZ and WANG ed., Elsevier applied science.

7. DESRUES (1983), "On the application of stereophotogrammetry to the measurement of large strains", Revue Française de Mécanique, no. 3, Grenoble (in French).

8. TORRENTI, BENAIJA (1990), "Stereophotogrammetry: a new way to study strain localization in concrete under compression", 9th International Conference on Experimental Mechanics, Copenhagen, pp. 1346-1354.

9. DESRUES, "Strain localization in granular materials", State Thesis, Grenoble, 1984 (in French).

10. KOTSOVOS,(1983),"Effect of testing techniques on the post-ultimate behavior of concrete in compression", Materials and structures, RILEM, vol.16, p 3- 12.

11. VONK, RUTTEN, VAN MIER and FIJNEMAN (1989), "Influence of boundary conditions on softening of concrete loaded in compression", Fracture of concrete and rock: recent developments, SHAH, SWARTZ, BAN ed., Elsevier Applied Science, Cardiff.

12. WANG, SCHREYER and RUTLAND (1990), "Internal deformation measurements with the use of real time X-rays", Micromechnics of failure of quasi brittle materials, SHAH, SWARTZ and WANG ed., Elsevier Applied Science.

13. TORRENTI, DESRUES, BENAIJA and BOULAY, "Stereophotogrammetry: a means of visualizing strain localization in concrete under compression", Revue Française de Mécanique, no. 1990-1 (in French).

PROBABILISTIC MODELLING OF BRITTLE FRACTURE STRENGTHS AND LOAD DURATION EFFECTS FOR CONCRETE

STUART G. REID
School of Civil and Mining Engineering
University of Sydney, NSW 2006, Australia

ABSTRACT

The statistical variability of brittle fracture strengths is commonly modelled using the statistical strength theory of Weibull. To account for the time-dependence of strengths due to slow crack growth, stochastic fracture models have been developed by combining the Weibull model with cumulative damage models based on the time-integral of applied stresses (raised to some power). The capabilities and limitations of such models are discussed, in relation to a more realistic stochastic crack growth model, and in relation to the modelling of concrete strengths.

INTRODUCTION

The statistical variability of brittle fracture strengths is commonly modelled using the statistical strength theory of Weibull [1]. The Weibull model accounts for fracture initiation due to spatially distributed random flaws, and hence it predicts statistical size effects for brittle fracture. The Weibull model can also account for the effects of different specimen geometries and dissimilar stress fields. However, modifications of the Weibull model are required for applications involving quasi-brittle fracture [2], or slow crack growth prior to brittle fracture. This paper concerns adaptations of the Weibull model to account for time-dependent strengths due to slow crack growth.

In order to produce stochastic (statistical time-dependent) models of fracture strengths, Weibull-type strength models have been combined with cumulative damage models of slow crack growth. Convenient models of cumulative damage have been proposed, based on the integral (with respect to time) of the applied stress raised to a high power. A simple model of this type was proposed by Mihashi and Izumi [3] to describe concrete fracture, and was applied by Zech and Wittmann [4] in a brief

investigation of the stochastic nature of concrete fracture. Also, a relatively sophisticated 'failure prediction model' of this type was developed by Brown [5] and refined by Beason and others [6] to describe the strength of glass, and it has been used extensively in the development of design standards for architectural glazing.

The statistical strength theory of Weibull, the stochastic theory for concrete fracture proposed by Mihashi and Izumi, and Brown's failure prediction model are briefly reviewed below and compared with a more realistic stochastic crack growth model [7].

FAILURE PREDICTION MODELS

Statistical Strength Theory of Weibull

According to the statistical strength theory of Weibull [1], the probability of failure of a brittle body due to internal flaws can be expressed

$$P_f = 1 - \exp[- \int_{Volume} k\sigma^m \, dV] \qquad (1)$$

where the integral of $k\sigma^m$ represents the expected number of flaws that would fail at a stress less than or equal to σ (the equivalent uniaxial tensile stress, accounting for the random orientation of flaws).

If the stresses σ within a body are proportional to a nominal applied stress σ_n, then

$$P_f = 1 - \exp[- kLV\sigma_n^m] \qquad (2)$$

where V is the total volume of the body and L characterises the relative stress distribution within the body. Hence for similar specimens differing only with respect to size, the Weibull model predicts a size effect such that the nominal strength σ_n is proportional to $V^{-1/m}$, for any particular fractile of the strength distribution.

Stochastic Strength Theory of Mihashi and Izumi

Mihashi and Izumi [3] proposed a simple stochastic model of fracture strength, similar to the Weibull model but with time-dependent parameters given by the time-integral of the applied stresses raised to a power β:

$$P_f = 1 - \exp[- \int_0^t kLV\sigma_n^{\beta}(t) \, dt] \qquad (3)$$

For 'ramp loads' applied at a constant nominal stress rate $\dot{\sigma}_n$, the corresponding distribution of failure stresses σ_f is

$$P_f = 1 - \exp[- kLV/[(\beta + 1) \, \dot{\sigma}_n] \, \sigma_f^{(\beta+1)}] \qquad (4)$$

Thus for nominally identical specimens, the nominal strength (for any particular fracture) depends on the stress rate, and the parameter β is given by

$$\beta = (ln \, \dot{\sigma}_n / ln \, \sigma_f) - 1 \qquad (5)$$

Zech and Wittmann [4] estimated β for concrete from the time-dependence of experimental results, and reported reasonable agreement between the model and the available data.

The exponent β characterises not only the time-dependence of the strengths, but also the statistical variability of the strengths. This implies a special relationship between the statistical variability and the time-dependence. If variations due to stress-history effects are eliminated by loading at a particular constant stress rate $\dot{\sigma}_n$, then the stochastic model (equation 4) reduces to the form of the Weibull model (equation 2), with the statistical variability (and associated size-effects) characterised by $(\beta + 1)$ equivalent to m. Zech and Wittmann [4] estimated β and m according to this implied relationship, on the basis of independent investigations of size effects and load-rate effects, and reported reasonable agreement between the results. However, it should be noted that the implicit relationship between β and m is simply a characteristic (and limitation) of the stochastic model, and not a characteristic of real fracture mechanics.

Brown's Failure Prediction Model

According to Brown's load-duration theory [5], glass fracture is caused by 'stress corrosion' and the failure criterion is expressed in terms of 'Brown's Integral':

$$\int_0^{t_f} \sigma(t)^n \, dt = D_f \qquad (6)$$

where t_f is the time to failure, and D_f is constant (for a given specimen). Brown's Integral was used to relate applied stresses to equivalent peak stresses σ_f for a particular strain rate.

Furthermore, Brown used a 2-parameter Weibull distribution to describe the distribution of equivalent peak stresses at failure (in effect assuming that D_f is Weibull distributed). Thus for a glass plate with surface flaws distributed over an area A,

$$P_f = 1 - \exp[- kLA\sigma_f^m] \qquad (7)$$

where L characterises the relative stress distribution. Brown estimated the Weibull

distribution parameter **m** from test results for geometrically similar glass plates of various sizes.

The current glass failure prediction model [6] is an extension of Brown's model incorporating the results of theoretical (geometrically non-linear) stress analyses of thin glass plates. Theoretical (time-dependent) stresses are converted to 'equivalent' stresses of 60 seconds duration, using Brown's Integral. The equivalent stresses are further 'corrected' to obtain equivalent uniform biaxial tensile stresses, and an 'equivalent stressed area' A^* is determined such that:

$$\int_{Area} k\sigma^m \, dA = k \, (\sigma_o)^m \, A^* \qquad (8)$$

where A^* is the 'equivalent area' at a biaxial tension of σ_o (sustained for 60 seconds).

Assuming a Weibull distribution of strengths, the critical 'equivalent area' A^* (the equivalent area required to produce failure) is exponentially distributed and consequently has a coefficient of variation of 1. Therefore the surface flaw parameters (**m** and **k**) are chosen to match experimental strength distributions, and to yield a coefficient of variation of A^* close to the theoretical value.

Clearly the glass failure prediction model is more realistic than the simple stochastic fracture model of Mihashi and Izumi [3], because the glass failure prediction model includes independent parameters **m** and **n** to characterise the statistical variability and the time-dependence, respectively. However, the model is still not realistic, because Brown's Integral implies that the probability of failure at or before time **t** is effectively independent of the applied stress at that time. Also, it should be noted that the model implies that the surface flaw parameter **m**, which characterizes the 'shape' of the strength distribution, is independent of the stress history, whereas realistic qualitative crack growth models indicate that the shape of the strength distribution changes with time [7].

Stochastic Crack Growth Model

The Weibull distribution of strength can be expressed (with regard to surface flaws)

$$P_f = 1 - \exp\left[- \int_{Area} \rho_o (\sigma/\sigma_o)^m \, dA \right] \qquad (9)$$

where ρ_o represents the density of flaws of strength less than or equal to σ_o and $(\sigma/\sigma_o)^m$ represents the cumulative distribution function of the relevant flaw strengths. Furthermore, the distribution of flaw strengths can be related to a distribution of flaw (micro-crack) sizes, and the time-dependence of the strength distribution can be expressed in terms of the time-dependence of the flaw size distribution [8].

In general, the time dependent strength distribution will be a complex function of the crack growth law and the stress history. In accordance with the principles of linear

elastic fracture mechanics, crack growth can be related to the stress intensity factor K_I, and failure can be assumed to occur at a critical value of the stress intensity factor K_{Ic}. If the crack growth law is

$$da/dt = C \, K_I(a)^n = C \, (\sigma Y \sqrt{a})^n \qquad (10)$$

where **a** is the crack size, **C** is a material property, σ is the nominal applied stress (normal to the crack), and **Y** is a factor dependent on the crack geometry; and if ramp loads are applied at a stress rate σ'; then a Weibull distribution of initial flaw strengths (equation 10) yields a time-dependent distribution of flaw strengths $F_{S(t)}(\sigma)$ [7]:

$$F_{S(t)}(\sigma) = (\sigma/\sigma_0)^m \left[1 + (n-2)/(2(n+1)) \; C \; Y^2 \; \sigma^3 \; K_{Ic}^{n-2} \; / \; \sigma'\right]^{m/(n-2)} \qquad (11)$$

where σ is the maximum stress attained at time **t**. Hence for slow rates of loading $F_{S(t)}(\sigma)$ is proportional to $\sigma^{m+3m/(n-2)}$, whilst for fast rates of loading, the strength distribution tends to the distribution function of initial flaw strengths, proportional to σ^m.

Comparison of the Failure Prediction Model and the Crack Growth Model for Concrete

Parameters of the failure prediction model (FPM) and the crack growth model (CGM) for concrete can be estimated from relevant published results, but the resultant estimates are variable and uncertain. To compare the models, representative values of the parameters have been taken to be: $Y^2 = 2/\pi$ (for penny shaped cracks); **m** = 12 (for the FPM), and **n** = 12 [4]; and K_{Ic} = 0.34 (MPa$\sqrt{m}$) [8] and **C** = 92 (m/s)(MPa$\sqrt{m}$)$^{-12}$. Hence, if the CGM is calibrated to match the FPM in the vicinity of a median flaw strength of 15 MPA, for a stress rate σ' of 1 (MPa/s), the FPM yields

$$F_S(\sigma) = 25.7 \times 10^{-18} \, \sigma^{13} \; / \; \sigma' \qquad (12)$$

and the CGM yields

$$F_S(\sigma) = (51.9 \times 10^{-15}) \left[1 + (465 \times 10^{-6}) \, \sigma^3 \; / \; \sigma'\right] \sigma^{10} \qquad (13)$$

Clearly, although the FPM and CGM have been calibrated to match in the vicinity of the median flaw strength for a stress rate of 1 Mpa/s, the models diverge for other stress ranges and stress rates. The CGM indicates that the effective FPM (Weibull) parameter **m** should decrease for relatively low strengths (e.g., for large specimens). Also, the CGM indicates that the FPM exaggerates the effects of load-duration (overestimating strengths for increased load rates). For example, for stress rates of 0.001, 0.1, and 10

(MPa/s), the FPM predicts median flaw strengths of 10.5, 15.0, and 21.4 (MPa), while the CGM indicates median flaw strengths of 10.6, 15.0, and 19.3 (MPa), respectively.

CONCLUSIONS

Stochastic models of fracture strength based simply on time-integrals of applied stresses are fundamentally flawed because they imply that the probability of failure is effectively independent of the stress at the time of failure. The stochastic model of Mihashi and Izumi [3] also imposes an unrealistic limitation on the relationship between the time-dependence and the statistical variability of strengths. Brown's failure prediction model [5] includes independent parameters of time-dependence and statistical variability, but it therefore implies that the 'shape' of the strength distribution is unaffected by the stress-history. A more realistic crack growth model indicates not only that the shape of the strength distribution changes with time, but also that Brown's failure prediction model exaggerates load duration effects. Therefore, the failure prediction model should not be used to extrapolate from one set of load conditions to another, but it could give useful results for concrete for standardised load conditions.

REFERENCES

1. Weibull, W., A statistical theory of the strength of materials. Handlingar Nr 151, Ingeniorsvetenskapsakademin, Stockholm, 1939.

2. Bazant, Z.P., Xi, Y., and Reid, S.G., Statistical size effect in quasi-brittle structures. Part 1: Is Weibull theory applicable ? Journal of Engineering Mechanics, ASCE, Vol. 117, No. 11, November 1991.

3. Mihashi, H., and Izumi, M., Stochastic theory for concrete fracture. Cement and Concrete Research, Vol. 7, 1977, pp. 411-422.

4. Zech, B., and Wittmann, F.H., Probabilistic approach to describe the behaviour of materials. Fourth International Conference on Structural Mechanics in Reactor Technology, 1977, pp. J1/11 1-14.

5. Brown, W.G., A load duration theory for glass design. Publication NRCC 12354, National Research Council of Canada, Ottawa, January 1972.

6. Beason, W.L., and Morgan, J.R., Glass failure prediction model. Journal of Structural Engineering, ASCE, Vol.110, No.2, February 1984, pp. 197-212.

7. Reid, S.G., Flaws in the failure prediction model of glass strength. Sixth International Conference on Applications of Statistics and Probability in Civil Engineering, Mexico City, June 1991, pp. 111-117.

8. Hu, X.-Z., Mai, Y.-W., and Cotterell, B., A statistical theory for time-dependent fracture for cementitious materials. SEM/RILEM International Conference on Fracture of Concrete and Rock, Houston, Texas, June 1987, pp. 53-64.

ASPECTS OF DAMAGE RELATED TO STRUCTURAL RESPONSE

J.F. Labuz, L. Biolzi, and C.N. Chen
Department of Civil and Mineral Engineering
University of Minnesota
Minneapolis, Minnesota 55455

ABSTRACT

A mechanical characterization of microcracking is presented based on the pressure-volume behavior of a brittle solid (granite). The damage estimate is measured by the linear and volumetric strain of an element where all microcracks close under high pressure, typically 50 MPa. The equivalent inclusion-average stress method and the measured properties are used to predict volume fraction. The global behavior of simple beams is related to this damage characterization and explained through an increase in the brittleness number.

INTRODUCTION

Several phenomena such as temperature fluctuation and fatigue or extreme loading produce an increase in microcracking for structures composed of rock-like materials. Furthermore, it is well known that microcracking has a pronounced effect on the behavior of these materials. For example, the presence of microcracks dominates the values of several mechanical properties such as modulus and strength [1-3].

Microcracking and its influence on the global response of a structure may develop competing features (Fig. 1). Although the reduction of the limit load is typically measured for a damaged structure, an increase in "ductility" may also be exhibited such that the system may require more energy to produce failure.

Microcracked solids

A microcracked solid is a special type of composite material, and as such, various methods are available for predicting effective properties. One popular approach is the self-consistent scheme [2], where it is assumed that a particle is embedded in a homogeneous body having unknown (effective) properties and subject to certain boundary conditions. This defines a boundary value problem that can be solved for an arbitrary ellipsoidal particle, resulting in uniform strain in the particle as a function of the effective properties. A shortcoming of self-consistent schemes is the mixing of the micro-variables of the particle with the mini-variables of the effective material--a violation of the so-called MMM principle [4]. Furthermore, self-consistent schemes do a poor job of predicting properties as microcrack density increases (> 0.1).

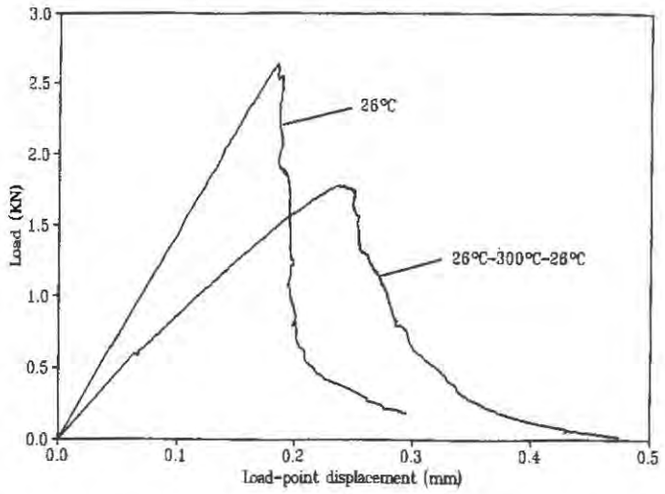

FIGURE 1. Global response of two identical (size and shape) granite beams in three-point bending. The 26°C beam was the virgin material; the other was damaged by heating to 300°C

The equivalent inclusion-average stress method [3], generally credited to Mori and Tanaka [5], gives a more realistic picture of the influence of damage on effective properties [3]. The Mori-Tanaka approach is a micromechanical model based on the equivalent inclusion idea of Eshelby, combined with eigenstrain and the concept of average stress in the matrix. Biolzi and Ferrari [6] have used this method successfully to predict the behavior of short-fiber composites. However, little experimental data are available on the detailed-mechanical response of solids containing microcracks to justify the use of various models in engineering practice. An attempt is made in this study to bridge this gap.

EXPERIMENTS

Because microcracks are very difficult to observe in materials such as rock and concrete, several researchers have proposed the use of hydrostatic pressure to characterize damage [1,7]. One such technique is called differential-strain analysis [7], a method developed to determine the physical properties of lunar rocks. A variation of this technique is employed for thermally-microcracked granite. Essentially, linear strain is measured as a function of hydrostatic pressure. At high enough pressure, typically 50 MPa, all microcracks close and the measured response is due to the solids. After transformation of the strain data, the principal values and the volume strain due to cracks closing can be determined (Fig. 2).

Fig. 2 illustrates the behavior of Charcoal granite (Cold Spring, MN), a rock with a porosity of less than 1%. It is interesting to note that the material (at this scale) is anisotropic: the application of hydrostatic pressure (the dilatational component) produces a shear strain (the deviatoric component); the principal directions of strain rotate with pressure as different microcracks close. The anisotropy is less pronounced on the macroscopic scale, and this rock is sometimes considered to be isotropic. This is certainly true when all cracks are closed. The y-intercept of tangents to the curve indicates the amount of crack-closure strain at a certain pressure; this information can be used to describe a crack distribution function.

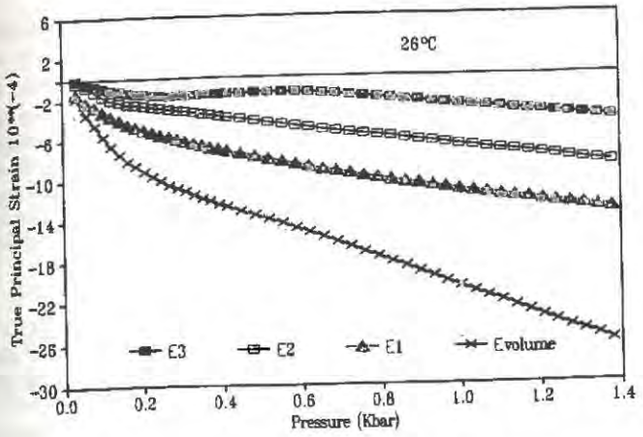

FIGURE 2. Pressure-strain response of a virgin Charcoal granite specimen.

Further damage was then induced by heating the rock at a thermal gradient of 2°C/min and holding the desired temperature for 4 hours. When a material such as rock is heated slowly and uniformly, intergranular thermal stresses develop independent from a gradient due to the nonhomogeneity of the matrix. When these stresses exceed the local fracture resistance, grain boundary and transgranular microcracking results [8]. In any given region of the matrix, the magnitude and location of the tensile stresses depend on the size and shape of the individual grains, the orientation of the crystal axes, and the degree of mismatch in the thermal properties.

The results of heating to 300°C are shown in Fig. 3. The damaged granite is still anisotropic, and the volumetric strain due to cracks closing has increased to from 6,700 microstrain for the virgin rock to 18,900 microstrain for the rock damaged at 300°C.

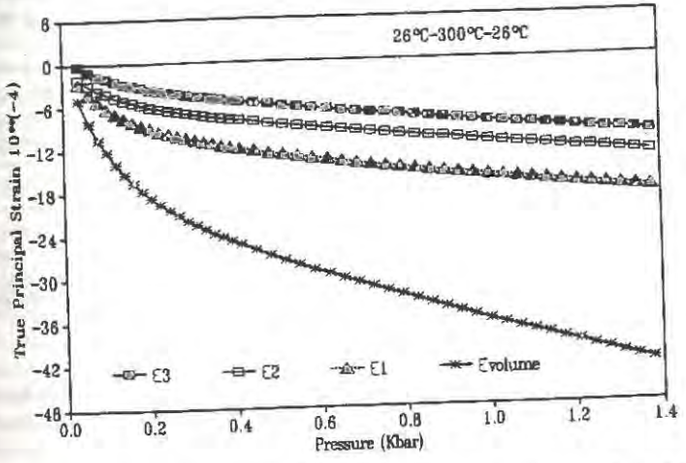

FIGURE 3. Pressure-strain response of a Charcoal granite specimen preheated to 300°C.

DISCUSSION

Specimens under hydrostatic pressure exhibit similar behavior: the initial portion of the pressure-strain curves are nonlinear due to closing of low aspect ratio cracks; at large enough pressure, all the curves are linear. The material is anisotropic at the scale (specimen size of 25 mm) and sensitivity (2×10^{-6}) of the pressure-strain experiments, but at larger scales the response of the rock tends to be isotropic. For a linearly elastic material, pressure p and volume strain e_v are related by

$$p = -\kappa e_v \tag{1}$$

where κ is the bulk modulus, and for an isotropic material, is given by $\kappa = E/[3(1 - 2\nu)]$. When the microcracks are closed, κ = constant. Assuming a Poisson's ratio of the solids to be the same as the virgin material, 0.15, the elastic modulus of the solids E_1 is 126 GPa.

Young's moduli of the virgin and damaged rock were measured indirectly in beam tests with core specimens [9]. The effective properties are 46.5 GPa for the natural granite and 27.1 GPa for the granite heated to 300°C. The experimental values were used to find the microcrack density through the Mori-Tanaka approximation [3].

Assuming a random distribution of penny-shaped cracks of aspect ratio α, the volume fraction was calculated (Table 1); little change in crack volume is predicted for $\alpha > 700$. It has been reported that the low aspect ratio cracks exist within Charcoal granite with α varying from 100 to 1000 [8]. Obviously, the virgin material contains damage, whereby the volume strain due to all cracks closing is 6700 microstrain and the porosity is estimated to be around 1%. When the rock was further damaged by heating to 300°C, crack closure strain increased by a factor of 2.8 and the porosity is predicted to increase a similar amount, approximately 2.1. It is important to note that small volume fractions produce dramatic changes in the modulus.

TABLE 1
The Mori-Tanaka prediction of microcrack porosity (volume fraction) of the measured moduli as a function of aspect ratio α for a random distribution of penny shaped cracks

Aspect ratio α	Porosity, E = 46.5 GPa	Porosity, E = 27.1 GPa
100	0.0375	0.0770
300	0.0130	0.0275
500	0.0083	0.0174
700	0.0065	0.0140

Structural response

Experiments were performed on granite beams 74 mm deep and 32 mm thick under three-point bend loading with a span length of 440 mm. Test control was provided by the crack-mouth displacement measured across a 3 mm notch cut in the middle of the beam. Four beams were tested, two fabricated from the virgin rock (labeled 26°C) and two damaged by heating to 300°C. The results are shown in Fig. 1. The limit load decreased 30%, from 2.6 to 1.8 kN, but the fracture energy, determined from the area under the load-displacement curve, increased slightly from 0.15 kN/m to 0.18 kN/m.

A striking feature of Fig. 1 is the change in global response: the virgin 26°C beam exhibits a condition of critical softening ($dv^t/dF = 0$) while the damaged 300°C beam softens in a stable manner. This is explained through the concept of "size effect" [10]. Consider a simple beam of rectangular cross-section under three-point bending. The total displacement v^t from a load (F) is due to an elastic part v^e and an inelastic (fracture) part v^f:

$$v^e = F\{L/(48EI) + \chi L(1+\nu)/(2EBT) + [5/(ET) + 0.2L/(ET)]\}, \tag{2}$$

where E is the effective Young's modulus, ν is the effective Poisson's ratio, χ is the form factor, L is the length, B is the height, T is the thickness, and I is the moment of inertia. The third term is from the diffusive nature of the point loads [10]. At the limit load, a cohesive fracture zone with a linear closing stress is approximated as being distributed over the full height of the beam. From geometrical considerations, the displacement v^f can be written as

$$v^f = G_f LB/(2\sigma_t). \tag{3}$$

If instead of the load the stress from elementary beam theory is introduced, the incremental stability condition for critical softening is $dv^t/d\sigma = 0$:

$$f(\lambda) = G_f E/(\sigma_t B), \tag{4}$$

where $f(\lambda) = \lambda/3 + 2\chi(1+\nu)/(3\lambda) + 4(5+0.2\lambda)/(3\lambda^2)$ and $\lambda = L/B$ is the slenderness of the beam. The right-hand side of (4) is referred to as a brittleness number [10], and can be used to explain the observed behavior.

Fig. 4 is a plot of (4); the regions formed by the horizontal lines, which represent the brittleness numbers, and the slenderness curve define the values of λ between which the response is stable. From tensile tests on the virgin material, the fracture energy (G_f) is estimated to be 0.25 kN/m with a peak stress (σ_t) of 8500 kN/m^2. The brittleness number for the 26°C beams is about 2.2 (solid line in Fig. 4), indicating that for this size and shape beam the response is near critical. Assuming the fracture energy to remain constant for the 300°C beams and the peak stress to decrease by 35% [9], the brittleness number increases to 3.0 (broken line in Fig. 4), which allows for a stable response at this geometry ($\lambda = 5.9$).

CONCLUSIONS

The mechanical behavior of microcracked solids is influenced strongly by the amount of damage within the material. For example, a Mori-Tanaka approximation shows that a volume fraction of about 1% reduces the effective modulus to less than one-half of the solids' modulus. Experiments indicate that by tripling the damage, which is measured by the volumetric strain due to cracks closing, the modulus is again halved. This may have important implications for structures composed of rock-like materials, as the global response of simple beams is altered by increasing the amount of damage within the brittle solid.

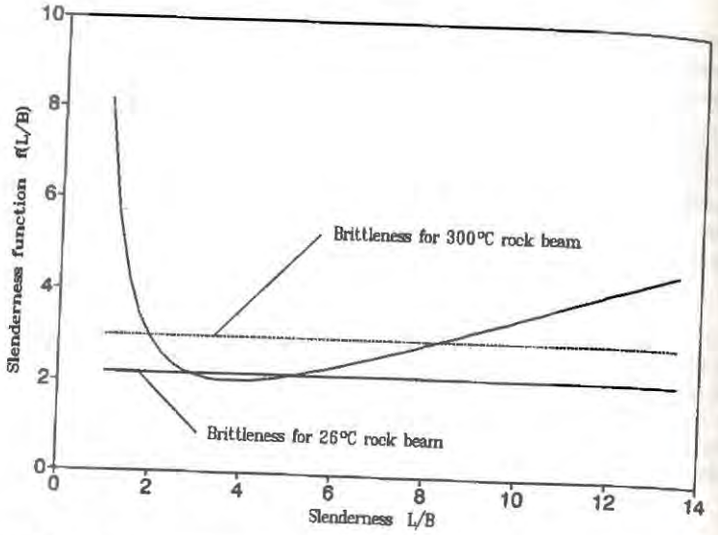

FIGURE 4. Stability regions of a simple beam for different brittleness numbers.

Acknowledgement
Partial support was provided by the National Science Foundation, grant number MSS-9109416

REFERENCES

1. Walsh, J.B., The effects of cracks on the compressibility of rocks. J. Geophys. Res., 1965, 70, 381-9.
2. Budiansky, B. and O'Connell, R.J., Elastic moduli of a cracked solid. Int. J. Solids Struct., 1976, 12, 91-7.
3. Benveniste, Y., A new approach to the application of Mori-Tanaka's theory in composite materials. Mech. Materials, 1987, 6, 147-57.
4. Hashin, Z., Analysis of composite materials--a survey. J. Appl. Mech., 50, 481-505.
5. Mori, T. and Tanaka, K., Average stress in matrix and average elastic energy of materials with misfitting inclusions. Acta Metal., 1973, 21, 571-4.
6. Biolzi, L. and Ferrari, M., Elastic response of macroscopically anisotropic PBT with short glass-fiber reinforcement. Composite Material Symp., ASME, 1991, Houston.
7. Simmons G., Siegfried, R.W., and Feves, M., Differential strain analysis: a new method for examining cracks in rocks, J. Geophys. Res., 1974, 79, 4383-5.
8. Bauer, S.J. and Johnson, B., Effects of slow uniform heating on the physical properties of the Westerly and Charcoal granites. In Proc. 20th U.S. Symp. Rock Mech., 1979, 7-14.
9. Labuz, J.F., Chen, C.N., and Berger, D.J., Microcrack-dependent fracture of damaged rock. Int. J. Fracture, 51, 231-40.
10. Biolzi, L. and Labuz, J.F., Submitted to Int. J. Solids Struct.

MICROPLANE–TYPE CONSTITUTIVE MODELS FOR DISTRIBUTED DAMAGE AND LOCALIZED CRACKING IN CONCRETE STRUCTURES

Ignacio Carol[1], Zdeněk P. Bažant[2] and Pere C. Prat[1]
[1]ETSECCPB — Technical University of Catalonia, 08034 Barcelona, Spain
[2]Dept. of Civil Engineering, Northwestern University, Evanston, IL 60208, USA

ABSTRACT — Two constitutive formulations adequate for representing distributed damage and localized cracking of concrete are described in this paper. They are derived using the same basic idea as the microplane model, i.e. the intrinsic material behavior can be specified on a plane of generic orientation, and the macroscopic relationships derived by accumulation of the contribution from all possible directions in space. In the first formulation, based on continuum damage mechanics, a new expression of a three-dimensional damage tensor, as an integral of the damage for each microplane, is obtained. The second formulation, assuming a statically constrained microstructure, is intended to represent macroscopic cracks within the framework of smeared finite elements analysis and fracture mechanics. In that sense, two of the model parameters are the fracture energies per unit volume under modes I and II, which is convenient for adjusting their values according to the element size so as to achieve the prescribed fracture energy per unit area.

INTRODUCTION

The two formulations described in this paper are based on the idea that the intrinsic material behavior can be defined as a relationship between stresses and strains on a plane of generic orientation, and the macroscopic behavior can be derived (by application of some variational principle) as an integral or summation over all the possible orientations in space. This is in fact an old idea: Taylor in 1938 [1] and Batdorf and Budianski in 1949 [2] used it in the *"slip theory of plasticity"* for metals, and later Zienkiewicz and Pande [3], and Pande and Sharma [4], in their *"multilaminate model"* for fractured rocks and soils.

KINEMATICALLY CONSTRAINED MICROPLANE MODEL AND DAMAGE TENSOR

The first application of this idea to concrete is due to Bažant and Oh [5] under the name of *microplane model*. The present structure of the model was proposed in [6] and an optimized version in [7]. A microplane is any plane cutting the material, defined by its unit normal vector of components n_i. Normal and shear stresses σ_N, σ_{T_r} and strains ϵ_N, ϵ_{T_r} are considered on each microplane. The normal components are further split into volumetric and deviatoric parts ($\sigma_N=\sigma_V+\sigma_D$, $\epsilon_N=\epsilon_V+\epsilon_D$). The strains on the microplane ϵ_V, ϵ_D, ϵ_{T_r} are assumed equal to the projection of the strain tensor ϵ_{ij} (kinematic constraint). The stress–strain behavior of the material is specified by explicit scalar stress-strain relations $\sigma_V=\mathcal{F}_V(\epsilon_V)$, $\sigma_D=\mathcal{F}_D(\epsilon_D)$ and $\sigma_T=\mathcal{F}_T(\epsilon_T)$. The application of the principle of virtual

work leads to the expression of the macroscopic stress tensor as an integral of the stress ten all the possible microplanes around a point:

$$\sigma_{ij} = \sigma_V \delta_{ij} + \frac{3}{2\pi}\int_\Omega \sigma_D n_i n_j d\Omega + \frac{3}{2\pi}\int_\Omega \frac{\sigma_{T_r}}{2}(n_i\delta_{rj} + n_j\delta_{ri} - 2n_i n_j n_r)d\Omega \quad (1)$$

In practice, integrals in (1) are performed numerically. A fixed number of "sample" directions are considerd, which serve as integration points and where, at the same time, history variables for the microplane laws are stored during computations. In [6,7] the model has proven to fit well a large number of test data under 1, 2 and 3-D loading conditions and be easy to implement and fast to run.

The microplane model can be reformulated as a continuum damage model, as described in [8]. The basic equation for a one-dimensional continuum damage model using the concepts of effective stress and strain equivalence is $\sigma=\alpha\tau$ where σ=macroscopic stress, τ=effective stress and α=damage variable of a geometric nature varying from 1 to 0. The corresponding expression in 3-D is $\sigma_{ij} = \alpha_{ijkm}\tau_{km}$, where damage is a fourth-order tensor (repetition of indices implies summation). The new microplane damage tensor is obtained by introducing, at the microplane level, three effective stresses τ_V, τ_D, τ_{T_r} and the corresponding damage variables α_V, α_D, α_T ($\sigma_V = \alpha_V\tau_V$, etc.). The corresponding laws for damage evolution are established in the form: $\alpha_V = \mathcal{G}_V(\epsilon_V)$, $\alpha_D = \mathcal{G}_D(\epsilon_D)$ and $\alpha_T = \mathcal{G}_T(\epsilon_T)$. The final expression gives the damage tensor as an integral of the damage in the microplanes of all possible orientations, in a purely geometric definition ("rheology" is introduced *via* the model for effective stresses τ_{km} exclusively):

$$\alpha_{ijpq} = \frac{\alpha_V}{3}\delta_{ij}\delta_{pq} + \frac{3}{2\pi}\int_\Omega \alpha_D n_i n_j\left(n_p n_q - \frac{\delta_{pq}}{3}\right)d\Omega + \\ + \frac{3}{2\pi}\int_\Omega \frac{\alpha_T}{4}(n_i n_p\delta_{jq} + n_i n_q\delta_{jp} + n_j n_p\delta_{iq} + n_j n_q\delta_{ip} - 4n_i n_j n_p n_q)d\Omega \quad (2)$$

Two examples of application of the microplane damage tensor are presented. In the first example, described in more detail in [8], the damage model has been used in conjunction with linear elasticity for the effective stresses. The example corresponds to a uniaxial test reported by van Mier in 1984 [9], in which both longitudinal stress and transverse strain were recorded. The results are represented in Fig. 1 by solid lines. The dots are the experimental data and the dashed lines are the results obtained with the previous version of the microplane model [7]. In the second example, the microplane damage tensor has been used in conjunction with aging viscoelasticity in the form of a Maxwell chain. The parameters of the chain have been determined according to the recomendations given in [10] to approach the values of the creep function for a concrete with compressive strength f'_c=36.8 MPa, fictitious depth of the specimen e=30 cm, and relative humidity h=90%. The chain ensures that for no damage ($\alpha_{ijkm} = \delta_{ik}\delta_{jm}$, $\sigma_{ij} = \tau_{ij}$) the aging viscoelastic behavior is approached satisfactorily by the overall model. The parameters of the damage model have also been assumed to vary with time so that the peak values of the instantaneous uniaxial σ–ϵ diagram at various ages coincide with the age dependence of f'_c. Various creep tests (consisting of a uniaxial step load applied at 28 days) with increasing values of the load value, have been run with the 3-D model. The stresses and strains along the axis of loading are represented in Fig. 2 showing a strain–time diagram and a stress–strain diagram with creep isochrones. Linear creep is obtained for low stresses (under about $0.4f'_c$), and nonlinear creep and failure under sustained load is obtained under high stresses. All these features agree with the well known behavior of concrete.

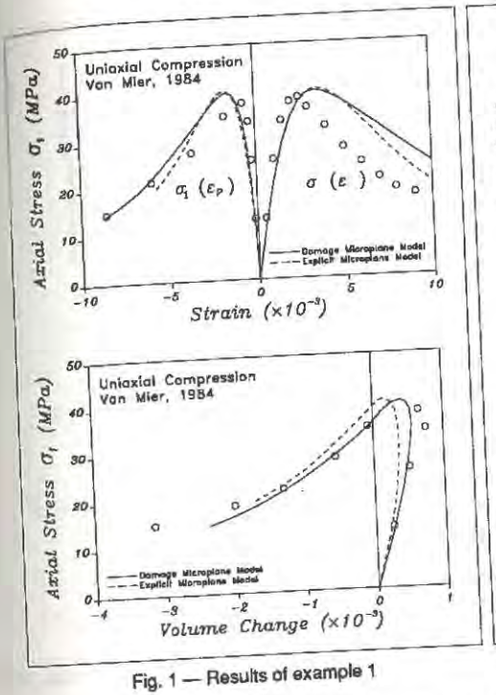

Fig. 1 — Results of example 1

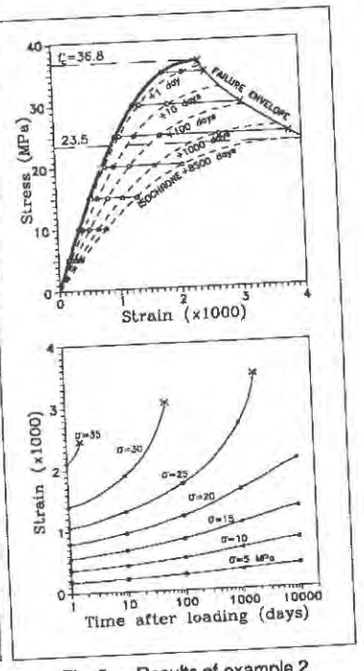

Fig. 2 — Results of example 2

MULTICRACK MODEL WITH STATIC CONSTRAINT

The multicrack model has been developed so far for 2-D analysis and is presented in more detail in [11-13]. As in other previous models for cracking, the stresses on a plane of potential cracking $\underline{s} = [\sigma, \tau]$ are assumed equal to the projection of the stress tensor on that plane $\underline{s}_i = \underline{N}_i^t \underline{\sigma}$ (static constraint), and the total macroscopic strain tensor is decomposed into the contributions of the continuum and crack components $\underline{\varepsilon} = \underline{\varepsilon}^{co} + \sum_{i=1}^{N_c} \underline{\varepsilon}_i^{cr}$ with $\underline{\varepsilon}_i^{cr} = \underline{N}_i \underline{e}_i^{cr}$. In these expressions

$$\underline{N}_i^t = \begin{bmatrix} \cos^2\theta & \sin^2\theta & 2\sin\theta\cos\theta \\ -\cos\theta\sin\theta & \cos\theta\sin\theta & \cos^2\theta - \sin^2\theta \end{bmatrix} \quad (3)$$

where θ is the angle between the normal to the plane of the ith crack and the x–axis; N_c the number of existing cracks, and $\underline{e}_i^{cr} = [\epsilon^{cr}, \gamma^{cr}]^t$= vector of crack strain in local coordinates.

The laws of formation and evolution of a crack on a generic plane are established in terms of the local stresses (σ, τ) and strains $(\epsilon^{cr}, \gamma^{cr})$ by means of a formulation with the structure of a nonassociated plastic model. A hyperbolic "cracking surface" $F(\sigma, \tau) = 0$ with three parameters χ, c and $\tan\phi$ is assumed (Fig. 3a). Two basic modes of fracture are defined together with their corresponding fracture energies. For pure tension, the traditional mode I with associated g_f^I; and, as a second mode related to shear, the asymptotic mode IIa is defined under shear and very high compression, with associated g_f^{IIa} (Fig. 3b). These two modes represent the limiting cases of crack formation and the hyperbola provides smooth transition in between. As the crack starts, parameter ϕ is assumed to remain constant,

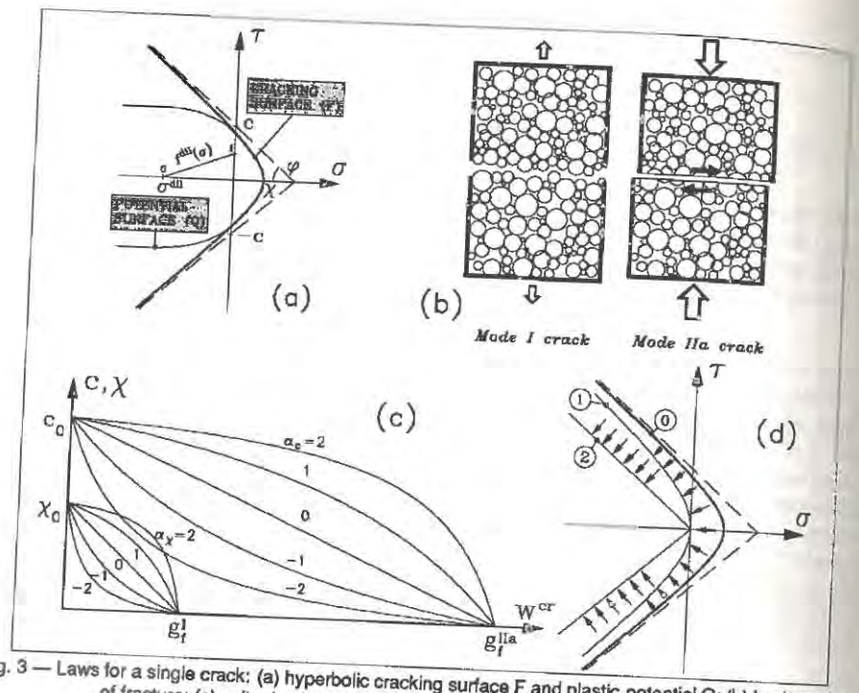

Fig. 3 — Laws for a single crack: (a) hyperbolic cracking surface F and plastic potential Q; (b) basic modes of fracture; (c) softening laws for χ and c; (d) evolution of the cracking surface

and parameters c and χ are assumed to vary with the softening variable w^{cr}, see Fig. 3c (different curves for each value of the additional parameters α_c and α_χ), where w^{cr} is the work spent on the fracture process, defined as $dw^{cr} = \sigma d\epsilon^{cr} + \tau d\gamma^{cr}$ in tension ($\sigma > 0$) and $dw^{cr} = (|\tau| - |\sigma| \tan\phi)|d\gamma^{cr}|$ in compression ($\sigma < 0$), to exclude the frictional work. As the crack progresses, the cracking surface shrinks from curve 0 in Fig. 3d to curve 1 when w^{cr} reaches g_f^I, and to the pair of straight lines 2 representing pure friction when w^{cr} reaches g_f^{IIa}. The direction of the crack strain (flow rule) is given by $d\underline{\varepsilon}_i^{cr} = [\partial Q/\partial \underline{s}]_i d\lambda_i$, with λ_i=plastic multiplier for the ith crack surface. The potential Q is defined so that the crack shows no dilatancy upon shear for high compressive stresses (Fig. 3a). As defined, the model has the structure of a plastic model with a number N_c of simultaneous yield surfaces. A classical derivation leads to the tangent stiffness matrix, which in this case involves the stiffness matrix of the undamaged material between the cracks:

$$d\underline{\sigma} = \underline{D}^{crco} d\underline{\epsilon}; \quad \underline{D}^{crco} = \underline{D}^{co}\left(\underline{I} - \sum_{i=1}^{N_c} \underline{N}_i \left[\frac{\partial Q}{\partial \underline{s}}\right]_i \left[\frac{\partial \lambda_i}{\partial \underline{\epsilon}}\right]^t\right) \quad (4)$$

The proposed cracking model has been implemented with linear elasticity for the intact material between the cracks. Twelve fixed directions equally spaced over the upper hemicircle, are checked at each stage of the computation for new cracks forming, and old ones progressing or stopping. The first example of application at constitutive level is the direct tension test. Only one crack perpendicular to the direction of tension develops. The results are represented in Fig. 4a for different values of the parameter g_f^I. Note that the

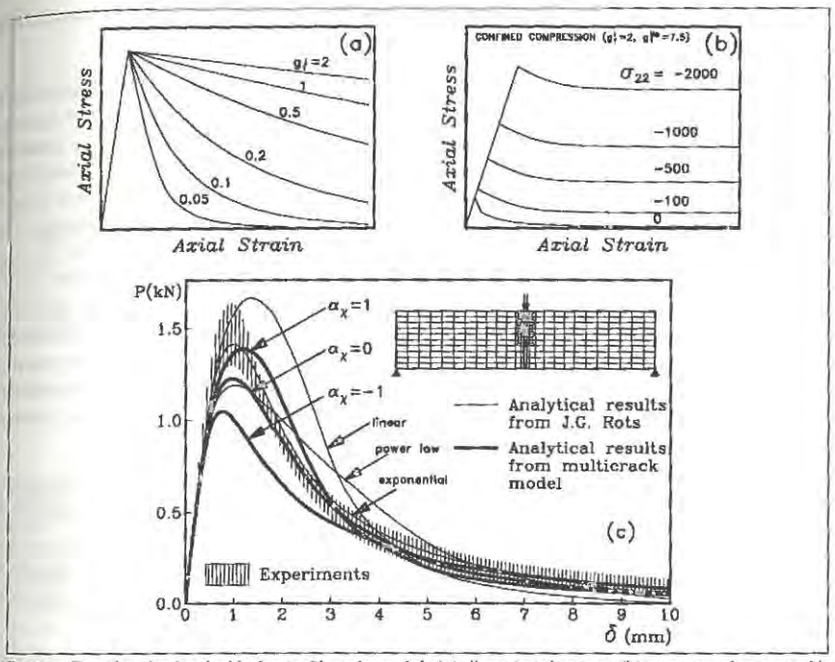

Fig. 4 — Results obtained with the multicrack model: (a) direct tension test; (b) compression test with lateral confinement; (c) finite element analysis of a three-point bending test [14]

resulting area surface under each one of the curves equals automatically the corresponding value of that parameter. The second example is a compression test with lateral confinement pressure. Two inclined cracks develop symmetrically with the inclination of about 30° on each side of the loading axis. The results for different values of the lateral pressure are represented in Fig. 4b. After the peak, the stress approaches asymptotically a final value that can be obtained from equilibrium considerations. The corner-shaped peak in the curves is due to the use of the elastic model for the continuum between the cracks. Finally, the model has been implemented in a finite element code and an example of a three-point bending beam has been analyzed. The fracture parameter g_f^I has been calculated from the experimental G_f and element size. The results obtained are shown in Fig. 4c together with experimental data [14] and numerical results from other authors [15].

CONCLUDING REMARKS

The basic idea of the microplane model, i.e. to define the basic material behavior on a plane of generic orientation and then accumulate the contributions over all possible orientations, is useful for developing new models that represent the behavior of materials undergoing damage and cracking. The new microplane damage tensor describes the geometric effects of distributed damage (microcracks). A kinematic micro–macro constraint is assumed, which corresponds to the preservation of material integrity. With the new damage tensor, the model can be combined with any existing model for the undamaged material in order to represent phenomena such as creep–damage interaction, etc. The multicrack model is intended to represent the effects of macrocracks in the context of a smeared–cracking finite element analysis of localized fracture. It is based on the static constraint, and only involves

the additional strain caused by cracks. It can be combined with any model representing the undamaged material between cracks.

The microplane model with kinematic constraint can also represent localized fracture (a crack). For the case of a pure tensile fracture (no shear crack), fracture always occurs on various microplanes within a certain range of inclinations. This might be seen unrealistic if the finite elements are large although microscopically inclined microcracks always occur. As described, the new model with static constraint cannot model complex triaxial behavior for fracture under compressive stresses, but might model a localized crack band or crack more efficiently when the narrow crack band or crack is parallel to the mesh lines and fracture can occur on microplanes of only one direction. The fracture model on these microplanes must represent frictional interlock of crack forces and dilatancy and can be specified independently of the microplane laws with kinematic constraint, which gives additional flexibility. With the kinematic constraint, the crack friction and dilatancy need not be represented by the microplane law because they are taken into account by the resistance and cracking of inclined microplanes [16], but then the shear resistance cannot be controlled independently of the opening fracture of the microplanes.

In contrast to the previous attempts at modelling of strain softening by microplanes with static constraint, this constraint is used here only for obtaining the cracking strain, while before [5] it was used for obtaining the total strains. This is the reason why previously the model turned out unstable in post-peak behavior, while the present model is stable. The kinematic constraint is not possible without calculating the total strain on the microplane level, including the elastic strain.

Acknowledgment. This paper was written during a sabatical leave of the first author at Northwestern University, funded by CIRIT (Generalitat de Catalunya, Barcelona, Spain). Financial support from research grant PB90-0598 funded by CICYT (Madrid, Spain), and from AFOSR grant 91-0141 to Northwestern University, is gratefully acknowledged.

REFERENCES

[1] G.I. Taylor (1938). *J Inst Metals* 62, 307–324.
[2] S.B. Batdorf, B. Budianski (1949). *National Advisory Committee for Aeronautics (N.A.C.A)*, Technical Note No.1871, Washington DC.
[3] O.C. Zienkiewicz, G.N. Pande (1977). *Int J Numer Anal Meth Geomech* 1, 219–247.
[4] G.N. Pande, K.G. Sharma (1983). *Int J Numer Anal Meth Geomech*, 7, 397–418.
[5] Z.P. Bažant, B.H. Oh (1983), in *Symp. on The Interaction of Non-Nuclear Munitions with Structures*, US Air Force Academy, Colorado, 49–55.
[6] Z.P. Bažant, P.C. Prat (1988). *J. of Eng. Mech* ASCE, 114(10), 1672–1702.
[7] I. Carol, Z.P. Bažant, P.C. Prat (1992). *Int. J. Sol. Struct.*, in press.
[8] I. Carol, Z.P. Bažant, P.C. Prat (1991). *J. Eng. Mech.* ASCE, 117(10), 2429–2448.
[9] J.G.M. van Mier (1984). Ph. D. dissertation, Univ. of Eindhoven, The Netherlands.
[10] Z.P. Bažant (1989). *Mathematical Modelling of Creep and Shrinkage of Concrete*. John Wiley.
[11] I. Carol, P.C. Prat (1990), in *Computer-aided analysis and design of concrete structures*, N. Bićanić and H. Mang (eds.), Pineridge Press (UK), vol.2, 919–930.
[12] I. Carol, P.C. Prat (1991), in *Fracture processes in brittle disordered materials*, J.G.M. van Mier et al. (eds.) Chapman & Hall.
[13] P.C. Prat, I. Carol, R. Gettu (1991), in *Mixed-Mode Fracture and Fatigue*, H.P. Rossmanith (ed.), Wien.
[14] H.A. Kormeling, H.W. Reinhardt (1983). Report 5–83–18, Stevin Lab., TU Delft, The Netherlands.
[15] J.G. Rots (1988). Ph.D. thesis at TU Delft, The Netherlands.
[16] Z.P. Bažant, P. Gambarova (1984). *J Struc Eng* ASCE, 110(9), 2015–2035.

MODELLING OF PROCESS ZONE FOR FRACTURE OF CONCRETE

B.K. RAGHUPRASAD and J.M. CHANDRA KISHEN
Department of Civil Engineering, Indian Institute of Science, Bangalore 560 012, India.

ABSTRACT

It is by now established that fracture of concrete is always preceded by microcracking in the so called process zone which is ahead of the crack tip. In this paper, the concrete in the process zone is modelled as it exists in reality, taking into consideration its heterogeneous nature. The specimen is modelled as a bi-phase material consisting of coarse aggregates and matrix. A tensile test specimen is analysed using FEM. The cracking of matrix as well as of the aggregates is assumed to follow softening law which is effected by applying a closing force after the stress reaches f_t, the limiting value of tensile stress. The results for three different configurations of coarse aggregates and matrix are compared with those available in the work of Bazant [1]. The results appear to be encouraging.

INTRODUCTION

By now, it has been quite well established that fracture of concrete follows laws of non-linear fracture mechanics rather than the elastic fracture mechanics. The main reason contributing to the above fact is the formation of microcrack zone ahead of the crack tip which is very familiarly called a process zone. The influence of the process zone on the non-linear fracture behaviour of plain concrete notched beam has been very well modelled by Hillerborg et al. [2] and has been called the Fictitious Crack Model, wherein an assumption that a crack closing force proportional to the crack opening acts following a linear softening law has been made. This of course, has been experimentally verified. But it still remains to be seen whether if the process zone is modelled as it exists in reality namely as a two-phase material consisting of aggregates and matrix, the results will still be more accurate and nearer to the actual behaviour. Towards this

end, there has been an attempt made by Bazant [3] in modelling fracture process zone as consisting of two-dimensional array of small circular penny shaped cracks at the initial stage of cracking and consisting of a two-dimensional array of small circular ligaments in the final stage. In the above paper, very interesting and useful results have been obtained regarding ligament tearing and the associated snapback instability. However, there has been an application of linear elastic fracture mechanics in analysing the effect of the penny-shaped cracks.

In the present paper, the same concept of modelling the uncracked ligament as a two-phase material has been followed with a slight deviation from the earlier approaches. The difference in the approach here is that as soon as the stress reaches a limiting value f_t in an element, the crack does not open out. A closing force is assumed to act and the crack opens out slowly as the value of closing force becomes zero.

DESCRIPTION OF THE MODEL

Geometrically similar tensile test specimens with depth, d = $3d_a$, where d_a = particle size (assumed constant throughout the specimen = 12 mm) and length L = 8d/3, where d = depth have been analysed. The specimens shown in Fig. 1 were subjected to prescribed longitudinal displacement at one end and restrained against displacements at the opposite end. Uniformly sized triangular plane stress elements were used.

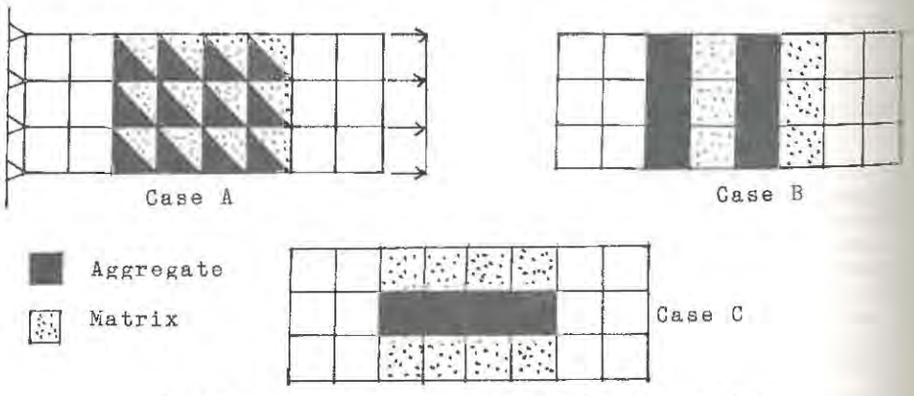

Figure 1. Aggregate matrix configurations

To obtain the applied load P and to prescribe the displacements, boundary spring elements were used. The material properties considered are shown in Table 1. To avoid the so called wall effect the elements at the fixed and displaced ends were considered to be of plain concrete.

TABLE 1
Material Properties

Property	Matrix	Aggregate	Concrete
Modulus of Elasticity (GPa)	30	180	40
Poisson's Ratio	0.15	0.25	0.20
Tensile Strength (MPa)	3	–	3

ANALYSIS

The specimen was subjected to a prescribed longitudinal displacement such that one of the elements reached a limiting value f_t of tensile stress. At this point, this element was removed and the nodes connecting this element was connected by a truss element. In all the cases considered, either a pair of internal elements reached f_t together as shown in fig. 2 or one end element reached the

Figure 2. Cracking patterns

limiting value. When a pair of internal elements reached f_t, these elements were removed and the nodes i and j were connected by a truss element. On the other hand, when an end element reached its limiting value, the element was removed and the nodes k and l was connected by a truss element. When the element reaches its limiting value, the crack does not open out completely. A closing force is considered to act and the crack opens out slowly. The maximum value of the closing force is taken to be equal to the stress times the area of cross section of the truss element. Again, here the area of cross-section of the truss element is arrived at by suitable iterations in such a way that when the closing force acts at the two nodes in opposite directions, the relative displacement between these two nodes tends to vanish. The analysis was carried out further with the closing forces decreasing by a constant value and by slowly incrementing the displacements. The load-displacement diagrams for the different cases considered are plotted as shown in fig. 3 and compared with those available in the work of Bazant [1]. The agreement appears to be good.

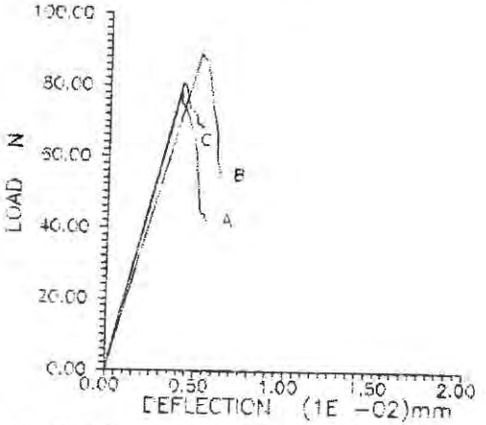

Figure 3. Load-deflection diagrams for Cases A,B,C

CONCLUSIONS

A simple heterogeneous model has been devised that exhibits a progressive loss in stiffness with increasing deformation. The behaviour of the model with different configurations of the two-phase material can be investigated solely by numerical computation. This approach is complementary to physical experimentation but has some important advantages.

The structure of the material with the cracking pattern can be examined at different stage of the loading process. The model can describe the post-peak declining load-deflection diagram which compares well with existing ones.

There are reservations which need further improvements in the use of the model. (1) The cross-sectional area of the truss members used to connect the nodes are not dependent on the distance between particles. (2) The closing force value is made to decrease by some arbitrary value.

REFERENCES

1. Bazant, Z.P., Mazen R. Tabbara, M.T. Kazemi, Giller Pijandier-Cabot, Random particle model for fracture of aggregate or fiber composites. Journal of Engineering Mechanics, 1990, 116, 8, 1686-1705.

2. Hillerborg, A., Modeer, M., and Petersson, P.E., Analysis of crack formation and crack growth in concrete by means of fracture mechanics and finite elements. Cement and Concrete Research, 1976, 6(6), 773-782.

3. Bazant, Z.P., Snapback instability at crack ligament tearing and its implication for fracture micromechanics. Cement and Concrete Research, 1987, 17(6), 951-967.

DAMAGE THEORY FOR CONCRETE BEAMS

B.K. RAGHUPRASAD and A GHOSH
Department of Civil Engineering, Indian Institute of Science, Bangalore 560 012, India.

ABSTRACT

Damage mechanics seems to offer parameters simpler in nature to represent more generally crack initiation, growth of microcracks and voids. With this in view, application of damage mechanics looks all the more relevant to concrete structures. An attempt is made to extend the concept of distributed damage theory to concrete elements with strain softening in tension considered.

INTRODUCTION

Since the early works of Kachanov [1] considerable progress has been made in applying damage mechanics to model the failure of structural elements. The concept of distributed defects in materials employed in structures not only leads to understanding of initiation of cracks but also of final fracture. The whole process could be considered as progressive deterioration (damage), which can be measured through loss of stiffness. The above ideas initiated the development of CDM by Janson and Hult [2] which was later applied to bending of beams by Krajcinovic [3].

It is by now well accepted that predictions of damage and failure of heterogenous material such as concrete and rock requires a mathematically correct and physically realistic description of the strain softening behaviour [4].

In the present paper, an effort is made to extend the model presented by Krajcinovic [3], incorporating the concept of strain softening.

ANALYSIS

Following Krajcinovic [3],as per the effective stress theory

$$\sigma = S\,(1-w) \qquad (1)$$

where, σ = nominal stress; S = effective stress = $E\varepsilon$

w = damage parameter; E = Young's modulus
ε = strain

$$w = \begin{cases} S/D \text{ for } S > 0 \\ 0 \text{ for } S \le 0 \end{cases} \quad (2)$$

D = damage modulus

E is known to remain constant in the prepeak region (of the σ-ε curve) and decrease in the post peak region. Thus the above relations are valid only in the pre peak region. In the post peak region, $S = E_n \varepsilon$, where E_n = effective modulus of elasticity as postulated by Loland [5].

There being insufficient experimental evidence regarding the variation of S in the post peak region, it is assumed that S decreases linearly at a rate equal to the softening modulus (E_T). Here it is worth elaborating about the variation of S. As S is defined as the load per unit effective area, after the peak, the load as well as the effective area decreases. Whether S decreases or increases in the post peak depends on whether load or the effective area decreases faster respectively. It is possible to express S as,

$$\text{Pre peak,} \quad S = E\varepsilon \quad (3)$$

$$\text{Post peak,} \quad S = E[\varepsilon_o(1+E^*)-E^*\varepsilon] \quad (4)$$

where $E^* = E_T/E$, ε_o = peak strain.

The variation of 'w' with 'ε' is assumed to be linear in both regions. An initial amount of damage is considered as w_i [5]. The value of w at failure is 1. Using these assumptions, we have:

$$\text{Prepeak,} \quad w = w_i + (w_o - w_i/\varepsilon_o)\varepsilon \quad (5)$$

$$\text{Postpeak,} \quad w = (\varepsilon-\varepsilon_o)(1-w_o)/(\varepsilon_u-\varepsilon_o)+w_o \quad (6)$$

where w_o is damage at strain ε_o and ε_u = ultimate strain (at zero post peak stress).
From eqns. (1), (3) and (5) and applying the condition that at $d\sigma/d\varepsilon = 0$; $\varepsilon = \varepsilon_o$, it is possible to show that

$$\text{Before peak,} \quad \sigma = S(1-S/D) \quad (7)$$

$$\text{After peak,} \quad \sigma = S(S/D) \quad (8)$$

Pure bending

The above model is now applied to a beam in pure bending, it is assumed that the cross sections remain plane after bending. The strain (ε_t) in the bottom fiber increases from zero to ε_o while S increases from 0 to S_o.
For $\varepsilon_b < \varepsilon_o$:

Resultant compressive force $N_c = 1/2\ b(h+y_o)S_c$ (9)

S_c = effective compressive stress at top fibre, S_t = effective tensile stress at bottom fibre, b = breadth of the beam's cross section, Y_o = distance of the neutral axis from the centroid of the section and 2h = depth of the section.

$$N_t = b \int_{Y_o}^{h} S(1-S/D) = 1/6(h-Y_o)b(3-2\,S_t/D)S_t \quad (10)$$

where, N_t = total tensile force.
Using eqn. of equilibrium, we get

$$1/2\ b(h+Y_o)S_c + b/6(h-Y_o)S_t(3-2S_t/D) = 0 \quad (11)$$

$$-2(h+Y_o)(2h-Y_o)S_t + (h-Y_o)[4h+2Y_o-S_t/D(3h+Y_o)]S_t = 12M/b \quad (12)$$

Also from the hypothesis of plane sections:

$$S_c = -(h+Y_o)/(h-Y_o)S_t \text{ (where, } S_t = E\,\varepsilon_t) \quad (13)$$

Thus with eqns. (11), (12) and (13) the beam problem can be solved.
Similar equations could be derived for $\varepsilon_b > \varepsilon_o$.

RESULTS AND CONCLUSIONS

Load-deflection curves were obtained from both models and were compared with existing experimental results (Figs. 1 and 2). Effective values of E and I have been taken as $I_{eff} = I(1-w_{av})$ (av = average over section) & $E_{eff} = E_{av}(1-w_{av})$ [6]. The value of D was taken as 3 x tensile strength of concrete, obtained by equating the tensile forces of present model and the linear σ-ε model. It is observed that the P_{max} values agree reasonably well with experimental values. The increasing effective stress concept gives higher values of

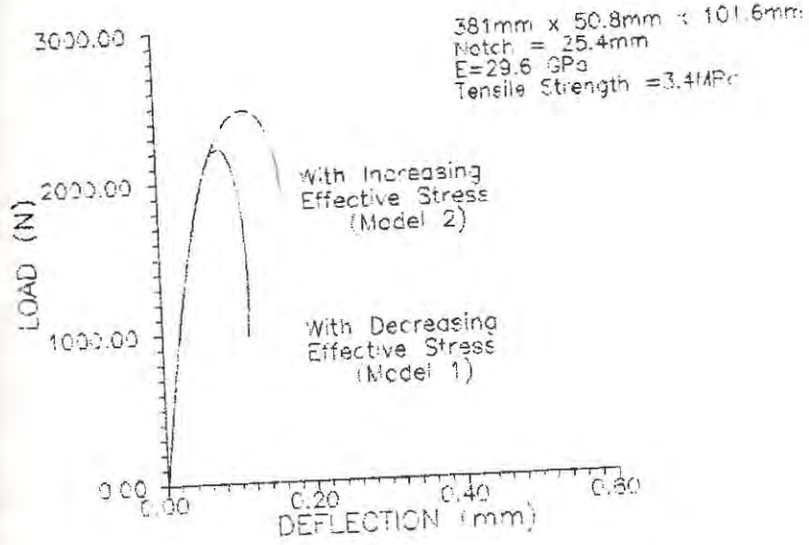

FIGURE 1 (Case 1)

P_{ult} (load at fracture of bottom fiber), while the decreasing stress concept gives closer values of P_{ult}. However, with both the concepts, the deflections are overestimated in one case while in another case they are very closely estimated.

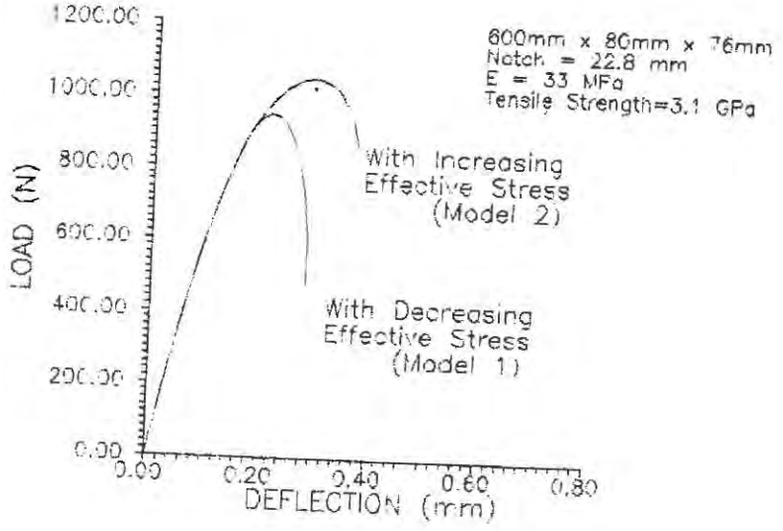

FIGURE 2 (Case 2)

REFERENCES

1. Kachanov, L.M., Time of the rupture process under creep conditions. Izv. Akad. SSR, Otd Tekh. Nauk 1958, 8, 23-31.

2. Janson, J., and Hult, J., Fracture mechanics and damage mechanics a combined approach. Journal de Mecanique Applique, 1977, 1, 68-84.

3. Krajcinovic, D., Distributed damage theory of beams in pure bending. Trans. ASME, Journal of Applied Mechanics, 1979, 4, 592-596.

4. Bazant, Z.P., Mechanics of distributed cracking, Applied Mechanics Review, 1986, 39, 5, 675-704.

5. Loland, K.I., Continuous damage model for load response estimation of concrete. Cement and Concrete Research, 1980, 10, 395-402.

6. Lemaitre, J., How to use damage mechanics. Nucl. Eng. Design, 1984, 80, 233-245.

NONLOCAL SMEARED CRACKING MODEL: CHARACTERISTIC LENGTH AND ENERGY DISSIPATION

FENG-BAO LIN AND ALFONSO WHU
Department of Civil and Environmental Engineering
Polytechnic University
Brooklyn, NY 11201

ABSTRACT

The tensile strength, the slope of the post-peak stress-strain curve, and the characteristic length are the three major parameters in the nonlocal smeared cracking model that affect its results in simulating concrete fracture behaviors. This paper is intended to give a systematic numerical study on the influence of characteristic length on energy dissipation. The purpose is to obtain the relationship among characteristic length, slope of the post-peak stress strain curve, and the energy dissipation as well as the relationship between characteristic length and the size of the fracture process zone.

INTRODUCTION

Many strain-softening damage models have been developed to predict the fracture behavior of quasi-brittle materials such as concrete which involves the simulation of the progressive growth of fracture process zones. When these models are applied to finite element analyses, problems associated with mesh-dependent results and zero energy dissipation at failure are encountered. Several approaches [2, 3, 4, 5, 6, 7, 8, 9, 10] have been proposed to prevent these problems. Among them, the nonlocal damage formulation proposed and developed by Bazant, Pijaudier-Cabot, and Lin [2, 4, 8] is an effective one. In this approach, the characteristic length is an important parameter that prevents the strain-softening damage from localizing into a zone

of one element width and thus to ensure the correct energy dissipation during the damage process.

The nonlocal smeared cracking model [2] is a particular example in applying the aforementioned nonlocal formulation to concrete fracture. In this model, the tensile strength, the slope of the post-peak stress-strain curve, and the characteristic length are the three major parameters that affect the softening behavior. It is essential to investigate the influence of the value of characteristic length on the amount of energy dissipation. The purpose of this study is to obtain the relationship among characteristic length, slope of the post-peak stress strain curve, energy dissipation, and the size of the fracture process zone.

CHARACTERISTIC LENGTH

The essential aspect of nonlocal damage formulation is that only those variables that cause damage should be considered as nonlocal [2, 4, 8]. Thus the damage ω in the nonlocal smeared cracking model is made nonlocal. This is accomplished by making strain ϵ_{11} nonlocal first because the damage ω is a function of ϵ_{11}. The nonlocal strain is defined as [2]:

$$\bar{\epsilon}_{11}(\mathbf{x}) = \frac{1}{V_r(\mathbf{x})}\int_V \alpha(\mathbf{s}-\mathbf{x})\langle\epsilon_{11}(\mathbf{s})\rangle dV = \int_V \alpha'(\mathbf{x},\mathbf{s})\langle\epsilon_{11}(\mathbf{s})\rangle dV \tag{1}$$

in which

$$V_r(\mathbf{x}) = \int_V \alpha(\mathbf{s}-\mathbf{x})dV, \quad \alpha'(\mathbf{x},\mathbf{s}) = \frac{\alpha(\mathbf{s}-\mathbf{x})}{V_r(\mathbf{x})} \tag{2}$$

The weighting function is chosen as the normal distribution function:

$$\alpha(\mathbf{x}) = e^{-(k|\mathbf{x}|/l)^2} \tag{3}$$

where κ is a constant whose value is 2 for two-dimensional cases, and l is the characteristic length of the material (Fig. 1).

The spatial averaging (nonlocal) of damage implies that

when damage occurs at a point, it spreads to some distance around the point rather than just at that particular location. This is a typical phenomenon observed in heterogeneous materials. The size of the spreading volume, which is defined by the characteristic length l, depends on the degree of heterogeneity of the material. In other words, the characteristic length measures the degree of heterogeneity of a material.

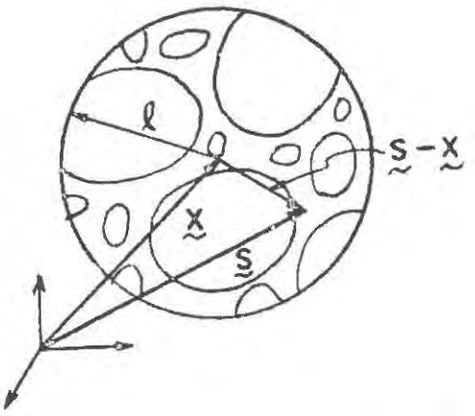

Figure 1. Characteristic length compared to aggregate size.

NUMERICAL STUDY

When a regular damage model is applied to a finite element analysis, it is found that damage happens always within a zone of one-element width with the surrounding elements unloaded. Because the energy dissipation per unit volume of the material under analysis is constant, different widths of the damage zone result in different energy dissipation during the fracture process. This unrealistic result can be prevented by using the nonlocal damage formulation.

In the nonlocal smearing cracking model, if the tensile strength and the slope of the post-peak stress-strain curve are kept constant, the size of the damage zone and the amount of energy dissipation are solely determined by the value of the characteristic length. To study the relationship among them, a three-point bending member with a notch at the midspan (Fig. 2)

is analyzed. Four-node quadrilateral isoparametric elements and step-by-step nonlinear iterations are used in the analysis. Various values of characteristic length are adopted in the analysis to obtain different damage zones and energy dissipation. The intent is to establish a quantitative relationship among those quantities. One of the damage zones obtained from the analysis is shown in Fig. 3.

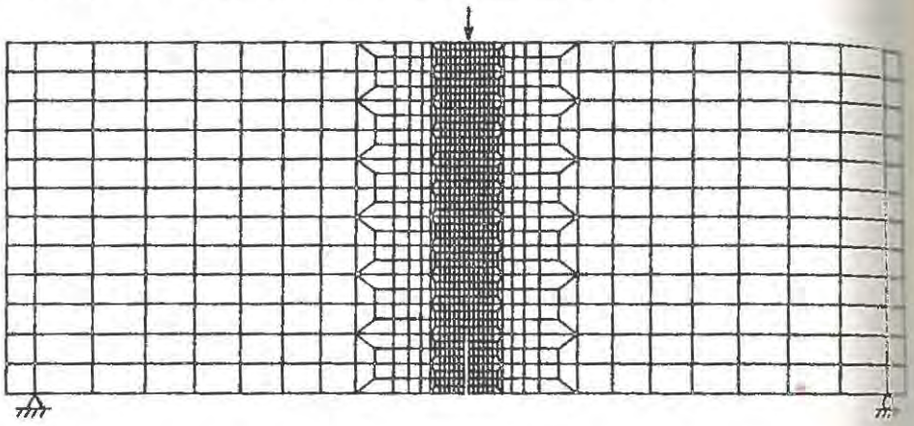

Figure 2. Finite element mesh used in the nonlocal analysis.

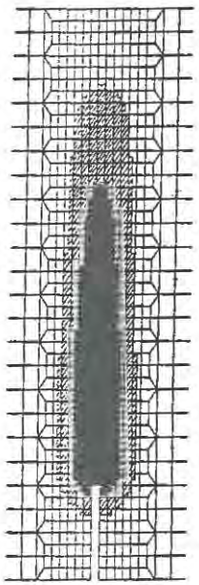

Figure 3. Damage zone (cross-hatched) and fracture zone (black).

Another study is on the influence of the slope of post-peak stress-strain curve on the energy dissipation when the characteristic length is kept constant. It is expected that from the results of this study the most suitable values of characteristic length and the slope of the post-peak stress-strain curve for the nonlocal smear cracking model can be decided when the fracture energy (obtained from experiments) or the maximum aggregate size of a concrete material is given.

REFERENCES

1. Bazant, Z. P. (1985), "Mechanics of Distributed Cracking," Applied Mechanics Reviews, ASME, Vol. 39. No. 5, pp. 675-705.

2. Bazant, Z. P., and Lin, F. B. (1988), "Nonlocal Smeared Cracking Model for Concrete Fracture," J. of Structural Engineering, ASCE, Vol. 114, No. 11, pp. 2493-2510.

3. Bazant, Z. P., and Oh, B. H. (1983), "Crack Band Theory for Fracture of Concrete," Materials and Structures, RILEM, Paris, France, Vol. 16, pp. 155-177.

4. Bazant, Z. P., and Pijaudier-Cabot, G. (1987), "Modeling of Distributed Damage by Nonlocal Continuum with Local Strain," Preprints, 4th intern. Conf. on Numerical Methods in Fracture Mechanic, Ed. by A. R. Luxmore, etc., held in San Antonio, Texas, March, pp. 411-432.

5. Hillerborg, A., Modeer, M., and Petersson, P. E. (1976), "Analysis of Crack Formation and Crack Growth in Concrete by Means of Fracture Mechanics and Finite Elements," Cement Concr. Res., 6(6), pp. 773-782.

6. Hillerborg, A. (1984), "Numerical Methods to Simulate Softening and Fracture of Concrete," Fracture Mechanics Applied to Concrete Structures, G. C. Sih, Ed., Martinus Jijhoff, The Hague.

7. Petersson, P. E. (1981), "Crack Growth and Development of Fracture Zones in Plain Concrete and Similar Materials," Report TVBM 1006, Lund Institute of Technology.

8. Pijaudier-Cabot, G. and Bazant, Z. P. (1987), "Nonlocal Damage Theory," J. Eng. Mech., ASCE, 113, pp. 1512-1533.

9. Pzietruszczak, S. T., and Mroz, Z. (1981), "Finite Element Analysis of Deformation of Strain-Softening Materials," Int. J. Numer. Methods Eng., No. 17, pp. 327-334.

10. Willam, K. J. (1984), "Experimental and computational aspects of concrete fracture," Intern. Conf. on

Computer-Aided Anlys. and Dsgn. of Concr. Struct., Split, Yugoslavia, Sep. 17-21, pp 33-69.

Chapter 3

Numerical Analysis of Concrete Fracture

Invited Paper

MESH ADAPTIVITY IN TRANSIENT FINITE ELEMENT ANALYSIS WITH A NONLOCAL MODEL

Antonio HUERTA[1], Gilles PIJAUDIER-CABOT[2] and Laurent BODE[2]

[1]ETS Ingenieros de Caminos, Dpto. de Matematica Aplicada III, Universitat Politecnica de Catalunya, Barcelona 08034, SPAIN.

[2]Laboratoire de Mécanique et Technologie, ENS Cachan / CNRS / Université P. et M. Curie, GRECO Géomatériaux, 61 Avenue du Président Wilson 94235 Cachan Cedex, FRANCE.

Abstract : Nonlocal models guaranty that finite element computations on strain softening materials up to failure remain sound from a theoretical and computational viewpoint. The nonlocality prevents strain localization in the form of a surface of discontinuity on which the global dissipation is zero, and thus finite element calculations converge upon mesh refinements more easily. One of the major drawback of these models is that the element size needed in order to capture correctly the localization zone is roughly of the order of the characteristic length. In practice, and if the location of the failure zone is not known a priori (or if the failure zone propagate), the total number of degree of freedom becomes rapidly prohibitive for most engineering applications and there is an obvious need for mesh adaptivity. After having recalled the principal theoretical properties attached to wave propagation in a nonlocal medium, i. e. wave dispersion, we apply in this paper the ALE description to transient dynamics in a nonlocal damageable material. Compared to other techniques the ALE description is better suited for this application and quite simple to implement since the mesh connectivity remains fixed. A general remeshing strategy is proposed based on an error which quantifies the jump of damage from one element to the next one. A one-dimensional example illustrates the capabilities of this technique.

1. INTRODUCTION

Nonlocal models are especially designed to handle the problem of progressive fracture and localization in strain softening materials. It has been demonstrated in statics that the spatial averaging of the variable that controls strain softening, or its differential equivalent in the form of gradient terms, prevents discontinuities of the rate of strain field [1], and thus prevents localization instability as studied classically by Rudnicki and Rice and others [2, 3]. Recently, it was also proved that the problem of localization in statics reduces to a bifurcation problem that can be cast in the same format as the localization analysis in a local continuum except that the number of possible solutions at the bifurcation point is finite and that the wave lengths of the localization modes are proportional to the characteristic length of the continuum [4, 5]. In this paper, we turn to transient analyses in such a nonlocal continuum. This type of problem finds its applications in the design and verification of concrete and reinforced concrete structures subjected to impacts loads or explosions for which the response of the structure up to failure is required. Before reaching the applications, there are a number of theoretical and computational problems that ought to be treated: First, it is necessary to investigate well

posedness of the problem in dynamics. In the first part of the paper; we recall briefly the main properties of the nonlocal continuum especially that wave propagation is dispersive.
In itself, the finite element implementation of the nonlocal damage model used in the present study is not a problem. It has already been described in 1987 by Pijaudier-Cabot and Bazant [6]. In practical engineering applications, there is however an acute need for interpolating the spatial variables with the lowest possible number of unknowns. Although the nonlocal model is designed to regularize the displacement field, the width of the localization zones remain of the order of magnitude of the characteristic length, which is a few aggregate diameters for concrete. If the localization zone is not known a priori, the number of degrees of freedom in a usual fixed mesh becomes totally prohibitive. Adaptive refinement, based in reducing the element size on the localization band are effective in steady state analyses, but they need to modify the mesh connectivity at each iteration and the elaboration of sophisticated algorithms in order to preclude an increase of the number of finite elements. We apply here another generalized spatial interpolation technique: the Arbitrary Lagrangian-Eulerian (ALE) formulation which is now well established in fluid mechanics and was recently extended to solid mechanics. This technique presents the advantage of keeping the number of degrees of freedom constant with the same connectivity.

2. WAVE PROPAGATION IN A NONLOCAL CONTINUUM

We use in this study the scalar continuous damage model proposed in Ref. 6. The constitutive relations read

$$\sigma_{ij} = C_{ijkl}(1 - D)\,\varepsilon_{kl} \tag{1}$$

in which σ_{ij} and ε_{ij} are the i,j (i,j $\in$ [1, 3]) components of the stress and strain tensors respectively, D is the damage variable and C_{ijkl} are the initial material moduli. If the initial equilibrium state is given by the stress σ^0_{ij} and the corresponding strain ε^0_{ij} along with the value of damage denoted as D^0, the rate constitutive relations are written as :

$$\dot{\sigma}_{ij} = (1 - D^0)\,C_{ijkl}\,\dot{\varepsilon}_{kl} - \dot{D}C_{ijkl}\,\varepsilon^0_{kl} \tag{2}$$

with the growth of damage defined as :

$$f(\bar{Y}) = \bar{Y} - \kappa$$

$$\begin{cases} \text{if } f(\bar{Y}) = 0 \text{ and } \dot{f}(\bar{Y}) = 0 \text{ then } \dot{D}(x) = \dfrac{\partial F(\bar{Y})}{\partial \bar{Y}}\,\dot{\bar{Y}}(x) \\ \text{if } f(\bar{Y}) < 0 \text{ or if } f(\bar{Y}) = 0 \text{ and } \dot{f}(\bar{Y}) < 0 \text{ then } \dot{D}(x) = 0 \end{cases} \tag{3}$$

In Eq. 3, F is the evolution law for damage, $f(\bar{Y})$ is the damage loading function, κ is the maximum between the quantity $\bar{Y}$ ever reached at the considered point of the solid during the loading history, and a damage threshold Y_0. $\bar{Y}$ is the average energy release due to damage :

$$\bar{Y}(x) = \frac{1}{V_r(x)} \int_\Omega \psi(s) Y(x + s)\, ds \tag{4}$$

$$Y(x) = \frac{1}{2}\,\varepsilon_{kl}\,C_{ijkl}\,\varepsilon_{ij} \tag{5}$$

Ψ is the weight function (Gaussian function) and Vr (x) is the representative volume at point x:

$$V_r(x) = \int_\Omega \psi(s - x)\, ds \tag{6}$$

$$\psi(s - x) = \exp(-|s - x|^2/2\ell_c^2)$$

ℓ_c is the characteristic length of the material . The evolution law for damage is taken as $F(\bar{Y}) = 1 - (1 + b_1(\bar{Y} - Y_0) + b_2(\bar{Y} - Y_0)^2)^{-1}$ with $b_1 = 605\ MPa^{-1}$, $b_2 = 5.423\ 10^4\ MPa^{-2}$ and $Y_0 = 60\ 10^{-6}$ MPa. The integral term in the rate constitutive relations is:

$$\dot{D}(x) = \frac{\partial F(\bar{Y})}{\partial \bar{Y}}\,\dot{\bar{Y}}(x) = \frac{\partial F(\bar{Y})}{\partial \bar{Y}}\,\frac{1}{V_r(x)} \int_\Omega \psi(s)\,C_{ijkl}\,\varepsilon^0_{ij}(x + s)\dot{\varepsilon}_{kl}(x + s)\, ds \tag{7}$$

In order to decide whether the problem of wave propagation is well posed or not, we need to study the conditions of possible propagation and in particular how the wave velocity varies in the softening regime. Such an analysis cannot be performed in a closed form if the problem is nonlinear. In the following, the linearization of the equations of motion is performed about an initially homogeneous steady state of deformation and damage (assumption 1). Furthermore, the nonlinearity due to the loading conditions (Eq. 3) is removed under the assumption that all the solid remains in the softening regime (linear comparison solid, assumption 2). Using the first assumption, the equation of motion becomes:

$$\dot{\sigma}_{ij,\,j} = \rho\,\frac{\partial^2 \dot{u}_i}{\partial t^2} \tag{8}$$

where ρ is the mass density, u_i is the i^{th} component of the displacement field. The second assumption is used in order to substitute in the equation of motion the linearized rate constitutive equations (Eq. 2) in which the rate of damage growth is given by Eq. 7.
The velocity field solution of the previous equation is expressed, without loss of generality, as:

$$\dot{u}_m = A_m \exp(-i\zeta(n_k x_k - ct)) \tag{9}$$

where ζ is the wave number, $\underset{\sim}{n}$ he wave propagation direction, A_m the amplitude, and c the wave celerity. Substitution of this velocity field and the rate constitutive equations into the equations of motion yields an eigenvalue problem (see Refs. [4,7]). In the particular case of a one dimensional bar (see also [8]) the resolution of the eigenvalue problem yields the expression of the admissible wave celerities, namely

$$c = c_o \sqrt{(1 - D^0) - E_o \varepsilon^{02}\,\frac{\partial F(\bar{Y})}{\partial \bar{Y}}\,\bar{\Psi}(\zeta)} \tag{10}$$

in which c_o is the initial wave velocity in the elastic medium and $\bar{\Psi}(\zeta)$ is the Fourier transform of Ψ , which is a function of the wave number. The main feature of this result is that wave propagation is dispersive. This is a classical result in nonlocal elasticity and it was observed also in the past with a gradient plasticity model [9]. Figure 1 shows the evolution of c normalized to the velocity of unloading waves as a function of the wave number normalized to the characteristic length. Several initial states of strain have been considered - before and after the strain at the peak stress denoted as ε^*. Before the peak stress all the waves can propagate. After the peak stress, short wave modes can propagate only. Thus, it is expected that the damage front in a bar can propagate even during softening.

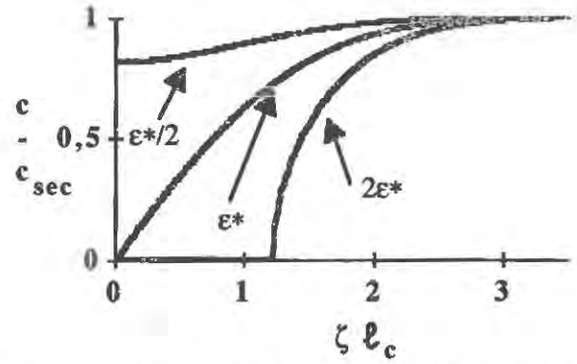

Fig. 1 Wave velocity as a function of the wave number and of the initial steady state of deformation.

It can be concluded from this analysis that the wave problem remains well posed for this nonlocal continuum. In view of computational applications, this is quite important since upon mesh refinement, strain will not localize into a single element. This implies that the nonlocal model will preclude mesh dependency for small enough elements; and moreover, the finite element model should have good convergence properties with no need for "zero" size elements to capture strain discontinuities.

3. ARBITRARY LAGRANGIAN-EULERIAN FORMULATION

In view of the previous conclusions, there is a need for remeshing capabilities for the analysis of real size structures. Among all the adaptive remeshing procedures available today, we have chosen the arbitrary Lagrangian-Eulerian (ALE) formulation [10], because it maintains the total number of the degrees of freedom as well as the mesh connectivity, it is automatically generalizable to higher spatial dimensions, and finally because the remeshing itself is embedded in the equations of motion.

Because of the shortcomings of purely Lagrangian and Eulerian descriptions, respectively element entanglement under large material distorsions and numerical difficulties for mapping material surfaces, among others, arbitrary Lagrangian-Eulerian techniques were developed. This formulation is already well established in the hydrodynamics and fluid structure interaction fields. Moreover, recent extensions to nonlinear continuum in transient analysis [13, 14] have increased the field of applicability of the technique.

The ALE approach is based on the arbitrary movement of the reference frame which is continuously rezoned in order to allow a precise description of the moving interface and to maintain the element shape. It is, therefore, concerned with the kinematic description, i.e., the relationship between the moving media and the computational grid. Following the notations of the previously cited references, the material region is denoted R_X and it is related to the particles or material points X, while R_x and x denote the spatial region, i.e. the laboratory configuration and coordinates. They represent the configurations of the body at the initial and current time t respectively.

The purpose of the kinematics is to define a simple procedure which relates material time derivatives and spatial derivatives. Spatial derivatives should appear because for simplicity the fundamental equations of motion are expressed in the spatial domain. On the other hand, both material and spatial domains are generally in motion with the reference R_χ which remains fixed throughout this formulation. Consequently, it is convenient to express the time derivatives in a referential form. This fundamental equation in ALE originally devised by Hughes [15], is:

$$\frac{\partial f}{\partial t}\Big|_X = \frac{\partial f}{\partial t}\Big|_\chi + c_i^* \frac{\partial f}{\partial x_i} \tag{11}$$

where f is given a physical property, and c* is the convective velocity defined as:

$$c^* = v - \hat{v} \quad \text{or} \quad c^*_i = w_j \frac{\partial xi}{\partial \chi_j} \tag{12}$$

In these equations, the following definitions are employed: v = material velocity, $\hat{v}$ = mesh velocity, and w = velocity of the material points in the referential domain, respectively:

$$v_i = \frac{\partial xi}{\partial t}\Big|_X ; \qquad \hat{v}_i = \frac{\partial xi}{\partial t}\Big|_\chi ; \quad w_i = \frac{\partial \chi_i}{\partial t}\Big|_X \tag{13}$$

Notice that the mesh velocity (or convective velocity) is arbitrarily chosen in order to optimize the spatial discretization, in the next section, a more detailed discussion on this procedure is presented. Once the kinematics are defined, the conservation of momentum that governs the motion of the continuum is written in the ALE description as:

$$\rho \frac{\partial v_i}{\partial t}\Big|_\chi + \rho\, c^*_i \frac{\partial v_i}{\partial x_j}\Big|_t = \frac{\partial \sigma_{ij}}{\partial x_j} \tag{14}$$

in which ρ is the mass density and no body forces are included.This equation is standard except for the convective terms which, on the other hand are standard in Eulerian problems. The ALE form of the constitutive equations for path-dependent materials is presented in [13,14], and it is simply:

$$\frac{\partial \sigma_{ij}}{\partial t}\Big|_\chi + c^*_k \frac{\partial \sigma_{ij}}{\partial x_k} = \alpha_{ij}\,(\rho, v, \sigma) \tag{15}$$

for a class of rate type constitutive relations. In Eqs. 14, 15 we can observe that the mesh motion is included in the governing equations which is not the case for standard remeshing techniques.

In order to evaluate the stress state at any material point Eq. 15 must be integrated. This is performed readily in the Lagrangian formulation by means of any time integration scheme because quadrature points at which stresses are evaluated coincide with the same material point throughout the computation. On the other hand, in the ALE formulation, a quadrature point corresponds at each time step to a different material point with a different loading history. It is very important to notice that Eq. 15 is in fact a scalar equation for each stress component, moreover any state variable which are needed have an evolution equation similar to Eq. 15. Therefore, the difficulty of implementing the ALE formulation is concerned here with the accurate time integration scheme for

$$\frac{\partial \tau}{\partial t}\Big|_\chi + c^*_k \frac{\partial \tau}{\partial x_k} = q \tag{16}$$

where q is a general nonlinear source term which depends on the state variables of the material. After several attempts to solve this problem in the context of fast transient dynamics and explicit finite element codes, stress update algorithms have been proposed [14] which appear to be well adapted to sharp wave problems. In the present application, the complexity is, however, tremendously reduced by the fact that the constitutive relations are given in an integrated form with respect to time.

4. REMESHING STRATEGY

The ALE description allows nodal points of the mesh to move arbitrarily in the Lagrangian coordinate system. The relative velocity field must be chosen now so as to optimize the mesh at each time step. In the present problem, we are interested in obtaining the best possible description of the damage localization zone which is characterized by propagating damage fronts as shown by the analytical study in §2. Therefore, we will assume that the optimum

mesh must be rather fine in the neighborhood of sharp variations of damage and coarse elsewhere. In order to use a remeshing procedure, we need to define a measure which quantifies the need for a finer or coarser grid at each point of the solid. This quantity denoted as K is defined here at each nodal point between elements k and k+1 as a function of the absolute value of the jump of damage across these elements:

$$K = a\,|[D]| + b \quad \text{with} \quad |[D]| = |D_{k+1} - D_k| \tag{17}$$

Constant b is set equal to one in order to avoid numerical difficulties when the error is equal to zero and constant a controls the amount of elements to be placed in the the region where K varies sharply as we will see further. The new positions of the nodal points are obtained from the solution of Eq. 18 which states that the flux of error must be kept constant at each point. In the one dimensional problem, we obtain the equation:

$$\frac{\partial}{\partial \chi}\left(K(x)\frac{\partial x}{\partial \chi}\right) = 0 \tag{18}$$

Note that the points at the boundary of the mesh are constrained to remain fixed. This equation which is similar to that solved in conduction problems can be conveniently generalized to 2D and 3D problems. If we call r_{max} the ratio of the maximum (Δx max) to the minimum length (Δx min) of the elements throughout the mesh, we obtain also after substitution in Eq. 17 :

$$r_{max} = \frac{\Delta x\ max}{\Delta x\ min} = \frac{K\ max}{K\ min} \tag{19}$$

Since D assumes values between 0 and 1, the maximum possible error is (a+b) and the minimum possible error is b. Thus the ratio r_{max} is bounded:

$$r_{max} \le \frac{a+b}{b} = 1 + \frac{a}{b} \tag{20}$$

and constant a controls the ratio of the minimum possible size to the maximum possible size of the finite elements in the mesh. Eq. 18 is a nonlinear elliptic partial differential equation which is solved iteratively. In practice, the number of iteration remains quite limited.

5. APPLICATION

In order to illustrate the capabilities of this computational method, we consider the well known problem of the interference of two constant strain waves propagating toward each other. The bar has a length 2L = 40mm and a cross section A = 1mm^2. The characteristic length of the material is 1 mm:

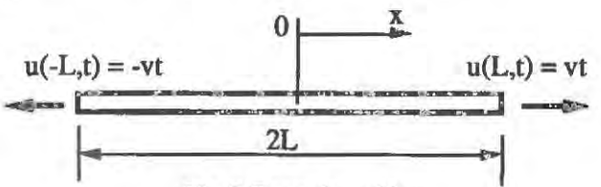

Fig. 2 Example problem

The velocity of the extremities of the bar is such that constant strain wave of amplitude 0.75e* propagate toward each other. They meet at the time t* and localization occurs in the middle of the bar.
Figure 3 shows the various damage profiles at different time steps obtained for a fixed mesh of 199 elements of constant length.We see that damage grows in a region located at the center of the bar and that the damage front propagate toward the extremities of the bar. The convergence of the finite element calculation with mesh refinement has been demonstrated on numerous occasions (see e.g. Ref. 6). The calculation has been performed here with a

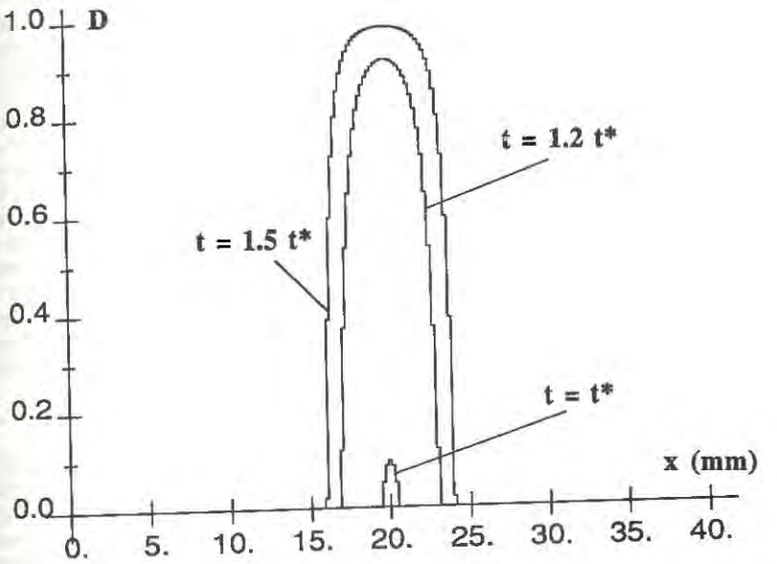

Fig. 3: Reference solution : evolution of the distribution of damage at different time steps

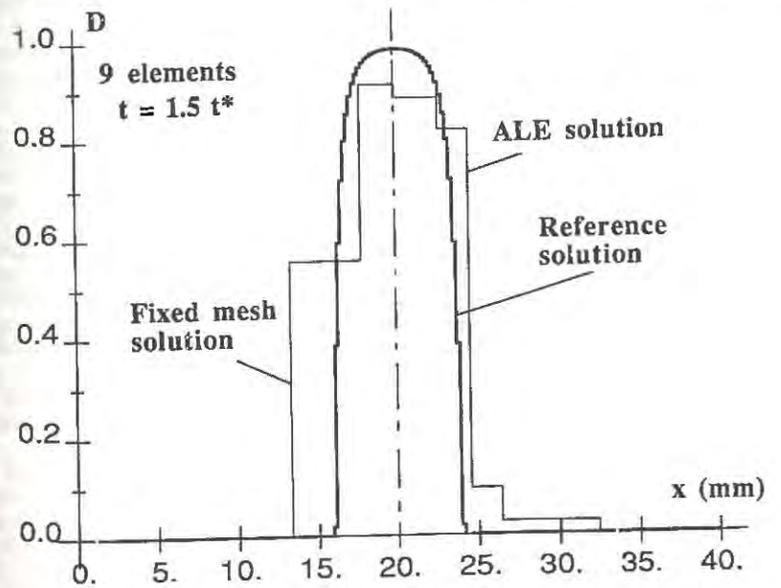

Fig. 4: Comparison of the ALE and fixed mesh solution with the reference solution at time t = 1.5t* (profiles of damage).

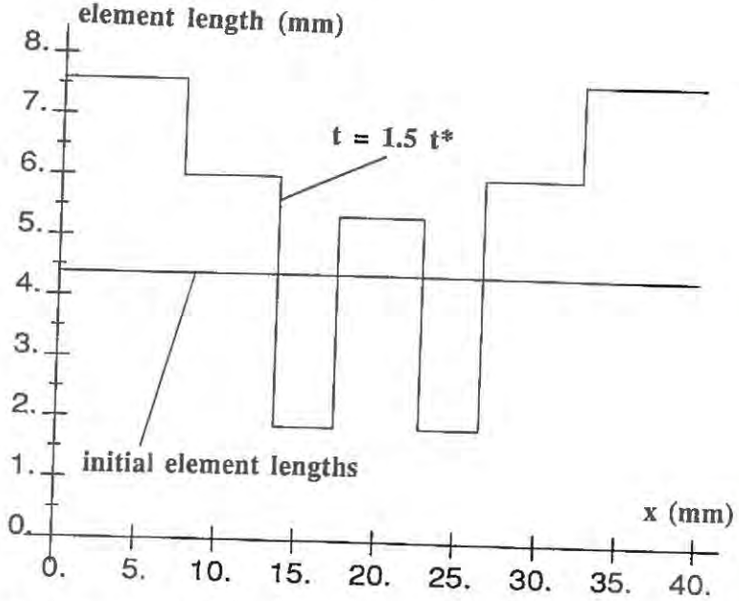

Fig. 5: Distribution of the element length throughout the mesh in the ALE solution at time t = 1.5t*.

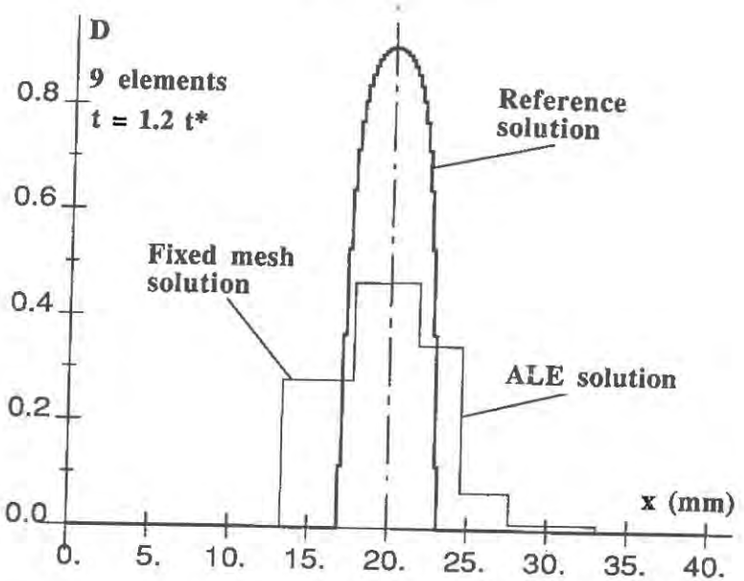

Fig. 6: Comparison of the ALE and fixed mesh solution with the reference solution at time t = 1.2t* (profiles of damage).

sufficient number of elements, therefore we will consider these results as a "reference solution" against which the ALE solution can be compared.
Figure 4 shows the profiles obtained from the ALE solution (a = 9) and a fixed mesh solution at time step 1.5t*. 9 elements of initially constant length were used for this computation. Compared to the reference solution, the approximation with a fixed mesh of 9 elements is poor but the ALE solution is quite close to the reference one. Figure 5 presents at the same time step the variation of element length throughout the mesh. The size of the elements has been divided by two near the damage front and accordingly it is multiplied by two outside the damage zone. The major drawback of the present remeshing strategy is that nodal points remain fixed if damage is constant. Upon a sudden variation of the damage field, that is at the inception of localization, The finite element mesh remain too coarse for a good approximation. This is exemplified on Fig. 6 which shows the profile of damage at the time step t = 1,2t*. This error is rapidly corrected during the next time steps. Another possibility would be to use an error which measure the discontinuity of the strain field. Such a strategy implies that remeshing starts at the beginning of the computation which is more time consuming.

5. REFERENCES

[1] Pijaudier-Cabot G. and Bodé L. (1991), Localization of Damage in a Nonlocal Continuum, Mech. Res. Communications, in press.
[2] Rudnicki J.W. and Rice J.R. (1980), A Note on Some Features of the Theory of Localization of deformations, Int. J. of Solids and Structures, 16, pp. 597-605.
[3] Benallal A., Billardon R., and Geymonat G. (1988), Some Mathematical Aspects of the Damage Softening Rate Problem, Cracking and Damage, J. Mazars et Z.P. Bazant Eds, Elsevier Pub., pp. 247-258.
[4] Pijaudier-Cabot G. and Benallal A. (1992), Strain Localization and Bifurcation in a Nonlocal Continuum, in preparation.
[5] de Borst R. and Muhlhaus H.B.(1991), "Continuum Models for Discontinuous Media", Fracture Processes in Concrete; Rock, and Ceramics, edited by J.G.M. Van Mier et al., E & FN Spon Pub., Vol. 2, pp. 601-618.
[6] Pijaudier-Cabot G. and Bazant Z.P. (1987), Nonlocal Damage Theory, J. of Engrg Mech. ASCE, 113, pp. 1512-1533.
[7] Pijaudier-Cabot G. and Huerta A. (1992), Wave Propagation in a Nonlocal Strain Softening Continuum, to be presented at the 9th ASCE Engrg. Mech. Specialty Conference, College Station, May 22-25.
[8] Pijaudier-Cabot G. and Bazant Z.P. (1992), Waves in a Nonlinear Elastic or Incremental Nonlocal Strain Softening Continuum, in preparation.
[9] Sluys L.J., de Borst R. and Muhlhaus H.B. (1991), Wave Propagation and Localization in a Gradient-Dependent Elastic-Plastic Solid, presented at the Int. Conf. Nonlinear Engrg Computations, Swansea, Sept. 16-20.
[10] Huerta A. and Liu W.K. (1988), Viscous Flow with Large Free Surface Motion, Comp. Meth. in Applied Mech. and Engrg., Vol. 69, pp. 277-324.
[11] Huerta A. and Liu W.K. (1989), ALE Formulation for Large Boundary Motion, Transactions of the 10th int. conf. on structural mech. in reactor technology, vol. B, pp 335-346.
[12] Zienkiewicz O.C. and Huang G.C. (1990), A Note on Localization Phenomena and Adaptive Finite Element Analysis in Forming Processes, Com. in Applied Num. Meth., Vol. 6, pp. 71-76.
[13] Huerta A., and Casadei F. (1992), New ALE Applications in Non-Linear Fast Transient Solid Dynamics, Engrg. Comput., (submitted).
[14] Huerta A., Casadei F. and Donéa J. (1992), Arbitrary Lagrangian Eulerian Formulation for Large Boundary Motion in Non Linear Continuum Mechanics", Report MA006/1991, ETS de Ingenieros de Caminos, Canales y Puertos, Universitat Politecnica de Catalunya.
[15] Hughes T.J.R., Liu W.K. and Zimmerman T.K. (1981), Lagrangian-Eulerian Finite Element Formulation for Incompressible Viscous Flows, Comp. Meth. App. Mech. and Engrg., Vol. 29, pp. 329-349.

Invited Paper

REMOVAL OF FINITE ELEMENTS IN STRAIN-SOFTENING ANALYSIS OF TENSILE FRACTURE

J.G. ROTS
Delft University of Technology / TNO Building and Construction Research,
P.O. Box 49, 2600 AA, Delft, The Netherlands

ABSTRACT

Many smeared crack models have difficulties in representing the final stage of separation after localized tensile fracture. The response will often be too stiff due to stress-locking. In this paper, it is shown that stress-locking can be avoided by removing heavily softened elements from the mesh. This creates a gap in the mesh such that the assumption of displacement continuity is lost and further rebuild of false stresses is avoided. Examples are given for mode-I fracture in concrete, showing correct stress relief at either side of the gap.

INTRODUCTION

Cracking in heterogeneous materials like concrete starts from various processes of internal damage, like micro-cracking and matrix-aggregate debonding. Upon further loading, micro-cracks and interfacial cracks bridge to finally form a geometrical discontinuity. Most existing smeared crack models have difficulties in correctly representing this final stage of mode-I separation. In many cases a too stiff response is found due to stress-locking [1], resulting from the assumption of displacement continuity, excessive shear stress transfer along the crack, false compressive strut action parallel to the crack and other reasons.

A possibility to overcome the above deficiency of the smeared approach is to remove finite elements from the mesh as soon as their tensile softening is completed. With this technique a blunt gap propagates through the mesh behind the micro-cracked zone, and the material at either side of the gap is allowed to fully relax (unload elastically) without any restraint from false element stiffness or continuity reasons. In the paper, methods are outlined that handle the unbalanced force due to element removal and the possible changes in topology. Three examples are included and a discussion is given in which also the parallels with isotropic softening models and micro-mechanics lattice models are drawn.

CRACK BAND MODEL

For the analyses in this paper a crack band model based on [2] has been used, embedded in a fixed smeared crack concept [1]. The crack band model aims at spreading the fracture zone

over the width h of a single element. This width has alternatively been called crack band width or characteristic length. The steepness of the softening branch is adjusted to h in order to release the correct amount of fracture energy G_f for creating the crack.

The length parameter h is related to the particular finite element configuration. The introduction of this parameter into the constitutive formulation can be seen as a first, coarse step towards a non-local model. Although non-local models [3] have been developed, it seems that these models call for a very fine element division, since at least one or more elements must be taken over the actual width of the fracture process zone which roughly equals three times the aggregate size. For engineering problems of large- and medium-scale structures, it is anticipated that crack band models will remain useful. Experiences [1] indicate that a reasonable choice for h is the square root of the element area for quadratic elements (six- and eight-node) and the square root of the element area times the square root of two for lower order elements (three- and four-node).

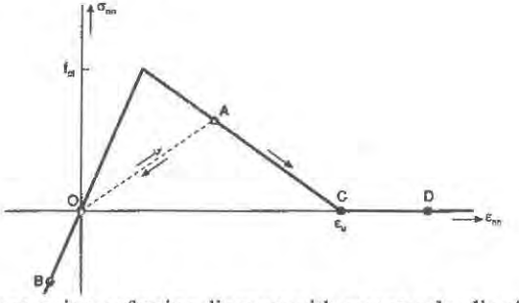

Fig. 1. Linear tension-softening diagram with secant unloading/reloading option.

REMOVAL OF ELEMENTS FROM THE MESH

When an element contains fully softened cracks, the assumption of displacement continuity in combination with residual shear stiffness and stiffness parallel to the crack, as is featuring in fixed as well as rotating smeared crack models, leads to a situation in which further straining in the localisation zone is no longer accompanied by continued unloading outside this zone. Instead, the stresses adjacent to the localisation zone tend to lock rather than to drop down to zero. To solve this problem, it has been suggested to remove elements from the mesh once their tensile softening is completed [1]. Also from experimental observations there is evidence to leave the assumption of displacement compatibility in the final stage, since a fully developed crack is identified as a geometrical *dis*continuity. The procedure is as follows:

a. At the end of a load step, a check is made on whether the fixed cracks in the integration points of an element have fully softened, i.e. have reached a strain beyond the ultimate strain ε_u of the softening diagram (in this paper a linear softening diagram will be considered, Fig. 1, such that $\varepsilon_u = 2G_f/(f_{ct}h)$ [2]).

b. If n or more than n integration points of an element have a fully softened crack, the element(s) is (are) removed from the mesh. If not, loading is continued in the usual manner. In this study $n=1$ was assumed for single-point integrated three-node elements, $n=2$ for four-point integrated four-node elements and $n=3$ for seven-point integrated six-node and nine-point integrated eight-node elements. However, different assumptions for n affected the results only slightly.

c. A new set of degrees of freedom is set-up. Strictly speaking, this is only necessary if element removal also leads to node removal, as occurs when higher-order elements are removed (Fig. 2a) or when a group of lower-order elements is removed (Fig. 2b). When only a single row of lower order elements is removed (Fig. 2c), the procedure becomes as simple as the initial topology can be preserved; in fact an equivalent situation to removal can then tried to be reached via regular iterations whereby all residual stress and stiffness components in the element are abruptly set to zero.
In the past, the need for changes in finite element topology has been considered as a major disadvantage and used as argument against e.g. discrete crack concepts with updates of the mesh. Nowadays, there is no longer any objection since even multi-purpose codes like DIANA offer facilities for changes in the topology during non-linear analysis, options initially developed for staged analysis of building processes [4].

d. Supports, tyings and the current external load vector are evaluated for the new mesh.

e. The new internal force vector is generated, based on the existing stresses in the remaining elements.

f. The unbalanced force (external minus internal) due to removal of the element(s) is eliminated via equilibrium iterations, as will be explained later.

g. New load steps are added and the process is repeated.

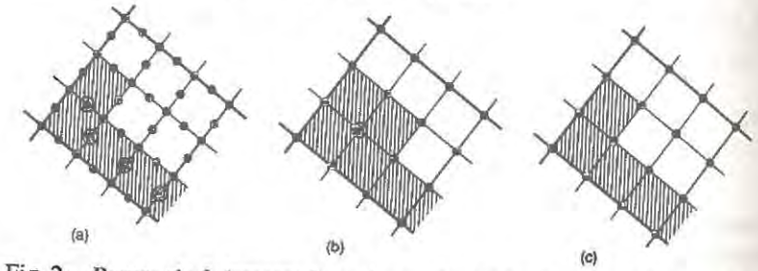

Fig. 2. Removal of elements from the mesh; (a) single row of eight-node elements, (b) group of four-node elements, (c) single row of four-node elements.

The method to get rid of the unbalanced force due to element removal plays a crucial role. Various procedures have been tested. First, equilibrium iterations were added to try and remove the entire unbalanced force in once. This must be done under load control or arc-length control. This method was not successful. Next, the unbalanced force was applied within several steps, in each of which equilibrium iterations were added. This method was partially successful, when only one element was removed at a time and when the element and its residual stresses were relatively small.

Although the wide range of arc-length schemes available has not yet been fully explored, a different procedure was followed in the final analyses reported in this paper. When the analysis indicates that an element or element(s) should be removed, the entire structure is unloaded, whereby a secant unloading branch in the tension-softening model is assumed according to path AOB in Fig. 1. In the unloaded stage, the element(s) is (are) removed and steps (c) to (f) are carried out. In the unloaded stage, the unbalanced force due to element removal will be almost zero and does not constitute a problem. Subsequently, the modified structure is reloaded whereby the fixed cracks are allowed to re-open in order to finally re-soften according to path BOACD in Fig. 1. The procedure requires the memory of the presence of cracks, their orientation and the maximum damage occurred (point A). It is possible with load control, arc-length control as well as displacement control.

EXAMPLE 1: SYMMETRIC NOTCHED BEAM

The first example is a four-point loaded symmetric notched beam which fails in mode-I fracture. The dimensions were taken according to experiments in [5]: span 450 mm, thickness 50 mm, height 100 mm, notch depth 10 mm. The distance between the symmetrically placed loading points is 150 mm. In order to illustrate the phenomena most clearly, a non-regular and non-symmetric mesh was adopted (Fig. 3), such that the fracture propagates through the mesh in a zig-zag manner as is typical for general fracture analysis. Four-point integrated four-node elements were used. The elastic parameters were taken as $E=38000\,\mathrm{N/mm^2}$, $\nu=0.2$ and the softening parameters as $f_{ct}=3.0\,\mathrm{N/mm^2}$, $G_f=60\,\mathrm{J/m^2}$ with a linear diagram.

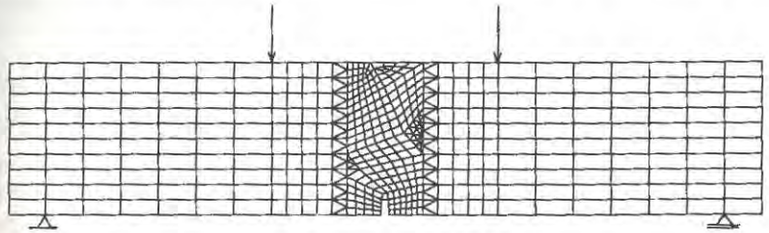

Fig. 3. Non-regular and non-symmetric mesh for symmetric notched beam.

First, two smeared crack analyses without element removal for shear retention factors $\beta=0.001$ and $\beta=0.05$ are compared with a reference analysis for a perfectly vertical predefined discrete crack in a regular mesh of the same fineness and with the same parameters. In a global sense, the problem involves pure mode-I with zero shear across the crack, as is represented by the discrete analysis. On a local level, however, the smeared analyses introduce shear effects and stress rotations in cracked elements because of the zig-zag path. The requirement is that such phenomena may not disturb the result. Consequently, the smeared results should match the discrete result. Fig. 4 shows that this is not achieved. Both smeared crack results are too stiff and show a false residual load plateau at 2.6 kN and 1.5 kN respectively, while the discrete crack analysis shows softening down to zero. For higher values of β, the effect becomes even worse and it also occurs when the rotating smeared crack concept is used [1]. The dramatic impact on the post-peak response is primarily due to stress-locking, Fig. 7a. (For the present problem the departure from the discrete result is larger than for the cases in [1]. Maybe, in addition to stress-locking other factors are important here, [6]).

Fig. 5. shows the effect of element removal. The analysis with $\beta=0.05$ was selected because it is most illustrative, but the same conclusions are reached for other values. The curve now correctly drops down after peak load, which is explained from the fact that false locked-in stresses have disappeared (Fig. 7b). Giving up the assumption of displacement continuity and removing any residual stiffness in the localisation zone obviously leads to correct relaxation of the two parts at either side of the separation. The stress relief in Fig. 7b is not yet perfect, as it is for the discrete crack result (Fig. 7c). This is attributed to imperfections in the crack closing/re-opening algorithm, whereby stress rotations in combination with

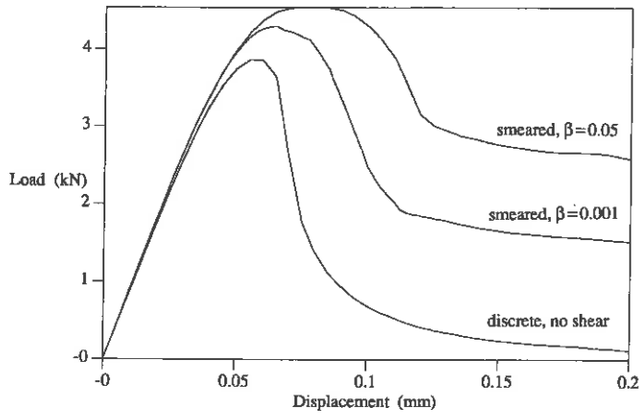

Fig. 4. Load F versus average loading point deflection for notched beam. Discrete and smeared analyses without element removal.

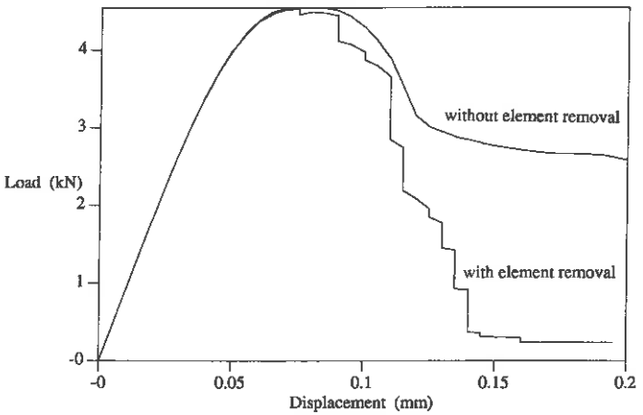

Fig. 5. Load F versus average loading point deflection for notched beam. Smeared analysis with and without element removal ($\beta=0.05$).

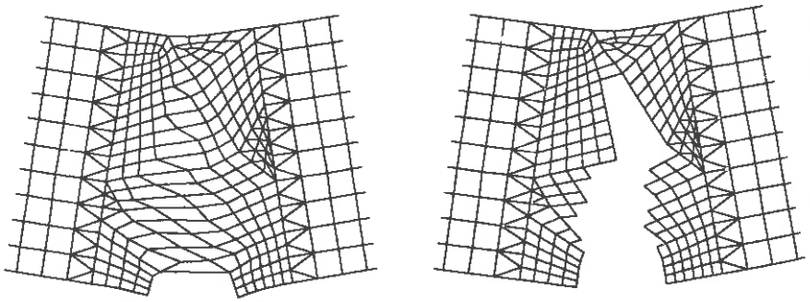

Fig. 6. Incremental displacements, corresponding to final stage in Fig. 5. (a) Smeared, without removal ($\beta=0.05$), (b) Smeared, with removal ($\beta=0.05$).

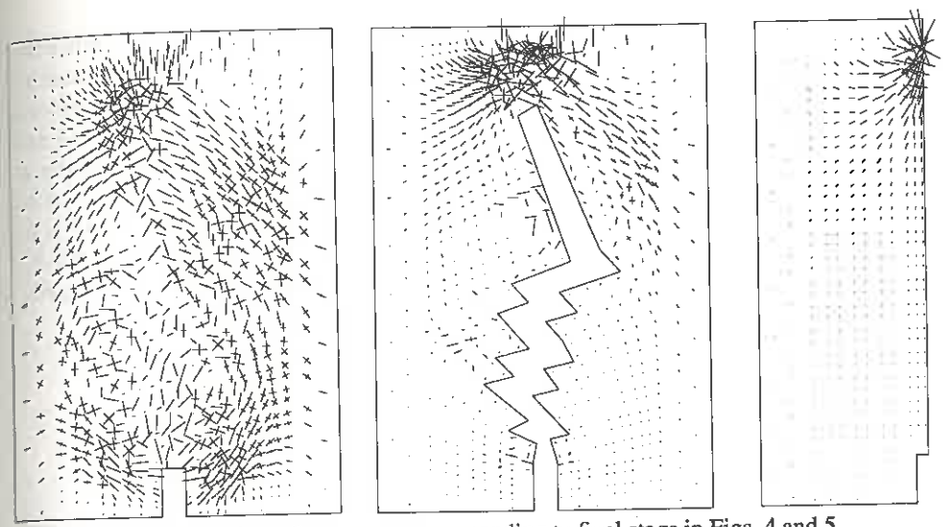

Fig. 7. Principal tensile stresses, corresponding to final stage in Figs. 4 and 5. (a) Smeared, without removal ($\beta=0.05$), (b) Smeared, with removal ($\beta=0.05$), (c) Discrete.

non-zero shear stiffness still left some (minor) residual stresses. In order to keep Fig. 5 clear, the unloading/reloading cycles for the analysis with element removal have been excluded from the plot, so that the drop of load due to element removal is indicated by a vertical line. The curve is discontinuous, but all solutions have converged. Fig. 6 shows the deformed meshes. In total, 19 elements have been removed in 12 stages, after which the analysis was terminated.

EXAMPLE 2: NON-SYMMETRIC NOTCHED BEAM

The second example is a non-symmetrically loaded single-notched shear beam which fails in curved mode-I fracture. Details of the way of modeling are given in e.g. [1]. The mesh of nine-point integrated eight-node elements is shown in Fig. 8. The mesh is too coarse to correctly predict the curved fracture path, but is sufficiently fine to illustrate the aspects intended here. The parameters were taken as $E=24800\,\mathrm{N/mm^2}$, $\nu=0.18$, $f_{ct}=2.8\,\mathrm{N/mm^2}$, $G_f=60\,\mathrm{J/m^2}$ with a linear diagram and $\beta=0.05$.

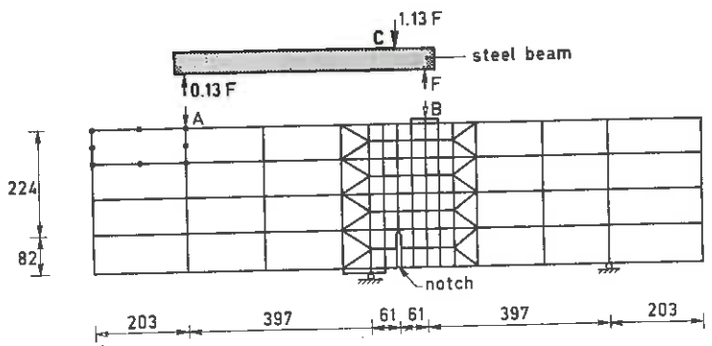

Fig. 8. Mesh for notched shear beam.

Fig. 9 shows the load F versus Crack Mouth Sliding Displacement for the analysis with and without element removal. Without element removal, a residual load plateau is found at about 55 kN, after which convergence could no longer be achieved because of spurious kinematic modes. With element removal, the load correctly drops down to zero which agrees with the discrete crack reference computation that has been presented in [1] (obtained for a finer mesh and slightly different parameters, therefore it has not been included in Fig. 9). The findings are fully in line with those of the previous example. Again, the explanation lies in the fact that false residual stresses near the localisation zone vanish when elements with fully softened tensile cracks are removed. This is evident from the stress plots of Fig. 11, corresponding to the displacement plots of Fig. 10.

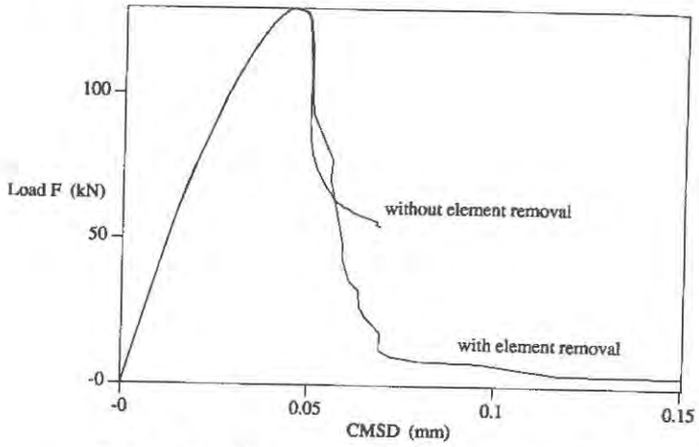

Fig. 9. Load F versus CMSD for notched shear beam.

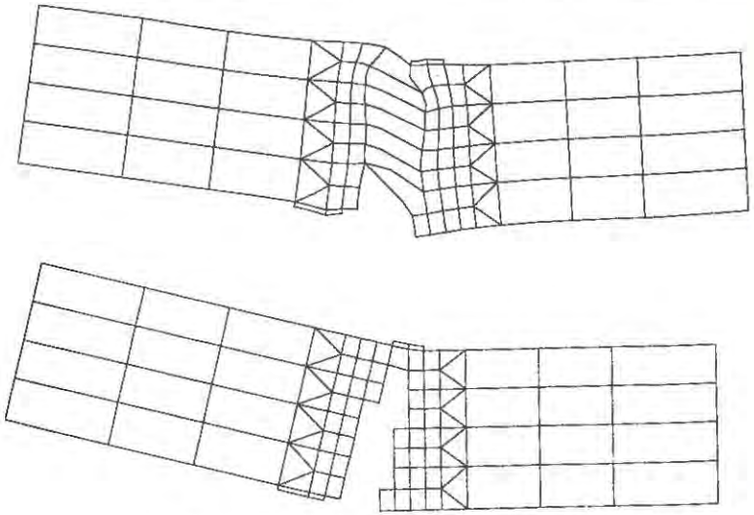

Fig. 10. Incremental displacements.
(a) Without element removal, (b) With element removal.

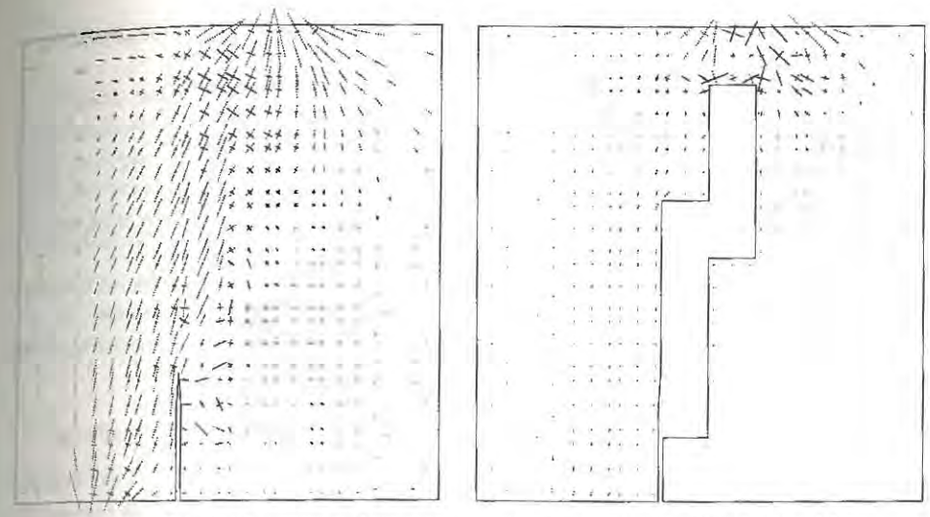

Fig. 11. Principal tensile and compressive stresses, corresponding to Fig. 10.
(a) Without element removal, (b) With element removal.

DISCUSSION AND CONCLUSIONS

The removal of cracked finite elements from the mesh improves smeared crack computations of localized tensile fracture. The initial assumption of displacement continuity is abandoned and the residual shear stiffness and lateral stiffness parallel to the crack, which are seen as the major contributors to stress-locking, are removed. This permits adjacent elements to fully relax, such that the loading/unloading process associated with fracture localisation is completed correctly. Further details and an additional example of a pull-out problem have been presented in [6].

The procedure is only applicable to localized fracture and/or relatively fine meshes. For global analysis of reinforced concrete structures, removal of the compression struts parallel to the cracks is at odds with the 'compression strut - and - reinforcement tie' philosophy, which forms the basic idea of reinforced concrete. This limitation also adheres to isotropic softening models in the context of damage mechanics or plasticity. Such models bear similarity with the present approach, since the residual shear and lateral stiffness also vanish, but gradually instead of abruptly. Recently, it was reported that isotropic damage models do not suffer from stress-locking and pose an attractive alternative to fixed and rotating smeared crack models [7]. This would be in line with the findings in the present paper. The example in [7], however, does not involve zig-zag fracture propagation, but propagation parallel to mesh lines so that stress-locking is likely to be less dominant. In preparing the present paper, the author has tried to solve the examples with isotropic softening plasticity. At first sight, stress-locking again occurred, but the computations suffered from the fact that the zero-normal-stress-condition for plane stress plasticity was not satisfied, which casts doubt on the correctness of the results. Further comparisons using isotropic softening models are intended to be presented at the conference.

Parallels also exist with micro-mechanics lattice models, e.g. [8]. Here, the heterogeneity of concrete is not modelled via a softening curve on continuum level, but directly, via statistical distributions of strength in extremely fine networks of beam (or truss) elements. Upon

adding load, the most critical beam (or truss) element is traced and subsequently removed, whereupon new load is added and the process is repeated [8].

Regarding spurious kinematic modes [9,10], the present approach is less critical than analyses without element removal. In fact, such was hinted at in [10]. However, when a quadratic element is removed, the mid-side node of the element ahead of the gap may start 'shaking', which temporarily hampers convergence. Problems with spurious modes and numerical stability are likely to increase upon using isotropic damage or plasticity models, since then the tangent stiffness is negative in all directions.

Further comparisons between smeared crack, damage, plasticity, removal, local, non-local, discrete, lattice and other models are required, since a recent round-robin [11] has shown that still unacceptable scatter occurs in results for localized fracture depending on the type of model adopted.

ACKNOWLEDGEMENTS

The research has been carried out using the DIANA finite element program of TNO Building and Construction Research. Financial support has been provided by the Royal Netherlands Academy of Sciences (KNAW) and by CUR Committee A30.

REFERENCES

1. Rots J.G., Computational modeling of concrete fracture. Dissertation, Delft Univ. of Techn., Dept. Civil Eng., 1988, 132 pp.
2. Bazant Z.P. and Oh B.H., Crack band theory for fracture of concrete. *RILEM Mat. & Struct.*, 1983, 16(93), 155-177.
3. Bazant Z.P., Belytschko T.B. and CHANG T.P., Continuum theory for strain-softening. *ASCE J. Eng. Mech.* 1984, 110, 1666-1692.
4. Visschedijk M.A.T., Phased analysis. DIANA User's Manual Vol. 9, Release 4.1, TNO Building and Construction Research, 1991.
5. Hordijk D.A., Local approach to fatigue of concrete. Dissertation, Delft Univ. of Techn., Dept. Civil Eng., 1991, 210 pp.
6. Rots J.G., Removal of finite elements in smeared crack analysis. In *Proc. Third Int. Conf. Computational Plasticity*, Pineridge Press, Swansea, april 1992.
7. Oliver J., Cervera M., Oller S, and Lubliner J., Isotropic damage models and smeared crack analysis of concrete. *Computer Aided Analysis and Design of Concrete Structures*, Eds. Bicanic N. and Mang H., Pineridge Press, Swansea, 1990, Part 2, 945-958.
8. Schlangen E. and Mier J.G.M. van, Boundary effects in mixed mode I and II fracture of concrete. *Fracture Processes in Concrete, Rock and Ceramics*, Eds. van Mier J.G.M., Rots J.G. and Bakker A., E & FN SPON / Chapman & Hall, 1991, Vol. 2, 705-716.
9. Borst R. de and Rots J.G., Occurrence of spurious mechanisms in computations of strain-softening solids. *Eng. Comp.* 1989, 6, 272-280.
10. Crisfield M.A., Difficulties with current numerical models for reinforced concrete and some tentative solutions. *Computer Aided Analysis and Design of Concrete Structures*, Eds. Damjanic F. et al., Pineridge Press, Swansea, 1984, Part 1, 245-260.
11. Elfgren L. (Ed.), Round-Robin analysis of anchor bolts. Preliminary report compiling various contributions, second draft, RILEM TC-90 FMA Fracture Mechanics of Concrete - Applications, Lulea Univ. of Techn., Sweden, 1991.

Invited Paper

SIMULATION OF ARBITRARY, COHESIVE CRACK PROPAGATION

T. N. BITTENCOURT[1], A. R. INGRAFFEA[1], J. LLORCA[2]
[1] Cornell Fracture Group, Cornell University, USA
[2] Department of Materials Science, Polytechnic University of Madrid, Spain

ABSTRACT

A new strategy for simulating the initiation and propagation of cohesive cracks is presented. The strategy is based on: interactive, effective crack length control; a criterion for propagation based on the fictitious crack tip opening profile; a local principal-stress-based criterion for direction of propagation; a dynamic relaxation solver for determining propagation length; automatic remeshing to accommodate arbitrary growth. In this new strategy, the user controls the simulation by indicating a crack growth increment in the predicted direction. The analysis proceeds to determine a load factor associated with this increment. Singular elements are not used at the fictitious crack tip. Rather, non-linear analyses are performed until a condition of zero-slope of the COD (crack opening displacement) at the tip is reached. The strategy is shown to be accurate and stable via a set of example problems which include Mode I with and without snap-back instability, and curvilinear propagation.

INTRODUCTION

In this paper an integrated strategy intended to simulate correctly and interactively the evolution of arbitrary, cohesive cracks is presented. The term 'integrated' emphasizes the first of two innovations described herein: fundamental capabilities for mesh and geometry representation, stress analysis, and non-linear fracture mechanics are combined in a single, engineering workstation-based system. In this context, the use of interactive computer graphics and sophisticated data structures to visualize and control geometry evolution is considered vital. This system is therefore both

useful and usable for applied research and solution of practical design and failure analysis problems involving the fracture of concrete.

The second innovation is the introduction of a crack stability criterion based on the fictitious crack-opening displacement (COD) profile. This criterion obviates the previous use of singular elements around the tip of the fictitious, cohesive crack. It also provides the most sensitive measure of convergence to simultaneous satisfaction of both global equilibrium and the local traction versus COD constitutive model for cohesive fracture.

First a brief literature overview will be presented. Then the integrated strategy will be described. Finally, two examples are presented to illustrate the accuracy and versatility of the strategy.

A STRATEGY FOR ARBITRARY, COHESIVE CRACK PROPAGATION

As noted by Shah [1], different known toughening mechanisms may be activated during crack propagation in ceramic materials: (a) surface energy dissipation, (b) microcracking, and (c) energy dissipation in the wake of the crack path, such as aggregate interlock and bridging. Depending on the assumption of the most important mechanism(s), different crack models have been proposed [2-8]. However, there is compelling evidence that the most important toughening mechanism in non-transforming ceramics at ambient temperature is energy dissipation in the crack wake [9-13]. The same can be stated for whisker- and fiber-reinforced ceramics [14-15], and other quasi-brittle material such as concrete, cement-based composites and rocks. In this case, a cohesive crack model (CCM) is usually employed to take into account the softening strain localization phenomenon. This model, proposed by Hillerborg *et al* [4,5] considers the energy dissipation in the wake of the crack path, while neglecting the other two toughening mechanisms. CCM is the state-of-the-art tool to analyze the fracture behavior of quasi-brittle materials, including concrete, cement-based composites, rocks, ceramics, and ceramic composites.

The applicability of CCM to general mixed-mode conditions has been the focus of recent attention. Throughout the 1980's, Ingraffea *et al* [16-21] have employed a strategy of singularity near-cancellation to handle mixed-mode crack evolution, with optional load or crack length control. Crack stability was controlled by iterating on the load or crack length until residual values of stress intensity factors were obtained at the tip of the fictitious crack. Direction of crack propagation was computed using these same

residual values. This criterion sometimes failed to predict accurately the critical load to produce crack extension because the singular elements at the crack tip perturbed the stress field in the cohesive zone. Moreover, use of these elements was inconsistent with the assumption of singularity cancellation inherent in the CCM.

Recently, an extension of the fictitious crack model to mixed mode propagation has been proposed by Bocca *et al* [8]. They employed a crack length control scheme with a stress-based crack stability criterion. The innovation in the present procedure is that stability is based on the most sensitive, and most easily computable, measure of conformance to the cohesive fracture constitutive model: the slope of the crack opening profile at the tip of the fictitious crack. The crack opening gradient must be zero at the tip for a purely cohesive fracture process.

The strategy which integrates this new criterion within a friendly and adaptable system is summarized in Figure 1. An important idea is to use self-complete modules for each of the basic elements of the system. The principle of modularity is crucial because it allows one to readily introduce new theoretical, numerical, or constitutive developments. The basic elements of this strategy are described next.

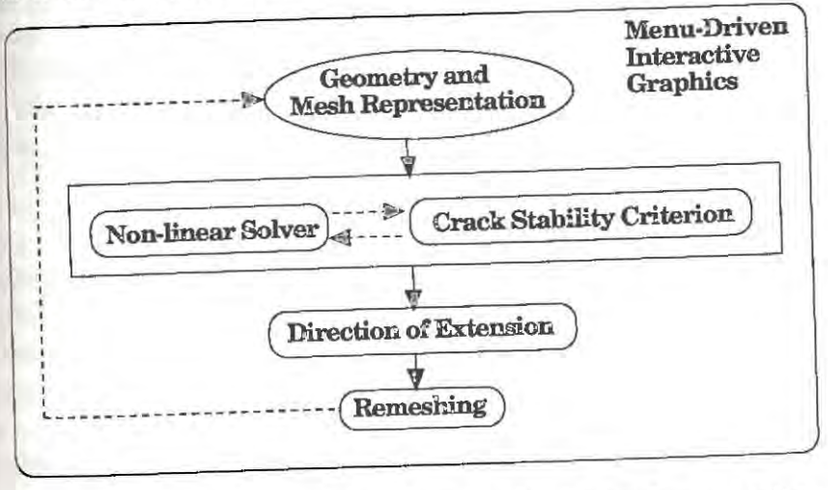

Figure 1 - Integrated strategy for arbitrary, cohesive crack propagation modeling.

Crack Length Control Scheme

It is well known that the load-displacement behavior of cracking ceramic-like structures is size dependent. Strain softening, as well as snap-back in-

stabilities, may occur for the same material depending on structure sizes. Softening can be handled with a displacement control procedure. However, snap-backs are more difficult to follow. As also recognized by Bocca *et al* [8], snap-back branches can be numerically captured when the loading process is controlled by an increasing function of the crack length. Crack length control assures uniqueness of the solution, being a natural and elegant way of handling snap-through and snap-back instabilities. In the present system, the simulation process is controlled through the specification by the user, via interactive graphics, of a crack length increment in the predicted direction.

Dynamic Relaxation Solver

In the present system, linear elastic quadrilateral and triangular elements are used in conjunction with zero-thickness interface elements in the fictitious crack. The behavior of the interface elements is determined, as previously [16], by non-linear softening constitutive models. Consequently, a non-linear solution technique is required. The dynamic relaxation (DR) technique has been selected for its applicability to potentially highly non-linear problems such as extreme softening and snap-back. A complete description of the solver is out of the scope of this paper, but can be found in Underwood [22]. DR, although robust, may be slow in some circumstances. This drawback is reduced here due to the stress-displacement information available from the previous steps of crack propagation. In addition, this explicit solution technique is very attractive for future substantial increases in solution speed via parallel computations.

Load Factor Computation; Crack Stability Criterion

The objective of this strategy is to determine a loading condition satisfying both global equilibrium and a crack stability criterion for a specified fictitious crack length. Distinct stability criteria that have been used include a tensile strength based criterion [4-5], and a fictitious stress singularity cancellation criterion [16-19].

A criterion based on the fictitious crack tip opening profile is implemented here. No singular elements are used at the fictitious crack tip. Rather, non-linear analyses are performed until a condition of zero-slope of the COD at the tip is reached. Considering the finite element discretization used here, with linear strain isoparametric elements, the condition of zero-slope can be verified when, Figure 2:

$$\partial w/\partial s \mid_{s=0} = (4w_B - w_A) / c = 0 \quad \text{or} \quad w_B/w_A = 1/4 \qquad (1)$$

where w is the opening of the fictitious crack, and A and B are nodes of the element adjacent to the crack tip. This criterion is a separate module in the overall simulation system. Although the profile gradient criterion has been applied in the simulations performed herein, the system is not limited to this criterion. Others may be introduced readily.

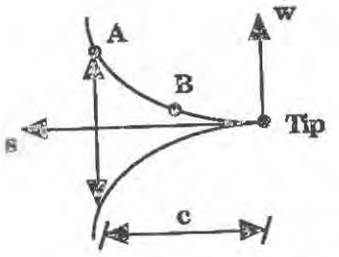

FIGURE 2. Zero-Slope Condition of the Opening Profile at the Fictitious Crack Tip.

The next step is to compute the load factor that satisfies the stability criterion for the current fictitious crack length. Monotonic and proportional loading is assumed. Initially, an overestimated value of the load factor is introduced. The dynamic relaxation solver then provides an equilibrated solution for that load factor. The profile gradient at the tip is computed through (1). If the gradient is greater than zero, the load factor is decreased. If the gradient is less than zero, or a closing condition is detected, the load factor is increased. The procedure is repeated until the zero-slope condition is satisfied, within a user specified tolerance.

An important detail of the load factor computation is the initial configuration used in the dynamic relaxation algorithm. The fictitious crack tip is always considered completely open at the beginning of the dynamic relaxation iterations. The cohesive closing forces are introduced within the dynamic iterative process. The last positive gradient configuration is stored and used as the initial configuration for the next candidate load factor. This procedure is necessary to avoid any confusion between admissible configurations in the increasing and decreasing branches of the load-displacement curve, allowing the crack length control scheme to produce a unique solution.

Computation of Crack Propagation Direction

When the stability criterion and global equilibrium are satisfied for a given crack length, the fictitious crack tip is propagated to a new position. The direction of crack extension is defined here by the maximum principal-stress direction due to the remote loading. A numerical search is performed around the fictitious crack tip to determine this direction. The search for maximum circumferential stress is performed along a circle centered at the tip. Here, the search is made along the circle closest to the second layer of Gauss points in the elements surrounding the crack tip. Once the direction is determined, the user graphically indicates the length of the desired increment.

Automatic Remeshing

Mesh generation is one of the most time consuming aspects of computational mechanics for moving boundary problems. It is an inevitable step if finite element methods are to be used to model discrete crack propagation. In this case, the mesh must be updated continuously to reflect the changing model geometry. An improved general triangulation meshing algorithm developed by Wawrzynek [23] has been implemented to regenerate the continuum mesh in the present system. A quadtree data structure is used [24] together with spatial decomposition and boundary contraction concepts. Simultaneously, additional interface elements are added along the new crack increment.

EXAMPLE PROBLEMS

Two examples are considered to demonstrate the applicability of the present strategy. A single edge notch in bending (SEN(B)) configuration is considered first. A range of softening responses, including snap-back, is demonstrated for this type of geometry. Next, the performance of an anchor bolt embedded in concrete, involving initiation and propagation of a curvilinear crack, is presented.

SEN(B) Configuration

The SEN(B) specimen of Figure 3 illustrates how size effects may completely change the behavior of the specimen, and how the presented strategy is capable of modeling all the possibilities. The relative geometry of the beam is preserved, while beam height varies from 50 mm to 300 mm. Plane stress is assumed. No initial notch is considered. Material properties and the interface softening model used in this analysis are presented in Figure 3.

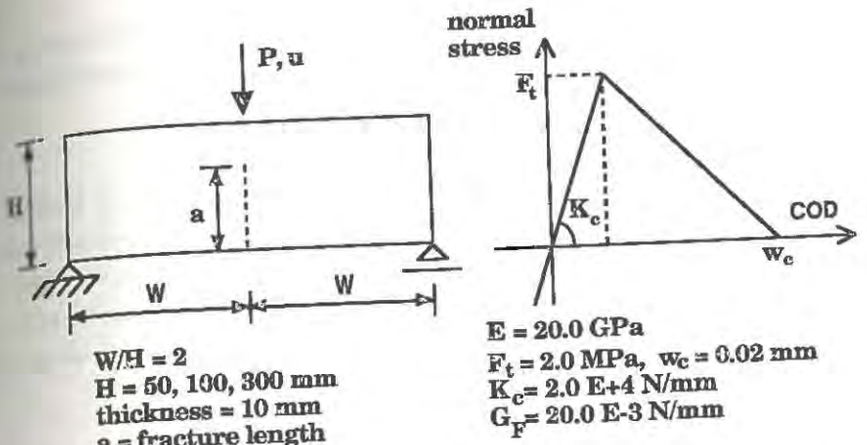

FIGURE 3 - SEN(B) Geometry, Interface Softening Model, and Material Parameters.

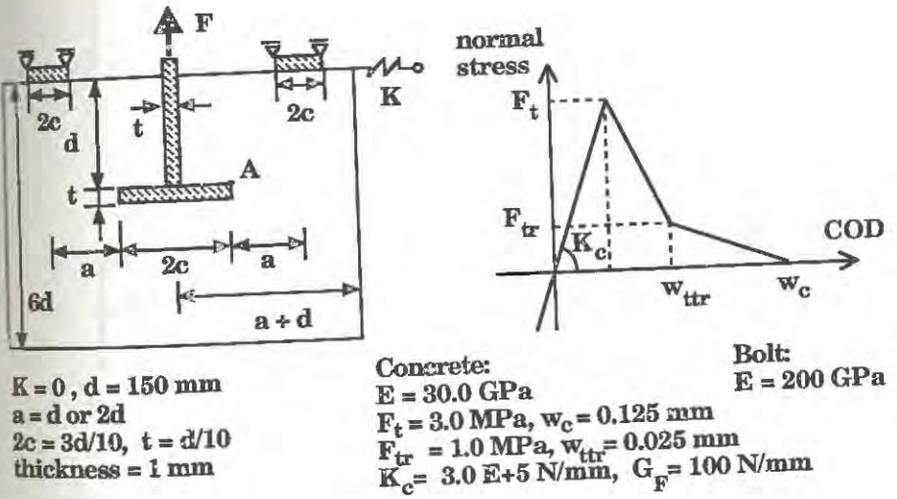

FIGURE 4 - Anchor Bolt Geometry, Material Properties, and Interface Softening Model.

Anchor Bolt Problem

This is part of the well-known round-robin analysis of anchor bolts embedded in concrete proposed by RILEM TC 90-FMA committee [22]. The geometry and material properties used are shown in Figure 4. A bilinear-softening

cohesive model is employed. Plane stress again is assumed. The concrete is in contact with the upper side of the bolt. Shear tractions in the propagating crack are not considered for this analysis.

Results

Figure 5 shows non-dimensional load-displacement curves for the SEN(B) structure. The normalized load term is the ratio Sigma N/F_t, where Sigma N = beam theory normal stress with no crack. It is clear that the present strategy is able to handle moderate and severe softening and, importantly, a snap-back instability. Crack length, as pointed out before, is an increasing function under the user's control (Figure 6).

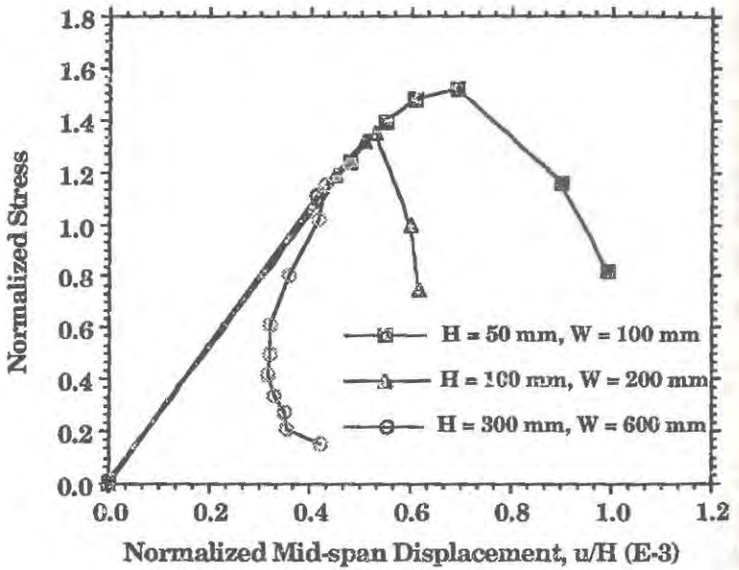

FIGURE 5 - Predicted load-displacement curves for the SEN(B) analyses.

The predicted load-displacement (vertical displacement of point A, Figure 4) curves for the anchor bolt problem are depicted in Figure 7. The deformed configuration at maximum load, for a = 2d, is also shown in Figure 8.

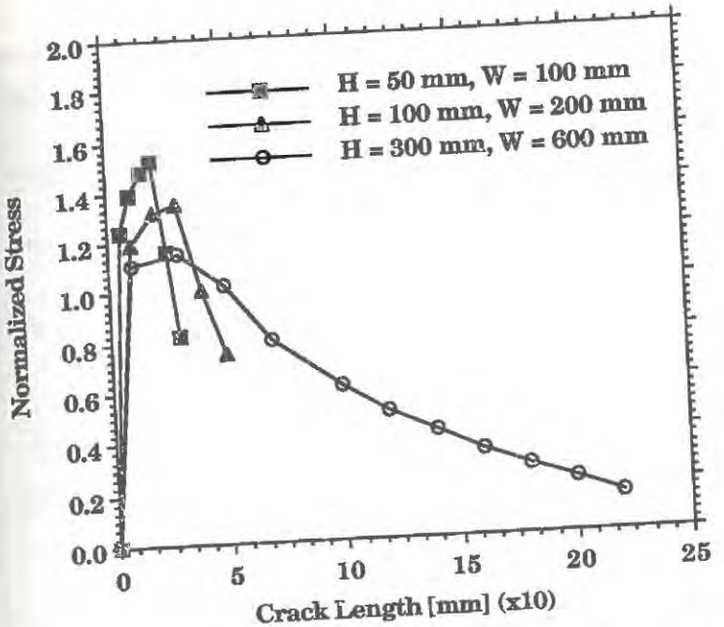

FIGURE 6 - Crack length (a) versus normalized stress for SEN(B) analyses.

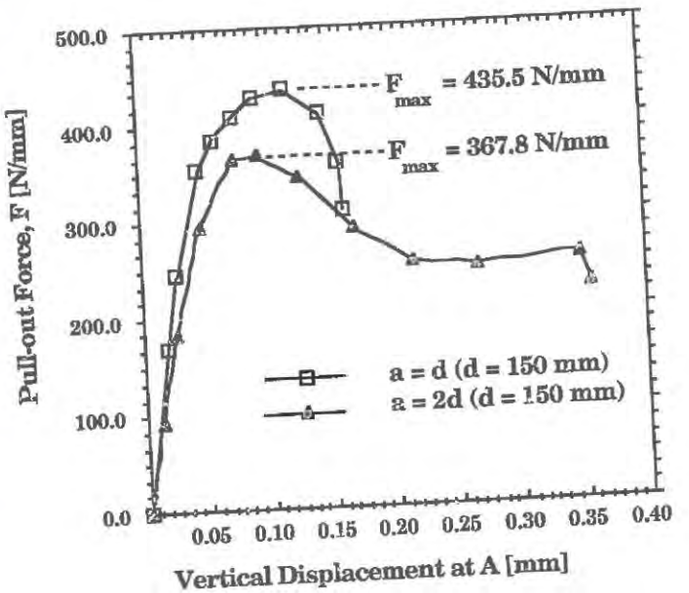

FIGURE 7 - Predicted load versus vertical displacement at A for the anchor bolt analyses.

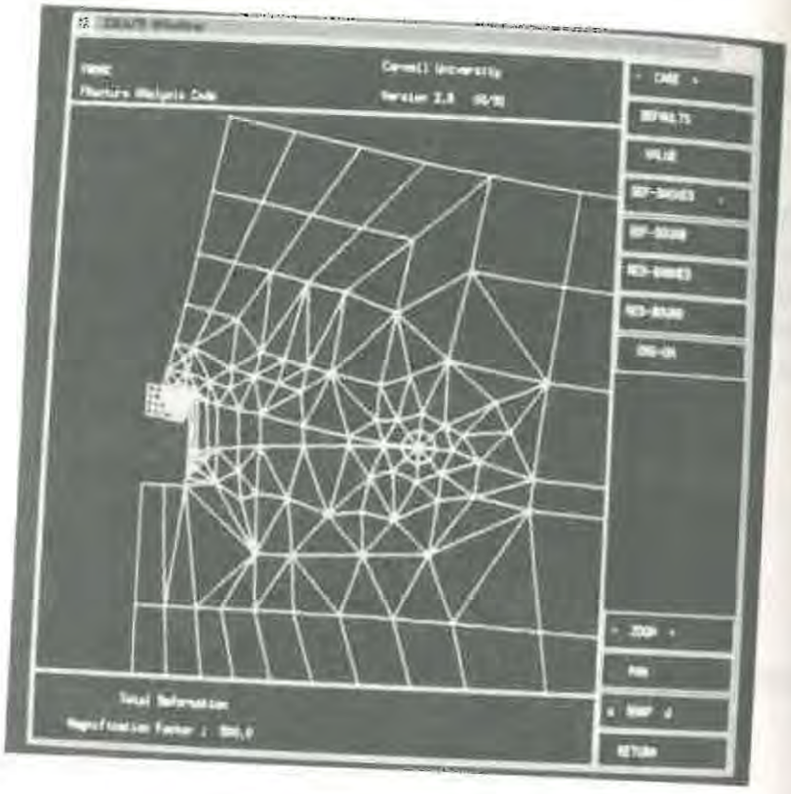

FIGURE 8 - Deformed configuration at maximum load for a = 2d. Amplification factor = 500.

DISCUSSION AND CONCLUSIONS

A new system for simulating the initiation and propagation of arbitrary, cohesive cracks has been presented. The system integrates geometrical and mesh representation, finite element, non-linear solution, non-linear fracture mechanics, and automatic remeshing techniques on an engineering workstation behind a graphical user interface. This system computes a load factor that simultaneously satisfies global equilibrium and a local crack stability criterion for a given fictitious crack length. The local criterion is based on zero-slope of the COD profile at the fictitious crack tip. The dynamic relaxation non-linear solution technique is capable of handling highly non-linear behavior, including snap-back, making it very general and powerful.

Current experience with the example problems indicates that there can be extreme sensitivity in load factor to small variation in the slope of the COD profile on the decreasing branch of the load versus displacement curves. Research is continuing to determine the range of acceptable tolerance on the zero slope condition that will insure both accuracy and stability of this numerical algorithm.

This system is heir to over a decade of work in modelling crack initiation and propagation in concrete and rock. It has been designed with data structure and code architecture in mind to allow it to receive new constitutive formulations and solution techniques gracefully.

ACKNOWLEDGEMENTS

All work was performed in the Program of Computer Graphics at Cornell University. The support provided by CNPq (Brazilian Agency) and Digital Equipment Corporation is deeply appreciated.

REFERENCES

1. Shah, S.P., "Whither fracture mechanics for concrete," Keynote Lecture, Fracture of Concrete and Rock: Recent Developments, Edited by S.P. Shah, S.E. Swartz, and B. Barr, Elsevier Science Publishers LTD, pp.1-4, 1989.
2. Saouma, V.E., Ingraffea, A. R. and Catalano, D.M., "Fracture toughness of concrete: K_{Ic} revisited," Journal of Engineering Mechanics Division, ASCE, Vol.108, Nº EM6, 1982.
3. Bazant, Z.P. and Oh, B.,"Crack band theory for fracture of concrete," Materials and Structures, Vol.16, Nº 93, pp.155-77, 1983.
4. Hillerborg, A., Modeer, M. and Petersson, P-E., "Analysis of crack formation and crack growth in concrete by means of fracture mechanics and finite elements," Cement and Concrete Research, Vol. 6, pp. 773-82, 1976.
5. Petersson, P-E., "Crack growth and development of fracture zones in plain concrete and similar materials," Report TVBM-1006/1-174, Division of Building Materials, Lund Institute of Technology, Lund, Sweden, 1981.
6. Carpinteri, A. "Interpretation of the Griffith instability as a bifurcation on the global equilibrium," Application of Fracture Mechanics to Cementitious Composites, NATO-ARW, pp.287-316, 1984.
7. Jenq, Y. and Shah, S. P, "Two parameter fracture model for concrete," ASCE, EMD, Vol.11, Nº 10, 1985.
8. Bocca, P., Carpinteri, A. and Valente, S., "Mixed mode fracture of concrete," International Journal of Solids and Structures, Vol.27, Nº 9, pp.1139-53, 1991.
9. Swanson, P. L., Fairbanks, C. J, Lawn, B. R, Mai, Y. W., and Jockey, B. J., "Crack interface grain bridging as a fracture resistance mechanism in ceramics: experimental study on alumina," Journal of American Ceramic Society, Vol. 70[4], pp. 279-89, 1987.
10. Vekinis, G., Ashby, M. F. and Beaumont, P. W. R.,"R-curve behaviour of Al_2O_3 ceramics," Acta Metallurgica, Vol. 38[6], pp.1151-62, 1990.
11. Rödel, J., Kelly, J. F. and Lawn, B. R.,"In situ measurements of bridged crack interfaces in the scanning electron microscope," Journal of American Ceramic Society, Vol. 73[11], pp. 3313-18, 1990.
12. Llorca, J. and Steinbrech, R. W., "Fracture of alumina: an experimental and numerical study," Journal of Material Science, Vol. 6, pp. 383-90, 1991.

13. Mai, Y. M., "Fracture and fatigue of non-transformable ceramics: the role of crack interface bridging," Fracture Processes in Concrete, Rock and Ceramics, Edited by Van Mier, J.G.M., London, 1991.
14. Becher, P. F., Hsueh, H., Angelini, P. and Tiegs, T. N., "Toughening behavior in whisker-reinforced ceramic matrix composites," Journal of American Ceramic Society, Vol. 71[12], pp. 1050-61, 1988.
15. Llorca, J. and Elices, M., "Fracture resistance of fiber-reinforced ceramic matrix composites," Acta Metallurgica, Vol. 38[12], pp. 2485-92, 1990.
16. Ingraffea, A. R. and Gerstle, W. H., "Non-linear fracture models for discrete crack propagation," Application of Fracture Mechanics to Cementitious Composites, NATO ARW, pp. 171-207, 1984.
17. Ingraffea, A. R., Gerstle, W. H., Gergely, P. and Saouma, V.,"Fracture mechanics of bond in reinforced concrete," Journal of Structural Engineering, ASCE, Vol.110, N° 4, pp. 871-89, 1984.
18. Hellier, A. K., Sansalone, M., Carino, N. J., Stone, W. C. and Ingraffea, A. R., "Finite element analysis of the pullout test using a nonlinear discrete cracking approach," Cement, Concrete, and Aggregates, Vol.9, N° 1, pp. 20-9, 1987.
19. Swenson, D. V., Ingraffea, A. R., "The Collapse of the Schoharie Creek Bridge: A Case Study in Concrete Fracture Mechanics", Int. Journal of Fracture, Vol. 51, pp. 73-92, 1991.
20. Wawrzynek, P., Boone, T., and Ingraffea, A. R., "Efficient Techniques for Modeling the Fracture Process Zone in Rock and Concrete, "Proc. of the Fourth International Conference on Numerical Methods in Fracture Mechanics, March 23-27, 1987, San Antonio, Texas, A. R. Luxmoore, D. R. J. Owen, Y. S. Rajapakse, and M. F. Kanninen, editors, pp. 473 - 482.
21. Ingraffea, A. R., "Theory of Crack Initiation and Propagation in Rock," Chapter 3 in Rock Fracture Mechanics, B. Atkinson, editor, Academic Press, Inc., 1987.
22. Underwood, P., "Dynamic Relaxation," Computational Methods for Transient Analysis, Edited by T. Belytschko and T. J. R. Hughes, Elsevier Science Publishers, pp. 245-65, 1983.
23. Wawrzynek, P. A., "Discrete modeling of crack propagation: theoretical aspects and implementation issues in two and three dimensions," Ph.D. Thesis, Chapter 6, Cornell University, 1991.
24. Samet, H., "The quadtree and related hierarchical data structures," ACM Computer Surveys, Vol. 16[2], 1984.
25. Elfgren, L., "Round-robin analysis of anchor bolts," RILEM TC-90 FMA Fracture Mechanics of Concrete-Applications, Preliminary Report, May, 1991.

Invited Paper

EXPERIMENTAL AND NUMERICAL FRACTURE MODELLING OF A GRAVITY DAM

ALBERTO CARPINTERI AND SILVIO VALENTE
Politecnico di Torino, Italy

GERARDO FERRARA
ENEL-CRIS, Milano, Italy

LORENZO IMPERATO
ISMES, Bergamo, Italy

ABSTRACT

Two scaled-down 1:40 models of a gravity dam are subjected to equivalent hydraulic and weight loading. An initial notch in the upstream wall propagates during the loading process towards the foundation. Crack mouth opening control is performed and the load vs. CMOD diagram is plotted. A numerical simulation of the experiments is carried out using a cohesive fracture model in Mixed Mode condition. The structural behaviour of the models and the crack trajectories are reproduced by the finite element idealization in a satisfactory way.

INTRODUCTION

Discrete and sharp cracks give rise to singular stress fields in the vicinity of the crack tip. The severity of the stress field is measured by the stress-intensity factors, which are valid only when damage and plastic zones are negligible and the material may be assumed to be linear elastic. Since the size of damage and plastic zones is hardly affected by the geometry of the structure, stress-intensity factors may only be used when dealing relatively large structures. For this reason, Linear Elastic Fracture Mechanics (LEFM) was first proposed [1,2] for the stability analysis of cracked dams.

Nevertheless, non-linear crack tip phenomena can be very important, to the point that LEFM might represent an oversimplification of reality. The damage zone at the crack tip may be either diffused or localised. In the latter case, a cohesive crack model was found to give very consistent results in describing ductile [3] as well as brittle fractures [4].

In applying Fracture Mechanics concepts to the crack analysis of dams, however, it proves necessary to take into consideration a large variety of crack growth mechanisms (e.g., fatigue, creep, etc.) and loading conditions (e.g., gravity, hydraulic, thermal, shrinkage, dynamic loads, etc.). Nowadays, it is difficult to say to what extent each factor affects the global problem. As a matter of fact, most of these factors are usually disregarded, including one which is not without importance, such as the three-dimensionality of the structure and the crack surface. A contribution to the general problem is provided by this experimental and numerical investigation, where two scaled-down and planar models of a gravity dam are subjected to equivalent self-weight and hydraulic loading.

EXPERIMENTAL MODELLING

Experimental tests were carried out on two bi-dimensional gravity dams (Fig. 1). Both models had a horizontal notch on the upstream side at a quarter of the dam height, with a notch depth ratio of 0.1 and 0.2 respectively. The geometric scale between prototype and model was taken as $S_L = 40$. A conventional concrete mix, used by ENEL-CRIS in several fracture mechanics

Figure 1. Gravity dam model.

experimental programmes, was employed [5,6], with maximum aggregate size of 25 mm. Compliance with material similitude requirements between prototype and model was taken into account, so that the modulus scale factor and strength factor was $S_E = 1$.

When the two previous independent quantities (length and specific force) are fixed, it is possible to obtain the scales of the remaining quantities that are normally involved in statics problems. The relationship between the specific weights is: $S_q = S_E \times S_L^{-1} = 1/40$, and the scale between the concentrated forces is: $S_F = S_E \times S_L^2 = 1600$.

TESTING SET-UP AND PROCEDURE

With the aim of reproducing the approximated stress distribution in the process zone due to self-weight, a fictitious system of discrete vertical forces was realized in order to solve the practical difficulty of complying with the scale relationship of the body forces. The method consists of artificially distributing in the model a sufficient and rational system of vertical forces, causing the minimum encumbrance, so as to disturb the static behaviour of the model as little as possible. The total volume of the model was subdivided into elementary portions and their centers of gravity and the intensity of the equivalent forces to be applied were estimated. This was done by means of a system consisting of cross bars connected by tie-rods to a steel framework placed under the foundation of the dam, and spring-dynamometers and balancing systems. The scheme of the testing set-up is shown in Fig. 2.

When the self-weight condition was reproduced in the model, the hydraulic thrust was applied onto the upstream side. The hydraulic load was generated by means of a servocontrolled actuator with 2000 kN capacity. This force was distributed into four concentrated loads, their intensity increasing with depth and acting directly onto the upstream wall through steel plates.

The crack mouth opening displacement (CMOD) signal was used as feedback to the servocontrolled actuator. During the initiation of the fracture process, the tests were carried out by increasing CMOD at a rate of 1.2 microns per minute. During the loading process, the following quantities were measured: self-weight, hydraulic thrust, displacement of the dam crest, CMOD and crack mouth sliding displacement (CMSD) on both the lateral walls.

NUMERICAL MODELLING

Experimental tests were simulated through the cohesive crack model, which is particularly suitable for the study of the non-linear behaviour of concrete-like materials characterized by strain-softening, i.e., by a decrease in load carrying capacity due to anelastic deformation. If an initial imperfection (such as a notch) is present in such a material, the non-linear zone localizes into a very narrow band, while the material outside the damage band retains a linear behaviour.

The cohesive crack model represents the narrow band as an extension of the real crack, which is called fictitious crack (or process zone). In this zone, though it is damaged, the material

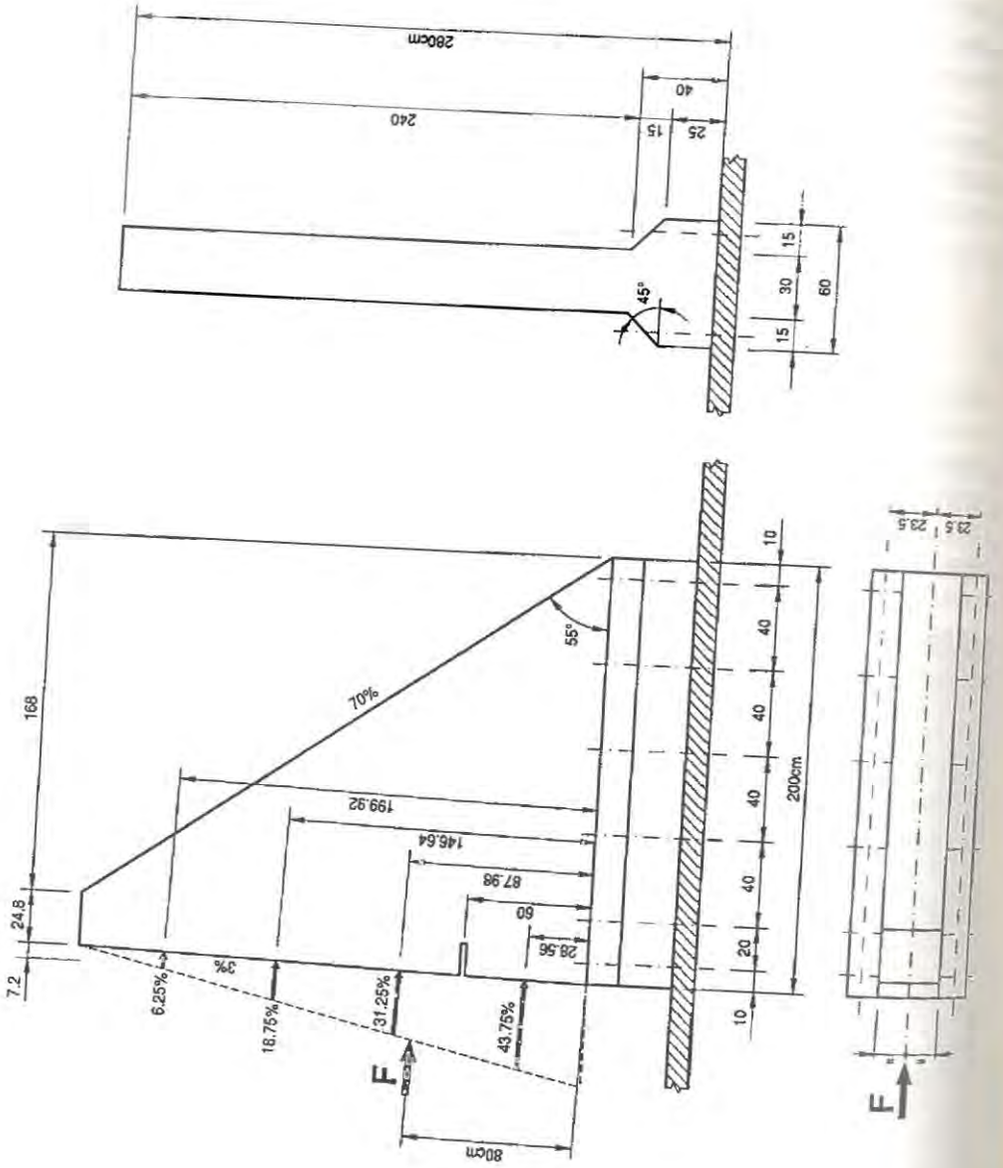

Figure 2. Testing set-up.

still able to transmit stresses that are decreasing functions of the displacement discontinuity. The ohesive crack model was applied initially to problems of collinear propagation (Mode I), where e crack trajectory is known a priori due to symmetry [3, 4]. Subsequently, the model was eneralized to problems of curvilinear propagation (Mixed Mode) by Carpinteri and Valente [7] nd applied successfully to the intepretation of experimental testing, i.e., four point shear [8,9] and ull-out [10,11].

The cohesive crack model can explain the transition between plastic collapse and brittle racture varying the scale. When the value of the brittleness number s_E [4] becomes very small, he model can predict and describe the catastrophic collapse through the snap-back instability branch.

The mechanical parameters assumed in the numerical simulation were:

Young's Modulus E = 35,700 MPa;

Poisson's ratio $\nu = 0.1$;

Tensile Strength $\sigma_u = 3.6$ MPa;

Fracture Energy $G_F = 184$ N/m^2.

The value of G_F was obtained from three point bend tests performed according to the RILEM Recommendation at the time when the first model was loaded to failure, i.e., 210 days after moulding.

If w_n stands for the component of the displacement discontinuity normal to the crack surface and σ_c and τ_c stand for the normal and tangential cohesive stress components respectively, the constitutive law was assumed to be the following:

$$\sigma_c = \sigma_u\left(1 - \frac{w_n}{w_c}\right) \quad , \text{ for } w_n < w_c \ ,$$

$$\sigma_c = 0 \quad , \text{ for } w_n \geq w_c \ ,$$

$$\tau_c = 0 \quad , \text{ always.}$$

Each dam model was discretized by using 6-noded triangular elements. The displacement field inside each element was approximated by quadratic shape functions. Numerical simulations were carried out by having the fictitious crack length serve as the control-variable (Fictitious Crack Length Control Scheme). Thus, this quantity always increases monotonically during the irreversible cracking process. With this technique, the external load is determined at each step so that the principal tensile stress at the fictitious crack tip achieves the ultimate tensile strength of the material, σ_u. The subsequent crack growth step occurs in the orthogonal direction.

Before accepting a step solution, a check on the real crack tip opening is made, so that $w_n \leq w_c$. If the preceding condition is not verified, the real crack tip advances until it is verified. The length of the process zone varies during crack growth. As the crack trajectory is not known a priori, an automatic remeshing was performed at each crack growth step (Fig. 3).

After the achievement of peak load, i.e. in the softening stage, for both the structural geometries tested, a particular condition was seen to occur involving two equal principal stresses at the fictitious crack tip. From that point onwards, crack growth was imposed as rectilinear and tangent to the previously developed trajectory.

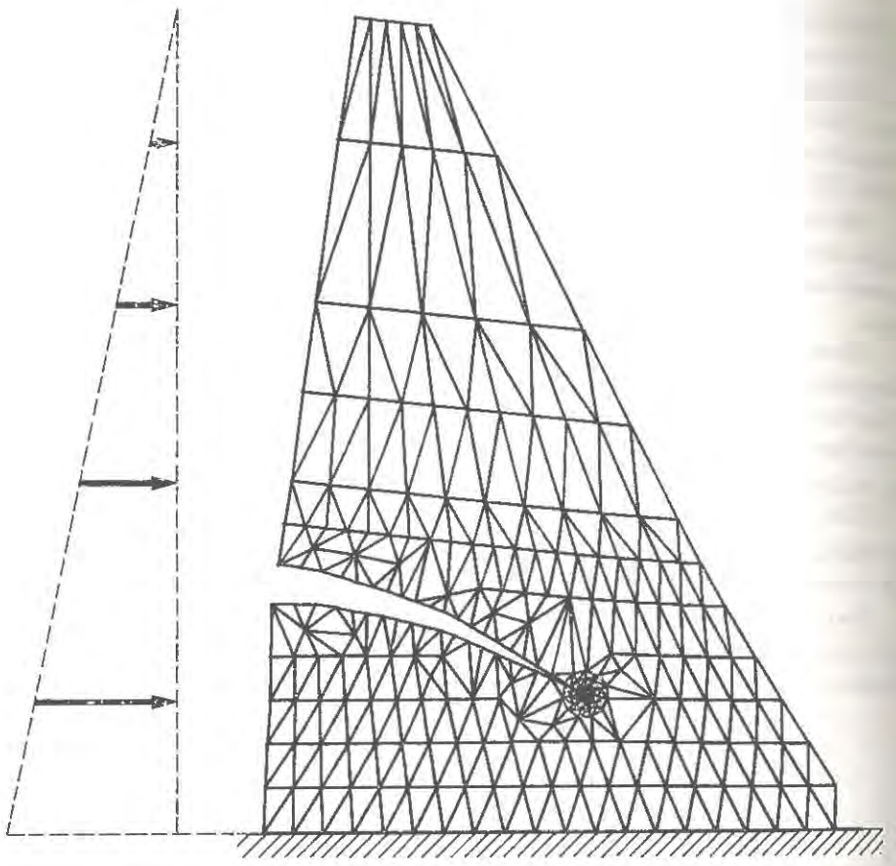

Figure 3. Test 3, mesh used at step 19 (displacements enlarged 300 times).

RESULTS AND DISCUSSION

The loading test of the first dam model (notch depth ratio = 0.1) stopped at the peak load, when unstable failure occurred at the weakest section of the foundation (Test 1). Then, the same dam model, glued and reinforced around the failure, was subjected to stable test without self-weight simulation (Test 2). Eventually, the second dam model (notch depth ratio = 0.2) was subjected to stable test without self-weight simulation (Test 3).

The experimental diagrams of hydraulic force versus crack mouth opening displacement are shown in Figs. 4 and 5, together with the numerical diagrams. The latter reproduce the former with an acceptable degree of accuracy. The experimental and numerical crack trajectories are illustrated in Fig. 6 and even in this case the finite element idealization appears satisfactory.

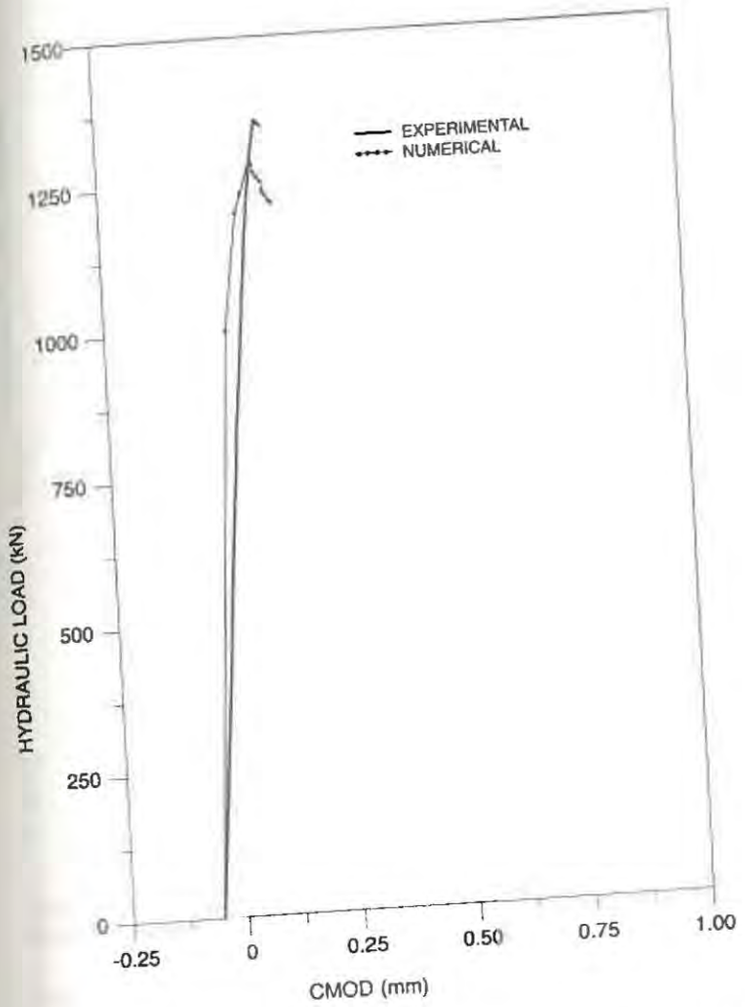

Figure 4. Hydraulic load versus Crack Mouth Opening Displacement (CMOD) diagrams: Test 1.

When self-weight was taken into account, the length of the process zone during crack growth was seen to decrease. It was therefore necessary to reduce the length of the crack growth step too, from 10 to 2 cm, in order to follow the phenomenon in a numerically stable manner. The mesh was therefore gradually refined as the failure process became more brittle.

The detaching of the model from the foundation and the elastic compliance of the foundation were not taken into account in the numerical simulation. By taking these factors into consideration we should probably obtain information on the energy dissipation due to friction between crack free surfaces.

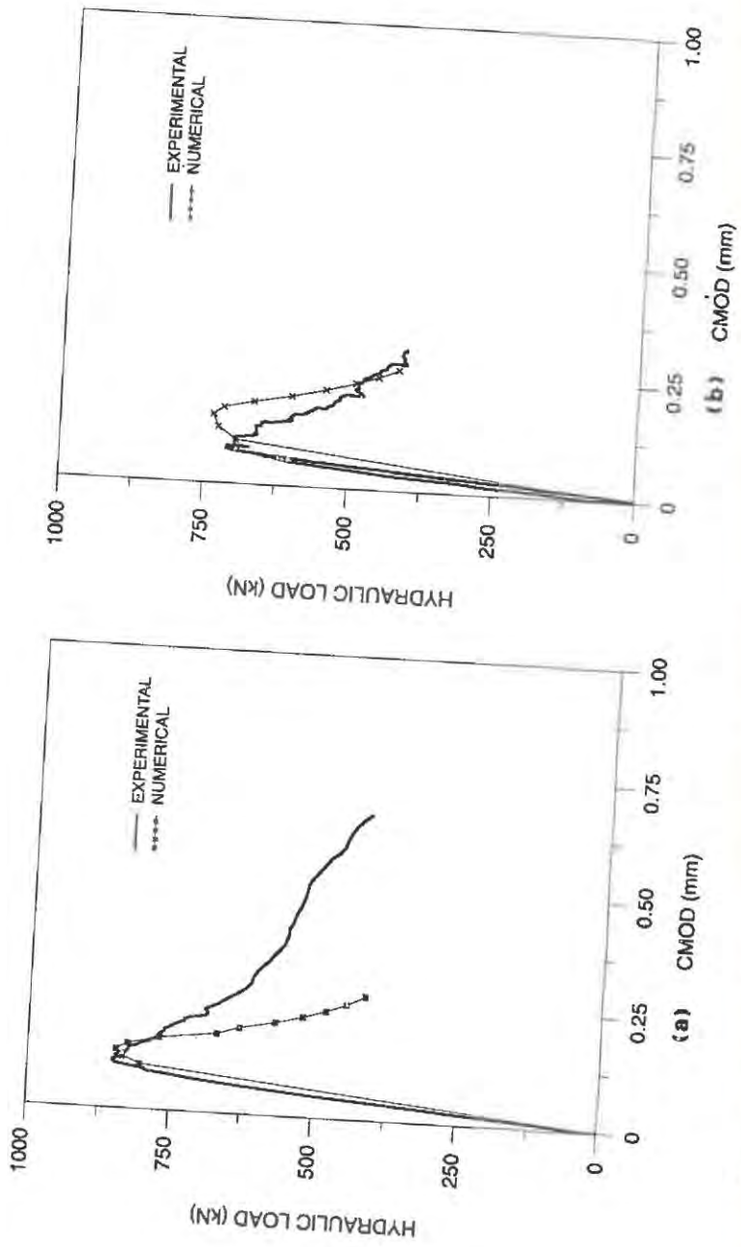

Figure 5. Hydraulic load versus Crack Mouth Opening Displacement (CMOD) diagrams: (a) Test 2; (b) Test 3.

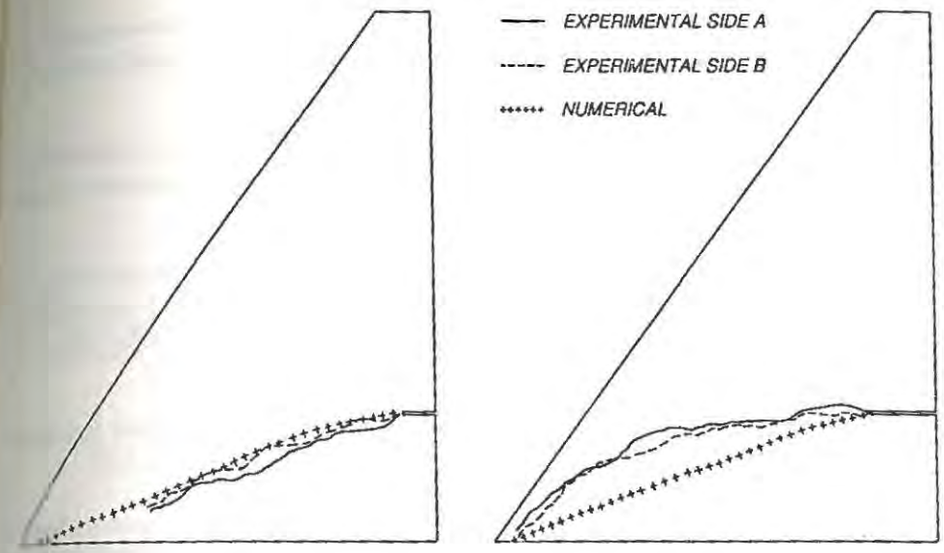

Figure 6. Crack trajectories: (a) Test 2; (b) Test 3.

REFERENCES

1. Ingraffea, A. R. and Chappel, J. F., A fracture mechanics investigation of the cracking of Fontana Dam. Report No. 81-7, Dept. of Structural Engineering, Cornell University, 1981.

2. Saouma, V. E., Ayari, M. L. and Boggs, H., Fracture mechanics of concrete gravity dams, SEM-RILEM Int. Conf. of Fracture of Concrete and Rock, Houston, June17-19, 1987, pp. 496-519.

3. Hillerborg, A., Modeer, M. and Petersson, P. E., Analysis of crack formation and crack growth in concrete by means of fracture mechanics and finite elements, Cement & Concrete Research, 1976, Vol. 6, pp.773-782.

4. Carpinteri, A., Interpretation of the Griffith instability as a bifurcation of the global equilibrium, N.A.T.O. Advanced Research Workshop on Applications of Fracture Mechanics to Cementitious Composites, Northwestern University, Evanston, 1984, pp. 287-316.

5. Carpinteri, A., Ferrara, G. and Melchiorri, G., Single edge notched specimen subjected to four point shear: an experimental investigation, Proceedings of the International Conference on Recent Developments on the Fracture of Concrete and Rock, Cardiff, 1989, pp. 605-614.

6. Carpinteri, A., Ferrara, G., Melchiorri, G. and Valente, S., The four point shear test on single edge notched specimens: an experimental and numerical analysis, Proceedings of the 2nd European Conference on Fracture, Torino, 1990, pp. 667-675.

7. Carpinteri, A. and Valente, S., Size scale transition from ductile to brittle failure: a dimensional analysis approach, France-U.S. Workshop on Strain Localization and Size Effect due to Cracking and Damage, Cachan, 1988, pp. 477-490.

8. Bocca, P., Carpinteri, A. and Valente, S., Size effects in the mixed mode crack propagation: softening and snap-back analysis, International Conference on Fracture and Damage of Concrete and Rock, Vienna, 1988; Engineering Fracture Mechanics, Great Britain, 1990, Vol. 35, pp. 159-170.

9. Bocca, P., Carpinteri, A. and Valente, S., Mixed mode fracture of concrete, International Journal of Solids and Structures, Vol. 27, Great Britain, 1991, pp. 1139-1153.

10. Bocca, P., Carpinteri, A. and Valente, S., Evaluation of concrete fracture energy through a pull-out testing procedure, Proceedings of the International Conference on Recent Developments of the Fracture of Concrete and Rock, Cardiff, 1989, pp. 347-356.

11. Bocca, P., Carpinteri, A. and Valente, S., Fracture mechanics evaluation of anchorage bearing capacity in concrete, Proceedings of the International Workshop on the Application of Fracture Mechanics to Reinforced Concrete, Torino, 1990, pp. 231-265.

THERMO-SEISMIC ANALYSIS OF CONCRETE GRAVITY DAMS

Sudip S. Bhattacharjee, Pierre Léger, and John Venturelli
Department of Civil Engineering and Applied Mechanics, McGill University,
817, Sherbrooke Street West, Montréal, Québec, Canada

ABSTRACT

A strain softening constitutive model has been developed for smeared crack propagation using the concrete parameters of strain energy density, and the specific fracture energy, as criteria for fracture initiation and propagation, respectively. The long-term effects of seasonal temperature induced stresses are considered with a simplified creep effects model for application in the two-dimensional finite element analysis of concrete gravity dams. The strain rate effects on fracture properties of concrete are considered by applying constant dynamic magnification factors. Results obtained from two-dimensional finite element analysis of typical concrete gravity dams are presented.

INTRODUCTION

Seasonal temperature change often causes severe degradation of the stiffness and strength properties of the concrete dams built in North-Eastern Canada. Recent seismic activity in that region, the 1988 Saguenay earthquake, has raised concern regarding the safety of the major dam installations. During the maximum credible earthquake, potential crack formations may endanger the ability of the dam to retain the reservoir. Several numerical investigations have been carried out in recent years to study the nonlinear seismic response of concrete gravity dams [1]-[3]. The influences of pre-seismic long-term stresses and strains, and the strain rate effects under seismic loads, have not been rigorously considered in those studies. A methodology to incorporate the experimentally observed [4] rate sensitive behaviour of concrete in fracture mechanics analysis of dams has been lacking in the literature.

The smeared fracture model proposed here considers both long-term and rapidly applied load effects on the behaviour of concrete. The time-dependent strain is divided into elastic and unrestrained strain, the elastic component is always related to the stress by the elastic modulus, E. The long-term creep effect that leads to relaxation of temperature induced stresses is modelled by modifying the elastic strain field that arises from restraints to thermal deformations. A modelling procedure to take account of strain rate sensitivity of fracture parameters is developed. The compatibility between the static and dynamic analysis models is achieved by using a constant elastic modulus E.

CONSTITUTIVE MODEL FOR FRACTURE ANALYSIS

For linear elastic isotropic behaviour, the plane stress material stiffness matrix [D], relating the strains to stresses, is given by:

$$[D] = \frac{E}{1-\nu^2}\begin{pmatrix} 1 & \nu & 0 \\ \nu & 1 & 0 \\ 0 & 0 & \frac{1-\nu}{2} \end{pmatrix} \quad (1)$$

where E is the 'elastic' modulus and ν the Poisson's ratio. Short-term laboratory tests with recovered dam concrete can be used to determine the value of E. The elastic isotropic material model is replaced by an orthotropic model when the principal tensile stress reaches the fracture process initiation stress (FPIS), σ_0 (Fig. 1a), which is calibrated such that the strain energy density, U_0, at the instant of fracture initiation is preserved.

$$\frac{\sigma_0^2}{2E} = \frac{(\kappa\sigma_t)^2}{2E} = U_0 = \int_0^{\epsilon_t}\sigma\, d\epsilon \quad (2)$$

where the integral on the right hand side represents the area under the tensile stress-strain curve up to the peak stress, σ_t, as determined from short-term laboratory tests. Assuming a linear softening relationship, the final strain, ϵ_f, of no tensile resistance in the softening direction, is obtained from the principle of conservation energy as:

$$\epsilon_f = \frac{2G_f}{\sigma_0\, h_c} \quad (3)$$

where h_c is the element characteristic dimension defined as the square-root of the element area (Fig. 1b).

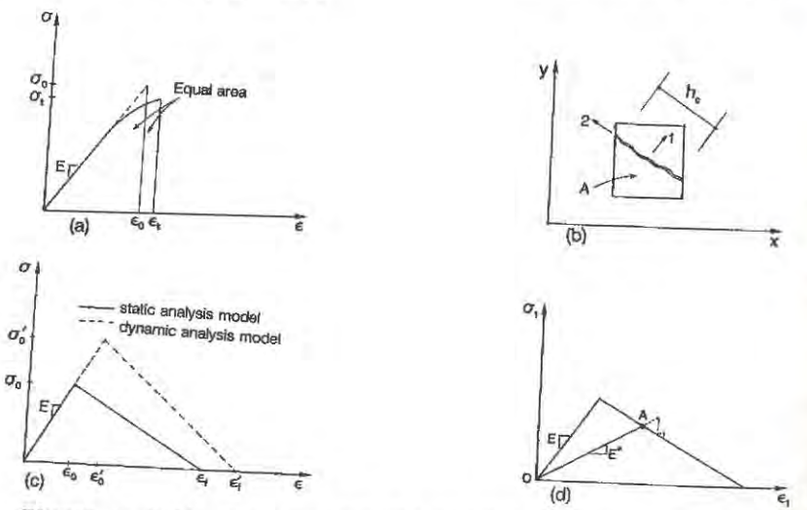

Figure 1. Softening constitutive model for fracture analysis.

In the present model, the elastic modulus is assumed to be strain-rate independent. Assuming strictly linear relationship up to the instant of fracture initiation, the dynamic magnification factor (DMF) for pre-peak elastic phase can be defined as:

$$DMF_e = \frac{\sigma_0'}{\sigma_0} = \frac{\epsilon_0'}{\epsilon_0} = \sqrt{\frac{U_0'}{U_0}} \quad (4)$$

where the primed quantities stand for dynamic parameters. The dynamic magnification of specific fracture energy is given by:

$$DMF_f = \frac{G_f'}{G_f} \quad (5)$$

Expressions (3)-(5) give the dynamic strain, ϵ'_f, of no tensile resistance as:

$$\epsilon_f' = \frac{DMF_f}{DMF_e}\,\epsilon_f \quad (6)$$

The influence of strain rate on the constitutive behaviour of concrete is demonstrated in Fig. 1c. During the softening state, the plane stress material stiffness, [D], in the local axis system 1-2 (Fig. 1.b) is given by:

$$[D] = \frac{E}{1-\eta\nu^2}\begin{pmatrix} 1 & \eta\nu & 0 \\ \eta\nu & 1 & 0 \\ 0 & 0 & \frac{1-\eta\nu^2}{2(1+\nu)} \end{pmatrix} \quad ; \quad \eta = E^*/E \quad (7)$$

where E^* is the softened modulus in the direction normal to the fracture plane. An iterative scheme is applied to simulate the strain softening phenomenon of decreasing stress with increasing strain. The unloading/reloading process follows the secant modulus path OA (Fig. 1d). With the initiation of fracture process in one direction, the material reference axis system is made irrotational. Presently, only one fracture plane is allowed per element. After complete fracture ($\epsilon=\epsilon_f$ or ϵ'_f), the parameter η in equation (7) becomes zero. A shear resistance reduction factor, β, can be applied at that state.

The creep effect on temperature stress, σ_T, induced over a long time period (t-t'), is represented as:

$$\{\sigma_T\} = [D]\,\{(1-\psi)\,(\epsilon-\epsilon_i)\} \quad ; \quad \psi = \frac{\chi\phi(t,t')}{1+\chi\phi(t,t')} \quad (8)$$

where $(\epsilon-\epsilon_i)$ is the elastic strain resulting from restrain effects on unrestrained temperature strain, ϵ_i, without taking creep effects into consideration, and ψ ($0 \le \psi \le 1$) is the relaxation coefficient defined in terms of the ageing coefficient, χ, and the usual creep coefficient, $\phi(t,t')$. Finite element analysis is performed for self-weight, hydrostatic pressure, and temperature loads at the first step. If the resultant static response exceeds the elastic range, the short-term strain softening model is activated to regulate the fracture propagation.

THERMAL ANALYSIS OF CONCRETE GRAVITY DAMS

The finite element model for structural and thermal analysis of the gravity dam subjected to yearly temperature cycles is shown in Fig. 2. The material properties are listed in Table 1. Transient heat transfer analyses accounting for air, reservoir, and foundation temperature variations as well as solar radiation have been performed with environmental data characteristic of the lower St. Lawrence region (Québec, Canada) where several dams are located.

Figure 3a shows the temperature contours for the condition corresponding to the coldest average temperature reached by the dam. The contours of the principal tensile stresses induced by temperature condition alone are presented in Fig. 3b. Significant tensile stresses occur near the downstream surface of the dam. The maximum stress 1.4 MPA at the toe results partly from the constraint effects caused by rigid foundation assumption. The bulk of the dam is not severely affected by temperature variations. The response of the dam remains linear elastic under the combined actions of self-weight, hydrostatic pressure, and the coldest average temperature condition.

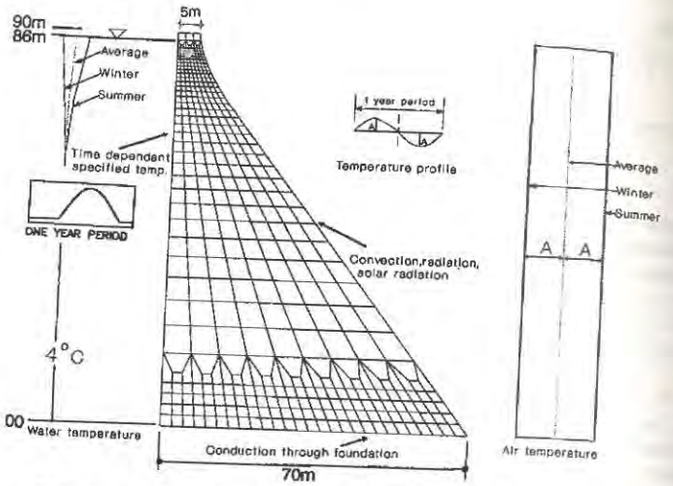

Figure 2. The concrete gravity dam model.

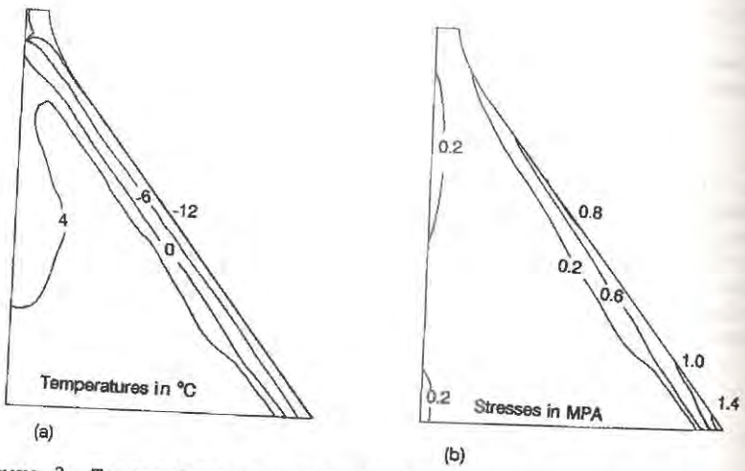

Figure 3. Temperature analysis of the concrete gravity dam.

TABLE 1
Material property data for concrete dam

Material parameters	Values	Material parameters	Values
Elastic modulus, E	27960 MPA	Thermal conductivity	2.62 W/m °C
Poisson's ratio, ν	0.2	Emissivity	0.88
Mass density	2400 kg/m^3	Convection	27.44 W/m^2 °C
Strength factor, κ	1.0	Solar absorbivity	0.50
Tensile strength, σ_t	2.0 MPA	specific heat	912 J/kg °C
Fracture energy, G_f	250 N/mm	Reference temp.	4 °C
DMF_s	1.1	Thermal Exp. Coeff.	6x10^{-6} /°C
DMF_f	1.1	Relaxation factor, ψ	0.35

THERMO-SEISMIC RESPONSE OF THE DAM

The proposed fracture analysis model has been implemented in a computer program FRAC_DAM. The dam model in Fig. 2 has been analyzed for a 3 sec segment of the S69E component of the Taft ground motion (Fig. 4a); the acceleration data has been scaled to different peak ground accelerations (PGA) to induce cracking in the dam. The structural damping has been defined to be mass proportional providing 5% damping in the fundamental mode response of the dam-reservoir system. The hydrodynamic interaction effects have been represented by Westergaard added mass, and added damping coefficients calibrated to provide low-level elastic response, consistent with the frequency-domain solution for the reservoir bottom wave reflection coefficient equal to 0.70 [5]. The foundation condition has been assumed rigid. The implicit Newmark integration method has been applied to solve the dynamic equilibrium equations with time step equal to 0.01 sec. Preliminary results obtained for different loading combinations are presented here.

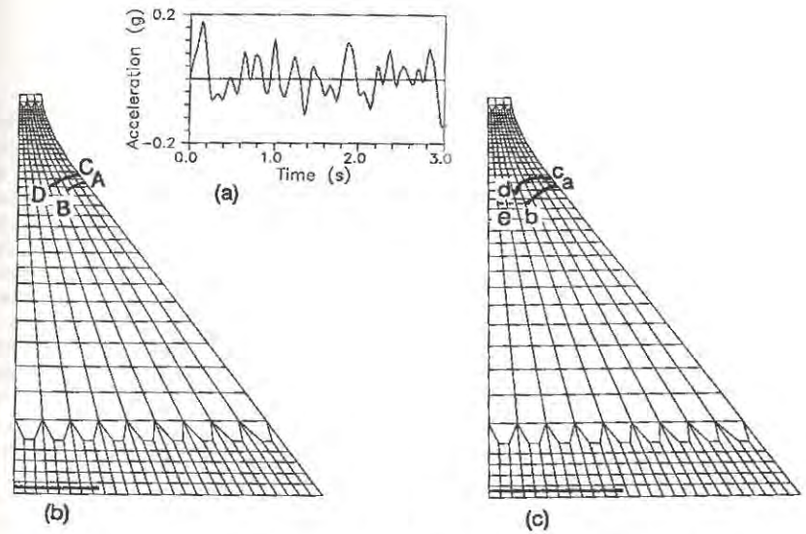

Figure 4. Seismic fracture in the concrete gravity dam.

Using the pre-seismic stress state determined for self-weight, hydrostatic pressure and coldest average temperature condition, the response of the dam has been studied under varying intensity of ground acceleration. Under seismic excitation with PGA equal to 0.25g, a crack initiates from the heel of the dam at 0.29 sec which eventually extends up to about 30% of the base area. The rigid base condition, assumed in the present study, causes an almost horizontal crack propagation along the dam-foundation interface. No other crack initiation is anticipated for this level of earthquake intensity. When the PGA is increased to 0.3g, the first crack initiates at 0.23 sec in the location A (Fig. 4b). The crack propagates horizontally through three elements and ceases propagation after curving down to point B. In the next load step (0.24 sec), a second crack is initiated at point C, which propagates up to point D in subsequent load steps. Further cracking takes place in the

elements surrounding these two crack profiles, meaning that the cracks did not effectively release the tensile stresses in that zones. Upon reversal of the dam motion in downstream direction, a crack initiates from the heel at 0.28 sec and extends about 30% of the base area. The cracks remain stable until 1.16 sec when the base crack extends up to about 70% of the base area. The program operation is terminated at 1.6 sec due to poor response prediction.

Nonlinear seismic analyses are then performed without taking into account any temperature induced stresses. For the PGA of 0.35g, only one crack is predicted which started from the heel at 0.29 sec and eventually extended up to about 40% of the base area. The PGA is scaled to 0.45g for studying the dam response under severe seismic excitation. At 0.23 sec, two cracks initiate at points a and c (Fig. 4c) and propagate up to points b and d in following steps. Some smearing of the cracks in vertical direction has also been observed. At 0.28 sec, when the downstream cracks are closed, a crack starts from the heel and propagates up to about 44% of the base area. At 1.37 sec, when the downstream cracks are open again, severe cracking occurs extending over the zone b-e (marked dotted in the Fig. 4c). The analysis was stopped at 2.5 due to poor response prediction after severe cracking.

CONCLUSIONS

The seismic safety of the concrete gravity dams appears to be reduced significantly when the severe winter temperature condition is taken into consideration. However, further investigations are necessary to determine conclusively the negative influences of seasonal temperature variations on the seismic safety of concrete dams. The smeared fracture model, applied in the present study, has shown a tendency to diffuse the crack profile in the direction normal to the primary crack propagation. Further refinements of the model are in progress to improve the performance. Nevertheless, the studies presented here, shows that the dam-foundation interface and the neck region on the downstream face are the two critical locations for cracking. The cracks initiating from the downstream face show a tendency of curving downward which is generally considered to be favourable from sliding stability considerations. In subsequent studies, the reservoir added damping has been observed to influence the seismic response of the dam by relieving the upstream face of high tensile stress that can initiate cracking.

REFERENCES

1. El-Aidi, B., and Hall, J.F., Non-linear earthquake response of concrete gravity dams. Part 1 & 2. Earth. Eng. Str. Dyn., 1989, 18, 837-865.
2. Ayari M.L., and Saouma, V.E., A fracture mechanics based seismic analysis of concrete gravity dams using discrete cracks. Eng. Frac. Mech., 1990, 35, 587-598.
3. Feltrin, G., Wepf D., and Bachmann, H., Seismic cracking of concrete gravity dams. Dam Eng., 1990, 1, 279-289.
4. Brühwiler, E., Fracture of mass concrete under simulated seismic action. Dam Eng., 1990, 1, 153-176.
5. Fenves, G., and Chopra, A.K., EAGD-84 a computer program for earthquake analysis of concrete gravity dams. Report no. UCB/EERC-84/11, 1984, University of California, Berkeley, California.

COMPUTER SIMULATION: SPLITTING TESTS OF CONCRETE THICK-WALLED RINGS

RADOMÍR PUKL
Research Engineer/Klokner Institute,
Czech Technical University of Prague
Šolinova 7, CS 166 08 Praha 6, ČSFR

BERND SCHLOTTKE
Research Engineer/Institut für Werkstoffe im Bauwesen

JOŠKO OŽBOLT
Research Engineer/Institut für Werkstoffe im Bauwesen

ROLF ELIGEHAUSEN
Professor/Institut für Werkstoffe im Bauwesen,
Stuttgart University
Pfaffenwaldring 4, D 7000 Stuttgart 80 - Vaihingen, Germany

ABSTRACT

Two non-linear program systems are used for a computer simulation of splitting failure of thick-walled concrete rings under internal radial pressure. Results of the numerical analyses for plane stress models, axisymmetrical model and 3D model are compared with available experimental data and empirical formulas. It is shown, that the behavior observed in experiments can be simulated using advanced material models, namely the nonlocal microplane model and SBETA material model based on the crack band theory. With increasing outer radius of the ring, a size effect can be observed.

Keywords: Splitting of concrete, Non-linear material models, Computer simulation, Finite element method, Fracture mechanics, Size effect

INTRODUCTION

The bond failure of deformed bars in reinforced concrete members is often caused by splitting of the concrete. A similar failure may occur in anchoring elements such as

headed-, expansion- or undercut anchors installed close to an edge. Until now, mainly experimental studies exist [4], [11]. Only a few analytical or numerical investigations, usually based on simplified material models, have been performed [10]. In order to investigate this problem, authors have performed an extensive numerical study of the splitting failure of concrete rings under internal radial pressure.

NON-LINEAR CONSTITUTIVE MODELS AND COMPUTER PROGRAMS

The present computer simulation was made with two computer codes, which were recently developed in Stuttgart: the microplane programs and SBETA.

The microplane program system, developed by Ožbolt [3], contains two non-linear computer programs, one for solution of two-dimensional problems (including axial symmetry) and another one for solution of three-dimensional problems. Both programs are using the same microstructural constitutive relation based on the nonlocal microplane material model. In this model a new level of discretization is introduced within material in the form of a final number of microplanes. The material behavior is an integral response of all microplanes. For each microplane are defined the stress-strain relations by special exponential functions. Parameters of these functions should be given in input data as material constants.

A nonlocal concept of this model avoids stress concentrations and spurious mesh sensitivity. The nonlocal concept means, that the stress at a material point depends not only on the strain in the same point, but on the weighted average of strains in a certain representative volume. This volume is defined by a characteristic length, which should be given as an input parameter. The proposed value of the characteristic length is three times the maximum aggregate size. Isoparametric quadrilateral (in two-dimensional program) or brick (in three-dimensional program) finite elements with two or three Gaussian points in each direction are used to model the analysed specimen. The microplane programs use an exponential iteration algorithm for the solution of the non-linear equations.

Another program used for this computer simulation was the commercially available program SBETA, developed by Červenka et al. [6], [7], [8]. This non-linear finite element program for plane stress analysis is based on the smeared material approach and the crack band theory [2] for modeling of concrete cracking. The softening modulus, which describes concrete toughness, is related to the fracture energy parameter G_f, crack band width and tensile strength of concrete. The crack band width is related to the element size. The mesh sensitivity is significantly reduced. A four-node quadrilateral finite element composed of two four-node subtriangles with an exact stiffness integration is used. The non-linear solution is performed by the arch-length method, which enables analysis of the post-peak behavior.

NUMERICAL MODELS

The geometry of the rings, shown in Fig.1, and material properties are taken from the experimental investigation [4]. The inner radius of the rings was constant ($R_i = 9$ mm).

The thickness of the rings was 30 mm. The outer radius of the rings was varied: 50 mm, 100 mm, 150 mm, 365 mm and 625 mm. Experimental results are available only for the first three values of outer radius. The last two values of outer radius are used according to [11], but experimental results obtained in [11] cannot be used for comparison in this study because of the different material properties of the test specimens. A symmetrical quarter of the ring was analyzed in most cases. Fine and coarse meshes with the minimal element side in radial direction of about 2.7 mm and 5.2 mm were used to observe mesh sensitivity; results for both types of meshes are almost the same.

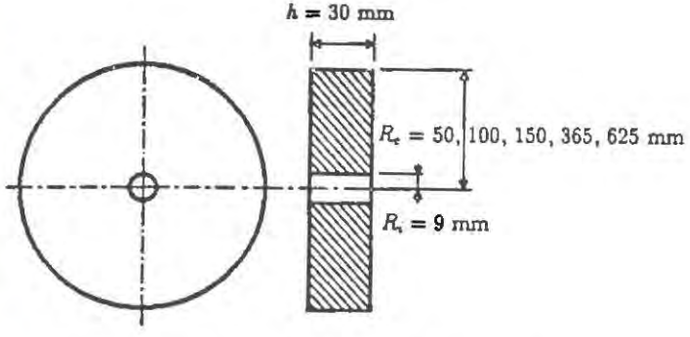

Fig.1 Geometry of the thick-walled concrete rings

Following material properties are given in [4]: Compressive cube strength f_c = 37.9 MPa, tensile strength f_t = 2.8 MPa, modulus of elasticity E = 28125 MPa, maximum aggregate size = 4 mm. These macroscopic material properties were used in SBETA analysis as input data. The material parameters of the microplane model were established from a correlation of the ring analysis with experiments [4] for the case of outer radius R_e = 100 mm, and for all three types of analysis (plane stress, axisymmetry, 3D). The same material parameters were used for the other values of outer radius R_e. A characteristic length of 12 mm was used in all cases. A study of the influence of the characteristic length for different types of analyses was performed. Results show, that the characteristic length influences the results differently in different types of analyses. In the splitting failure of the thick-walled concrete rings the influence of the characteristic length on the peak load in axisymmetrical and 3D models is relatively small; in plane stress model the peak internal pressure increases significantly with increasing characteristic length.

NUMERICAL RESULTS, COMPARISON WITH EXPERIMENTS AND WITH EMPIRICAL EQUATIONS

Table 1 contains a review of the peak values of internal pressure from analysis, experiments [4] and those calculated from the empirical formulas presented in [10]. Fig.2 shows the peak internal pressure as a function of the relative outer radius of the rings

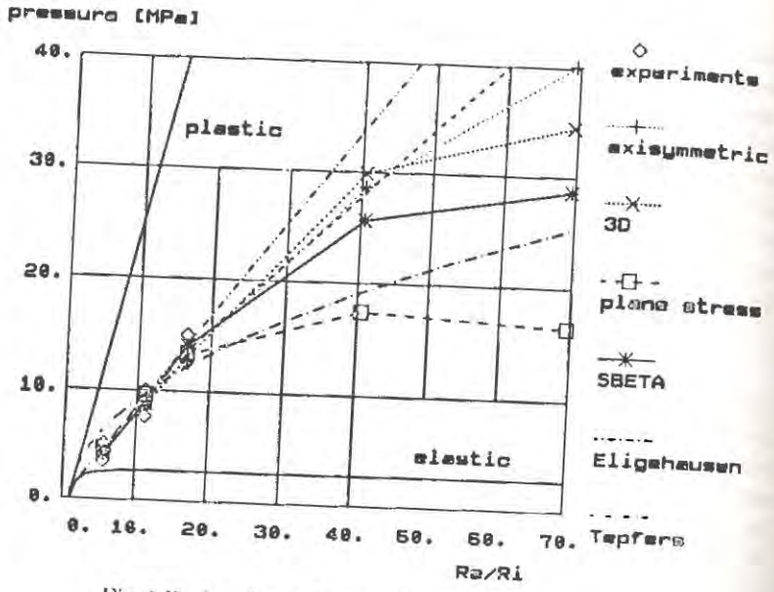

Fig.2 Peak values of internal radial pressure

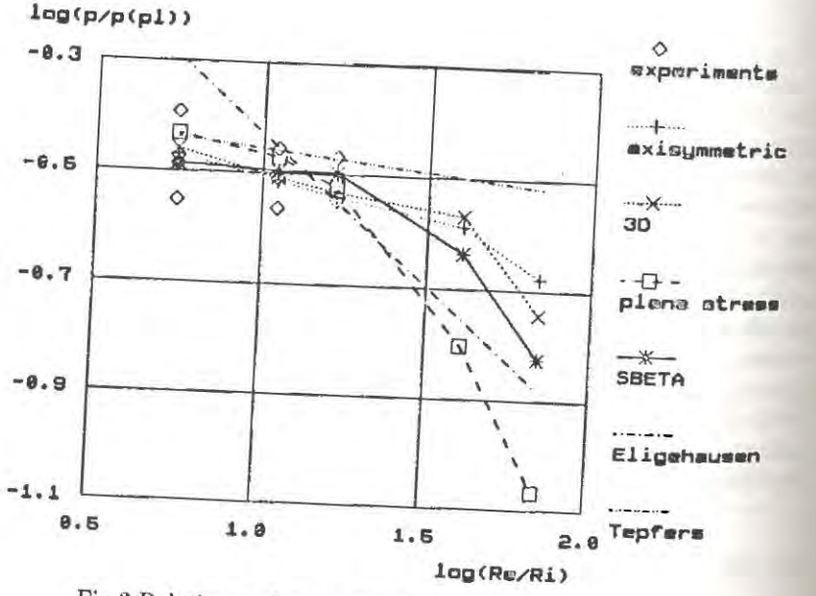

Fig.3 Relative peak pressures in logarithmic scale

ratio R_e/R_i). In Fig.3 the peak internal pressure related to the value valid for plastic analysis is plotted as a function of the relative outer radius in double logarithmic scale. A size effect can be observed from the results obtained by computer simulation. The nature of this size effect observed from Fig.3 is similar to the size effect law proposed by Bažant [1].

TABLE 1

Peak values of internal radial pressure						
Pressure p [MPa]						
outer radius R_e	[mm]	50.	100.	150.	365.	625.
ratio $r = \frac{R_e}{R_i}$		5.56	11.11	16.67	40.56	69.44
experiments [4]	serie 1	3.58	7.73	12.43	-	-
	serie 2	4.17	8.79	13.55	-	-
	serie 3	5.18	9.91	14.92	-	-
experiments	mean	4.31	8.81	13.63	-	-
microplane	plane stress	4.73	9.59	13.17	17.43	16.38
	axisymmetric	4.34	8.68	12.66	28.61	40.17
	3D	4.44	8.80	12.91	29.89	34.53
SBETA	plane stress	4.18	9.05	13.97	25.66	28.68
elastic	$f_t.\frac{r^2-1}{r^2+1}$	2.62	2.76	2.78	2.80	2.80
Tepfers [12]	$c_1.f_t.r$	4.68	9.35	14.03	34.12	58.42
Eligehausen [9]	$c_2.f_t.\sqrt{r-1}$	6.51	9.69	12.07	19.18	25.22
plastic	$f_t.(r-1)$	12.77	28.31	43.88	110.77	191.63

CONCLUSIONS

Computer simulation of the splitting failure of concrete rings was performed by two finite element codes, namely, the microplane system and SBETA. With suitable material parameters the behavior observed in experiments can be succesfully simulated using computer material models. Deviations of numerical results from the mean experimental values did not exceed the scatter of the experiments. With increasing outer radius of the ring, a size effect in simulated results can be observed.

This paper was prepared under the terms of a research cooperation between the Institute of Material Science, Stuttgart University, Germany, and the Klokner Institute, Technical University Prague, ČSFR.

REFERENCES

[1] Bažant, Z.P., Size Effect in Blunt Fracture: Concrete, Rock, Metals. ASCE Journal of the Engineering Mechanics Division, 110, 1984, pp. 518-538.

[2] Bažant, Z.P., Oh, B.H., Crack Band Theory for Fracture of Concrete. Mater Struct. RILEM, Paris, France, 16, 1983, pp. 155-177.

[3] Bažant, Z.P., Ožbolt, J., Nonlocal Microplane Model for Fracture, Damage and Size Effect in Structures. ASCE Journal of the Engineering Mechanics Division, 116, No.11, Nov. 1990, pp. 2485-2505.

[4] Bilčik, J., Priechodský, V., Stresses and Strains in Model Ring under Internal Radial Pressure. IABSE Colloquium Structural Concrete, Stuttgart, Germany, April 1991, pp. 755-760.

[5] Červenka, V., Eligehausen, R., Pukl, R., Computer Models of Concrete Structures IABSE Colloquium Structural Concrete, Stuttgart, Germany, April 1991, pp. 311-320.

[6] Červenka, V., Eligehausen, R., Pukl, R., SBETA Computer Program for Nonlinear Finite Element Analysis of Concrete Structures. Mitteilungen des Instituts für Werkstoffe im Bauwesen No.1990/1, Universität Stuttgart, Germany, 1990.

[7] Červenka, V., Eligehausen, R., Pukl, R., Simulation of Cracking and Failure of Concrete Structures, STRUCENG & FEMCAD, Grenoble, France, October 1990, pp. 323-328.

[8] Červenka, V., Pukl, R., Eligehausen, R., Fracture Analysis of Concrete Plane Stress Pull-out Tests. RILEM Conference Fracture Processes in Concrete, Rock and Ceramics, Noordwijk, Netherlands, June 1991, pp. 899-908.

[9] Eligehausen, R., Übergreifungsstösse zugbeanspruchter Rippenstähle mit geraden Stabenden. Deutscher Ausschuss für Stahlbeton, Verlag Wilhelm Ernst & Sohn, Berlin, Germany, Heft 301, 1979 (in German).

[10] Eligehausen, R., Kreller, H., Querschnittsbericht zur Rissbildung in Stahl- und Spannbetonkonstruktionen. Deutscher Ausschuss für Stahlbeton, Verlag Wilhelm Ernst & Sohn, Berlin, Germany, Heft 393, 1988, 57 p. (in German).

[11] Neuner, J., Stöckl, S., Grasser, E., Versuche an dickwandigen, unbewehrten Betonringen mit Innendruckbeanspruchung. Deutscher Ausschuss für Stahlbeton, Verlag Wilhelm Ernst & Sohn, Berlin, Germany, Heft 299, 1978, 63 p. (in German).

[12] Tepfers, R., A Theory of Bond Applied to Overlapped Tensile Reinforcement Splices for Deformed Bars. Chalmers University of Technology, Division of Concrete Structures, Publication 73:2, Göteborg, Sweden, 1973.

NUMERICAL STUDY OF GRANULE INFLUENCES ON THE CRACK PROPAGATION IN CONCRETE

J. WANG, P. NAVI, C. HUET
Ecole Polytechnique Fédérale de Lausanne
Département des Matériaux
Laboratoire de Matériaux de Construction
Switzerland

ABSTRACT

A fully automatic computer program of mesh generation for the granular materials like concrete with microcracks embedded in the matrix is presented. At the present stage the granules are represented as circles, around which the microcracks are introduced. The principles of linear elastic fracture mechanics is applied to calculate the crack propagation in this multi-cracked 2D heterogeneous material by the finite elements method. The crack arresting due to the existence of granules is observed by this numerical method. Examples concerning the influences of the volume content and the distribution of granule on the load-displacement curve are given. The load-displacement curve of the body made of the microcracked granular material subjected to the tensile loading is compared to the cases of the corresponding homogeneous body

INTRODUCTION

Generally with a servo-controlled test machine experiments can be made on the notched concrete specimen subjected to tension under the condition of the rupture control to get the post-peak (or strain softening) curve. The dominant tendency in the recent years on the fracture study of concrete is to consider the strain softening as a property of the material. It is known, for example, as shown in the references [1, 2], that according to the linear elastic fracture mechanics (LEFM) the stability of the crack propagation and the shape of the post-peak part of the load-displacement curve of the homogeneous material is highly dependent on the geometry of the specimen, the mode of loading control, the size and the rate of concentration of the pre-existing microcracks and their distribution inside the material.

One way to examine the intrinsic nature of the post-peak behavior of the concrete body is to study its development in strict relation between the micro and macro fracture process (micro-macromechanics). For that purpose one should not ignore the heterogeneity of concrete and the pre-existing of microcracks inside it. As the components of concrete (mortar and aggregates) are nearly brittle materials, LEFM can be used to study crack propagation, crack arresting and crack branching in these materials.

In this investigation concrete is simulated numerically as a two-phase material made of the granules and matrix. The microcracks (geometric discontinuities) are embedded around the

granules in the matrix. The crack propagation in this microcracked composite is calculated through the application of LEFM. A computer program of a fully automatic mesh generation has been developed to compute the stress intensity factors and the evolution of crack propagation. The mechanism of the crack arresting due to the presence of the granules is observed by this numerical simulation. The global load-displacement curves are obtained in relation with the microcrack propagations in the matrix. The phenomenon of instability occurring in the post-peak region is discussed in terms of the volume content and the distribution of the granules and the homogeneous counterpart.

MESH GENERATION

The numerical generation of the modeled concrete starts with the determination of the center of the granules represented as circles from a random generator and the size distribution from Fuller curve of the particle size distribution. An automatic mesh generation process triangulates the composite structure of the specimen. The microcracks are introduced around the granules in the matrix to simulate the interface layer between the aggregates and hydrated cement paste, which is believed to be the weak part of normal concrete. In order to calculate precisely the stress intensity factors, eight equilateral quarter-point triangular elements are produced around the crack tip. Our computer program of mesh generation for the microcracked composite can follow the whole process of crack propagation in a fully automatic way, although the topology of the specimen changes with each loading step. Figure 1 gives an example of such a mesh generation of the microcracked concrete material and mesh details around one crack tip.

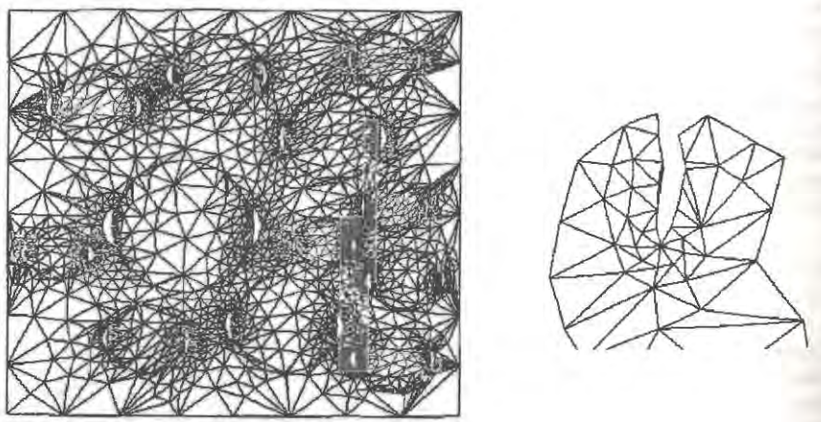

(a) (b)

Figure 1. (a) Mesh generation of the specimen with 12 granules and 24 microcracks around the granules. (b) mesh details around one crack tip.

DESCRIPTION OF THE ANALYSIS

The stress intensity factors K_I and K_{II} are calculated in the same way as [3] from the values of the node displacement of the quarter point triangular elements surrounding the crack tip. The onset and the angle of the crack propagation are obtained according to the maximum principle stress criterion [4]

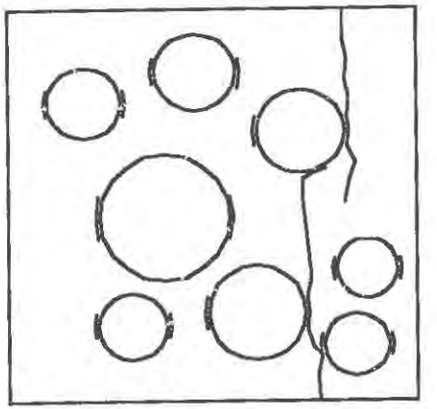

(a)

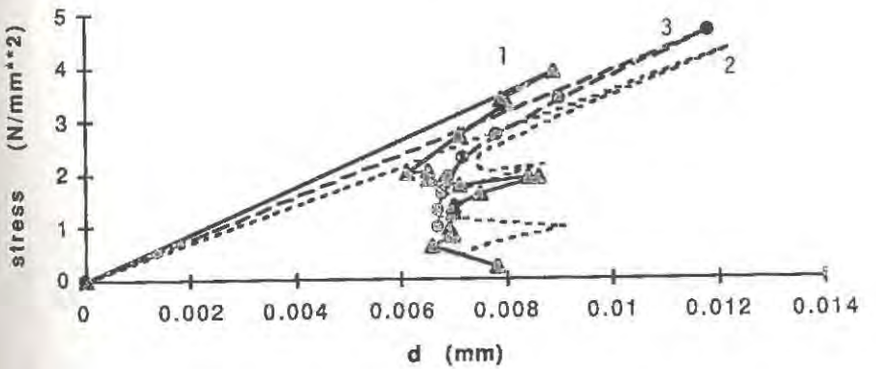

(b)

Figure 3. (a) The crack trajectory of the specimen with 8 granules. (b) The corresponding nominal stress-displacement curve.Curve 1, 2 and 3 are the cases of the heterogeneous body, the homogeneous body with same crack pattern as the heterogeneous one and the homogeneous body of one crack,respectively.

It is shown from the analytical solutions [5] that when the crack approaches the interface between two different materials with perfect bounding, the stress intensity factors decrease if second material in front of the crack has a greater Young's modulus. The stress intensity factors become zero when the crack terminates at the interface because the order of the stress singularity is bigger than -0.5. To consider this factor as well as the existence of the interface layer between the mortar and the aggregates, an arbitrary small distance between the circumference of the granule and the crack tip is maintained. There are two possible paths for the crack to propagate when it encounters the granule. One is that the crack goes further around the granule to the right hand of its original position, the other is left. It is shown from our analytical solution for the semi-infinite crack terminating at the material's interface the cleavage

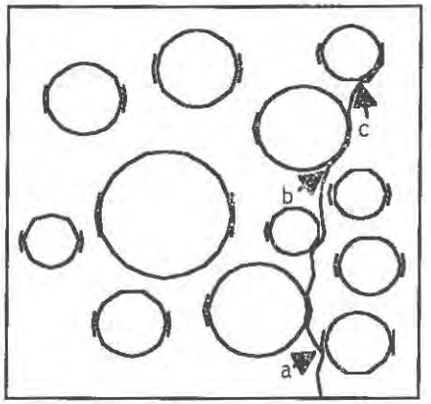

(a)

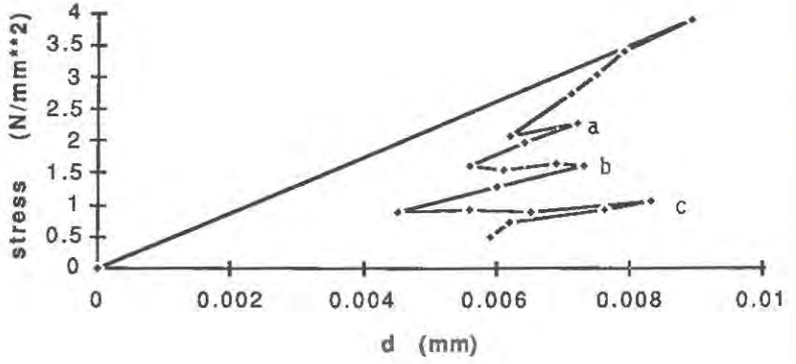

(b)

Figure 4. (a) The crack trajectory of the specimen with 12 granules. (b) The corresponding nominal stress-displacement curve.The situations of the crack encountering the granules are marked by letters a, b and c.

stress ($\sigma_{\theta\theta}$) is much larger on the plane of interface with a larger angle with the crack than the one with smaller angle. For this reason we assume that when the crack meets the granule and satisfies the criterion given in [4], it starts to propagate around the granules with a larger angle between the tangent of the granule and its original position. A simple criterion below is used to determine whether the crack still propagates around the granule or deviates into the matrix. For $\vec{n}_c \cdot \vec{n}_g \geq 0$ the crack will deviate into the matrix and for $\vec{n}_c \cdot \vec{n}_g < 0$ the crack will still go around the granule, where $\vec{n}_c$ is the direction vector of the crack propagation calculated

from the angle of the crack propagation according to [4] and $\vec{n}_g$ is unit vector of the outer normal of the granule.

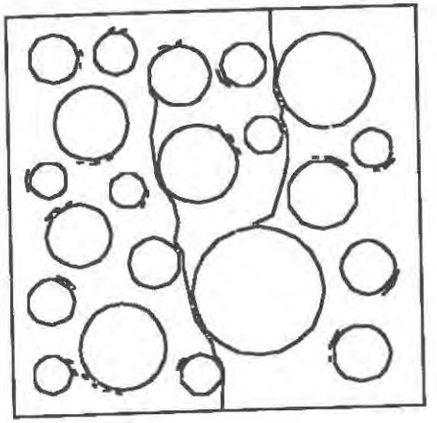

(a)

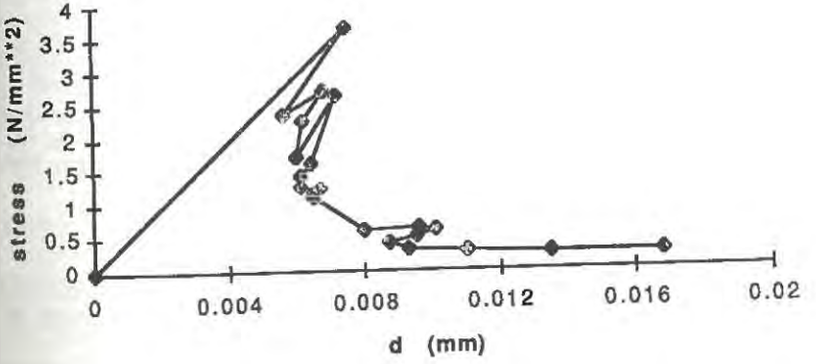

(b)

Figure 5. (a) The crack trajectory of the specimen with 21 granules. (b) The corresponding nominal stress-displacement curve.

During the fracture process the stress intensity factor K_I may become negative for some microcracks . The negative K_I means the crack closing. The situations of crack closing are also taken into consideration in our calculations. The incremental length of the crack propagation is used as the controlling parameter and is given prior to the analysis. The specimen is loaded with a fixed displacement along the opposite sides of the specimen in x

direction. The corresponding tensile reaction forces are computed for each step. In this way the equilibrium curve of the load-displacement is determined and the crack trajectory can be followed from the beginning up until the specimen is ruptured completely. The Young's modulus and Poisson's ratio of the granule and the matrix are taken as 60 GPa, 0.2 and 20 GPa, 0.2 respectively. The material toughness K_{IC} of the matrix is given as 20.0 $N/mm^{-3/2}$

RESULTS AND DISCUSSION

The numerical results are plotted in the Figures 3, 4 and 5 for the volume contents of granules as 27.8% (8 granule), 32.8% (12 granules) and 39.6% (21 granules) respectively. Figures 3(a),4(a) and 5(a) give the crack trajectories and Figures 3(b), 4(b) and 5(b) give the corresponding nominal stress-displacement curves. The initial cracks shown in Figures 3(a) and 4(a) are embedded on the left and right sides of each granules, whereas the position and the length of the initial cracks shown in Figure 5(a) are generated randomly.

In Figure 3(b) the nominal stress-displacement curves of the heterogeneous material, its homogeneous counterpart with the same crack pattern and the homogeneous body with only one crack are shown by the curve 1, 2 and 3 respectively. It is recognized that the post-peak parts of the load-displacements are different from each other due to the different structures of the material.

The situations of the crack encountering the granules are shown by the arrows and letters a, b, and c in Figure 4(a). The points corresponding to the crack approaching the granules are indicated with the same letters a, b, and c in Figure 4(b). These figures demonstrate that when the crack encounters a stiff inclusion the corresponding external force increases.

Because of the increase of the volume content of the granules, the crack trajectory in Figure 5(a) is composed of two large different cracks instead of one given in Figure 3(a) and 4(a). The two previous examples given in Figures 3 and 4 show that the instability happens right after the peak load until the complete rupture of the specimen. Whereas in the specimen with high volume content of granule this situation is different from the previous examples. As shown in Figure 5(b) although the instability occurs after the peak load, the stable situation appears after the phase of instability. We think that the volume content of the granules playing the role of the crack arresting has an important influence on the stability of the crack propagation. Actually the volume content of aggregates in normal concrete is about 70% which is much higher than what we have simulated in the numerical calculation.

REFERENCES

1. C. Huet, Méthode de détermination de l'énergie spécifique de rupture et application aux céramiques et à divers matériaux, I: Bases théoriques, Cahiers du Groupe Français de Rhéologie, novembre, 1973, **t. 3, n° 3.**

2. C. Huet, Méthode de détermination de l'énergie spécifique de rupture et application aux céramiques et à divers matériaux, II: Conséquences pratiques et expérimentation , Cahiers du Group Français de Rhéologie, septembre, 1974, **3, n° 4.**

3. C.E. Freese, D.M. Tracey, The Natural Isoparametric Triangle versus Collapsed Quadrilateral for Elastic Crack Analysis, Int. J. Fracture, 1976, **12**, pp. 767 - 770.

4. F. Erdogan, G.C. Sih, On the crack Extension in Plates under Plane Loading and Transverse Shear, J. Basic Engng., 1963, **85**, pp. 519 - 527.

5 Y. Murakami (Editor-in-chief), Stress Intensity Factors Handbook, Pergamon Press, 1987, pp. 429-640.

THE USE OF VARIOUS CRACK MODELS IN F.E. ANALYSIS OF REINFORCED CONCRETE PANELS

PETER H. FEENSTRA and RENE DE BORST
Delft University of Technology, Department of Civil Engineering /
TNO Building and Construction Research,
P.O. Box 5048, 2600 GA Delft, Netherlands.

ABSTRACT

The paper describes two crack models embedded in a total strain concept, the fixed orthogonal crack model and the coaxial rotating crack model. Within this concept, a model for reinforced concrete is presented. The salient feature in this model is the stress decomposition into a stress contribution of the concrete with a strain softening model, a stress contribution of the reinforcing steel with a elasto-plastic model and a stress contribution owing to the interaction between concrete and reinforcement. The model capabilities are demonstrated in simulations of three reinforced concrete panels.

INTRODUCTION

Fracture of concrete can be modeled following several approaches. One of the most promising approaches for implementation in a finite element program is the phenomenological approach, in which fracture is described within a continuum, the smeared crack model. Generally an elastic-softening behavior is assumed in which a gradual decrease of the stress occurs after the crack is initiated. These constitutive models can be embedded in different concepts, the decomposed strain concept and the total strain concept. The first concept is based on a strain decomposition into an elastic part and an inelastic part and has been treated comprehensively in the work of de Borst and Nauta [1] and Rots [2]. The second concept is the total strain formulation in which the stress is assumed to be a function of the total strain. The constitutive behavior of models embedded in both concepts is highly dependent upon the modeling of the shear stress-strain relation. This has resulted in different crack models, the fixed smeared crack model and the rotating smeared crack model. In this study the fixed and the rotating crack model embedded in a total strain concept will be treated.

CRACK MODELS IN A TOTAL STRAIN CONCEPT

Within a smeared crack approach the cracked material is considered as a continuum, for

which the notions of stress and strain are defined. This means that the constitutive relation can be described in terms of stress-strain relations. Commonly, and this has also been done in this study, the constitutive relation in the uncracked state is restricted to linear-elasticity. When a tension cut-off criterion is violated, this linear-elastic relation is replaced by an orthotropic stress-strain law with the axes of orthotropy in accordance with the directions of the principal strains. The explicit application of the orthotropic elasticity theory to cracked concrete is not straightforward. Indeed, the concept of a fully orthotropic material has not yet been applied to describe smeared cracking. Instead, it is assumed that cracking only influences the diagonal terms in the compliance matrix, as proposed by Bažant and Oh [3]. Then the total stress-strain relation in a plane-stress configuration is given by the following stiffness relation in the crack coordinate system n,s :

$$\sigma^c_{n,s} = \begin{bmatrix} \frac{\alpha_n E}{1-\alpha_n\alpha_s\nu^2} & \frac{\alpha_s\alpha_n E\nu}{1-\alpha_n\alpha_s\nu^2} & 0 \\ \frac{\alpha_n\alpha_s E\nu}{1-\alpha_n\alpha_s\nu^2} & \frac{\alpha_s E}{1-\alpha_n\alpha_s\nu^2} & 0 \\ 0 & 0 & \beta_s G \end{bmatrix} \varepsilon_{n,s} \qquad (1)$$

As a first approximation it is assumed that the reduction factors α_n and α_s for the Young's modulus E are only functions of the tensile strains in the considered directions, and that the shear retention factor β_s has a constant value.

The constitutive relation, eq.(1), has been expressed in the local coordinate system. Using the strain transformation matrix $\mathbf{T}(\phi)$ the relation in the global coordinate system is given by:

$$\sigma^c_{x,y} = [\, \mathbf{T}(\phi)^T \, D^c_{n,s} \, \mathbf{T}(\phi)] \, \varepsilon_{x,y} \qquad (2)$$

in which the superscript T denotes the transpose and ϕ is the angle between the local crack coordinate system and the global coordinate system. The tangential stiffness matrix which is needed in a non-linear analysis which employs a Newton-Raphson procedure is given by:

$$\dot{\sigma}^c_{x,y} = \left[\mathbf{T}^T(\phi) \frac{\partial \sigma^c_{n,s}}{\partial \varepsilon_{n,s}} \mathbf{T}(\phi) + \frac{\partial \mathbf{T}^T(\phi)}{\partial \phi} \sigma^c_{n,s} \frac{\partial \phi^T}{\partial \varepsilon_{x,y}} \right] \dot{\varepsilon}_{x,y} \qquad (3)$$

Fixed crack model - in the fixed crack model the principal axes of orthotropy are kept fixed during the post-cracking phase. This results in the following constitutive model:

$$\sigma^c_{x,y} = [\, \mathbf{T}^T(\phi_0) \, D^c_{n,s} \, \mathbf{T}(\phi_0)] \, \varepsilon_{x,y} \qquad (4)$$

in which ϕ_0 the constant angle between the global coordinate system and the crack coordinate system. Because $\partial \mathbf{T}^T / \partial \phi = 0$, the tangential stiffness matrix reads:

$${}^t D^c_{x,y} = \mathbf{T}^T(\phi_0) \left[\frac{\partial \sigma^c_{n,s}}{\partial \varepsilon_{n,s}} \right] \mathbf{T}(\phi_0) \qquad (5)$$

This model has also been used by Rots, Nauta, Kusters and Blaauwendraad [4] as an extension of the fixed crack model proposed by Bažant and Oh [3]. A more fundamental treatment

of the fixed crack model is given in the inspirational work of Willam, Pramono and Sture [5].

Rotating crack model - the rotating crack model differs notably from the fixed crack model in the post-cracking phase. The principal axes of orthotropy are not kept constant, but rotate coaxially with the principal strains during crack propagation. The constitutive model is now defined by the full expression of eq.(2) with $\mathbf{T}(\phi)$ a function of the global strains. The tangential stiffness matrix ${}^t D^c_{x,y}$, is more complicated because of the introduction of the spin of the principal stress axes and is given by the full expression of eq.(3). The first term of the tangential stiffness matrix is equal to the tangential stiffness matrix that follows from the fixed crack approach, and can be considered as the material tangent stiffness. The second term, due to the spin of the principal axes, is a function of the stresses and the angle ϕ between global coordinate system and crack coordinate system. The rotating crack model does not involve an independent shear-retention factor β, but the coaxiality condition results in a shear stiffness that is associated with the rotation of the principal axes.

CONSTITUTIVE MODEL FOR REINFORCED CONCRETE

The constitutive model for reinforced concrete used in this study is based on the assumption that reinforced concrete is a composite material. With this assumption it is possible to decompose the total stress in the stress components of the constituent materials, concrete and steel, and a stress component due to the interaction between concrete and steel. The reinforcing steel is modeled with an embedded formulation in which it is assumed that the strain for both materials is equal. The total stress is now given by:

$$\sigma_{x,y} = \sigma^c_{x,y} + \sigma^s_{x,y} + \sigma^{ia}_{x,y} \qquad (6)$$

in which the superscript c denotes the concrete, s the reinforcing steel and ia the stresses due to the interaction between concrete and reinforcement. The constitutive relation for the concrete has already been derived (cf. eq.(2)):

$$\sigma^c_{x,y} = [\mathbf{T}^T(\phi) \, D^c_{n,s} \, \mathbf{T}(\phi) \,] \, \varepsilon_{x,y}$$

The constitutive relation for the reinforcing steel looks very similar:

$$\sigma^s_{x,y} = [\, \mathbf{T}^T(\theta) \, D^s_{p,q} \, \mathbf{T}(\theta) \,] \, \varepsilon_{x,y} \qquad (7)$$

with θ the inclination angle between the reinforcing grid and the global x,y-coordinate system. The constitutive relation for the reinforcing grid is given by the matrix:

$$D^s_{p,q} = \mathrm{diag}(\, \rho_p E^{ep}_s \, , 0 \, , 0 \,) \qquad (8)$$

with ρ_p the reinforcing ratio in the p-direction of the grid and E^{ep}_s the secant elasto-plastic modulus for the considered direction.

The stress contribution owing to the interaction between concrete and reinforcement is given by:

$$\sigma^{ia}_{x,y} = [\, \mathbf{T}^T(\theta) \, D^{ia}_{n,s} \mathbf{T}(\theta) \,] \, \varepsilon_{x,y} \qquad (9)$$

with the constitutive relation for the interaction in the reinforcement directions:

$$D^{ia}_{n,s} = \text{diag}(\cos\alpha\, E_{bp} , 0 , 0)$$

with α the angle between reinforcement and the normal of the crack. The secant stiffness modulus E_{bp} is the result of the bond stresses between the reinforcement and the concrete between the cracks. This contribution to the stiffness of the structure is commonly known as the tension-stiffening effect. The tension-stiffening modulus E_{bp} is a function of the strain in the reinforcement. This tension-stiffening component is assumed to be a tri-linear function according to Cervenka, Pukl and Eligehausen [6].

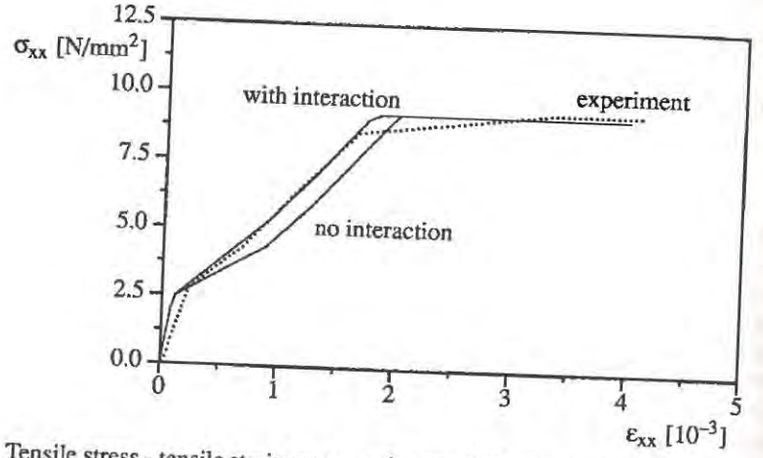

Figure 1. Tensile stress - tensile strain response for panel PB25, uniaxial tensile loading.

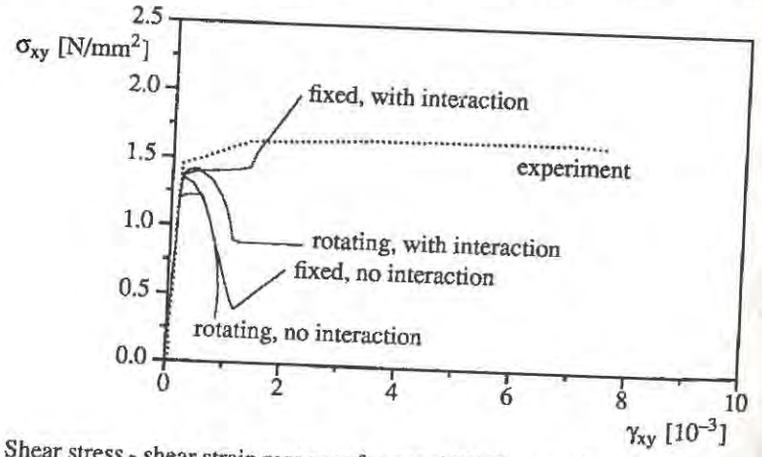

Figure 2. Shear stress - shear strain response for panel PB18, pure shear loading.

UNIAXIALLY REINFORCED CONCRETE PANELS BHIDE AND COLLINS

Numerical simulations with the above described model for reinforced concrete were carried

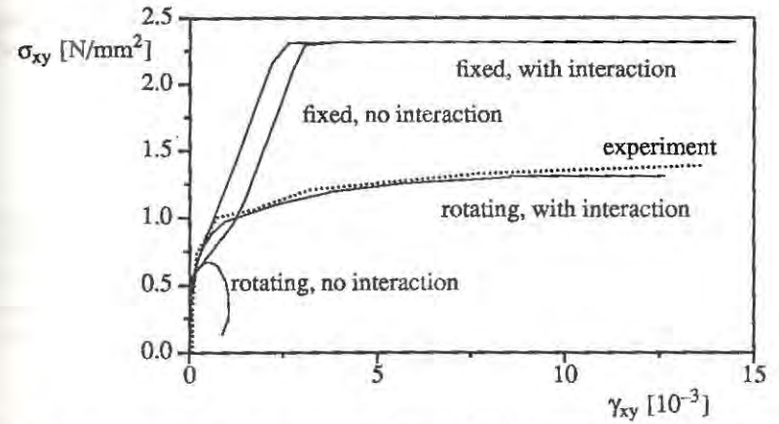

Figure 3. Shear stress - shear strain response for panel PB21, combined tension-shear loading.

out for three uniaxially reinforced panels of Bhide and Collins [7] with dimensions 890x890x70 [mm³]. The panels were selected from group III, with a reinforcement ratio of 2.195 % in the element x-direction and a reinforcement ratio of 0.0 % in the element y-direction. The concrete has been modeled with a Young's modulus $E_c = 20000$ [N/mm²], Poisson's ratio $\nu = 0.2$, compressive strength $f_{cc} = 21$ [N/mm²], a tensile strength $f_{ct} = 1.51$ [N/mm²] and a fracture energy $G_f = 0.1$ [Nmm/mm²]. A crack spacing of 100 [mm] has been assumed which means that 8–9 cracks are distributed over the element size. The total amount of energy consumed in the panel is then 8–9 times the fracture energy for one crack. The total strain concept and linear tension softening have been used. Both the rotating crack model and the fixed crack model have been utilized. For the latter model a shear retention factor $\beta = 0.2$ has been adopted. The behavior of the concrete under compression has been assumed to be linear elastic. The compressive stresses in the panels remain small, as has been observed in pilot calculations, which justifies the assumption of linear-elastic behavior under compression. The reinforcing steel has been modeled with a elasto-plastic model with a Young's modulus $E_s = 210000$ [N/mm²] and a yield stress $f_{sy} = 420$ [N/mm²].

The finite element configuration for the analysis is one four-noded element with four integration points for both the reinforcement and the concrete. The panel has been loaded in three different cases: uniaxial tension in the element x-direction, panel PB25; a pure shear loading, panel PB18; and a combined uniaxial tension - shear loading, panel PB21.

The tensile stress - strain response for panel PB25, see Figure 1, has been used to calibrate the parameters of the interaction model, which have been used in the simulation of the other two experiments. Both crack models give the same results, because the crack does not rotate. The panel loaded in pure shear, panel PB18, gives an entirely different shear stress - shear strain response for the different crack models, see Figure 2. The ductile behavior of the experiment could not be simulated in either case. The analyses show a much more brittle response. The fixed crack model shows a linear stress - strain relation after the crack has fully developed, which is a consequence of the assumption of a constant shear retention factor.

This behavior becomes very dominant in the combined tension - shear loaded panel PB21 as has been depicted in Figure 3. The fixed crack model, with or without the tension-stiffening effect shows a much too stiff behavior and ultimately fails because of yielding of the reinforcement. The rotating crack model without the tension-stiffening shows a softening

behavior after cracking and is not capable of describing the ductile behavior of the panel. If the tension-stiffening effect is taken into account, the rotating crack model shows a good approximation of the experimentally measured response of the panel.

CONCLUDING REMARKS

The results of the simulation of the reinforced panels demonstrate the capabilities of the proposed model for simulating reinforced concrete behavior. The main advantage of the model is the separate treatment of the softening behavior of the concrete and the tension-stiffening behavior of the reinforced concrete due to bond stresses between the cracks. Unidirectionally reinforced concrete panels are very sensitive to the inclusion of the tension-stiffening effect and the modeling of the shear resistance of the cracked concrete.

ACKNOWLEDGEMENTS

The calculations have been carried out with the DIANA finite element code of TNO Building and Construction Research. The financial support by the Netherlands Technology Foundation (STW) under grant DCT-71.1405 and by the Commission of the European Communities through the Brite-Euram program (project BE-3275) is gratefully acknowledged.

REFERENCES

1. de Borst, R. and Nauta, P. (1985). Non-orthogonal cracks in a smeared finite element model. *Eng. Comput.* , (2), p. 35-46.
2. Rots, J.G. (1988). Computational modeling of concrete fracture. Dissertation, Delft University of Technology, Delft, Netherlands.
3. Bažant, Z.P. and Oh, B.H. (1983). Crack band theory for fracture of concrete. *Materials and Structures* , RILEM, 93(16), p. 155-177.
4. Rots, J.G., Nauta, P., Kusters, G.M.A. and Blaauwendraad, J. (1985). Smeared crack approach and fracture localization in concrete. *Heron* , 30(1), p. 3-48.
5. Willam, K.J., Pramono, E. and Sture, S. (1987). Fundamental issues of smeared crack models, in *Proc. SEM/RILEM Int. Conf. Fracture of Concrete and Rock* , eds. S.P. Shah et al., Houston, p. 142-157.
6. Cervenka, V., Pukl, R. and Eligehausen, R. (1990). Computer simulation of anchoring technique in reinforced concrete beams, in *Proc. Int. Conf. Computer Aided Analysis and Design of Concrete Structures* , Part I, eds. N. Bićanić et al., Pineridge Press, Swansea, p. 1-21.
7. Bhide, S.B. and Collins, M.P. (1987). Reinforced concrete elements in shear and tension. Publication 87-02, Univ. of Toronto, Dept. of Civil Engrg., Canada.

FINITE ELEMENT ANALYSIS OF CONCRETE STRUCTURES WITH SMEARED HETEROGENEITY

RAUL ROSAS E SILVA
Associate Professor
ROQUE LUIZ DA SILVA PITANGUEIRA
Graduate Student
Department of Civil Engineering
Pontificia Universidade Catolica do Rio de Janeiro
Marques de Sao Vicente 225, Rio de Janeiro, RJ 22453, Brazil

ABSTRACT

Usual models of cracking and fracture phenomena in concrete and reinforced concrete structures consider the concrete as a material matrix with initially isotropic homogeneous properties. Upon cracking or damage the material becomes anisotropic and heterogeneous. This paper presents a two-dimensional finite element model which includes the initial heterogeneity of concrete in a simple manner, similar to the smeared approach used for the post-damage effects in most homogeneous models. The enhancement in understanding and visualization of cracking is demonstrated by example of a pull-out test.

INTRODUCTION

The representation of the mechanical behavior of concrete structures benefits much from developments in the area of constitutive modelling. However, the microstructure of concrete should also be considered in a rational model for realistic prediction.

Models of crack propagation in concrete can be discrete [1] or smeared [2]. The smeared crack approach considers the cracks as regions of damaged material in the finite elements and appears to be a more convenient tool for approximate modelling of the propagation of cracking patterns occurring in concrete structures. Similar considerations apply to concrete under compression in the inelastic range.

An attempt to model the constituents of concrete by using a discrete approach would amount to considerable computer effort. However, the microstructure can be accounted for in a simple manner, by considering the material as initially heterogeneous and assigning to each element (or integration point) different properties. This approach should involve an

approximation similar to that introduced by the post-damage high degree of heterogeneity in the usual smeared models.

Herein the concrete is considered as a statistical combination of constituent materials with different properties (aggregate, paste and interface material). Several benefits are obtained from this approach: first, undue singularities are avoided (similar to buckling analysis of imperfect structures); second, certain effects of brittleness and nonlinearity may appear which are not present in the homogeneous model; third, a better understanding of progressive damage phenomena is provided.

MODEL FOR PROPERTIES OF CONCRETE

The mechanical properties of concrete are related to the low strength of the interface region between the mortar and the aggregate [3]. Solid concrete can be represented as a three-phase material with aggregate, paste/mortar and interface material. Experimental results are available [3,4]. The parameters h (characteristic size of the material), G_f (energy per unit area of fracture surface) and $g_f = G_f/h$ (energy per unit volume of smeared cracked or damaged material) are utilized, following Bazant [2].

The stiffness matrix of a finite element is obtained by numerical integration, Eq. 1, where **K** is the stiffness matrix, t is the element thickness, $\mathbf{D}_{jk}$ is the constitutive matrix, $\mathbf{B}_{jk}(r,s)$ is the matrix which gives the strain-nodal displacement relations, and $J(r_j,s_k)$ is the determinant of the transformation matrix from global x,y coordinates to natural r,s coordinates in the usual parametric mapping, j and k are indexes for the integration points, r_j and r_k are the respective coordinates, w_j and w_k the associate weights, and NG is the number of points in each direction.

$$\mathbf{K} = t \sum_{j=1}^{NG} \sum_{k=1}^{NG} w_j\, w_k\, \mathbf{B}^T(r_j, s_k)\, \mathbf{D}_{jk}\, \mathbf{B}(r_j, s_k)\; J(r_j, s_k) \qquad (1)$$

In the usual models, matrix $\mathbf{D}_{jk}$ is the same for all integration points, in the start of the analysis; with deformation, this matrix is modified to account for damage in tension and compression. Herein, the initial properties of each Gauss point are associated to the components of concrete, according to a random number generator and a constant probability corresponding to the volume fraction of each material in the mixture, as illustrated in Fig. 1. The values presented correspond to the data in [4] and the fraction of interface material (15%) was assigned in order to give consistent results in standard tension and compression tests.

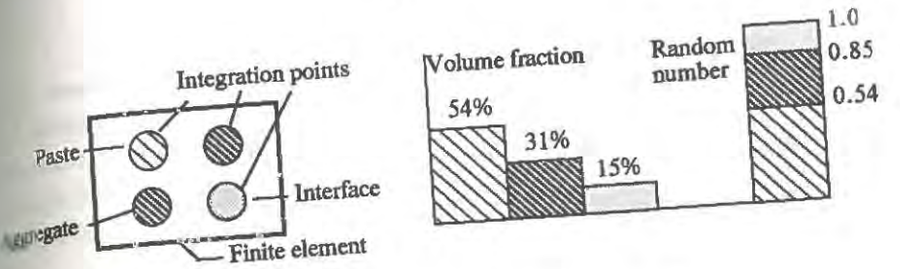

Figure 1. Concrete materials and finite element model.

EXAMPLE

The pull-out test is modelled for both initially homogeneous and heterogeneous materials. The equivalent homogeneous material corresponds to the experimental data of Bazant and Pfeiffer [4] and Monteiro [3], with 15% of interface material having 1 % of the strength of the cement paste.

Figure 2 provides a picture of the result for the heterogeneous model. The homogeneous model, in this case, reached collapse with very small previous cracking, at 80% of the maximum load level for the heterogeneous model; the force along the rod was less concentrated at the the point of load application in the heterogeneous model.

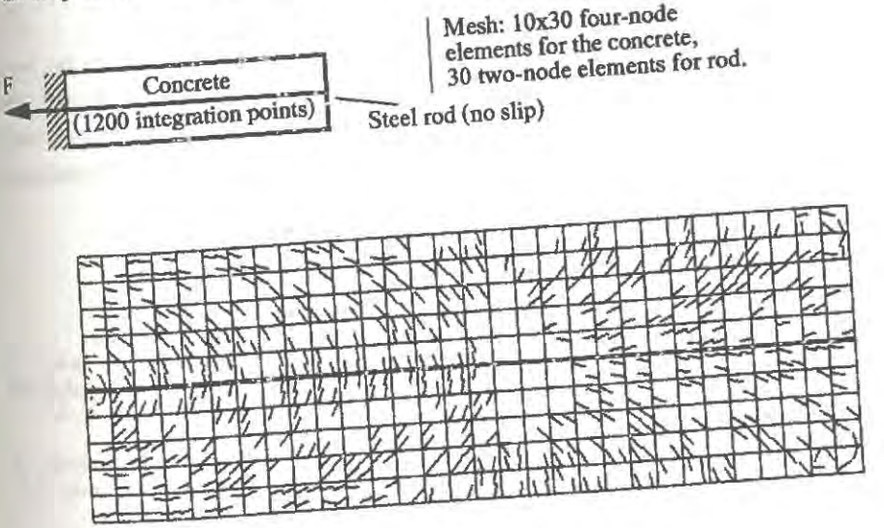

Figure 2. Pull-out example data and cracking pattern for heterogeneous model.

A detailed view of the cracks shows that they emanate from the aggregate poles. Figure 3 presents such a view for a simple tension test (triangles are aggregate particles; lines are cracks; paste and interface are dots with different densities); similar results are obtained for simple compression (with cracks parallel to the force direction) and more general situations. Thus, despite the smeared nature of the analysis, stress gradients are introduced which provide realistic crack patterns.

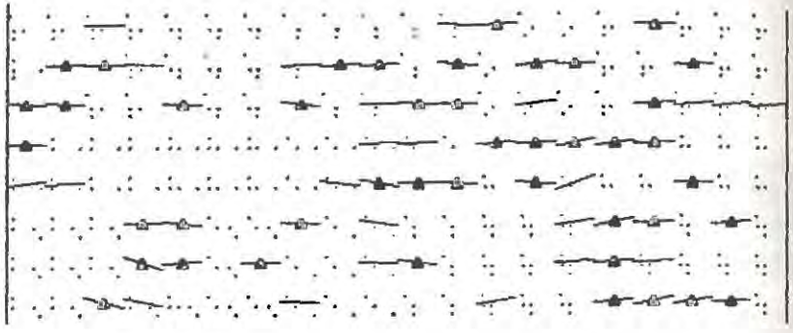

Figure 3. Detailed view of crack pattern in simple tension.

FINAL CONSIDERATIONS

The proposed heterogeneous model avoids premature instabilities and allows for better understanding and visualization of progressive damage in concrete. However, few test results are available for the individual components of concrete. Further work is necessary to develop a three-dimensional realistic model which takes into account the spatial distribution and interaction of the constituent materials.

REFERENCES

1. Ingraffea, A.R. and Saouma, V., Numerical Modeling of Discrete Crack Propagation in Reinforced and Plain Concrete. In Fracture Mechanics of Concrete: Structural Application and Numerical Calculation, eds. G.C. Sih and A. Ditommaso, Martinus Nijhoff, 1985, 171-225.

2. Bazant, Z.P., Mechanics of Fracture and Progressive Cracking in Concrete Structures. In Fracture Mechanics of Concrete: Structural Application and Numerical Calculation, eds. G.C. Sih and A. Ditommaso, Martinus Nijhoff, 1985, 1-94.

3. Monteiro, J.P.M., Microstructure of Concrete and its Influence on the Mechanical Properties. Ph.D. thesis, Department of Civil Engineering, Univ. of California, Berkeley. 1985.

4. Bazant, Z.P. and Pfeiffer, P.A., Determination of Fracture Energy from Size Effect and Brittleness Number. ACI Materials Journal, 1987, 84, 463-480.

Chapter 4

Experimental Methods and Determination of Fracture Characteristics

Principal Lecture

FRACTURE PROCESS ZONE AND FRACTURE ENERGY

FOLKER H. WITTMANN
Institute for Building Materials
Swiss Federal Institute of Technology, ETH Zürich
8093 Zürich, Switzerland

ABSTRACT

The fracture process zone is described in a phenomenological way. In the damaged zone stresses are transferred by friction and interlocking of aparticles. If the width of the specimen at the crack tip is not wide enough the full interlocking mechanisms can not be activated. Further it is assumed that the fracture process zone is confined close to the notch tip and when the crack approaches the end of the ligament. In the center part of the ligament the fracture process zone can extend until a maximum is reached. Under these conditions a maximum of fracture energy is consumed. To describe this effect a local fracture energy which varies along the ligament is introduced. An analytical expression is deduced which allows us to determine the local fracture energy if the global fracture energy has been measured on identical specimens having different notch lengths. Experimental results are presented. It is found that a ligament width of about four times the maximum aggregate size is needed to fully activate friction and interlocking in the fracture process zone. Within a given specimen geometry fracture energy increases with increasing ligament length. The local fracture energy is found to increase initially and then decrease as the crack approaches the end of the ligament. This effect explains why the fracture energy depends on the ligament length.

INTRODUCTION

Many years ago it has been realized that linear elastic fracture mechanics can not be applied. to predict crack formation in a composite material such as concrete. Several alternatives have been developed in the meantime. It has been widely agreed by now that concrete must be considered to be a material with a characteristic strain softening. This approach is essentially based on the work of Hillerborg and his coworkers [1,2].

In order to apply this concept numerically we need four material parameters. First we need the specific fracture energy, that is the energy necessary to create a crack divided by the cross section of the broken ligament. Then we need the tensile strength of the material and at least two parameters to characterize the softening branch. If we assume a simple power law to describe the bridging stresses σ behind the fictitious crack tip the strain softening can be characterized by the critical crack width w_c at which no stress is transferred any more and the shape coefficient n.:

$$\frac{\sigma}{f_t} = \left[1 - \frac{w}{w_c}\right]^n \qquad (1)$$

A RILEM Recommendation on how to determine fracture energy has been published in 1985 [3]. The remaining three material parameters are often determined by means of a least squares fit using complete and stable stress strain diagrams. As a first approximation for standard concrete a bilinear strain softening branch has proved to be useful [4].

It is obvious that the four material parameters mentioned above depend on the concrete composition, the age, and the rate of loading. All properties of concrete depend, by the way, on these factors. But are the parameters of nonlinear fracture mechanics independent of the size of a specimen? This question is vital if we want to apply properties determined on laboratory specimens for the prediction of the behaviour of real structures.

After a phenomenological description of the fracture process zone some experimental data will be presented in this contribution in order to elucidate the influence of width and length of the fracture process zone on the corresponding fracture energy.

PHENOMENOLOGICAL DESCRIPTION OF THE FRACTURE PROCESS ZONE

In a bending or direct tension test we can assume that the fracture process zone is in average as wide as the ligament. In Fig.1 a schematic representation of the fracture process zone is shown [5]. We subdivide the damaged zone ahead of a real crack in an inner zone with interacting microcracks. The remaining bridging stress is transferred by friction and aggregate interlock. This inner zone is surrounded by a zone in which isolated microcracking takes place.

If the width of the fracture process zone is equal to about one maximum aggregate size, then cracks as shown in the inner zone in Fig.1 have a certain probability to run through the entire specimen. It is not likely that strong interlocking can be built up under these conditions. If the fracture process zone, however, is wide enough full interlocking of the separating particles in the composite structure can be developed.

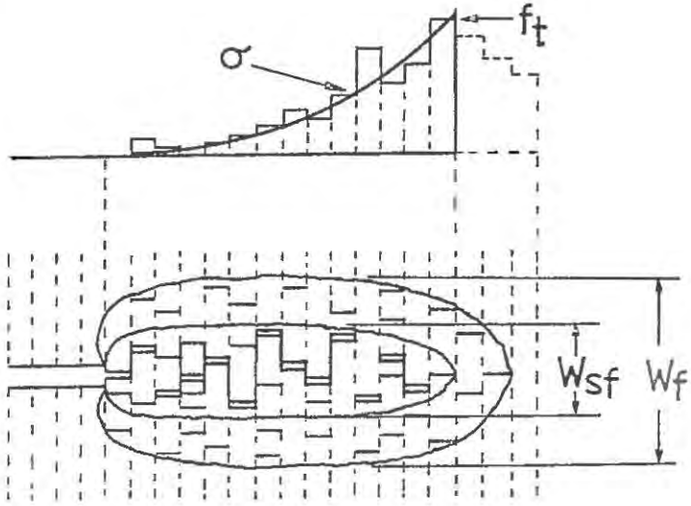

Figure 1. Schematic representation of the fracture process zone and the corresponding bridging stresses. The fracture process zone is subdivided into an inner softening zone and an outer micro fractured zone [5].

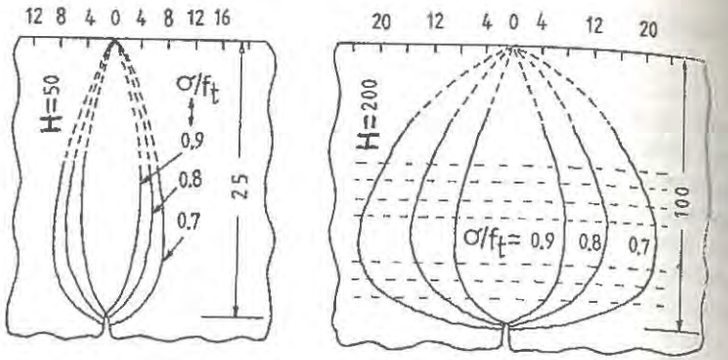

Figure 2. Lines of identical maximum values of the first principal stress for two beams under bending [6]. Results of beams with H = 50 mm and H = 200 mm are shown, respectively. In both cases a notch with a length of half the beam height is assumed. The first principal stress is related to the tensile strength.

Petersson has already pointed out that the width of the area within the lines of equal first principal stress increases with the height of the beam [6]. Results of this analysis are shown in Fig.2 for beams having a height H = 50mm and H = 200 mm, respectively. Lines of equal maximum values of the first principal stress related to the tensile strength of the material are shown.

Let us assume that microcracking within the area enclosed by the principal stress isolines of $\sigma / f_t = 0.8$ contributes to the measured fracture energy. Then in the case of H = 50 mm the maximum width of this zone is about 12 mm while it is about twice as wide if H = 200 mm. It is plausible to assume that in the latter case more energy is consumed to separate the ligament.

INFLUENCE OF THE WIDTH OF THE SPECIMEN

In order to investigate the influence of the width of the ligament on the fracture energy two series of experiments have been carried out. Cubes of 200 x 200 x 200 mm have been cast with a maximum aggregate size of 8 mm and 32 mm, respectively, and having both a water/cement ratio of 0.5. From these cubes slices ranging from 10 mm to 160 mm thickness have been cut. On these slices fracture energy has been

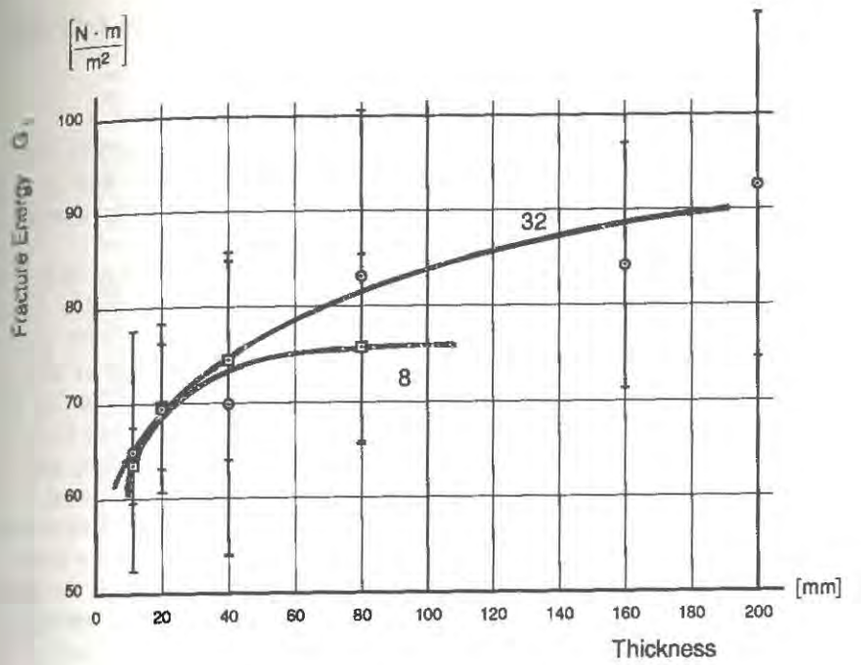

Figure 3. Experimentally determined fracture energy of concrete as function of the width of the ligament. Results of concrete having a maximum grain size of 8 mm and 32 mm, respectively, are shown.

determined after an age of 28 days with the wedge splitting technique [7]. More details on the preparation of the specimens and the test procedure are given in [8].

In Fig.3 the measured fracture energy is shown as function of the width of the specimens. As expected, concrete with bigger maximum aggregate size has a higher fracture energy. But it can be seen that for both types of concrete the fracture energy increases with increasing width of the fracture process zone and finally reaches a constant value. From these results we can conclude that a width corresponding to about four times the maximum aggregate size is necessary in order to fully activate the interlocking mechanisms in the fracture process zone.

DEVELOPMENT OF THE FRACTURE PROCESS ZONE ALONG THE CRACKING LIGAMENT

In order to study the extension of the fracture process zone in preloaded specimens we developed the multi-cutting method [9,10]. Wedge splitting tests are used in this case. A fracture process zone is created by preloading until a certain crack mouth opening is reached.

Then the damaged ligament is removed by successive cutting. In Fig. 4 a typical example is shown. In this case the total ligament length is mm. The lower solid line shows the compliance of the specimen as function of the increase Δa of the notch. Due to the damage by an applied load the initial compliance increases to the value given by the horizontal dashed line in Fig.4. As long as we remove by successive multi-cutting parts of the ligament which are not load bearing any more the compliance remains constant. When we remove partially load bearing material, that means material from the fracture process zone then the compliance starts to increase again. Finally, when we have removed the fracture process zone completely by cutting, the measured compliance must be identical with the compliance of the undamaged specimen.

In the example shown in Fig.4 the fracture process zone is determined to be 34 mm. This value has been measured on specimens made with a water/cement ration of 0,4 and a maximum grain size of 4 mm.

In Fig.5 results obtained by the multi-cutting method are shown. It can be seen that the length of the fracture process zone decreases as the tip of the fictitious crack approaches the back of the specimen. The predicted values shown in Fig.5 have been obtained by evaluating loading and unloading cycles measured on identical specimens [11].

We can conclude that the length of the fracture process zone increases, reaches its maximum when the real crack starts to grow, and then decreases as the fictitious crack approaches the end of the ligament.

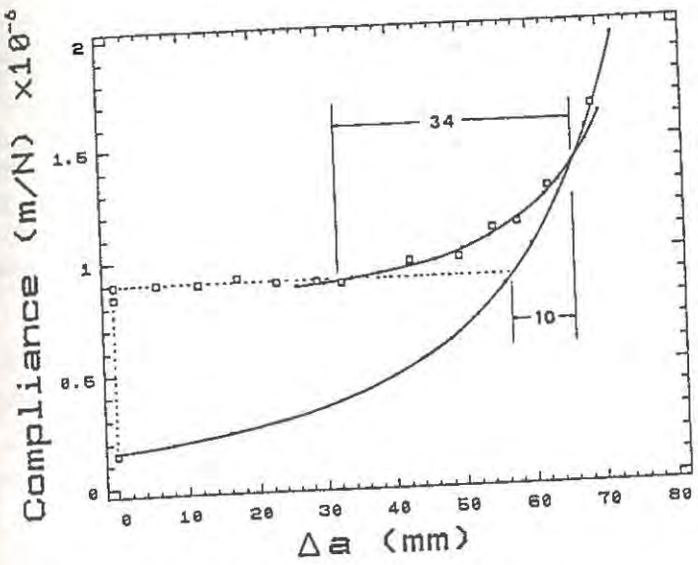

Figure 4. Typical example of a result of the multi-cutting method. The compliance of a wedge splitting specimen is first measured as function of the length of the initial notch. Then a fracture process zone induced by loading is removed by successive cutting while the compliance is measured after each cut.

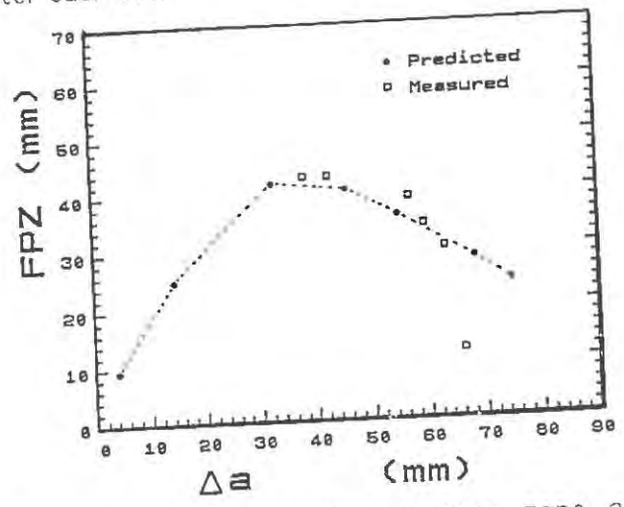

Figure 5. Length of the fracture process zone as determined experimentally by the multi-cutting method as function of the increase Δa of the initial notch. For comparison, values obtained from loading unloading cycles are shown.

LOCAL FRACTURE ENERGY

We have seen in the preceding section that the length of the fracture process zone varies along the ligament. When we described the development of the fracture process zone phenomenologically we have seen that not only the length but also the height varies along the ligament. Both at the beginning and at the end of the ligament the potentially damaged zone is strongly confined. From this we can expect that fracture energy also varies along the ligament. For this reason we introduce here a local fracture energy g_f.

Let P be the applied load, δ the displacement in the loading plane, a the initial crack length or notch, and (W-a) B the projected fracture area. The specific fracture energy G_f is then given by:

$$G_f(a) = \frac{1}{(W-a)\,B} \int P\, d\delta \qquad (2)$$

Now we introduce an x-axis along the ligament with x = 0 at the initial crack tip. When g_f is the local fracture energy for the infinitesimal area B d x on the x-axis, then the total fracture energy for a ligament with length (W-a) is given by:

$$G_f = \int P\, d\,\delta \quad = B \int_0^{W-a} g_f(x)\, dx \qquad (3)$$

From equ (3) and (2) we find

$$(W-a)\,B\;\; G_f(a) = \int P\, d\,\delta = B \int_0^{W-a} g_f(x)\, dx \qquad (4)$$

and for the specific fracture energy G_f it follows

$$G_f(a) = \frac{1}{(W-a)} \int_0^{W-a} g_f(x)\, dx \qquad (5)$$

After having introduced some simplifying assumptions we can deduce from equation (5) an expresson for $g_f(a)$ [5]:

$$g_f(x) = G_f(a) - (W-a)\,\frac{dG_f(a)}{da} \qquad (6)$$

If $G_f(a)$ is constant we find $G_f = g_f$.

Wedge splitting tests have been carried out on specimens with three different sizes, i.e. 150 x 150 x 60 mm, 200 x 200 x 60 mm, and 500 x 500 x 100.mm. For all three test series the ligament length has been varied. The water/cement ratio was always 0,5 and the maximum aggregate size 32 mm. For more details on the experimental procedure see [8].

In Fig.6 the measured specific fracture energy G_f for all three test series is shown as function of the initial notch length related to the height of the specimens. As the ligament decreases the specific fracture energy decreases as well.

If we plot the data shown in Fig.6 as function of the ligament length we obtain Fig.7. In this case the values observed on large specimens (500 x 500 x 100 mm) have been corrected for a ligament width of 60 mm in order to be comparable with results obtained on small and medium size specimens. The specific fracture energy of the small and medium size specimens increases with the ligament length and values follow the same function within the experimental error. The corresponding function obtained on large specimens, however, is shifted towards lower fracture energies. This tendency can be explained by the higher eccentricity in large specimens for the same ligament length and this effect is discussed in more detail in another contribution to this volume [12].

If we use equation (6) we can calculate the local fracture energy along the ligament $g_f(x)$ if $G_f(a)$ is known. One typical example is shown in Fig.8. In this case data shown in Fig.6 for the medium size specimen are evaluated. It can be seen that the local fracture energy first increases and after having reached a maximum decreases again as the crack approaches the end of the ligament. This variation can be interpreted by the changes of the fracture process zone as discussed in this contribution. At the beginning and towards the end the fracture process zone is confined.

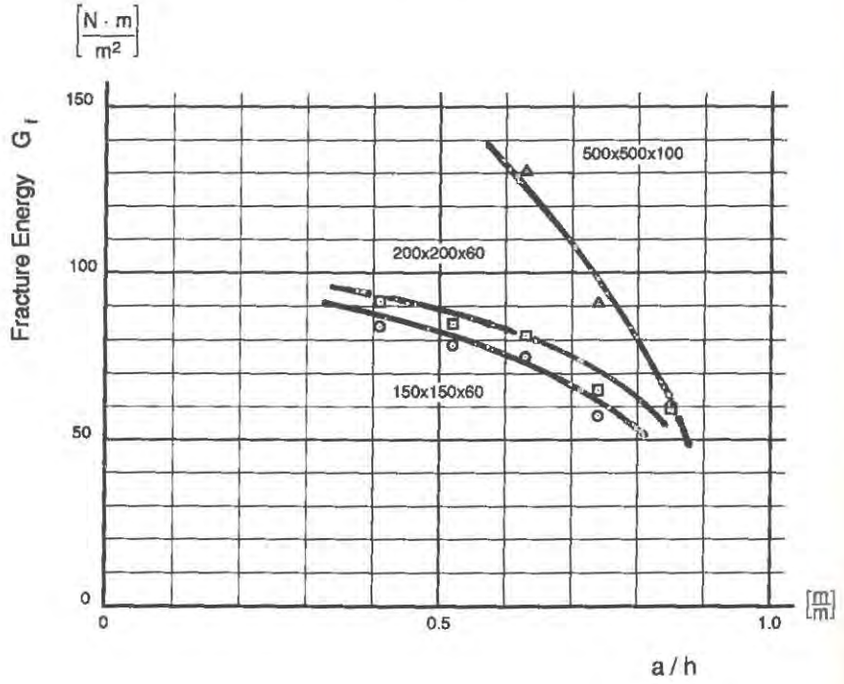

Figure 6. Specific fracture energy as determined by means of the wedge splitting method on concrete specimens with three different dimensions (small = 150 x 150 x 60 mm, medium = 200 x 200 x 60 mm and large = 500 x 500 x100 mm) as function of the related notch length

For every large specimens this border effect loses its significance and, hence, G_f becomes independent of size. This result confirms earlier findings [13, 14].

CONCLUSIONS

It is been shown that in the fracture process zone of concrete the full interlocking mechanisms can be activated only if the crack front has a width of at least four times the maximum aggregate size. For thinner specimens the fracture energy decreases accordingly.

The recently developed multi-cutting technique has proved to be a powerful tool to study the extension of the fracture process zone in concrete quantitatively.

At the notch tip and towards the end of the ligament the fracture process zone is confined. As a consequence the corresponding local fracture energy is decreased at both ends. This means that in a small ligament the specific fracture energy G_f is decreased by this border effect. If the ligament is long enough, the border effect loses its significance and the specific fracture energy depends on size by the Weibull statistics only.

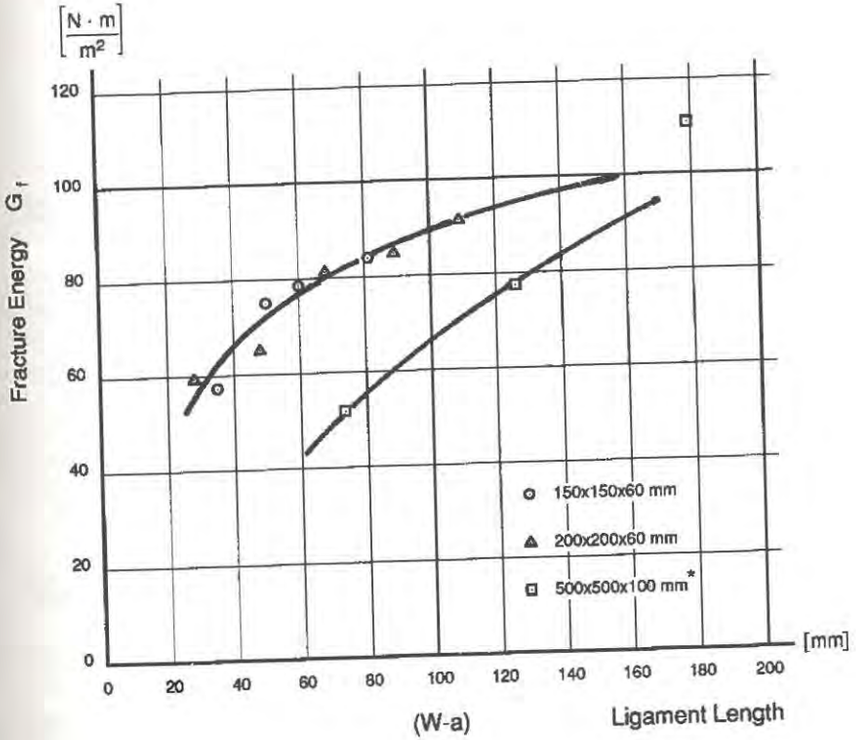

Figure 7. Same results as shown in Fig. 6 but plotted as function of the ligament length. Values for large specimens have been corrected for a ligament width of 60 mm.

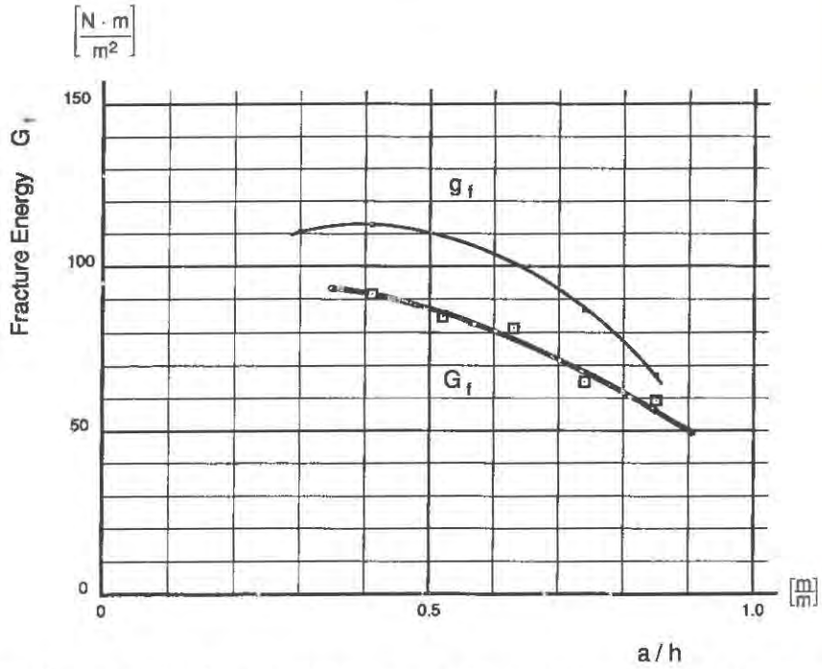

Figure 8. The specific fracture energy G_f as measured on the medium size specimens (200 x 200 x 60mm; see Fig.6) is shown as function of the related notch length. In addition g_f as determined with equ.(6) is shown.

REFERENCES

1. Hillerborg, A., Modeer, M., and Petersson, P.-E., Analysis of crack formation and crack growth in concrete by means of fracture mechanics and finite elements. Cem.Concr.Res 6, 773-782 (1976).

2. Hillerborg, A., Analysis of one single crack, in Fracture Mechanics of Concrete, ed. F.H.Wittmann, Elsevier Amsterdam, 223-249 (1983).

3. RILEM Draft Recommendation (50-FMC), Determination of the fracture energy of mortar and concrete by means of three-point bend test on notched beams, Materials and Structures 18, 285-290 (1985).

4. Wttmann, F.H., Roelfstra, P.E., Mihashi, H., Huang, Y.-Y., Zhang, X. and Nomura, N., Influence of age of loading, water/cement ratio, and rate of loading on fracture energy of concrete, Materials and Structures 20, 103-110 (1987).

5. Hu, X.-Z., and Wittmann, F.H., Fracture energy and fracture process zone, (to be published in Materials and Structures 1992).

6. Petersson, P.-E., Crack growth and development of fracture zones in plain concrete and similar materials, Report TVBM-1006, Division of Building Materials, Lund Institute of Technology (1981).

7. Brühwiler, E., and Wittmann, F.H., The wedge splitting test, a new method of performing stable fracture mechanics tests, in Fracture and Damage of Concrete and Rock, ed. H.P.Rosmanith, Pergamon Press, Oxford (1990), pp. 117-125.

8. Zhong, H., Some experiments to study the influence of size and strength on fracture energy, Institute for Building Materials, Swiss Federal Institute of Technology Zürich, Internal Report (1991).

9. Hu, X.-Z., and Wittmann, F.H., Experimental method to determine extension of fracture process zone, J. of Materials in Civil Eng. 2, 15-23 (1990).

10. Hu, X.-Z., Fracture process zone and strain softening in cementitious materials, Institute for Building Materials, Swiss Federal Institute of Technology, Zürich, Research Report No 1 (1990).

11. Wittmann, F.H. and Hu, X.-Z., Fracture Process Zone in cementitious materials, Int. J. of Fracture 51, 3-18 (1991).

12. Slowik, V., and Wittmann, F.H, Influence of strain gradient on fracture energy, Contribution to this volume.

13. Wittmann, F.H., Mihashi, H., and Nomura, H., Size effect on fracture energy of concrete, Eng.Fract.Mechanics 35, 107-115 (1990).

14. Brühwiler, E., Bruchmechanik von Staumauerbeton unter quasi-statischer und erdbebendynamischer Belastung, PhD-Thesis No.739, Swiss Federal Institute of Technology Lausanne (EPFL), Lausanne 1988.

Invited Paper

FRACTURE MECHANICS of CONCRETE DAMS; Overview of Research at the University of Colorado

Victor Saouma, Jan Červenka, Scott Keating, Ron Reich, Fletcher Waggoner
Associate Professor and Graduate Research Assistants
Department of Civil Engineering, University of Colorado
Boulder, CO 80309-0428

Abstract

The following paper will summarize the experimental and computational research undertaken by our group over the past four years in the area of dam fracture. The experimental component includes fracture properties based on large size specimens, uplift pressure distribution along a propagating crack under both static and dynamic loading, effect of biaxial confinement on fracture properties, field tests to determine elastic and fracture properties, and centrifuge testing to assess numerical models. The computational aspect hinges on both the development of a general purpose fracture mechanics 3D finite element program, as well as case studies of actual dams perceived to be unsafe under flood conditions using traditional analysis methods.

1 Introduction

Although few new dams are being currently constructed, there is a renewed interest in assessing dam safety of the numerous existing ones under extreme conditions which may not have been adequately considered during their design. Examples of such extreme conditions include new probable maximum flood (PMF) specified by hydrologists on the basis of accumulated data, and earthquake loading. Historically, gravity dams have been dimensioned on the basis of the linear elastic beam formula (which was the only known applicable equation when they were designed), and is still in use when assesing dam stability. Such an analysis must be performed every five years by publically owned dams as part of a relicensing process with the Federal Energy Regulatory Commission [1].

Should the extreme conditions result in unacceptably long cracks, then post-tensioning must be performed. The cost of such a rehabilitation, compounded by the perceived inadequacy of traditional analysis methods have prompted the Electric Power Research Institute (EPRI, Palo-Alto, CA) to look into alternative analysis methods.

Dams being designed to achieve very low tensile stresses, and as massive unreinforced concrete structures they constitute an ideal application for fracture mechanics. Already, the US Army Corps of Engineers has recognised the role of fracture mechanics in analysis [2], and most recently a specialized conference was held [3] with over 100 attendees from 18 countries, which was in turn preceded by a specialized workshop [4].

As such, our group has been involved in a research and development effort in the application of fracture mechanics to concrete dams. Being supported by Industry, and focusing on immediate practical problems related to the integrity of our decaying infrastructure, the research is both comprehensive and goal oriented. Hence, by its very origin, this research effort provided us with not only numerous technical challenges (which led to unusual experiments), but the greatest one of them was to reconcile scientific accuracy with engineering reality to solve the mechanics of a complex practical problem.

This paper will provide the reader with an overview of our research, and more detailled information could be found in the referenced ones.

2 Experimental Aspects

2.1 Fracture Properties of Concrete Dams

As most, if not all, previous concrete fracture tests have been limited to small scale specimens, there is a well justified concern that Dam Engineers may have difficulties accepting the corresponding fracture parameters. Henceforth, initial tests on wedge splitting specimens (WS) up to 5 ft in size and 3" with maximum size aggregate were undertaken [5, 6]. The WS specimen was selected as it has a large fracture area compared to the concrete volume, approximately 4.6 times greater than a commonly used three-point bend (TPB) beam geometry [7] of equal volume. Three specimen sizes were selected: 1, 3, and 5 ft in size and maximum size aggregate (MSA) was 0.75, 1.5, and 3 in. In addition to regular specimens, a series of cold-jointed specimens were tested to quantify the fracture properties existing at lift joints. From these tests, constant fracture toughness value K_{Ic} and fracture energy G_F were determined independently from aggregate or specimen sizes.

2.2 Effect of Internal Hydrostatic Pressure

Following completion of the WS test series, the testing procedure was refined to assess: 1) Uplift pressure distribution along a fracture process zone; and 2) Degradation of material properties (tensile strength, fracture toughness, and fracture energy) due to high water pressure (or stress corrosion). The original WS test was thus altered to enable the application of both an external mechanical (through the wedge), and an internal hydrostatic (through water under controlled pressure) loads, Fig. 1, [8], [9].

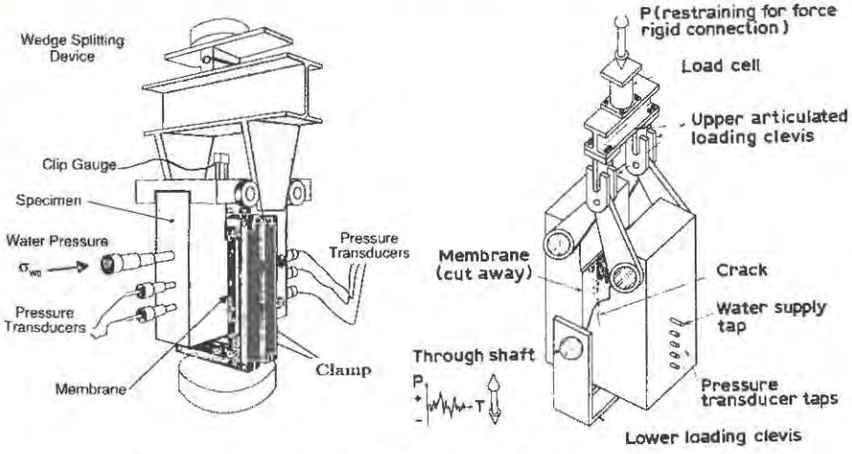

Figure 1: Set-Up for "Wet" Static (a) and Dynamic Wedge Splitting Tests

The mechanical load F induced by the wedge simulates the (horizontal) water load along the dam's upstream face, while the water pressure σ_W acting along the entire crack simulates (vertical) uplift pressure within cracks inside the dam. Following formation of the FPZ, water penetrates into it and hydrostatic pressure is *gradually* built up.

Based on numerous experiments conducted on both 1 and 3 ft specimens, it was determined that: 1) Due to the water pressure, there is a decrease in fracture properties, tensile strength, and process zone length; and 2) The water pressure distribution along the FPZ is also inversely proportional to the crack opening displacements, and is not constant as commonly assumed.

Finally, by reinforcing some well known facts, and shedding light on others, this task has clearly improved our basic understanding of what "really goes on" deep inside a crack buried in a dam.

2.3 Dynamic loading

Two commonly asked question by Engineers who perform dynamic analysis of concrete dams are: 1) How many excursions of the Gauss point tensile stress, in terms of duration, beyond the tensile strength does it take for concrete to "crack"? and 2) In a dynamically propagating crack, is there water penetration?

Presently, empirical rules (rules-of-thumb) are used to judge the importance of excursions beyond tensile strength in dams. Also, it is commonly assumed that no water penetrates propagating cracks in dams during earthquakes. This may prove to be an unconservative assumption (as trapped uncompressible water during crack closure may act as a wedge resulting in tensile stresses on the opposite dam face).

To conduct those tests, a variation of the WS tests was developed, Fig. 1. It should be emphasized that determination of dynamic fracture mechanics properties not being the objective of these tests, they are conducted under closed loop load (rather than strain) control. Furthermore, a load controlled dynamic experiment with reverse loading is not only easier to perform than one under strain or stroke control (due to the potential "slacks" in the system) but it is also easier and more intuitive to apply a load rather than a displacement.

Henceforth, following preliminary static tests (required to determine the peak load), two series of tests are being conducted: 1) Harmonic loading, with increased frequencies (up to 15Hz), and amplitude (exceeding the static peak load); and 2) Variable amplitude loading as determined from a time history seismic analysis of a dam and the computed stress history of a Gauss point.

In the second ("wet") phase, the specimens will also have internal hydrostatic pressure. These tests will constitute the culmination of all previous ones, as dynamic loading will be applied to a specimen subjected to internal hydrostatic pressure inside a propagating crack, and this will provide an indication of the water pressure distribution inside a propagating crack with *opening/closure* during an earthquake. Of particular importance, are the following measurements: 1) The frequency of crack opening/closing at which water (at a specific pressure) is able to penetrate the crack; 2) The location within the crack of the water front (detected by electrical circuit completion); 3) The time history of pressures at specific locations within the specimen (monitored by pressure transducers); and 4) The additional crack propagation (if any) caused by the "wedge effect" of the water present in the crack during closing.

2.4 Effect of Confinement

While it is well known that concrete strength increases with confinement, there is ample evidence that fracture strength of rock does also increase with confinement, [10].

Hence, a testing procedure originally developed by Zoback [11] for small rock specimens, and subsequently adapted to concrete by the authors, [12], was again used to assess the effect of biaxial confinement on concrete fracture strength.

Using a concrete mix previously used for standard wedge splitting specimens, 24 3x3x3 ft cubical specimens with a maximum size aggregate of 3" were cast, Fig. 2. On each specimen, a standard 3-inch

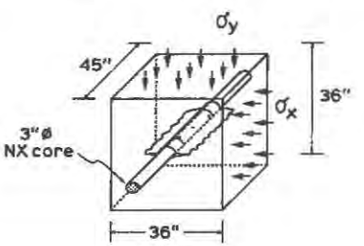

Figure 2: Cubical Tests to Determine Effects of Confinements on Fracture Properties

diameter, NX-size diamond core drill was utilized to bore a hole through the specimens. Specimens were subsequently subjected to biaxial confinements and 3 replica of each test were performed.

Testing was accomplished by pressurizing the borehole through a special probe while recording diametral changes, and acoustic emissions. The probe consists of an elastomer-skinned expandable bladder

with deformation sensors, or linear variable differential transducers (LVDT), embedded in circumferentially staggered positions $\pi/4$ radians apart. LVDT's in the probe measure diametrical changes (to the nearest 0.001mm) of the borehole during pressurization.

Preliminary conclusions from these tests indicate that: 1) Young's modulus and tensile strength, determined from the cubical tests compared with the experimentally determined ones (on cylindrical specimens) within 20%; 2) Distinct measurable increase in fracture properties were obtained only when confinement exceeded 200 psi; 3) A simple relationship between fracture toughness and confinement was determined:

$$K_{Ic}^{eff}(\text{Ksi}\sqrt{\text{in}}) = 1.12 + 1.2\sigma_x(\text{Ksi}) \tag{1}$$

2.5 Field Test

Satisfied by the laboratory tests, one field test was undertaken, [12]. Preliminary results of this test highlighted the substantially higher *in-situ* fracture toughness values over the laboratory obtained one.

As limited data were gathered from this first test (which entails local fracturing inside the dam), two additional ones are scheduled for the near future.

Finally, it should be noted that while it may be premature to rely on the full *in-situ* determined value of K_{Ic} for safety evaluation, this test has great potential in continuously monitoring and quantifying concrete degradation when alkali-aggregate reaction is suspected.

2.6 Centrifuge Test Validation

Despite the numerous analytical and numerical models for dam analysis, there have been few, if any, model validations. In order to respect all the similitude laws in model testing, the acceleration of gravity must be inversely proportional to the dimensional scale. For most models this requirement is of no importance, however for gravity dams it is essential. The only mean of artificially scaling acceleration of gravity is through a centrifuge. Hence to evaluate our (and others) computational/analytical models, the University of Colorado Civil Engineering Department 400 G-ton centrifuge (capable of subjecting a 2 ton payload to an acceleration of 200 g) is being used to test models of concrete dams.

This investigation was preceded by an extensive evaluation of fracture mechanics tests under high g levels. Laws of similitude for fracture testing were derived and then validated on the basis of fracture toughness testing of both aluminum and concrete compact tension specimens, [13].

Currently we are testing 3 ft high models of gravity dams, Fig. 3, and have only recently overcome two

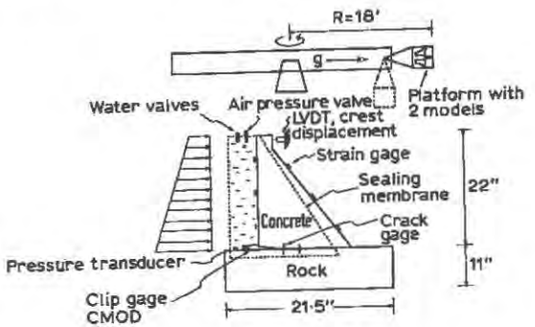

Figure 3: Centrifuge Testing of Concrete Dams

major difficulties: 1) properly sealing the water; and 2) obtain reliable crest displacements and CMOD (a few thousandths of an inch), and strains (about 10 micro-strain) measurements from a specimen subjected to 150 g's!

Immediate future plans include casting concrete dam models on different types of rock bases, and inducing failure through overpressurization of water (simulating overtopping).

When all these tasks will be successfully completed, dynamic testing in the centrifuge may be considered.

3 Computational Issues

Analysis capabilities are provided by a finite element program, **Merlin**, which includes numerous extensions for fracture mechanics based analysis. **Merlin** is based on the standard displacement formulation of the finite element method and incorporates an iterative solution strategy based on a discretization the Hu-Washizu variational principle known as the Mixed-Iterative Method [14]. The Mixed-Iterative Method, which is described in Section 3.1, facilitates the computation of C^0 continuous nodal strain- and stress-fields. The availability of nodal strain and stress values greatly simplifies computations associated with fracture mechanics techniques such as the evaluation of contour integrals (see Section 3.2.2) or the implementation of principal stress criteria for crack propagation in nonlinear fracture analysis (see Section 3.3).

3.1 Mixed-Iterative Method

A topic that has recently received some attention in the literature is the solution of problems in linear elasticity using mixed methods and iterative solution strategies [14, 15]. The Hu-Washizu three-field variational principle is the foundation of the mixed-iterative method implemented in **Merlin**

$$\Pi_{HW} = \int_\Omega \frac{1}{2}\,\epsilon^T \mathbf{E}\epsilon \, d\Omega - \int_\Omega \sigma^T(\nabla \mathbf{u} - \epsilon)\, d\Omega - \int_\Omega \mathbf{u}^T \mathbf{b}\, d\Omega - \int_{\Gamma_t} \mathbf{u}^T \bar{\mathbf{t}}\, d\Gamma \tag{2}$$

where the functional Π_{HW} is the total potential energy of the system and $\mathbf{u} \equiv \tilde{\mathbf{u}}$ is enforced on Γ_u. The variations of Equation 2 constitute the weak forms of the three basic equations of elasticity

$$\begin{aligned} \int_\Omega \delta\sigma^T(\nabla \mathbf{u} - \epsilon)\, d\Omega = 0 \qquad \int_\Omega \delta\epsilon^T(\mathbf{E}\epsilon - \sigma)\, d\Omega = 0 \\ \int_\Omega \delta(\nabla \mathbf{u})^T \sigma \, d\Omega - \int_\Omega \delta\mathbf{u}^T \mathbf{b}\, d\Omega - \int_{\Gamma_t} \delta\mathbf{u}^T \bar{\mathbf{t}}\, d\Gamma = 0 \end{aligned} \tag{3}$$

(i.e., strain-displacement, constitutive, and equilibrium, respectively) as the subsidiary conditions. Within a finite element framework, the three field variables are approximated over an element domain using shape functions

$$\mathbf{u} = \mathbf{N}_u \overline{\mathbf{u}} \qquad \epsilon = \mathbf{N}_\epsilon \overline{\epsilon} \qquad \sigma = \mathbf{N}_\sigma \overline{\sigma} \tag{4}$$

Substituting $\mathbf{N}_u$, $\mathbf{N}_\epsilon$, and $\mathbf{N}_\sigma$ for $\delta\mathbf{u}$, $\delta\epsilon$, and $\delta\sigma$, respectively, the resulting discretization of Equation 3 yields the following system of equations:

$$\begin{bmatrix} \mathbf{A} & \mathbf{C} & \mathbf{0} \\ \mathbf{C}^T & \mathbf{0} & \mathbf{D} \\ \mathbf{0} & \mathbf{D}^T & \mathbf{0} \end{bmatrix} \begin{Bmatrix} \overline{\epsilon} \\ \overline{\sigma} \\ \overline{\mathbf{u}} \end{Bmatrix} = \begin{Bmatrix} \mathbf{f}_1 \\ \mathbf{f}_2 \\ \mathbf{f}_3 \end{Bmatrix} \tag{5}$$

where

$$\mathbf{A} = \int_\Omega \mathbf{N}_\epsilon^T \mathbf{E} \mathbf{N}_\epsilon \, d\Omega \qquad \mathbf{D} = \int_\Omega \mathbf{N}_\sigma^T \mathbf{B}\, d\Omega \qquad \mathbf{C} = -\int_\Omega \mathbf{N}_\epsilon^T \mathbf{N}_\sigma \, d\Omega \tag{6}$$

$$\mathbf{f}_1 = \mathbf{f}_2 = \mathbf{0} \qquad \mathbf{f}_3 = \int_\Omega \mathbf{N}_u^T \mathbf{b}\, d\Omega + \int_{\Gamma_t} \mathbf{N}_u^T \bar{\mathbf{t}}\, d\Gamma \tag{7}$$

In order to initiate the iterative process, an approximation for one the three field variables is required. Upon examining Equation 5, the obvious choice is the displacement field. The most convenient method of computing displacements is the standard displacement method stiffness matrix $\mathbf{K}$, which augments Equation 5 to become

$$\begin{bmatrix} \mathbf{A} & \mathbf{C} & \mathbf{0} \\ \mathbf{C}^T & \mathbf{0} & \mathbf{D} \\ \mathbf{0} & \mathbf{D}^T & \mathbf{K} \end{bmatrix} \begin{Bmatrix} \overline{\epsilon} \\ \overline{\sigma} \\ \overline{\mathbf{u}} \end{Bmatrix} = \begin{Bmatrix} \mathbf{f}_1 \\ \mathbf{f}_2 \\ \mathbf{f}_3 - \mathbf{K}\overline{\mathbf{u}} \end{Bmatrix} \tag{8}$$

The iterative procedure is defined by

$$\begin{aligned} \overline{\mathbf{r}}^n &= \mathbf{D}^T \overline{\sigma}^n - \mathbf{f}_3 \\ \overline{\mathbf{u}}^{n+1} &= \overline{\mathbf{u}}^n - \mathbf{K}^{-1}\mathbf{r}^n \\ \overline{\epsilon}^{n+1} &= -\mathbf{C}^{-1}\mathbf{D}\overline{\mathbf{u}}^{n+1} \\ \overline{\sigma}^{n+1} &= \mathbf{E}\overline{\epsilon}^{n+1} \end{aligned} \tag{9}$$

and initial values of the three field variables are identically set to zero, $\overline{\mathbf{u}}^0 = \overline{\epsilon}^0 = \overline{\sigma}^0 = \mathbf{0}$. It should be noted that the displacements for the first iteration, $\overline{\mathbf{u}}^1$, correspond to that of the standard displacement method solution. Since the iterative solution procedure depends on the stiffness matrix of the displacement method, the mixed-iterative method is implemented as an extension to a displacement method program.

The third step in the iterative procedure, the computation of the continuous nodal strain field from the discontinuous element strain fields, involves computing the inverse of the strain projection matrix C. Diagonalization or lumping of the strain projection matrix greatly reduces the computational effort without significantly effecting the quality of the projected strain field [16].

3.2 Extraction of SIF

In a LEFM analysis, the computation of accurate values of the stress intensity factors (SIF) is essential. There are basically two schools of thought regarding how to perform this task: use special elements to model the stress singularity at the crack tip [17, 18] or use contour integrals based on the conservation laws of elasticity or reciprocal work theorems to avoid modeling the stress singularity at the crack tip [19, 20, 21]. Both approaches have been implemented within **Merlin** for 2D and 3D analyses.

3.2.1 Displacement Correlation Method

For a crack on a bi-material interface, such as rock/concrete, the use of singular elements becomes highly questionable since the order and nature of singularity in the stress-field differs significantly from the case of a crack in a homogeneous medium. For a crack in a homogeneous medium the order of the singularity is $\sigma \sim \frac{1}{\sqrt{r}}$ and for a crack on a bi-material interface the order of the singularity is $\sigma \sim \frac{1}{\sqrt{r}} \begin{pmatrix} \sin(\lambda_j \log r) \\ \cos(\lambda_j \log r) \end{pmatrix}$ where λ_j is a function of the elastic properties of the two materials [22]. The order of the singularity in the quarter-point element exactly matches that of the strain- and stress-fields for the homogeneous case, but the addition of the transcendental terms for the bi-material case make it impossible for an element using an assumed displacement-field based on a polynomial expansion to match the order of the singularity in the stress-field.

3.2.2 Contour Integral Methods

Independently, Eshelby and Rice [23, 19] proposed a path-independent contour integral based on a conservation law of elasticity that has been come to be known as the J-integral

$$J = \oint_\Gamma \left[W\, dy - t_i \frac{\partial u_i}{\partial x}\, ds \right] \tag{10}$$

where $t_i = \sigma_{ij} n_j$. For problems in linear elasticity the computed value of J is equivalent to the fracture energy release rate G which is, in turn, related to the mode I and II stress intensity factors

$$G = \frac{K_I^2 + K_{II}^2}{E'} \tag{11}$$

For the case of pure mode I, K_I can be evaluated directly from J, but for mixed mode fracture more elaborate techniques are required.

Based on an observation by Knowles and Sternberg [24], in which the J-integral is identified as one component of a vector quantity

$$J_i = \oint_\Gamma \left[W n_i - t_j \frac{\partial u_j}{\partial x_i} \right] ds \tag{12}$$

Using Equation 12 as the starting point, it is a relatively straightforward task to extend the J-integral from a 2D line integral to a 3D surface integral [25, 26]. A representation of the surfaces associated with the 3D J-integral is shown in Figure 4. The 3D J-integral follows the form of Equation 12

$$G_i = \frac{1}{L}\left\{\oint_{\Gamma_1 \cup \Gamma_2 \cup \Gamma_3} [W\delta_{ij} - \sigma_{kj}u_{k,i}]\, n_j d\Gamma + \oint_{\Gamma^+ \cup \Gamma^-} [W\delta_{ij} - \sigma_{kj}u_{k,i}]\, n_j d\Gamma - \int_\Omega b_j u_{j,i} d\Omega\right\} \quad (13)$$

where G_i is the energy release rate per unit extension of the crack front; $i = 1, 2$; the surface integral over $\Gamma^+ \cup \Gamma^-$ accounts for tractions on the crack surface; and the volume integral accounts for the body forces.

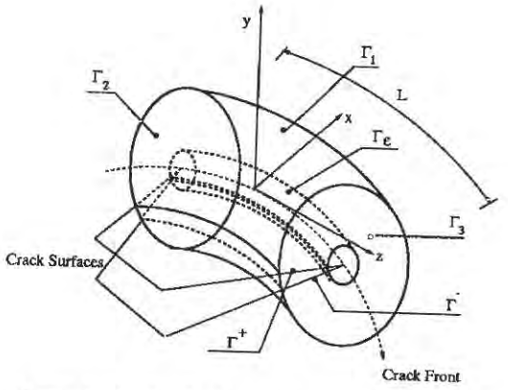

Figure 4: Tubular Surface Around the Crack Front

Other contour integrals based on reciprocal work theorems or conservation laws using auxiliary equilibrium states to compute the SIF directly have also been proposed [20, 21]. The extension of a contour integral based on a reciprocal work theorem [20] to include the effect of tractions on the crack surface and body forces is relatively simple

$$\oint_\Gamma (u_i \hat{t}_i - \hat{u}_i t_i)\, ds - \oint_{\Gamma_t} \hat{u}_i t_i\, ds - \int_\Omega \hat{u}_i b_i\, ds = 0 \quad (14)$$

where u_i, t_i, and b_i are from the finite element solution; $\hat{u}_i$ and $\hat{t}_i$ are from the auxiliary solution; the contour integral over Γ_t accounts for surface tractions; and the volume integral accounts for body forces. The authors experience indicates that these methods are more realiable and accurate than the J-interal for the computation of SIF for mixed mode fracture. However, they are limited by the availability of the appropriate auxiliary solutions for the case of cracking in a bi-material medium and it may be difficult to extend them to 3D analyses retaining the effect of body forces on the SIF.

Regardless of the type of contour integral used, the contour path is defined by element edges for 2D analyses and element surfaces for 3D analyses. This approach simplifies the computation of the contribution to the SIF from body forces, which is evaluated using a volume integral over elements on the interior of the contour path, but requires nodal displacement gradients and stresses. The mixed-iterative method, with its C^0 continuous displacement gradient and stress fields, allows for a simple and efficient implementation of contour integral methods.

3.3 Nonlinear Fracture

Nonlinear fracture mechanics based analyses of plain concrete structures is performed using an incremental form of the Fictitious Crack Model (FCM) [27]. Casting the FCM into an incremental form allows for the presence of nonlinear constitutive laws within the continuum away from the crack to be treated using standard techniques for nonlinear finite element analysis. The applied loads for a given increment

are scaled such that the principle stress in the continuum at the crack tip is equal to the uniaxial tensile strength (i.e., stress continuity is maintained between the fictitious crack and the continuum).

The criteria for crack propagation is the value of the maximum tensile principle stress at the crack tip and the direction of crack propagation is perpendicular to this principle stress. This approach, which requires nodal values of stress, is currently used whether a ficititious crack is present or not. The nodal values of stress used with the crack propagation criteria are computed using the variational projection technique of the mixed-iterative method. The effect of using a stress criteria for crack propagation from an initial notch on the overall structural response is currently being investigated.

Stress transfer in the ficititious crack is facilitated through continous interface elements. The constitutive model defining the tractions in the ficititious crack currently accounts for only normal tractions; resistance to sliding and, consequently, dilatation are ignored. In addition, time and rate effects are ignored in the current constitutive model. The addition of these effects should be a strainghtforward task once the numerical models to account for them have been formulated.

3.4 Automatic Remeshing and 3D Graphical Post-Processor

Parallel to Merlin, two separate modules are currently being developed. An automatic mixed mode remesher for 2D applications, and a separate one for both "pseudo-3D" (straight crack front) and full 3D. Also under development is a general purpose 3D interactive graphical post-processor.

In both cases, C is used for programing, Phigs for the graphics, and OpenWindow (a superset of X) for graphical user interface.

4 Acknowledgments

The financial support of the Electric Power Research Institute under contract No. RP-2917-8, Doug Morris Project Manager and Howard Boggs Project Monitor, is gratefully acknowledged. Furthermore, the authors would like to thank EPRI's Hydroelectric Advisory group for their continuous review and evaluation.

References

[1] Anon. Engineering guidelines for the evaluation of hydropower projects. Technical report, Federal Energy Regulatory Commission, Office of Hydropower Licensing, 1987.

[2] Anonymous. Fracture mechanics analysis of concrete hydraulic structures. ETL 1110-8-16, US Army Corps of Engineers, 1991.

[3] V.S. Saouma, R. Dungar, and D. Morris, editors. *Proceedings Dam Fracture*, Boulder, September 1991. Electric Power Research Institute (EPRI), Palo Alto, CA.

[4] R. Dungar, V. Saouma, and F. Whittman. Conference report: The application of fracture mechanics to dam engineering. *Dam Engineering*, 2(1):3–20, 1991.

[5] V.E. Saouma, J.J. Broz, E. Brühwiler, and H.L. Boggs. Effect of Aggregate and Specimen Size on Fracture Properties of Dam Concrete. *ASCE, Journal of Materials in Civil Engineering*, 3(3):204–218, August 1991.

[6] Brühwiler, E., Broz, J.J., and Saouma, V.E.,. Fracture Model Evaluation of Dam Concrete. *ASCE, Journal of Civil Engineering Materials*, 1991. in print.

[7] Anon. RILEM Draft Recommendation (50–FCM): Determination of the Fracture Energy of Mortar and Concrete by Means of Three–Point Bend Tests on Notched Beams. *Materials and Structures*, 18:287–290, 1985.

[8] E. Brühwiler and V.E Saouma. Water fracture interaction in cracked concrete dams. Technical report, Dept. of Civile Engineering, University of Colorado, December 1990. Report submitted to EPRI.

[9] Brühwiler, E. and Saouma, V.E. Water fracture interaction in cracked concrete dams. In V.E. Saouma, R. Dungar, and D. Morris, editors, *Proceedings of the Int. Conference on Dam Fracture*, pages 551–567, Palo-Alto, Ca, September 1991. Electric Power Research Institute, GS-7491.

[10] R. Schmidt and C. Huddle. Effect of confining pressure on fracture toughness of indiana limestone *International Journal of Rock Mechanics, Mining Science & Geomechanics Abstract*, 14:289–293 1977.

[11] Zoback, M.D., Rummel, F., Jung, R. and Raleigh, C.B.,. Laboratory Hydraulic Fracturing Experiments in Intact and Pre-Fracture Rock. *Int. J. Rock Mech. Min. Sci. & Geomech. Abstr.*, 14:49–58. 1977.

[12] V.E. Saouma, J.J. Broz, and H.L. Boggs. In-situ Field Testing for Fracture Properties of Dam Concrete. *ASCE, Journal of Materials in Civil Engineering*, 3(3):219–234, August 1991.

[13] Broz, J. and Saouma, V.E. and Brühwiler, E. and Boggs, H. Fracture mechanics experiments in a centrifuge. In H.Y Ko and McLean F.G., editors, *Centrifuge-91*, pages 575–581, Boulder, CO, June 1991. Balkema.

[14] O. C. Zienkiewicz, J. P. Vilotte, S. Toyoshima, and S. Nakazawa. Iterative method for constrained and mixed approximations. an inexpensive improvement of fem performance. *Computer Methods in Applied Mechanics and Engineering*, 51(1–3):3–29, 1985.

[15] M.A. Crisfield. *Finite Elements and Solution Procedures for Structural Analysis*, volume 1, Linear Analysis. Pineridge Press, Swansea, UK, 1986.

[16] O. C. Zienkiewicz and R. L. Taylor. *The Finite Element Method*, volume 1, Basic Formulation and Linear Problems. 4th ed., McGraw-Hill, London, 1989.

[17] R.S. Barsoum. On the use of isoparametric finite elements in linear fracture mechanics. *International Journal of Numerical Methods in Engineering*, 10(1):25–37, 1976.

[18] V.E. Saouma and E.S. Sikiotis. Stress intensity factors in anisotropic bodies using singular isoparametric elements. *Engineering Fracture Mechanics*, 25(1):115–121, 1986.

[19] J. R. Rice. A path independent integral and the approximate analysis of strain concentration by notches and cracks. *Journal of Applied Mechanics*, 35(2):379–386, 1968.

[20] M. Stern, E.B. Becker, and R.S. Dunham. A contour integral computation of mixed mode stress intensity factors. *International Journal of Fracture*, 12(3):359–368, 1976.

[21] J. F. Yau, S. S. Wang, , and H. T. Corten. A mixed-mode crack analysis of isotropic solids using conservation laws of elasticity. *Journal of Applied Mechanics*, 47(2):335–341, 1980.

[22] M. L. Williams. The stresses around a fault or crack in dissimilar media. *Bulletin of the Seismological Society of America*, 49(2):199–204, 1959.

[23] J.D. Eshelby. The continuum theory of lattice defects. *Solid State Physics*, 3:79–144, 1956.

[24] J. K. Knowles and E. Sternberg. On a class of conservation laws in linearized and finite elastostatics. *Archive for Rational Mechanics and Analysis*, 44(3):187–211, 1972.

[25] C. F. Shih, B. Moran, and T. Nakamura. Crack tip integrals and domain integral representation for three-dimensional crack problems. In *Analytical, Numerical and Experimental Aspects of Three Dimensional Fracture Processes*, New York, N.Y., 1988. American Society of Mechanical Engineering. AMD 91.

[26] R. Reich, J. Cervenka, and V.E. Saouma. Numerical techniques for 2d and 3d nonlinear fracture mechanics based analysis of dams. In V.E. Saouma, R. Dungar, and D. Morris, editors, *Proceedings of the Int. Conference on Dam Fracture*, pages 163–182, Palo-Alto, Ca, September 1991. Electric Power Research Institute, GS-7491.

[27] A. Hillerborg, M. Modéer, and P.E. Petersson. Analysis of crack formation and crack growth in concrete by means of fracture mechanics and finite elements. *Cement and Concrete Research*, 6(6):773–782, 1976.

FRACTURE MECHANICS OF CONCRETE, ROCK AND INTERFACE

A. K. MAJI[1], J. WANG[2] and C. V. CARDIEL[3]
Department of Civil Engineering
University of New Mexico, Albuquerque, NM 87131, USA.

ABSTRACT

A study of the interface between concrete and different types of rocks is important for understanding the role of aggregates in a cement matrix. More recently, concrete seals are being proposed to seal off nuclear waste repositories in rocks. A study of the interface characteristics, such as fracture toughness, crack openings, and permeability is therefore necessary to ensure the proper functioning of the seals, and to prevent the transport of radioactive materials. This paper compares the fracture process zone in concrete, rocks and their interfaces, in order to investigate the applicability of fracture mechanics.

Electronic Speckle Pattern Interferometry, a laser based nondestructive inspection tool, has been used to study rock, concrete and interface fracture characteristics. The laser technique permits the in-situ observation of crack propagation with high sensitivity. Laboratory size Compact Tension specimens of Indiana limestone, concrete, and the interface were prepared. Fracture characteristics of the interface was measured with the aid of finite element computations. Fractured limestone specimens were subsequently tested to determine the permeability of water through the natural fractures generated by the tests.

The research allows us to visually observe the formation of the process zone, its propagation leading to complete loss of load carrying capacity, and the presence of crack-face ligament connections. The investigation provides a comparative analysis of the fracture mechanisms in concrete, rock and interfaces.

INTRODUCTION

The characteristics of the aggregate/cement interface has been of great interest to the concrete community (Mindess and Shah 1988). This interest has grown in the context of high strength concrete where the interface, as the weakest link in the system, is the limiting factor. Recently, the properties of the concrete/rock interface is under scrutiny with relevance to nuclear waste repositories. Concrete seals will be used to plug the shafts leading to the underground storage facilities (AECL 1990). Injection of cement grout into cracks in rocks has also been proposed for reducing permeability (Hoorelbeke and Potier 1991). Experiments are currently under way in several countries to address the design of these facilities.

---

1 Assistant Professor of Civil Engineering
2 Graduate Research Assistant and PhD Candidate
3 Undergraduate Research Assistant.

The strength and fracture toughness of rocks have been subject of ongoing investigation in its relation to blasting and hydofracturing operations (Rossmanith 1983). Fracture of concrete and other cementitious materials have also been the subject of numerous investigations, and attempts have been made to incorporate some of the evolving concepts into structural design (Bazant and Li 1989). The fundamental aspects of fracture in rocks, concrete, ceramics are similar (Shah 1990). Little quantitative information is however available on the fracture of the concrete-rock interface, which is the subject of this investigation.

EXPERIMENTAL PROGRAM

Fracture Tests

Compact Tension specimens 6" x 6" (15.2 cm x 15.2 cm) and 1" (2.54cm) thick (Figure 1) were prepared. The mortar specimens were cast in a plexiglass mold with a mix ratio 2:1:0.5 of sand, Type III cement, and water. A 2" (5.08 cm) long sharp notch was cast into the specimen with a 1mm thick steel plate. The blade was removed 6 hrs. after casting. The specimens were removed from the mold after 24 hrs. and placed in a lime water bath (at 150° F) for another 48 hours prior to testing. The limestone specimens were saw cut in the specimen preparation laboratory of the Department of Geology. The two 1/2" (12.7mm) diameter loading holes were drilled into the specimens by a rotary diamond core-drill.

The specimens were tested on a 3 kip (13 KN) manual loading frame. Electronic Speckle Pattern Interferometry (ESPI) was used in to monitor the crack propagation in the specimens as they were loaded. This technique uses interference of laser beams create fringe pattern corresponding to the displacements on the specimen surface. The fringes are formed on a video screen and are sensitive to a fraction of a micrometer changes in the displacement field. The discontinuities in the fringe pattern as observed during loading indicate the extension of the crack from the original notch-tip. It is therefore possible to observe the crack propagation in real time. Details of the ESPI experiments conducted on the limestone specimens have been reported in details elsewhere (Maji and Wang 1992).

The interface specimens were fabricated with the fractured limestone specimens. The naturally fractured halves of the limestone were placed in the molds and the mortar was cast on its side. The specimens were cured and subsequently tested as described above. Three specimens of each of the three types of materials were tested.

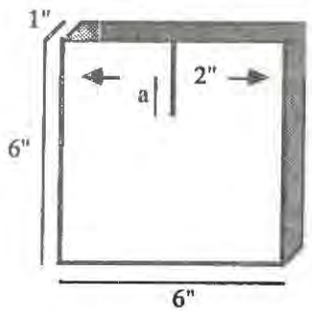

Figure 1. Compact-Tension Specimen

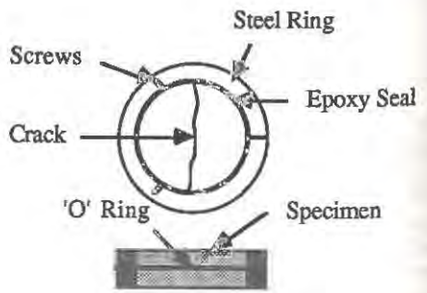

Figure 2. Permeability Test Specimen Holder

Permeability Tests

A modification of the ASTM Standard D4525: 'Permeability of Rocks by Flowing Air' was used to determine the flow of water through natural fractures. Flow of gases and water are both of importance in waste repositories. Part of the test device is shown in Figure 2. A cylindrical specimen (2.75", 7cm in diameter and 1", 2.54cm thick) was cored out of the fractured limestone specimen and placed in the steel ring with the same external diameter. Three screws on the sides of the steel ring were used to hold the specimen in place, and to adjust the width of the crack in the specimen. A rubber 'O'-ring was used to prevent seepage of water around the steel ring. The edges of the specimen were also epoxy sealed. A constant head of 8 feet (2.43 meters) of water was used to study the permeability through both fractured and intact specimens.

In addition, petrographic thin section analysis of the rock was also done. A sample of the rock is mounted to a microscopic slide with a clear epoxy, and ground to the dimensions of 40mm x 40mm x 30 microns. It is then possible to seen the microstructure of the rock under a microscope. Using the ESPI technique, it was possible to determine the extension of the natural crack. Specimens were subsequently unloaded before complete fracture and thin-sections were made of the natural cracked section.

Figure 3. Ligament Connection

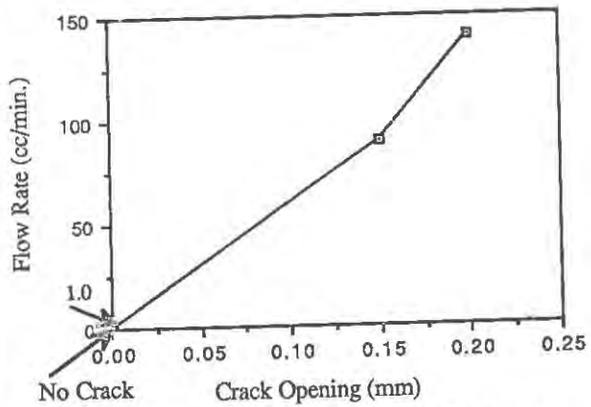

Figure 4. Flow Through Fractured Limestone

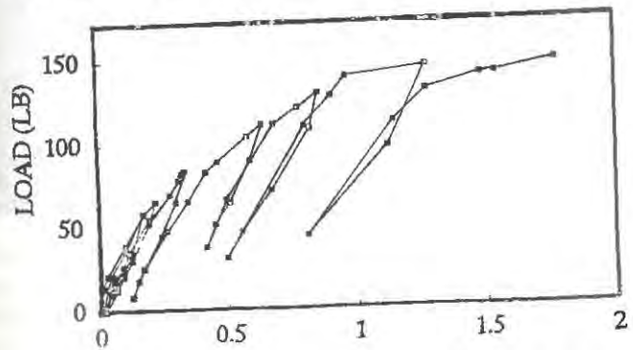

Figure 5. Load vs. CMOD for Interface Specimen

TEST RESULTS

The grain size of the limestone varied from 0.1mm to 5 mm, and the porosity was 15 to 20%. The optical microscope very clearly shows ligament connections across the open crack (Figure 3). The permeability test results are shown in Figure 4. It is evident from this Figure that the permeability of water through the limestone will be due primarily to the flow through the fractures, in spite of its porosity. Although this has been known for many years and used for modeling the porosity of water and cement grout in rock fissures (Snow 1968), it reiterates the importance of interface cracks in the proper functioning of the plugs in the nuclear repository seals.

The Load vs. Crack Mouth Opening Displacement (CMOD) data for an interface specimen is presented in Figure 5. The CMOD measurements were obtained from a miniature LVDT. It is evident from this Figure that the interface demonstrates significant pre-peak nonlinearity. The specimen fails along the interface, through the center of the specimen. The loading-unloading curves also demonstrate large plastic deformation, in addition to damage (degradation of the unloading modulus). The ESPI technique readily captures pre-peak crack propagation which is responsible for the pre-peak nonlinearity.

The extent of pre-peak crack propagation was about 2" (5.08cm). Figure 6 shows a typical ESPI fringe pattern. Notice the much larger fringes on the right, the smaller fringes on the left, and the discontinuities in the fringe pattern all the way through the picture.

The most interesting aspect of the ESPI techniques is that it allows one to observe the development of strain concentrations at the crack tip immediately before failure. In Figure 6 the fringe discontinuities show the crack extension. There is no concentration of fringes at the crack-tip. The crack is steadily growing at this phase. However, immediately prior to unstable crack propagation, i.e., at or near the maximum load, the fringe pattern resembles a fan (Figure 7). The concentration of fringes at the crack-tip demonstrates the region of strain-concentration.

Figure 6. ESPI Fringe Pattern

Showing Crack Extension

Figure 7. ESPI Fringe Pattern

Immediately prior to Failure

ANALYSIS OF RESULTS

The Finite Element Method (FEM) was used to evaluate the fracture toughness and the energy release rate of the three materials tested. The code used (Pantaki and Gerstle) applies quarter point singular elements to determine the Stress Intensity Factors (SIF). The right value of the Elastic Modulus (E) for both the mortar and the limestone were determined from the experimentally observed load vs. CMOD of the specimens during the initial elastic stages of loading, and the load vs. CMOD measurements from the FEM analysis.

The interface specimen was also analyzed using the value of E determined as stated above, and using a value of the Poisson's ratio (ν) as 0.18. The SIFs obtained from this analysis showed the existence of the K_{II} term, as is expected for interface cracks subject to pure mode I loading. The significance of SIFs in interface cracks is not well understood, and lead to oscillatory stresses in the open crack situation in our experiment (Williams 1959, Rice 1988). The Energy Release Rate (G) of the three materials were compared, assuming that for the rock and mortar :

$$G = K_I^2/E \qquad (1)$$

For the interface analysis, G was determined as:

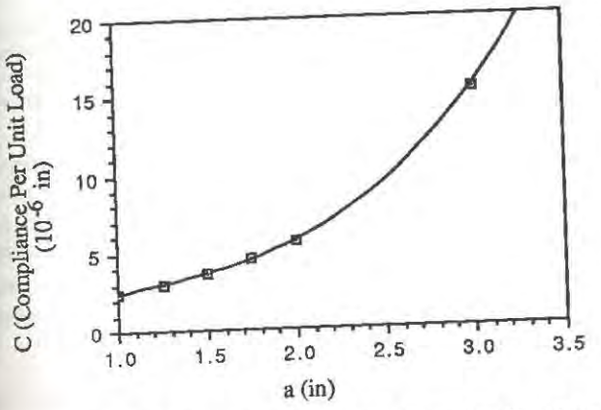

E1=3.2 x 10^6 psi
E2=4.5 x 10^6 psi
ν1=ν2= 0.18

Figure 8. Compliance vs. Crack Extension (FEM Analysis)

Table 1. Comparison of Test Data

	Rock	Concrete	Interface
Max Load (lbs.)	350	270	150
pre-peak crack growth (in.)	0.6	2.0	2.0
E (x 10^6 psi.)	4.5	3.2	-
K_I (psi.√in.)	700	540	-
G (lb.in./in^2)	0.109	0.09	0.026

(1 lb. = 4.448 N)
(1 in = 2.54 cm)
(1psi.=6.895 kPa)

$$G = \frac{P^2}{2B}\frac{\delta C}{\delta a} \qquad (2)$$

where C is the compliance at the point of application of the external loads, P is the applied load, B is the specimen width (1", 2.54cm), and 'a' is the crack length from the line of applied loading (see Figure 1). The Compliance vs. 'a' relationship obtained from the FEM analysis has been plotted in Figure 8. A third order polynomial shown below was used in this Figure to fit the FEM data using the least squares approach :

$$C = (-1.1920 + 5.9049\,a - 3.4633\,a^2 + 1.1114\,a^3) \times 10^{-6} \qquad (3)$$

Table 1 shows a comparison between the average values obtained for the three materials using the maximum load and the initial crack length of 2" (5.08cm). Accounting for the pre-peak crack extension will increase the values of K_I and G reported here.

CONCLUSIONS

It was discussed that the interface is primarily responsible for permeability of rocks. The interface behavior is quasi-brittle in nature, and the fracture characteristics are similar to that of concrete and rocks. Pre-peak crack extension along the interface is similar in magnitude to that in the mortar. The Energy Release Rate of the interface was compared to that of the two component materials.

ACKNOWLEDGEMENT

This research was supported partially by a National Foundation Grant (No. MSS-8918121). C. V.Cardiel was supported by New Mexico's Waste Management Education and Research Consortium (WERC).

REFERENCES

AECL (Atomic Energy of Canada Limited), "Managing Canada's Nuclear Fuel Wastes", Publication no. WWM-89-05-01, 1989.

Bazant Z. P. and Li V., (editors), - "Fracture Mechanics - Applications to Concrete", ACI-SP 118, 1989.

Hoorelbeke J. M. and Potier, "Design and Operating Criteria of the French Deep Repository for High Level Radioactive Waste", Proc. of 2nd Annual Int. Conf. on High Level Radioactive Waste Management, Las Vegas, NV, April-May 1991, pp. 334-339.

Maji A. K. and Wang J., "Experimental Study of Fracture Processes in Rocks", Rock Mechanics and Rock Engineering, Feb-Mar 1992.

Mindess S.and Shah S.P., (editors),"Bonding in Cementitious Composites", MRS Proceedings V 114, 1988.

Pantaki M. J. and Gerstle W., "A New Integrated Computer Graphics Design Tool", Technical Report RSI-039, Respek Inc., Albuquerque, NM, August, 1988.

Rice J.R., "Elastic Fracture Mechanics Concepts for Interfacial Cracks", Transactions of the ASME, V 55, March 1988, pp. 98-103.

Rossmanith H. P., (editor), "Rock Fracture Mechanics", Springer-Verlag, 1983.

Shah S. P., (editor), "Toughening Mechanisms in Quasi-Brittle Materials", Proc. of NATO Advance Research Workshop, Evanston, IL, July 1991.

Snow D. T., "Rock Fracture Spacing, Openings, and Porosities", ASCE J. of Soil Mech. and Foundations Div., January 1968, pp. 73-91.

Williams M. L., "The Stresses Around a Fault or Crack in Dissimilar Media", Bulletin of the Seismological Society of America", V 49, No. 2, April 1959, pp. 199-204.

FRACTURE ENERGY OF CONCRETE AND EQUIVALENT CRACK LENGTH

BYUNG HWAN OH
Department of Civil Engneering
Seoul National University
Kwanak-ku, Seoul, Korea

ABSTRACT

A method to determine the fracture energy of concrete is investigated. A simple and accurate formula to predict the fracture energy of concrete is proposed. An equivalent crack length concept is then devised to predict the maximum failure loads of concrete beams. A simple formula for the equivalent crack length is also proposed. The concept enables to satisfactorily predict the maximum loads without resort to the complete fracture analysis or the R-curve analysis.

INTRODUCTION

It is becoming increasingly recognized that fracture toughness of concrete cannot be evaluated using linear elastic fracture mechanics without any appropriate modification. This is due to the fact that large size of nonlinear zone exists in front of the crack tip in concrete. This nonlinear zone in concrete, called the fracture process zone, is caused by microcracking ahead of the crack tip. The fracture process zone in concrete is known to be very large compared with those of metals or other engineering materials(2-7,10,14). This causes difficulties to measure the fracture toughness of concrete. Another difficulty lies in measuring the crack length increments during loading process since the crack tip is blurred by a microcracking zone in concrete. One possible remedy is to use the complete load-deflection diagram to determine the fracture energy of concrete.

The purpose of this paper is, therefore, to investigate the method of three-point bend test to determine the fracture energy of concrete and then to propose a simple formula to predict the fracture energy of a given concrete. The second objective is to devise a so-called equivalent crack length concept to calculate the maximum failure loads of the concrete beams. This concept will enable one to calculate the maximum loads of the beams

without resort to the complete nonlinear fracture analysis or the R-curve analysis.

FRACTURE TESTS

Several series of concrete beams were tested to measure the maximum failure loads of the beams and to determine the fracture energy of concrete. Five series of test beams were made and the compressive strengths were ranged from 20N/mm² to 28N/mm².

The dimension of the test beams was 100x100x400mm. The concrete beams for each series had four different initial notch depths,i.e., a_o/H = 0.0,0.2,0.4,0.6 in which ao = initial notch depth and H = beam depth. The reason for the different initial notch depths was to investigate the effect of initial notch depth ratio on the fracture energy of concrete. The concrete beams were tested in three-point loading condition. The test specimens were loaded in the Instron testing machine. The cross head speed (or loading velocity) was 0.05mm/min and was maintained constant throughout the tests. The load-deflection curves were generated by the plotter attached to the machine.

FRACTURE ENERGY

The fracture energy of concrete, G_F, can be determined from the area under the complete load-defection diagram. The area under the curve represents the amount of energy consumed when the crack propagates through the concrete beam.

Now, the contribution from the self-weight of the beam must be considered to calculate the fracture energy. The fracture energy per one unit of area may then be calculated by the following equation.

$$G_F = \frac{\int_0^{\delta_o} p(\delta)d\delta + mg\delta_o}{B(H-a_o)} \qquad (1)$$

in which δ_o = maximum deflection, m = mass of the beam, g = gravitational acceleration, B = beam width, H = beam depth, and a_o = initial crack length.

The fracture energy for each series of concrete has been calculated according to Eq.1. It was found in this study that the contribution of the self-weight of a beam to the fracture energy was very small and it was only about 2-6 percent of the total G_F value.

The fracture energy, G_F, must be known in advance as a material property in order to perform the fracture analysis of concrete structures. This requires a certain prediction formula to determine the fracture energy of concrete.

The progressive microcracking in the fracture process zone may be described by a stress-strain relation that exhibits strain-softening. The strain-softening uniaxial stress-strain relation may be well-idealized as a bilinear stress-strain diagram. The fracture energy may then be expressed as

$$G_F = W_c A = \frac{1}{2} W_c \varepsilon_o f_t' \qquad (2)$$

which W_c = width of microcrack band = $c_o d_a$(3,6), d_a = maximum aggregate size, A = area under the stress-strain curve, ε_o = strain at zero stress, f_t' = tensile strength of concrete, and E_c = its elastic modulus.

The recently-published good experimental data for the fracture energy of concrete have been used to determine the fracture energy equation. It was identified from this study that the fracture energy varies linearly with the tensile strength. The best prediction equation for the fracture energy of concrete was found from the test data as follows.

$$G_F = 58.4 f_t' d_a / E_c \qquad (3)$$

in which G_F is in N/mm, f_t' and E_c in N/mm²(or MPa), and d_a in mm. When the value of E_c is not given, the usual relation $E_c = 4{,}733\sqrt{f_c'}$ may be used(1) in which f_c' is the compressive strength of concrete in N/mm²(or MPa).

EQUIVALENT CRACK LENGTH

A stable crack grows as the applied load increases. One may then need to know how far the crack propagates at which the applied load reaches its maximum value. It is, however, very difficult to measure the actual amount of crack growth since the crack tip of concrete is blurred by a large size of microcracking zone. Even though one can make the measurements on the crack length increments, there may be some doubts as to whether the measured crack length is real.

To avoid the difficulties to measure the actual crack length increments and to be free from those doubts on the real crack, one may devise a certain efficient concept, called the equivalent crack length concept.

The equivalent crack length represents here a certain effective crack length which is a sum of the initial crack length and the crack increment at the maximum failure load. The crack length increment at the maximum load may be obtained from the relation between the load P and the fracture energy G_F as described below.

The stress intensity factor K_I for a three-point bend specimen(4, 8) can be written as

$$K_I = \sqrt{\pi \cdot a}\,\frac{P \cdot L}{B \cdot H^2}\, f(z) \qquad (4)$$

$$f(z) = 1.635 - 2.603z + 12.30z^2 - 21.27z^3 + 21.86z^4 \qquad (5)$$

in which z = a/H, a = crack length, H = beam depth, B = beam width, L = beam span, and P = applied load. Since $G_F = K_I^2/E$ for the plane stress state, one may rewrite Eq.4 as the following form.

$$P = \sqrt{\frac{E}{\pi \cdot a}}\,\frac{B \cdot H^2}{L \cdot f(z)}\,\sqrt{G_F} = F_1(a) \cdot G_F \qquad (6)$$

Eq.6 enables one to calculate the proper crack length "a" for a given load and fracture energy. So, one may evaluate the equivalent crack length a_{eq} from Eq.6 if the maximum failure load P_{max} and the fracture energy G_F are known from the experimental data.

The equivalent crack lengths have been calculated from the experimental data for various cases. It is enough only to know the maximum load P_{max} of the concrete beam since G_F may be obtained from Eq.3.

Conversely, it is also possible to predict the maximum failure load P_{max} once the equivalent crack length a_{eq} is determined. This can be done if a_{eq} can be predicted. To derive a simple formula for a_{inc}, the various variables have been investigated. The present study indicates that a_{inc} has certain correlations with the maximum aggregate size, the beam depth, and the relative crack depth ratio, but not with the tensile strength. The various equations have been tried to obtain the best formula and the following equation was found to give the best prediction for a_{inc}.

$$a_{inc} = [\ 0.80 + 0.258(1-z)H\ ]\ d_a^{0.5} \qquad (7)$$

in which $(1-z)H = H - a_o$ = ligament, H, a_o and d_a are given in cm.

Now, Eqs.3, 6 and 7 enable one to predict the maximum failure loads of the beams. One may write from Eq.6 as

$$P_t = F_1(a_{eq})\sqrt{G_F} \qquad (8)$$

in which P_t = theoretical maximum load, $a_{eq} = a_o + a_{inc}$ (Eq.7), and $F_1(a_{eq})$ comes from Eq.6.

The theoretical maximum loads have been calculated from Eq.8 and then compared with the various experimental data. Despite the simplified analysis for the maximum loads, the present method yields relatively good results which are not inferior to the complete analysis or the R-curve analysis.

CONCLUSIONS

1. The present experimental study indicates that the fracture energy is decreased as the initial notch-to-beam depth ratio increases. The appropriate ratio of initial notch-to-beam depth to determine the fracture energy of concrete is found to be 0.5.

2. It is found that the influence of the self-weight of a beam to the fracture energy is very small and it amounts to only several percent of the fracture energy.

3. A simple and accurate formmula for the fracture energy of concrete is proposed. The fracture energy is a required value to perform the fracture analysis of concrete structures. The fracture energy of concrete depends on the aggregate size and tensile strength and is about 80-130 N/m in value for normal aggregate concrete.

4. An equivalent crack length concept is devised to predict the maximum failure loads of concrete beams. A simple formula for the equivalent crack length is proposed. The concept enables to calculate the maximum loads without resort to the complete analysis or the R-curve analysis.

ACKNOWLEDGMENT

The financial support from the Korea Science and Engineering Foundation to this research is gratefully acknowledged.

REFERENCES

1. ACI 318-83, "Building Code Requirements for Reinforced Concrete," American Concrete Institute, 1983.
2. Bazant, Z. P., "Crack Band Model for Fracture of Geomaterials," Proceedings, 4th International Conference on Numerical Methods in Geomechanics, Edmonton, Alberta, Canada, Vol.3, Z. Eisenstein, ed., June, 1982, pp.1137-1152.
3. Bazant, Z. P., "Size Effect in Blunt Fracture : Concrete, Rock, Metal," Journal of Engineering Mechanics, Vol.110, No.4, April, 1984, pp.518-535.
4. Bazant, Z. P., and Cedolin, L., "Approximate Linear Analysis of Concrete Fracture by R-curves," Journal of Structural Engineering, Vol.110, No.6, June, 1984, pp.1336-1355.
5. Bazant, Z. P., and Cedolin, L., "Blunt Crack Band Propagation in Finite Element Analysis," Journal of the Engineering Mechanics Division, ASCE, Vol.105, No.EM2, Apr., 1979, pp.297-313.
6. Bazant, Z. P., and Oh B. H., "Crack Band Theory for Fracture of Concrete," Materials and Structures(RILEM, Paris), Vol.16, 1983, pp.155-177.
7. Bazant, Z. P., and Oh, B. H., "Rock Fracture via Strain-Softening Finite Elements," Journal of Engineering Mechanics, ASCE, Vol.110, No.7, 1984, pp.1015-1035.
8. Gjørv, O. E., Sørenson, S. I., and Arnesen, A., "Notch Sensitivity and Fracture Toughness of Concrete," Cement and Concrete Research, Vol.7, 1977, pp.333-344.
9. Kaplan, M. F., "Crack Propagation and the Fracture of Concrete," American Concrete Institute Journal, Vol.58, No.11, Nov., 1961.
10. Pertersson, P. E., "Fracture Energy of Concrete : Method of Determination," Cement and Concrete Research, Vol.10, 1980, pp.78-89, and "Fracture Energy of Concrete : Practical Performance and Experimental Results," Cement and Concrete Research, Vol.10, 1980, pp.91-101.
11. Raphael, J. M., "Tensile Strength of Concrete," Journal of the American Concrete Institute, March-April, 1984, pp.158-165.
12. Shah, S. P., and McGarry, F. J., "Griffith Fracture Criterion and Concrete," Journal of the Engineering Mechanics Division, ASCE, Vol.97, No.EM6, Proc. Paper 8597, Dec., 1971, pp.1663-1676.
13. Walsh, P. F., "Fracture of Plain Concrete," The Indian Concrete Journal Vol.46, No.11, Nov., 1979, pp.469, 470, and 476.
14. Wecharatana, M., and Shah, S. P., "Slow Crack Growth in Cement Composites," Journal of Structural Engineering Division, ASCE, Vol.108, No.ST6, June, 1982, pp.1400-1413.

INFLUENCE OF STRAIN GRADIENT ON FRACTURE ENERGY

VOLKER SLOWIK, FOLKER H. WITTMANN
Institute for Building Materials, Swiss Federal Institute of Technology,
8093 Zurich, Switzerland

ABSTRACT

The effect of different strain gradients in a concrete ligament on the fracture energy is investigated. The strain gradient considered is that at maximum load in the linear elastic range. Experiments to determine fracture energy on specimens with identical ligament size but with different strain gradients have been carried out. Different strain gradients are imposed by the specimen geometry and by the loading conditions. Comparative tests have been run with direct tension specimens, wedge splitting specimens having different cantilever length and three-point bending specimens. The influence of the strain gradient on the total specific fracture energy and the strain softening behaviour has been determined. Results serve to understand the difference in fracture energy and strain softening as determined under direct tension, with a wedge splitting test and three-point bending specimens.

INTRODUCTION

Fracture energy and strain softening have proved to be material parameters which allow us to describe crack formation in concrete in a realistic way. Soon it was found, however, that fracture energy depends on both specimen geometry and ligament size. It should be kept in mind that compressive and tensile strength of concrete depend on geometry and size too. In the case of fracture energy it may be anticipated that it varies as differently shaped fracture process zones will develop in specimens having different geometry. One aim of this contribution is to show for a given ligament size that the strain gradient has an influence on the observed fracture mechanics parameters. It will be shown that different components contribute to the global size effect. Strain gradient being one component of the global size effect is studied here in particular.

FRACTURE ENERGY AS INFLUENCED BY GEOMETRY

The size and geometry depedence of the fracture energy can not be properly described if only one geometric parameter is considered. There are several geometric effects, all having different physical origins. These effects have to be investigated separately in order to be able to compare fracture energies obtained under different conditions and to predict the behaviour of a structural element under given geometry and loading conditions. The semi-

empirical size effect law by Bazant /1/ allows to determine fracture mechanical material parameters for infinite large structures and to estimate critical loads for geometric similar members. It is not directly applicable for the above mentioned purpose. There are at least three geometric influences on the fracture energy, i.e. (1) the ligament size, (2) the strain gradient, and (3) the size of the highly stressed volume. The first and the third effect are related to the flaw and particle distribution and have to be described by means of a statistical approach. The third effect is caused by bulk energy dissipation in addition. The second effect can be explained by a different confinement of the fracture process zone.

Experimental investigations of the size effect on fracture energy performed by Hu /2/ included wedge splitting tests using mortar specimens with different notch length but constant total length. The measured fracture energy has been used to determine the local fracture energy along the concrete ligament. The variation of the local fracture energy can be explained by geometry and size effects. Zhong /3/ and Brühwiler /5/ performed wedge splitting tests with concrete specimens having different ligament and cantilever lengths. Nomura /4/ determined the fracture energy for geometric similar compact tension specimens made of concrete. In the experiments mentioned above both the ligament length and the strain gradient were changed simultaneously. In the experiments presented here the strain gradient is varied for a constant ligament length. In this context we consider the strain gradient at maximum load in the linear elastic range. It starts with the value of zero in the case of direct tension tests and reaches a maximum in bending tests, always for the same ligament length. In wedge splitting tests the strain gradient depends on the cantilever length.

PREPARATION OF SPECIMENS AND EXPERIMENTS

Preparation of specimens

The concrete mix used for all specimens had a maximum grain size of 32 mm. The cement content was 300 kg/m^3 and the water-cement ratio 0.5. The resulting compressive strength after 28 days is 41 MPa, the modulus of elasticity is 43 GPa and the density 2480 kg/m^3. The beams for the three-point bending tests were stored at 90% relative humidity. All other specimens were water cured. The age at testing was 28 d. The used specimen geometries are shown in Figure 1. Table 1 contains the corresponding dimensions. The ligament length and the specimen width amounted to 100 mm for all specimens. The notches in the wedge splitting specimens with the smallest size and in the bending beams were introduced by sawing. The notches in the other specimens were moulded by using a steel plate with a 1mm thick paraffin layer on both sides. Before demoulding the paraffin was heated to avoid any damaging of the concrete ligament. This was done with the specimen standing upside down to prevent the penetration of paraffin into the concrete ligament.

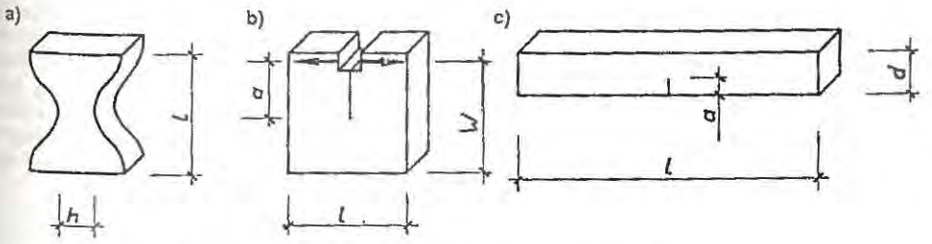

Figure 1. Specimen geometry: (a) dog bone for direct tension, (b) wedge splitting specimen, and (c) three-point bending specimen.

TABLE 1
Specimen dimensions, strain gradients and eccentricities of the equivalent normal force.

	direct tension	wedge splitting	wedge splitting	wedge splitting	wedge splitting	wedge splitting	three point bending
Serie	D	W1	W2	W3	W4	W5	B
dimension [mm] width=100 mm	h = 100 l = 300	w = 185 a= 85 l=200	285 185 300	485 385 500	645 545 500	985 885 500	d = 150 a = 50 l = 1000
max. strain gradient in el. range gradε	0	$3f_t(W+a)/(2W+a)/E/h$ f_t...tensile strength; E...modulus of elasticity; h...ligament length					$2f_t/Eh$
relative strain gradient gradε*E*h/f_t	0	1.78	1.87	1.93	1.94	1.96	2
eccentr. of equi. normal force	0	135	235	435	595	935	∞

Direct tensile tests
We intended to mimimize the bulk energy dissipation and therefore we used a dog-bone shaped specimen for the direct tension test. The end faces of the specimen were glued to steel plates connected with the testing machine. To increase the machine stiffness steel bars were clamped parallel to the specimen. All tests were run under deformation controlled conditions using a servo-hydraulic testing machine.

Wedge splitting tests
An electro-mechanical testing machine was used. The tests were carried out under crack opening control. For the determination of the fracture energy the specimen's self-weight was taken into consideration in two different ways. A horizontal force F_{cor} acting at the loading point can be determined from the equilibrium conditions. This force represents an additional splitting force. In addition the fracture energy was determined by numerical simulation using the fictitious crack model. In this case gravitational forces were taken into account. In this way the fracture energy and the parameters of the bilinear strain-softening diagram can be obtained by fitting the numerically calculated load-displacement curve with the experimental values.

Three-point bending tests
The span between the rolling supports amounted to 760 mm. The tests were carried out under deflection control using an electro-hydraulic testing machine with vertical loading direction. Two masses were applied to the outer ends of the beam for self-weight compensation. The measured load-deflection curves showed a very long tail at a very small force. We assume that this is caused by friction at the supports. To exclude this additional energy numerical simulations using the fictitiuos crack model were performed to determine fracture energy and strain-softening parameters. In this latter evaluation the long tail is of no significance.

RESULTS

In Table 2 the fracture energies obtained experimetally and numerically and the critical crack openings are given. Both the directly determined experimental fracture energy G_f^{exp} and the numerically calculated value G_f^{num} are given in Table 2. With the exception of the value for the direct tension test all critical crack openings given in Table 2 have been determined numerically. In the numerical simulation special attention was paid to a good agreement between the experimental and numerical load-displacement curves and therefore the fracture energies are not necessarily the same.

TABLE 2
Fracture energy G_f^{exp} as determined directly for the load-displacement diagrams, fracture energy G_f^{num} as obtained by numerical simulation, and critical crack opening w_c.

Serie	D	W1	W2	W3	W4	W5	B
number of samples	5	5	6	3	3	3	9
G_f^{exp} [N/m]	142.11 ±29.13	118.39 ± 9.97	97.56 ± 16.98	82.87 ± 16.0	75.82 ± 4.5	69.06 ± 15.40	114.28* ±9.16
G_f^{num} [N/m]	142.11	95.0	74.8	71.0	68.2	58.5	73.2
w_c [mm]	0.5	0.26	0.19	0.18	0.17	0.17	0.16

*This value is corrected for the long tail of the load-displacement curve.

Figure 2 shows the obtained fracture energies as function of the eccentricity of the equivalent normal load. Figure 3 contains representative strain softening curves for all test series. A bilinear softening behaviour has been assumed.

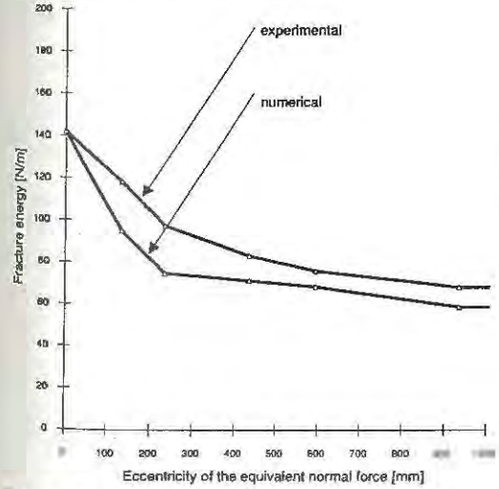

Figure 2. Fracture energy versus eccentricity of the equivalent normal load.

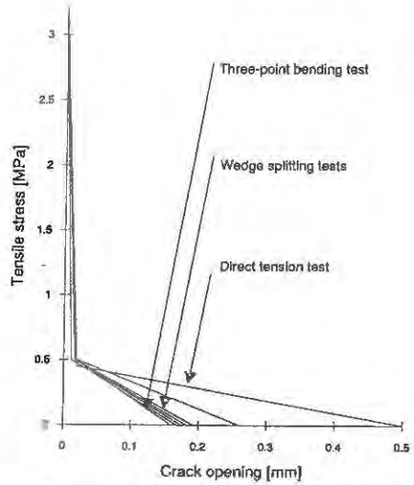

Figure 3. Strain softening diagrams.

DISCUSSION AND CONCLUSIONS

It has been shown that the fracture energy depends on the strain gradient in the concrete ligament. We explain this dependence by the varying length and width of the fracture process zone. For higher strain gradients the length of the fracture process zone decreases and the width becomes more confined. The strain softening diagrams calculated for the series with different strain gradients have nearly the same maximum tensile stress and the first steep descending branch ends at approximately the same stress. The critical crack openings, however, differ significantly. The tensile strength seems not to be influenced by the size of the fracture process zone. The wider the fracture process zone can develop the higher will be the resulting critical crack opening. Hu /2/ also concluded that the local fracture energy depends on the width of the fracture process zone.

The three-point bending tests have given higher maximum tensile stresses. This may explain why the fracture energy is comparatively high. At this moment we are unable to explain this effect. It can not be excluded that experimental inaccuracies are the origin of this discrepancy.

Fracture energy can be represented as function of the ligament length h and as function of the eccentricity e of the equivalent normal force in a three dimensional diagram. It is assumed that the specimen width is kept constant or is large enough so that there is no significant influence on the fracture energy. The influence of the size of the highly stressed volume is neglected in this representation. In Figure 4 some experimenal data are compiled. These data have been used to determine a surface for the fracture energy by a least square fit. The resulting surface is shown in Figure 5. Hillerborg /6/ presented results of comparative tests of three-point bending beams and concluded that the fracture energy becomes 20% higher if the beam depth changes by a factor of 2 and 30% higher for a factor of 3. These results have been considered in the approximation of the function mentioned above.

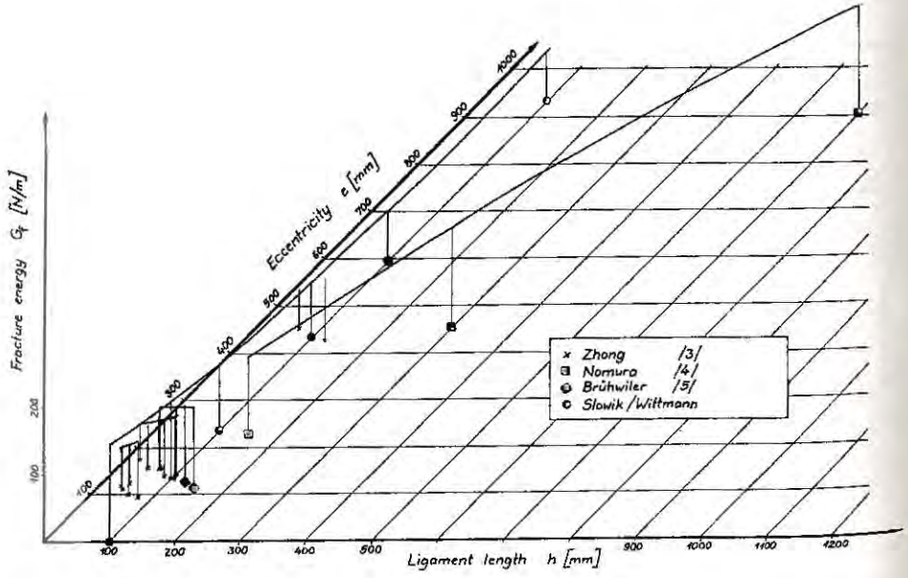

Figure 4. Compiled experimental data to demonstrate the influence of ligament length and eccentricity on fracture energy.

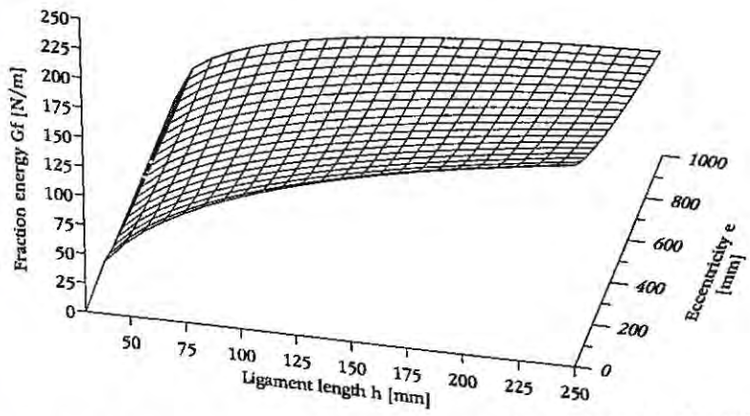

Figure 5. Fracture energy versus ligament length and load eccentricity as determined on the basis of the data shown in Figure 4.

It has been shown that the fracture energy depends both on the ligament length and on the eccentricity of the equivalent single force. The load eccentricity determines the strain gradient in the concrete ligament. The variation of the fracture energy in the range of usual specimen dimensions is of the same order of magnitude as the variation of the compressive strength at different specimen size. For the practical application of the concept of fracture energy appropriate conversion coefficients should be made available. This will enable us to predict the behaviour of large structural elements on the basis of laboratory tests.

REFERENCES

/1/ Bazant, Z.P., Kim, J.-K., Pfeiffer, P., Determination of nonlinear fracture parameters from size effect tests. Application of fracture mechanics to cementitious composites, NATO-ARW, September 4-7 1984, Northwestern University, USA, pp. 143-169.

/2/ Hu, X., Fracture process zone and strain-softening in cementitious materials. Postdoctoral report, Institute for Building Materials, Swiss Federal Institute of Technology Zurich, Switzerland, 1989.

/3/ Zhong, H., Size effect and fracture energy. Research report, Institute for Building Materials, Swiss Federal Institute of Technology Zurich, Switzerland, 1991.

/4/ Nomura, N., Fracture mechanics approach to study the tension softening behaviour in fracture process zone of concrete, Doctoral thesis, Tohoku University Sendai, Japan, 1990

/5/ Brühwiler, E., Bruchmechanik von Staumauerbeton unter quasi-statischer und erdbebendynamischer Belastung. Thése No 739, Département des Materiaux, Ecole Polytechnique Fédérale de Lausanne,1988

/6/ Hillerborg, A., Results of three comparitive test series for determining the fracture energy G_f of concrete. Materials and Structures, 1985, 18, 407-413.

MATERIAL BRITTLENESS FROM NONLINEAR FRACTURE MECHANICS

RAVINDRA GETTU*, PERE C. PRAT* and MOHAMMAD TAGHI KAZEMI#

*Technical University of Catalunya, ETSECCPB-UPC,
Campus Nord, Gran Capitán s/n, E-08034 Barcelona, SPAIN; and

#Department of Civil Engineering, Sharif University of Technology,
P.O.Box 11365-8639, Azadi Ave., Tehran, IRAN

ABSTRACT

Based on nonlinear fracture mechanics models, several investigators have proposed measures of the brittleness of materials such as concrete. These quantities can be obtained experimentally from tests of simple fracture specimens. Some of the methods, including those of Bažant, Shah, Carpinteri and Hillerborg, are discussed, and typical values of their parameters are presented. The material brittleness quantified on the basis of fracture mechanics has potential for use as a parameter in both structural and material design.

INTRODUCTION

The failure of quasi-brittle materials (i.e., materials that are aggregated, disordered and weak in tension) is generally a consequence of cracking. It is rational, therefore, that fracture mechanics be applied for studying the behavior of materials such as concrete. One aspect that is of major importance is the brittleness with which structures fail. In high strength concrete, for example, modifications to the microstructure have caused an alarming increase in brittleness, forcing designers to confine the concrete with steel in order to prevent catastrophic failure, especially under seismic loading. Furthermore, an increase in brittleness implies a decrease in nominal strength [1]. Obviously, a less brittle material would make designs more economical and safer. Several measures of brittleness based on fracture mechanics criteria have been proposed. These can be used in future design codes that take the brittle nature of failure into account. Also, with dependable methods of quantifying brittleness, materials can be engineered to be not only stronger but also less brittle.

Most brittleness measures are related to the size or some other aspect of the fracture process zone that precedes the crack in quasi-brittle materials, and reflect the "pseudo-ductility" of the material (or the inverse of its brittleness). The nonlinear fracture models that define these quantities also provide means of determining the crack resistance, and have two or more basic parameters. When the brittleness is very high, the response of these models tends towards linear elastic fracture

mechanics (LEFM) criteria based on only one parameter. The parameters discussed here have been verified extensively and shown to be practically independent of specimen size. However, there is a possibility that they may be geometry-dependent, and therefore, the data presented pertains mainly to notched beam tests which have been the most common.

Structural brittleness (or the brittleness of structural failure) is a function of the material and the structure. Generally, larger structures are more brittle. This is reflected in several of the brittleness numbers in the literature. In addition, the shape of the structure should be included in the "true" determination of structural brittleness [2].

MATERIAL BRITTLENESS BASED ON FRACTURE MECHANICS

Hillerborg's Characteristic Length, ℓ_{ch}

Hillerborg [3] combined the three material parameters of the fictitious crack model [4] for fracture in concrete, into a characteristic length:

$$\ell_{ch} = EG_F/f_t^2 \qquad (1)$$

where E = modulus of elasticity, G_F = fracture energy, and f_t = tensile strength. The value of G_F used in Eq. (1) is usually obtained from the area under the load-deflection curve of a notched specimen [3]. Note that ℓ_{ch} can be a true material parameter only if sufficiently large specimens are used to experimentally determine G_F and f_t, as they are dependent on the specimen size and geometry.

A quantity similar to ℓ_{ch} was suggested by Irwin as the size of the plastic zone, and is of significant importance with respect to the ductile-brittle transition in fracture behavior of metals. In quasi-brittle materials, ℓ_{ch} is related to the fracture zone size, and decreases with increase in material brittleness. Some of the values given in the literature for various materials are listed in Table 1.

A code-type relation for ℓ_{ch} has recently been proposed [6]:

$$\ell_{ch} = 600\, a_d\, f_{cm}^{-0.3} \qquad (2)$$

where f_{cm} = compressive strength in MPa; and a_d = 4, 6 & 10, for maximum aggregates sizes of 8, 16 & 32 mm, respectively. This equation fits available data satisfactorily, and may be used in the absence of test data.

TABLE 1
Typical values of ℓ_{ch}

Material	value	Ref.
Glass	≃ 1 μm	[5]
Dense Silica Cement Paste	≃ 1 mm	[5]
Cement Paste	5-15 mm	[3]
Mortar	100-200 mm	[3]
High Strength Concrete (50-100 MPa)	150-300 mm	[6]
Normal Concrete	200-500 mm	[3]
*Dam Concrete: m.a.s. = 19 mm	≃ 0.6 m	[7]
m.a.s. = 38 mm	≃ 0.7 m	
m.a.s. = 76 mm	≃ 0.9 m	
Glass Fiber Reinforced Mortar	0.5-3 m	[3]
Steel Fiber Reinforced Concrete	2-20 m	[3]

m.a.s. = maximum aggregate size
*values obtained from wedge-loaded compact tension specimens

Carpinteri's Brittleness Number s_E

Carpinteri [8] defined a dimensionless number based on finite element analysis of the scale effects in notched beams using the fictitious crack model [4]:

$$s_E = \frac{G_F}{f_t\, d} \tag{3}$$

where G_F = fracture energy, defined as the area under the stress-separation relation $f(w)$ of the fictitious crack, f_t = tensile strength, and d = size of structure or specimen. For a linear $f(w)$ relation, $s_E = w_c/2d$, where w_c is the critical separation when the cohesive stress becomes zero [4]. A larger s_E implies that the structure fractures in a less brittle manner. For specimens with identical shape and size, s_E depends only on G_F/f_t or w_c. Therefore, these two quantities can be taken as the measures of material pseudo-ductility according to this model.

Jenq-Shah Model

The two-parameter fracture model [9] of Shah considers an effective (or elastically equivalent) crack in a specimen that is identical to the concrete specimen but elastic. Failure (peak load) occurs when the effective stress intensity factor and the effective crack-tip opening reach the material parameters K_{Ic}^S and $CTOD_c$, respectively. The effective critical crack extension, a_c, is determined from the unloading compliance (load versus crack-opening) of a notched specimen, at its peak load. Subsequently, K_{Ic}^S and $CTOD_c$ are computed, using classical LEFM equations.

Two size-independent parameters based on the Jenq-Shah model have been taken to quantify material brittleness. One of them is $CTOD_c$, and the other is a length parameter defined by [9]:

$$Q = \left(\frac{E\ CTOD_c}{K_{Ic}}\right)^2 \tag{4}$$

Typical values of Q and $CTOD_c$ are shown in Table 2. The effective crack extension a_c has also been used as a measure of the material brittleness [10,11] but it is dependent on specimen geometry, unlike the others.

TABLE 2
Typical values of Q and $CTOD_c$

Material	Q	$CTOD_c$	Ref.
Cement Paste with 10% silica fume	5 mm	0.002 mm	[11]
Cement Paste	50 mm	0.005-0.008 mm	[9]
Mortar	100 mm	0.008-0.013 mm	[9]
Concrete	300 mm	0.01-0.02 mm	[9]
*Dam Concrete: m.a.s. = 19 mm	50-300 mm	0.016-0.025 mm	[7]
m.a.s. = 38 mm	130-230 mm	0.020-0.034 mm	
m.a.s. = 76 mm	190-300 mm	0.025-0.044 mm	
High Str. Concrete (110MPa)	90 mm	0.011 mm	[10]

m.a.s. = maximum aggregate size
*values obtained from wedge-loaded compact tension specimens

Bazant's Process Zone Size

Based on experimental observations, a phenomenological relation for the failure stresses of geometrically similar specimens and structures was proposed by Bažant [1,12]:

$$\sigma_N = \frac{B}{\sqrt{1+\beta}}, \qquad \beta = d/d_0 \tag{5}$$

where σ_N = maximum nominal stress (peak load/gross cross-sectional area), d = characteristic specimen size, and B and d_0 = empirical parameters. Eq. (5) can be also put in a linear form that is convenient for linear regression analysis:

$$Y = AX+C, \text{ where } X = d,\ Y = \sigma_N^{-2}, \text{ and } B = C^{-1/2},\ d_0 = C/A \tag{6}$$

From the size effect model, unambiguous fracture parameters which are independent of specimen size and shape [12,2] have been derived. One such

parameter is the effective process zone size, which is the crack extension at the peak load of an infinitely large specimen of the same material. It can be obtained from the peak loads of geometrically similar notched specimens of different sizes using Eqs. (5) or (6) [13]:

$$c_f = \frac{g_0}{g_0'} d_0 = \frac{g_0}{g_0'} \frac{C}{A} \tag{7}$$

where g_0 and g_0' are constants dependent on the specimen geometry used [13]. The value of c_f reflects the effectiveness of the toughening or crack-shielding mechanisms in the material. These mechanisms include aggregate-bridging, microcracking, and crack-deflection. A larger c_f implies that energy is dissipated, during fracture, in a larger zone, and that, consequently, fracture is less brittle. Typical values of c_f are shown in Table 3, along with K_{Ic} (fracture toughness) and the statistical parameters obtained with the procedure recommended by RILEM [13].

Table 3
Linear regression analysis for fracture parameters
based on the size effect method

Material & Environ. Conditions	A		C		m	K_{Ic}		c_f		Ref.
	mean mm^3/N	ω	mean mm^4/N^2	ω		mean $MPa\sqrt{mm}$	ω	mean mm	ω	
Concrete	0.0060	0.07	0.470	0.15	0.15	31.4	0.03	13	0.17	[12]
Mortar	0.0091	0.04	0.100	0.67	0.13	25.6	0.02	2	0.67	[12]
[1]HSC	0.0130	0.01	0.424	0.39	0.26	33.1	0.06	6	0.41	[14]
[2]LS	0.0704	0.05	3.66	0.06	0.08	29.9	0.03	9	0.80	[15]
[3]LS	0.1100	0.01	2.19	0.03	0.01	23.9	0.01	4	0.03	[16]
[4]Concrete	0.0039	0.26	0.408	0.25	0.34	39.2	0.13	18	0.36	[17]
[5]Concrete	0.0100	0.11	0.0748	0.16	0.01	24.3	0.06	1	0.20	[17]
[6]Concrete	0.0085	0.09	0.295	0.46	0.24	26.5	0.05	6	0.47	[18]
[7]Concrete	0.0143	0.06	0.341	0.41	0.16	20.4	0.03	4	0.41	[18]
[8]Concrete	0.00243	0.13	0.563	0.11	0.15	76.4	0.07	45	0.17	[19]

ω = co-efficient of variation; m = relative width of scatter

[1]High strength concrete at 14 days (86 MPa)
[2]Indiana limestone (arrester orientation)
[3]Indiana limestone (divider orient.) - precracked with ≃ 7 fatigue cycles
[4]Concrete loaded with time to failure of ≃ 1.4 seconds
[5]Concrete loaded with time to failure of ≃ 3 days
[6]Concrete tested dry at 65°C
[7]Concrete tested wet at 65°C
[8]Saturated concrete tested at -70°C

It can be seen from Table 3 that c_f decreases with increase in temperature, loading time and compressive strength. Note that the upper limits suggested for m, and ω-values for A and C are 0.2, 0.1 and 0.2, respectively. Since several of the test data in Table 3 violate these recommendations, it seems that more testing is required before the observed trends can be generalized. Also, it has been observed that the values of the parameters obtained depend on whether linear or nonlinear regression analysis is used (e.g., see Ref. [2]).

CONCLUDING REMARKS

Generally, brittleness of concrete decreases with increase in aggregate size, and increases with increase in compressive strength. The addition of fibers to concrete decreases the brittleness considerably. Note that the quantities described here may depend on specimen shape, and therefore, it is best that the brittleness of different materials be compared only when parameters have been obtained by the same method.

Acknowledgements

R.Gettu is grateful for support by a grant from the Ministry of Education and Science, Government of Spain (Supervisor: Prof. I.Carol). The help of Padma Gettu with the statistical analysis is appreciated.

REFERENCES

1. Bažant, Z.P., Size effect in blunt fracture: concrete, rock, metal. J. Engng. Mech., 1984, **110**, 518-535.

2. Bažant, Z.P. and Kazemi, M.T., Determination of fracture energy, process zone length and brittleness number from size effect, with application to rock and concrete. Int. J. Fract., 1990, **44**, 111-131.

3. Hillerborg, A., Analysis of a single crack. In Fracture Mechanics of Concrete, ed. F.H.Wittmann, Elsevier Science, Amsterdam, 1983, pp. 223-249.

4. Hillerborg, A., Modéer, M. and Petersson, P.-E., Analysis of crack formation and crack growth in concrete by means of fracture mechanics and finite elements. Cem. Concr. Res., 1976, **6**, 773-782.

5. Bache, H.H., Fracture mechanics in design of concrete and concrete structures. In Fracture Toughness and Fracture Energy of Concrete, ed. F.H.Wittmann, Elsevier Science, Amsterdam, 1986, pp. 577-586.

6. Hilsdorf, H.K. and Brameshuber, W., Code-type formulation of fracture mechanics concepts for concrete. Int. J. Fract., 1991, **51**, 61-72.

7. Brühwiler, E., Broz, J.J. and Saouma, V.E., Fracture model evaluation of dam concrete. J. Materials in Civil Engng., 1991, **3**, 235-251.

8. Carpinteri, A., Di Tommaso, A. and Fanelli, M., Influence of material parameters and geometry on cohesive crack propagation. In Fracture Toughness and Fracture Energy of Concrete, ed. F.H.Wittmann, Elsevier Science, Amsterdam, 1986, pp. 117-136.

9. Jenq, Y.S. and Shah, S.P., A two parameter fracture model for concrete. J. Engng. Mech., 1985, **111**, 1227-41.

10. John, R. and Shah, S.P., Fracture mechanics analysis of high-strength concrete. J. Materials in Civil Engng., 1989, **1**, 185-198.

11. Lange, D.A., Relationship between microstructure, fracture surfaces and material properties of portland cement. Ph.D. Dissertation, Northwestern Univ., Evanston, USA, December 1991.

12. Bažant, Z.P. and Pfeiffer, P.A., Determination of fracture energy from size effect and brittleness number. ACI Mater. J., 1987, **84**, 463-480.

13. RILEM Committee TC89-FMT Fracture Mechanics of Concrete — Test Methods, Size-effect method for determining fracture energy and process zone size of concrete. Mater. Struct., 1990, **23**, 461-465.

14. Gettu, R., Bažant, Z.P. and Karr, M.E., Fracture properties and brittleness of high-strength concrete. ACI Mater. J., 1990, **87**, 608-618.

15. Bažant, Z.P., Gettu, R. and Kazemi, M.T., Identification of nonlinear fracture properties from size effect tests and structural analysis based on geometry-dependent R-curves. Int. J. Rock Mech. Min. Sci., 1991, **28**, 43-51; Corrigenda, 1991, **28**, p.233.

16. Schmidt, R.A., Fracture-toughness testing of limestone. Expt. Mech., 1976, 161-167.

17. Bažant, Z.P. and Gettu, R., Rate effects and load relaxation in static fracture of concrete. Report 90-3/498r, Center for Advanced Cement-Based Materials, Northwestern Univ., Evanston, USA, 1991; also ACI Mater. J., 1992, in press.

18. Bažant, Z.P. and Prat, P.C., Effect of temperature and humidity on fracture energy of concrete. ACI Mater. J., 1988, **85**, 262-271.

19. Maturana, P., Planas, J. and Elices, M., Evolution of fracture behaviour of saturated concrete in the low temperature range. Eng. Fract. Mech., 1990, **35**, 827-834.

THE INFLUENCE OF AGGREGATE/PASTE BONDING AND STRENGTH ON MODE I FRACTURE MECHANICS PROPERTIES OF CONCRETE

STUART SWARTZ, YU-CHENG KAN
Department of Civil Engineering
Kansas State University
Manhattan, KS 66506
USA

ABSTRACT

The mode I fracture properties of concrete obtained by proposed standard testing methods are determined using beams in three point bending with a view to evaluating the suitability of these methods for mixtures with widely-varying parameters. In this paper, the results of an initial portion of this study are presented in which extremes of aggregate/paste strength and - to a limited extent - bonding were used in the concrete mixtures.

INTRODUCTION

The acceptability of fracture mechanics to the design of concrete structures presupposes the availability of methods of testing to obtain appropriate material properties (in addition to the sole property normally used in concrete design, f'_c). To date, a number of such methods have been proposed to RILEM eg. Hillerborg (and RILEM Committee TC 50)[1], G_F; Bazant, G_f[2]; and Jenq/Shah, K^s_{IC}, $CTOD_c$[3]. These methods determine the indicated mode I fracture properties as well as brittleness number, characteristic dimension and effective crack length. These methods and comparisons between equivalent results, as well as other methods, are given in a report by Karihaloo and Nallathambi[4].

Since the processes of initiation and growth of cracks which lead to fracture in concrete must surely be influenced by aggregate - paste bonding and strength relationships (as well as other conditions) it would be desirable to verify if these proposed testing methods are valid for wide extremes in these mixture parameters.

An extensive testing program at KSU, which is in progress, attempts to do this through using beams in three point bending. The methods of Hillerborg[1], Jenq and Shah[3,4] and Karihaloo and Nallathambi[4] are used, compared to each other and to the method of Go/Refai/Swartz[5]. The results presented here are preliminary in nature and incomplete.

PREVIOUS WORK

An early attempt to evaluate the influence of mixture parameters on values of K_{IC} was done by Naus and Lott[6]. To the writers' knowledge, this is the only study where the effects of a wide range of mix variables on K_{IC} were investigated. Variables included water/cement (W/C), air content, mortars-pastes-concretes, curing time, percent fine aggregate, fineness modulus of aggregate, and percent coarse aggregate. Unfortunately, their results are flawed because of the testing method employed. Basically, small beams were used and slow crack growth and process zone effects were not considered. Of course, at that date (1969) the importance of these effects was not recognized.

A number of tests to evaluate the influence of aggregate size, aggregate surface roughness (crushed - rounded) and W/C on effective crack length a_e and fracture toughness K_{IC} were conducted by Nallathambi, et al.[7-9]. The most striking results were an increase in K_{IC} with crushed versus rounded aggregate and a decrease in K_{IC} with increase in W/C.

Although many results are available for different fracture properties from many investigators, these are by and large for a single mix in each case - or at most a limited number of mixes. This is essentially true even for the round robin tests reported by Hillerborg[10].

TESTING PROGRAM

The entire testing program comprises twenty four groups of beams with variations in: W/C; sand gradation; types of aggregate - crushed limestone, polished limestone, crushed quartzite, river gravel, expanded shale; and use of flyash or silica fume.

Based on earlier work, it was decided to use beams with span = 40 in. (1016 mm), depth = 10 in. (254 mm) and width = 5 in. (127 mm). It has

been shown that this size is sufficient to develop a process zone completely for the maximum aggregate size used here (< 0.75 in. or 19 mm) and that K_{IC} is crack length independent for crack/depth ≤ 0.7[11].

The results presented here are for W/C = 0.64, 0.30; crushed limestone; polished limestone; and crushed quartzite as summarized in Table 1.

Table 1

Mix parameters for beam testing program

I.D.	W/C	Limestone Crushed	Limestone Polished	Quartzite Crushed
NC-.64-S1	0.64	X		
NC-.30-S1	0.30	X		
NP-.64-S1	0.64	X	X	
NP-.30-S1	0.30	X	X	
HC-.64-S1	0.64			X
HC-.30-S1	0.30			X

Note: All coarse aggregates, 3/4 in. minus; well-graded sand; Type I Portland Cement

All beams were cast in steel molds along with companion 3 in. x 6 in. (75 x 150 mm) cylinders. After curing one day, the specimens were demolded and placed in a fog room for 84 days. They were then removed and placed in an air-dried environment for 7 days and tested on the 92nd day. On the test day, four beams and companion cylinders were tested. The cylinder tests included uniaxial compression (f'_c and stress-strain) and split-cylinder tension. The fracture tests reported here are for beams notched at midspan to one third the depth. All tests were conducted using strain control on the crack mouth opening displacement and load-displacement plots were obtained. The load point displacement was measured using a reference bar and was to the side of the beam away from the load[12].

TEST RESULTS

Average values of the various test results are presented in Table 2.

An empirical equation relating K^s_{IC} and f'_c was given by John and Shah[13].

$$K^s_{IC} = 1.3\ (f'_c)^{0.75} \qquad (1)$$

In this f'_c is psi and K^s_{IC} is lb-in.$^{-3/2}$. This equation is plotted in Fig. 1 along with the Jenq/Shah[3] data values from Table 2.

Table 2

Fracture test results, average values

		NC-.64	HC-.64	NP-.64	NP-.30	HC-.30	NC-.30
f_c', psi x 10^3		5.74	5.83	6.20	8.88	9.52	9.82
MPa		39.5	40.2	42.7	61.2	65.6	67.7
f_t', psi x 10^3		0.74	0.87	0.78	1.17	1.16	1.22
MPa		5.1	6.0	5.4	8.0	8.0	8.4
E_c, psi x 10^6		4.50	5.08	4.74	5.46	5.54	6.03
GPa		31.0	35.0	32.7	37.2	38.2	41.6
K_{IC} lb-in$^{-3/2}$	ref. 3	922	1206	980	1266	1523	1308
		1015	1327	1078	1392	1676	1439
kN-m$^{-3/2}$	ref. 4	1009	1494	999	1349	1732	1489
		1110	1643	1099	1484	1905	1638
Fracture Energy lb/in	ref. 1	0.565	0.824	0.570	0.727	0.952	0.679
		99.0	144.4	99.9	127.4	166.8	119.0
	ref. 3	0.245	0.470	0.232	0.364	0.627	0.480
N/m		42.9	82.3	40.6	63.8	110.0	84.1
	ref. 4	0.335	0.639	0.296	0.486	0.678	0.521
		58.7	112.0	51.9	85.1	118.8	91.3
$CTOD_c$, μin.		966	1873	965	988	1536	1331
μm		24.5	47.6	24.5	25.1	39.0	33.8

Note: All sand series S1.

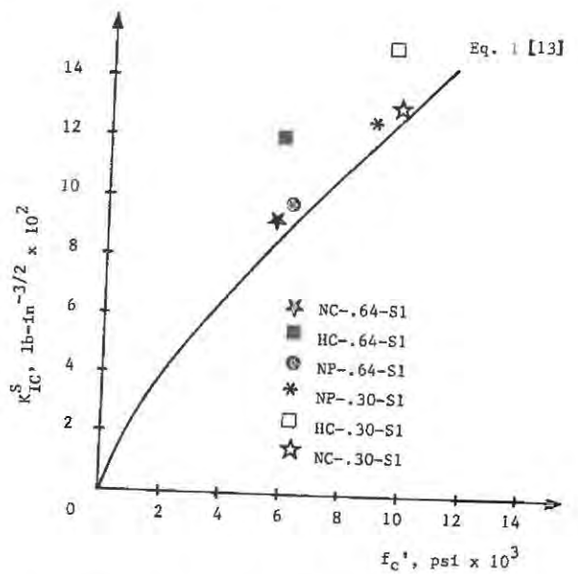

Figure 1. Variation of fracture toughness with compressive strength

CONCLUSIONS

The results of this initial portion of a much larger study into the effects of various mixture components on fracture mechanics properties of concrete lead to the following conclusions.

1. The fracture toughness of the concrete with limestone is not much different for crushed versus polished aggregate and the variation of values with f_c' is quite similar to the prediction of Eq. 1 given by John/Shah[13].

2. For a given W/C, the f_c' for quartzite is not significantly different from that for limestone - crushed or polished, but the fracture toughness values are considerably higher.

3. The fracture toughness results between the Jenq/Shah and Karihaloo/Nallathambi methods are quite similar for every mix reported here.

ACKNOWLEDGMENT

The research reported here is supported by the National Science Foundation, Grant No. MSM-8919449. This support is gratefully acknowledged.

REFERENCES

1. RILEM, 50-FMC, Determination of the fracture energy of mortar and concrete by means of three-point bend tests on notched beams. Mat. and Stru, 18, 106, 1985.

2. RILEM, 89-FMT, Size-effect method for determining fracture energy and process zone size of concrete. Mat. and Stru., 23, 138, 1990, 461-65.

3. RILEM, 89-FMT, Determination of fracture parameters (K_{IC}^S and $CTOD_c$) of plain concrete using three-point bend tests. Mat. and Stru., 23, 138, 1990, 457-60.

4. Karihaloo, B.L. and Nallathambi, P., Notched beam test: mode I fracture toughness. In Fracture Mechanics Test Methods for Concrete, eds. S. P. Shah and A. Carpinteri, Chapman and Hall, London, 1991, pp. 1-86.

5. Swartz, S.E. and Refai, T., Cracked surface revealed by dye and its utility in determining fracture parameters. In Fracture Toughness and Fracture Energy - Test Methods for Concrete and Rock, eds. H. Mihashi, H. Takahashi and F. A. Wittmann, A. A. Balkema, Rotterdam, 1989, pp. 509-20.

6. Naus, D.J. and Lott, J.L., Fracture toughness of portland cement concretes. ACI Jnl., 66, 6, 1969, 481-89.

7. Nallathambi, P., Karihaloo, B.L. and Heaton, B.S., Effect of specimen and crack sizes, water cement ratio and coarse aggregate texture upon fracture toughness of concrete. Mag. Concr. Res., 36, 129, 1984, 227-36.

8. Nallathambi, P., Karihaloo, B.L. and Heaton, B.S., Various size effects in fracture of concrete. Cem. & Concr. Res., 15, 1, 1985, 117-26.

9. Nallathambi, P. and Karihaloo, B.L., Determination of specimen-size independent fracture toughness of plain concrete. Mag. Concr. Res., 38, 135, 1986, 67-76.

10. Hillerborg, A., Results of three comparative test series for determining the fracture energy G_F of concrete. Mat. and Stru., 18, 107, 1985.

11. Kan, Y.-C. and Swartz, S.E., Influence of curing conditions and width on the fracture of concrete beams. In Proceedings of 1989 SEM Spring Conference on Experimental Mechanics, Cambridge, MA, May 29-June 1, 1989, pp. 196-201.

12. Swartz, S.E. and Kan, Y.-C., On the validity of indirect measurement of the LPD for SEN concrete beams. In Fracture Processes in Concrete, Rock and Ceramics, eds. J.G.M. vanMier, J.G. Rots, A. Bakker, E&FN SPON, London, 1991, pp. 771-778.

13. John, P. and Shah, S.P., Fracture mechanics analysis of high-strength concrete. Jnl. Mat. C.E., 1, 4, 1989, 185-98.

WHY DIRECT TENSION SPECIMENS FLEX AND BREAK AT MIDLENGTH

ZDENĚK P. BAŽANT
Walter P. Murphy Professor of Civil Engineering
Northwestern University
Evanston, Illinois 60208

LUIGI CEDOLIN
Professor of Structural Engineering
Politecnico di Milano
Milano, Italy 20133

ABSTRACT

In a direct tension test, unnotched specimens of quasibrittle materials that exhibit post-peak strain softening do not deform symmetrically. The equilibrium path bifurcates and the thermodynamic criterion of stable path requires the specimen to flex to one side, even if the geometry is perfect and if the straightening effect of the moment of the axial force about the centroid of the deflected cross section is taken into account. In absence of rotational restraints at the ends, the specimen fails right after the peak load. But if the attachments to the loading machine exert a sufficient restraint against rotation, the flexing to the side is retarded and failure occurs at midlength. The phenomenon (which is similar to the recently discovered behavior of notched tensile fracture specimens) is illustrated using a simple model in which the specimen consists of two bars of unequal length, joined by a strain-softening link.

INTRODUCTION

For brittle or quasibrittle materials which exhibit strain softening, for example concrete, rock or ceramics, the interpretation of the direct tensile test is not easy. As Rots and de Borst [8, 9] and Hordijk, Reinhardt and Cornelissen [6] have recently shown, symmetrically notched prismatic specimens subjected to centric tension do not deform symmetrically but flex to one side as cracks propagate from the notches. A similar loss of symmetry and lateral flexing was analytically demonstrated by Bažant [1, 2] and Bažant and Tabbara [11]. Subsequently Bažant [3] and Bažant and Cedolin [4] analyzed bifurcation and stable response path of a simple model of a centrically tensioned unnotched specimen, and they again found that this idealized

specimen, too, flexes to one side if certain, not abnormal, conditions are met. A similar phenomenon was demonstrated by Pijaudier-Cabot and Akrib [7] by layered finite element analysis. The objective of this paper is to present a summary of the results obtained in Ref. [5] through a generalization of the previously presented model.

RIGID-BAR MODEL

Let us consider the tensile specimen in Fig. 1a, which consists of two rigid bars of unequal lengths L_1 and L_2 , and denote by N the axial (tensile) load and by u the corresponding axial displacement. The bars are linked by two deformable short flanges of length h ($h \ll L$, $L \simeq L_1 + L_2$) and cross section areas A_f , each of negligible width and located at distances b from the cross section center. These flanges can exhibit strain-softening, characterized by tangent softening modulus E_t ($E_t < 0$, Fig. 1d). The specimen is supported at the ends by hinges with springs of rotational stiffnesses C . Let w be the deflection of the link, and θ_1 and θ_2 the inclination angles of bars L_1 and L_2 , respectively. The link is assumed to transmit a shear force without deforming in shear.

Let us assume that initially $\theta_1 = \theta_2 = 0$ (perfect structure). In general the equilibrium path in the (P, u) plane bifurcates, with two possible branches: (1) the primary (symmetry preserving) branch $\delta\theta_1 = \delta\theta_2 = 0$, for which both flanges are loading, obeying modulus E_t ; and (2) the secondary (symmetry breaking) branch $\delta\theta_1 \neq \delta\theta_2 \neq 0$, for which one flange is loading, obeying modulus E_t ($E_t < 0$), and the other is unloading, obeying unloading modulus E_u ($E_u > 0$, $E_u \leq E$ = initial elastic modulus). For the latter path, writing the equilibrium conditions of each bar for vertical forces and for moments about the center of the link, expressing the strains in the left and right flanges of the link in terms of displacements, and assuming that the right flange is loading and the left flange is unloading, one can show (see Ref. [5]) that the condition that the left flange during this deformation unloads requires that

$$-E_t \geq \bar{E}_t = \frac{h}{4b^2 A_f}\left[N\frac{L}{2} + C - 2\Delta^2\left(\frac{N}{L} - 2\frac{C}{L^2}\right)\right] \tag{1}$$

where $\Delta = (L_1 - L_2)\ /2$ = distance of the location of failure from the specimen midlength, and $\bar{E}_t$ represents the minimum magnitude of E_t for which flexing to the side can occur. From this equation one can see that $\bar{E}_t$ (1) increases with the value of C, i.e. with the stiffness of the rotational restraints at the bar ends ; and (2) increases

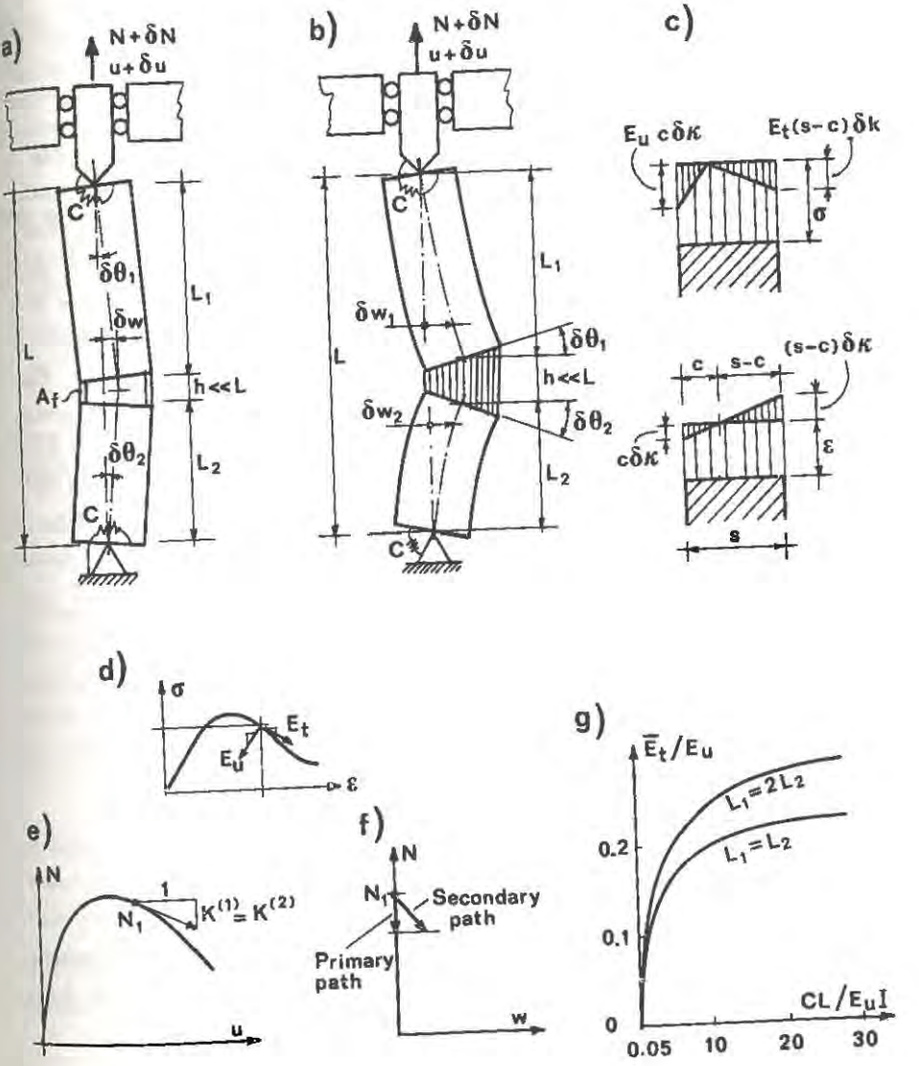

Figure 1. (a) Rigid-Bar Model; (b) Deformable Bar Model; (c) Variations of Stresses and Strains in Strain-Softening Slice; (d) Loading and Unloading Tangential Moduli; (e, f) Bifurcation of Equilibrium Path; (g) Minimum Magnitude of the Loading Tangential Modulus at Bifurcation.

with distance Δ provided that $C > NL/2$, i.e. that the rotational restraint at the ba: ends exceeds a certain limit. If this condition is met, the smallest $\overline{E}_t$ occurs fo: $L_1 = L_2$.

In the same Ref. [5] it is also shown that the value of $K^{(2)}$ corresponding to $E_t = -\overline{E}_t$ coincides with the tangent stiffness $K^{(1)} = 2A_f E_t/h$ for the primary branch, for which $\delta\theta_1 = \delta\theta_2 = 0$ and symmetry is preserved (Fig. 1e, f). As shown by thermodynamic arguments in Ref. [4] (Sec. 10.2 - 10.3), the equilibrium path branch that actually occurs is that for which the tangent slope given by $K^{(1)}$ or $K^{(2}$ is steeper. Thus, the symmetry-breaking secondary branch must occur when $K^{(2)} < K^{(1)}$, and it is found that this condition is always satisfied for $E_t < -\overline{E}_t$. This means that, assuming a softening stress-strain diagram with a gradually steepening donward slope, the specimen will flex to the side as soon as the limit condition $E_t = -\overline{E}_t$ is attained. Furthermore, comparing the $\overline{E}_t$ values for various Δ values for a specimen with rotational end restraints, we see that the minimum slope occurs for $\Delta = 0$. This proves that the direct tensile specimen must break at midlength.

The foregoing analysis shows that, if there is a rotational restraint of nonzero stiffness at the specimen ends, the minimum magnitude of the tangential modulus for which flexing to the side occurs is attained when the specimen breaks in the middle and increases with C . It appears, then, that in order to increase the stability of the primary path, one should increase the stiffness of the rotational restraints at the bar ends.

The limit condition $E_t = \overline{E}_t$, expressed through Eq. 1, gives an implicit equation [5] exactly analogous to that which defines Shanley's load in compression [10]; for a review see for example Ref. [4] (Sec. 8.1 and 10.2-10.4). Overall we may conclude that the strain-softening feature of the constitutive law engenders bifurcation of the equilibrium path in tension (Fig. 2f), a fact that has not been suspected.

DEFORMABLE-BAR MODEL

A more realistic analysis requires consideration of a deformable specimen, as shown in Fig. 1b, which has a rectangular cross section of width r and height s . We assume that strain softening, if it occurs, must be localized in a beam slice of a short length h ($h \ll L$), located at distances L_1 and L_2 from the specimen top and bottom (Fig. 1b); $L_1 + L_2 \simeq L$ = specimen length. Outside the slice, there is no loading anywhere. The variations of the rotations of the ends of the slice at the moment of bifurcation are denoted as $\delta\theta_1$ and $\delta\theta_2$. The variation of curvature in the slice is $\delta\kappa =$

$(\delta\theta_1 + \delta\theta_2)/h$. The variations of strains at the left and right faces of the slice are $c\delta\kappa$ and $(h-c)\delta\kappa$ where c is the distance from the left face to the neutral axis, which separates loading from unloading (Fig. 1c). Finally, the variation of the axial deformation of the link is expressed by $\delta\epsilon = \delta u/h = (s/2 - c)\,\delta\kappa$.

Writing the appropriate equilibrium and compatibility equations, and taking into account the nonlinear geometric effects, one can show [5] that the limit condition $\ldots = 0$ gives for $K^{(2)}$ a value which coincides with $K^{(1)}$, similarly to what we found for the rigid bar specimen. The corresponding value of E_t is given by

$$-E_t = \overline{E}_t = \frac{12G_2 h}{kG_1 r s^3} \tag{2}$$

where $G_1$and G_2 are known expressions. Again one finds that, for $E_t < -\overline{E}_t$, the condition $K^{(2)} < K^{(1)}$ is always satisfied.

Numerical calculations show that the effects of the stiffness of the end restraints and of the position of the strain-softening zone along the bar are analogous those found for the rigid-bar specimen. This is illustrated by Fig. 1g , which shows the value of $\overline{E}_t$ as a function of the stiffness C for different values of the ratio L_1/L_2 , for the case that $L = 100$ cm , $h = s = 5$ cm, $r = 10$ cm , $I = 500$ cm^3, $N = 15000$ N and $E_u = 3\times10^6$ N/cm^2. One can see that the effect of increasing the stiffness of the end restraints is to enhance the stability of the primary path (provided that $C > C_{lim} = 0.05\,E_u I$) .

CONCLUSIONS

1. The equilibrium path in a direct tension test of a strain softening material exhibits a bifurcation in which the secondary, symmetry-breaking path corresponds to flexing of the specimen to the side.

2. The lateral flexing can be retarded by providing rotational restraints at the specimen ends. The stiffer they are, the steeper is the post-peak slope of the strain-softening diagram at which bifurcation occurs.

3. The analysis shows that lateral flexing favors a break at midlength of the specimen over a break away from the middle.

4. The bifurcation behavior is analogous to Shanley's bifurcation in elastoplastic columns.

ACKNOWLEDGEMENT

Partial financial support under AFOSR grant 91-0140 to Northwestern University is gratefully acknowledged.

REFERENCES

1. Bažant, Z.P., Stable States and Paths of Structures with Plasticity or Damage, *J. Engrg. Mech.*, ASCE, 1988, 114(12), 2013-2034.

2. Bažant, Z.P., Stable States and Stable Paths of Propagation of Damage Zones and Interactive Fractures, in *Cracking and Damage – Strain Localization and Size Effect*, ed. by J. Mazars and Z.P. Bažant, Elsevier, London and New York, 1989, pp. 183-206 (Proc. of France-U.S. Workshop held at ENS, Cachan, September 1988).

3. Bažant, Z.P., Lectures on "Stability of Structures," Course 720-D24, 1989. Northwestern University, Evanston, Ill.

4. Bažant, Z.P. , and Cedolin. L., *Stability of Structures – Elastic, Inelastic, Fracture, and Damage Theories*, Oxford University Press, New York and Oxford. 1991.

5. Bažant, Z.P. , and Cedolin. L., Why Direct Tension Test Specimens Break Flexing to the Side , submitted for publ., *J. Struct. Engrg.*, ASCE, 1991.

6. Hordijk, D.A., Reinhardt, H.W., Cornelissen, H.A.W., Fracture Mechanics Parameters of Concrete from Uniaxial Tensile Tests as Influenced by Specimen Length," Preprints, SEM-RILEM, *Conference on Fracture of Concrte and Rock*, Houston, TX, 1987, S.P. Shah and S.E. Swartz, eds., 138-149.

7. Pijaudier-Cabot, G., and Akrib, A., Bifurcation et résponse postbifurcation de structures en béton, Preprint, *Colloquium GRECO on Rhéologie des Géomateriaux*, 1989, France.

8. Rots, J.G., and de Borst, R., Analysis of Mixed-Mode Fracture in Concrete, *J. Engrg. Mech.*, ASCE, 1987, 113(11), 1739-1758.

9. Rots, J.G., and de Borst, R., Analysis of Concrete Fracture in Direct Tension, *Int. J. Solids Struct.*, 1989, 25(12),1381-1394.

10. Shanley, F.R., Inelastic Column Theory, *J. Aero. Sci.*, 1947, 14(5), 261-268.

11. Bažant, Z.P. , and Tabbara, M. , Bifurcation and Stability of Structures with Interacting Propagating Cracks, *Int. J. of Fracture*, 1991, 51, in press.

CHARACTERISTIC MATERIAL VALUES OF CONCRETE UNDER UNIAXIAL TENSION

Frank Blaschke, Gerhard Mehlhorn
Civil Engineering Department
Kassel, Germany

ABSTRACT

Experimental investigations of the characteristic material values of concrete under uniaxial tension are presented. The concrete fails under tension in a limited cross-section. A special gum is used to join both halves of the already cracked specimens. Therefore it is possible to identify several lokal crack opening displacements. The analytical consideration of concrete parameters with the FE-System ADINA shows the influences of the shape of the stress-strain relationship and fracture energy on the maximal carrying capacity of a concrete bar under bending loading.

INTRODUCTION

Due to the increasing importance of finite element calculations it is necessary to know the material behaviour of concrete exactly. Therefore the properties of the tensile behaviour of concrete are becoming more and more important. The comparision of experimental investigations of several authors shows differences in the effektive tension stress f_t, the fracture energy G_F and the characteristical length l_{ch}. The research results vary greatly [4] because of the used concrete (composition, curing), the different conditions in laboratories and the material behavior of concrete under tension.
The question was, in which dimension do the mechanical properties of concrete in our region under conditions similar to the practice vary and which effects are provoked by very different fracture energies and the form of the stress-strain relationship in numerical calculations.

MATERIALS AND METHODS

The behavior of concrete (B35; characteristic value of the cube strength of concrete under compression 35 N/mm^2, corresponding to a concrete cylindrical strength $f_c' \approx 30$ N/mm^2) under uniaxial tension was investigated using 130 concrete specimens under axial tension tests. The investigations should give information about the influence of the specimen's measurements (geometry, size), the load installation (centrical, uniaxial eccentrical with $e/d \leq 1/6$, biaxial eccentrical with $e_x/d_x + e_y/d_y \leq 1/6$) the free crack opening displacement on a specimen with regard to the characteristic material values of concrete under tension.
The tension specimens were made of Portland cement PZ 35F and natural unbroken aggregate with a maximum grain size of 16 mm. The concrete specimens had to stay 5 days after casting under wet conditions (90%) humidity) and after a total of 28 days under dry conditions. This storage of the test specimens creates shrinkage stresses which depend on the specimen's age, geometry and size which in turn affects the test results. The age of the concrete specimen's when tested was 100 days after casting. The specimen's measurements were 100/200/1000, 200/200/1000, 141/283/1400, 283/283/1400 [mm]. The relations between length and width was constant with l/d=5. The tensile tests carried out were deformation-controlled with inductive strain gages, which were placed on the specimens directly. The tests took place in the central laboratories of the Civil Engineering Department , University of Kassel.
The tensile force was introduced using a special gum (epoxy) and steelplates. The eccentricity of loading was enabled by using biaxial moveable steelplates, which in turn during the experiment could affect the eccentricity of the load. Biaxial load eccentricities were calculated with $e_x/d_x + e_y/d_y$ otherwise with an ideal related load eccentricity. The ideal load eccentricity considers the square root of the addition of the squares of the individual biaxial load eccentricities in both directions in relation to the diameter of the equivalent cross-section of a circle or an ellipse depending on the shape of the cross-section used for the test specimen wether it is a square or a rectangle respectively.
The loading rate was always 0,01‰/min which acts on the maximum stressed side of the specimen.

RESULTS

The crack opening displacement of test specimen Z1Q020 appeared 30 cm from th top of the body. In addition to the four normal measuring lengths, there were two measuring lengths placed between the bottom and the middle of the specimen (Curve 8). In consequence of the different measuring lengths we noticed two different shapes of stress-deformation relationships (Figure 1).

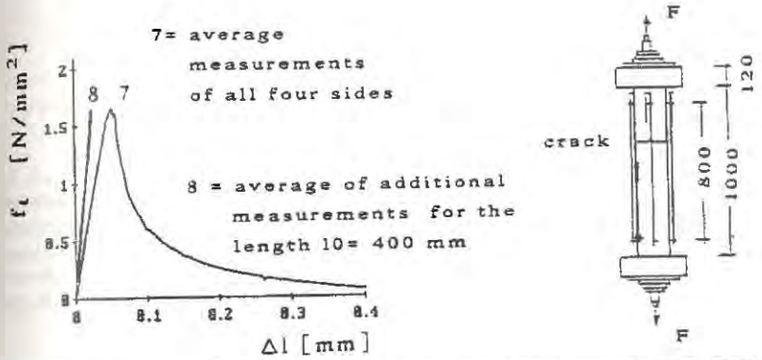

Figure 1 Stress-deformation relation for test specimen Z1Q020

After the peak-load, the deformations outside the crack opening displacements came back to the starting point. The concrete outside the fracture process zone behaves linearly. Residual deformations were not detected in all tested cross-sections of the tension specimens. The fracture energy G_F is equal the hatched area in figure 2. The results of the fracture energy are valid for the fracture process zone. Calculation of G_F in this way without including the residual deformations, results consequently in values which are 1-2% higher than otherwise calculated by other authors. (e.g. Hillerborg [5])

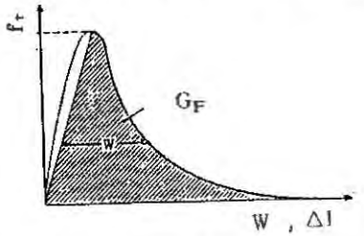

Figure 2 Description for the determination of the fracture energy

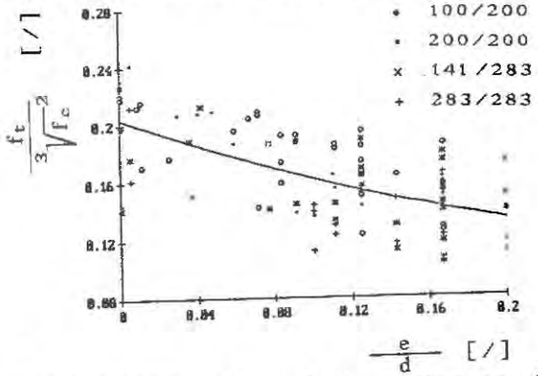

Figure 3 Related tensile strength depending on the eccentricity

$$\frac{f_t}{\sqrt[3]{f_c^2}} = 0.62\left(\frac{e}{d}\right)^2 - 0,48\,\frac{e}{d} + 0.204 \qquad (1)$$

A significant influence of the cross-section's shape and size in the researched area with regard to the material values with an equivalent length/width ratio could not be confirmed. A clear connexion between the given load eccentricity (defined at 85% of the maximum load) and the fracture energy G_F could not be established. The tested concrete specimens under centric tensile loading have shown the following values for maximum load:

- a fracture energy of 250 N/m
- a characteristical crack width of 0,13 mm
- a characteristical length of 1900 mm

With an increasing related load eccentricity e/d, the

- average concrete stresses
- fracture energies
- average strains

become less, and the

- maximum stresses
- characteristical crack widths
- characteristical lengths
- maximum strains.

become higher.

Figure 4 shows three stress-deformation relationships noticed for one concrete specimen.

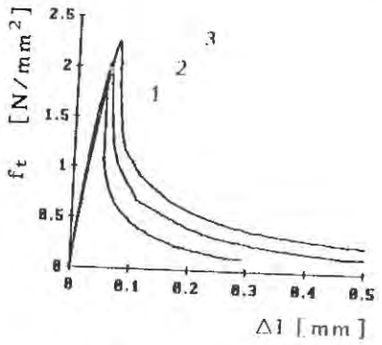

Figure 4 Stress-deformation relations

The distribution of crack opening displacements along the test specimen was made possible. The first separated parts of the test specimen were glued together before applying a next loading. In this way it was possible to detect with only one test specimen up to eight crack opening displacements.

Table 1

tension test	f_t [N/mm^2]	ε_m [‰]	G_F [N/m]	l_{ch} [mm]	w_{ch} [mm]	FPZ distance from bottom [mm]
1	1,83	0,062	163	1752	0,089	700
2	2,03	0,069	239	1972	0,118	890
3	2,25	0,086	371	2345	0,165	790

The stress-deformation relations in figure 4 show that a preloading of the tension body has no negative influence on the tensile strength. It was noticed that the material values for one concrete specimen vary greatly depending on the lokalization of an imperfect area, which creates consequently the fracture prozess zone (FPZ).

EXAMPLE FOR THE USE OF THE MATERIAL MODEL IN FINITE ELEMENT ANALYSIS INCLUDING THE "TENSION SOFTENING" EFFECT

A bending beam was chosen to demonstrate the use of the influence of the material model including the "Tension Softening"effect.

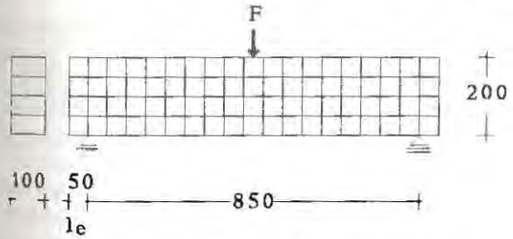

Figure 5 Element mesh of the beam

The calculation was made using the Finite Element Programm ADINA 84 which has been further developed to contain the Tension Softening effect [2].
The fracture energy was considered for four plain stress elements in the middle of the beam under bending and the shape of the stress-strain relation is determined with a factor $X = f_t' / f_t$ (Figure 7).

$$G_F = f_t \times \varepsilon_t \times l_e/2 + X \times f_t \times n \times \varepsilon_t \times l_e/2 \qquad (2)$$

Figure 6 shows the calculated peak-load of a beam depending on the selected fracture energy.

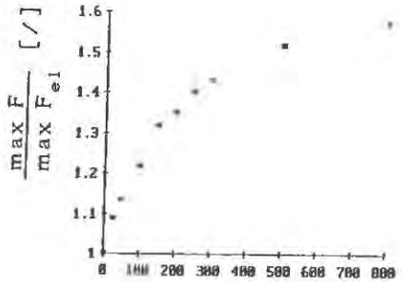

Figure 6

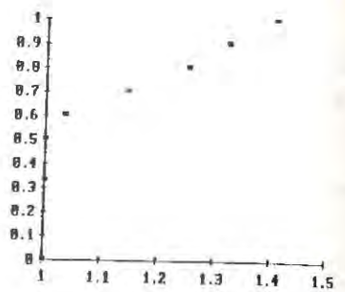

Figure 7

Figure 7 shows the calculated peak-load of the beam in dependence of the shape of the stress-deformation relationships with a fixed fracture energy of 250 N/m.

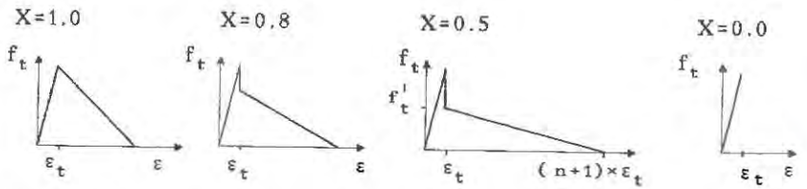

Figure 7 Description for the factor X

In future the influence of a decending expontial curve for the Tension Softening effect on the maximum tensile load would be investigated.

REFERRENCES

1. Blaschke, F.; Mehlhorn, G. : Verhalten von Beton unter exzentrischer Zugkraft Forschungsbericht Nr. 17 aus dem Fachgebiet Massivbau der Gesamthochschule Kassel, 1991

2. Abuassab, W.; Schulz, J. U.; Mehlhorn, G. : Erweiterung des Betonmodels von Bathe/Ramaswamy Forschungsbericht Nr.18 aus dem Fachgebiet Massivbau der Gesamthochschule Kassel, 1991

3. Blaschke, F.; Schulz, J. U.; Mehlhorn, G. : Numerische Untersuchung der Tragfähigkeit von unbewehrten Betonbalken mit verschiedenen "Tension Softening" Annahmen Forschungsbericht Nr. 19 aus dem Fachgebiet Massivbau der Gesamthochschule Kassel, (in preparation)

4. Hordijk, D.A. : Deformation-controlled uniaxial tensile tests on concrete Report 25.5-89-15/VFA Delft, University of Technology 1989

5. Hillerborg, A. : Reliance upon Concrete Tensile Strength IABSE Colloquium Structural Concrete Stuttgart, 1991

FRACTURE IN CONCRETE UNDER BIAXIAL LOADING - NUMERICAL EVALUATION OF WEDGE SPLITTING TEST RESULTS

ELMAR TSCHEGG
Associate Professor, Technical University of Vienna, Austria

HARALD KREUZER
Consulting Engineer, TFB Wildegg, Switzerland

MARCUS ZELEZNY
Research Assistant, Technical University of Vienna, Austria

ABSTRACT

Generally, concrete of massive structures is stressed multiaxially when fracture occurs. To account for this condition fracture parameters are evaluated using the results of biaxially loaded wedge splitting tests. Load-deformation diagrams for concrete with three different max. size aggregates and at different compressive preloading are compared. Fracture energy and bilinear softening functions are used as criteria to assess the fracture behavior under biaxial loading. It is found that the fracture energy changes non-uniformally with increasing compressive stress level and that an interaction of microcracking and aggregate interlock influence the fracture mechanism. Further research is necessary to confirm these results.

INTRODUCTION

If cracking occurs in massive concrete structures such as dams it is forced to propagate through an already stressed material. In order to account for this situation an experimental study was performed by which cubes under a preset compressive load were split and the crack opening displacement was measured. Experimental results were evaluated and presented at the International Conference on Dam Fracture in Boulder, Colorado [1]. This paper tries to further outline the test results by means of a numerical simulation with the purpose to

specify fracture energy values and to obtain strain softening functions under a changing tensile/compressive state of stress.

EXPERIMENTAL INVESTIGATIONS

The test equipment is shown on Fig.1. It consists of the wedge splitting equipment and the compressive load application device. The former induces the tensile σ_2-stress, the latter the compressive σ_1-stress. Together they create a biaxial state of stress in the specimen. Equipment and principle of the wedge splitting test are described in more detail in [2].

Figure 1.
Test equipment showing the wedge of the splitting device, between the σ_1-compressive load application structure with 4 screws (2 with strain gauges), one of the 2 LVDT's for COD recording.

Concrete was tested for three maximum size aggregates (MSA) on 15cm notched cubes at an age of about 30 days. Mix designs corresponding to dam concrete were chosen, however, with the experimental restriction of the smaller MSA as compared to real dam concrete. Concrete properties are given in [1].
Biaxial states with five different compressive preloading levels were tested, ie. σ_1= 0(uniaxial case), 25%, 40%, 60% and 70% of the corresponding compressive strength f'_c.

ANALYTICAL EVALUATION

In a process to simulate numerically the experimental results of the 56 force-deformation diagrams a finite-element package, SOFTFIT/FRACTURE I [3], was extended with Dr. Roelfstra to accommodate biaxial loading. SOFTFIT/FRACTURE, is a widely used data fit program, which correlates iteratively measured and calculated softening curves by minimizing the square-root sum of squares between them. Then, bilinear softening curves are developed using the four parameters f_t, s_1, w_1, and w_2, see Fig.2.

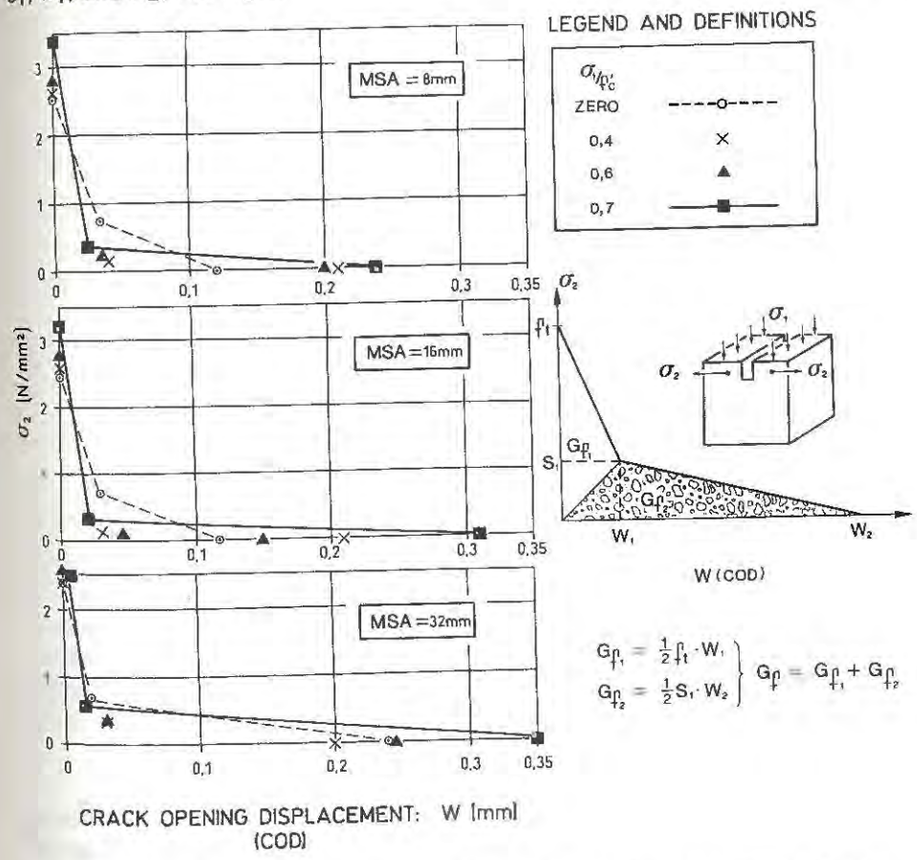

Figure 2. Bilinear softening diagrams for the three investigated concrete types

The main parameters resulting from the numerical analysis for selective softening diagrams, considered to be representative, are shown on Table 1 and Fig. 2. As an indicator for quality of compliance measured vs. calculated Gf-values are added.

TABLE 1
Parameters of bilinear strain-softening functions

MSA - σ_1/f'_c mm	f_t N/mm^2	s_1 N/mm^2	w_1 mm	w_2 mm	G_f/G_{fc} N/m
8 - 0	2.5	0.71	0.032	0.127	84/80
8 - 0.4	2.6	0.16	0.040	0.212	69/67
8 - 0.6	2.8	0.20	0.037	0.200	69/72
8 - 0.7	3.4	0.35	0.025	0.237	75/81
16 - 0	2.5	0.70	0.029	0.117	77/74
16 - 0.4	2.6	0.13	0.032	0.210	56/56
16 - 0.6	2.8	0.10	0.048	0.150	74/75
16 - 0.7	3.2	0.30	0.020	0.308	74/78
32 - 0	2.4	0.70	0.020	0.240	104/99
32 - 0.4	2.4	0.37	0.032	0.200	74/71
32 - 0.6	2.7	0.35	0.032	0.244	81/82
32 - 0.7	2.5	0.57	0.017	0.346	110/116

G_f/G_{fc} = measured/calculated spec. fracture energy

DISCUSSION AND CONCLUDING REMARKS

1. Test results, on the one hand, are described in [1] and outlined in Fig.3, upper diagram. It is interesting to note that G_f decreases within the elastic range of σ_1-loading and that at the onset of microcracking G_f starts to increase again prior to total material disintegration. This unsteady development ensues from restraints in the expansion of the fracture process zone for the descending G_f-branch and from aggregate interlock for the rising branch.

2. Discussing, on the other hand, results from the numerical evaluation, a distinction between the two branches of the softening function is suggested, as discussed by several authors [4 to 8], particularly [9]. From this it follows, that energy along the upper branch is consumed by microcracking, along the lower branch by overcoming friction and tortuosity of aggregate interlock. Fracture energies related to these two phenomena are designated as G_{f1} resp. G_{f2} in Figures 2 and 3.

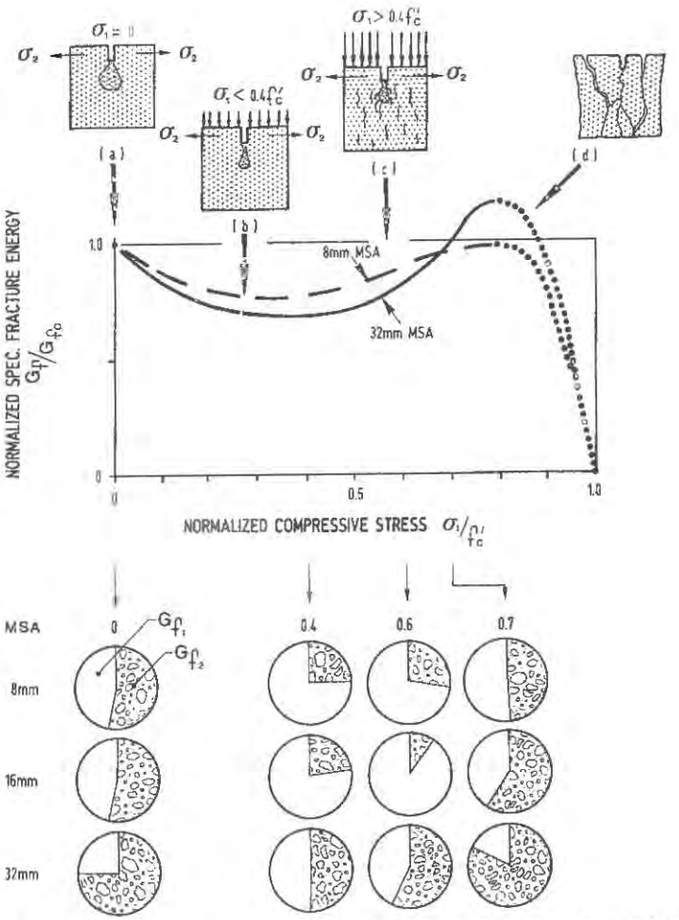

Figure 3. Course of fracture energy G_f for different preloading,(a) to (d), and distribution of two G_f-portions related to microcracking (G_{f1}) and aggregate interlock (G_{f2}) respectively.

Given this perspective one may conclude that σ_1-loading has a stabilizing influence on microcracking, or in other words: the preloading impedes crack opening and propagation, confining it within a narrow FPZ. The material reacts more brittle and more energy is stored in the microcracked concrete. This is evident from both the steep first softening branches and the increase of G_{f1} for

$$0.6>\sigma_1/f'_c>0.$$

Aggregate interlock increases with increasing MSA, see Fig.3, lower diagram. This is valid for all σ_1-loadcases.

These preliminary findings need further research. They may, however, be useful to formulate damage models, especially for assessing post-earthquake stability of massive concrete structures.

ACKNOWLEDGEMENTS

The authors are indebted to the generous support of the study by Prof. W.Wilk, President of the Technical Research & Advisory Institute of the Swiss Cement Industry, and to the assistance of Mr. M. Elser for designing the loading equipment and performing the testing.

REFERENCES

1. Kreuzer, H., Tschegg, E., Wilk, W., Fracture parameters in concrete under biaxial loading, Proc. of the International Conference on Dam Fracture, eds. V.Saouma, R.Dungar, D.Morris, Boulder, Colorado, Sept. 1991, pp. 445-57.

2. Tschegg, E., New Equipments for Fracture Tests on Concrete, Materialprüfung/ Materials Testing, C. Hanser Verl., 33. Jg., 1991, pp.338-42.

3. Roelfstra, P.E., Wittmann, F.H., Numerical method to link strain softening with failure of concrete, Fracture toughness and fracture energy of concrete, ed. F.H. Wittmann, Elsevier Applied Science Publishers, Amsterdam, 1986, pp. 163-75.

4. Hsu,T.C., Slate, F.O., Sturman, G.M., Winter,G., Microcracking of plain concrete and the shape of the stress-strain curve, ACI Journal, Proc. Vol.60 Nr.2, Title Nr. 60-14, April 1962, pp. 209-22.

5. Carpinteri, A., Colombo, G., Ferrera, G., Guiseppetti G., Numerical simulation of concrete fracture through a bilinear softening stress-crack opening displacement law, SEM/RILEM International Conference on Fracture of Concrete and Rock, Houston, Texas, June 1987, eds. S.P. Shah, S.E. Swartz, A.A. Balkema, Amsterdam, 1989, pp.131-41.

6. Rossi,P., Brühwiler,E., Chhuy,S., Jenq,Y.S., Shah,S.P., Fracture properties of concrete as determined by means of wedge splitting tests and tappered double cantilever beam tests, in Fracture Mechanics - Test Methods for Concrete, eds. S.P.Shah & A.Carpinteri, Rilem Report 5, Chapman &Hall, London, pp.87-128.

7. Mier, J.G.M., Nooru-Mohamed, M.B., Fracture of concrete under tensile and shear-like loading, International Workshop on Fracture Toughness and Fracture Energy, Sendai, Oct.1988, A.A.Balkema,1989, pp.449-63.

8. Mier, J G.M., Mode I fracture of concrete: discontinuous crack growth and crack interface grain bridging, Cement and Concrete Research, Vol. 21, Pergamon Press, USA, 1991, pp. 1-15.

9. Nomura, N., Mihashi, H., Izumi, M., Correlation of fracture process zone and tension softening behavior in concrete, Cement and Concrete Research, Vol. 21, Pergamon Press, USA, 1991, pp. 545-50.

FRACTURE PARAMETERS OF CONCRETE AS DETERMINED BY MEANS OF WEDGE SPLITTING TEST

Wang Xinyou and Wu Keru
Department of Materials Science and Engineering
Tongji University, Shanghai 200092, China

ABSTRACT

In this paper, the fracture parameters of concrete, such as fracture toughness, fracture energy, and so on, have been obtained by means of wedge splitting test. The influence of water–cement ratio, the maximum aggregate size, test age and compressive strength of concrete, as well as the initial notch depth on the fracture properties of concrete has been studied. Several empirical relations between the compressive strength and other parameters studied are also obtained.

INTRODUCTION

The fracture parameters are not only the measurement of fracture behaviour of concrete, but also the important basis of the fracture models for concrete. In past researches, three–point bending test was a primary test method used in determining the fracture parameters of concrete. However, it has some disadvantages. The fracture area of specimens is small compared to the whole volume, and correction for the influence of the dead weight must be done based on the point of the load–displacement curve. The wedge splitting (WS) test seems to be one of the most promising testing methods for determination of the fracture parameters of concrete, when a servo–controlled testing machine is available. The idea of WS test was initially proposed by Linsbauer and Tschegg (1) . Then the testing machine is improved and refined by Brubwiler et al (2) , and a detailed reserch on WS test is carried out by authors (3) . In this paper, the fracture properties of concretes with different water–cement ratio W / C, the maximum aggregate size d_{max}, test age t and compressive strength f_c have been obtined by means of WS test, and the influence of the initial nothch depth a_0 on the test results has also investigated.

WEDGE SPLITTING TEST

The set–up and specimen of WS test are illustrated in Fig.1 and Fig.2 respectively. During the test, the applied load Pv (vertical component) and the crack opening displace-

ment (COD) are measured. The splitting force Ph is measured by using a clip gauge. In a closed–loop servo–hydraulic testing machine, the test is controlled by means of value of COD. The energy necessary to split the specimen into two halves is represented by the area under the Pv–COD curve. Fracture energy G_F and fracture toughness K_{IC} can be calculted on the basis of certian formulae through the P_V–COD curve and the peak load P_{vmax} . These calculation formulae have been inferred by authors [3] according to the loading and geometry conditions for wedge splitting test.

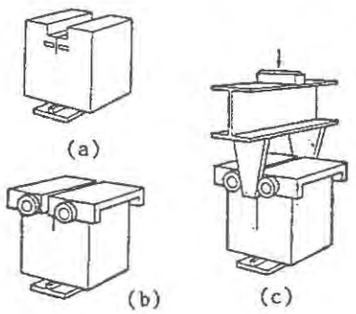

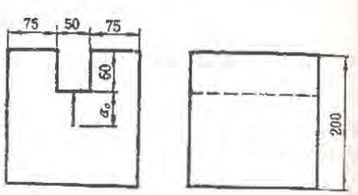

Fig.1 Set–up of WS test Fig.2 Size and geometry of the specimen

MATERIALS AND MIX PROPORTION

The concrete specimens were prepared using following materials: No. 525 Portland cement, river gravel, river sand, and high efficiency water reducer type NF when preparing high strength concrete. In this study, five series tests of concrete were designed, their mix proportions are listed in Table 1. All specimens were casted according to the standard methods, cured at room temperature for 24hr, demolded, and then moved to the standard curing room to the test time. The compressive strength for every concrete was also obtained using cube specimen measuring 100mm × 100mm × 100mm.

TEST RESULTS AND DISCUSSION

The complete P_V–COD curves can be stably measured by means of WS test. Fig.3 and Fig.4 show two groups of typical P_V–COD curves for concrete with different W / C and d_{max} values. The fracture parameters of concrete, e.g. fracture toughness K_{IC} , fracture energy G_F , the peak load P_{vmax}, value of COD at the peak load COD_0 can be obtained from the complete P_V–COD curves. All experimental results are given in Table 2.

The test results indicated that the initial notch depth has quite big influence on fracture energy and fracture toughness. The complete P_V–COD curve is not able to be measured for no notch specimen. Fracture energy, fracture toughness and compressive strength have almost same changing tendency with increasing water–cement ratio. The maximum aggregate size has bigger effcet on fracture energy than on compressive strength and the peak load. This may be explained by different failure mechanism, that is different cracking pathes. Because the cracks propagate around the coarse aggregate particles in concrete, the fracture surface is more tortuous and fracture area is bigger in the actual failure of concrete when large aggregate are used. Like water–cement ratio, test age has almost same effect on the fracture properties and compressive strength. It is noted from Table 2 that for all test series COD_0 values increase with the increase of compressive strength.

Table 1 Mix proportions of concrete

No	W / C	d_{max} (mm)	t (days)	a_0 (mm)
OA_1	0.50	15	28	0
OA_2	0.50	15	28	25
OA_3	0.50	15	28	50
OA_4	0.50	15	28	75
OB_1	0.40	15	28	50
OB_2	0.45	15	28	50
OB_3	0.50	15	28	50
OB_4	0.60	15	28	50
OB_5	0.70	15	28	50
OC_1	0.50	10	28	50
OC_2	0.50	15	28	50
OC_3	0.50	20	28	50
OC_4	0.50	30	28	50
OC_5	0.50	40	28	50
OD_1	0.50	15	3	50
OD_2	0.50	15	7	50
OD_3	0.50	15	14	50
OD_4	0.50	15	28	50
OE_1	0.71	10	28	50
OE_2	0.55	15	28	50
OE_3	0.46	20	28	50
OE_4	0.38	30	28	50
OE_5	0.31	40	28	50

Table 2 Test results of concrete

No	f_c (MPa)	P_{vmax} (N)	COD_0 (mm)	G_F (N / m)	K_{IC} (kN / $m^{3/2}$)
OA_1	43.2	11050	0.039	–	1597
OA_2	43.2	8850	0.040	258	1279
OA_3	43.2	6000	0.052	159	867
OA_4	43.2	4600	0.041	86	665
OB_1	47.0	7875	0.060	218	1138
OB_2	45.7	6750	0.054	163	977
OB_3	43.2	6000	0.052	159	866
OB_4	31.1	4000	0.042	116	578
OB_5	18.6	3825	0.036	99	553
OC_1	32.9	4350	0.048	104	629
OC_2	43.2	6000	0.052	159	866
OC_3	44.3	6875	0.057	173	993
OC_4	44.5	6950	0.060	181	1005
OC_5	44.6	7200	0.062	197	1049
OD_1	18.3	3100	0.036	61	449
OD_2	30.2	3750	0.042	121	543
OD_3	36.9	4750	0.046	154	686
OD_4	43.2	6000	0.052	159	866
OE_1	20.3	3500	0.044	53	506
OE_2	32.1	5675	0.051	117	819
OE_3	46.6	6125	0.053	181	885
OE_4	51.1	8125	0.060	212	1176
OE_5	53.7	8125	0.064	235	1176

The test results show that the peak load and fracture energy increase with increasing compressive strength of concrete. According to data listed in Table 2, the following empirical relations between the compressive strength and other parameters studied here were obtained by means of the linear regressive method.

$$G_F = 4.5 f_c - 22.6 \quad , \quad r = 0.936 \tag{1}$$

$$K_{IC} = 18.8 f_c + 141.2 \quad , \quad r = 0.926 \tag{2}$$

$$f_c = 26.6(C / W) - 15.1 \quad , \quad r = 0.938 \tag{3}$$

$$f_c = 0.9t + 20.6 \quad , \quad r = 0.914 \tag{4}$$

$$f_c = 7.3 lg(d_{max}) + 19.9 \quad , \quad r = 0.791 \tag{5}$$

Where, C / W is cement–water ratio, r is the correlation coeificiency.

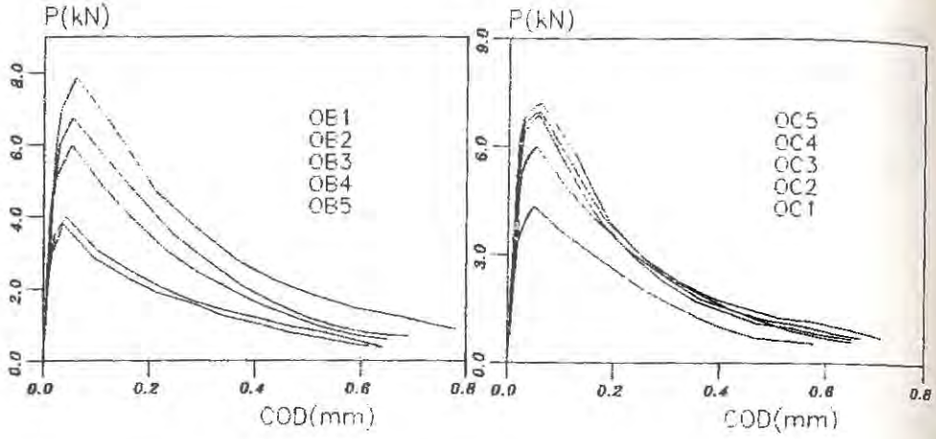

Fig.3 The complete P–COD diagrams measured of concrete series OB

Fig.4 The complete P–COD diagrams measured of concrete series OC

Except the relation between f_c and d_{max} , there are good agreement between the compressive strength and other parameters. It is noted that the above equations are only suitable for concrete having the compressive strength range of 20–60 MPa, and equation(4) is only suitable for test age less than 28 days.

CONCLUSIONS

1. The initial notch depth has quite big influence on fracture energy and fracture toughness of concrete.

2. Fracture energy, fracture toughness and the compressive strength have almost same changing tendency with inceasing water–cement ratio and test age. The maximum aggregate size has bigger effect on fracture energy than on the compressive strength and peak load.

3. Except relation between the compressive strength and the maximum aggregate size, there are good aggrement between the compressive strength and other parameters studied in this paper.

REFERENCES

1. Tschegg, E. K. and Linsbauer, H. N., Test method for the determintion of fracture mechanics properties, Patent Specification No. A–233 / 86, Austrian Patent Office, 1986.

2. Bruhwiler, E., Wittmann, F. H. and Rokugo, K., Influence of rate of loading on fracture energy and strain softening of concrete, Trans of 9th SMIRT, Lausanne, Vol. H, 1987, pp.25—33.

3. Wang Xinyou and Wu Keru, Study on wedge splitting test for determining fracture parameters of concrete, Journal of Shanghai Institute of Building Materials, Vol.3, No.4, 1990, pp.357–367(in Chinese).

TENSILE PROPERTIES OF A HIGH PERFORMANCE CONCRETE

Per Anders Daerga
Department of Civil Engineering
Luleå University of Technology, S – 91 857 Luleå, Sweden

ABSTRACT

Controlled uniaxial tensile tests are performed under restrained rotating boundary conditions on a high performance concrete. Notched solid cylindrical specimens of equal geometry (height/diam. = 75/74 mm) and of a single quality are used. In all, six specimens are tested.

The obtained material parameters are in average: tensile strength f_t = 5.15 MPa; initial static modulus of elasticity E_c = 36830 MPa; experimental fracture energy G_{FE} = 211.8 Nm/m^2; apparent fracture energy G_{FA} = 223.9 Nm/m^2; ultimate elongation δ_u = 426 μm and characteristic length l_{ch} = 316 mm.

Keywords: Uniaxial Tension, Boundary Conditions, Fracture Mechanics Parameters, High Strength Concrete.

INTRODUCTION

Controlled uniaxial tensile tests on concrete and other cementitious materials can nowadays be carried out with the purpose to determine fracture mechanics parameters. These parameters serve as input to fracture mechanics models such as *the fictituos model* of Hillerborg and *the band model* of Bažant.

Published results on the tensile properties of high strength concrete are still scarce. In this paper results from a small test series on a high performance concrete are presented. More details are provided in [1].

EXPERIMENTAL PROCEDURE

Mix Proportions, Curing Conditions and Specimen

A low heat ordinary Portland cement and crushed aggregates of a granitic type were used in the mix. A naphthalene superplastizer called M150 was added. No silica was used. The mix proportions together with specimen data and mechanical properties are shown in Table 1.

The specimens are all solid cylinders of equal shape with a laithed notch at midheight. They were made from drillcores taken from a plain concrete block, with the cylinder axis oriented parallell to the casting direction. Each drillcore produced two specimen. The drilling was done some weeks before testing and approximately 3 months after casting.

Table 1: Mix proportions and material properties of the high performance concrete.

Mix Proportions				
Cement (kg/m^3)	Sand 0–8 mm (kg/m^3)	Gravel 8–16 mm (kg/m^3)	W/C	Superplasticizer M150
480	775	1167	0.25	4% of C
Mechanical Properties[1]			*Specimen Data*	
$f_{cc}(28d)$ (MPa)	$f_{cspl}(28d)$ (MPa)	$f_{cspl}(115d)$ (MPa)	height/diam. (mm)	notchdepth/width (mm)
93	5.7	5.9	75/74	10/2

[1] Average of three tests performed on 100 mm cubes.

Test Set-Up, Control and Data-acquisition

The test arrangement consisted of a separate rig/actuator system. A tensile fixture served as an interface between the specimen and the actuator/frame. The actual rotational stiffness of the equipment has not been determined. As an infinite rotational stiffness is in practice unachievable, the term *restrained rotating boundary conditions* is prefered before *nonrotating boundary conditions*, and will therefore be used in the following.

The elongation was measured by two Extensometers and two COD-gauges (*Crack Opening Displacement*) mounted across the notch, evenly spaced around the circumference. The measuring length was $30mm$. The overall control was excercised by a PC-program called Regula, [2]. Data-acquisition was done at regular displacement intervals of $0.5\mu m$, and the result stored on the hard-disk of the PC. All tests were performed in *displacement control* with the average of the four displacement gauges constituting the feed-back signal. The accuracy of the displacement gauges and the loadcell were better than $0.7\mu m$ and $75N$, respectively.

RESULTS

Nonlinear Fracture Mechanics Parameters

Figure 1 comprises all the obtained $\sigma - \delta_{mean}$ curves and Table 2 summarizes the corresponding material parameters. The shape of the descending branches vary from rather smooth curves to ones containing obvious plateaux.

The fracture energy is evaluated according to a classification scheme introduced by Elices and Planas in [3], where a distinction is made between theoretical and experimental fracture energy. The *experimental* fracture energy G_{FE} is defined as the external energy supplied divided by the crack surface. If there is no energy dissipation other than for crack formation and a single crack develops, G_{FE} equals G_F, the *theoretical* fracture energy. Consequently, G_{FE} corresponds to the area under the $\sigma - w$ curve, where w is the average crack opening. The total energy supplied for completely fracturing the material per unit area of crack is denoted the *apparent* fracture energy G_{FA}, and corresponds to the area under the $\sigma - \delta$ curve, where δ is the average total elongation.

The values of E_c apply to the section within the measuring length (including the notch). The gauge readings are averaged and divided by the measuring length to obtain an equivalent $\sigma - \varepsilon$ relation. A regression analysis is then applied on datapoints between 10 and 40% of the maximum stress. This procedure only yields an approximative value of the initial static

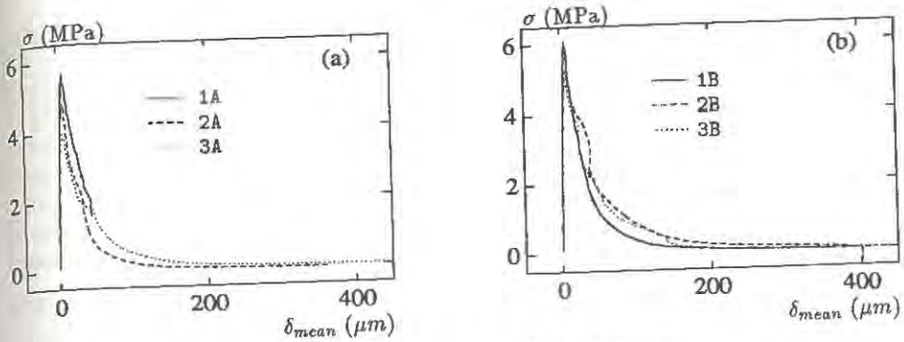

Figure 1: $\sigma - \delta_{mean}$ response of all specimens.

Table 2: Experimental fracture mechanics parameters.

Specimen	boundary condition	E_c (MPa)	f_t (MPa)	G_{FE} (Nm/m^2)	G_{FA} (Nm/m^2)	δ_u^1 (μm)	l_{ch} (mm)
1A[2]	restrained	36020	5.76	–	–	–	–
1B	restrained	42870	6.09	199.4	211.5	360	230
2A	restrained	37140	4.84	136.9	148.8	360	217
2B	restrained	38080	5.26	291.7	305.5	430	401
3A	restrained	33080	3.96	192.8	204.1	550	407
3B	restrained	33770	4.96	238.1	249.4	430	327
average		**36827**	**5.15**	**211.8**	**223.9**	426	316

[1] Rounded off to the nearest multiple of ten. [2] The complete descending branch was not obtained.

modulus, since both the strain and the stress distribution are disturbed due to the presence of the notch.

The tensile strength f_t is the maximum load divided by the area of the notched cross-section. Quite large differences exist between the specimens. To some extent it can be explained by the amount of penetrated aggregates. The specimens also contained some air pores of various sizes at the fractured surface, especially 3A exhibited three large pores (up to $6mm$ in width) which probably contributed to the relatively poor tensile strength. A systematic difference in strength can also be observed in that the B specimens are stronger than the corresponding A, which may be due to the fact that the A specimens usually were taken from the upper part of the core while the B specimens were taken from the lower part. The values of the tensile strength are in good agreement with the values for the splitting tensile strength, see Table 1.

The experimental fracture energy G_{FE} shows a rather large scatter, even for specimens originating from the same core. The individual differences can be correlated to the tortuousity of the crack path (the rougher the crack the higher the fracture energy). The apparent fracture energy G_{FA} is 5-9% higher than G_{FE}.

The ultimate elongation δ_u corresponds to a stress-free crack surface. The obtained values varies between 360 and $550\mu m$. The numbers are rounded off to the nearest multiple of ten due to the uncertainty in the evaluation. The values correspond well to those cited for normal concrete by Hordijk, van Mier and Reinhardt in [3].

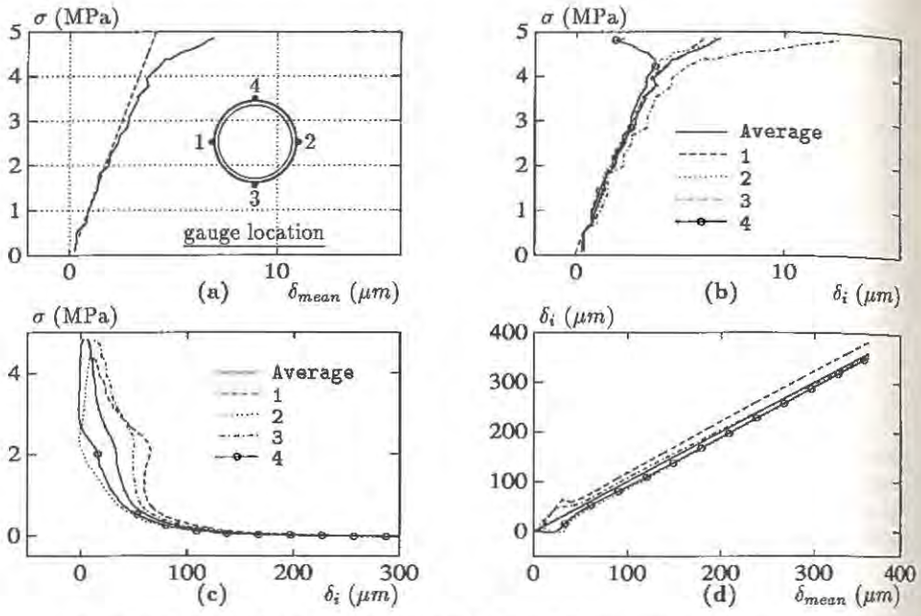

Figure 2: Prepeak (a and b) and postpeak (c and d) response for specimen 2A.

Prepeak and Postpeak Characteristics

Figure 2 exemplifies the prepeak and the postpeak response of specimen 2A. The prepeak gauge readings are fairly uniform up to a level which roughly coincides with the *proportionality limit*. From there and up to the peak the $\sigma - \delta_{mean}$ curve starts to soften and the individual readings begin to deviate, especially gauge 3 and 4, Figure 2(b). Almost all of the prepeak curves gave a positive indication on a connection between the *proportionality limit* and the onset of the scattering of the gauges. For some of the specimens the deviation started at small stress levels. This behaviour resemblances that of testing under free rotating boundaries, and is believed to be influenced by initial load eccentricity.

The boundary conditions at the loading grips are known to be very important for the postpeak behaviour. Under free rotating boundary conditions, the descending branch of the $\sigma - \delta_{mean}$ curve generally shows a smooth curvature with a monotonically increasing nonuniform crack opening to failure. Under restrained rotating boundary conditions, the descending branch is more disturbed and oftenly displays a characteristic *bump*. The location and extension of the bump depends on the rotational stiffness of the boundaries as demonstrated by [4], and on the flexural stiffness of the specimen. The nonuniform crack opening increases to the beginning when the descending branch is entered. It attains a maximum which, for most of the tests performed, coincides with the end of the *bump plateau*. The plateau is followed by a drop of load, at which the nonuniform opening starts to revert. The recession continues until a fairly uniform opening is attained. Quite often, a residual opening prevailed to the end, Figure 2(d). This may have several reasons, for example can it be caused by initial load eccentricity or by a bending moment introduced when the loading grips were attached to the tensile fixture and centered in position. Sometimes the direction of the principal crack opening rotated during fracturing, Figure 2(c).

The divergence of the gauges indicates that localization of strains into a fracture process zone occurs before the peak load is attained. This suggests that the proportionality limit reflects the

formation of a macroscopic defect and the subsequent onset of macrocrack growth, at least in case of notched specimens. Prepeak localization is also reported by those using full field surface measurements techniques such as the *Moiré interferometry*, [5].

The measurements also reveal that the load drop at the bump is a manifestation of a redistribution of stresses. The region of the notched section which is most tensed undergoes a *snapback*, while at the opposite side the deformation alters from being compressive to becoming tensile. The loaddrop that succeed the plateu level is interpreted as a column buckling of a core of relatively intact material. For the long tail, the stress transferring capacity is thought to be governed mainly by *crack interface bridging* and *crack boundary sliding* as suggested in [6].

CONCLUSIONS

- The high performance concrete tested does not appear to be more brittle than normal strength concrete. The *characteristic length*, $l_{ch} = E_c G_{FE}/f_t^2$, is of the same order as is reported in the literature for normal concrete.
- The displacement measurements indicates that localization of strains occur before the peak load is attained. The stress level at which the fracture process zone appears to form and starts to propagate coincides fairly well with the *proportionality limit*.
- If a macroscopic defect forms and begins to propagate before the peak, then *the apparent fracture energy* G_{FA} is a more appropriate measure of the energy dissipation within the process (fracture) zone than *the experimental fracture energy* G_{FE}.

ACKNOWLEDGEMENT

The work has been supported by the Swedish Council for Building Research.

References

[1] Daerga P. A. , Some Experimental Fracture Mechanics Studies in Mode I of Concrete and Wood. *Licentiate Thesis, Luleå University of Technology, 1992, (To be published).*

[2] Daerga P. A. and Sundqvist J. , Material Testing with Regula – Demonstration and Verification. *Technical Report 1991:28T, Luleå University of Technology, 1991, 80 p.*

[3] Elfgren L. (Editor), Fracture Mechanics of Concrete Structures, From Theory to Applications. *RILEM Report prepared by the Technical Committee 90 – FMA, Fracture Mechanics of Concrete – Applications, Chapman and Hall, London, 1989, 407 p.*

[4] Hillerborg A. , Stability Problems in Fracture Mechanics Testing. *In Fracture of Concrete and Rock – Recent Developments, (Ed. S.P. Shah, S.E. Swartz, B. Barr), Elsevier, 1989, pp. 369–378.*

[5] Raiss M. E. , Dougill J. W. and Newman J. B. , Development of Fracture Process Zones in Concrete. *Magazine of Concrete Research, 42, No. 153, 1990, pp. 193–202.*

[6] van Mier J. G. M. , Crack Face Bridging in Normal, Highstrength and Lytag Concrete. *In Fracture Processes in Concrete, Rock and Ceramics (Ed. J. G. M. van Mier, J. G. Rots, A. Bakker), Chapman and Hall, London, 1991, pp. 27-40.*

TENSILE BEHAVIOUR OF HIGH-STRENGTH CONCRETE (HSC)

GERT KÖNIG*, GERD REMMEL**
*Institut für Massivbau, Technische Hochschule Darmstadt, Germany
**Philipp Holzmann AG, Frankfurt/Main, Germany, presently at Institut für Massivbau

ABSTRACT

In order to obtain more information on the tensile behaviour of HSC, deformation-controlled tensile tests and bending tests on plain concrete were carried out. Both test methods showed the existence of tensile softening, even for concrete with a cylinder strength of 125 MPa. The results are compared with the characteristics of normal-strength concrete (NSC). In addition, the influence of different curing conditions on the tensile behaviour is investigated.

INTRODUCTION

Although the tensile capacity is generally neglected for the design of ultimate limit states of reinforced and prestressed concrete structures, in many cases it is taken into account, e.g. shear capacity of longitudinally reinforced members, bond and anchorage of reinforcing bars. Models, which include the tensile softening, as e.g. the "Fictitious Crack Model" by Hillerborg, give a better understanding of the bearing behaviour of R.C. members. Furthermore, they are able to explain size dependencies, e.g. of the flexural tensile strength. With the basic knowledge of the tensile behaviour of HSC (f_c > 60 MPa), it will be possible to extend existing design concepts for NSC to concrete with higher strengths.

DIRECT TENSILE TESTS

Deformation-controlled tensile tests give direct information on the tensile behaviour. In order to obtain a stable test course, a low stiffness of the specimens (fig. 1) was selected compared to the stiffness of the test frame (9000 MN/m). The specimens were fixed in the test machine by means of an epoxy-based resin. The rotation of the end platens was prevented to avoid an instable, zipperlike failure.

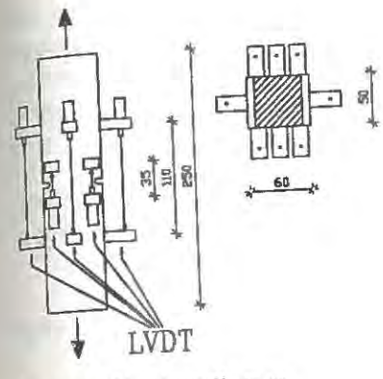

Figure 1. Direct tensile tests

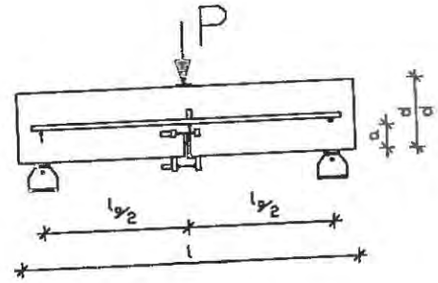

Figure 2. Three-point bending tests

The test specimens were weakened by cutting 2 notches at opposite sides. Their depth was 5mm resp. 7mm, depending on the maximum aggregate size d_{max}, 16mm resp. 8mm. By coupling 4 LVDT's near the notch tips, it was possible to control the tests in a stable manner, even when an eccentric crack opening occurred. To reduce the elastic part of the deformation, a minimal measurement length was chosen (35mm). This kind of test control was already used by Hordijk and Reinhardt [1]. 4 other LVDT's on the middle of each specimen side gave information on the distribution of the deformation over the cross section. The panels (400/300/60mm), from which the specimen were sawn, were cured in water for a period of 1 - 3 months. After sawing the specimens and providing them with the notches, they were stored at 60% relative humidity until 1 day before the test.

Figure 3a) shows the load-deformation curve of a HSC specimen. The specimen shows linear elastic behaviour up to 95% of the maximum load (P_{max}). After maximum load is reached, the curve shows a steep decay at first - until about 0,20 P_{max}. After another very flat decrease, no more load is transferred at a deformation value of ~150 µm.

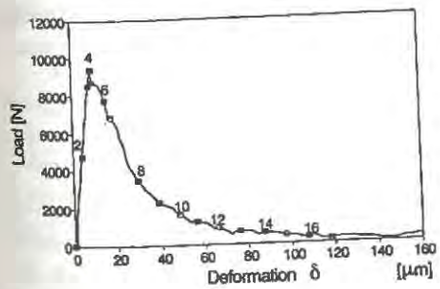

Figure 3.a) Load-deformation curve

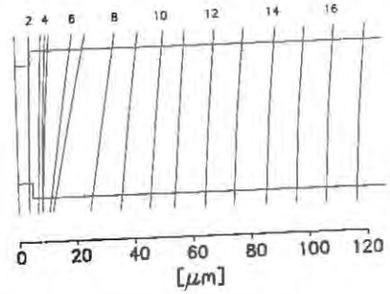

b) Distribution of the crack-opening over the cross section

The distribution of the deformation over the cross section is shown in figure 3b). The deformation is nearly even with increasing load. In the region of P_{max} the deformation on one specimen side grows stronger. After surpassing the maximum load the crack develops from this side over the whole cross section. Towards the end of the test this eccentricity is removed due to the flexural restraint of the specimen.

The load-deformation curves of 4 different concrete mixtures are presented in figure 4. The HSC (mixes 5 and 8), containing 8 - 10% (of the cement mass) silica fume, show a substantial steeper decay after the maximum load was reached.

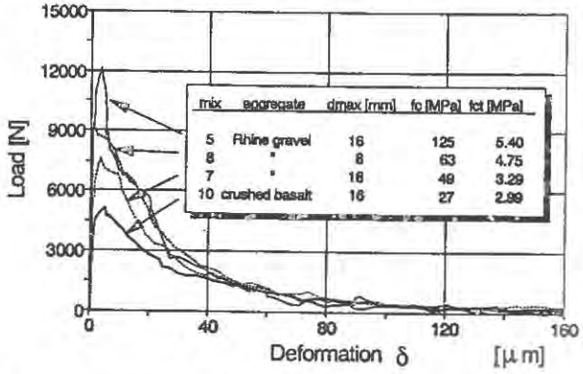

Figure 4. Load-deformation behaviour of NSC and HSC

Corresponding with the fictitious crack model by Hillerborg the nonlinear stress-crack-opening (σ-w) relation can be obtained by substracting the elastic deformations from the results of the direct tensile tests. Eventual eccentricities are neglected. They will be considered in the ongoing investigations.

A fitting of existing mathematical formulations to the measured curves showed that these functions, which are derived from test results with NSC, represent the tensile behaviour of HSC only with a strong correction of the original parameters. The following modification of a proposal by König and Duda [2] was chosen to describe the extracted nonlinear tensile behaviour:

$$\sigma_{ct}(w) = \sigma_a \cdot e^{-(w/w_a)^c} + \sigma_b \cdot (1-w/w_b), \quad 0 \le w \le w_b \text{ with } \sigma_a + \sigma_b = f_{ct} \qquad (1)$$

The exponential function describes the steep decay due to the successive failure of material bridges at the beginning, whereas the following flat part, representing the stress transfer by friction of the crack surfaces, is reflected by a straight line (fig. 5a). w_b represents the crack opening where the transfered stress becomes zero. The test data showed that for a gravel concrete w_b tends to be 150 μm and for a concrete with crushed aggregate 200 μm. The other parameters of the proposed formulation were found by means of an opti-

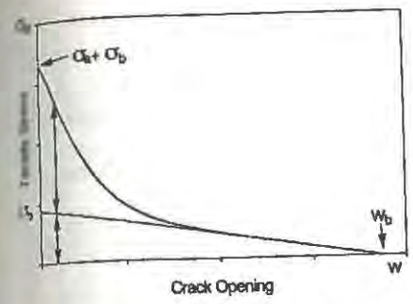

Figure 5. a) Course of σ-w-relation

mix	5	7	8	10
f_c [N/mm²]	125.1	48.8	83.4	27.0
f_{ct} [N/mm²]	5.40	3.29	4.75	2.99
σ_a [N/mm²]	4.99	2.41	4.16	2.01
w_a [μm]	21.3	22.4	24.4	30.0
σ_b [N/mm²]	0.41	0.88	0.59	0.98
w_b [μm]	150.	150.	150.	200.
c [-]	1.30	1.35	1.35	1.67

b) Parameters of σ-w-relation

mization algorithm (fig. 5b). The results show that the parameters w_a and c are nearly independant from the concrete strength, whereas with increasing concrete strength the stress parts σ_a and σ_b increase or decrease, resp. The decrease of σ_b supports the supposition that the stress part, transfered by friction, decreases for HSC. Since the crack breaks right through the aggregates, the aggregate interlock is omitted. On the contrary, NSC with crushed aggregates shows a distinct interlock and thus a relatively ductile tensile behaviour. This is reflected by the augmentation of the parameters w_a and c.

THREE-POINT BENDING TESTS

In addition to the direct tensile tests, three-point bending tests on plain NSC and HSC were carried out. Standard specimens with the dimensions l/d/d = 700/150/150 mm and 500/100/100 mm with spans of l_0 = 600 mm and 400 mm, resp., were used (fig. 2). A notch with a depth of d/3 was sawn at midpsan. The beams were supported by roller bearings, which allowed rotation also in the lateral direction. Thus, the crack could propagate freely without any constraint. The tests were controlled by the notch opening, measured at the lower side of the specimen. Its increase was chosen so that the ultimate load was reached 30 - 60 s after the beginning of loading. Additionally, the crack opening at the notch tip and the deflection of the beam were recorded, each at both sides.

These bending tests are carried out with 12 different concrete mixes, variing concrete strengths, kind of aggregate (gravel, crushed basalt) and maximum aggregate size. With some, the influence of different curing conditions on the specimen behaviour was investigated. Most of the specimens were cured in water until ~1 hour before testing ('wet'). In some cases, the beams were stored in the laboratory at ~20°C and ~50% rel. humidity after 7 days of water curing ('dry'). The tests were performed 28 days after the concreting.

Figure 6 illustrates the influence of the curing conditions on the specimen behaviour for a HSC (mix 5), exemplarily. The beams cured in water show a ~25% higher ultimate load compared to the 'dry' cured specimen. This phenomenon may be explained by cracks,

which are caused by shrinkage of the 'dry' cured specimen. However, after the peak load these beams show a more ductile behaviour compared to the 'wet' ones.

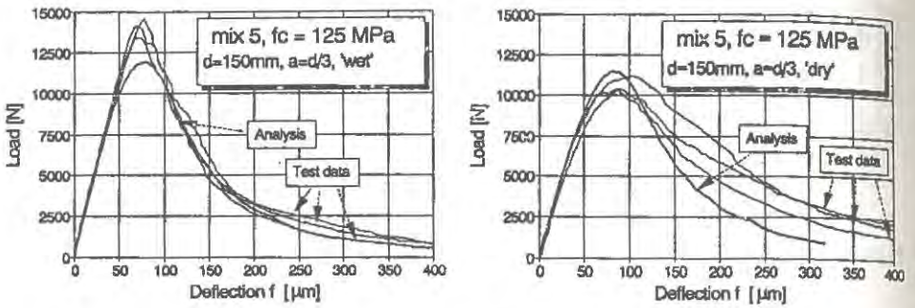

Figure 6. Load-deflection curves for different curing conditions

Additionally, the measured specimen behaviour (fig. 5) is compared with load-deflection curves, which are calculated on the basis of the proposed σ-w-relation (1) with the parameters of fig. 4b by means of the finite-element method. This analysis produces an ~15% lower ultimate load than the measured ones of the 'wet' cured beams, whereas the post-peak response agrees well with the test data. However, the ductility of the 'dry' specimen is underestimated by the analysis. An explanation of this difference can be deduced from a consideration of the fracture energy.

FRACTURE ENERGY, TENSILE STRENGTH AND DUCTILITY

The fracture energy G_f, which is determined from the area under the load-deformation curve, shows a similar dependency from the concrete strength for the water-cured bending- and the uniaxial tensile tests (fig. 7). For lower concrete strengths (~25MPa) G_f is ~100N/m. Then G_f increases up to a strength of 80 - 90 MPa to ~150 N/m. For higher strengths it stays nearly constant. Bending tests with 'dry' cured specimen produce fracture energies, which are on an average 50 N/m higher. These results agree with the values, reported by Olson [3].

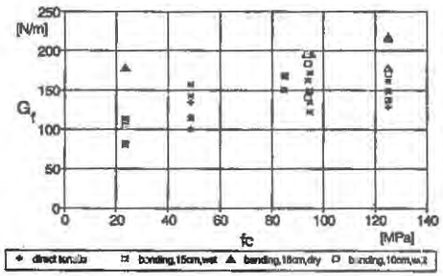

Figure 7. G_f/f_c - dependency

mix	E [MPa]	G [N/m]	B/l [1/m]	l [mm]
5	39960	134	5.47	183
7	32790	117	2.82	354
8	38410	145	4.06	247
10	31290	149	1.91	523

Table 1: Ductility indices

As with the fracture energy, the tensile strength shows a similar dependency from the strength. For f_c higher than 80 - 90 MPa no substantial increase is observed. This is valid for the direct tensile strength (fig. 8), the net flexural tensile strength, which is received from the notched bending tests, and the splitting strength (fig. 9). The own test data and results from Loland [4] indicate a lower increase of f_{ct} as most of the existing formulas reflect (fig. 8).

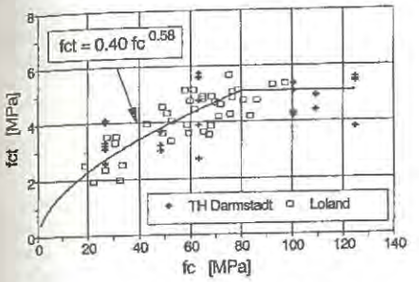

Figure 8. Direct tensile strength

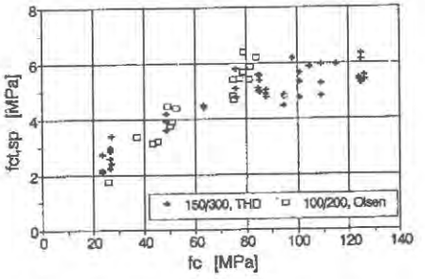

Figure 9: Tensile splitting strength

The ductility of tensile loaded concrete can approximately be described by the brittleness number $B = (l \cdot f_{ct}^2)/(E \cdot G_f)$. It is deduced for a uniaxial tensile member with the length l and a material with the modulus of elasticity E [5]. Using the results of the uniaxial tensile tests, the ductility decreases with increasing concrete strength (table 1). The HSC (mix 5) behaves 2x more brittle than a NSC (mix 7) and 3x more brittle than a NSC with crushed aggregates, which is especially ductile due to its distinct aggregate interlock.

CONCLUSION

The experimental results show that HSC possesses a substantial tensile softening simular to NSC. The fracture energy as well as the tensile strength increase with increasing concrete strength. Both show substantial further increase for strengths higher than 80 MPa. However, the ductility decreases for higher strengths. A HSC behaves 2-3x more brittle than a NSC. This loss of ductility has to be taken into account for future design rules.

REFERENCES

1. Hordijk, D.A., Reinhardt, H.W.: Influence of Load History on Mode I Fracture of Concrete, In: Fracture Toughness and Fracture Energy, Mihashi et.al.(ed.), 1989
2. Duda, H., König, G.: Rheological Material Model for the Stress-Crack-Width Relation of Concrete Under Monotonic and Cyclic Tension, ACI Materials Journal, May-June 1991
3. Olson, N.H.: The Strength of Overlapped Deformed Tensile Reinforcement Splices in HSC, Technical University of Denmark, ABK, Serie R, No 234, 1990
4. Loland, K.E.: Rapport BML 81.101, University Trondheim, Norway, 1991
5. Elfgren, L. (ed.): Fracture Mechanics of Concrete Structures, pp. 399-401, 1989

PASSIVE AND ACTIVE EVALUATION OF STABILITY IN CONCRETE STRUCTURES

RUSSELL J. MILLER and JOZEF M. DESCOUR
Mining Engineering Department

ALFRED H. BALCH
Geophysics Department

Colorado School of Mines
Golden, Colorado 80401

ABSTRACT

Geophysical techniques have long been used for evaluating internal conditions and stability of earth structures. These same techniques can be used for examining concrete structures and determining the relative stability of those structures. Passive techniques such as microseismic monitoring can locate progressive failures, determine their magnitude, and establish a relative degree of threat to the structure. Active techniques such as radar or seismic probing can actually peer into the structure to evaluate problems such as cold joints, fractures, and the condition of reinforcing steel. Recent tests at the Colorado School of Mines have confirmed the effectiveness of these techniques for evaluating concrete structures.

This paper is intended to identify geophysical techniques applicable to the evaluation of concrete structures, illustrate examples of successful application of those techniques , and indicate other potential applications of geophysics to concrete structures.

INTRODUCTION

It is well known that the nation's existing infrastructure is in a state of deterioration, and that significantly more infrastructure is required to meet current and future needs. Since much of the infrastructure will need to be repaired or replaced over time, it is important to be able to evaluate the state of deterioration and the remaining useful life of these constructed facilities.

Visual inspection of the surface of a structure can often provide a qualitative evaluation of its remaining strength, but information is required on internal conditions to be able to quantify the degree of deterioration and remaining useful life. Sampling the internal materials destroys part of the structure, must be repaired, and may provide a pathway for future adverse intrusion. For these reasons it is preferable to use nondestructive internal evaluation techniques.

Nondestructive evaluation of metals is fairly common, but techniques for examining construction materials such as concrete used in bridges, highway/airports, buildings, tun-

nels, dams, offshore structures, harbors, waste repositories, piers, and other facilities, are not well developed. Instruments and analysis techniques are needed to allow the quantitative evaluation of the safety of a structure and to estimate adequately its remaining life.

Geophysical techniques have been used successfully for many years in evaluating subsurface conditions in geologic environments, and geologic materials can have the same complicated geometries and non-uniform composition as concrete structures. There is a direct comparison, though at different scales, between the geophysical evaluation of geologic structures and the evaluation of structures containing common construction materials. Recent tests at the Colorado School of Mines have confirmed the effectiveness of these techniques for evaluating concrete structures.

BACKGROUND

As mentioned, geophysical techniques have been used to probe the underground for many types of features: oil and gas traps, mineral deposits, geologic conditions, faults, cavities, tunnels, etc.. Concrete structures also contain features we would like to be able to identify and characterize such as: reinforcing, aggregate, fractures, cold joints, segregation, and deterioration. The scale of the features is of course different; requiring the use of higher frequencies, which is possible due to the lower penetration distances necessary in most concrete structures. There are several potential techniques applicable to evaluating stability in concrete structures. Those currently being evaluated include:

Passive Seismic - With this technique we are "listening" for signs of structural distress. Any structure consisting of a brittle material will experience microseismic emissions when local stresses cause micro-failures within the structure. These micro-failures create stress waves that travel through the structure and can be measured by sensors placed on or in the structure. Through the use of several sensors, the source of the emissions can be located, and the severity of the problem determined. Passive seismic makes an excellent reconnaissance tool, being able to quietly and cheaply sit by and monitor a structure's stability. When any instability begins to develop, the system can alert the proper authorities who can then investigate the problem further with more detailed analyses of the passive seismic signals, or apply one of the following active techniques.

Active Seismic - Instead of just listening to the structure, one can generate seismic waves in the material and measure how their propagation is affected by conditions in the structure. Wave propagation phenomena of reflection, transmission, refraction, and attenuation can be used to characterize material properties and identify anomalies such as fractures, voids, or deterioration. Seismic techniques are fairly easy to apply, have good penetration in concrete, and have demonstrated reasonable resolution.

Pulsed Electromagnetics - Similar to active seismic in application except that electromagnetic waves are used instead of seismic waves. Again, reflection, transmission, refraction, and attenuation are used to characterize the material or anomaly through which the waves pass. Electromagnetic techniques are slightly more complex in application and have a problem with moisture in the concrete, but can have good resolution and make an appropriate companion to other techniques.

RF or Microwave Transmission - Transmitting radio-frequency electrical signals through geologic material has been demonstrated to be an effective delineator of structure and material properties. Similarly, RF or microwave transmission through concrete is expected to identify zones of differing material properties, and certainly the presence of conductive reinforcing. In fact, conductive reinforcing may dominate the signal path, obscuring other features. It remains to be determined if continuous wave energy can be effective in evaluating the condition of reinforcing.

Resistivity - Measures the resistance to the flow of electricity of a material. Can measure variations in material properties resulting in resistance changes. Can detect moisture, and particularly corrosive fluids. The high contrast between the conductivity of metal-

lic reinforcing and the surrounding concrete makes the reinforcing easy to find, but the domination of the current path by the rebar causes the same problem as for continuous wave transmission. It is hoped resistivity will be effective in evaluating the condition of reinforcing.

Tomographic Reconstruction - Similar to a CAT scan, the data from seismic or electromagnetic probing can be used to reconstruct the conditions within the structure. In addition to showing where things are within the structure, signal analysis should also be able to identify the condition of the concrete or reinforcing for stability evaluation. This technique has already been successfully demonstrated in the laboratory, with field units under development.

LABORATORY TESTS

As discussed previously, geophysical techniques are effective in probing geologic materials, and it was desired to determine their applicability to the stability analysis of concrete structures. Toward this end, several models plus actual concrete structures were fabricated. Both passive and active techniques are being evaluated. Results to date are summarized here.

Passive Seismic

The simplest, yet most promising, approach to be evaluated was passive seismic. A special concrete test block reinforced with several 1-inch diameter smooth steel bars/tubes was constructed (fig.1). The block was 47-in wide, 54-in high, and 7.5-in thick. The steel bars of different geometrical arrangement contributed to a nonuniform distribution of mechanical properties in the block. The effect of stress concentration produced by corrosion was simulated by a pair of thick-wall tubes with 12-inch long segment of each tube replaced by a rubber hose. By pumping a hydraulic fluid into the system a build-up of radial stress was generated which resulted in a series of internal structural failures (hydrofracing). Stress/deformation changes associated with each failure migrated through the structure and were detected as stress waves (fig.2) by the array of 8 seismic sensors (accelerometers) attached to the surface of the block (fig.1). Signals generated by the sensors in response to passing waves were digitally recorded by the data acquisition system designed for monitoring microseismic activity in mines. The data acquisition was conducted with a sampling rate of 500,000 samples per second, ten times higher than used in mines. Because of a high rate of crack occurrence, the data were acquired automatically (trigger) and processed off line. The typical waveforms measured from cracks generated in the block resembled waveforms detected in underground mines [1]. Using the arrival times of the first wavelets detected by the sensors (fig.2) along with the coordinates of these sensors, the coordinates of the center of energy release and the average group velocity were computed for individual cracks.

Three cycles of hydraulic loading and unloading were conducted. During the first cycle a total pressure on the order of 650 psi was reached in four steps: 0 to 150 psi, 120 to 250 psi, 200 to 275 psi, and 235 to 650 psi. All 17 events detected during the first step were dominated by strong signals (fig.3) of a resonant frequency on the order of 8 kHz (detailed frequency analysis of all data will follow). Their source appeared associated with the adjustment of the structure and reinforcing steel to the geometry of loading, and could be related to the slippage along reinforcing bars between steel and concrete. The estimated source location based on raw data pointed toward the top right steel tube of the pair (fig.1). First records typical for structural failures (fig.2) in the concrete between the two hose lines were detected when the pressure reached 600 psi. They were characteristic of a dominant frequency on the order of 20 kHz followed by 8 kHz signals of a generally insignificant amplitude. The second loading cycle was conducted in two steps: 0 to 600 psi, and 500 to 1000 psi. No significant events were observed during the first step. When the pressure

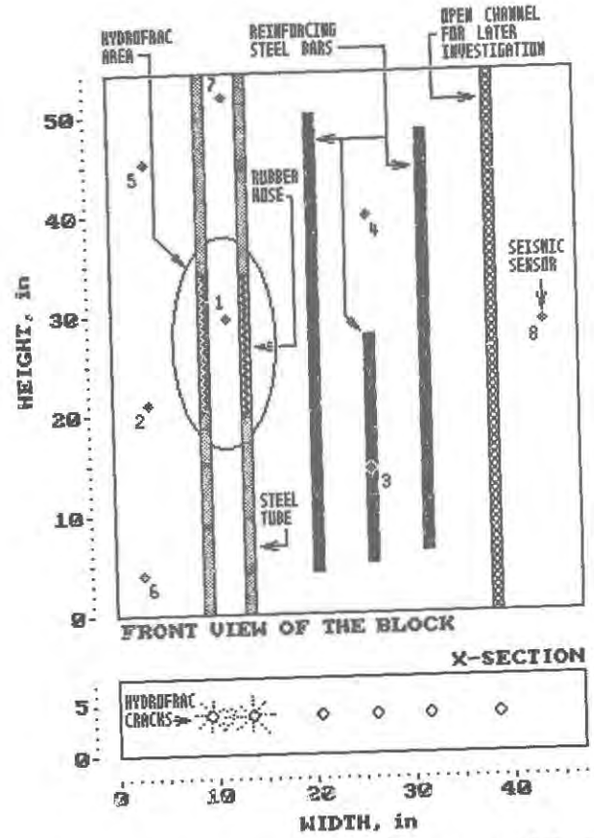

FIGURE 1. Concrete test block, the array of seismic sensors, and the grid of source points for testing the velocity distribution.

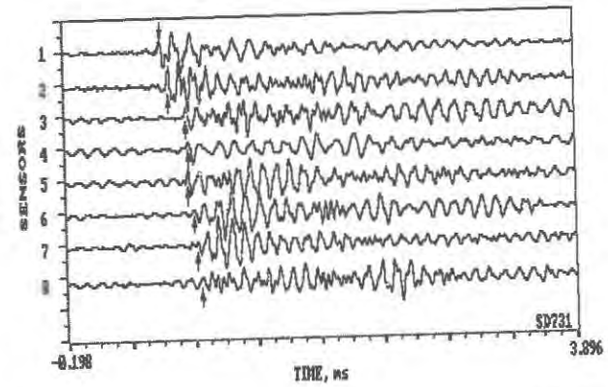

FIGURE 2. Waveforms of stress waves from a failure in the concrete block. Arrows mark arrival times used for source location.

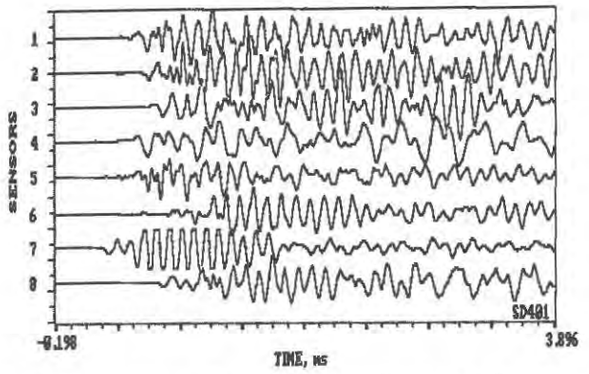

FIGURE 3. Typical waveforms which appear associated with stress release along reinforcing steel.

approached 1000 psi, a long series of strong events occurred, 64 of which were recorded. Figure 4 presents locations of these events. After initial dispersion of the first weak events, a series of stronger events were concentrated in a location approximately in the middle of the hydrofraced area. The decrease of pressure was accompanied by a significant number of events which appeared related to the relaxation of stressed material (based on parallel audio-monitoring). Only 32 events were detected during the last cycle of loading from 0 to 1000

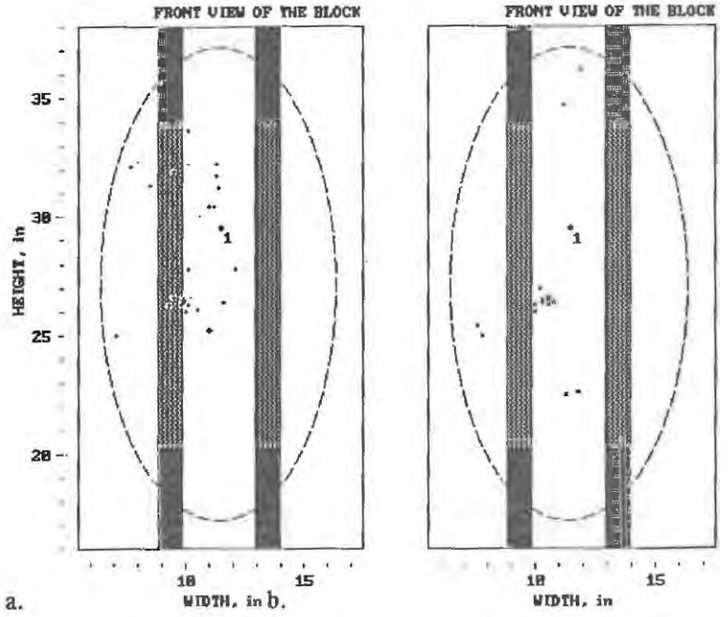

FIGURE 4. Location of micro-failures caused by hydrofracing during the second loading cycle (600 to 1000 psi)(a), and the third cycle (0 to 1000 psi)(b).

psi. Most of them occurred when the pressure approached 1000 psi. The majority of them were concentrated in the same location detected in the second cycle (fig.4).

An average group velocity on the order of 6,200 ft/s was obtained as a by-product of the source location. Considering the velocity of stress waves in the concrete on the order of 11,680 ft/s for P-waves, and 7,090 ft/s for S-waves [2], the detected velocity appears characteristic for flexural waves in bounded materials [3]. Also, there were practically no P-wave arrivals in front of detected waveforms. This same characteristic was observed in the underground mines.

Stress Wave Tomography

Two active source techniques have been tested: stress wave tomography (travel time and amplitude), and stress wave reflection imaging. In the first case we observe a direct wave arrival for a great multiplicity of source-receiver combinations. Then we mathematically deduce a velocity (or attenuation) distribution that is consistent with the first arrival times (or amplitude). The approach is analogous to the medical CAT scanner. In the second case we utilize internal reflections and diffractions to create images of reflecting/diffracting bodies.

An example of tomography as applied to a concrete specimens shown in figure 5. The two dark zones, or blotches, in the middle correspond almost exactly to two voids in the concrete specimen. The dark area near the top corresponds to a high velocity (strength) zone, due to differential curing [4].

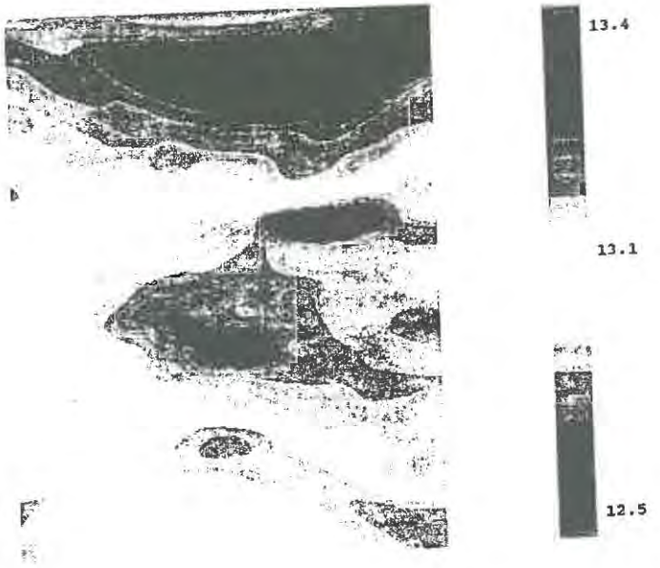

FIGURE 5. Typical stress wave velocity tomogram obtained from a concrete specimen with two voids in it. High velocity anomaly near top is due to differential curing.

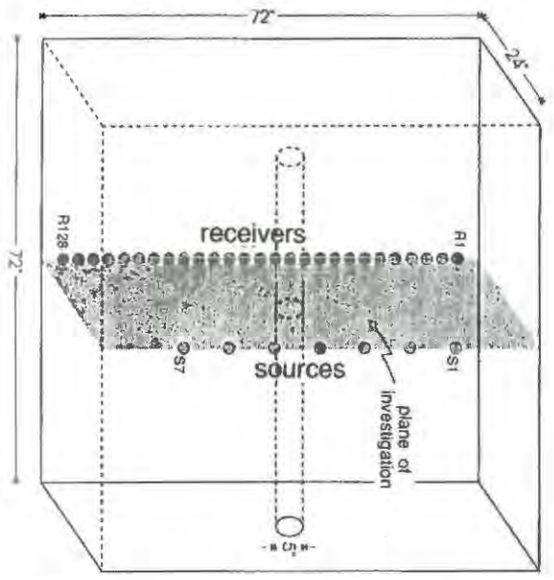

FIGURE 6. Schematic of source-receiver geometry used to explore a sample concrete specimen using reflection imaging.

As an example of the second technique, reflection/diffraction imaging, a specimen of concrete containing a cylindrical void was instrumented as shown in figure 6 [5]. A cross medium data set is shown in figure 7. The figure 7a type data are then imaged and yield the result shown in figure 7b. Images of the top and bottom of the hole, and the top and bottom of the specimen are clearly seen.

DISCUSSION

Passive and active geophysical techniques have been used successfully for the stability analysis and probing of subsurface materials. Instrumentation, processes and analysis have been fine tuned principally for minerals exploration, but it is clear many of these techniques are applicable to the construction and environmental areas. Concrete, in particular, has a strong similarity to natural geo-materials - it is composed of rock products, displays heterogeneous properties, and has similar targets of interest (fractures, voids, linear features). Differences are principally in scale - large targets at significant depth versus small targets at relatively shallow depth. This is important because resolution and penetration are strongly related. To have any reasonable resolution, the wavelength of the applied signal should be equal to or preferably shorter than the dimension of the target of interest. However, effective penetration distance falls off with increasing signal frequency (decreasing wavelength), limiting the depth and resolution attainable. For seismic techniques the maximum depth/target size ratio is about 10 to 1. Electrical methods have a similar geometric maximum range, but are complicated by being highly dependent on material electrical properties as well.

In addition to using passive and active geophysical techniques to locate problems or

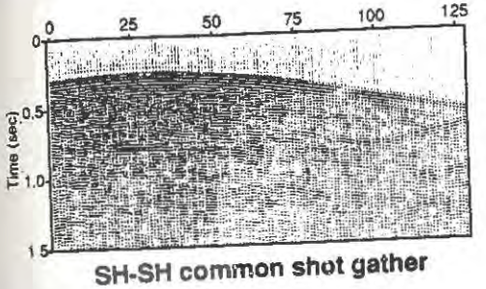

a.

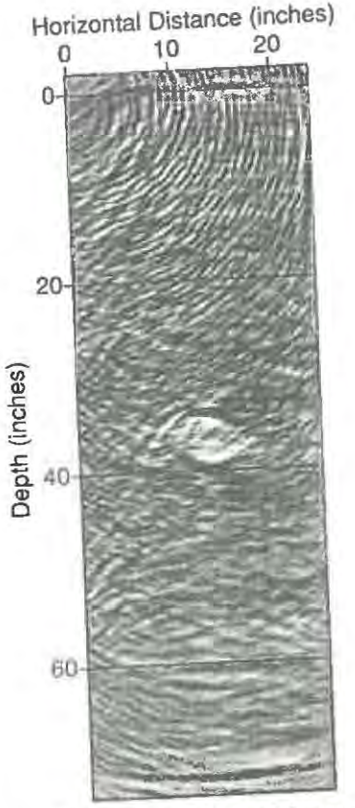

b.

FIGURE 7. Typical data set obtained from the specimen shown in figure 6 (a), and the image of cylindrical hole in the specimen (b). Both the top an bottom of the hole are delineated, as well as top and bottom of the specimen itself.

anomalies in a concrete structure, signal analysis can be applied to the data and more information about the structure obtained. Perturbations of the signal while passing through a material indicate material properties, the "quality" or deterioration of the material, and help estimate the remaining useful life of a structure. Analysis of the passive seismic emissions of a structure can warn of a developing instability, estimate its rate of progression, determine its size, and possibly predict a time to failure. Passive seismic can even monitor stability in areas related to the concrete structure such as scour and foundations or embankments.

As demonstrated in the tests described here, the passive and active systems used worked very well in analyzing a reinforced concrete structure. The passive monitoring was able to locate a developing instability, follow its progression, determine when a fracture has occurred, and identify its extent. The active seismic probing of a concrete block demonstrated that a target of the size of interest could be "seen" at a depth of interest. Even the residual stresses from the concrete curing process could be identified. Work is continuing to determine if conditions such as corroded reinforcing or deteriorated concrete can be quantified.

REFERENCES

1. Descour, J.M. and Miller, R.J., Coal Mine Bump Monitoring. U.S.BoMines Contract No.J0245009, OFR 32-88, Denver, December 1987.

2. Carmichael, R.S., Practical Handbook of Physical Properties of Rocks and Minerals, CRC Press, Inc., Boca Raton, 1989, pp. 532.

3. Kolsky, H., Stress Waves in Solids, Dover Publications, New York, 1963, pp. 41-86.

4. Schneider, W.A., Ranzinga, K., Balch, A.H. and Kruse, C., A Dynamic Programming Approach to First Arrival Travel-Time Computation, in Media with Arbitrally Disturbed Velocities. Geophysics, 1992, V.57, No.1.

5. Balch, A.H. and Chang, H., Seismic Cross Hole Imaging of 2- and 3-D Elastic Models Using Prestack, Reverse Time Migration. 61st S.E.G, Houston, 1991.

DETECTION OF FRACTURE PROCESS ZONE IN CONCRETE BY MEANS OF X-RAY WITH CONTRAST MEDIUM

KOJI OTSUKA
Department of Civil Engineering, Tohoku Gakuin University,
13-1, Chuo-1, Tagajo City, Miyagi Pref. 985 JAPAN

ABSTRACT

The purpose of the present investigation is to detect and to evaluate the fracture process zone of concrete by means of x-ray with contrast medium. The specimen used for this experiment is a rather compact tension test specimen. The contrast medium was filled in the small holes of the specimen during the loading and the x-ray exposing. Photographs and figures of fine cracks in concrete detected using this technique have been shown. Before the peak of the load, the start of fine cracks' in concrete could be observed at the tip of the initial notch. As the crack opening displacement increased, developing fracture process zones were visualized. A correlation was obtained between the pattern of fracture process zone and the maximum size of aggregate.

INTRODUCTION

Cracking processes in concrete are important influences on the mechanical behavior of concrete. Therefore to know the pattern and size of fracture process zone in concrete is important. There are many procedures to detect the fracture process zone of concrete and almost are the ways to measure them on the surface of concrete. However, to know the real figures of them, it is important to detect them in the concrete under loading condition by nondestructive methods. For the purpose, an ordinary x-ray nondestructive inspection method seems to meet the condition. However, it is impossible to detect fine cracks in concrete by ordinary x-ray methods. The uniqueness of the method used in this experiment is to use a new x-ray technique [1] -[4] with contrast medium for injecting in cracks.

MATERIALS AND METHODS

CONCRETE

Maximum sizes of aggregate of the concrete were 5, 10, 20 and 25 mm. The compressive strength of the concrete was about 27 MPa.

SPECIMEN

Fig. 1 shows details of the test specimen. The thickness of the specimen was 50 mm that was decided by preparatory x-ray experiments. There are four injecting holes (diameter: 3 mm) for contrast medium in a specimen. A notch of the specimen was cut using a diamond saw.

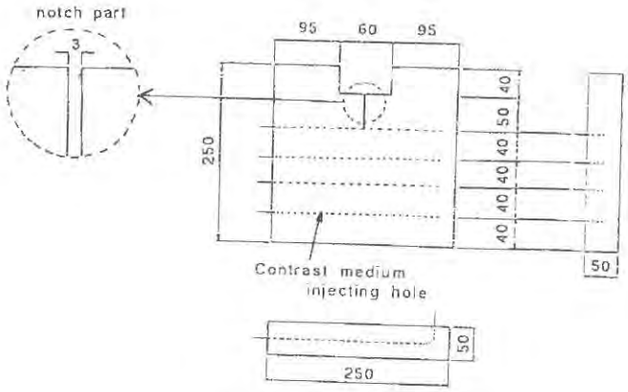

Fig. 1 Details of test specimen.

CONTRAST MEDIUM

X-ray contrast media are generally used in medical fields to increase the contrast between the internal organs to be inspected and other organs around them. Many contrast media on the market were investigated and offered to the comparison test considering the conditions as follows.

1. Contrast efficiency.
2. Permeability for fine cracks.
3. Chemical stability and safety for handling.
4. Reasonable price.

A contrast medium was selected for this experiment. It was an organic iodine type that was used for blood vessel. The density of the organic iodine is 440 mg/ml.

LOADING EQUIPMENT

Fig. 2 shows the loading equipment and a test specimen. The specimen was pulled toward up and down directions through two steel plates that were bonded using adhesive agent to the specimen. The tension loads and crack opening displacements were measured by a load cell and a clip gage.

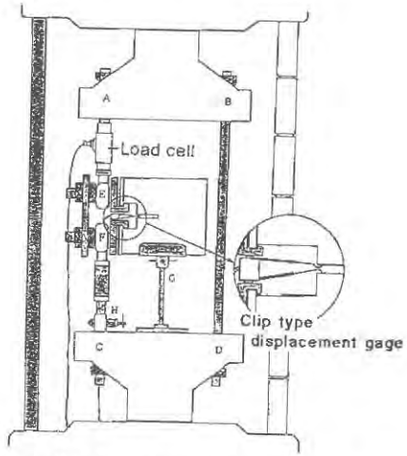

Fig. 2 Loading equipment and a test specimen.

X-RAY EQUIPMENT

An x-ray equipment for industrial use was used. The voltage was in the range of 60 ekv to 120 ekv and the electric current was 2 mA. The distance from x-ray equipment to the test specimen was 60 cm. The crack detection system used for this test were two modes. One was a direct x-ray film mode and the other was a x-ray TV image processing mode. In the case of film mode, it had to wait about 3 minutes for the exposure time, but it could be taken more clear figure of fine cracks in the concrete than the case of TV image processing mode.

RESULTS

LOAD-CRACK OPENING DISPLACEMENT CURVES

Fig. 3 shows an example of a relationship between the load and the crack opening displacement. In this case maximum aggregate size was 25 mm. The value of Gf calculated from this curve is 131 N/m. Peaks and valleys on the curve are points where x-ray exposures were taken place and the numbers in circles are corresponding to those of x-ray film.

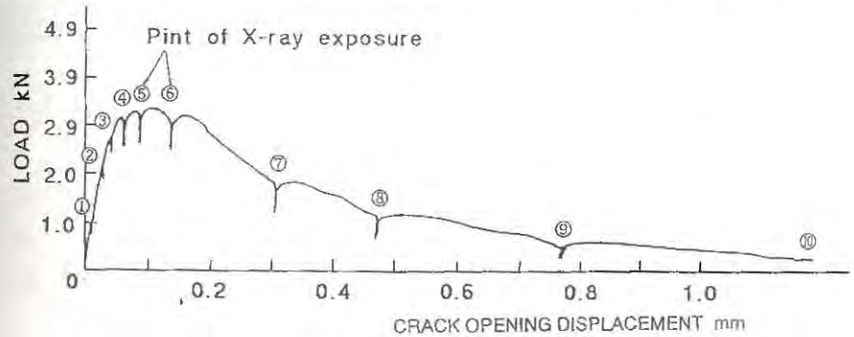

Fig. 3 Example of a load-crack opening displacement.

DETECTION OF FINE CRACKS

Fig. 4 shows a photograph printed from the No. 3 film taken from the same specimen of Fig. 3 and at the point No. 3 on the curve. Though this stage is before the peak of the load, the start of fine cracks can be seen at the tip of the notch. The crack opening displacement at this time was 0.04 mm.

Fig. 4 Start of fine cracks at the tip of the notch.

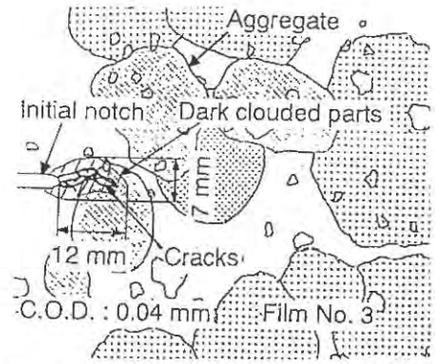

Fig. 5 A drawing of fine cracks and adjacent aggregates traced from the film No. 3.

Fairly fine cracks can be observed directly from x-ray film using film reading apparatus with naked eye. However, it becomes rather difficult to observe them in photographs printed from films and only clear cracks can be observed. Then drawings traced from the films were provided to indicate the figure of fairly fine cracks and the adjacent aggregates as shown in Fig. 5, 7, 9 and 11. In these photographs, slightly clouded dark parts could be observed near the group of fine cracks. It can be considered the existence of micro cracks that could not be recognized as cracks because of the limitation of accuracy of this technique. Fig. 6 and 7 show a photograph printed from No. 5 film and a corresponding drawing. This stage is just at the peak of the load and the crack opening displacement is 0.09 mm. Fig. 8 and 9 show a photograph printed from No. 6 film and a corresponding drawing. This stage is just after the peak of the load and the crack opening displacement is 0.13 mm.

Fig. 6 Fine cracks at the peak of load.

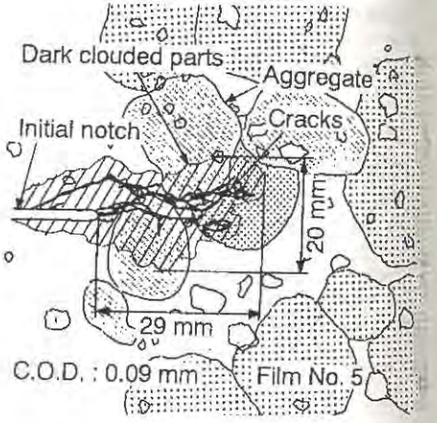

Fig. 7 A drawing of fine and the adjacent aggregate traced from film No. 5.

Fig. 8 Fine cracks just after the peak of load.

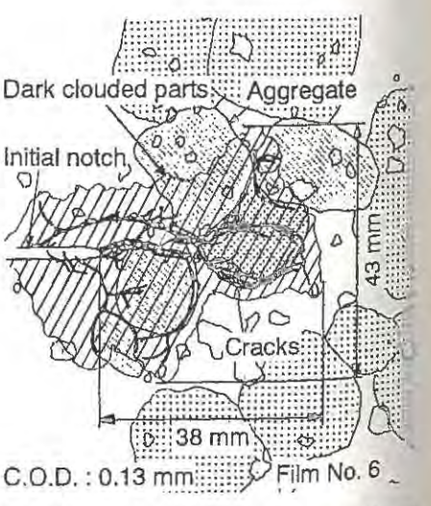

Fig. 9 A drawing of fine cracks and adjacent aggregate traced from film No. 6

Fig. 10 shows a photograph printed from No. 7 film. This stage is on the descending branch and the crack opening displacement is 0.30 mm. Many fine cracks are developing farther.

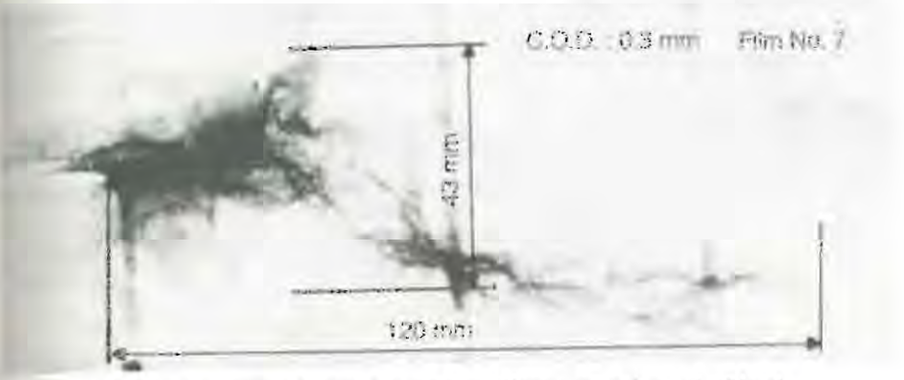

Fig. 10 A zone of fine cracks and clouded parts after the peak of load.

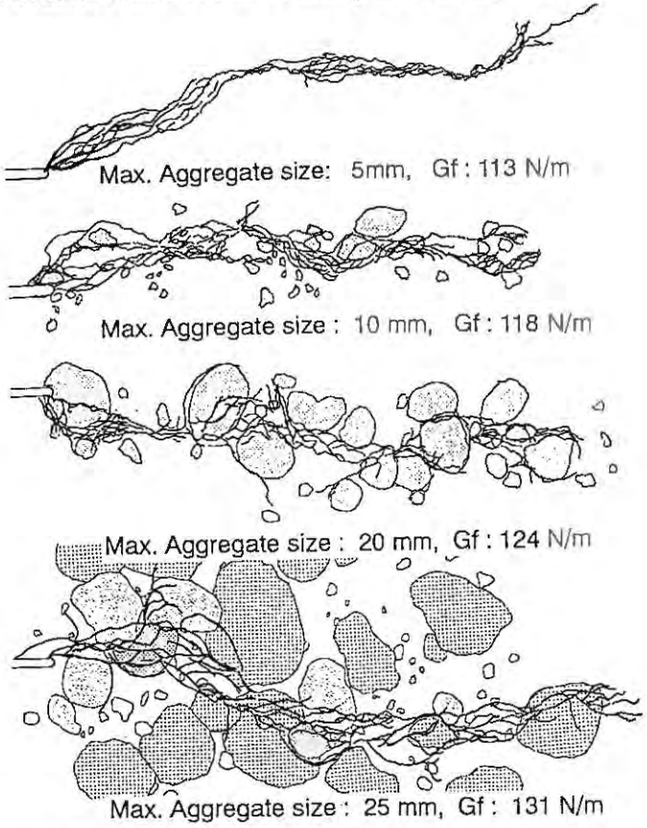

Fig. 11 Comparison of patterns of fine cracks detected in the specimens of different maximum aggregate sizes.

Fig. 11 shows four drawings of fine cracks and adjacent aggregates that were obtained from different specimens. They had been made from the concrete of different maximum aggregate sizes; 5 mm, 10 mm, 20 mm and 25 mm. All the stages of them are just before the cracks reach to the end of specimens. Cracks are forced to curve around aggregates and many complicated cracks are forming. The relationship is very clear between the maximum aggregate size and the areas of fine cracks zone including slightly dark clouded parts. According to the maximum size of aggregate become larger, the area of the zone increase.

FRACTURE ENERGY Gf

Fracture energies Gf was measured from only a limited number of specimens. The values of Gf were 113,118,124 and 131 N/m corresponding to the maximum aggregate sizes 5, 10, 20 and 25 mm respectively. They are shown in Fig. 9. According to the maximum aggregate sizes become larger, the value of fracture energy increase.

CONCLUSION

An independent experimental technique (X-ray with contrast medium) has been used to detect fine cracks in concrete. Photographs and drawings of fine cracks detected using this technique have been shown to study the fracture process zone of concrete.

Before the peak of the load, start of fine cracks' cloud be observed at the tip of the initial notch. As the crack opening displacement increased, developing fracture process zones in concrete were visualized.

A correlation was observed between the pattern of fracture process zone and maximum aggregate size. A tendency was also observed that the values of fracture energy increase according to the maximum aggregate size become large.

ACKNOWLEDGMENTS

The author wishes to express his gratitude to Prof. Hirozo Mihashi for frequent, stimulating, and helpful suggestions and comments. The author is also deeply indebted to his students Hiroaki Katsube for his contribution to obtain the x-ray photographs and drawings.

REFERENCES

1. Otsuka, K. , X-ray technique with contrast medium to detect fine cracks in reinforced concrete. Fracture Toughness and Fracture Energy, A. A. Balkema, Rotterdam, 1989, pp. 521-534.

2. Otsuka, K. and Shoji, Y., Detection of fracture process zone by x-ray with contrast medium, JCI colloquium on fracture mechanics of concrete structures, 1990, pp. 1-4.

3. Otsuka, K., Detection of fine cracks in reinforced concrete using x-ray with contrast medium, Proceedings of JCI, 1988, Vol. 10, No. 3, pp. 145-150.

4. Otsuka, K., Morohashi, K. and Naruse, Y., X-ray inspection of crack in concrete. Abstracts of the annual scientific presentation meeting, Tohoku branch of JSCE, 1987, pp. 398-399.

DETECTION OF CRACK DEVELOPMENT BY REAL-TIME HOLOGRAPHIC INTERFEROMETRY

GUNTER KRÜGER, GOTTFRIED SAWADE
FMPA BW Otto-Graf-Institut
Pfaffenwaldring 4, D-7000 Stuttgart 80, Germany

ABSTRACT

Sandstone was characterized by a fracture mechanical description. Further the effect of stone strengthening due to the cementation of cracks was investigated. The mechanical parameters and properties were evaluated from 3-point-bending tests. Real-time holograhic interferometry in conjunction with phase-shift technique was applied for crack length determination.

INTRODUCTION

Mechanical and thermal-hygrical loading of natural stone in conjunction with chemical and biological detoriation can lead to the formation of cracks and in the end to a complete mechanical destruction. In particular this applies to mineral building materials with low tensile strength such as sandstone. The consolidation of deteriorated material by stone strengthener is aimed at regaining the original state with respect to strength and porosity [1] and to a certain degree to produce stress transfer over existing cracks.

Therefore it is important to know about the fracture behaviour of the material and effect of cementation by a stone strengthener with respect to the cementation of cracks and the generation of stress transfer over cracks.

For the visualization of crack processes and the experimental determination of crack lengths holographic interferometry in conjunction with digital image processing is a very useful tool because of the high range of sensivity and the possibility of extensive observation [2],[3].

THEORY

During the crack formation and crack growth elastic energy is converted to surface energy. However, when the fracture energy G is evaluated on the basis of linear fracture mechanics (LEFM) from notched samples of mineral building material, a strong size dependence is observed [4]. This effect is attributed to nonlinear slow crack growth occuring prior the peak load; stable crack growth appears with increasing load.

The modeling of this behaviour in LEFM is based on the assumption, that a crack-processing-zone exists, where stress transfer depending on the crack opening w is possible [5]. The fracture energy G(w) is then assumed to be a material typical function of the crack opening with regard to the specific total crack surface energy G_f and the tension strength β_s. Approximately, the energy balance due to the crack developement can be stated in generalization of LEFM as

$$1/E \cdot K_I^2(a)da = \int_0^{a+da} G[w(x,a+da)]dx - \int_0^{a} G[w(x,a)]dx, \quad (1)$$

where K_I, E, a and w(x,a) are the stress intensity factor, the Young's modulus of elasticity, the crack length and the crack opening (obtained from LEFM).

PHASE-SHIFTING HOLOGRAPHIC INTERFEROMETRY

In holographic interferometry fringes are formed by reconstruction of double-exposure holograms or by superposition of the reconstructed wave field and the real-time image of the deformed object. The interfering wave fields correspond to different deformation states of the investigated object. The sinusoidal fringe patterns can be analysed qualitatively for nondestructive testing and quantitatively to obtain surface displacements and strains [2]. The interference phase Φ is related to the surface displacement vector **d**, as follows:

$$\Phi = 2\pi/l \cdot (\mathbf{d} \cdot \mathbf{e}) \quad (2)$$

The sensitivity vector **e** with $|\mathbf{e}|=2\cdot\cos(\alpha/2)$ is directed along the bisector of the angle α between the direction of illumination and viewing. l is the wavelength of the illuminating laser light.

Fig.1 shows a principle of the real-time interferometer used in this work, that allows a continual observation during the tests. Holograms were recorded using a thermoplastic camera system, which permits rapid in situ processing. Small tilts to the object beam were introduced to compensate rigid body movements, which lead to a large number of fringes and poor fringe contrast.

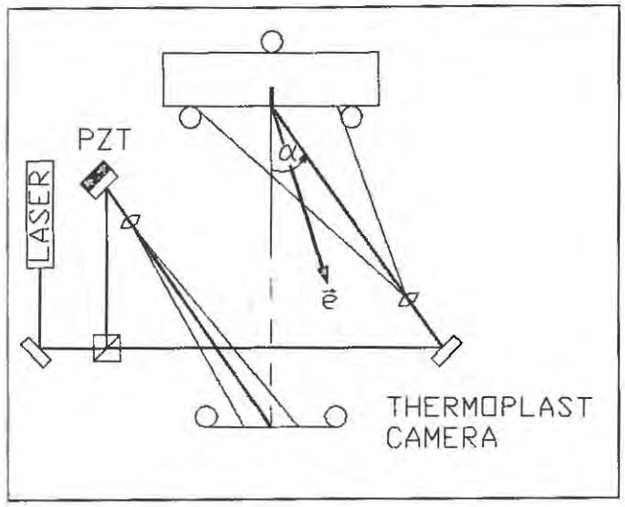

Figure 1.
Optical setup

The interferograms viewed by a CCD camera were processed by a microcomputer and an image memory board. Cracks are detected from lines of discontinuity (Figure 2). The accuracy in the localization of the crack tip can be improved, when the phase-shift technique [7] is applied, to calculate the interference phase.

Figure 2.
Interferogram of a loaded specimen

Figure 3.
Interference phase modulo 2π

The interference phase modulo 2π can be evaluated from four by 90° phase stepped interferograms. To vary the phase, the reference mirror was mounted on a piezoelectric transducer (PZT)

and controlled by a digital I/O device. The intensity $I_n(x,y)$ at any point x,y of the detector array of the CCD chip can be written as

$$I_n(x,y) = I_0(x,y)\cdot[1 + \Gamma(x,y)\cdot\cos(\Phi(x,y) + n\cdot 90°)] \qquad (3)$$

$$n = 0,1,2,3,$$

where $I_0(x,y)$ is the average intensity and $\Gamma(x,y)$ is the fringe contrast. The phase $\Phi(x,y)$ is given by

$$\Phi(x,y) = \arctan\cdot \frac{I_3(x,y) - I_1(x,y)}{I_0(x,y) - I_2(x,y)} . \qquad (4)$$

Fig.3 showes the interference phase modulo 2π which has an improved signal to noise ratio and contrast in comparison to the fringe pattern of figure 2.

TEST PROCEDURE

Three different kinds of sandstone were investigated: Schilfsandstein, Grünsandstein and Stubensandstein. In a first step notched beams ($200\cdot40\cdot45mm^3$) were tested in a three-point bending arrangement. The notch length and the support span were 15mm and 180mm respectively. The external load and the centre deflection were recorded by an electronic data acquisition system. The test was stopped when the crack reached a length of 80% related to the crack ligament. After the first test the specimens containing cracks were cemented using a stone strengthener. In the same manner as before a second bending test was made on the strengthened samples.

RESULTS

In table 1 the mean values of the maximum load, the fracture energy G_f and the stress intensity factor are listed. K_I was calculated from the crack length and the maximum load by means of LEFM.

TABLE 1

	Schilf-sandstein	Grün-sandstein	Stuben-sandstein	
peak load [kN]	0.30	0.34	0.73	first loading
G_f [N/mm]	0.061	0.029	0.060	
K_I [$N/mm^{1,5}$]	12	16	36	
peak load [kN]	0.25	0.33	0.29	after cement.
G_f [N/mm]	0.029	0.028	0.030	
K_I [$N/mm^{1,5}$]	64	130	145	

As an example in figure 4 the calculated (according to equ.1) and the experimental load-deflection diagrams of the untreated and the strengthened samples are given.

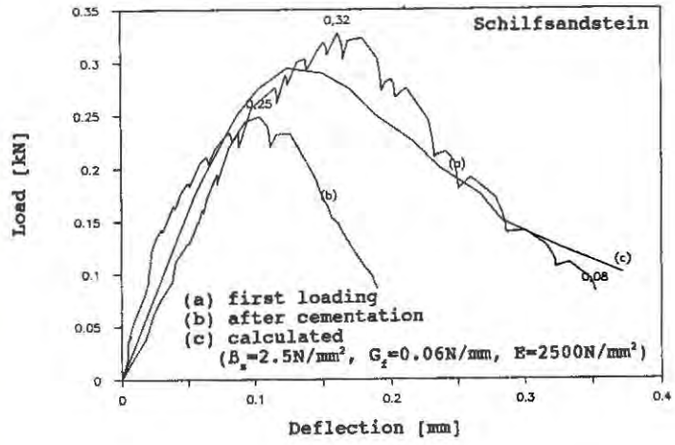

Figure 4. Load deflection curves

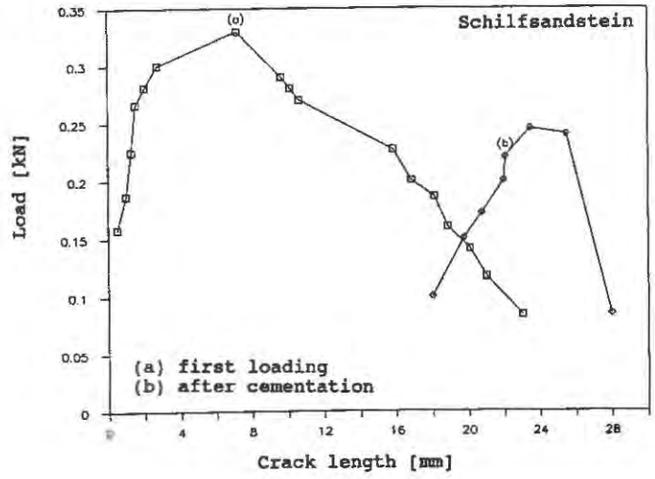

Figure 5. Crack growth

In all samples crack formation prior the peak could be obser-

ved. The crack length at maximum load was approxiately 20-30% related to the crack ligament. A typical crack length versus load diagram is given in figure 5.

The sandstones show a nonlinear fracture behaviour. In comparison to the untreated specimens the maximum load of the strengthened samples is reached at considerably high crack lengths; the crack produced by the first loading opens completely at rather small loads.

CONCLUSIONS

Real-time holographic interferometry is useful for the contactless measurement of crack lengths in fracture mechanical tests. Due to noise reduction and contrast enhancement the use of phase-shift techniques allowes a precise localization of the crack tip.

All investigated sandstones showed undercritical crack growth predicted from the existence of a nonlinear crack-zone. Therefore the fracture mechanical description has to follow the nonlinear fracture approach.

However, the peak loads and the fracture energies at the first loading are quite different for the different kinds of material investigated, the peak loads of all strengthened samples are approximately equal. This leads to the conclusion, that the deformation behaviour of the strengthened specimen is mainly independent of the mechanical properties of the stone. The effect of the strengthening is not the complete cementation of cracks, but the improvement of stress transfer over the crack at large deformations.

REFERENCES

[1] Snethlage, R., Steinkonservierung, Forschungsprogramm des Zentrallabors für Denkmalpflege 1979-1983, Arbeitsheft 22, ed. Bayrisches Landesamt für Denkmalpflege.

[2] Erf, R., Holographic Nondestructive Testing, Academic Press, New York, 1974

[3] Breuckmann,B. and Thieme,W., Computeraided ananlysis of holographic interfrograms using the phase-shift method; Appl.Opt., 1985, **24**

[4] Jenq, Y.S. and Shah, S.P., A two Parameter Model for Concrete. J.of Engeneering Mechanics, ASCE 111, 1985, **10**

[5] Hillerborg,A., Analysis of One Single Crack Developments. Fracture Mechanics of Concrete, Elsevier 1983

[6] Eligehausen ,R. and Sawade, G., Verhalten von Beton auf Zug. Beton & Fertigteilwerk-Technik, 1985, **7/8**

[7] Carré,P.: Installation et utilisation du compateur photoelectrique et interferential du Bureau International des Poids et Mesures; Metrologia **2**, 13, 1966

TENSILE MODELING AND EXPERIMENTAL DETERMINATION OF FRACTURE ENERGY OF EARLY AGE CONCRETE

DENZIL R. LOKULIYANA
Graduate Student,
Dept. of Civil Engineering,
Nagoya Univ., Nagoya, Japan

KINYA KASHIMURA
Research Engineer,
Konoike Const. Co.,
Osaka, Japan

TADA-AKI TANABE
Professor,
Dept. of Civil Engineering,
Nagoya Univ., Nagoya, Japan

ABSTRACT

On the basis of fracture mechanics, a constitutive model is proposed to describe the tensile softening behaviour of early age concrete with the corporation of classical plasticity theory. In the present analysis, the localized failure of concrete under uniaxial tension is considered. Fracture energy of early age concrete was obtained from the direct tensile test using a double notched test specimen.

INTRODUCTION

In view of the need to identify the fracture energy of early age concrete a plastic modeling is constructed on the basis of fracture energy concept in terms of Mode I type of cracking. Drucker-Prager type failure surface, is used to describe the shape of failure surface, and its evolution is considered to be governed by cohesion and the angle of internal friction. Finally, the applicability of the proposed model is verified through available test data.

THEORETICAL CONSIDERATION OF THE MODEL

When the stress in concrete which is subjected to direct tensile test reaches its strength, initiation of micro cracks occur. With further increase of strain these microcracks start to develop gradually to produce the final complete crack. Hence in the region where the progressive development of microcracking occurs, which also can be called as the softening region, the stiffness orthogonal to the direction of crack reduces gradually to zero. The following relation can be written for the uniaxial stress σ_e and strain ϵ_e (Fig. 1) in the strain softening region.

$$\sigma_e = \mu E_{t0} \varepsilon_e \tag{1}$$

where E_{t0} is the Young's modulus at time t_0 and the term μ counts for the degradation of stiffness. Here, μ is defined as softening parameter and, continuous transition from crack free state to the fully cracked state may be very simply obtained by continuously varying the softening parameter μ between the limits of one and zero.

In the strain softening region, the cohesive properties of concrete will start to deteriorate and as a result of this mechanism, the strength of concrete also starts to reduce in the same manner. Hence, in spite of the paucity of experimental data for early age concrete, the degradation characteristic of cohesion may be rationalized to take the form similar to strength reduction and the following assumption for the variation of cohesion with softening is considered to be appropriate as far as the experimental tendency is examined (Fig. 2).

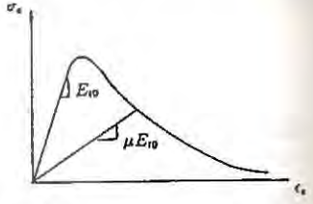

Figure 1. Uniaxial Stress-Strain Relation

$$c = c^*_{t0} \ \mu \ exp(1-\mu) \tag{2}$$

where c^*_{t0} is the cohesion just before cracking.
In this analysis since Mode I type of fracture is considered, the cohesive properties of the material is assumed to dominate over the frictional properties and hence, unlike in compressive failure the frictional properties in tensile failure is considered to remain unchanged.

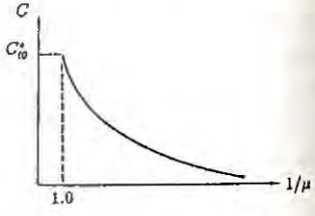

Figure 2. Variation of Cohesion

When the idealized process of progressive cracking is considered as the cracking has no effect on lateral strains the amount of fracture energy at time t_0 can be calculated as

$$Gf_{t0} = \int_{\mu=1}^{0} dG(\mu) = w_c \int_0^{\varepsilon^f_e} \sigma_e d\varepsilon^f_e \tag{3}$$

in which w_c is the width of crack band. Here, superscript 'f' refers to the fracture process zone.

DECOMPOSITION OF TOTAL STRAIN OF CRACKED CONCRETE

The total strain increment vector within the fracture process zone where both cracked and uncracked concrete exists, can be decomposed into two components which are contributed from micro defects and intact material in between (Fig. 3). Then an average process describe the average total strain increment by

$$d\varepsilon_{ij} = d\varepsilon^e_{ij} + \beta_{ik} d\varepsilon^f_{kj} \tag{4}$$

where, the superscript ' e ' stands for intact material. Here, β_{ij} is introduced to define the ratio of the width of the fracture process zone or the crack band width to the length of the concrete element. This can be defined as follows.

$$\beta_{11} = \frac{w_c}{l_0}, \qquad \beta_{22} = \gamma \frac{w_c}{l_0}, \qquad \beta_{33} = \eta \frac{w_c}{l_0} \tag{5}$$

Here, l_0 is the length of the concrete element and γ and η count the effect of micro cracks to the other directions. For the idealized crack bands where major cracks are assumed to be orthogonal to the applied load the values of γ and η can be taken as zero.

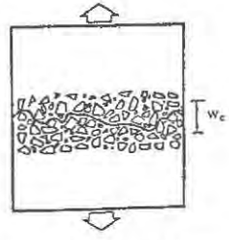

Figure 3. Partially Cracked Element

MODELING OF CONCRETE AT EARLY AGES FOR TENSION

In the present modeling which follows the basic concept of classical plasticity theory, the current loading surfaces are assumed to change continuously in size depending on the accumulation of the defects on the material as a function of stress state σ_{ij} and energy consumed $G(\mu)$ which is defined as a function of softening parameter μ, during fracturing. This can be written as follows.

$$f = f(\sigma_{ij}, G(\mu)) \tag{6}$$

The consistency condition $df = 0$, which the stress tensor must satisfy during loading, can be expressed as

$$df = \frac{\partial f}{\partial \sigma_{ij}} d\sigma_{ij} + \frac{\partial f}{\partial G(\mu)} dG(\mu) = 0 \tag{7}$$

The normality condition of the failure surface with associated flow rule can be expressed as

$$d\varepsilon^f_{ij} = d\lambda \frac{\partial f}{\partial \sigma_{ij}} \tag{8}$$

where $d\lambda$ is a scalar quantity.
Now from the elastic stress strain relation

$$d\sigma_{ij} = D^e_{ijkl} d\varepsilon^e_{kl} \tag{9}$$

and both consistency condition (eqn. (7)) and normality condition (eqn. (8)) the constitutive relation for cracked concrete can be expressed as

$$d\sigma_{ij} = \left[D^e_{ijkl} - D^e_{ijpq} \frac{\beta_{pv} \frac{\partial f}{\partial \sigma_{vq}} \frac{\partial f}{\partial \sigma_{mn}} D^e_{mnkl}}{\frac{\partial f}{\partial \sigma_{rs}} D^e_{rstu} \beta_{tw} \frac{\partial f}{\partial \sigma_{wu}} - w_c \frac{\partial f}{\partial G} \sigma_{ij} \frac{\partial f}{\partial \sigma_{ij}}} \right] d\varepsilon_{kl} \tag{10}$$

In the literature [1], different approaches have been done to define the failure surface for concrete material. Out of these, a smooth approximation to the Mohr-Coulomb surface was given by Drucker and Prager and is assumed in the present numerical calculations. The Drucker-Prager failure surface with the time dependent material parameters at time t_0 can be expressed as

$$f = \alpha_{t0} I_1 + \sqrt{J_2} - k_{t0} \tag{11}$$

Here, $I_1 = \sigma_{kk}$ and $J_2 = \frac{1}{2} s_{ij} s_{ij}$ are the first invariant of stress tensor σ_{ij} and the second invariant of the deviatoric stress tensor s_{ij}, respectively and, α_{t0} and k_{t0} are material constants which varies with time and progressive failure. Since the present analysis is considered only on the tensile behaviour of concrete, the two failure surfaces i.e. Mohr-Coulomb Drucker-Prager, are matched along the tensile meridian and hence,

$$\alpha_{t0} = \frac{2sin\phi}{\sqrt{3}(3 + sin\phi)} \quad \text{and} \quad k_{t0} = \frac{6ccos\phi}{\sqrt{3}(3 + sin\phi)} \tag{12}$$

where c and ϕ are the values of mobilized cohesion and friction angle which varies with the cracking parameter.
Now from eqns. (11) and (12),

$$\frac{\partial f}{\partial G} = \left\{ \frac{\partial f}{\partial \alpha_{t0}} \frac{\partial \alpha_{t0}}{\partial \mu} + \frac{\partial f}{\partial k_{t0}} \frac{\partial k_{t0}}{\partial \mu} \right\} \frac{\partial \mu}{\partial G} \tag{13}$$

Now from the equivalent uniaxial stress-strain relation of eqn. (1) and using the relation of eqn. (2) the term $\frac{\partial \mu}{\partial G}$ of the above equation will become

$$\frac{\partial \mu}{\partial G} = -\frac{1}{w_c E_{t0} \varepsilon_e^2} \tag{14}$$

Then from the substitution eqns. (13) and (14) into eqn (10), the proposed constitutive relation for the cracked concrete element can be obtained.

VERIFICATION OF THE PROPOSED MODEL

Numerical simulation was carried out for uni-axial test specimens to verify the applicability of the proposed model. Firstly, the model was checked with the test results of Evance et. al. [2]. Next, the test results of Gopalaratnam [3] and Klisinski [4] were compared with the proposed model. It can be seen that the model agrees well with the experiments. These are shown in Fig. 4.

Now, according to the definition of β_{11}, from the results of uniaxial test data together with analytical results obtained from the model analysis, the width of the fracture process zone can be calculated. Now from eqn. (3), when the area of the stress-strain curve at $\beta_{11} = 1.0$ is W_f the value of fracture energy becomes

$$Gf_{t0} = w_c W_f \tag{15}$$

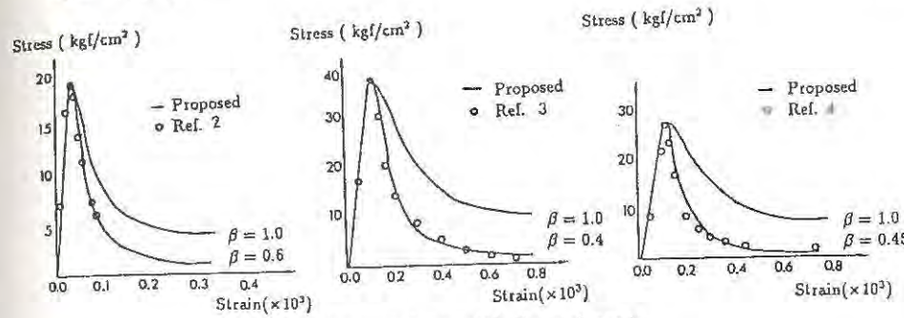

Figure 4. Comparison with Experiments

The results obtained for crack band width, crack width and fracture energy are listed in Table 1.

TABLE 1. Summary of the Obtained Results

Test	Age (days)	β_{11}	l_0 (mm)	$w_c = \beta_{11} l_0$ (mm)	ε_{cr} $\times 10^6$	w_{cr} (mm)	Gf_{t0} (N/m)
Evans 2)	70	0.60	24.5	14.7	4000	0.059	27.85
Gopalaratnam 3)	28	0.45	83.0	37.3	800	0.029	50.31
Klisinski 4)	-	0.40	-	-	900	-	-

EXPERIMENTAL INVESTIGATION

Uniaxial tensile test was carried out for rectangular prismatic specimen having length of 300mm, width of 140 mm and 40 mm thickness. Two notches were introduced at the center of the specimen having length of 25 mm and 4 mm width. The Displacement Transducer type (DT-F) strain gages were used to measure the strains along the fracture process zone. Two testing machines were used in the experiments. High stiffness testing machine having maximum tensile loading capacity of 150 kN was used to test the specimens with ages more than 11 hrs. Very young age concrete was tested by another testing machine having maximum tensile loading capacity of 50 kN.

Testing was carried out for several number of specimens at different ages. Test specimens were made by concrete having cement:sand:aggregate ratio of 1:2.5:3 with water:cement ratio of 0.55. Tests were performed for concrete at 8, 9, 12, 18, 22, 25, 42 hr. after casting of the specimens. The values for tensile strength, Young's modulus and fracture energy are obtained from the direct tensile test are illustrated in Table 2.

TABLE 2. Proposed Values of Material Properties

Age hr.	Tensile Strength kgf/cm^2	Young's modulus ($\times 10^5$) kgf/cm^2	Fracture Energy kgf-cm/cm^2
8	0.8	0.080	0.004
9	1.4	0.083	0.008
12	1.4	0.139	0.012
18	3.9	0.363	0.024
22	4.4	0.180	0.048
25	7.9	0.444	0.028
42	12.6	1.805	0.036

CONCLUSION

The proposed model can be used to present the softening behaviour of concrete at early ages. The behaviour of the model is mainly governed by the material properties of concrete such as cohesion, angle of internal friction and Young's modulus. Hence when the values of these parameters at any time is known, the constitutive relation for the softening region of early age concrete can be obtained.

Since the present model was constructed by considering the localized failure, the size of the fracture process zone can be estimated with the aid of test results of direct tensile test. From this estimated value of the width of fracture process zone, the width of crack and the value of fracture energy can be evaluated. However, more experimental investigation is necessary on the determination of the values of fracture parameters.

REFERENCES

1. Chen, W.F., Plasticity in Reinforced Concrete, McGraw-Hill Book Company, 1982.
2. Evans, R. H. and Marathe, M. S., Microcracking and Stress-Strain Curves for Concrete in Tension, Materials and Structures (Paris), No. 1, Jan.-Feb., 1988, pp. 61-64.
3. Gopalaratnam, V. S. and Shah, Surendra P., Softening Response of Plain Concrete in Direct Tension, ACI Journal, Proceedings V. 82, No.3, May-June, 1985, pp. 310-323.
4. Klisinski, M., Degradation and Plastic Deformation of Concrete, Polish Academy of Sciences, Warsaw, IFRT Report No. 38, 1985, pp.198.

DISCONTINUOUS CRACK GROWTH AS FRACTURE PROCESS ZONE THROUGH SEM ANALYSIS

Bascoul, A. and Turatsinze, A.,
Laboratoire Matériaux et Durabilité des Constructions
I.N.S.A.-U.P.S. Complexe Scientifique de Rangueil
31077 TOULOUSE CEDEX - FRANCE.

ABSTRACT

Microscopical observations by means of the replica technique and SEM are presented. They concern the damage of mortar specimens subjected to mode I crack opening. Within the material a discontinuous process of crack growth can be regarded as the process zone. Its length is compared with the effective crack length from Effective Crack Model and Two Parameter Model.

INTRODUCTION

Non linear models have been developed whether to describe the behaviour of specimens subjected to crack growth or to identify the intrinsic parameters which govern the crack growth. Through all these models, it is always assumed that there is a microcracked zone - process zone - ahead of the macroscopic crack. Whereas it is generally thought that microcracks are distributed in a volume, the process zone is always modelised by a crack line with closing pressure except in the crack band model[1].

Direct observations are needed to valid the concept of microcracked zone and the associated models. Replica method makes it possible. Some previous observations by means of the replica technique and SEM were presented at International Conference in Cardiff (Sept 89) [2]. Now it is possible to present an extensive study on mode I crack propagation.

EXPERIMENTAL PROGRAM

Three point bending tests were carried out on notched mortar specimens. Their final dimensions were always obtained by cutting (loading span, S=320 mm - depth, H=80 mm - width, B=50 mm - notch depth a_0=40 mm). The displacement of the applied load was imposed with a rate of 20 µm/minute.

Observations were carried out on the outside lateral surface for 14 specimens and in the longitudinal median plane, after cutting, for 20

specimens. Replica method has been already described [3]. It allows to observe the imprint of the mortar surface on a material insensitive to the atmosphere of the SEM cell. The minimum crack opening which can be detected is of the order of 0.1-0.25 µm at usual magnification of X200-X400. Higher magnifications (up to X10000) are used when there are some doubts about the interpretation of pictures from replicas, the resolution of which is of 0.1 µm.

The observations on the lateral surfaces give an important information about the resolution of the method. In that case comparisons can be made between replicas of loaded and unloaded specimens. They show the same very fine line at the same place of the path end. Thus the crack cannot close completely when the specimens are unloaded which induces an imprint of the same length. As a result of these comparisons it can be considered that there is no loss of resolution concerning the observations within the material in spite of the necessary unloading.

DISCONTINUOUS MICROCRACKING AS PROCESS ZONE

The first damages are observed soon before the peak load (around 70% of maximum load). They can be detected approximately by taking successive replicas on the lateral surface from zero loading. So the beginning of the cracking appears to be formed by only one microcrack which is initiated somewhere at the tip of the notch. No microcracks are observed in the neighbourhood. The beginning of the propagation does not result from a phenomenon of coalescence of microcracks. Inside the material such a process is also pointed out. As it is impossible to follow the damaging on a same sample, arbitrary cuttings are necessary before the maximum load is reached. In that case one single microcrack is observed but at higher load levels.

When the load displacement is increased two different processes are observed outside and inside the specimen. Outside the material there is a single tortuous crack path with some branchings. No microcracks can be detected beside this path neither ahead of the tip of the crack. Within the material, the damages are formed by a continuous path which starts from the notch and next discontinuous microcracks which draw the path along which the crack will go for upper load displacement [2]. These phenomenons are illustrated on figure 1. The lengths of the damaged ligament are almost identical inside and outside the specimen. Such a result has been found on the set of our tests.

Through our method, discontinuous microcracks have always been observed within the material whereas no damages of this kind were detected by the overall techniques of impregnation [4] [5] . This leads to consider that there are isolated microcraked surfaces which cannot be reached by the liquids. But the discontinuous paths may also result from a tortuous shape of the front of the macro-fracture surface as well as from material bridgings. In fact the three phenomenons are likely to combine and all these fractures are distributed over a surface and not within a volume. Let us write the total length of damaged ligament L_{tf} as the sum of the length of continuous fracture L_{cf} and the length of discontinuous fracture L_{df}:

$$L_{tf} = L_{cf} + L_{df}.$$

The term L_{df} may be considered as the length of the process zone.

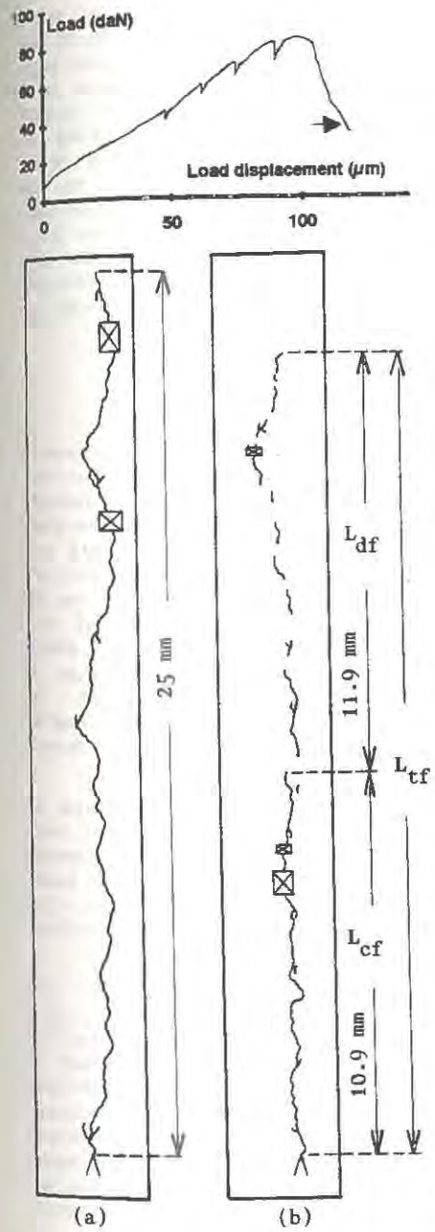

Figure 1 : Maps of the cracks
(a) lateral surface
(b) longitudinal median plane

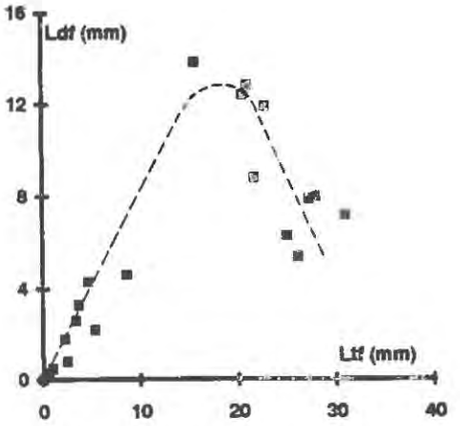

Figure 2 : Discontinuous fracture length according to total damaged ligament length

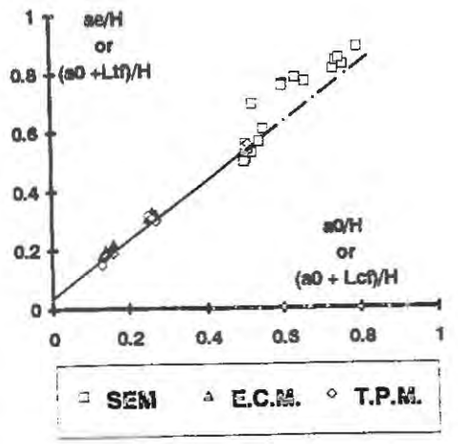

Figure 3 : Comparison between ECM or TPM results and observations through SEM

Table I gives the values of the three terms L_{tf}, L_{cf} and L_{df} which were measured. It can be seen that the process zone length is nearly equal to the total length at the beginning of the crack propagation, before the mean displacement δ_m at the peak load (δ_m = 78 µm). Beyond δ_m value there is a steep increase in L_{tf} with some discrepancy whereas the process zone length appears to be bounded. On figure 2, L_{df} values are plotted according to L_{tf} values. Two domains of variation can be pointed out. At the beginning of the propagation, the process zone length increases proportionally to the total length L_{tf}. The peak of the curve is reached when the tip of the last microcrack is close to the middle of the ligament. Next the process zone decreases. It cannot develop through lack of space and microcracks are connected as the crack mouth opening is increased. Such a variation compares with the one deduced by means of compliance and multi-cutting method [6].

COMPARISON BETWEEN MODELS AND OBSERVATIONS

Through Effective Crack Model or Two Parameter Model an effective crack length a_e is calculated which integrates the process zone effects at the tip of an artificial notch when the critical load is reached. The process zone length can be evaluated by means of the difference (a_e-a_0). By varying the artificial notch a_0 the relationship between the the crack growth and the process zone length can be approached. Such tests have been carried out and the results are published in the report of RILEM Technical Committee 89 - FMT [7]. Effective crack lengths a_e are given in table II. (a_e-a_0) and L_{tf} values can be directly compared for the specimens which have a notch depth ratio equal to 0.5. L_{tf} values corresponding to the mean value δ_m of the critical load displacements are only to be compared to (a_e-a_0) values. In that case it can be seen from table I that the lengths measured in the test number 6, 7 and 8 are of the same order as the process zone length (a_e-a_0) from table II.

The theoretical relationship between a_e and a_0 can be considered as linear, (figure 3). In order to compare the evolution of the process zone length proposed by the models with the one deduced from the measurements the terms (a_0) and (a_e) have to be identified respectively to the terms (a_0+L_{cf}) and (a_0+L_{tf}). The experimental points as defined above are also plotted on figure 3. It can be seen that these points are distributed around the theoretical straight line.

The evolution of the process zone length deduced from E.C.M. and T.P.M. cannot remain valid when the notch depth ratio tends to the unit. But it appears to be roughly in accordance with the evolution as observed througth the tests. When the load displacement corresponding to the test is around the mean peak value, the points are very close to the theoretical line. In fact they are in accordance with the assumptions of the models. Next the points are above the extrapolated straight line and the process zone is greater than the predicted one, particularly when the continuous crack is not very developed. However when the continuous crack has reached the middle of the ligament the points are close again to the line because the process zone is confined.

TABLE 1
Measured damage lengths

Test N°	δ (µm)	Lcf (mm)	Ldf (mm)	Ltf (mm)	(a0+Lcf)/H	(a0+Ltf)/H
1	35	0.5	1.8	2.3	0.51	0.53
2	41	0.5	0.5	1	0.51	0.51
3	50	0.4	0.3	0.7	0.51	0.51
4	50	0.4	3.3	3.7	0.51	0.55
5	55	0	0	0	0.50	0.50
6	60	1.7	0.8	2.5	0.52	0.53
7	71	3.2	2.2	5.4	0.54	0.57
8	80	0.8	2.6	3.4	0.51	0.54
9	98.4	18.8	6.3	25.1	0.74	0.81
10	102	4.1	4.6	8.7	0.55	0.61
11	109	0.4	4.3	4.7	0.51	0.56
12	116	1.8	13.8	15.6	0.52	0.70
13	117	8.2	12.8	21	0.60	0.76
14	119.3	10.9	11.9	22.8	0.64	0.79
15	119.5	19.4	7.9	27.3	0.74	0.84
16	120	8.1	12.4	20.5	0.60	0.76
17	120	20.8	5.4	26.2	0.76	0.83
18	120	20	8	28	0.75	0.85
19	124	23.8	7.2	31	0.80	0.89
20	131.8	12.9	8.8	21.7	0.66	0.77

δ: load displacement
Lcf: length of continuous fracture
Ldf: length of discontinuous fracture
Ltf: total length of damaged ligament

TABLE 2
Effective crack lengh ae from models [7]

H (mm)	a0 (mm)	ECM ae (mm)	TPM ae (mm)
40	10	12.4	12.8
39	10.1	12.5	12.1
40	10.8	12.8	12
80	40.8	44.8	44
80	40	43.2	44
80	40.8	44.8	44.8
80	20.8	25.4	24.8
83	21.6	27.4	25.7
83	21.6	27.4	25.7
80	10.4	14.4	12
83	13.3	18.3	15.8
83	11.6	16.6	14.9

CONCLUSIONS

Three point bending tests were carried out on a lot of notched specimens in order to study the crack growth by means of the replica technique and SEM.The results from this study can be summarized as follows:

a) A single microcrack (of the order of maximum grain size) was detected at the beginning of the fracture process inside the specimens as well as on the lateral surfaces, before the peak load was reached.

b) On the lateral surfaces a continuous path was always observed sometimes with some branchings.

c) Inside the specimens, discontinuous microcracks were always located ahead of the continuous crack on a tortuous line without any other microcracks in the neighbourhood.

d) It can be concluded that there is a discontinuous process of crack growth inside the specimens as it is generally assumed in concrete fracture mechanics. But these discontinuities are distributed on a surface instead of a volume as it is often proposed. This fracture process has to be regarded as the process zone, the length of which has been measured by our technique. The lengths of the overall damages have been compared to the effective crack lengths from ECM and TPM models. Both models are in good agreement with the experimental results.

REFERENCES

1.Bazant, Z.P. and Oh, B.H., Crack band theory for fracture of concrete, Materials and Structures,Vol.16 N°93, 1983.

2.Bascoul, A., Détriché, C-H., Ollivier, J-P. and Turatsinze, A., Microscopical observation of the cracking propagation in fracture mechanics of concrete. Fracture of concrete and rock. Recent developments. Edited by S.P. Shah, S.E. Swartz, B. Barr. Elsevier Applied Science.

3.Ollivier, J-P., A non destructive procedure to observe the microcracks of concrete by scanning electron microscopy. C.C.R., vol.15, 1985.

4.Bascoul, A., Kharchi, F., Maso, J.C., Concerning the measurement of the fracture energy of a micro-concrete according to the crack growth in a three point bending test on notched beams. Fracture of Concrete and Rock. SEM-RILEM International Conference, 1987, Houston, TX, USA. Edited by S.P. Shah and S.E. Swartz.

5.Swartz, S.E., Dye techniques to reveal the fracture surface of concrete in mode I. Experimental technniques. May - June 1991.

6.Hu,X.Z., and Wittmann, F.H., Fracture process zone and Kr-curve of hardened cement paste and mortar.Fracture of Concrete and Rock. Recent developments. Edited by S.P. Shah, S.E. Swartz, B. Barr. Elsevier Applied Science.

7.Karihaloo, B.L., and Nallathambi, P., Notched Beam Test: Mode I Fracture Toughness. RILEM REPORT 5. Fracture Mechanics Test Methods for Concrete. Edited by S.P. Shah and A. Carpinteli. Chapman and Hall.

HYDRAULICALLY DRIVEN FRACTURE OF CONCRETE AND ROCK: A NEW TEST CELL.

J.H.M. VISSER and J.G.M. VAN MIER
Delft University of Technology, Stevin Laboratory,
P.O.Box 5048, 2600 GA Delft, The Netherlands.

ABSTRACT

A new test cell is presented for hydraulically fractured laboratory scaled specimen. The cylindric concrete specimens were loaded on the circumference by water pressure only. The tests were all deformation controlled and the deformation rate was kept constant. Similarity between the load-displacement curves of the hydraulic tests and the uniaxial tests indicate a pure mode I fracturing mode. This is supported by the peak load of the specimens which is equal to the tensile strength of the material. The pressure cell seems to be a powerful experimental set-up for gaining a better insight in hydraulic fracturing process and parameters involved.

INTRODUCTION

Fluid driven fracture of concrete and rock is a widely observed phenomenon. Examples of situations where it may occur are concrete dams, offshore platforms and hydraulic fractures made for the stimulation of oil well production. The fundamental interaction between fluid and solid is barely understood. Important parameters are the permeability of the (cracked) material and the fluid flow in the crack. Fracture propagation theories form an essential ingredient in establish relations between these parameters and the fracture geometry.

In order to determine the influence of the hydraulic fracturing parameters on the fracturing process, a simple pressure cell has been developed by which fluid driven fractures can be obtained in laboratory scale specimens. Concrete or rock cores of diameter 100 mm are subjected to axial tension or compression and lateral fluid pressure up to 100 bar. The system has been developed primarily for surveying triaxial tension-compression-compression states of stress.

In the paper, the construction of the test-cell will be described, together with some preliminary experimental results on concrete. The experiments should reveal the fracture energy and failure mechanism of the material for situations where the fluid pressure interacts with the process zone.

MATERIALS AND SPECIMENS.

The specimens used in the pressure cell are mortar (d_{max} = 2 mm) cylinders of 300 mm length and 100 mm diameter. The composition of the concrete is given in [1]. In order to obtain homogeneous specimens, they are casted as blocks of 300x300x350 mm. After 2 days, the blocks are demoulded and stored under high moisture conditions (90 % RH) to prevent drying out. At an age of 14 days, four cylinders with a diameter of 101 mm are drilled from one block and from both ends of the cylinders, 25 mm is sawn to obtain a cylinder length of 300 mm. Immediately after sawing, the cylinders are restored under high-moisture condition. A week before testing, the cylindrical surfaces are polished to obtain a diameter of exact 100 mm. In order to be able to centre the specimen when polishing, steel discs of 30 mm thickness are glued with epoxy resin to the ends of the cylindrical specimen. An additional advantage of the steel plates is that an axial force can now be applied on the specimens.

Further preparation of the specimens consists of notching them to define the region of fracturing and sealing the ends of the cylinder. A circular notch of 5 mm depth and 5 mm width is sawn 100 mm from the top of the specimen. Sealing the ends of the cylinders is done to prevent leakage of water from the test cell along the specimen due to irregularities like air bubbles. Sealing of the cylinder ends is done with epoxy resin. After application of the epoxy resin, the ends are polished to obtain a perfectly smooth surface. In Fig. 1, a schematic cross sectional figure of the cylindrical specimen is shown.

With each batch, six 150 mm cubes are produced and cured under the same conditions as the cylinder specimens. After 28 days, the cubes are used for the determination of the compressive and splitting tensile strengths. The compressive strength f_c and the tensile splitting strength f_{spl} determined from the 150 mm cubes are 45.1 ± 0.5 and 3.4 ± 0.1 MPa respectively.

EXPERIMENTAL SET-UP

The cylindrical cell

The pressure cell has been developed primarily for triaxial tension-compression-compression states of stress. Therefore, the pressure cell, of which a cross sectional view is given in Fig. 2, consists of three parts: an upper plate, a circular shaft and a lower plate which are held together by safety bolts. The upper and lower plate of the cell are not solid, but contain a circular hole of 100 mm diameter in which the cylindrical specimen is contained. In this way, the specimen can move freely in longitudinal direction. Also, an axial force (either compressive or tensile) can be applied on the specimen ends. Radial compressive forces on the specimen can be applied by pressurizing the water in the cell. As can be seen in Fig. 2, not the total length of the circumference of the specimen is pressurized, but only 200 mm of the specimen is surrounded by water. Rod seals between the upper c.q. lower plate and the specimen prevent water leakage from the cell.

In the upper plate of the cell, a filler cap and a valve are inserted so the cell can be filled with water before pressurization. On top of the upper plate, a safety plate is attached to prevent the specimen from shooting out of the cell in case of uncontrollable fracture.

In the lower plate of the cell, a small channel has been drilled to the water reservoir of the cell through which water can be transported either in or out the cell in order to adjust the pressure. Four additional channels are leading the LVDT-wires out of the cell. A second plate is attached under the lower plate. The specimen can be attached to this so-called

base-plate, and an axial force can be applied to the specimen. The base-plate itself is standing on three adjustment screws and a hinge by which the cell can be put perfectly horizontal. The hinge plate finally is attached to a frame which is fixed to the floor of the laboratory.

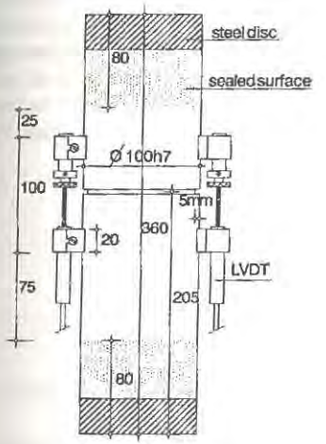

Figure 1. Specimen

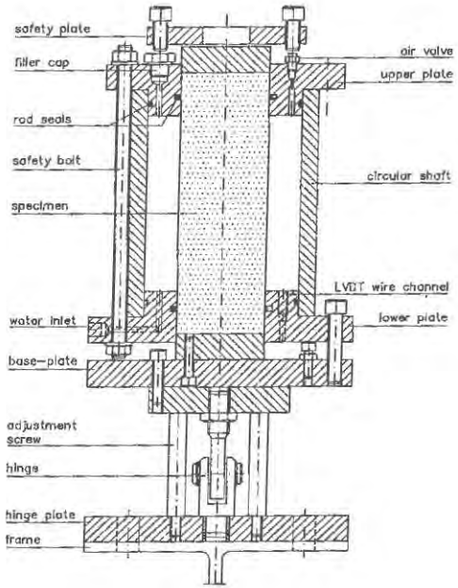

Figure 2. Pressure cell.

Regulation system

In Fig. 3, a schematic reproduction of the regulation system is given. As can be seen, only two parameters can be measured in the pressure cell. The first parameter is the pressure in the cell, which can be measured with a pressure transducer. The second variable is the axial elongation of the specimen which is measured with two high pressure LVDT's (type W1S/6S, linear stroke +/- 1 mm, measuring length 80 mm) 180 degrees apart. The LVDT's can be used up to pressures of 200 bar. The LVDT's are attached to the specimen by holders glued to the specimen surface. The holders are placed symmetrical to the notch in longitudinal direction and are 80 mm apart (see Fig. 1). Only the mean deformation of the two LVDT's is registered.

The tests done with the hydraulic cell are all deformation controlled. The prescribed deformation is generated by a function generator and consists of a linearly increasing deformation at a rate of 0.12 μm\s. The pressure necessary for a certain deformation is controlled by a servo valve (Moog valve, type 76-315 S/N D129), which obtains its basic pressure from a hydraulic pump.

When the prescribed deformation equals the mean measured deformation, the control signal for the servo valve, generated by a P.I.D.-amplifier, is zero and the valve is closed. However there is a leakage current entering the valve via pressure inlet P and leaving the valve via return outlet R.

If the prescribed deformation is larger than the measured deformation, the control signal is positive and the valve opens so water is pumped in the cell, giving rise to higher pressures and an increasing deformation. Via inlet P, the valve and outlet C1, water can be pumped into the cell. The hydraulic system works on oil, whereas the hydraulic cell contains water. Therefore, an oil-water separator was placed between the valve and the cell. This separator consists of a tube in which oil floats on water by density contrast only.

When the pressure in the cell has to be reduced, the valve shifts to the left, and the water flows back to the hydraulic pump via tube C1, the valve and return tube R, either stopping further deformation or slowing it down. When the pressure in the cell has to be decreased instantly, not enough oil can be pumped back via the valve, so a bypass tap K1 has been added. The tap is opened only slightly, because otherwise the pressure of the hydraulic system will drop to the pressure of the test cell and the servo valve will not have enough pressure available to regulate properly. In the present set-up, no active reduction of axial deformation can be obtained unless a compressive axial force is applied. In order to keep the pressure in the valve low when it shifts to the left, a third outlet tube (C2) is added. Tap K2 is opened only slightly to prevent the pressure to become too low.

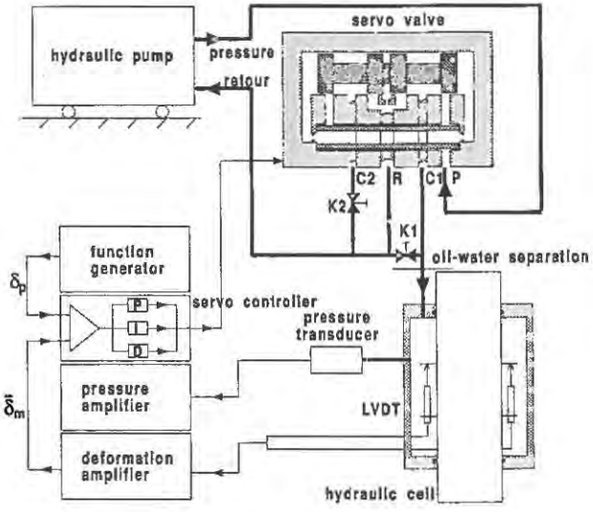

Figure 3. Regulation system.

EXPERIMENTS.

The experiments have been performed using water as a pressure fluid in the cell. The cylindrical specimen was loaded at the circumference only. Control variable in the experiments was the axial elongation of the specimen. The prescribed deformation rate was kept constant at 0.12 μm/s. Measuring length of the LVDT's was 80 mm.

Only four succesfully controlled tests have been performed so far. Most of the specimens broke outside the LVDT-range during the experiments. This might be due to the presence

of high stress concentrations at the boundaries of the glued areas (from the sealing and gluing of the LVDT-holders). A notch depth of 5 mm seems for these specimens not deep enough to predefine the fracture area but no experiments have yet be done with deeper notches. For two different types of specimens, controllable experiments could however be performed. The first type of specimens were sealed to the notch, so no glue boundaries were present. The second type of specimens were partly saturated. With partly saturated is meant that the specimens have been immersed in a water basin for one week. In this way it is not possible to completely saturate the specimen. The pressure-displacement curves for the four succesful tests are given in Fig.4.

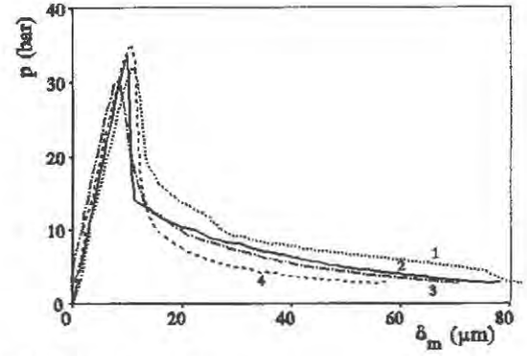

Figure 4. Load-displacement curves.

The results show a rather consistent response. This can also be seen in table I, in which the most important parameters are given.

Table I.
Parameters of the hydraulic fracture tests.

Curve no.	Type of specimen	E-modulus (GPa)	p_{max} (MPa)	$d(p_{max})$ (μm)	d_{max} (μm)
1	sealed	27.0	3.2	10.4	82.0
2	sealed	28.2	3.4	10.0	78.2
3	sealed	27.7	3.0	8.2	70.0
4	saturated	31.1	3.5	10.4	57.4

The Young's moduli, given in table I, show a slightly higher value for the saturated specimen. Regarding the variance in E- moduli for the sealed, or unsaturated, specimen, it is difficult to say at this stage of the research if the slightly higher value in E-modulus for the saturated specimen is due to the saturation.

The peak loads are for both the sealed and the saturated specimens similar. This is probably due to the fact that for both type of specimen no fluid can seep through the surface of the specimens. The only possible fracture initiation mechanism is the external load, except maybe for a small contribution of loading of the notch. The notch effect will be lower for the unsaturated specimen because water can seep in the concrete, reducing the effective stress. But regarding the difference in peak load for both types of specimen, this reduction

can not be high. It seems that fracture initiation is totally due to the external loading [2]. Once a fracture has been initiated, fluid will leak off in the surrounding concrete in the unsaturated specimen. This is however not the case for the partly saturated specimen. Although it is only partly saturated, it seems that the porosity is reduced enough to prevent a large leak-off current in the concrete. Therefore, pressure can be built up faster, giving rise to a higher crack propagation speed. In other words, less pressure is needed for a similar crack speed as for the unsaturated specimen. Because the pressure in the cell can not become lower than 3 bar, crack speed can not be reduced any further when a pressure of less than 3 bar is needed. This point is reached sooner for the saturated specimen. Thus, the maximum displacement which still could be measured (see table I) is much lower for the saturated specimen. Whereas crack initiation seems determined by the external loads only, crack propagation seems to be influenced by the pressure distribution in the crack as well. At this stage of the research it is however not possible to say anything about possible mechanisms of crack propagation.

The peak strengths of the curves in Fig.4 are almost equal to the tensile strength of the mortar, as derived from the cubic tensile splitting tests (f_{spl} = 3.4 ± 0.1 MPa). It thus seems that the fracturing mode of the specimens is purely tensile, or mode I. This is also confirmed by the fact that the pressure-displacement curves in fig.4 have a remarkable similar shape with the load- displacement curves from the uniaxial tests of Schlangen and van Mier [1] for the same 2 mm mortar. For the pressure tests, we also find a steep descending branch beyond the peak, followed by a stable tail until complete separation occurs. The main difference between the curves, is that the pressures curves can only be measured unto about 40 mm. This is due to the fact that the pressure in the cell can not become lower than 3 bar.

CONCLUSIONS.

Although the results are only preliminary, it seems that the pressure cell is a powerful experimental set-up for measuring the most important parameters of the hydraulic fracturing process and will give without doubt a better insight in the mechanism of the hydraulic fracturing process.

ACKNOWLEDGEMENT.

The authors are greatly indebted to the valuable assistance of Mr. G. Timmers with the experiments. The research was made possible through a grant of Delft University (Committee Beek) and the Commission of the European Community.

REFERENCES.

1. Schlangen, E. and van Mier, J.G.M., Experimental and numerical analysis of micromechanisms of fracture of cementbased composites. Report 25.5-91-1/VFC, T.U.Delft, 1991.

2. Clayton, N. and Grimer, F.J., The diphase concept, with particular reference to concrete. In Developments in concrete technology-1, ed. F.D. Lydon, Applied Science Publishers Ltd., London, 1978, pp. 283-318.

Chapter 5

Measurements of Damage and Size Effect

Invited Paper

SIZE EFFECT OF THE CONCRETE CONE FAILURE LOAD OF ANCHOR BOLTS

ROLF ELIGEHAUSEN
Professor/Institut für Werkstoffe im Bauwesen,
Stuttgart University, Germany

PETR BOUŠKA
Research Engineer/Klokner Institute
Czech Technical University of Prague, CSFR

VLADIMIR ČERVENKA
Červenka Consulting, Prague, CSFR

RADOMÍR PUKL
Research Engineer/Klokner Institute

ABSTRACT

The concrete cone capacity of headed anchor bolts subjected to axial tension load was experimentally investigated using 35 concrete specimens of three different sizes. The dimensions of the test specimens were varied in proportion to the embedment depth h (h = 50, 150 and 450 mm). Material properties were measured on accompanying specimens. The measured failure loads are compared with other experimental and numerical investigations. According to the present results the failure loads increase in proportion to $h^{1.6}$, that means close to the prediction by linear fracture mechanics.

INTRODUCTION

Fastening elements such as headed-, expansion- and undercut anchors are often used in the construction industry to transfer loads into concrete structures. The design of such fastenings is mainly based on the results of experimental investigations [3]. One of the open problems is the so-called size effect of the concrete cone failure load.

An experimental investigation of the pull-out strength of headed anchors was recently conducted at the Klokner Institute of the Czech Technical University in Prague in cooperation with the Institute for Building Materials of the Stuttgart University. The main objective of the investigation was to verify the size effect of the concrete cone failure load.

EXPERIMENTAL PROGRAM

Specimens and headed anchor bolts of three different sizes of the same geometrical shape were used. For corresponding dimensions the ratio 1 : 3 : 9 was applied, while the actual embedment length was 50, 150 and 450 mm. Furthermore two different diameters of the

anchor heads were used. All specimens were made from concrete of nominally identical quality with a specified cube strength f_{cc} = 30 MPa. The specimens were cast in six series. Each series of specimens was cast from the same concrete mix, 18 specimens were tested in series I to III [1] and 17 specimens in series IV to VI [2].

TEST SPECIMENS

The shape of the specimens in plan view was a square (small and medium sizes of series I to III) or an octagon respectively (all other specimens). The dimensions of the specimens are shown in Fig. 1 and listed in Table 1. The diameter of head type A was with $d_h \sim 1.9\ d_0$ (d_0 = shaft diameter) relatively large. For head type B the head diameter d_h was chosen such that the stresses under the head at peak load were kept almost constant ($\sigma_u \sim 14\ f_{co}$). The concrete mix was transported from an industrial plant by mobil mixers to the laboratory, where the specimens were cast. Composition and properties of the mix are described in Table 2. The results of the accompanying material tests (average value of at least 3 tests) performed at the time of testing (concrete age about 45 days), are also given in Table 2. To avoid a splitting failure the specimens of series I to III were reinforced by an orthogonal ribbed reinforcement placed near the top surface and anchored by hooks. In series IV to VI the specimens were constrained by a welded orthogonal steel frame which was placed around the top of the specimens and slightly prestressed to ensure direct contact.

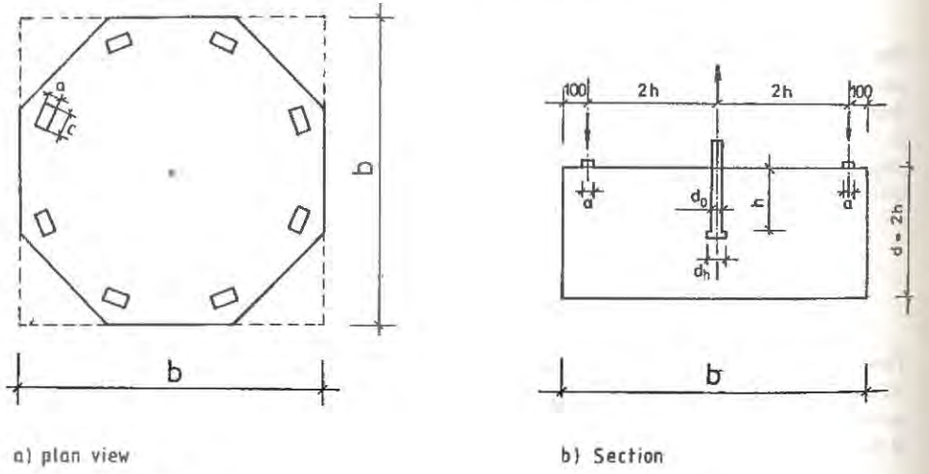

a) plan view b) Section

Fig. 1 Test specimen

TEST PROCEDURE

The tensile force was transferred to the anchor through a shaft with two spherical hinges to minimize bending moments on the anchor. Three types of loading systems were used: for small specimens 100 kN hydraulic machine Amsler, for medium specimens a pair of 250 kN jacks and for large specimens a pair of 1500 kN jacks. However, in series I to III the anchor

bolts with h = 50 mm ruptured before a concrete cone was formed because of a too low steel strength. Therefore a hole was drilled from the back side of the specimens and the anchors were loaded by a compression force on the anchor head. In all other tests the anchor bolts did not yield. The support reaction was taken up by a special orthogonal structure resting on eight supports located on a circle (see Fig. 1).

TABLE 1
Dimension of specimens in mm

Size	Anchor				Specimen		Support	
			d_h					
	h	d_0	head A	head B	b	d	a	c
small	50	8	15.0	12.7	400	100	10	40
medium	150	24	45.6	32.9	800	300	30	100
large	450	72	135.5	88.5	2000	900	100	180

TABLE 2
Concrete mix and properties

Series	Cement[1]	Water	W/C	Aggregates[2] size in mm		Ligo-plast SF	Slump	f_{cc} [3]	f_t [4]	E_c	G_f [5]
				0 - 4	8 - 22						
	kg/m³	kg/m³		kg/m³	kg/m³	kg/m³	mm	MPa	MPa	GPa	N/m
I								32.6	2.97	26.2	169
II	350	195	0.57	890	905	2	110	29.7	2.85	29.8	170
III								33.2	3.00	26.4	167
IV								29.3	2.76	30.1	126
V	350	200	0.58	880	890	2	150	28.3	3.09	30.5	146
VI								34.4	3.17	31.5	152

[1] Slag-Portland cement SPC 325
[2] natural round aggregates
[3] measured on cubes (side length 200 mm)
[4] tensile splitting strength
[5] measured on notched beams (d = 100 mm) in 3 point bending according to RILEM [11]

The loading was performed under displacement control by manual operation of the hydraulic system. The time-displacement relation was kept approximately linear. For each size of specimen a special calibrated load cell was used. During the test the anchor load, the relative displacement between the loaded end of the anchor bolt and the top surface of

the specimen and the strains on the surface of the shaft were measured by Peekel Instruments data acquisition system Autolog controlled by a PDP computer 11/23. In series IV to VI also the displacement of the anchor head was measured.

TEST RESULTS

In all tests failure was caused by pushing (Series I to III, h = 50 mm) or pulling out (all other tests) a concrete cone. The shape of this cone was approximately similar for all embedment depths. In general the diameter of the cone on the concrete surface was < 4h. However, in some tests with large anchors (h = 450 mm), the formation of the failure cone was restricted by the supports.

In Fig. 2 typical load displacement curves for anchors with head type B and an embedment depth h = 50, 150 and 450 mm are plotted. In Table 3 the concrete cone failure load of anchors with head type B are listed. The concrete compression strength varied between 28 and 34 MPa. Therefore the failure loads were normalized to the average compression strength f_{cc} = 31 MPa by multiplying the measured values with the factor $(31/f_{cc})^{0.5}$. The weighted coefficient of variation of the normalized failure loads amounts to V ~ 11 %. This coefficient of variation is quite common for such tests. A much larger value must be expected, if the concrete mix is varied. For anchors with a larger head (type A), the average failure load was 10 % (h = 50 mm), 14 % (h = 150 mm) and 6 % (h = 450 mm) higher than for anchors with head type B. This is due to the much smaller concrete stresses under the head at peak load (~ 3.6 (h = 450 mm) to 8.6 f_{cc} (h = 50 mm)) which lead to smaller displacements of the anchors with a larger head.

The test results for the deepest anchors (h = 450 mm) might have been influenced favourably by two effects: (1) The concrete compression strength was measured on cubes which were cured as the test specimens. Because of hydration heat generated in the large specimens, the concrete strength might have been somewhat higher than measured on control specimens. (2) In some tests, the formation of the failure cone was hindered by the supports. However, it is believed that the combined effect of both influencing factors is small.

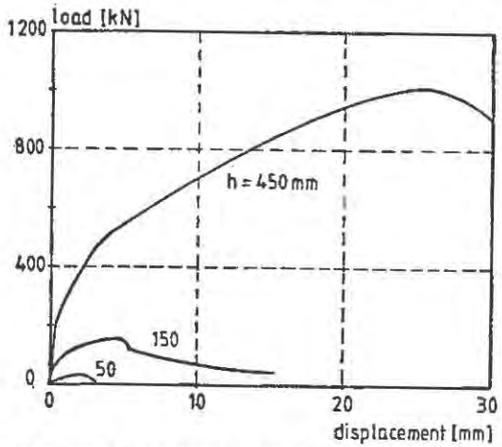

Fig. 2 Typical load-displacement relationships

TABLE 3
Failure loads of anchors with head type B

Series	f_{cc}	F_u [kN] for h in [mm]			F_{ul} [1)] [kN] for h in [mm]		
	MPa	50	150	450	50	150	450
I	32.6	25.8	150.0	1087	25.2	146.3	1060
II	29.7	(40.2)	161.7	1108	(41.1)	165.2	1132
III	33.2	35.6	131.4	1162	34.4	127.0	1123
IV	29.3	27.2	133.3	937.2	28.0	137.1	964.0
		26.1	181.7		26.8	186.9	
V	28.3	21.5	160.7	989.0	22.5	168.2	1035
		30.2	165.7		31.6	173.4	
VI	34.4	29.3	151.5	1221	27.8	143.8	1159
		33.2	167.7		31.5	159.2	
		29.6			28.1		
		35.6			33.8		
Average	31.2	29.4[2)]	160.0	1084	29.0[2)]	156.3[1)]	1079
V [%]	7.9	15.3	10.2	9.8	13.1	12.3	6.8

[1)] $F_{ul} = F_u \cdot \sqrt{31/f_{cc}}$ [2)] without result of Series II

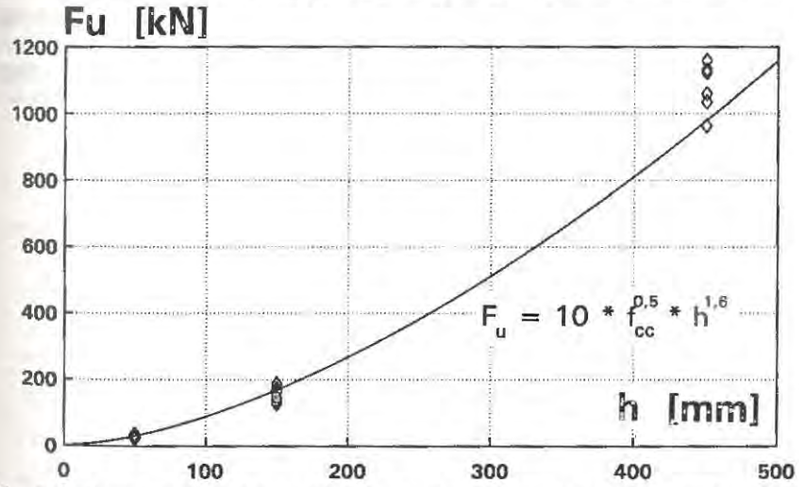

Fig. 3 Failure loads (head type B) as a function of the embedment depth

In Fig. 3 the normalized failure loads are plotted as a function of the embedment depth. The average values can be approximated by Eqn. (1). This equation is sufficiently accurate for practical purposes (compare Table 4).

$$F_u = 10 \cdot f_{cc}^{0.5} \cdot h^{1.6} \quad (1)$$

DISCUSSION OF RESULTS

In [4] the following empirical equation is proposed. It assumes the greatest possible size effect which will be obtained when applying linear fracture mechanics [5]. The formula is based on approximately 200 results of tests with headed anchors from different sources. The embedment depth was varied between d = 40 mm and d = 525 mm.

$$F_u = 15.5 \cdot f_{cc}^{0.5} \cdot h^{1.5} \quad (2)$$

In [7] another empirical equation is given, which does not take into account a size effect

$$F_h = 0.96 \cdot f_{cc}^{0.5} \cdot h^2 \, (1 + d_h/h) \quad (3)$$

According to Bazant's size effect law [8], the nominal concrete strength, $\sigma_N = F_u/A_c$, on the failure cone surface A_c is given by Eqn. (4)

$$\sigma_N = B \cdot f_t \left(1 + h/h_0 \right)^{-0.5} \quad (4)$$

where B and h_0 are empirical constants. Eqn. (4) predicts a gradual transition from a plastic solution (no size effect) for small embedment depths to a linear fracture mechanics solution (largest size effect) for large embedment depths. Assuming a diameter of the projected cone of 3h [3] the test results yield B = 0.62 and h_0 = 101 mm. In Fig. 4 the ratio $\sigma_N / (B \cdot f_t)$ is plotted as a function of the ratio h/h_0 in double logarithmic scale. It can be seen, that for h = 450 mm the test results are close to the linear fracture mechanics solution. With $f_t = 0.5 \cdot f_{cc}^{0.5}$ and $A_c = \pi \cdot (3h)^2/4$ one gets from Eqn. (4) the following failure load.

$$F_u = 2.2 \cdot f_{cc}^{0.5} \cdot h^2 (1 + h/100)^{-0.5} \quad (5)$$

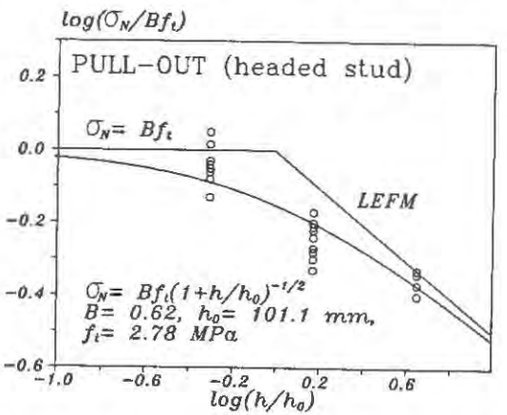

Fig. 4 Size effect of the average tensile stress over the failure cone area

In Fig. 5 the measured failure loads related to the average value for h = 50 mm are plotted as a function of the embedment depth in double-logarithmic scale. In this scale, Eqns. (1) to (3) are straight lines with different slopes and Eqn. (5) gives a slightly curved line. The figure shows, that the size effect law (Eqn. (5)) agrees rather well with the test results. While Eqn. (2) slightly overestimates, Eqn. (3) significantly underestimates the size effect.

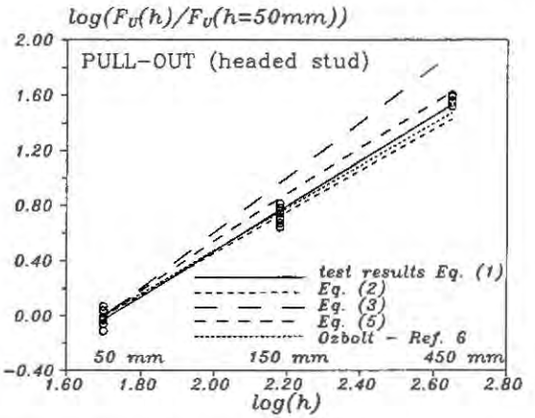

Fig. 5 Related failure loads as a function of the embedment depth

In Table 4 the test results are compared with the predictions according to Eqns. (1) to (3) and (5). As expected, Eqn. (1) gives the best representation of the test results. Eqn. (3) agrees worst with the test results, because the average value of the ratio measured failure load to calculated value decreases significantly with increasing embedment depth and the coefficient of variation of the ratio $F_{u,test}/F_{u,calculated}$ is about 3 times larger than the coefficient of variation of the measured failure loads. Equation (2) is conservative for h = 450 mm.

TABLE 4
Comparison of test results with various predictions

h	average failure load [1]	F_u [kN] predicted according to Eqn. [1]				$F_{u,test} / F_{u,calculated}$ according to Eqn.			
mm	kN	(1)	(2)	(3)	(5)	(1)	(2)	(3)	(5)
50	29.0	29.1	30.5	16.8	25.0	1.00	0.95	1.73	1.16
150	156.3	168.8	158.5	146.6	147.3	0.93	0.99	1.07	0.90
450	1079	979	824	1295	1058	1.10	1.31	0.83	1.20
[1] f_{cc} = 31 MPa					$\bar{x}$	1.0	1.05	1.27	1.03
					V [%]	12.9	17.7	32.9	16.0

In an earlier study [5] headed anchors (h = 130, 260 and 520 mm) were embedded in one large concrete block (d = 600 mm) and loaded in tension. Failure occured by pulling out a concrete cone. In Fig. 6 the failure loads related to the value for h = 130 mm are plotted as a function of the embedment depth in double logarithmic scale. The increase in failure load is almost correctly predicted by Eqn. (1), slightly underestimated by Eqn. (2) and significantly overestimated by Eqn. (3). It should be mentioned that these tests have been criticized because of the too small member depth. However, in the light of the present results, this criticism seems not to be justified.

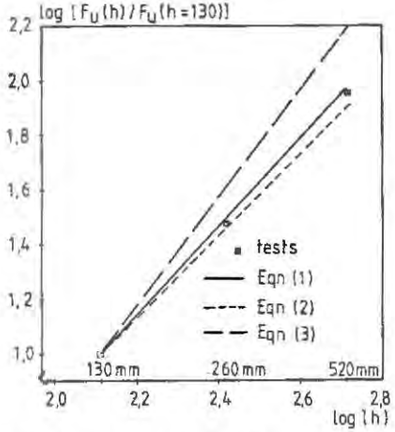

Fig. 6 Related failure loads as a function of the embedment depth, tests according to [5]

In [6], [9] a non-linear finite element simulation of the present tests was performed. While in [6] the investigation was based on the non-local microplane model [10], in [9] a new thermodynamical model was applied. Both material models take non-linear fracture mechanics into account. The results of the two studies compare very favourably. The results of [6] are also plotted in Fig. 5. It can be seen, that they agree quite well with the experimental results.

The size effect might be influenced by the concrete mix. Therefore, similar tests as described here are needed with a variation of the concrete mix.

CONCLUSIONS

Based on the present study, the following conclusions can be drawn

(1) The concrete cone failure load shows a significant size effect which is rather close to the solution according to linear fracture mechanics. This can be explained by the high strain gradient and the relatively small fracture process zone [5, 6].

(2) The size effect should be taken into account in the design of fastenings, because otherwise the strength of fastenings with a small embedment depth is overestimated and those with a large embedment depth is underestimated.

REFERENCES

1. Bouška, P., Červenka, V., Experimental Investigation of Anchoring Bolts, Research report, Klokner Institute, Technical University Prague, 1991.

2. Bouška, P., Experimental Investigation of Anchoring Bolts in 1991, Research report, Klokner Institute, Technical University Prague, 1991.

3. Rehm, G., Eligehausen, R., Mallée, R., Befestigungstechnik, Betonkalender 1988, part 2, pp. 569 - 663, Ernst & Sohn, Berlin, 1988.

4. Eligehausen, R, Ick, U., Mallée, R., Reuter, M., Schimmelpfennig and Schmal: Tragverhalten von Kopfbolzenverankerungen bei Zugbeanspruchung, Bauingenieur, in press.

5. Eligehausen, R., Sawade, G., A fracture mechanics based description of the pull-out behaviour of headed studs embedded in concrete, Fracture Mechanics of Concrete Structures, Report of RILEM TC-90-FMA, Ed. L. Elfgren, Chapman and Hall, London New York, 1989, pp. 281 - 299.

6. Ožbolt, I., Round-Robin Analysis Of Anchor Bolts. Report to RILEM-TC-90-FMA, March 1991.

7. ACI 349-85, Code Requirements for Nuclear Safety Related Concrete Structures, Appendix B, Steel Embedments, American Concrete Institute, Detroit, 1985.

8. Bažant, Z. P., Size effect in Blunt Fracture: Concrete, Rock, Metal. Journal of Engineering Mechanics ASCE, 1984, 110 (4), pp. 518 - 535.

9. Sawade, G. and Eligehausen, R., Analysis of Headed Steel Anchors Embedded in Concrete Using a Non-linear Fracture Model, Proceedings, First International Conference on Fracture Mechanics of Concrete Structures, Breckenridge, June 1992.

10. Bažant, Z. P. and Ožbolt, I., Non-local microplane model for fracture, damage and size effect in structures. Journal of Engineering, Mechanics, ASCE, 1990, 116 (11), pp. 2485 - 2504.

11. RILEM draft recommendation: Determination of the fracture energy of three point bend tests on notched beams. Materials and Constructions, July - August 1985, 106, pp. 285 - 296.

Invited Paper

DUCTILE FRACTURE IN CEMENTITIOUS MATERIALS?

VICTOR C. LI and T. HASHIDA
Advanced Civil Engineering Materials Research Laboratory,
Department of Civil and Environmental Engineering,
University of Michigan, Ann Arbor, MI 48109-2125

ABSTRACT

This paper describes a newly discovered phenomenon -- ductile fracture in cementitious materials. This behavior is made possible by a pseudo strain-hardening process generated by the stress transfer capability of properly designed fiber reinforcements in the cementitious composite. The ductile fracture phenomenon has been recorded in a double cantilever beam (DCB) fracture specimen fabricated from a specially designed cement reinforced with polyethylene fibers. The off-crack-plane microcracked zone is found to be shaped like an onion with its base located near the crack tip. In the present set of experiments, this inelastic zone spreads to the edge of the specimen, covering an area of more than 500 cm^2 in the large size DCBs. Fracture energy consumed in the fiber bridging fracture process zone, and in the inelastically deformed material off the crack plane, are determined for various specimen sizes using the J-based method. The results show that the off-crack-plane energy consumption can be as large as, and when steady state is achieved likely to be even larger than, the fiber pull-out energy consumed on the main crack plane.

INTRODUCTION

The two types of fracture that have been observed in cementitious materials are brittle and quasi-brittle. Brittle fracture can be observed in hardened cement paste material. It is characterized by a very small microcrack zone at the crack tip (Figure 1a) typically of sub-millimeter scale, low fracture energy of the order of 0.01 kJ/m^2, and a linear load versus load point displacement curve from a fracture test. Quasi-brittle fracture can be observed in concrete and in most fiber reinforced cement or concrete (FRC). It is characterized by a bridging process zone in addition to the small microcrack zone at the crack tip (Figure 1b). The bridging action provides additional energy absorption through aggregate and/or ligament bridging in concrete, and through fiber bridging in FRC, in the wake of the crack front. For quasi-brittle materials, the fracture energy extends a large range, from 0.1 kJ/m^2 in concrete to several kJ/m^2 in the case of FRC. Correspondingly, the process zone size extends from

mm scale to cm scale. The load versus load line displacement curve from a fracture test may involve a small non-linear region near the peak load with a significant post-peak tension-softening behavior. Research in quasi-brittle materials in the last decade has been extensive (see, e.g. [1,2] for a recent collection of papers on the subject).

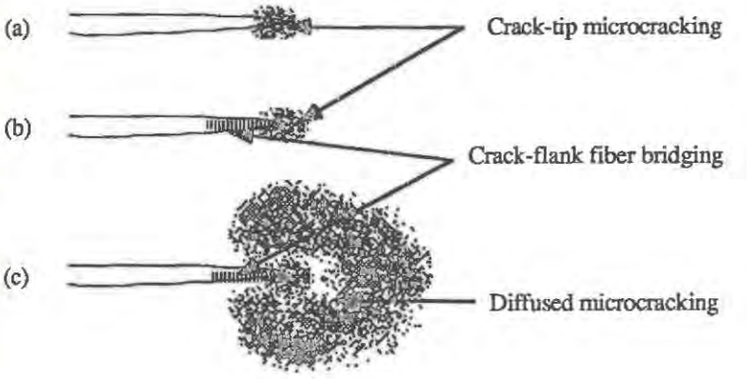

Figure 1. Fracture process zone in (a) Brittle cement, (b) Quasi-brittle concrete and FRC, and (c) Ductile SHCC.

This paper describes a new type of fracture in cementitious material which has heretofore not been observed. It may be labelled 'ductile fracture' because it involves extensive off-crack-plane inelastic energy absorption, as shown schematically in Figure 1c. However, unlike ductile metals, the present strain-hardening cementitious composite (SHCC) also involves extensive energy absorption on the crack plane. The total energy absorption level and the mechanisms involved place the SHCC in a separate class of materials in comparison to ordinary quasi-brittle fiber reinforced concrete. The load versus load line displacement curve from a fracture test such as that of the DCB is also expected to deviate from that of a quasi-brittle material.

This brief paper attempts to achieve two objectives: 1) to demonstrate the concept of ductile fracture in cementitious material using an SHCC designed, fabricated and tested at the ACE-MRL at the University of Michigan, and 2) to provide a measure of the relative magnitude of energy absorption via the in-plane fiber bridging mechanism, and the off-plane strain-hardening mechanism. Greater details and further experimental results, can be found in a companion paper [3].

PSEUDO STRAIN-HARDENING AND DUCTILE FRACTURE

All brittle materials may be made to exhibit pseudo strain-hardening, provided proper fiber reinforcement is introduced to transfer the stress away from a matrix crack plane. Pseudo strain-hardening has been demonstrated in a number of brittle matrix materials, including ceramics reinforced with continuous fibers (e.g. [4]) and in cements reinforced with continuous fibers (e.g. [5,6]) or with discontinuous randomly distributed fibers (e.g. [7,8]).

The conditions under which pseudo strain-hardening can occur in the latter material have recently been worked out [9,10] based on micromechanics principles. An SHCC designed in this manner using polyethylene fiber exhibits a strain-hardening behavior with strain capacity more than 100 times that of the matrix alone. While the material strength is low, it serves as an excellent model material for studying the multiple cracking and ductile fracture processes as the micro-crack widths are large enough to be visible without any sophisticated imaging needs. This means that real-time inelastic deformation can be followed and captured on an ordinary camera.

A material which strain-hardens implies that under strain-concentration, such as that at the tip of a notch, stress redistribution will occur so that localized fracture will be delayed. This suggests that in a SHCC, an expanded zone of matrix cracking must surround the crack tip prior to crack propagation. This expanded zone is created by the stress transfer capability of the reinforcing fibers, in a manner similar to the multiple cracking process in a uniaxial tensile specimen. Of course, because the stress field surrounding the notch tip is different from the uniform stress field in a uniaxial tensile specimen, the resulting crack pattern will also be different. At any rate, such an extensive volumetric cracking process must involve considerable energy absorption, and it is this off-crack-plane inelastic energy absorption which may be expected to give rise to a ductile fracture behavior.

When the crack tip strain reaches the failure strain capacity of the SHCC, stable crack propagation will occur, although the crack flanks will still be bridged by fibers, and energy absorption by fiber pull-out will take place. In a SHCC therefore, the total composite fracture energy J_c comes from two components, an off-crack-plane matrix cracking component J_m and an on-crack-plane fiber bridging component J_b.

In the following, we describe briefly an experimental program which utilizes a uniaxial tensile test to determine J_b, and a DCB to determine the total fracture energy J_c. The off-crack-plane fracture energy can then be deduced from the difference between J_c and J_b.

THE EXPERIMENTAL PROGRAM

The material selected for testing was a polyethylene fiber reinforced mortar. The constituent materials used and their mix proportions are given in Table 1. Type I Portland cement was used to form the matrix of the composite. The fiber length and diameter were 12 mm and 38 μm, respectively. The fiber volume fraction was 2 %. It has been shown that the material system selected for this study can produce a strain-hardening behavior with fiber volume fractions greater than 1 % [8, 10].

Table 1 Mix Proportions of Composite Tested

Materials	Portland Cement (Type I)	Silica Fume	Super-plasticizer	Water	Fiber
Mix Proportions (by weight)	1.0	0.20	0.03	0.27	0.02*

* Volume Fraction

The uniaxial tensile specimen and the DCB specimen, as illustrated in Figure 2, were used to determine the strain-hardening behavior of the material. DCB specimens of two different sizes were prepared to examine the effect of specimen size on the fracture behavior; the specimen width, W was 127 mm for the small beam, and 310 mm for the large beam. Two notched uniaxial tensile specimens were also used for the fracture energy determination. The specimens were cast using Plexiglass moulds. After casting they were allowed to harden at room temperature for one day prior to demolding and then cured in water for 2 weeks before testing.

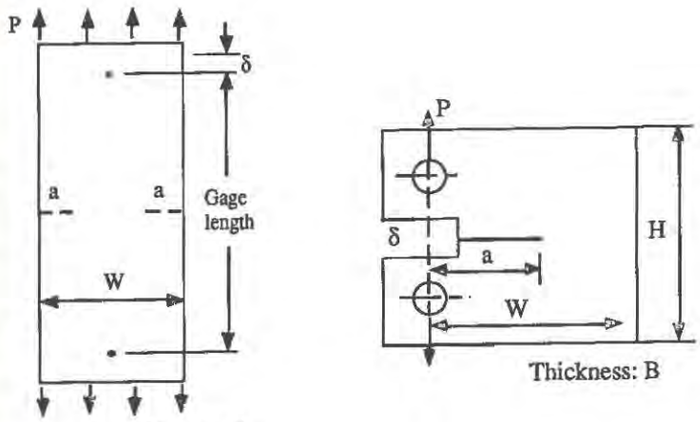

	W (mm)	B (mm)	a (mm)	No. of specimens
Unnotched	76	13	-	2
Notched	76	13	15, 20	2

	W (mm)	B (mm)	H (mm)	a (mm)	No. of specimens
Small beam	127	35	153	65, 74	2
Large beam	310	61	300	117, 148	2

Figure 2. Specimen configurations used

The uniaxial tensile tests and fracture toughness tests were conducted in a closed loop testing machine. The specimens were loaded to complete failure with a constant cross head speed; the testing time was typically 40 minutes for all tests. The load, P and load-line displacement, δ were measured using linear variable differential transducers (LVDT's). The relative displacement between the two points on the specimen surface was monitored to measure the elongation in the uniaxial tensile tests (see Figure 2). The gage length for the measurement was approximately 200 mm. The total fracture energy was determined by means of the J-based technique described in [11], and using a set of DCB specimens with different notch lengths (Figure 2). Concurrently with the tests, damage evolution on the specimen surface was recorded using a camera. To facilitate fracture observation, a white brittle paint (pure lime, CaO) was applied to the specimen surface.

RESULTS

The stress-deformation curve obtained from a uniaxial tensile test is shown in Figure 3. The designed composite exhibits a strain-hardening behavior, as predicted by the micromechanical model [8, 9, 10]. Real-time observation showed that multiple cracking occurred with many sub-parallel cracks across the specimen during strain-hardening. The averaged strain at peak stress is approximately 3.5 %. Beyond peak stress, localized crack extension occurred accompanied by fiber bridging. The fracture energy J_b due to the fiber bridging may then be computed by integrating the post-peak stress-displacement relation:

$$J_b = \frac{U}{A_{lig}} \tag{1}$$

where U is the area under the post-peak stress-crack opening curve, and A_{lig} is the net cross sectional area. Test results on the notched uniaxial specimens were also used to determine J_b. There has been no significant difference in the J_b values of the unnotched and notched specimens; 11.8 and 14.8 kJ/m^2 for the unnotched specimens, and 9.7 and 12.5 kJ/m^2 for the notched specimens. A theoretical model for bridging fracture energy [12] based on the frictional fiber pull-out mechanism predicts J_b to be 9.2 kJ/m^2 (assuming an interfacial frictional bond strength of 1.02 MPa [13], and a snubbing coefficient of 0.5 [12]). The higher value from experimental measurement may be due to the non-planar fracture behavior, even in the notched specimens. This notion is also supported by the length of the post-peak load-displacement curve being more than half the fiber length. In this preliminary study, an average of the J_b values (= 12.2 kJ/m^2) is taken as an estimate of fiber bridging fracture energy, but this should be regarded as an upper bound of the true value, in light of the discussion above.

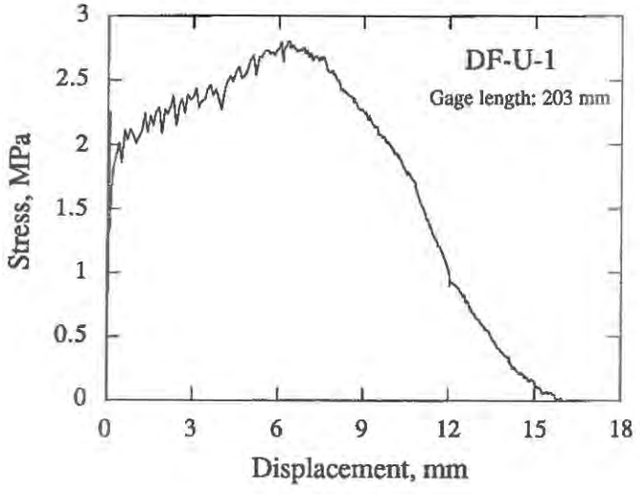

Figure 3. Stress-deformation relation

An example of load-displacement record is shown in Figure 4 for the large-sized DCB specimen. It is seen that despite the presence of the deep notch the material produces a significant strain-hardening behavior subsequent to the bend over point. Figure 5 presents the damage evolution recorded for various load-line deformation values indicated in Figure 4. It is particularly noted that an extensive microcracking zone spreads around the notch tip before the localized crack starts to grow. The microcracking zone is seen to expand close to the beam outer boundary at the peak load. The final shape of the fully developed inelastic zone appears like an onion with its base located near the notch tip. As clearly shown in Figure 5, the strain-hardening behavior is attributable primarily to the extensive off-crack-plane microcracking process.

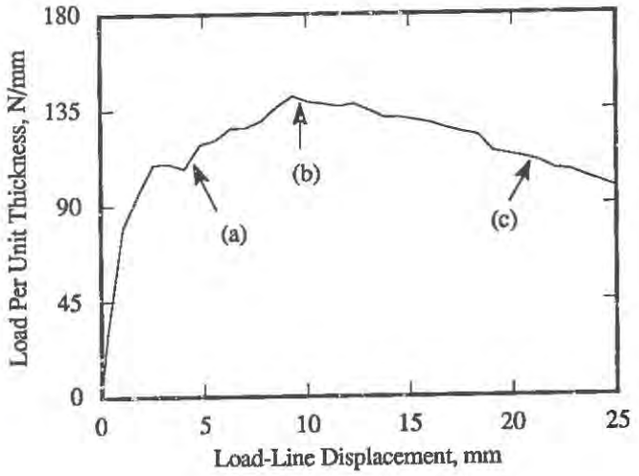

Figure 4. Load-displacement record for large DCB specimen

In the following we deduce the fracture energy contribution J_m from the off-crack-plane microcracking using the J-based technique. The total fracture energy J_c can be evaluated using the equation;

$$J_c = \frac{1}{(a_2 - a_1)} \int_0^{\delta} \left(\frac{P_1}{B_1} - \frac{P_2}{B_2} \right) d\delta = \frac{S}{a_2 - a_1} \tag{2}$$

where subscripts, 1 and 2 refer to the two different notch lengths, and S is the area between P/B-δ curves of the two specimens, as exemplified in Figure 6 for the large DCBs. For the notched uniaxial tensile specimens, the crack length a in Eqn. (2) is replaced by 2a. Figure 7 summarizes the results of the J-based tests, showing the J_c values as a function of specimen size. The ligament length is selected as a representative specimen dimension. The area of the microcracking zone observed is also indicated in the parenthesis. Based on the observation

(a)

(b)

(c)

Figure 5. Damage evolution as a function of deformation
(a) δ=4.94 mm (b) δ=9.64 mm (c) δ=21.12 mm

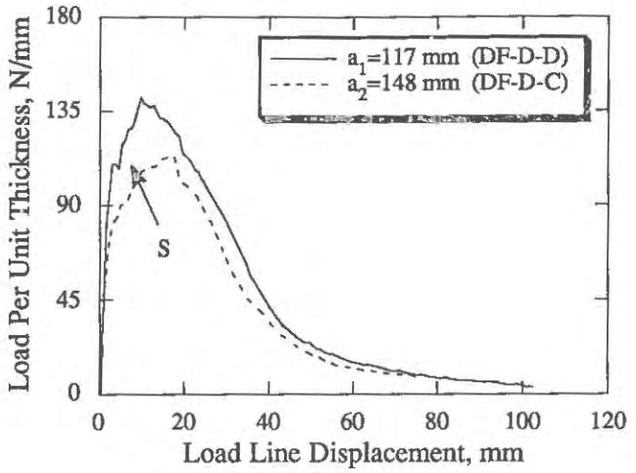

Figure 6. J-based method used to determine J_c

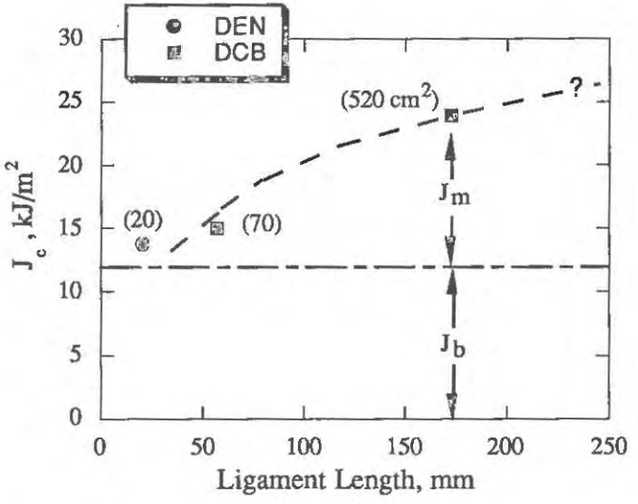

Figure 7. Summary of J_c measurements, showing the contribution of J_m and J_b. The numbers in brackets indicate the maximum size of the inelastic microcracked zone.

of the damage evolution, the J_c measured can be interpreted as a sum of the two components, J_m and J_b. Thus, the J_m may be obtained from the difference between the J_c and J_b values. As shown in Figure 7, the J_m component increases with increasing specimen size because of the enlarged microcracking zone in larger specimens. In the large DCB specimens the J_m component amounts to 50 % of the total fracture energy. It has been observed in the DCB specimens that the microcracking zone spread almost up to the dimension of the beam height. This observation suggests that no steady state crack growth has been achieved in the limited specimen sizes tested in this study. It is expected therefore that further increase of the J_m contribution may be possible under steady state condition.

CONCLUSIONS

1. It is demonstrated that cementitious materials can be made to fail in a ductile fracture mode if the material is properly reinforced with fibers so that strain-hardening occurs when loaded beyond its tensile cracking strength.

2. In such a SHCC, ductile fracture occurs by development of a microcracked inelastic zone covering an area of more than 500 cm^2 in the material and large specimens used in this study.

3. The energy absorbed in the off-crack-plane inelastic zone is of the same order of magnitude as that absorbed by fiber bridging in the crack wake. For the present study, a total fracture energy of 24 J/m^2 is measured for the large specimens. However, it should be pointed out that the onion shaped inelastic zone has reached the full height of even the large size specimens. The steady state value of off-crack-plane energy absorption and the total fracture energy may therefore be expected to be even higher. Further experimental study is needed to confirm this.

4. The ductile fracture mode of a SHCC enhances the margin of safety in a structure subjected to high strain. Strain imposition on a structure may come from ground motion induced by earthquakes, from movement of substructures, or from deformation near acute geometries such as a shear key. Even the expanding debris of a corroding re-bar imposes tensile strain on the surrounding concrete. In addition, the large energy absorption through combined on- and off-crack-plane inelastic mechanisms delays structural instability associated with fracture formation. The stress redistribution capability of a SHCC also enhances structural durability by producing fine cracks rather than large fractures when overloaded, thus reducing the amount of aggressive elements from penetrating the interior of a structure. It is suggested that further development of SHCC coupled with fundamental understanding of its failure mode can lead to improved structural safety and durability.

ACKNOWLEDGEMENTS

This work has been supported by a grant from the National Science Foundation to the Advanced Civil Engineering Materials Research Laboratory at the University of Michigan, Ann Arbor. The Program Manager at NSF is Dr. Ken P. Chong. The authors acknowledge helpful discussions with Dr. H.C. Wu and technical assistance from M. Maalej.

REFERENCES

1. Shah, S.P. (ed.), Toughening Mechanisms in Quasi-Brittle Materials, NATO ASI Series E, Vol. 195, 1991.

2. Van Mier, J.G.M, Rots, J.G. and Bakker, A. (eds.) Fracture Processes in Concrete, Rock and Ceramics. Chapman and Hall, 1991.

3. Li, V.C., Hashida, T., Maalej, M., in preparation, 1992.

4. Marshall, D.B. and Evans, A.G., Failure mechanisms in ceramic-fiber/ceramic-matrix composites, J. Am. Ceram. Soc. 1985, **68**, 225.

5. Aveston, J., Mercer, R.A. and Sillwood, J.M., Fiber reinforced cements -- scientific foundations for specifications. In Composites Standards Testing and Design, Conf. Proc. National Physical Laboratory, IPC Science and Technology Press, Guildford, UK., 93-103, 1974.

6. Krenchel, H. and Stang, H., Stable microcracking in cementitious materials. 2nd International Symposium on Brittle Matrix Composites -- BMC 2, Cedzyna, Poland, 1988.

7. Krenchel, H., New receipes and new production techniques for high performance frc-materials. To appear in High Performance Fiber Reinforced Cement Composites, eds. H. Reinhardt and A. Naaman, Chapman and Hall, 1992.

8. Li, V.C., and Wu, H.C. , Pseudo Strain-Hardening Design in Cementitious Composites. To appear in High Performance Fiber Reinforced Cement Composites, eds. H. Reinhardt and A. Naaman, Chapman and Hall, 1992.

9. Li, V.C. and Leung, C.K.Y., Theory of steady state and multiple cracking of random discontinuous fiber reinforced brittle matrix composites. Accepted for publication in ASCE J. of Engineering Mechanics, 1992.

10. Li, V.C. and Wu, H.C., Conditions for pseudo strain-hardening in fiber reinforced brittle matrix composites. Submitted for publication in Applied Mechanics Review, 1992.

11. Li, V.C., Chan, C.M., and Leung, C.K.Y., Experimental determination of the tension-softening relations for cementitious composites. Cement and Concrete Research, 1987, **17**, 441-452.

12. Li, V.C., Post-crack scaling relations for fiber reinforced cementitious composites. ASCE J. of Materials in Civil Engineering, 1992, **4**, 1, 41-57.

13. Li, V.C., Wang, Y., and Backer, S., Effect of inclining angle, bundling, and surface treatment on synthetic fiber pull-out from a cement matrix. J. Composites, 1990, **21**, 2, 132-140.

INFLUENCE OF DISORDER ON THE FRACTURE PROCESS OF MORTAR.

BREYSSE D., FOKWA D.
L.M.T., C.N.R.S., UNIV. PARIS 6
61 Avenue du Pdt Wilson, 94235 Cachan Cedex, France

ABSTRACT

The response of 210 (14 series of 15 specimens) mortar beams of 50*50*170 mm³ loaded in four points bending is analyzed. Two degrees of disorder are considered : (a) a 'material' disorder related to the intrinsic inhomogeneities of the material (sand, hydrated cement paste, ...), (b) a 'macroscopic' disorder created by the presence of cylindrical holes which cross the specimen. The diameter, number and relative position of the holes vary from one serie to another. A statistical analysis (successive linear regressions) is first performed to take into account and to eliminate the effect of several spurious parameters (exact specimen size, age of the mortar, porosity). Comparisons are made between series which show that the reduction of the carrying capacity (maximum load) can generally be correctly predicted with a simple criteria based on the 'worse located defect'. It is shown that an 'effective stress concentration factor' around a hole has to be defined which takes into account the non locality of the material behaviour. The use of a damage model through a finite element code shows little practical interest. The effect of the interactions between holes and between the two degrees of disorder (material and macroscopic) is finally discussed.

INTRODUCTION

Mortar being a composite material, the existence of inhomogeneities plays a significant role on the creation and development of the microcracks. The two main consequences of the local disorder are the localization of the degradation in volumes of limited size and the variability of the macroscopic properties.

The response of 210 (14 series of 15 specimens) mortar beams of 50*50*170 mm³ loaded in four points bending is analyzed. Two degrees of disorder are considered : (a) a 'material' disorder related to the intrinsic inhomogeneities of the material (sand, hydrated cement paste, ...), (b) a 'macroscopic' disorder created by the presence of cylindrical holes which cross the beam from the front face to the rear face (these holes have been artificially introduced by the presence of steel rods crossing the formwork).

Some series (Figure 1a) contain a number of holes distributed on a regular mesh, designed such as to separate the effects of : (a) size of the holes (1 mm, 2 mm, 3mm), (b) number of the holes, (c) total area of the holes. Other series contain only few holes such as to study the effect of 'bad located' defect (Figure 1b), or randomly distributed holes (Figure 1c),

to study the effect of hazard. Finally a serie contains no hole. It serves as a reference, where only a 'material disorder' is present.

The mortar is made with a Seine sand (maximal size 1 mm) and a CPJ 45 cement. Practical constraints lead us to mould the specimens in two mixes with the following ratios :
mix A : w/c = 2.29, s/c = 3.00 mix B : w/c = 2.21, s/c = 2.99

Control on 6 cylindrical specimens have shown a difference of 16 % between the compressive strength of the two series (mix A : 16.8 MPa ; mix B : 20.0 MPa).

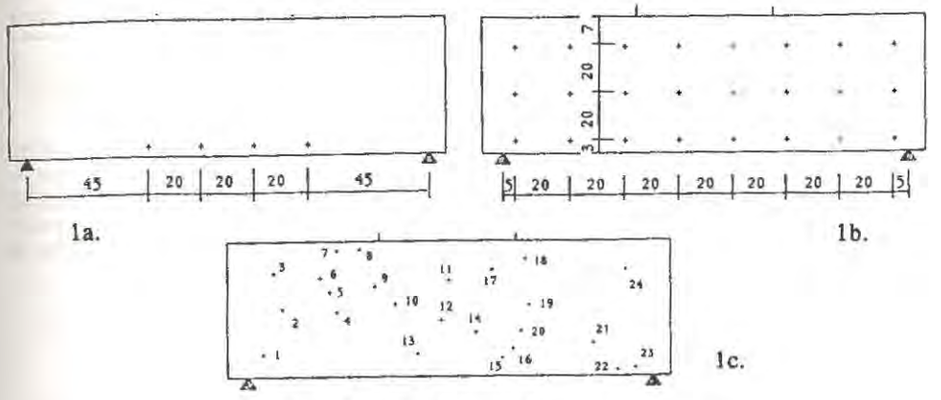

Figure 1a-c. Definition of three series.

EXPERIMENTAL RESULTS

The specimens are loaded in four point bending until failure and the load-displacement curves are systematically recorded. The deflection is measured on the median fiber, the effect of crushing of the supports being therefore eliminated. The deflection under the maximal load is around 20 microns for a load ranging [3 kN, 5 kN]. The load-deflection curve is approximately linear during the first stage (load under 2.5 or 3 kN), then a non-linearity appears and the failure is brittle. The specimen is finally splitted into two parts. Strain gauges fixed on some specimens have shown strong local non-linearities (or unloadings) when the global response remains more or less linear (Figure 2a-b).

The failure surface is approximately plane and it tends to cross some of the existing holes, but not always the same ones in a given serie. For the reference serie (without hole), the position of this surface is equally distributed in the pure bending zone between the two loads, whose abscisses are 60 mm and 110 mm (Figure 3).

The statistical results are very dispersive within each serie, the coefficient of variation (C.V. = standard deviation / average value) varying from 8.3 % to 16.7 %. This prevents a direct analysis of

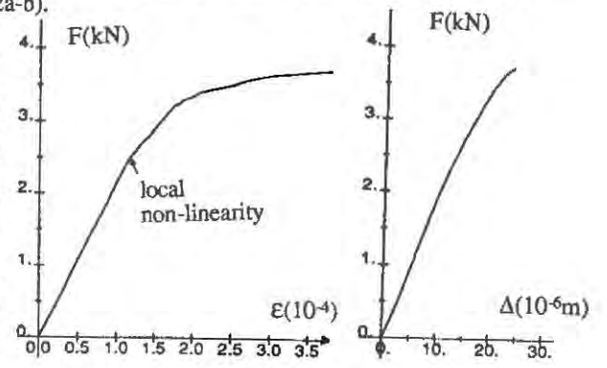

Figure 2a-b. Global and local responses.

the results, and makes necessary the reduction of the noise due to spu-rious sources. These sources are : differences between the two mixes, differences in the age of the specimen (between 100 and 132 days at the time of test), differences in the exact dimensions of the specimens (the lateral faces are directly given by the formwork and the height results from a simple trowel surfacing).

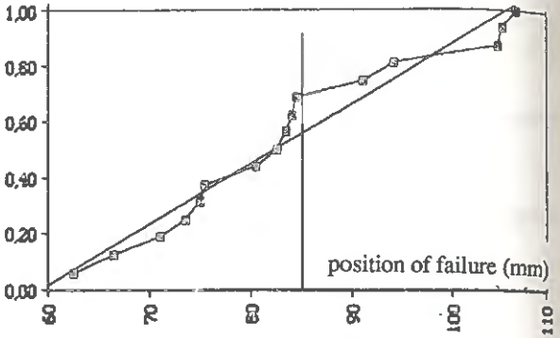

Figure 3. Cumulative probability of failure.

STATISTICAL ANALYSIS : NOISE REDUCTION

The aim is to (a) obtain significative average values for each serie, (b) increase the separability level between series. We perform several linear regressions such as to successively eliminate the deterministic bias due to the three parameters indicated above. If Fp is the value (in Newtons) of the maximal load, we obtain different corrected values :

$$Fp1 = k1 * Fp \quad (1)$$

where k1 is deduced from the compressive strengths measured for the two mixes,

$$Fp2 = Fp1 + 16.83\ (age_{ref} - age) \quad (2)$$

and

$$Fp3 = Fp2 + 4.282\ (W_{ref} - W) \quad (3)$$

where age_{ref} and W_{ref} are reference values and where age and W are the specimen characteristics. These linear corrections are justified by correlations similar to that presented on Figure 4 and they lead to final corrected values Fp3, where the effects of three spurious factors have been eliminated.

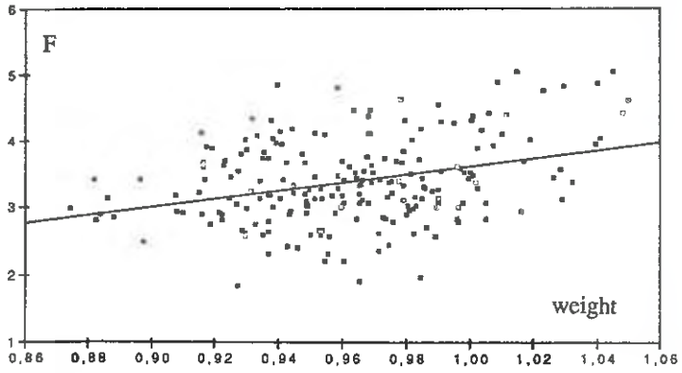

Figure 4. Correlation between the weight W (in kg) and the maximum load F (in kN).

The Table 1 summarizes the results for the the reference serie (P) and three series R1, R2 and R3 containing respectively 75 holes of 1 mm of diameter, 24 holes of 2 mm and 10 holes of three mm, the total area of the holes remaining quite the same for the three series. Extensive results are available in [1].

TABLE 1.
Direct and corrected results for the failure load.

serie	Fp (N) average	C.V. (%)	Fp3 (N) average	C.V. (%)
P	3768	12.53	4410	7.54
R1	4370	13.64	3829	11.74
R2	2939	16.21	3401	14.96
R3	3219	9.24	3063	7.58

The two aims of the statistical treatment are reached : the separability between the series is effective and the internal variance is reduced in each serie (even if it remains a significant variance). It is for instance possible, assuming a gaussian distribution of the maximum loads for each serie, to compute the probability for one specimen randomly drawn one given serie (Ri) to have a strength higher than one specimen issued from any other serie (Rj). These results are summarized in Table 2.

TABLE 2.
Level of separability between series.

i	j	p (FP3(Ri) > Fp3(Rj)
1	2	0.735
1	3	0.925
2	3	0.726

EFFECTS OF DISORDER. INTERACTIONS.

The comparisons between series with few holes (see [1] for further details) have shown that the effect of interaction between the holes is not very important. The minimum distance between two holes of diameter 2 mm is 5 mm and Fond [1] has computed that under uniaxial tension, the stress concentration factor k_t is in this case 2.93 instead of 3.00 for a single hole in an infinite medium. With the same tool [2], issued from previous works [3, 4], it has been shown that the interaction between a hole and a side leads to a value of 3.25 of the stress concentration factor k_t . These values are two important to explain why the reduction of the carrying capacity between the reference serie and any other serie never exceeds 21 %. It is then clear that the failure of the specimen does not follow directly a local failure (as it is seen on figure 2) and that a brittle approach can not be correct. An other possibility is to consider that a wholly local stress concentration factor has no meaning and that it has to be replaced by a 'averaged' stress concentration factor. This average has to be made on a representative volume of material. If we, for instance, consider the variation of k_t on a segment between the lower face of the specimen and the nearest hole (the center of the hole being distant 3 mm), it gives an average value of 1.416 which would cause a decrease of 29 % of the carrying capacity. An average computed both on this segment and on a perpendicular one would certainly be better, but this result is sufficient to confirm our reasoning and the idea of 'non-locality' of the criteria.

ANALYTICAL MODELS

Both a deterministic non-local scalar damage model [5,6] and a probabilistic local damage model [7] have been used to simulate the non-linear response of the specimens for three series.

The quantitative (normalized, the loads being divided by the strength of the reference serie) results are presented on Table 3. The accuracy of the computations is very dependent on the quality of the mesh around the holes. A two coarse mesh gives approximated values of the stresses/strains in these areas and if the spatial development of the the damage process is correctly described (figure 5), the quantitative results are not completely satisfactory.

TABLE 3. Experimental and computed results for three series.

serie	experimental value	deterministic damage model	probabilistic damage model
P (reference)	1.000	1.000	1.000
U (4 holes, see fig. 1a)	0.840	0.914	0.949
R2 (24 holes, see fig. 1b)	0.771	0.893	0.966

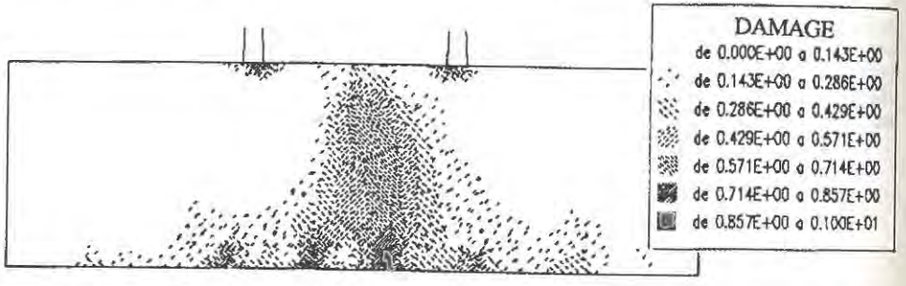

Figure 5. Pattern of damage (probabilistic model) for a specimen with four holes (serie 'U').

As we have shown the low influence of the interactions, it is possible to analyze the predictive capacity of a simple model, based on a 'strength of materials' ('s.o.m.') approach. The uniaxial bending stress near a hole can be written :

$$\sigma(M) = \sigma_{réf} * k_1(M) * k_2 * k_3(M) \qquad (4)$$

where $\sigma_{réf}$ is the maximum value of the uniaxial stress in the reference specimen and $k_1(M)$ is a scalar whose value depends only on the position of M and on the decrease of inertia due to the presence of a hole in the cross-section containing M. k_2 takes into account the non-local effect of the stress-concentration around the hole and $k_3(M)$ measures the influence of the interactions. These two last parameters are unknown.

We can plot (figure 6) the 's.o.m.' reduction (i.e. $1/k_1(M)$) against the effective experimental reduction (average value of a serie divided by the value of the reference serie) for each serie. We then obtain an average value for the product $k_2 * k_3(M)$ which can be estimated to 0.94. If we assume that the very simple model for $k_1(M)$ is sufficient, we see once more that the effect of the stress concentration around the hole is very limited (here to 6 % if $k_3(M)$ is taken unity).

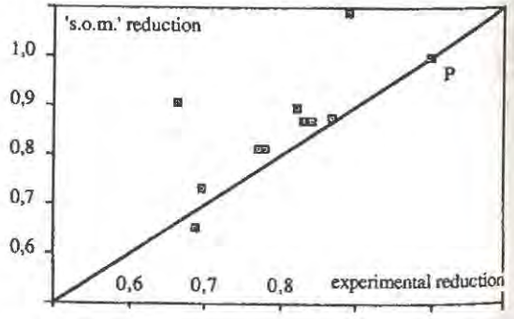

Figure 6. Prediction of the strength with a simple model.

In reality, the results are a little more complex. The predictions of this very simple model are very good, excepted for two series. One of these serie (called 'A2') being that presented on fig. 1c. We studied three series with the same number of holes (24) of the same diameter (2 mm), the only change being their position (regular for one serie, randomly distributed for the two others). Big differences appear between these series (up to 20 % on the strength), which show that the knowledge of parameters like the size and the number of the defects is unsufficient to predict the response of the specimen. They suffice only when the number of defects is great enough to consider then as equally diluted within the specimen.

The same considerations can be done for the 'material disorder'. Its knowledge is directly impossible and it can only be studied through its effects on the macroscopic response (e.g. the variability of the response within a given serie). For instance, we have found that the greater the number of holes, the greater the variability (the five series whose C.V. exceeds 11 %) are those which contains 24 holes or more. It is clear that this parameter is a source of disorder, but it is unclear for the moment if this influence is only due to working up problems (segregation increased when many rods cross the moulds) or to more fundamental reasons.

CONCLUSION

The response of 210 mortar beams has been analyzed. The influence of the macroscopic disorder has been studied after a previous statistical treatment which eliminated the influence of spurious parameters. The presence of the holes affects the strength of the specimen at a degree which can be explained only if an averaged 'non local' stress-concentration factor is considered. The failure can then be predicted quite accurately with a simple model based on strength of materials assumptions. The use of numerical damage model makes possible the prediction of the failure patterns. Finally, we have studied the possibility of interaction between the two levels of disorder (microscopic and macroscopic) and we we have shown that the material disorder (microscopic level) does not influences the mean strengths but only the variability.

REFERENCES

[1] Breysse D. et al, 'Approche expérimentale et numérique pour la prise en compte d'un désordre initial', Rapport ATP Matériaux Hétérogènes, CNRS, LMT, 1992 (in french).
[2] Fond C., Berthaud Y., "Interactions entre défauts dans une matrice élastique.", GRECO Géomatériaux, Aussois, France, 1991 (in french).
[3] Kachanov M., "Elastic solids with many cracks - asimple analysis", Int. J. Solids and Structures, V. 23, n. 1, pp. 23-43, 1987.
[4] Benveniste Y. et al, "On interacting cracks and complex configurations in linear elastic media.", Department of Civil Engineering, Rensselaer Institute, Troy, New York, USA (may1988).
[5] Mazars J, "Application de la Mécanique de l'Endommagement au comportement non linéaire et à la rupture du béton de structure.", Thèse d'Etat, LMT Cachan, 1984 (in french).
[6] Saouridis C., " Identification et numérisation objectives des comportements adoucissants : une approche multi-échelle de l'endommagement du béton", Univ. Thesis, LMT Cachan, 1988 (in french).
[7] Breysse D.,"Probabilistic formulation of damage evolution law of cementitious composites.", J. Eng. Mech. ASCE, 116, n 7, pp. 1389-1410, 1990.

DOWEL ACTION: EXPERIMENTAL ANALYSIS OF LOCAL DAMAGE

MARCO DI PRISCO and PIETRO G. GAMBAROVA
Department of Structural Engineering
MIlan University of Technology, Milan, Italy 20133

ABSTRACT

Crack formation and propagation and damage accumulation along and close to the shear plane in a R.C. specimen subjected to a dowel force are investigated within a comprehensive research project on Dowel Action. Two situations, with the dowel pushing against either the concrete core or cover, are analysed using the moiré technique in the former case, instrumented stirrups (for the study of tension stiffening) in the latter case and LVD Transducers in both cases. The results, which regard damage accumulation in the concrete mass, as well as in the reinforcement and at the interface, may be instrumental in the validation of recently proposed approaches based on non-local damage theories.

INTRODUCTION AND NATURE OF PROBLEM

The modelisation of R.C. local behavior is still a challenging problem, since concentrated loads, geometric discontinuities and steel-concrete interaction make the local stress and strain field highly nonlinear, due to damage accumulation caused either by concrete crushing or microcracking.

Only recently, a comprehensive theoretical approach has been developed for aggregate-type materials, within the so-called "Continuum Damage Mechanichs" [1,2]. In this way, the energy dissipation due to microcracking can be modeled efficiently, so much so that a few successful applications to local problems have been carried out recently (see for istance [6]), by implementing existing F.E. codes with damage models.

Because of the considerable strain softening of aggregate-type materials, F.E. analysis of local problems in R.C. is highly mesh-dependent and the "local" models are of limited validity, since mesh size cannot be smaller than a certain "characteristic length" below which the concept of "material" no longer holds. To overcome this problem, "nonlocal" models have been developed recently. These models, which are based on different assumptions and theories (denial of the concept of "local internal force" [3,4], introduction of the strain gradient in the constitutive laws, Cosserat's theory [5]), turn out to be quite complex, though very promising [6]; consequently, an adequate amount of comprehensive, detailed and dedicated test data is necessary, in order to allow a better formulation of the models through best-fitting techniques, and to pinpoint the different capabilities

of the models in the description of local benchmark problems. To this end, data on concrete displacements, strains and microcracking, as well as on steel plastic deformations associated with Dowel Action (Fig.1) are here presented: 6 block-type R.C. specimens (Fig.2), simulating both the "strong" mechanism of Dowel Action (Fig.2a) and the "weak" mechanism (Fig.2b), were tested within a comprehensive research project on Dowel Action (60 specimens tested so far [7,10]), which is a very efficient shear transfer mechanism, characterized by the predominant role of concrete and steel local behavior.

DOWEL BAR PUSHING AGAINST CONCRETE CORE

The tests were carried out by applying a monotonically increasing displacement to the dowel section flush with the shear plane (Section 1, Fig.2a); the maximum value of the displacement was limited to 0.25 d_b and was reached in 20-65 steps. The average displacement rate was 12 μm/min for $V < 2/3V_u$ and 7 μm/min up to the end of each test (V_u was evaluated according to the well-known Dulacska's equation). A simple but efficient and stiff mechanical loading machine was used [7]. Both the dynamometer and the LVD transducers were connected to a data-acquisition unit, which was controlled by a HP Personal Computer.

The displacements of the dowel bar were monitored by means of a set of up to 14 millesimal transducers (spacing 13 mm, Fig.3a), while 12 transducers were used to monitor the displacements within the concrete mass. Special plastic ducts were embedded in the concrete to allow the LVDT stems to measure the displacements at selected locations. The ducts were glued either to the dowel surface or to special bushings held in position (prior to casting) by thin aluminium strips (Fig.3b).

The vertical displacements along the shear plane, underneath the dowel, were measured by means of moiré interferometry: a 40 lines per mm grid was glued to the forefront of the specimens, after concrete hardening (a polished plexiglass formwork guarantees perfect smoothness to specimen surfaces). Due to a slight mismatch between the "specimen" grid and the "reference" grid, a set of parallel fringes appears in the no-load situation (initial mismatch), and these fringes multiply and get distorted at increasing load level (Figs.6a,b). The fringe pattern are the contour lines of the displacement at right angles to grid alignement, once the initial mismatch is deducted. Moiré sensitivity is here of 1/80 of a mm. Microcracks and concrete crushing are clearly shown by sharp zigzags along the fringes. Of course, at high load levels, the fringes get blurred close to the dowel, due to the formation of a concrete flake (Figs.4c,d), which impairs a perfect adhesion between the two grids.

The load-displacement curves of Specimens B7, B8 and B9 are shown in Fig.4a (Δ_1 is the displacement of the loaded section, Section 1, Fig.2a): response nonlinearities arise from both concrete crushing underneath the dowel and dowel yielding, the latter playing the leading role in the plastic plateau. Dulacska, Rasmussen and -to a lesser extent- Soroushian's equations (see Refs. in [7]) provide a satisfactory estimate of ultimate capacity (Fig.4b). The size of the concrete flake, which starts to detach at 4/5 of V_{max}, is slightly dependent on bar diameter (Fig.4c).

In Fig.5 the diagrams of the displacements and curvatures of the dowel are shown, for different load levels: the latter diagrams were obtained by resorting to a highly sophisticated interpolation process applied to the displacements [7]. At increasing load level, the plasticization of the dowel affects an increasing bar length ($\chi/\chi_y > 1$, χ_y= curvature at the onset of yielding = $2\varepsilon_y/d_b$, $\varepsilon_y = f_y/E_s = 0.22\%$, with $f_y = 432$ MPa, $E_s = 200000$ MPa).

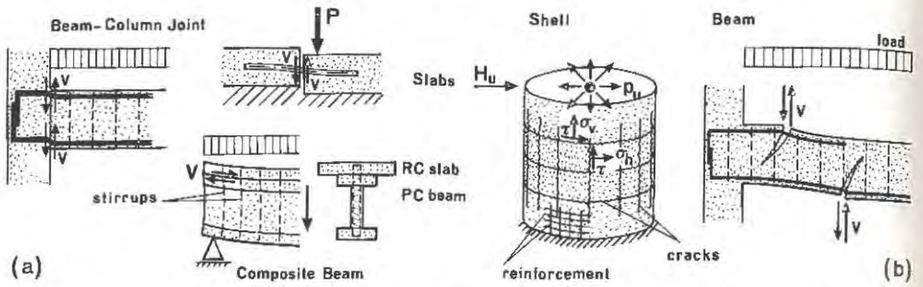

Figure 1. (a) Working loads: Dowel Action acting on built-in interfaces. (b) Ultimate loads: Dowel Action acting on stress-induced interfaces.

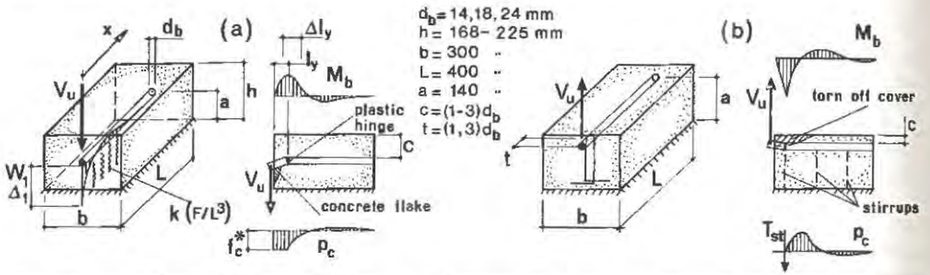

Test	d_b (mm)	c (mm)	f'_c (MPa)	V_{max} (kN)	V_u (kN)
B7	18	51	35	38.9	36.0
B8	14	51	31	30.1	29.6
B9	24	73	30	83.5	83.5

Test	d_b (mm)	c (mm)	t (mm)	f'_c (MPa)	V_{max} (kN)	V_u (kN)
D1	14	28	14	25	15.8	17.3
D5	18	36	18	24	33.5	37.5
D14	24	48	24	34	69.5	65.3

Figure 2. Relevant parameters in the study of Dowel Action and summary of specimen characteristics: Dowel Action pushing against concrete core (a) and concrete cover (b). W , Δ = displacements from theory , from tests. $V_u = V_{max}\sqrt{30/f'_c}$ – reference strength = 30 MPa.

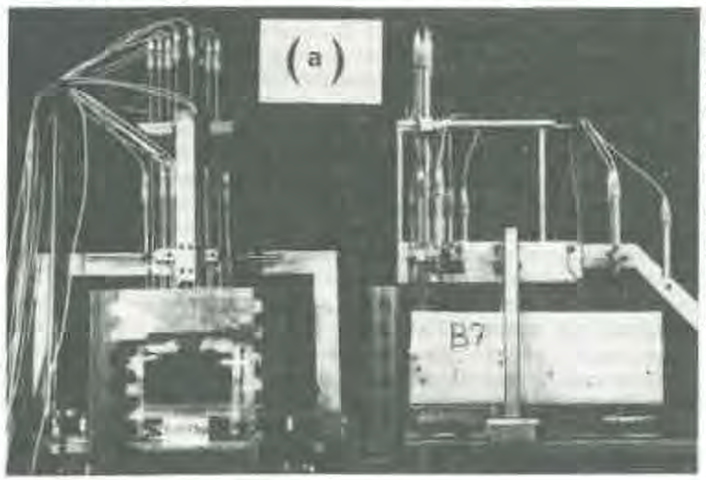

Figure 3. (a) Views of Specimen B7; (b) ducts of LVD transducers monitoring concrete and steel displacements.

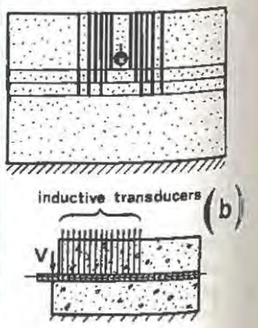

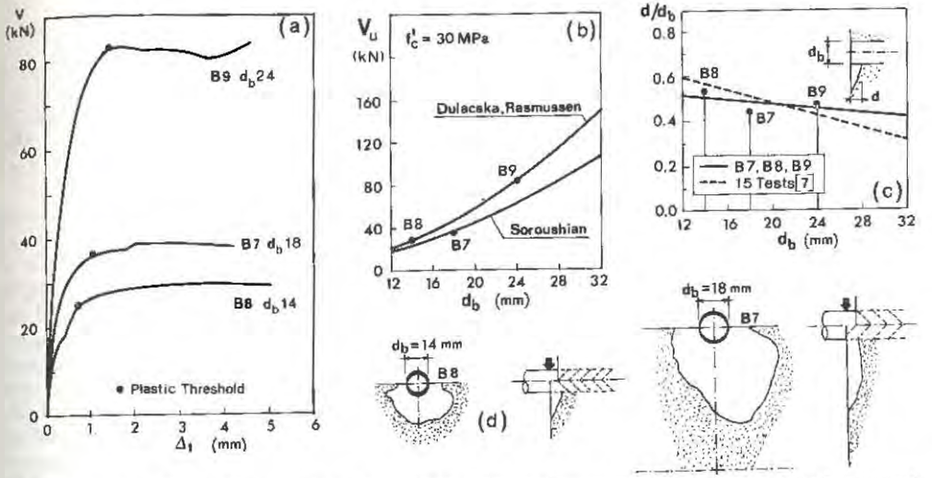

Figure 4. Dowel Action pushing against concrete core: (a) force-displacement response; (b) ultimate capacity versus bar diameter; (c,d) concrete flake.

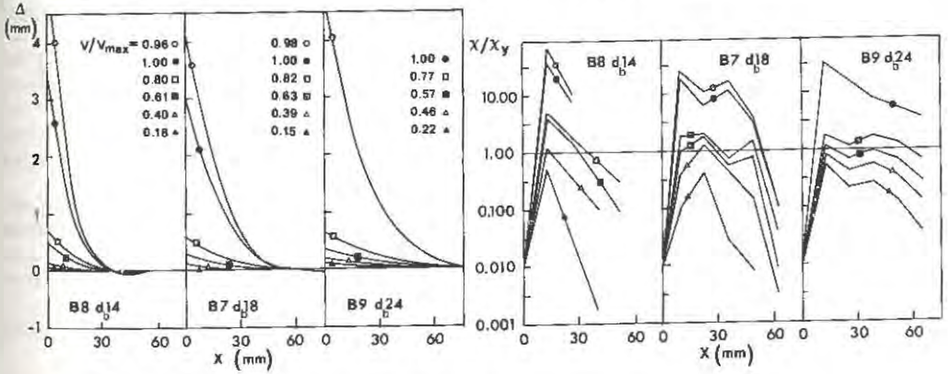

Figure 5. Displacement and curvature diagrams plotted along the dowel-bar.

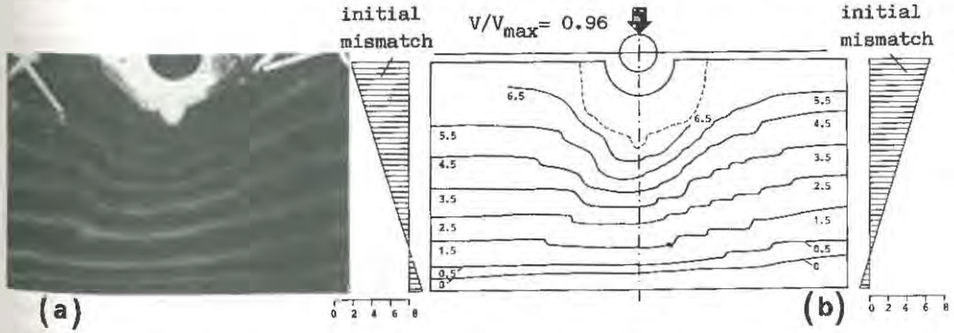

Figure 6. Specimen B8 : (a) photograph of moiré fringes and (b) contour lines of the vertical displacement, initial mismatch included.

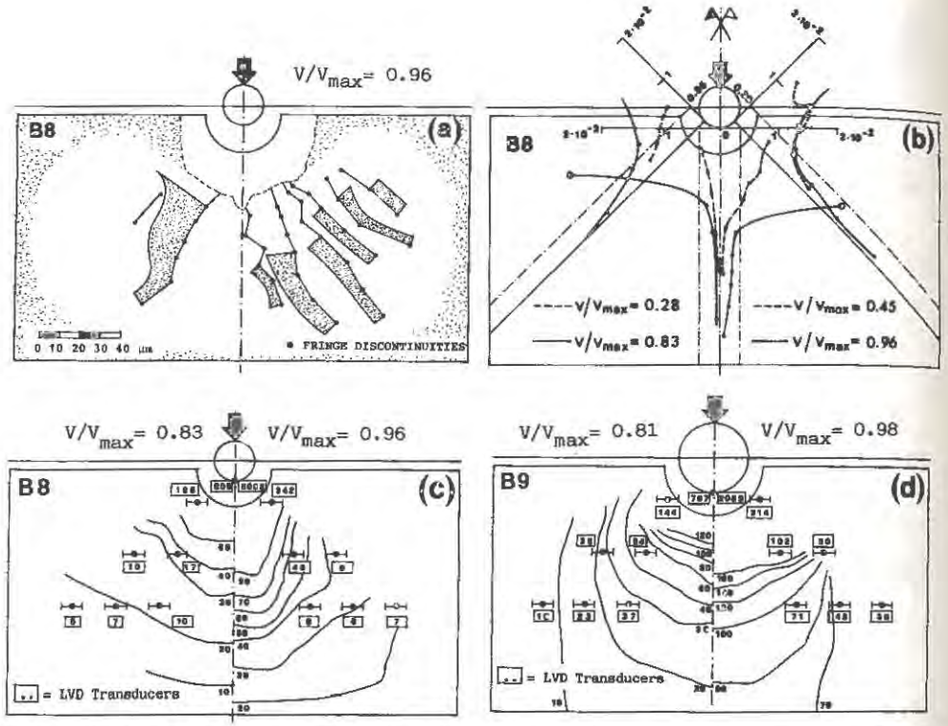

Figure 7. Specimens B8 and B9: (a) microcracks on specimen forefront and diagrams of crack opening; (b) diagrams of the normal strain in the radial direction; (c,d) contour lines of the vertical displacement.

The moiré fringes of Specimen B8 at 96% of peak load are shown in Figs. 6a,b. The microcracks on specimen forefront (Fig.7a) can be visualized by connecting the discontinuity points ("zizgzag" points) along the fringe patterns. The diagrams in Fig.7a refer to the vertical component of crack opening. In Fig.7b the diagrams of the normal strain in the radial direction are presented, while the contour lines of the vertical displacement, for B8,B9 specimens, are shown in Figs.7c,d. The numbers in squares refer to LVDT-detected displacements, in the points shown in Fig.3b where the displacements are certainly smaller than on the forefront, since these points are 10 to 25 mm behind the shear plane. Fig.7e shows how the strains were evaluated. The grid size is 140x80 mm.

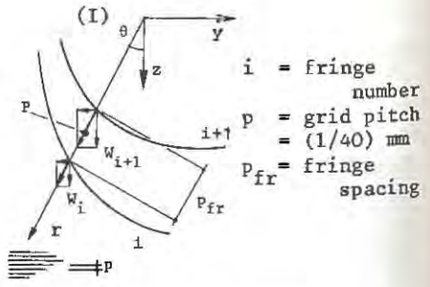

Figure 7e. (I) Sketch of the contour lines; (II) definition of the radial strain. The strain field is assumed to be merely radial, ε_r.

DOWEL BAR PUSHING AGAINST CONCRETE COVER

As in previous tests, a monotonically increasing displacement was applied to the front section of the bar (Fig.2b, average displacement rate 8 μm/min). The displacements were still measured with LVD transducers, but in Specimen D14 the first stirrup was instrumented with 4 electric strain gages (Fig. 10c), to study bond-induced tension-stiffening effects.

The weak mechanism of Dowel Action is by far more complex than the strong mechanism, since the failure mode is strongly related to geometry (concrete cover and bar free interspace) and to stirrup-dowel interaction. As well known, the closer the first stirrup is to the shear plane, the more efficient the Dowel Action is, as shown in Figs.8a,d. Only in Specimen D14 the first stirrup (d_{st}= 8 mm, 2 legs) yields before the bar, since the latter has a great intrinsic stiffness (d_b= 24 mm). Such behavior is shown by the diagrams in Fig.8b, where there are no common points, unlike Specimens D1 and D5 (d_{st}= 6 mm, mostly elastic behavior of the stirrups). Due to the early yielding of the stirrup in Specimen D14, the plasticized length of the bar is considerable at high load levels (Fig.8c).

As shown in Fig.9, tension stiffening effects on the first stirrup are quite remarkable far from the dowel (gages 3 and 4), because of limited or nil concrete damage, while the opposite is true close to the dowel (gages 1 and 2), where concrete is micro- and macrocracked, and -in the end- the cover is torn off (Fig.10a). The very complex resistant mechanism can be reduced to a simple (albeit quite rough) scheme (Fig.10b), where k_b , k_{st} and k_m stand for the stiffnesses of the bar, stirrup and thin mortar layer between the bar and the loop of the stirrup. Assuming a linear distribution for the strains in the stirrup (Fig.10d), the strains and stiffness of the mortar layer were evaluated, and also the overall stiffness of the stirrup and its force-displacement response (Fig.10e).

Considering the dowel as an elasto-plastic beam resting on a nonlinear elastic subgrade (with the subgrade modulus suggested in [9]) and introducing also the non linear response of the stirrup, the diagrams of Fig.11 were obtained by solving the problem with a F.E. code, and the fitting of both displacements and curvatures turned out to be quite satisfactory (Figs. 11a,b), while the subgrade response seems reasonable (Fig.11c: the peak stands for the concentrated force exerted by the stirrup).

CONCLUDING REMARKS

Concrete has been ad always will be plagued with poor tensile strength and ductility, which means that fracture is the major problem in R.C. structures, being either a nuisance or a virtue, depending on the different points of view.

It is a nuisance for durability, strength and stiffness, as well as for appearance and serviceability, but it is a virtue for adaptability to settlements and restraint redundancies, and -ironically- for theoretical and experimental research, since the more challenging the problems are, the more sophisticated and high-profile the research has to be.

With regard to research, even the more comprehensive and refined mathematical models would be of limited value, should appropriate test results be scanty or even unavailable, since fracture and damage often develop in limited zones, where high stress-and-strain gradients occur. Consequently, accurate tests for model validation are required.

Keeping this in mind, the very scope of this paper is to present a typical local problem -a dowel embedded in a concrete mass and subjected to shear- with high stress-and-strain- gradients, fracture localization and

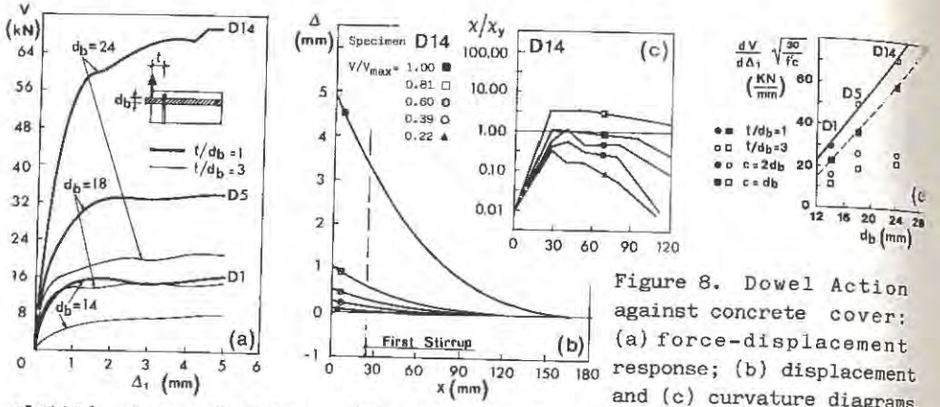

Figure 8. Dowel Action against concrete cover: (a) force-displacement response; (b) displacement and (c) curvature diagrams plotted along dowel-bar; (d) initial stiffness versus bar diameter (first stirrup ● ■close to-, ○ □far from- specimen forefront = shear plane).

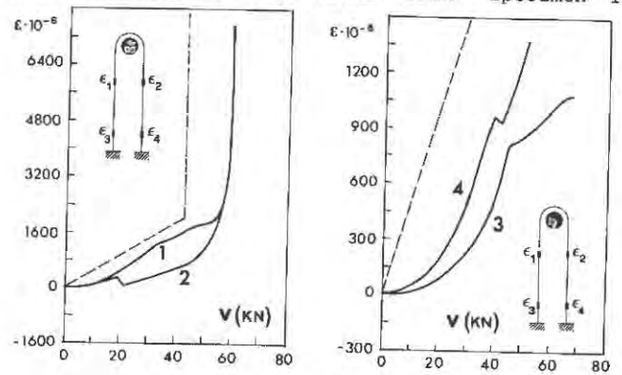

Figure 9. Diagrams of the strain versus dowel force, first stirrup, Specimen D14 (– – – – no tension stiffening = bare stirrup).

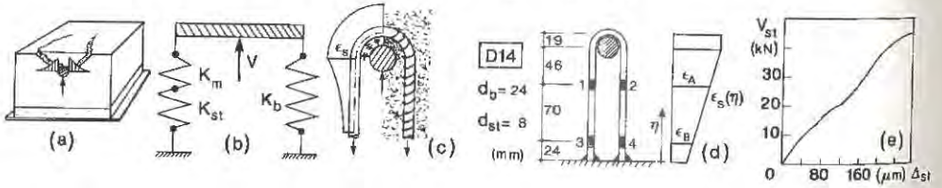

Figure 10. (a) Cover cracking; (b) dowel-stirrup interaction: simplified model; (c) actual strains and (d) assumed strains in the 1st stirrup (1,2,3, 4 electric strain gages, Specimen D14); (e) force-displacement response.

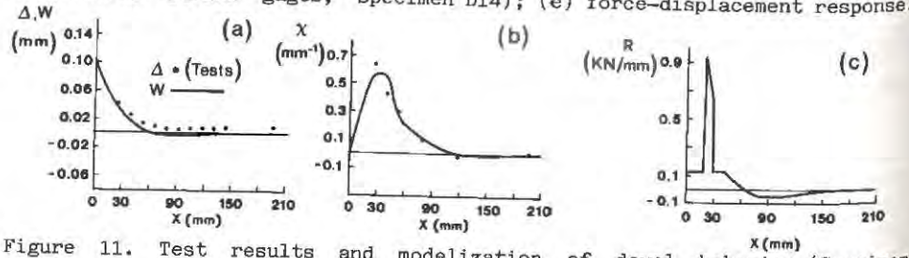

Figure 11. Test results and modelization of dowel behavior (Specimen D14, V/V_{max}= 0.22, W_1= 0.098 mm): (a) displacements; (b) curvatures and (c) bar-concrete reaction, stirrup effects included.

extended damage. The values of bar and concrete displacements, as well as those of the strains (even in the stirrups) may represent a reference mark for assessing the reliability of damage and fracture models, even more so because the measures were obtained by means of an unusual and innovative test set-up and of different experimental techniques, based on LVD transducers, moiré interferometry and electrical strain gages. In this way, a better understanding of an important shear transfer mechanism was also achieved.

ACKNOWLEDGEMENT

The authors wish to acknowledge the financial support of the Italian Ministry for University and Scientific-Technological Research (MURST, Funds 60%, 1988-1990) for this study, which was carried out within a comprehensive research project on dowel action, under the guidance of Prof. Sandro Dei Poli Director of the School for the Design of R.C. Structures.

REFERENCES

1. Chaboche, J.L., Continuum damage mechanics: present state and future trends. Nuclear Engineering and Design, Vol. 105, 1987, pp. 19-33.

2. Mazars, J. and Pijaudier-Cabot, G., Continuum damage theory: application to concrete. Journal of Engineering Mechanics, ASCE, 89(2), pp. 345-365.

3. Bazant, Z.P. and Ozbolt, J., Nonlocal microplane model: tensile and compression fractures, and triaxial damage. Proc. SCI-C 1990, Second Int. Conf. on Computer Aided Analysis and Design of Concrete Structures, Zell am See (Austria), April 1990, pp. 809-829.

4. Pijaudier-Cabot, G. and Bazant, Z.P., Nonlocal damage theory. Journal of Engineering Mechanics, ASCE, 87(10), pp. 1512-1533.

5. De Borst, R., Simulation of localisation using Cosserat theory. Proc. of SCI-C 1990, Second Int. Conf. on Computer Aided Analysis and Design of Concrete Structures, Zell am See (Austria), April 1990, pp. 21-32.

6. Pijaudier-Cabot, G., Mazars, J. and Pulikowski, J., Steel-concrete bond analysis with nonlocal continuous damage. Journal of Structural Engineering, ASCE, 91(3), pp. 862-882.

7. Dei Poli, S., Di Prisco, M. and Gambarova, P.G., Shear Response, Deformations and Subgrade Stiffness of a Dowel Bar Embedded in Concrete. ACI Structural Journal (accepted for publication, December 1991).

8. Vintzeleou, E.N. and Tassios, T.P., Mathematical models for dowel action under monotonic and cyclic conditions. Magazine of Concrete Research, Vol. 38, No. 134, March 1986, pp. 121-161.

9. Furuuchi, H. and Kakuta, Y., Deformation behavior in dowel action of reinforced bars. Transactions of the Japan Concrete Institute, Vol. 7, 1985, pp. 263-294.

10. Di Prisco, M. and Gambarova, P.G., Test results and modelling of dowel action in normal, high-strength and fiber-reinforced concrete. Proc. of the First Bi-annual Environmental Specialty Conference of the Canadian Society of Civil Engineers, Vol. 2, Hamilton (Ontario, Canada), May 1990, pp. 792-722.

EFFECT OF SIZE AND COMPRESSIVE STRENGTH ON THE FRACTURE ENERGY OF PLAIN CONCRETE

PHILIP C. PERDIKARIS AND ALBERTO ROMEO
Department of Civil Engineering
Case Western Reserve University
Cleveland, Ohio 44106, U.S.A.

ABSTRACT

A series of concrete beams were tested (3-point bending) under CMOD control using a closed-loop servo controlled testing machine. Three beam sizes, one maximum aggregate size and two compressive strengths are considered. The beams have a single edge notch a_0=0.3d (d=height) sawed at midspan. The applied CMOD rate is either kept constant or is such that the peak load is reached in approximately 10 min. Representative load-CMOD and load-LPD diagrams are presented. The vertical LPD (relative vertical displacement at midspan between the bottom and midheight of the beam) is measured using a specially designed aluminum frame attached to the specimen. The experimental results are discussed in terms of the effect of compressive strength of concrete, specimen size and applied CMOD rate on the fracture energy computed according to the RILEM method proposed by Hillerborg [1,5], Bazant's size effect law [2,3], Jenq-Shah's two-parameter model [10] and LEFM.

INTRODUCTION

The determination of fracture toughness parameters as material properties is truly challenging for several reasons. Firstly, concrete is a heterogeneous material which could behave nonlinearly at relatively low load levels. It is well known that the size of its microstructure (aggregate vs. matrix) and macrostructure (specimen size) influences the standard fracture parameters. The validation of a size effect law of broad applicability is still a controversial issue [1,3,8,10]. Furthermore, the influence of the compressive strength on the specific fracture energy of concrete has not yet been adequately investigated. The sensitivity of test results to the loading rate is not fully understood. Finally, the influence of the method for measuring the load-point-deflection (LPD) on the load-LPD diagram and subsequently on the predicted fracture energy based on the RILEM method is undoubtedly of major importance.

The presented work is part of a broader project aimed at determining the influence of the macro- and micro-structure, compressive strength of concrete, loading rate, and method of measuring the LPD on the fracture process of concrete.

TESTING PROGRAM

The testing program involves beam specimens of three (3) sizes (range 1:4) and two (2) uniaxial compressive target strengths for concrete. The beams are notched at midspan (nominal a_0/d=0.3) and tested under 3-point bending (the dead-weight of the beam is acting in the same direction as the applied load). The span-to-height ratio is kept equal to 4 for all sizes. The beam width is also constant (nominal b=127 mm). The specific beam dimensions, uniaxial compressive strength , f_c', and Young's modulus, E_{co}, measured by instrumenting 10.2 x 20.4 and 15.2 x 30.4 cm concrete cylinders, are shown in Table 1. Only one (1) maximum aggregate size (D1=6.4 mm) is considered.

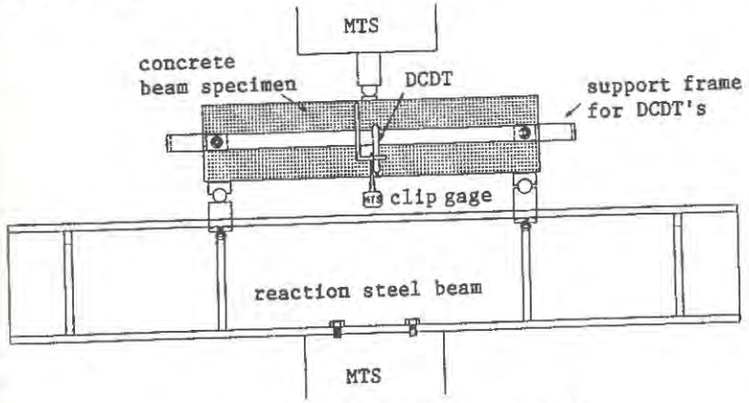

Figure 1. Testing setup (3-point bending).

A sketch of the testing setup is shown in Fig.1. To avoid undesirable constraints, the beam is simply supported on a steel pin/plate system at one end and a steel sphere/plate system at the other end; the midspan load is applied through a steel sphere/plate assembly. All bearing steel plates, proportional in size to the beam dimensions, are attached to the concrete surface with hydrostone. The vertical LPD of the beam is measured by means of two DCDT's (one on each side) attached to a specially designed aluminum frame mounted around the specimen at midheight, in an effort to minimize the spurious influence of any localized damage at the regions of applied load and support reactions. The CMOD is measured by a clip-gage attached to two knife edges at the crack mouth midway the beam width. Two loading schemes are considered: a group of specimens was tested under a constant CMOD rate (0.0001 mm/sec), and another group under a CMOD rate so that the peak load P_{peak} is reached in approximately 10 min. The former loading condition corresponds to a constant crack growth in different sized specimens, while the latter induces the same degree of damage in the same time period.

As soon as the peak load was reached, the specimen was unloaded and reloaded. In the post-peak softening region, further unloading-reloading was performed prior to the complete fracture of the beam. The complete load-CMOD, load-LPD and load-stroke responses were recorded for each specimen.

TABLE 1
Beam dimensions and concrete properties

	Nominal Specimen Size (mm)			Compr. Strength fc' (MPa)		Elastic Modulus Eco (GPa)	
	S1	S2	S3	C1	31*	C1	32.8*
Span	254	508	1016		39**		35.5**
Height	63.5	127	254	C2	80*	C2	39.5*
Width	127	127	127		71**		42.0**
Maximum aggregate size = 6.4 mm							

(*) Cylinder size = 10.2x20.4 cm

(**) Cylinder size = 15.2x30.4 cm

EXPERIMENTAL RESULTS - FRACTURE ENERGY PREDICTIONS

Representative load-CMOD and load-LPD curves for the three beam sizes and the higher compressive strength mix (C2D1), under a CMOD rate such that the peak load is reached in about 10 min., are shown in Figs. 2 and 3, respectively. The responses of the beams under the constant CMOD rate independently of the compressive strength and beam size appears to be similar to that depicted in Figs. 2 and 3.

A rather mild size dependence is observed for the specific fracture energy values, G_F^R, determined according to the RILEM recommendations (see Table 2). For both loading schemes and mixes, calculated G_F^R values increase slightly with beam size. A 4 times larger beam size results in a 15-35% increase in G_F^R. Largely responsible for this is the work-of-fracture due to the self-weight, which is as high as 33% for the largest specimens (S3) and as low as 4.5% for the smallest ones (S1). An interesting aspect of the experimental findings is that G_F^R values of the higher strength concrete mix (C2D1) are either similar or slightly lower than those of the lower strength mix (C1D1).

The predicted values for the specific fracture energy, G_f^{SEM}, according to the size effect method(SEM) proposed by Bazant [2,3] are included in Table 2. The elastic modulus, E_{co}, used in Bazant's formulation is computed from uniaxial compressive tests on cylinders. As already reported by other authors [3,6,8], the predicted G_f^{SEM} values of 13 and 53 N/m are lower than G_F^R values, the ratio G_F^R/G_f^{SEM} being about 6.3 to 8.5 for the low-strength mix and 1.3 to 1.8 for the high-strength mix. This contradicts the size effect law definition of G_f [4]. Higher G_f^{SEM} values are found if the elastic modulus is derived from the initial stiffness of the load-LPD diagram. The RILEM specific fracture energy, G_F^R, based on the experimental load-LPD curves, and Bazant's G_f^{SEM} are compared in Fig.4 together with G_F^{LEFM} values, based on LEFM, and G_F^{JS} values predicted by Jenq/Shah's two-parameter model [10]. For the two latter models, higher compressive strength results in consistenly higher fracture energy values and a considerable size effect. The G_f^{SEM} values appear to be almost the upper-bound limit of both LEFM and two-parameter model fracture energy predictions, especially for the higher strength concrete.

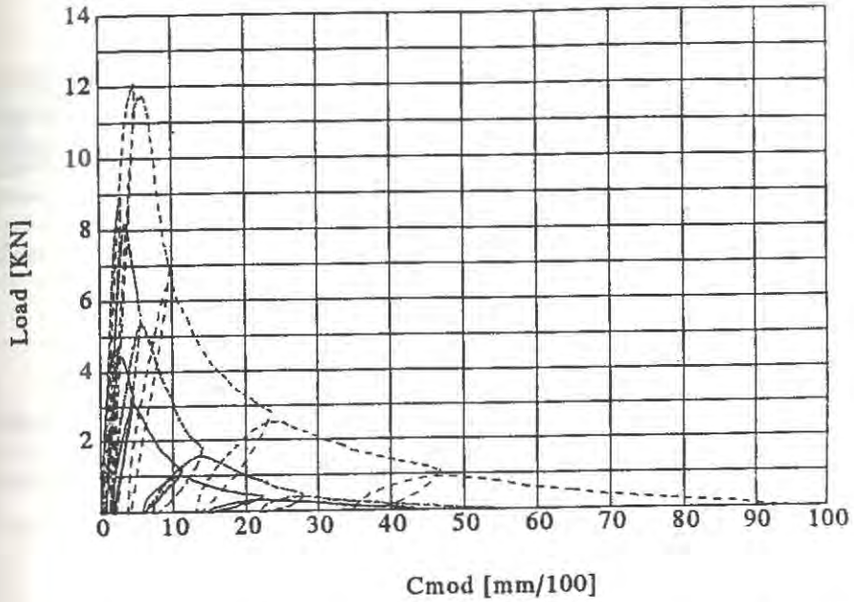

Figure 2. Load-CMOD diagram (pre-peak regime in 10 min.) for high strength mix C2D1.

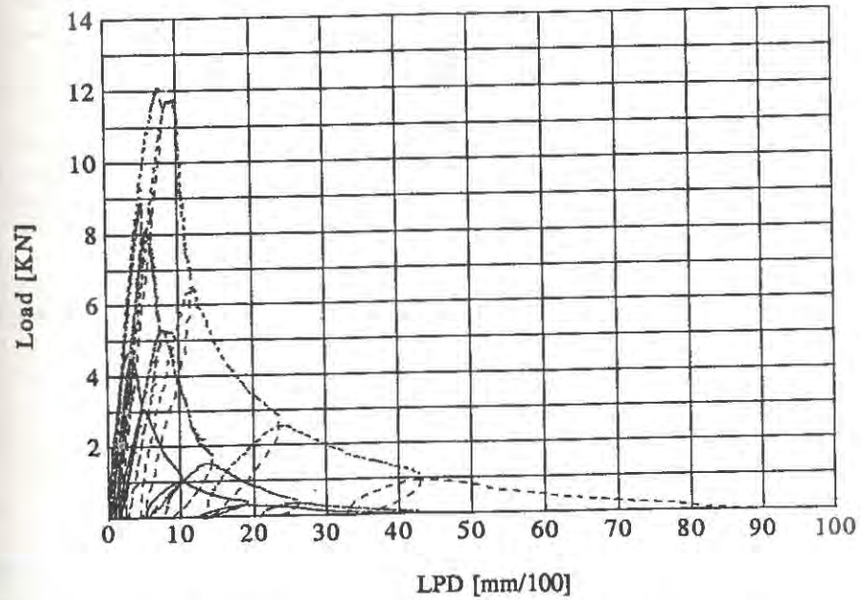

Figure 3. Load-LPD diagram (pre-peak regime in 10 min.) for high strength mix C2D1.

TABLE 2
Experimental results and calculated specific fracture energy

Mix	Size	d [mm]	b [mm]	ao/d	Ppeak [KN]	Defl.u [mm/100]	Specific Fracture Energy RILEM [N/m]	LEFM [N/m]	Jenq [N/m]	Bazant [N/m]
C1D1	S1[a]	63.0	127.5	0.322	2.767	73	76	9	21	
	S2[a]	128.0	128.7	0.307	4.670	110	94	12	20	
	S3[a]	254.7	129.8	0.309	7.037	120	118	15	20	13
	S1[b]	63.2	127.2	0.309	2.903	87	87	9	20	
	S2[b]	126.7	126.7	0.302	4.685	98	91	12	22	
	S3[b]	253.0	130.0	0.299	5.712	105	103	10[d]	12[d]	
C2D1	S1[a]	63.8	126.5	0.313	4.672	40	69	20	34	
	S2[a]	127.0	129.3	0.307	8.953	55	82	37	47	
	S3[a]	253.5	130.0	0.310	12.112	90[c]	118	36	49	53
	S1[b]	63.3	128.3	0.348	4.631	53	68	21	35	
	S2[b]	126.3	129.3	0.299	8.453	62	79	33	45	
	S3[b]	255.0	127.7	0.298	13.363	67	98	41	54	

(a) The peak load is reached in 10 min.
(b) Constant CMOD rate (0.0001 mm/sec).
(c) Fracture surface revealed possible spurious constraints.
(d) Suspect data.

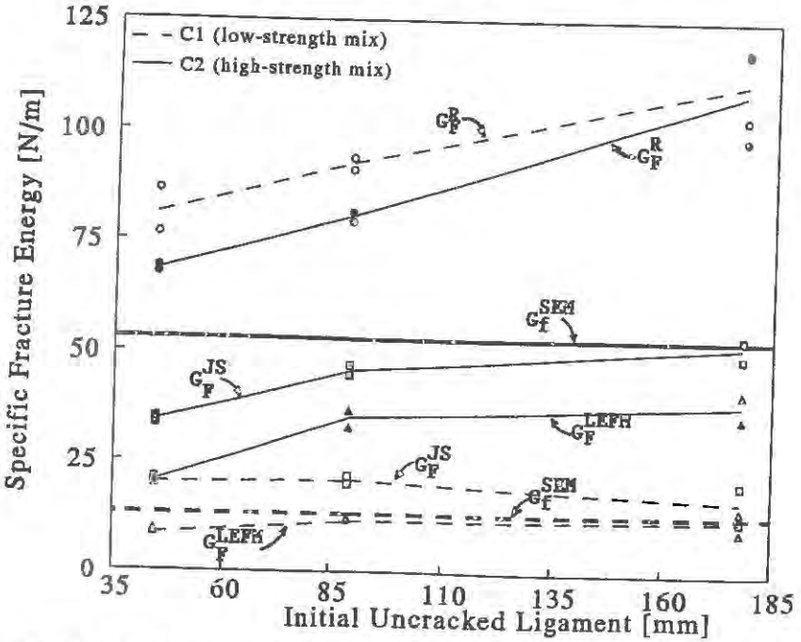

Figure 4. Comparison of specific fracture energy according to different methods.

CONCLUSIONS

The data presented confirm some results already detected by other researchers regarding the size dependence of the RILEM fracture energy, although the present tests reveal a rather mild size effect. It is interesting that the G_F^R values, which appear consistent with other findings in the literature [9], for a concrete compressive strength twice as much higher are similar or slightly lower than those for the lower strength. While the predicted G_f^{SEM} appears to be much lower than G_F^R contradicting the size effect law definition of G_f, it appears to be an upper-bound limit for both LEFM and two-parameter fracture energy predictions.

ACKNOWLEDGMENTS

Support of this research was provided by the Concrete Materials Research Council (CMRC) of the American Concrete Institute (ACI) and the Department of Civil Engineering at Case Western Reserve University.

REFERENCES

1. RILEM TC-50 FMC, Determination of the fracture energy of mortar and concrete by means of three-point bend tests on notched beams. Materials and Structures, 1985, **18**, No.106,285-290.
2. Bazant, Z.P., Kim, J.K., Pfeiffer, P.A., Nonlinear fracture properties from size effect tests. Journal of Structural Engineering, ASCE, 1986, **112**, No.2 ,289-303.
3. Bazant, Z.P., Gettu, R., Kazemi, M.T., Determination of fracture energy and process zone length by the size effect method. Materials and Structures, Nov. 1990 (Report to RILEM Committee 89-FMT: Test Methods).
4. Bazant, Z.P., Kazemi, M.T., Size dependence of concrete fracture energy determined by RILEM work-of-fracture method. International Journal of Fracture, 1991, **51**, 121-138.
5. Hillerborg, A., The theoretical basis of a method to determine the fracture energy G_F of concrete. Materials and Structures, 1985, **18**, No.106, 291-296.
6. Planas, J.,and Elices, M., Fracture criteria for concrete: Mathematical approximation and experimental validation. Engineering Fracture Mechanics, 1990, **35**, No.1/2/3,87-94.
7. Gettu, R., Bazant, Z.P.,and Karr, M.E., Fracture properties and brittleness of high strength concrete. ACI Materials Journal, Nov.-Dec. 1990, **87**, No.6, 608-618.
8. Planas, J.,and Elices, M., Size effect and experimental validation of fracture models. Fracture Mechanics of Concrete Structures, RILEM TC90-FMA, L.Elfgen (Ed.), Chapman and Hall, London, 1990, 99-127.
9. Hillerborg, A., Results of three comparative test series for determining the fracture energy G_F of concrete. Materials and Structures, 1985, **18**, No.107, 407-413.
10 Jenq,Y.S.,and Shah,S.P., Two-parameter fracture model for concrete. Journal of Engineering Mechanics, ASCE, 1985, 111, No. 10, 1227-1241.

SIZE EFFECT IN STRENGTH OF REINFORCED CONCRETE COLUMNS

ZDENĚK P. BAŽANT[1] AND YOUNG WUNG KWON[2]
[1]Walter P. Murphy Professor of Civil Engineering,
Northwestern University, Evanston, Illinois 60208
[2]Visiting Scholar, Northwestern University;
Associate Professor on leave from Incheon University, Seoul, Korea

ABSTRACT

The results of tests of geometrically similar tied reinforced concrete columns of different sizes, with size ratio 1:2:4 and slendernesses 16, 32 and 48, are reported. The model columns were made of reduced-size aggregate with maximum size 1/8 in. and reduced-size steel bars. It is found that, for all slendernesses, there exists a strong size effect in which the nominal stress at maximum load decreases as the size is increased. This contradicts the current design codes. The results are in good agreement with the previously proposed size effect law. The higher the slenderness, the stronger is the size effect.

INTRODUCTION

The diagram of axial load versus the load-point deflection (axial shortening) of reinforced concrete columns does not exhibit a horizontal plateau after the maximum load is reached, as would be expected for short columns if the assumptions of plastic limit analysis, serving as the basis of the current design codes, were valid. Rather, the columns, both short and long, exhibit post-peak softening. This can be caused only by fracture phenomena and implies that size effect ought to be at play.

Although important advances have been made in the past in understanding the behavior of reinforced concrete columns [1,2] (for further references see also [3,4]), the size effect in columns escaped attention so far. But no physical phenomenon is understood until the scaling law is understood, and this applies to concrete columns, too. The objective of this study is to briefly report the initial results of an experimental investigation of the size effect in columns. A detailed report will be given in a forthcoming article [5].

TEST SPECIMENS AND EXPERIMENTAL PROCEDURE

The test specimens (Fig. 1) were tied reinforced concrete columns of square cross sections with sides $D = 0.5$, 1 and 2 in. Three column slendernesses $\lambda = 16$, 32, and 48, were used ($\lambda = L/r = L/D$). The corresponding column lengths were $L = 2.5$, 5, and 7.5 in. for the smallest

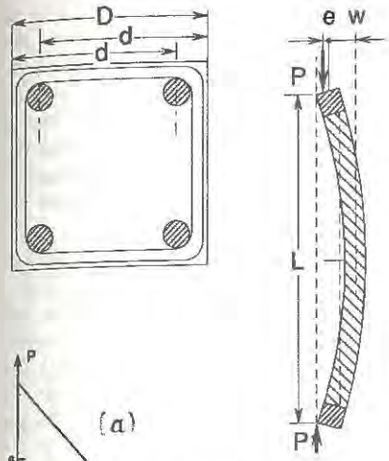

Fig.1 Column specimens tested.

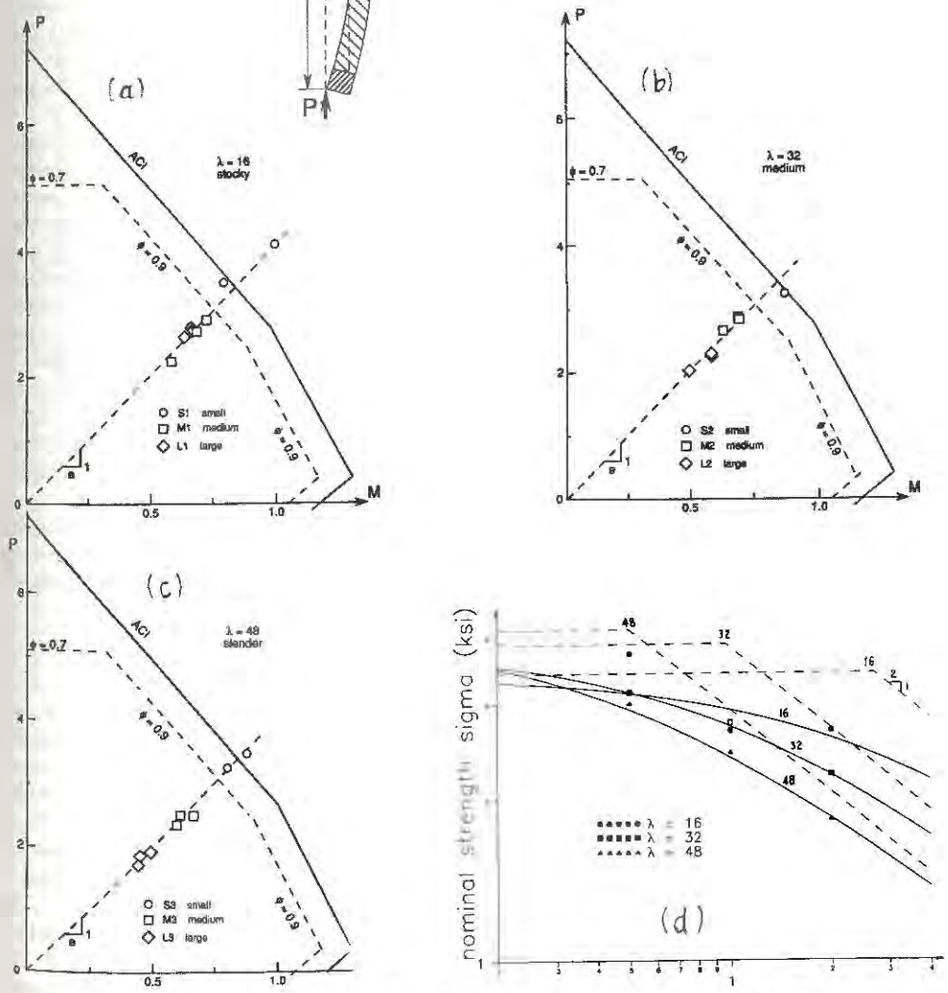

Fig. 2 Test results: (a-c) Interaction diagrams, (d) Size effect plots.

cross section, $L = 5$, 10, and 15 in. for the middle cross section, and $L = 10$, 20, and 30 in. for the largest cross section. The columns in each group of the same slenderness and different sizes were geometrically similar. The geometric similarity was enforced scrupulously—the reinforcing bars, their locations and cover, as well as the diameter and spacing of the ties, were all scaled in proportion to the characteristic column dimension D, taken as the cross section side. Because of the unavailability of deformed reinforcing bars of sufficiently small diameter, smooth steel bars were used. This nevertheless should have caused no problems with bond slip, because the column ends were provided with steel cover plates (Fig. 1c) at which the vertical bars were anchored by threaded nuts.

The columns were simply supported, and the load P was applied with end eccentricities e which were geometrically similar; $e = D/4$. Each column had four longitudinal bars (Fig. 1) of diameters $d_b = 1/16$, 1/8, and 1/4 in. for the smallest, middle and largest column sizes. The corresponding diameters of the steel ties were one half of the foregoing values. The center-to-center spacing of the ties was 0.3, 0.6 and 1.2 in. for the smallest, middle and largest cross sections, but near the ends the spacings were reduced to 0.2, 0.4 and 0.8 in., respectively, and very near the ends to 0.1, 0.2 and 0.4 in., respectively. The loads were applied onto the steel platens through steel balls and steel plates.

The average uniaxial compression strength of concrete, measured on 28-day-old companion cylinders of diameter 3 in. and length 6 in., was $f'_c = 4{,}200$ psi (28.96 MPa). The concrete (actually a micro-concrete or mortar) was made of Type I Portland cement with water-cement ratio 0.65 (for easy workability) and aggregate-cement ratio 2.5 (by weight). The aggregate used in the mix was an air-dried siliceous sand of maximum grain size 0.132 in., passing through sieve No. 6. All the specimens were cast from one and the same batch of concrete. The steel had Young's modulus $E_s = 29{,}000{,}000$ psi (200 GPa) and yield strength $f_y = 80{,}000$ psi (552 MPa). This value of yield strength was higher than that permitted for reinforced concrete structures, however this could not have had any significant effect since the calculated stresses reached in the steel bars before the peak load did not exceed 60,000 psi (414 MPa). The thickness of the concrete cover of longitudinal bars, measured from the bar center to the surface, was $d_c = 0.2D$.

The columns were cast in forms made of plywood with a smooth hard varnish-painted surface. The forms were stripped after one day, after which the columns, as well as the companion cylinders, were cured until 28 days of age in a water bath at 20°C temperature. At the age of 28 days, the columns were tested in a closed-loop (MTS) testing machine. The lateral deflection at the midheight of column was measured by an LVDT gauge (Fig. 1d). The stroke rate was kept constant in each test and was chosen so as to reach the peak load for any column size and slenderness within about 15 min.

RESULTS OF MEASUREMENTS AND THEIR ANALYSIS

The test results are summarized in Table 1 (1 kip = 1,000 lb.). In the specimen labels, S, M, and L mean the small, middle, and large cross sections; the subsequent numbers 1, 2, and 3 mean the low, middle, and high slenderness. Three identical specimens were tested for all cases, except S1 and S3. The corresponding mean nominal stresses at maximum load, defined as $\sigma_N = P/D^2$, are also given. Furthermore, Table 1 shows the values of the nominal bending moment Pz at midspan, in terms of the parameter $m_N = Pz/D^3 = \sigma_N(e + w)/D$; $z = e + w$ = deflection ordinate at midspan at maximum load, $e = D/4$ = eccentricity of the load, w = deflection at midspan. The mean values of m_N for each group of identical specimens are also given. The interaction diagram of maximum (ultimate) axial load P vs. the corresponding bending moment M, calculated according to the standard procedure [1,2], is shown by the solid line in Fig. 2. The dashed lines show the reduced interaction diagrams (in which ϕ are the ACI capacity reduction factors).

TABLE 1. Measured axial load P (of end eccentricity $e = D/4$) and midheight deflection w, with corresponding bending moment M, nominal stress $\sigma_N = P/D^2$ and nominal moment $m_N = M/D^3 = \sigma_N(e + w)/D$, for various column slendernesses λ and cross-section sizes D.

D (in.)	λ	Specimen	Prepeak State		Peak Load State		Postpeak State		Peak Load State				
			P	w	P	w	P	w	M	σ_N	Mean σ_N	m_N	Mean m_N
			(kip)	(in.)	(kip)	(in.)	(kip)	(in.)	(kip x in.)	(kip/in²)	(kip/in²)	(kip/in²)	(kip/in²)
0.5	16	S1-1	0.205	0.005	1.03	0.025	0.208	0.118	0.13	4.12	3.72	1.04	0.92
		S1-2	0.202	0.039	0.83	0.023	0.20	0.011	0.10	3.32		0.80	
	32	S2-1	0.203	0.014	0.86	0.044	0.24	0.14	0.11	3.44	3.15	0.88	0.80
		S2-2	0.205	0.025	0.80	0.063	0.20	0.14	0.10	3.20		0.80	
		S2-3	0.208	0.024	0.70	0.055	0.26	0.08	0.09	2.80		0.72	
	48	S3-1	0.208	0.019	0.875	0.035	0.20	0.149	0.11	3.52	3.01	0.88	0.75
		S3-2	0.205	0.019	0.807	0.087	0.20	0.171	0.10	3.24		0.80	
1.0	16	M1-1	1.015	0.031	2.76	0.049	1.0	0.163	0.69	2.76	2.85	0.69	0.71
		M1-2	1.02	0.049	2.93	0.023	1.0	0.179	0.73	2.93		0.73	
		M1-3	1.02	0.011	2.32	0.038	1.0	0.105	0.58	2.32		0.58	
	32	M2-1	1.01	0.045	2.62	0.095	1.0	0.230	0.66	2.62	2.76	0.66	0.69
		M2-2	1.01	0.028	2.83	0.090	1.0	0.203	0.71	2.83		0.71	
		M2-3	1.01	0.021	2.82	0.079	1.0	0.195	0.71	2.82		0.71	
	48	M3-1	1.01	0.0302	2.49	0.148	1.01	0.370	0.62	2.49	2.44	0.62	0.61
		M3-2	1.02	0.038	2.37	0.165	1.0	0.377	0.59	2.37		0.59	
		M3-3	1.0	0.050	2.47	0.188	1.03	0.252	0.62	2.47		0.62	
2.0	16	L1-1	2.0	0.0068	10.85	0.0869	2.10	0.0346	5.43	2.71	2.67	0.68	0.67
		L1-2	2.0	0.0048	10.67	0.0767	4.16	0.276	5.34	2.67		0.67	
		L1-3	2.02	0.015	10.53	0.0525	2.0	0.371	5.27	2.63		0.66	
	32	L2-1	2.0	0.010	9.42	0.244	2.07	0.980	4.71	2.36	2.22	0.59	0.56
		L2-2	2.05	0.015	9.21	0.227	2.0	0.885	4.61	2.30		0.58	
		L2-3	2.0	0.012	8.04	0.098	2.0	0.203	4.02	2.01		0.50	
	48	L3-1	2.0	0.016	7.38	0.360	2.0	0.902	3.69	1.85	1.84	0.46	0.46
		L3-2	2.0	0.006	7.02	0.298	2.0	0.657	3.51	1.76		0.44	
		L3-3	2.0	0.002	7.64	0.284	2.32	1.0	3.82	1.91		0.48	

The most interesting aspect of the results is that: (1) with increasing size, the data points generally move toward the origin of the interaction diagram, and (2) the size effect exists and is quite significant. These observations disagree with all the existing design codes. The maximum load points that lie inside the interaction diagram represent situations in which the code does not provide the required safety margin. For more slender columns, as expected, the response path moves more to the right and describes a wider loop.

Consider now the plots of the nominal strength $\sigma_N = P/D^2$ vs. log D. Fig. 1d gives such plots for all the slenderness, and each data point represents the average of a group of three like specimens. The plots clearly indicate a strong size effect. Based on previous theoretical arguments (cf. [3], chapters 12 and 13), the size effect should follow the approximate size effect law proposed by Bažant (1984) $\sigma_N = Bf'_t(1+\beta)^{-1/2}$ with $\beta = D/D_0$, in which Bf'_t and D_0 are two empirical constants (f'_t = tensile strength). The optimal fits by this size effect law are shown in Fig. 1d as the solid curves. Note that for a more slender column the size effect is stronger, with the response lying closer to the linear elastic fracture mechanics asymptote of slope -1/2. This is not surprising, since a more slender column of the same cross section stores more energy than a stockier column.

CONCLUSIONS

1. Tied reinforced concrete columns exhibit a strong size effect of fracture mechanics type.
2. The present test results are in agreement with the previously proposed size effect law.
3. The higher the slenderness, the stronger is the size effect.
4. The size effect ought to be introduced into the code provisions for columns. Until this is done, very large columns will have a significantly smaller safety margin than required.

ACKNOWLEDGMENT.—Partial financial support for the underlying theoretical studies of the size effect was received under AFOSR Grant No. 91-0140 to Northwestern University. The second author wishes to express his gratitude for a fellowship from the Korean government supporting him during a one-year appointment as Visiting Scholar at Northwestern University. Thanks are due to Milan Jirásek, graduate research assistant, for his expert help in data evaluation after Y.W. Kwon returned to Korea.

REFERENCES

1. McGregor, J.G., *Reinforced Concrete: Mechanics and Design*, Prentice Hall, Englewood Cliffs, NJ, 1988 (799 pp.)
2. Nilson, A.H., and Winter, G., *Design of Concrete Structures*, 10th ed., McGraw Hill, New York, 1986 (730 pp.)
3. Bažant, Z.P., and Cedolin, L., *Stability of Structures: Elastic, Inelastic, Fracture and Damage Theories* (textbook and reference volume). Oxford University Press, New York, 1991 (1010 pp.)
4. Bažant, Z.P., Cedolin, L., and Tabbara, M.R., New method of analysis for slender columns. *ACI Structural Journal* 1991, 88 (4), 391–401.
5. Bažant, Z.P., and Kwon, Y.W., Size effect in failure of short and slender reinforced concrete columns. Structural Engineering Report 91-9/456s, Northwestern University, Sept. 1991; submitted to *Journal of Structural Engineering ASCE.*

Fracture Energy of Concrete with Different Specimen Size and Strength by Wedge Splitting Test

J.K.KIM*, H. MIHASHI**, K. KIRIKOSHI** and T. NARITA**

* Dept. of Civil Engineering, KAIST, Daejeon, Korea
** Dept. of Architecture, Tohoku Univ. Sendai, 980 Japan

ABSTRACT

It has been investigated and is now known that the fracture energy estimated does strongly depend on the specimen size and evaluation method even though concrete is identical. In this paper, some experiments were carried out to study such influence on fracture energy of concrete, For this purpose, 9 three-point bending specimens of 100 x100 x840mm and 36 wedge-splitting specimens with four different sizes of 100 x 100 x 100mm, 100 x 100 x 120mm, 200 x 240 x 120mm and 400 x 480 x 120mm were tested for three different compressive strength levels of 20MPa, 60MPa and 100MPa. A load-CMOD curve and 2 load-CTOD curves for each specimen were obtained with unloading curves after peak load. The experimental results were analyzed and discussed by RILEM recommendation, 2 RILEM draft recommendation methods, and wedge splitting test method. The fracture characteristics of concrete resulted by this experiment depended on the specimen size strongly.

INTRODUCTION

It has been generally observed that fracture behavior of concrete is quite different with its strength, and fracture energy of concrete depends on the specimen size and shape. The principal objective of this paper is to show the comparison between results obtained by wedge splitting test and analytical results by RILEM recommendation method(1), i.e., three-point bending test method, 2 RILEM draft recommendation methods, i.e., size-effect method(2) and two-parameter method(3), and wedge splitting test method proposed by F.H.Wittmann(4).

EXPERIMENTAL PROGRAM AND RESULTS

Concrete Properties

Three different strengths of concrete, i.e., 20MPa, 60MPa and 100MPa were designed. The mix proportion and test results of compressive strength, splitting tensile strength, static and dynamic elastic moduli are given in Table 1.Three batches for each strength level were prepared, and 6 cylinders of ϕ100 x 200mm for each batch were casted, i.e., three for compressive strength and three for splitting tensile strength. Therefore the values of f'_c, f_{sp}, E_c and E_d in

Table 1 are average values of 9 specimens. The maximum aggregate size used for all mix proportions was 7 mm.

TABLE 1
Mix Proportion and Test Results of Concrete

Strength level	C (kg)	Si (kg)	W (kg)	S (kg)	G (kg)	S.P (l)	W/C	f_c' (MPa)	f_{sp} (MPa)	E_c (GPa)	E_d (GPa)
20MPa	349	0	227	721	1006	0	0.65	20.9	2.36	22.7	27.3
60MPa	340	60	160	721	1006	8.95	0.47	59.1	3.83	35.3	41.8
100MPa	444	111	111	721	1006	25.31	0.25	106.3	6.08	39.8	46.6

Preparation of Test Specimens
A beam specimen of 100 x 100 x 840mm and two wedge splitting specimens of 200 x 240 x 120 and 400 x 480 x 120mm with groove of 10mm each side were casted from each batch. The notch was cast for all the specimens with acrylic plate. The small wedge splitting specimens of 100 x 100 x 100 and 100 x 100 x 120mm were made by cutting the beam specimen after testing. Their initial notch and the groove for 100 x 100 x 120mm specimen were also made by diamond saw. This means that three identical specimens in each strength level were casted. All the specimens were cured in 100% humidity curing room during 28 days until the test. Just before testing each specimen was prepared for clip gauges and loading device.

Experimental Procedures
A servo-controlled hydraulic machine of 20 ton capacity was used for all test. Three-point bending test was followed the RILEM recommendation(1), and wedge-splitting specimens were controlled by crack mouth opening displacement(CMOD). CMOD and two crack tip opening displacements(CTOD) in each side as well as the applied load were recorded. The load-CMOD and 2 load-CTOD curves were fully obtained. During the test of wedge-splitting specimen the applied load was manually unloaded at about 95% of the peak load as possible, and was consquently unloaded several times. The rate of loading was properly changed with the size of specimen, i.e., the rate of CMOD was increased with increasing of specimen size. After the test the dimension of specimen and ligament was measured for the analysis of test results. Horizontal component of maximum applied load(H), initial stiffness(D_i), unloading stiffness(D_u), and crack tip opening displacement at peak load(CTOD) were given in Table 2. It was, however, impossible to unload exactly at 95% of the peak load. Therefore D_u values in Table 2 were obtained by regression from several unloading stiffnesses at different stress levels.

ANALYSIS OF TEST RESULTS

RILEM Recommendation
The average fracture energies of 3 specimens by RILEM recommendation(1) for three-point bend tests are 87.08 N/m, 111.36 N/m and 97.36 N/m for 20MPa, 60MPa, and 100MPa respectively. For the measured G_f the correction for the effect of dead weight was carried out according to RILEM recommendation.

Wedge Splitting Test Method
The fracture energy of concrete by wedge splitting test method(4) can be directly obtained from load-CMOD curve, i.e., total area under load-CMOD curve/total ligament area of specimen, and is given in Table 2.

Size Effect Method
For the application of size effect method, it is required to test geometrically similar notched concrete specimens of different sizes(2). Three different sizes of specimens were tested for this purpose with geometrical similarity as possible. The stress for each specimen was calculated by Eq.(1) with considering the effect of vertical component of applied load.

$$\sigma_N = 2\,kd\,H/(bL_o(2kd-L_o)) \tag{1}$$

where $kd = L_o(3a_o+ 2L_o+ 3hV/H)/3(2a_o+ L_o+ 2hV/H)$; distance of neutral axis from crack tip, V/H=0.084; ratio of vertical force component to horizontal component, h=31mm; distance to bearing center of loading device from initial notch line, b; thickness excluding grooves, $L_o=W-a_o$; initial ligament length, a_o; initial notch length (intial notch plus the distance to bearing center from specimen surface(15mm)), W; specimen depth, S; specimen width.
The geometry correction factor $F(\alpha)$ of wedge splitting specimens for S/W = 100/115 of A,B series, S/W = 240/215 of C series, and S/W = 480/415 of D series were evaluated by finite element analysis as given in Eq.(2).

$$F_A(\alpha) = F_B(\alpha) = 0.7603+2.0061\,\alpha-6.1724\,\alpha^2+4.444\alpha^3+0.0024\alpha^4$$

$$F_C(\alpha) = 1.0588-1.5788\alpha+2.7631\alpha^2- 2.9136\alpha^3+ 1.4258\alpha^4 \tag{2}$$

$$F_D(\alpha) = 1.2317-3.46\alpha+9.1658\alpha^2-12.004\alpha^3+6.1047\alpha^4$$

The relationship of σ_N, $F(\alpha)$ as given in Eqs.(1) and (2), and K_I for LEFM in this case can be written as Eq.(3). And the nondimensional energy release rate and fracture energy are calculated by Eq.(4) and Eq.(5) respectively.

$$K_I = \sigma_N \sqrt{W-a}\,F(\alpha) = \sigma_N\sqrt{L}\,F(\alpha) \tag{3}$$

$$g(\alpha) = (1-\alpha)\,(F(\alpha))^2 \tag{4}$$

$$G_f = g(\alpha_o)/E_cA \tag{5}$$

where $\alpha=a/W$, E_c; Young's modulus of concrete, A; slope of linear regression line for $X_j=W_j$ and $Y_j=(1/\sigma_N)^2$. But specimen proportion with sizes are slight different due to using the same size of loading device. If the specimen proportion is not equal to each other, but slight different, then the nominal stress σ_N obtained by Eq.(1) can be modified to that for the reference proportion under assumption of the same K_I, i.e.,

$$\sigma_{N,R} = \sigma_N\,F(\alpha)/F_R(\alpha) \tag{6}$$

where $F_R(\alpha)$ is geometry correction factor of the reference specimen proportion. For specimens with the same S/W but different a/W, the modification can be achieved by the same approach, i.e., $\sigma_{N,R} = \sigma_N\sqrt{L}\,F(\alpha)/\sqrt{L_R}F(\alpha_R)$. In this paper, the specimen proportion of C series, i.e., S/W = 240/215 and a/W = 115/215 was taken as the reference proportion, and results were shown in Table 2.

Two-Parameter Method
To estimate the parameters K_{Ic}, $CTOD_c$ and E_c, geometry correction factor functions, $V(\alpha)$ and $F(\alpha)$ for displacement and stress intensity factor as well as the initial and unloading compliances should be obtained from the load-CMOD curve(3). Young's moduli were calculated by Eq.(7), and were given in Table 2. The critical effective crack length a_c was determined by Eq.(8) with using an iteration process suggested in Ref. 3, and unloading stiffness D_u which was obtained by experiment was also given in Table 2.

$$E_c = (D_i/B)\,V(\alpha_o) \tag{7}$$

$$E_c = (D_u/B)\, V(\alpha_c) \quad (8)$$

where D_i; the initial stiffness from load-CMOD curve which is given in Table 2, B; total thickness of specimen, and $V(\alpha)$ is the geometry correction factor function which was obtained by regression from the results in Ref. 5, and is given in Eq.(9)

TABLE 2.
Experimental and Analytical Results of Wedge Splitting Test

Specimen No.	H (N)	D_i (N/mm)	D_u (N/mm)	$CTOD_c$ (mm)	E_c (MPa)	$\sigma_{N,P}$ (MPa)	K_{Ic} (MPa$\sqrt{m}$)	G_f (WST) (N/m)	G_f (SEL) (N/m)
20-A1	1472	42732	23721	0.0095	29471	3.585	0.9220	57.60	
20-A2	1619	40790	20581	0.0158	28622	3.869	1.0457	79.14	
20-A3	1619	38887	23181	0.0125	26974	3.912	0.9758	63.69	
20-B1	1207	41555	23269	0.0125	24725	2.949	0.7559	63.66	
20-B2	1383	43380	26458	0.0103	25811	3.430	0.8497	67.74	80.05
20-B3	1354	37984	25222	0.0130	21582	3.339	0.7888	48.69	(60.38)*
20-C1	3198	62421	43154	0.0188	25345	3.493	1.1997	80.44	
20-C2	2914	65354	38102	0.0194	26117	3.163	1.1883	67.78	
20-C3	2825	62500	35620	0.0181	25377	3.087	1.1759	64.49	
20-D2	5347	68954	44959	0.0250	24739	2.850	1.4230	93.34	
20-D3	5356	70818	48648	0.0213	25672	2.883	1.4015	78.06	
60-A1	2423	45106	31480	0.0100	32583	6.037	1.4047	89.56	
60-A2	2825	56437	36120	0.0095	41250	6.920	1.6785	87.04	
60-A3	2865	55986	33589	0.0133	39059	6.988	1.7359	109.64	
60-B1	2413	67434	41133	0.0110	41073	6.035	1.4922	76.77	
60-B2	2560	68484	46911	0.0100	42207	6.392	1.5050	81.25	79.25
60-B3	2943	67944	42124	0.0105	41141	7.291	1.7833	89.25	
60-C1	4581	91704	57320	0.0165	37235	4.984	1.8006	97.85	
60-C2	4581	87338	62009	0.0150	35274	4.961	1.6802	92.94	
60-C3	5140	89987	61783	0.0165	36732	5.620	1.9342	95.99	
60-D1	9398	96638	69004	0.0231	34851	4.976	2.3738	98.61	
60-D2	8083	82747	64540	0.0203	29996	4.294	1.9527	92.95	
60-D3	9133	101661	72869	0.0233	36285	4.810	2.2373	102.95	
100-A1	3051	59419	38622	0.0110	42673	7.440	1.7900	96.57	
100-A2	3345	62500	48118	0.0070	45414	8.264	1.8476	82.86	
100-A3	3286	64108	40388	0.0100	46040	8.124	1.9751	81.89	
100-B1	3640	75390	57300	0.0093	44857	8.627	1.9038	78.27	
100-B2	3169	74448	50031	0.0114	45613	8.117	1.9187	90.73	115.00
100-B3	3640	74939	53572	0.0098	43819	8.955	2.0685	89.51	
100-C1	6171	101072	77931	0.0173	41257	6.761	2.1956	88.17	
100-C2	6612	101779	77656	0.0170	41107	7.127	2.2263	96.62	
100-C3	6406	101651	78274	0.0150	40838	7.065	2.2982	94.33	
100-D2	10507	109588	83287	0.0218	39726	5.624	2.6111	92.33	
100-D3	12635	123449	91351	0.0235	44291	6.265	2.8653	107.09	

* fracture energy excluding the results of 20-B series

$$V_A(\alpha)=V_B(\alpha)=(1+\alpha/1-\alpha)^2(-0.04903+54.564\alpha-253.68\alpha^2+765.37\alpha^3 -1447.2\alpha^4+1496.5\alpha^5-679.01\alpha^6+67.53\alpha^7)$$

$$V_C(\alpha)= (1+\alpha/1-\alpha)^2(1.6025+22.948\alpha-79.255\alpha^2 +193.18\alpha^3 -351.29\alpha^4 +371.74\alpha^5-172.04\alpha^6 +17.11\alpha^7) \quad (9)$$

$$V_D(\alpha)= (1+\alpha/1-\alpha)^2(1.8726+17.778\alpha-50.73\alpha^2 +99.602\alpha^3 -172.06\alpha^4 +187.8\alpha^5-89.129\alpha^6+8.8642\alpha^7)$$

The critical stress intensity factor K_{Ic} was determined by Eq.(10).

$$K_{Ic} = (H/b\sqrt{W})\, F(\alpha) \quad (10)$$

in which $F(\alpha)$ was evaluated by finite element analysis as shown in Eq.(11).

$$F_A(\alpha)=F_B(\alpha)=6.5284+31.420\alpha+2.5852\alpha^2-182.19\alpha^3+244.90\alpha^4$$

$$F_C(\alpha)=30.435-184.97\alpha+638.43\alpha^2-976.19\alpha^3+610.55\alpha^4 \quad (11)$$

$$F_D(\alpha)=28.802-176.50\alpha+621.24\alpha^2-965.10\alpha^3+612.00\alpha^4$$

DISCUSSION OF EXPERIMENTAL AND ANALYTICAL RESULTS

RILEM Recommendation

Fracture energy obtained in this study by RILEM method shows the same trend as that by other research, i.e., the effect of dead weight on the fracture energy is decreased as the higher strength of concrete. The ratio of fracture energy by dead weight to total fracture energy is 46%, 33% and 27% for 20MPa, 60MPa and 100MPa respectively. And it has been observed that fracture energy of 60MPa concrete is higher than that of 100MPa.

Wedge Splitting Test Method.

The load-CMOD curve by this method usually had very long tail comparing with RILEM method. Especially the smaller size and lower strength of concrete shows the longer tail. This might be due to some other factors not due to fracture process. Therefore it was excluded for the estimation of fracture energy by cutting at the point with zero slope in load-CMOD curve even though it was very ambiguous in some cases. The fracture energy by this method depends on the specimen size as shown in Table 2. The average fracture energies of A and B, C, D series are 63.42, 70.90, and 85.70N/m for 20MPa, 88.92, 95.59, and 98.17N/m for 60MPa, and 86.64, 93.04, and 99.71N/m for 100MPa respectively. And it has been also observed that the average fracture energy, 92.90N/m for 60MPa is higher than that for 100MPa, 90.76N/m.

Size Effect Method

As known, the definition of fracture energy in this method which is the energy for infinite large specimen, is different from other methods. LEFM can be applied for infinite large specimen, but it is impossible to obtain the stress for infinite large specimen by test . Therefore the stress for infinite large specimen is obtained by extrapolation using size effect law from stresses of small size specimens. The size effect law is, however, inherently an appoximation, in other word, it is not accurate enough for estimation of fracture energy because the stress of infinite large specimens is required, even though it is resonable enough for the prediction of stress for large member in construction field. It has been generally observed that the fracture energy by this method is smaller than that by other methods even it is expected larger because it is the energy for infinite large specimen. This is partially due to that the stress of infinite large specimen extrapolated by size effect law gives smaller value than exact, and partially due to that

the specimens at failure is usually not similar each other even though they are originally similar. Some of the results are also summerized in Table 2. As mentioned in previous section specimens are not exactly similar each other. Therefore, all stresses were modified to those of 2 reference shapes, i.e., the shapes of C series and A series according to Eq.(6). and the fracture energies calculated for 2 different reference shapes were almost same. This means that this approach can be used if the shape of specimen is not much different. In spite of it is the most promised method, it seems that this method needs to be refined.

Two-Parameter Method

Based on the results obtained in this limited investigation, it seems that two parameters, K_{Ic} and $CTOD_c$ do depend much on the specimen size unlike the results by the proposer of this method. As shown in Table 2, $CTOD_c$ which was directly obtained from clip gauges on both sides at initial crack tip depends strongly on the size, but Young's modulus obtained is almost same as the value by compressive stress test. More researches for the dependence of the K_{Ic} and $CTOD_c$ on the specimen size would be needed for different shapes of specimen and specimens with large ligament size.

CONCLUSIONS

Based on the results obtained in this limited investigations it would be concluded that; 1) The fracture energy, G_f and two parameters K_{Ic} and $CTOD_c$ in wedge splitting test depend on the specimen size, 2) The fracture energy do not proportionally increase with increasing the compressive strength. It comes to the conclusion that a more comprehensive method is required to accurately estimate fracture characteristics of concrete.

REFERENCES

1. RILEM Draft recommendation(TC50-FMC), Determination of the fracture energy of mortar and concrete by means of three-point bend test on notched beams, Materials and Structures, 1985, 18, pp. 285-290

2. RILEM Draft recommendation(TC89-FMT), Size-effect method for determining fracture energy and process zone size of concrete, Materials and Structures, 1990, 23, pp. 461-465

3. RILEM Draft recommendation(TC89-FMT),Determination of fracture parameters(K_{Ic} and $CTOD_c$) of plain concrete using three-point bend tests, Materials and Structures, 1990, 23,pp. 457-460

4. E. Brühwiler, and F.H.Wittmann, The wedge splitting test, a method of performing stable fracture mechanics tests, International Conference on Fracture and Damage of Concrete and Rock, 1988, Vienna, Austria

5. Y.Murakami, Stress intensity factors handbook; vol. 1, Pergamon Press, 1987, pp.13-32.

Fracture Toughness of Cementitious Materials Using Small Size Specimens

W. Jiang, X. Wu and D.M. Roy
Materials Research Laboratory, The Pennsylvania State University
University Park, PA 16802, USA

ABSTRACT

The topic of this paper is focusing on fracture toughness of cementitious and concrete materials and lab technology. The objective of the present investigations is to develop the experimental technique based the *J*-integral to obtain K_{1c} and G_{1c} in an indirect way using small size specimens. Getting what was wanted for with high-toughness concrete, the different strengthening mechanisms were studied.

INTROUCTION

Earlier investigations in the fracture of quasi-brittle materials assume the validity of linear-elastic fracture for the laboratory specimens employed and their toughness parameters such as K_{1c} and G_{1c} are determined. However, such parameters as obtained from normal laboratory sized specimens are found to be dependent on the specimen size. As a result, very large specimens (over 1 meter) are required to obtain the true K_{1c} value. Such specimens sizes are clearly impractical in the laboratory.[1,2]

J-integral

The *J*-integral introduced by Rice can be interpreted as the area of tension-softening curve [1], which is defined as the functional curve between the traction across a crack plane and the separation distances of the crack faces in a uniaxial tension specimen quasi-statically loaded to complete failure. The path independent nature of this integral allows the integration path to be taken close or sufficiently far from the crack tip.[3,5] It is equivalent to the critical energy release rate G_c under small scale yielding condition. G_c is related to through the equation

$$J_c = G_c = (K_{1c})^2 / E \qquad \text{(for plane stress conditions)}$$

Hence, from this relation, the linear-elastic fracture parameter K_{1c} can be obtained. *J*-integate can be obtained experimentally from a compliance test by loading two precracked specimens with slightly different crack lengths. If the load P and the load point displacement Δ are measured simultaneously in the test, *J* can be obtained in terms of d from the area *A* (Δ) between the two *P*-Δ curves up to a load point displacement value of Δ.

$$J\ (\Delta) = (1/B)[A\ (\Delta)/(a_2-a_1)]$$

Where *B* is the width of the specimen and (a_2-a_1) is the difference in crack length.

Strengthening and toughening mechanisms

The history of the attempts to strengthen concrete is almost the history of engineering. Numerous mechanisms for strengthening of concrete have been advanced. New concrete have been developed with and without such knowledge. Table 1 gives the description of some of the mechanisms involved and the processes employed.

TABLE 1
Major concrete strengthening mechanisms

Mechanisms	Associated effect
Admixture-modified	
a) Chemical	effective dispersant promotes denser packing, reducing water requirement
b) Mineral	DSP(densfied systems containing homogeneously arranged, ultra-fine particles-silica fume or fly ash)
c) Polymer (water soluble)	MDF(macro-defect-free); allows high shear processing
Mechanical compaction	utilizes intense mechanical compaction which overcomes the inter-locking surface forces and pack the concrete as densely as permitted
Fiber reinforcing	the cracks are stopped or deflected by the presence of the fibres at the interface and the work of fracture is often dramatically increased
Polymeric reinforcing	polymer fills tiny pores and flaw, increases density, improves the cement-aggregate bonding, reduces stress concentrations
Autoclave curing	fine and close in the texture, well and high percentage crystalline hydrate

EXPERIMENTAL

Cement used in this research was the Lafarge product "Secar 71" high alumina cement. Fine aggregates were ASTM standard sand. Coarse aggregate is sieved before use so that the maximum sized aggregate pass through a No. 8 screen. The mix proportions: for concrete, cement: sand: aggregate :water :: 1.0: 2.75: 2.75: 0.35; for mortar, 1.0: 2.75: 0 : 0.3. Specimen size dimensions: for mortar and concrete, 350x80x40, for cement paste 60x10x10mm. The two different a/w (crack depth/beam depth) ratios were 0.4 and 0.5. The notch was cut in a tension side of beam using a 0.2mm thick diamond saw. Table 2 lists the preparations of specimens tested in this work. The details can be found in respective reference.

The specimens were tested at an age of 28 days. The measurement of fracture toughness of cement paste, mortar, and concrete have been conducted by the single-edge-notch-beam method, in the three-point bending test, the load and load point displacement are measured simultaneously. Signal output was recorded by computer data acquisition system and sent immediately to an IBM PC where the data were stored. The data are analyzed numerically. For each set of raw data, values are obtained by interpolation. The averaged values of P and δ for each crack length at the pre-selected Δ values are then computed as $P_1(\Delta)$, $\delta_1(\Delta)$, $P_2(\Delta)$ and $\delta_2(\Delta)$, respectively. Two specimens with various crack lengths are prepared and loaded to fracture as indicated in Figure 1. At each Δ, we compute $J(\delta)$ by numerical integration of $P_1(\Delta') - P_2(\Delta')$ from $\Delta' = 0$ to Δ and divided by $B(a_2-a_1)$. Also, δ is obtained from $(\delta_1(\Delta) + \delta_2(\Delta))/2$. Hence, a J-δ curve can be obtained.(Figure 3)

Young's modules of elasticity was obtained from the flexure of a beam using the equation

$$E = (kl^3/4bd^3)*10^{-3}$$

Where E is Young's modulus of elasticity (GPa), k the slope of the load-deflection plot (Nmm^{-1}), b the beam width (mm), d the beam depth (mm) and l the beam span (mm).

TABLE 2
The preparations of specimens

Materials	Preparation	Reference
1. hcp (hydrated cement paste)	water/cement = 0.3	
2. hot pressing paste	50,000 psi, 80 °C	[6]
3. MDF paste		[7]
4. mortar	ASTM C109	
5. polymer impregnated mortar		[8]
6. plain concrete	ASTM C116	
7. DSP concrete	5% silica fume	[11]
8. PIC (autoclaved)		[8]
9. carbon FRC	8% Vol, 6mm (Stackpole)	[9]
10.polypropelene FRC	2%, 0.5"	[10]

PIC = polymer impregnated concrete; FRC = fiber reinforced concrete.

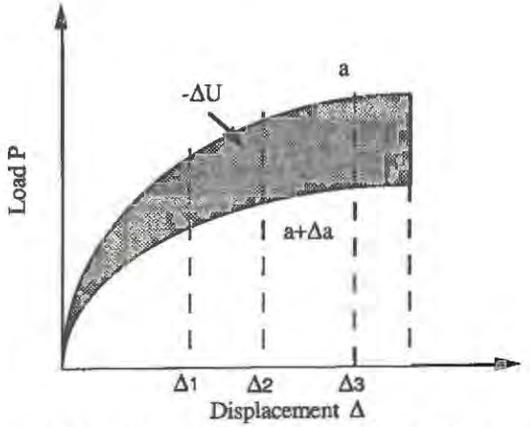

Figure 1 Load-displacement curves for speciments having crack lengths of a and a + Δa.

RESULTS AND DISCUSSION

Figure 2 schematically illustrates the typical load vs load point displacement characteristics exhibited by paste, mortar and concrete. All specimens were same size, but the paste was specially made by MDF cement.

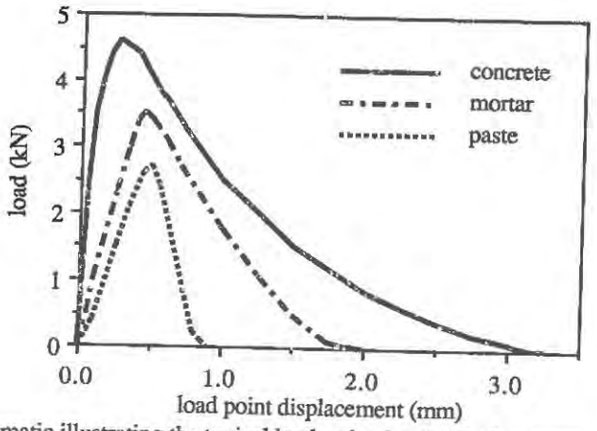

Figure 2. Schematic illustrating the typical load vs load point displacement .

Experimental results of toughness under effect of different toughening mechanisms are shown in Figure 3.

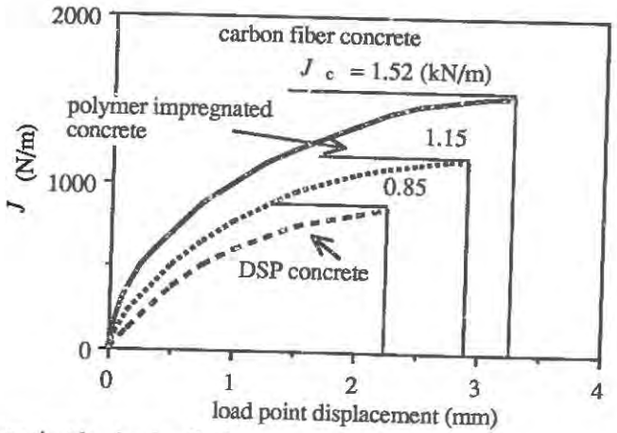

Figure 3. J against load point displacement curve.

Figure 4 shows the range of fracture energy obtained for variety of concrete, mortar and paste, based on J-integral of the multiple-specimen method.

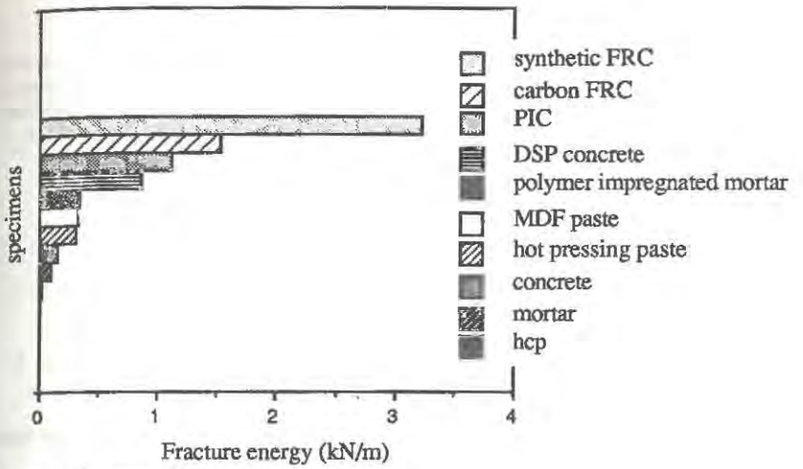

Figure 4. Fracture energy of specimens.

Table 3 lists J-integral, Young's modulus of elasticity, E which were from test, and critical stress intensity Factor, K_{1c} which was calculated from the equation of $J_c = (K_{1c})^2/E$ for different concrete, mortar and paste.

TABLE 3
J-integral, Young's modulus of elasticity and critical stress intensity Factor

Materials	J-integral (kN/m)	E (GPa)	K_{1c} (MPa·m$^{1/2}$)
1. hcp (hydrated cement paste)	0.016	19	0.304
2. hot pressing paste	0.31	24	2.78
3. MDF paste	0.32	25	2.82
4. mortar	0.11	20	1.48
5. polymer impregnated mortar	0.35	26	3.01
6. plain concrete	0.16	22	1.87
7. DSP concrete	0.85	28	4.88
8. PIC (autoclaved)	1.12	30	5.79
9. carbon FRC	1.52	32	6.97
10.polypropelene FRC	3.23	36	10.78

The difference between the J-integral technique we use here and the RILEM GF test [4] is that In their test, pre-cracked specimens with only one crack size is need and only the apparent critical energy release rate can be determined, in our test, two kind of crack size are used and more information is provided. Also it is thought that the value of G_c we obtained will be subject to a much smaller size dependence than RILEM test value. The size dependence is mainly due to damages outside the cracking plane which tends to increase with the specimen size. In our case, G_c is obtained from the different in energy of two specimens with slightly different crack size. The irrecoverable losses will tend to compensate each other for the two specimens and hence the size dependence can be greatly reduced.

CONCLUSIONS

J-integral, an indirect experimental technique is developed to obtain the critical stress intensity Factor, K_{1c}. Three-point bending test was employed. The test involved only laboratory-sized specimens and can be easily performed without the need of mortification of testing machines. Our results are found to be in good qualitative agreement with those obtained by the other tests.

REFERENCES

1. Leung, C.K.Y. and Li, V.C., Determination of fracture toughness parameter of quasi-brittle materials with laboratory-size specimens. J. Mater. Sci., 1989, **24**, 854-62.

2. Ouyang, C. and Shah, S.P., Geometry-dependent R-curve for quasi-brittle materials. J. Am. Ceram. Soc., 1991, **74** [11], 2831-36.

3. Westerlind, B.S., Carlsson, L.A. and Andersson, Y.M., Fracture toughness of liner board evaluated by the *J*-integral, J. Mater. Sci., 1991, **26**, 2630-36.

4. Karihaloo, B., Fracture Mechanics Test Methods for Concrete, ed. S.P Shah and A. Carpinteri, Chapman and Hall, London, 1991, pp. 1-69.

5. Gdoutos, E.E., Fracture Mechanics Criteria and Applications, Kluwer Academic Publishers, The Netherlands, 1990, pp. 171-76.

6. Roy, D.M. and Grouda, G.R., High strength cement paste, hot pressing, Cem. Concr. Res. 1973, **3**, pp. 807-20.

7. Park, C.K., Silsbee, M.R. and Roy, D.M., Toughening of MDF-OPC Composites, Mat. Res. Soc. Symp. Proc. Vol. 211, 1991, pp. 237-246.

8. Feldman, D., Polymeric Building Materials, Elsevier Science Publishers, England, 1989, pp.209-251.

9. Li, V.C., Fracture Resistance Parameters for Cementitious Materials and Their Experimental Deterinations, In Application of Fracture Mecanics to Cementitious Composites, ed. S.P. Shsh, HATO-ARW, 1984, pp.431-449.

10. Li, V.C., Backer, S., Wang, Y., Ward, R. and Green, E, Toughened Behavior and Mechanisms of Synthtic Fiber Reinforced Normal Strength and High Strength Concrete, In Fiber Reinforced Cements and Concrete: Recent Developments, ed. E.N. Swamy and B. Barr, Elsevier Science Publishers, England, 1989, pp.420-433.

11. Bache, H.H., CBL report No. 40 from Aalborg Portland, Denmark, 1981.

DAMAGE DETECTION FOR CONCRETE PILES USING A SIMPLE NONDESTRUCTIVE METHOD

MOHAMAD HUSSEIN
Partner, Goble Rausche Likins and Associates, Inc., Orlando, Florida 32809
JOHN GARLANGER
Principal, Ardaman and Associates, Inc., Orlando, Florida 32809

ABSTRACT

Piles are often used as deep foundations to support structural loads. Concrete piles may be either precast and installed with a pile driving hammer, or cast-in-place in a preformed hole. Both pile types can be damaged during installation and also during service. This paper discusses a nondestructive testing method for pile structural integrity assessment. The test is performed by affixing an accelerometer to the pile top and then impacting the pile top with a hand held hammer. The measured acceleration-time record is integrated, the resulting velocity-time record is displayed as a function of pile length, and then studied using elastic one dimensional wave propagation theories. One case history is presented in which a large percentage of the piles so tested were found to be damaged.

INTRODUCTION

Subsurface conditions and structural requirements often dictate the employment of deep foundation systems to support structural loads. Elements for deep foundations (i.e., piles) may be made of timber, steel, concrete, or a combination of these materials. Concrete piles may be precast and installed with a pile driving hammer, or cast-in-place in a preformed hole. They vary in size from 10 to over 100 inches in diameter and can be more than 150 ft in length.

Precast concrete piles may be regularly reinforced, prestressed, or post-tensioned and are mostly square in shape. They are installed with drop, air, steam, hydraulic, or diesel hammers. During driving, piles are subjected to a complex combination of compressive, tensile, torsional, and bending forces. Overstressing the pile material causes damage; fatigue may result in pile damage at lower stress levels. While the installation process itself constitutes a "test" for the soundness of the pile in-place, it can also be the cause of pile structural failure. Common modes of driving-induced pile damage include: crushing at the pile head, toe, or shaft, vertical and horizontal cracking, and failure of splices. Dynamic pile testing by the Case Method is often performed during installation to assess pile driving axial stresses and to evaluate pile structural integrity [1]. In cases where piles are not instrumented during driving, questions sometimes arise concerning their structural integrity.

Cast-in-place piles are produced by excavating holes in the ground and filling them with concrete. A steel reinforcing cage may, or may not, be used. A common method is the continuous-flight auger (CFA) where concrete grout is placed under pressure through the toe of the auger stem starting at the bottom of the hole during auger withdrawal. The constructed shape and structural integrity of this pile type is dependent on: concrete quality, soil conditions, workmanship, and construction procedures. Common modes of pile structural deficiencies are: separation of concrete in pile shaft, necking, inclusions, or voids. Both driven and cast-in-place concrete piles may also be damaged after installation by large lateral movements from impacts of heavy equipment, or slope or retaining wall failures.

This paper presents a method called the Pile Integrity Test (P.I.T.), which is based on low strain impacts and one dimensional wave propagation and reflection mechanics. A case history illustrating the applicability and validity of the method is also discussed.

Low Strain Integrity Testing

Background. With the advent of electronic instrumentation and data processing, there exists today a number of testing techniques to evaluate the structural integrity of deep foundations [2]. Other procedures are excavation around the pile, or drilling and coring through its shaft. Some tests require that the pile be prepared and/or instrumented prior to, or during installation making its random application prohibitively expensive. Stress wave tests can be either "high" or "low" strain [3]. High strain testing requires the presence of a pile driving hammer, or a large drop weight on site. The simplest and most readily applicable method is the low strain technique requiring minimal instrumentation and testing effort.

Wave Mechanics. One dimensional wave mechanics applies to a linear elastic pile that has a length an order of magnitude greater than its width. When impacted at the top, a stress wave travels down the pile shaft at a wave speed, c, which is a function of the material elastic modulus, E, and mass density, ρ (i.e., $c = \sqrt{E/\rho}$). Pile impedance, Z, is the product of cross sectional area, A, and elastic modulus divided by the stress wave speed and is, therefore, a measure of pile cross sectional size and quality.

When the impact induced stress wave, Fi, arrives at a point along the pile length where the impedance changes from Z1 to Z2, part of the wave is reflected up, Fu, and part transmits down, Fd, such that both continuity and equilibrium are satisfied. The downward and upward propagating waves are related to the impact wave by:

$$Fd = Fi[2Z2/(Z2 + Z1)] \quad (1)$$

$$Fu = Fi[(Z2 - Z1)/(Z2 + Z1) \quad (2)$$

For a uniform pile (Z2 = Z1), the impact wave travels unchanged. An example of extreme "nonuniformity" is a free pile end (Z2 = 0), the impact wave will be completely reflected upward and the resulting Fu will be of the opposite sign.

Figure 1 shows that for a compressive downward travelling wave which encounters an impedance reduction at distance, a, from pile top, an upward travelling tension wave will be observed at the pile top a time 2a/c after impact. The figure also shows that a compressive upward travelling wave is generated by soil resistance R at location, b, and is felt at time 2b/c after impact. Other reflections monitored at the pile top are those from the pile toe and the secondary reflection at 4a/c. Low strain integrity testing is based on the premise that changes in pile impedance and soil resistance produce predictable wave reflections at the pile top.

Instrumentation. The testing system consists of an accelerometer (15 g/v), a hand held hammer, dedicated software, and a field data acquisition system capable of converting analog signals to digital form and data processing. The system and method is commonly referred to as the P.I.T. tester. The impact generates accelerations in the 10 to 100 g range and pile strains around 10^{-5} micro strain.

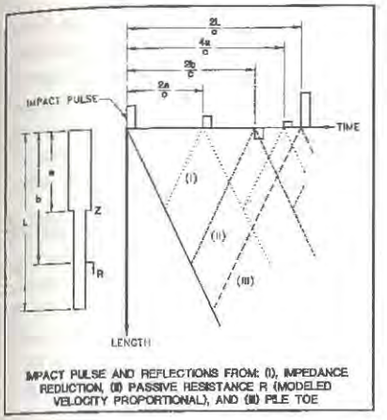

IMPACT PULSE AND REFLECTIONS FROM: (I), IMPEDANCE REDUCTION, (II) PASSIVE RESISTANCE R (MODELED VELOCITY PROPORTIONAL), AND (III) PILE TOE

Figure 1. Impact and Wave Reflections at Pile Top.

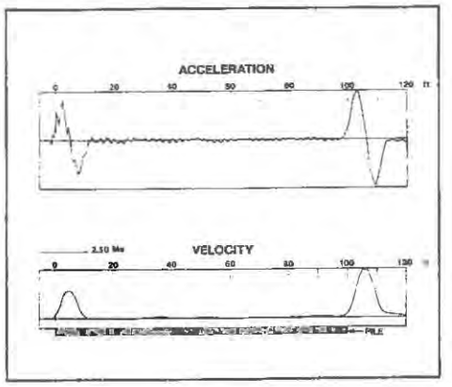

Figure 2. Pile Top Dynamic Data.

Testing and Data Interpretation. Pile preparation simply involves smoothing and leveling of a small area of the pile top. The accelerometer is affixed to the pile top using a jell type material and a hammer blow is imposed to the pile top. The acceleration record created by the impact is integrated and the resulting velocity record is displayed as a function of pile length. Time to length conversion is done using the wave speed. Figure 2 presents a measured acceleration and its integrated velocity record obtained from a test performed before installation of a 24-in square prestressed concrete pile 100 feet in length. An analysis option in the program is an exponential (with time) amplification routine. This option is used to amplify wave reflections which are very small due to pile and soil damping. Another analysis option allows the user to average a number of records. Normally, 4 to 6 test blows are taken for each pile and averaged. The technique is useful in separating effects of random mechanical and electronic noise from relevant reflections.

In addition to visual inspection of the velocity records for wave reflections, additional rigorous dynamic analysis, called PITWAP, can be performed on the measured data to obtain pile shape as a function of length in an interactive signal matching process [3].

Limitations. Wave reflections coming from locations greater than 30 to 40 pile diameters are generally too weak to be detected at the pile top, especially if high soil resistance is present. Gradual changes in pile impedance over a long distance can not be detected since they do not produce sharp wave reflections. Mechanical splices, or severe damage may screen deficiencies from the lower parts of the pile. Cast-in-place piles with greatly varying cross sections, especially in layered soils, can not be analyzed with confidence.

Case History

This case history describes a project where low strain dynamic testing was performed on cast-in-place concrete piles. The job involved the construction of both 1- and 3-story building additions adjacent to an existing 6-story structure, with provisions that another 3 stories may be added to the proposed 3-story building addition in the future. The new construction area had plan dimensions of approximately 60 by 180 ft. Subsurface investigations included 9 SPT borings, 8 CPT soundings, and a ground penetrating radar survey. Geotechnical investigation results indicated a complex, irregular, and nonuniform stratigraphy. The overburden included soft clays, clayey sand, and cemented silts. The bearing layer was limestone containing solution cavities.

Considering the subsurface conditions, structural loads, and the proximity of construction to the existing structure, foundation recommendations were to use nondisplacement deep foundations.

A total of 95 cast-in-place concrete piles were used. The piles were 16 inch in diameter, varied in length between 25 and 95 ft, and were constructed using the CFA method. Because of the potential for damage resulting from heavy construction equipment moving over and around heads of the constructed piles, the presence of cavities in the underlaying rock, and the unexpectedly large amounts of concrete needed to form the piles, it was decided to test a number of the piles for structural integrity.

A total of 46 piles were tested randomly covering the range of soil conditions and pile lengths. Twelve of the tested piles were found broken at locations 2 to 10 ft below pile tops. Four piles had impedance reduction below 18 ft. Two piles indicated bulging in their shafts. Breakage was verified by soil excavation around the broken piles. Fortunately, most of the breakage was above the eventual pile top cutoff elevations. When the piles were broken below cutoff elevations, the broken section was removed, the pile retested, and the pile top was built-up to the requires elevation. Pile impedance reduction or increase could not be verified due to

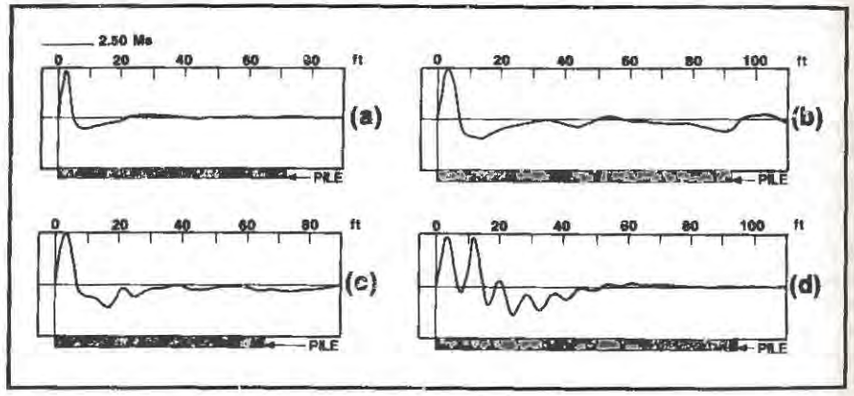

Figure 3. Pile Top Dynamic Records, Case History Piles.

its location at greater depths. Figure 3 presents plots of four velocity histories from four piles, Figure 3a shows a good pile, 3b a pile with a bulge at 35 ft and toe reflection at 95 ft, 3c a pile with impedance reduction at 18 ft, and 3d a pile broken at 8 ft below pile top.

REFERENCES

1. Hussein, M., and Rausche, F., Determination of Driving Induced Pile Damage. Foundations Profondes, Presses Ponts et Chaussies, Paris, 1991, pp. 455-62.

2. Fleming, W.G., Weltman, A.J., Randolph, M.F., and Elson, W.K., Piling Engineering, Surrey University Press, London, 1985, pp., 283-300.

3. Rausche, F., Likins, G., and Hussein, M., Pile Integrity by Low and High Strain Impacts, Application of Stress Wave Theory to Piles, ed. Bengt H. Fellenices, BiTech Publishers, Vancouver, 1988, pp. 44-55.

A TORSIONAL DAMAGE TEST FOR THE ASSESSMENT OF THE DETERIORATION OF CONCRETE

B.I.G. BARR[+], N.J.S. GORST[+] and J.G.M. WOOD[++]
[+] School of Engineering, UWCC, Cardiff, U.K.
[++]Mott MacDonald Group, 20-26 Wellesley Road, Croydon, U.K.

ABSTRACT

A number of tests have been developed for the structural appraisal of alkali-silica reaction (ASR) damaged structures. In one test, cores are subjected to a low cyclic uniaxial compressive load to determine the Damage Index. In another test, cores are subjected to torsional loading which may be considered as an indirect tensile test on the concrete. The main objective of the work reported here was to combine the above two tests by incorporating a Damage Index test into the torsion test - by subjecting cores in the torsion rig to low cyclic loading prior to taking the specimens up to failure. Initial results are presented for three Grades of concrete, lightweight aggregate concrete and polymer concrete.

INTRODUCTION

Standard strength tests to evaluate concrete quality generally involve testing specially prepared and cured control specimens (cubes, cylinders or prisms) cast during the construction period. However, when appraising concrete structures in which concrete quality is uncertain due, in particular, to degradation with time, strength tests must be based on cores taken from the actual concrete in the structure. It is known that with some forms of deterioration, the normal relationships of tensile to compressive strength break down. For example, Nixon and Bollinghaus (1) tested a number of cubes and cylinders suffering from alkali-silica reaction (ASR) and found that ASR appeared to reduce the tensile strength of concrete to a greater extent than the compressive strength.

ASR in concrete produces a gel which, in the presence of sufficient moisture, can expand causing cracking in concrete structures. The Mott MacDonald Group in conjunction with others has developed a number of tests for the structural appraisal of ASR damaged structures. In one of these tests, cores taken from damaged structures are initially tested under a low cyclic uniaxial compressive load and the strain response is measured. This test (known as the Stiffness Damage Test (2)) yields a number of parameters including the Damage Index which is the area of the hysteresis loops (over 4 cycles) normalised over the stress range.

A second test which has been developed is one in which concrete cores are subjected to torsional loading (3). The resulting shear stress state, on a representative volume of concrete, is used to evaluate the shear strength properties of the concrete. The application of torsion alone to a concrete core (or cylinder) will produce pure shearing stresses on certain planes equal in magnitude to the principal stresses (i.e. diagonal tension and compression stresses). Thus the torsion test may be considered as an indirect tensile test on the concrete cores.

The main objective of the work reported here was to combine the benefits of the above two test methods into one test. The Damage Index test method has been added to the torsion test so that Damage Index results are obtained by subjecting cores in the torsion rig to low cyclic loading prior to taking the specimens up to failure.

EXPERIMENTAL DETAILS

The loading arrangement for applying torsion to the cores/cylinders is illustrated in Fig.1. Two supports provide upward reactions, a third support provides a downward reaction and the load P is applied at the free end. As the load P is applied, corresponding reactions of P are induced at the three supports. The load is transferred into the cores/cylinders via a set of split collars. The collars are attached at both ends by means of an adhesive. Only standard 100mm diameter cylinders, 200mm long, were used in the work reported here. The collars were 30mm wide, leaving a clear length of 140mm being subjected to the torsional stress state.

Three concrete mixes were designed to give 28 day cube strengths of 30, 55 and 75 N/mm^2. The mix proportions for these three mixed are given in Table 1. The Grade 75 mix contained 10% microsilica (by weight of the cement content). In addition a lightweight concrete mix and a polymer concrete mix were prepared in this study.

TABLE 1
Details of concrete mixes

Ref. No.	f_{cu} (N/mm^2)	cement : sand : coarse agg.	W/C ratio
1	30	1 : 2.9 : 5.6	0.7
2	55	1 : 1.8 : 2.8	0.5
3	75	1 : 1.8 : 2.8	0.4

A typical load-displacement graph is shown in Fig.2. Fig.2 shows a typical response recorded via the Instron machine and is a record of the load V. displacement of the point of application of the load, i.e. there is considerable uncertainty regarding the actual response of the test specimen itself in this case. Fig.2 shows a linear relationship up to point A and thereafter a limited amount of softening is observed up to the maximum load at point B. Generally point A corresponds to approximately 80% of the maximum load. All the cylinders failed in diagonal tension with the inclination of the failure plane being in the range 40^o to 50^o to the longitudinal axis.

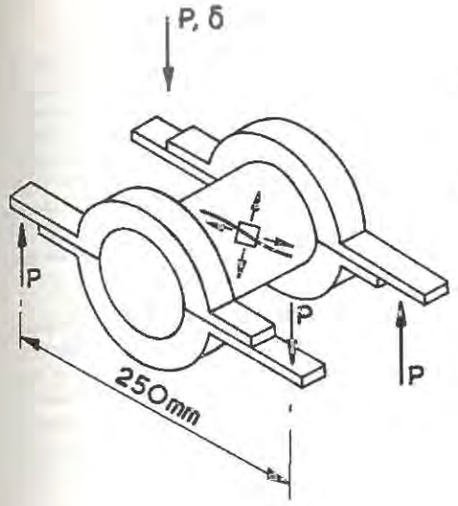

Fig.1 Torsion test rig

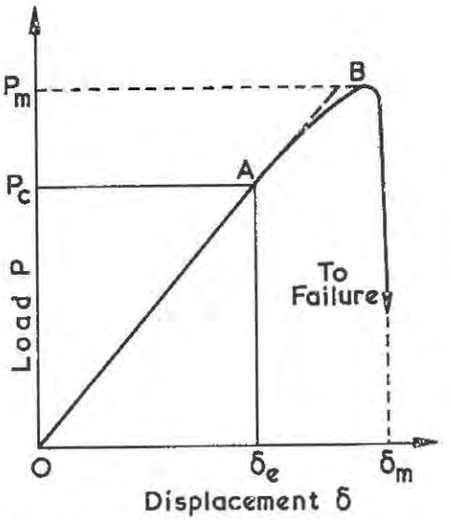

Fig.2 Typical load-deflection graph from Instron machine

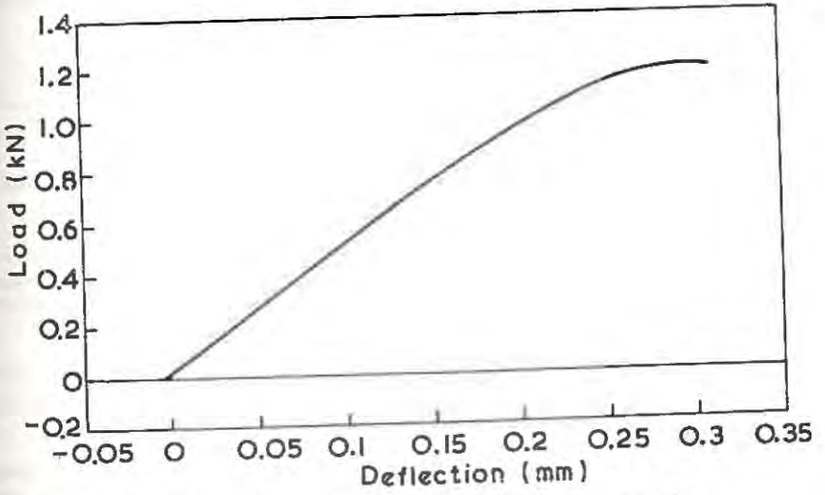

Fig.3 Typical load-deflection graph for actual test specimen

Recently the torsion test has been developed further by the addition of more instrumentation. A device has been developed which allows the actual rotation of the cylinder over a 120mm gauge length to be determined. This information is recorded by a PC and a typical load-deflection graph is shown in Fig.3. Fig.3 gives the load-deflection graph corresponding to the actual response of the test specimen over a 120mm gauge length. Fig.3 differs significantly from Fig.2 and shows that microcracking is taking place at a much lower load than that suggested by Fig.2.

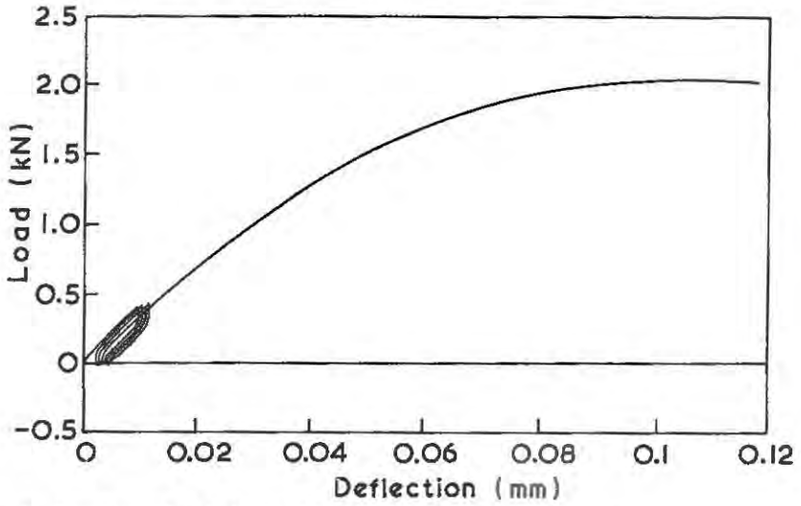

Fig.4 Complete load-deflection graph for combined test

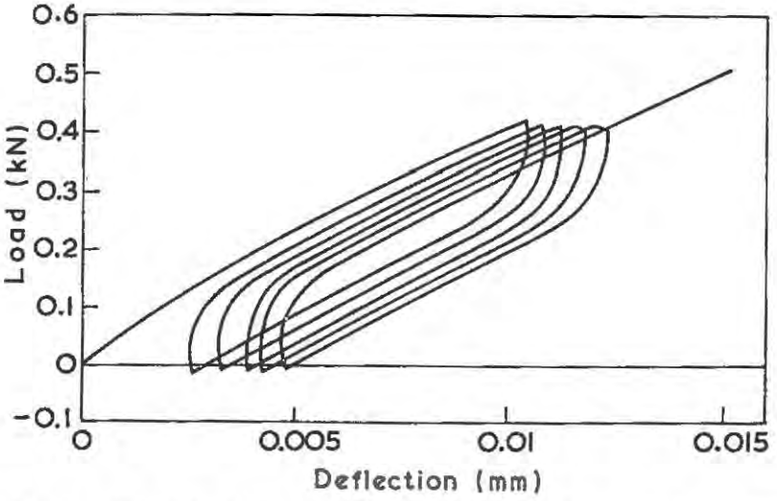

Fig.5 Expanded view of load-deflection graph due to cyclic loading

Figs.4 and 5 show a typical result obtained by incorporating the Damage Index test into the torsion test. Fig.4 shows the complete load-displacement curve for a given test whereas Fig.5 shows an enlarged view of the load-displacement response due to the 5 loading-unloading cycles generated at the start of the test. The results illustrated by Fig.5 were stored on a compacter and a program has been developed to measure directly the area contained within each of the last four hysterisis loops. The average area was then determined and divided by the load range used in the loading-unloading cycles to give the Damage Index for the test specimen. Thus the Damage Index is measured in mm.

RESULTS AND DISCUSSION

A typical set of results is presented in Table 2. Three Grades of normal density concrete, a lightweight aggregate (Lytag) concrete and a polymer concrete have been studied. The three normal density concretes represent typical low, medium and high strength concretes. The lightweight aggregate concrete was designed to have the same strength as the low strength concrete and was studied, in particular, in terms of the fracture planes developed. The polymer concrete mix is typical of that which has been studied extensively in the same laboratory in terms of its mechanical and physical properties.

The average shear strengths (which are also the values of the tensile strengths) for the three normal density concretes are as expected. As the strength is increased the Damage Index results decrease - also as expected. The strength of the lightweight concrete is slightly higher than the strength of the nominal Grade 30 concrete and the Damage Index is also higher at 2.84. This result is also as expected since more microcracks are developed at the matrix-aggregate interface in the case of lightweight concrete.

All the fracture planes were within the range 40^{o} to 50^{o} for the angle between the fracture plane and the longitudinal axis. The fracture planes tended to go around the coarse aggregate for all the normal density concretes, whereas in the case of the lightweight aggregate the fracture

TABLE 2

Typical results for Damage Index and Shear Strength

Material	f_{cu} (N/mm^2)	P_{max} (N)	Average shear strength (N/mm^2)	Damage Index (mm x 10^{-3})	Average Damage Index (mm x 10^{-3})
Grade 30 Concrete	29.0	2020		2.25	
		1945	2.51	2.43	2.41
		1958		2.54	
Grade 55 Concrete	57.5	2479		1.99	
		2737	3.19	2.42	2.24
		2292		2.31	
Grade 75 Concrete	74.6	3426		1.93	
		4005	4.68	1.93	1.99
		3604		2.11	
Grade 30 Lightweight Concrete	32.5	2047		3.46	
		2212	2.64	2.27	2.84
		1958		2.80	
Polymer	38.0	3848		9.88	
		3673	5.17	9.09	10.75
		4665		13.28	

planes continued directly through the aggregate. The polymer concrete fracture planes tended to show a more typical spiral fracture surface than that observed for the ordinary concrete specimens.

In addition to the three test results given in Table 2 (for the five concretes) a companion set of three cylinders were tested. This second series of tests was carried out without the low cyclic loading at the start of the test, i.e. the loading was continuous from the start to the point of fracture. The objective of these companion tests was to investigate whether the low cyclic loading had an effect on the fracture load. The results showed that the load at failure was not affected by the cyclic loading.

The test results obtained from the polymer concrete specimens are of interest. Although the compression strength was only 38 N/mm^2, the average tensile strength was almost two times that of comparable ordinary concrete. The Damage Index results were greater as expected - polymer exhibits a well-known hysterisis effect with cyclic loading.

CONCLUSIONS

The work reported here shows that it is possible to combine the Damage Index test and the Torsion test into one test. The initial test results, obtained for five concretes, are commensurate with common sense. Further research is required in this promising area so that damage and tensile strength (determined from tests on cores) can be used to assess the strength of existing structures and, in particular, structures which are being attacked by ASR. Work is currently under way to investigate the major parameters which may affect the response of cores and/or cylinders to torsion - these include size effects, aspect ratio, compression strength, aggregate size and shape etc.

REFERENCES

1. Nixon, P.J. and Bollinghaus, R., The effect of alkali aggregate reaction on the tensile and compressive strength of concrete, Durability of Building Materials, Elsevier Applied Science Publishers, London, 1985, Vol.2, pp243-248.

2. Chrisp, T.M., Wood, J.G.M. and Norris, P., Towards quantification of microstructural damage in AAR deteriorated concrete. In Fracture of Concrete and Rock: Recent Developments (Eds: Shah, Swartz and Barr), Elsevier Applied Science Publishers, London, 1989, pp419-427.

3. Norris, P., Wood, J.G.M. and Barr, B., A torsion test to evaluate the deterioration of concrete due to alkali-aggregate reaction, Magazine of Concrete Research, 1990, Vol.42, No.153, pp239-244.

ACKNOWLEDGEMENTS

The second author has been supported partly by an SERC studentship. The authors also wish to acknowledge the contribution made by the Natural Resources Group plc towards supporting this project - in particular the work on polymer concrete. The authors also wish to acknowledge the contribution of Dr. Z.A.Y. Tokatly in the early days of the development of the torsion rig.

Long Term Tests on Concrete According to Micromechanics of Damage

H. Schorn

Introduction

Tests for measuring long term behaviour of concrete as creep and long term strength usually are planned in accordance to the strength of the material. Using strength as a reference value contains two important disadvantages:

1. Due to unavoidable scattering results of measurements of strength according to the microscopical inhomogenious concrete structure, strength only can be known as an average. In long term loading of a particular body the percentage of strength actually existing cannot be known exactly.
2. In long term deformation mechanisms of deformation caused by viscosity of material and caused by microcrack formation and propagation cannot be distinguished from each other.

Thus prediction of long term behaviour depends on some unknown conditions and is accordingly inaccurate. It seems better not to use the strength as a reference value for long term loading but a reference in better accordance to micromechanics of damage of material structure.

Crack formation and propagation

In previous work [1] it has been shown that damage process of concrete can be divided into three parts. Fig. 1 shows these parts at a load elongation curve of an ideal uniaxially tensile loaded unnotched concrete structure. In the zero point of the diagram some irregular situated and orientated microcracks are existant due to internal stress states in the microstructure. During the loading process these microcracks do not propagate - contrary to commmon assumption! Instead of propagation of existing microcracks new microcracks will be formed in loading process. Microcrack forming does not stop at point of strength. It continues even in the unloading branch of the curve up to point B in fig. 1. From B a macrocrack propagation is starting which can be fully described by (non linear) fracture mechanics.

From the zero point up to point A in the ascending branch of the curve the new formed microcracks are distributed stochastically and orientated irregular. Between point A and point B in the descending branch of the curve zones of microcrack

accumulation occur which lead to strength and form a transition to the begin of macrocrack opening, point B in fig. 1. These microcrack accumulation cannot be described by fracture mechanics easily. There is needed a particular method for determing fracture energy, e.g. using the proposal of Hillerborg [2].

The first formation of microcrack accumulation characterizes that state of material structure which determines strength. Using a very precisely working test apparatus you can stop the loading process so quickly that crack accumulation in the body will occur but will not become critical. A description of this testing method using unnotched tensile loaded specimens is given in [3]. Important alterations of material structure occur in point A as well as in point B in fig. 1. Point B marks the begin of a material structure and a crack propagation process which fulfills the conditions of (non linear) fracture mechanics. Using this point as a reference for long term loading seems not ideal for practical purposes; usually a long term loaded body is not strained beyond the point of strength.
Point A in fig. 1 in the ascending branch of the curve is more suitable as reference. The irregular distributed microcracks now begin to form microcrack accumulation zones which are mainly orientated normally to uniaxial tensile load direction. Certainly at point A the microcrack forming process has not yet finished; but a material structure as characterized by microcrack accumulation zones at point A will alter its structure under long term load mainly by propagating microcrack accumulations, less by forming new cracks. The influence of new formed microcacks is negligible.

From the point of view of fracture mechanics, B in fig. 1 is undoubtedly the characteristic point in alteration of material structure. From the point of practice it seems better to choose A in the ascending branch of the curve which marks the first characteristic alteration in material structure due to loading by forming a microcrack accumulation zone. Which point, A or B, ever will be chosen, the specimens do not become destroyed in short time loading. The characteristic microcrack pattern becomes imprinted on the material structure. Thus the long term test can be carried out using the same body loaded in short time test before. The disadvantage number 1 as named in the introduction does not exist.

Long term damage process

For tests specimens of a size of 40 mm x 40mm x 160 mm were made from concrete with a maximum size of aggregete of 4 mm. The mix proportions are put together in table 1. In tensile tests the specimens became tensile loaded as

described in [3]. Using this test device the position of microcrack accumulation (see point A in fig. 1) can be identified. Now the specimens became deloaded. In the following long term loading the deformation can be measured including the accumulation zone as well as excluding, see distances 1 and 2 in fig. 2.

If measurement 1 and 2 show the same increase of elongation under sustained load, the stress obviously is low enough for being irrelevant for any crack propagations. Higher stress levels lead to very different results of deformation measurements in 1 and 2. The deformation in 1 increases rapidly and up to high values. Fig. 3 contains a diagram as measured for the distance 1, fig. 2, containing the microcrack accumulation zone. At all times the fracture energy can be determined in a specimen destroying test as usual. Determing fracture energy after different periods of time on several specimens quantifies the improvement of crack propagating during the long term loading.

You not only can find that level of stress which leads to crack propagating under sustained load. All other influences on crack propagating, e.g. dynamic loading, can be studied in the same way. Using this method you have not to wait a long time until the stress and strain states have formed a propagating microcrack pattern - contrary to commom methods. And you are sure that you are measuring the crack propagation process separately from other superimposing influences. Even corrosion processes may be quantified by this method if they lead to an alteration of material structure by crack opening or crack propagating.

Conclusions

In common long term tests you cannot distinguish influences of viscosity and microcrack formation from crack propagation. To avoid this disadvantage an experimental method can be used as follows:
- Specimens become preloaded in a very precisely tensile test just before point of strength. In the body a microcrack accumulation zone will occur.
- Measuring microcrack affected as well as microcrack non-affected zones of the same body, the influence of crack propagation can be shown indepedent from influence of viscosity and microcrack formation due to long term loading.

References

[1] Schorn, H.: Strength-independent evaluation of fracture energy (G_F) of brittle materials. International Conference Fracture Processes in Brittle Disordered Materials. Noordwijk, NL, June 1991.
[2] Hillerborg, A.: Analysis of One Single Crack. Fracture Mechanics of Concrete, edited by F.H. Wittmann. Elsevier Science Publishers, Amsterdam 1986.

[3] Schorn, H.; Berger-Böcker, T.: Test Method for Determing Process Zone Position and Fracture Energy of Concrete. Experimental Techniques, June 1989, pp 29-33.

portland cement	315 kg/m^3
aggregate	1733 kg/m^3
emulsion	139 kg/m^3
w/c ratio	0.50
p/c ratio	0.28

Table 1: Mix proportions of a polymer modified concrete with high polymer content (as example)

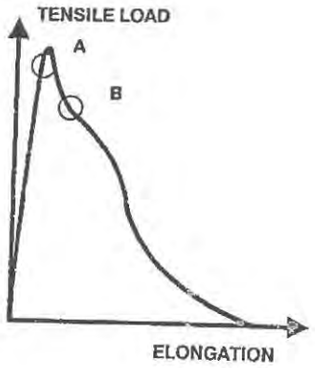

Fig. 1: Tensile load elongation curve

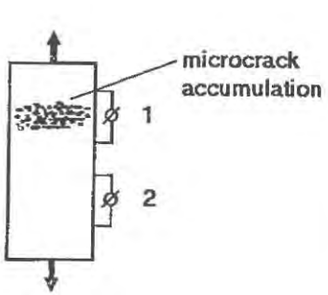

Fig. 2: Specimen of 40 mm x 40 mm x 160 mm size, containing a microcrack accumulation zone in 1

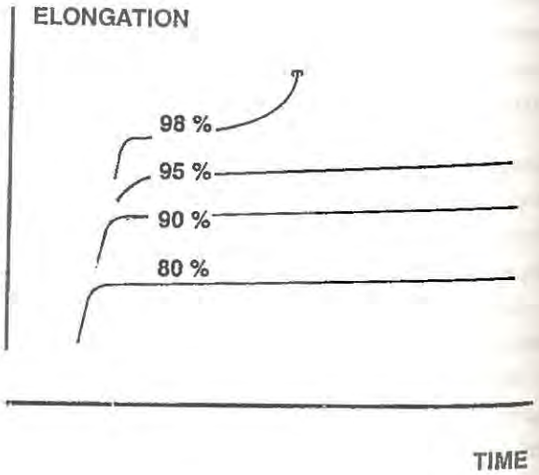

Fig. 3: Elongation due to loading and suatained load for specimens of the same material, loaded in percentage of that load microcrack accumulation was detected (see point A in fig. 1)

The diagram shows the first 5 minutes of the test.

STRAIN MEASUREMENTS FROM THE GREY LEVELS OF REAL TIME X-RAY IMAGES

CRAIG A. RUTLAND, Capt, USAF, MING L. WANG, HOWARD L. SCHREYER
Departments of Civil and Mechanical Engineering
The University of New Mexico, Albuquerque, New Mexico 87131

ABSTRACT

Recent tests [1] have shown that X-ray equipment is now sufficiently sensitive so that changes in densities due to changes in loads on specimens can be detected when X-ray images of the specimen are enhanced and compared. Prism specimens of aluminum and cement mortar were tested in uniaxial compression and simultaneously X-rayed. The grey levels from X-ray images taken during loading are compared. Results show that the strains in the specimen can be determined from the changes in the grey levels.

INTRODUCTION

X-ray radiography has been widely used to determine density distributions and displacement fields within various materials and, in particular, soils. Using X-ray radiographs of sand specimens, Vardoulakis [5] has shown that dilatation occurred in a thin shear zone at failure and that the density of this zone was qualitatively different from the soil outside of this shear zone. Similar changes in the density of cementitious specimens has been shown [1].

In this study the possibility of using these qualitative changes in X-ray images to determine strains within a specimen is investigated. The theoretical relationship between strain and image intensity is first derived for general loading situations. Simplifying assumptions are made to make the relationship tractable. Experimental data are given to show the feasibility of the procedure for measuring strains. The basic principle of this technique is that changes in the X-ray intensity passing through a specimen represents changes in the density of the material and/or the X-ray path length.

THEORETICAL ANALYSIS

At various times during the test, images are digitized (captured) and stored on a computer for later analysis. When an image is captured it is broken into discrete elements called pixels. The shade of grey (grey level) of each pixel

is a measure of the average light (X-ray) intensity. Each pixel represents an area that is parallel to the X-ray detector and perpendicular to the path of the X-rays.

In general, the intensity of X-rays passing through a material can be calculated using the following formula [6]:

$$I = I_0 \, \beta(\mu x) \, e^{-(\frac{\mu}{\rho})\rho x} \qquad (1)$$

where I_0 is the intensity of the X-rays entering the material and I is the transmitted intensity of the X-rays. The linear attenuation factor is denoted by μ and ρ is the mass density. The mass attenuation factor is μ/ρ which is only a function of the material composition and the energy of the photons of the X-ray. The path length that the X-rays must travel through the material is denoted by x. $\beta((\mu/\rho)\rho x)$ is the build-up factor or forward scatter and is a function of the mass attenuation factor, mass density, path length, and beam geometry. For narrow beam tests $\beta((\mu/\rho)\rho x) = 1$. When small deformations and strains occur the buildup factor in the strained state is essentially the same as that in the unstrained state and the ratio of build-up factors can be set to 1.

As a specimen is loaded, the density and/or the X-ray path length change, causing a change in the transmitted intensity of the x-rays. These changes in path length and density are functions of the applied strain (ϵ) and the lateral extension (Poisson) ratio (υ)[1]. If a specimen is loaded in pure shear, there is no change in density, however, the X-ray path length may change depending on the orientation of the X-rays.

Suppose a specimen with nominal height, width, and depth of H, W, and D, is subjected to a multiaxial strain. One face of the specimen is perpendicular to the X-rays which pass through a material path of length D. ρ_1 and D_1 represent the density and X-ray path length prior to loading. The density and X-ray path length after loading are expressed in terms of ρ_1 and D_1:

$$\rho_2 = \frac{\rho_1}{(1 + \varepsilon_{vol})} \qquad D_2 = D_1(1 + \varepsilon_d) \qquad (2)$$

where tension is positive. The normal components of strain in the H, W, and D directions are ϵ_h, ϵ_w, and ϵ_d. By substituting these relations into equation (1), the change in intensity, ΔI, for a given strain is obtained:

$$\Delta I = I_1 - I_2 = I_1 \left[1 - \left(\frac{B_2}{B_1}\right) e^{(\frac{\mu}{\rho})\rho_1 D_1 (1 - \frac{1 + \varepsilon_d}{1 + \varepsilon_{vol}})}\right] \qquad (3)$$

During the test only one measure of ΔI is obtained for a load increment. Equation (3) has two unknowns (ϵ_{vol} and ϵ_d or ϵ_h and ϵ_w). Therefore, additional measures of the strains must be obtained or the number of unknowns must be reduced to make this procedure tractable.

[1] Lateral extension ratio is used in lieu of Poisson ratio to emphasize that this ratio may not be constant for some materials.

In the case of uniaxial stress the change in intensity (ΔI) is:

$$\Delta I = I_1 \left[1 - \left(\frac{B_2}{B_1}\right) e^{(\frac{\mu}{\rho})\rho_1 D_1 (1 - \frac{1}{(1 + \varepsilon_h)(1 - \upsilon\varepsilon_h)})}\right] \qquad (4)$$

where X-rays pass through the depth (D). One equation with two unknowns (ϵ_h and υ) is obtained. Similar equations can be developed for other load paths.

EXPERIMENTAL TECHNIQUE

Equipment
All specimens were loaded in uniaxial compression using an Instron 1323 Biaxial Loading System. Continuous X-rays of the specimens were taken with an IRT IXRS 160/3200 Industrial X-ray System. The fluoroscopy was accomplished using a six inch image intensified area X-ray detector and a CCD camera. Images from the tests were digitized using an IMAGING Technologies, Inc. FG100-1024 Video capturing board in an IBM AT computer.

Specimens
Six prismatic specimens were tested. 3 aluminum blocks (3" X 2" X 1.5") and 3 cement mortar blocks (1.5" X 1.5" X 3") were tested. Strain gauges were attached to opposite sides of the specimens. Two gauges were placed on each side, one for axial strain, the other for lateral strain. Each set of gauges was placed at the mid height of the specimen. These gauges were used to determine the lateral extension ratio and to provide a measure of the axial strain to compare with the results obtained from the changes in grey levels.

Test Procedure
The aluminum specimens were compressed uniaxially to 100 Kips. The mortar samples were compressed uniaxially to failure. No steps were taken to relieve the friction between the platens and the specimen for the aluminum and two of the mortar specimens. The failure zones of the mortar were angled and passed through the corners of the specimens. The friction was reduced for the third mortar specimen by placing a .01 inch thick sheet of rubber between the platens and the specimen. The resulting failure zone was characterized as vertical splitting. Load-displacement, strain, and X-ray data were collected.

In all tests a piece of aluminum (not loaded) was placed near the specimen so that it could be seen in the X-ray images. This aluminum acted as a control, which allowed the images to be corrected for slight temporal variations in the X-ray intensity. For the materials and energy levels used the expected change in grey levels are approximately .1% to .5% of the intensity of the original image, I_1. Therefore, it is critical that any changes in the intensity of the source X-ray beam be accounted for.

Data Reduction and Analysis
The average grey level of the unloaded image (I_1) was calculated. The difference in grey levels between to the loaded and unloaded images was calculated ($\Delta I = I_1 - I_2$). The average differences were normalized by dividing by the average intensity of the original image, I_1. The normalized average differences in grey levels were plotted against the axial strain.

Data from the strain gauges were used to determine the value of the

lateral extension ratio and how it varies (mortar) with axial strain. The lateral extension ratios obtained from these gauges were used to obtain the theoretical relationship between change in grey level and axial strain. The theoretical relation between axial strain and normalized change in grey level was plotted and compared to experimental results.

RESULTS

ALUMINUM

The lateral extension ratio that was determined from the strain gauge data was .32 for the aluminum. The linear attenuation factor, μ, for aluminum X-rayed at a photon energy of 100 Kev was taken from reference [12] to be 1.1684/in. Figure 1 shows predicted and experimental values of the normalized average change in grey level, $\Delta I/I_1$, versus the strain for the three aluminum samples. The predicted values follow the observed values closely.

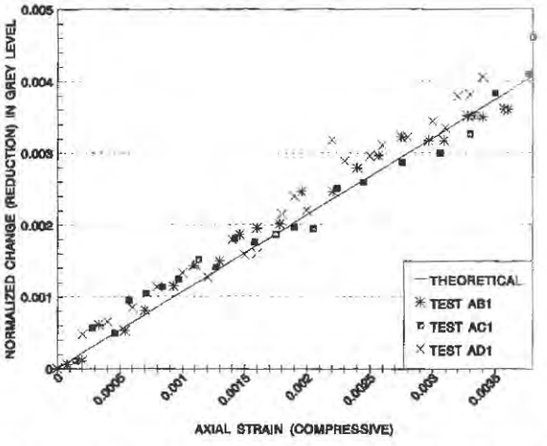

Figure 1: Normalized change in grey levels axial strain for aluminum

MORTAR

A plot of the lateral extension ratio versus the axial strain is shown in Figure 2 for the first test without relief of end confinement. Figure 2 also shows the values of the lateral extension ratio that were used to analyze the data from that test. Figure 3 shows the predicted and observed average change in grey level versus axial strain. The observed values show that there is more compaction than predicted. Dilatation occurred later than predicted. The specimen begins to dilate in the center much sooner than in the regions close to the platens. The failure zone for the specimen was angled and passed through the corners of the specimen. Such results are consistent with confinement on the specimen from the platens.

Figure 4 shows the results of the test with rubber sheets between the platens and the specimen. The specimen begins to dilate at approximately .0005 (in/in), while the predicted dilatation doesn't occur until an axial strain of .0019 (in/in) is attained. Investigation of smaller regions of the

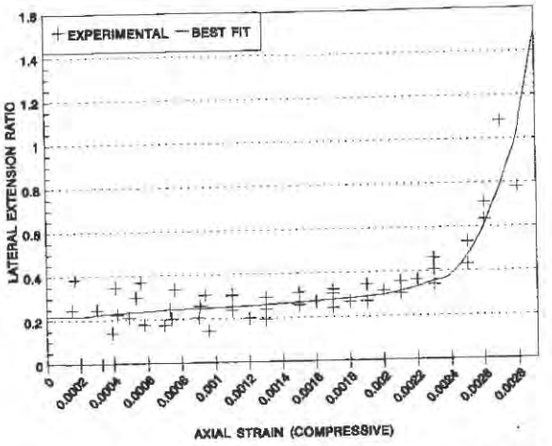

Figure 2: Lateral extension ratio vs axial strain for mortar. No relief of platen friction.

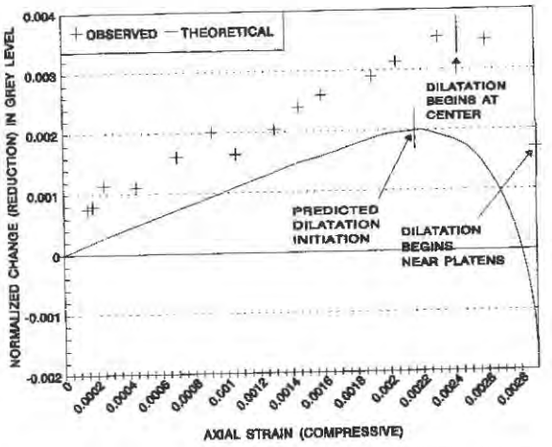

Figure 3: Normalized change in grey level vs axial strain for mortar. No relief of platen friction.

images shows that dilatation occurs at the ends of the specimens almost immediately. The center of the specimen dilates at a strain of .0019 (in/in). This matches well with the predicted behavior indicating that the center of the specimen is fairly close to uniaxial conditions. The failure zone of this specimen is characterized as vertical splitting. These results are consistent with an outward lateral shear stress being applied at the ends of the specimen by the rubber.

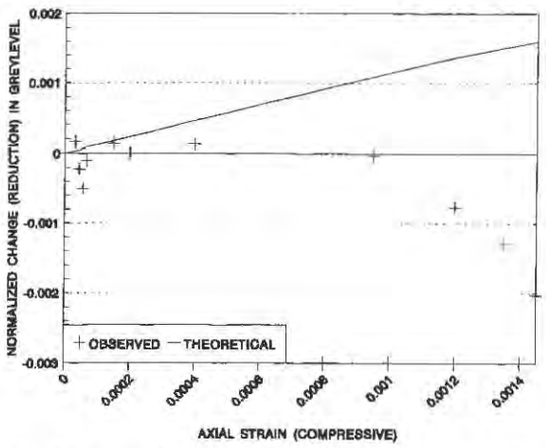

Figure 4: Normalized change in grey level vs axial strain for mortar. Platen friction reduced with rubber sheet.

CONCLUSIONS

Strain data can be obtained by measuring the change in grey level of X-ray images. With some knowledge of the lateral extension effect and loading conditions, strains can be obtained with very little computation. Therefore, the technique may be used as a non-invasive means to provide strain control for materials testing. This technique will provide a means of quantifying how well an experimental setup simulates a homogeneous state of strain under uniaxial and biaxial states of stress. If this technique can be applied to a specimen in several directions, for example by utilizing tomographic techniques, it may be possible to derive a complete description of the strain field solely from the change in grey levels.

The Authors greatfully acknowledge the support of Dr. Spencer Wu and the Air Force Office of Scientific Research.

REFERENCES

[1] M.L. Wang, H.L. Schreyer, and C.A. Rutland, Internal Deformation Measurements Using Real Time X-rays, Exp. Tech., Jul-Aug 1991, pp. 43-47.

[5] I. Vardoulakis and B. Graf, Calibration of Constitutive Models for Granular Materials Using Data from Biaxial Experiments, Geotechnique, Vol. 35, No. 3, 1985, pp. 288-317.

[6] R.C. McMaster, The Society for Nondestructive Testing, Nondestructive Testing Handbook, 1959, Vol. 1, pp. 13.17-15.39.

[12] L.E. Bryant and P. McIntire, The Society for Nondestructive Testing, Nondestructive Testing Handbook, Vol. 3, Radiography and Radiation Testing, 1985, pp. 836-878.

SPALLING FRACTURE AND CONTINUOUS DAMAGE IN ELASTIC-BRITTLE MATERIALS (EXPERIMENTS & EVALUATIONS)

JERZY NAJAR
Department of Mechanics (A)
Technical University Munich
Arcisstr. 21, Munich, Germany

ABSTRACT

An experimental procedure for the determination of the spalling strength of elastic-brittle materials, like concrete, ceramics or rock, has been developed in accordance with the basic demands of a simple specimen geometry, lack of on-specimen gages, controlability of the uniaxial stress history in the spalling plane, versatility with respect to the data evaluation procedures for a variety of nonlinear material responses prior to failure. In particular, wave dispersion effects due to both specimen geometry and to the development of the continuous damage at tensile loading can be taken into account. Low costs of the non-instrumented specimens allow for large experimental series, resulting in proper distinction between the scatter of material characteristics and the errors of measurement and evaluation.

INTRODUCTION

Concrete, rock and ceramics fail under dynamic loading mainly in the spalling mode, i.e. under the action of dynamic tensile stresses. For quite a few reasons, however, the most widely used apparatus for dynamic testing, the split Hopkinson pressure bar (SHPB), can be applied neither to the investigation of the mechanisms of the tensile failure in these materials nor to the determination of the corresponding stress levels. The main reason is due to the fact that the original SHPB arrangement as well as its 1-D evaluation procedure, (1), assume multiple wave reflections within the wafer-shaped specimen, which should lead to quasi-static yielding, (2). This should hardly apply to brittle fracture, where the spalling process developes within a single wave passage, provided the stress amplitude is sufficiently high, (3). Various versions of the SHPB apparatus, (4-6), developed specifically for direct tensile tests, are equally non-suitable for brittle spalling experiments due to their comlicated geometry and the necessity to accomodate for gripping

devices. The wide variety of the Charpy-type tensile set-ups in use, e.g. (7-8), lacks the main advantage of the SHPB, which is the non-instrumented specimen of a most simple geometry. Added to a complicated wave pattern, which necessitates applying of doubtfull numerical procedures for the description of the spalling failure, as well as to the unresolved question of specimen grips' influence on the test results for brittle materials, the disadvantages of these arrangements for experiments with concrete, rock and ceramics become all too clear. Finally, the plate impact apparatus, (9), although superb for basic research of spalling phenomena in metals and other crystallic matters, appears to be rather forbiddingly expensive, when applied to testing of large numbers of samples, as it is usually the case with materials of a high natural scatter of mechanical properties. It becomes obvious, that an advantageous experimental arrangement aiming specifically at the applications for spalling tests of materials under consideration needs not only to incorporate possibly all advantages of the set-ups listed above, but to use also some peculiarities of these materials: a very high compressive-to-tensile strength ratio, (10), low fracture tuoghness and extremely short fracture delay time, (11).

EXPERIMENTAL SET-UP

The experimental set-up developed at the Department of Mechanics, Technical University of Munich, combines the principles of the pulse initiation and stress measurement and evaluation, characteristic for the SHPB scheme, with the tensile dynamic loading of the specimen developing in result of the reflection of the compressive pulse from the free end of the specimen, typical for the impact spalling scheme. Opposite to the latter one, however, a uniaxial state of stress can arise in the specimen prior to its spalling failure, due to its high slenderness ratio, Fig. 1. Within the framework of the 1-D treatment of the uniaxial waves in long rods, (1), under the assumption of a linear elastic-brittle response of the tested materials, one can deduce from the knowledge of the stress pulse transmitted into the specimen and the location of the spalling plane the level of stress developed at spall.

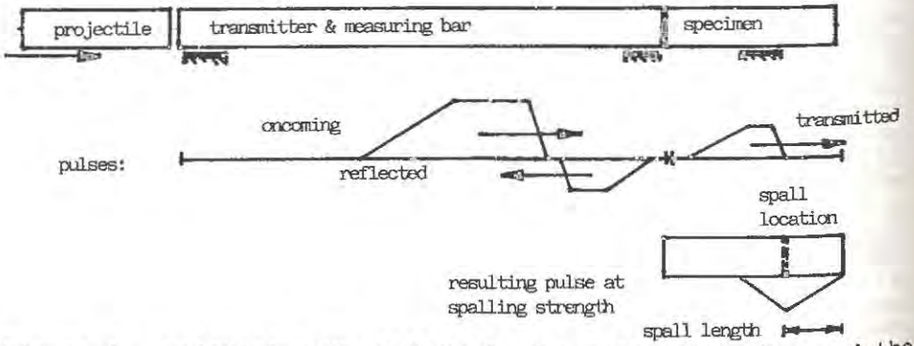

Figure 1. Uniaxial wave pattern in the transmitter bar and the specimen up to spalling.

The apparatus itself consists of four main components: the projectile launcher, the instrumented wave transmitting bar, the adjustable specimen mount for cylindrical test samples and the fragments collector, all lined up in a horizontal arrangement flexible enough to accomodate for various elastic-brittle materials, with the corresponding demands on the dimensions of the specimens. In the following, the technical data quoted apply to spalling tests of alumina ceramics.

The launcher represents a compressed air gun (barell 2.5 m caliber 20.5 mm), directly connected at the breech end with the pressure vessel (volume 6 l, pressure up to 25 atm). The projectile remains under the pressure until the holder is electrically released, triggering the measuring block at the same time. The whole assembly rests on a heavy cast base equipped with optional grips. The cylindrical steel projectile's length and diameter are chosen according to the optimal pulse length and its needed shape. Mounted into a teflon sabot liner, it can be propelled with necessary muzzle velocity (more than 100 m/s) to induce upon collision with the transmitting bar (length 1000 mm slenderness ratio up to 100) high compressive stress pulses. The induced pulse propagates along the instrumented bar until the contact with the cylindrical specimen, where a part of the compressive pulse gets reflected and registered. Another part gets transmitted into the specimen, according to the effective impedances of the two bars. From the stored oncoming and reflected pulses one obtains the transmitted pulse propagating further along the specimen.

In the experiments referred here to, cylindrical bar specimens of diameter less then the diameter of the pressure bar and slenderness ratio between 30 and 40 were applied, although tubular specimens and lower slenderness ratios would be admissible. The lower limit on the slenderness is connected with the shape of the transmitted pulse: the wavelength of the highest substantial Fourier component of the pulse must be sufficiently larger than the diameter of the specimen in order to preserve the applicability of the 1-D wave pattern to the evaluation procedure. At the same time, the length of the specimen should exceed substantially, at least by an order of magnitude, its diameter, which is necessary to accomodate for the wave transition cross-sections at both ends of the specimen and at the plane of spalling. When testing a new material, initial tests are therefore needed to win the impedance data and to determine the most favourable and feasible slenderness of the specimens.

Under the conditions listed above, the uniaxial compressive wave reflects from the free end of the specimen with reversing into a tensile one, (2); the superposition of these two wave-trains results in tensile stresses increasing from the end when properly shaped pulses are transmitted into the specimen, Fig. 2. As soon as the peak stress of the resulting pulse arrives at the level of the spalling strength, spall occurs and the trapped momentum in the spall length of the specimen detaches it from the rest of the material, flying in the same axial direction. To avoid secondary fracture in the specimen one needs to arrange both for soft collection of the fragments and for not overshooting the spalling stress level too far.

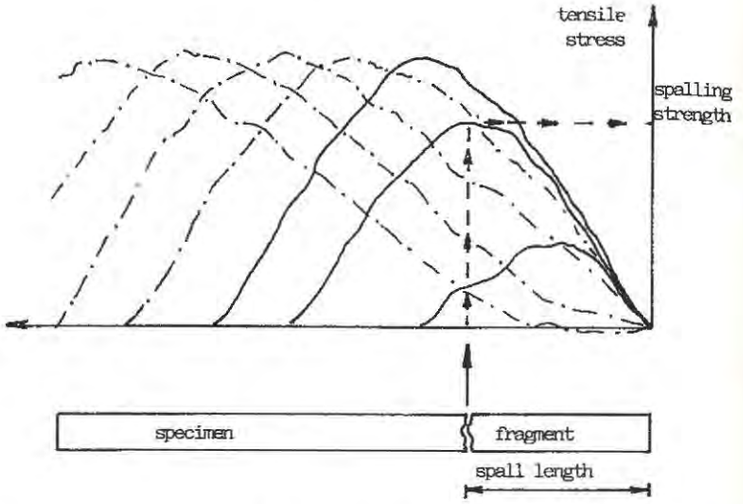

Figure 2. Time sequence of the resulting tensile stress pulses in the specimen: spall length determines the strength

EVALUATION PROCEDURE

The evaluation procedure consists of three steps of approximation: the uniaxial linear elastic estimation, the correction for geometrical dispersion effects and the correction for the material non-linearities due to continuous damage phenomena in the vicinity of the spalling plane.

The linear elastic estimation of the spalling strength consists of the computation of the time sequence of the resulting tensile stresses in the specimen on the basis of the uniaxial bar wave model, (1). The recorded oncoming and reflected pulse in the transmitter bar yields hereby the compressive pulse in the specimen, which in turn is numerically superposed with the reflected tensile pulse of the same shape. Supplying the length of the spalled fragment, one obtains the spalling strength by equating it with the maximal stress of the resulting pulse, who se maximum coincides with the spalling plane, Fig. 2.

Obviously, the estimation procedure applies only for materials with mechanical properties deviating only negligibly from the elastic-brittle response; it is assumed also that the compressive strength is much higher than the tensile one, and that the fracture delay time, i.e. the activation period of the failure mechanisms under sufficiently high tensile stresses, is negligibly small as compared to the carrying frequence of the registration cirquits (here: 10 MHz). As already mentioned, it is necessary also to assure the univocal determination of the spalling strength by introducing a properly shaped compressive pulse, which yields a monotonous increase of the amplitude of the resulting tensile stress simultaneously with the monotonous shifting of location of the stress maximum away from the free

end of the specimen. All these conditions apply to most kinds of concrete, ceramics and rock or can be implemented at their testing, (11), in the first approximation.

Exact measurements of the pulse propagation show, however, some dispersion effects even in the transmitter bar, although it is loaded below its linear elastic limit. They are connected with the lateral wave reflections; their effects on the longitudinal wave in the cylindrical rod can be incorporated into the uniaxial scheme on the basis of the Pochhammer-Chree corrective term, (12). According to this model, the phase velocity c_1 of a harmonic wave with with the length l depends on the ratio of the wavelength to the rod's radius r: the shorter the wave, the lower the velocity c_1. A typical stress pulse, consisting of a number of harmonic components, undergoes thus some dispersion of purely geometrical character, as it propagates in the transmitter bar and the specimen. Experiments with alumina ceramics, (13), conducted at low stress levels, confirm this effect. Due to the high bar wave velocity c_0 in alumina (twice as high as in the steel pressure bar) the corresponding wavelength of the Fourier's components of the transmitted pulse are twice as large as those in the oncoming stress pulse, resulting thus in a lower geometrical dispersion in the specimen. Still, the dispersion correction is incorporated into the evaluation procedure of the spalling test both for the transmitter bar and for the specimen.

The correction for material's non-linear response due to the development of the damage prior to the spalling is based on the continuous damage model, (14), as applied to concrete, (15) or similar materials. According to it, damage developes through activation of initial damage sources (pores, microcracks) in the course of the tensile loading, Fig. 3. The non-linearity of the stress-strain relation yields incremental waves of stress-dependent velocity c_s: with rising stresses the velocity becomes lower, resulting in dispersive effects in the specimen.

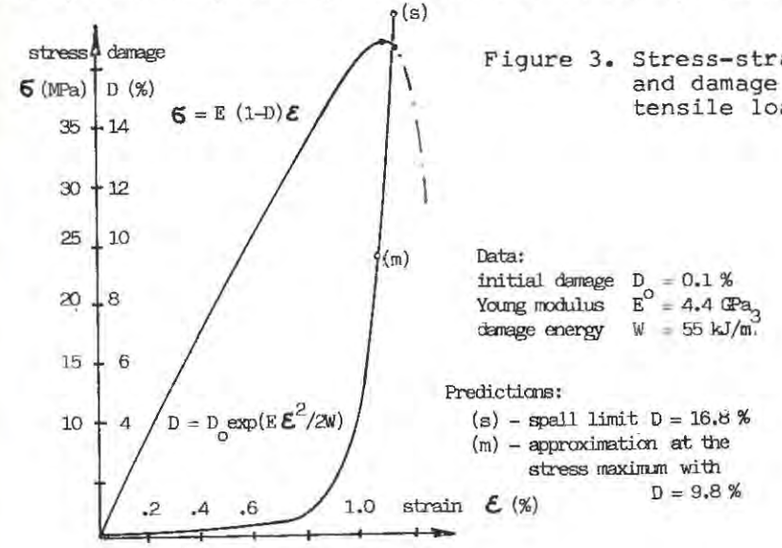

Figure 3. Stress-strain and damage in tensile loading

The corresponding numerical procedure is based on the method of characteristics as applied to the part of the wave propagation path corresponding to the tensile resulting stresses, while for the compressive path the previous procedures hold. Two parts of the procedure can be distinguished, in the first one the material parameters D_o and W being taken from the static experiment while further corrected for possible strain-rate dependence of damage energy W, if needed.

As an example of the experimental results, the following data were obtained in spalling tests with alumina ceramic rods diameter 8 mm, length between 247 and 333 mm: for oncoming pulses between 179 and 214 MPa and corresponding transmitted pulses between 249 and 302 MPa the spall length was 60 to 93 mm and the corresponding values of the spall strength were 219 to 277 MPa; the average spall strength of the 5 tested specimens was calculated at 245 MPa, with the standard deviation 10%.

REFERENCES

1. Davies, R.M., A critical study of the Hopkinson pressure bar Phil. Trans., London Royal Soc., ser. A, 1948, 240, p. 375.
2. Kolsky, H., Stress waves in solids, Oxford Univ. Press, 1953
3. Rajendran, A.M., Cook, W.H., A comprehensive review of modeling of impact damage in ceramics, Report AFATL-TR-88-143, Univ. Dayton Res. Inst., Dec. 1988.
4. Goldsmith, W., Dynamic loading of several concrete-like mixtures, J. Str. Div., 1968, p. 1803-1827.
5. Hauser, F., Techniques for measuring stress-strain relations at high strain rates, Exp. Mech.,1966, 6, p. 395-402.
6. Nicholas, Th., Tensile testing of materials at high rates of strain, Exp. Mech., 1981, 21, p. 177-185.
7. El Magd, E., Application of the FEM to elasto-plastic wave propagation in metals, Eng. Comput., 1985, 2, p. 114-120.
8. Kussmaul, K., Demler, T., Klenk, A., Advanced testing method for rotating disc impact machine, in Materials at high strain rates, Inst. Phys. Conf., ser. no 102, Oxford, 1989, IOP Publ., p. 157-164.
9. Barker, L.M., Lundergan, C.D., Herrmann, W., Dynamic response of aluminium, J. Appl. Phys., 1964, 35, p. 1203-1212.
10. Vutukuri, V.S., Lama, R.D., Saluja, S.S., Handbook on mechanical properties of rocks, Trans Tech Publ., 1974.
11. Duffy, J., Nakamura, T., Yeshurun, Y., Suresh, S., Dynamic fracture of ceramics, in Materials at high strain rates, Int Conf., Inst. Phys. Conf., ser. no 102, Oxford, 1989, p. 355.
12. Kolsky, H., An investigation of the mechanical properties of materials at very high strain rates of loading, Proc. Phys. Soc., sec. B, 1949, p. 676-700.
13. Bierwirth, S., Najar, J., Dispersion der Wellenausbreitung in Stäben bei der Untersuchung der dynamischen Zugfestigkeit von Al_2O_3, in DVM-Arbeitskreis Bruchvorgänge, 23. Vortragsveranst., Berlin, 1991, p. 423-432.
14. Najar, J., Continuous damage of brittle solids, in Continuum damage mechanics, ed. by D. Krajcinovic and J. Lemaitre, Springer, Wien-N.York, 1987, p. 233-294.
15. Najar, J., Transition from continuous damage to failure, in Cracking and damage, ed. J. Mazars, Z.P. Bažant, Elsevier, 1989, p. 150-163.

Chapter 6

Dynamic Fracture

Invited Paper

DYNAMIC FRACTURE

J. Isenberg[1], Z. P. Bazant[2], S. Mindess[3], W. Suaris[4] and H. W. Reinhardt[5]

[1]Weidlinger Associates, 4410 El Camino Real, Los Altos, CA 94022
[2]Northwestern University ,The Technical Institute, Evanston, IL 60201
[3]University of British Columbia, 2324 Main Hall,Vancouver, BC , Canada V6T 1Z4
[4]University of Miami, P.O. Box 248294, Coral Gables, FL 33124
[5]Tech Hochschule Darmstadt, Alexanderstrasse 5, D-6100, Darmstadt, W. Germany

ABSTRACT

This paper summarizes the results of experiments in which the properties of concrete subjected to dynamic loads are investigated. The macroscopic strength and stiffness of concrete in both compression and tension are found to increase with loading rate. In experiments on notched specimens loaded in tension, it is found that prepeak crack growth varies inversely with rate. Some evidence suggests that the bond between cement paste and aggregate is higher at higher rates, leading to the initiation of fracture within the paste. The rate dependence of bond between steel and concrete has been attributed to rate dependence of local crushing of concrete by bar deformations. Computational modeling of localized failure under dynamic loading must consider mesh objectivity and proper posedness; the latter requires a localization limiter such as that provided in the non-local continuum approach.

INTRODUCTION

Concrete structures may experience dynamic effects when subjected to rapidly applied loads of short duration, such as impact, explosions and earthquakes. Under dynamic loading, both structural and material responses depend on the applied loading rate; in this paper, we are concerned primarily with material effects. Strain rates of about 10^{-5} sec^{-1} to 10^{3} sec^{-1} are considered.

The microstructural origin of the rate dependence lies partly in the creep or viscoelastic character of the hardened cement paste. A second origin of rate dependence is the time dependent nature of crack growth wherein bond ruptures leading to growth of fracture surfaces are thermally activated and require some time. At a larger scale, termed the meso level, the tendency of cracks to meander less during high rate loading means that the cracks are more likely to intersect aggregate particles. These possess a higher fracture toughness than cement paste and impart a higher toughness to the material overall. Opposing this effect at very high rates is the tendency for the fracture process zone to decrease, which adds to the brittleness of the material. At the macro level, where concrete is idealized as homogeneous, models of strain rate effects consider the velocity at which energy can be transferred to the new crack surfaces to

be limited to about 10% of the Rayleigh wave velocity; thus the velocity at which cracks can propagate is restricted. Inertia is not considered to play a major role in rate dependence of concrete fracture.

With regard to computational modeling of crack propagation and postpeak behavior of concrete specimens and structures, special difficulties arise. In addition to the problems of mesh objectivity which occur in static and dynamic problems alike, care must be exercised in the postpeak regime. This is because, if strain softening is represented by local rate independent stress-strain relations, wave speeds become imaginary and the governing equations of motion are altered from hyperbolic to elliptic. The behavior of the resulting model can be completely different from what was intended. Introducing rate dependence or other localization limiter into continuum models of postpeak behavior leads at a minimum to a system of properly posed equations. Methods based on non-local continuum idealizations are promising from the theoretical point of view.

EXPERIMENTAL EVIDENCE OF RATE EFFECTS

Tensile (Mode I) Failure

Mode I failure is studied by applying macroscopic tensile stress across the fracture process zone in advance of the crack. Strain rates higher than about 0.1 sec^{-1} are achieved by a Hopkinson split-bar test or an impact test using either a drop weight or pendulum. Explosive and flyer plate testing have also been used, though quantitative data from these sources are scarce.

Typical data shown in Fig. 1 were obtained in direct tension (1).

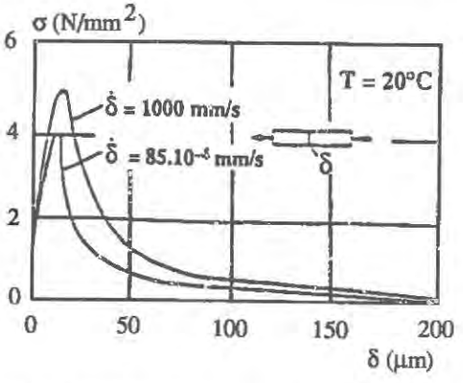

Figure 1. Uniaxial tension stress-strain curves of concrete at two different rates of loading, (1).

Data shown in Fig. 2 were obtained in flexure (2). John and Shah (3) have successfully modeled the strength- or quality-dependence of the rate effect on tensile strength. The initial secant modulus of cement mortar in flexure, defined as the slope of a line through (0.4 x peak load), is virtually insensitive to increase in strain rate (2). The secant modulus defined as the slope through peak flexural load exhibits a modest rate dependence. This may represent a decrease in prepeak nonlinearity or simply the same amount of prepeak nonlinearity with higher strength or both.

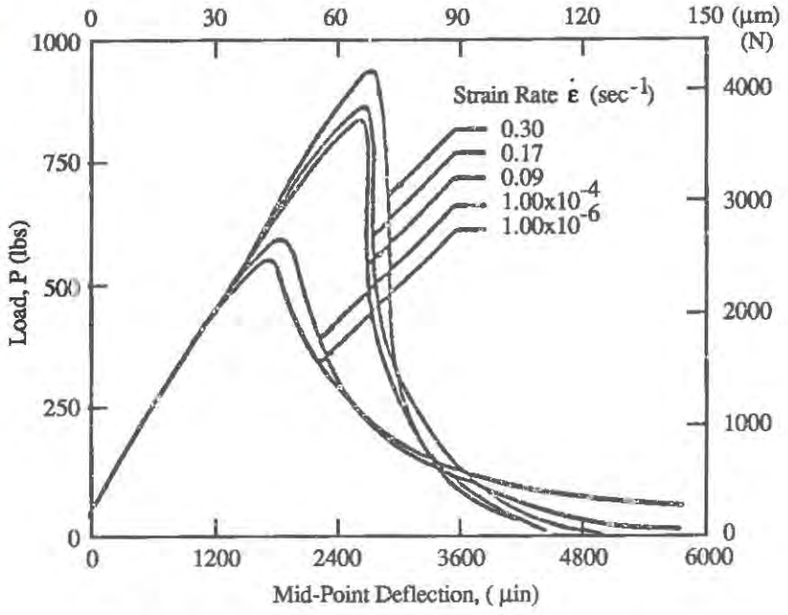

Figure 2. Typical load-deflection response of concrete in bending at different rates of loading, (2).

Brooks and Samaraie (4) conducted direct tensile tests and 3- and 4-point bending tests on concrete specimens to investigate the sensitivity of prepeak stress/strain relations and the peak stress to loading rate. Their results confirm those of (5)with respect to the increase in secant modulus up to peak stress with increasing stress rate. They also note that the "limit of proportionality" in stress and strain, which may be due to the onset of microcracking, increases with increasing rate. The origin of this effect, which is a central factor in rate dependence of Mode I fracture, has not been identified, however. Finally, the results of (4) and (5) conflict with respect to the initial tangent modulus of concrete, which the latter say is unaffected by stress rate.

The rate effect in very slow (static) loading was measured by Bazant and Gettu (6,7), who used the size effect method to determine the dependence of the effective fracture energy and the effective (elastically equivalent) length of the fracture process zone on the time to reach the peak load for conditions of constant-rate loading. The time to peak load ranged from one second to approximately 10^5 seconds, and the specimens were notched three-point bending beams. As expected, the fracture energy was found to decrease as the loading rate decreased, but a surprising conclusion was that, for these rates, the fracture process zone length decreased as the loading rate decreased, which means the response became more brittle, closer to linear fracture mechanics (in the sense of the effective elastic modulus approximation of viscoelasticity). This effect appears to be due to creep or stress relaxation in the fracture process zone, which supplements the creep that occurs in the bulk of the specimen.

The idea of reduced prepeak crack growth is supported by the data reported in (8), which indicates that prepeak crack growth in notched beams decreases with increasing rates. A similar trend was also observed in (9) based on tests in uniaxial tension; in (10) and in (11) in compression; and in (12) in flexure based on load versus crack mouth opening responses of

notched beams at impact rates. Reinhardt (1) reported that the secant modulus increases with increasing rate based on impact tensile tests; his results suggest that the increase was about 25% at strain rate of 1 sec^{-1}. This also supports the hypothesis that prepeak crack growth is reduced at higher strain-rates. The conventional LEFM approach of assuming slow crack growth to be negligible is not appropriate when applied in cases of quasistatic loading (8); significant slow growth precedes fracture.

Mindess et al (13) interpreted the results of drop hammer tests using the expression for critical stress intensity factor, or fracture toughness K_{ID}, given in (14). The results summarized in Fig. 3 show that the dynamic value of the fracture toughness K_{ID} is much larger than the static value K_{IC}.

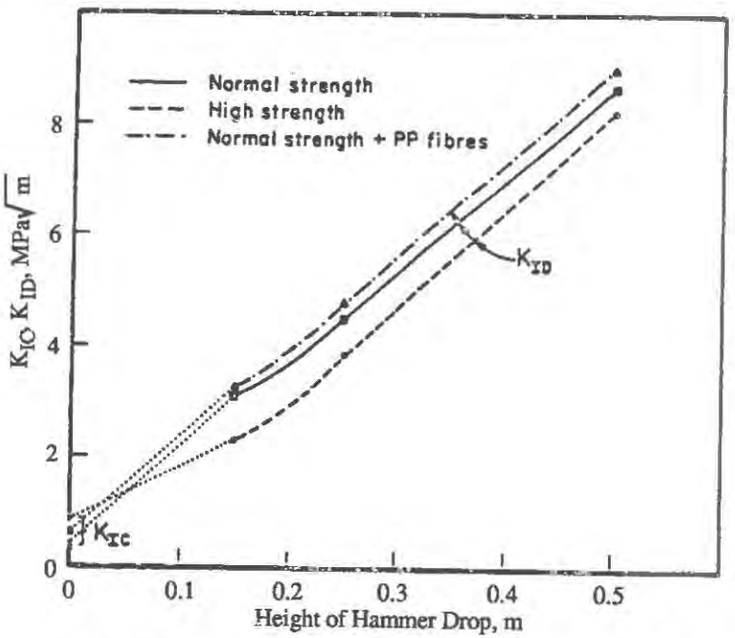

Figure 3. Fracture toughness as a function of hammer drop height, (13).

Nonlinear fracture mechanics was used in (15) to analyze the results of notched, 3-point bending specimens subjected to loading through a fast-acting dynamic load cell. The maximum strain rate in the fracture process zone was about 0.2 sec^{-1}. Relative to static loading, the dynamic tensile strength, f_{td}, is about 88 % greater for the strain rate of 0.2 sec^{-1}.

Compressive Failure

Deformation and strength characteristics of concrete subjected to macroscopic compressive stress have been investigated by drop weight, Hopkinson split bar, rapid hydraulic loading and controlled explosive loading tests. The experimental facility used by Malvern et al. (16) is a typical Kolsky apparatus in which a striker bar impacts axially the incident pressure bar. Malvern et al. tested specimens of concrete made from four different aggregates (Andesite, Seattle gravel, manufactured limestone and a lightweight aggregate called Solite). Results from

their tests show 50 -100% increases in strength relative to the static values over the strain rate range considered.

Results reported in (17) were obtained by Hopkinson bar testing of cement paste specimens up to strain rates of 10^3 sec^{-1}. These show that compressive strength increases with strain rate up to about 250 sec^{-1} and then tends toward a limiting value. Results similar to those of (17) were reported in (18,19) in which specimens of cement paste and cement-sand mortar were subjected to direct compression. Fully saturated samples of these materials were tested at rates from about 3 x 10^{-7} sec^{-1}. to about 4 x10^{-1} sec^{-1}. The results indicate a monotonic increase with rate in strength of paste and mortar over this range. These results agree with Jawed et al in that the stronger specimens (lower W/C) tend to gain slightly more strength at higher rates than do the weaker specimens. The influence of quality indicated by data obtained under compressive loading appears to differ from the influence of quality on rate sensitivity in tension.

Dropweight tests reported in (5) investigated whether the increase in strength at strain rates of about 15 sec^{-1} relative to strength under static load is accompanied by a similar increase in the value of strain at maximum stress. Strength under dynamic load is greater by a factor of about 1.7 than strength measured statically. The strain at maximum dynamically applied stress also increases relative to the static value by a factor of about 1.4. This is consistent with data reported in (11) and with results obtained under tensile loading as is reported in (1), under flexure (2) and in (20).

Bond Failure

The behavior of structural concrete is strongly affected by the various types of bonds, including bonds between cement and aggregate; between concrete and steel reinforcement; and between the matrix and discontinuous fibers. A review of the various bonds and their significance under static loading has been provided in (21). The great difficulty of carrying out measurements of cement-aggregate bond under static loading has been noted; the present writers are aware of no studies dealing directly with dynamic loading effects on cement-aggregate bond. Indirect evidence from high strain rate studies of concrete strength may permit some information to be inferred. For normal strength concrete under static load, cracks tend to go around aggregate particles, whereas for high strength concrete they may go through or around aggregate particles. In contrast, for dynamic loading, neither in normal strength nor in high strength concrete is bond necessarily the weakest link, (22), (23), (24).

A study on the bond between concrete and steel reinforcement under dynamic loading (25) found that, for smooth bars, loading rate had no significant effect on the maximum bond resistance nor on the bond stress versus displacement relationships. However, for deformed bars, both bond resistance and bond stiffness increase markedly with loading rate, the influence of loading rate being more pronounced for weaker concretes. The influence of loading rate could be described by a power function similar to that used to describe the effect of loading rate on strength of plain concrete. This is presumably because with deformed bars, failure is due to the local crushing of the concrete by the bar deformations. Recent results (26) obtained from drop weight impact tests show that the average bond stress and fracture energy increase slightly (up to about 20%), depending on hammer drop height, in comparison with that under static loading. This is observed in both normal and high strength concretes. Takeda (27) concluded that the strain distribution around the deformed reinforcing bars is different under dynamic and static loading. He suggested that the distributed area of strain is much narrower under dynamic loading, which could cause fracture of the reinforcement in reinforced concrete structures because the deformations are limited to a small length of the reinforcing bars. This argument was also applied (22), (28) to the failure of steel reinforcement under impact loading of reinforced concrete beams, in which enhanced concrete-steel bond limits the deformations to the small area under the point of impact, leading to ductile fracture of the steel.

COMPUTATIONAL MODELING OF LOCALIZED FAILURE UNDER DYNAMIC LOADING

The main challenges in numerical modeling of failure or postpeak weakening in concrete are to avoid dependence on the choice of mesh size and to ensure that wave propagation problems have solutions. Since strain softening is not a true local property of materials, constitutive equations which assume that stress, strain, density, etc. exist as in a continuum, that no characteristic dimensions are present, and that behavior of an infinitesimal element is the same as a finite volume of material are not appropriate for computational modeling of post peak behavior. Despite this, the temptation to express postpeak behavior in terms of a constitutive model is strong in order to capitalize on the advantages of continuum finite element or finite difference modeling.

A dynamic finite element model was developed by Du et al (29) that incorporates the static Crack Opening Displacement (COD)-Crack Closing Stress (CCS) distribution. A dynamic tensile strength that governs CCS in the neighborhood of the crack tip was derived from the static tensile strength using the assumption that the rate dependence is the same as work to fracture measured in (8). The finite element model was used to simulate the growth of the fracture process zone during modulus of rupture tests on notched specimens. The analysis showed that the dynamic tensile strength of the fracture process zone is less strain-rate dependent than the tensile strength determined from impacted modulus of rupture specimens. In addition the experimental observation in (8) that the length of the fracture process zone decreases with increasing strain rates was confirmed by the analytic model.

An effective and possibly realistic way to overcome difficulties due to strain-softening is provided by the nonlocal continuum concept. The nonlocal continuum is a continuum in which the stress-strain relation involves spatial averaging over a certain representative volume of the material surrounding the point. An effective approach, in which the stress and the total strain are local and the only variables that are nonlocal are those associated with the strain-softening damage (microcracking, smeared cracking), was proposed in (30), (31). The nonlocal constitutive law is obtained from the local law by replacing the local damage with a nonlocal damage parameter.

As is demonstrated in (32), (33), attempts to represent dynamic loading of a continuum whose strain softening constitutive equations are derived from load-deflection experimental data are unsuccessful. The modulus becomes negative. Whereas the resulting lack of mesh objectivity can be overcome, an additional difficulty arises in that the only element of a dynamically loaded bar, for example, for which postpeak behavior occurs is the one adjacent to the load. All others unload elastically before the peak is reached. As the mesh size is reduced to zero, none of the material undergoes softening. It is not possible to construct a time-marching solution for such a system when arbitrary initial conditions are prescribed. However, it is also shown in (31) that introducing rate dependence leads to dynamically well-posed problems. An example in which a rate dependent model is applied to a problem involving dynamic strain softening is in (34). Non-local theories may produce similar results and may be the only reasonable way of making static behavior equivalent to the long time limit of dynamic behavior under slow loading.

SUMMARY

Experimental data on rate effects have been obtained primarily by subjecting concrete specimens to flexure or to unconfined direct tension or compression. Compression, flexural and direct tension tests confirm that strength increases with increasing rate of loading. Direct tension and bending tests show that prepeak nonlinearity, apparently an indicator of microcracking, is less at higher rates. In notched beams prepeak crack growth decreases with increasing rates. Similar experiments show that the critical stress intensity factor, or fracture toughness K_{1D} is much larger than the static value K_{1C}. Rate dependence of bond between concrete and reinforcing has been identified with local crushing of the concrete around deformation of the bar. Hence, the rate dependence of bond in such cases has the same origin as that for plain concrete and has roughly the same quantitive relationship to strain rate. At high loading rates, enhanced concrete-steel bond limits deformations to a small length of reinforcing bar, promotes fracture of the bar and may lower the overall ductility of reinforced concrete members.

Computational models of localized failure under dynamic loading must give proper consideration to objectivity with regard to mesh size and, for wave propagation problems, to proper posedness. The non local continuum approach has been suggested as a method of providing a localization limiter, preventing strain-softening damage from becoming localized into a zone of zero volume. Using rate dependence to represent softening has been proposed and has been adopted by some workers as a method of preserving the hyperbolic nature of governing equations in wave propagation problems.

REFERENCES

[1] Reinhardt, H. W., in "Cement Based Composites: Strain Rate Effects on Fracture," Materials Research Society Symposium, (S. Mindess and S. P. Shah, eds., 1986).

[2] Gopalaratnam V. S. and S. P. Shah, " Properties of Steel Fiber Reinforced Concrete Subjected to Impact Loading," J. ACI, V. 83 No. 8, pp. 117-126, Aug. 1985.

[3] John, R. and S. P. Shah, "Constitutive Modeling of Concrete Under Impact Loading," in Proc. of SMIRT-9-Post Conference Seminar: Impact, Lausanne, Switzerland, Aug. 1987.

[4] Brooks, J. J. and N. H. Samaraie, "Influence of Rate of Stressing on Tensile Stress-Strain Behaviour of Concrete", Int. Conf. on Recent Developments in Fracture of Concrete and Rock, Cardiff, UK, Elsevier, Sept. 1989.

[5] Curbach, M., J. Eibl "Nonlinear Behaviour of Concrete Under High Compressive Loading Rates", Int. Conf. on Recent Developments in Fracture of Concrete and Rock, Cardiff, UK, Elsevier, Sept. 1989.

[6] Bazant, Z.P. and R. Gettu "Determination of Nonlinear Fracture Characteristics and Time Dependence From Size Effect," Int. Conf. on Recent Developments in Fracture of Concrete and Rock, Cardiff, UK, Elsevier, Sept. 1989.

[7] Bazant, Z. P. and R. Gettu "Size Effect In Concrete Structures and Influence of Loading Rates", in Serviceability and Durability of Construction Materials, Proc., 1st Materials Engineering Congress of ASCE, Denver, CO, Aug. 1990.

[8] John, R. and S. P. Shah "Fracture of Concrete Subjected to Impact Loading," Cement, Concrete and Aggregates, ASTM, Vol. 8, No. 1, pp. 24-32, 1986.

[9] Tinic, C. and E. Bruhwiler, "Effects of Compressive loads on the Tensile Strength of Concrete at High Strain Rates," Int. J. of Cement Composites and Lightweight Concrete, Vol. 7, No. 2, pp. 103-108, 1985.

[10] Suaris, W. and S. P. Shah, "Rate Sensitive Damage Theory for Brittle Solids," J. of Struc. Eng., Proc. ASCE, Vol. 111, No. 3, pp. 563-576, March 1985.

[11] Ahmad, S. and Shah, S. P., "Behavior of of Hoop Confined Concrete Under High Strain Rates," J. ACI, pp. 634-647, Sept.-Oct. 1985.

[12] John, R., "Strain Rate Effects on Fracture of Cement-based Composites," Ph. D. Thesis, Dept. of Civ.Eng'g, Northwestern University, Evanston, IL, 1988.

[13] Mindess, S., Banthia, N. and Yan, C., "The Fracture Toughness of Concrete Under Impact Loading," Cement and Concrete Research, V. 17, pp. 231-241, 1987.

[14] Broek, D., Elementary Engineering Fracture Mechanics, Martinus Nijhoff Publishers, The Netherlands, pp. 76 1982.

[15] Yon, J-H N. M. Hawkins and A. S. Kobayashi "Dynamic Fracture Testing of Concrete Bend Specimens", Proc, Fracture Toughness and Fracture Energy - Test Methods for Concrete and Rock, Sendai, Japan, Balkema, Rotterdam, 1989.

[16] Malvern, L. E., et al, "Dynamic Compressive Testing of Concrete," Proc. of the 2nd Symp. on The Interaction Non-Nuclear Munitions With Structures, Panama City Beach, FL, pp. 194-199, 15-18 April 1985.

[17] Jawed, I. et al., "High Strain Rate Behavior of Hydrated Cement Paste," Cement and Concrete Research, Vol. 17, No. 3, pp. 433-440, 1987.

[18] Harsh, S., Z. Shen and D. Darwin "Strain-Rate Sensitive Deformation of Cement Paste and Mortar in Compression", ACI Materials Journal, V. 87, No. 5, Sept.-Oct. 1990.

[19] Harsh, S., Z. Shen and D Darwin, "Strain-Rate Sensitive Deformation of Cement Paste and Mortar in Compression", SM Report No. 22, to AFOSR, Univ of Kansas Center for Research, March 1989.

[20] Birkimer, D. L. and Lindeman, R., "Dynamic Tensile Strength of Concrete Materials," J.ACI , pp. 47-49, January 1971.

[21] Mindess, S., "Bonding in Cementitious Composites: How Important is it?," in Bonding in Cementitious Composites, Materials Research Society Symp. Proc., Vol. 114, Materials Research Society, Pittsburgh, 1988.

[22] Bentur, A., S. Mindess and N. P. Banthia, "The Fracture of Reinforced Concrete Under Impact Loading," in Cement Based Composites: Strain Rate Effects on Fracture, Materials Research Society Symposia Proceedings, Vol. 64, Pittsburgh, 1986.

[23] Yumei, Zhang, Cao Jianguo and Guo Guilan, "The Experimental Research of Dynamic Fracture Properties of Concrete," Fracture Toughness and Fracture Energy of Concrete, Elsevier, Amsterdam, pp. 491-496, 1986.

[24] Alford, N. McN., "Dynamic Considerations of Fracture in Mortars," Materials Science and Engineering, Vol. 56, pp. 279-287, 1982.

[25] Vos, E. and H. W. Reinhardt, "Influence of Loading Rate on Bond Behaviour of Reinforcing Steel and Prestressing Strands," Materiaux et Constructions, Vol. 15, pp. 3-10, 1982.

[26] Yan, C and S. Mindess "Bond Between Concrete and Steel Reinforcing Bars Under Impact Loading", in Brittle Matrix Composites 3, Elsevier Appl. Sci., 1991

[27] Takeda, J.-J., "Strain Rate Effects on Concrete and Reinforcements, and Their Contributions to Structures," Cement-Based Composites: Strain Rate Effects on Fracture, Materials Research Society Symposia Proc., Vol. 64, Materials Research Society, Pittsburgh, pp.15-20, 1986.

[28] Banthia, N. P. "Impact Resistant of Concrete," Ph.D Thesis, University of British Columbia, Vancouver, Canada, 1987.

[29] Du, J. , Kobayashi, A. S. and Hawkins, N. M., "FEM Dynamic Fracture Analysis of Concrete Beams," J. of Eng. Mech., ASCE, Vol 115, No. 10, pp. 2136-2149, Oct. 1989.

[30] Pijaudier-Cabot, G., and Bazant, Z. P. "Nonlocal Damage Theory," *J. of Engng. Mechanics ASCE*, 113, (10), 1512-1533, 1987.

[31] Bazant, Z. P., and Pijaudier-Cabot, G. "Modeling of Distributed Damage by Nonlocal Continuum with Local Strains," Numerical Methods in Fracture Mech., Pineridge Press, Swansea, U. K.,1987

[32] Sandler, I.S. "Strain Softening for Static and Dynamic Problems," Constitutive Equations: Macro and Computational Aspects, Winter Annual Meeting, ASME, New Orleans, LA, pp. 217-231, Dec. 9-14, 1986.

[33] Sandler, I and Wright, J.P. "Summary of Strain Softening. Theoretical Foundations for Large Scale Computations of Nonlinear Material Behavior," DARPA-NSF Workshop, S. Nemat-Nasser, ed. Northwestern University, 1985.

[34] Isenberg, J., E. Richardson and H. S. Levine, "A Rate Dependent, Strain-Softening Model for the Dynamic Collapse of Beams in Flexure and Shear," Winter Annual Meeting of ASME, New Orleans, LA , pp. 205-216, 9-14 Dec. 1984.

ANALYSIS OF IMPACT FRACTURE IN A DOUBLE-NOTCHED SPECIMEN INCLUDING RATE EFFECTS

L.J. SLUYS and R. DE BORST
Delft University of Technology, Department of Civil Engineering /
TNO Building and Construction Research, Delft, Netherlands,
P.O. Box 5048, 2600 GA Delft, The Netherlands.

ABSTRACT

Rate-dependence is included in the material description of a cracked medium to obtain a well-posed initial value problem. As a result thereof the numerical simulation of failure, initiated by localisation of deformation, no longer exhibits an excessive mesh dependence. This is demonstrated by means of the analysis of an impact test on a double-notched specimen.

INTRODUCTION

As a consequence of micro-structural changes during concrete fracture we observe, at a macro-level, a decreasing tensile force at increasing deformation. This phenomenon is commonly called softening and is attended by the formation of narrow bands of intense straining.

From a mathematical point of view boundary value problems as well as initial value problems that involve softening become ill-posed. For dynamic problems the field equations lose hyperbolicity which is accompanied by the presence of imaginary characteristics of the solution. The wave speeds become imaginary and no longer have physical significance.

From a mechanical point of view solutions of initial value problems (Bazant and Belytschko 1985) show localisation zones of zero thickness without consumption of energy. Wave reflection on the localisation zone is similar to refection on a free boundary. Numerical analyses try to capture this solution and therefore suffer from an excessive mesh dependence.

To correct the above-mentioned deficiencies we incorporate a dependence on the strain rate in the constitutive equations (Wu and Freund 1984, Needleman 1988, Sluys and de Borst 1991). First, the rate-dependent crack model will be treated and next the simulations are presented of the impact tensile tests on double-notched specimens. These specimens have been analysed for the rate-dependent model to assess the performance with respect to mesh refinement.

FORMULATION OF A RATE-DEPENDENT CRACK MODEL

The rate-dependent crack model has been implemented within the framework of the fixed

smeared crack concept (de Borst and Nauta 1985). In this concept a cracked zone is conceived to be a continuum which permits a description in terms of stress-strain relations. The stress rate-strain rate relation can be written as

$$\dot{\boldsymbol{\sigma}} = \mathbf{D}_e \left[\dot{\boldsymbol{\varepsilon}} - \dot{\boldsymbol{\varepsilon}}_{cr} \right] . \tag{1}$$

with the matrix $\mathbf{D}_e$ that contains the instantaneous moduli of the concrete. A superimposed dot denotes differentiation with respect to time. We use crack stress - crack strain ($\boldsymbol{t}_{cr} - \boldsymbol{e}_{cr}$) laws in a local coordinate system aligned with the crack. This necessitates a transformation between the crack strain rate $\dot{\boldsymbol{\varepsilon}}_{cr}$ in the global coordinate system and the crack strain rate $\dot{\boldsymbol{e}}_{cr}$ in the local coordinate system via $\dot{\boldsymbol{\varepsilon}}_{cr} = \mathbf{N}\,\dot{\boldsymbol{e}}_{cr}$, where $\mathbf{N}$ is the transformation matrix. The relation between the local crack strain rate and the local crack stress rate is

$$\dot{\boldsymbol{t}}_{cr} = \mathbf{D}_{cr} \dot{\boldsymbol{e}}_{cr} . \tag{2}$$

with $\mathbf{D}_{cr} = diag[h, \beta G]$, in which h the mode-I softening modulus ($h < 0$), which has been assumed to be a constant for the sake of simplicity. The shear stiffness in the crack is obtained by a multiplication of the elastic shear stiffness G with a shear reduction factor β. In the rate-dependent crack model not only the crack stress t_{cr} but also a rate-dependent stress t_{rd} is transmitted in the crack. We define the rate-dependent stress rate as

$$\dot{\boldsymbol{t}}_{rd} = \mathbf{M}\,\ddot{\boldsymbol{e}}_{cr} , \tag{3}$$

in which $\mathbf{M} = diag\ [m, 0]$, so that only mode-I rate effects are considered. The relation between local tractions and global stress now becomes

$$\dot{\boldsymbol{t}}_{cr} + \dot{\boldsymbol{t}}_{rd} = \mathbf{N}^T \dot{\boldsymbol{\sigma}} . \tag{4}$$

If we substitute eq.(2) and (3) into eq.(4) we obtain

$$\mathbf{D}_{cr} \dot{\boldsymbol{e}}_{cr} + \mathbf{M} \ddot{\boldsymbol{e}}_{cr} = \mathbf{N}^T \dot{\boldsymbol{\sigma}} . \tag{5}$$

Premultiplying eq.(1) by $\mathbf{N}^T$ and combining the result with eq.(5) yields the relation between the local crack strain rate and the global strain rate

$$\dot{\boldsymbol{e}}_{cr} = (\mathbf{N}^T \mathbf{D}_e \mathbf{N} + \mathbf{D}_{cr})^{-1} [\mathbf{N}^T \mathbf{D}_e \dot{\boldsymbol{\varepsilon}} - \mathbf{M}\,\ddot{\boldsymbol{e}}_{cr}] . \tag{6}$$

This equation can be substituted in eq.(1), which gives the global constitutive equation

$$\dot{\boldsymbol{\sigma}} = \mathbf{D}_e [\mathbf{I} - \mathbf{N} (\mathbf{N}^T \mathbf{D}_e \mathbf{N} + \mathbf{D}_{cr})^{-1} \mathbf{N}^T \mathbf{D}_e] \dot{\boldsymbol{\varepsilon}} + \mathbf{D}_e \mathbf{N} [\mathbf{N}^T \mathbf{D}_e \mathbf{N} + \mathbf{D}_{cr}]^{-1} \mathbf{M}\,\ddot{\boldsymbol{e}}_{cr} . \tag{7}$$

For sake of simplicity only one crack has been considered in this derivation, but it is possible that due to the rotation of principal stresses new cracks arise. The algorithmic aspects of the model have been discussed in detail by Sluys (1992).

The mathematical background of inclusion of rate dependence as a proper regularisation method has been elucidated in a study by Sluys (1992). The initial value problem of the rate-dependent strain-softening medium has been proved to remain well-posed with real characteristics. From an analysis of the wave motion it can be shown that the wave speeds in the strain-softening medium remain real. In contrast to the rate-independent medium, wave propagation is dispersive which means that waves can be transformed into stationary localisation waves. Furthermore the rate-dependent model contains an internal length scale l

$$l = \frac{2mc_e}{E} , \tag{8}$$

with E the Young's modulus and c_e the elastic wave speed.

IMPACT TENSILE TEST ON A DOUBLE-NOTCHED SPECIMEN

In the Stevin Laboratory of Delft University of Technology impact tensile tests have been carried out on notched, prismatic concrete specimens (Figure 1). The tests have been performed with a Split-Hopkinson bar apparatus by Weerheijm and Reinhardt (1989). The specimen is kept between an upper bar (6.7 m) and a lower bar (3.5 m) and the tensile pulse is applied at the bottom of the experimental set-up.

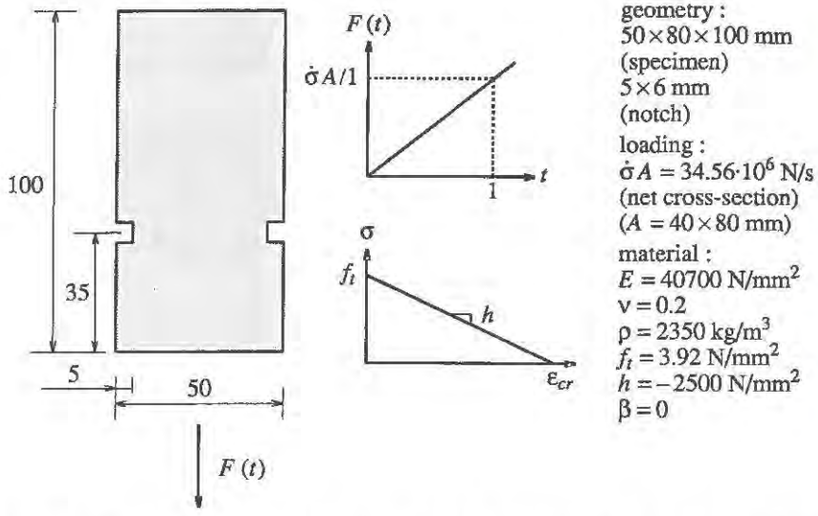

geometry :
50×80×100 mm
(specimen)
5×6 mm
(notch)
loading :
$\dot{\sigma}A = 34.56 \cdot 10^6$ N/s
(net cross-section)
($A = 40 \times 80$ mm)
material :
$E = 40700$ N/mm^2
$\nu = 0.2$
$\rho = 2350$ kg/m^3
$f_t = 3.92$ N/mm^2
$h = -2500$ N/mm^2
$\beta = 0$

Figure 1. Impact tensile test on a double-notched specimen : geometry and input data.

For the numerical modelling of the Split-Hopkinson bar we use a discretisation with special boundary elements (Sluys 1992). For the specimen itself three finite element discretisations have been used with one, two and four rows of elements in the notched section, respectively. The elements are eight-noded quadrilaterals with a nine-point Gauss integration. The elastic and inelastic properties are given in Figure 1. The parameters are derived by a straightforward translation of experimental data. Because a notched specimen yields a lower value for the impact tensile strength the dynamic value for f_t is taken from empirical relations derived in former programmes (Zielinski 1982). A simple linear strain-softening model is used and in a classical way, using the homogenisation technique, the constant softening modulus h was derived from the ultimate deformation measured in the experiment. In the numerical analyses a section of 5×6 mm in front of the left notch was given a material imperfection in the sense that the tensile strength was reduced by 20 %. The time integration of the field equations has been done with a Newmark scheme ($\delta = 1/2$, $\alpha = 1/4$) and a time step $\Delta t = 5 \cdot 10^{-7}$ s. A consistent mass matrix has been used for all analyses.

For the analyses with the rate-dependent crack model we take the material rate sensitivity $m = 0.1$ Ns/mm^2. In combination with the parameter set from Figure 1 this results in a length scale parameter $l = 20.5$ mm (eq.(8)).

The computational results differ markedly from the results obtained with the rate-independent crack model (Sluys 1992). Now, a localisation band occurs that is independent of the choice of the finite element discretisation. At the notches the very local stress concentration

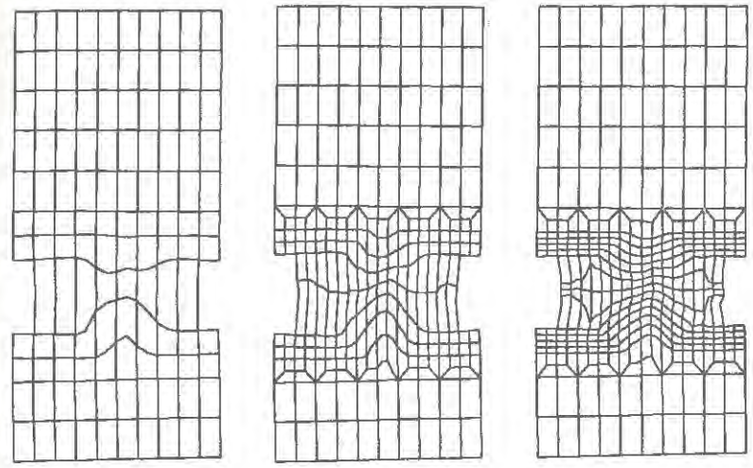

Figure 2. Incremental displacement patterns at $t = 0.45 \cdot 10^{-3}$ s.

zones keep the band small but the width of the localisation band increases when the crack propagates to the centre of the specimen. This can be seen from the deformation patterns for the three meshes, plotted in Figure 2, which not only show the mesh independence but also the misalignment of the localised deformations with the mesh. In contrast to the calculations for the rate-independent model in which the deformation localises along the horizontal mesh lines (Sluys 1992), the cracks branch off and the deformation band becomes wider, independent of the mesh lines. A small mesh dependence appears in the results due to the presence of stress singularities in the notches of the specimen.

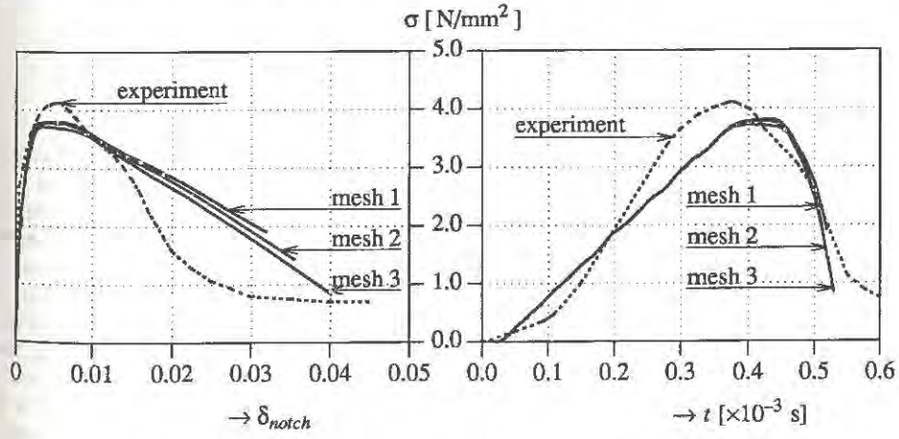

Figure 3. Stress-deformation curve inside the fracture zone (left) and stress-time curve of the transmitted loading pulse (right) for the rate-dependent model.

The numerical results have been compared with the experimental data. The stress-deformation curves for the numerical analyses as well as for the experiment are plotted in Figure 3. We observe not only mesh independence, but also a reasonable similarity between numerical analysis and experiment. The calculated maximum tensile stress is slightly smaller and the application of a linear strain-softening model prevents the proper simulation of a nonlinear softening branch, which is measured in the experiment. Another comparison between experiment and calculation is made in Figure 3 for the loading pulse which is transmitted by the fracture zone. The results for the three meshes are identical but differ slightly from the measured pulse. The rate-dependent crack model is a very simple model and it was not the prime aim of this study to exactly simulate experiments. Rather it was meant to provide a solution technique for mesh sensitivity. The second step is now to calibrate the model to experiments, for instance these impact tensile tests.

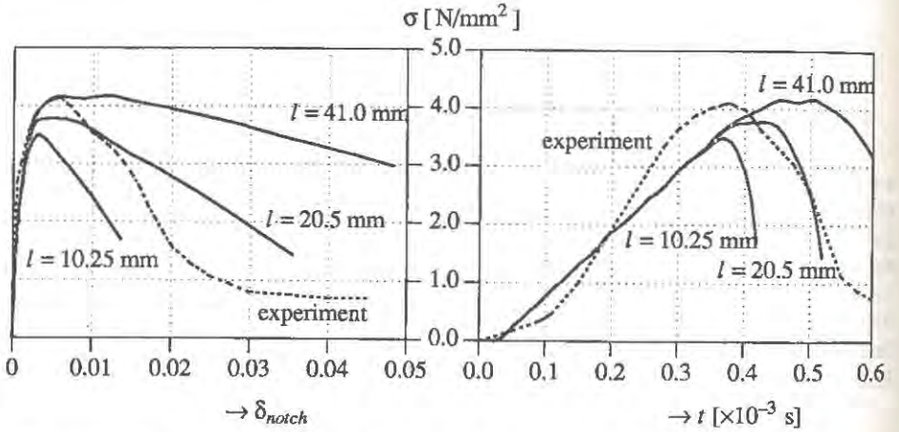

Figure 4. Stress-deformation curve inside the fracture zone for (left) and stress-time curve of the transmitted loading pulse (right) for different values for the length scale parameter l.

Finally, the length scale parameter l has been varied through a variation of the material rate-sensitivity parameter m in the numerical analysis. In the stress-deformation curve in Figure 4 the influence of the parameter l is clear : a smaller value for l leads to a steeper drop in the curve and to a more brittle behaviour, whereas an increase of l yields a more ductile response, although the maximum stress is predicted more accurately. Hence, l is a parameter which behaves in a fashion similar to that of the fracture energy G_f. Because the length scale parameter also determines the width of the band, brittleness of a material and the width of the localisation zone are related phenomena. In Figure 4 the influence of l on the shape of the loading pulse, which passes the crack plane, is also shown. A larger value for l slows down the failure process and enables the cross-section to redistribute the stress, which leads to a larger maximum stress value. It turns out that the behaviour close to the peak load is very important and determines the crack propagation speed and the extent of redistribution of stresses.

ACKNOWLEDGEMENTS

The calculations described in this paper have been carried out using the DIANA finite element package of TNO Building and Construction Research. This project is partially funded by the Prins Maurits Laboratory of TNO. The authors appreciate the stimulating discussions with J. Weerheijm on the experiments.

REFERENCES

Bazant, Z.P. and Belytschko, T.B. 1985. Wave propagation in a strain softening bar - exact solution. ASCE J. Engrg. Mech., 111(3), 381-389.

de Borst, R. and Nauta, P. 1985. Non-orthogonal cracks in a smeared finite element model. Eng. Comput., 2(1), 35-46.

Needleman, A. 1988. Material rate dependence and mesh sensitivity on localisation problems. Comp. Meth. Appl. Mech. Eng., 67, 69-86.

Sluys, L.J. and de Borst, R. 1991. Solution methods for localisation in fracture dynamics. In Proc. Conf. on Fracture Processes in Concrete, Rock and Ceramics, (eds J. van Mier, J.G. Rots and A. Bakker), Chapman and Hall, London, 661-671.

Sluys, L.J. 1992. Wave propagation, localisation and dispersion in softening solids. Dissertation, Delft University of Technology, Delft, Netherlands.

Weerheijm, J. and Reinhardt, H.W. 1989. Concrete in impact tensile tests. In Proc. First Int. Conf. on Struct. under Shock and Impact, Cambridge Massachusetts.

Wu, F.H. and Freund, L.B. 1984. Deformation trapping due to thermoplastic instability in one-dimensional wave propagation. J. of Mech. Phys. Solids, Vol.32 no.2, 119-132.

Zielinski, A.J. 1982. Fracture of concrete and mortar under uniaxial impact tensile loading. Dissertation, Delft University of Technology, Delft, Netherlands.

FRACTURE OF CONCRETE UNDER TORSIONAL IMPACT LOAD CONDITIONS

N.J.S. GORST AND B.I.G. BARR
School of Engineering, UWCC, Cardiff, U.K.

ABSTRACT

In recent years a number of investigators have tested concrete cylinders and cores in torsion. Some of these tests were on notched test specimens, with the aim of evaluating some Mode III fracture parameters, whereas others were on solid test specimens, in which case the torsion test was in effect yet another indirect tensile test. The work reported here extends the above studies to include the impact resistance of cylinders under torsional loading. The specimens have been tested by means of a repeated drop weight impact test apparatus. The same apparatus had previously been used to study the fracture of notched beams in bending and notched prisms and cylinders subjected to a predominantly shear-type of failure. Some of the initial results on a Grade 55 concrete are presented.

INTRODUCTION

In Fracture Mechanics there are three basic modes of fracture or crack extension - Modes I, II and III. Many investigators have proposed a range of Mode I test specimens for concrete and fibre reinforced concrete (FRC). More recently, the concrete fracture community has made significant progress with mixed-mode fracture in concrete - in which the shear mode is significant and in some cases dominant. In the last few years some investigators have tested concrete cylinders and cores in torsion. Some of these tests were on specimens with circumferential notches and the objective was to develop a Mode III type of fracture in the specimens.

At the same time that the above developments were taking place in Fracture Mechanics, the use of FRC in construction was developing rapidly. A range of new fibres and composites has been proposed and a significant amount of research effort has taken place to determine the physical and mechanical properties of both the fibres and the composites. In particular, the toughness energy absorption and impact strength of FRC have received considerable consideration. In the past, more attention has been given to the development of test methods for evaluating toughness than to evaluating the impact resistance of FRC materials. However, increasing attempts are being made to evaluate the impact properties of FRC materials.

The main objective of the work reported here was to bring together the above two areas of research. This study extends previous work to include the impact resistance of cylinders or cores under torsional loading. Some initial results are presented for ordinary concrete.

A number of researchers have proposed test geometries and loading arrangements to test circumferentially notched cylinders under Mode IIItype of loading conditions. These researchers include Bazant and Prat (1), Xu and Reinhardt (2) and Luong (3). In all these cases the torsion was induced in the test specimens by means of point loads creating equal and opposite torques. A similar loading arrangement to that proposed in (1) was developed by Tokatly (4) who has carried out an extensive study on the torsional strength of cylinders and cores. Some of his tests were on notched specimens, with the aim of evaluating some of the Mode III fracture parameters, whereas the remaining tests were on solid test specimens, in which case the tests were in effect another form of indirect tensile tests.

The work of Tokatly (4) has been extended to develop a torsion test to evaluate the deterioration of concrete due to alkali-aggregate reaction (5). In this test concrete cores taken from a number of structures have been subjected to torsional loading and the resulting shear stress state is used to evaluate the shear strength/indirect tensile strength properties of the concrete. Some further development of this torsion test on cylinders and cores is reported in a companion paper (6).

As more FRC materials and products have been developed, the determination of their fracture characteristics has become a subject of some considerable research interest. Most of the tests reported to date have used static loading conditions rather than dynamic loading. Most of the machines which have been developed to test FRC materials under impact conditions fall into one of two categories - machines of the pendulum type (modified Ozod and Charpy machines) and machines of the drop weight type (7).

A repeated drop weight testing machine was developed by Barr and Baghli (8) for testing notched beams in bending. After suitable modifications by Mahjoub-Moghaddas (9), this impact machine has been used for testing a number of geometries in which the loading was primarily of the shear type. The impact test results obtained by this apparatus can be considered at two levels (10). In the first case, the impact resistance is given simply in terms of the number of blows to cause fracture which, in turn, can be converted to energy. Additionally, the instrumentation allows the investigators to determine with some degree of confidence the influence of the passage of the shock wave through the test specimens and the amount of energy dissipated in various processes, e.g. inertial effects. This repeated drop weight machine is currently being used to investigate the fracture of concrete under torsional impact load conditions and some of the initial results are reported here.

EXPERIMENTAL DETAILS

The loading arrangement for applying torsion to the cylinders is illustrated in Fig.1. Two supports provide upward reactions, a third provides a downward reaction and the applied load is imposed at the free end. The load (static or dynamic) is transferred into the cylinders via a set of split collars. The collars are attached at both ends by means of an

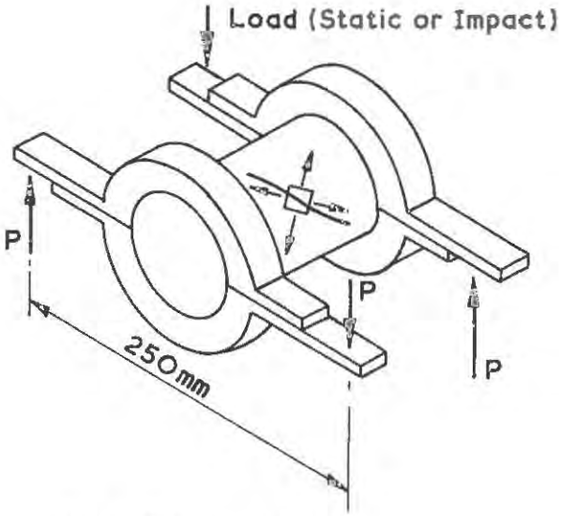

Fig.1 Torsion test rig

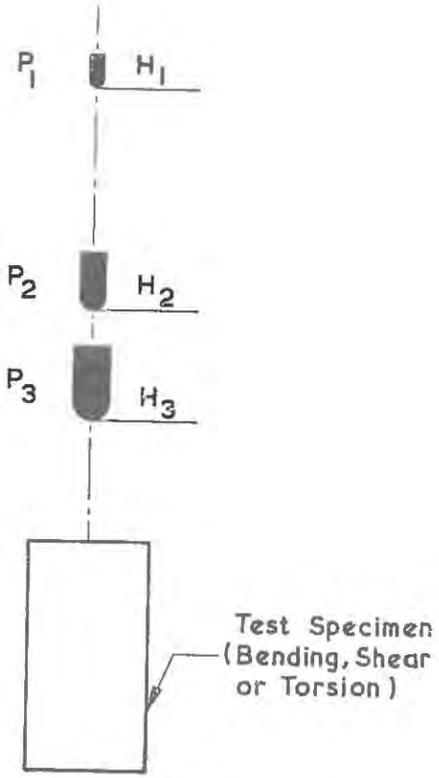

Fig.2 Schematic view of impact test apparatus

adhesive. Only standard 100mm diameter cylinders, 200mm long, have been tested to date. The collars were 30mm wide, leaving a clear length of 140mm being subjected to the torsional stress.

A schematic view of the repeated drop weight apparatus is given in Fig.2. A number of variables can be investigated using the apparatus. Various masses, P, ranging from 1 to 4 kg together with various drop heights, H, ranging from 0.5 to 2m, have been studied. Suitable combinations of drop heights and masses can be used with this test apparatus - for example to provide the same impacting energy but covering a range of impacting velocities. In addition to the variables provided by the apparatus, the test specimens can also be varied - a range of Mode I and Mixed-Mode fracture test specimens have already been tested by means of this apparatus. In this particular study, the impacting mass, P, was dropped onto the free arm of the testing arrangement shown in Fig.1.

The torsion test specimens were supported as illustrated in Fig.1 and subjected to a series of impacts by the falling masses. The number of blows required to completely fracture the specimens was taken as the measure of the impact resistance. In common with other similar test methods, it is important to realise that this method of testing is subject to energy dissipation during the impact event, including vibration, inertial effects, strain energy in the testing system, damage at the point of impact etc.

A full description of the instrumentation is beyond the scope of this paper. Gauges were fixed to the loading arm of the test rig to monitor the impacting load. An accelerometer was attached to the "free end" of the test specimen to monitor inertial effects. Each impact event was recorded by means of a 16-channel Signal Memory Recorder. The data collected during the impact tests were stored on a floppy disk and analysed later.

In this study three types of concrete materials have been investigated - ordinary concrete (cube strength of 55 N/mm^2), lightweight aggregate concrete (cube strength of 50 N/mm^2) and Polymer Concrete (cube strength of 40 N/mm^2). Only the initial results for the ordinary concrete are presented here. The mix used had a water/cement ratio of 0.5 and mix proportions of 1:1.8:2.8 representing cement (OPC) : fine aggregate (sea-dredged sand) : coarse aggregate (10mm crushed limestone aggregate). The specimens were cured under water for 27 days and tested at 28 days.

RESULTS AND DISCUSSION

A typical set of results is presented in Table 1. Even the limited test results given here illustrate a number of interesting points. Impact testing of plain concrete is not an easy area to research. If the impacting mass/drop height combination is below a threshold level then fracture will not occur. On the other hand, an impact which is only marginally greater than the threshold level will result in fracture in a relative small number of blows - hence accurate consistent results are difficult to obtain for plain concrete specimens. In contrast, FRC materials are much easier to test in the impact mode than the corresponding plain concrete test specimens. The next objective of this study is to extend the work to include FRC materials.

Specimens 1 and 3 in Table 1 had impacting energies of 5 Nm whereas the other three specimens had impacting energies of 10Nm. The results given in Table 1 show that the number of blows to fracture are greater in the cases where the drop height is greater (for the same impacting energy). This suggested that a heavier mass, travelling at a lower velocity, is more effective in transmitting energy into the test specimen and hence a smaller number of blows is required to cause failure of the test samples. This conclusion confirms earlier work on Mode I fracture test specimens (8) and is also in agreement with theoretical predictions.

Fracture angle results are also presented in Table 1. Generally the angle between the fracture plane and the longitudinal axis is approximately 45^{o}. It is of interest to note that the fracture planes are invariably in the central portion of the test specimens i.e. the results are not affected by the loading arrangements via the split collars.

TABLE 1

Torsional impact strength results for a Grade 55 concrete

Ref. No.	Impacting Mass (kg)	Drop Height (m)	Number of blows	Fracture angle (^{o})
1	1	0.5	10	43.6
2	1	1.0	3	45.6
3	2	0.25	8	35.5
4	2	0.5	2	49.6
5	4	0.25	1	42.8

CONCLUSIONS

A repeated drop weight impact testing apparatus has been successfully used to evaluate the impact torsional resistance of plain concrete cylinders. The impact resistance has been determined initially in terms of the number of blows required to fracture the test specimens. However, the apparatus and test specimens have been instrumented so that full details of the impact event (in terms of load-time response at impact and accelerations) are known and will be reported later. The study reported here brings together two current active research themes - torsional testing of cylinders and/or cores and impact testing.

Only results for plain concrete (Grade 55) are reported here. The impact results show that larger masses, travelling at lower velocities (but with the same energy at impact), are more efficient in producing impact fracture in torsion test specimen. This conclusion is similar to that reported earlier for notched beams in bending (Mode I fracture) and test specimens subjected to a predominantly shear type of loading. This conclusion is also supported by earlier theoretical studies.

This is an interesting area of research and work is currently being undertaken on lightweight aggregate concrete and polymer concrete. However, the main objective in the future will be to extend the work to include a study of the torsional impact strength of FRC materials.

REFERENCES

1. Bazant, Z.P. and Prat, P.C., Measurement of Mode III fracture energy, Nuclear Engineering and Design, Vol.106, 1988, pp1-8.

2. Xu, D. and Reinhardt, H.W., Softening of concrete under torsional loading. In Fracture of Concrete and Rock : Recent Developments (Eds: Shah, Swartz and Barr). Elsevier Applied Science, 1989, pp39-50.

3. Luong, M.P., Fracture behaviour of concrete and rock under Mode II and Mode III shear loading. In Fracture of Concrete and Rock : Recent Developments (Eds: Shah, Swartz and Barr). Elsevier Applied Science, 1989, pp18-26.

4. Tokatly, Z.A.Y., Torsional and Mode III strength of concrete, Ph.D. Thesis, University of Wales, 1991, pp341.

5. Norris, P., Wood, J.G.M. and Barr, B., A torsion test to evaluate the deterioration of concrete due to alkali-aggregate reaction, Magazine of Concrete Research, 1990, Vol.42, No.153, pp239-244.

6. Barr, B.I.G., Gorst, N.J.S. and Wood, J.G.H., A torsional damage test for the assessment of the deterioration of concrete. In proceedings of International Conference on Fracture Mechanics of Concrete Structures, Breckenridge, Colorado, 1992, pp

7. Banthia, N.P., Impact resistance of concrete, Ph.D. Thesis, The University of British Columbia, Vancouver, 1987, pp313.

8. Barr, B.I.G. and Baghi, A., A repeated drop-weight impact testing apparatus, Magazine of Concrete Research, 1988, Vol.40, No.144, pp167-176.

9. Mahjoub-Moghaddas, H., Tensile and shear strength of concrete and fibre reinforced concrete, Ph.D. Thesis, University of Wales, 1991, pp409.

10. Mahjoub-Moghaddas, H. and Barr, B.I.G., Impact shear strength of FRC Materials. In RILEM Symposium on Fibre Reinforced Cement and Concrete (Ed. R.N. Swamy), Ed F.N. Spon, July 1992, pp.

ACKNOWLEDGEMENTS

The second author has been supported partly by an SERC studentship. The authors also wish to acknowledge the contribution made by the Natural Resources Group towards supporting this project in various ways. Finally the authors also wish to acknowledge the contributions of Dr. Z.A.Y. Tokatly and Dr. H. Mahjoub-Moghaddas in the early days of the development of the torsion tests and the instrumented impacted testing apparatus respectively.

FRACTURE CHARACTERIZATION IN BLAST-LOADED CONCRETE STRUCTURES

Dr F B A Beshara and Prof K S Virdi
Structures Research Centre
Department of Civil Engineering
City University
Northampton Square, London EC1V 0HB, UK

ABSTRACT

The paper describes a finite element based analysis of reinforced concrete plane and axisymmetric structures under blast loading conditions. The method provides the possibility of activating different fracture mechanisms and failure modes characteristic of reinforced concrete structures. The rate sensitivity effects are also accounted for in the constitutive relations adopted for the materials in both tension and compression. The significance of history and rate dependent characterization is illustrated by means of examples.

INTRODUCTION

An understanding of the structural behaviour under blast loading is of concern in many aspects of military and civil engineering. For more realistic analysis of two dimensional reinforced concrete structures exposed to blasts, the nonlinear finite element method offers many advantages, especially in spatial discretisation. The method lends itself to convenient modelling of material nonlinearities and different fracture mechanisms. The paper briefly describes the method, but a fuller description of the theory and implementation can be found in [1-4].

MODELLING OF CONCRETE FRACTURE IN COMPRESSION

Concrete is idealized as a rate and history dependent elasto-viscoplastic strain hardening-softening material. The dynamic fracture of concrete in compression is modelled by generalizing the failure stress concept within the viscoplasticity theory by means of a set of variables, the values of which can be determined from empirical data. The viscoplastic behaviour is controlled by two bounding rate dependent surfaces in the stress space, the initial yield surface F_o and a failure surface F_f. The failure surface predicts failure if the state of stress satisfies the following condition

$$F_f\left(I_1, J_2, \sigma_{cd}\right) = f\left(I_1, J_2\right) - \sigma_{cd} = 0 \qquad (1)$$

where $f\left(I_1, J_2\right)$ is the failure function which is assumed to be a function of the first stress invariant I_1 and the second deviatoric stress invariant J_2. In the above equation, σ_{cd} is the dynamic compressive strength of concrete and is a function of its static strength and of the effective strain rate dependent magnification factor [1]. The following function has been developed for the representation of the failure surface of concrete in the principal stress space:

$$f\left(I_1, J_2\right) = a\, I_1 + \sqrt{b\, I_1^2 + 3\, c\, J_2} \qquad (2)$$

where a, b, c are material constants which have been evaluated elsewhere [1], using Kupfer's test results [5]. In the above formulation, the initial yield surface defines the onset of viscoplastic behaviour. When the stress state lies within this surface, concrete response is assumed to be linear elastic. Once concrete has been stressed beyond the elastic limit, a subsequent new loading surface develops. The new loading surface is assumed to have the same shape in stress space as that of the failure surface. Thus, the general form of the loading surface is proposed as

$$F_o\left(I_1, J_2, \tau\right) = f\left(I_1, J_2\right) - \tau = 0 \qquad (3)$$

in which τ is the effective stress which is assumed to be a function of the effective viscoplastic strain ε_{vp}, and the effective strain rate, $\dot{\varepsilon}_{eff}$.

Concrete crushing

To model the crushing mechanism for concrete, its ultimate deformation capacity under biaxial stress state is defined as a strain controlled phenomenon. This is achieved by converting the failure function described in terms of stresses to that in terms of strains such that

$$C\left(I_1', J_2', \varepsilon_{cu}\right) = a\, I_1' + \sqrt{b\, I_1' - 3cJ_2'} - \varepsilon_{cu} = 0 \qquad (4)$$

where I_1' is the first invariant of strain, J_2' is the second deviatoric strain invariant, and ε_{cu} is concrete ultimate strain (0.003-0.005).

Degradation of concrete compressive strength

To include the plastic stiffness degradation effects in the pre- and post-failure regimes, the parameter τ in Eqn (3) is derived as function of a history dependent plastic damage variable, effective viscoplastic strain, to fit quasi-static experimental results. Based on empirical rate sensitivity factors, this function is extended for dynamic problems. For the prefailure range, an isotropic hardening rule is developed which assumes the uniform expansion of the loading surface to be rate and history dependent. In Ref [1], the normalized effective stress is defined by the following hardening function

$$\frac{\tau}{\sigma_{cd}} = \frac{2}{C}\left[1 - C + \frac{2C}{\varepsilon_{cd}}\varepsilon_{vp}\right]^{1/2} - \frac{2}{C}\left[1 - C + \frac{C}{\varepsilon_{cd}}\varepsilon_{vp}\right] \quad (5)$$

in which ε_{cd} is the dynamic peak compressive strain and C is a constant derived as a function of concrete elastic limit. In the postfailure range, the loading surface shrinks with the increase in viscoplastic strain. A rate dependent softening rule has been defined [1] in which the effective stress is assumed as a function of the dynamic compressive strength and the postfailure viscoplastic energy, κ, such that

$$\tau = \sigma_{cd}\, e^{-\beta\kappa} \quad (6)$$

in which β is a concrete softening constant. Excellent agreement [1] has been obtained with Kupfer's results [5] for both the hardening and softening functions. To evaluate the viscoplastic strain rate vector, $\dot{\varepsilon}_{vp}$, the classic flow rule is modified to include rate dependence of inelastic deformations. The evolution law for the internal variable of associated rule, the fluidity parameter γ, is derived as a semi-empirical function of the effective strain rate.

$$\dot{\varepsilon}_{vp} = \gamma\left(\dot{\varepsilon}_{eff}\right) < \phi\,(F_o) > \mathbf{a} \quad (7)$$

where $\phi\,(F_o)$ is the flow function and **a** is the flow vector. From the governing uniaxial elasto-viscoplastic stress strain relation [1], and the curve fitting of experimental results, the fluidity parameter is found as a function of the effective strain rate and the concrete compressive strength.

IDEALIZATION OF CONCRETE TENSILE FRACTURE

Tensile fracture is modelled here by treating concrete as a linear elastic strain softening material [1, 4] with smeared fixed crack formulation.

Crack initiation criterion
The onset of tensile cracking is assumed to be governed by a rate sensitive strain criterion. The influence of deformation velocity is considered by raising the cracking strain to relative the static condition using a rate dependency factor.

$$\varepsilon_{cr} \geq \varepsilon_{td} \quad (8)$$

where ε_{td} is the dynamic cracking strain of concrete which is defined [1] as a function of the corresponding static strain and an empirical effective strain rate dependent magnification factor.

Degradation of tensile strength of cracked concrete
Upon cracking the gradual loss of tensile strength of concrete is governed by a nonlinear reversible tension softening rule based on the concrete fracture energy G_f, the crack characteristic length L_c, the static tensile strength σ_{ts} and static cracking strain ε_{ts}

$$\sigma = \sigma_{ts}\, e^{\frac{-\varepsilon + \varepsilon_{ts}}{\psi}}, \quad \psi = \left(G_f - 0.5\,\sigma_{ts}\,\varepsilon_{ts}\,L_c\right) \;/\; \sigma_{ts}\,L_c \quad (9)$$

The fracture energy concept leads to a nonlocal format of the equivalent softening relation necessary to meet objectivity of analysis with respect to mesh elements size.

CHARACTERIZATION OF CONCRETE FRACTURE IN SHEAR

Degradation of shear strength of cracked concrete
Considerable shear can be transferred across cracks due to aggregate interlock and dowel action of steel bars. In the smeared crack approach, the shear modulus of cracked concrete is obtained by using a reduction factor, which depends on the tensile strain ε across the crack.

$$\beta_c = 1 - \frac{\varepsilon_t}{0.004}\;;\; \beta = 0 \text{ if } \varepsilon_t \geq 0.004 \quad (10)$$

Detection of fracture localization and diagonal shear cracks
Under blast conditions, sudden and extensive diagonal cracking occurs within a few time steps. Some recommendations on computational strategies to be adopted are now given, based on numerical results [1]. First, displaying only full cracks, i.e. cracks for which the normal strain is beyond the ultimate strain of the tensile softening branch, is necessary to reveal any fracture localization in the structure behaviour as well as to uncover the shear-type cracks in the predicted crack patterns. Second, the use of Gaussian quadrature with a reduced 2x2 order for the integration of stress fields proves to be a successful means of avoiding stress-locking phenomena associated with strain localization mechanism [1]. This results in a partial release of the continuity requirements imposed by shape functions assumed for the finite elements.

MODELLING OF YIELDING OF STEEL REINFORCEMENT

Steel is modelled as a uniaxial strain rate dependent elasto-viscoplastic material in tension and compression in which the yield stress σ_{yd} is rate dependent. Beyond yield, the effective stress level is governed by a linear strain hardening function such that

$$\tau = \sigma_{yd} + H\,\varepsilon_{vp} \quad (11)$$

where H is the hardening modulus of steel. To calculate the viscoplastic strain rate, the associated flow rule is modified in a similar fashion to concrete where the fluidity parameter is derived as a semi-empirical function of the strain rate [1].

FINITE ELEMENT IMPLEMENTATION AND NUMERICAL APPLICATIONS

For the spatial discretisation of the nonlinear dynamic equilibrium equations, 8-node isoparametric elements have been employed for concrete with embedded bars to simulate reinforcement. Perfect bond is assumed

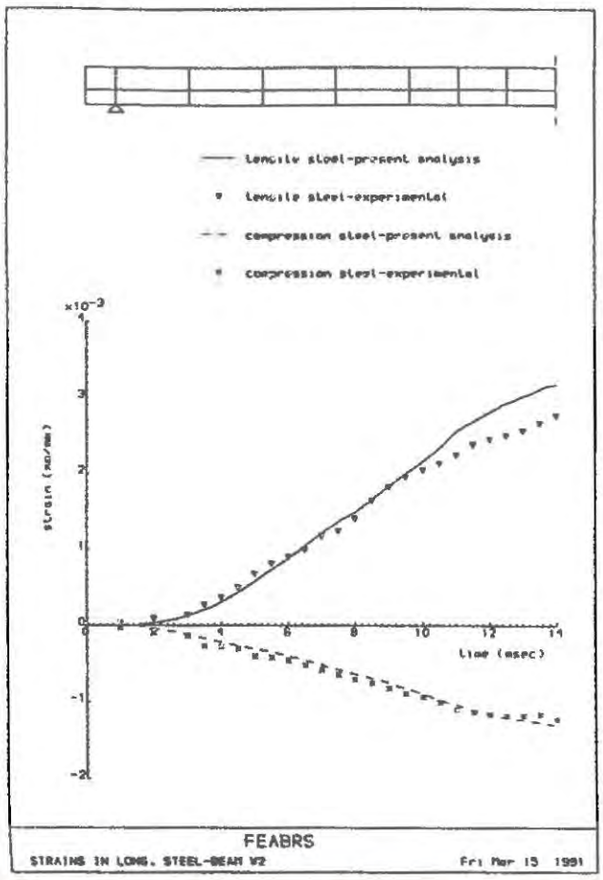

Fig 1: Strain history of steel

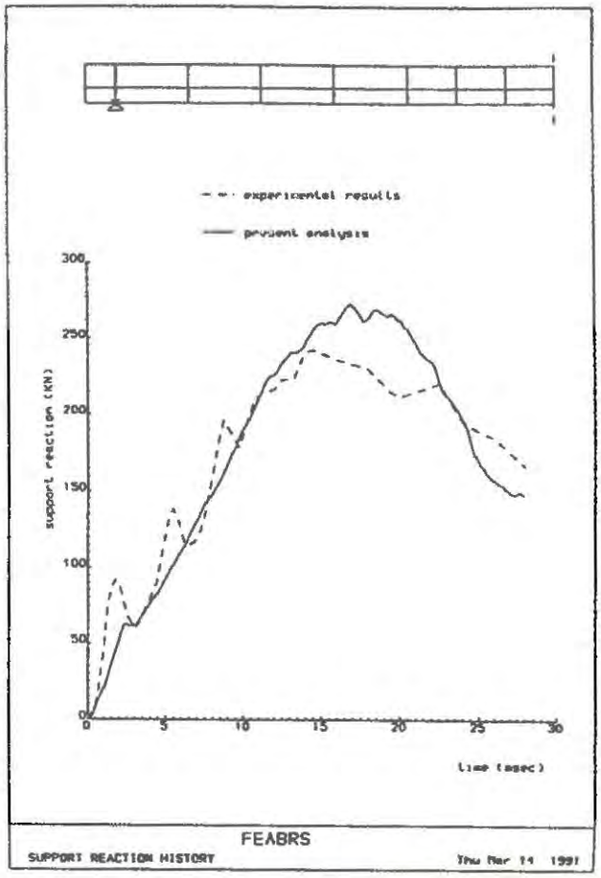

Fig 2: End reaction history

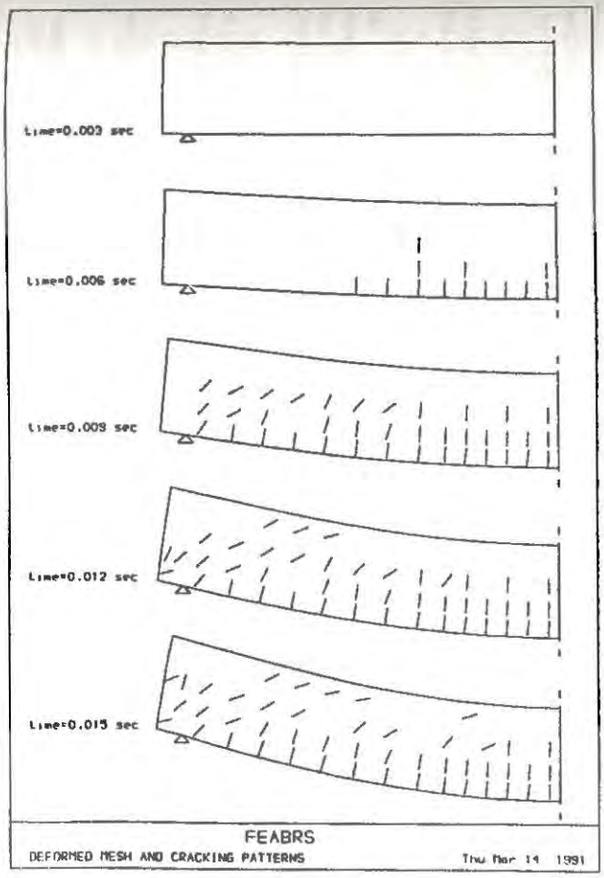

Fig 3: Cracking patterns

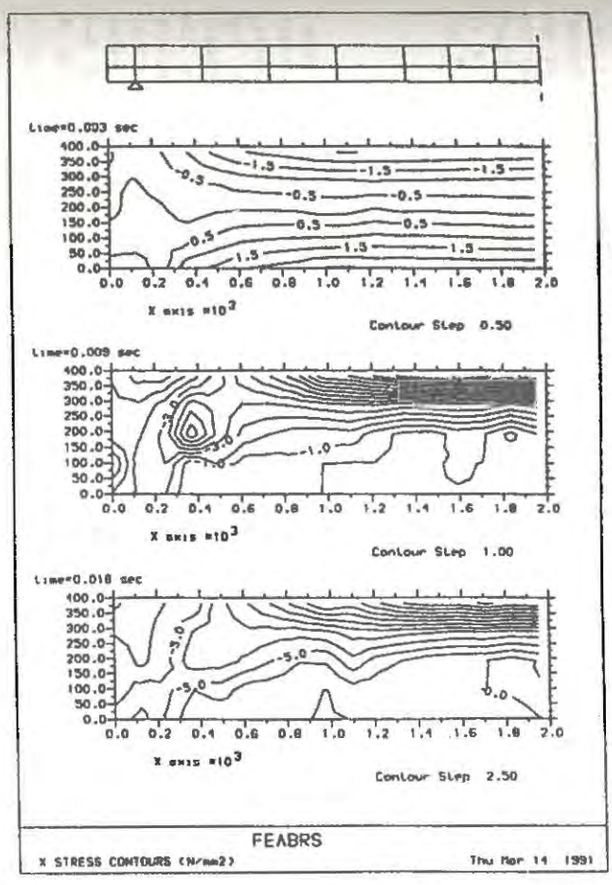

Fig 4: Longitudinal stress

between steel and concrete. Explicit central difference scheme has been used for temporal discretisation of dynamic equations while explicit Euler integration has been adopted for time rate constitutive relations [1, 4]. To implement the proposed fracture models, a versatile computer program, FEABRS, has been developed for linear and nonlinear dynamic analysis of two dimensional concrete structures. The program has been used to study the response characteristics of several structures under impulsive and blast loading [1-4]. In Figs 1-4, comparisons are made with test results of Ref [6] where many aspects of concrete fracture and the generality of the proposed models are well demonstrated by the analysis.

CONCLUSION

For the finite element analysis of concrete structures, a numerical model is presented for characterization of fracture mechanism under blast loading. The proposed rate and history elasto-viscoplastic constitutive model which includes strength degradation effects in the pre- and post-failure regimes, is suitable for modelling the concrete dynamic fracture in compression. For idealization of concrete tensile fracture, the adopted rate sensitive cracking condition in conjunction with fracture energy dependent tension softening rule proved to be a powerful numerical tool. In addition to a fracture strain based-shear retention factor, some recommendations are described for detecting diagonal shear cracks and fracture localization mechanisms. Steel yielding is considered by a modified viscoplasticity theory. An illustrative example is included.

REFERENCES

1. Beshara, F B A, Nonlinear finite element analysis of reinforced concrete structures subjected to blast loading, *PhD Thesis*, Structures Research Centre, Department of Civil Engineering, City University, London, June 1991.

2. Beshara, F B A and Virdi, K S, Nonlinear finite element dynamic analysis of two dimensional concrete structures, *Computers and Structures*, 1991, **41**, pp 1281-1294.

3. Beshara, F B A and Virdi, K S, A computational strategy for the cracking process in concrete structures under shock and earthquake loading conditions, *Proceedings of Int. Conf. on Earthquake, Blast and Impact*, SECED, held at University of Manchester Institute of Science and Technology, Manchester, 1991, pp 249-263.

4. Beshara, F B A and Virdi, K S, Time integration procedures for finite element analysis of blast-resistant reinforced concrete structures, *Computers and Structures*, 1991, **40**, pp 1105-1123.

5. Kupfer, H, Hilsdorf, H K, and Rüsch, H, Behaviour of concrete under biaxial stresses, *ACI Journal*, 1969, **66**, pp 656-666.

6. Seabold, R H, *Dynamic shear strength of reinforced concrete beams, Part 2*, Naval Civil Engng. Lab., Port Hueneme, Calif., AD 644823, 1967.

CONCRETE SLAB TESTS USING A SHOCK TUBE : HOW TO QUANTIFY CONCRETE DYNAMIC FRACTURE ?

FRANCOIS TOUTLEMONDE , CLAUDE BOULAY
Laboratoire Central des Ponts et Chaussées (LCPC)
58 bd Lefebvre 75732 Paris CEDEX 15, FRANCE

CHRISTIAN GOURRAUD
Laboratoire d'Essais d'Abris (LEA), BP2 46500 Alvignac, FRANCE

ABSTRACT

To study the high strain rate behaviour of structures, at a realistic scale for this material, and with the required test quality to obtain quantitative results and validate numeric codes, an experimental process for slabs has been developped at the LEA with the Concretes Department of the LCPC. Particular care has been taken concerning control of the loading (using the shock tube) and boundary conditions, instrumentation and data acquisition. This process has been used in order to determine the main parameters characterizing concrete dynamic behaviour and fracture, completing other dynamic tests carried out by the GRECO (French Group of Coordinated Researches in the field of Geomaterials). First results are getting available concerning the role of porosity and free water content in plain concrete slabs submitted to progressive shocks .

OBJECTIVES

The convergence of varied approaches and requirements presently leads to a growing interest in high strain rate behaviour of concrete structures, namely: (i) a demand of owners (power companies for nuclear plants, oil companies for off-shore structures, defence conctruction departments, etc.) who wish designs to reflect dynamic and accidental loadings more accurately; (ii) an increasing activity of scientific organizations in dynamics of materials, undoubtedly in connection with aerospace and military applications, and with the development of calculation resources that make it at least possible, if not yet easy, to solve these difficult numerical problems; (iii) a pressing necessity of improving design rules and processes to allow for shocks or rapid loading, in civil engineering and construction fields (bridge piers,

explosions inside or beside buildings).

Current knowledge however lacks for a rational engineer's approach in evaluating security/cost ratios of structures, because dynamic constitutive laws usable for concrete in design codes are not physically based, because well-controlled tests for validating calculations are rare, and because very few good probabilistic modelizations of accidental loadings exist.

Given this state of the art, we decided in the frame of the GRECO Géomatériaux - project "Dynamics of concretes", to develop a physically-based experimental analysis associating varied test facilities of highest reliability. Works by Pierre ROSSI who manages this project have highlighted the main role of free water and porosity in strain rate effects observed on concrete. Therefore one objective of the proposal is to confirm and quantify this influence, in order to adapt if necessary the concretes mix designs when impact or dynamic resistance is required. The other objective is to deliver reliable experimental results in varied loading conditions to help modelization.

Beside dynamic compression and traction facilities, a flexural dynamic slab test using a shock tube has thus been developped in cooperation between LCPC (French National Research Center for Public Works) Concrete Department and the LEA (French Laboratory for Shelters), members of this GRECO-project. The test covers a wide range of strain rates (typically 10^{-3} to $10\ s^{-1}$) corresponding to hard shocks and explosions. The same facility may also generate quasi-static loadings. Available data are described hereafter, allowing to validate "fine" computations including explicit cracking or to suggest "cruder" moment/curvature laws.

TESTING PROCESS AND MEASUREMENT

Principle

In a shock tube, a quasi-plane shock wave is generated by bursting the diaphragm which separates the reservoir filled with compressed air (up to 6,000 kPa) from the expansion zone (35 m) where the wave is guided and regularized. At the end of the tube, the wave hits the sample and is reflected. The concrete slab which is tested is simply supported and loaded uniformly and instantaneously. The pressure versus time profile is a step, the intensity of which (maximum about 1,700 kPa) depends on the inflation pressure and the duration of the plateau (10 to 100 ms) on the length of the reservoir (1.5 to 19 m). Successive shots with increasing maximum pressure allow bracketting the value of the ultimate structural load, and following the evolution of its rigidity and of its fissuration scheme. The load profile is very well controlled (pyrotechnic know-how) and reproducible, as it has been verified experimentally. The size of the tube (diameter = 666 mm) leads to rather big laboratory samples (diameter = 90 cm, thickness = 8 cm), so that realistic concrete mix-designs with 0 to 16 mm aggregates can be tested, and classically reinforced or fiber reinforced concrete slabs at a sufficiently large scale.

To avoid echoes of the shock wave, a relief area is provided in such a way that a "single" shock (considering damage to the slab) is applied at each shot. Realization of well controlled boundary

conditions required a specific mould with reduced margins and a specific supporting device where the slab is pinched between two circular ribs with special steel-rubber distribution rings. Control of the global mechanical behaviour of the slab is achieved by low pressure level quasi-static tests and measurement of the principal natural frequency: the result is very near to a simple support.

Measurement

Sixteen channels are available to characterize the sample's mechanical state. One is devoted to pressure, another to support acceleration for taking inertial forces into account. Local strain measurements are carried out by nine gauges bonded to concrete (inner side, and outer side for plain concrete) or to reinforcement (three gauges bonded to the welded wire mesh classically reinforcing the slab). The necessity to measure global deformations along a radius, when concrete gets cracked, leads to use five displacement sensors regularly spaced from center to support and edge of the slab. Their specifications are: linearity over 20 mm, distortion-free frequency response up to 500 Hz, precision of about 1 %, low cost. Gauge fork-shaped sensors in zicral and their connection to the slab and a fixed support had to be specially designed.

To get a fine analysis of transient behaviour at the shock time, without eliminating following of the whole sollicitation history, a dual time base (0.01 ms for 24 ms, 0.1 ms for 170 ms) is used on a first 16 channel recorder, while a 4 channel digital oscilloscope tracks for 1 s the main macroscopic variables: pressure, displacement of the support, central deflection and rotation on support. A perfect control of triggering, despite spike-current delivered by the exploder required specific electronic arrangements.

A precise survey of cracks, as soon as they appear and the axisymmetry of the test vanishes, of their position on inner and outer side and of their opening widths, and if possible clichés during the shock using a fast camera (4,000 images/second) complete the recorded data, stored on diskettes and processed for further analysis.

AVAILABLE DATA

The test has been undergoing development and validation campaigns for two years, and is now operational. A programme of tests has been carried out to confirm the role of free water content and porosity as main relevant parameters for concrete strain rate effects. Mix designs and storage conditions isolating these parameters have been used, and results are now being processed. Series of reinforced concrete slabs of different concrete qualities are to be tested, to give (if possible quickly) data for validating computations and drawing preliminary semi-quantitative conclusions for engineers.

REFERENCES

1. TOUTLEMONDE, F., BOULAY, C., GOURRAUD, C., Shocktube tests of concrete slabs, proposed for publication in Materials and Structures, 1992

2. TOUTLEMONDE, F., PASUTTO, S., Essai de dalles de béton au tube à choc, Scientific report of GRECO Géomatériaux, Project 1.3, 1990

3. TOUTLEMONDE, F., BOULAY, C., PASUTTO, S., GOURRAUD, C., progress report, Scientific report of GRECO Géomatériaux, project 1.3, 1991

4. TOUTLEMONDE, F., RINGOT, J.F., video-film Dalles soufflées à la Quercynoise, coproducted by LCPC & LEA, Copyright LCPC 1991

5. ROSSI, P., VAN MIER, J., TOUTLEMONDE, F., Dynamic behaviour of concretes, Report Euro-GRECO, project N°3, 1991

6. ROSSI, P., Influence of cracking in the presence of free water on the mechanical behaviour of concrete, Magazine of Concrete Research, 1991, **43**, N°154, 53-57

7. ROSSI, P., BOULAY, C., Influence of free water in concrete on the cracking process, Magazine of Concrete Research, 1990, **42**, N°152, 143-146

Figure 1. Cracked plain concrete slab at the end of the tube.

THE TRANSIENT SOLUTION OF MODE-I CRACK PROPAGATING WITH TRANSONIC SPEED

YEN-LING CHUNG
Department of Construction Engineering
National Taiwan Institute of Technology
P.O. Box 90-130, Taipei, Taiwan, R. O. C.

ABSTRACT

The transient problem of a mode-I centered crack propagating in an unbounded isotropic linear elastic body with the crack-tip speed larger than the S-wave speed and less than the P-wave speed is studied. The method of self-similar potentials with the function-theoretic approach has been successfully applied. Attention is focused on the stress singularity and it is found that the asymptotic solution of the stress field near the crack tips is of order -(1/2+m), where m = 0 for the crack-tip speed equal to the P-wave as well as S-wave speeds and m= 1/2 for the crack-tip speed equal to $\sqrt{2}$ of S-wave speed.

INTRODUCTION

Most of the studies on dynamic crack propagations have been based on the premise that for sub-Rayleigh cases the stress singularity is of order -1/2. However, experimental work by Winkler *et al.*[4] indicates the possibility of super-Rayleigh cases of crack propagation. Some analytical work has been carried out in the transonic and super-Rayleigh ranges using homogeneous function techniques by Brock [5], in the transonic range using the highly questionable steady-state approach discused in [6,7], and in the transonic range using the steady-state and transient methods of the mode-II propagating cracks studied by Freund[8]. Therefore, it would be of interest to solve the transonic crack problems without the steady-state assumption.

The method used in the present study is the self-similar potentials which was first developed by Smirnov and Sobolev [9] in 1930's. The method of self-similar potentials in conjunction with the Schwarz integral theorem provides an extremely powerful technique to solve the boundary value problems with much less mathematical manipulation [12]. However, for the crack problems which are the mixed-boundary problems, the Schwarz integral theorem cannot be used directly. and therefore a function-theoretic integral equation approach could be applied. Whereas, it was found for the corresponding indentation problem[10] that the transonic range was the most challenging aspect of the solutions. Thus, for the transonic crack problems, a special approach is required to overcome the difficulty.

It is known that the stress singularity for the subsonic case is of order -1/2. However, the singular behavior of the transonic case both the mode-I crack [7] and the mode-II [6,8] is different from that of the subsonic case. The singular behavior obtained here independently agrees with that studied by Broberg[7] for the steady-state solution.

THE PROBLEM OF MODE-I CRACK

Consider an unbounded homogeneous, isotropic elastic medium which has shear modulus μ and longitudinal and transverse wave velocities a and b. The material is at rest at time $t \le 0$. A crack begins to extend symmetrically from zero length along the x-axis with a constant speed s for time $t \ge 0$. The crack-tip speed s is taken in the transonic region, i.e., it is larger than the S-wave speed and less than the P-wave speed. A tensile loading in the y-direction of magnitude q acts at infinity so that the extension occurs in mode I. Further suppose that the remote tension q is taken such that the state of deformation is one of plane strain. The problem can be solved in two parts. Part I: The body without the crack under the external load q is considered; part II: The body with the crack on which the surface $|x| < st$, $y = 0$ is subjected to tractions opposite to that derived from part I is investigated. Then the final solution will be the sum of the contributions from part I and part II. Only the evaluation of part II is of present concern.

With the symmetry about the x-axis, consideration can be limited to the region $y \ge 0$ subjected to the following boundary conditions :

$$\sigma_y(x,0,t) = -q \qquad |x| < st \tag{2.1a}$$

$$\tau_{xy}(x,0,t) = 0 \qquad -\infty < x < \infty \tag{2.1b}$$

$$u_y(x,0,t) = 0 \qquad |x| \ge st \tag{2.1c}$$

Eqs.(2.1) indicate that the boundary tractions are homogeneous functions of degree zero in x and t. Therefore, eqs.(2.1) can be expressed in terms of the self-similar potentials. With the absence of the shear stress on the entire surface $y = 0$, the boundary conditions in eqs.(2.1) can be reduced to two equations which are: [1, 9, 10]

$$\sigma_y(\theta_0) = \mathrm{Re}\int_0^{\theta_0} \frac{-\mu b^2 R(\theta^2)}{\sqrt{a^{-2}-\theta^2}} V_y^{*\prime}(\theta)\, d\theta = -q \qquad |\theta_0| > s^{-1} \tag{2.2a}$$

$$V_y(\theta_0) = \mathrm{Re}\int_0^{\theta_0} V_y^{*\prime}(\theta)\, d\theta = 0 \qquad |\theta_0| < s^{-1} \tag{2.2b}$$

where θ_0 parameterizes the characteristic surface of the wave equations on the surface $y = 0$, i.e., $\theta_0 = t/x$; $R(\theta^2)$ is the Rayleigh function and $V_y^{*\prime}(\theta)$ is a unknown function. Therefore, the problem is now to solve the dual integral equations of eqs.(2.2) which involve an unknown function $V_y^{*\prime}(\theta)$.

SOLUTION OF THE PROBLEM

The boundary conditions in eqs.(2.2) will be satisfied if the following conditions are met: (i) The integrand of eq.(2.2a) is analytic for $|\theta_0| > s^{-1}$; (ii) The integrand of eq.(2.2b) is

analytic for $|\theta_0| < s^{-1}$. In a manner similar to the subsonic case[1], the quantity $V_y^{*\prime}(\theta)$ is found straightforwardly :

$$V_y^{*\prime}(\theta) = \frac{i\,F(\theta)}{(s^{-2}-\theta^2)^{3/2}} \tag{3.1}$$

where $F(\theta)$ is a function to be determined. When substituting eq.(3.1) to eqs.(2.2), we find that the function $1/\{(a^{-2}-\theta^2)^{1/2}(s^{-2}-\theta^2)^{3/2}\}$ in eq.(2.2a) has branch cuts in $a^{-1} < |\theta_0| < s^{-1}$ and the function $(s^{-2}-\theta^2)^{3/2}$ in eq.(2.2b) has branch cuts from $\pm s^{-1}$ to $\pm\infty$ on the real axis of the θ-plane. Thus, conditions (i) and (ii) can be rewritten as:

(i) $R(\theta^2)F(\theta)$ is analytic and real in $|\theta_0| > s^{-1}$; (3.2a)

(ii) $F(\theta)$ is analytic and real in $|\theta_0| < s^{-1}$ (3.2b)

Moreover, because the real load applied at the origin of the real plane, which corresponds to the infinite of the θ-plane, is finite, the order of the integrand in eqs.(2.2) must be less than -2. This means that the order of $F(\theta)$ must be zero as $\theta \to \infty$, i.e.,

(iii) $\lim_{\theta\to\infty} F(\theta) \to$ constant (3.2c)

A real complex function implies that the argument of that complex function, which is equal to the imaginary part of logarithm of the complex function, is zero. Hence, eqs.(3.2) can be rewritten as:

$$\mathrm{Im}\log F(\theta) = \begin{cases} -\mathrm{Im}\log R(\theta) & s^{-1} \le |\theta_0| < b^{-1} \qquad (3.3a) \\ 0 & |\theta_0| < s^{-1} \text{ and } |\theta_0| > b^{-1} \qquad (3.3b) \end{cases}$$

$$\lim_{\theta\to\infty} \log F(\theta) \to 0 \tag{3.3c}$$

The range $|\theta_0| > s^{-1}$ has been changed to $s^{-1} < |\theta_0| < b^{-1}$. This is caused by the fact that the Rayleigh function $R(\theta^2)$ is real and analytic for $|\theta_0| < b^{-1}$. Eqs.(3.3) show that the function Im log $F(\theta)$ is known on the entire boundary of the half space, therefore the Schwarz integral theorem [11] for the half space can be used to obtain the general solution for the function $F(\theta)$ which satisfies eqs.(3.3). The unknown function $F(\theta)$ is then found to be:

$$F(\theta) = B\,\beta(\theta^2), \quad \beta(\theta^2) = \exp\left\{\frac{1}{\pi}\int_{s^{-2}}^{b^{-2}} \frac{-\mathrm{Im}\log R(\xi^2)}{\xi^2-\theta^2}\, d\xi^2\right\} \tag{3.4}$$

where B is a real constant to be determined. It is noted that the solution approach was first developed by Thompson and Robinson for the corresponding indentation problem[10]. To obtain the value of constant B, the boundary condition $\sigma_y(\theta) = -q$ at $|\theta_0| < s^{-1}$ needs to be imposed. Therefore, it follows from eqs.(2.2), (3.1), and (3.4) that

$$B = \frac{q}{\mu b^2 J}, \text{ where } J = \mathrm{Re}\int_0^{\theta_0} \frac{i\, R(\theta^2)\, \beta(\theta^2)}{\sqrt{a^{-2}-\theta^2}\ (s^{-2}-\theta^2)^{3/2}}\, d\theta, \text{ for } |\theta_0| > s^{-1} \qquad (3.5)$$

The quadrature in eq.(3.5) can be easily calculated as accurately as desired by choosing any path off the real axis of the θ plane. It is easy to show that the function $\beta(\theta^2)$ at crack tips can be expressed as:

$$\beta(\theta^2) = \frac{\gamma(\theta^2)}{(s^{-2}-\theta^2)^{H(\theta^2)}}, \quad \gamma(\theta^2) = (b^{-2}-\theta^2)^{H(\theta^2)} \mathrm{Exp}\left\{ \int_{s^{-2}}^{b^{-2}} \frac{H(\xi^2) - H(\theta^2)}{\xi^2 - \theta^2}\, d\xi \right\} \qquad (3.6)$$

where $H(\theta^2) = -\ \mathrm{Im}\ \log R(\theta^2)/\pi$ and $H(\xi^2) = -\ \mathrm{Im}\ \log R(\xi^2)/\pi$. It follows directly that the value of $H(\theta^2)$ is always positive for $a^{-2} \le \theta^2 \le b^{-2}$, equal to zero for $\theta^2 = a^{-2}$ or $\theta^2 = b^{-2}$, and equal to 1/2 for $\theta^2 = b^{-2}/2$. The curve of function $H(\theta^2)$ is plotted in FIGURE 1. It is clear that $\gamma(\theta^2)$ is a smooth function at the crack tips, and the function $\beta(\theta^2)$ has singularity of $H(s^{-2})$ at the crack tips.

DYNAMIC STRESS INTENSITY FACTOR

For the subsonic case in which the crack-tip speed is less than the Rayleigh-wave speed, the stress intensity factor of a mode-I crack is defined by:

$$K_I = \lim_{\varepsilon \to 0} \left\{ \sqrt{2\pi\varepsilon}\ \sigma_y(\varepsilon, y=0) \right\}$$

However,It is apparent from eqs.(2.2), (3.1), and (3.6) that for the transonic case the stress field has singularities with the order of $-(1/2+H(s^{-2}))$, instead of -1/2. Therefore, we defined the stress intensity factor for the transonic case as:

$$K_I = \lim_{\varepsilon \to 0} \left\{ (2\pi\varepsilon)^{1/2+H(s^{-2})}\, \sigma_y(\varepsilon, y=0) \right\}$$

After some manipulations, the dynamic stress intensity factor for the transonic case is found as:

$$K_I = q\sqrt{\pi s t}\ (\pi s^3 t)^{H(s^{-2})}\, \frac{s^2 (b^{-2}-2s^{-2})^2\, \gamma(s^{-2})}{\left(1+2H(s^{-2})\right)\sqrt{s^{-2}-a^{-2}}\ J}$$

where J is given in eq.(3.6) and is negative. Since $\gamma(s^{-2})$ and $H(s^{-2})$ are all positive when the crack-tip speed s is in the transonic range, the value of K_I is therefore negative for positive load q. A graph of the ratio $K_I/q\sqrt{\pi s t}\ (\pi s^3 t)^{H(s^{-2})}$ versus s/a is shown in FIGURE 2 for the P-wave speed a = 6326 m/sec and the S-wave speed b = 3463 m/sec. FIGURE 2 shows that the

value of $K_I/q\sqrt{\pi s t}\ (\pi s^3 t)^{H(s^{-2})}$ is approximated to -0.5 when s = b, stays about -0 when b < s < a, and approaches to $-\infty$ when s = a. From the viewpoint of physics, the negative stress intensity factor means a healing crack. However, when a crack is subjected to a tensile external load, the crack surface is going to open, not to close. This means that the mode-I crack propagating with transonic velocity is impossible, which independently agrees with the Broberg's study[7].

ACKNOWLEDGMENTS

This article was supported by the National Science Council of Taiwan under grant NSC-80-0410-E011-11. The author would like to express her appreciation to the professor A. R. Robinson of Civil Engineering in the University of Illinois at Urbana-Champaign for his suggestions.

REFERENCES

1. Chung, Y. L., "The Transient Solutions of Mode-I, Mode-II, and Mode-III Cracks Problems," *Journal of the Chinese Institute of Civil and Hydraulic Engineering*, Vol. 3, No. 1, pp. 51-61, 1991.

2. Freund, L. B., "Crack Propagation in an Elastic Solid Subjected to General Loading - I Constant Rate Extension," *Journal of the Mechanics and Physics Solids*, Vol. 20, pp. 129-140, 1972.

3. Kanninen, M.F. and Popelar, C. H., *Advanced Fracture Mechanics*, Oxford University Press, New York, 1985.

4 Winkler, S., Shockey, D. A., and Cruuan, D. R., "Crack Propagation at Supersonic Velocities: I,"*International Journal of Fracture Mechanics*, Vol. 6, No. 2, pp. 151-158, 1970.

5 Brock, L. M., "Two Basic Problems of Plane Crack Extension: A Unified Treatment, " *International Journal of Engineering Science*, Vol. 15, pp. 527-536, 1977.

6 Georgiadis, H. G., "On the Stress Singularity in Steady-State Transonic Shear Crack Propagation," *International Journal of Fracture Mechanics*, 30, pp. 175-180, 1986.

7 Broberg, K. B.,"The Near-tip Field at High Crack Velocities," *International Journal of Fracture*, Vol. 39, pp. 1-13, 1989.

8 Freund, L. B.,"The Mechanics of Dynamic Shear Crack Propagation," *Journal of Geophysical Research*, Vol. 84, No. B5, pp 2199-2209, 1979.

9 Smirnov, V. I., *A Course of Higher Mathematics*, Vol. III, part 2, Addison-Wesley, Reading, Mass, 1964.

10 Thompson, J. C. and Robinson, A. R., "Exact Solutions of Some Dynamic Problems of Indentation and Transient Loadings of an Elastic Half Space," Civil Engineering Studies, *SRS* 350, University of Illinois, Urbana, Illinois, 1969.

11 Churchill, R. V., *Complex Variables and Applications*, Fourth Edition, MaGraw-Hill, New York, 1984.

12 Johnson, J. J. and Robinson, A. R., "Wave Propagation in Half Space Due to an Interior Point Load Parallel to the Surface," Civil Engineering Studies, *SRS* 388, University of Illinois, Urbana, Illinois, 1972.

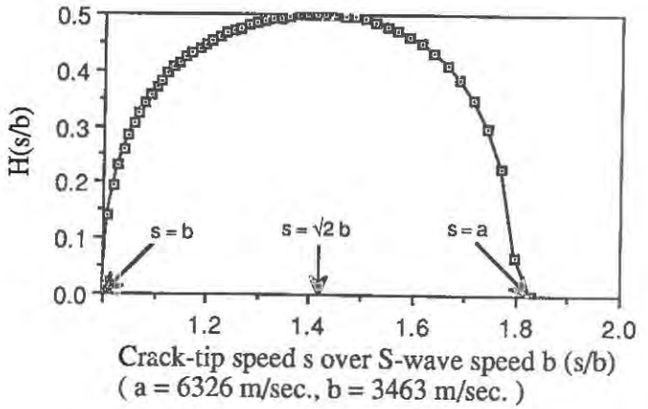

FIGURE 1 The curve of the function H(θ).

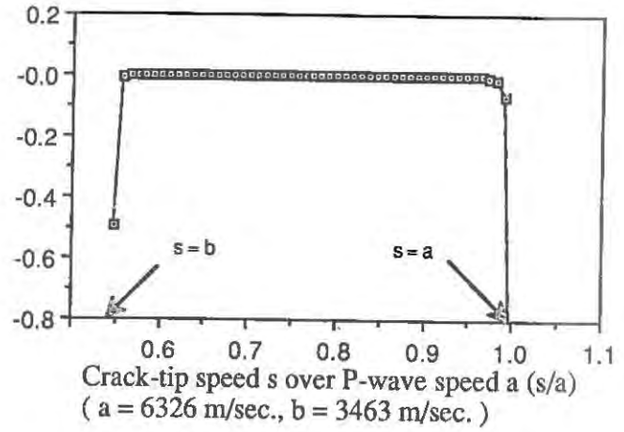

FIGURE 2 The ratio of $K_I / q\sqrt{\pi st}\ (\pi s^3 t)^{H(s^{-2})}$ versus the ratio of s/a

IS THE DYNAMIC BEHAVIOUR OF CONCRETE INFLUENCED BY THE PRESENCE OF FREE WATER ?

P. ROSSI (1), J.G.M. VAN MIER (2), F. TOUTLEMONDE (1)
(1) Laboratoire Central des Ponts et Chaussées, Paris Cedex 15, France.
(2) Stevin Laboratory, Delft University of Technology, Delft, The Netherlands

ABSTRACT

Direct tensile tests were performed on a microconcrete and miniconcrete at loading rates between 0.02 and 80000 MPa s-1. It is shown, experimentally, that the presence of free water in these concretes causes the increase in strengths observed at a high loading rate.

INTRODUCTION

In the context of European co-operation (scientific co-operation programme of the European Community) between the LCPC (Laboratoire Central des Ponts et Chaussées) in Paris, and the Stevin Laboratory of Delft University of Technology, Delft, Netherlands, the dynamic tensile behaviour of concrete has been studied. Particular interest was taken in the influence of free water on the increase of strength with loading rate. Two series of tests were performed respectively on a microconcrete and a miniconcrete using the Split Hopkinson Bar at Delft University [1]. In order to determine the possible influence of free water, two internal moisture conditions were studied: completely wet (no exchange of moisture with the exterior) and completely dry (the specimens, once matured, are oven dried with a gradualincrease of temperature to 105°C). The results concerning the microconcrete were the subject of a publication [2]. They showed that the dry microconcrete exhibited a very small rate effect, while the tensile strength of the wet microconcrete increased substantially with the strain (or stress) rate. So, the study on the miniconcrete was to verify whether this effect exists in a concrete made with coarser aggregates too.

EXPERIMENTAL INVESTIGATION

Characteristics of the concrete and of the specimens tested

The composition of the microconcrete, and of the miniconcrete is given respectively in tables 1 and 2.

TABLE 1
Microconcrete mix

constituents	amount (Kg/ m3)
Normalized sand (Leucate) 0/2 mm	1783
Portland cement type 1 (CPA HS)	400
Mixing water	200
Melment Plast Superplasticizer	12

TABLE 2
Minicroconcrete mix

constituents	amount (Kg/m3)
microgranite (Pont de Colonne) 6/10 mm	1162
sand (Bernières) 0/4 mm	681
cement CPA HP (Cormeilles)	365
eau	185

The specimens were 74 mm in diameter and 100 mm long. They were released from the moulds at 17 days for the microconcrete and at 36 days for the miniconcrete. Half of them was protected from drying, while the other half was dried in an oven by gradual heating up to 105°C.
The specimens were protected from exchanges of free water with the exterior by wrapping them in a thin sheet of plastic paper covered with two thicknesss of self-adhesive aluminium foil (following a method develloped at LCPC [3]).
The specimens were then tested at ages ranging from 29 to 40 days for the microconcrete and from 37 to 57 days for the miniconcrete. The ends of the specimens were sawn, ground, then glued to the Hopkinson bar. It should be noted that the protective wrapping was left on the specimens (except at the ends) during the tests.

Experimental procedure

As we have stated, the tests were performed on the Split Hopkinson Bar of the Stevin Laboratory Delft University [4]. The principle of this test is shown schematically in figure 1. The stress in the specimen is measured using two strain gauges (half-bridge mounted to give a mean), fixed to the upper the aluminium bar. By varying the mass of the hammer, its drop height, and the type of contact between the hammer and the bottom of the bar (impact more or less hard depending on the thickness of the rubber interlaye), it is possible to vary the shape of the pulse, i.e. the rate and energy of loading.
In our study we fixed the drop height of the hammer and varied its mass (two mass values) and the thickness of rubber (three different thicknesses). Three loading rates, between 1500 and 80000 MPa/s, covering the range of loading rates (from slowest to fastest) attainable by the Split Hopkinson Bar of Delft and sufficient to cause failure of the concrete specimens, were selected in this way.

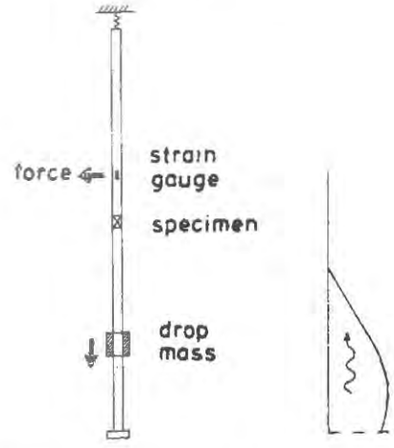

Figure 1. Schematic diagram of the Hopkinson bar.

The static uniaxial tensile tests, were carried out using the tensile apparatus developed at Delft University [5] for the microconcrete, and a classical hydraulic machine in LCPC for the miniconcrete.
The static tests were carried out at an imposed displacement rate of 0.08 µm/s for the microconcrete, and at an imposed stress rate for the miniconcrete. Concerning this last one, two stress rates were studied: 5 10-5, and 5 10-3 GPa/s.
It should be emphasized that we had, for the microconcrete, great difficulty performing the dynamic tests on the wet microconcrete because of the poor bond between the specimen and the aluminium bar: the glue used polymerizes rather poorly in the presence of

the wet surface of the specimen, and there were many cases in which failure occurred in the glue or at the glue-concrete interface. We solved this problem by making a notch in the perimeter of the specimens, at mid-height (for the wet specimens only). This created a preferential zone of failure in the specimen and so eliminated the failures in the glue. This solution was of course used in the static tests. The geometry of the notch is 10 mm deep and 4 mm wide.

EXPERIMENTAL RESULTS

As for the determination of the loading rate, we made the assumption that the failure of the specimen is a function of the couple (σ, $\dot{\sigma}$) and that in consequence the loading rate that must be used is the one that exists at the time of failure of the specimen. This choice differs using a mean stress rate when its evolution versus time is nonlinear (the greater the thickness of rubber at the point of contact between the mass and the bottom of the bar, the more nonlinear this evolution becomes).
As the results concerning the microconcrete have been previously presented in details [2], we will resume them in considering only the ratio $\sigma dyn./\sigma stat.$ for the two internal moisture conditions:this ratio is equal to 4.1 for the wet concrete, and to 1.14 for the dry concrete.
The results relative to the miniconcrete are given in the table 3.

TABLE 3
Results relative to the miniconcrete

	static		dynamic	
internal moisture	$\dot{\sigma}$ GPa/s	σrmean MPa	$\dot{\sigma}$mean GPa/s	σrmean MPa
dry	5 10-5 5 10-3	3.1 3.4	1.9 5.9 34.6	4.0 4.1 4.4
wet	5 10-5 5 10-3	3.6 4.8	2.0 5.9 47.3	5.7 6.5 7.5

The index mean is relative to the average of 10 values.

If we make the same analysis than for the microconcrete, we find that the ratio $\sigma dyn./\sigma stat.$ is equal to 1.38 for the dry miniconcrete wherreas this ratio is equal to 2.08 for the wet miniconcrete.

Considering the results relative to the microconcrete and to the miniconcrete, we can make the following comments: *With sand or coarser aggregates the wet concrete is subtantially more rate dependent that the dry concrete.*

The remaining small rate effect migth probably be caused through another, still unknown, physical mechanism. But, two others assumptions can also be advanced to explain this small rate effect:

1. The first one may be derived from the fact that the specimens regarded as dry are not completely dry. It is, in fact, very difficult to dry the micropores (with diameter of, approximatively, 10-8 m) of concrete in which the physical forces between the water and the solid skeleton are very strong. Perhaps the thermal treatment in the oven was not sufficient to warrant a completely dry specimen.

2. The extent forces of inertia in the bar-specimen system, which are not taken into account in our analysis, could affect the results.

The second assumption being very difficult to verify, we have choosen to study, in a first time, the validity of the first assumption. To do that, we have applied to 6 specimens of miniconcrete a thermal treatment which was different that for the others specimens. Instead of 3 weeks in the oven at 105°c, these 6 specimens stayed only 1 week at 105 °c.
These specimens were tested in static condition using two stress rates: 5 10-5 (3 specimens), and 5 10-3 GPa/s (3 specimens).
We have considered the ratio between the tensile strength relative to each stress rate for the three conditions of thermal treatment: without thermal treatment (wet specimens), 1 weeks at 105°c, and 3 weeks at 105°c. The results are given in table 4.

TABLE 4
Influence of the thermal treatment of the specimens on the rate effect

	dry concrete condition 1	dry concrete condition 2	wet concrete
$\sigma r1/\sigma r2$	1.10	1.23	1.35

$\sigma r1$: tensile strength relative to the stress rate of 5 10-3 GPa/s,
$\sigma r2$: tensile strength relative to the stress rate of 5 10-5 GPa/s,
condition 1: thermal treatment during 3 weeks,
condition 2: thermal treament during 1 week.

From the above results, the following conclusion can be drawn: its seems obvious that the rate effect observed on the dry specimens is principally due to the fact that the thermal treatment is not sufficient to dry completely the micropores of the concrete.

CONCLUSIONS

In this article, we have presented some experimental results which permit to obtain this important information: *the presence of free water in concrete explains practically all of the increase of tensile strength of this material at higher loading rates*.

ACKNOWLEDGMENTS

We thank the Commission of the European Community in charge of co-operation programs, without whose help this study could not have been performed.

REFERENCES

1. Reinhardt, H.W., Rossi, P., Van Mier, J.M.G., Joint investigation of concrete at high rates of loading. Materials and Structures, 1990, vol. 23, pp. 213-216.

2. Rossi, P., Van Mier, J.G.M., Boulay, C., Le Maou, F., The dynamic behaviour of concrete: influence of free water. To be published in Materials and Structures in 1992.

3. Attolou, A., Belloc, A., Torrenti, J.M., Méthodologie pour une nouvelle protection du béton vis à vis de la dessiccation. Bulletin de Liaison des LPC, 1989, n°164.

4. Reinhardt, H.W., Körmeling, H.A., Zielinski, A.J., The split Hopkinson bar, a versatile tool for impact testing of concrete. Materials and Structures, 1986, vol. 19, pp. 55-63.

5. Hordijk, D.A., Reinhardt, H.W., Cornelissen, H.A.W., Fracture mechanics parameters of concrete from uniaxial tensile tests as influenced by specimen length. Proceedings of the International Conference on the fracture of concrete and rocks, Houston, published by Shah and Swartz, 1987, pp. 138-149.

NONLINEAR DYNAMIC ANALYSIS OF DAMAGE IN CONCRETE

Minh Phong LUONG and Hui LIU
CNRS URA 317
Laboratoire de Mécanique des Solides
Ecole Polytechnique 91128 Palaiseau, France

ABSTRACT

Concrete structures, subject to strong ground motions, undergo repeated deformations, respond inelastically and accumulate damage which may lead to failures. Therefore, the nondestructive detection of the nonlinear response as well as the potential for damage accumulation has to be considered as an aid to delay and to control the post-cracking and post-yield behaviour of concrete. This paper describes experimental results, obtained in the laboratory, using specific testing methods to assess damage accumulation. The damaging process of a concrete specimen has been detected by analysing the signal evolution of ultrasonic pulses travelling through the specimen subject to increasing loads. A nonlinear analyser based on a multidimensional Fourier transform permits to separate the linear and nonlinear part of the concrete response.

INTRODUCTION

Concrete is widely used as construction material because of its many favourable characteristics. It presents a high strength-cost ratio in many applications. It may easily be cast in forms at ordinary temperatures to produce almost any desired shape. The exposed face may be developed into a smooth or rough, hard surface, capable of withstanding the wear of truck or airplane traffic, or it may be treated to create desired architectural effects. In addition, it has high resistance to fire and penetration of water.

But concrete has also disadvantages. Quality control is sometimes less rigourous than for other construction materials, because it is often mixed on the site under conditions where responsability for its production cannot be pinpointed. Concrete is generally weak and brittle in tension compared to its capacity in compression. There is a need for a better control of the mechanical performance as well as the post-cracking and post-yield tensile behaviour [1].

In seismic areas, concrete structures, subject to strong ground motions, undergo repeated deformations, respond inelastically and accumulate damage which may lead to failures [2]. Therefore the nondestructive detection of the nonlinear response as well as the potential for damage accumulation has to be considered as an aid to delay and to monitor the post-cracking and post-yield response of concrete.

This paper describes special testing devices in use for measuring experimentally the occurrence of damaging nonlinearities and specific testing methods to assess damage accumulation. As damage accumulates in a structural system, its strength diminishes. It is assumed that dissipated energy is a measure of concrete damage. As the energy is dissipated by the concrete structure, the residual strength decreases. The damaging process of concrete specimen has been detected by analysing the signal evolution of ultrasonic pulses propagating through the specimen which is subjected to increasing loads. A nonlinear analyser based on a multidimensional Fourier transform permits to separate the linear and nonlinear part of the concrete response.

NONLINEAR ANALYSER

Experimental methods have traditionally been used to obtain information concerning deformations, strains, structural integrity and failure mechanisms. Common experimental methods include extensometers, photoelasticity, moiré interferometry [3], ultrasound and radiography, as well as acoustic [4] and thermographic [5] methods. Measurement of the elastic moduli using ultrasound has become fairly routine. The connection between the speed of sound c, density ρ and Young's modulus E is strictly valid for an ideally linear elastic and homogeneous material; it remains valid for heterogeneous materials so long as a key assumption is satisfied, namely, the wavelength is large compared to any characteristic length of the material. Acoustic emission AE is applied in a broad sense to the sounds which are internally generated in a material which is under stress. AE testing is relatively simple needing only a sensor (usually piezoelectric), basic signal-analysis equipment (amplifier, filter, data-processing equipment) and some means of loading the structure. There is a wide variety of mechanisms known to be responsible for AE generation, ranging from dislocation motion to crack propagation. Therefore, the basic AE monitoring techniques are applicable to a wide class of materials and structures. Unfortunately the interpretation of results still remains a delicate affair.

Linear analysers based on one-dimensional Fourier transforms (FTs) and modal analysis programmes are popular tools used by experimentalists in linear structural dynamics. In this experimental work, an input-output non-parametric approach [6] has been chosen to portray the nonlinear behaviour of concrete subject to tension.

A nonlinear functional Volterra series has been used to detect the occurrence of the nonlinear behaviour of concrete subject to increasing tensile loading. In this functional, the total response of the system y(t) is decomposed into components of various orders.

$$y(t) = y_1(t) + y_2(t) + \ldots + y_n(t) \tag{1}$$

Each component is defined by a functional

$$y_n(t) = \int_{-\infty}^{\infty} \ldots \int_{-\infty}^{\infty} h_n(\tau_1,\tau_2,\ldots,\tau_n) \prod_{k=1}^{n} x(t-\tau_k)\, d\tau_k \tag{2}$$

The first order component is described by linear convolution

$$y_1(t) = \int_{-\infty}^{\infty} h_1(\tau)\, x(t-\tau)\, d\tau \tag{3}$$

where x(t) denotes the input function and $h_1(t)$ the first order impulse response that describes the linear behaviour of the system.

The other components require more than one time variable and multidimensional signal processing is needed. As an example, let us describe the second order (nonlinear) component of the response. From Eq.(2), we have the following expression :

$$y_2(t_1,t_2) = \int_{-\infty}^{\infty}\int_{-\infty}^{\infty} h_2(\tau_1,\tau_2)\, x(t_1-\tau_1)\, x(t_2-\tau_2)\, d\tau_1 d\tau_2 \tag{4}$$

where τ_1,τ_2 are the two time variables and $h_2(\tau_1,\tau_2)$ denotes the second order impulse response. Within this mathematical framework, two dimensional Fourier transform is appropriate for the study of the material behaviour in the frequency domain.

$$\mathcal{F}_2\,[h_2(\tau_1,\tau_2)] = \int_{-\infty}^{\infty}\int_{-\infty}^{\infty} h_2(\tau_1,\tau_2)\, \exp(-j\omega_1\tau_1 - j\omega_2\tau_2)\, d\tau_1 d\tau_2 \tag{5}$$

This expression defines the second order transfer function $\mathcal{H}_2$ with two circular frequency variables ω_1 and ω_2 . $\mathcal{F}$ is the Fourier transform operator.

$$\mathcal{H}_2\,(\omega_1,\omega_2) = \mathcal{F}_2\,[h_2(\tau_1,\tau_2)] \tag{6}$$

In this application, a single impulse has been used as input

$$x(t) = a\,\delta(t-T)$$

Then from (1) and (2), we obtain :

$$y(t) = \sum_{i=1}^{n} y_i(t) = \sum_{i=1}^{n} \int_{-\infty}^{\infty} \ldots \int_{-\infty}^{\infty} h_i(\tau_1,\tau_2,\ldots\tau_i) \prod_{k=1}^{i} a\,\delta(t-T-\tau_k)\, d\tau_k$$

$$= \sum_{i=1}^{n} a^i\, h_i(t-T) \tag{7}$$

From the single impulse of m different test magnitudes, Eq.(7) gives :

$$y^m(t) = \sum_{i=1}^{n} a_m^i\, h_i(t-T) \tag{8}$$

where m denotes the m^{th} test.

Under matrix form, Eq.(8) is as follows :

$$\{y\} = [a]\,\{h\} \tag{9}$$

where

$$\{y\} = (y^1(t),y^2(t),\ldots,y^m(t))^T$$

$$\{h\} = (h_1(t-T),h_2(t-T),\ldots,h_n(t-T))^T \tag{10}$$

$$[a] = \begin{bmatrix} a_1^1 & a_1^2 & \cdots & a_1^n \\ a_2^1 & a_2^2 & \cdots & a_2^n \\ \cdots & \cdots & \cdots & \cdots \\ a_m^1 & a_m^2 & \cdots & a_m^n \end{bmatrix} \quad (11)$$

or

$$\{h\} = [a]^{-1} \{y\} \quad (12)$$

This equation gives the impulse response of various orders with only one time variable.

TEST PROCEDURE AND EXPERIMENTAL RESULTS

Large specimens have been prepared and maintained during testing by a steel frame (Figure 1) in order to keep the main advantages of the proposed cylindrical test specimen, described in [7]. The tests were performed on a closed-loop electro-hydraulic loading machine of 50 kN capacity. Four electro-mechanical extensometers of 30 mm and 60 mm gauge length were glued onto the specimens to measure the deformation at different locations. One LVDT measured the deformation over the crack zone.

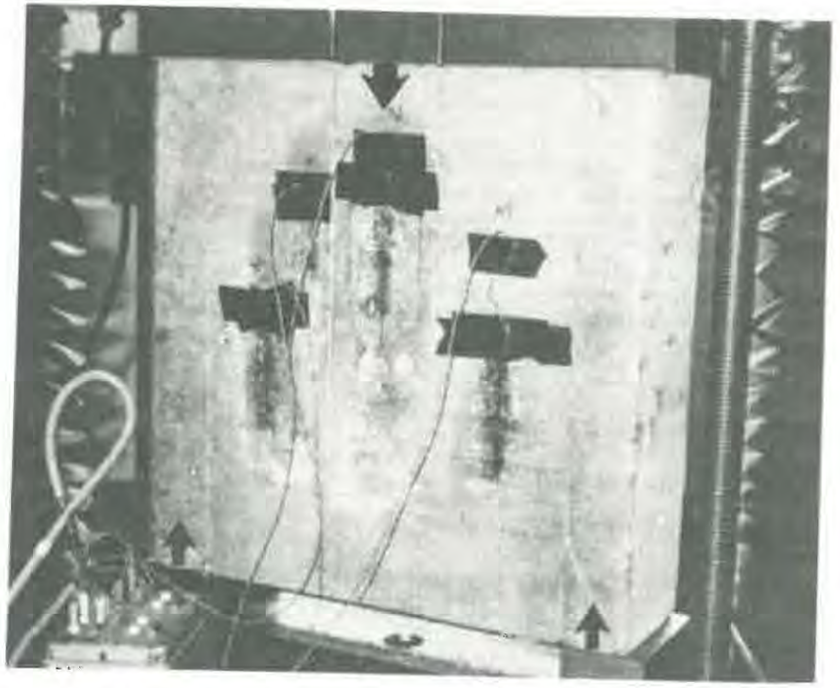

Figure 1. Large tensile test specimen equipped with extensometers.

Concrete mix

The mix used is (per m³)

Aggregate size	12.3/20 mm :	485 kg
	8/12.5 mm :	359 kg
Sand	1.6/5 mm :	156 kg
	0/1.6 mm :	701 kg
Cement (CPA HP Ciment Lafarge Saint Vigor) :		385 kg
Superplasticizer Sikament HR 401 :		9.6 kg
Mixing water :		137 litres
Dramix steel fibres	(length : 60 mm) :	40 kg

The curing conditions employed during a fortnight period are : ambient temperature (20 °C) and relative humidity : > 95 % (mist conditioning room). The compressive strength at 28 days old, measured on the standard cylinders (0.16 m in diameter and 0.32 m high), are 56.2 MPa, 57.3 MPa and 59.9 MPa.

Using Hillerborg's technique [8], the characteristic length of the tested cementitious composite has been determined thanks to the relationship :

$$\ell_{ch} = EG_F / f^2_t = 248 \text{ mm}$$

The pulse-transmission method, using videoscan piezoelectric transducers V150 (0.25 MHz), have been applied as a nondestructive testing, in conjunction with a pulser-receiver Panametrics 5052PR which provides high-energy broadband performance. The pulser section produces an electrical pulse to excite a piezoelectric transducer, which emits an ultrasonic pulse. The pulse travels through the specimen which is subjected to a given static tension, to a second transducer acting as a receiver. The transducer converts the pulse into an electric signal which is then amplified and conditioned by the receiver section and made available for nonlinear analysis.

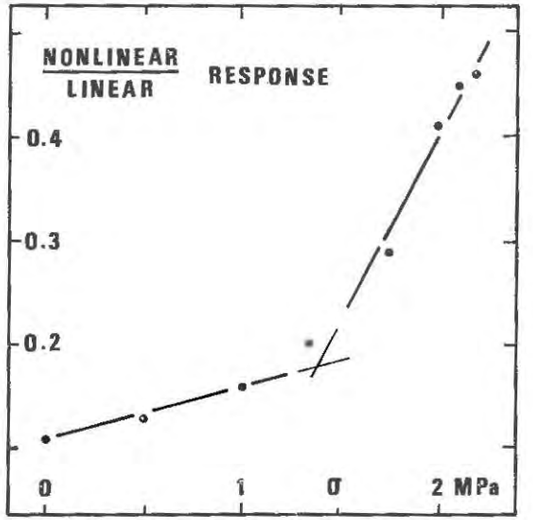

Figure 2. Variation of the ratio nonlinear/linear response of the ultrasonic pulse travelling through the specimen under static tension loading.

Signal records have indicated the evolution of the ultrasonic pulse travelling through the specimen which is loaded by increasing static tensile forces. They have evidenced (1) the occurrence of tensile cracking which modifies the longitudinal part (the faster) of the pulse signal and (2) the effects of microcracking which affect its transversal part (the slower). Figure 2 presents the variation of the ratio nonlinear/linear response of the ultrasonic pulse. The slope change of the experimental curve suggests that the concrete presents two different behaviours : the former is stable ,the latter may lead to failure because of microcracking which generates nonlinear effects affecting the ultrasonic wave propagation mechanisms. The traditional "ductility factor μ", commonly used for the design of earthquake resistant structures, seems to be defined in reference to this threshold of nonlinearity appearance.

CONCLUDING REMARKS

The proposed testing arrangement for direct tensile strength measurements simplifies the loading equipment by the use of a uniaxial test machine with the combined compression loading frames. It is practical and reliable. The method does not require special testing equipment and/or ancillary mechanical components.

The nonlinear analyser reveals to be very useful for the detection of the microcracking process announcing the occurrence of propagating damage in the concrete subject to tension. It can be used to monitor nondestructively and continously the whole fatigue damage process of concrete so that the damage mechanisms can be quantitatively explained.

The experimental results provides a basis for selecting a ductility factor in earthquake resistant design, because ductile hysteretic response is a manner of transforming and dissipating the seismic energy or accumulating damage during successive events.

REFERENCES

1. Chern, J.C., Young, C.H. and Wu, K.C., A nonlinear model for mode I fracture of fiber reinforced concrete, Fracture Mechanics : Application to Concrete, ACI SP-118, 1989, pp. 91-112.
2. Rosenblueth, E., Design of earthquake resistant structures, Pentech Press, London, 1980, pp.142-194.
3. Yon, J.H., Hawkins, N.M., Guo, Z.K. and Kobayashi, A.S., Fracture process zone associated with concrete fracture, Proc. Int. RILEM/ESIS Conf. Chapman & Hall, 1991, pp. 485-494.
4. Ouyang, C., Landis, E. and Shah, S.P., Damage assessment in concrete using quantitative acoustic emission, J.Engng.Mech., 117(11), Nov., 1991, pp. 2681-2698.
5. Luong, M.P., Infrared thermography of fracture of concrete and rock, SEM/RILEM Int. Conf. on Fracture of Concrete and Rock, Houston, 1987, pp. 343-353.
6. Liu, H. and Vinh, T., Multidimensional signal processing for nonlinear structural dynamics, Mechanical Systems and Signal Processing, 5(1), 1991, pp. 61-80.
7. Luong, M.P., Tensile and shear strengths of concrete and rock, Engineering Fracture Mechanics, 35, 1990, pp. 127-135.
8. Hillerborg, A., Fracture mechanics and the concrete code, Fracture Mechanics : Application to Concrete, ACI SP-118, 1989, pp. 157-169.

NONLINEAR DYNAMIC ANALYSIS OF IMPACT FAILURE MODES IN CONCRETE STRUCTURES

Ayaho MIYAMOTO*, Michael W. KING* and Manabu FUJII**

* Dept. of Civil Engineering, Kobe University, Nada, Kobe 657, JAPAN

** Dept. of Civil Engineering, Kyoto University, Sakyou, Kyoto 659, JAPAN

ABSTRACT

A nonlinear dynamic layered finite element method is applied for analytically predicting the failure modes in reinforced concrete structures subjected to soft impact loads. The effects of material nonlinearity, concrete plasticity, concrete element cracking and also the loading and unloading phenomena in the plastic regions, are included into the analytical procedure. The analytical results are then compared with the results from full-scale experiments to verify the validity of the analysis. It is found that the ultimate behaviors as well as failure modes can be predicted accurately. Finally, the effects of different loading rates on material states as well as failure modes are studied. Three different failure modes, i.e., bending, bending to punching shear and punching shear, are analytically defined. The bending failure mode is dominant at slow loading rates while a fast loading rate would cause punching shear failure to occur.

INTRODUCTION

The failure modes for concrete structures subjected to soft impact loads [1] are dependent on the characteristic of the impact load-time function and also the energy absorption capacity of the structure itself. Determining the failure modes for different impact load functions can be considered to be the major task that a structural engineer has to overcome, in order to design a concrete structure efficient enough to withstand a given impact load. An analytical procedure, based on the nonlinear dynamic layered finite element method, is employed for studying the failure mechanism, ultimate states and also failure modes in reinforced concrete slabs during soft impact loadings.

ANALYTICAL PROCEDURE [2,3]

A nonlinear dynamic step-by-step finite element method is employed for analysis of reinforced concrete slabs. Reinforced concrete slabs with doubly reinforced sections are modeled as shown in Fig.1. The slab is divided into eight hypothetical layers, six of concrete and two of steel reinforcement. The layering approach allows the in-plane strains and in-plane stresses to be varied with member thickness and permits the inclusion of steel reinforcement at proper levels within the slab. The finite element employed here is the four-node Mindlin-type rectangular element. Each element nodal-point has five degrees of freedom, i.e., in-plane displacements (u,v), transverse displacement (w) and sectional rotations around the x- and y-axes (θ_x,θ_y). The element consists of in-plane, plate-bending and coupling effects. The extensional-bending coupling effect becomes

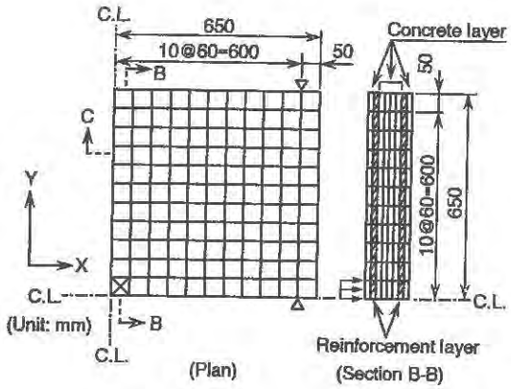

Fig.1 Layered finite element meshes

more pronounced due to the shifting of the neutral axes, as cracks progress through the slab. Furthermore, the transverse shear stresses for the concrete slab are extrapolated from the equation of equilibrium and then included into the analysis as it is assumed to affect not only the ultimate behaviors but also the failure modes. The external impact force is applied to the slab at midspan, as indicated in Fig.1.

The theory of plasticity is applied for modeling of concrete. A provision for material nonlinearity, cracking in concrete elements and the loading and unloading phenomena are adopted in the analysis. A 4-parameter triaxial failure model for concrete proposed by Ottosen [4] is applied here. The Ottosen model is capable of reproducing the main features of a triaxial failure surface. The yield surface for concrete is selected as a reduced shape of the failure surface. The shape of the yield surface is based on a nonuniform hardening model. A plastic potential other than the loading function is used to define the flow rule as inelastic volume dilatation can be expected to occur in concrete materials near the ultimate stress. The Drucker-Prager type of function is applied here.

Concrete is treated as an orthotropic material after cracking. The elastic strain energy in the cracked element is then converted into equivalent nodal forces. The numerical representation of cracking is based on a 2-dimensional smeared crack approach in the in-plane direction, where the effects of aggregate interlock and dowel action after cracking can be expressed in terms of a shear retention factor.

Static material properties are used throughout this study for defining the material characteristics of concrete and reinforcement. It is considered that the dynamic material properties during soft impact loadings can be properly simulated in the dynamic finite element procedure through application of static material test results, as the effects of inertia and viscous damping have been incorporated into the analysis.

VERIFICATION OF ANALYTICAL PROCEDURE

The validity of the analytical procedure was verified through comparison with available experimental data. Reinforced concrete slabs with a dimension of 130x130x13 cm were subjected to failure tests. The apparatus used for the impact test was a pendulum-type impact testing machine, which was specially designed to derive only one sine-wave impact. The falling weight had a mass of 500 kgf. To derive soft impacts, a 1 cm thick rubber pad was placed on a square steel loading plate 15x15x2.5 cm at the impact face. The impact load-time relation was measured by acceleration sensors attached to the falling mass. Measurements for deflection, acceleration response and crack widths were carried out. The measuring system consisted of noncontact displacement tranducers, acceleration sensors, crack gages and an analog data recorder.

Two series of concrete slabs were tested, i.e., normal strength reinforced concrete (RC) slabs and high-strength reinforced concrete (HRC) slabs. Material test results such as Young's

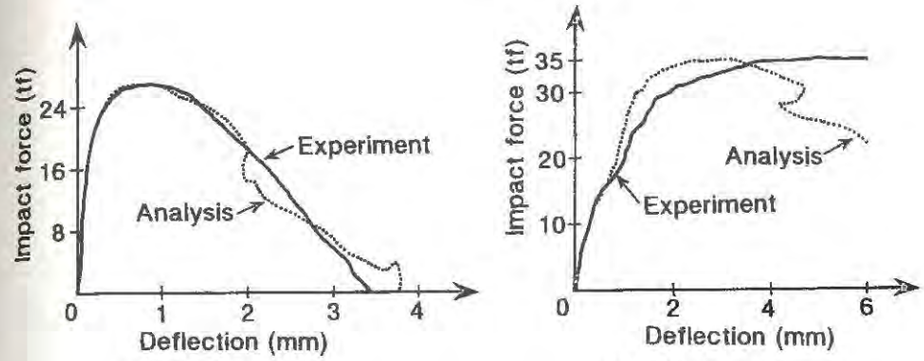

(a) RC slab (h=60 cm) (b) HRC slab (h=80 cm)

Fig.2 Impact force-midspan deflection curves

modulus, Poisson's ratio and uniaxial material characteristics from uniaxial compressive (concrete) and tensile (concrete and steel reinforcement) tests are used as input data for the materials. The uniaxial material test results are converted into the effective stress-effective strain relation [2] before application into the analysis.

Fig.2(a) shows the impact force-midspan deflection curves for the analysis and experiment of a typical RC slab while Fig.2(b) is the result for an HRC slab. The height of fall of the impacting mass (500 kgf) in the experiments, h, are indicated in brackets. The results show that the analysis gives a very good prediction of the ultimate behaviors of RC slabs, even after the point of maximum impact force. A small difference between the calculated values and the experiments begin to appear after the maximum impulsive load, i.e., when the unloading process begins. In Fig.2(b), it is clear that the analytical results are a little different from the experiment after the initial cracking stages. But in general, the analysis is able to give a rough estimate of the overall deformation behavior. Other ultimate states and behaviors, such as the crack patterns at failure and failure modes, are also compared and found to be similar with the experiments. Therefore, the analysis can be considered to give a good prediction of the overall response of concrete slabs under soft impact loads.

ANALYSIS OF FAILURE MODES

The two main failure modes that can be associated with soft impact loads are the bending (flexural) failure mode and the punching shear failure mode. Furthermore, an intermediate failure mode between these two distinct failure modes, where the bending mode is dominant at the early stages followed by a transition into the punching shear mode, is expected. The failure modes can be analytically defined based on the following indexes [3]:

Index *I*: The distribution of deflection (deformation) throughout the slab,

Index *II*: The impact force-midspan deflection curves from zero to ultimate load,

Index *III*: The propagation of cracks through cross-sections and crack patterns at failure.

The first two indexes will be employed here in the discussions as they provide good indications of the failure modes. More detailed information about the indexes are given in Reference [3]. A series of analyses were carried out to study the dynamic behaviors at ultimate states and also the failure modes of reinforced concrete slabs subjected to different loading rates. The term "loading rate", v_l, is defined as the average gradient of the impact force-time function at failure [3]. The range of the loading rate considered were between 5.0 tf/msec and 140.0 tf/msec.

Fig.3 shows the effects of loading rate on different material states of concrete and steel reinforcement. The cracking of concrete, initial yielding of concrete (plasticity) under compression and steel reinforcement yielding behave in a similar manner as the loading rate is increased, that is, the load for each material state increases as the loading rate is increased. This shows that the different material states are under the influence of inertia during impulsive loadings. The effects of inertia grow larger as the loading rate is increased but the increase in load

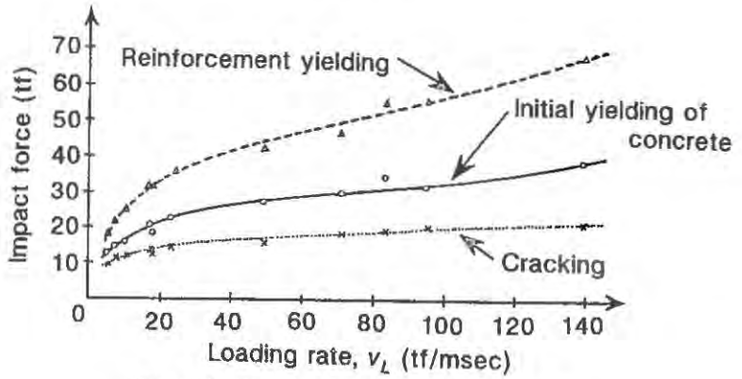

Fig.3 Effects of loading rate on material states

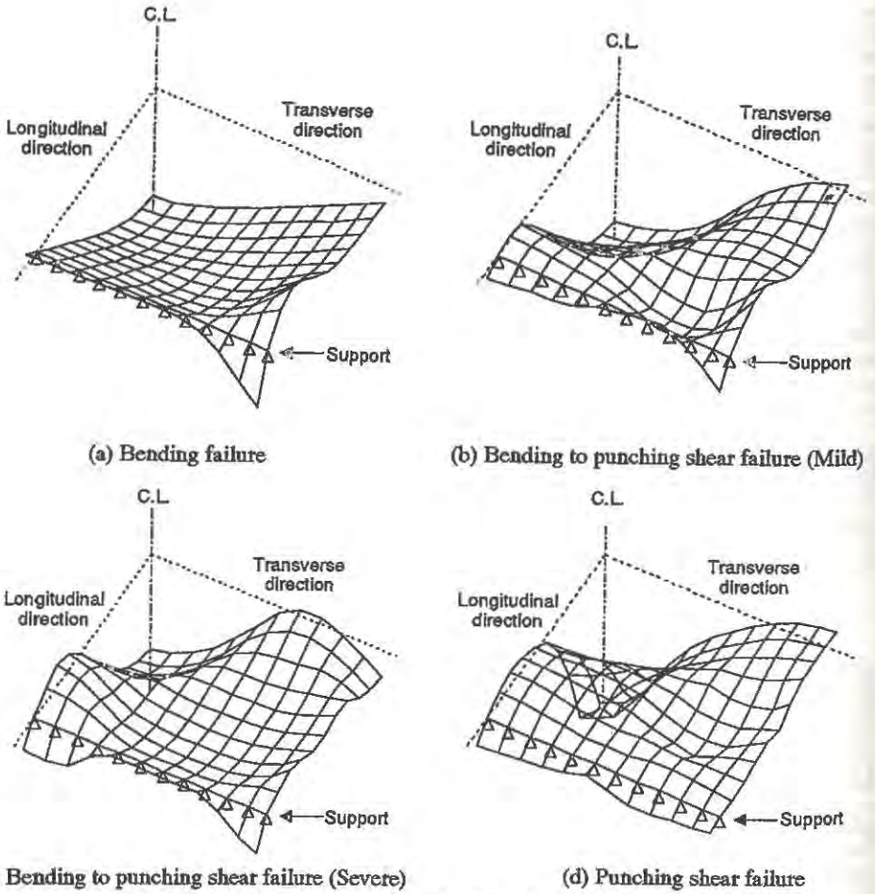

Fig.4 Typical deformation (failure) modes for RC slabs under impact loads

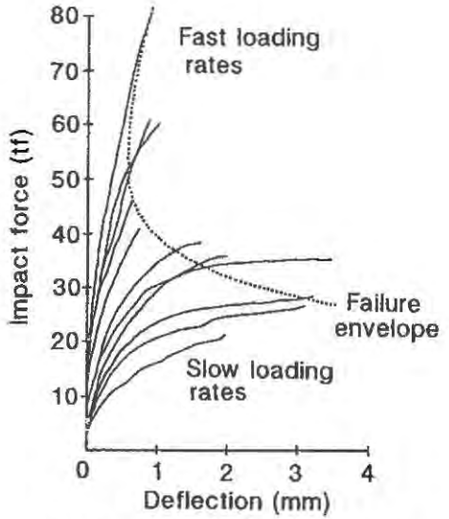

Fig.5 Failure envelope for impact loads

for concrete cracking is comparatively small at high loading rates. Therefore, concrete cracking is not influenced as much as steel reinforcement under soft impact loads. In general, concrete cracking occurs first, followed by initial yielding of concrete under compression, and finally yielding of reinforcement.

Fig.4 shows four typical deformation (failure) modes, obtained during different loading rates, at the final failure stage. Under a slow loading rate, as in Fig.4(a), deformation is spread throughout the entire slab and total structural failure is expected. The failure mode here can be classified as the bending failure mode. During this failure mode, crushing of edge concrete elements at the center of the slab or along the central transverse axis is noticed together with yielding of steel reinforcement throughout the entire slab. Both Fig.4(b) and 4(c) indicate the deformation mode for a medium loading rate. The loading rate in Fig.4(c) is relatively faster than in Fig.4(b), thus indicating the severity of the degree of punching shear mode in the final failure mode. Furthermore, the effects of higher modes of vibration, indicated by the shape of the distribution of deformation along the longitudinal and transverse axes, are much more prominent in Fig.4(c). Concrete crushing occurs at approximately 1/4 portion of the span of the slab, where the relative deformation is comparatively large. Fig.4(d) indicates the deformation mode at a very fast loading rate. Deformation is concentrated toward the middle of the slab and local failure is expected. The failure mode for this figure can be classified as the punching shear failure mode. During this failure mode, concrete crushing and yielding of steel reinforcement are concentrated around the area where relative deformation is comparatively large.

Fig.5 shows the impact force-midspan deflection curves, from zero to ultimate load, for different loading rates. The curves with large impact force at failure occur during fast loading rates while curves with a relatively small impact force at failure are those under slow loading rates. During fast loading rates, the initial gradients of the curves are relatively large and not much deflection is noticed at failure. This phenomena can be attributed to the effects of inertia in the concrete slab. Therefore, punching shear (brittle) failure can be expected. As for the slower loading rates, the initial gradients are relatively smaller, and a rapid increase in deflection at the ultimate stages, due to the yielding of reinforcement throughout the slab, is clearly noticeable. Thus, bending (ductile) failure can be expected for a slow loading rate.

From the results in Fig.5, a failure envelope for reinforced concrete slabs under soft impact loads can be obtained. The failure envelope is indicated in Fig.5, in the shape of a parabolic curve, by dotted line. The impact force at failure increases with increasing rate of loading, but the corresponding deflections at both fast loading rates and slow loading rates are greater than at the medium loading rates. This fact is significant, as it indicates that the failure mechanism and also

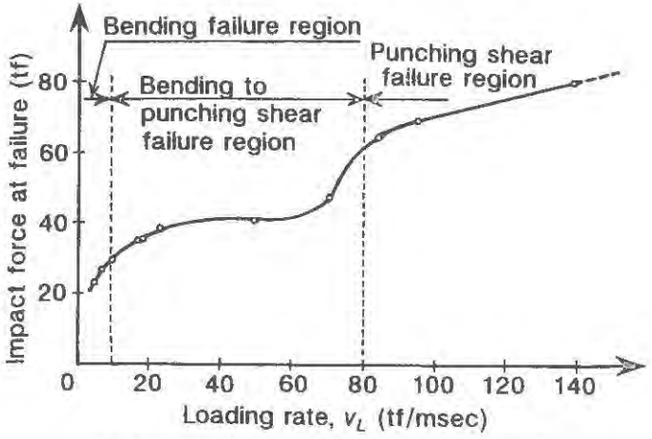

Fig.6 Effects of loading rate on impact force at failure

failure modes are different for different regions of loading rate.

The impact force at failure for different loading rates are shown in Fig.6. The results above are also included into this figure, where the region for bending failure, bending to shear failure and punching shear failure modes, are indicated. The bending failure mode region can be classified as up to approximately 10 tf/msec, while the punching shear failure mode region is for loading rates above 80 tf/msec. Note that a transition in impact force at failure occurs between each failure region. The loading rate v_L can be classified into three different categories based on the failure modes, i.e., slow loading rate ($v_L \leq 10$ tf/msec), medium loading rate (10 tf/msec $< v_L \leq$ 80 tf/msec), and fast loading rate ($v_L > 80$ tf/msec).

CONCLUSIONS

The main conclusions from this study can be summed up as follows:
(1) The nonlinear dynamic layered finite element method, together with the Ottosen failure model and the Drucker-Prager plastic potential, is capable of giving good predictions of the ultimate behaviors of concrete slabs under soft impact loads.
(2) The different material states of concrete and reinforcement due to different loading rates, i.e., concrete cracking, concrete plasticity under compression and steel reinforcement yielding, can be simulated in the analysis by including the effects of inertia. A fast loading rate is found to have a comparatively smaller effect on concrete cracking, in comparison with steel reinforcement.
(3) Three different failure modes are analytically identified in reinforced concrete slabs under soft impact loads. The failure modes are: (i) Bending failure mode, (ii) Intermediate (bending to punching shear) failure mode, and (iii) Punching shear failure mode. The three failure modes correspond to three different ranges of loading rate. The bending failure mode occurs at a slow loading rate region while punching shear failure is dominant at a fast loading rate region.

REFERENCES

1. Concrete structures under impact and impulsive loading - Introductory report, RILEM, CEB, IABSE, IASS Interassociation Symposium, Berlin (BAM), June 2-4, 1982, 148pp.
2. Miyamoto, A., King, M.W. and Fujii, M., Nonlinear dynamic analysis of reinforced concrete slabs under impulsive loads. ACI Structural Journal, V.88, No.4, July-Aug. 1991, pp.411-419.
3. Miyamoto, A., King, M.W. and Fujii, M., Analysis of failure modes for reinforced concrete slabs under impulsive loads. ACI Structural Journal, V.88, No.5, Sept.-Oct. 1991, pp.538-545.
4. Ottosen, N.S., Failure criterion for concrete, Journal of the Engineering Mechanics Division, ASCE, V.103, EM4, 1977, pp.527-535.

Chapter 7

Fracture Under Shear

Principal Lecture

SHEAR FRACTURE IN CEMENTITIOUS COMPOSITES PART I: EXPERIMENTAL OBSERVATIONS

J.G.M. VAN MIER, E. SCHLANGEN and M.B. NOORU-MOHAMED
Delft University of Technology, Stevin Laboratory,
P.O. Box 5048, 2600 GA Delft, The Netherlands

ABSTRACT

Results are presented of "shear" fracture tests on concrete. Two different but unique test methods were used. In the first approach, double-edge-notched quadratic plates are subjected to combined tension and shear. During loading the boundaries of the plates are kept parallel. Depending on the exact boundary conditions and the load-path, a set of curved or straight overlapping cracks develops from the two notches The behaviour seems governed by mode I cracking only. Beam tests are carried out in a sophisticated apparatus where the boundary conditions can be varied. Tests can either be carried out between fixed or rotating supports. It is found that the actual boundary condition has a significant effect on the crack mode. Under fixed supports, the overlapping curved crack mode is found, and final failure occurs through splitting. This situation resembles the results obtained in the plate experiments. When on the other hand the supports in the beam tests are allowed to rotate, a single mode I crack dominates the behaviour of the single-edge-notched and double-edge-notched four point shear beams. The results are confirmed by simulations with a simple lattice model, which are presented in another contribution to this conference [8]. Shear failure, defined as an array of inclined microscopic tensile cracks seems only be possible when secondary cracking can be prevented (1) through confinement on the parts of the specimen outside the expected shear zone, (2) under dynamic loading, or (3) in fibre reinforced cement composites where secondary cracking is prevented by the fibres.

INTRODUCTION

In classical fracture mechanics, three different crack modes are distinguished - opening, in plane shear and out-of-plane shear - which can occur in any combination. Although mode I is the situation which has been investigated most thoroughly in the concrete community, it seems to be the exception in practice. This is the reason which is most frequently used by researchers to justify mixed-mode I and II, mode II and mode III fracture studies. But do these latter modes really occur in heterogeneous materials like concrete ? Or is our view blurred because several initial assumptions must be made, which often go back to classical

strength theory and fracture mechanics ? The answer to these questions is not straightforward. Important to realise is that the level at which we define tensile or shear cracks is of eminent importance. In the discussion two levels will be distinguished: (1) the macroscopic level at which continuum theories are assumed to be valid, and (2) the meso-level, where individual aggregate particles are distinguished. The characteristic size range for the first level is in the order of 100 mm or more, at the meso-level details in the order of 1 mm are distinguished.

In the past, Bažant & Pfeiffer [1] claimed that true macroscopic shear (mode II) fracture occured in double notched shear beams with a narrow shear zone. Mode III fracture was observed among others by Bažant & Prat [2]. In all these tests, the main emphasis was on determining the maximum load for specimens of different size. The post-peak response was of less interest, and tests were conducted in stroke control.

Many researchers have questioned the results of the mode II experiments by Bažant & Pfeiffer. For example Ingraffea & Panthaki [3], and Swartz & Taha [4] tried to demonstrate both through experiments and finite element analysis that actually a splitting type of failure occured in the four point shear beams with narrow shear zone, after primary cracks nucleated from the notches along curvilinear paths. There are however several uncertainties in the discussion. First, the level of observation is not specified. Secondly, and more important, the boundary conditions may have an important influence on the behaviour of the specimens. This latter point is mentioned in [2] and [4], but has never been investigated in detail. The effect of boundary conditions has been studied in the past by the authors for mode I and mixed-mode I and II test geometries [5], [6].

In this paper an overview of the experiments carried out at the Stevin Laboratory will be presented. Two unique but different test set-ups are used. In a sophisticated biaxial apparatus, square double-edge-notched plates are subjected to combined tensile and shear loads. The specimens are loaded between fixed end-platens, which can only have minor rotations caused by the stiffness of the supports. In the second test set-up single-edge-notched or double-edge-notched beams are subjected to four point shear. This apparatus has been designed in order to allow for variation of boundary conditions, i.e. fixed or rotating supports. Results of experiments carried out in these machines are discussed and compared with results from literature. The findings are (partly) supported by results obtained with a recently developed lattice model [7]. The numerical results are presented in another contribution to this conference [8]. When discussing mixed-mode fracture below, always mixed-mode I and II is assumed.

OVERVIEW OF THE EXPERIMENTS IN DELFT

The biaxial apparatus in the Stevin Laboratory was designed for mixed-mode fracture studies of concrete [9]. The machine can however also be used for studying shear fracture, creating a situation similar to the loading of a narrow shear zone in a four point shear beam. This was done in the so-called load-path 4, 5 and 6 experiments. After a short description of the testing technique, relevant results will be presented.

The four point shear experiments that have been carried out on single-edge-notched beams were part of the round robin test designed by Carpinteri [10]. However, it was felt that the boundary conditions might have a significant effect on the experimental result.Carpinteri et al. [11] claimed an increase of fracture energy under mixed-mode loading. However, recently it was shown that much of the increase of the so-called mixed-mode fracture energy must be traced back to boundary effects [12]. In this paper, the respective influences will be shown. Moreover the experiments have been extended to double-edge-notched beams as well. The mode II fracture test of Bažant & Pfeiffer [1] have been repeated using exactly the same beam geometry, but now under varying boundary conditions.

Biaxial loading frame

Biaxial tension/shear experiments were carried out in the test set-up of Fig. 1. In this machine, which is extensively described in detail in [10] and [13], axial tension and lateral shear can be applied independently in displacement control.

The boundary conditions in the experiments are shown schematically in Fig. 2. Two opposite sides of the specimen are forced to remain parallel to each other during the entire test. If the end-faces can indeed be kept parallel, will depend to a large extent on the stiffness

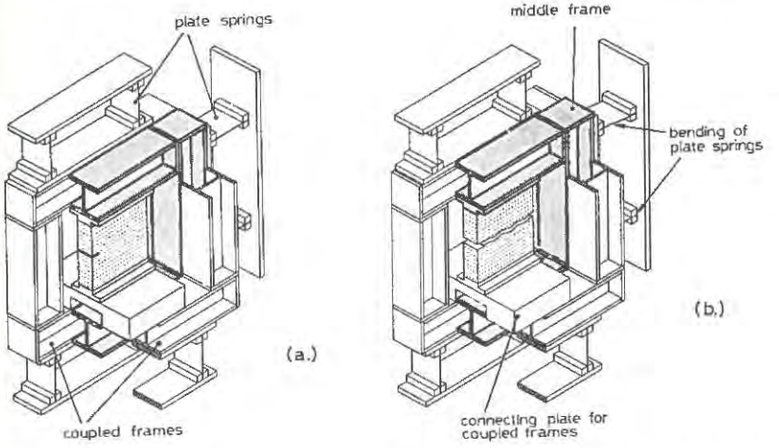

Figure 1. Sectional view of the biaxial test-rig in two stages: (a) before and (b) after cracking due to loading in the vertical direction. Note the bending of the plate springs in figure (b).

of the plate springs that are used for fixing the two independent loading frames in the overall test frame (see Fig. 1). Carefully conducted callibration tests showed that the rotational stiffness of the springs is relatively high, but in spite of this, non-uniform loading of the specimen is caused by non-uniform fracturing of the specimen [14].

As mentioned, axial tension (P, δ) and lateral shear (P_s, δ_s) can be applied independent of each other. The global axial crack opening is measured with four LVDTs (gauge length 65 mm) mounted near the notches at the surface of the specimen. The shear displacement

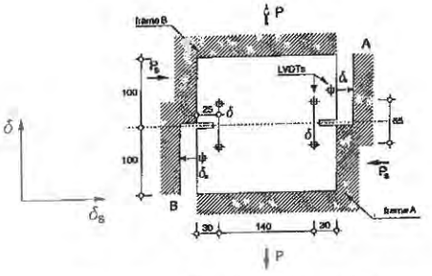

Figure 2. Boundary condition for a double-edge-notched specimen subjected to combined tension and shear.

is defined as the average displacement measured with two LVDTs placed at diagonal opposite positions at the front and back face of the specimen. In addition to this, the local crack opening is measured using clip gauges with a measuring length of 35 mm.

Specimens of three different sizes have been tested, viz. 50 x 50 mm, 100 x 100 mm and 200 x 200 mm, all with a thickness of 50 mm. The notch depth was a constant ratio of the specimen size: a/d = 0.125. Four different materials were tested. The main results presented in this paper were obtained on a cement mortar with d_{max} = 2 mm. Further details of the concretes tested are included in [13].

Biaxial results

The total scope of the biaxial experiments was rather wide [13], [14], and here only limited number of results are included. In one of the load-paths (i.e. load-path 4), a specimen was first loaded in shear up to a given lateral shear load P_s = -5 kN, -10 kN or equal to $P_{s,max}$ (the maximum shear load that the specimen could sustain). During the application of the lateral shear, the axial load was kept constant at P = 0. Following this, axial tension was applied in displacement control while P_s was kept constant.

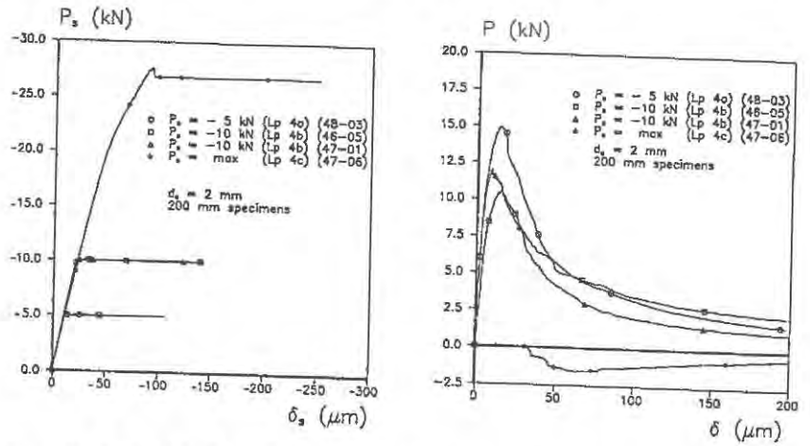

Figure 3. P_S-δ_S (a) and P-δ (b) curves for load-path 4 experiments on square plates of 200 mm.

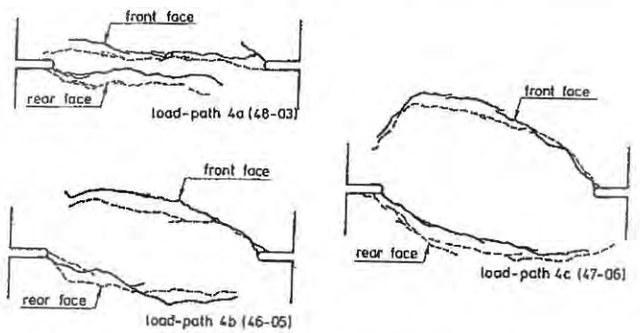

Figure 4. Crack patterns for load-path 4a, 4b and 4c experiments.

Another load-path of interest was load-path 6 where shear and tension were applied simultaneously in a constant ratio of δ/δ_S = 1.0, 2.0 and 3.0. At δ/δ_S = 3.0, tension is dominant, at smaller values, the effect of shear becomes more important.

In Fig. 3 the P_S-δ_S and P-δ response for the load-path 4 experiments on specimens of 200 mm are shown. The graphs contain a duplicate test with P_S = - 10 kN (load-path 4b) during tension. The P_S-δ_S curves show where the test control was changed from load-control in the lateral (shear) direction to displacement control in the axial direction. The tensile response of the specimens depends to a large extent on the level of the shear loading. A decreasing maximum axial load is measured when the level of P_S increases. For load-path 4c, when the shear-load is kept constant at $P_{S,max}$, the axial load P even becomes compressive (Fig. 3b, specimen 4706). The reason for this becomes clear when the crack patterns are studied. In the load-path 4c test, a set of overlapping curved cracks developed from the two notches as shown in Fig. 4c. During the experiment the lower crack branch was visible, whereas the upper branch developed during axial loading. Similar crack patterns were observed in the two other tests, the difference being the distance between the two overlapping cracks (see Figs. 4a and 4b). In the load-path 4a and 4b tests, no cracking was observed

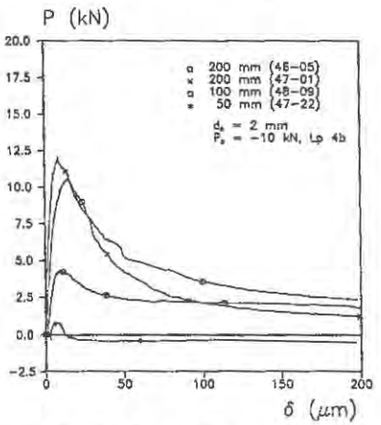

Figure 5. P-δ curves for load-path 4b experiments on specimens of different size.

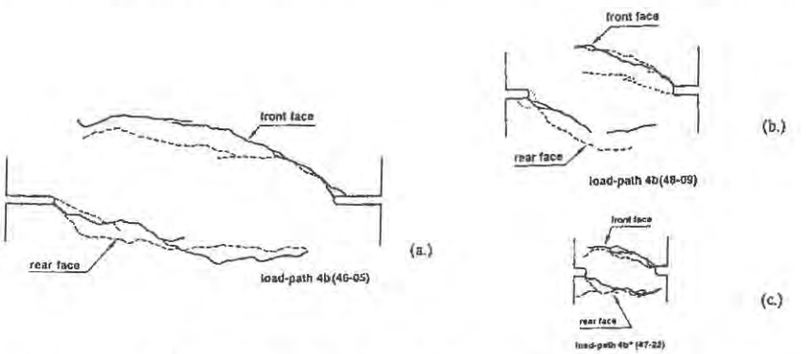

Figure 6. Crack patterns for load-path 4b experiments on specimens of three different sizes.

during the shearing regime. This can also be deduced from the P_s-δ_s curves for these tests (Fig. 3a), which are almost linear up to the required level of -5 kN and -10 kN respectively.

The effect of specimen size is shown in Fig. 5. Load-path 4 experiments were carried out on specimens of three different sizes as mentioned above. The P_s-δ_s curves are not shown here because they resemble the curve of Fig. 3a for P_s = - 10 kN. Note that the shear-load for the 50 mm specimens was reduced to - 9 kN because a shear-load of - 10 kN was too close to the maximum shear load for these small specimens. This explains why the axial tensile peak is so low. The crack patterns for the experiments of Fig. 5 are shown in Fig. 6. In spite of the fact that the relative level of shear stress was different in the three specimen sizes, the crack patterns were surprisingly self similar. The same overlapping cracks developed in the specimens and seemed to scale according to the scaling of the specimens.

Interesting results were also obtained in the load-path 6 experiments. In Fig. 7, P/P_{max}-δ and P_s-δ_s curves are shown for load-path 6a tests (δ/δ_s = 1.0) for specimens of three different sizes. In these tests, cracking is caused by the tensile loading; during crack opening

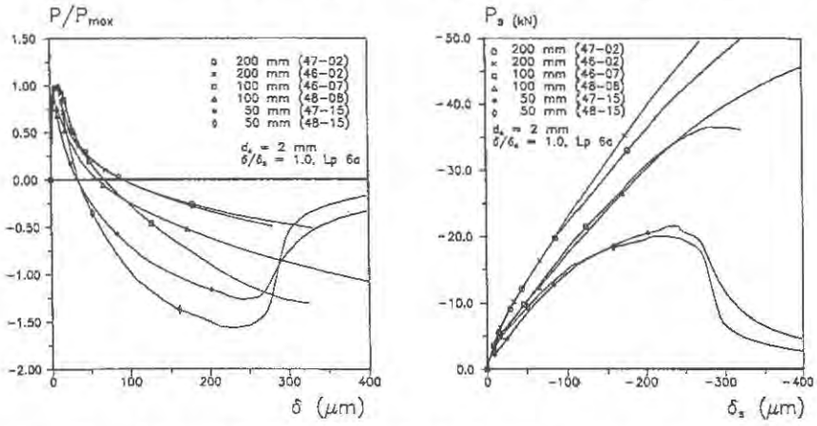

Figure 7. P/P_{max}-δ (a) and P_s-δ_s (b) curves for load-path 6a experiments on specimens of three different sizes.

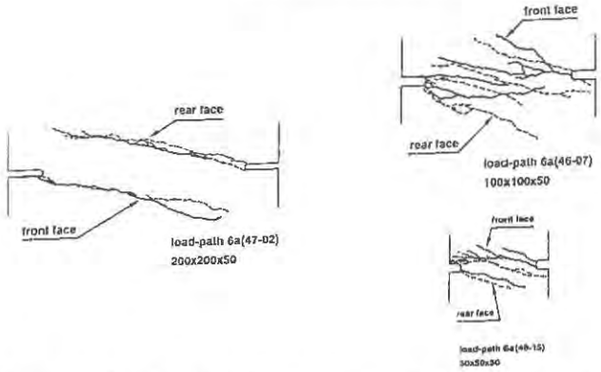

Figure 8. Crack patterns for the load-path 6 experiments of Fig. 7.

the effect of shear becomes prominent and the axial load changes from tension to compression. Note that the y-axis in Fig. 7a is dimensionless: all results are divided by the maximum load for the respective experiments. The only specimen which could be 'failed' was the 50 mm specimen, which showed a decrease of axial compressive load for larger crack-openings ($\delta > 250\,\mu$m). In Fig. 8 the crack patterns pertaining to these tests are shown. For the larger size specimens, the overlapping crack mode was found, except that the crack branches were more straight now than in the load-path 4 tests. The experiments revealed also a change in fracture mode for the smaller specimens. The crack patterns were more distributed for several 50 mm and 100 mm experiments, although this was not consistent for all tests.

Beam tests

Beam experiments were carried out in a recently developed test-rig where the boundary conditions could be varied. In Fig. 9, an overview of the loading configuration is shown. Single-edge-notched or double-edge-notched beams are loaded in four point shear between hinged pendulum bars. In this situation, the supports are free to rotate. By inserting diagonal bars between the pendulums (dashed lines in Fig. 9), the supports are prevented from rotating. In this manner the effect of boundary restraint on the fracturing of the specimens can be studied. Note that the test set-up is completely anti-symmetric. The concrete specimen is loaded with pendulums between steel bars that are fixed through a

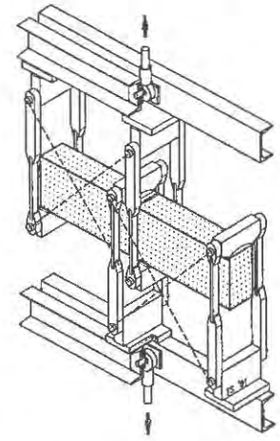

Figure 9. Set-up for testing single-edge-notched or double-edge-notched four point shear beams.

hinges to the overall loading frame. The test set-up is extremely unstable because of all the hinges, and a stable displacement controlled test can only be carried out succesfully when a constantly increasing deformation is chosen as control variable. Moreover, the specimen dimensions must be exact, and the sides to which the loads are applied must be completely plan-parallel. In addition to this, the pendulum bars must be placed at exactly the correct position, and no eccentricities are allowed. When all these conditions are fulfilled, experiments can be carried out with extremely small scatter as shown in Fig. 11 for three small beam tests with rotating supports.

Single-edge-notched four point shear beams. The test set-up was originally developed to study mixed-mode fracture of concrete following the Round Robin proposal of RILEM Technical Committee 89 FMT [10]. The set-up proposed in [10] was changed because the

impression was that the reported increase of fracture energy under mixed-mode conditions could well be explained by the effects of the supports when a beam is loaded in compression in a conventional test apparatus. The beams are loaded in displacement control using δ_2, as defined in Fig. 10a, as control parameter in the closed loop system. The average signal measured with two LVDTs mounted at the front and back side of the beam was used as feed back signal. Six additional LVDTs were fixed to the specimen in order to measure δ_1, CMOD en CMSD. Local deformations in the crack zone were measured with clip gauges. The loads F_1 and F_2, and the support reactions F_{1R} and F_{2R} were measured with the instrumented pendulum bars. For a detailed description of the test procedure the reader is refered to [6], [12].

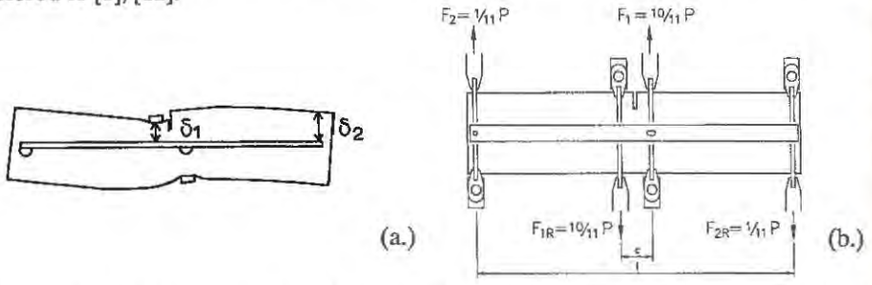

Figure 10. Deformations δ_1 and δ_2 (a); loads F_1, F_2 and reactions F_{1R}, F_{2R} (b) for the single-edge-notched beam.

The experimental results presented below were obtained on a 8 mm normal concrete. For the single-edge-notched beams several different materials were tested, but these results will be presented elsewhere. Details concerning the concrete mix are given in [12]. Beams of two different sizes were tested, viz. small beams (440 x 100 x 100 mm), and large beams (840 x 200 x 100 mm) with a notch depth of 20 and 40 mm respectively. The specimens were always tested with the notch at the top side. Previous tests showed that the effect of notch position was negligible [12].

The load-deformation curves (P-δ_2) are given in Fig. 11. Results are shown for small and large beams loaded either between fixed or free supports. Always the descending branch was higher for the beams tested between fixed supports. Moreover the ratio's F_1/F_2

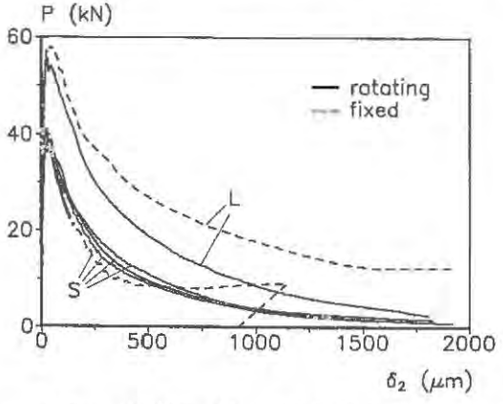

Figure 11. P-δ_2 curves for small (S) and large (L) single-edge-notched beams loaded between freely rotating or fixed supports.

and F_{1R}/F_{2R} would remain constant at 10/1 when a beam was tested between free rotating supports. In contrast, this ratio would deviate strongly when the supports were fixed. The reason for this behaviour can be found when the crack patterns in the respective tests are studied, see Fig. 12. When a beam is loaded between free rotating supports, a crack will start to grow from the notch at an angle. The crack will subsequently propagate along a curved path as shown in Fig. 12a. Because the pendulum bars can rotate away as shown, the crack will open as a mode I crack, see also [12]. When on the other hand diagonal bars are fixed between the pendulums, the free movement of the concrete specimen is restricted, and after the growth of crack 1, a flexural crack developed at the unnotched side of the beam (see figure 12b). Fig. 12 shows the fracture modes for the small beams, for the large beams in both cases only crack 1 developed.

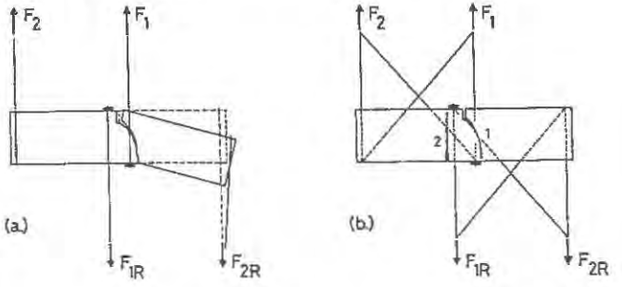

Figure 12. Failure mechanisms for the small single-edge-notched beams loaded between rotating (a) and fixed supports (b).

An analysis of the amount of energy involved in the fracturing of the single-edge-notched four point shear beams showed that the effect of mode II on the fracture energy was negligible [12]. Although it appeared that the analysis of G_f was dependent on assumptions regarding the tail of the softening curves, the reported 19-30 % increase of fracture energy in [11] could not be found.

Double-edge-notched four point shear beams. At present, the beam set-up is used for loading double-edge-notched four point shear beams as well. In fact the tests of Bažant & Pfeiffer [1] are duplicated, and the effect of boundary conditions is studied. Only two sizes were tested, viz. d = 150 mm and 300 mm (specimen thickness 37.5 mm; d is defined in Fig. 13). The average signal of the two CMSD gauges and the two CMOD gauges was used as feed back signal in the closed-loop servo control. CMOD is negative before peak for this geometry, whereas the CMSD showed snap-back response beyond peak. Consequently the best choice was to control the experiment by using the average signal of CMSD and CMOD.

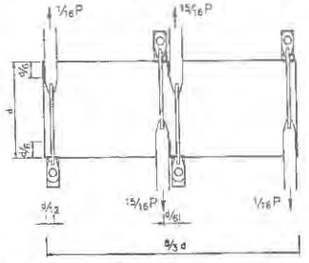

Figure 13. Double-edge-notched four point shear beam tested between pendulum bars.

The double-edge-notched geometry is shown in Fig. 13. The experimental results were obtained for the same 8 mm concrete as was used for the tests on the single-edge-notched beams.

In Fig. 14, the total load P is plotted against the average crack sliding and opening (CMSD + CMOD), which was the control signal in the experiment. The tests are carried out at present, and not all variable combinations have been tested. The results show large resemblance to the results for the single-edge-notched beams: loading the specimen between fixed supports gives always a higher descending branch, irrespective of the size of the beam. As far as the crack patterns are concerned, almost the same mechanisms as found

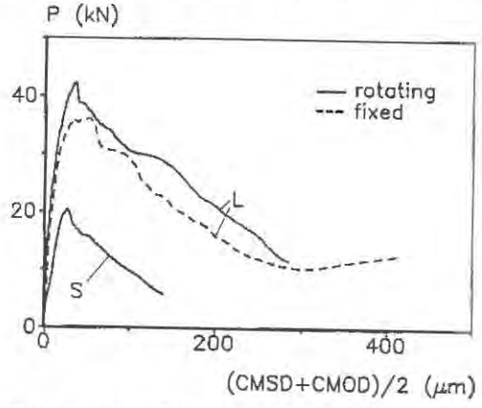

Figure 14. Load (P) - average CMSD + CMOD curves for small (S) and large (L) double-edge-notched beams and loaded between fixed or rotating supports.

in the single-edge-notched beams are observed as shown in Fig. 15. When a specimen is loaded between rotating supports, initially two cracks start to grow from the two notches. However, at a certain moment only one crack wil propagate. This causes failure of the specimen. When on the other hand, the specimen is loaded between fixed supports, two overlapping curved cracks (no. 1, 2 in Fig. 15b) develop from the two notches, and final rupture of the beam is through the growth of a third splitting crack (no. 3 in Fig. 15b) in between of the two curved cracks. No difference in behaviour was observed for the small and the large double-edge-notched beams, at least for beams loaded between freely rotating supports.

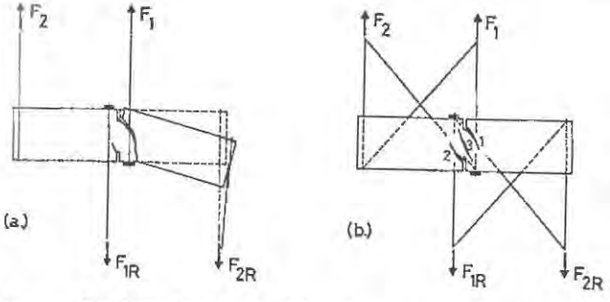

Figure 15. Failure mechanisms for the double-edge-notched beams loaded between rotating (a) and fixed supports (b).

DISCUSSION OF RESULTS

When the fracture modes in the plate experiments are compared to those obtained in the double-edge-notched shear beams loaded between fixed supports a striking resemblance is observed. The boundary conditions in both experiments show large similarities. In the plate tests in general a single curved crack intitiated from one of the notches, causing a large eccentricity in the specimens, because the boundaries of the plates were forced to remain parallel. At some stage of loading a second crack would appear at the other side of the specimen, and in fact a situation similar to testing a specimen in tension between fixed end-platens is created [5]. The fractures will develop as a symmetric set of curved overlapping cracks, and the distance between the crack branches seems mainly determined by the amount of shear as found in the load-path 4 tests on plates. Of course, as will be directly clear from Fig. 15, a bending moment will also develop in the beam tests where fixed supports are used. Again this causes a symmetric failure mode.

The results of the beam tests can be compared with findings by others, for example [1], [3] ,[4]. Both in references [3] and [4], the overlapping curved crack mode was reported. Swartz and Taha [4] found that the overlap would be more narrow when an additional axial load was introduced in the beam. The results of Ingraffea & Panthaki [3] were based on a numerical simulation only. Comparison of the present results with those reported in [1] shows that contradictory results are found. No macroscopic 'shear' cracks are found in the present experiments, and the impression is that the findings in [1] can probably be explained from the way these experiments were controlled. In [1] the beams were loaded in stroke control, and not as in the present series in displacement control. This would imply that explosive failures occured as soon as the peak load was reached, which might trigger the developement of a single shear fracture as recently demonstrated by Davies [15].

This brings us to the question when true macroscopic 'shear' fractures can be expected. A survey of the literature indicates three possible situations: (1) triaxial compression, (2) dynamic loading and (3) addition of fibres to the concrete. These situations are elaborated in detail in [13], and here only a few remarks will be made. The case of triaxial compression may be straightforward. In this case however, high shear stresses will develop in the localized shear band. Addition of fibres has a similar result as confining a specimen with external loads. The fibres act as an internal confinement, and prevent the development of secondary tensile cracks. Macroscopic shear cracks were recently reported in ordinary fibre reinforced cements [16], as well as in Slurry Infiltrated Fibre Concrete [13]. In the latter case, the material structure is rather anisotropic, and shear fractures may develop in weak planes between the fibre layers, whereas the fibres prevent (or delay) the growth of inclined secondary cracks.

CONCLUSION

In this paper results of 'shear' tests on plate specimens and beam specimens are discussed. The results were obtained by using two different, both unique, test set-ups in the Stevin Laboratory. The main conclusion is that shear fracture is not possible under static loading conditions in materials with a low tensile strength like concrete. The experiments on plates and beams are quite indicative, wheras recent numerical simulations with a simple lattice model confirm this conclusion [8]. Moreover there seems to be a definite effect of specimen size on fracture mode, at least as was observed in the plate tests.

Comparing the present results with data from literature indicates that true shear fractures (defined as an aray of inclined microscopic cracks) can only be found when parts of the specimens outside the shear fracture zone are confined in such a way that secondary cracks are prevented. This might be done by external confinement either applied actively

or derived from a carefully designed test geometry, or by an internal confinement for example by adding fibres to the concrete [13], [16]. Moreover, shear fractures seem also possible under dynamic loading as recently shown in [15].

ACKNOWLEDGEMENT

Part of the research was sponsored through a grant from the Dutch Technology Foundation (STW), which is gratefully acknowledged. The authors are indebted to Mr. A. Elgersma and Mr. G. Timmers for their expert help in the experiments.

REFERENCES

[1] Bažant, Z.P. and Pfeiffer, P.A., Shear fracture tests of concrete, *Materials & Structures*, 1986, **19**, 111-21.

[2] Bažant, Z.P. and Prat, P.C., Measurement of mode II fracture energy of concrete, *Nuclear Engineering and Design*, 1988, **106**, 1-8.

[3] Ingraffea, A.R. and Panthaki, M.J., Analysis of shear fracture tests of concrete beams, in *Finite Element Analysis of Reinforced Concrete Structures*, Tokyo, 1985, pp. 151-73.

[4] Swartz, S.E. and Taha, N.M., Mixed mode crack propagation and fracture in concrete, *Engineering Fracture Mechanics*, 1990, **35**, 137-44.

[5] Van Mier, J.G.M. Fracture of concrete under complex stress, *HERON*, 1986, **31(3)** , 1-90.

[6] Schlangen, E. and Van Mier, J.G.M., A FE-supported investigation of mixed mode fracture in concrete, in *Proceedings of the 9th Int'l. Conference on Experimental Mechanics*, Technical University of Copenhagen, Aaby Trick Publishers, 1990, pp. 1403-12.

[7] Schlangen, E. and Van Mier, J.G.M., Lattice model for numerical simulation of concrete fracture, in *Proc. Int'l. EPRI Conference on Dam Fracture* (eds. V.E. Saouma, R. Dungar and D. Morris), Boulder, Colorado, Sept. 11-13, 1991, Electric Power Research Institute, Palo Alto, Ca 94304, USA, pp. 511- 27.

[8] Schlangen, E. and Van Mier, J.G.M., Shear fracture in cementitious composites, Part II: Numerical simulations, *this Conference*.

[9] Reinhardt, H.W., Cornelissen, H.A.W. and Hordijk, D.A., Mixed mode fracture tests on concrete, in *Fracture of Concrete and Rock* (eds. S.P. Shah and S.E. Swartz), Springer Verlag, New York, 1989, pp. 119-130.

[10] Carpinteri, A. and Swartz, S.E., Mixed mode crack propagation in concrete, Chapter 3 in *Fracture Mechanics Test Methods for Concrete* (eds. S.P. Shah and A. Carpinteri), Chapman & Hall Publishers, London/New York, 1991, pp. 129-191.

[11] Carpinteri, A., Ferrara, G., Melchiorri, G. and Valente, S., The four point shear test on single notched specimens: an experimental and numerical analysis, in *Fracture Behaviour and Design of Materials and Structures* (ed. D. Firrao), EMAS Publishers, UK, 1990, pp. 667-75.

[12] Schlangen, E. and Van Mier, J.G.M., Boundary effects in mixed mode I and II fracture of concrete, in *Fracture Processes in Concrete, Rock and Ceramics* (eds. J.G.M. van Mier, J.G. Rots and A. Bakker), Volume II, Chapman & Hall Publishers, London/New York, 1991, pp. 705-16.

[13] Van Mier, J.G.M., Nooru-Mohamed, M.B. and Timmers, G., An experimental study of shear fracture and aggregate interlock in cementbased composites, *HERON*, 1991, **36(4)**, 1-102.

[14] Nooru-Mohamed, M.B. Mixed mode fracture of concrete: an experimental approach, *PhD-thesis*, Delft University of Technology, (in preparation).

[15] Davies, J., Numerical and experimental study of development of fracture path under mixed mode loading, in *Fracture Processes in Concrete, Rock and Ceramics* (eds. J.G.M. van Mier, J.G. Rots and A. Bakker), Volume II, Chapman & Hall Publishers, London/New York, 1991, pp. 717-26.

[16] Arslan, A., Hughes, T.G. and Barr, B.I.G., Mixed mode fracture - Including torsion in a new compact test specimen geometry, in *Fracture Processes in Concrete, Rock and Ceramics* (eds. J.G.M. van Mier, J.G. Rots and A. Bakker), Volume II, Chapman & Hall Publishers, London/New York, 1991, pp. 737-46.

SHEAR FRACTURE IN CEMENTITIOUS COMPOSITES PART II: NUMERICAL SIMULATIONS

E. SCHLANGEN and J.G.M. VAN MIER
Delft University of Technology, Stevin Laboratory,
P.O. Box 5048, 2600 GA Delft, The Netherlands

ABSTRACT

Numerical simulations with a simple lattice model are shown of single-edge-notched and double-edge-notched concrete beams loaded in four point shear and compared with experimental results presented in [2]. No cracks occur in the region where shear stress dominates as claimed by Bažant and Pfeiffer [4]. In a heterogeneous material like concrete cracks seem propagate in a direction which is perpendicular to the maximum tensile stress, even when the shear stress is high, but they also follow the weakest links in the material.

INTRODUCTION

In the research on the influence of shear on the fracture process in concrete structures a distinction has to be made between the initiation and propagation of a crack tip, and the opening of an existing crack under mode II or mixed mode loading. From the latter experimental results can be found in [1,2]. Many researchers are interested in mode II and mixed-mode crack initiation, see for instance [3,4,7,8].

In this paper the results of experiments on single-edge-notched beam specimens (Fig. 1a) loaded in four point shear using the geometry and dimensions proposed for a round robin organised by RILEM committee 89 FMT, and tests on double-edge-notched beams (Fig. 1b) following the geometry of Bažant & Pfeiffer [4] are simulated, using a simple lattice model in which the heterogeneity of the concrete is implemented as quenched disorder. First the model and assumptions are explained, followed with a comparison of experimental results presented in [2].

LATTICE MODEL

For the simulation of the experiments a lattice type model, originally developed in theoretical physics for simulating fracture processes in materials [5], is adopted. The material is modelled as a triangular lattice of brittle breaking beam elements [6]. The model is based on a linear elastic finite element model (DIANA). Fracturing of the material takes

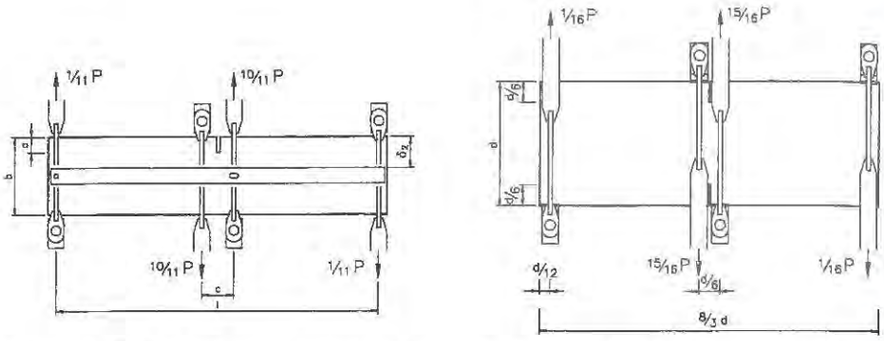

Figure 1. Loading scheme for single-edge-notched (a) and double-edge-notched beams (b).

place by removing in each load step the beam element with the highest stress (relative to its strength). The stress is calculated from the following fracture law:

$$\sigma_t = \beta*(F/A+\alpha*\max(|M_i|,|M_j|)/W)$$

where F is the normal force in the beam element, M_i and M_j are the bending moments in nodes i and j of the beam element respectively, $A = b*h$ is the cross-sectional area of the beams, and $W = b*h^2/6$. The coefficient α is introduced in order to select a failure mode where bending plays either a dominant or a restricted role. The coefficient β is a scaling factor for the global maximum stress.

For introducing the heterogeneity of the concrete a grain structure is generated. For the distribution of aggregate particles in the concrete mix a Fuller curve has been chosen. Using statistical formulas the distribution of circle diameters in a certain cross section can be generated, see [6]. The triangular lattice is projected on top of the generated grain structure, and different strengths and stiffnesses are assigned to the respective beam elements, see Fig. 2. When a beam element is situated inside an aggregate particle, the stiffness and the failure strength of the aggregate will be assigned to this element; a beam element located on the boundary between aggregate and matrix will get a low strength. Matrix properties will be assigned to those beam elements projected on the cement matrix in the generated two-phase material.

SIMULATIONS

The input parameters have been determined from a parameter study. For this purpose simulations were carried out of a uniaxial tensile experiment. The specimen and mesh as well as the experimental and simulated stress-deformation curve obtained with the input

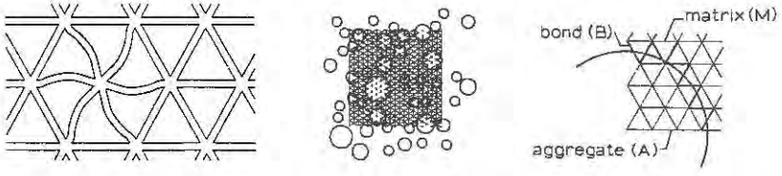

Figure 2. Triangular lattice and projection on generated grain structure.

parameters of Table 1 are shown in Fig. 3. From a comparison of the stress-deformation curves it can be concluded that the simulated descending branch is too low. It is the author's opinion that a three dimensional simulation would probably give better results. Firstly because in that case the material bridges that still connect the two crack surfaces will also be three dimensional, which gives probably a more ductile response. Secondly because in the experiments the deformation is measured on the surface, which seems to crack first [9]. The average deformation will give a less ductile response.

Using the same input parameters the four point shear experiments are simulated. Only the part in the mesh were cracks are expected contains the triangular lattice. The remainder of the specimen is modelled using isoparametric eight-noded plane stress elements available in DIANA. Simulations are carried out of the small single-edge-notched beam and double-edge-notched beams of three different sizes, see figure 5. For the double-edge-notched beams also the situation where the horizontal movement of the supports is restricted by the diagonal bars [2], is simulated for one specimen size. The horizontal displacement of the four supports is fixed in this case.

TABLE 1

beam elements: l = 5/3mm, b = specimen thickness, h = 0.68*l					
σ_A	= 10 MPa	E_A	= 70 GPa	α	= 0.005
σ_M	= 5 MPa	E_M	= 25 GPa	β	= 2.0
σ_B	= 1.25 MPa	E_B	= 25 GPa		

DISCUSSION OF RESULTS

The load-displacement curves of the simulations are compared with the experimental results [2], see Fig. 4. For the single-edge-notched beams the total load P is plotted versus the deformation δ_2, see Fig. 1 and [2]. In the experiments on the double-edge-notched specimens the average of CMSD and CMOD at both the notches is used as feed-back signal. In Fig. 4 the total load P is plotted versus this average deformation. The crack patterns for the simulations and for the experiments presented in [2] are plotted in Fig. 5.

In the experiments on the single-edge-notched beams one curved crack is observed starting at the notch and running to the opposite support. If the horizontal movement of

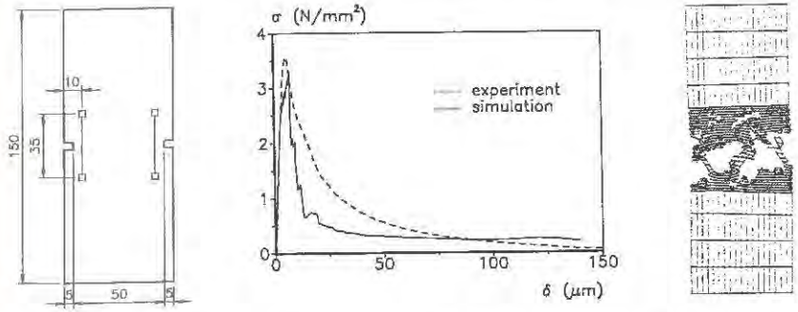

Figure 3. Uniaxial tensile specimen; stress deformation curves of experiment and simulation; cracked and deformed mesh.

the supports is restricted by the diagonal bars the descending branch is higher and the load distribution deviates from the theoretical ratios, see Fig. 1 and [3]. In the small beams the load even increases which leads to a flexural crack as shown in Fig. 5.

In the double-edge-notched beams two growing cracks can be observed before the peak. After the peak only one crack will continue due to the heterogeneity of the material. In the situation with the horizontaly fixed supports also in the double-edge-notched beams the load at the end of the descending branch increases again, which leads to a second curved crack and finally to a third tensile splitting crack which starts in the middle of the specimen. The simulations with the lattice model show the same results as the experiments. In the single-edge-notched beams one curved crack developed. In the double-edge-notched beams up till peak load two cracks developed; after peak only one crack propagated further. In all three beam sizes the same fracture mechanism occured. If the horizontal movement of the supports is restricted this leads to first one curved crack, then a second curved crack and finally a splitting crack between the notches. It has to be mentioned that a complete fixation of the supports as is possible in simulations never can be reached in the experiments.

The main error in the numerical simulations published in [7,10] of the DEN beams is the assumption of a homogeneous material which leads automatically to two curved cracks. The simulations of Rots et.al. [11] resulted in one curved crack, because they gave a material imperfection to the element at the bottom notch. The curvature they found was less than in the experiments and the simulations with the lattice model presented in this paper. Rots and coworkers believe that mode I and mode II softening has to be implemented in order to get a correct representation of the fracture mechanism that occured in this test.

The experimental results presented here and in a previous publication [3] indicate that the fracture mechanism is pure mode I. In the simulation with the lattice model no softening for mode I and no for mode II is implemented. Instead local brittle failure of the elements leads to a global ductile response and crack patterns show a good resemblance with the experiments. The cracks obtained with the lattice model are not continuous (Fig. 5), but there are still pieces material left connecting the two crack surfaces. These crack interface bridges, see also [9], can still transfer stress as the crack already has reached the opposite side of the beam, which results in a rather ductile global response. Compared with the experimental load-displacement curves the numericaly obtained response in too brittle, but as pointed out in the previous section three dimensional simulations will probably give better results. Nevertheless the crack patterns and maximum loads found with the two dimensional simulations are realistic.

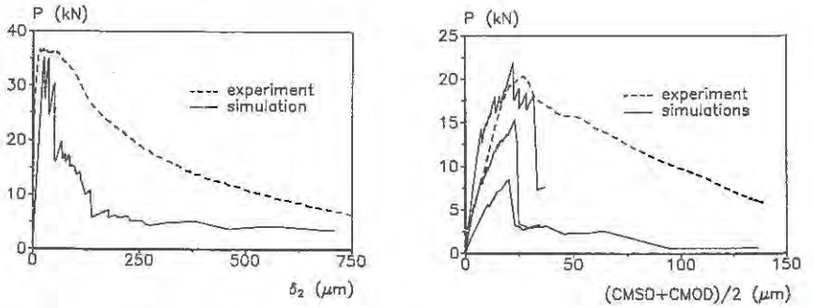

Figure 4. Load-displacement curves for experiments and simulations of single-edge-notched beams (a) and double edge-notched beams (b). Only curves of experiments and simulations with free rotating supports are shown.

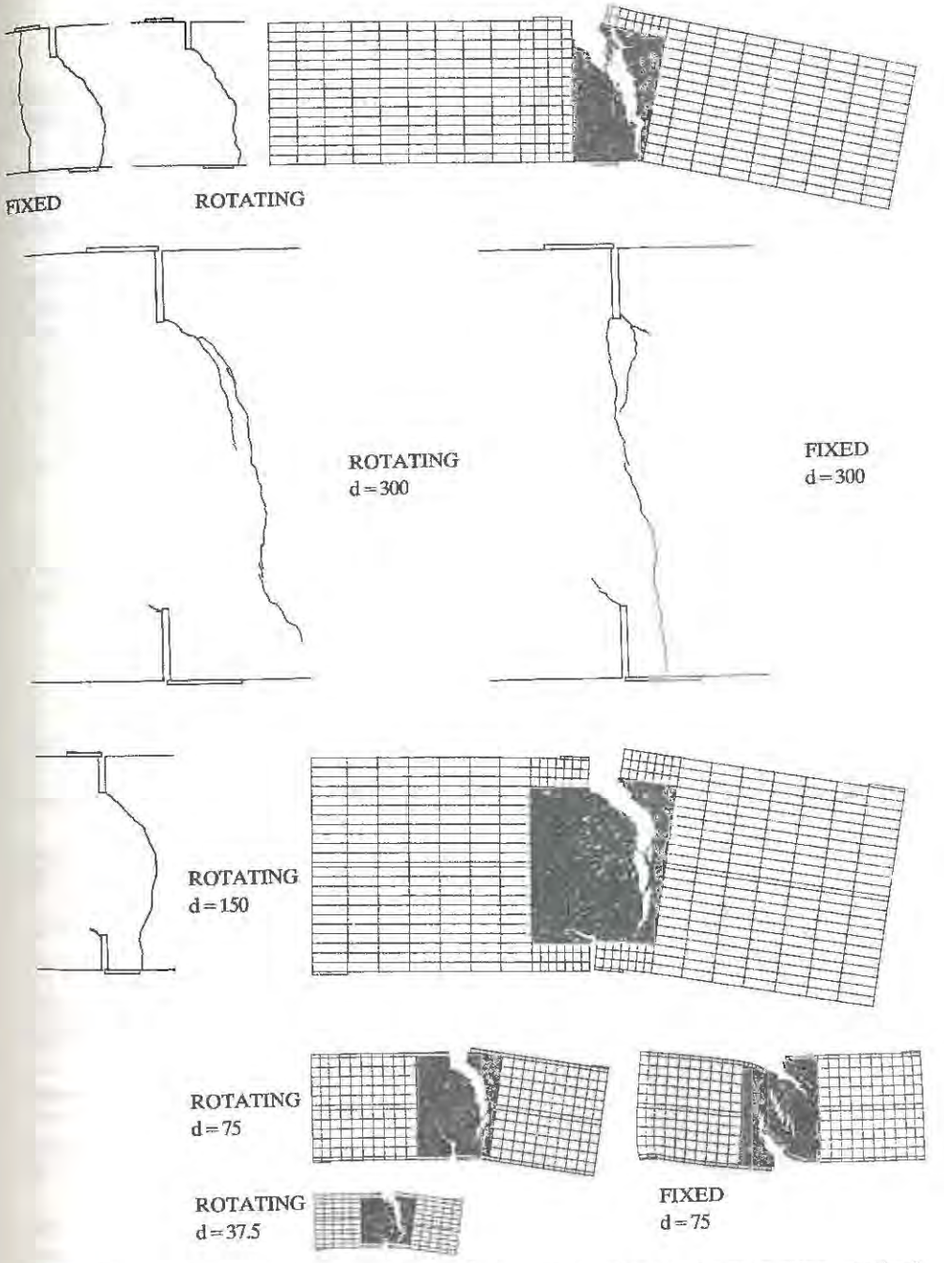

Figure 5. Experimental and numerical crack patterns for the small single-edge-notched (a=20, b=100, c=40, l=400 and t=100 mm) and double-edge-notched (d=300, 150, 75, 37.5 mm and t=37.5 mm) beams.

CONCLUSIONS

From the experiments and simulations of single-edge-notched and double-edge-notched beams it can be concluded that fracture grows under mode I, even when the external loading is mixed-mode.

In contradiction to the experimental results published in [4] there will occur one curved mode I crack in the double-edge-notched specimen loaded in shear. A straigth crack between the middle supports is obtained only if the supports are fixed in the horizontal direction. In that case a tensile splitting crack is observed.

The results obtained with the lattice model show a good resemblance with the experiments. Due to the implementation of the heterogeniety of the material only one crack in the double-edge-notched beam will propagate beyond peak load. The lattice model is able of simulating fracture in different beam sizes. Crack interface bridges, which cause a ductile load-displacement response beyond the peak, are found with the lattice model. The simulated load displacement response is too brittle. It is expected that a three dimensional simulation will give better results.

ACKNOWLEDGEMENT

The authors are greatly indebted to Mr. A.S. Elgersma for his substantial assistance in carrying out the experiments. The work was sponsored through a grant from the Dutch Technology Foundation (STW).

REFERENCES

[1] Nooru-Mohamed, M.B. Mixed-Mode Fracture of Concrete: An Experimental Approach, *PhD-thesis*, Delft University of Technology, (in preparation).

[2] Van Mier J.G.M., Schlangen E. and Nooru-Mohamed M.B., Shear fracture in cementitious composites; part I: Experimental observations, *this Conference.*

[3] Schlangen E. and Van Mier J.G.M., Boundary effects in mixed mode I and II fracture of concrete. In *Fracture Processes in Concrete, Rock and Ceramics*, eds. J.G.M. van Mier, J.G. Rots and A. Bakker, Chapman & Hall Publishers, London/New York, 1991, pp. 705-16.

[4] Bažant Z.P. and Pfeiffer P.A., Shear fracture test of concrete. *Materials and Structures*, 1986, **19**, 111-21.

[5] Herrmann H.J., Patterns and scaling in fracture. In *Fracture Processes in Concrete, Rock and Ceramics*, eds. J.G.M. van Mier, J.G. Rots and A. Bakker, Chapman & Hall, London/New York, 1991, pp. 195-212.

[6] Schlangen E. and Van Mier J.G.M., Lattice model for numerical simulation of concrete fracture. In *Proceedings International EPRI Conference on Dam Fracture*, eds. V.E. Saouma, R. Dungar and D. Morris, EPRI, Boulder, Colorado, 1991, pp. 511-27.

[7] Swartz, S.E. and Taha, N.M., Mixed mode crack propagation and fracture in concrete. *Engineering Fracture Mechanics*, 1990, **35**, 137-44

[8] Carpinteri A., Ferrara G., Melchiorri G. and Valente S., The four point shear test on single notched specimens: an experimental and numerical analysis, in *Fracture Behaviour and Design of Materials and Structures*, ed. D. Firrao, EMAS Publishers, UK, 1990, pp. 667-75.

[9] Van Mier J.G.M., Mode I fracture of concrete: discontinuous crack growth and crack interface grain bridging, *Cement & Concrete Research*, **21**, 1-15.

[10] Ingraffea A.R. and Panthaki M.J., Analysis of "shear fracture" tests of concrete beams. In *Finite Element Analysis of Reinforced Concrete Structures*, eds. Meyer and Okamura, ASCE, Tokyo, 1985, pp. 151-73.

[11] Rots J.G., Kusters G.M.A. and Blaauwendraad J., Strain-softening simulations of mixed-mode concrete fracture. In *Proceedings SEM/RILEM International Conference on Fracture of Concrete and Rock*, Houston, Texas, 1987, eds. S.P. Shah and S.E. Swartz, pp. 175-88.

MIXED MODE FRACTURE IN CONCRETE

L.J. MALVAR
Civil Engineering Department
University of California, Davis

ABSTRACT

Two smeared crack approaches to fracture of concrete in mixed mode are implemented in two-dimensional nonlinear concrete elements: (1) tensile stress transfer across cracks and (2) tensile plus shear stress transfer across cracks. To corroborate the analytical model a notched beam under mixed mode loading is analyzed. In both cases the stiffnesses normal and parallel to the crack were modified to insure a positive definite stiffness matrix. Stresses were corrected and set as functions of the crack slip and crack opening. Equilibrium iterations were implemented to redistribute stress. In both cases, acceptable agreement was found between analytical predictions and experimental results. Consideration of shear stress transfer did, however, improve the numerical prediction.

Introduction

Although it is generally recognized that crack initiation in concrete occurs in Mode I (opening), crack propagation is more likely to take place in mixed mode, i.e., involving Mode I and II (shearing) or III (tearing).

Mixed mode crack propagation involves considering the transfer of tensile and shear forces across cracks. Constitutive relations representing the transferred stresses were evaluated (1). In the present report these constitutive relations are implemented in a general purpose finite element program developed by ADINA R&D Inc. (2). A benchmark experiment by Arrea and Ingraffea (3), (4) is then modeled, with and without considering transfer of shear stresses.

Problem

The mixed mode problem considered is depicted in Fig. 1 and concrete properties used are reported in Table 1. In many cases the problem was approached without considering shear transfer across the crack. Initial

attempts at modeling the shear transfer using a constant shear retention factor β (typically $\beta \leq 0.1$) yielded results with almost no softening after peak load (5), (6). Better representations were obtained either assuming the existence of a Mode II fracture energy (7), or using a predetermined crack path (8). In this study the consideration of a shear transfer model is attempted and its effects observed.

TABLE 1. Concrete Properties

Fracture Energy	G_f = 0.055 N/mm (.314 lb/in)
Compressive Strength	f'c = 45.5 N/mm^2 (6600 psi)
Tensile Strength	f_t = 2.80 N/mm^2 (406 psi)
Modulus of Elasticity	E = 24.8 GPa (3600 psi)

TABLE 2. Stress - Crack Width Relationship

w/w_o	σ/f_t
0.00	1.0000
0.05	0.7082
0.10	0.5108
0.15	0.3817
0.20	0.2986
0.25	0.2446
0.30	0.2080
0.40	0.1596
0.60	0.0904
0.80	0.0361
1.00	0.0000

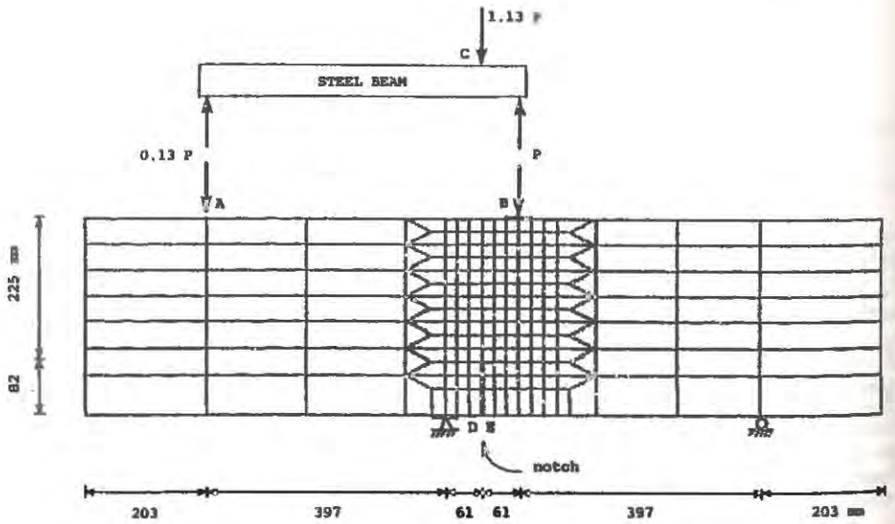

FIG 1.
Experimental setup and finite element mesh.

Tensile Stress Transfer

The transfer of tensile stresses across a crack had already been implemented with a smeared crack approach (9) using the Crack Band Model (CBM). This tension softening behavior involved a negative stiffness, C_s, for the cracked element. The CBM was implemented assuming zero stiffness (actually a very small value was used to avoid a singular stiffness matrix) and then resetting the stresses as a function of the crack opening. These stresses are then redistributed during equilibrium iterations. The stress transferred versus crack width relationship is tabulated in Table 2 (10) in nondimensional form.

The fracture energy, G_f, is related to the stress versus displacement relationship by:

$$G_f = w_o \, f_t \int_0^1 \sigma/f_t \, d(w/w_o)$$

where w = crack width or crack opening
σ = stress transferred at crack width w
w_o = crack width beyond which no stress is transferred
f_t = tensile strength

In a first analysis on the mixed mode problem the CBM alone was used in order to evaluate the importance of considering shear transfer.

Versions of ADINA (2) acknowledge the importance of strain softening by including a linear stress release as a function of strain after cracking (11). This stress release can be directly linked to fracture energy. However, it has been shown that linearizing the highly nonlinear post peak stress versus strain relationship negatively affects results (9). Due to its modular form, the program was easily modified to include the nonlinear strain softening relationship indicated in Table 2.

Arc-Length Procedure

The solution of the finite element incremental equations of motion was first attempted using the spherical arc-length and the constant increment of external work procedures described in (12). The post-peak numerical analysis of this experiment has shown to be highly unstable (5). The adopted approaches did not yield converged equilibrium states past peak load and, thus, were modified.

A type of indirect displacement control (13) was then adopted: in the arc-length procedure the norm of displacement (involving all nodal points) was replaced by the distance between the two points at the edges of the notch (points D and E on Fig. 1). The vertical component of this distance is referred to as CMSD (Crack Mouth Sliding Displacement). During the analysis, the CMSD is a monotonically increasing parameter which stabilizes the algorithm. In the experiment, the CMSD had been used as feed-back control parameter.

Failure Envelopes

The failure envelopes used in ADINA (14) are largely based on biaxial concrete strength experimental results by Kupfer at al. (15). In the plane stress analytical model, the crack path showed sensitivity to the tensile envelope representation close to the tension/tension zone ($\sigma_1>0$, $\sigma_2>0$, $\sigma_3=0$) (Fig. 2). The existing linear envelope in the tension/compression zone was then modified to better match experimental results. The following power relationship was used:

$$\sigma'_t = \sigma_t \left[1 - \left(\frac{{}^t\sigma_i}{\sigma'_c} \right)^n \right]$$

where σ_t = uniaxial cut-off tensile stress

σ'_t = uniaxial cut-off tensile stress, multiaxial conditions

σ'_c = uniaxial compressive failure stress, multiaxial conditions

${}^t\sigma_i$ = principal stress in direction i at time t

$n = 1$ if $\sigma'_c \geq 8000$ psi (563 kp/cm²)

$= 1 + 0.0002(8000-\sigma'_c)$ if $\sigma'_c < 8000$ psi

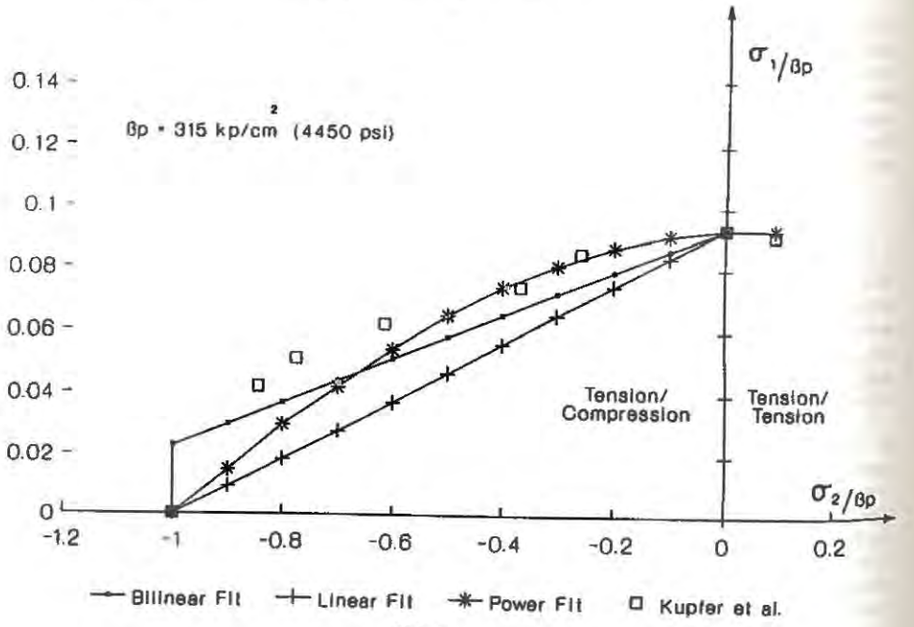

FIG 2.
Tension-compression failure envelope.

Both linear and power envelopes are shown in Fig. 2, together with Kupfer et al. results for βp = 315 kp/cm² (4450 psi). βp is the uniaxial compressive strength of 50 by 50 by 200 mm (2 by 2 by 7.9 in.) prisms. Later versions of ADINA improved the original curve fitting, using (11):

$$\sigma'_t = \sigma_t \left[1 - 0.75 \frac{{}^t\sigma_i}{\sigma'_c} \right]$$

From Fig. 2 it is apparent that the present modification still yields a better match close to the tension/ tension zone.

Finite Element Model

The finite element mesh used is depicted in Fig. 1. Loads of 0.13P and P were applied at points A and B, respectively. In the computer program this is accomplished using an automatic step incrementation method, where the level of externally applied loads is adjusted automatically. In the experiment, a single total load of 1.13P was applied at point C, on a steel beam which was itself bearing on rollers at points A and B.

Shear Transfer

Cracks in reinforced concrete are able to transmit shear forces across crack faces. This transfer is traditionally neglected on the assumption that this would be a conservative simplification. However, Bazant et al. showed that this assumption can be an over simplification (16), (17). Crack dilation occurs with shear slip. However, crack dilation is prevented by forces normal to the crack faces which will have to be compensated by tensiles forces in the reinforcement across the crack.

Shear stresses can be transferred across a crack in three ways:

1. Aggregate interlock as a result of the roughness of the crack faces
2. Dowel action or shear resistance of the reinforcement across the crack
3. The axial tensile force component in the reinforcement oblique to the plane of cracking.

For members with low reinforcement and for small crack widths, aggregate interlock is the main mechanism of shear transfer. Tests carried out on beams without web reinforcement showed that aggregate interlock accounted for up to 75 percent of the shear transfer (18). Hence, most attention will be given to this first mechanism of transfer.

Shear Transfer Model

Three accepted empirical models which represent the nonlinear relationships between shear stress and slip are: the Rough Crack Model (RCM) in its original form (12), or in a modified form (MRCM) (19), and the Two-Phase Model (TPM) (20), (21). The MRCM constitutive laws are as follows:

$$\sigma_{nn} = - a_{12} \frac{r}{(1+r^2)^{0.25}} \sqrt{\delta_n \sigma_{nt}} \quad \text{(always compressive)} \tag{1}$$

$$\sigma_{nt} = \tau_o \left(1 - \sqrt{\frac{2\delta_n}{d_a}}\right) r \frac{a_3 + a_4 |r|^3}{1 + a_4 r^4} \tag{2}$$

in which δ_n = crack opening ($\delta_n \geq 0$)
δ_t = relative slip
$r = \delta_t / \delta_n$
σ_{nn} = interface normal stress
σ_{nt} = interface shear stress

$a_{12} = 0.62$
$a_3 = 2.45/\tau_o$
$a_4 = 2.4(1-2/\tau_o)$
$\tau_o = 0.25 f'_c$

and
$$\begin{bmatrix} d\sigma_{nn} \\ d\sigma_{nt} \end{bmatrix} = \begin{bmatrix} B_{nn} & B_{nt} \\ B_{tn} & B_{tt} \end{bmatrix} \begin{bmatrix} d\delta_n \\ d\delta_t \end{bmatrix} = B \begin{bmatrix} d\delta_n \\ d\delta_t \end{bmatrix} \tag{3}$$

where B is the crack stiffness matrix. The derivation of B is shown in Appendix A.

Implementation in Finite Element Program

Transfer of shear stresses was implemented by combining the MRCM and the CBM. The incremental flexibility matrix due to the solid concrete and including strain softening in tension is given by (22): $\{d\varepsilon\} = D^{sc} \{d\sigma\}$ or

$$\begin{bmatrix} d\varepsilon_{nn} \\ d\varepsilon_{tt} \\ d\varepsilon_{nt} \end{bmatrix} = \begin{bmatrix} 1/E & -\mu/E & 0 \\ -\mu/E & 1/E & 0 \\ 0 & 0 & 1/G \end{bmatrix} \begin{bmatrix} d\sigma_{nn} \\ d\sigma_{tt} \\ d\sigma_{nt} \end{bmatrix} \tag{4}$$

where μ = Poisson's ratio.

In addition, since we assume strain softening in tension to be present, the slope C_s of the strain softening branch has to be taken into account. The crack stiffness is then:

$$C^{cr} = \begin{bmatrix} wB_{nn} + C_s & wB_{nt} \\ wB_{tn} & wB_{tt} \end{bmatrix} \tag{5}$$

For very small values of the crack opening, C_s is large but B_{nn} is almost zero; whereas when the crack opening reaches about 0.1 mm, the opposite holds.

The incremental stiffness matrix can be obtained from:

$$C = D^{-1} = \left[D^{sc} + C^{cr-1}\right] \tag{6}$$

This yields an incremental stiffness matrix which is not symmetrical and is not guaranteed to be positive definite. Since ADINA considers only symmetric

matrices, the solution was attempted using a modified stiffness, and then correcting the stresses at every iteration for each load step increment. The following simplifications were then implemented: $\mu = 0$, and to insure positive definiteness $C_{11} = 0+$ if $C_{11} < 0$ and $C_{31} = C_{13} \leq \sqrt{C_{11} C_{33}} - 0+$ where 0+ is a small positive number.

Model Representation

To evaluate the effects of shear transfer, a 100 by 100 by 100 mm (4 by 4 by 4 in.) concrete finite element was first cracked in tension, then sheared in the perpendicular direction (Fig. 3), in displacement control. Given the nodal displacements, strains at the Gauss points are evaluated, then an iterative process determines crack slip, crack dilatation and concrete deformation using Eq. (1), (2), C_s, and (23):

$$\delta_n = (\varepsilon_n - \sigma_{nn}/E)w \quad \text{and} \quad \delta_t = (\varepsilon_t - \sigma_{nt}/G)w$$

The model behavior is predicted using all three formulations (RCM, MRCM, TPM). For each case, Fig. 4 shows the shear and normal loads transferred. The TPM values were capped to the maximum predicted by the RCM. It is observed that the dilatancy induces vertical compression (along the z axis). If reinforcing bars perpendicular to the cracks were present, the dilatancy would increase the tension in the bars at the crack locations.

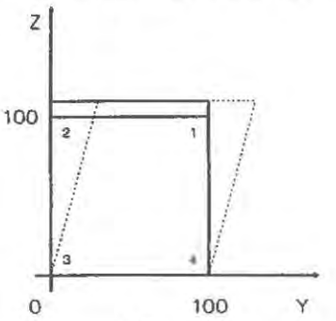

FIG 3.
Shear transfer experiment.

From Fig. 4, it is apparent that all three models yield very similar shear transfer capacity, but the normal stress due to dilatation is significantly higher for the RCM. In the mixed mode analysis, the more recent MRCM formulation was chosen, since it appeared close to the TPM formulation but presents no discontinuity in the stress gradient.

Results

In order to evaluate the importance of modeling stress transfer across cracks, the analytical model was first run with no transfer, i.e., assuming total stress release right after cracking. Since the standard algorithms did not converge, the indirect displacement method was used, with a very low fracture energy (0.0002 N/mm) equivalent to a sudden stress release. Results for this first run are shown in Fig. 5.

The analysis was then carried out considering only tensile stress transfer across the cracks (CBM). Finally, the MRCM was added and a new analysis completed (CBM+MRCM). Results for both cases are shown in the form of load versus CMSD (Fig. 5) and load versus vertical displacement at point C (Fig. 6). The vertical displacement at point C was derived by linear interpolation of the vertical displacements of points A and B. Data points indicating the reported range of experimental results (3) are also shown in Fig. 5.

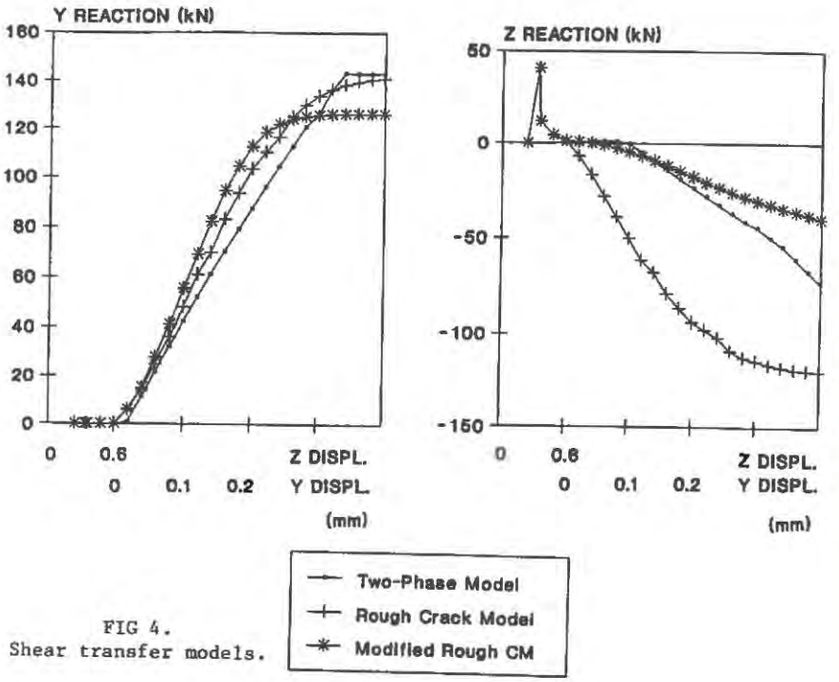

FIG 4.
Shear transfer models.

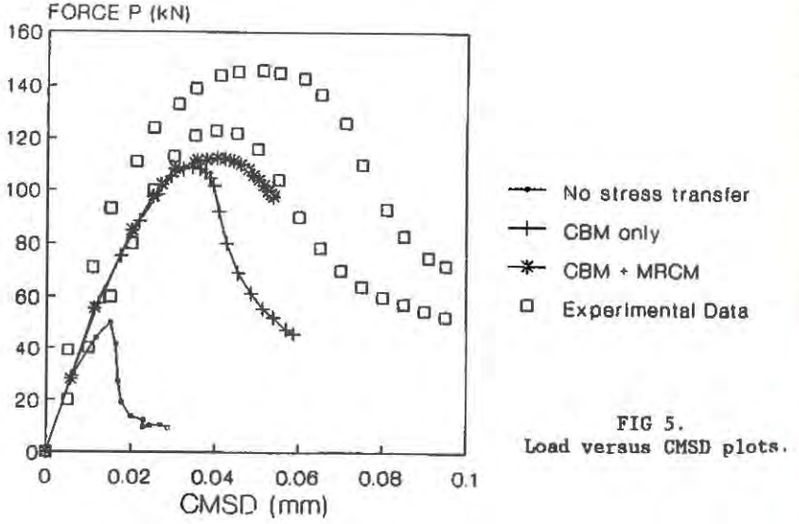

FIG 5.
Load versus CMSD plots.

Convergence of the arc-length algorithm was only obtained for carefully chosen control parameters. These parameters control the size of the step in the load-CMSD space (ALFA), the maximum number of iterations allowed for each time step (ITEMAX), the maximum displacement at control point E (DISPP), and energy convergence criteria (ETOL) (12). In each case they were respectively:

Parameter	No Transfer	CBM	CBM+MRCM
ITEMAX	45	45	30
ETOL	10^{-6}	10^{-6}	5.10^{-4}
DISPP	-0.015	-0.015	-0.015
ALFA	0.4	0.4	0.5

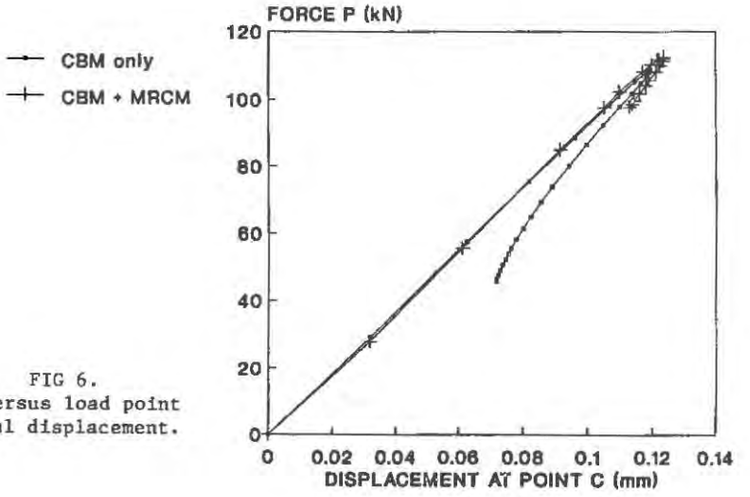

FIG 6.
Load versus load point vertical displacement.

The crack pattern and the deformed shape for the last loading step are shown in Figs. 7 and 8 (CBM case).

Discussion

Fig. 6 indicates that the displacement at point C presents a sharp snap-back past peak load. This explains why displacement control at that point cannot yield the post peak response. The displacement at both points A and B shows a similar behavior, which explains why the norm of displacement in the arc-length procedure was unsuccessful.

Fig. 5 shows that considering tensile stress transfer alone yields a conservative behavior prediction. The maximum load is underestimated by about 20 percent and the post peak load carrying capacity is lower. However, the shape of the strain softening portion is similar. A higher value of G_f would yield a better match to the experimental peak load and post peak response (8).

The crack pattern (Fig. 7) still differs from the reported experimental crack path. It was, however, observed that a small variation in the mesh size, or initially larger load step sizes, would affect the path or result in bifurcation points. Similarly, stiffer bearing plates would bring the crack path closer to the notch plane. The crack path would easily follow any of the different directions indicated in Fig. 7. This would explain the discrepancies in crack paths found by different authors (24), (25), (26), (27), using a similar but symmetrical specimen. For example, the experimental crack path obtained in (24) coincides with the analytical crack pattern shown in Fig. 7.

Should tensile stress transfer not have been considered, the maximum load carrying capacity of the analytical model would have been reached as soon as the first tensile cracks had formed (around 50 kips) (Fig. 5). This is obviously an inadequate representation of the experimental behavior.

Transfer of both tensile and shear stress is considered best in matching experimental behavior. The peak load is higher and the post peak behavior is closer to experimental results. However, in order to obtain a more accurate post peak behavior, a non-symmetrical stiffness matrix would have to be considered. This would present additional difficulties, such as implementation in a different program with a non-symmetrical solver, and increase in computation time. In this case, the crack pattern remained similar to the previous one.

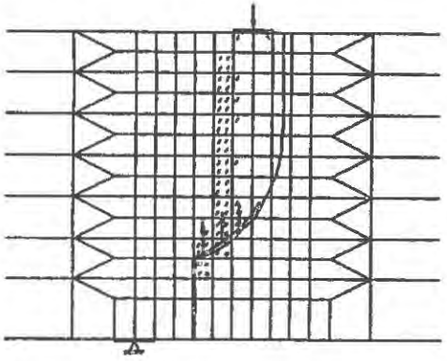

FIG 7.
Crack pattern, experimental and alternate crack paths.

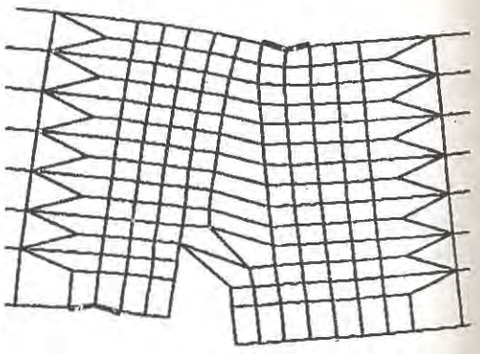

FIG 8.
Deformed shape at failure.

Conclusions

The consideration of shear stress transfer across the propagating cracks yielded a better prediction of the experimental results. However, the resultant stiffness matrix is non-symmetrical and more accurate results would be obtained by using a non-symmetric solver.

The exclusive consideration of tensile stress transfer yielded good results up to peak load. Beyond this point, the loads are underestimated, although the shape of the unloading branch matches the experimental trend. This could be an acceptable representation of mixed mode behavior as long as it is kept in mind that a conservative post peak behavior will be obtained.

Finally, it was shown that inadmissible results are obtained if both tensile and shear stresses are assumed to completely vanish upon cracking.

Acknowledgment

Support provided by the Naval Civil Engineering Laboratory, Port Hueneme, CA, and the Naval Facilities Engineering Command, Alexandria, VA, is gratefully acknowledged. The author wishes to express his appreciation to Dr. G.E. Warren, NCEL, for his continued support throughout this investigation.

References

1. L.J. Malvar and G.E. Warren, Analytical modeling of reinforced concrete in tension, Technical Report 926, NCEL, Port Hueneme, California (1989).
2. ADINA R&D Inc. ADINA: A finite element program for Automatic Dynamic Incremental Nonlinear Analysis, Watertown, Massachusetts (1987).
3. M. Arrea and A.R. Ingraffea, Mixed-mode Crack Propagation in Mortar and Concrete, Report 81-13, Dept. Struct. Eng., Cornell Univ., Ithaca, New York (1981).
4. RILEM Tech. Committee 90-FMA, Fracture Mechanics of Concrete/Applications, Second Draft Report over the State of the Art, Division of Struct. Eng., Lulea University of Technology, S-951 87 Lulea, Sweden (1987).
5. J.G. Rots, P. Nauta, G.M.A. Kusters and J. Blaauwendraad, HERON, 30(1), (1985).
6. Concrete Mechanics, Cooperative Research between Institutions in the Netherlands and the USA, Third Meeting, Delft Univ. of Technology (1983).
7. J.G. Rots and R. de Borst, J. of Eng. Mechanics, 113(11), 1739 (1987).
8. J.G. Rots, Computational Modeling of Concrete Fracture, PhD Dissertation, Delft Univ. of Technology (1988).
9. L.J. Malvar and G.E. Warren, Experimental Mechanics, 28(3), 226 (1987).
10. L.J. Malvar and M.E. Fourney, Eng. Fract. Mechanics, 35(1/2/3), 251 (1989).
11. K-J. Bathe, J. Walzack, A. Welch and M. Mistry, Computers and Structures, 32(3/4), 563 (1989).
12. K-J Bathe and E.N. Dvorkin, Computers and Struct., 17(5/6), 871 (1983).
13. R. de Borst, Nonlinear Analysis of Frictional Materials, PhD Dissert., Delft Univ. of Technology (1986).

14. K-J. Bathe and S. Ramaswamy, Nuclear Eng. and Design, 52, 385 (1979).
15. H. Kupfer, H. Hilsdorf and H. Rush, ACI Journal, 66, 656 (1969).
16. Z.P. Bazant and T. Tsubaki, J. Struct. Div., 105(ST2), 327 (1979).
17. Z.P. Bazant and P. Gambarova, J. Struct. Div., 106(ST4), 819 (1980).
18. S. DeiPoli, P.G. Gambarova and C. Karakoc, J. of Struct. Eng., 113(1), 1 (1987).
19. R.C. Fenwick and T. Paulay, J. Struct. Div., 94(ST10), 2325 (1968).
20. J.C. Walraven and H.W. Reinhardt, HERON, 26(1A), (1981).
21. H.W. Reinhardt and J.C. Walraven, J. Struct. Div., 108(ST1), 207 (1982).
22. Z.P. Bazant and B.H. Oh, Matls. Struct., 16(93), 155 (1983).
23. G. Valente, Smeared crack analysis using nonlinear fracture and aggregate interlock models for concrete, Proc., Intl. Conf. on Fracture and Damage of Concrete and Rock, Technical University, Vienna, (1988).
24. Z.P. Bazant, and P.A. Pfeiffer, Matls. Struct., 19(110), 111 (1985).
25. A.R. Ingraffea and M.J. Panthaki, Analysis of "Shear Fracture" Tests of Concrete Beams, Finite Element Analysis of RC Struct., Proc. of a Seminar Japan Soc. Prom. Science and US NSF, Tokyo, Japan, 151 (1985).
26. Z.P. Bazant and P.A. Pfeiffer, Comment on Ingraffea and Panthaki's Analysis of Shear Fracture Tests of Concrete, F.E.A. of RC Struct., Proc. Seminar Japan Soc. Prom. Science and US NSF, Tokyo, 174 (1985).
27. S. Melin, Materials and Structures, 22(127), 23 (1989).

Appendix A: Derivation of Crack Stiffness Matrix B

The MRCM formulation can be rewritten as

$$\sigma_{nn} = -a_{12} r\sqrt{\delta_n}\,\sigma_{nt}/h \quad \text{and} \quad \sigma_{nt} = \tau_o(1-\sqrt{2\delta_n/d_a})r(f/g)$$

where $f = a_3 + a_3 |r^3|$, $g = 1 + a_4 r^4$, $h = (1+r^2)^{0.25}$

and by derivation:

$$f_n = \partial f/\partial n = -3a_4|\delta_t^3/\delta_n^4|, \quad f_t = \partial f/\partial t = 3a_4\delta_t|\delta_t/\delta_n^3|$$

$$g_n = \partial g/\partial n = -4a_4(\delta_t^4/\delta_{n5}), \quad g_t = \partial g/\partial t = 4a_4(\delta_t^3/\delta_n^4)$$

$$h_n = \partial h/\partial n = (1+r^2)^{-0.75}(-2\delta t^2/\delta_n^3)/4, \quad h_t = \partial h/\partial t = (1+r^2)^{-0.75}(2\delta_t/\delta_n^2)$$

The crack stiffness terms are then:

$$B_{nn} = -a_{12}\left((-h\delta_t/\delta_n^2 - h_n r)\sqrt{\delta_n}\sigma_{nt}/h^2 + r\delta_n^{-0.5}\sigma_{nt}/2h + r\sqrt{\delta_n}B_{tn}/h\right)$$

$$B_{nt} = -a_{12}\left((-h_t r + h/\delta_n)\sqrt{\delta_n}\sigma_{nt}/h^2 + r\sqrt{\delta_n}B_{tt}/h\right)$$

$$B_{tt} = \tau_o(1-\sqrt{2\delta_n/d_a})\,[f/\delta_n g + r(f_t g - f g_t)/g^2]$$

$$B_{tn} = \tau_o\left(-fr/(g\sqrt{2d_a\delta_n}) + (1-\sqrt{2\delta_n/d_a})[(f_n g - f g_n)r/g^2 - f\delta_t/(g\delta_n^2)]\right)$$

FRACTURE OF STEEL FIBER REINFORCED CONCRETE BEAMS SUBJECTED TO SHEAR AND AXIAL FORCE

JENN-CHUAN CHERN, AN-TAI CHANG, HUI-SHENG CHIU
Department of Civil Engineering
National Taiwan University
Taipei, Taiwan, ROC

ABSTRACT

Mixed mode fracture tests were performed to investigate the fracture energy, crack propagation and failure of Iosipescu-type concrete beams with and without inclusion of steel fibers. Some concrete beams were subjected to both shear and compression. The effect of axial load, volume fractions of steel fiber, and the distance between interior load points on fracture of concrete specimens are discussed. The test results of mixed mode fracture of steel fiber reinforced concrete are presented.

INTRODUCTION

Recent advancements in the use of fracture mechanics concepts to explain crack initiation and failure of concrete has brought great attention to researchers and engineers. Following the steps to explore the mechanical behavior of concrete subjected to tensile-type of loading, more research efforts are now been devoted to situations in which crack growth in a body under complex state of stress [1,2,3]. The mechanical behavior of concrete, regarded as frictional material, is sensitive to the effect of confining stress. Some recent researches [1,4] show that it is more reasonable to analyze the shear failure of beams using fracture mechanics concept. How axial loads affect the fracture energy, crack initiation and propagation, and failure of concrete beams is of great concern. This paper will present the results of a testing program conducted, considering the effect of different spacings of the interior load points for four-point bending (4PB) and the degree of axial force. Steel fiber-reinforced concrete (SFRC) and plain concrete beams were used for the test.

EXPERIMENTAL INVESTIGATION

The test specimens were beams of constant rectangular cross section and constant length-to-depth ratio 4:1. To determine the size effect, geometrically similar specimens of various depths, d = 63.5, 127, and 254 mm, were used. The thickness of specimens were the same; b = 101.6 mm. The double-sided notch, of depth a sixth of d at midth of beam, was cut by a designed cutting table with a diamond saw into the hardened specimens. All specimen were cured in moist condition for 28 days until the day of testing. A testing system composed by a 100-ton servo-controlled closed loop MTS testing machine and a rigid frame for 4PB test was used. The steel brush platens were used to eliminate the unwanted shear stress which might occur on lateral surfaces of concrete beam during the application of axial force. The spacings of the interior load points of the beams are 0.32 d, 0.72 d, and 1.12 d. The axial force was applied through a motorized constant hydraulic pressure system so that the pressure was maintained constant throughout the test.

The materials used were Type I portland cement, steel fibers, local crushed limestone aggregate with a maximum aggregate size, d_a, 1/2 in. (12.7 mm). The grading of coarse aggregate meets the requirements of ASTM C33. Fine aggregate, with maximum aggregate size 4.76 mm, used has a fineness modulus 2.67 and a grading satisfying ASTM C33 requirements. Steel fibers used are Fibercon 3/4 in. (19 mm) carbon steel fibers, which is straight type with a shallow notch on one side of fiber. The equivalent diameter of the fiber is 0.017 in. (0.43 mm); the corresponding aspect ratio is 44. Cementitious mixes designed for plain concrete and SFRC are shown in Table 1. Number of specimens and the major parameters of the mix are listed in Table 2. Companion cylinders 6 in. (15.24 mm) in diameter and 12 in. (30.48 mm) in length were cast from each batch of concrete; three cylinders of each mix were for compressive strength tests and three specimens for splitting tensile tests.

RESULTS AND DISCUSSIONS

Strength

Table 3 shows the result of compressive strength and splitting tensile strength of cylindrical specimens made of various fiber contents. Results shown in Table 3 indicate that the higher the fiber content in concrete the higher the tensile and compressive strength of specimen. Fig. 1 shows the mean failure load for plain concrete beams and beams made of two different volume fractions of steel fiber. Also shown in Fig. 1 are the effect on ultimate load due to the axial compression and the distance between interior loading points. The trend of results due to volume fractions of fiber are similar to that found in the compressive test and splitting tensile test for steel fiber reinforced mixes; the load capacity of beams is greatly enhanced with the increase of axial compression. When both effects due to fiber and axial compression are considered, shown in Fig. 2 and 3, it was found that axial compression has

a dominant contribution to the increase of failure load and fracture energy; i.e. the influence influence of friction and aggregate interlock of concrete is higher than the stiffening and bridging effect due to fiber. No clear relationship among failure load of beams loaded at different distance between interior loading points were found. Further numerical analyses are required to verify the test results.

Fracture pattern

Numerous tests were performed on plain concrete beams with Iosipescu geometry, however, different crack paths in 4PB tests were reported [1,2,3]. Ballatore et al. indicated [3] that different crack paths may develop for different spacings of the interior load points of the beam. Bazant and Pfeiffer reported a macroscopic failure pattern consisting of a vertical line connecting the crack tips, which they stated was due to a Mode II shear failure using a very closely spaced interior loading points (0.167 d). Fracture of concrete beams can be summarized in four patterns as shown in Fig. 4. Pattern I and II appears in the situations when concrete beam was loaded at close loading points, 0.32 d; the central zone subjected to high shear stress. For all three sizes of specimen, the fracture patterns are all consistent. Plain concrete beams and 1% SFRC beams fails in pattern I, while 2% SFRC beams fracture in Pattern II. The authors also found that the fracture block in the midth of beam is much smaller of 1% SFRC beam as compared to that of plain concrete beam. Therefore, one may conclude that the addition of fibers to concrete, which changes the mechanical behavior of concrete, leads to the alternation of failure pattern from I to II. However, all concrete beams fail identically in Pattern II when there were subjected to axial compression.

As the distance between interior loading points, c , increase, the contribution of flexural stress to the failure of concrete beam increase. For the case of c equals to 0.72 d, the crack pattern for all specimens, with or without fiber and axial compression, is Pattern III. When the maximum load was reaches, two cracks develop simultaneously from the notch tips. Following the peak load, these cracks stabilized and another crack, denoted as 2, started at mid-span almost at mid-depth. This crack finally propagate through the beam depth and connect two interior load points. When c equals to 1.12 d, all specimens fail in Pattern IV. Two cracks develop from the opposite side of interior load points at the same time, these cracks propagates toward the interior load points until failure.

Size effect law

Size effect is the most important consequence of application of fracture mechanics on concrete structures [1]. Geometrically similar double-edge notched beams, of three different sizes, made of cementitious mixes at various fiber volume fractions were used for the mixed mode size effect tests. Fig. 5 shows the results of experimental studies on size effect of plain concrete and SFRC beams subjected to shear

and compression. For the case c= 0.32 d and 0.1 f'c axial compression, Fig. 5 shows that the range of applicability of nonlinear fracture mechanics of SFRC is wider than that of plain concrete. However, the size effect in SFRC beams is less pronounced as compared to that made of plain concrete. Similar result was found for concrete beams tested without axial force. The test results indicate that the appication of linear fracture mechanics to SFRC structure is feasible only with much larger specimens as compared to plain concrete.

Fig. 6 shows the size effect plot for the beams subjected to various distance, c , between two interior load points in 4PB tests. Concrete beams loaded with larger c exhibits a more significant size effect. The size effect in Mode I loading condition is much apparent than the conditions when shear load is involved. The case with strong shear load, i.e. c = 0.32 d, shows less pronounced size effect as compared to two other cases shown in Fig. 6. The mechanisms lead to this finding need more deeper study, however the contribution of energy due to shear friction, which yields higher Mode II fracture energy in Bažant's test, along the crack surface to the fracture of concrete seems to the reason for that.

CONCLUSIONS

(1) The addition of fiber increases both strength and fracture energy of plain concrete beam subjected to mixed load conditions; the effect of confining pressure was found to have much more effect on the fracture properties of concrete than that due to fiber.

(2)The size effect is less pronounced when the distance between two interior loading points in 4PB test is smaller and the shear force is greatly involved.

ACKNOWLEDGEMENT

Financial support from the National Science Council of Republic of China under Grant No. NSC79-0410-E002-22 to National Taiwan University is gratefully acknowledged.

REFERENCES

1. Bažant, Z.P. and Pfeiffer, P.A.,"Shear Fracture Tests of Concrete," Materials and Structures (RILEM), Vol. 19, No. 110, pp. 111-121 (1986).
2. Swartz, S.E. and Taha, N.M.,"Crack Propagation and Fracture of Plain Concrete Beams Subjected to Shear and Compression," ACI Structural J., Vol. 88, No. 2, pp. 169-177 (1991).
3. Ballatore E.,Carpinteri A.,Ferrara G.,Melchiorri G.,"Mixed Mode Fracture Energy of Concrete," Engineering Fracture Mechanics, Vol. 35, No. 1/2/3, pp. 145-147 (1990).
4. Bažant, Z.P. and Kazemi, M.T.,"Size Effect on Diagonal Shear Failure of Beams without Stirrups," ACI Structural J., Vol. 88, No .3, pp. 268-276 (1991).

5. Tarng, K.M., Chern, J.C. and Chen, H.W.,"Determination of R-Curves of Steel Fiber Reinforced Concrete from Size Effect Tests," J. of the Chinese Institute of Engineers, Vol. 14, No. 2, pp. 173-183 (1991).

TABLE 1 Mix proportions (kg/m^3)

Mix	water cement ratio	cement	water	coarse aggr.	fine aggr.	fiber
plain concrete	0.53	383	203	958	766	
SFRC(1%) (2%)	0.50	428	214	856	856	81 162

TABLE 2 Strength of cylindrical specimens

Mix (v_f)	Compressive strength* (kg/cm^2)	Split tensile strength* (kg/cm^2)
0%	351	30
1%	385	31
2%	410	32

* average of three specimens

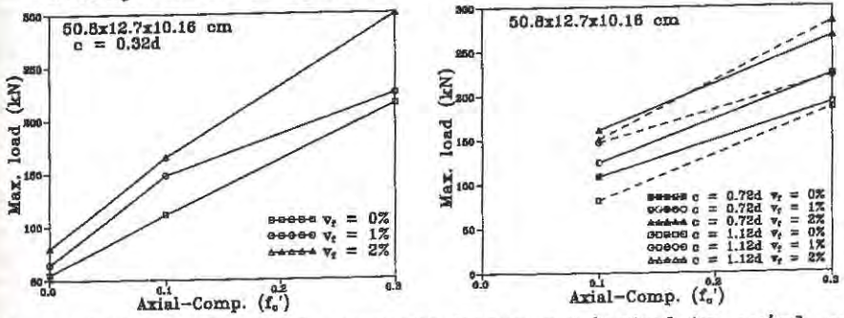

Fig. 1 Ultimate load of concrete beams subjected to axial compr.

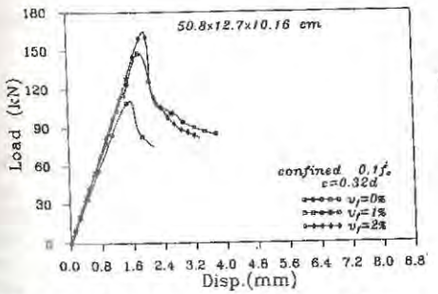

Fig. 2 Effect of fiber volume fractions on load-displ. curve

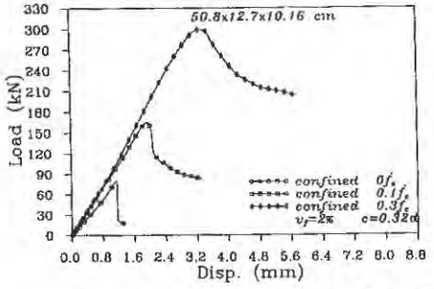

Fig. 3 Effect of lateral compr. loads on load-displacement curve

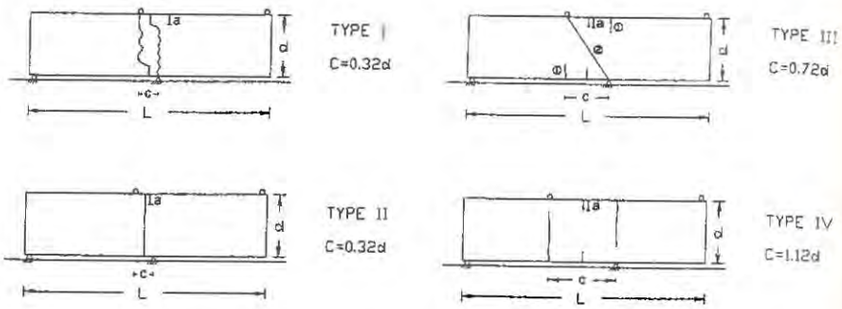

Fig. 4 Fracture patterns of concrete beam.

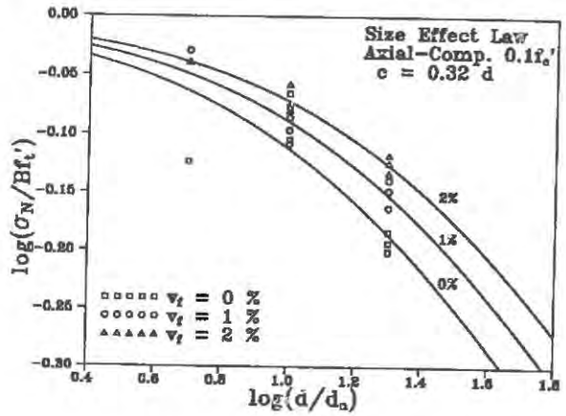

Fig. 5 Size effect of concrete beams subjected to shear and compression.

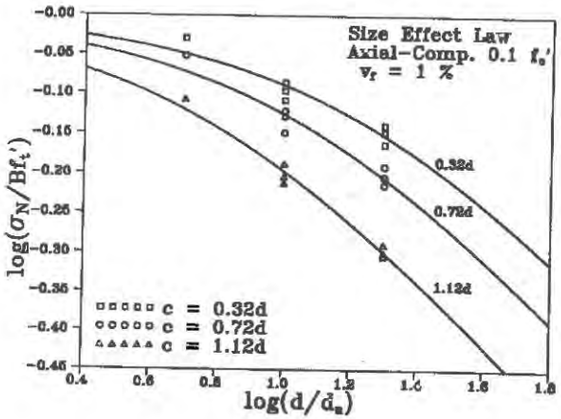

Fig. 6 Size effect of SFRC beams subjected to load at various interior distances.

MIXED MODE CONCRETE FRACTURE - AN EXPERIMENTAL ANALYSIS

Z. K. Guo*, A. S. Kobayashi* and N. M. Hawkins**
*Department of Mechanical Engineering
University of Washington, Seattle, WA 98195
**Department of Civil Engineering
University of Illinois at Urbana-Champaign, Champaign, IL 61801-2397

ABSTRACT

The development of a fracture process zone associated with a subcritical crack growth in a three-point bend concrete specimen with an off-centered, precracked, single-edge crack was studied using a hybrid analysis based on moire interferometry finite element method. The crack closing and shearing stresses due to aggregate bridging and interlocking, respectively were determined and the energy dissipation rate at the fracture process zone was found to be larger than that of an equivalent concrete specimen without aggregate interlocking.

INTRODUCTION

The most common mixed mode type of fracture in concrete structure is the diagonal tension failure of a reinforced concrete beam. That cracking usually develops from initial cracks generated by fracture along the tension edge of the beam. Those initial cracks propagate perpendicularly from the edge of the beam and kink only after extending beyond the reinforcement. Since aggregate interlock exits in these crack prior to kinking, the kinking angle as well as subsequent crack extension may be influenced by the interface shear forces.

The purpose of this study was to quantify interlocking as well as bridging forces in plain concrete beam specimens under such offset loading conditions.

EXPERIMENTAL PROCEDURE

Specimen

Two three-point bend specimens, were made using a steel mold and a high early strength Portland cement, an aggregate of 6.4 mm maximum size and a local Seattle sand. The concrete strength at the time of the test, as determined from cylinder tests, was 48 MPa. A notch of 0.3 mm width and 19 mm depth machined in the bottom of the specimen and an initial crack of about 13 mm depth was extended from that notch by Mode I loading. Mixed mode loading was then applied by rearranging the loading points so that the notch was offset from the central loading point.

Moire Interferometry

A four beam moire interferometer [1] was used to record sequentially the vertical and horizontal displacements [2] surrounding the extending crack with a motorized Nikon camera. An orthogonal moire grating of 600 lines/mm with a fringe multiplication of two provided the two displacement fields from which the crack opening and crack sliding displacements (COD and CSD) were computed.

NUMERICAL ANALYSIS

A hybrid experimental-numerical procedure was used to compute the fracture parameters. The entire specimen had to be modelled for this mixed mode fracture analysis. Since the boundary conditions were completely prescribed by the experimental data, the solution to this finite element boundary value problem should have provided the sought answers directly as in [3]. In practice, however, the solution was erratic, possibly due to its sensitivity to the minute variations in displacements along the crack Thus the better conditioned but time consuming inverse procedure [4] was used in this study.

The numerical procedure was to find the crack closing stress (CCS) versus crack opening displacement (COD) and the crack shearing stress (CSS) versus crack sliding displacement (CSD) relations which, together with the applied load, provided the COD's and CSD's which coincided with their measured counterpart during kinked crack extension. The sum of the work done by the CCS acting on the COD and the CSS acting on the CSD for unit crack extension represents the energy dissipation rate in the fracture process zone (FPZ). The energy release rate was computed directly by incrementing the crack tip one finite element node and computing the difference in elastic energies stored in the specimen prior to and after incremental crack extension.

The modes I and II stress intensity factors, K_I and K_{II}, were computed directly from the COD and CSD. First the finite element model was numerically calibrated for accurate stress intensity factor determination by using known K_I and K_{II} solutions. Then the K_I and K_{II} for a beam with an offset three point bend load but without the CCS and CSS prescribed on the FPZ were determined. A superposition of the K_I and K_{II} of an unloaded beam with the prescribed CCS and CSS on the FPZ comprised the sought mixed mode stress intensity factors.

RESULTS

Experimental Results

Figure 1 shows the measured load versus computed load-line displacement relations for the mixed mode loading of one of the specimen. The load-line displacement, which was measured on one side of the specimen (the side without the moire grating), did not provide accurate results due to uneven local crushing at the load point and thus the computed load-line was used in this figure.

Figure 2 shows a typical pair of moire interferometry patterns corresponding to the orthogonal displacement fields of u_x and u_y of a kinked crack in a three point bend specimen.

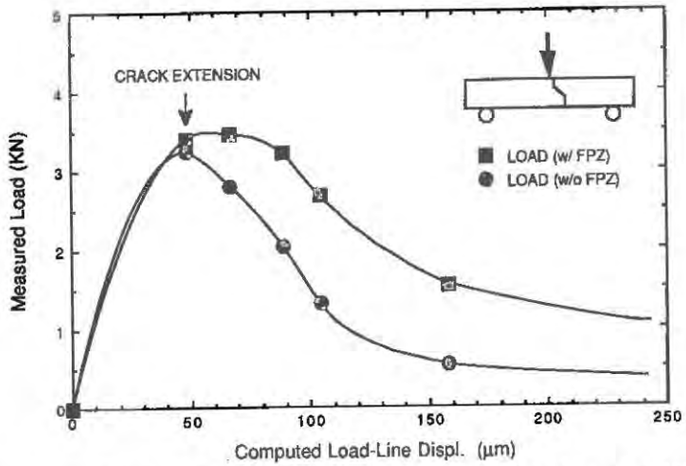

Figure 1. Averaged load and displacement variations with kinked crack extension.

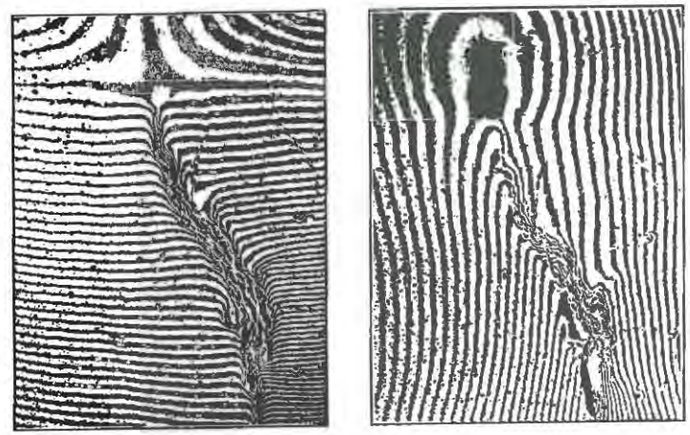

Figure 2. Typical x- and y-moire patterns.

Figure 3 is a composite figure. It shows the COD and CSD variations along the initial and kinked crack for increasing crack extensions expressed in terms of the total crack length. The curves are the displacements obtained from moire interferometry and the data points are computed results. The CSD along the kinked portion of the crack are negligible. On the other hand, the CSD's along the initial precrack and the first kinked portion of the crack after the second kinking are constant, thus indicating rigid body slidings along the initial and the first portion of the twice kinked crack.

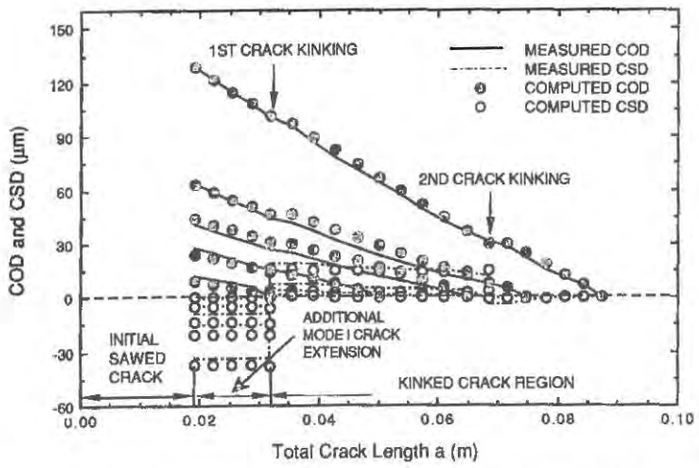

Figure 3. Measured and computed crack opening (COD) and sliding (CSD) displacements.

Numerical Results

The inverse analysis provided good matches between the measured and computed COD and CSD as shown by the curves and the data points, respectively in Figure 3. Figure 4 shows the CCS versus COD and the CSS versus CSD relations which provided the best fit between measured and computed COD's and CSD's. The CCS versus COD relation of Figure 4 shows a crack closing stress, i.e. the crack bridging forces, of approximately forty percent larger than that derived previously for pure mode I crack opening [3]. Probably that increase is due to the additional frictional forces generated by the interlocking forces.

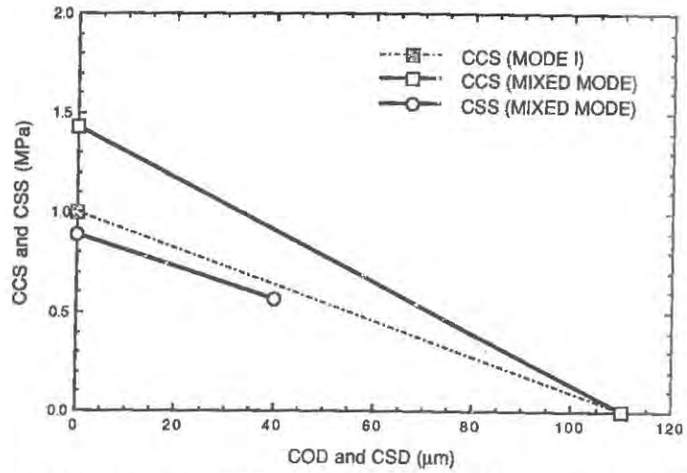

Figure 4. Crack closing stress (CCS) versus COD and crack shearing stress (CSS) versus CSD relations

The mode II CSD versus CSS relation, which is far from complete due the short FPZ in a three-point bend specimen, shows that the interlocking forces generated a shearing stress approximately sixty-five percent of the mode I crack closing stress for the same crack displacement.

Figure 5 shows the variations in mode I and II stress intensity factors, K_I and K_{II}, with crack extension. K_I increases with crack extension whereas K_{II} remained essentially zero.

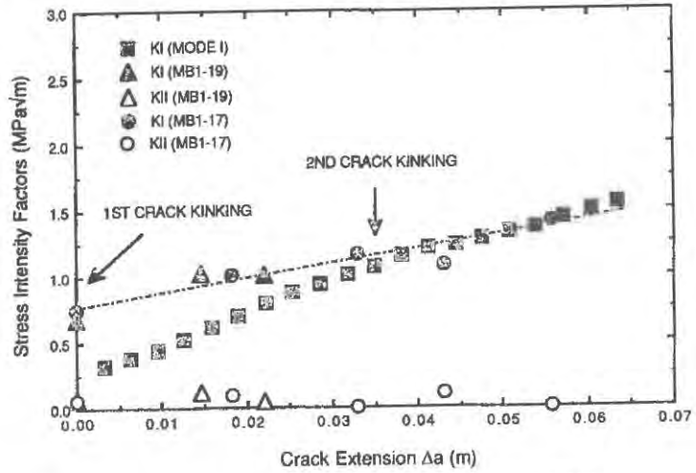

Figure 5. Variations in stress intensity factors with crack extension.

Figure 6 shows the energy release and dissipation rates with crack extension. This energy dissipation rate relates only to the FPZ and does not include other energy sinks, such as micro-cracking ahead of the crack tip, crushing at the load and support points and aggregate-mortar debonding.

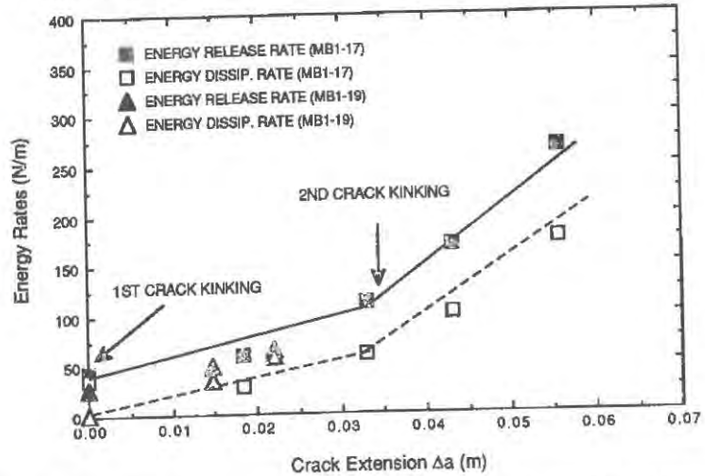

Figure 6. Energy rates in three-point bend specimen with doubly kinked crack.

The energy release rate represents the resistance curve for this mixed mode fracture process. This energy dissipation rate should have remained constant during subsequent crack extension after the FPZ was fully developed, Figure 6 shows that this was not the case.

DISCUSSIONS

The practical significance of the FPZ is illustrated by the second load curve "without FPZ" in Figure 1. This load was computed by applying the computed load-line displacement to the specimen and the FPZ. This figure shows that the FPZ enhances the load carrying capacity of the concrete specimen in the strain softening region.

CONCLUSIONS

1. Constitutive relations for crack bridging and interlocking forces for a off-set three-point bend concrete specimens were obtained.

2. The dominant energy dissipation mechanism in concrete fracture is crack bridging and interlocking in the fracture process zone without which the load carrying capacity in the strain softening region is reduced.

ACKNOWLEDGEMENT

This research was supported by the US Air Force Office of Scientific Research grant AFOSR-91-0218. The authors wish to thank Dr. Spencer Wu, AFOSR for his continuing support and encouragement during the course of this investigation.

REFERENCES

1. Post, D, Moire interferometry. Handbook on Experimental Mechanics, ed. A.S. Kobayashi, Prentice-Hall, Inc., 1987, 314-387.

2. Dadkhah, M.S., Wang, F.X. and Kobayashi, A.S., Simultaneous on-line measurement of orthogonal displacement field by moire interferometry. Experimental Technique, vol. 12, 28-30, 1988.

3. Guo, Z.K., Yon, J.-H., Hawkins, N.M. and Kobayashi, A.S., Fracture energy dissipation mechanism of concrete. To be published in Fracture Mechanics, 23rd Symposium, ASTM.

4. Yon, J.-H., Hawkins, N.M. and Kobayashi, A.S., Fracture process zone in dynamically loaded CLWL-DCB specimens. To be published in ACI Materials Journal.

A STUDY OF THE MIXED MODE FRACTURE USING DISK SPECIMEN

by A. Castro-Montero[1], Z. Jia[2] and S.P. Shah[3]

Center notched diametrically loaded disc specimens (Brazilian Test) were used to investigate the mixed mode fracture process zone in mortar. Three dimensional displacement fields were measured using a multiple sensitivity vector holographic arrangement. The specimens were tested in a closed loop testing system with a feedback controller designed to satisfy interferometric stability requirements. Image analysis techniques were used for enhancement and evaluation of the holographic images.

The size of the fracture process zone was determined based on the difference between experimentally measured and linear elastic fracture mechanics strain fields. The size of the fracture process zone obtained by this method was found to be dependent on the fracture mode.

A relationship was observed between the strain distribution prior to crack initiation and the crack initiation location and propagation sequence. Also, comparison with strain field measurements on Mode I fracture process zone showed that there is a relationship between the level of strain prior to crack initiation and the state of stress (e.g. uniaxial, biaxial)

Introduction

Linear elastic fracture mechanics (LEFM) has been used to model quasi-brittle behavior of cement-based materials. Indirect methods such as the multicutting technique[1] and experimental observations using acoustic emission[2] and holographic interferometry[3] have demonstrated that there is tensile stress transfer between the crack faces. Cohesive crack models and otherwise conventional LEFM have been used to model Mode I fracture in concrete[4,5,6].

Since Mode I tests can be conducted easily in laboratories compare to other fracture modes, cohesive model and other several methods have been proposed to characterize Mode I crack propagation in concrete[7,8,9]. However, many structural applications behave under mixed-mode loading conditions. It is necessary to verify if an extension of the Mode I model can be applied in the cases where both tensile and shear forces associated with crack opening and sliding are transfered through the crack faces. The objective of this study was to measure the strain distribution in the fracture process zone in mixed mode specimens in order to provide the information required to develop a cohesive crack model similar to those for Mode I.

1 Assistant Professor of Civil and Environmental Engineering, University of Houston, Houston, TX.
2 Graduate Research Assistant, Northwestern University, Evanston, IL.
3 Director, NSF-Center for Advanced Cement-Based Materials, Professor of Civil Engineering, Northwestern University, Evanston, IL.

Experimental Program

Center notched disk specimens were loaded in the Brazilian test configuration (diametral compression) using a 120 Kip capacity loading frame. The fracture mode can be changed by rotating the notch inclination angle with respect to the loading direction[10].

Applied load, load-point displacement and diametrical displacement were measured during testing. A cylindrical load cell was designed for accurate load measurement and holographic stability. The load point displacement was measured using a dual LVDT transducer and a modified MTS clip gage Model 632.02B.20 transducer was used to measure diametral displacement perpendicular to the loading direction (DD). A linear combination of the load and DD was used as the control signal for closed loop testing.

A three sensitivity vector holographic arrangement was used to measure three dimensional displacement fields. Digital image processing techniques were used for the evaluation of interferograms and the sensitivity vector linear approximation was used for the computation of displacements[11].

Specimens were tested with five notch inclination angles (β=0°, 18°, 36°, 54° and 72°), but it was not possible to make holographic recordings for β = 36° during crack propagation due to the brittleness of the response. After the control signal reached the range limit, loading was continued under stroke control up to collapse, in order to obtain the final failure mode (Figure 1).

Strain Fields (β=0°)

Figure 2 shows the load-DD curve. In this plot, the stars correspond to holographic recordings. Stable crack growth occured between Holograms 7 and 10 (2105 lb and 2429 lb resp.). The first macroscopic evidence of nonlinearity (in the load-DD curve) is after Hologram 10 when the crack has already propagated through the specimen.

Figure 3 shows the measured strain distribution at three loading levels corresponding to elastic or pre-cracking state (Hologram 3), crack initiation stage (Hologram 7) and failure stage (Hologram 10). In this figure, the bold line represents the crack extension. The strain concentration around the notch tips starts to be evident in the strain distribution corresponding to Hologram 3. At the crack initiation stage (Hologram 7), the strain distribution around both the top notch tip and the bottom crack tip are similar because a crack is just about to initiate at the top notch tip (verified in Hologram 8; not shown). The crack propagation trajectory can be approximately predicted from the same strain distribution (Hologram 7). Strain around the top notch tip are slightly higher on the left side while the strain distribution around the bottom crack tip is symmetric. In fact, the same trends begin to appear during the elastic stage at load levels less than 50% of the crack initiation stage.

The strain distribution prior to failure (Hologram 10) shows that the crack growth corresponds to the strain distribution at earlier loading stages. Even though the size of the

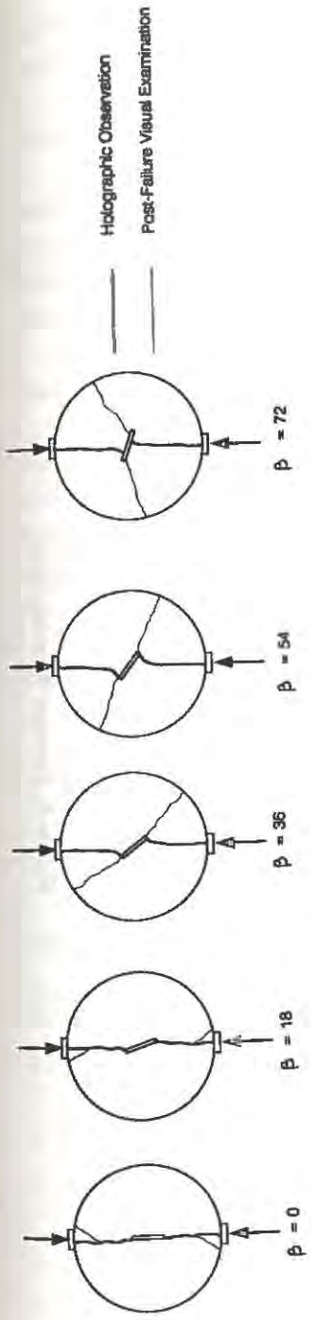

Figure 1. Failure Mode.

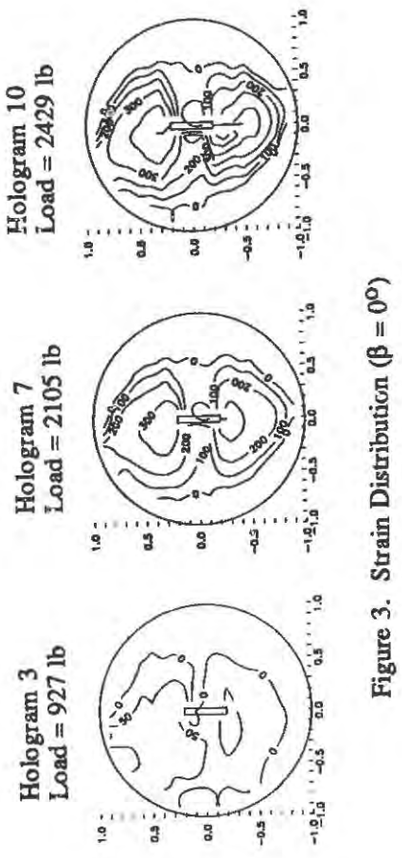

Figure 3. Strain Distribution (β = 0°)

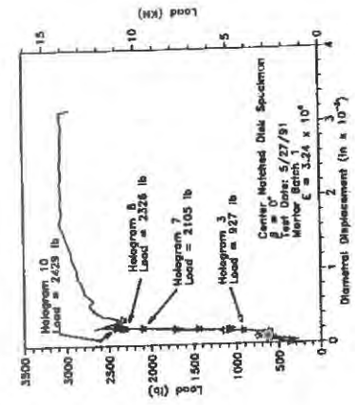

Figure 2. Load-DD Curve (β = 0°)

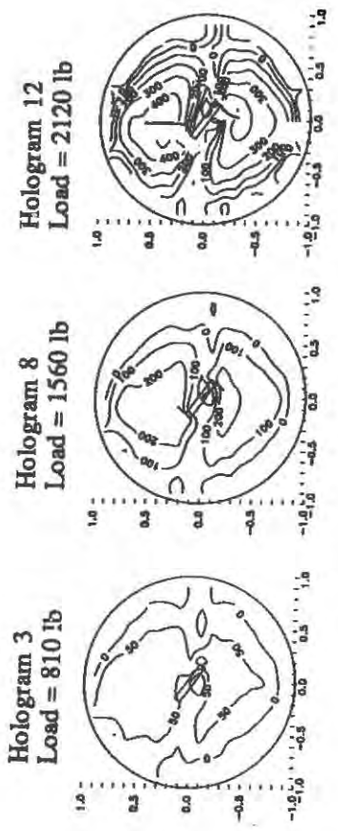

Figure 5. Strain Distribution ($\beta = 54^o$)

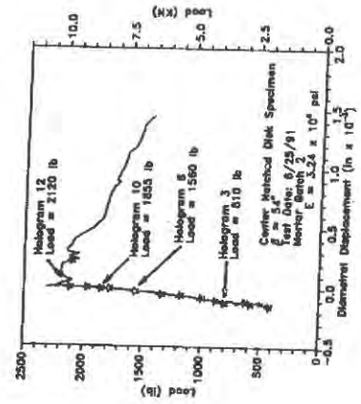

Figure 4. Load-DD Curve ($\beta = 54^o$)

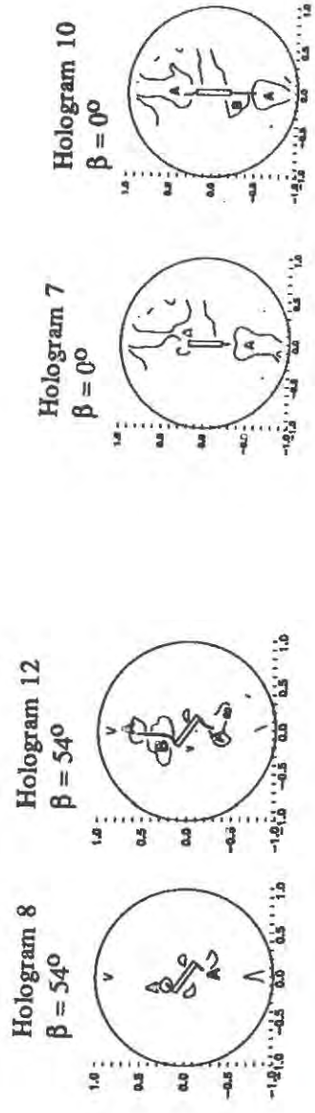

Figure 6. Fracture Process Zone.

specimen limits the size of stable crack growth, from the same strain distribution it can be concluded that there is stress transfer between the crack faces.

Strain Fields (β=54°)

Figure 4 shows the load-DD curve and Figure 5 shows the strain distribution in the elastic, crack initiation and failure stage (Holograms 3,8 and 12 respectively). Even though the shape of the load-DD curve changed due to the change in fracture mode, there is no apparent difference in the strain distributions. Consistently higher strain levels on the top half of the specimen can be related to the failure sequence shown in Hologram 12.

Fracture Process Zone

The fracture process zone (FPZ) was defined as the zone of deviation from linearity exceeding 60 $\mu\varepsilon$[12] (note that ε_{xx} was used). Figure 6 shows a comparison of the FPZ at crack initiation and failure stages for β=0° and β=54°. The size of the FPZ in Mixed Mode is smaller than that in Mode I for short crack lengths. For longer crack lengths, after the crack adopted a straight line trajectory, the FPZ in the Mixed Mode specimen approaches the dimension of the FPZ in Mode I.

Conclusions

1. Crack initiation occurs at less than 70% of the ultimate load for both failure modes. However, the failure mode seem to affect the post peak response.
2. Examination of the strain distribution at early loading stages can give an indication of the crack growth sequence.
3. The size of the FPZ defined as a function of the tensile strain distribution can give an indication of the fracture mode.

Acknowledgement

This study was made possible through the support of the Air Force Science and Engineering Center (Contract No. F08635-89-C-0182), Program Manager Dr. Allen Ross and the NSF Center for Advanced Cement-Based Materials.

References.

1. Hu, X.Z. and Wittmann, F.H. (1990) "An Experimental Method to Determine the Extension of the Fracture Process Zone," ASCE J. Mats. and Engineering.
2. Maji, A.K. and Shah, S.P. (1988) "Process Zone and Acoustic Emission Measurements in Concrete," Experimental Mechanics.
3. Miller, R.A., Castro-Montero, A. and Shah, S.P. (1991) "Cohesive Crack Models for Cement Mortar Examined Using Finite-Element Analysis and Laser Holographic Measurements," J. of the American. Ceramic Soc.
4. Cook. R.F., Fairbanks, C.J., Lawn, B.R. and Mai. Y-W (1987) "Crack Resistance by Interfacial Bridging: Its Role in Determining Strength Characteristics," J. of Mat. Res.
5. Cedolin, L., DeiPoli, S. and Iori, I. (1987) "Tensile Behavior of Concrete," ASCE J. of Engg. Mech.

6. Roelfstra, P.E. and Wttmann, F.H. (1986) "A Numerical Method to Link Strain Softening to Failure of Concrete," Fracture Toughness and Fracture Energy of Concrete, F.H. Wittmann, Ed.
7. Bazant, Z.P. and Oh, B.H. (1983) "Crack Band Theory for Fracture of Concrete," Materials and Structures.
8. Hillerborg, A., Modeer, M. and Petersson, P.E. (1977) "Analysis of Crack Formation and Crack Growth in Concrete by Means of Fracture Mechanics and Finite Elements," Cement and Concrete Research.
9. Jenq, Y.S. and Shah, S.P. (1985) "A Two Parameter Fracture Model for Concrete," ASCE J. of Engg. Mech.
10. Atkinson,C., Smesler, R.E. and Sanchez J. (1982) "Combined Mode Fracture Via the Cracked Brazilian Disk," Int. J. of Fracture.
11. Castro-Montero, A. (1991) Mixed-Mode Fracture of Concrete at High Strain Rates," PhD Dissertation, Northwestern University.
12. Castro-Montero, A, Shah, S.P. and Miller, R.A. (1990) "Strain Field Measurement in Fracture Process Zone," ASCE J. of Engg. Mech.

POST-PUNCHING BEHAVIOUR OF A WAFFLE FLAT SLAB FLOOR

GUILHERME S.S.A. MELO
PUC/Rio - Civil Engineering Department
Rua Marques de São Vicente 225, Gávea
22 453 - Rio de Janeiro - BRAZIL

PAUL E. REGAN
Polytechnic of Central London
Civil Engineering Department
35 Marylebone Road - London NW1 5LS - ENGLAND

ABSTRACT

In order to investigate the post-punching behaviour of a complete floor and its relation to progressive collapse, four tests were made on a sixteen column and nine panels (5.75 x 5.75 m overall) waffle flat slab floor already tested until ultimate load. It was quite clear from the tests that horizontal spreading of failure after punching is a real possibility in flat slabs and that the post punching resistance of an internal connection in the absence of bottom bars through the column is very low. This work was part of a research on the post punching resistance of flat slabs after local failure at the Polytechnic of Central London [1] where besides the four tests described in this paper eight quarter scale (75 mm thick) solid slab specimens, twelve large scale (150 mm thick) specimens and four real size column models (300 x 300 mm) were tested to study the post-punching behaviour of a floor system.

INTRODUCTION

Progressive collapse is defined as a chain reaction or propagation of failure, following damage to a relatively small portion of a structure, in which the resulting damage is characteristically out of proportion to the damage which initiated the collapse. It achieved world prominence when a corner of the Ronan Point apartment block collapsed in London in 1968 [2]. A 16-storey apartment building that collapsed in 1971 in Boston [3] and a planned 26 storeys structure that collapsed during the casting of the 24th floor in Virginia in 1973 [4] are examples of progressive collapse in flat slab structures.

The need to minimize the risk of progressive collapse applies to most structures but some types of construction require more attention than others. Many normal types of construction already have hidden resistance against progressive collapse. Most monolithic concrete frames and continuous steel frame constructions with infill panels are examples.

The codes have inserted requirements that the layout of the structural system and interaction between structural members should normally ensure a robust and stable design with sufficient redundancy and that the structure should possess a satisfactory level of structural integrity in the event of an accident [5]. The provisions in the codes are fundamentally based on precast structures (the requirements concentrate on tying, etc.) and seem quite appropriate for this purpose.

For flat slabs, only the Canadian Code CAN3-A23.3 [6] has so far inserted provisions that are based on actual behaviour. These requirements of the Canadian Code are derived from works at McGill University in Montreal [7].

Irrespective of the initial causes of the failures, excessive loading during or just after casting, early dismounting of the propping, wrong positioning of the top reinforcement, the presence of holes in the slab or the utilization of low quality materials are some possible causes of a punching failure that can lead to a generalized collapse.

Given that the initial failure in a flat slab building is likely to be by punching at a slab/column connection, the post punching behaviour of such connections is likely to be important in determining the progress (or otherwise) of a collapse. If little or no load can continue to be transmitted by the failed connection, the slab spans in both directions will be doubled and the loads and moments applied to the surrounding connections will be greatly increased and likely to cause further failures.

TEST RESULTS

Four tests (PSP1 to PSP4) were made on a waffle flat slab floor to investigate the post-punching behaviour of a complete slab. The floor was designed and tested by LUCIO [8] at the PCL laboratory, with sixteen columns and nine slab panels (5,75 x 5,75 m overall) designed in accordance with BS 8110 [9] to study the behaviour of this kind of structure under vertical and horizontal loading. Some details of the structure and reinforcement are shown in Figures 1 and 2. Loading was applied by 9 jacks at 16 points per panel to simulate a uniform distribution. The loading points are shown in Figure 1 (left). It is noteworthy that there were no bottom bars passing through any of the interior columns. At the edges there were bars through the columns at the South and East sides (section AA' in Figure 2) but not at the North and West (section BB' in Figure 2).

Among more than thirty tests made by LUCIO, three were "Ultimate Load Tests" (ULT1 to ULT3) that in the end left the slab punched around columns 6, 8, 9 and 10. As the waffle flat slab was lightly reinforced almost all reinforcement had yielded before the punching of the slab. Tests ULT1 and PSP1 to PSP3 are now described;

Ultimate load test 1 (ULT1)

Uniformly distributed vertical loading was applied in steps on all the slab as shown in Figure 3 (left). Up to the step immediately prior to failure vertical reactions for all the columns were measured for each step by load cells located under each column. Typical panel load versus column reaction graphs for an internal (column 10), an edge (column 9), and a corner (column 13) column are shown in Figure 3 (right).

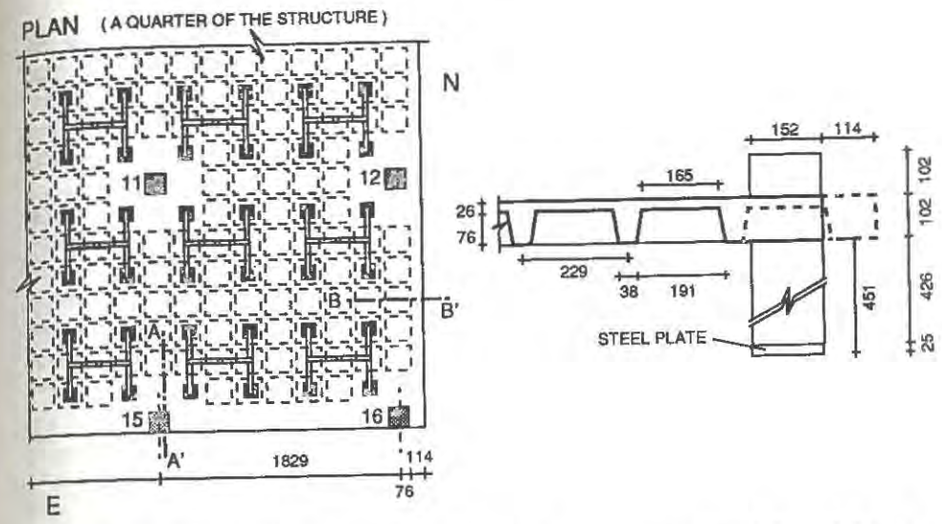

Figure 1. Dimensions of the waffle flat slab and loading system details (left) and detail of the waffle flat slab (right)

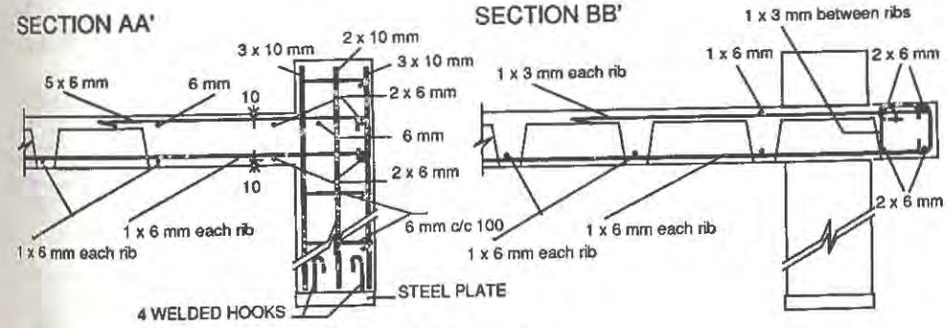

Figure 2. Details of the connections reinforcement

At a load of 80 kN per panel (23.9 kN/m^2), column 10 and then column 9 punched through the slab (Figure 3 left) and the test was stopped. This is a quite good example of horizontal spreading of failure in a flat slab. As column 10 could only sustain a reduced load after failure, the slab around column 9 failed as well.

Post-punching test 1 (PSP1)

The four panels around column 6 were loaded (Figure 4 left) with the purpose of studying the behaviour of this part of the structure after the internal column had failed. As the line between columns 9 and 11 was quite damaged due to the previous tests this was properly propped. Vertical reactions were recorded at columns 1 to 3 and 5 to 7.

The load was applied in steps until the system could not sustain any more load. The maximum load reached was 70 kN per panel (20.9 kN/m^2) and the column 6 reaction was

21.8 kN - 24.9 % of the maximum reaction obtained in LUCIO's ULT3 test for this column - (see Figure 4 right). The slab around column 5 failed at this stage and, even though it seemed that this column connection could sustain more load, the test was discontinued due to much degradation of the slab around column 6. As this connection had only top reinforcement going through the column and the bars were not continuous this was the behaviour expected (reaching a maximum of a quarter of the previous load).

Graph for column 5 is shown in Figure 5 (right). It can be seen that after the reaction reached it's maximum and the connection failed (note point 4 in the PSP1 graph) with an immediate loss of resistance there was a later increase in the reaction (note the points 6, 7 and 8). This increase in the reaction even after failure of the slab was possible due to the presence of continuous top and bottom bars in this particular connection (see reinforcement details on Figure 2 - section AA'). As it seemed that column 5 could sustain more load a second test was then made loading only the panels adjacent to it - see test PSP2 below.

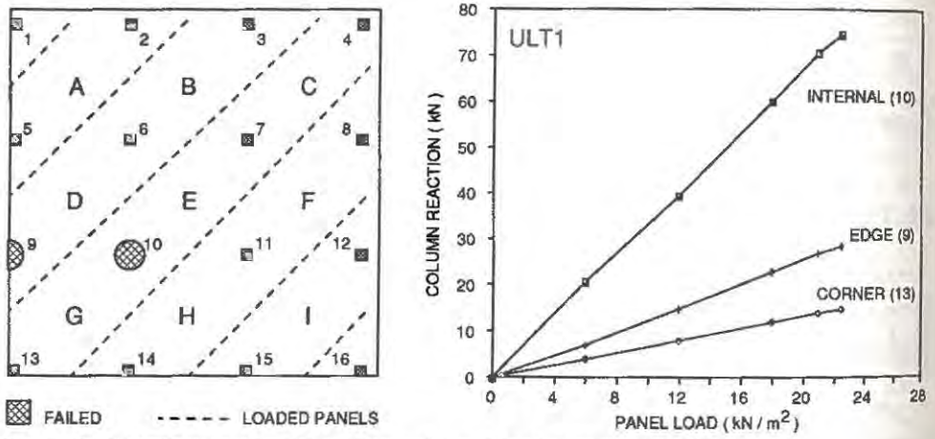

Figure 3. LUCIO's test ULT1 and typical panel load v column reactions

Post-punching test 2 (PSP2)

For this test panels A and D were loaded (Figure 5). In addition to the line between columns 9 and 11, the region around column 6 was propped. As can be seen from Figure 5 (right), the connection in this test was capable of sustaining more load (30.6/28.4 = 1.08) than it had sustained up to punching (PSP1 test) because of the continuous top and bottom bars through the column present there (see section AA' in Figure 2). It went on until the bottom bar through the column broke and the system could not sustain any more load. It is remarkable that the connection resisted more load than it had resisted before failure by punching.

As columns 1 and 2 were relatively undamaged at this point, a third test was carried out applying load around these columns.

Post-punching test 3 (PSP3)

Panels A and B were loaded and the line between columns 5 and 6 was propped due to the previous failures. At a load of 85 kN per panel (25.4 kN/m^2) column 2 punched the slab and the test was stopped because there was no connection at all between the column and the slab and it was just going down all the way (Note the reinforcement detail on

Figure 2 - section BB'). This differs significantly from the situation of column 5 (Reinforcement detail in section AA' - Figure 2) in test PSP2. At column 2 the peripheral top and bottom bars that made the connection and resisted the load at column 5 were away from the column and in the overhang of the slab.

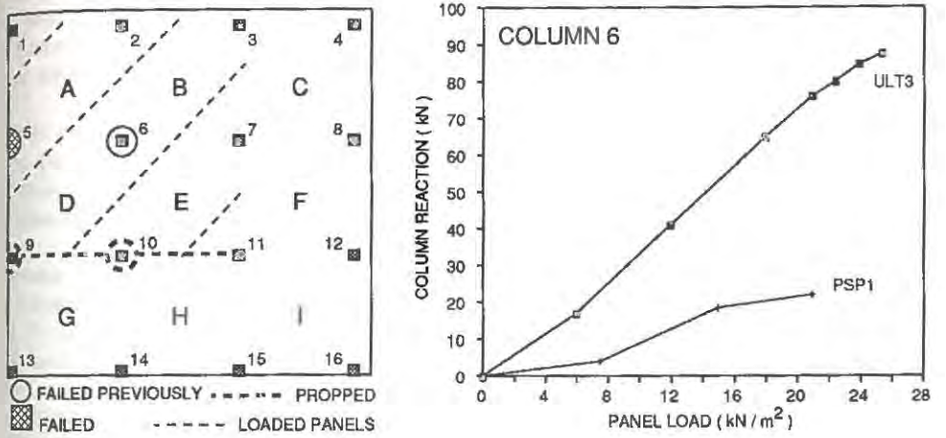

Figure 4. Post-punching test 1 (PSP1) and panel load v column reaction - Column 6 -

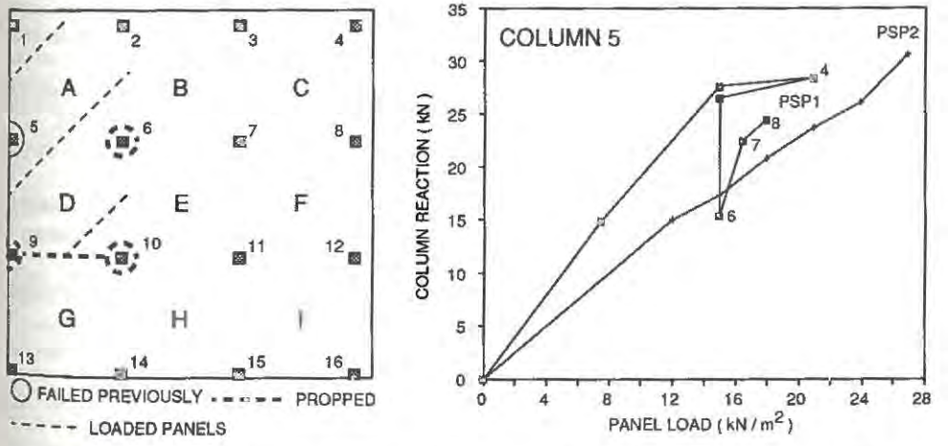

Figure 5. Post-punching test 2 (PSP2) and panel load v column reaction - Column 5 -

CONCLUSIONS

It was quite clear from tests ULT1, PSP1 and PSP4 that horizontal spreading of failure after punching is a real possibility in flat slabs. After a punching failure top bars are easily pulled out of the slab and provide little resistance. After shear failure has occurred the top

reinforcement "rips-out" of the top surface of the slab and becomes ineffective in carrying the load [7 and 10]. Deeply embedded bottom bars passing through the columns and anchored in the slab however, provide significant resistance initially by dowel action, and then at larger deformation by being kinked. Bottom bars do not seem to increase the initial punching strength but are a very effective measure to lessen the loss of capacity at a connection and could significantly reduce the demands on the rest of the slab and its supports in the event of a punching failure. Besides this they are very easy to install if compared with shear reinforcement that could be another alternative to improve the post punching behaviour of the connection.

Unless they are positioned continuously through the column at the bottom of the slab, the presence of ties (according to BS 8110 [9]) is not enough to guarantee any post punching resistance of a connection in a flat slab and consequently provide resistance to progressive collapse. This can be seen from the behaviour of the column 2 connection in test PSP3.

Apart from the above described experimental work a finite element elastic analysis was performed to make comparisons with the tests and to study the effect of the partial or total loss of a column on the behaviour of the remaining slab, a flexural resistance of the slab following the partial loss of support at a column was verified by the yield line method and possible damage scenarios of failure of slab-columns connections were considered and design recommendations were proposed [1, 11 and 12].

REFERENCES

1. MELO, G.S.S.A., "Behaviour of reinforced concrete flat slabs after local failure", Ph.D. Thesis, Polytechnic of Central London, 1990.
2. GRIFFITHS, H., PUGSLEY, A., SAUNDERS, O., "Report of the inquiry into the collapse of flats at Ronan Point,", Her Majesty's Stationery Office, 1968, pp. 71.
3. LITLE, W.A. (1975), "The Boston collapse at 2000 Commonwealth Avenue", Symposium on Progressive Collapse, ACI Annual Convention, April, Boston.
4. LEYENDECKER, E.V., FATTAL, S.G., "Investigation of the Skyline Plaza collapse in Fairfax County, Virginia", Building Science Series N. 94, National Bureau of Standards, Washington, D.C., February, 1977, 91 pp.
5. FIP on Prefabrication, "Ductility of tie connections for concrete components in precast structures", Technical Report, Fed. Int. Precontrainte, England, 1982, pp. 40.
6. CAN3-A23.3-84, "Design of concrete structures for buildings", Canadian Standards Association, 1984.
7. MITCHELL, D., COOK, W. (1984), "Preventing progressive collapse of slab structures", Journal of Struct. Eng., ASCE, V. 110, N. 7, July, pp. 1513-1531.
8. LUCIO, V.J.G., "Investigation of waffle slab structures under vertical and horizontal loading", Ph.D. Thesis, Superior Technical Institute, Lisbon, (to be published).
9. BS 8110, "The structural use of concrete", British Standard Institution, Part I, London, 1985.
10. REGAN, P.E. (1981), "Behaviour of reinforced concrete flat slabs", CIRIA Report 89, London, pp. 89.
11. MELO, G.S.S.A., REGAN, P.E., "Exper. study post-punching resistance of flat slab / column connections", XXV Sth. Ame. J. Str. Eng., Brazil, 1991, Vol. III, pp. 319-342.
12. MELO, G.S.S.A. e REGAN, P.E., "Post punching resistance of connections between flat slabs and interior columns", 1992, (under preparation)

MACROSCOPIC STUDY OF CRACK FACE BRIDGING PHENOMENON IN MIXED - MODE LOADING

J. DAVIES
The Department of Civil Engineering and Building,
The Polytechnic of Wales,
Pontypridd CF37 1DL, UK

ABSTRACT

Mixed-mode I and II loading is a combination of tensile and in-plane shear loading. Investigation showed that crack evolution in this mixed mode is more complex than that in tension. It was observed that discontinuous cracks were initiated at several locations in the ligament and the growth consisted of partly tensile splitting and also shearing cracks. The crack face bridges were observed between two overlapping crack tips. In some cases initial tensile cracks closed during the shearing process, this phenomenon suggested that compressive struts developed in the specimen. This very complex tensile/shearing crack interaction was found in most of the tested specimens.

INTRODUCTION

The understanding of cracking process in cementitious materials is improving very rapidly with the advances made in both computational and experimental mechanics. Large number of test geometries have been used to study fracture mechanisms when subjected to tensile loads (Mode I type of failure) and it was generally accepted that tensile cracks propagate in the direction perpendicular to maximum tension. Tensile failure is usually due to one main crack extending throughout the ligament and may be accompanied by other secondary branching cracks or microcracks accumulated around the crack tip. This region has been defined as the fracture process zone.

One of the major problems in the study of the fracture process zone is the difficulty in observing it directly and on the basis of available observations to determine what failure mechanisms have actually taken place. Various techniques e.g. microscopy, interferometric techniques or acoustic emissions, have been used to investigate the early development of the

microcracked zone and the start of the main crack path.

Understanding of the initiation of microcracking and the point at which the main crack path begins to form is essential if the results of laboratory tests are to be meaningfully applied in subsequent modelling and design criteria for concrete structures.

MATERIALS AND METHODS

This contribution deals with the development of the fracture process zone in mortar and badly compacted concrete specimens having various geometries. The testing machine used throughout the investigation was a closed-loop servo controlled stiff testing machine, Instron 8582. All tests were carried out in a displacement controlled mode at the speed of 0.003mm/sec and at the room temperature of about 21 C. Samples were positioned in a testing rig and a video recording of every test has been made using a fast zoom video camera with the shutter speed 500 -1000 frames/sec. The experiments were viewed with the aid of a MERLYN - X vision mixer with effects enabling us to split a fracture process into frames 1/25 seconds apart. The frames were frozen and then photographed from the television screen using a PENTAX P30N still camera.

The specimens were made of mortar and badly compacted concrete containing an excessive amount of voids. The reason behind this experiment was to observe how the fracture process zone would form if an excessive amount of voids were present in the concrete matrix. The geometry of test specimens is shown in Figure 1.

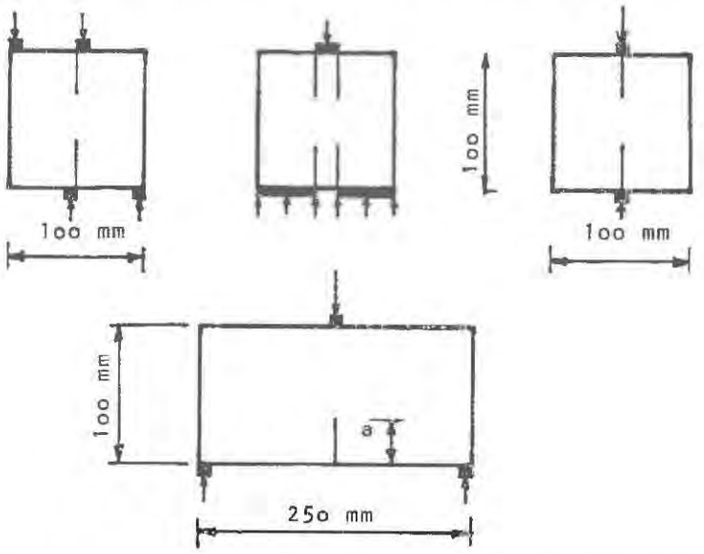

Figure 1. The geometry of specimens used in experiments

We have also studied the effect of friction,between the platens and punch - through shear specimen, on the basic characteristics of fracture process zone. One set of tests was carried out with a slight lateral restraint and without any agent preventing the friction between the platens and specimen. The other set was carried out without the lateral restraint and with a graphite agent applied on the contact surfaces to minimize the friction.

RESULTS

The photographs in Figure 2 and 3 show a typical set of results obtained from these tests. The basic characteristic of fracture process zone in specimens with the restraint and friction, Figure 2, was the formation of a superficial tensile crack, followed by the formation of multiple discontinuous fissures between the slots. The main crack faces overlapped and were joined by compressive struts at several places. The initial tensile crack either closed partly or completely during the subsequent fracture process. The final fracture was a narrow crush zone with the clear signs of the abrasive action on the internal surfaces of the specimen.

Figure 3 shows a typical set of the results obtained from specimens made of badly compacted concrete and with the minimum friction between the specimen and platens. The first stage of cracking process seemed to be very similar to that previously described, but the subsequent crack extension and propagation showed a completely different characteristic. Multiple discontinuous cracks overlapped and opened with the increasing load and the crack interface bridges could be clearly seen. The compressive struts or signs of crushing during the load descend, the characteristic feature of the restrained specimen, were not detected. Instead of that only the crack opening has been observed, indicating that Mode I was predominant in this case. This experiment clearly indicated that the boundary conditions would significantly affect the fundamental characteristic of the fracture mechanism.

Experiments on punch through shear cubes indicated that the first hairline tensile cracks appeared at about 40% of the maximum load and the full formation of the fracture process zone was observed at about 78 - 85% of the maximum load. It was interesting to see that specimens made of badly compacted concrete, and with the same boundary conditions, exhibited almost identical behaviour regarding the appearance of the first tensile crack and the full fracture process zone. The maximum load was, however, considerably lower as expected.

Figure 4 shows a formation of fracture process zone in a cube subjected to direct compression. The failure mechanism in this case is due to indirect tension (splitting). It can be seen from the photographs that the initial discontinuous cracks open during the loading process and finally the tips curve towards the adjacent crack producing a final fracture. This failure mechanism is very brittle and there is no reserve in the load carrying capacity after the first crack appearance.

Figure 2. Formation of crack face bridges and compression struts in punch through shear specimen

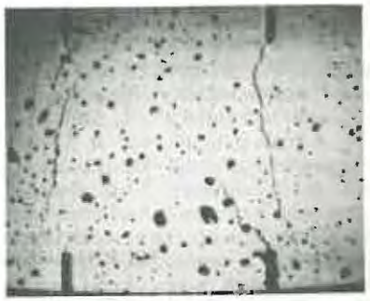

Figure 3. Fracture processes in badly compacted concrete with minimized friction at contact surfaces

Figure 5 is a photograph of a final failure pattern for a cube subjected to a concentrated shear force in the ligament. Figure 6 shows a crack pattern obtained in the beam subjected to three point bending. The principal characteristic of a tensile fracture is a formation of one single crack originating from a series of discontinuous fissures, and the characteristic of a mixed mode fracture with the Mode II predominant is a formation of a narrow crush zone originating from a series of discontinuous fissures which are jointed by compressive struts.

Figure 4. Double notch split cube ... fracture process

Figure 5. Double notch shear cube

Figure 6. Crack development in 3-pt bending beam

CONCLUSIONS

The experiments described in this investigation were aimed to highlight the differences in the formation of the fracture path when tensile and mixed mode loading is applied to the specimen. The crack face bridging phenomenon as observed by vanMier [1,2] was noted in all experiments carried out on punch-through shear cubes, split cubes, shear cubes and three point bending beams. It can be said therefore that the first phase of crack formation,ie. the set of discontinuous fissures occurring between the slots, seems to be identical irrespective of the type of loading or geometry of the specimen. The size of crack face bridges, however, seemed to depend on the type of loading. The larger size and more numerous were observed in specimens subjected to mainly Mode II (punch-through shear cube, shear cube).

The difference in the fracture mechanisms seems to be during the second phase of cracking process, ie. during the formation of the full fracture zone. It was observed that when Mode II is predominant the failure of crack face bridges is largely due to the crushing of intact ligaments between two overlapping crack tips [3]. A similar observation was reported by Bazant et al [4] when testing beams in shear. The crack face bridges failure in specimens subjected to predominantly Mode I loading seems to be due to extension of one of the crack tips and producing a single continuous crack. Further work is in progress to establish whether the size of the specimens and strain rate will have any influence on the fracture process.

ACKNOWLEDGMENT

The author wishes to express her gratitude to the members of the Media Resources Department, namely Viv Cole, John Thomas and Malcom Coundley for their infinite patience during the production of still photographs. The efforts of Mr. Pg Backar are also gratefully acknowledged.

REFERENCES

1. Vonk,R.A.,van Mier,J.G.M. and Fijneman,H.J., Micromechanical simulation of concrete softening,Fracture Processes in Concrete, Rock and Ceramics, ed. J.G.M.vanMier, J.G.Rots and A.Bakker,Chapman and Hall, London, 1991, pp. 129 - 138

2. vanMier,J.G.M, Crack Face Bridging in Normal, High Strength and Lytag Concrete, Fracture Processes in Concrete, Rock and Ceramics, Chapman and Hall, London, 1991, pp. 27 - 38.

3. Davies,J., Numerical and Experimental Study of Development of Fracture Path under Mixed Mode Loading, Fracture Processes in Concrete,Rock and Ceramics, Chapman and Hall, London, 1991, pp. 717 - 726.

4. Bazant,Z. and Pfeiffer,P.A, Shear Fracture tests of Concrete Mat. Const. 1986, 19 , pp. 111 - 121

MIXED-MODE AND MODE II FRACTURES IN CONCRETE

MAKOTO IROBE
Department of Transportation and Construction Engineering,
College of Scince and Technology,
Nihon University.
Narashinodai 7-24-1
Funabashi,Chiba 274. Japan

SONG-YING PEN
Engineering Department
Miura Boiler Co.,Ltd.
8 Copernicus Boulevard
Branfort, Ontario
Canada,N3P 1K5

ABSTRACT

A center notched circular disk subjected to the splitting load is discussed in the context of the linear elastic fracture mechanics (LEFM). Various stress states can be generated in the disk according to the notch length as well as the crossing angle of the loading direction to the notch plane. Stress intensity factors K_I and K_{II} for the notch are calculated by the theory of elasticity, and for comparison by the finite element method (FEM). Results of experiments for the notched concrete disks are presented. Mode I and mode II fracture toughnesses of the concrete are obtained from the load intensities at the initiation of crack propagation.

INTRODUCTION

In the past decades the nature of concrete has been investigated widely and deeply from the view-point of fracture mechanics. The testing methods and the numerical techniques have been advanced concuurently to solve both linear and non-linear problems in this field. In consequence problems such as post peak softening, size effect, and fracture process zone become now popular for concrete investigators as research subjects. Still now these problems remain to be solved.

The mixed-mode fracture of concrete has taken a growing interest, since Bažant[1] criticized the investigation by Ingraffea[2]. They conducted shear tests for single notched and double notched concrete beams by four-point loading. Recently Rots analyzed the

mixed-mode fracture in the four-point shear beams by using the elastic softening constitutive relation in the smeared crack model [3,4]. He is cautious in using the words mode II and mixed-mode fractures for concrete in the reference[4]. Hawkins[5] proposed a mixed-mode loading device for CLWL-DCB concrete specimens. In the reference, however, observation of the mode II fracture is not mentioned. More recently, Bocca[6] extended the cohesive crack model to mixed-mode crack propagation, and performed confirmation experiments by the same method as seen in the reference[1]. Among crack trajectories shown in reference[6] the mode II patterns are observed.

In this paper the stress intensity factors for the center notched circular disk are solved under the splitting load whose direction crosses the notch plane. Using the solution results of splitting test for concrete are analyzed. The relation between stress intensity factors, K_I and K_{II} , at crack initiation in the concrete is presented.

STRESS INTENSITY FACTORS IN A NOTCHED CIRCULAR DISK

The stress state of the notched disk shown in Figure 1 left is obtained by superposing as illustrated in the righthand side of the same figure. The disk without notch shown in center has no relation to the stress singularity. Therefore, the stress intensity factors of the disk in right yield those of the notched disk in left.

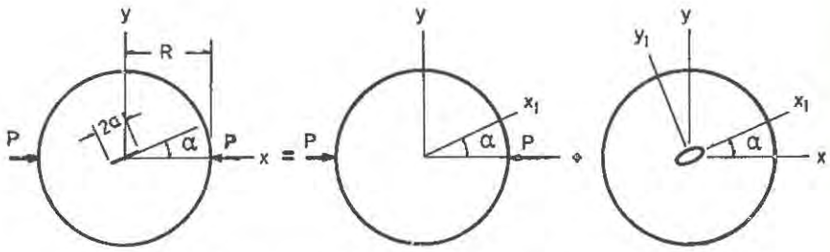

Figure 1. Decomposition for solving a notched disk.

Normal and tangential stresses σ_{y_1} and $\tau_{x_1 y_1}$ along the axis x_1 in the disk without notch are given by:

$$\sigma_{y_1} = \frac{P}{\pi R}\left[\frac{2(1+2\rho^2)(\cos 2\alpha - 1) - 2\rho^4(\cos 2\alpha - 1)(2\cos 2\alpha + 1)}{(1-2\rho^2\cos 2\alpha + \rho^4)^2} + 1\right] \qquad (1a)$$

$$\tau_{x_1 y_1} = \frac{P}{\pi R}\frac{2(1-\rho^2)(1-\rho^4)\sin 2\alpha}{(1-2\rho^2\cos 2\alpha + \rho^4)^2} \qquad (1b)$$

in which α is a crossing angle of the axis x_1 to the axis x and ρ is a normalized distance r/R from the center of disk. As the notch length 2a decreases, stress intensity factors for the disk approximate to those for an infinite plate with a crack of length 2a subjected to the same tractions on its inner surface. Stress intensity factors for the infinite plate are obtained by:

$$K_I = \frac{1}{\sqrt{\pi a}}\int_{-a}^{a} -\sigma_{y_1}\sqrt{\frac{a+x_1}{a-x_1}}\,dx_1 \qquad (2a)$$

$$K_{II} = \frac{1}{\sqrt{\pi a}}\int_{-a}^{a} -\tau_{x_1 y_1}\sqrt{\frac{a+x_1}{a-x_1}}\,dx_1 \qquad (2b)$$

It is easily found that the sign of stress σ_{y_1} changes from plus to minus for the crossing angle near 30° in case of a/R=0.1. The elastic solution determined in this way does not completely satisfy the boundary condition of the disk. In order to confirm the solution, therefore, the stress intensity factors are solved by the FEM. The FE solution is obtained by superposing a solution for symmetric loading to that for antisymmetric loading as shown in Figure 2.

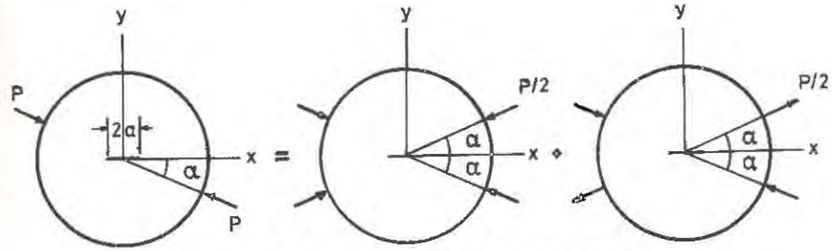

Figure 2. Decomposition of loading.

The FE analysis was performed by using two patterns of the element discretization, as shown in Figure 3. In both case, quarter point triangular elements are arranged at the notch tip. And the ratio of the side length of triangular element to the radius of disk is 1/30. In one pattern a side of the triangular element is collinear to the axis of symmetry, and in the other pattern a center line of the triangular element is on the axis of symmetry.

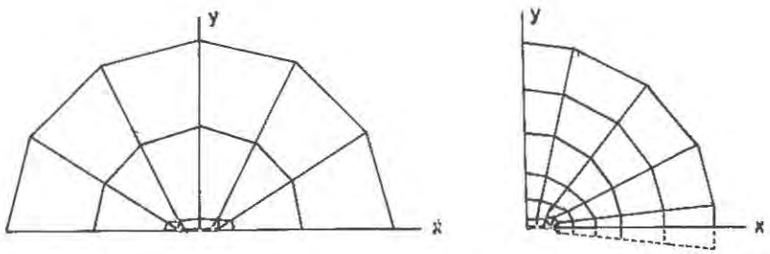

(a) Pattern-A. (b) Pattern-B.

Figure 3. Finite element discretization.

K_I and K_{II} are obtained by Ingraffea's formula[7]. Considering a size of test specimen, the plane strain was assumed in calculation. The stress intensity factors are determined for dimensions of the disk, i.e. R=7.5 cm, a=0.75 cm, and a side legth of quarter point triangular element on the notch surface l=0.25 cm. Figure 4 shows the normalized stress intensity factors F_I and F_{II} versus the crossing angle α. Three different solutions are presented. The correct solution is thought to exist between two FE solutions.

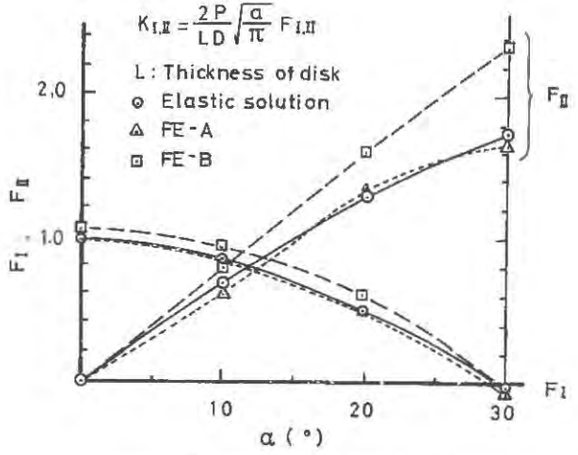

Figure 4. Normalized stress intensity factors versus α.

Figure 5 shows nondimensional stress $\sigma_y \pi R/P$ at Gauss points on the x axis of the notch end triangular element which were derived by the FE discretization pattern-B. It gives also the relation of

the notch length to the nondimensional stress. Although the FE discretization pattern-A gives a good estimation for stress intensity factors, it does not yield such a smooth stress distribution as patter-B. This suggests that the crack propagation problems must be solved for the entire geometrical form. The fracture process zone is expected to be very small from Figure 5.

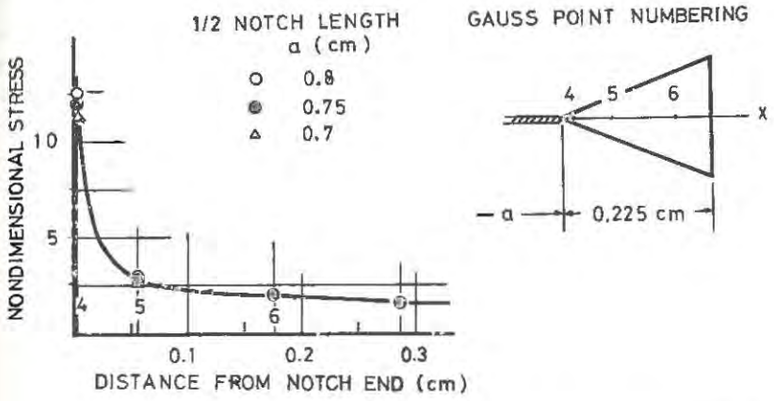

Figure 5. $\sigma_y \pi R/P$ distribution along x axis near notch tip.

EXPERIMENTAL RESULTS

Two kinds of concrete of the usual mix were used. Table 1 shows

Table 1.
Mix proportions and properties of concrete used.

	mix-1	mix-2
water with additive (kgw/m³)	178	174
cement	300	283
gravel (max. size 1.5cm)	871	871
sand	824	840
f_c' (kN/cm²)	3.00	2.40
E (MN/cm²)	3.24	2.55
Poisson's ratio	0.21	0.22

the mixing proportions and the mechanical properties.
A center notch was formed by setting thickness less than 2 mm and width 15 mm steel bar in cylinder moulds at casting of concrete. After three times repetition of preloading up to one third of the splitting failure load was applied to the specimen, the load was increased under a constant slow crosshead rate to failure. The yield point was found at about one half of the failure load. Typical load strain curves are shown in Figure 6. One is the case of $\alpha=0°$, and the other is the case of $\alpha=30°$.

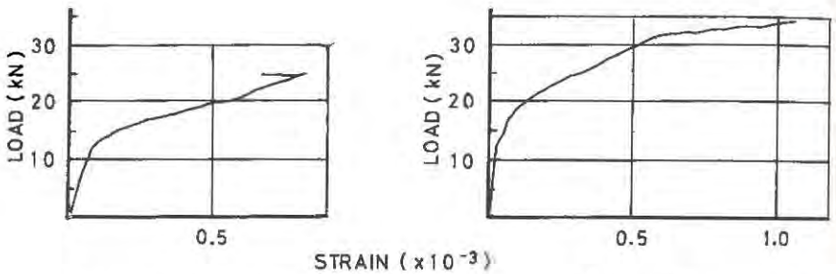

(a) $\alpha=0°$, Mix-1. (b) $\alpha=30°$, Mix-2.

Figure 6. Typical load strain curve.

Writers considered the load of yield point as the microcrack initiation load to determine the stress intensity factors. Table 2 shows the crack initiation loads . From the curve for FE-A in Figure 4 and the yield loads in Table 2 fracture toughnesses are derived.

TABLE 2.
Mean crack initiation loads

α (°)	mix-1(MN)	mix-2(MN)
0	13.04	12.19
10	22.06	14.54
15	22.85	——
20	17.95	15.16
25	16.28	——
30	15.50	17.26

$K_{IC}=146$ N/cm$^{1.5}$ and $K_{IIC}=228$ N/cm$^{1.5}$ for mix-1, and $K_{IC}=113$ N/cm$^{1.5}$ and $K_{IIC}=267$ N/cm$^{1.5}$ for mix-2 are obtained. The perfect sliding test for $\alpha=30°$ is difficult to be performed in order that the crack may not close. This is the reason why mix-2 concrete gains a larger K_{IIC} than mix-1, in spite of smaller f_c'.
The relations of K_I/K_{IC} to K_{II}/K_{IC} for the two kinds of concrete are depicted with the fracture locus of the maximum stress theory in Figure 7. All of the experimental data is plotted outside of the theoretical locus as like as the result of fracture test for PMMA, which behaves as a brittle fracture material under a room temperature, presented by Takamatsu[8].

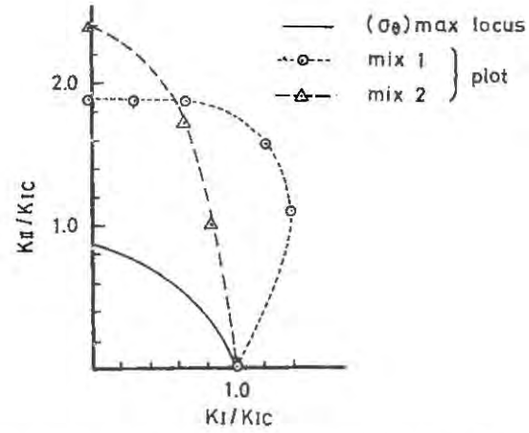

Figure 7. Comparison between experimental fracture plots and theoretical fracture locus.

The discrepancy between the theory and the experimental facts for these materials is considered to depend upon a large energy requirement for inducing the mixed-mode and sliding mode fractures. Especially for the concrete the existence of aggregates cannot be disregarded in this fracture process.

CONCLUSIONS

This investigation was performed for the usual concrete in the scope of the LEFM. Nevertheless, interesting conclusions are obtained.

1. The center notched cicular disk is an advantageous specimen to investigate the cracking process of concrete.
2. Both mixed-mode and sliding mode fractures exist for concrete.

3. It is not recommendable to use the symmetrical and antisymmetrical conditions with the singular element for the numerical analysis of crack problem.
4. Microcrack propagation in concrete does not obey the maximum stress theory.

ACKNOWLEDGEMENT

The writers would like to thank their colleagues and students at Nihon University, for their support.

REFERENCES

1. Bažant, Z.P. and Pfeiffer, P.A., Shear fracture tests of concrete. Materiaux et Constructions, Vol.19, No.110, 1986.
2. Arrea, M. and Ingraffea, A.R., Mixed-mode crack propagation in mortar and concrete. Department of Structural Engineering, Cornell University, Report No.81-13, 1982.
3. Rots, J.G. and Borst, R., Analysis of mixed-mode fracture in conrete. Journal of EM Div. ASCE, Vol.113,No.11, November 1987.
4. Rots, J.G., Stress rotation and stress locking in smeared analysis of separation. International Workshop on Fracture Toughness and Fracture Energy. Tohoku University, Japan, 1988.
5. Hawkins, N.M., Du, J., Yin, X. and Kobayashi, A.S., Fracture testing of CLWL-DCB specimens. International Workshop on Fracture Toughness and Fracture Energy. Tohoku University, Japan, 1988.
6. Bocca, P., Carpinteri, A. and Valente. S., Mixed mode fracture of concrete. Int.J. Solids Structures Vol.27, No.9, 1991.
7. Ingraffea, A.R. and Manu, C., Stress-intensity factor computation in three dimensions with quarter-point crack tip elements. Int. J. Numer. Meth. in Engng. Vol.12, No.6, 1978.
8. Takamatsu, T. and Ichikawa, M., Ductile fracture behavior of sheet cracked specimens under the mode I -II mixed-mode loading condition. Journal of JSME, Vol.56, No.532, Paper No.90-0127A, Dec. 1990 (in Japanese).

Chapter 8

Fracture of Reinforced Concrete

SIZE EFFECT IN BENDING FAILURE OF REINFORCED CONCRETE BEAMS

WALTER H. GERSTLE, PARTHA P. DEY, PAKAL RAHULKUMAR and MING XIE
Department of Civil Engineering,
University of New Mexico,
Albuquerque, N.M. 87131

ABSTRACT

In a singly reinforced concrete specimen in flexure, the effect of reinforcement and initial crack length on the fracture mechanics size effect is investigated using a simple analytical model. An unprenotched and/or reinforced beam exhibits a lower limit to the size effect; however a prenotched unreinforced beam demonstrates no lower limit in strength as the size increases. A parametric study indicates for which regime the size effect is most prominent. The importance of the size effect for a practical beam is demonstrated with the aid of an example.

INTRODUCTION

The fracture mechanics size effect in concrete structures has been introduced by Bazant (1), and has been experimentally observed (2). It is now necessary to evaluate the importance of the size effect in practical design situations, and particularly to determine whether justification exists for alteration of the design code, ACI-318 (3) in light of the size effect.

To answer this question, we study a singly reinforced concrete specimen in flexure. This is a particularly good specimen to study because it involves only Mode I cracking and is therefore easy to model analytically; because it is expected to produce a large size effect; and because this is the most common type of reinforced concrete element in practice.

A simple analytical model has been developed. This model makes use of the fictitious crack model (FCM) (4,5), linear elastic fracture mechanics (LEFM) (6), and includes elastic behavior of the concrete and elastic-plastic behavior of the steel.

The predictions produced by the model are briefly summarized in this paper, and the importance of the size effect in practical regimes is evaluated.

ANALYTICAL MODEL

An analytical model has been developed to predict the behavior (up to peak load and beyond) of a singly reinforced concrete beam. With respect to Fig. 1, the model takes into account eight normalized parameters:

$$\beta \equiv \frac{f'_t\, h}{E_c\, COD_{cr}} \quad \text{(normalized depth of beam);}$$

$$M \equiv \frac{m}{f'_t\, b\, h^2} \quad \text{(normalized applied moment);}$$

$$A = \frac{a}{h} \quad \text{(normalized length of fictitious crack} = a_o + a_1\text{);}$$

$$A_0 = \frac{a_0}{h} \quad \text{(normalized initial crack length);}$$

$$\rho \equiv \frac{A_s}{bh} \quad \text{(reinforcement ratio);}$$

$$n \equiv \frac{E_s}{E_c} \quad \text{(modular ratio of steel to concrete);}$$

$$\gamma \equiv \frac{\sigma_y}{f'_t} \quad \text{(normalized yield strength of steel);}$$

$$\delta \equiv \frac{f'_c}{f'_t} \quad \text{(normalized compressive strength of concrete)}$$

where f'_t is concrete tensile strength, h is beam depth, E_c and E_s are Young's moduli for concrete and steel respectively, COD_{cr} is the crack opening displacement beyond which the concrete carries no tensile stress, m is the moment applied to the beam, b is the beam width, a is the crack length, a_0 is the initial crack length, σ_y is the yield strength of the steel and f'_c is the compressive strength of the concrete.

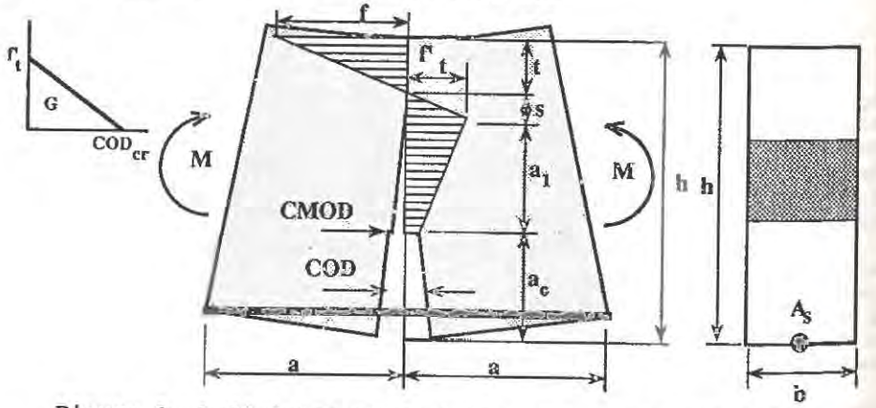

Figure 1. Definition of Variables in Analytical Model

The assumptions made by the model are:

(1) At a horizontal distance of **a** (see Fig. 1) from the crack, plane sections of the beam remain plane after deformation (from Saint Venant's principle and Timoshenko beam theory).

(2) Fictitious crack surfaces remain plane after deformation.

(3) Closing tractions acting on the fictitious crack follow a linear stress-COD curve for $0<COD<COD_{cr}$.

(4) Fiber bending stress in the concrete at the level of the notch tip is assumed constant and equal to the traction normal to the crack mouth at the notch tip.

(5) The concrete is linear and elastic in the stress range between the compressive strength, f'_c, and the tensile strength, f'_t.

(6) The steel is elastic up to stress σ_y, at which point it becomes perfectly plastic.

(7) The steel can slip with respect to the concrete over a distance **a** from the crack surface. Beyond this distance, the steel cannot slip with respect to the concrete (a representation of bond-slip behavior).

(8) The centroid of the steel is located at the bottom of the beam (this assumption is not necessary, but reduces the number of variables in the problem for ease of presentation). This implies that beam depth h = d.

(9) Once the stress in the top fiber of the beam reaches the compressive strength of concrete, f'_c, the beam can carry no additional moment.

(10) At a given traction-free crack length, the beam carries the minimum moment predicted by either the FCM or by LEFM.

RESULTS OF ANALYTICAL MODEL

The analytical model described in the previous section was implemented in a simple computer program which generated normalized moment, M, versus normalized crack length, A, curves, shown for a small, medium, and large beam in Figs. 2(a-c), respectively. The interesting features are that for small beams, the strength is determined by the FCM and by yielding of the steel, for medium beams the strength is determined by an interaction between the FCM and the LEFM models, and for large beams, the strength is determined by either LEFM or by the strength properties of the steel and concrete.

Also, the computer program was capable of producing size effect curves, several typical of which are shown for a unprenotched and a prenotched beam in Figs. 3(a) and 3(b), respectively. The interesting features of the curves shown in Fig. 3 are:

1. The size effect is most pronounced in an unreinforced, prenotched concrete beam.
2. The size effect in an unreinforced, unprenotched concrete beam has a ratio of $\frac{M(\beta_{small})}{M(\beta_{large})} = \frac{3\delta - 1}{\delta + 1}$ between the upper and the lower shelves of the size effect curve. This effect has also been predicted by Kim et al. (7).
3. For unreinforced beams, the transition region between the upper and the lower shelves on the size effect curves occur approximately in the size regime $-2 < \log_{10}(\beta) < +2$, as

shown in Fig. 3(a). For typical concretes (E_c=4143 ksi, f'_c=6 ksi, f'_t=0.6 ksi, COD_{cr}= 0.0025"), this corresponds to a beam depth of 0.173" < h < 1730". Thus the range of sizes of unreinforced nonprecracked concrete members falls within the range within which the size effect is most pronounced.

4. As the reinforcement ratio ρ increases, the ratio between the upper and lower shelves of the size effect curve is reduced radically. Also, the transition regime is shifted toward very small beam sizes as ρ increases.

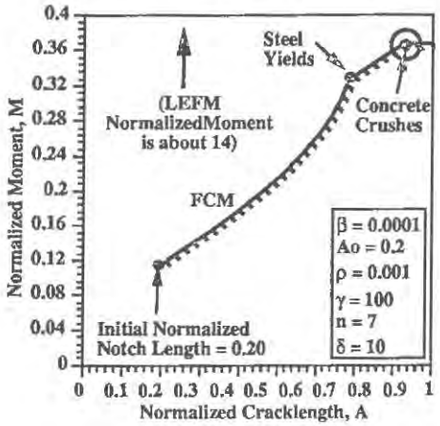

(a) Small Beam

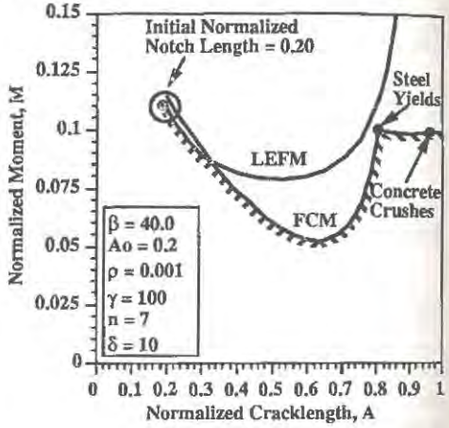

(b) Medium Beam

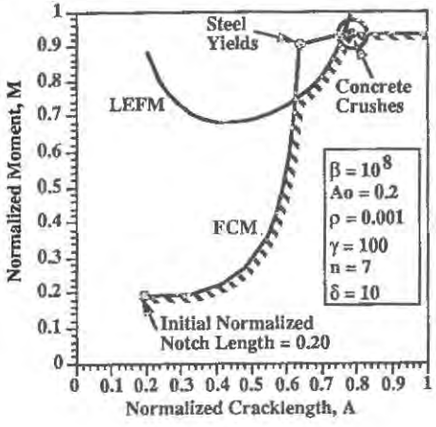

(c) Large Beam

Figure 2. Typical Normalized Moment versus Normalized Crack Length Curves Generated by the Analytical Model.

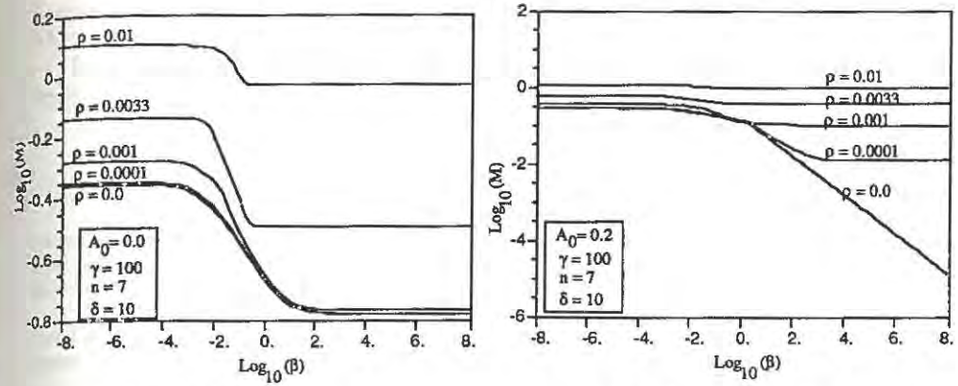

(a) Unprenotched (b) Prenotched

Figure 3. Typical Size Effect Curves Generated by the Analytical Model.

EXAMPLE PROBLEM

Consider a fairly typical 12" deep by 6" wide singly reinforced concrete beam with one #4 grade 60 reinforcing bar whose centroid is located 10" below the top of the beam. Assume the following properties describe the beam: d=h=10"; b=6", f'_t =0.6 ksi; f'_c=6 ksi; E_c=4143 ksi; E_s=29000 ksi; σ_y=60 ksi; A_s=0.20 in^2; K_{Ic} = 1.77 ksi-sqrt(in). COD_{cr} is calculated to be 0.0025". The normalized parameters for this beam are: β=0.58; A_0=0; ρ=.0033; γ=100; n=7; δ=10. $Log_{10}(\beta)$ = -0.237. From Fig. 3(a) it is found that for this value of β, the value of $log_{10}(M)$=-.491 is already on the lower shelf. A failure moment of 116 k-in is thus predicted. The ACI code (3) predicts a nearly identical failure load of 118 k-in.

If a similar beam of one-half the size were investigated (6" deep), (this might be a floor slab, for example), $log_{10}(\beta)$ = -0.537, and the size effect would barely begin to become evident, as can be seen in Fig. 3(a). From Fig. 3(a), $log_{10}(M)$= -.490, from which the predicted resisting moment is 14.58 k-in. The ACI code predicts a resisting moment of 14.44 k-in. For such a beam, the moment predicted by the analytical model is about one per cent greater than that predicted by the ACI Code (3).

For yet a another similar beam of one-quarter the original size (3" deep), (as for example a flange of a precast tee beam), the size effect is expected to be quite important. For this beam, $log_{10}(\beta)$ = -0.839. From Fig. 3(a), $log_{10}(M)$=-.4617, from which the predicted resisting moment is 1.943 k-in. The ACI code predicts a resisting moment of 1.82 k-in. The ACI Code under predicts the strength by about 7 per cent.

A specimen smaller than 3" deep would be very difficult to

create with a typical concrete because the aggregate size would approach the depth of the beam. However, for any beam with $\log_{10}(\beta)$ less than -2.5, as shown in Fig. 3(a), $\log_{10}(M)=-.140$. The analytical model predicts a failure moment about 93 per cent higher than predicted by the ACI Code (3).

CONCLUSIONS

The size effect is very pronounced in some cases:

1. For large, unreinforced, prenotched concrete beams, the size effect may be extremely large. As can be deduced from the size effect law, for a doubling of beam size the predicted nominal strength decreases by 41 per cent.
2. For unreinforced, unprenotched beams, the ratio of nominal strength for a very small beam to nominal strength of a very large beam is given by $\frac{M(\beta_{small})}{M(\beta_{large})}=\frac{3\delta-1}{\delta+1}$. For normal concrete, δ=10, and the ratio in normalized moments is only 2.63.
3. As the amount of reinforcement increases, the size effect decreases rapidly.

The size effect does not seem to be important for typical concrete beams in typical size ranges with typical reinforcement ratios. The size effect is, however, very important for unreinforced, or very lightly reinforced, concrete beams. The ACI Code (3) should be appended to cover these cases.

REFERENCES

(1) Bazant, Z.P., Size Effect in Blunt Fracture; Concrete, Rock, Metal. Journal of Engineering Mechanics, ASCE, 1984, Vol. 110, pp. 518-535.

(2) Bazant, Z.P. and Sener, S., Size Effect in Torsional Failure of Concrete Beams. Journal of Structural Engineering, ASCE, 1987, Vol. 113, No. 10, pp. 2125-2136.

(3) ACI, Building Code Requirements for Reinforced Concrete. American Concrete Institute Standard 318-89.

(4) Hillerborg, A., Modeer, M., and Petersson, P.E., Analysis of Crack Formation and Crack Growth in Concrete by Means of Fracture Mechanics and Finite Elements. Cement and Concrete Research, 1976, Vol. 6, No. 6, pp. 773-782.

(5) Petersson, P. E., Crack Growth and Development of Fracture Zone in Plain Concrete and Similar Materials. Report TVBM-1006, Lund Institute of Technology, 1981.

(6) Broek, D., Elementary Engineering Fracture Mechanics, Fourth Revised Edition, Klewer Academic Publishers, 1986.

(7) J.K. Kim, S.H. Eo, and H.K. Park, Size Effect in Concrete Structures without Initial Cracks. Fracture Mechanics, ACI SP 118-9, 1989, pp. 179-195.

SCALE EFFECT ON PLASTIC ROTATIONAL CAPACITY OF R.C. BEAMS.

CRESCENTINO BOSCO, ALBERTO CARPINTERI and PIER GIORGIO DEBERNARDI
Department of Structural Engineering - Politecnico di Torino
24, Corso Duca degli Abruzzi, 10129 Turin, Italy.

ABSTRACT

The results obtained from an extensive experimental program show the scale dependency of plastic rotational capacity of reinforced concrete beams. This is verified both when failure occurs with large deformation of bars (low steel percentage) and when crushing of concrete prevails (high steel percentage).

A numerical simulation, on the basis of material constitutive stress-deformation relationships proposed by standard codes, is performed in the attempt of representing the behavior of the beam cross-section. Numerical results do not comply with the experimental ones and then the model based on the hypothesis that plane sections remain plane does not seem applicable to evaluate inelastic behavior of r.c. structures.

INTRODUCTION

Plastic rotational capacity is a fundamental characteristic for providing reinforced concrete structures with a sufficient ductility. It allows them to tolerate imposed deformations, such as settlements of supports, thermal effects, etc., to redistribute load-effects, to exploit the strength of the structure and to dissipate energy provoked by seismic events.

Theoretical evaluation of plastic rotation is however a complex question because of the interaction of several phenomena: concrete confinement, bond characteristics of reinforcing bars, shear effects, shape of bending moment diagram, mechanical properties of concrete, strength and ductility of steel, etc. The influence of size on the inelastic rotational capacity, has not been clarified yet; in fact the experimental data available, mostly obtained by load controlled tests on concrete beams reinforced with high ductility bars [1], [2], [3], show a considerable dispersion.

Test results discussed in the following [4], deal with concrete beams reinforced with new types of steel, recently defined in the European Codes [5], [6], that present characteristic of ductility lower than the traditional ones. The displacement-controlled experimental procedure allows the correct evaluation of the behavior of the beam in the plastic range, characterized by large deformations and displacements at maximum load and, generally, by a descending branch before the failure of the element.

The influence of the cross-sectional dimensions of the elements on the structural ductility has been numerically evaluated in terms of mean plastic curvature at maximum load, for different percentages of reinforcement, and compared to the experimental results, for verifying the applicability of the models given by Codes.

EXPERIMENTAL REFERENCE AND DEFINITIONS

The 44 simply supported reinforced concrete beams described in Table 1, are subdivided into eleven classes of four specimens, of which two with steel of high ductility and two with steel of normal ductility, symmetrically loaded by one or three loads according to the scheme shown in Fig. 1.

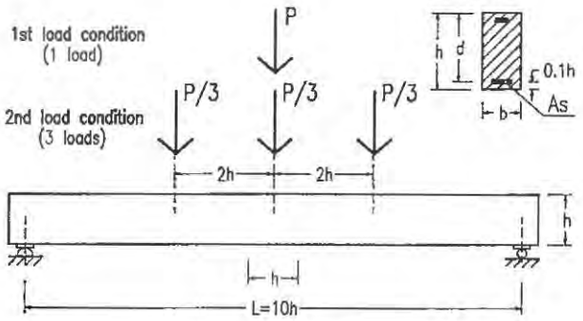

Figure 1. Testing scheme and loading conditions.

TABLE 1
Geometrical characteristics of the beams and percentages of steel

Beam type	b(mm)	h(mm)	L(mm)	Tensile reinforcement	Percentage
1	100	200	2000	1φ12	0.56
2				2φ12	1.13
3				3φ12	1.70
4	200	400	4000	2φ12	0.28
5				4φ12	0.56
6				8φ12	1.13
7				12φ12	1.70
8	300	600	6000	2φ12	0.13
9				4φ12	0.25
10				9φ12	0.56
11				18φ12	1.13

The mechanical parameters of the high bond bars type A and B, given in Table 2, are represented by the ultimate (f_t) and yielding (f_y) stresses while the ductility is represented by the ratio f_t/f_y and by the elongation at maximum load (ε_u).

TABLE 2
Mechanical characteristics of high bond steel reinforcement (mean values)

	Type A	Type B
f_t (N/mm²)	672	641
f_y (N/mm²)	587	596
f_t/f_y	1.15	1.076
ε_u	7.00%	4.18%

The following parameters are constant, see Fig. 1: L/h = 10; h/b = 2; d/h = 0.9. Mean cylindrical strength of concrete f_{cm} is 25.6 N/mm² and the compressive reinforcement is represented by 2 bars of 12, 10 and 8 mm respectively, for the three beam depths. Stirrups of 8 mm every 100, 200 and 150 mm, are provided for the beams type 1-3, 4-7 and 8-11, respectively.

Plastic rotation Θ_p is defined according to Eurocode 2 [5] and Model Code 90 [6] and obtained by integration, along the plastic zone (where the stress in the tensile reinforcement is higher than its yielding limit), of the difference between mean curvature $1/r_m$ and that at yield limit of steel, $1/r_{my}$. The average curvature, allowing for tension stiffening, can be deduced from the average strain ε_{sm} of tension chord and the average strain ε_{cm} at the extreme compression fibre of concrete, according to $1/r_m = (\varepsilon_{sm} - \varepsilon_{cm})/d$, where d is the effective beam depth (Fig. 1).

Two values of plastic rotation are considered: at maximum load (Θ_{pm}) and at the ultimate value (Θ_{pu}) on the descending branch, at a bending moment equal to 90% of the maximum value. When this level is not reached, the value recorded at the ultimate bending moment is considered. When the yielding of steel is not clearly identificable (this occurs for high percentages of steel) a fictitious yielding point is considered, corresponding to a 0.1% of the proof curvature in the cracked range.

The experimental mean plastic curvature is measured in the central part of the beam, with a length equal to the beam depth.

THEORETICAL APPROACH

Non linear analysis of the behavior in the plastic range, up to failure, is performed by a numerical method using mean stress-strain relationships and based on material properties appropriate for the considered limit state.

As a simplification, some assumptions are considered valid up to failure. The first one corresponds to assume that plane sections remain plane up to the ultimate limit state is reached. While this hypothesis is valid for small deformations, it can certainly be considered rough close to the ultimate state. Nevertheless, often it is a useful reference for avoiding more complex calculations.

Other aspects that greatly affects the deformation of the beam are represented by bond relationship between concrete and steel and by the spacing of cracks.

For what concerns the behavior of concrete in compression, we observe increased characteristic of strengths and strains, linked to the degree of confinement of the compression chord. On the other hand the bars in compression can provoke, at ultimate limit state, instability phenomena that anticipate the crushing of concrete.

A further aspect, affecting the experimental results, is represented by the loading system; the extent of the loading zone influences the local stress distribution, the local crack propagation and the deformability, in particular at failure.

The formulation of a consitutive model for representing all these aspects in the plastic range of beams in flexure is then rather difficult. For comparing numerical and experimental values, a first tentative of simulating the actual behavior of concrete structures can be performed on the basis of simple analitical relationships given in [6], for concrete in compression and steel. This means to assume the curvature as a parameter of comparison. In the present analysis, reference is made to curvature at midspan cross-section and at peak load, without considering the tension-stiffening beyond the steel yielding, neither the contribution of the phenomena developing in the fracture process zone.

For numerical calculation, the cross-section depth is subdivided in strips 1 cm deep and the curvature at maximum moment is obtained by imposing equilibrium and congruence conditions. The idealized stress-strain curve for concrete presents the peak stress (mean cylindrical value obtained from the specimens) at a strain of 0.0022. The ultimate strain ε_{cu} is assumed 5 times the strain corresponding to half the peak stress in the descending branch (ε_{cu}=0.0168). The linear elastic-linear hardening curve of steel is characterized by the yielding (f_y) and ultimate (f_t) mean stresses and the ultimate strain value ε_u reported in Table 2.

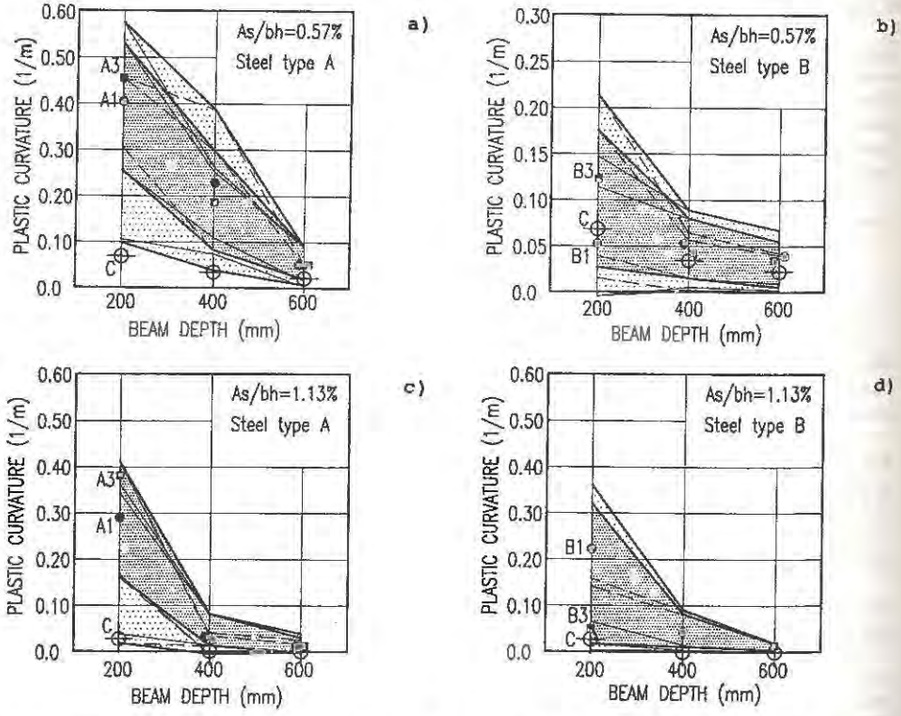

Figure 2. Plastic curvature vs. beam depth for percentages of steel equal to 0.57 and 1.13.

DISCUSSION AND RESULTS

The actual trend of the experimental moment-curvature diagrams, for ordinary percentages of steel, is normally characterized by an extended "plateau" in the plastic range, without important variations of bending moment around its maximum value. This is more evident as the ductility characteristic of steel increases (the ductility of steel type A is higher than that of steel type B). But even for very low or very high percentages of steel (beams type 8 or types 3 and 7, see Table 1), it is possible to observe the relatively extended plastic part of diagrams.

For representing these aspects, together with the curvature at maximum bending moment, also the curvature at the ends of the range given by bending moments equal to 95% and 98% of the maximum value (in the ascending and descending part of the diagrams), are reported. All these values are plastic values, net from the curvature measured at yielding limit.

In Figs. 2 a to d, the theoretical and experimental plastic curvatures for two percentages of steel (0.53 and 1.13) are compared, the last ones referred to the central part of the beam. The labels A1 and A3 (or B1 and B3) indicate the experimental mean plastic curvatures at maximum bending moment for beams reinforced with steel type A (or B) loaded with one or three loads respectively. The bold lines bound the range of variation of the experimental values. The internal range (dense dotted zone) is referred to the 98% of maximum moment; the external range (scattered dotted

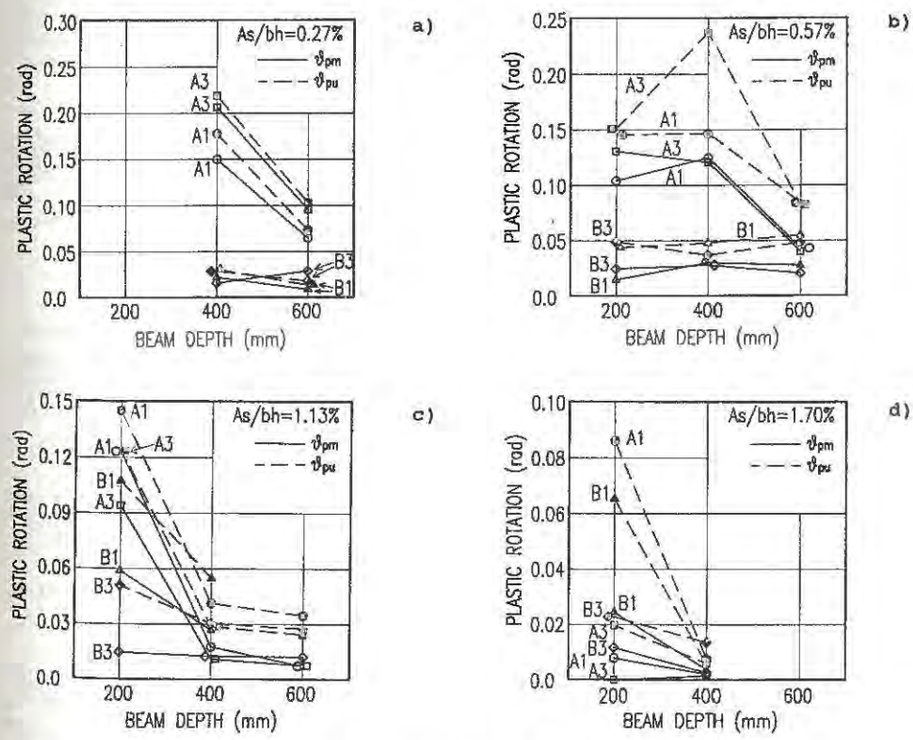

Figure 3. Experimental plastic rotation vs. beam depth.

zone) containing the previous one, defines the variations at 95% of maximum moment. In the same Figures the labels C represent the calculated values by numerical analysis for the cracked section; these values tend to locate in the lower part of the experimental curve of 95%.

In any case, the numerical results are far from representing the experimental ones, for any percentages of reinforcement, even though the latter are largerly scattered. The same results are not inversely proportional to the beam depth, as theoretically predicted, because the actual percentage of compressive steel is not proportional to the scale of the elements.

In Figs 3 a to d, on the other hand, the experimental plastic rotations are reported for the four considered percentages of steel. The dashed lines refer to the ultimate rotations, while the continuous ones indicate the values at maximum moment. For this parameter it is possible to observe a general trend of decreasing values as the beam depth increases, while the rotation calculated on the basis of theoretical curvature is independent of the beam depth.

CONCLUSIONS

From the examination of the experimental results, the influence of the scale on the rotational capacity of reinforced concrete beams appears evident. In fact the experimental mean curvature with steel type A (high ductility), decreases more than 8 times for percentage of 0.57 and more than 28 times for percentage of 1.13, as the beam depth increases from 200mm to 600mm. For steel type B (normal ductility) the variations are 2.7 and 9.4 times, respectively.

The numerical results obtained using the relationships proposed by standard codes and the hypothesis that plane sections remain plane does not seem to reproduce the experimental behavior in terms of mean plastic curvature and, as a consequence, in terms of plastic rotation.

REFERENCES

1. Mattock, A. H., Rotational capacity of hinging regions in reinforced concrete beams. Proceedings of the International Symposium on Flexural Mechanics of Reinforced Concrete, Miami, ACI SP12, Nov.1964, pp.143-181.
2. Corley, W. G., Rotational capacity of reinforced concrete beams. J. Struct. Div., ASCE, Oct. 1966, 92, pp.121-146.
3. Siviero, E., Rotation capacity of monodimensional members in structural concrete. Bulletin d'information CEB, Feb.1974, n.105, pp. 206-222.
4. Bosco, C. and Debernardi, P.G., Influenza della duttilita' degli acciai sulla capacita' di rotazione plastica delle strutture in cemento armato. Atti Congresso A.I.C.A.P., Spoleto, Italy, 16-18 Maggio 1991, pp. 45-62. In Italian.
5. Commission of the European Communities. Industrial Processes - Building and Civil Engineering. Eurocode n. 2. Design of Concrete Structures. Part 1. General Rules and Rules for Buildings. 1990.
6. Comitée Euro-International du Béton (C.E.B.)., Model Code 1990.
7. Carpinteri, A., Stability of fracturing process in RC beams. J. Struct. Eng.,(ASCE), 110, 1984, pp. 544-554.
8. Bosco, C., Carpinteri, A. and Debernardi, P.G., Minimum reinforcement in high-strength concrete, J. Struct. Eng., (ASCE), 1990, 116 (2), pp. 427- 437.

CRACK SPACING AND CRACK WIDTH IN REINFORCED CONCRETE FLEXURAL MEMBERS

LUCIE VANDEWALLE
Civil Engineering Department - K.U.Leuven
de Croylaan 2 - 3001 Heverlee - Belgium

ABSTRACT

Crack spacings and crack widths in reinforced concrete flexural members can be analyzed by means of methods, based on the τ-δ-relation of a reinforcement bar in concrete. At the Civil Engineering Department of the K.U.Leuven, the τ-δ-relation is mathematically approached by the expression :

$$\tau = \tau_u (1 - \mu e^{-\lambda \delta}).$$

To check the accuracy of the developed model, eighteen reinforced concrete beams were tested to failure. Comparisons of the calculated crack spacings and crack widths with the obtained test results show satisfactory agreement.

INTRODUCTION

Cracks in reinforced concrete structures may be expected at service load because of the low tensile strength of concrete. This cracking has a major influence on the stiffness of the structure and the resistance to corrosion of the reinforcement. It is therefore, necessary to control cracking in reinforced concrete structures.

There has been a common consensus by several investigators that the bond between steel and concrete has a pronounced influence on the control of cracking.

FROM τ-δ-RELATION TO CRACKING

The bond between the reinforcement bar and the concrete may be described in an idealized way as a shear stress between the surface of the reinforcement bar and the surrounding concrete. The bonding mechanism may be expressed by

the relation between the shear stress τ (=bond stress) and the relative displacement δ between the reinforcement bar and the concrete.

On the basis of the results of an extensive test program of beam tests on deformed bars, both at normal as well as at cryogenic temperatures, executed at the Civil Engineering Department of the K.U.Leuven [1], the τ-δ-relation is mathematically approached by the expression :

$$\tau = \tau_u \, (1 - \mu e^{-\lambda \delta}) \qquad (1)$$

in which τ_u is a function (mathematical expression) of the concrete cover on the reinforcement bar, the concrete quality and the temperature; μ and λ are constants. This formula holds both for normal as well as for cryogenic temperatures, and moreover for both small as well as for large values of δ.

For a reinforced concrete beam, loaded by a constant moment and normal force along the axis of the member, the transfer of a portion of the tensile force N in the bar to the surrounding concrete is, for an elementary part dx, described by the following equation (figure 1) [2] :

$$\frac{d^2\delta}{dx^2} = \tau_x \frac{4}{\phi} \left[\frac{1}{E_s} + \frac{2 A_s (v - d_{st})(m - 1)}{E_c v^2 b m}\right] \qquad (2)$$

$$m = \frac{E_s}{E_c} .$$

Only the tensioned zone of the cross-section of the beam is considered in the calculations. After substituting (1) in (2) and numerically solving the differential equation (2), one obtains the anchorage length ℓ_d corresponding to the cracking force N_{cr}.

Using the above-mentioned model for "force-transfer", crack spacings (L_{cr}) and crack widths (w_{cr}) belonging to first order ($L_{cr} \geq 2\ell_d$) and second order cracks ($\ell_d \leq L_{cr} < 2\ell_d$) can be determined [2],[3].

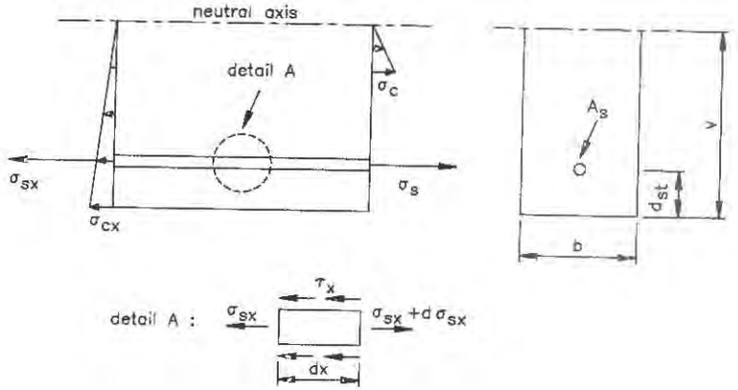

Figure 1 : Eccentrically loaded reinforced concrete tensile bar.

TEST PROGRAM

Specimens

The influence of the following parameters on the cracking behaviour of a reinforced concrete beam was examined :

- diameter of the reinforcement bar (ϕ = 16 - 20 - 25 mm)
- ratio between the concrete cover on the bar (d) and the diameter of the bar (ϕ)(d/ϕ = 1 - 1.5).

For every combination of the two parameters, three specimens were cast. So the test program consisted of a series of 18 beams. The beams were 100 x 250 mm in cross-section and had a length of 1300 mm. The under-reinforcement consisted of one deformed bar (= parameter) and the upper-reinforcement of two bars (ϕ=6 mm) (figure 2).

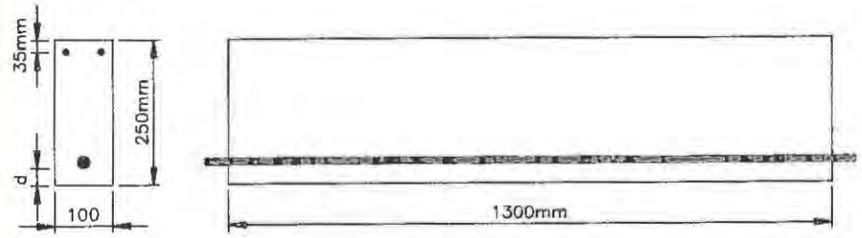

Figure 2 : Specimen.

Material properties

The concrete mixture ($1m^3$) was composed of : gravel 4/14, 1300 kg; sand 0/5, 550 kg; cement HK40, 400 kg; water, 165 l; W/C, 0.413.

Compressive strength obtained on cubes (150 mm) at an age of 28 days was 55.2 Mpa on the mean [4].

Test procedure

Immediately after demoulding, the specimens were stored in a fog room (20°C, R.H.>95%). Loading tests were performed at an age of 28 days. The specimens were set up vertically. The constant bending moment and normal force along the axis of the member were realized by applying at both ends of the beam a tensile force N on the rebar.

At each load increment the evolution of the crack formation was indicated on the beam and the crack width of the different cracks was measured by means of a small microscope.

TEST RESULTS

Crack spacing

The evolution of the crack spacing (L_{cr}) as a function of the steel stress in the under-reinforcement (σ_s) at the place of the crack is for different specimens shown in figure 3. The horizontal dotted line in this figure

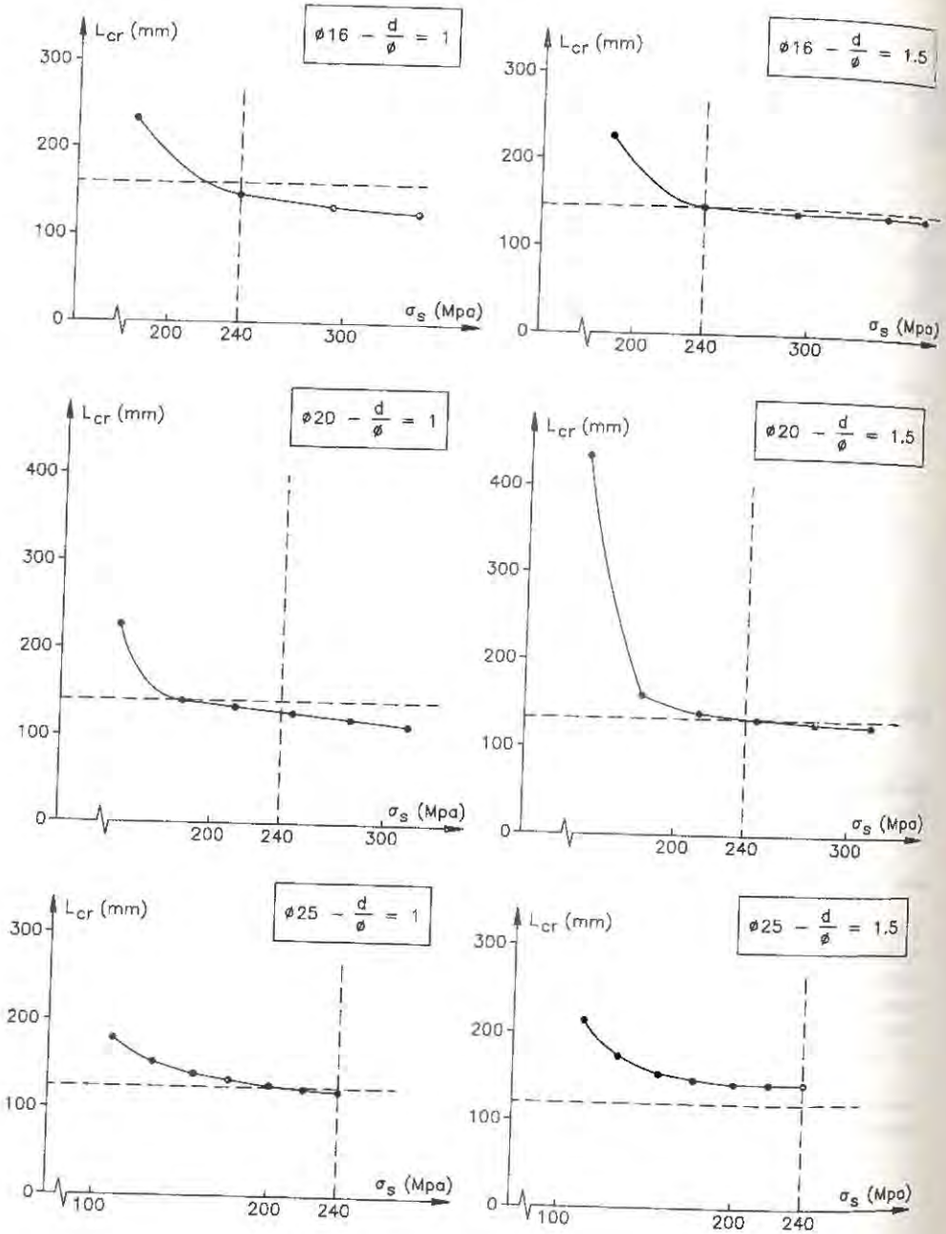

Figure 3 : Crack spacing as a function of steel stress.

represents the theoretically calculated anchorage length ℓ_d corresponding to the cracking force N_{cr} [2].

From figure 3 it follows that the measured mean crack spacing at service load (σ_s=240 Mpa) corresponds good with the value of ℓ_d.

Crack width

In table 1 the following observed quantities are given for a load level about service load (σ_s=240 Mpa) : the maximum (w_{max}), the minimum (w_{min}) and the mean crack width (w_m). The mean crack width (w_t) at this load level has also been calculated using the developed theory [2] and is given in the last column of table 1.

From table 1, it follows that there is a satisfactory agreement between theoretically obtained results and test results.

TABLE 1
Crack width

Specimen	w_{min} (mm)	w_{max} (mm)	w_m (mm)	w_t (mm)
ϕ 16/1	0,04	0,18	0,11	0,13
ϕ 16/1.5	0,08	0,16	0,12	0,12
ϕ 20/1	0,04	0,14	0,08	0,13
ϕ 20/1.5	0,04	0,18	0,12	0,12
ϕ 25/1	0,08	0,18	0,12	0,12
ϕ 25/1.5	0,06	0,24	0,16	0,11

CONCLUSIONS

From this study it follows that for reinforced concrete beams, loaded by a constant moment and normal force along its axis, crack spacings and crack widths can be calculated using the theory that is developed at the Civil Engineering Department of the K.U.Leuven.

However, in reality the crack distribution is very irregular because it is determined by stochastic effects. The concrete tensile strength is indeed a quantity which is liable to a relatively great spread. Therefore strictly speaking only minimum and maximum values can be given for the crack spacing and crack width. A mean value for those quantities, obtained by carrying out the calculations with the mean concrete tensile strength, is accordingly to be interpreted with caution.

REFERENCES

1. Vandewalle, L., Hechting tussen wapening met verbeterde hechting en beton bij gewone en cryogene omstandigheden, Ph.D.-thesis, K.U.Leuven, March 1988.

2. Vandewalle, L., Ankerlengte, scheurafstand en scheurwijdte in balken met rechthoekige sektie, Internal report 33-ST-18, K.U.Leuven, August 1991.

3. Vandewalle, L., Crack spacing and crack width in reinforced concrete members, Eight European Conference on Fracture, Torino, 1-5 October 1990.

4. Vandewalle, L., Proeven op gewapend betonnen elementen, excentrisch belast, Internal report 34-ST-19, K.U.Leuven, August 1991.

CRACKWIDTH IN R.C. BEAMS - A FRACTURE MECHANICS APPROACH

H. ANANTHAN
Department of Civil Engineering, Malnad College of Engineering, Hassan, India

K.T. SUNDARA RAJA IYENGAR and B.K. RAGHUPRASAD
Department of Civil Engineering, Indian Institute of Science, Bangalore 560 012, India

ABSTRACT

An analytical procedure is developed to predict crackwidth of a single dominant crack in R.C. beams at various stages of loading using fracture mechanics principles. The comparison between the predicted values with the experimental values available in literature is found to be good. The influence of the tensile strength of concrete on the performance of the model is ascertained by performing a sensitivity analysis.

INTRODUCTION

The determination of crackwidth in reinforced concrete (R.C.) beams is important to ensure the limit state of serviceability in design. At present the crackwidths and crack spacings are calculated based mostly on empirical approaches using the results of large amount of experimental data available in the literature (1,2). From these investigations, it can be seen that, in addition to the primary variable namely stress or strain in steel, many other variables are considered to influence the crackwidth. Each approach differs from the other with respect to the selection of other variables only. In the authors' opinion, no satisfactory theory exists to enable the accurate prediction of the cracking behaviour of R.C. structures. In the existing design approaches, the cause for cracking in R.C. i.e. tensile stress is neglected. Considering the tensile strength of concrete, it is possible to evolve more rational methods to predict the crackwidth. One such method is described in this paper.

PROPOSED MODEL

The proposed formulation to predict crackwidths in a R.C. beam is based on the method developed by the authors (3) to evaluate the crack opening displacements (COD) at various locations on the cracked surfaces and at various stages of loading in a plain concrete beam. In this method, the COD is obtained by a simple multiplication of the local angular rotation of the cracked surfaces, Θ with the radial distance measured from the point of instantaneous centre of rotation to the point at which COD is to be evaluated. The latter is fixed in a concrete beam at the tip of an effective crack $a_{eff} = a+L_p$ where a is the notch depth and L_p is the length of the process zone. The crack of given length a is replaced by a effective crack of length $(a+L_p)$ subjected to the same external bending moment M as well as to a crack closing force F, which is being determined from the knowledge of stress distribution in the fracture process zone across the uncracked ligament. The force F being eccentric is replaced by an equivalent axial force F and a moment M. The expression for Θ (4) is given by

$$\Theta = \frac{(12.56(1-\nu)^2)/(Eb w^2)}{(\xi_1^2)/(1-\xi_1^2)/(1+2\xi_1)^2} \; [V_M(\xi_1)M^* - 0.167(1+2\xi_1)V_{FM}(\xi_1)Fw] \quad (1)$$

where $\xi_1 = (a+L_p)/W$, a = initial cracklength, b = breadth of the beam, w = overall depth of the beam, E = modulus of elasticity of concrete, ν = Poisson's ratio, $V_M(\xi_1)$ and $V_{FM}(\xi_1)$ are tabulated by Okamura and Watanable (4). To apply this simple procedure to a R.C. beam, the extension of the softening beam method (SBM) developed by the authors (5) is used. Fig. 1 shows the schematic diagram of the procedure. M^* in equation (1) is obtained as the resultant of external moment M, moment M_c due to the tensile force carried by the

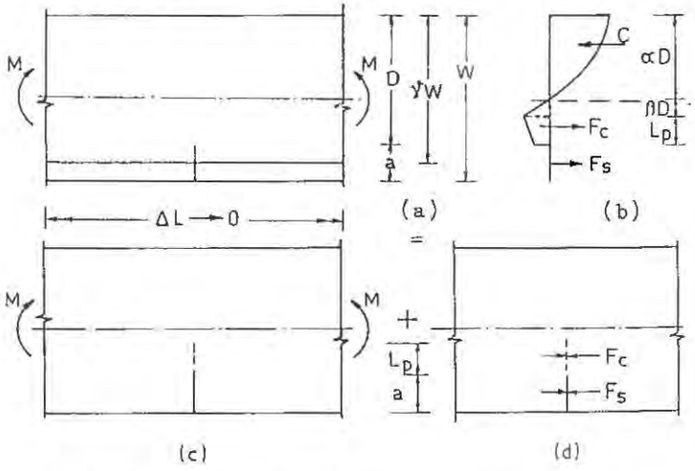

Figure 1. Schematic diagram of the procedure

concrete along the extended length of crack and M_s due to the tensile force carried by steel. Similarly F in equation (1) is the sum of F_c and F_s, being the tensile forces carried by concrete or steel. The procedure described is to obtain the crackwidth of a single crack at midspan. However in R.C. beams multiple cracks develop. Still the procedure is assumed valid since the experimental crack patterns in a R.C. beam indicate that they can be regarded as noninteracting ones (6).

RESULTS

The theoretically predicted values of crackwidth according to the proposed procedure are compared with the most important test results of Clark (7), Hognestad (8) and Base et al (9). The computed values of statistical quantities like average crackwidth, standard deviation and coefficient of variation are given in Table 1.

TABLE 1
Statistical quantities relating to the prediction of crackwidths

Sl No	Experimental Investigator	Number of observations	$\frac{W_{pre}}{W_{exp}}$		
			Mean value	Standard deviation	Coeff.of variation
1	Clark (7)	250	0.950	0.430	45.20
2	Hognestad (8)	117	1.400	0.412	29.42
3	Base et al (9)	147	1.104	0.180	16.26

Results given in Table 1 are for tensile strength = 1/10 x compressive strength of concrete. In order to understand the influence of tensile strength, a sensitivity study is performed. 24 beams tested by Base et al (9) are considered for comparison as given in Table 2.

TABLE 2
Comparison of average crackwidths at 6 and 10 tonne loads*

Load	Predicted average crackwidth x 10^{-3} inch*			Measured average crackwidth x10^{-3} inch
	1	2	3	
6 t	4.850	6.038	6.819	5.6
10 t	11.275	12.410	13.145	12.1
6 t	4.839	6.007	6.774	6.0
10 t	11.275	12.410	13.145	12.1

1 inch = 25.4 mm
* Note: Values tabulated under columns 1, 2 and 3 are obtained by assuming tensile strength equal to 1/8th, 1/10th and 1/12th of compressive strength, respectively. The first two rows are for steel of type GK60 and the 3rd and 4th row are for mild steel. From the results, it can be seen that the tensile strength has considerable influence on crackwidth.

CONCLUSIONS

The approximate analytical procedure developed using fracture mechanics principles to predict crackwidth of a single dominant crack in a R.C. beam is found to yield results within the accuracy expected in the case of a R.C. beam. The performance of the model is found to be sensitive to the value of tensile strength of concrete.

REFERENCES

1. Park, R. and Paulay, T., Reinforced Concrete Structures. John Wiley and Sons, New York 1975.
2. Desayi, P. and Ganeshan, N., An investigation on spacing of cracks and maximum crackwidth in flexural members. Materials and Structures (RILEM), March-April 1985, 18, 104.
3. Ananthan, H., Raghuprasad, B.K. and Sundara Raja Iyengar, K.T., Influence of strain softening on the fracture of plain concrete beams. International Journal of Fracture, 1990, 45, 195-219.
4. Okamura, H. and Watanabe, K.,Deformation and strength of cracked members under bending moment and axial force. Engineering Fracture Mechanics, 1975, 7, 531-539.
5. Raghuprasad, B.K.,Ananthan, H. and Sundara Raja Iyengar, K.T., Fracture behaviour of reinforced concrete beams. under publication in Journal of Structural Engineering, Madras, India, 1992.
6. Sundara Raja Iyengar, K.T., Raghuprasad, B.K. and Ananthan, H., Effect of interaction of macrocracks on the stress intensity factor in a beam. Engineering Fracture Mechanics, 1989, 32, 3, 379-386.
7. Clark, A.P., Cracking in reinforced concrete flexural members. Journal of Am. Concr. Inst. 1956, 27(8), 851-862.
8. Hognestad, E., High strength bars as concrete reinforcement, Part 2. Control of flexural cracking. Journal of PCA, Research and development laboratories, 1962, 4, 46-63.
9. Base, G.D., Read, J.B., Beeby, A.w. and Taylor, H.P.J., An investigation of the crack control characteristics of various types of bars in reinforced concrete beams. Parts 1, 2 and 3, Research Report 41.018, Cement and Concrete Association, England, 1966.

EFFECT OF DIFFERENT CRACK LENGTHS ON THE FRACTURE TOUGHNESS OF CONCRETE WITH REINFORCING BARS

Yu Hu, Jian Wang, Chaoxin Zhang and Qin Sun
Department of Civil Engineering
Huazhong University of Science and Technology, Wuhan, China
Xiaoyu Hu
Department of Metallurgy and Materials Science
Polytechnic University, Six Metrotech Center, Brooklyn, N.Y.11201, U.S.A.

ABSTRACT

The effect of different crack lengths on the fracture toughness of concrete with 0.3% reinforcing bars was studied. In this study, fracture toughness tests were carried out on three groups of reinforced concrete specimens and a group of pure concrete specimens. By a direct measurement or a calculation from the crack mouth opening displacement for the effective crack length, similar fracture toughness was obtained from both methods. Also, from experimental results, it reveals that when a_0, the initial crack length, equals to 25 and 50 mm, the fracture toughness of reinforced concrete are approximately the same for both cases. However, these values are lower than that in the case a_0 = 80 mm. This behavior is similar to that of pure concrete.

INTRODUCTION

Recently, there has been considerable interest in the study of the fracture toughness of concrete with reinforcing bars. In their earlier work, with the energy and the strength criteria, Bazant et al [1,2] analyzed the spacing and width of a group of parallel cracks for reinforced concrete. The asymptotic solutions for the crack spacing and width were analytically derived. Carpiteri [3] studied the stability of fracturing process in reinforced concrete beams with the type I crack when the different reinforcement ratios were considered. Rokugo et al [4] applied the fracture energy of concrete in compression to discuss the ductility of reinforced concrete beams under bending and axial forces. In terms of the initial crack length, De-Pei Chen et al [5] found a maximum 14% difference in the fracture toughness between reinforced and pure

concrete. Byung Howm Oh and Young-Jin Kang [6], on the basis of recently developed crack theory, calculated the maximum crack width and the average crack spacing in the flexed member for reinforced concrete. The calculations were in agreement with the experimental results. By assuming that yielding of steel bars in concrete and the first cracking occur simultaneously, Bosco et al [7] calculated the minimum reinforcement ratio in high strength concrete by dimensional analysis.

In previous work [8], without changing the initial crack length, the effect of different reinforcement ratios on the fracture toughness of concrete was studied. It was found that when the initial crack length was used to carry out the calculation, the fracture toughness increased rapidly with an increase of reinforcement ratio. In present paper, the effect of different crack lengths on the fracture toughness of reinforced concrete will be reported.

MATERIALS AND METHODS

A. Specimen Preparation

Materials of specimens consist of slag portlant cement (mark 525), general medium sand (grain Size is less than 0.5 mm) and crushed stone of quartz sand stone (grain size is from 5 to 10 mm). The mixed proportion of concrete was: cement: sand: stone: water = 1: 1.39: 2.3: 0.48.

Specimens were casted in the cast steel form and the vibrating needle was used to tamp concrete. Steel bars were used for reinforcing elements in concrete. A 1 mm thick crack was precasted with steel sheet. After the initial coagulation of concrete, the cast steel form was removed and the specimens were cured in the curing room.
Three groups of reinforced concrete were prepared. There were four specimens in each group. For the comparison purpose, one group of three pure concrete specimens was also prepared. Totally fifteen specimens were used in experiments. The configuration of specimens and the arrangement of reinforcing bars are shown in Fig.1. The dimensions and the reinforcement ratio, ρ, of specimens are given in Table 1.

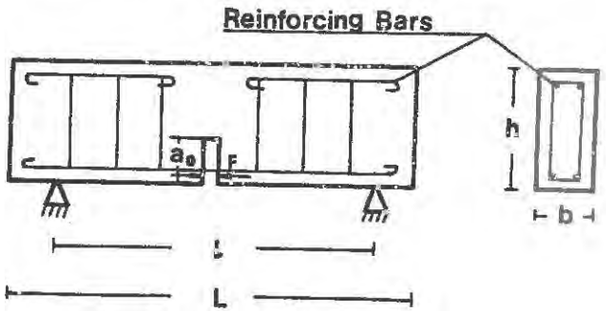

Fig.1 The Configuration of Specimen and the Arrangement of Reinforcing Bars

Additionally, with the same mixed proportion, six 100 mm x 100 mm x 100 mm cube specimens and four 100 mm x 100 mm x 300 mm prism specimens were prepared to determined the uniaxial compression strength, Young's modulus and Poisson ratio.

TABLE 1 Dimensions and Reinforcement Ratios of Specimens

Specimen Group	Number of Specimens	Reinforcement Ratio ρ	L mm	l mm	h mm	b mm	a_0 mm
A	4	0.3%	900	800	200	100	80
B	4	0.3%	900	800	200	100	50
C	4	0.3%	900	800	200	100	25
E	3	0.0%	900	800	200	100	80

B. Mechanical Test

The three point bending test was carried out to measure the fracture toughness of specimens, as shown in Fig.1. All uniaxial properties of materials were determined in compression test and are given in Table 2.

TABLE 2 Mechanical Properties of Pure and Reinforced Concrete

Material	Compressive Strength	Tensile Strength	Yield Limit	Poisson Ratio	Young's Modulus
Pure Concrete	39.5Mpa	3.5Mpa		0.198	2.82×10^4Mpa
Reinforced Concrete			310Mpa		18.0×10^4Mpa

C. Formulation of Fracture Toughness

If the tension, F, of the reinforcing bar is thought of as the external force applied to the specimen at the location of crack, Fig.1, then, the stress intensity factor of concrete with reinforcing bars, k_{IC}, is the difference between k_{IC}^p, the stress intensity factor produced in a three point bending specimen at load p, and k_{IC}^F, the stress intensity factor produced by a tension force F on the crack surface in an infinite strip. The fracture toughness of reinforced concrete k_{IC} is calculated as follows [9,10].

$$k_{IC}=k_{IC}^p-k_{IC}^F \quad (1)$$

$$k_{IC}^p=1.5\frac{pb}{h^{3/2}b}F_1\left(\frac{a}{b}\right) \quad (2)$$

$$F_1\left(\frac{a}{b}\right)=\sqrt{A}\frac{1.99-A(1-A)(2.15-3.93A+2.7A^2)}{(1+2A)(1-A)^{3/2}} \quad (3)$$

$$k_{IC}^F=2\frac{F}{\sqrt{\pi a}}F_2(X,Y) \quad (4)$$

$$F_2(X,Y)=\frac{3.52(1-X)}{(1-Y)^{3/2}}-\frac{4.35-5.28X}{(1-Y)^{1/2}}$$

$$+\left[\frac{1.30-0.30X^{3/2}}{\sqrt{1-X^2}}+0.83-1.76X\right]\left[1-(1-X)Y\right] \quad (5)$$

where $A=a/h$, $X=C/a$ and $Y=a/h$. a is called the effective crack length and will be discussed subsequently. The definition of b, c, h can be found in Fig.1

When the reinforcing bars are removed, the second term of right side of Eq.1 disappears. Then, Eq.1 will be reduced to an expression of the fracture toughness only for pure concrete.

RESULTS AND DISCUSSION

A. Effective Crack Length and the Fracture Toughness

Two methods were employed to determine the effective crack length.

1. *The Direct Method.* In this method, the increment of crack, Δa, was directly measured from the strain gage which was adhered on the top of the crack. The effective crack length can be expressed as $a=a_0+\Delta a$, where a_0 is the initial crack length.

2. *The Indirect Method.* In this method, the effective crack length was calculated from the crack mouth opening displacement (CMOD) by the try and error procedures. The crack mouth opening displacement was also measured experimentally. The expression for CMOD is given by

$$CMOD=6\frac{pla}{h^2bE}V\left(\frac{a}{h}\right) \quad (6)$$

$$V\left(\frac{a}{h}\right)=0.76-2.28A+3.87A^2-2.04A^3+\frac{0.66}{(1-A)^3} \quad (7)$$

where A, a, b, h have the same definition as described earlier. E is Young's modulus. l can also be found in Fig.1.

Substituting the effective crack length, a, determined by the above two methods, in Eqs.1-5, the corresponding fracture toughness for both reinforced and pure concrete can be obtained. The fracture toughness, together with the effective crack lengths, are listed in Tables 3 and 4. k_{Ic}^d in Tables 3A and 4A are the fracture toughness calculated from direct method, and k_{Ic}^i in Table 3B and 4B are the fracture toughness calculated from indirect method. p_c in Table 3A and B is the load at the initial cracking point, while p_{max} in Table 4A and B is the maximum load in the load-displacement curve. All of the effective crack lengths, CMOD, p_c, p_{max} and the fracture toughness are average values over the specimens in each group.

For both reinforced and pure concrete, these tables reveal that the effective crack lengths obtained from the two methods are similar for a given initial crack length. Thus, one would expect that the fracture toughness calculated from these two effective crack lengths are similar.

Comparing Table 3A with 4A or 3B with 4B, it can be found that, for a given

initial crack length, a_0 = 80 mm, the fracture toughness is higher for reinforced than pure concrete. As in earlier work [8], it was noted that the size of microcrack zone decreased with an increase of the reinforcement ratio, ρ. Therefore, the microcrack zone in the front of the crack tip would be expected to be smaller in the presence of the reinforcing bars than that in pure concrete. Thus, this smaller microcrack zone in the front of the crack tip would limit the crack opening. As a result, the fracture toughness in reinforced concrete increases.

For reinforced concrete, Table 3 (either 3A or 3B) indicates that when a_0 equals to 25 and 50 mm, the fracture toughness are approximately same. However, these values are lower than that in the case in which a_0 = 80 mm. The similar behavior was also found in pure concrete in earlier investigation [6].

TABLE 3 Fracture Toughness of Reinforced Concrete

A. Calculated from Direct Measurement of Crack Length

Specimen	a_0 (mm)	a(mm)	p_c (KN)	k_{Ic}^d (Mpa/mm$^{1/2}$)
A1-A4	80	90	8.71	1.31
B1-B4	50	75	7.55	1.08
C1-C4	25	55	8.33	1.02

B. Calculated from Measurement of CMOD

Specimen	a_0 (mm)	CMOD (mm)	a (mm)	p_c (KN)	k_{Ic}^i Mpa/mm$^{1/2}$
A1-A4	80	0.109	99	8.71	1.36
B1-B4	50	0.045	72	7.55	1.00
C1-C4	25	0.039	62	8.33	1.01

TABLE 4 Fracture Toughness of Pure Concrete

A. Calculated from Direct Measurement of Crack Length

Specimen	a_0 (mm)	a (mm)	p_{max} (KN)	k_{Ic}^d (Mpa/mm$^{1/2}$)
E1-E3	80	113	3.82	1.16

B. Calculated from Measurement of CMOD

Specimen	a_0 (mm)	CMOD (mm)	a (mm)	p_{max} (KN)	k_{Ic}^i(Mpa/mm$^{1/2}$)
E1-E4	80	0.07	113	3.82	1.14

B. Critical Load at initial Cracking Point

It was noted that when the crack begins to open, the crack opening extends

rapidly to the entire zone of ligament in pure concrete. In this case, it is difficult to determine the load at initial cracking point. Therefore, the maximum load in load-displacement curve is usually used in the formulation of the fracture toughness, i.e. p_{max} in Table 4A and B.

However, for the specimens of concrete with reinforcing bars, when the crack begins to open, the stress of reinforcing bars increases suddenly. By the method of flexibility [11], this sudden increase in the stress leads to an obvious change on the curve of flexibility- displacement. Thus, the load at initial cracking point, p_c in Table 3A and B, can be easily and reliably determined from a combination of curves of load-displacement and flexibility-displacement. Consequently, the measurement of the fracture toughness would be expected to be more accurate and more reliable in reinforced concrete than in pure concrete.

CONCLUSIONS

1. Two methods were employed to determine the effective crack length. It was found that the effective crack length obtained by these two methods were similar. Therefore, similar fracture toughness calculated from these two methods would be expected to be obtained.

2. The fracture toughness of reinforced concrete at the initial cracking load is higher that of pure concrete at the maximum load for given initial crack length. For reinforced concrete, the fracture toughness at a_0 = 25 and 50 mm are almost same, but lower than the value of a_0 = 80 mm. This behavior is similar to that of pure concrete.

3. If the specimens of concrete with reinforcing bars are used to measured the fracture toughness, the initial load at cracking point can be determined easily because of a sudden increase of the stress on the reinforcing bars.

REFERENCES

1. Z.P.Bazant and B.H.Oh, J. Structural Engineering, 1983, 109, 2066-85.
2. Z.P.Bazant and B.H.Oh, J. Structural Engineering, 1983, 109, 2207-12.
3. A.Carpinteri, J. Structural Engineering, 1984, V.110, 554-58.
4. K.Rokugo, Proceedings of the International Conference on Fracture Mechanics of Concrete, Edited by F.H.Wittmann, Lausanne, Switzerland, Oct., 1985, 587-96.
5. De-Pei Chen, Proceedings of the International Conference on Fracture Mechanics of Concrete, Edited by F.H.Wittmann, Lausanne, Switzerland, Oct., 1985, 607-13.
6. Byung Hwan Oh and Young-Jin Kang, ACI. Structural Journal, 1987, 84, 103-12.
7. C.Bosco, J. Structural Engineering, 1990, 116, 427-37.
8. Chaoxin Zhang, Jian Wang and Yu Hu, Proceedings of the Fourth Congress on Fracture and Strength of Rock and Concrete, Changsha, China, Oct., 1989, 220-25.
9. Y.S.Jenq and S.P.Shah, J. Engineering Mechanics, 1985, 111, 1227-41.
10. Y.S.Jenq and S.P.Shah, J. Engineering Mechanics, 1985 111, 1055-69.
11. Yu Hu, Chaoxin Zhang and Jian Wang, J. Huazhong University of Science and Technology, 1987, 15, 7-11.

INFLUENCE OF THE TENSILE BEHAVIOUR ON THE SHEAR STRENGTH OF LONGITUDINALLY REINFORCED CONCRETE MEMBERS

GERD REMMEL

Philipp Holzmann AG, Frankfurt/Main, Germany,

presently at Institut für Massivbau, TH Darmstadt, Germany

ABSTRACT

Shear tests on high-strength concrete (HSC) beams with different reinforcement- and shear span/depth ratios have been carried out. On the basis of their results and about 100 other test results on normal- and high-strength concrete, which are reported in literature, a formulation for the shear strength of slender, longitudinally reinforced concrete members is deduced. This empirical relation takes into account the effects of the ratio of reinforcement, of the depth, and, especially of the strength and ductility of tensile loaded concrete.

INTRODUCTION

In normal-strength concrete (NSC) cracks usually develop at the interface between the aggregates and the cement paste. This leads to a distinct aggregate interlock of the crack faces, to which a substantial part of the shear capacity of longitudinally RC-members is ascribed. On the contrary, cracks in HSC (f_c > 60 MPa) break right through the aggregates. The consequence is: relatively smooth crack surfaces. Additionally, the tensile strength increases only underproportionally with increasing compression strength, and the ductility of tensile loaded concrete decreases for HSC [10]. Since a correlation between the shear strength and the tensile strength is usually assumed and because of the missing aggregate interlock, a relatively lower shear strength of HSC-members is expected compared to NSC.

EXPERIMENTAL INVESTIGATIONS

In total, 6 tests on longitudinally reinforced HSC-beams with three different shear span(a)/ depth(d) ratios were carried out at the Institut für Massivbau (fig. 1). The material

characteristics of the concrete and of the deformed reinforcing bars for the two series, with different ratios of longitudinal reinforcement, were nearly identical (TAB. 1). Rhine gravel with a maximum size of 16 mm was used for coarse aggregate. The concrete contained silica fume (8% of cement mass) for the augmentation of the compression strength.

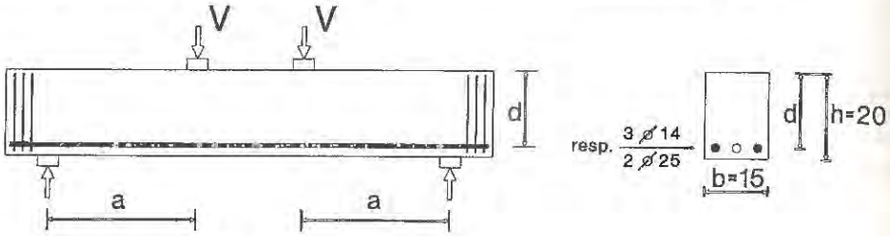

Figure 1. Geometry of the beams

TABLE 1. Material characteristics

Serie	f_c [MPa]	$f_{ct,sp}$ [Mpa]	G_f [N/m]	f_y [MPa]
1	85.1 ±0.9	5.30 ±0.30	162 ±10	523
2	84.5 ±1.4	5.25 ±0.31	157 ±10	554

TABLE 2. Test results

Serie	d [mm]	ρ[%]	a/d	v_u [MPa]
1	165	1.87	2.3	4.51
			3.06	1.94
			4.0	1.87
2	160	4.09	2.3	6.08
			3.06	2.51
			4.0	2.40

The failure of the slender beams (fig. 2), a/d = 3.06 and 4.0, is characterized as follows: Near the abutments inclined cracks develop from vertical bending cracks. After a steep inclination at the beginning, the crack propagates in the region of the ultimate load V_u from the middle of the beam diagonally towards the abutments. For both tests with a/d = 4 inclinations of 35° - 37° and crack widths of 0,30 - 0,35 mm were registered at the surfaces shortly before V_u was reached. In addition, horizontal cracks along the position of the reinforcement indicate a bond failure at the abutment side of the inclined crack.

The beams with a/d = 2.3 showed a totally different behaviour. After 0.5 V_u was reached, the crack pattern was closed. Then the load was directly transmitted by compression struts into the abutments. The crack width reached a value of ~2.0 mm with increasing loads. The failure of the beam was finally caused by a local failure in the region of the load platen. The different bearing mechanisms led to high shear strengths, $v_u = V_u/(b \cdot d)$, for the deep beams, which were twice as high compared to the slender ones (TAB. 2). A doubling of the reinforcement ratio increased v_u to 30 and 35 % for the slender and deep beams, respectively. The following investigation is restricted on slender members because a strong influence of the geometry and the stiffness of the load platens on the shear strength of beams and plates with a/d<3 is expected, and the dimensions of the load introducing systems are seldomly reported in literature.

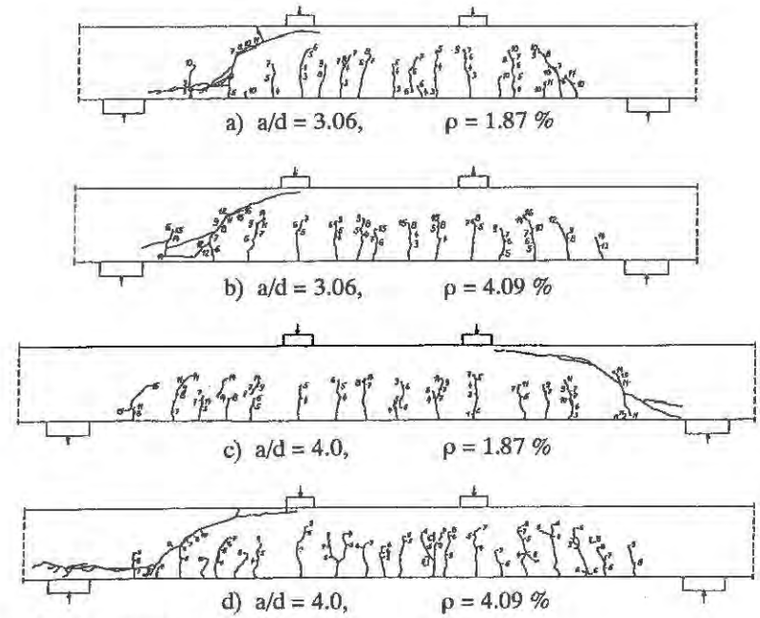

Figure 2. Crack patterns of slender beams

EMPIRICAL FORMULATION FOR THE SHEAR STRENGTH

For the derivation of a formulation to determine the shear strength of both NSC and HSC, additional test results from literature were used. Shear tests on HSC-beams have been carried out in the USA [1, 2, 3] and in Norway [4, 5]. In order to ensure the applicability of the formulation in demand for NSC, other investigations with a wide range of influencing parameters were included also [6, 7, 8, 9]. In one case [10] some beams had a h/b-ratio > 10, and therefore, they seem to be endangered to instabilities. These results as well as the test data, where an anchorage failure determined the ultimate load, were not taken into account.

The diagonal shear failure is determined decisively by the stress state in the vicinity of the tip of the inclined crack (fig. 3), which depends on different parameters:

1. TENSILE BEHAVIOUR OF THE CONCRETE

The tensile strength and the tensile softening behaviour decide whether or not the inclined crack propagates into the compression zone and finally causes the shear failure. The tensile strength f_{ct} increases only underproportionally with higher compression strengths f_c (cylinder 150/300 mm) and reaches an upper limit for f_c ~80 MPa [10].

$$f_{ct}(f_c) = 0.40 \cdot f_c^{0.58}\ [MPa], \quad f_c < 80\ MPa \tag{1}$$

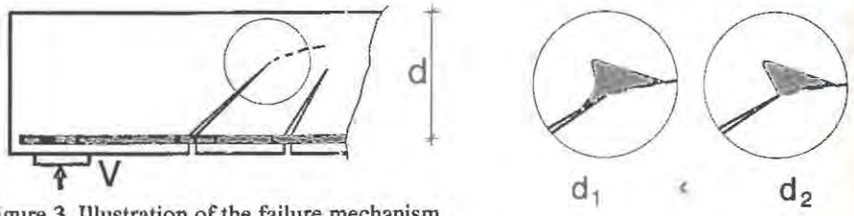

Figure 3. Illustration of the failure mechanism

The ductility of a tensile loaded concrete is determined by its capacity to continue to transfer tensile stresses with further increasing deformation after the tensile strength has been reached. It can be approximately described by the characteristic length $l_{ch} = E \cdot G_f/f_{ct}^2$. The fracture energy G_f represents the energy which is necessary to open a crack to its full extend. Tensile and bending tests on NSC and HSC with gravel (d_{max} = 16 mm) as coarse aggregate showed for G_f a similar dependancy as for the tensile strength. It increases up to a strength of ~80 MPa and then stays nearly constant for higher strengths. The formulation for the modulus of elasticity E was taken from MC1990 [11].

$$v_u \sim \left(\frac{E \cdot G_f}{f_{ct}^2 \cdot c_1}\right)^{c_2} \quad \text{with : } E = 8500 \cdot f_c^{1/3}\ [MPa] \qquad (2)$$

$$\text{and } G_f = \begin{cases} 100 N/m & f_c \le 25\ MPa \\ 150 N/m & f_c \ge 80\ MPa \end{cases} \quad \begin{matrix} \text{(Intermediate values} \\ \text{are interpolated linearly)} \end{matrix}$$

The characteristic length is divided by c_1 = 425 mm, which corresponds to l_{ch} of a NSC (B25 (DIN 1045)). The later regression analysis showed that the shear strength is proportional to the normalized characteristic length with a power c_2 = 0.5 (2). In addition to the decrease resulting from the only underproportionally increasing tensile strength, this ductility factor reduces the shear strength of a HSC (f_c = 80 MPa) by 24%, compared to a NSC (f_c = 25 MPa) (fig. 4).

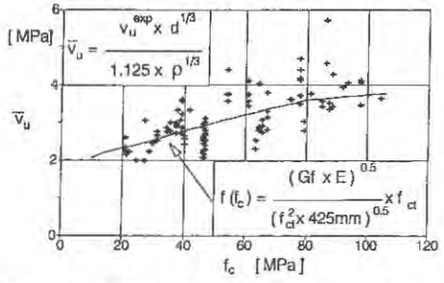

Figure 4. Effect of compression strength

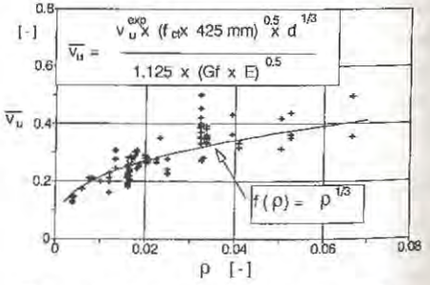

Figure 5. Effect of reinforcement ratio

2. LONGITUDINAL REINFORCEMENT

The amount of the reinforcement and its bond properties determines the longitudinal stiffness of the tensile chord, and by this, the crack width and the further crack propagation (fig. 3). In the case of shear failure, yield stress usually is not attained; therefore, an effect of

the yield stress is not expected. Furthermore, a contribution to the shear capacity is assigned to the dowel action of the reinforcement. It depends on the flexural stiffness of the reinforcement and is limited by the tensile capacity of the concrete in the layer of the reinforcing bars. Since in some tests (fig. 2) horizontal cracks occurred at a load level, substantially lower than V_u, the contribution of the dowel action seems to be questionable. The dependency chosen, $v_u \sim \rho^{1/3}$, takes into account the decreasing bond stiffness for larger bar diameters with higher reinforcement ratios (fig. 5).

3. DEPTH

The shear strength of longitudinal reinforced concrete members decreases with increasing depth d. A reason might be deduced from the analogy to the size dependency of the flexural tensile strength. The region, where a nonlinear stress transfer takes place due to the tensile softening behaviour, becomes smaller for increasing depths (fig. 3). From tests on NSC [6, 7, 8, 9] it was found, that v_u is proportional to $d^{-1/3}$. The test results of Iguro et al. [7] indicate that this is valid for d < 1.5 m (fig. 6). For d > 1.5 no further substantial decrease occurs. For HSC, tests with d > 50 cm are not available.

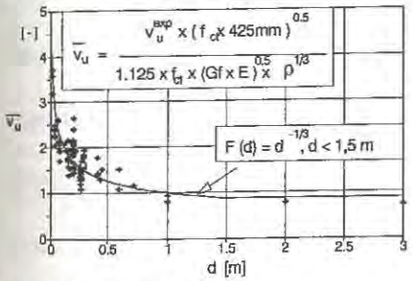

Figure 6. Effect of depth

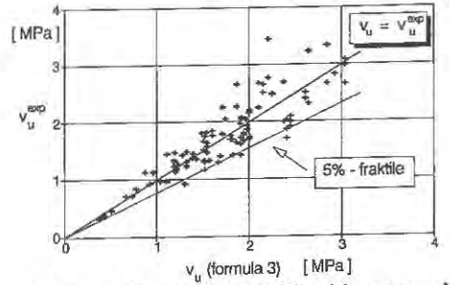

Figure 7. Comparison of (3) with test results

Concerning the contribution of the aggregate interlock to the shear strength, investigations of Walraven et al. [12] indicate an underproportional increase of the shear friction capacity for higher concrete strengths. However, no test results are available for f_c > 70 MPa. For higher concrete it is supposed, that the natural roughness and the higher stiffness and strength of the crack faces compensate the loss of the aggregate interlock. For the following a correlation of the crack-face interlock with the tensile strength (1) is assumed. The preceding study of the parameters, which effect the shear strength, shows that they influence one another. Therefore, it seems to be justified to combine them to a multiplicative formulation (3). For the same reason, the effects of the depth and of the ductility are considered indepently from each other, contrary to [13]. For example, the bond splitting failure depends on the tensile strength as well as on its ductility.

$$v_u = C \cdot \sqrt[3]{\frac{\rho}{d[m]}} \cdot \left[\frac{G_f \cdot E}{f_{ct}^2 \cdot 425mm}\right]^{0.20} \cdot f_{ct} \qquad (3)$$

The constant C is received from a regression analysis: C = 1.125 for the mean value and C = 0.87 for the 5%-fractile (fig. 7). For G_f ,E, f_{ct} and their restrictions, see equations (1-2). According to (3), 5%-fractile, the admissible shear strength for a NSC (f_c = 25 MPa) with d = 25 cm and ρ = 0.50% is 0.023 f_c. The corresponding value for an HSC (f = 80MPa) amounts 0.011 f_c. However, this relative decrease means an absolute increase of ~50%.

CONCLUSION

The results of shear tests on longitudinal reinforced concrete members without shear reinforcement and the formula (3), which is deduced from them, show: The underproportional increasing tensile strength f_{ct} and the decrease of the ductility result in a relative decrease of the shear strength. For concrete strengths higher than 80 Mpa no further increase, but also, no further decrease of the shear strength is observed. This corresponds with the dependency of both the fracture energy and the tensile strength from the compression strength. This underlines the strong influence of the tensile behaviour on the shear capacity.

REFERENCES

1. Mphonde, A.G., Frantz, G.C.: Shear Tests of High- and Low-Strength Concrete Beams Without Stirrups, ACI Journal, July-August 1984, pp 350-357
2. Ahmad, S.H., Khaloo, A.R., Poveda, A.: Shear Capacity of Reinforced High-Strength Concrete Beams, ACI Journal, March-April 1986, pp 297-304
3. Elzanathy, A.H., Nilson, A.H., Slate, F.O.: Shear Capacity of Reinforced Concrete Beams Using HSC, ACI Journal, March-April 1986
4. Bernhardt, C.J., Fynboe, C.C.: High-Strength Concrete Beams, in Nordic Concrete Research, Norske Betongforening, Oslo 1986
5. Thorenfeldt, E., Drangsholt, G.: Shear Capacity of Reinforced High-Strength Concrete Beams, in Utilization of High-Strength Concrete, Symposium, Berkeley, May 1990
6. Leonhardt, F., Walther, R.: Schubversuche an einfeldrigen Stahlbetonbalken mit und ohne Schubbewehrung, Deutscher Ausschuß für Stahlbeton, No 151, 1962
7. Iguro, M., Shioya, T., Nojiri, Y., Akiyama, H.: Experimental Studies on the Shear Strength of Large Reinforced Concrete Beams Under Uniformly Distributed Load, Proceedings, Japan Society of Civil Engineers No 348, pp 175-184, Tokio 1984
8. Walraven, J.: Scale Effects in Unreinforced Webs, Loaded in Shear, In: Progress in Concrete Research, Vol. 1, TU Delft 1990
9. Bazant, Z.P., Kazemi, M.: Sice Effect on Diagonal Shear Failure of Beams Without Stirrups, ACI Structural Journal, May-June 1991
10. König, G., Remmel, G.: Tensile Behaviour of High-Strength Concrete, FraMCoS1
11. CEB-FIP Model Code 1990, Bulletin d'Information, Nr. 203-205, Lausanne 1991
12. Walraven, J.C., Frénay, J., Pruijssers, A.: Influence of Concrete Strength and Load History on the Shear Friction Capacity of Concrete Members, PCI-Journal, 1987, No 1
13. Gustafsson, P.J., Hillerborg, A.: Sensitivity in Shear Strength of Longitudinally RC Beams to Fracture Energy of Concrete, ACI Structural Journal, May-June 1988

EVALUATION OF STEEL STRESSES IN REINFORCED AND PRESTRESSED CONCRETE CRACKED ELEMENTS - A FRACTURE MECHANICS APPROACH.

ALI SHERIF SALAH EL DIN
Professor of Strength of Materials, The University of Tanta, Tanta, Egypt
and
Associate of DAR AL-HANDASAH CONSULTANTS (SHAIR AND PARTNERS), Cairo, Egypt.

ABSTRACT

A theory, named the Arrest-Propagation Verge theory, is developed for the stability of cracks in reinforced and prestressed concrete elements. The theory is applied to predict the cracking moment and the load-steel stress relationship for cracked reinforced and prestressed concrete beams tested by other investigators. It is believed that the general form of the theory makes it readily applicable not only to beams but also to other structural concrete elements.

INTRODUCTION

Reinforced and prestressed concrete structures are designed to generally satisfy two limit states, namely, the limit state of strength and the limit state of serviceability. The latter state usually requires the analysis of cracked concrete members, under service loads, to evaluate the stresses in each of the concrete and the steel. There are several conventional theories that are in use for such analysis, but none of them is based on a real consideration of the mechanism of cracking of the concrete and the crack arrest offered by the reinforcing or the prestressing steel. For this reason each one of the conventional theories has its own limited range of applicability.

The concepts of Linear Elastic Fracture Mechanics, LEFM, offer a viable alternative for developing a general unified theory for the analysis of cracked concrete elements. Early attempts of using LEFM for cracked reinforced concrete element were made by Naus et al. [1] in 1970 and followed by Carpinteri [2] in 1981. Models developed in those two studies were not readily applicable for quantitative analysis of cracked concrete members. The author [3] in 1989, has developed a theory based on the concepts of LEFM for the analysis of cracked concrete elements which were verified by successfully evaluating the steel stress in a number of reinforced and prestressed concrete beams of rectangular sections. In this paper, this theory is re-introduced under the name " Arrest-Propagation Verge" theory. Also the validity of the theory is reaffirmed by applying it to predict the cracking moment as well as the entire load- steel stress diagram from the onset of cracking up to the yielding of steel in reinforced and prestressed beams of different configurations.

THE ARREST-PROPAGATION VERGE THEORY

The Arrest-Propagation Verge theory postulates that "When concrete cracks propagate in a reinforced or prestressed concrete element the reinforcement develops constraining forces of magnitude just enough to bring the cracks to the verge of arrest". The theory will be explained here with the help of the model shown in fig. 1 for a crack propagating in the pure bending zone of a reinforced or prestressed concrete element.

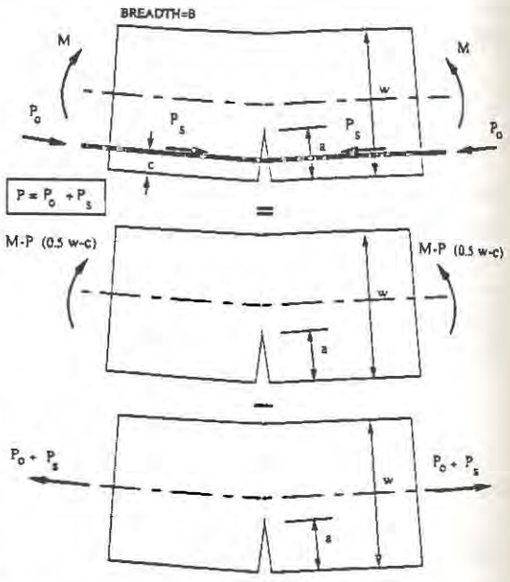

Figure 1 . Model for crack propagation in pure bending zone

Suppose an initial crack of size a_o is subjected to the driving action of the applied moment M and the constraining action of the force in the steel P. The force in the steel consists of the initial force P_o such as the prestressing force and the increase of the force in the steel due to concrete cracking, P_s. According to LEFM this crack is at the verge of propagation if the combined stress intensity factor K_I due to the driving and the constraining actions becomes equal to fracture toughness of the concrete K_{Ic}. At this stage let the driving action M be gradually incremented to $M_1 = M + \Delta M$, then K_I will exceed K_{Ic} and the crack will start propagating. If due to crack propagation the system is not capable of developing its constraining action, or it can only develop little additional constraining action, the crack will continue to propagate as in the cases a and b of fig. 2. This situation represents the condition when yielding or slippage of the steel occurs.

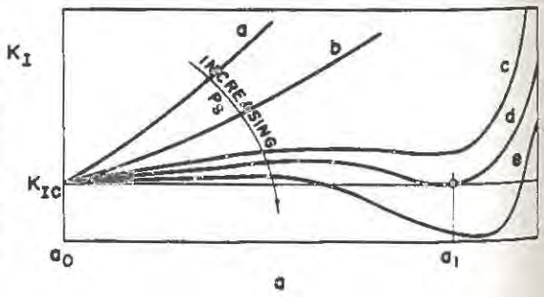

Figure 2 . Schematic K-a relation

If , however, the system is capable of developing an ever increasing constraining action with crack propagation, the K-a curve starts to move downward and bend forming a spoon like curve, curves c, d and e in fig. 2. As the curve continues to move downward the trough of the spoon head reaches first the level of K_{Ic} and it is at this point the crack is brought to the verge of arrest at a size equals a_1 and under the action of a driving action M_1. Once this point is reached the system ceases to develop its constraining action anymore and curve e in fig. 2 can never be formed. At this same point the crack is also at the verge of propagation because any slight increase of M_1 will cause the crack to propagate. Therefore, it can be said that cracks in concrete structures are always at the Arrest-Propagation Verge; APV, at which the following two conditions are true:

$$K_I = K_{Ic} \quad (1)$$

$$dK_I / da = 0 \quad (2)$$

The above two conditions are enough to determine the unknowns in any cracked concrete element; i.e., the crack size a and the constraining action (steel force) P_s at the APV. The steel stress can then be calculated by dividing the obtained value of P_s by the cross sectional area of the steel provided. It can also be argued that the smallest driving action at which the above two conditions are simultaneously satisfied represents the cracking moment of the concrete element M_{cr}.

MORE VERIFICATION OF THE APV THEORY

The APV theory has been verified [3] by applying it to predict the steel stresses in 7 reinforced and 7 prestressed concrete beams of rectangular sections. It was found that the theory predicts steel stresses higher than those obtained by conventional theory and by

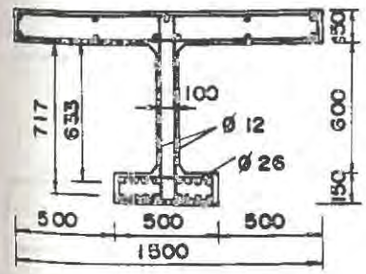

CROSS SECTION OF BEAM T1

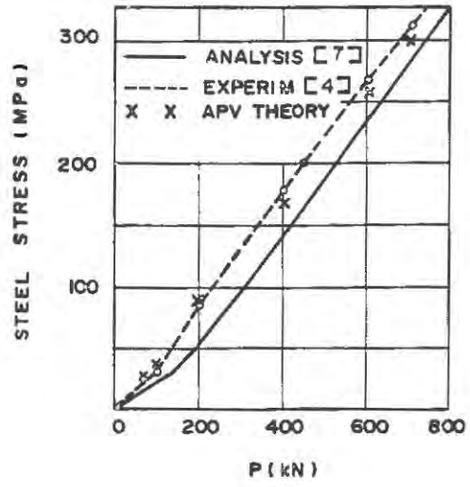

Figure 3 . Details and comparison with beam tested in Ref. [4]

measurements with an average value of 10.3% and 7.9% respectively.

In this paper, the APV theory is applied to predict the cracking moment and the entire load-steel stress relationship for 3 beams tested by Leonhardt and Walther [4] (data obtained from reference [7]), Rogowsky et al. [5] and Shenoy and Frantz [6]. The expressions for the stress intensity factor required for the application of the APV theory are given in reference [3]. Figures 3, 4 and 5 show details of the tested beams and comparisons between the experimental load - steel stress relationship and that obtained by the APV theory using K_{Ic} =

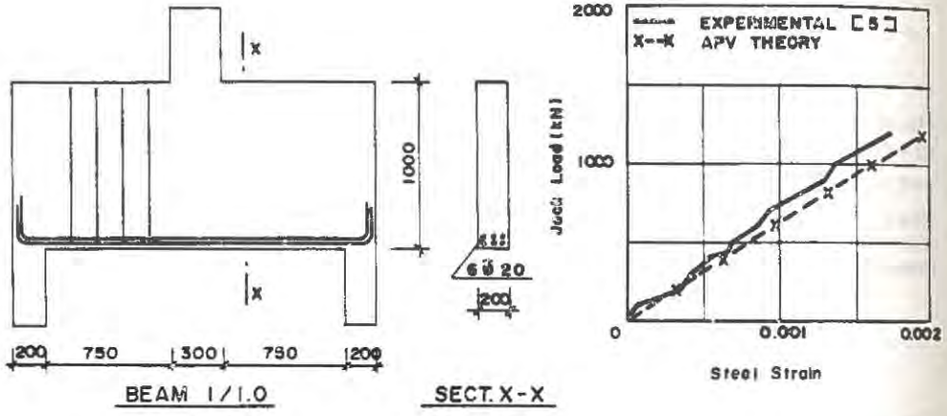

Figure 4 . Details and comparison with beam tested in Ref. [5]

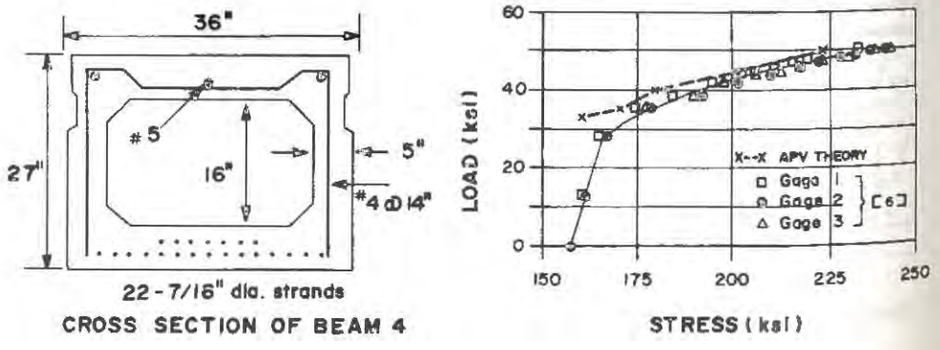

Figure 5 . Details and comparison with beam tested in Ref. [6]

900 KN/m$^{3/2}$. Reasonable to good agreement between the experimental and the APV theory is evident from these figures. It can also be seen from fig. 3 that the agreement between the results obtained by the APV theory and the experimental data of reference [4] is much better than that between the latter and the results obtained using the layer finite element model [7].

Figure 6 shows the predicted values of the steel stress against the corresponding measured values. The figure includes all the data of this study and those published in reference [3]. It can be seen that most of the predicted values lay within a range of 85% to 115% of the measured values. The discrepancies between the APV predicted steel stresses and the measured stresses may be attributed to one or more of the following reasons:

1- Approximations in the expressions of the stress intensity factor used in the application of the APV theory.

2- The fact that the APV theory predicts steel stresses at the centroid of the steel area whereas most of the measured stresses are for the lower layer of the steel bars.

3- The fact that the APV theory predicts steel stresses at the concrete crack whereas the measured values represent the steel stress at the location of the gauge which does not necessarily coincides with the crack.

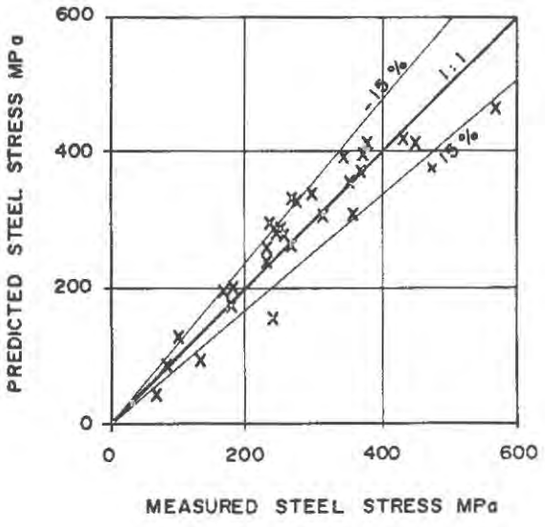

Figure 6. APV predicted virsus measured steel stresses

The APV theory is also used to predict the cracking loads shown in table 1 for those three tested beams [4-6].

TABLE 1
Predicted and observed cracking load.

Beam No. Ref. No.	Predicted values of cracking load P_{cr}	Conc. tensile stress at predicted P_{cr} (N/mm^2)	Observed values of cracking load
T1 Ref.[4]	74.8 KN	3.2	----
1/1.0 Ref.[5]	163.2 KN	3.1	----
4 Ref.[6]	33 Kip	----	35.5 Kip

It can be seen that for beams T1 and 1/1.0 the concrete tensile stress corresponding to the predicted cracking loads are in the expected range of the flexural strength of concrete . Also the predicted cracking load for beam number 4 of 33 kip is close to the experimentally observed load of 35.5 kip.

CONCLUSIONS

A general theory for crack stability in structural concrete elements has been developed. The theory is based on the concepts of LEFM and is assigned the name "Arrest-Propagation Verge (APV) theory. It is found that the APV theory is capable of evaluating the cracking load and the load-steel stress relationship from the onset of concrete cracking to the yielding of steel for reinforced and prestressed concrete beams. The APV theory is readily applicable to other structural concrete elements provided that the expresions for the stress intensity factor for the case in hand are available.

REFERENCES

1. Naus, D., Rejali, H. M., Lott, J. L. and Kesler, C. E., Cracking of concrete, Bulletin 504, Engineering Experiment Station, College of Engineering, University of Illinios, 1970.

2. Carpinteri, A., A fracture mechanics model for reinforced concrete collapse, IABSE Colloquium on Advanced Mechanics of Reinforced Concrete, Delft, 1981.

3. El Din, A. S. S., A LEFM approach for evaluating steel stresses in reinforced and prestressed concrete cracked elements, Proceedings of The Third Arab Structural Engineering Conference, U.A.E. University, U.A.E., 1989, Vol. 4, pp. 315-32.

4. Leonhadt, F., and Walther, R. Stuttgarter Schubversuche 1961, Special issue, Beton und Stahlbeton, Ernest & Sohn, Berlin, Germany, 1962, (in German).

5. Rogowsky, D., M., MacGregeor, J.,G., and Ong S.,Y., Tests of reinforced concrete deep beams, ACI Journal, V. 83, No. 4, July-August 1986, pp. 614-23.

6. Shenoy, C., V., and Frentz, G., C., Structural tests of 27-year-old prestressed concrete bridge beams, PCI Journal, V. 36, No. 5, September-October 1991, pp. 80-90.

7. Rericha, P., Layer model of bending-shear failure in RC plates and beams, J.. Struct. Engrg., ASCE, Vol. 107, No. 10, October 1991, pp. 2865-83.

FRACTURE OF REINFORCED CONCRETE CLWL-DCB SPECIMENS

S. N. Bullington*, N. M. Hawkins**, and A. S. Kobayashi***
*INCA Engineers Inc., Bellevue, WA 98005
**Department of Civil Engineering, Univ. of Illinois, Urbana, IL 61801
***Department of Mechanical Engineering, Univ. of Washington
Seattle, WA 98195

ABSTRACT

Tests were made on CLWL-DCB fracture specimens, with and without reinforcing bars crossing the precast starter notch, to examine use of fracture mechanics concepts developed from tests on plain concrete for reinforced concrete analyses. Those tests showed that realistic analyses must include the creep strain in the concrete and the residual forces developed in the concrete and steel due to shrinkage effects.

INTRODUCTION

The use of fracture mechanics concepts for reinforced concrete design requires use of standard finite element programs capable of modeling fracture process zone (FPZ) effects, overall material behavior, and any additional effects introduced by reinforcement. Analyses (1) of crack line wedge loaded-double cantilever beam (CLWL-DCB), specimens tested previously (2) using the finite element program ANSYS (3) showed that commercial programs could accurately model the behavior of plain concrete specimens. This study was to determine what modifications were needed for the finite element model for plain concrete to accurately predict the response of reinforced concrete CLWL-DCB specimens.

EXPERIMENTAL PROCEDURE

Ten CLWL-DCB specimens were made using steel forms, high early strength Portland cement, a local Seattle sand, and a gravel aggregate of 1/4 in. maximum size. The geometry and instrumentation for a typical specimen are shown in Fig. 1. A notch of 1/4 inch width and 7 inch length was precast in the specimen and a No. 3 or No. 4 reinforcing bar extended the width of the specimen at 3 inches from one edge. When a No. 4 bar was used a half inch length, centered on the notch,

was machined to 0.397 inch diameter. All specimens were effectively continuously moisture cured until one day prior to test. Specimens 1 through 7 contained No. 3 bars and were tested at an average age of 160 days. Specimens 8 through 10 contained No. 4 bars and were tested an average age of 50 days. Concrete strengths at time of test were as follows: specimens 1 through 4, 4440 psi; specimens 5 through 7, 6770 psi; and specimens 8 through 10, 6250 psi. The yield stresses for the No. 3 and No. 4 bars were 66,930 and 71,990 psi, respectively. For specimen 8, the reinforcing bar was cut with a hacksaw, where it crossed the notch, immediately prior to the start of testing. Displacement controlled tensile loads were applied to the protruding ends of the bar and crack lengths for increasing displacements were measured using a replica film technique (2). Clip gages measured the crack opening displacements at the locations $2V_1$ and $2V_2$ in Fig. 1 and electrical resistance gages of 1/4 inch gage length measured bar strains for the protruding ends and the notch. Specimens were loaded to failure in approximately seven equal displacement increments.

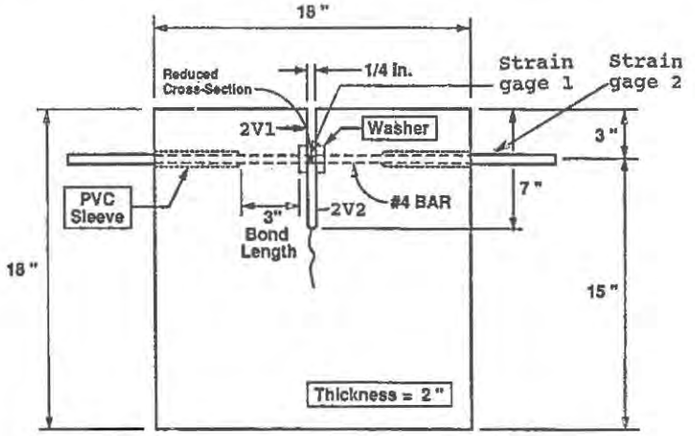

Figure 1. Typical test specimen and instrumentation

TEST RESULTS

Effect of Creep Strains

Shown in Fig. 2 is the force versus $2V_1$ relation for specimen 8 compared to that predicted for the same strength plain concrete specimen using the computer program ANSYS and the FPZ model of Ref. (4). The two responses are very similar except for the decrease in the capacity of specimen 8. Restraint of concrete shrinkage by the reinforcement caused compression in that reinforcement that was balanced by an equal concrete tension. That tension caused a creep strain. Severance of the reinforcement released that compression and the balancing elastic tension in the concrete. However, it could not release the creep strain caused by that tension. The result for specimen 8 showed clearly the significance of the residual force caused by shrinkage but not the magnitude of that force. The result showed the fictitious

force, F_E, that produced an elastic strain in the specimen equal to the magnitude of that creep strain. The force F_E was 534 lbs for a specimen which, if it had been plain concrete, would have had a capacity of about 1800 lbs. Clearly the crack closure stresses, (CCS), in the FPZ are strain rather than stress dependent.

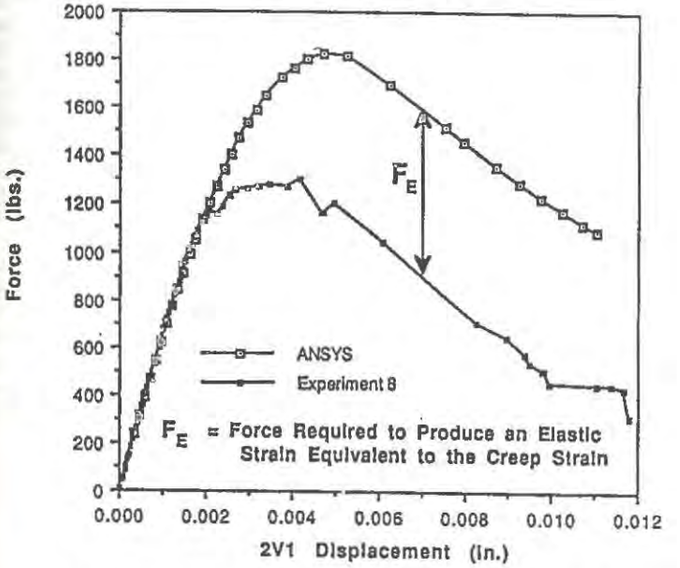

Figure 2. Effect of creep strain on response Comparison of ANSYS and specimen 8 results

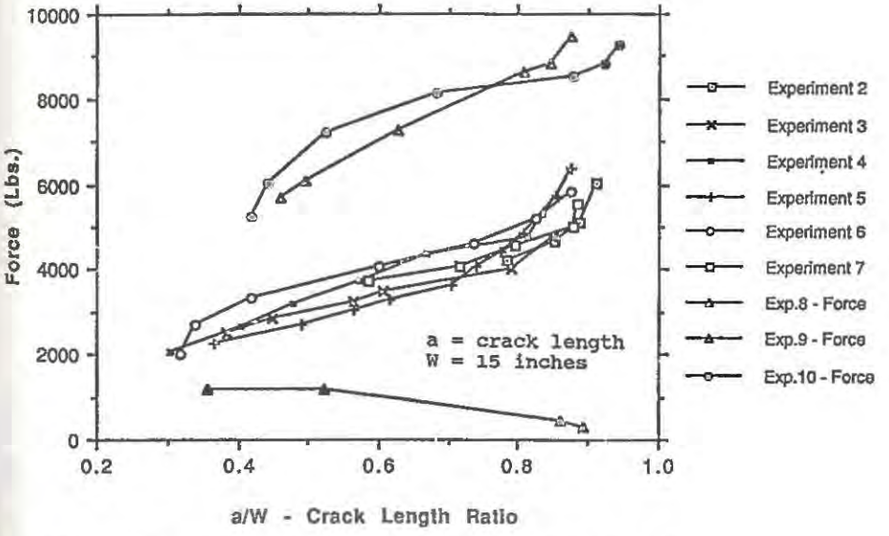

Figure 3. Force versus crack lengths ratios

Force Versus Crack Length Ratios

Shown in Fig. 3 are force versus crack length ratios for all specimens. Those with No. 3 bars cracked at smaller forces than those with No. 4 bars. That result was not due to concrete strength differences since specimens 5 through 7 had similar strengths to specimens 9 and 10. Nor was it due to different bar areas since the cross-section at the notch was almost the same for all specimens. Only differences in residual force, or bond length parameters could have caused those differences. Residual forces and creep strains were different for the specimens with No. 3 and No. 4 bars, but analysis showed that effect did not explain the differences in behavior. Only the variations in bonded bar length and size could have caused the differences. For a given applied load, No. 3 bar specimens experienced more strain due to their smaller size. That strain was transferred to the concrete over a longer bond length, producing greater strains on the crack line than for No. 4 bar specimens. This result shows the need, for fracture applications, to better understand interaction effects caused by crack spacing and bond.

Crack Profile and Bar Strain

Shown in Fig. 4 is a comparison between $2V_1$ and $2V_2$ displacements and crack length ratios for specimens 8 and 10. Cutting the bar did not change substantially the crack profile characteristics. Clearly direct comparisons of the behavior of plain and reinforced specimens are valid.

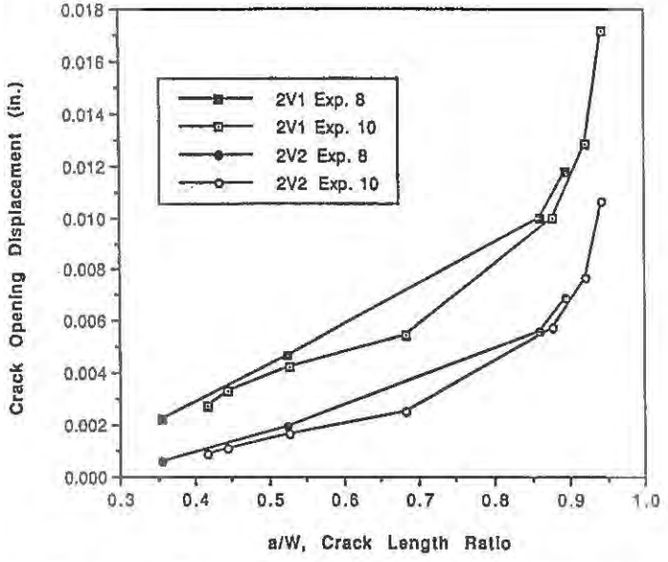

Figure 4. 2V1 and 2V2 displacements versus crack length ratio

The relation between bar strains at the notch and $2V_1$ was linear initially. However, once the steel's stress-strain relation became non-linear the bar pivoted about the crack. Between a strain of 0.002 ($2V_1$ = 0.004in) and yield $2V_1$s increased faster than strains. However, after yielding at a strain of 0.0027, the non-linearity direction reversed.

NUMERICAL ANALYSIS

For analysis a distinction must be made between absolute and apparent forces. The fracture behavior, in terms of absolute forces, was similar for specimens 8 and 10. The relation of the absolute concrete force to $2V_1$ and the crack length was almost the same for both specimens and the relation of the absolute steel force to the bar strain for specimen 10 was the same as the relation for that bar tested in air. The experimental techniques measured apparent forces only. They measured neither the initial compressive force in the steel caused by concrete shrinkage nor the change in force recorded by the load cell of the testing machine due to progressive transfer of that shrinkage force to the testing machine as the capacity of the specimen deteriorated. The latter transfer causes a drift in load cell values that directly affects post-peak values. As shown in Fig. 5, "apparent" concrete force versus $2V_1$ values for specimen 10 exhibited a post-peak slope steeper than for specimen 8 even though in absolute terms the forces were descending along the same curve. For Fig. 5, the curve for specimen 10 was moved to the left by the amount of the $2V_1$ value necessary to create a force, at a $2V_1$ value of zero, equal to the F_E force for specimen 8.

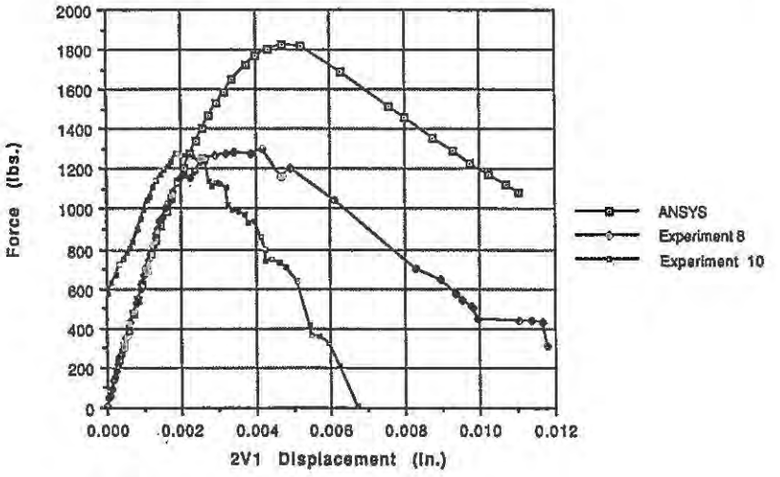

Figure 5. Effect of residual force - comparison of analytical and experimental results

A finite element analysis procedure was developed (1) to account for creep and residual force effects. Shown in Fig. 6 is the result for specimen 10, the calculated contributions to the overall resistance by steel and concrete, and the ANSYS result when creep and residual force effects were neglected. There was still tension in the concrete when the bar yielded. The failure behavior of reinforced concrete is always expressed in terms of apparent forces in the concrete and steel. Use of fracture mechanics for reinforced concrete will require procedures

that consider absolute forces and the creep strains they create. Those results will then have to be translated into apparent force effects.

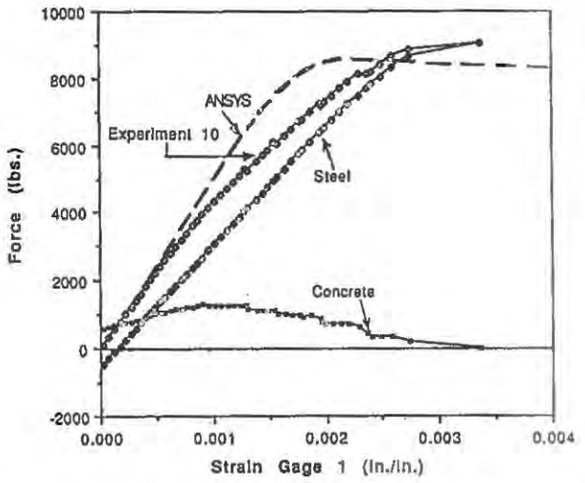

Figure 6. Total force, steel force, and concrete force versus strain at gage 1 for specimen 10

CONCLUSIONS

Finite element modeling of the fracture of reinforced concrete that account be taken of creep strains in the concrete, the residual force acting between the steel and the concrete due to shrinkage, and the transfer of that residual force to the supports with loading. Neglect of those effects results in strength predictions, for lightly reinforced members, considerably different to those obtained in physical tests.

REFERENCES

1. Bullington, S. N., Fracture in reinforced concrete DCB specimens - an experimental and analytical study. MSCE Thesis, University of Washington, Seattle, WA 1991.

2. Barker, D. B., Hawkins, N. M., Jeang, F. L., Cho, K. Z. and Kobayashi, A. S. Concrete failure in CLWL specimens. J. Engrg. Mech. ASCE 111, 1985, 623-638.

3. DeSalvo, G. J. and Gorman, R. W., ANSYS engineering analysis user's manual. Swanson Analysis Systems, Houston, PA, May 1989.

4. Liaw, B. M. et al., An improved non-linear model for concrete fracture. J. Engrg. Mech., ASCE 116 (2), 1990, 429-445.

Flexural Failure Behavior of Lightly Reinforced Concrete Beams

Keitetsu ROKUGO, Yuichi UCHIDA and Wataru KOYANAGI
Department of Civil Engineering, Gifu University
Yanagido, Gifu, 501-11, JAPAN

ABSTRACT

The results of bending tests on lightly reinforced concrete (RC) beams (reinforcement ratio: 0.10 ∿ 0.40%, effective depth: 16, 31 and 47 cm) were reported. The softening and hardening behavior and the localization of fracture were focused. When the cracking load Pcr was greater than the ultimate load Pu, only one visible flexural crack propagated and then tension reinforcing bar was broken soon after yielding. In these cases, it was observed through measured strain distribution that additional invisible cracks existed. This can be explained through the fictitious crack concept.

INTRODUCTION

The size dependent properties of strength and ductility, the localization of fracture, and the stability of failure are interesting subjects in the field of the Fracture Mechanics of Concrete. These are all relating to the softening behavior.

The failure behavior of lightly reinforced concrete beams and the minimum reinforcement ratio have been investigated [1,2,3]. In this contribution, the flexural failure behavior of lightly reinforced concrete beams differing in size is discussed on the basis of the softening concept.

OUTLINES OF EXPERIMENTS

Specimens and Testing Procedures

Seven kinds of singly reinforced concrete (RC) beams with a rectangular cross-section were tested. The sizes and the reinforcement ratios are shown in Table 1. The beams of A-series were differing in the reinforcement ratio and the width. The beams of B-series had the same reinforcement ratio (p=0.1%) but different effective depths. Two specimens were tested for each kind, except for B-2050 (one specimen). Deformed bars of D6 (diameter: 6.35 mm) were used. The yield and tensile strengths of the bars were 42.9 kgf/mm^2 and 57.0 kgf/mm^2. The compressive strength, the

TABLE 1
Kinds of specimens.

Specimen	Specimen size (cm) width, depth, length	Effective depth (cm)	Reinforcing bars	Reinforcement ratio (%)	Loading span (cm)
A-1018	**10**x18x170	15.7	2D6	**0.40**	150
A-2018	**20**x18x170	15.7	2D6	**0.20**	150
A-3018	**30**x18x170	15.7	2D6	**0.13**	150
A-4018	**40**x18x170	15.7	2D6	**0.10**	150
B-2018	20x**18x170**	**15.7**	1D6	0.10	**150**
B-2034	20x**34x330**	**31.2**	2D6	0.10	**300**
B-2050	20x**50x490**	**47.2**	3D6	0.10	**450**

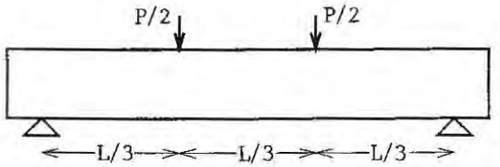

Figure 1. Loading test on RC beams.

splitting tensile strength and the flexural strength (modulus of rupture) of the concrete at the testing age (53-56 days) were 321 kgf/cm^2, 28.5 kgf/cm^2 and 52.5 kgf/cm^2, respectively.

The beams were loaded at the third points, as shown in Fig. 1. The shear span to depth ratio (a/d) was 3.2. The applied load and the loading point displacement were recorded. The strain distributions on the top (compression side) and the bottom (tension side) concrete surfaces were measured with strain gauges (length: 30 mm), which were glued continuously in the moment span.

DETERMINATION OF CRACKING LOAD, YIELD LOAD AND ULTIMATE LOAD

Experimental Determination

Cracking load Pcr: The cracking load Pcr was defined as the load when the slope of the load-displacement curve firstly changed.

Yield load Py: The yield load Py of the beams was defined as the load when the slope secondly changed. When the load dropped after cracking, Py was taken to be the bottom value of the load.

Ultimate load Pu: The ultimate load Pu was taken as the maximum load after the yielding.

Calculation through Rough Method

Cracking load Pcr1: The cracking load Pcr1 was calculated as the load when the stress in concrete reached the flexural strength.

Yield load Py1: When calculating the yield load Py1, the tensile resistance of concrete was neglected.

Ultimate load Pu1: The ultimate load Pu1 was calculated according to JSCE code [4], assuming the safety factors to be 1.0. The work hardenin of steel bars was considered. The tensile strength of steel bars was used instead of the yield strength when the reinforcement ratio was smaller than 0.13 %.

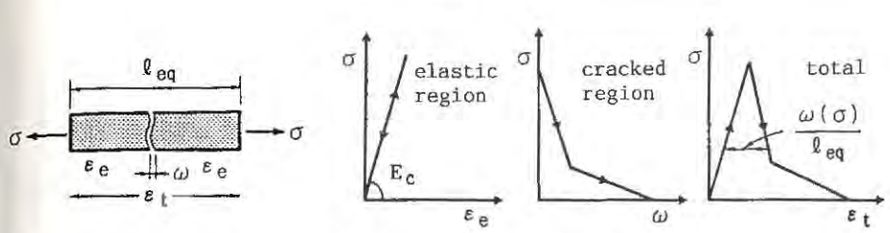

$$\varepsilon_t = \sigma / E_c \qquad (\varepsilon_t \leqq f_t / E_c)$$
$$= \sigma / E_c + \omega(\sigma) / \ell_{eq} \qquad (\varepsilon_t > f_t / E_c)$$

where,

$$\frac{\ell_{eq}}{\ell_{ch}} = 1 - (1 + 0.5\,(d/\ell_{ch}))^{-1.6}$$

$$\ell_{ch} = E_c G_F / f_t^2$$

ℓ_{eq}: equivalent length, σ: tensile stress, ε_t: tensile strain, E_c: elastic modulus, $\omega(\sigma)$: function of tension softening curve, G_F: fracture energy, f_t: tensile strength, d: beam depth.

Figure 2. Tensile stress-strain curve of concrete [5].

Calculation through Refined Method Considering Concrete Tension Softening

Cracking load Pcr2 and yield load Py2: The cracking load Pcr2 and the yield load Py2 were calculated through the so-called discrete element technique in which the tension softening diagram of concrete was taken into account as shown in Fig. 2 [5].

TEST RESULTS AND DISCUSSIONS

Test results are tabulated in Table 2. The values in Table 2 are the average of two specimens except for B-2050. The values of loads in Table 2 are modified considering the effect of the beam weight. The load-displacement curve, the final crack map, and the strain distributions on compression and tension concrete surfaces are shown in Figs. 3 to 8.

TABLE 2
Test results.

Specimen	Crack load (kgf)			Yield load (kgf)			U. load (kgf)			Number
	Exp.	Calculation		Exp.	Calculation		Exp.	Cal.	Pu	of
	Pcr	Pcr1	Pcr2	Py	Py1	Py2	Pu	Pu1	Pcr	cracks
A-1018	1040	1130	910	1800	1580	1680	2070	1790	1.99	12
A-2018	1670	2270	1730	1870	1620	1820	2210	2020	1.32	6
A-3018	2780	3400	2560	[2080]	1630	1940	2360	2210	0.85	1
A-4018	3270	4540	3380	[1980]	1640	2050	2300	2240	0.70	1
B-2018	1670	2270	1690	[1050]	820	1030	1170	1120	0.70	1
B-2034	2730	4050	2760	[2070]	1630	1830	2400	2230	0.88	1
B-2050	3750	5830	3800	[3140]	2470	2690	3690	3370	0.98	1

[ ]: bottom value of load after cracking.

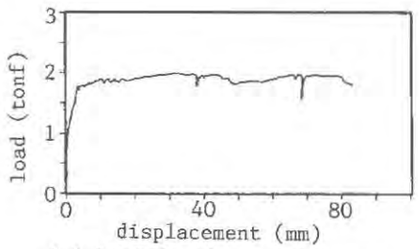

(a) Load-displacement curve

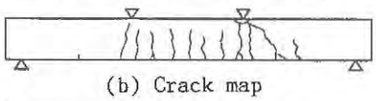

(b) Crack map

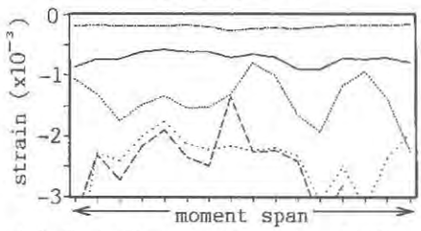

(c) Distribution of comp. strain

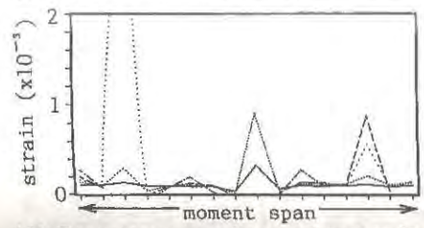

(d) Distribution of tensile strain

Figure 3. A-4018 specimen (p=0.40%).

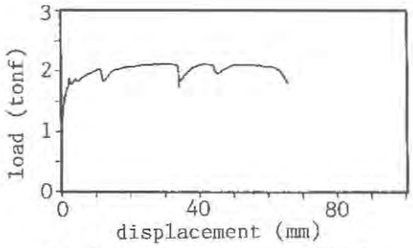

(a) Load-displacement curve

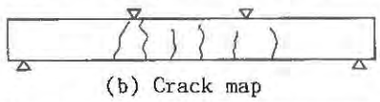

(b) Crack map

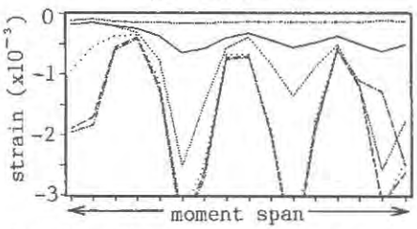

(c) Distribution of comp. strain

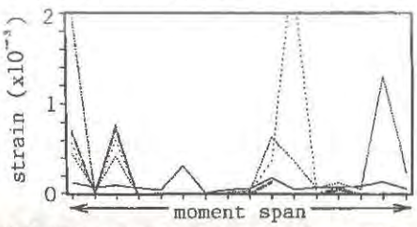

(d) Distribution of tensile strain

Figure 4. A-2018 specimen (p=0.20%).

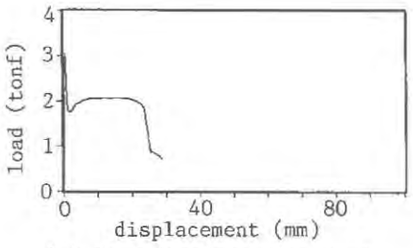

(a) Load-displacement curve

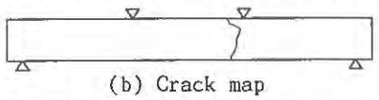

(b) Crack map

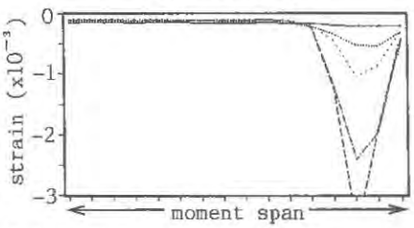

(c) Distribution of comp. strain

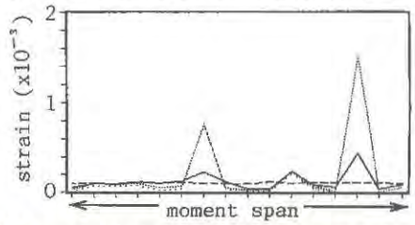

(d) Distribution of tensile strain

Figure 5. A-4018 specimen (p=0.10%).

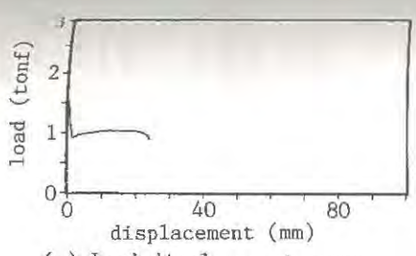

(a) Load-displacement curve

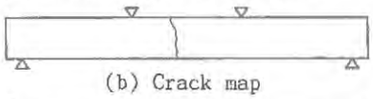

(b) Crack map

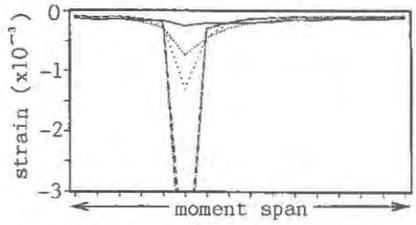

(c) Distribution of comp. strain

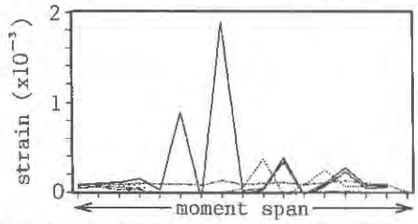

(d) Distribution of tensile strain

Figure 6. B-2018 specimen (p=0.10%).

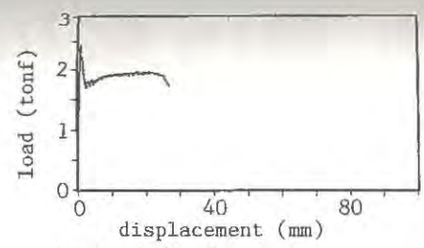

(a) Load-displacement curve

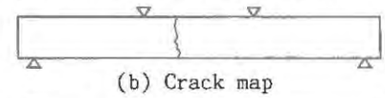

(b) Crack map

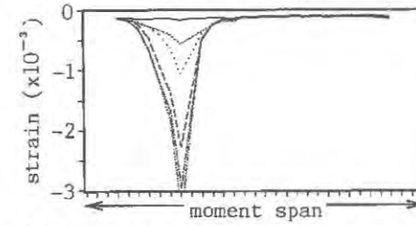

(c) Distribution of comp. strain

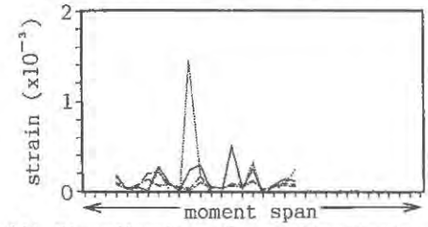

(d) Distribution of tensile strain

Figure 7. B-2034 specimen (p=0.10%).

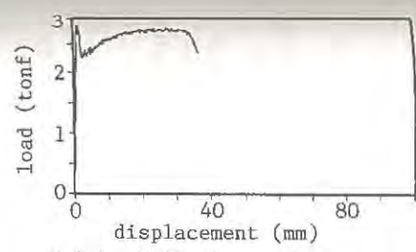

(a) Load-displacement curve

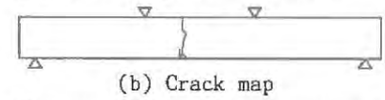

(b) Crack map

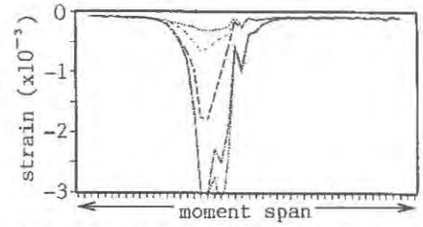

(c) Distribution of comp. strain

Figure 8. B-2050 specimen (p=0.10%).

Figures for A-3018 beam, which were similar to those for A-4018 beam, are omitted to save space.

Failure Behavior and Number of Cracks

A-1018 beams (p=0.40%) exhibited ductile failure mode as typical RC beams with many bending cracks and large displacement. In the final stage of these beams, the concrete in compression crashed but the tension reinforcing bars did not rupture. A-2018 beams (p=0.20%) also failed in the ductile mode, while the tension reinforcing bars finally ruptured.

In the cases of the other beams (p≤0.13%), the load suddenly dropped after only one macro bending crack appeared. The load slightly increased with displacement due to the work hardening of the steel. Then the tension reinforcing bars soon ruptured at smaller beam displacement due to the concentration of the deformation.

Distribution of Strain

The strain in compression was relatively uniform for A-1018 beam (Fig. 3), but was localized at the top of the bending crack for the beams with only one macro crack (Figs. 5 to 8).

For beams with only one macro crack, there are many peaks in the strain distribution in tension. This means that additional invisible micro cracks were detected with strain gauges. This can be explained through the fictitious crack concept. That is, in the case of concrete beams in bending, the load at opening of a visible flexural crack is higher than the load when the stress in the tension surface reaches the tensile strength and the fictitious crack stars because of the tension softening properties of concrete.

Comparison of Measured and Calculated Loads

The calculated cracking loads Pcr2, which were calculated considering the tension softening of concrete, are in good accordance with the measured cracking loads Pcr. The calculated yield loads Py2 with tension softening of concrete are also better than the values of Py1 calculated through the rough method. It can be concluded that the tension softening properties of concrete should be considered when calculating the cracking load and the yield load, especially for lightly reinforced concrete beams.

The ultimate loads Pu1, which were calculated using the tensile strength of steel bars instead of the yield strength, are close to the measured values of Pu.

Failure Mode of RC Beams and Minimum Reinforcement Ratio

In the softening process (load decreases with deformation) the failure zone tends to localize, but in the hardening process (load increases with deformation) the failure zone spreads. This is the nature of the failure phenomena.

The hardening process is needed after the cracking in order that RC beams fail in ductile mode with plural cracks. The ultimate load Pu must be greater than the cracking load Pcr. This is the basic concept for the minimum requirement for the tension reinforcement ratio. Precise calculation of both Pu and Pcr is important especially for lightly reinforced concrete beams. The concept of this minimum reinforcement ratio would be effective also for the combined use of new materials such as resin concrete, high strength concrete, high strength reinforcing bars, FRP rods, etc.

The relation between Pcr and Pu for B-series is shown in Fig. 9. Pu is almost proportional to the effective depth d, but Pcr is not. Therefore, it is expected from Fig. 9 that Pu becomes greater than Pcr (the relation

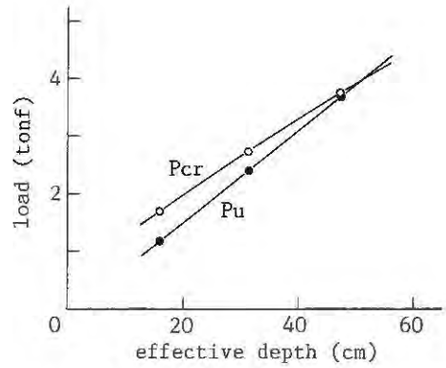

Figure 9. Relation between Pcr and Pu obtained from experiments.

is reversed) and the beam fails in the ductile mode if the effective depth d is larger than 60 cm. The effective depth of RC beams is one of the factors affecting on the minimum reinforcement ratio of RC beams, because the cracking load Pcr is size-dependent.

CONCLUSIONS

When the cracking load Pcr was greater than the ultimate load Pu, only one visible flexural crack propagated and then tension reinforcing bar was broken soon after yielding. The effective depth of RC beam is one of the factors affecting the minimum reinforcement ratio.

It is pointed out that the tension softening properties of concrete must be taken into account for the precise calculation of the flexural cracking load Pcr and the yield load Py especially for lightly reinforced concrete beams.

For the case of RC beams failed with one main crack, the fracture zone of concrete in compression localized at the top of the crack. It was observed through measured strain distribution that additional invisible cracks existed. This can be explained through the fictitious crack concept.

REFERENCES

1. Bosco, C., Carpinteri, A. and Debernardi, P.G., Size effect on the minimum steel percentage for reinforced concrete beams. Fracture of Concrete and Rock: Recent Developments, Elsevier Applied Science, 1989, pp.672-681.
2. Shima, H., Niwa, J. and Okamura, H., Prevention of brittle failure of beams with low reinforced ratio in bending. Proc. of JSCE, No.378, 1987-2, pp.231-237 (in Japanese).
3. Ikeda, S, Yamaguchi, T. and Goto, Y., Study on the flexural behavior of reinforced concrete beams with low reinforcement. Concrete Research and Technology, JCI, Vol.1, No.1, 1990, pp.51-59 (in Japanese).
4. JSCE, Standard specification for design and construction of concrete structures, 1991.
5. Uchida, Y., Rokugo, K. and Koyanagi, W., Application of fracture mechanics to size effect on flexural strength of concrete. Proc. of JSCE, No.442, 1992-2 (in Japanese).

CHOOSING THE RIGHT CONCRETE FOR PILES: AN APPLICATION IN CONCRETE FRACTURE MECHANICS

MANUEL ELICES, GUSTAVO V. GUINEA and JAIME PLANAS
Dpto. Ciencia de Materiales, Universidad Politécnica de Madrid,
E.T.S. Ingenieros de Caminos, Ciudad Universitaria, 28040-Madrid. Spain.

ABSTRACT

This contribution provides an example of an application of Fracture Mechanics concepts to a practical concrete problem. Reinforced concrete piles made with two concretes having the same standard mechanical properties (compressive and tensile strength and elastic modulus) behaved in a different way; one set of piles was more brittle than the other. Fracture mechanics concepts provided some clues for solving this problem by disclosing the relevant parameter, the fracture energy G_F, and by suggesting procedures to improve its value.

INTRODUCTION

Although reinforced concrete piles have proved their ability to take a great amount of punishment without structural damage, sometimes fracture occurs during hammering. This paper presents an example of pile damage during driving and how this problem was analyzed using Fracture Mechanics concepts applied to concrete.

A Company producing concrete piling, found that the piles coming from one of their two pile precast factories (Factory A) occasionally showed brittle behaviour when being hammered. The design of the reinforced piles was the same as that of the other factory (Factory B). Figure 1 shows a typical section of these piles, whose length is usually 12 m, and Fig. 2 an example of a brittle failure during hammering.

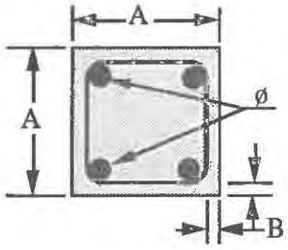

A = 235, 270 or 300 mm.
B = 25 mm.
ø= 12 or 20 mm.

Figure 1. Cross-section of concrete piles.

Figure 2. Example of brittle fracture of a pile made of concrete A.

Concrete mixes were nominally identical for both factories, but the aggregates came from different quarries. The mechanical properties of both concretes, as measured through tensile and compressive stresses, and Young modulus, were almost the same or even better for concrete from factory A. No classical approach could explain the differen behaviour of the two concretes, since the conventional strengths of the *brittle* concrete A were never below those of the *well behaved* concrete B.

Looking for fracture parameters, the specific fracture energy G_F was measured in both concretes. It turned out that G_F and the characteristic length were much lower for concrete A than for concrete B, so that the theoretical brittleness correlated well with the observed brittleness. Such measurements and some actions undertaken to improve concrete A are described in detail in the next sections.

CONCRETE PILE PROPERTIES

Strong concrete is usually required for piles. The mixix design of both concretes, A and B, was the same —as already mentioned— and is shown in Table 1.

TABLE 1
Proportional mixing of concrete, A and B, by weight

Cement	Coarse aggregate	Fine aggregate	Water
1	2.64	2.46	0.43

Cement content 390 kg/m^3.

The cement was a rapid-hardening Portland (ASTM type III). Natural rounded aggregates, classified as siliceous, were used for concrete B and crushed dolomitic aggregates were used for concrete A. In both concretes, maximum aggregate size was 25 mm. Also 4,2 kg/m^3 of superplasticizer *Fluinel 1*® was added to the mixes.

Mechanical properties were measured from cylindrical specimens of 300 mm length and 150 mm diameter, according the ASTM standards: Compressive Strength (C.39), Tensile Strength (C.496) and Modulus of Elasticity (C.469). Average results of three samples at 28 days, are shown in Table 2.

The specific fracture energy G_F was measured according the procedure proposed by RILEM TC-50 [1], and taking into account additional refinements suggested by the authors [2, 3, 4]. Test specimens were notched beams of 100 x 100 x 850 mm.

Testing was performed in a 100 kN servohydraulic testing machine INSTRON 8501, run in actuator position control mode. Loads were measured with a 5 kN load cell with a resolution of 5 N and 0.5 percent accuracy.

TABLE 2
Concrete properties (28 days)

Concrete Type	Compressive Strength (MPa)	Tensile Strength (MPa)	Elastic Modulus (GPa)
A	57.5	5.7	48
B	43.5	4.5	36

Deflection was measured as the relative displacement of the control loading head and the line defined by the points on the upper surface of the specimen located on the verticals of the lower supports. The displacement was measured by an extensometer of accuracy better than 5 μm. In all tests, weight compensation was used.

The load-displacement curves corresponding to four tests are shown in Fig. 3.

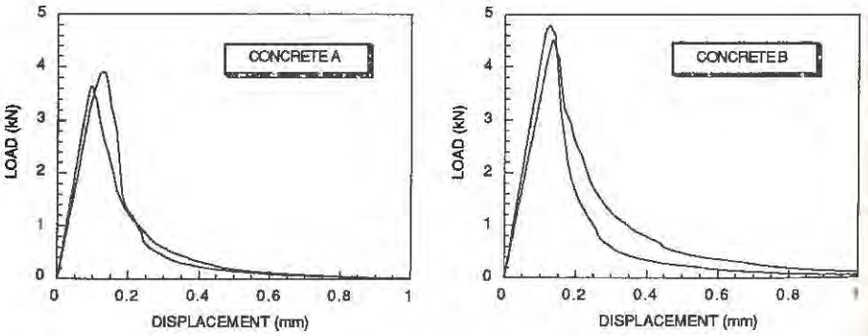

Figure 3. Load-displacement curves for concrete A and for concrete B.

Table 3 summarizes the experimental results of the specific fracture energy G_F, as well as the computed values of the characteristic size [5],

$$l_{ch} = \frac{G_F E}{f^2_t} \qquad (1)$$

where E is the elastic modulus and f_t the tensile strength.

TABLE 3
Concrete fracture properties

Concrete Type	G_F (J/m^2)	$G_{F,average}$ (J/m^2)	l_{ch} (mm)
A	102, 104	103	152
B	130, 153, 169	151	268

Fracture energy results clearly show that concrete B is tougher than concrete A — even though the standard properties are almost the same— a fact that probably is at the root of the superior performance of concrete B during hammering.

Several parameters have been proposed to characterize the brittleness of concrete structures. A useful one is the brittleness number [6]:

$$B = \frac{L}{l_{ch}} \qquad (2)$$

where L is a characteristic dimension of the structure. A higher brittleness number indicates increased brittleness. However, this number has not an absolute meaning, because the structural dimension L is open to choice. It is useful only when comparing geometrically similar structures. Since the piles from the two factories are geometrically identical, one can in principle determine the relative brittleness of the two concretes to be 1.8. Hence concrete A may be estimated to be nearly twice as brittle as concrete B, which again supports the observed field behaviour (For this to be exact, the two concretes should display a softening curve with exactly the same shape. This is probably not so, but the existing experience with other concretes tends to show that the difference must be slight)

A fractographic analysis of the broken samples revealed that, for concrete B, most of the aggregates were debonded, while for concrete A they were broken. Representative pictures of broken surfaces for both concretes are shown in Fig. 4.

Figure 4. Typical specimen fracture surfaces for concrete A (left) and B (right).

IMPROVING CONCRETE TOUGHNESS

The fractographic evidence suggests that the low toughness values of concrete A as compared with concrete B are due to its weaker aggregates. Toughness of concrete A can be improved in either of two ways: by improving the strength of aggregates, avoiding aggregate fracture and forcing the crack to bend round the aggregates, or by improving the toughness of the cementitious matrix.

The second solution was selected for economic reasons, and the matrix toughness was improved by fibre reinforcement. Polipropilene fibres (Concrefib®) of 40 mm length were used. Concrete mix and curing procedures were as previously described. For comparison purposes another set of samples similar to concrete A, henceforth called A2, were also tested.

The load-displacement curves corresponding to the RILEM tests are shown in Fig. 5 for some representative samples. It is worth noticing the large tail due to fibre reinforcement in the P-δ curves for FRC. Table 4 summarizes the main mechanical properties.

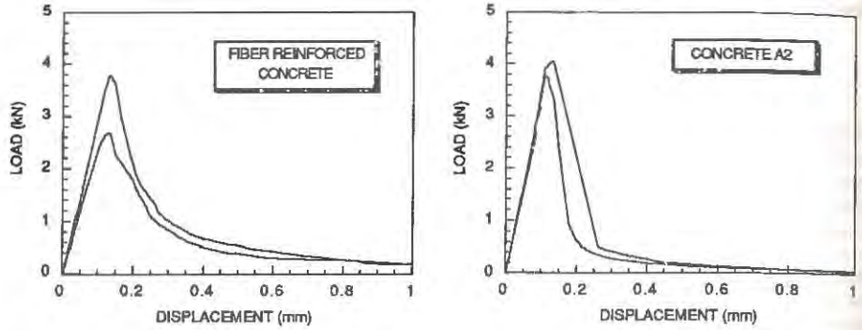

Figure 5. Load-displacement curves for fibre reinforced concrete and for concrete A2.

TABLE 4
Mechanical properties of reinforced and A2 concretes

Concrete Type	Compressive Strength (MPa)*	Tensile Strength (MPa)	Elastic Modulus (GPa)	G_F (J/m^2)	l_{ch} (mm)
Fibre Reinforced	59.4	5.0	45	157	283
A2	57.7	5.0	40	101	162

* 28 days

The specific fracture energy for fibre reinforced concrete is the average value of four measurements (115, 144, 169 and 187 J/m^2), and the corresponding value for A2 the average value of three tests (92, 101 and 123 J/m^2). The fractographic analysis of broken samples revealed that the majority of the aggregates were broken, a result expected from previous tests with concrete A. Representative pictures of broken surfaces for fibre reinforced concrete and concrete A2 are shown in figure 6.

Figure 6. Typical fracture surfaces for fibre reinforced (left) and A2 (right) concretes.

The increased toughness of fibre reinforced concrete, similar to that of concrete B, suggested the possibility of using it for piles, even though the aggregates were still weak. Further tests on piles made with FRC showed good performance during hammering and, at present, sufficient experience has been accumulated to permit safe and economic utilization of these fibre reinforced concrete piles.

FINAL COMMENTS

This research has shown —quantitatively— that concrete A is more brittle than concrete B and fibre reinforced concrete. Hence, under the same circumstances, piles made with concrete A should exhibit more brittle behaviour than piles made with the other concretes.

There is still some controversy on the measurement of *absolute* values of G_F because the results may depend on the specimen size [2, 3, 4] and on the measurement procedure (RILEM, Bazant, Shah, etc.) [7]. Sometimes, it is not necessary to reach an agreement about this point to solve the problem. This is an example where the absolute value of G_F is not needed, only relative values are of interest; an increase of 50 percent in G_F is all that was needed to drive the concrete to safe grounds.

Fracture Mechanics concepts provided a procedure for solving this problem; after pointing to the *relevant parameters*—specific fracture energy G_F and brittleness number—, this technique offered a way to *quantify* this properties and finally suggested procedures to *improve* them up to values that previous experience had shown acceptable.

ACKNOWLEDGEMENTS

The authors gratefully acknowledge partial financial support for this research provided by the Comisión Interministerial de Ciencia y Tecnología, CICYT, Spain, under grant PB90-0276, and by the Polytechnic University of Madrid under grant A-91 0020 02-31.

REFERENCES

1. RILEM TC-50 FMC (Draft recommendation), Determination of the fracture energy of mortar and concrete by means of three-point bend tests on notched beams. *Materials and Structures*, 1985, **18**, 285-90.

2. Guinea, G.V., Planas, J. and Elices, M., Measurement of the fracture energy using three oint bend tests:1. Influence of experimental procedures. *Materials and Structures*, 1992, in press.

3. Planas, J., Elices, M. and Guinea, G.V., Measurement of the fracture energy using three oint bend tests: 2. Influence of bulk energy dissipation. *Materials and Structures*, 1992, in press.

4. Elices, M., Guinea, G.V. and Planas, J., Measurement of the fracture energy using three oint bend tests: 3. Influence of cutting the P-δ tail. *Materials and Structures*, 1992, in press.

5. Hillerborg, A., Existing methods to determine and evaluate fracture toughness of aggregative materials-RILEM recommendation on concrete. In Fracture Toughness and Fracture Energy, ed. Mihashi et al., Balkema, 1989, pp. 145-51.

6. Elfgren, L., Applications of fracture mechanics to concrete structures. In Fracture Toughness and Fracture Energy, ed. Mihashi et al., Balkema, 1989, pp. 575-90.

7. Elices, M. and Planas, J., Size effect and experimental validation of fracture models. Chapter 8, in Analysis of Concrete Structures by Fracture Mechanics, eds. L. Elfgren and S.P. Shah, Chapman and Hall, 1991, pp. 99-127.

EVALUATION OF THE SHEAR BEHAVIOR OF REINFORCED CONCRETE BEAMS - A COMPARISON OF CODE AND FRACTURE MECHANICS PREDICTIONS

Tainshing Ma
Graduate Research Assistant
Civil Engineering Department
University of Kansas
Lawrence, KS 66045

Junichiro Niwa
Associate Professor of Civil Engineering
Nagoya University
Nagoya 464-01, Japan

Steven L. McCabe
Associate Professor of Civil Engineering
University of Kansas
Lawrence, KS 66045

ABSTRACT

This study evaluates the analytical behavior of a class of reinforced concrete beams without shear reinforcement. The behavior is predicted using finite element analysis and incorporates fictitious crack modeling of specified diagonal tension crack locations. The results of this analysis are compared against traditional ACI Code predictions as well as the existing provisions found in the Japanese Society of Civil Engineers (JSCE) and Comite Euro-International du Beton (CEB) concete codes.

The results of this study clearly show that the shear behavior of reinforced concrete beams can successfully be predicted using the fictitious crack model. Nonductile behavior is exhibited, as would be expected, under the types of loading and fracture planes defined in this study. Perhaps more importantly, the results indicate that there is indeed a size effect which can be clearly seen in the finite element results. Sufficient analytical work has been done to show that the size effect is a phenomenon that can be evaluated using this type of fracture model when shear behavior is considered. The comparisons of the analytical results with JSCE and CEB provisions indicate that these codes predict the behavior of the analytical specimens within an acceptable degree of accuracy, while the traditional ACI approach is less accurate.

INTRODUCTION

The shear behavior of reinforced concrete members is an important consideration in the analysis and design of concrete systems. The complexity and nonductile behavior exhibited in shear failures of reinforced concrete members makes it imperative that the capacity be

accurately predicted and potential overloads under shear be avoided. There have been numerous experimental and analytical studies over the years that have indicated that the traditional approach utilizing ACI whereby a constant value of shear stress capacity, v_c, is computed for any size member, may not be in keeping with the actual behavior exhibited.

These observations are not new. ACI-ASCE Committee 326 [1] in 1962 observed that the "approximate exact" expressions found in the ACI 318 building code [2], where effects did not predict actual behavior for members, and were recognized that the time to be interim formulations, ones that were to be improved upon in the following years. This area, of course, has been the subject of wide research. However, the basic code expressions have not changed in the intervening years in part because the alternatives offered by researchers are complex and also are not reliably accurate under all loading and geometric configurations. However, research done in the United States, in Canada, in Japan, and in Europe has increasingly pointed towards the application of alternative analytical means as the way that the shear problem can be attacked. Recently the application of fracture mechanics to the shear problem has shown great promise [3,6,13,14]. In all of these alternative approaches, the idea is to analytically capture the behavior and failure of members under shearing forces and then to provide the designer with a simplified approach that can be readily used in the design office.

The intent of the study reported herein was to investigate the analytical behavior of a class of reinforced concrete beams, without shear reinforcement, to identify the basic behavior involved so as to provide a framework whereby additional research could provide needed analytical refinements and simplification for design purposes. This study utilized finite element analysis together with fictitious crack modeling of identified diagonal tension crack locations firstly, to investigate the application of fracture mechanics in the form of the fictitious crack model to the shear problem, and to compare the results predicted in this analysis with those predicted through ACI, Japanese, and European code equations. The overall intent was to evaluate this approach for its viability and as a means of suggesting further steps to be taken in the determination of design equations for use.

FRACTURE IN CONCRETE

Fracture mechanics of concrete is a well-established area of research where there are three predominant analysis philosophies involved. Analysts have the option of utilizing the discrete crack approach whereby actual crack paths are determined and the finite element mesh in the cracked regions modified to physically model a cracking process. The cracking behavior is based upon maximum principal stresses or other key parameters that when exceeded produce a tension crack, in this case caused by interaction of tension and shear stresses generally causing a curved crack trajectory. A second option is a so-called smeared crack behavior whereby the effects of cracking are anticipated and modeled within the element itself, reducing its stiffness by appropriate amounts keyed to the behavior involved. Once again, the trajectory is determined via the analysis and the element stiffness is reduced accordingly. A third approach is a fictitious crack model. This approach, developed by Hillerborg et al. [9], is based on an energy formulation where the amount of energy required to advance the crack, a unit amount, is modeled in rod element located perpendicular to the pre-defined crack plane. The advantages of this approach are the simplicity of the fracture modeling and the disadvantages include the need for a pre-defined crack plane.

In this study, the decision was made to utilize the fictitious crack model because of its application to other areas of reinforced concrete research and its ease of application and analytical reduction of the finite element results. Accordingly, the shear model to be investigated consisted of linear elastic finite element models with a pre-defined crack trajectory with zero length rod elements joining one side to the other across the crack plane. These rods were modeled using nonlinear material properties to simulate the stress-crack opening width behavior where the amount of energy dissipated through the advance of the crack is determined via experimental results and defined prior to running the analysis.

The parameters included in this analysis were the crack orientation, that is the angle with which the crack intercepts the member horizontal axis, as well as its location. The angle and the location both are functions of the loading, the end conditions, and the interaction of the shear-span-to-depth ratio of the member. In this particular study, a simply supported singly reinforced concrete member was modeled without shear reinforcement with crack locations and trajectories being varied, so as to obtain an estimate of the effects of these parameters on the overall shear capacity of the member. Loading was imposed by increasing displacements

along the beam center line and measuring the amount of load required.

Results were compared against the ACI 318 [2] design equations 11-3 and 11-6:

$$V_c = 2\sqrt{f'_c}\, b_w d$$

$$V_c = \left[1.9\sqrt{f'_c} + 2500\rho_w \frac{V_u d}{M_u}\right] b_w d$$

where V_c is the shear capacity, f'_c is the concrete strength, b_w is the member width, d is the effective depth, ρ_w is the reinforcement ratio and V_u and M_u are the factored shear and moment, respectively.

In addition, the JSCE [10] and CEB [8] concrete codes, also were evaluated and compared against these results. These equations are as follows:

JSCE:

$$V_c = \left[0.19\ (100\rho_w f'_c)^{1/3}\ d^{-1/4}\right] b_w d$$

CEB:

$$V_c = \left[0.12\ (100\rho_w f'_c)^{1/3}\ (1 + \sqrt{0.2/d})\right] b_w d$$

where f'_c is in MPa and d is in m, the other parameters are as defined earlier.

It is important to note that the Japanese and European codes incorporate the size effect in their formulation. The size effect proportional to $d^{-1/4}$ or $[1 + \sqrt{0.2/d}]$ is significant because it recognizes that the shear behavior of smaller members will be different than that of larger members; behavior that is not identified in current U.S. practice, but has been observed by a number of researchers [4-7].

Thus, the intent of this investigation was to ascertain the viability of fictitious crack modeling to the "correct" behavior of reinforced concrete members subjected to shear and whether or not this approach could be accurate in the overall prediction of behavior. In the section that follows, the results will be presented for this analytical procedure and the accuracy of this approach, as compared with JSCE and CEB equations, will be evaluated.

ANALYTICAL SHEAR STRENGTH AND COMPARISON WITH DESIGN EQUATIONS

To investigate the size effect on the shear strength of reinforced concrete beams without shear reinforcement, finite element analyses using the fictitious crack model were performed. In the analyses, simply supported rectangular beams subjected to concentrated load at the span center were considered. The location and orientation of the fictitious crack, simulating the diagonal crack, were pre-defined. Diagonal cracks were oriented in the following three angles, 26°, 35°, and 45°. These angles were determined considering the range of typically observed diagonal cracks. The location where the diagonal crack intersects the bottom of beam was assumed at d, the effective depth away from the support. For the diagonal crack of 45°, another location, 2d, was also assumed. Finite element meshes for these four types of beams are shown in Fig. 1. Each type of beam was analyzed with five different sizes; however, these five beams are geometrically similar. All of the five beams have the same size proportions in the length of shear span (a), width (b), and height (h), 60:7.5:16. The effective depth (d) was 7/8 of the height (h); therefore, the effective depth of these five beams are 0.875, 4.375, 14.0, 21.875 and 43.75 in., respectively.

Rod elements having the Mode I fracture energy, G_f = 100N/m (0.57 lb/in.), were provided perpendicularly along the pre-defined crack surface. In reality, shear cracks are supposed to have the Mode II fracture energy. However, Mode II fracture energy can be neglected and replaced by Mode I fracture energy if the crack plane is properly modeled [3]. A bilinear tension softening curve, shown in Fig. 2, was adopted in the analysis, along with linear and trilinear curves. The tensile strength of concrete is 0.4 ksi, and all of concrete

elements are assumed to be elastic (E_c = 4000 ksi, nu = 0.2). The elastic modulus of reinforcing bars, E_s, is 30,000 ksi.

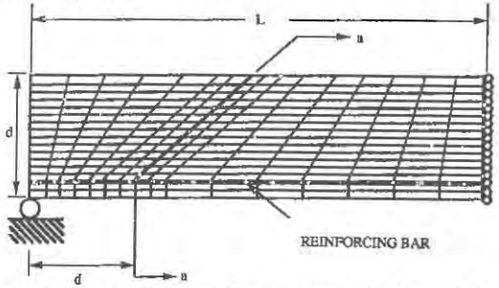

Fig. 1 Finite Element Mesh for Reinforced Concrete Beam with Flexural Shear Crack Inclined at 45 degrees (Type 1), 35 degrees (Type 2), and 26 degrees (Type 3), d from the Support. Type 4 Model has the Flexural Shear Crack Inclined at 45 degrees and 2d from the Support

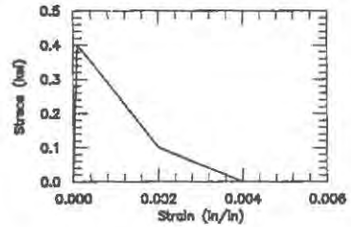

Fig. 2 Bilinear Approximation for Tension Softening Curve

Size Effect. The analytical results on shear strength are shown in Table 1. It can be confirmed that the location and inclination of diagonal crack definitely affects the shear strength of the beams. The area of the diagonal crack surface associated with the total fracture energy changes with the crack orientation resulting in the different behavior. The location of the diagonal crack also affects the behavior of beams. In this study, analytical results of Type 3 beams are selected as the typical results and compared with the design equations of shear strength in ACI [2], CEB [8], and JSCE [10] in Fig. 3.

According to this figure, the tendency of the shear strength to decrease with an increase in beam size was obtained from finite element analyses and shows the good agreement with CEB and JSCE design equations, in which the size effect has been incorporated. For the smallest beam (d = 0.875 in.), the analysis shows the significant increase in the shear strength and a decrease with increasing size. The size effect on the shear strength of beams without shear reinforcement can be concluded as being significant, yet the ACI design equations do not consider this phenomenon. In fact, ACI design equations are likely to overestimate the shear strength of large-sized beams; therefore, it can be pointed out that the safety margin would change depending on the beam size.

Cracking Type	d = 0.875"	d = 4.375"	d = 14"	d = 21.875"	d = 43.75"
1	413.43	178.47	125.03	116.62	94.16
2	350.36	170.86	118.34	107.06	89.12
3	288.18	159.45	114.72	95.82	81.95
4	288.43	135.30	104.80	83.46	63.46

Table 1 Numerical Results of Nominal Stresses (in psi) due to Different Cracking Types and Sizes

Effect of tension softening curve. Besides the bilinear tension softening curve, linear, and trilinear softening curves having the same amount of the fracture energy have been adopted in the analysis. In these analyses, the crack pattern of Type 3 was adopted. In order

to enhance the numerical stability, the smallest beam of the effective depth 0.875 in. was chosen as the subject. The strain energy accumulated within the beam increases with the increase in the beam size. Failure mode of large-sized beams becomes brittle because of the sudden release of this large amount of accumulated strain energy. Therefore, it becomes gradually difficult to get the stable solution with the increase in beam size. To avoid numerical stability problems in the solution, the smallest sized beam was used, results are shown in Fig. 4. Depending on the tension softening curve applied, the shear strength and post-peak responses of load-displacement relationship exhibit the definite difference. The linear softening curve results in stiffer behavior than the other two softening curves and exhibits higher shear strength, however the descending behavior is more brittle.

Effect of reinforcement ratio. In addition, the effect of longitudinal reinforcement ratio on the shear strength of beams was investigated. The crack pattern of Type 3 was used. The reinforcement ratio was increased from 1% to 2% and the results are shown in Table 2. The results indicate that the shear strength is significantly increased for the small beams with increasing reinforcement ratio; however, for the large beams, the shear strength is only slightly increased.

Steel Ratio %	d = 0.875"	d = 4.375"	d = 14"	d = 21.875"	d = 43.75"
1	288.18	159.45	114.72	95.82	81.95
2	437.21	171.30	126.63	113.95	94.89

Table 2 Results for the Same Beam Geometry and Crack Pattern (Type 3) for 1% & 2% Steel Ratios (ρ)

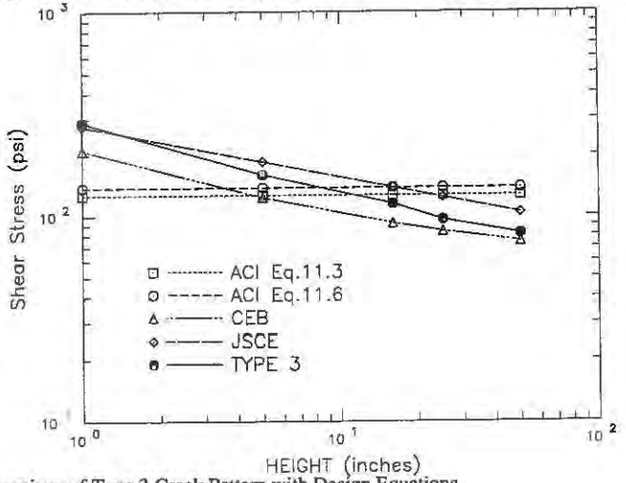

Fig. 3 Comparison of Type 3 Crack Pattern with Design Equations

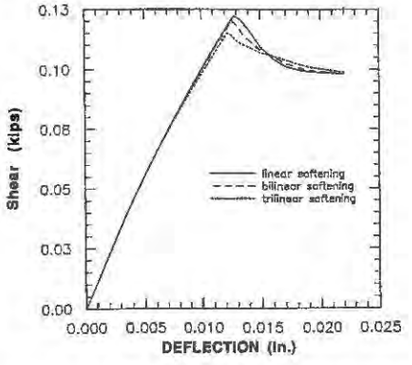

Fig. 4 Load-Deflection due to Different Tension Softening Curves (Type 3 Crack Pattern, d = 0875 in.)

OBSERVATIONS AND RECOMMENDATIONS FOR ACI 318

As can be seen by the foregoing evaluation, the fictitious crack modeling approach yields excellent results when compared with JSCE and CEB equations. It can be observed that there is indeed a size effect that is present that can be analytically shown to exist when investigated using a finite element technique. Moreover, the fictitious crack modeling approach yields reliable, accurate results with ease of modeling that can indeed predict this behavior in conformance with internationally accepted shear relationships. The question of whether the size effect is $d^{-1/4}$ as proposed in the JSCE and $[1 + \sqrt{0.2/d}]$ in the CEB relations or as has been proposed by others was not an area that was investigated in this study. However, it is an important question as to how exactly the shear capacity does vary. The assumption in this present work was that the JSCE and CEB relationships would be evaluated against the results of this study. And, as can be seen, the results match quite well.

In an overall sense, one is led to the conclusion that the ACI expressions found in Chapter 11 of the 318 Code must be improved if our ability to correctly predict shear behavior is not to be doubted. There is indeed an effect that occurs that is a function of the member geometry and one that is not currently identified in the ACI 318 expressions. This omission leads to conservatism in one class of member sizes and perhaps more alarmingly under-conservatism in the other extreme. Neither over-design or under-design can be tolerated, and steps need to be taken to improve the existing shear expressions while at the same time providing designers with a viable and easy to use procedure. The authors have investigated the required modifications to these equations needed to include a size effect and the results indicate that relatively minor modifications can be made to the expressions to include a size effect. However, the question of the form and the approach to be used is one that clearly deserves further study, and is one that should be given a top priority in the fracture area.

REFERENCES

[1] ACI-ASCE Committee 326, "Shear and Diagonal Tension," *Journal of the American Concrete Institute*, Vol. 59, No. 2, Feb. 1962, pp. 277-333.

[2] ACI Committee 318, *ACI Building Code Requirements for Reinforced Concrete*, American Concrete Institute, Detroit, MI.,1989, pp. 353.

[3] Blaauwendraad, J. and Wang, Q. B., "Systematic Fracture Mechanics Study of Shear Failure in Beams under Distributed Load," *IABSE Colloquium on Structural Concrete*, Vol. 62, 1991, pp. 637-642.

[4] Bazant, Z. P., "Size Effect in Blunt Fracture: Concrete, Rock, Metal," *Journal of Engineering Mechanics*, ASCE, Vol. 110, EM 4, 1984, pp. 518-535.

[5] Bazant, Z. P. and Cedolin, L., "Fracture Mechanics of Reinforced Concrete," *Journal of the Engineering Mechanics Division*, ASCE, Vol. 106, No. EM6, Dec. 1980, pp. 1287-1306.

[6] Bazant, Z. P. and Kazemi, M. T., "Size Effect on Diagonal Shear Failure of Beams without Stirrups," *Journal of American Concrete institute*, Vol. 88, No. 3, May-June 1991, pp. 268-276.

[7] Carpinteri, A., "Size Effects on Strength, Toughness, and Ductility," *Journal of Engineering Mechanics* ASCE, Vol. 115, No. 7, July 1989, pp. 1375-1392.

[8] CEB, CEB-FIP Model Code 1990 (Final Draft). *Bulletin d'Information* No. 203-205, 1991.

[9] Hillerborg, A., Modeer, M., and Petersson, P. E., "Analysis of Crack Formation and Crack Growth in Concrete by Means of Fracture Mechanics and Finite Element," *Cement and Concrete Research*, Vol. 6, No. 6, Nov. 1976, pp. 773-782.

[10] JSCE, *Standard Specification for Design and Construction of Concrete Structures, part 1 (Design)*, 1st ed., Tokyo, 1986.

[11] Niwa, J., Yamada, K., Yokozawa, K., and Okamura, H., "Revaluation of the Equation for Shear Strength of Reinforced Concrete Beams without Web Reinforcement," *Proceeding of JSCE*, No. 372, Vol. 5, Aug. 1986.

[12] Okamura, H. and Higai, T., "Proposed Design Equation for Shear Strength of Reinforced Concrete Beams without Web Reinforcement," *Proceeding of JSCE*, No. 300, Aug. 1980.

Chapter 9

Interaction Between Concrete and Reinforcement

Principal Lecture

Bond Properties in Fiber-Cement and Aggregate-Cement Paste Interfaces

Surendra P. Shah and Zongjin Li
NSF Center for Science and Technology of Advanced Cement-Based Materials
Northwestern University
Evanston, IL 60208

ABSTRACT

Analytical and experimental studies of the interfacial zone between fiber-cement and aggregate-cement paste were undertaken. A simple theoretical model is proposed for calculating interface properties from pull-out or push-out tests. The model enables calculating of the following material parameters: the parameter of shear stiffness of the fiber or aggregate-matrix boundary layer, the shear bond strength, the frictional bond strength and the specific interfacial fracture energy. These parameters can be determined from the slope of the load-slip curve, the maximum pull-out load and the corresponding slip value. Slip-controlled, multiple-fiber pull-out tests and aggregate push-out tests were conducted in a closed-loop test system. Various factors such as, embedment length of fibers, treatment of aggregate surface, mixing process and incorporation of silica fume for aggregate specimens were investigated.

The transition zone of aggregate specimen was further investigated by using backscattered electron imaging and energy dispersive analysis of x-rays (EDAX) to characterize the microstructure of the interface of aggregate-cement paste. The relationship between mechanical properties and microstructure of interfacial zone was studied.

INTRODUCTION

It has been long recognized that the mechanical behavior of concrete and fiber reinforced concrete is largely affected by the properties of interfacial zone between aggregate or fiber and cement. A number of studies have been conducted to characterize the chemical nature, morphology of cement hydrated product and mechanical properties of interfacial zone. There is general agreement that the interface between aggregate-cement or fiber-cement is the weak link in concrete or fiber reinforced concrete since it has more porosity than bulk matrix.

The microstructure of the interfaces for both fiber-cement and aggregate-cement has been investigated using scanning electron microscopy[1][2][3][4]. For the aggregate-cement paste case, the formation of a calcium hydroxide film adjacent to the aggregate surface has been observed. On this film, a thin layer of C-S-H forms and thus a transition zone. By using EDAX the presence of ettringite and the preferentially oriented calcium hydroxide crystals in the interfacial zone has been demonstrated[1]. Backscattered electron imaging has been used to quantify the transition zone[5]. It was found that the porosity at the interface is relatively high, and decreases towards the bulk paste. The width of the interfacial zone was observed to be approximately 50μm. Similar phenomena were observed in the fiber-cement interface. For example, Al Kalaf and Page[2] found that the microstructure of the transition zone could be described as a discontinuous polycrystalline layer of portlandite with a thickness from 0.5 to 40 microns. Pinchin and Tabor[3] observed that there was a marked decrease in strength within 0.75 mm from the wire surface. Furthermore, Bentur, Midness and Diamond[6] indicated that a near-fiber layer had higher porosity, i.e., had lower stiffness than bulk matrix. The tendency of the occurrence of the microcracks around the aggregate [7] and the development of longitudinal cylindrical shear microcracks around fiber[8][9] were also observed.

Attempts have been made to characterize the mechanical properties of the interface. Micro-hardness tests around the interface[10][11] showed that the hardness of the interfacial zone (about 20-60 μm from aggregate or fiber) is lower than that of the bulk matrix. To measure aggregate-cement bond strength, different types of test methods, such as bending test[12], direct tensile test[13][14], axial compression test and shear bond test[15], have been employed. It has been shown that bond strength varies with curing condition, type of aggregate, and type of cement. For the fiber-cement case, single fiber pull-out tests were carried out on specimens consisting of different steel wires as fiber and either cement paste or mortar as matrix[16][17]. Moreover, Laws[18] and Gopalaratnam[19] conducted multiple fiber pull-out test by using cement paste as matrix and either glass fiber strand or steel wires as fiber. To better characterize the bond behavior, one needs to know the bond-slip response of the interface and the influence of the microstructure of interface on the mechanical properties. However, few studies have concentrated on these subjects.

This paper explores the bond behavior for the interface of aggregate-cement and fiber-cement by analyzing the measured load-slip curve. Interfacial mechanical properties such as interfacial stiffness, shear bond strength and interfacial surface energy were obtained. The relationship between mechanical properties and microstructure of the transition zone for aggregate-cement case was also investigated. This might lead to better understanding of the toughening mechanism of concrete.

THEORETICAL MODEL

To interpret the results of fiber pull-out and aggregate push-out tests, a simple method is developed. The theoretical background for the method is described below. Figure 1 represents the schematic reference model in which L and A represent the fiber or aggregate embedment length and cross-sectional area. The fiber or aggregate are assumed to be elastic with Young's Modulus of E. The matrix is assumed to be rigid except for a thin boundary layer idealized as a elastoplastic shear layer. The effect of Poisson's ratio is neglected for both fiber and matrix.

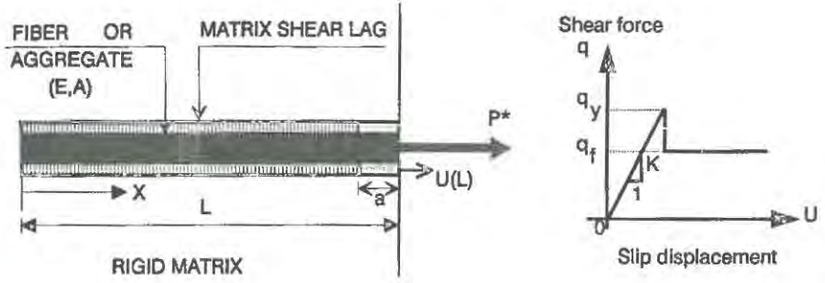

Figure 1 Theoretical model and constitutive relationship for interface

It is assumed that debonding has occurred over a certain length, a, starting at x=L. Treating the boundary layer as a shear lag and assuming that a constant shear stress are acting at the debonded interface, the following equations can be written,

$$q = \begin{cases} kU(x) & 0 < x < L-a \\ q_f & L-a < x < L \end{cases} \tag{1}$$

where k is the stiffness per unit length of the interfacial layer for small deformation, q is the shear force per unit length acting on the fiber or aggregate, q_f is the frictional shear force per unit length, and U(x) is the fiber or aggregate displacement.

Introducing the equilibrium equation and the constitutive relationship for the fiber (aggregate), the following differential equation for U can be obtained,

$$\begin{aligned} U_{,xx} - \omega^2 U &= 0 \qquad 0 < x < (L-a) \\ U_{,xx} - \frac{q_f}{E\,A} &= 0 \qquad (L-a) < x < L \end{aligned} \tag{2}$$

Where, subscript comma "," indicates differential operator. The quantity ω is defined as:

$$\omega = \sqrt{\frac{k}{E\,A}} \tag{3}$$

Equations (2), together with boundary conditions and continuity conditions, constitute a complete set of equations for the determination of $U(x)$. Solving this set of equations the following closed form expression for the slip displacement at the loading end, U^*, is obtained as:

$$U^* = U(L) = \frac{P^* - q_f a}{E_a A\,\omega}\coth(\omega(L-a)) + \frac{P^* - 0.5 q_f a}{E_a A}a \tag{4}$$

Furthermore, it can be shown[20] that the relationship between the external force and debonding length, a, derived from both the shear strength (q_y) criterion and fracture energy (Γ) criterion take the following forms.

For the shear strength criterion:

$$P^* = q_f a + \frac{q_y \tanh\omega(L-a)}{\omega} \tag{5}$$

For the fracture energy criterion:

$$P^* = q_f a + \left[\frac{q_f}{2\omega} + \sqrt{\left(\frac{q_f}{2\omega}\right)^2 + 2E_a A p \Gamma}\right]^{0.5} \tanh(\omega(L-a)) \tag{6}$$

Where, Γ is the specific fracture energy.

The interfacial frictional forces, q_f, the interfacial yield parameter, q_y, and the specific energy, Γ, can be computed by using the following formula, Eq.7, 8 and 9, respectively,

$$q_f = \frac{\omega P^*_{max}}{a\omega + Sinh(\omega(L-a))Cosh(\omega(L-a))} \tag{7}$$

$$q_y = q_f Cosh^2(\omega(L-a)) \tag{8}$$

$$2E_f A p \Gamma = (\frac{q_f}{\omega})^2 [Cosh^4(\omega(L-a)) - Cosh^2(\omega(L-a))] \tag{9}$$

Note that an addition equation (Eq. 10) is needed to determine the debonding length, a.

$$P^*_{max}\frac{0.5(\omega a)^2 + Cosh^2(\omega(L-a)) + \omega a\, Sinh(\omega(L-a))Cosh(\omega(L-a))}{\omega a + Sinh(\omega(L-a))\, Cosh(\omega(L-a))} - U^*_{peak}E_{af}\omega = 0 \tag{10}$$

In Eq. (10) U^*_{peak} represents the slip displacement corresponding to the peak load.

The shear strength, τ_y, and frictional stress, τ_f, can be obtained by dividing q_y and q_f by perimeter of the fiber or the aggregate.

MULTIPLE FIBER PULL-OUT EXPERIMENT

Experimental details

In order to identify and evaluate the interfacial properties, multiple fiber pull-out tests were carried out using different types of fibers. The results for steel fiber are discussed here. The continuous steel wires were obtained from Bekaert Co. Chicago. IL with a diameter of 0.2032 mm.

Fabrication of the specimens was achieved by using a brass mold which is similar in construction and assembly to the mold developed by Laws[17]. Sixteen steel wires were used in each specimen. A brass guide-plate with 16 holes was used to provide alignment of fibers during construction. During testing this guide plate was used to separate the pullout section of the specimen from the anchored end and provide for the transfer of the load. Neat cement paste with a water/cement ratio of 0.35 was used. To facilitate the workability, 3.86 ml superplasticizer per kilogram of cement was also used. The specimens were cast horizontally with the embedded fiber perpendicular to the direction of casting. Specimens were tested after either 14 days or 28 days of curing.

The specimen being held in the mechanical fixture is shown in Fig. 2. The specimen is connected to the "U" shaped loading fixture by means of a stainless steel rod (loading rod) 6.3 mm in diameter. The loading fixture is connected to the servohydraulic actuator and the entire specimen-fixture moves with the actuator. A restraining frame which can make contact with the specimen's brass guide plates is connected to the load cell and is used to resist the upward movement of guide plate. Subsequently, load is transferred from the brass guide plate to the matrix. This load is being reacted against by the fibers which are the only means of connecting the top and bottom portion of the specimen. The load is transferred to the top of the specimen and thereafter to the loading fixture through bending of the loading rod.

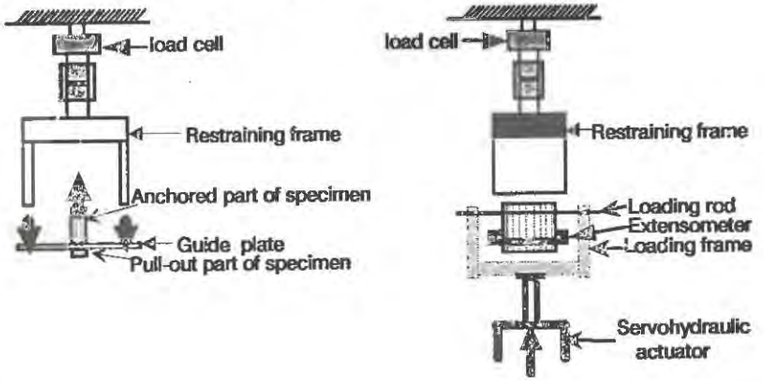

Figure 2 Specimen setup for multiple fiber pull-out experiments

Two extensometers (1.905 mm in. range) mounted across the guide plate using a 12.5 mm gage length were used to measure the slip displacement of fiber debonding and pull-out. The average output of extensometers was used as the feedback signal in the control of the servohydraulic system. The pull-out tests were performed at a rate of 0.0254 mm opening of extensometer transducers per minute. Once the magnitude of slip was to exceed the transducers range, the mode of the control was switched to stroke control and the entire fiber length was pulled out of the matrix. A digital oscilloscope was utilized in the data acquisition.

Experimental results

A typical load vs. slip displacement curve is shown in Fig. 3. Evaluation of the load-slip behavior indicates that the curve can perhaps be divided into three stages, linear-elastic deformation stage, partial debonding stage and full debonding followed by a frictional pull-out stage.

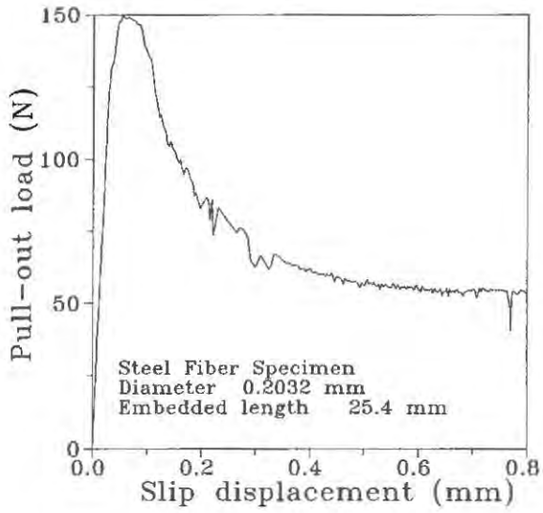

Figure 3 Typical load-slip displacement curve for steel fiber pull-out specimen

The interfacial layer of the fiber and matrix may be characterized by the parameter of the shear stiffness, ω. The experimental results of ω are obtained from the initial slop of load-slip curve. Other bond properties of interface, i.e. $q_f(\tau_f)$, q_y (τ_y) and Γ can be calculated from the values of P^*_{max} and the corresponding slip displacement at P^*_{max} by using Eqs. (7), (8), and (9). These values are listed in Table 1. It can be seen from the table that the values of ω are in general independent of the embedded length, hence one can use ω as a material property. Furthermore, it is shown that ω increases almost two fold as the duration of curing increases from 14 to 28 days. Thus it can be used to assess the development of the bond and the extent of hydration reactions at the interface. Note that the magnitude of the shear bond strength, τ_y, agrees with the lower bound values obtained by other researchers[16]. The agreement is also observed for the values of the frictional bond strength, τ_f, comparing with the values acquired by previous studies. The specific surface energy, Γ, obtained in present study is not far from the surface energy of hardened cement paste[21]. However, comparing with the surface energy of fiber reinforced cementitious composite[21], the values of specific surface energy for the fiber/matrix interface obtained in present study are significantly lower. This indicates that the interface is a weak link in fiber reinforced cementitious composites.

Table 1 Test results for steel fiber specimens

L (mm)	P_{max} (N)	ω (1/m)	τ_y (MPa)	τ_f (MPa)	Γ (N/m)	Curing (days)
10.31	246.98	75.15	2.74	1.97	17.2	28
12.90	244.75	76.00	2.35	1.42	17.7	
7.2	80.1	45.86	1.12	1.05	2.01	14
11.4	97.9	42.99	0.90	0.79	2.54	
12.0	134.2	44.84	1.18	1.00	4.81	
25.4	150.0	44.30	0.78	0.43	6.86	

AGGREGATE PUSH-OUT TEST

Mechanical experimental procedures

An aggregate push-out method was developed to measure the bond properties of aggregate-cement interface. The materials used in the study were Type I ordinary Portland cement, condensed silica fume slurry, and Indiana limestone and granite.

Aggregate was cored out from stone block as a 12.7 mm diameter cylinder. The surface of some aggregates were pre-treated with several kinds of processing such as painting cement and SF slurry on aggregates and exposing them in room temperature (20°C) for 1 hour before casting. After mixing cement paste matrix, aggregate was put in the center of the 50.8 mm diameter cylindrical mold and then covered with matrix. Specimens were cured in water under the temperature of 20°C. Cylindrical specimen were sliced into appropriate thickness and ground and polished on both top and bottom surface before push-out test.

The set-up for aggregate push-out test is shown schematically in Fig.4. The specimen was put on a flat circular plate which was connected with a servohydraulic actuator of an MTS machine through a hollow cylinder. The entire specimen-fixture could move up with the actuator. A steel rod, which was connected to load cell, made the contact with the top surface of the aggregate and by resisting the upward movement of loading fixture pushed the central cylindrical aggregate downwards. Two LVDTs, which were fixed between circular plate and the rigid wings of the steel rod, were used to measure slip displacement of the top of the aggregate relative to the surface of the cement matrix annulus. The average output of the LVDTs was used as feedback signal to control the servohydraulic system. The push-out test was performed at a rate of slip displacement of about 1 mm per hour. Slip displacement at the bottom of the aggregate was also measured by another LVDT. Push-out load, slip displacement of aggregate and stroke of the actuator of MTS were recorded by using a data acquisition computer.

Twelve groups of specimens were tested with different water/cement ratio, coating process, matrix and aggregate type as variables. Two water to binder ratios (0.35 and 0.65), eight coating methods, two kinds of matrix (cement paste and the mixture of cement with 10% by weight of silica fume), and two kinds of aggregate (limestone and granite) were used. Push-out tests were carried out at the specimen age of 14 and 28 days. Three specimens for each mixture were tested.

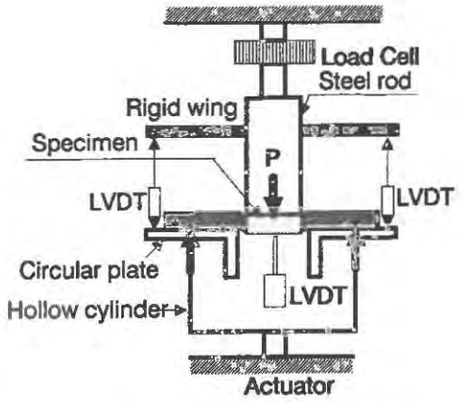

Figure 4 Specimen set-up for aggregate push-out experiment

Microscopic study for aggregate-cement interface

In order to quantify microstructural properties of the interface in these push-out specimens, samples were also cast for study in a scanning electron microscope by using the same procedures described earlier. These specimens were cut perpendicular to the cored aggregate axis into thin slices with a thickness about 1 mm on a diamond saw at 14 and 28 days. Epoxy impregnation of the thin slices was performed by replacing water with ethanol followed by replacing ethanol with low viscosity epoxy. After impregnation, specimens were dry ground. Lapp cloths impregnated with diamond paste of 6 μm, 3 μm, 1 μm and 0.25 μm were used to bring the samples to a 0.25 μm polish. Finally, the polished samples were carbon coated.

The interfacial zone was examined with a scanning electron microscope with an energy dispersive x-ray analysis system. An image magnification of 400x was selected based on precedence of work by Scrivener[5] and others. Each region of different brightness in the images was analyzed to identify the different chemical components, such as unhydrated cement (anhydrous phase), calcium hydroxide, C-S-H and pores. The two phases of interest in this study are anhydrous and porous phases. These two phases lie at opposite ends of the grey spectrum. The grey-level thresholds associated with these two phases in cement were selected by picking the suitable values which appear to best segment these two regions from other solid phases in the image.

Each image of the aggregate-paste interface was subdivided into bands with a width of 20μm and up to 200μm away from the aggregate surface. Binary images of the unhydrated phase and the porosity phase were then created for each subdivided image according to the threshold of grey level. The area percentage, which is representative of the volume fraction of a randomly distributed material, was measured for each band. Gradient plots for anhydrous material and pore space were created by plotting the average area percentage versus the distance from the aggregate surface for each image.

Experimental results

The bond properties, such as ω, τ_y, τ_f and Γ were calculated by using the method introduced earlier. The calculated results of these parameters for five groups of typical push-out specimens are listed in Table 2.

Table 2 Test results for aggregate-cement specimen with 28-day curing

No.	Comments	ω (1/m)	τ_y (MPa)	τ_f (MPa)	Γ (N/m)
1	w/c=.35, cement matrix no coating, limestone	20.30	4.07	3.98	4.74
2	w/c=.65, cement matrix no coating, limestone	19.09	3.76	3.73	2.01
3	w/c=.35, cement matrix no coating, granite	13.09	3.33	3.26	3.67
4	w/c=.35, 10% SF matrix no coating, limestone	23.02	5.88	5.71	9.64
5	w/c=.35, 10% SF matrix C+SF coating, limestone	27.36	11.44	10.34	59.02

A typical image of the interface for specimen group 1 is shown in Fig.5. A clear, porous transition zone is observed.

Figure 5 Backscattered electron micrograph of an interface for specimen No. 1

The effect of w/c ratio is shown in Fig. 6. It can be seen from Fig.6(a) that the specimen with w/c of 0.35 has the higher push-out load and steeper initial slope. Consequently, it can be shown that all the interfacial properties decrease with the increase of the w/c ratio, especially the fracture energy which becomes less than half (Table 2). Fig. 6(b) shows an obvious difference of the porosity gradient of for two different w/c ratio. It can be observed from the figure that the higher w/c ratio the higher the porosity. Note that one of the reasons of the existence of the interfacial zone is that bleed water stays under coarse aggregate and creates a porous zone under aggregate. Therefore, the higher the w/c ratio, the greater the bleeding and the more porous will be the interfacial zone. This phenomena is helpful to explain the reduction in bond mechanical properties.

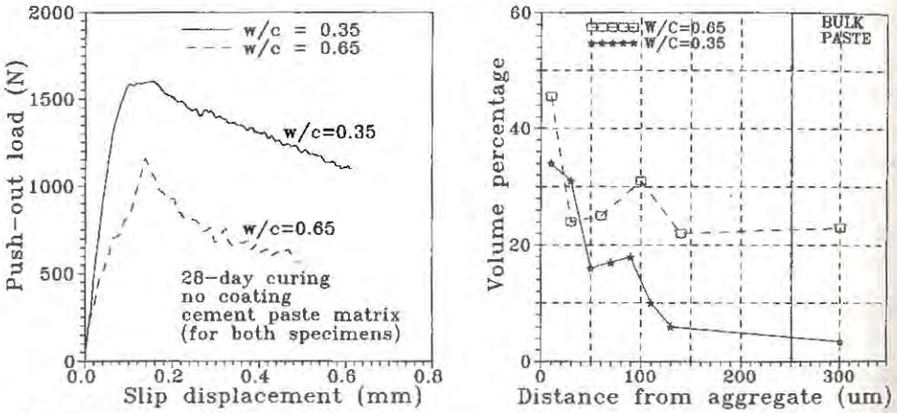

Figure 6 Effect of water cement ratio on the aggregate-cement interfacial behavior

The effects of silica fume can be attributed to the fact that it reacts with calcium hydroxide in concrete and makes the structure dense through pozzolanic reaction and a "packing" effect due to smaller particle size. As a result, the amount of interfacial porosity is reduced. This is verified in the observation of present study. A dramatic reduction of the porosity within the transition zone is observed for a specimen with a silica fume modified matrix. Moreover a significant increase in the value of interfacial surface energy is demonstrated in Table 2. The additional effect is obtained from the coating the aggregate with slurry of the cement plus silica fume. It was demonstrated that for the specimen incorporated with silica fume both in matrix and surface coating, the porosity of the interface was further reduced. And the maximum push-out load significantly increased. The influence of silica fume modification is graphically illustrated in Fig. 7. It can be seen that incorporating silica fume improved all the interfacial properties, especially the interfacial specific fracture surface energy. The surface fracture energy increased about two times for the specimens with SF modified matrix and about 10 times for the specimens with SF modified matrix together with cement and SF slurry coating when compared with the control specimen.

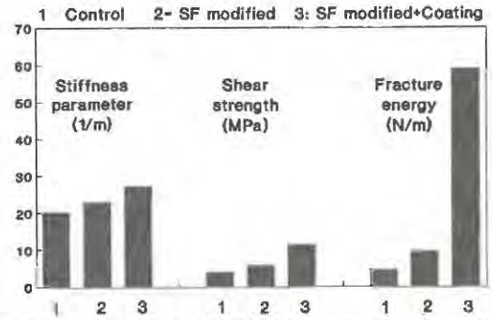

Figure 7 Effect of incorporation of silica fume in matrix and coating

CONCLUSIONS

A simple and objective method of determining interfacial properties has been developed and multiple fiber pull-out test has been conducted. It is shown that bond properties for fiber-cement and aggregate-cement interfaces can be reliably measured. For the fiber-cement interface, it seems that these parameters are more or less independent of embedded length for the majority of the experimental results except for the longest embedment length case.

Examination of the aggregate-cement interface by using backscattered electron imaging shows that porosity of the interfacial zone is largely influenced by w/c ratio. The microstructure of the interface can be significantly improved by lowering w/c ratio and incorporation of silica fume into the cement paste matrix. The pre-coating of aggregate with cement and silica fume slurry can further reduce the porosity of the transition zone. Direct comparison of the gradients of the porosity in transition zone and the interfacial mechanical properties reveals that the microstructure of the interface is the key factor which determines the mechanical behavior.

ACKNOWLEDGEMENTS

The authors gratefully acknowledge the financial support of the National Science Foundation Center for Science and Technology of Advanced Cement Based Materials (NSF-ACBM).

REFERENCES

1. Grandet and Oliver, "The aggregate mortar interface", C.C.R., Vol.15, 1985.
2. Al Kalaf, M. N. and Page, C. L., "Steel/mortar interfaces: Microstructural features and Mode of failure", Cem. Concr. Res., 9(2), 1979, PP 197-207
3. Pinchin, D., J. and Tabor, D., "Interfacial phenomena in steel fiber reinforced cement I: structure and strength of interfacial region", Cem. Concr. Res., 8(1), 1978, pp 15-24
4. Barnes, B. D., Diamond, S. and Dolch, W. L., "Contact zone between portland cement paste and glass aggregate surface", Cem. Concr. Res., 8(2), 1978, PP 233-243
5. Scrivener and Pratt, "Quantitative characterization of the transition zone in high strength concrete", Advances in Cem. Res. Vol.1, 1988.

6. Bentur, A., Mindness, S. and Diamond, S., "Pull-out process in steel fiber reinforced cement", International J. of Cement Composite and Lightweight Concrete, Vol. 7, No. 1, Feb., 1985, PP 29-37
7. Maji and Shah,"Initiation and Propagation of bond cracks as detected by Laser holography and acoustic emission", MRS symp., Proc. 114, 1988.
8. Kelly, A., "Interface effect and the work of fracture of a fibrous composites", Proc. Ray. Soc., Vol. A319, 1970, PP 95-102.
9. Selvadurai, A. P. S., "Concentrated body force loading of an elastically bridged penny shaped flaw in a unidirectional fiber reinforced composite", Int. J. of Fracture, 21, 1983, PP 149-159.
10. Lyubimova and Pinus,"Crystallization structure in the contact zone between aggregate and cement in concrete", Colloid Jour., 24, 5, 1962.
11. Wei, S., Mandel, J. A. and Said, S., "Study of the interface strength in steel fiber reinforced cement based composites", ACI Journal, 1986, PP 597-605.
12. Iwasaki and Tomiyama,"Bond strength between cement paste and aggregate",Annual report of cement technology, Vol.28, 1974.
13. Shah and Slate,"Internal microcracking, mortar-aggregate bond, and the stress strain curve of concrete", Int. conf. on the structure of concrete, 1968.
14. Hsu, T.T.C. and Slate, F. O., "Tensile bond strength between aggregate and cement paste or mortar", J. of ACI, Proceedings, Vol. 60, No.3, March, 1963, PP 371-390
15. Taylor and Broms,"Shear bond strength between coarse aggregate and cement paste or mortar", ACI J., Aug., 1964.
16. Gray, R. J., "Analysis of the Effect of Embedded Fiber Length on Fiber Debonding and Pullout From an Elastic Matrix, Part 2, Review of Theories", J. Mat. Science, V. 19, 1984, PP. 1680-1691.
17. Bartos, P., "Analysis of pull-out tests on fibers embedded in brittle matrices", Journal of Material Science, V. 15, 1980, PP 3122-3128.
18. Laws, V.,"The Glass Fiber/Cement Bond", Journal of Material Science , 1986, 21, PP 289-296.
19. Gopalaratnam, V. S. and Abu-Mathkour, H. J., "Investigation of the pull-out characteristics of steel fibers from mortar matrixes", Proceedings of the International Symposium on Fiber Reinforced Concrete, Dec. 16-19, 1987, Madras, India, PP 2.201-2.211
20. Li, Mobasher and Shah, "Characterization of interfacial properties in fiber reinforced cementitious composites", J. of American Cer. Soc., Sep. 1991.
21. Mindness, S.,"Fracture toughness testing of cement and concrete", Fracture Mechanics of Concrete, Edt. A. Carpintenri and A. R. Ingraffea, Martinus Nijhoff Publishers, 1984, 67-107

Principal Lecture

BOND OF STEEL TO STRAIN-SOFTENING CONCRETE TAKING ACCOUNT OF LOADING RATE

HANS W. REINHARDT
FMPA BW Otto-Graf-Institute and Stuttgart University
Pfaffenwaldring 4, D-7000 Stuttgart 80, Germany

ABSTRACT

Bond of reinforcing and prestressing steel is an essential requirement for serviceability and loading capacity of reinforced and/or prestressed concrete structures. Bond is assured by adhesion, friction and mechanical interlock the effectiveness of which depends on the geometry of the steel bars, the mechanical properties of concrete, and the loading conditions.

In the present paper, concrete is modelled as a strain softening material. It is discussed how the governing parameters like Young's modulus, tensile strength, fracture energy depend on loading rate. The ultimate bond stress is calculated as function of cover to steel bar diameter and loading rate. The results are compared with usual short-term results.

INTRODUCTION

The bond between reinforcing bars and concrete is an essential requirement of reinforced concrete. It relies upon three mechanisms: adhesion, friction, and mechanical interlock. Adhesion contributes to the bond resistance only at small forces during the first loading whereafter friction may become active at smooth steel surfaces. The most important part plays mechanical interlock which develops due to the lugs on a steel bar when it is pulled-out.

However, mechanical interlock causes also forces transverse to the bar which have to be supported by the surrounding concrete. If concrete cover is small these forces may lead to splitting which, on its turn, leads to bond failure. The bond resistance is thus governed by the mechanical properties of the concrete.

The mechanical behaviour should be modelled in best agreement with the actual behaviour. The moment being to model concrete as a strain-softening material is most appropriate and will be introduced into the analysis.

There are extraordinary loading cases with high loading rates such as impact, explosions, earthquake or pile driving. It should be also known for those loading cases whether the bond resistance remains reliable or whether special measures should be taken.

In the following, the bond resistance of a strain-softening material will be analysed taking rate effects into account.

ANALYTICAL MODEL FOR THE SPLITTING FAILURE MECHANISM

Elastic and plastic modelling

Bond forces emenate from the steel ribs of a deformed bar and spread into the surrounding concrete at an angle α as schematically shown by Fig. 1. The bond force is composed of a radial and a tangential component. The radial compressive component is balanced by a tensile ring force in the concrete. Tepfers [1] has assumed that the radial component can be regarded

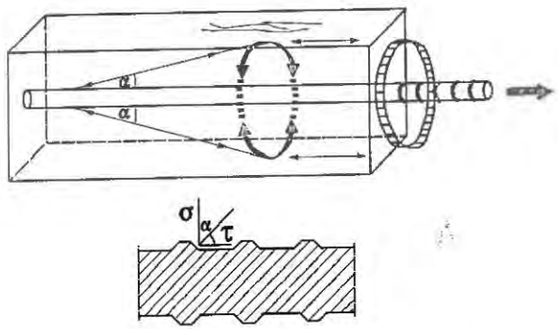

Figure 1. Equilibrium of bond forces around a deformed bar according to Tepfers

as the action of a hydraulic pressure on a thick-walled ring formed by the concrete around the steel bar. The wall thickness of the ring is determined by the smallest available dimension which is given by the least thickness of the cover, c.

If the wall material is elastic a splitting crack occurs in the concrete at the steel bar surface and the maximum bond force is reached. For that case, Tepfers [1] has given the relation expressed in critical bond stress τ_{cr}

$$\tau_{cr} = \frac{f_{ct}}{\tan\alpha} \frac{(c + r_s)^2 - r_s^2}{(c + r_s)^2 + r_s^2} \qquad (1)$$

with f_{ct} tensile strength, α angle of inclination, c cover, and r_s half bar diameter. Tepfers has also considered the case that a inner part of the cover is cracked and cannot transfer any tensile stress what led to the relation

$$\tau_{cr} = 0.3 \frac{f_{ct}}{\tan\alpha} \left[\frac{c}{r_s} + 1 \right] \qquad (2)$$

and, finally, a plastic material with a yield strength equal to the tensile strength of concrete what resulted in

$$\tau_{cr} = \frac{f_{ct}}{\tan\alpha} \frac{c}{r_s} \qquad (3)$$

The three cases are schematically shown by Fig. 2.

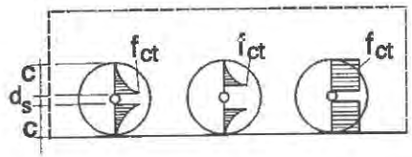

Figure 2. Distribution of tangential stresses around a deformed reinforcing bar: (1) elastic, (2) partly cracked elastic, (3) plastic. (d_s = steel bar diameter, c = concrete cover, f_{ct} = tensile strength of concrete.)

None of these three classical cases can apply to concrete since it is known that concrete is a strain-softening material. It is anticipated that the consideration of the softening behaviour will lead to better agreement with experimental results.

Strain-softening model

The basic assumption of Tepfers [1] that a concrete ring is loaded by a hydraulic pressure will also be adopted. It is assumed that a certain region around the steel bar is cracked

and that stress transfer is still possible as long as the concrete did not reach the stress-free crack opening.

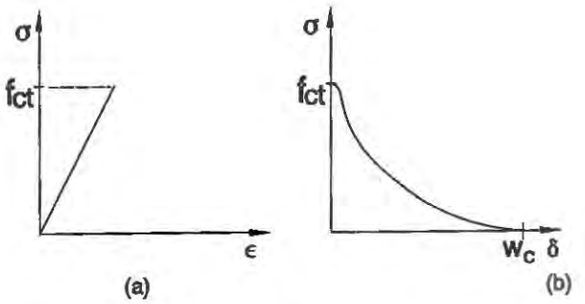

Figure 3. Stress displacement diagram of concrete
a) elastic part, b) softening part

Fig. 3 shows the stress-displacement curve of concrete with the relevant quantities: Young's modulus E_c, tensile strength f_{ct}, the strain at maximum stress ϵ_{cr}, stress-free crack opening w_c, and specific fracture energy G_F. With this material behaviour, the geometry and the stress disribution become like in Fig. 4 is schematically given. As long as the crack can transfer stresses it is called a ficticious crack [2].

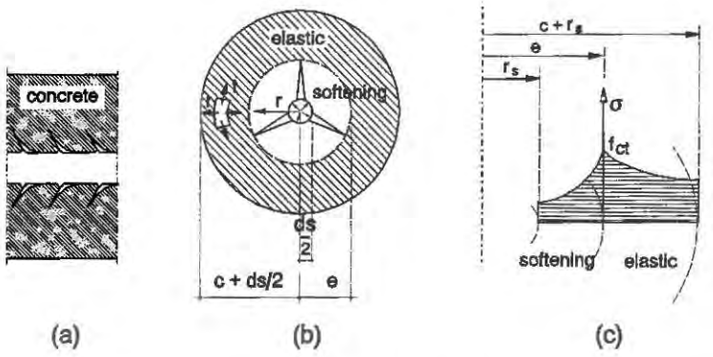

Figure 4. Steel bar with surrounding concrete ring.
(a) Longitudinal section with secondary cracks,
(b) cross-section indicating material state,
(c) stress-distribution in cincrete ring.

The resistance of the concrete ring is built up by the outer

elastic part and the inner softening part. According to Tepfers [1], the elastic part is given by

$$\tau_{cr} = \frac{e\ f_{ct}}{r_s \tan\alpha} \frac{(c+r_s)^2 - e^2}{(c+r_s)^2 + e^2} \qquad (4)$$

The second part is approximated in the following [3,4]. It is assumed that the bond stresses cause a hydraulic pressure on the concrete which deforms. The total tangential elongation of the concrete at a distance r consists of concrete strain ϵ_t and crack opening nw

$$\delta_{tot} = 2\pi r\epsilon_t + nw \qquad (5)$$

with n the number of cracks. At r = e, the tensile strength is reached at the edge of the ficticious crack. There, the total elongation reads

$$\delta_{tot} = 2\pi e\epsilon_t = 2\pi e \frac{f_{ct}}{E_c} = 2\pi e\epsilon_{cr} \qquad (6)$$

neglecting Poisson's effect. The radial displacement u_r is assumed to be constant, i.e. a rigid-body displacement of the inner part occurs. This is shown by Fig. 5.

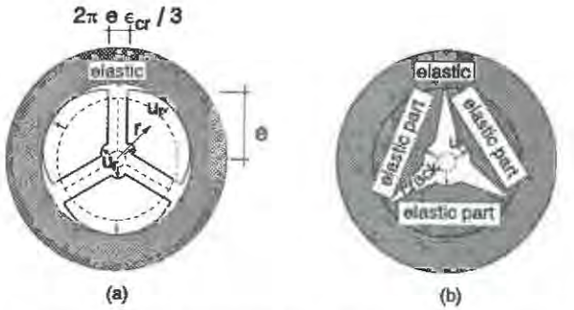

Figure 5. Rigid-body displacement of the inner part of the concrete ring, (a) without tangential stesses in the cracks (b) with tensile stesses across the cracks

The radial displacement is $u_r = \epsilon_{cr} e$. In case of Fig. 5a, the tensile stress at r = e reaches just the tensile strength which leads to compatibility between the cracked and uncracked parts of the concrete ring. At a distance r the tangential displacement is given by eq. (5) which is, due to the rigid-body displacement, equal to eq. (6)

$$\delta_{tot} = 2\pi r\epsilon_t + nw = 2\pi e\epsilon_{cr} \qquad (7)$$

The analysis is facilitated with the assumption of $\epsilon_t = \epsilon_{cr}$ which leads to

$$nw = 2\pi\epsilon_{cr}\,(e-r) \tag{8}$$

This assumption is justified because the elastic contribution in the cracked part is small compared to the contribution due to strain-softening. The tangential bond force per unit length in the cracked part becomes

$$F_b = \int_{r_s}^{e} \sigma_t \, dr \tag{9}$$

and the bond resistance due to this force

$$\tau_{cr} = \frac{F_b}{r_s \tan\alpha} \tag{10}$$

The total bond resistance is the sum of eq. (4) and eq. (10). To evaluate the contribution of the cracked part a suitable softening relation has to be applied to the concrete. For that purpose, an exponential expression will be used which had been derived from numerous uniaxial tensile tests [5]. This reads

$$\frac{\sigma}{f_{ct}} = \left[1 + \left(C_1 \frac{w}{w_c}\right)^3\right] \exp\left(-C_2 \frac{w}{w_c}\right) - \left(1 + C_1^3\right) \exp\left(-C_2\right) \tag{11}$$

with C1 and C2 being constants. Inserting eq. (8) into eq. (11) leads to the following expression

$$\frac{\sigma_t}{f_{ct}} = \left\{1 + \left[C_1 \beta (e-r)\right]^3\right\} \exp\left[-C_2 \beta (e-r)\right] - \left(1 - C_1^3\right) \exp\left(-C_2\right) \tag{12}$$

with the short hand notation $\beta = 2\pi\epsilon_{cr}/(nw_c)$. The bond force follows from integration between $r=r_s$ and $r=e$ (eq. (9).

$$\frac{F_b}{f_{ct}} = \frac{1}{f_{ct}} \int_{r_s}^{e} \sigma_t \, dr = \frac{1}{C_2\beta} \left\{1 - \exp\left[-C_2\beta a\right] + \frac{6C_1^2}{C_2^4\beta} - \frac{(C_1\beta)^3}{C_2\beta} \cdot \right.$$
$$\left. \cdot \exp\left(-C_2\beta a\right)\left[a^3 + \frac{3a^2}{C_2\beta} + \frac{6a}{(C_2\beta)^2} + \frac{6}{(C_2\beta)^3}\right] - \left(1 + C_1^3\right) \exp\left(-C_2 a\right) \right. \tag{13}$$

with $a = e - r_s$ which are the integral boundaries. With this result, all relations are known for the computation of the critical bond stress at the onset of splitting of the concrete cover. [1] The next step is to account for the loading rate effect.

[1] Ref. [4] contains an error which is rectified by eq. (13). The numerical effect was however negligeable.

Loading rate effect

At high rates of loading the strength of concrete increases whereas at low rates the strength decreases. This general feature has been demonstrated experimentally [6] and has also been derived theoretically [7]. This behaviour should also apply to the bond strength and to the splitting of the concrete cover due to bond forces since the loading capacity is determined by the tensile behaviour of concrete. That this hypothesis is acceptable has been demonstrated for a deformed bar embedded in concrete and pulled-out of the concrete [8]. The failure was due to the crushing and cracking of concrete around the lugs of the steel bar. The increase of pull-out force at high loading rates followed the corresponding increase of tensile and compressive strength of concrete at high loading rates.

The same idea will be applied to the splitting failure of concrete cover. For that purpose quasi-static loading conditions are assumed but with rate dependent mechanical properties of concrete. The relations will be applied as collected in [6]. It is assumed that the angle of inclination α does not change from static to dynamic loading.

The quantities involved are the tensile strength f_{ct}, the fracture energy G_F, the stress-free crack opening w_c and the elastic modulus E_c. From f_{ct} and ϵ the critical strain ϵ_{cr} is derived.

First, w_c shall be examined. This is a geometrical quantity which depends on the grading curve of concrete, the maximum aggregate size, the shape of the aggregates, and the volume fraction. The dependence of w_c on this quantities has been shown by a model[9]. There is no reason to assume a rate dependence of w_c.

The rate dependance of the tensile strength can be described by

$$\frac{f_{ct}}{f_o} = \left[\frac{\dot{\epsilon}}{\dot{\epsilon}_o}\right]^b \tag{14}$$

with the subscript o denoting the respective value at usual "static" loading which is in the order of $\epsilon_o = 3\ 10^{-6}\ s^{-1}$. Fracture energy G_F is the integral under the stress-crack opening curve. There are a few test results available which show that the shape of the descending branch is similar for various loading rates [10]. With this fact and no rate dependence of w_c it follows that

$$\frac{G_F}{G_o} = \left[\frac{\dot{\epsilon}}{\dot{\epsilon}_o}\right]^b = \left[\frac{\dot{w}}{\dot{w}_o}\right]^b \tag{15}$$

i.e. it follows the same relation as the tensile strength. This result has not been anticipated since the prepeak and the postpeak mechanism need not to be the same - bond breaking vs. aggregate interlock and friction. Furtheron, the descending branch relates on displacement (crack opening) while the ascending branch is given in terms of strain.

The elastic modulus depends on strain rate according to

$$\frac{E_c}{E_o} = \left[\frac{\dot{\epsilon}}{\dot{\epsilon}_o}\right]^C \qquad (16)$$

which leads to the rate dependence of the critical strain $\epsilon_{cr} = f_{ct}/E_c$ as

$$\frac{\epsilon_{cr}}{\epsilon_{o,cr}} = \left[\frac{\dot{\epsilon}}{\dot{\epsilon}_o}\right]^{b-c} \qquad (17)$$

If the rate dependence of tensile strength and Young's modulus were the same ϵ_{cr} remained unchanged. In reality there is a small difference which may be neglected because the contribution of the softening part is by far greater than that of the elastic part. With this approximation, the coefficient ß in eq. (12) is independent on strain rate.

The result of this deliberation is that the critical bond stress - at onset of splitting failure of the cover - depends in the same way on loading rate as the tensile strength does.

EVALUATION

The lower bound to eq. (13) is obtained for one single crack in the concrete ring, i.e. n = 1. This case will be evaluated and the results plotted in normalized form as τ_{cr}/f_{ct} both quantities being rate dependent. The following static quantities will be varied.

- tensile strength f_o = 3, 4.5 MPa
- fracture energy G_o = 100, 140 J/m²
- Young's modulus E_o = 30, 45 GPa
- bar diameter α_s = 10, 40 mm
- concrete cover c = 1 to 6 times diameter d_s
- angle of inclination α = 45°

From these quantities, the critical strain ϵ_{cr} and the stress-free crack opening w_c follow via

$\epsilon_{cr} = f_o/E_o$ and $w_c = 5.14\ G_o/f_o$ [11] with $C_1 = 3$ and $C_2 = 6.93$

to $\epsilon_{cr} = 100*10^{-6}$ and $w_c = 0.171$ mm for the first combination and

$\epsilon_{cr} = 100*10^{-6}$ and $w_c = 0.160$ mm for the second combination.

The influence of the strain rate on tensile strength can be estimated from [6]; the power becomes

$$b = (10 + f_{cm}/2)^{-1}$$

with f_{cm} the static cube compressive strength.
This leads for the first concrete with average strength f_{cm} = 30 MPa to b = 0.04 and the second with high strength f_{cm} = 50 MPa to 0.028.

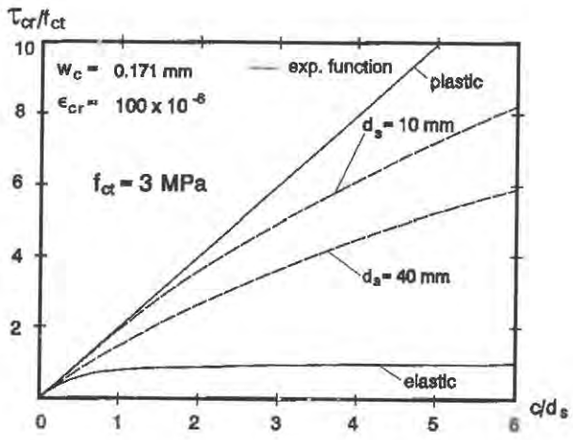

Figure 6. Bond stress at onset of failure versus thickness of concrete cover. Conrete with average strength.

Fig. 6 shows the prediction for the average strength concrete with τ_{cr}/f_{ct} vs. c/d_s. The bond resistance increases with increasing cover as expected. The bond resistance increases less for a thick bar than it does for a thinner bar or, expressed in another way, for the same bond resistance the cover has to be relatively larger. The solution for the plastic model surmounts the softening solution and the elastic solution leads always to considerably lower results. This had

to be expected since the formation of a first crack in the vicinity of the bar will not lead to failure except at very small covers.

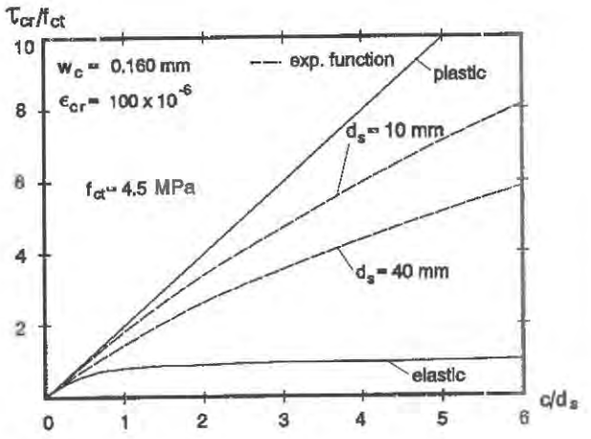

Figure 7. Bond stress at onset of failure versus thickness of concrete cover. High strength concrete.

The results for the higher strength concrete are presented in Fig. 7. Comparing the two figures 6 and 7 there is not much difference. This means that the relative strength values reamain almost the same although concrete strength has absolutely increased. The reason for that is the small difference in ϵ_{cr} and w_c in the two cases. It has been shown earlier that an increase in w_c, for instance by large aggregate, can shift the curves close to the plastic behaviour.

For better understanding, the absolute values of τ_{cr} are plotted against relative strain rate in Fig. 8 in order to show that the high strength concrete has larger advantages at low (static) loading rate while at high rates the average concrete increases the bond resistance more and can come close to the high strength concrete. This may mean in reality that the failure mechanism of a beam changes from anchorage or bond failure to another type at high loading rates in case of average concrete but that the failure type of high strength concrete remains unchanged or that bond failure will occur at high strength concrete. This last statement is a hypothesis which has not yet been proven by experiments as far as the author is aware of.

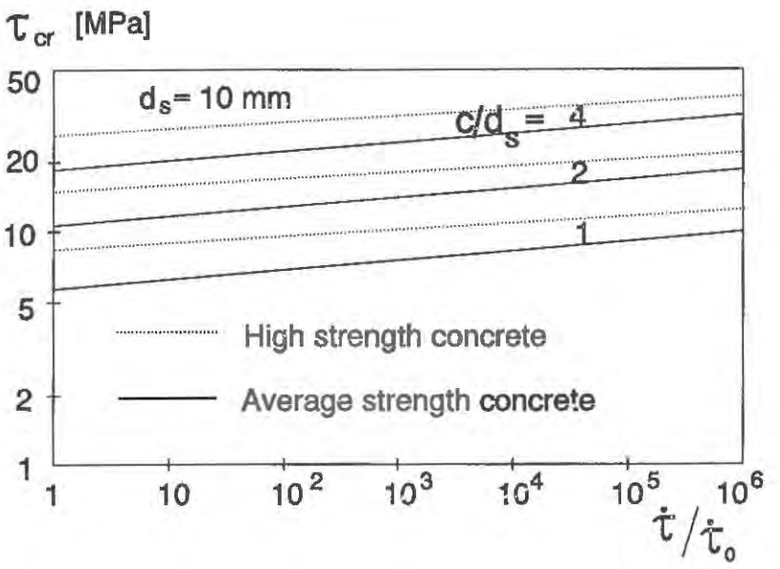

Figure 8. Critical bond stress as function of loading rate for two concrete qualities

CONCLUSIONS

From this study a few conclusions can be drawn with respect to splitting failure of concrete cover due to bond forces. First, the assumption of strain-softening behaviour of concrete seems to be an appropriate model. Second, the relation between bond stress at onset of failure and tensile strength is uneffected by strain rate. Third, the increase of bond strength due to high loading rates is smaller for high strength concrete than it is for average strength concrete. This last conclusion would justify research on beams or slabs of high strength concrete at high rates of loading in order to investigate the failure mode as affected by loading rate.

REFERENCES

1. Tepfers, R., A theory of bond applied to overlapped tensile reinforcement splices for deformed bars. Report 73-2, Chalmers University of Technology, Göteborg 1973, 328 pp.

2. Hillerborg, A., Analysis of fracutre by means of the fictitious crack model, particularly for fibre reinforced concrete. Int. J. Cement Composites 2 (1980), pp 177-184.

3. Van der Veen, C., Cryogenic bond stress-slip relationship. Thesis, Delft University of Technology, Delt 1990, 111 pp.

4. Reinhardt, H.W., Van der Veen, C., Splitting failure of a strain-softening material due to bond stresses. In "Applications of Fracture Mechanics to Reinforced Concrete", (Ed.) A-Carpinteri, Elsevier Sci. Publ. 1991, Chapter 13.

5. Reinhardt, H.W., Cornelissen, H.A.W. & Hordijk, D.A., Tensile tests and failure analysis of concrete. J. Struct. Div. (ASCE), 112 (11) (1986) 2462-77.

6. CEB "Concrete structures under inpact and impulsive loading", Bulletin No. 187, Lausanne, 1988.

7. Reinhardt, H.W., Strain rate effects on the tensile strength of concrete predicted by thermodynamic and fracture mechanics models. In "Cement-Based Composites: Strain rate Effects on Fracture", Eds. S. Mindess, S. P. Shah - Mat. Res. Soc. Symp. Proc. Vol. 64, Pittsburg, PA, 1986, pp 1-13.

8. Reinhardt, H.W. Blaauwendraad J. & Vos. E., Prediction of bond between steel and concrete by numerical analysis. Materials & Structures, 17 (100) (1984) 311-20.

9. Duda, H., Bruchmechanisches Verhalten von Beton unter monotoner und zyklischer Zugbeanspruchung. Deutscher Ausschuss für Stahlbeton, Bulletin No. 419, Beuth, Berlin 1991, 60 pp.

Invited Paper

CHARACTERISATION OF INTERFACIAL PROPERTIES IN STEEL FIBRE-CEMENT MORTAR MATRIX COMPOSITES

JANG-KYO KIM, LI-MIN ZHOU & YIU-WING MAI
Centre for Advanced Materials Technology
Department of Mechanical Engineering
University of Sydney, Sydney, NSW 2006, Australia

ABSTRACT

An improved theoretical analysis developed on the basis of the concept of fracture mechanics has been successfully used to characterise the debonding and frictional pull-out behaviours in steel fibre reinforced cement mortar matrix composites. It is shown that the maximum debond stress σ_d^* predicted using the instability criterion developed by the authors agrees well with experiment over the whole range of embedded fibre length L studied. However, the theory overestimates the post-debond frictional pull-out stress σ_{fr}, particularly for long L, if the same parameters are used for prediction. This discrepancy seems to be a direct result of the decay of frictional bond at the interface region after complete debonding due mainly to compaction of the porous cement mortar surrounding the fibre. This effectively reduces the residual clamping stress q_0 arising from shrinkage of the cement matrix. Therefore, a correct theoretical prediction is made for the frictional pull-out stress σ_{fr} using a lower value of q_0 while other parameters are kept constant, which gives good agreement with experimental results. It is noted that the interfacial properties determined in the present study compared favourably with the values reported in the literature.

INTRODUCTION

The recognition of the importance of the interfacial properties has led to an increased effort in both micromechanical and experimental characterisation of the fibre-matrix interface in various loading configuration including fibre pull-out. There are two distinct approaches to the theoretical analysis of fibre pull-out: one is based on a maximum shear

stress criterion such that debonding occurs when the interfacial shear stress exceeds the shear bond strength τ_b; and the other is based on the concept of fracture mechanics where the debonded region is considered as an interfacial crack and its propagation is dependent on the energy balance in terms of interfacial fracture toughness G_{ic}. In the authors' previous study [1] an improved analysis has been developed on the basis of the concept of fracture mechanics, in which the differential total elastic energy stored in the composite constituents at both bonded and debonded regions are equated to the interfacial fracture toughness. Poisson contraction of the fibre when subjected to tension is considered which results in a more-generalised non-uniform friction along the debonded region. Excellent agreement was obtained for the maximum debond stress and the initial frictional pull-out stress after complete debonding between theories and fibre pull-out experiments of several composite systems with epoxy and ceramic matrices. The principal aim of the present study is to characterise the interfacial properties by comparing the theory with published data for steel fibre-cement mortar matrix systems. Causes of anomaly observed in the fibre pull-out experiments of this material are clarified in terms of the relationship between microstructure and failure mechanisms at the fibre-matrix interface region, and their effects are correctly reflected for the interfacial properties.

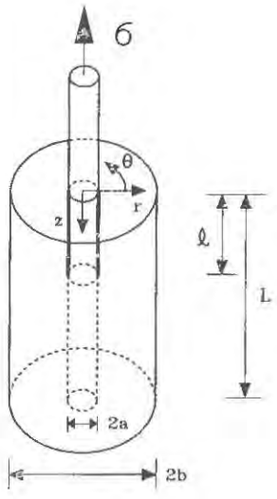

Figure 1. A schematic of fibre pull-out model.

THEORY

A simple shear lag model shown in Figure 1 consists of a fibre (of radius a) which is embedded at the centre of a coaxial cylindrical shell of matrix (of an outer radius b). L is the total embedded fibre length with a partial debonded region ℓ from the fibre free end. In experiment the matrix is fixed at one end (z=L) and a tensile stress σ is applied to the other end (z=0) of the embedded fibre. Shear lag analysis for other boundary conditions with restrained matrix top and fixed matrix and fibre bottom ends are given elsewhere [2]. The external stress σ is represented by σ_0, σ_d^P, σ_d^* and σ_{fr} for frictionless (initial) debond stress, partial debond stress, maximum debond stress and initial frictional pull-out stress after complete debonding, respectively, at different stages of the fibre pull-out process. In our previous study [1] the solution for the partial debond stress σ_d^P during progressive debonding was formulated as a function of the debond length ℓ and the crack tip debond stress σ_ℓ which is the fibre axial stress acting at the boundary between the bonded and debonded regions ($z=\ell$):

$$\sigma_d^P = \sigma_\ell + (\bar{\sigma} - \sigma_\ell)\frac{\omega\,[\exp(\lambda\ell) - 1]}{1 + \omega\exp(\lambda\ell)} \approx \sigma_\ell + (\bar{\sigma} - \sigma_\ell)[1 - \exp(-\lambda\ell)] \qquad (1)$$

Therefore, using Eq. (1) the initial debond stress σ_0 is determined for an infinitesimal debond length (i.e. $\ell \to 0$) and the maximum debond stress σ_d^* determined at load instability [3,4]. Further, the solution for the initial frictional pull-out stress σ_{fr} after complete debonding was obtained when the debond length ℓ reaches the embedded length L and $\sigma_\ell = 0$:

$$\sigma_{fr} = \frac{\omega\,\bar{\sigma}\,[\exp(\lambda L) - 1]}{1 + \omega\exp(\lambda L)} \approx \bar{\sigma}\,[1 - \exp(-\lambda L)] \qquad (2)$$

λ is the reciprocal length giving the effective friction shear stress transfer distance and $\bar{\sigma}$ is the asymptotic debond stress for long embedded length L. These parameters are related to the coefficient of friction μ and the residual clamping stress q_0 (caused by the matrix shrinkage and differential thermal contraction between fibre and matrix) by:

$$\lambda = 2\mu k/a \qquad (3)$$

$$\bar{\sigma} = -(q_0/k)\,[1 + (\gamma/\alpha)(\nu_m/\nu_f)] \qquad (4)$$

where $\alpha = E_m/E_f$, $k = (\alpha\nu_f + \gamma\nu_m)/[\alpha(1 - \nu_f) + 1 + \nu_m + 2\gamma]$, $\gamma = a^2/(b^2 - a^2)$ and $\omega = \alpha\nu_f/(\alpha\nu_f + \gamma\nu_m)$. ν_f and ν_m are the fibre and matrix Poisson ratios. The partial debond stress σ_d^p in Eq. (1) is composed of two components: a crack tip debond stress σ_ℓ which is a function of G_{ic} and the debond length ℓ relative to L; a friction stress component which is directly proportional to $(\overline{\sigma} - \sigma_\ell)$ and is also a function of λ.

TABLE 1
Interfacial properties of steel wire-cement mortar matrix composites

σ_0 (GPa)	λ (mm^{-1})	$\overline{\sigma}$ (GPa)	G_{ic} (J/m^2)	μ	q_0 (MPa)	z_{max} (mm)
0.106	0.0269	0.780 (1.62)[a]	2.50	0.082	-24.2 (-50.3)[a]	1.20

[a] Uncorrected values

RESULTS AND DISCUSSION

Published data for steel fibre-cement mortar (or paste) composites having similar elastic properties and radii of the constituents are compared with theoretical predictions. Only those with both the maximum debond stress and post-debond frictional pull-out stress available are selected [5-9] so that the interfacial parameters λ, $\overline{\sigma}$ and σ_0 (and thus μ, q_0 and G_{ic}) can be determined simultaneously. Properties and radii of the constituents given by Gray [5] who measured the pull-out stresses for a wide range of embedded fibre length L are used for prediction: E_f = 207 GPa, E_m = 30.4 GPa, ν_f = 0.27, ν_m = 0.17, a = 0.19 mm, b = 12.7 mm. The interfacial properties are determined by evaluating experimental results with regard to λ, $\overline{\sigma}$ and σ_0 in a procedure similar to that presented previously [4], and are summarised in Table 1. Using these interfacial properties (including the uncorrected value $\overline{\sigma}$ = 1.62 GPa or q_0 = -50.3 GPa), specific results of the partial debond stress σ_d^p are calculated against debond length ℓ for two different embedded fibre lengths as shown in Figure 2. It is clear that the cement matrix composite is typical of frictional bonding at the fibre-matrix interface as evidenced by the major contribution of the friction stress component to the partial debond stress σ_d^p

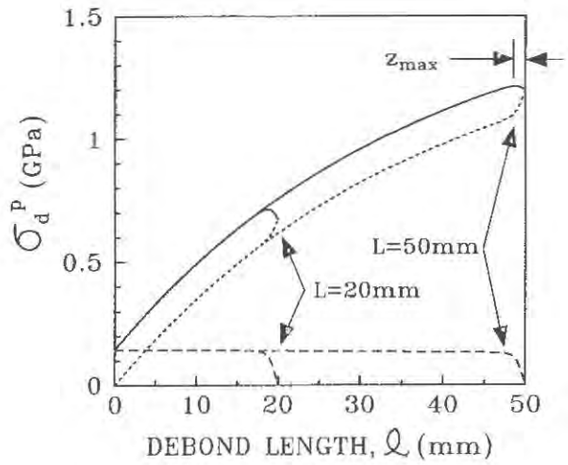

Figure 2. Plots of partial debond stress σ_d^p as a function of debond length ℓ for different embedded fibre length L for steel fibre-cement mortar matrix composites: —— partial debond stress σ_d^p; - - - - crack tip debond stress σ_ℓ; ------ friction stress component.

(i.e. over 80% at instability for L = 50 mm). This is further manifested by the very small z_{max} (= 1.2 mm) which is the maximum bond length for unstable debonding. The instability condition described in the authors' previous paper [3] requires that the derivative of σ_d^p with respect to the remaining bond length (L-ℓ) is equal to or less than zero. This implies that the debond process becomes unstable if L or (L-ℓ) is smaller than z_{max}, where the maximum debond stress σ_d^* is obtained. It is predicted that a two-fold increase in the interfacial fracture toughness G_{ic} (and thus the corresponding increase in the frictionless initial debond stress σ_0 from 0.106 GPa to 0.15 GPa) would result in only a negligible increase in the partial debond stress σ_d^p. This further confirms that the chemical bond (which is represented either by the interfacial fracture toughness G_{ic} or shear bond strength τ_b) makes up only an insignificant contribution to the total bond quality at the interface of this material.

The maximum debond stress σ_d^* and the initial frictional pull-out stress σ_{fr} obtained just before and after load instability, respectively, are compared with experimental results in Figure 3. The predictions for the maximum debond stress σ_d^* agree well with experiment over the whole range of embedded fibre length L considering

the data scatter expected for different testing methods and materials (Figure 3(a)). However, the theory overestimates the initial frictional pull-out stress σ_{fr}, particularly for long L (Figure 3(b)), if the same interfacial parameters are used for prediction. This discrepancy is considered to be a direct result of the decay of frictional bond at the debonded region which effectively reduces the frictional pull-out stress σ_{fr} measured in experiments. There are several reasons for the degradation of the frictional resistance: the compaction or densification of cement mortar near the fibre surface [10-12]; the microcracking and virtual breakdown of the cement mortar at the interface due to the high stiffness and hardness of the fibre relative to the matrix material [10,11]; the permanent plastic deformation of the steel fibre, particularly at a high debond stress for a long embedded fibre. Among these the first is the most likely, which is related to the porous nature of cement mortar. Bentur et al. [13] have explained the microstructure of this material in terms of a transition zone which consists of a duplex film of cement, a CH rich layer, a porous layer and the bulk material from the fibre surface. The weakest region of the transition zone is not necessarily at the actual interface, but is in the porous layer as evidenced by the low microhardness at a distance approximately 20 to 40 μm away from the interface [14]. The weak porous layer is compacted upon fibre slip after debonding, resulting in enlargement of the matrix hole.

Therefore, the gross effect turns out to be a significant reduction in the residual clamping stress q_0 [10, 12] arising from the matrix shrinkage, rather than a reduction in the coefficient of friction μ. Further, a significant portion of the relaxation of residual clamping stress appears to have occurred at the end of and/or just after the debonding process as suggested by the progressive load drop (as opposed to the rapid unstable load drop in polymer- and ceramic-based composite systems) after the maximum in the pull-out load versus displacement record for this material [5, 9, 12]. Therefore, a correct theoretical prediction is made for the frictional pull-out stress σ_{fr} using a lower value of q_0 (reduced from -50.3 MPa to -24.2 MPa) while other parameters are kept constant. The new prediction gives excellent agreement with experimental results as shown in Fig. 3(b). It is noted that the interfacial properties determined in the present study (i.e. $G_{ic} = 2.5\,J/m^2$, $q_0 = -24.2$ MPa, $\mu = 0.082$ and the initial frictional shear bond strength $\tau_{fr} \approx -\mu q_0 = 1.98$ MPa) compared most favourably with the values reported in the literature (e.g. $q_0 = -24.6$ MPa, $\mu = 0.09$ [5], $\tau_{fr} = 1.4 \sim 1.8$ MPa [12] and $G_{ic} = 2.41 \sim 2.53\,J/m^2$, $\tau_{fr} = 1.3$ MPa [15]).

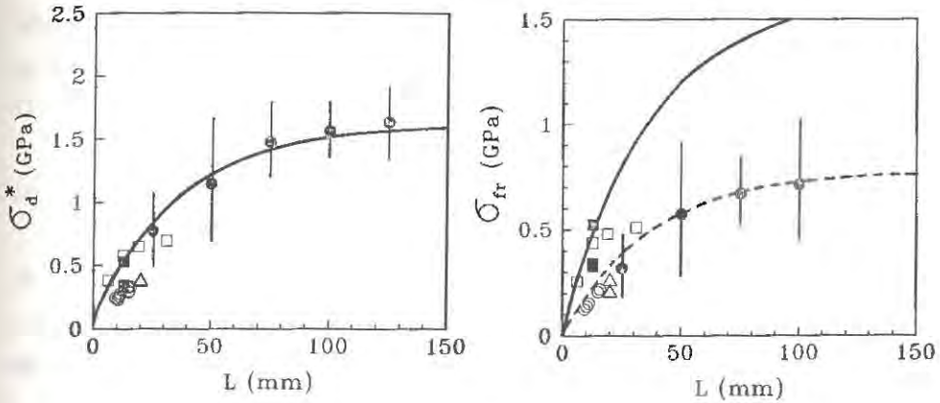

Figure 3. Comparison between experimental results and theoretical predictions of (a) maximum debond stress σ_d^* and (b) initial frictional pull-out stress σ_{fr} as a function of embedded fibre length L for the steel fibre-cement mortar matrix composites. Experimental data taken from (◉) Gray (1984); (○) Maage (1977); (□) Beaumont and Aleszka (1978); (▩) Naaman and Shah (1976); (△) Mandel et al. (1987). Predictions: ——— with residual clamping stress $q_0 = -50.3$ MPa; - - - - - with corrected $q_0 = -24.2$ MPa for σ_{fr} prediction.

CONCLUSION

Using an improved theoretical analysis developed by the authors on the basis of the concept of fracture mechanics, interfacial properties have been characterised with regard to the debond and frictional pull-out stresses in steel fibre reinforced cement mortar matrix composites. The interfacial properties including the interfacial fracture toughness G_{ic}, residual clamping stress q_0 and the coefficient of friction μ are determined in a procedure suggested previously. It is shown that the maximum debond stress σ_d^* predictions agree well with the experimental results over the whole range of embedded fibre length L studied. However, the theory overestimates the post-debond frictional pull-out stress σ_{fr}, particularly for long L, if the same interfacial properties are used for prediction. This discrepancy is presumably a direct result of degradation of frictional bond at the debonded interface due mainly to compaction of the porous cement mortar surrounding the fibre. This effectively reduces the residual clamping stress q_0 arising

from shrinkage of the cement matrix. Therefore, a correct theoretical prediction is made for σ_{fr} using a lower value of q_0 while other properties are kept constant, which gives good agreement with experimental results.

ACKNOWLEDGMENTS

The authors wish to thank the Australian Research Council for the continuing support of this work which forms part of a larger project on "Development of High Strength and High Fracture Toughness Fibre Composites with Controlled Interfaces." Thanks are also due to B. Cotterell for many useful suggestions and stimulating discussions.

REFERENCES

1. Zhou, L.M., Kim J.K. and Mai, Y.W., Interfacial debonding and fibre pull-out stresses: Part II. a new model based on the fracture mechanics approach. J. Mater. Sci., 1992, **27**, in press.

2. Zhou, L.M., Kim J.K. and Mai, Y.W., On the single fibre pull-out problem: effect of loading methods. Composite Sci. Technol., 1992, in press.

3. Kim, J.K., Baillie C. and Mai, Y.W., Instability of interfacial debonding during fibre pull-out. Scripta Metall. Mater., 1991, **25**, 315-320.

4. Kim, J.K., Baillie C. and Mai, Y.W., Interfacial debonding and fibre pull-out stresses: Part I. a critical comparison of existing theories with experiments. J. Mater. Sci., 1992, **27**, in press.

5. Gray R.Y., Analysis of the effects of embedded fibre length on fibre debonding and pull-out from en elastic matrix. J. Mater. Sci., 1984, **19**, 1680-1691.

6. Maage M., Interaction between steel fibers and cement based matrices. Mater. Struct., 1977, **10**, 297-301.

7. Beaumont P.W.R. and Aleszka J.C., Cracking and toughening of concrete and polymer-concrete dispersed with short steel wires. J. Mater. Sci., 1978, **13**, 1749-1760.

8. Naaman A.E. and Shah S.P., Pull-out mechanism in steel fiber-reinforced concrete. J. Struct. Div. ASCE, 1976 , **102**, 1537-1548.

9. Mandel J.A., Wei S. and Said S., Studies of the properties of the fiber-matrix interface in steel fiber reinforced mortar. ACI Mater. J., 1987, **12**, 101-109.

10. Pinchin D.J. and Tabor D., Interfacial phenomena in steel fiber-reinforced cement II: Pull-out behavior of steel wires. Cement Concr. Res., 1978, **8**, 139-150.

11. Wang Y., Li V.C. and Backer S., Modelling of fibre pull-out from a cement matrix. Intern. J. Cement Composites Lightwt. Concr., 1988, **10**, 143-149.

12. Naaman A.E., Narmur G.G., Alwan J.M., Najm H.S. (1991)., Fiber pullout and bond slip. I: Analytical study. J. Struct. Eng. ASCE, 1991, **119**, 2769-2790.

13. Bentur A., Diamond S. and Mindess S., The microstructure of the steel fibre-cement interface. J. Mater. Sci., 1985, **20**, 3610-3620.

14. Wei S., Mandel J.A. and Said S., Study of the interface strength in steel fiber-reinforced cement-based composites. ACI J., 1986, **83**, 597-605.

15. Morrison J.K., Shah S.P. and Jenq Y.S., Analysis of fiber debonding and pullout in composites. J. Eng. Mech. ASCE, 1988, **114**, 277-294.

INFLUENCE OF THE STATE OF STRESS IN CONCRETE ON THE BEHAVIOR OF THE STEEL CONCRETE INTERFACE

C. La Borderie and G. Pijaudier-Cabot

Laboratoire de Mécanique et Technologie, ENS Cachan / CNRS / Université P. et M. Curie, 61 Avenue du Président Wilson 94235 Cachan Cedex, FRANCE.

Abstract : - Predictions of the response of civil engineering structures cannot be correctly performed if the behaviors of concrete, steel and of the steel concrete interface are not well captured. In this paper, we are interested in the response of the interface between concrete and steel fibers or bars. Several results from pull out tests are presented. This study is aimed at obtaining reliable data on the effect of the state of stress in concrete on the response of the interface. It is found that the confinement stress has no effect on the fiber-concrete interface and that is has a significant influence on the response of the interface between reinforcing bars and concrete. These results will eventually help at identifying debonding and friction laws.

1. INTRODUCTION

There exist in the literature a large number of experimental set-ups designed for performing pull-out tests:

- In the case of pull-out on reinforcing bars, the usual procedure is that tension is applied at both ends of the bar which protrudes from concrete [1]. Unfortunately this test set up is quite inappropriate because the concrete block fails usually in tension and the mode of failure has nothing to do with testing the interface between the two materials. Retaining concrete with a sleeve (see e.g. [2]) while the bar is pulled is the easiest method. Nevertheless such boundary conditions cause compression to develop in concrete and perturbs the state of stress about the fiber at the interface. Casting the block of concrete into a rigid hollow cylinder which remains fixed during test is most probably the set up which produces less perturbations on the state of stress in concrete near the interface [3].

In the case of fiber there are some additional choices: the number of fiber pulled is a parameter [4], their orientation is another one, and finally the shape of the specimen can be quite different from one study to another [5].

Despite the large bulk of data, the effect of the state of stress in concrete on the response of the interface is surprisingly lacking. In usual structures, the state of stress in concrete about the steel reinforcement is complex. The effect of lateral confinement on the interface properties of concrete is a question which needs an answer beyond the knowledge of the variation of the shear strength. Indeed, the models for the steel concrete interface need to be consistent with the material description, i.e. progressive fracturing in concrete and plasticity in steel. Consistency calls for models that describe the response of the interface entirely and include the debonding and slipping regime observed in real failure of concrete members [6].

In order to decide upon the type of friction model which should be used for the interface it seems reasonable to think that the state of stress in concrete can be a very sensitive variable. If the effect of confinement on debonding and crack propagation at the interface is not clear, the residual strength of the interface due to friction should vary with the confinement. With a Tresca friction model for example, the amount of relative slip between the fiber and the matrix should not depend on the hydrostatic stress at any given pull-out load. Furthermore, the

unloading-reloading behavior of the specimen measured in term of shear stress versus relative slip is expected to be quite dependent on the type of friction law [7]. The variation of the state of stress in concrete is one of the originality of these results. Another valuable information is that fibers are pulled out of concrete and not mortar as it was done usually in the past.

2. TEST SET-UP AND SPECIMENS

The specimen tested are cubes of 80 x 80 x 80 mm in which a fiber or a reinforcing bar is embedded at the center. The concrete grade chosen is C30/37 with a compressive strength of about 25 MPa measured on cylinders (Ø = 16 cm, h = 32 cm). The maximum size of the aggregate is 16 mm so the size of the concrete cube corresponds to the smallest possible in view of the homogeneity of the state of lateral stress in the specimen without fiber which must be achieved and considering the capacity of our testing frame. The embeddement length of the fibers corresponds to half the fiber lengths and the embeddement length of the reinforcing bars is 45 mm (Ø 8 mm bars).The specimens were cast 28 days (average) before testing, removed from the molds 24 h after casting and kept at room temperature. In order to equilibrate the pull-out force applied to the fiber (or bar), the concrete block was retained by a circular sleeve. It was checked with finite element calculations (nonlinear) that this configuration did not generated uncontrolled compressive stresses on the interface. The lateral confinement was applied using brush-platens The testing frame for these experiments was a SCHENK multiaxial testing system. The lateral confinement was applied with four hydraulic jacks (100KN) and the pull-out force was applied with another pair of jacks of capacity 250 KN each. Load or displacement control was available on each jack. The pull-out force was applied while the displacement was controlled ($\dot{u} = 8{,}3\ 10^{-3}$ mm/s) and the lateral forces were constrained to remain constant. The pull-out force was measured with load cells of capacity 250KN, 500N and 22N depending on the type of fiber tested and the relative slip was measured with a LVDT.

3. PULL-OUT TESTS ON FIBERS

Two types of fibers were tested : smooth fibers (WIREX) of length 40 mm and diameter 0.6 mm (embeddement length 20 mm) and hooked fibers (DRAMIX) of length 60 mm and diameter 0.8 mm (embeddement length 30 mm). Three different confinement stresses were applied of 0, 7.5 and 15 MPa respectively. The confinement was applied first on each specimen and then it was kept constant under load control conditions. Then, the fiber was pulled out and unloading-reloading cycles were carried out every time the fiber was pulled of 2,5 mm starting at the peak load.

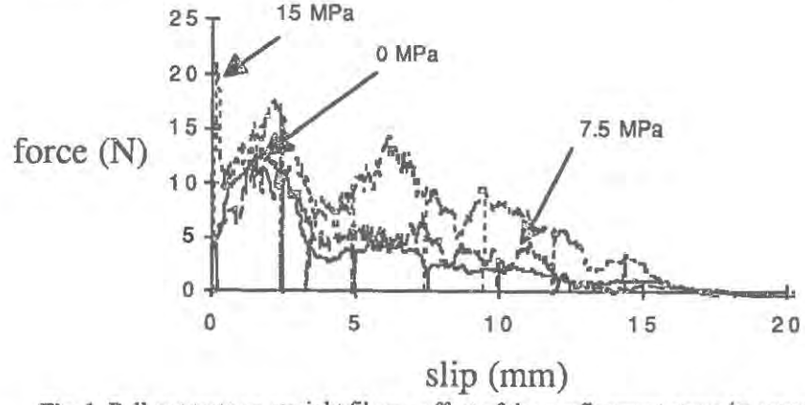

Fig. 1: Pull-out tests on straight fibers - effect of the confinement stress in concrete.

Fig. 1 presents the results of the tests on the smooth fibers for the various confinement stresses. The pull-out strength is of the order of 10N (accuracy 0.1N). At such a low level, any misalignment between the fiber and the load, or any particle touching the fiber can cause the load to change sensitively.

In most cases the pull-out force versus relative slip curve exhibits a peak and then a long tail during which the fiber is progressively pulled out of concrete. In some instances this peak is not very acute. Overall, the peak load does not seem to be affected by the confinement pressure.

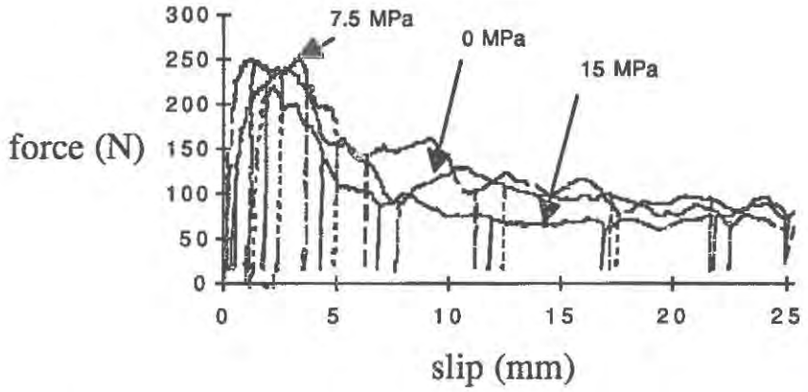

Fig. 2: Pull-out tests on hooked fibers - effect of the confinement stress in concrete.

The same program of experiments has been carried out with the DRAMIX fibers which have a hooked extremity. Fig. 2 presents the results for the three lateral stresses. Again, the results do not exhibit any significant influence of the confinement on the pull-out strength. As opposed to the experiments on the WIREX fibers, the dispersion seems to be within an acceptable range. The level of strength is 10 to 20 times what is measured for the smooth fibers. This indicates that geometrical effects such as a hook on the fibers produce the mechanisms in fiber reinforced concrete which provide the increase of ductility observed usually in tensile or bending tests. The fiber is constrained to become straight during pull-out and the yield stress of steel must be reached in order to deform the hook at the extremity of the fiber [4]. The failure mechanism is controlled by the deformation of the fiber and most probably friction in the region of the hook. This phenomenon is extremely localized since the bond provided by the rest of the fiber which is embedded is negligible. As a consequence, the response during the pull-out test is not really sensitive to the confinement applied to concrete.

4. PULL-OUT TEST ON REINFORCING BARS

Over the range of possible confining pressures between 0 and 15 MPa, four types of tests were carried out in which the pressure was increased by 5 MPa for each type. The loading procedure was kept the same than that described in §3. The results are plotted on Fig. 3. It shows that there is a definite effect of the lateral stress on the response of the interface : the strength increases with the confinement stress and the interface softens less beyond the peak for high values of the relative slip at the interface. The increase of strength is 35% and corresponds quite accurately to what ROBINS and STANDISH [8] measured. Therefore, we can state that such a variation is significant of the interface response. From the loading-

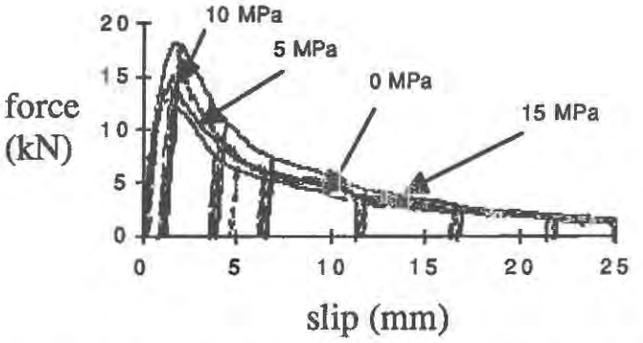

Fig. 3: Pull-out tests on reinforcing bars - effect of the confinement stress in concrete.

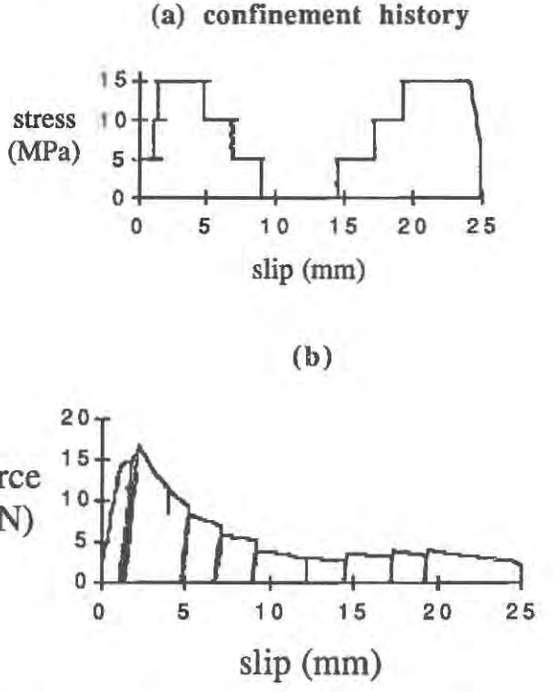

Fig. 4: Pull-out tests on reinforcing bars - effect of the variation of confinement stress in concrete.

unloading cycles in which the lateral stress has been changed, we see that the confinement has a very sensitive effect on friction properties of this interface. The variation can be of the order of 33 % for a confinement decreasing of 5 MPa. (Fig. 4).

5. DISCUSSION OF THE RESULTS

In an attempt to summarize the results of this test program, we have plotted on Figs. 5-6, the effect of the confinement on the pull-out strength in each test. It seems that such an influence is negligible for the fibers. For reinforcing bars, the influence of the confining pressure exists. It affects also the shape of the force-slip curve and friction at the interface.

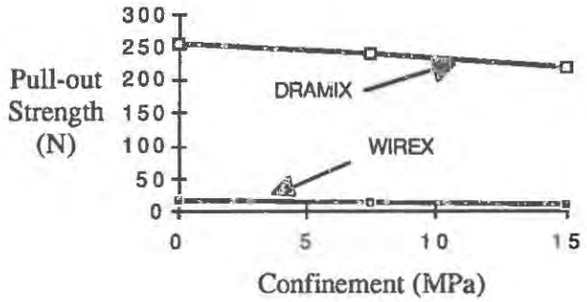

Fig. 5 : Pull-out strength v.s. confinement stress for fibers

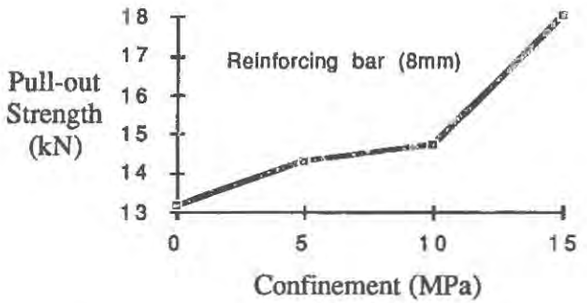

Fig. 6 : Pull-out strength v.s. confinement stress for bars

The pull-out test on smooth fibers show that the bond is not the important mechanism which provide the increase of mechanical properties of FRC. Hooked fibers have a pull-out strength which is 20 times higher than smooth fibers. The effect of the confining pressure is negligible.

The strength and response of the interface between a deformed bar and concrete is mainly controlled by cracking in concrete. Debonding seems to be affected by the confinement of concrete. The effect of the lateral pressure on the residual load due to friction is observed.

Acknowledgements : Financial support of the Commission of the European Communities through the Brite-Euram Programme (Project BE-3275) and of Electricité de France (under contract I 70/1F 3146) is gratefully acknowledged.

6. REFERENCES

[1] GOTO Y. (1971), "Crack Formed in Concrete Around Tensile Bars", J. American Concrete Inst., Vol. 68, pp. 244-251.

[2] BAZANT Z.P. and SENER S. (1988). "Size Effect in Pull-Out Tests" ACI Materials Journal, Sept-Oct., pp. 347-351.

[3] ADROUCHE K. , LORRAIN M. (1987), "Influence des Paramètres Constitutifs de l'Association Acier-Béton sur la Résistance de l'Adhérence aux Chargements Cycliques Lents", Materials and Structures RILEM, vol. 20, n° 118, pp. 315-320.

[4] CHANVILLARD G. (1990), "Interaction fibres d'acier-matrices cimentaires", coll. du GRECO Géomatériaux.

[5] BARTOS P. (1981), "Bond in Fibre Reinforced Cements and Concretes", Int. J. of Cement Composite and Lightweight concrete, Vol. 3, pp. 1 - 18.

[6] LA BORDERIE C. (1991) , "Phénomènes Unilatéraux dans un Matériau Endommageable. Modélisation et Application à l'Analyse de Structures en Béton". Thèse de Doctorat, Université P. et M. CURIE.

[7] BUI H.D. (1991), "Failure Mechanics of Fiber-Reinforced Concrete and Pre-Damaged Structures, Task Report n° 3", Brite Euram Project P-3275, Report n° 816-07 Dept. Mécanique et Modèles Numériques, Electricité de France.

[8] ROBINS P.J. and STANDISH I.G. (1984), "The Influence of Lateral Pressure Upon Anchorage Bond", Mag. of Concrete Res., Vol. 36, pp. 195-202.

FRACTURE MECHANICS IMPLICATIONS IN THE BOND AND DEVELOPMENT OF REINFORCEMENT IN CONCRETE

Steven L. McCabe
Associate Professor of Civil Engineering
University of Kansas
Lawrence, KS 66045

David Darwin
Deane E. Ackers Professor of Civil Engineering
University of Kansas
Lawrence, KS 66045

Abstract

Based on work performed over the past decade by the authors and others, it has become apparent that the interaction of reinforcing bars with concrete is a structural process and that the characteristics of the overall system are important. Bond failures can be explained through the use of structural evaluation methods including fracture mechanics.

One can evaluate the generation of microcracks around the region of a bar, followed by the growth of these cracks into larger macrocracks, ultimately leading to slippage of the bar and failure of the system as on-going fracture process. If this approach is taken, it can lead to an understanding of the importance of design parameters such as bar spacing, cover, and the degree of confinement provided by transverse reinforcing steel.

Using fracture as the key cause of splitting bond failures, this approach is used to make observations regarding the design considerations for reinforced concrete. The paper evaluates aspects of bond as observed in the laboratory and through analytical studies conducted by the authors, and observations are made regarding the overall process of bonding reinforcement to concrete. Parameters include the concrete strength, the bar surface, the characteristics of the member, including the bar spacing and cover. The paper concludes with a summary of the findings to date and the anticipated research efforts that need to be undertaken to further extend the application of fracture mechanics to bond evaluation in full scale structures.

INTRODUCTION

The bond and development of reinforcement in concrete structures is a key factor in the overall structural performance of these systems. Proper attachment of reinforcement to the surrounding concrete to attain strain compatibility is an underlying assumption in the design of reinforced concrete structures. Without proper attachment of the reinforcing steel to the surrounding concrete, bar slippage and structural failure will result. Thus, determination of the required length to develop the full yield capacity of the bar is a critical step in design.

Since the early days of the reinforced concrete industry, when the original smooth surface bars were replaced with deformed bars, researchers have attempted to quantify and model the bond process to allow designers to accurately select the development length. The goal has been to obtain a safe estimate of the length required, without producing overly conservative and expensive predictions that compromise the cost effectiveness of reinforced concrete structures. Traditionally, bond strength has been considered to be a material property – one that is related to the characteristics of the concrete and the reinforcing bar. Using this approach, studies of bond have been conducted in a localized sense, and bond failure has been viewed as a failure of the materials involved rather than as a failure of the structure as a whole.

This attitude, however, is changing. Over the past decade, there have been a number of studies performed by the authors and others that have investigated the bond of epoxy-coated and uncoated deformed steel bars in specimens with a variety of geometries. This work has provided insight that leads one to conclude that the bond process can indeed be explained through a structural engineering approach, where stresses, strains, structural geometry, and material properties come into play.

This paper summarizes some of the research conducted by the authors at the University of Kansas into the overall question of bond and development of reinforcement and addresses a very promising area of endeavor, the application of fracture mechanics to this problem. It will be shown that the bond process and the prediction of development lengths for reinforcing bars in concrete can be founded upon a fracture mechanics approach and that the design community can benefit from a fracture mechanics-based philosophy when determining the proper development lengths for use in design.

BOND AND DEVELOPMENT BACKGROUND

Over the last several decades, there have been a number of important studies of bond and development of reinforcement to concrete including those by Tepfers [21,22], Ferguson [9-12], and others [1, 18, 19]. These studies have greatly enhanced our understanding of the lengths needed to fully develop a bar to its yield strength. Work by Orangun, Jirsa, and Breen [19], Treece and Jirsa [23], Cleary and Ramirez [7], Darwin et al. [3,4,14,15] have focused additional attention on this important process. However, a shift has gradually occurred over the past ten years caused in part by the advent of computer-based analysis techniques, in particular finite element analysis and more recently fracture mechanics. If one looks at the earlier studies of bond, one observes that most of this research has been experimental in nature. A large number of specimens have been tested, evaluating various bar sizes, concrete strengths, and geometric configurations. Empirical equations have been developed depicting the behavior of these specimens under load. These empirical equations have been refined and made more accurate over the years, as the pool of data has increased; once a reliable and accurate empirical equation is identified, then an equation for design use can be developed. The foremost example of this approach is the ACI-318 [2] equation for development length.

$$l_d = 0.04\, A_b f_y / \sqrt{f'_c} \qquad (1)$$

This equation represents the development length, l_d, of the bar in terms of the bar area, A_b, the bar nominal yield, f_y, and the nominal strength of the concrete, f'_c. Equation 1 and the Orangun, Jirsa, Breen expression [20], Eq. 2 below, are examples of empirical equations where curves are fit to the data. This approach can accurately represent behavior provided the test parameters upon which the equations are founded are not violated by the designer.

$$l_d = \frac{10{,}200 d_b}{\sqrt{f'_c}\,(1 + 2.5\frac{C}{d_b} + K_{tr})\,\phi} \qquad (2)$$

$$K_{tr} = \frac{A_{tr}\, f_{yt}}{600\, s d_b} \leq 2.5$$

where C is the cover or one-half the clear spacing and A_{tr} is the transverse steel area.

The empirical approach begins with an hypothesis, that is represented in some fashion by the testing parameters involved and can lead to greater insight into the bond process. However, it is significant that no underlying model *per se* is proposed prior to the testing. Rather, the results are reduced and a form of empirical model results from the testing activity in the laboratory.

Recent work by the authors has begun to show that one can effectively join the laboratory to the analytical environment and that experimental work can be verified through straightforward, relatively simple analytical procedures which, in turn, may lead to the development of future design expressions.

One such process has occurred over the past five years at the University of Kansas where a large-scale National Science Foundation study has involved tests of approximately 500 beam-end specimens and 50 splice specimens. The goal of the study has been to experimentally determine the behavior of epoxy-coated and uncoated bars as a function of bar size and geometry, concrete strength, and specimen geometry. In this study, the experimental results have been evaluated using traditional methods, but the behavior observed in a laboratory has been analytically verified using fracture mechanics concepts and finite element techniques. The following section provides additional background on this study.

EXPERIMENTAL AND ANALYTICAL RESULTS

In the NSF study at the University of Kansas, it has been consistently observed that. at bond failure, both the beam-end specimens and the splice specimens undergo a splitting process in which a crack plane(s) is generated at the center line of the bar and propagates either to a free surface or to adjacent bars. In no tests were so-called pullout failures observed. This is due, in part, to the design of the specimens which involved bar placement geometries and covers matching those found in practice [3,4,14,15]. Typical failures from loading of the beam-end specimens reveal a splitting plane located on the specimen center line with two other planes located at 120 degree intervals. The splitting occurred nearly instantaneously, and failure occurred in a nonductile manner. It can be qualitatively observed that when bond failure occurs, as the bar deformations attempt to slip past the surrounding concrete, the concrete is forced outward and "rides up" on the bar deformations. This induces transverse tensile strains and stresses in the concrete. This process could continue until the deformations have slid completely up and the bar is free to slide out of the surrounding concrete. Prior to this occurring, however, the specimen fails by splitting due to the slip-induced tensile stresses. Tepfers [21] observed this phenomena early on and attempted to evaluate this process using the thickwall cylinder analogy. While this analogy is not viable for design and can severly underestimate bond strength, it does provide a starting point for more accurate evaluation of the state of stress using finite element techniques.

At the University of Kansas, the beam-end specimen has been extensively analyzed using linear elastic finite elements, together with fracture mechanics modeling to better understand the failure process observed in the laboratory. Typical models include one-half of the beam-end specimen with a predefined fracture plane located along the specimen center line. The specimen is joined to the model center line by zero length rod elements. The rod elements allow the crack opening behavior to be represented by the Fictitious Crack Model first developed by Hillerborg et al. [16]. The model is based on the concept that the cracking

process is principally controlled by the fracture energy, G_f, the energy required to open a crack of a unit area.

The reinforcing bar is modeled as a linear elastic material joined to the surrounding concrete by a Mohr-Coulomb slip surface. In this way, once the adhesion between the bar and the surrounding concrete is exceeded, the bar slips with respect to the concrete and the only properties still active in bond are friction at the bar-concrete interface and the mechanical interlock of the deformation itself with the surrounding concrete. Thus, the models have two sources of nonlinearity, the bar-concrete interface and the fracture plane located at the specimen center line.

The behavior predicted by the simple finite-fracture approach matches quite closely with that obtained in the laboratory. For example, Darwin et al. [3,14] demonstrated that the fracture mechanics approach correctly captures the experimentally observed effects of cover on bond strength. The close agreement between analytical and experimental behavior is important because it reveals, for the first time, that bond failure can accurately be modeled using fracture mechanics and emphasizes that bond failure must be characterized correctly as a structural, rather than a material, failure. The failure of the concrete surrounding the bar results from dilation of the concrete surrounding the bar caused by the wedging action of the bar. Eventually the cracks allow the bars to separate from the concrete and to slip relative to the specimen. Based on this behavior and the close match of the analytical model with the laboratory specimens, one can formulate observations which can, in turn, provide insight into design that can optimize the bond and development relationships.

OBSERVATIONS FOR BOND AND DEVELOPMENT

Based on the foregoing analysis, it can be seen that fracture mechanics can be used to explain splitting bond failures, and, thus, any geometric or material changes that affect the fracture behavior of the specimen will affect the bond and development characteristics of the bars embedded in the specimen. Therefore, parameters can be identified from the experimental and analytical studies shown to be important, and using the fracture mechanics context provide observations as to their affects on the overall performance. First and foremost of these are bar spacing and concrete cover.

The fracture mechanics approach used in this study indicates that the bond strength is controlled by splitting and, thus, is related to the amount of energy that the cover and the concrete between bars can absorb before the bar slips relative to the concrete. Thus, if bars are spaced further apart and if they are provided with greater amounts of cover, there is a greater reservoir of concrete through which bond slip-induced cracks must be driven prior to failure. The greater the "concrete reservoir," the greater available fracture energy which, in turn, increases the bond force that the member can take prior to failure. These factors have been suspected in the past. Ferguson and Breen [9], among others, correctly observed that widely spaced bars, and bars with higher amounts of cover, indeed produce larger bond forces than bars with closer spacings and smaller amounts of cover. The fracture mechanics model, however, provides a unique perspective. It allows researchers to investigate the failure process by using a fracture-based philosophy which allows closer matching of behavior than material strength-based approaches. Thus, the geometry of the bar placement as a parameter in determining bond force and development length requirements can be explained with fracture mechanics. The results suggest that cover and spacing requirements may be tied to absolute dimensions (inches or mm) rather than dimensions as a multiple of bar diameter, as reflected in Ref. 2.

Another geometry related parameter is the geometry of the reinforcing bar itself. Current deformation patterns were first studied in depth by Clark [5,6] in the late 1940's, when the available reinforcing bar patterns were compared experimentally. As a result of Clark's studies, the weak patterns were eliminated from the commercial market, leaving the patterns that exist today. The use of a fracture mechanics-based analysis approach allows the researcher to investigate the effects of bar geometry. In a current study at the University of Kansas, parameters such as deformation spacing, deformation height, and inclination of the deformations, are being evaluated in terms of their effects of bond performance using the

fracture mechanics approach described earlier.

On the concrete materials side, the overall basis behind the fracture mechanics model is the stress-crack width relationship which ultimately determines the functional force at the bar-concrete interface. It is interesting to note that the development of bars in high strength concretes may well be less favorably affected by the higher strength concretes than one would first think. A pilot study by Hadje-Ghaffari et. al [14] indicated that the bond strength may not be a consistent square root function of f'_c, as it is for "normal" strength concretes. There may in fact be a tailing off in the expected increase in strength when the compressive strength exceeds 10,000 psi. This behavior has been observed, not only in bond tests, but in other applications. This effect can be explained in part using a fracture mechanics approach. High strength concretes are generally produced with smaller sized aggregates and decreased aggregate contents. These modifications tend to decrease, rather than increase, the fracture energy. Thus, there is a tradeoff that occurs, and ultimately the amount of fracture energy that is available is not as great as expected based on observations of normal strength concrete [13]. The fact that higher strength concretes have a relatively low fracture energy helps explain observations that high strength concretes do not produce significant decreases in required development lengths. Thus, in the arena of high strength concretes, fracture mechanics helps explain the observed phenomena.

Another area of interest is the role of transverse reinforcement on the behavior of bars embedded in concrete. The addition of transverse steel has been shown in many studies to be effective in producing more ductile behavior and greater strength in bond specimens than obtained in bond specimens without confining steel. The presence of transverse steel provides a confining force that helps reduce crack width and redistribute the load as localized fracture occurs. This effect has been noted in several studies [9,10,11,14,15,20,22] when comparing the behavior of splice specimens with and without confining steel. Specimens with unconfined three bar splices tend to fail at lower bar bond forces than those with two bar splices. This behavior may be explained by the "weak link" theory, where the weakest splice of the group controls the overall load of the specimen. If a fracture plane is produced (in splice specimens it tends to be horizontal running from one splice pair to the next) the failure plane initiated at one location will control the strength of the entire specimen. More splices produce the possibility of more fracture planes and, thus, three bar splices produce lower average bar bond strengths than two bar splices. The addition of transverse steel, however, changes this situation, because the transverse steel keeps the crack widths small, limiting the separation of the cracked surfaces and allowing load to be transferred across the partially open cracks. The steel also allows load redistribution to occur and localized effects to be removed, eliminating the weak link behavior and transferring load that is shed by the localized fracture into the remaining splices. Thus, the role of transverse steel and its beneficial effects in load redistribution and more ductile behavior can be explained, in part, using fracture mechanics.

CONCLUSIONS

As the foregoing discussion illustrates, fracture mechanics can play an important role in explaining the bond of reinforcing steel to concrete. In reality, the limitation of crack width, crack propagation, and even crack formation itself are underlying goals in increasing bond forces and decreasing required development lengths. Excessive bond forces can lead to the formation of cracks and ultimately the slippage of the bar relative to the concrete. Thus, it is important to depict the bond process in a way that accurately models the state of stress in the concrete and the failure process that occurs as bars slip relative to the concrete and bar spacing, improved bar geometries, and the use of transverse steel can lead to improved bond performance. Behavior also can be impaired through the use of aggregates and mix designs that provide an optimum fracture capability. For example, improved performance may be produced by high strength concretes that sacrifice some compressive strength in exchange for greatly enhanced fracture and tensile properties, obtained through the use of larger aggregates. The application of fracture mechanics to the overall bond question has been shown to be a viable means of analysis. If our ability to predict and improve the bond characteristics of reinforcing steel to concrete is to occur, additional work needs to be performed using more

sophisticated and detailed three-dimensional models of members with a variety of geometries containing both unconfined and confined bars. In this way, the development length expressions used in design will evolve from the current empirically based relationships to analytically based relationships that will have experimental verification. The results will be rational design procedures that produce structures with greater reliability, safety, and economy than are produced today.

REFERENCES

[1] Abrams, D. A. (1913). "Tests of Bond between Concrete and Steel," *Bulletin No. 71*, Engineering Experiment Station, University of Illinois, Urbana, IL, 105pp.

[2] ACI Committee 318. (1989)., *Building Code Requirements for Reinforced Concrete, Code ACI-318 and Commentary ACI-318R*, American Concrete Institute, Detroit, MI, 353 pp.

[3] Choi, Oan C., Darwin, David, and McCabe, Steven L. (1990). "Bond Strength of Epoxy-Coated Reinforcement to Concrete," *SM Report No. 25*, University of Kansas Center for Research, Lawrence, Kansas, July, 217 pp.

[4] Choi, Oan Chul, Hadje-Ghaffari, Hossain, Darwin, David and McCabe, Steven L. (1991). "Bond of Epoxy-Coated Reinforcement: Bar Parameters" *ACI Materials Journal*, Vol. 88, No. 2, March-April, pp. 207-217.

[5] Clark, A. P. (1946). "Comparative Bond Efficiency of Deformed Concrete Reinforcing Bars," Journal of American Concrete Institute, *Proceedings* Vol. 43, No. 4, December, pp. 381-400.

[6] Clark, A. P. (1949). "Bond of Concrete Reinforcing Bars," Journal of American Concrete Institute, *Proceedings* Vol. 46, No. 3, November, pp. 161-184.

[7] Cleary, D. B. and Ramirez, J. A. (1989). "Bond of Epoxy Coated Reinforcing Steel in Concrete Bridge Decks," *Joint Highway Research Project Informational Report*, JHRP 89-7, Purdue University, 127 pp.

[8] Donahey, Rex C. and Darwin, David. (1985). "Bond of top-Cast Bars in Bridge Decks," Journal of the American Concrete Institute, *Proceedings* Vol. 82, No. 1, January-February, pp. 57-66.

[9] Ferguson, P. M. and Breen, J. E. (1965). "Lapped Splices for High Strength Reinforcing Bars," Journal of the American Concrete Institute, *Proceedings* Vol. 62, No. 9, September, pp. 1063-1078.

[10] Ferguson, P. M. and Krishnaswamy, C. N. (1971). "Tensile Lap Splices -- Part 2: Design Recommendations for Retaining Wall Splices and Large Bar Splices," *Research Report No. 113-3*, Center for Highway Research, University of Texas at Austin, April, 60 pp.

[11] Ferguson, Phil M. and Thompson, J. Nellis. (1962). "Development Length of High Strength Reinforcing Bars in Bond," Journal of the American Concrete Institute, *Proceedings* Vol. 59, No. 7, July, pp. 887-927.

[12] Ferguson, P. M. and Thompson J. N. (1965). "Development Length for Large High Strength Reinforcing Bars," Journal of the American Concrete Institute, *Proceedings* Vol. 62, No. 1, January, pp. 71-91.

[13] Gettu, R., Bazant, Z. P. and Korr, M. E. (1990). "Brittleness of High Strength Concrete" *Proceedings of First Materials Engineering Congress*, ASCE, New York, pp. 976-985.

[14] Hadje-Ghaffari, Hossain, Darwin, David and McCabe, Steven L. (1991). "Effects of Epoxy-Coating on the Bond of Reinforcing Steel to Concrete," *SM Report No. 28*, University of Kansas Center for Research, Lawrence, Kansas, 288 pp.

[15] Hester, Cynthia J., Salamizavaregh, Shahin, Darwin, David and McCabe, Steven L. (1991), "Bond of Epoxy-Coated Reinforcement to Concrete: Splices," *SL Report 91-1*, 66 pp.

[16] Hillerborg, A., Modeer, M., and Petersson, P. E. (1976). "Analysis of Crack Formation and Crack Growth in Concrete by Means of Fracture Mechanics and Finite Elements," *Cement and Concrete Research*, Vol. 6, No. 6, November, pp. 773-782.

[17] Johnston, D. W. and Zia, P. (1982). "Bond Characteristics of Epoxy Coated Reinforcing Bars," *Report No. FHWA-NE-82-002*, Federal Highway Administration, Washington, DC, 163 pp.

[18] Lutz, L. and Gergely, P.. (1967). "Mechanics of Bond and Slip of Deformed Bars in Concrete," Journal of the American Concrete Insitutue, *Proceedings* Vol. 64, No. 11, November, pp. 711-721.

[19] Mathey, Robert G. and Clifton, James R. (1976). "Bond of Coated Reinforcing Bars in Concrete," *Journal of the Structural Division*, ASCE, Vol. 102, ST1, January, pp. 215-229.

[20] Orangun, C. O., Jirsa, J. O., and Breen, J. E. (1977). "A Reevaluation of Test Data of Development Length and Splices," Journal of the American Concrete Institute, *Proceedings* Vol. 74, No. 3, March, pp. 114-122.

[21] Tepfers, R. (1979). "Cracking of Concrete Cover Along Anchored Deformed Reinforcing Bars," *Magazine of Concrete Research*, Vol. 31, No. 106, March, pp. 3-12.

[22] Tepfers, R. (1982). "Lapped Tensile Reinforcement Splices," *Journal of the Structural Division*, ASCE, Vol. 108, No. ST1, January, pp. 283-301.

[23] Treece, R. A. and Jirsa, J. O. (1989). "Bond Strength of Epoxy-Coated Reinforcing Bars," *ACI Materials Journal*, Vol. 86, No. 2, March-April, pp. 167-174.

STRESS TRANSFER BETWEEN FIBER AND MATRIX IN A FIBER-REINFORCED BRITTLE MATRIX COMPOSITE

L. Gu and P. L. Mangonon
Department of Mechanical and Aerospace Engineering
Florida Institute of Technology, Melbourne, FL 32901

ABSTRACT

The fracture mechanics model of matrix cracking in uniaxially fiber-reinforced brittle matrix composites depends significantly on the load transfer mechanism between the fiber and the matrix. A stress transfer model was developed theoretically under uniform tension in the direction parallel to the fibers and normal to the crack plane in the presence of residual stress and interfacial friction. It was assumed that the fibers are strong enough to remain intact when the matrix cracks. The stress transfer mechanisms were based on a typical cylindrical composite cell as stress free at the external surface of the matrix. A comprehensive analysis of stress distributions in both the fiber and the matrix in the slip and non-slip regions, was obtained by introducing a fictitious friction coefficient at the fiber-matrix interface in the non-slip region. The analytical solutions of the stress distributions in both the fiber and the matrix differ from other methods currently available in the literature. The methodology is much simpler, yet yields the same results as those from more complicated solutions. The present model may be extended to the case when the fiber is broken.

INTRODUCTION

The stress transfer between the fiber and the matrix in the fiber-reinforced composite material is very important mechanical factor. The most common model of a composite material is to assume it as an assemblage of circular cylinder cells. Then the stress distribution in both the fiber and the matrix is analyzed by considering the fiber as the inner solid cylinder, surrounded by a ring of the matrix. Smith and Spencer [1] investigated the stress and displacement distributions of elastic materials reinforced by strong fiber. Gao et al. [2] developed a shear lag model, which included friction at the slip interface and the Poisson contraction of the fiber to solve the fiber-matrix slip problem. However, axial residual stress was ignored when the stress-strain relations were used. Sigl & Evans [3] developed a modified shear lag model to analytically solve the problem of matrix crack and

fiber pull-out in a brittle matrix composite by considering the effect of residual stress from the thermal expansion mismatch between the fiber and the matrix, as well as frictional slip. However, stress and displacement are not considered in the non-slip region. Hutchinson & Jensen [4] proposed a model for the slip of a fiber embedded in a brittle matrix, which was restricted to a system having a residual compressive stress acting across the fiber-matrix interface. Their analyses contained, however, the same shortcomings as the analyses of [2] & [3]. McCartney [5] developed a theoretical model of stress transfer between fiber and matrix in a uniaxially fiber-reinforced composite. However, in order to satisfy the conditions of displacement and stress-strain-temperature, the analysis restricted to averaging the values and resulted in a rather complex solution.

The present study illustrates a much simpler solution to the stress distributions in both the slip and non-slip regions. The solutions satisfy the boundary conditions at both ends of the crack plane and the far field, respectively, and at the external surfaces, as well as the continuity conditions at the fiber-matrix interface. The slip length in a typical cylindrical composite cell can be calculated. The present analysis is validated by the excellent agreement of the results with the more complicated solution [5].

MATHEMATICAL FORMULATION

For mathematical convenience, the composite is also assumed to be an assemblage of circular cylindrical cells. A typical composite cell is shown in Figure 1 for axially symmetrical stress distribution when matrix cracks and fibers remain intact. It is composed of an inner solid cylindrical fiber with radius, R, surrounded by a concentric circular matrix shell with outer radius of $R/V_f^{1/2}$. The cylindrical coordinates r and z are symmetrical, respectively, around the crack opening and the long fiber axis, with the origin at the crack plane. The slip length, L, is measured along the fiber from the origin. At the crack plane, there is a traction T in the fiber but not in the matrix (stress free), since the matrix is assumed to be cracked [6]. The composite cell is from $z=0$ (crack plane) to ∞, where the stress, σ_∞, is applied to the composite in the direction parallel to the fibers and normal to the crack plane. Residual stress in the fiber and the matrix exists as well as at the interface, because of difference in manufacture and application temperatures.

The stress transfer mechanisms between the fiber and the matrix are analyzed in two regions, i.e., the slip and non-slip regions. In non-slip region, $L \le z < \infty$, it is assumed there is no slip at the interface between the fiber and the matrix, i.e., the fiber and matrix have the same displacements in z direction. For the slip region, $0 \le z \le L$, it is assumed that there has been some frictional slip at the fiber-matrix interface [4]. The stress-strain-temperature relations of an elastic body are

$$E\epsilon_r = \sigma_r - \nu(\sigma_\theta+\sigma_z)+E\alpha_T\Delta T;\quad E\epsilon_\theta = \sigma_\theta - \nu(\sigma_r+\sigma_z)+E\alpha_T\Delta T;\quad E\epsilon_z = \sigma_z - \nu(\sigma_r+\sigma_\theta)+E\alpha_T\Delta T \quad (1)$$

where ΔT denotes the difference between manufacture and application temperatures and α_T is linear thermal expansion coefficient. E and ν denote the Young's modulus and the Poisson's ratio, respectively. It should be pointed out that the above material properties, and stress and strain components indicate either the fiber or the matrix, and superscripts or subscripts of "f" and "m" are used when referred to the fiber and the matrix, respectively.

Interfacial boundary conditions ($z \geq 0$, $r=R$) [3] are

$$\epsilon_\theta^f(R,z) = \epsilon_\theta^m(R,z); \qquad \sigma_r^f(R,z) = \sigma_r^m(R,z); \qquad \tau_{rz}^f(R,z) = \tau_{rz}^m(R,z) \tag{2}$$

The stress free boundary conditions at the external matrix cylindrical surface are

$$\sigma_r^m\left(\frac{R}{V_f^{1/2}},z\right) = 0; \qquad \tau_{rz}^m\left(\frac{R}{V_f^{1/2}},z\right) = 0 \tag{3}$$

The boundary conditions for σ_z in the z direction are

$$\sigma_z^f(r,0) = T; \quad \sigma_z^f(r,\infty) = \sigma_\infty^f; \quad \sigma_z^m(r,0) = 0; \quad \sigma_z^m(r,\infty) = \sigma_\infty^m \tag{4}$$

where T is the fiber traction at the crack plane. σ_∞^f and σ_∞^m are the applied stresses to the fiber and matrix in the z direction at $z = \infty$ [5], respectively. The uniaxial stress applied to the composite in the z direction is expressed in the form of far field stress components of the fiber and matrix,

$$\sigma_\infty = V_f\sigma_\infty^f + V_m\sigma_\infty^m \tag{5}$$

In the slip region, friction slip occurs because the shear contact stress equals that prescribed by the Coulomb friction law. The relationship between the radial and the shear contact stresses at the fiber-matrix interface is

$$\tau = -\mu\sigma_r^f(R,z) \qquad \text{at} \quad 0 \leq z \leq L \tag{6}$$

where μ is the interfacial friction coefficient and τ is the shear contact stress at the interface and is a function of z, since the fiber radial contact stress is also function of z. The radial contact stress is assumed here to be compressive, because the compressive contact radial stress is desired in a real composite material. For this to occur, the thermal expansion coefficient of the fiber is assumed to be less than that of the matrix.

In the non-slip region, there is no slip at the fiber-matrix interface. The displacements in z direction at the interface and the relationship between contact shear and radial stresses are

$$u_z^f(R,z) = u_z^m(R,z); \qquad \tau < -\mu\sigma_r^f(R,z) \qquad \text{at} \quad L \leq z < \infty \tag{7}$$

It is assumed, for simplicity, that the stresses in the z direction, σ_z^f and σ_z^m, are the average values across the cross section, i.e., the axial stresses are functions only of z. The relationship between axial and contact shear stresses [2] are

$$\frac{d\sigma_z^f}{dz} = -\frac{2\tau}{R}; \qquad \frac{d\sigma_z^m}{dz} = \frac{2\tau V_f}{RV_m} \tag{8}$$

By introducing the result from the Lame problem [7] in the fiber domain (solid cylinder), the stress components and radial displacement at any cross section may be written as

$$\sigma_r^f = -T_r; \qquad \sigma_T^f = -T_r; \qquad \epsilon_\theta^f = \frac{1}{E_f}[-T_r(1-\nu_f) - \nu_f\sigma_z^f] + \alpha_f\Delta T \tag{9}$$

where T_r is assumed as the compressive stress at the fiber-matrix interface. In the matrix domain (cylindrical ring),

$$\sigma_r^m = \frac{T_rV_f}{V_m}\left(1-\frac{R^2}{r^2V_f}\right); \quad \sigma_\theta^m = \frac{T_rV_f}{V_m}\left(1+\frac{R^2}{r^2V_f}\right); \quad \epsilon_\theta^m = \frac{1}{E_m}\left\{\frac{T_rV_f}{V_m}\left[1-\nu_m+\frac{R^2}{r^2V_f}(1+\nu_m)\right]-\nu_m\sigma_z^m\right\}+\alpha_m\Delta T \tag{10}$$

By substituting Eq. (9) and (10) into the continuity condition Eq. (2), the radial contact stress, T_r, is expressed as below

$$T_r = \frac{\beta}{\alpha}\sigma_z^m - \frac{\gamma}{\alpha}\sigma_z^f + q_o \tag{11}$$

where $\alpha = E_f(1+V_f+\nu_mV_m)+E_mV_m(1-\nu_f)$, $\beta = E_fV_m\nu_m$, $\gamma = E_mV_m\nu_f$, and $q_o = E_mV_mE_f(\alpha_f-\alpha_m)\Delta T/\alpha$.

Slip Region

The shear contact stress τ is caused by initial pressure q_o and radial contact stress T_r. In this region, Coulomb friction is applied, i.e.,

$$\tau = \mu T_r \tag{12}$$

Substituting Eqs. (11) and (12) into Eqs. (8), the governing equations may be rewritten as follows

$$\frac{d\sigma_z^f}{dz} = -\frac{2\mu}{R}\left[q_o+\frac{\beta}{\alpha}\sigma_z^m-\frac{\gamma}{\alpha}\sigma_z^f\right]; \qquad \frac{d\sigma_z^m}{dz} = \frac{2\mu V_f}{RV_m}\left[q_o+\frac{\beta}{\alpha}\sigma_z^m-\frac{\gamma}{\alpha}\sigma_z^f\right] \tag{13}$$

Eqs. (13) are first order differential equations and can be solved simultaneously and analytically by using Eqs. (4) at $z = 0$. The resulting axial stresses of the fiber and the matrix in the z direction are, respectively,

$$\sigma_z^f = T-\eta(e^{\lambda z}-1)(T_o-T); \qquad \sigma_z^m = \eta\frac{V_f}{V_m}(e^{\lambda z}-1)(T_o-T); \qquad \tau = \frac{\mu\lambda}{\alpha}(T_o-T)e^{\lambda z} \tag{14}$$

where T_o, η and λ are defined below

$$T_o = \frac{\alpha q_o}{\gamma} = \frac{E_f}{\nu_f}(\alpha_f-\alpha_m)\Delta T; \qquad \eta = \frac{E_mV_m\nu_f}{E_mV_m\nu_f+E_fV_f\nu_m}; \qquad \lambda = \frac{2\mu}{\alpha R}(E_mV_m\nu_f+E_fV_f\nu_m) \tag{15}$$

Non-slip Region

It should be noted that the shear contact stress and the normal stresses of both the fiber and matrix in the z direction are still functions of z. The following continuity conditions of stress and displacement components at $z = L$ should be satisfied between slip and non-slip zones.

$$\sigma_z^f(L^+)=\sigma_z^f(L^-); \quad \sigma_z^m(L^+)=\sigma_z^m(L^-); \quad \tau(L^+)=\tau(L^-); \quad u_z^f(L^+)=u_z^f(L^-); \quad u_z^m(L^+)=u_z^m(L^-) \tag{16}$$

where the signs, (+) and (-), indicate the non-slip region and the slip region, respectively. The limiting values from each region as one approaches at $z = L$ are equated.

In order to satisfy the continuity conditions Eqs. (16), a fictitious friction coefficient μ^* is introduced to derive the stress and the displacement components in the non-slip region. μ^* is a function of z and should satisfy two boundary conditions, i.e., $\mu^*(L) = \mu$ (the real Coulomb friction coefficient) and μ^* vanishes at $z = \infty$. The latter condition is the reason for calling μ^* the fictitious friction coefficient, because the real friction coefficient, μ, can not be zero. Based on the two boundary conditions, $\mu^*(z)$ may be expressed as

$$\mu^*(z) = \mu\, e^{L-z} \tag{17}$$

The relationship between the contact shear and the radial stresses is similar to Eq. (12), but the friction coefficient μ is replaced by the fictitious friction coefficient, μ^*, and is expressed as

$$\tau = \mu^* T_r \tag{18}$$

The difference between Eqs. (12) and (18) is that the real friction coefficient is used in the slip region and the fictitious friction coefficient issued in the non-slip region. Thus, the equilibrium equations of the fiber and the matrix are rewritten, similar to Eqs. (13) in the slip region, by using μ^* (instead of μ) in the non-slip region. These are

$$\frac{d\sigma_z^f}{dz} = -\frac{2\mu^*}{R}[q_o + \frac{\beta}{\alpha}\sigma_z^m - \frac{\gamma}{\alpha}\sigma_z^f]; \qquad \frac{d\sigma_z^m}{dz} = \frac{2\mu^* V_f}{RV_m}[q_o + \frac{\beta}{\alpha}\sigma_z^m - \frac{\gamma}{\alpha}\sigma_z^f] \tag{19}$$

By solving Eq. (19) and substituting Eq. (18) and the boundary conditions Eqs. (4) at $z = \infty$, the axial stress components in the z direction in the non-slip region are

$$\sigma_z^f = -\eta(T_o + \frac{\beta V_f}{\gamma V_m}T)(e^{-\lambda g(z)} - 1) + \sigma_\infty^f e^{-\lambda g(z)}; \quad \sigma_z^m = \frac{V_f}{V_m}[T + \eta(T_o + \frac{\beta V_f}{\gamma V_m}T)(e^{-\lambda g(z)} - 1) - \sigma_\infty^f e^{-\lambda g(z)}] \tag{20}$$

where $g(z) = e^{(L-z)}$ and $L \le z < \infty$. The contact shear stress in the non-slip region is

$$\tau(z) = \frac{\gamma\mu g(z)}{\alpha}\left[(T_o + \frac{\beta V_f}{\gamma V_m}T)\, e^{-\lambda g(z)} - \frac{1}{\eta}\sigma_\infty^f e^{-\lambda g(z)}\right] \tag{21}$$

It should be noted that Eq. (21) yields $\tau(\infty) = 0$ in the far field, as expected.

By using the continuity condition Eq. (16) and the stress and displacement components in both regions, the slip Length, L, can be calculated and expressed as,

$$L = \frac{1}{\lambda}\ln\left\{\frac{T + \eta(T_o + \frac{\beta V_f}{\gamma V_m}T)(e^{-\lambda} - 1) - \sigma_\infty^f e^{-\lambda}}{\eta(T_o - T)} + 1\right\} \tag{22}$$

It is worth noting that the radial stresses of the fiber and matrix at the interface are still continuous at $z = L$. When the fiber traction T at the crack plane is less than the critical slip stress, non-slip occurs throughout the fiber-matrix interface.

The above derivation completes the solution of the frictional stress transfer problem described in the beginning. All the stress and the displacement components satisfy the boundary conditions and the continuity conditions at the fiber-matrix interface and between the slip and the non-slip regions.

RESULTS AND DISCUSSION

In order to validate the solutions derived from the present model, it is necessary to compare the results with those currently available in [5]. The material parameters used are

$E_f = 220$ GN/m^2 $\quad \nu_f = 0.1$ $\quad V_f = 0.4$
$E_m = 70$ GN/m^2 $\quad \nu_m = 0.2$ $\quad \Delta T = -550$ °C
$\alpha_f = 5.5\times10^{-6}$ /°C $\quad \alpha_m = 1.0\times10^{-5}$ /°C

Another new parameter, applied strain $\epsilon' = \epsilon - \alpha_c\Delta T$, is introduced, where α_c is the axial thermal expansion coefficient of the composite material and is defined in [5], and ϵ is axial strain in the non-slip region. The slip length and stress components for the case of matrix cracking with frictional slip are compared.

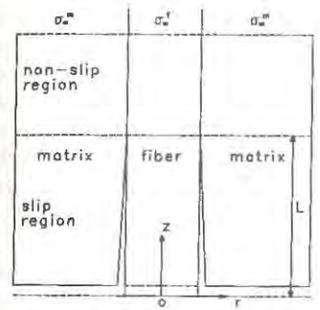

Figure 1. Schema of matrix crack opening in a typical cylindrical composite cell.

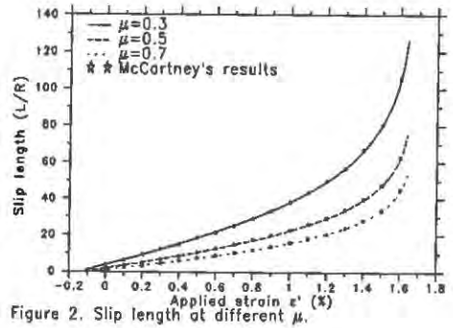

Figure 2. Slip length at different μ.

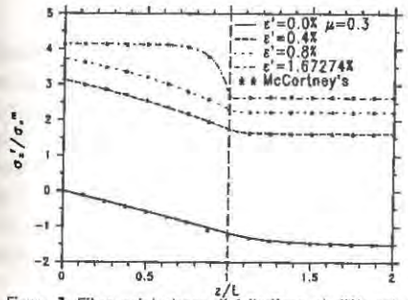

Figure 3. Fiber axial stress distributions at different ϵ'

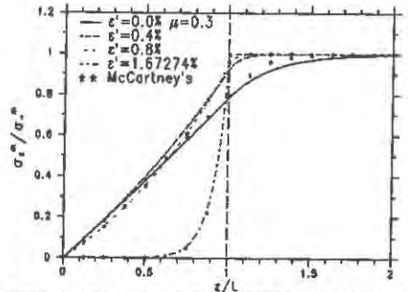

Figure 4. Matrix axial stress distributions at different ϵ'.

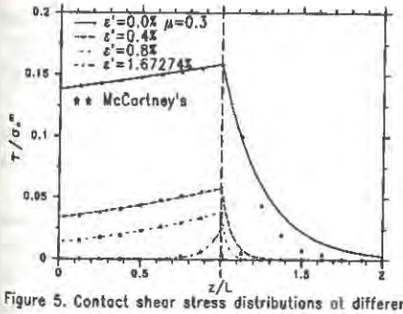

Figure 5. Contact shear stress distributions at different ϵ'.

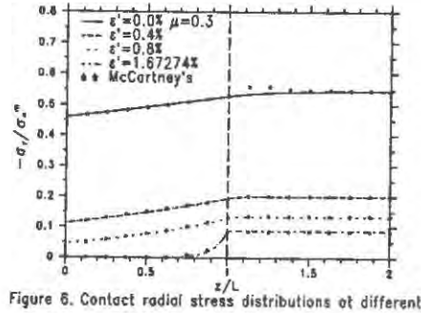

Figure 6. Contact radial stress distributions at different ϵ'.

Figure 2 shows the variation of the normalized slip length, L/R, on the applied strain for five different values of frictional coefficient, μ = 0.3-0.7. * indicates the data points directly taken from [5] and therefore may be subject to error. It is also significant to note that when $\epsilon'=0$, i.e., before any applied stress is imposed on the composite, slip length already exists, i.e., L/R>0. This arose because of the residual stress due to ΔT. Figures 3 - 6 show stress distributions at the interface between the fiber and matrix, σ_z^f, σ_z^m, τ and σ_r, respectively, normalized with respect to the far field matrix stress, σ_∞^m, at different applied strain with μ = 0.3. The very good agreement between the present solution and McCartney's solution in the above figures is the validation of the current solutions. Since the figures are essentially the same as those of [5], the description and more discussion on the figures are referred to [5]. The discussion of difference of contact stresses at z=0 is referred to [6].

SUMMARY AND CONCLUSIONS

The stress distributions in both the fiber and the matrix were calculated in a typical cylindrical composite cell using a modified shear lag model. The model incorporates variable interfacial contact stresses and assumes that the axial stresses of the fiber and the matrix vary only along the axial direction, but independent of radius. A fictitious friction coefficient is used in the non-slip region, where the Coulomb friction law can not be imposed, to make it possible to derive stress and displacement components in both the slip and non-slip regions. The slip length can be determined by the continuity conditions between the slip and non-slip regions. The present much simplified solutions are validated by the excellent agreement with McCartney's [5] results from more complicated solutions.

REFERENCES

1 Smith, G. E. & Spencer, A. J. M., 1970, "Interfacial Tractions in a Fiber-Reinforced Elastic Composite Material", Journal of Mech. Phys. Solids, Vol. 18, pp. 81-100

2 Gao, Y., Mai, Y. & Cotterel, B., 1988, "Fracture of Fiber-Reinforced Materials", Journal of Applied Mathematics and Physics (ZAMP), Vol. 39, pp. 550-569

3 Sigl, L. S. & Evans, A. G., 1989, "Effect of Residual Stress and Frictional Sliding on Cracking and Pull-out in Brittle Matrix Composites", Mechanics of Material, No. 8, pp. 1-12

4 Hutchinson, J. W. & Jensen, H. M., 1990, "Model of Fiber Debonding and Pullout in Brittle Composites with Friction", Mechanics of Materials, No. 9, pp. 139-163

5 McCartney, L. N., 1989, "New Theoretical Model of Stress Transfer Between Fiber and Matrix in a Uniaxially Fiber-Reinforced Composite", Proceedings of the Royal Society, London A, Vol. 425, pp. 215-244

6 Gu, L., 1991, "Fracture Mechanics of Fiber-Reinforced Brittle Matrix Composite Materials", Ph.D. thesis, Florida Institute of Technology

7 Timoshenko, S. & Goodier, J. N., 1951, Theory of Elasticity, McGraw-Hill Book Company, Inc., pp. 58-63

DEVELOPMENT OF CONCRETE TENSILE FRACTURE AND CONCRETE/REBAR BOND STRENGTH MODELS

Gregory J. Kay, Sanjay Govindjee,
Tod Laursen and Brad Maker
Lawrence Livermore National Laboratory
P.O. Box 808
Livermore, California 94550

ABSTRACT

A model has been developed to simulate accumulated damage in plain concrete and the bond strength between concrete and steel reinforcement bars. The constitutive model utilizes a continuum approach to describe microcracking and crack coalescence in plain concrete for the prediction of concrete tensile fracture. The smeared crack model accounts for inelastic strains and progressive strength degradation while maintaining a macroscopically continuous displacement field. The constitutive equations which form the basis for the model are derived using the principle of maximum dissipation and softening in the model is related to fracture mechanics concepts. Concrete/rebar interaction in the model is achieved through the use of one dimensional beam elements which interact with three dimensional continuum elements through a one dimensional contact algorithm. The prescribed stick/slip interactions between the concrete and rebar are expressed in terms of the interface stress or the internal damage variables of the concrete damage model.

INTRODUCTION

Detailed finite element analysis of reinforced concrete structures by means of three dimensional continuum elements could refine analytical results in critical regions and, when used in conjunction with laboratory tests, could offer a more complete method for the determination of critical loads and failure modes of reinforced concrete structures. In what follows a brief sketch of the model is given and the relative importance of one of its features is shown.

CONCRETE DAMAGE MODEL

A concrete constitutive model has been developed which accounts for tensile and shear damage accumulation and which utilizes a characteristic length method to properly account for the energy which is dissipated in creating new crack surfaces (on a per unit volume basis)[1]. A tensile stress criterion is used in the small deformation

model to initiate a smeared crack perpendicular to the direction of the maximum principal stress. Once a crack has formed its existence and direction in the material are fixed and the crack can never heal. Upon load reversals the crack can open and close. As the tensile load bearing capacity of the model decreases, the shear bearing capacity is proportionally decreased and vice versa. The tensile and shear fracture planes in the crack model form an open ended failure surface in stress space. Fracturing in the model is governed by criteria which includes the normal and shear tractions on the crack plane, the concrete tensile strength f_t, the shear strength f_s and the direction of the smeared crack normal $\boldsymbol{n}$. The tensile damage is governed by the criterion

$$\phi_t^d(\boldsymbol{\sigma}, q) = \boldsymbol{n} \otimes \boldsymbol{n} : \boldsymbol{\sigma} - f_t + q \leq 0$$

where the damage stress $q = H_t \alpha$, α being the damage variable, and $\boldsymbol{\sigma}$ is the Cauchy stress tensor. The softening modulus H_t is a function of the fracture energy required to produce virtual cracks in the direction defined by the smeared crack normal $\boldsymbol{n}$. Shear fracture in the model, a function of the shear stress traction on the crack plane, is governed by the following criterion

$$\phi_s^d(\boldsymbol{\sigma}, q) = \left\| (\mathbf{I} - \boldsymbol{n} \otimes \boldsymbol{n}) \cdot (\boldsymbol{\sigma} \cdot \boldsymbol{n}) \right\| - f_s + q \frac{f_s}{f_t} \leq 0$$

where $\mathbf{I}$ is the identity tensor and $\| \cdot \|$ represents the Euclidean norm.

In the model the total strain is assumed to be decomposed additively into elastic, tensile fracture and shear fracture strain components, i.e.,

$$\boldsymbol{\epsilon} = \boldsymbol{\epsilon}^e + \boldsymbol{\epsilon}_t^d + \boldsymbol{\epsilon}_s^d$$

Assuming a free energy function for the material as:

$$\Psi(\boldsymbol{\epsilon}, \boldsymbol{\epsilon}_t^d, \boldsymbol{\epsilon}_s^d, \alpha) = \frac{1}{2} \boldsymbol{\epsilon}^e : \mathbf{C} : \boldsymbol{\epsilon}^e - \frac{1}{2} H_t \alpha^2$$

the Second Law of Thermodynamics may be invoked using standard arguments to show that the Cauchy stress is given by

$$\boldsymbol{\sigma} = \mathbf{C} : (\boldsymbol{\epsilon} - \boldsymbol{\epsilon}_t^d - \boldsymbol{\epsilon}_s^d)$$

where $\mathbf{C}$ is the elastic stiffness tensor. Further, assuming the principle of maximum dissipation, one also has the evolution laws for the internal damage variables as:

$$\dot{\boldsymbol{\epsilon}}_t^d = \lambda_t \frac{\partial \phi_t^d(\boldsymbol{\sigma}, q)}{\partial \boldsymbol{\sigma}}$$

$$\dot{\boldsymbol{\epsilon}}_s^d = \lambda_s \frac{\partial \phi_s^d(\boldsymbol{\sigma}, q)}{\partial \boldsymbol{\sigma}}$$

$$\dot{\alpha} = \lambda_t + \lambda_s \frac{f_s}{f_t}$$

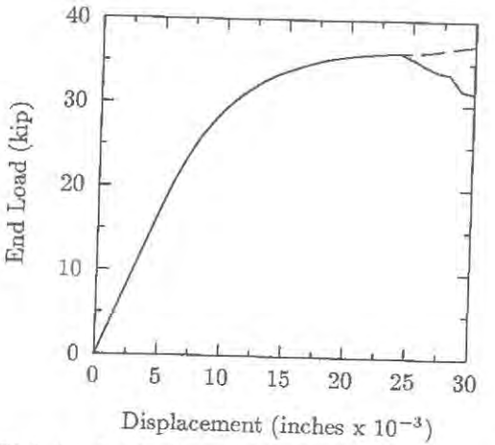

Figure 1. Global softening in a short plain concrete cantilevered beam as displacement controlled loading is increased.

where λ_t and λ_s are scalar tensile and shear loading parameters governed by the conditions:

$$\lambda_t \geq 0 \quad \phi_t^d(\boldsymbol{\sigma}, q) \leq 0 \quad \lambda_t \phi_t^d(\boldsymbol{\sigma}, q) = 0$$

$$\lambda_s \geq 0 \quad \phi_s^d(\boldsymbol{\sigma}, q) \leq 0 \quad \lambda_s \phi_s^d(\boldsymbol{\sigma}, q) = 0$$

The damage accumulation parameter α is bounded from above by f_t/H_t to preclude negative work cycles.

The relative importance of including the shear degradation in the model can be seen in Figure 1, where the load–displacement curve for the failure of a short plain concrete cantilevered beam with an aspect ratio of 1.7 under displacement controlled end loading is shown. As can be seen, the calculation where shear degradation is ignored, the dashed line, is above the calculation where shear damage is considered, the solid line, in regions where acute failure of the beam has occurred.

CONCRETE/REBAR CONTACT SURFACES

A one dimensional slideline algorithm was added to NIKE3D[3] to model the interaction of beam elements with solid concrete elements. The algorithm constrains beam elements to move along the edges of solid elements until the axial force in the beam segments exceeds a prescribed value or the internal variable α in the concrete exceeds a prescribed value, after which the beam elements may slide along the solid elements. The constraints in the algorithm may be considered as two independent actions: axial and normal.

Normal constraints insure that the beams move along the solid element edges. No gaps are allowed. The normal constraints are implemented using a penalty method, within an optional augmented Lagrangian iteration loop[2]. Gap vectors

are initially computed between nodal points on the beam and solid element sides of the interface. These gaps are decomposed into components parallel (axial) and perpendicular (normal) to the axis of the beam. Penalty springs are then generated which act to close the normal components of the gap vectors.

Axial constraints act to restrict the relative sliding of the beam and solid elements. The axial constraints are also implemented using a penalty method. Fictitious springs are inserted between nodes on opposing sides of the interface. As relative sliding occurs these springs are stretched, generating equal and opposite axial forces across the interface. To simulate prestressing of concrete, birth and failure mechanisms have been included in the axial constraint. The axial constraint,initially inactive (frictionless), is activated at a specified birth time during the analysis allowing a preload to be added to the rebar beam elements before they interact with the concrete elements. Failure of the interface bond occurs when either the axial contact stress or the internal variable α in the concrete exceeds prescribed values. After failure occurs, beam elements are allowed to slide with respect to solid elements.

REFERENCES

1. J. Oliver, "A Consistent Characteristic Length for Smeared Cracking Models," Int. J. Num. Meth. Eng., **28**, 461-474(1989)

2. Simo, J.C. & T. A. Laursen [1991], "An Augmented Lagrangian Treatment of Contact Problems Involving Friction," Comp. Struc., to appear.

3. Maker, B.M., Ferencz, R.M. & Hallquist, J.O., "NIKE3D A Nonlinear, Implict, Three-Dimensional Finite Element Code for Solid and Structural Mechanics," LLNL, UCRL-MA-105268 (1991).

ANALYSIS OF HEADED ANCHORS EMBEDDED IN CONCRETE USING A NONLINEAR FRACTURE MODEL

GOTTFRIED SAWADE[1)], ROLF ELIGEHAUSEN[2)]
[1)]FMPA BW Otto-Graf-Institut, [2)] IWB, Universität Stuttgart
Pfaffenwaldring 4, D-7000 Stuttgart 80, Germany

ABSTRACT

This paper represents an energetical model of the fracture behaviour of concrete where crack opening is considered as time dependent dissipative process. States of mechanical equilibrium can be obtained by simulation of a relaxation process. Application of this model to calculations of the bearing capacity of anchorages confirms recent approachs based on linear fracture mechanics.

INTRODUCTION

The use of fastenings systems such as headed -,expansion- or undercut anchors in the building construction industry is on the increase. At present, the design of fastenings is mainly based on empirical equations/1/.In order to get a better understanding of the anchor behaviour, fracture mechanics must be used. However, due to the complicated fracture process (mixed mode crack propagation) few theoretical investigations are available only /2,3/.Therefore numerical studies were performed to investigate the behaviour of headed anchors embedded in a large concrete block. In the investigations a newly developed energetical model based on the linear irreversible thermodynamics was employed.

THERMODYNAMICAL MODEL

In this model /4/ damage due to tension stresses are considered as discontinuities of the field of displacements on the crack surface S_{Re}. Therefore in a finite element V_e an additional strain $\underline{\varepsilon}_{fr}$, depending on the average crack opening $\underline{w}_e$ follows as:

$$\underline{\varepsilon}_{fr} = \frac{S_{Re}}{V_e} \underline{N}(\Omega_e) \cdot \underline{w}_e \qquad (1)$$

with: $\underline{w}_e^T = [w_n, w_t]$ - crack opening normal and tangential to crack surface,

$\underline{N}$ describes the transformation from the global to the local coordinates of the crack surface. The entropy production L_e in the element V_e due to crack opening is:

$$L_e = S_{Re} \cdot \underline{w}^T \cdot \underline{K} \cdot \tag{2}$$

$\underline{K}$ is the thermodynamical force of crack opening with:

$$\underline{K} = \{\underline{N}^T[\underline{D} \cdot \underline{B} \cdot \underline{l} - \underline{\epsilon}_{fr}] - \underline{G}_{,w}\} \tag{3}$$

$\underline{D}$ is tensor of elasticity, $\underline{l}$ is the vector of nodal displacements. $\underline{G}_{,we}$ is the partial derivation of crack surface energy:

$$\underline{G}_{,w}^T = [\delta G/\delta w_n, \delta G/\delta w_t] \tag{3a}$$

Equ. (4) contains a simple ad hoc approach for G, with G_f as specific surface energy, β_n and β_t as tension-strength and shear-strength of concrete respectively:

$$G = G_f \cdot \{1 - \exp(-[\frac{\beta_n}{G_f} \cdot w_n + \frac{\beta_t}{G_f} \cdot |w_t|])\} \quad , w_n \geq 0 \tag{4}$$

Assuming linear irreversible thermodynamics, the following relation for the crack-opening rate is valid:

$$\underline{w}' = \underline{R} \cdot \underline{K} \tag{5}$$

with:

$$\underline{R} = \begin{vmatrix} r_n & 0 \\ 0 & r_t \end{vmatrix} \quad ; \quad r_s = \begin{cases} 0 & \text{for } K_s < 0 \\ r_{os} & \text{for } K_s \geq 0 \quad s=n,t \end{cases} \tag{6}$$

The phenomenological parameters r_{on} and r_{ot} are assumed to be equal for reasons of simplicity. In case of previously unknown crack orientation, the direction of a newly generated crack increment follows from the principle of maximum entropy production. The necessary condition is therefore:

$$\delta\{\underline{K}^T \cdot \underline{R} \cdot \underline{K}\}_{w=0} / \delta\Omega_e = 0 \tag{7}$$

In case of isotropic behaviour of G and $\underline{R}$, the crack orientation calculated with respect to equ. (7) is in accordance with the usual normal-tension criterium.
The loading of the specimen results from the vector $\underline{d}_o(t)$ of prescribed displacements in some selected nodal points. The remaining unknown displacements $\underline{d}(t)$ are obtained from:

$$\underline{K}_{red} \cdot \underline{d}(t) = \underline{f}[\underline{d}_o(t)] + \Sigma\, \underline{g}_e[\underline{w}_e(t)] \tag{8}$$

$\underline{K}_{red}$ is the reduced stiffness matrix, $\underline{f}$ and $\underline{g}$ are linear functions of $\underline{d}_o(t)$ and $\underline{w}_e(t)$ respectively. Solving of the differential equation system (5,7,8) is done by means of discrete

time steps $t_k = k \cdot dt, k=0,1,.M$. For k=0 the crack opening is assumed to be zero, meaning no damage of the specimen at the beginning of loading. The calculation-scheme is as follows:

1. nodal displacement at time t_k:
$$\underline{d}(t_k) = \underline{K}_{red}^{-1}\{\underline{f}[\underline{d}_o(t_k)] + \Sigma \underline{g}_e[\underline{w}_e(t_k)]\} \tag{9}$$

2. orientation of cracks in at present uncracked elements :
$$\delta\{\underline{K}[\underline{l}(t_k)] \cdot \underline{R} \cdot \underline{K}[\underline{l}(t_k)]\}/\delta\Omega = 0 \tag{10}$$

3. crack opening displacement at time t_{k+1}:
$$\underline{w}_e(t_{k+1}) = dt \cdot \underline{R} \cdot \underline{K}[\underline{l}(t_k), \underline{w}_e(t_k)] + \underline{w}_e(t_k) \tag{11}$$

This scheme is simple as at any time step the vector of nodal displacements and the crack opening can be calculated from the values of the previous time step. It is especially advantagous that $\underline{K}_{red}$ remains unchanged during the whole process. To obtain thermodynamical equilibrium ($\underline{K}$=0), the loading function $\underline{d}_o(t_k)$ has to be expressed by means of a step-function:

$$\underline{d}_o(t_k) = p(t_k) \cdot \underline{d}_{oo} \tag{12}$$

$$p = p_m \quad ; \quad t_m \leq t_k < t_m + dt \cdot M$$

where $\underline{d}_{oo}$ is a unit displacement, and M an integer.
Loading is kept constant during the relaxation interval M·dt. At sufficiently high relaxation times, the thermodynamical force $\underline{K}$ tends to zero. The stress vector at the crack surface depends only on the crack-opening in aggreement with the Hillerborg-model.

MODELLING OF ANCHORAGES

ASSUMPTIONS

For the calculation of the bearing capacity of axially loaded headed anchors,the following assumptions are made:
1. Loading is axial-symmetrical
2. The headed stud is assumed to be rigid.
3. Crack growth takes place only in the r-z-plane (circumferential cracking)
4. The ultimate load results from the load-displacement curve, in each loading-step the thermodynamic equilibrium is reached because the loading process is sufficient slow.

The elasticity tensor is assumed to be orthotropic with respect to circumferential stresses:

$$\underline{D} = \frac{E(1-\mu)}{(1-2\mu)(1+\mu)} \begin{vmatrix} 1-\mu & \mu & c\mu & 0 \\ \mu & 1-\mu & c\mu & 0 \\ c\mu & c\mu & c(1-\mu) & 0 \\ 0 & 0 & 0 & 2(1+\mu)^{-1} \end{vmatrix} \tag{13}$$

If circumferential stress is to be excluded (e.g.in case of anchors in intersecting cracks) c has to be set to zero.
In the finite element discretization the nodal points form a

regulary spaced grid with the coordinates (r_i, z_j) (see Fig.1)

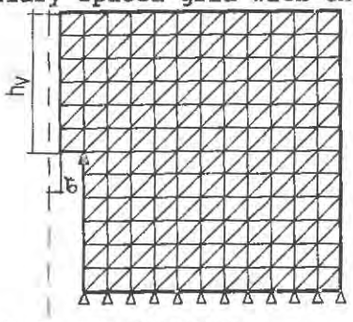

$$r_i = r_0 + i\cdot\Delta z \qquad 0\le i\le N_i$$
$$z_j = j\cdot\Delta z : \qquad 0\le j\le N_j$$
$$\Delta z = h_v/6$$
$$r_0 = 1\ \text{mm}$$

Fig.1 FE-Idealization

The quotient S_{Re}/V_e in equ. (1) was set approximately to $1/\Delta z$. The time interval dt was normalized to $dt=0.2\cdot\Delta z/(E\cdot r_{on})$. In the following described calculations the influence of embedment depth h_v, the concrete stengths β_z, β_t and circumferential stresses (c) was investigated. The Youngs-modulus E, the specific surface energy G_f and the Poisson-modulus μ was set to:

- $E=30000\ N/mm^2$, $\mu=0$, $G_f=0.1\ N/mm$

For each of the load-displacement curves, 150 loading steps were considered, the relative duration of one relaxation interval being M=100.

RESULTS

Table 1 contains the cases considered and the results obtained.

Table 1

No.	h_v mm	β_z N/mm²	β_t N/mm²	c -	F_{max} kN	$\frac{F_{max}}{\sqrt{EG_f}\cdot h_v^{1.5}}$	emp. equ.(15) kN
1	50	3	0	1	36	1.85	41
2	150	3	0	1	203	2.01	212
3	450	3	0	1	1168	2.23	1103
4	150	6	3	1	236	2.34	212
5	150	3	0	0	100	1.00	-

Fig. 2 shows the load-displacement curve for case 2. The crack contour for this case at 0.95 F_{max} is shown in Fig.3. The anchorage fails due to the propagation of a single circumferential crack, growing in a stable manner. Comparison of case 2 and case 4 yields little influence of β_z and β_t on ultimate load. The failure load is dependent mainly on the embedment depth, the Youngs-modulus and the total specific crack surface energy.

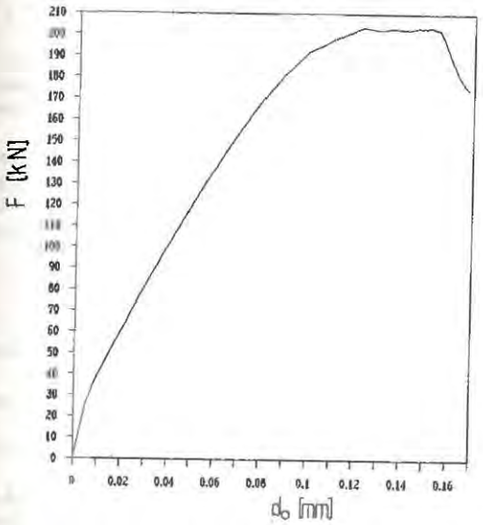

Fig. 2 Load-displacement curve case 2, (h_v=150 mm)

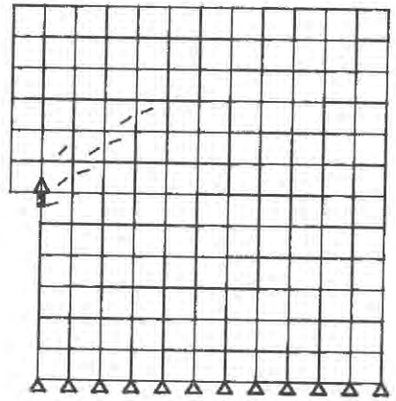

Fig. 3 Crack contour at $0.95\cdot F_{max}$

Considering the size-effect, the ultimate load of case 1-4 is expressed as a function of the embedment depth:

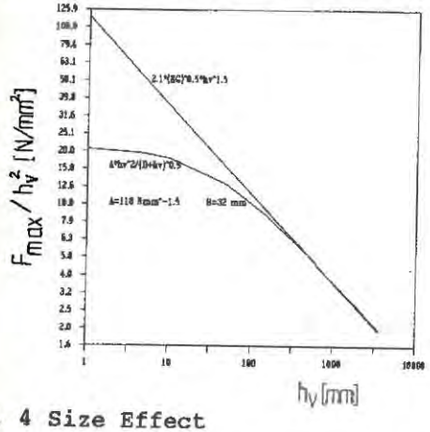

Fig. 4 Size Effect

$$F_{max} = A\cdot h_v^2/(B+h_v)^{0.5} \qquad (14)$$

In Fig.4 the ratios F_{max}/h_v^2 calculated from equ.(14) are plotted as a function of the embedment depth in double-logarithmic scale. For comparision the result of a linear fracture mechanics solution /5/ with:

$$F_{max}=2.1\sqrt{EG_f}\cdot h_v^{1.5} \qquad (14a)$$

is plotted as well.

Obviously, the above nonlinear dissipative model gives ultimate loads with agree rather well with results obtained by means of linear fracture mechanics (see column 7 of table 1). This is valid for $h_v > 50$mm.
In column 8 of table 1 the above calculated ultimate loads are compared with results of the empirical design formula (17)/1/:

$$F_{max} = 15.5\sqrt{\beta_b}\cdot h_v^{1.5} \qquad (15)$$

The compression strength was calculated to β_b=55 N/mm² according to FIP-CEB Model-Code /6/, assuming a maximum grain diameter of 16mm. Comparision of theoretical and empirical values shows sufficient agreement.
Neglecting the circumferential stresses gives an ultimate load of only one half of the value valid for uncracked concrete (case 5). This is confirmed by empirical results /1/ obtained with anchors in crosswise cracked specimens, where the ultimate load was in range of 40-70% compared to uncracked specimens.

CONCLUSIONS

The essential features of the described energetical model are as follows:
-The rates of crack opening displacements can be obtained as a function of the corresponding thermodynamical force.
-The crack contour can be determined by the principle of maximum production of entropy
-The displacements and crack-openings can be treated as a relaxation problem. This model allows the solution of a nonlinear boundary-problem by a simple step by step procedure.
The application of the case of headed anchors embedded in a large concrete block yields the following results:
-The ultimate load is essentially influenced only by the embedment depth, the Youngs-modulus and the total specific crack-surface energy.
-For an embedment depth h_v> 50 mm, the ultimate load follows the linear fracture mechanics.

RFERENCES

/1/Rehm,G.;Eligehausen,R;Malle,R.:Befestigungstechnik,in: Beton-Kalender (77) Teil 2. pp.569-663, Berlin 1988
/2/Ballarini,R.;Shah,S.P.:Fractur mechanics based analyses of pull-out tests an anchor bolts ,in: Analysis of concrete structures by fracture mechanics,RILEM- proceedings (Elfgren,L.;-Shah,S.P. ed.) London 1990
/3/Ozbolt,J.;Eligehausen,R.:Numerical analysis of headed studs embbeded in large plain concrete blocks, Rep. No.4/10 - 90/9 Universität Stuttgart ,Inst. f. Werkstoffe i. Bauwesen,1990
/4/Sawade,G.:Ein energetisches Materialmodell zur Berechnung des Tragverhaltens von zugbeanspruchtem Beton, (i.german), Thesis submitted to Universität Stuttgart 1992
/5/Eligehausen,R.;Sawade,G.:A fracture mechanics based description of pull-out behaviour of headed studs, Fracture mechanics of concrete structures ,Rep. of the technical commitee 90 FMA RILEM,(Elfgren,L. ed.),London 1989
/6/CEB-FIP Model Code 1990 (1988) First Predraft; Chapter 1-5. CEB Bulletin No. 190a

EXPERIMENTAL RESEARCH ON ANCHOR BOLTS IN ROCK

AHMED FATHY, JAIME PLANAS, MANUEL ELICES and GUSTAVO V. GUINEA
Departamento de Ciencia de Materiales.Universidad Politécnica de Madrid
E.T.S. Ingenieros de Caminos. Ciudad Universitaria s/n 28040 MADRID

ABSTRACT

This paper presents a first approach to the in-plane simulation of anchor bolts in quasi-brittle materials. The experimental work was carried out on granite plates, with special care to achieve well defined remote boundary conditions. Four different specimen sizes were tested to investigate the size effect. Linear elastic fracture mechanics computations were performed to ascertain the large size behaviour of the specimens. The fracture pattern records show that except for 25 percent non-symmetric failures, the crack path is quite symmetric, roughly as predicted by LEFM, nearly perpendicular to the loading axis, much in discordance with the wedge-shaped pattern one would expect by direct extrapolation of the most usual axisymmetric pullout tests.

EXPERIMENTAL RESEARCH

Twelve granite plates were tested, of the geometry depicted in Fig. 1. This corresponds to the geometry recommended by the RILEM TC 90 "Fracture Mechanics of Concrete, Applications" for the numerical round robin on anchor bolts [1]. For this geometry, four sizes were tested, of d = 30, 50, 75 and 150 mm, to study the size-effect phenomena.

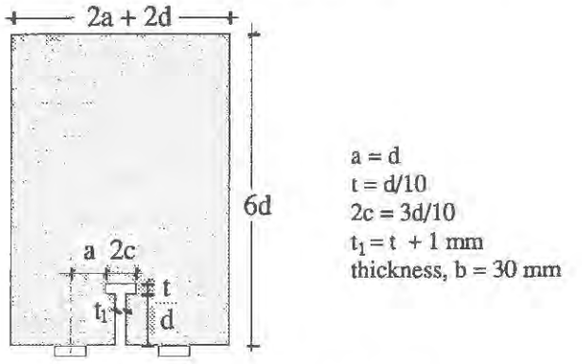

Figure 1. Specimen geometry

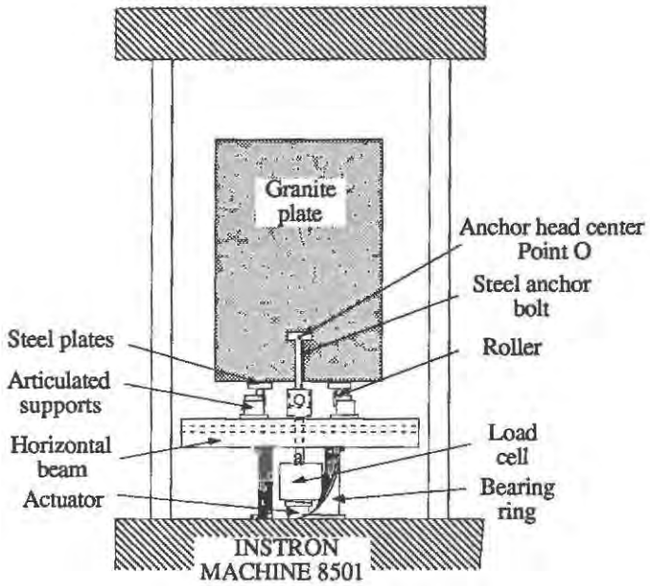

Figure 2. Experimental set-up

Specimens were cut from a plate of commercial granite, 30 mm thick, always keeping the same direction to avoid bias in the results due to possible anisotropy of the material. The anchor housing was water-jet cut to a strict tolerance.

A sketch of the experimental set-up is given in Fig. 2. The load system was based on a hydraulic testing machine INSTRON Mod. 8501. The granite specimen rested on two articulated lateral supports over a horizontal beam, and was loaded through the anchor bolt connected to the machine actuator.

The anchor bolts were made of steel, with a conventional yield limit of 325 MPa. Their shape was in accordance with that of the anchor housing given in Fig. 1, except that a 0.5 mm gap was allowed all around it to avoid uncontrolled contact with the rock.

The bolt head displacement was measured at the centre of the bolt head, point O in Fig. 2, with respect to the load frame. To account for possible rotations of the specimen ,two measures were taken, one on each face of the plate. All tests were performed in actuator position control, at constant displacement rate. Peak load was reached after 3 or 4 minutes from the test start.

Granite properties were experimentally determined by means of complementary tests. Brazilian indirect tensile tests and notched three point bend tests were conducted to ascertain Young modulus, tensile strength and the specific fracture energy of granite. The results are shown in Table 1. Additional information about these tests is given in [2].

TABLE 1.
Granite properties

Property	Mean ± Std.Dev	Test Method
Young Modulus, E (GPa)	39 ± 4	Notched Three Point Bend, CMOD Compliance
Tensile Strength, f_t (MPa)	12.6 ± 1.1	Brazilian
Fracture Energy, G_F (J/m^2)	173 ± 17	Notched Three Point Bend

NUMERICAL ANALYSIS

The first approach to modelling the fracture of granite plates was achieved using linear elastic fracture mechanics. The simulation was conducted using the finite element code FRANC©. Although granite is thought to behave as a cohesive material rather than linear elastically, LEFM provides useful insight into the large size limiting behaviour.

The model geometry was as depicted in Fig. 1, and the elastic properties input to the model were that of Table 1. A maximum circumferential stress criterion was used, with a critical stress intensity factor K_{Ic} = 2.60 MPa$\sqrt{m}$ (obtained from the plane stress relationship $K_{Ic} = \sqrt{EG_F}$).

The initial mesh and the boundary conditions for the half plate are shown in Fig. 3. The steel support and the anchor bolt were modelled with E = 200 GPa and ν = 0.3. The contacts between steel and granite were modelled as perfectly adherent by connecting the relevant nodes of the meshes. The load was uniformly distributed at the end of the anchor shaft.

To enable LEFM calculations, a short initial crack ($\Delta a \approx 0.02$ d) was introduced at the lower corner of the anchor housing in a direction such as to give zero mode II stress intensity factor (more precisely, $K_{II} = 0 \pm 0.01K_{Ic}$). As the crack propagated, the mesh was automatically rebuilt along the crack, leaving element dimensions at the crack tip unchanged. At each propagation step the load, crack mouth displacements and anchor head displacement were recorded

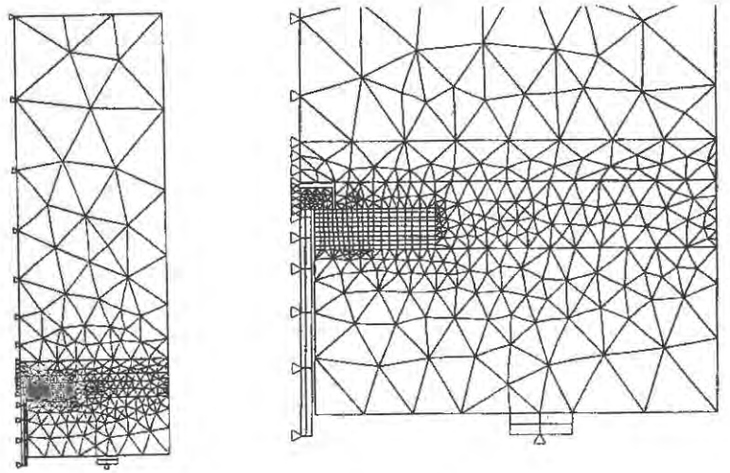

Figure 3. Initial mesh and boundary conditions

RESULTS AND DISCUSSION

A dimensionless plot of the load (P) v.s. displacement of the central point of the head bolt (δ) is shown in Fig. 4, both for the experiments and for LEFM predictions. With the coordinates used (which contain the size) the curve for LEFM becomes size-independent.

The experimental curves are typical curves for each size and show dependence on the size. These curves are the plots of raw results, and include the initial nonlinear portion due to settlement at the contacts, which is grossly exaggerated for the small specimens due to the scales used.

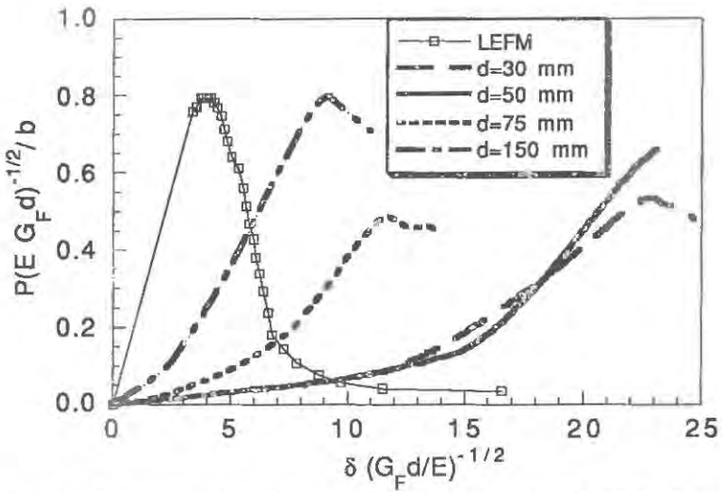

Figure 4. P-δ curves for the sizes tested and for the numeric LEFM simulation

Although hardly appreciable in this plot, the LEFM simulation shows a stable crack growth region prior to the peak. This means that (except perhaps for very short cracks where LEFM would never be applicable for any practical size) this geometry is negative, as defined by the authors [3]. When the evolution of K_I along the crack path is analyzed, a minimum of K_I at constant load is found at a crack extension $\Delta a \approx 0.1$ d, with a value

$$K_{Imin} \approx 1.25 \frac{P}{b\sqrt{d}} \qquad \text{for } \Delta a \approx 0.1\, d \tag{1}$$

The experimental failure patterns display a tendency towards non-symmetric modes, although some specimens showed paths close to symmetry. Fig. 5 shows the envelope of the experimental crack paths together with the crack path obtained in the LEFM simulation. This latter has numerically enforced symmetry. A non-symmetric LEFM path is perhaps possible, but has not been investigated yet.

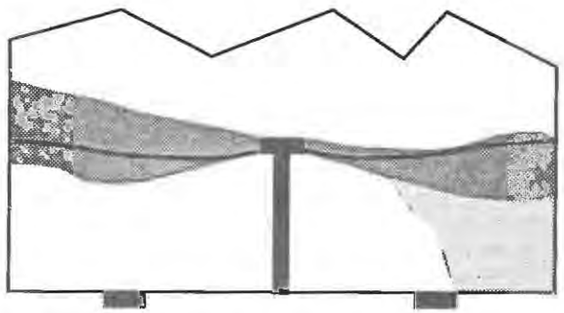

Figure 5. Dashed area is the envelope of the 12 experimental cracks, 9 of which run through the darker regions. The heavy line is the symmetric LEFM crack path.

It is interesting to note that in general the failure occurs through a single bilateral crack which runs roughly perpendicular to the loading axis. This means that the failure kinematics for this 2D case is essentially different from the conically shaped failure observed in axissymmetric pull out tests.

The difference in crack pattern with respect to the experiments performed by Helbing *et al.* [4] in which multiple branching was observed, may be due to differences in the roller supports which in our case were completely free to roll, while in theirs they were inserted in a groove.

These results also indicate that the symmetric LEFM solution may give a reasonable estimate of the crack path, but that this geometry is close to a bifurcation towards a non-symmetric path. Moreover, preliminary work changing the interfacial conditions at the bolt head contact has shown appreciable sensitivity of the predicted LEFM solution to the detailed load bearing conditions. This is a matter requiring further analysis.

Fig. 6 illustrates the size effect for peak load. The figure is a log-log plot of the nominal peak stress versus specimen size for this geometry. The strength theory line was estimated using the rigid plastic mechanism sketched in Fig. 7. The LEFM solution is obtained by setting $K_{Imin} = K_{Ic} = 2.6$ MPa$\sqrt{m}$ in Eq. (1).The experimental results lie under the horizontal line, which represents the strength theory, and under linear elastic fracture theory, but they are much closer to LEFM, as expected for a negative geometry [3].

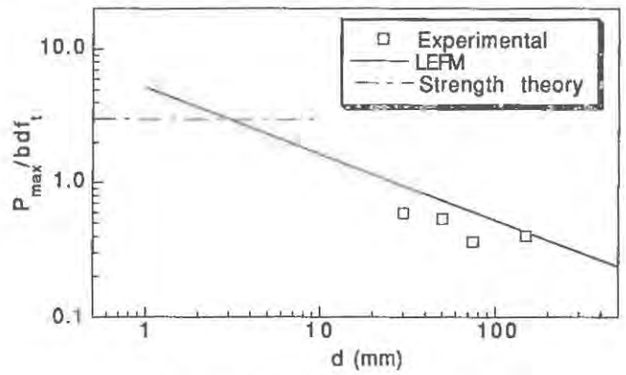

Figure 6. Peak load size effect

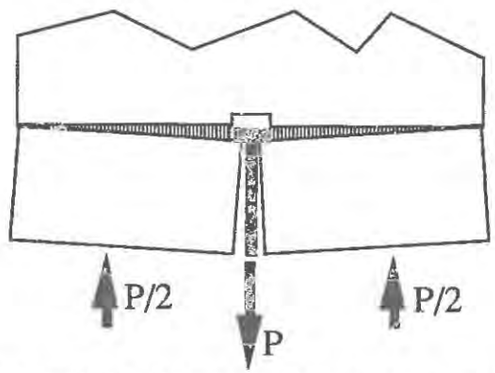

Figure 7. Simplified rigid-plastic mechanism to estimate small size strength.

CONCLUSIONS

The objective of the work presented in this paper was to obtain test results for both crack paths and P-δ curves with the aim of providing trustworthy data to check different rock fracture models. A preliminary study was performed with the help of the FRANC© program for LEFM modelling. At this stage, the following conclusions may be drawn:

1. Symmetry-enforced LEFM calculations predict crack paths reasonably close to those observed experimentally for symmetric mode. However, the experimental P-δ curves are much more compliant than the prediction, probably due to the fact that excessively compliant connections was included in the measuring train.

2. The stress intensity factor along the crack path first decreases and goes through a minimum for a crack extension of about 0.1 d. This means that the geometry is negative, and hence brittle [3].

3. This later tendency is confirmed by the size effect plot which shows that the experimental peak loads are much closer to LEFM than to the strength of materials limit.

4. For this type of geometry, both LEFM and the experiments indicate that the failure tends to be through a single bilateral crack roughly perpendicular to the load axis. However a tendency to non-symmetric failure is experimentally observed.

5. At any rate, the failure mechanism for this slender 2D model is never conical, and no extrapolation can be made to 3D axisymmetric pullout tests.

ACKNOWLEDGEMENTS

The authors gratefully acknowledge Prof. A. Ingraffea for providing them with FRANC© and Dr. Javier Llorca for helping with computation. Also, financial support for this research provided by the Comisión Interministerial de Ciencia y Tecnología, CICYT, Spain, under grant PB90-0276, and by the Polytechnic University of Madrid under grant A-91 0020 02-31.

REFERENCES

1. RILEM TC90-FMA, Round-Robin Analysis of Anchor Bolts-Invitation, Materials and Structures, 1990, 23, 78.

2. Fathy A., Application of Fracture Mechanics to Rock Materials, Ph.D. Thesis. Universidad Politécnica de Madrid, 1992.

3. Planas, J. and Elices, M., Anomalous structural size effect in cohesive materials like concrete, in Serviceability and Durability of Construction Materials, Vol. 2, ed. B. A. Suprenant, American Society of Civil Engineers, New York, 1990, pp. 1345-1356.

4. Helbing, A., Alvaredo, A. M. and Wittman, F. H., contribution to Round-Robin Analysis of Anchor Bolts, RILEM TC-90 FMA, preliminary report, second edition, compiled by L. Elfgren, Division of Structural Engineering, Luleå University of technology, S-951 87 LULEÅ, Sweden, May 1991.

ROUND ROBIN ANALYSIS AND TESTS OF ANCHOR BOLTS

LENNART ELFGREN
Department of Civil Engineering
Luleå University of Technology, S-95187 Luleå, Sweden

ABSTRACT

RILEM Technical Committee TC 90-FMA Fracture Mechanics of Concrete - Applications has invited to Round Robin Analysis and Tests of Anchor Bolts. In this paper some preliminary results are given.

INTRODUCTION

Anchorage problems have great practical importance. Design loads for a specific type of anchor are mostly determined by testing or by simplified empirical formulae. In these, the influence of the size of the anchor is sometimes underestimated (i e for large size anchors the empirical formulae are sometimes unconservative).

The problem is challanging from a theortical point of view and it should be possible to analyse it with fracture mechanics methods. The problem is complicated as shear is involved which means that mixed modes appear.

INVITATION

Based on discussions in RILEM Technical Committee TC-90 FMA (Fracture Mechanics of Concrete - Applications) an invitation was issued in 1989/90 to a Round Robin Analysis of Anchor Bolts [1]. Sixteen contributions were submitted. They were compiled in a preliminary report and discussed during a meeting in Torino in October 1990. There was quite a scatter in the results and it was decided to give more precise rules for what to be calculated and what to be presented. It was also decided to invite actual testing of the proposed loading cases. In order to make testing possible, some of the parameters to be analysed were changed slightly. A second invitation was issued, see Fig. 1 and Table 1 [2].

Seventeen contributions were submitted. The contributions which were submitted before the end of May 1991 were compiled in a second preliminary report which was discussed during a meeting in Delft in June, 1991. The results are very interesting and give a possibility to compare different methods of analysis. A part of the scatter seems to be due to different choices of mesh orientation and mesh size in FEM calculations. In order to make the results available to a wider audience it was decided to publish the contributions in a RILEM Report [3]. In this paper some preliminary results form the report will be presented.

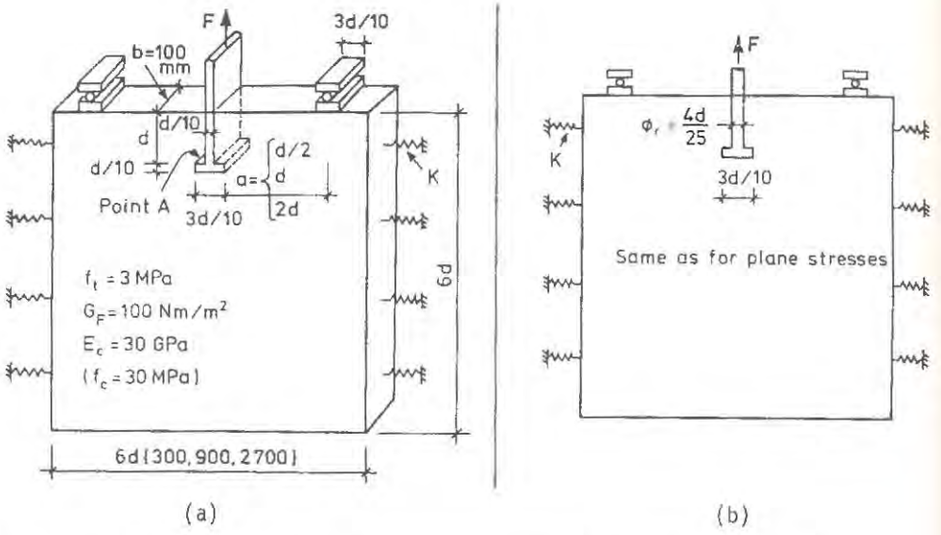

Figure 1. Invitation to Round Robin Analysis and Tests of Anchor Bolts [2]. Analyse and/or test any or both of the problems in Fig (a), plane stresses, and Fig. (b) axi-symmetric stresses. Give the following results: (a) Description of model of analysis and/or test method; (b) Peak load; (c) Displacement of upper edge of anchor (Point A in Figure (a)) at peak load; (d) Failure mechanism. If possible, please also give: (e) Load - displacement curve; (f) Crack pattern at peak load and at termination of analysis/test; and (g) load at onset of cracking.

TABLE 1
Recommended values of parameters in Fig. 1.

Plane stresses

K = 0				K = ∞
d =	50	150	450	150
a = d/2		x		
a = d		x		x
a = 2d	x	X	x	x

Axi-symmetric stresses

K = 0		K = ∞		
d =	150	50	150	450
a = d/2			x	
a = d	x		x	
a = 2d		x	X	x

PLANE STRESSES

Some results from the contributions regarding plane stresses are illustrated in Fig. 2.

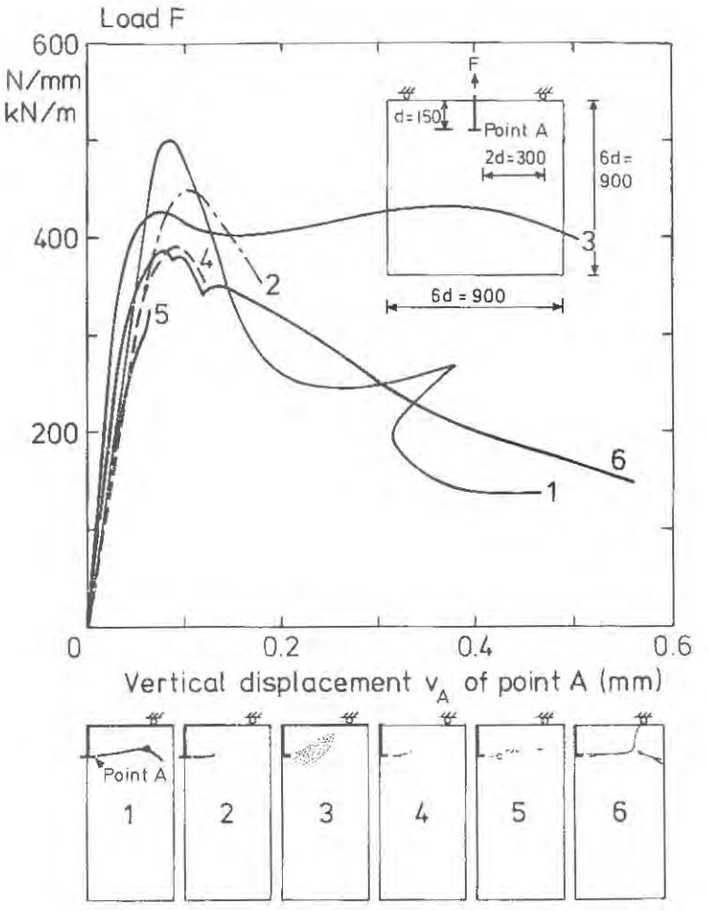

Figure 2. Preliminary results from analysis and tests with plane stresses. The six load-deflection curves and the accompanying crack patterns illustrate the following methods:
1. Linear Elastic Fracture Mechanics
2. Non Linear Fracture Mechanics. Fixed smeared crack concept. Almost zero shear-retention factor.
3. Non Local Continuum Damage
4. Non Linear Fracture Mechanics. Fixed smeared crack concept.
5. Linear Elastic - Brittle Failure in Tension
6. Test

AXI-SYMMETRIC STRESSES

Some results from the contributions regarding axi-symmetric stresses are illustrated in Fig. 3.

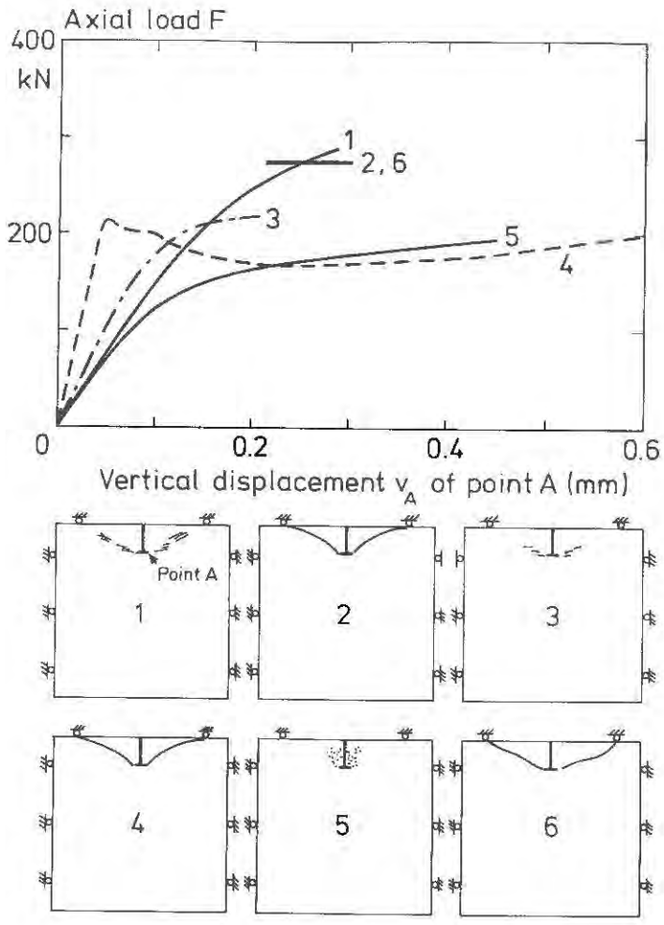

Figure 3. Preliminary results from analysis and tests with axi-symmetric stresses.The six load-deflection curves and the accompanying crack patterns illustrate the following methods:
1. Non Linear Fracture Mechanics. Fixed smeared crack concept. Almost zero shear-retention factor.
2. Theory of Plasticity, no tensile strength.
3. Non Linear Fracture Mechanics. Fracture and aggregate interlock
4. Non Linear Fracture Mechanics. Discrete crack concept.
5. Non Local Microplanes
6. Test

CONCLUSIONS

There is still some scatter in the predictions of the ultimate loads. However, most of the predictions give reasonable results. Size effects can be calculated in an accurate way with many of the methods.

AKNOWLEDGEMENT

The contributions from the various research groups are much appreciated.

REFERENCES

[1] RILEM TC 90 - FMA Fracture Mechanics of Concrete - Applications: Round Robin Analysis of Anchor Bolts - Invitation. **Materials and Structures**, Vol 23, January 1990, p.78.

[2] RILEM TC 90 - FMA Fracture Mechanics of Concrete - Applications: Round-Robin Analysis and Tests of Anchor Bolts - Invitation. Supplement to **RILEM News** 1991:1, 1 p.

[3] Elfgren, L., Eligehausen, R. and Rots, J., editors: **Round Robin Analysis and Tests of Anchor Bolts**. RILEM Report to be published in 1992.

ANALYSIS AND DESIGN OF ANCHOR BOLT WITH CONSIDERATION OF FRACTURE MECHANICS

KYUICHI MARUYAMA AND KEIJI SHIMIZU
Department of Civil Engineering
Nagaoka University of Technology
1603-1 Nagaoka, Niigata 940-21, JAPAN

ABSTRACT

It was discussed in this paper how the anchor bolt system carried the load, and what was the proper design formula with wide applicability. The authors conducted the pull-out test of anchor bolts which were mounted singly in concrete with embedment length of 4 through 24 cm. With careful observation of the behavior of specimen during test and with measurement of the ruptured cone shape, the stress transfer mechanism was examined. The fracture mechanics was, then, introduced to analyze the micro behavior in the cracked region. Comparing the analytical results with the test results, the authors proposed a design formula for the maximum capacity.

INTRODUCTION

Post-installed anchor bolts have been widely used for fastening accessories to concrete structures, and for strengthening the existing structures against earthquakes. A lot of effort has been done to evaluate the pull-out capacity of anchor bolts. The results, however, were limited to short anchor bolts having the embedment length of 10 cm or less.

Since the anchorage has become an important problem in reinforced concrete columns or in steel towers, the above study should be extended to large size of anchor bolts. In order to develop a rational model for design purposes, it is necessary to examine the stress transfer mechanism of the anchor bolt system in detail.

First, the static pull-out test was conducted on the anchor bolts with the embedment length of 4 through 24 cm. The analysis on the stress transfer mechanism was, then, done with help of the elastic finite element method. In particular, the fracture mechanics was introduced to express the stress condition of concrete near the tip of a crack. Comparing the analytical results with the experimental ones, the stress transfer model was proposed and the discussion was extended to the load-bearing mechanism of anchor bolt. Based on the findings, a rational equation was proposed for estimating the ultimate capacity of anchor bolts.

PULL-OUT TEST

ANCHOR BOLTS

The shapes of bolt are shown in Figure 1 and the dimension is summarized in Table 1. Bolts with 4 through 10 cm embedment length were commercially prevailed undercut type ones, and the other two types were specially manufactured for providing the larger embedment length of 16 or 24 cm. Since there was no drilling device for the latter bolts, they were placed at the right position of form work in advance of casting of concrete. The similarity to the post-anchor bolt was taken into account by eliminating the frictional resistance between the bolt and concrete using vinyl tape to wrap the bolt.

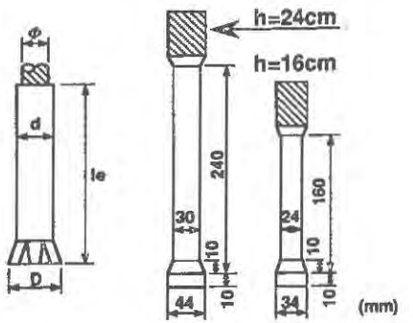

Figure 1. Shape of bolt.

Main features of concrete were, usage of high early strength cement, 25 mm of maximum aggregate size, 8 cm of design slump value and the target nominal strength between 150 and 350 kgf/cm^2. The dimension of concrete block was varied according to the size of bolt as shown in Table 1. The compressive strength of concrete was obtained using cylinder specimens with dimension of Φ100x200 mm. The results are shown in Table 2.

TESTING METHOD

After installation of a bolt, the appropriate initial torque was applied to the bolt for providing enough interlock action. Then, setting a reaction frame and a center hole typed oil jack, the bolt was pulled out statically up to failure of concrete. The applied load and the displacement of bolt were monitored and recorded continuously. These data were stored in a micro-computer through a dynamic strain meter and an A/D converter. In order to eliminate the influence of compressive stress produced near the supports of the reaction frame, the distance between the bolt specimen and the support points was designed to be three times of the embedment length (for h=4-10 cm) or 55 cm (for h=16 and 24 cm).

TABLE 1
Dimension of specimen

Size of bolt (mm) d	le	Φ	D	Initial torque (kgf·cm)	Concrete block (mm) W x L x H		
14	40	M10	18	240	500	500	220
14	60	M10	18	360	600	600	300
18	80	M12	24	360	600	600	300
22	100	M12	28	1200	1200	600	300
	160	24	34	---	1200	1200	1200
	240	30	44	---	1200	1200	1200

TEST RESULTS

Typical shape of ruptured cone of concrete is shown in Figure 2. Due to the observation during test and the measurement of ruptured cone, the failure process was summarized as the following steps: (1) initiation of crack at a steeper inclination (40-55 degree) just around the bottom end of bolt; (2) propagation of crack at a slower angle (20-35 degree); and (3) rupture of concrete with scaling at a shallow angle near the outskirts of cone. The last stage, however, appeared after passing the peak load. The portion of concrete near the surface could not contribute to the ultimate capacity [1]. Since the second stage was considered to determine the ultimate capacity, the crack inclination at this stage was measured in details and the results were summarized in Table 2. Here, the measured crack angles in the four directions are shown, and the section 1 and 2 indicate the orthogonal direction to each other.

The ruptured cone shape was not necessarily the same in each specimen, but the average angle of 28.4 degree was similar in any case despite of the difference of embedment length.

Figure 2. Ruptured cone

TABLE 2
Test results

Bolt d	Bolt le	Bolt Φ	f'_c kgf/cm^2	f_t kgf/cm^2	P_{max} tonf	θ (degree) sec. 1		sec. 2		$\theta_{ave.}$
14	40	M10	196	17.9	2.11	28	20	48	25	28.6
					2.12	24	30	27	27	
14	60	M10	395	29.0	4.50	26	20	27	45	
					5.62	29	27	27	25	25.4
					3.92	15	18	21	25	
18	80	M12	320	22.9	6.32	30	30	25	30	
			395	29.0	6.70	24	35	21	29	31.6
			381	25.7	5.61	21	26	23	22	
22	100	M16	381	25.7	9.24	37	28	24	38	
					8.80	30	30	31	16	30.0
					11.10	34	32	--	--	
	160	24	280	21.0	17.90	22	34	13	22	
					18.70	37	30	26	30	27.2
					18.10	31	29	26	26	
	240	30	280	21.0	35.40	29	34	22	31	29.4
					35.30	32	30	26	31	

STRESS TRANSFER MECHANISM

FINITE ELEMENT ANALYSIS

Since the test results showed that the shape of ruptured cone of concrete was almost identical in all the cases where the embedment length varied from 4 cm to 24 cm, the analysis was conducted only on the case of 8 cm embedment length with 60x60x30 cm concrete block. Using the rectangular elements with four nodal points, the linear elastic finite element analysis was done taking the axi-symmetric procedure.

Assuming a crack to propagate along the given route obtained by the test results, the stress distribution in concrete was computed at the each loading level. The crack propagation was judged when the principal tensile stress in the element exceeded the tensile strength of concrete. Once the cracking was recognized in the element, remeshing of element was proceeded so as to eliminate the stress transfer along the cracked surface.

ANALYTICAL RESULTS

According to the elastic analysis, the maximum pull-out capacity was evaluated when the crack propagated up to 0.43 of the assumed full crack length. This seemed to coincide the result by Eligehausen and et al [2] which showed the ratio of 0.45 by non-linear finite element analysis. However, the computed capacity of 3.1 tonf at the maximum load was far below the test result of 6.3 tonf. This was because the analysis did not count the stress transfer in the cracked region. Then, the linear elastic analysis was, again, repeated so that the cracked element could bear the tensile stress in inverse proportion to the crack width. Such resistances were applied to the element as the nodal forces as shown in Figure 3.

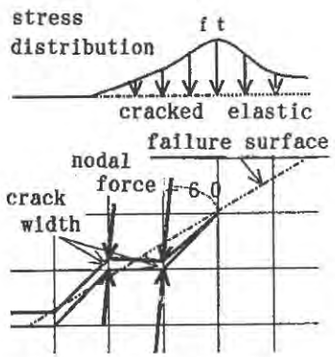

Figure 3. Crack model

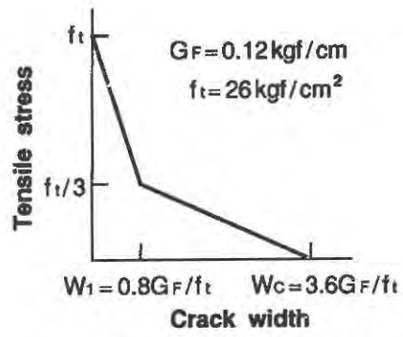

Figure 4. Stress-crack width [3]

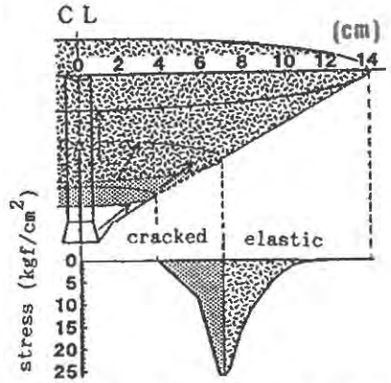

Figure 5. Stress distribution

The resistant stress was evaluated by Petersson's model [3] as shown in Figure 4. The region where this stress was acting could be called as the fracture process zone, and the zone was actually observed by Ohtsuka using X-ray technique [4].

In order to obtain the appropriate magnitude of the tensile resistant stress in the fracture process zone, the computation was repeated until the proper coincidence was obtained between the crack width and the corresponding stresses. In detail, it was necessary to determine the principal direction of stresses in the fracture process zone. Since the nominal direction of the principal stress in the elastic range was computed as about 60 degree to the assumed failure plane at the maximum load, the stresses in the fracture process zone were, then, supposed to act in the same manner (Figure 3). Finally, the stress distribution at the maximum load of 6.3 tonf was obtained as shown in Figure 5.

PROPOSED FORMULA FOR PULL-OUT CAPACITY

In order to extend the analytical results, the stress distribution in Figure 5 should be examined with relation to the embedment length. Since the shape of ruptured cone was identical irrespective of the embedment length, the stress acting area in the elastic range should increase proportionally to the second power of the embedment length (h). It is because both the band width and the periphery length of the elastic stress zone increase in proportion to (h).

On the contrary, the band width of stress acting area in the cracked zone could be constant because it depends upon the absolute crack width. The periphery length is only proportional to the embedment length (h). Comparing the analytical results with the test results, the proposed equation for the maximum capacity is, then, expressed as follows:

$$P_{max} = 18.0 \cdot f_t (0.9 \cdot h + 0.1 \cdot h^2) \quad (1)$$

where, f_t;tensile strength of concrete ($= 0.58 \cdot (f'_c)^{2/3}$, f'_c;compressive strength of concrete, kgf/cm^2) and h;embedment length (cm). P_{max} is expressed in (kgf).

The applicability of Eq.(1) was examined by the test data of this program and the results are shown in Figure 6 in which the equation proposed by Eligehausen [2] was compared. His equation was as follows:

$$P_{max} = 15.5 (f'_c)^{0.5} \cdot h^{1.5} \quad (2)$$

where, f'_c; (N/mm^2) and h; (mm).

When the embedment length was short, little difference was recognized between the two equations. With increase of the embedment length, the difference became large. Examination of Eq.(1) with 74 test specimens resulted in 99.8 % of correlation factor. Figure 7 shows the required embedment length to attain a given value of the maximum capacity with relation to concrete strength. The effect of compressive strength was evaluated larger by the proposed equation than by Eq.(2).

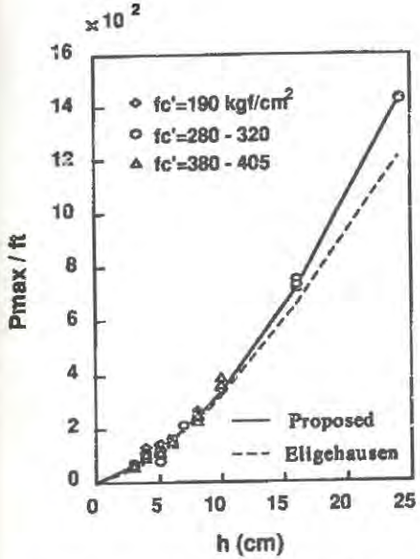

Figure 6. Influence of embedment length on capacity

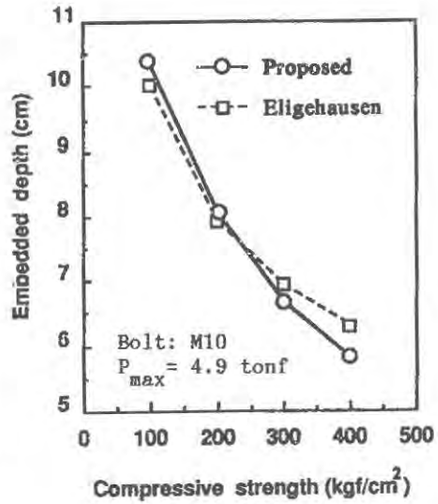

Figure 7. Influence of concrete strength on embedment length

CONCLUSIONS

The followings were concluded from this study.

(1) The shape of ruptured cone was almost identical irrespective of the embedment length.

(2) The proposed model for the maximum capacity had high applicability in the wide range of embedment length. In the model, the contribution of cracked zone was expressed as a linear function of the embedment length whereas that of elastic zone was taken as proportional to the second power of the embedment length.

REFERENCES

1. Maruyama, K., Momose, M., Shimizu, K. and Hashimoto, C., Load-bearing mechanism of undercut type fixings. Transactions of the JCI, Vol.12, 1990, pp.499-506.
2. Eligehausen, R. and Sawade, G., Verhalten von Beton auf Zug (Behavior of concrete in tension). Betonwerk + Fertigteil-Technik, No.5 and No.6, 1985. (in German and English)
3. Petersson, P.E., Crack growth and development of fracture zones in plain concrete and similar materials. Report TVBM-1001, Division of Building Materials, Lund Institute of Technology, Sweden, 1981.
4. Ohtsuka, K., X-ray technique with contrast medium to detect fine cracks in reinforced concrete. Fracture Toughness and Fracture Energy edited by Mihashi, H. and Wittmann, F.,H., Balkema, 1989, pp.521-534.

INFLUENCE OF CRACK WIDTH ON THE CONCRETE CONE FAILURE LOAD

Rolf Eligehausen and Joško Ožbolt
Institut für Werkstoffe im Bauwesen, Stuttgart University, Germany.

ABSTRACT

In the present paper the influence of the crack width on the concrete cone failure load of headed anchors embedded in concrete is analyzed. The analysis is carried out on a reinforced concrete thick plate specimen using three-dimensional finite elements and the nonlocal microplane model. In order to introduce pre-cracking into the specimen before loading the headed anchor, the specimen is loaded in longitudinal direction by applying tension forces through reinforcement. At different crack levels pull-out of the fastening element is performed. Results of the analysis show that the concrete cone failure load is decreasing with increasing crack width up to $w \sim 0.15$ mm to approximately 70 % of the failure load obtained for non-cracked concrete. Further increase of the crack width does not cause further decrease of the failure load. Comparison between numerical and experimental results indicates good agreement.

INTRODUCTION

Presently a number of tests have been performed on fastening elements consisting of one anchor that is embedded in uncracked or cracked concrete [1]. Tests in cracked concrete are usually arranged in a way that the crack plane is passing through the anchor axis. Crack initiation as well as the crack width is controlled by reinforcement that is perpendicular to the crack plane. Comparison between concrete cone failure loads obtained for uncracked and cracked specimens indicate a decrease of the failure load in the case of cracked concrete. Measurements show that by increasing the crack width to $w > 0.3$ mm the concrete cone failure load of headed or undercut anchor decreases to about 50 - 80 % of the failure load obtained for uncracked concrete [1]. However, in spite of the number of experiments the failure mechanism is not yet quite well explained and understood.

In order to better understand the failure mechanism in such a complicated stress-strain situation, where the anchor is pulled out from the concrete that has been previously damaged, a numerical analysis is performed [2]. Due to the complexity no numerical study of the present problem has been reported in literature.

SPECIMEN GEOMETRY AND FINITE ELEMENT ANALYSIS

The influence of the crack width on the concrete cone failure load is studied on a reinforced concrete thick plate of dimensions 1000 x 1040 x 300 mm (Fig. 1). In the center of the specimen a single headed anchor is embedded with an embedment depth h_{ef}= 120 mm. The diameters of the steel stud and anchor head are 22 and 35 mm respectively. In order to initiate crack propagation in the anchor plane, a notch of length 100 mm is introduced on both vertical sides of the specimen (see Fig.1). The crack width in the specimen is controlled through 12 reinforcing bars of diameter 16 mm. The plate is vertically supported around the bottom edges as well as around the anchor at a distance $2h_{ef}$.

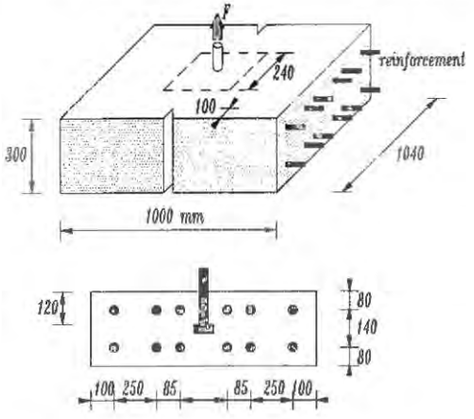

Figure 1. Geometry of the specimen

The loading procedure used in the analysis is the same as it is common in the experiments. Tensile stresses are introduced first through the reinforcement bars (displacement control) producing a crack of a certain width. In the next step the reinforcement extension is fixed and pulling out of the anchor is performed (load control). This is repeated for different tension stresses in the reinforcing bars i.e. for different crack widths.

In the finite element analysis three-dimensional eight-nodes finite elements with eight integration points are used. A finite element mesh is shown in Fig. 2. Only 1/4 of the specimen is modeled i.e. symmetry is employed. Since in the analysis a smeared crack approach is used the crack width that is introduced through the reinforcement can not be obtained explicitly from the analysis. Due to this, the empirical formula [3] is used in order to calculate the average crack width w from the known reinforcement strains:

$$w = s_m \epsilon_{sm} \tag{1}$$

$$s_m = 40 + 12.5 d_s/\mu \tag{2}$$

where ϵ_{sm}= average steel strain in longitudinal reinforcement, s_m = average crack spacing (in mm), d_s= bar diameter (in mm) and μ is reinforcement ratio (in %).

The basic material properties used in the nonlocal microplane model [4], Young modulus and Poisson's ratio, are chosen as follows: E= 30000 MPa and ν= 0.20. Microplane model parameters are chosen such that the calculated uniaxial concrete compression strength (material level) yields $f_c \cong 34$ MPa and the uniaxial concrete tensile strength $f_t \cong 1.8$ MPa.

In order to be able to represent the concrete fracture correctly, it is necessary to set the characteristic length, l, of the nonlocal continuum properly. Since no explicit relation between fracture energy, G_F, and l exists, the characteristic length is chosen such that together with the used material parameters the finite element calculation yields a correct pull-out failure load for the uncracked specimen. The reference failure load F_u (in N) for uncracked concrete specimen is calculated using the empirical expression [1]:

$$F_u = k\sqrt{f_{cc}}h_{ef}^{1.5} \tag{3}$$

where $k = 15.5$ is introduced in order to calibrate Eq. (3) and to assure dimensional correctness, f_{cc} represents concrete cube compression strength (in MPa) and h_{ef} is embedment depth (in mm). According to this the characteristic length is chosen as $l = 25$ mm.

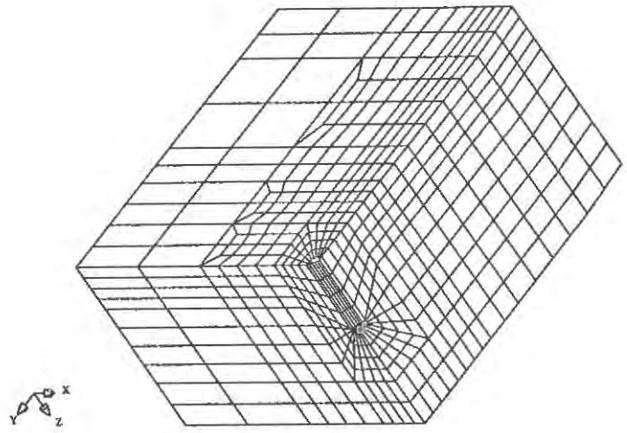

Figure 2. Three-dimensional finite element mesh - one quarter of the specimen

RESULTS OF THE ANALYSIS

In Fig. 3 the concrete cone failure load in cracked concrete related to the value valid for uncracked concrete is plotted as a function of the crack width. For comparison results of tests with headed anchors evaluated in [5] are plotted as well. It can be seen that the calculated failure load decreases with the increase of the crack width rather fast up to a crack width $w \sim 0.15$ mm. For further increase of the crack width the failure load is constant and amounts to approximately 70 % of the failure load obtained for uncracked concrete (w= 0). The calculated influence of the crack width on the concrete cone failure load agrees well with test results.

In order to understand the failure mechanism at different crack widths the fields of the stresses in the direction tangential to the concrete cone and in vertical (anchor) direction for the uncracked and the cracked specimens at peak load are analyzed. In cracked concrete the maximum tangential stress as well as the vertical tensile stress in the fracture process zone close to the anchor head are slightly smaller than in the case of uncracked concrete. This is a consequence of the fact that the tensile strength in the fracture process zone is reduced due to the damage introduced by stressing the reinforcement. In the plane perpendicular to the crack plane, the magnitude of the tangential tensile stresses are similar to the value for uncracked concrete. However, the zone of relatively high tangential tensile stresses is much larger than in the case of uncracked concrete. In the crack plane no tangential stresses exist because the concrete is cracked. For cracked concrete approx. 75 % of the pull-out load is transferred through the supports that lies on a line that is parallel to the crack plane. In contrast to this, in uncracked concrete in both support directions (direction parallel and perpendicular to the crack) about 50 % of the applied pull-out load is taken up.

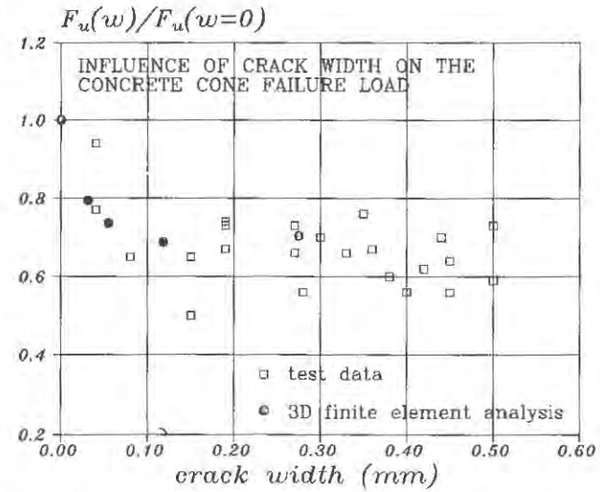

Figure 3. The calculated and measured relation between crack width and failure load

Based on the results of the analysis a simplified mechanism of the load transfer in uncracked and cracked concrete is shown in Fig. 4. In uncracked concrete the anchor load is distributed equally into the concrete (Fig. 4a). Tensile tangential (hoops) stresses are needed for equilibrium. No or only small shear stresses exist on the failure cone surface. However, in the crack plane tangential tensile stresses can not be taken up (Fig. 4b). Therefore, in this plane concrete resistance in direction perpendicular to the concrete cone surface consists only of tensile stresses acting in the direction of the crack plane i.e. there is no spatial effect. However, in the plane perpendicular to the crack plane beside these stresses significant tangential stresses in the imagined concrete cone exist

and contribute to the total resistance, stiffening the concrete cone in this direction, i.e. a spatial effect exists that is similar as in the case of uncracked concrete. A continuous drop of the tangential tensile stresses from the maximum value in the plane perpendicular to the crack plane, to zero value in the crack plane, is due to shear stresses acting in the concrete cone. Therefore, theoretically the projection of the concrete cone on the concrete surface can not have the form of a circle, as in uncracked concrete, since in such a case no change of the tangential stresses is possible. The form of the concrete cone projection should be approximately an ellipse, such that change of tangential stresses is possible.

According to this simplified model, the load transfer in the crack plane is mainly due to local bending i.e. no significant spatial effect exists and the situation is similar to a case of plane stress state. However, in the plane perpendicular to the crack plane significant tangential stresses exist. As a consequence, this plane behaves much stiffer and most of the pull-out force is transferred into the direction of this plane.

This load transfer mechanism is basically the same as in the case of an anchor in the vicinity of an edge if the edge distance of the anchor is small or zero [6]. However, there are three differences: (1) While in cracked concrete a full cone is formed, anchor at the edge will generate a half cone only for a zero edge distance. (2) Anchoring at the edge might produce a lateral local failure in the region of the head (so called blow-out failure). This failure mode is not possible for an anchor in a crack because a large lateral expansion of the concrete under the head will cause crack closing and thus confinement. (3) Anchor in uncracked concrete at the edge can utilize the full concrete tensile capacity. In contrast to that, for anchors in crack the concrete tensile capacity is reduced as explained above.

The above mechanism is activated soon after crack opening starts since the capability of the tangential load transfer in the crack plane decreases relatively fast with increasing crack width. This is demonstrated in Fig. 3 where it is shown that the concrete cone failure load decreases rather fast at small crack widths and is about constant for a crack width larger than a critical value ($w \sim 0.15$ mm).

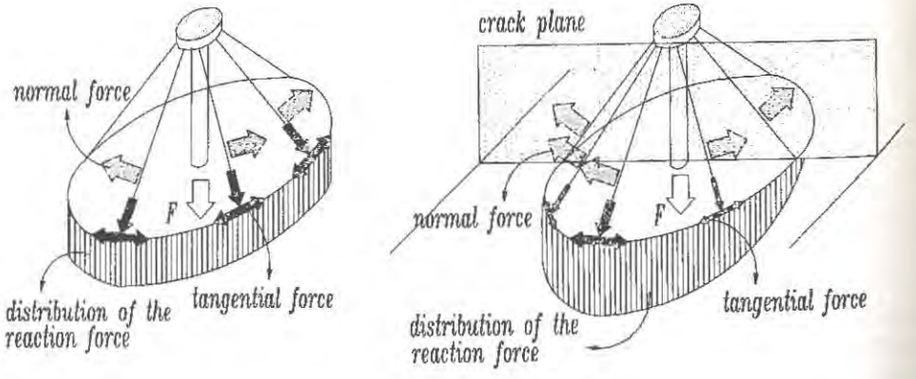

Figure 4. Simplified load-transfer mechanism, (a) uncracked and (b) cracked concrete

CONCLUSIONS

1. Similar as in the experiments the analysis confirms that the concrete cone failure load in cracked concrete decreases relatively fast with increasing crack width and reaches for $w \sim 0.15$ mm approximately 70% of the failure load valid for uncracked concrete. A further increase of the crack width has no influence on the failure load since the final load transfer mechanism has been formed.

2. In the case of uncracked concrete the load transfer in any vertical plane is the same and an axisymmetrical type of analysis can be used. Because of the axisymmetry, the forces in the concrete cone are equally distributed around the anchor. Tangential tensile (hoops) stresses exist for equilibrium reasons.

3. In cracked concrete the flow of forces is not axisymmetrical to the anchor. In the crack plane tangential stresses do not exist and the load transfer in this plane is similar as in the case of plane stress state. However, in the plane perpendicular to the crack plane the flow of forces is similar as in uncracked concrete i.e. a spatial effect exists. The change of the tangential stresses around the circumference of the cone is caused by shear stresses. As a consequence the concrete cone in the plane perpendicular to the crack plane is much stiffer than in the crack plane and approx. 75 % of the pull-out force is transferred through the support lines that are parallel to the crack. This change in load transfer mechanism causes the above mentioned failure load in cracked concrete to 70 % of the value valid for a uncracked concrete.

REFERENCES

1. Rehm, G., Eligehausen, R., and Mallie, R., Befestigungstechnik. Betonkalender 1988, Teil 2, Wilhelm Ernst & Sohn, Berlin, 1988.

2. Ožbolt, J., Influence of the crack width on the concrete cone failure load of headed stud anchors. Report Nr. 4/13-91/12, Institut für Werkstoffe im Bauwesen, Stuttgart University, November 1991, not published.

3. Rehm, G., and Martin, H., Zur Frage der Rissbegrenzung im Stahlbetonbau. Beton - und Stahlbetonbau, 1968, **8**, Berlin, 1-8.

4. Bažant, Z.P., and Ožbolt, J., Nonlocal microplane model for fracture, damage, and size effect in structures. Journal of Engineering Mechanics, ASCE, 1990, 116(**11**), 2485-2504.

5. Eligehausen, R., and Balogh, T., Ultimate tensile capacity of single anchors in cracked concrete. Report to ACI committee 355, Washington D.C., March 1992, in preparation.

6. Ožbolt, J., The edge influence on the pull-out failure load of the headed stud anchors. Report Nr. 4/12-91/11, Institut für Werkstoffe im Bauwesen, Stuttgart University, November 1991, not published.

Chapter 10

Fatigue and Rate Effects

Invited Paper

ARE FRACTURE MECHANICS-BASED METHODS USEFUL FOR CHARACTERIZING FATIGUE DAMAGE IN CONCRETE BEAMS?

STUART SWARTZ
Dept. of Civil Engineering
Kansas State University
Manhattan, KS 66506
USA

ABSTRACT

Fracture mechanics-based methods for predicting fatigue crack growth rates and life estimates which have been used extensively - and successfully - for metals would appear to be ideally suited for concrete. This paper reviews recent work on evaluation of the fatigue behavior of plain concrete beams in the context of fracture mechanics concepts including the fictitious crack model, size effect law, effective crack length model and such LEFM concepts as fracture toughness and Paris' law. The applicability of these approaches to reinforced concrete where the fatigue failure mechanism may be due to crack propagation through the concrete matrix as opposed to debonding or rupture of the reinforcement is proposed by considering test results from model beams.

INTRODUCTION

Fatigue of plain and reinforced concrete structural members has been studied for many years. The most recent extensive summaries of this work may be found in references 1 and 2. The process of fatigue, which is due to progressive and irreversible deterioration, may lead to excessive deformations, excessive crack widths, debonding of reinforce-ment, and rupture of reinforcement and/or matrix leading to structural collapse. The latter possibility - crack propagation through the matrix leading to failure before some other mechanism controls - has not often been considered.

Empirical methods using Wöhler - or S-N curves - have traditionally been used in conjunction with statistical treatment of the data as, for instance, by Oh [3] in which the relative dispersion about the mean is seen to increase with decreasing stress ratio and in-creasing fatigue life for plain concrete beams in bending.

For metals, the use of methods of fracture mechanics for fatigue life estimates has become standard practice. As stated by Barsom and Rolfe [4], "The field of fracture mechanics has become the primary approach to controlling brittle fracture and fatigue failures in structures". Why not then for the "brittle" material concrete?

DAMAGE METHODOLOGIES

The use of the method of damage mechanics is directed to obtaining damage indices to describe the reduced function of the structural component in terms

of load cycles. Typically, the damage function is of the form

$$\Psi = \Psi_{ref}(1-D) \qquad (1)$$

where Ψ is the current stiffness parameter, Ψ_{ref} is the original (considered to be undamaged) reference state and D is a damage parameter. As noted by Alliche and Francois [5], this approach to describing damage--as opposed to considering stresses--yields less scatter and therefore strain--or equivalently deflection--may be better correlated with damage. They describe three distinct stages as shown in Fig. 1. Using stages II and III, they assume dD/dN to be a scalar function of strain and the stress ratio ($R = P_{min}/P_{max}$).

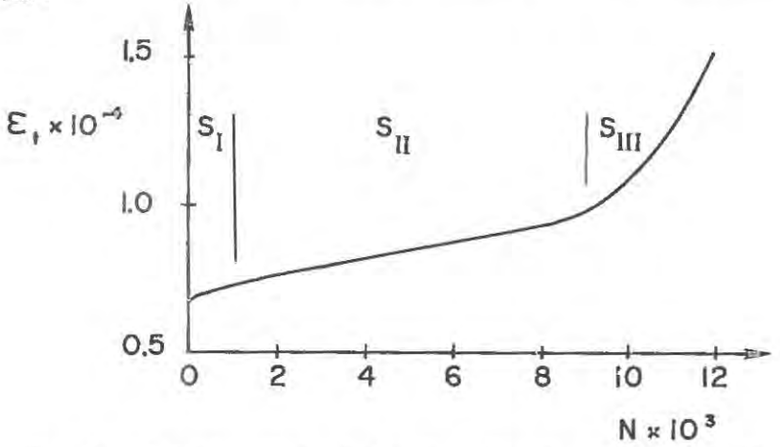

Fig. 1. Evolution of ϵ_t with number of cycles (after ref. 5)

The life estimates obtained from this approach showed a reasonable correlation with their experimental data.

This concept may be utilized with fracture mechanics methods to model the damage process directly. Apparently, Gylltoft [6] was the first to use a fracture mechanics model in this way to study low-cycle fatigue behavior of a plain concrete beam. More recently, this approach has been used by Hordijk [7] and Hordijk and Reinhardt [8]. As more details will be found elsewhere in this volume only a brief description of their method will be given here.

The basic idea is that damage accumulates in each load cycle, where $F_{upper} < F_{MAX}$ (static load), until some cycle when F_{upper} coincides with a point on the softening branch of the static, uniaxial load - COD curve. At this point, the crack propagation is unstable and failure occurs.

The model was implemented in the DIANA finite element program and applied to a beam in four-point bending with a central notch of half the beam height (Fig. 2). It is seen that the deflection response with load cycle N is very similar to that observed experimentally (cf. Fig. 1[5]). Although this approach is very time-consuming (computing intensive) it nevertheless appears to be realistic.

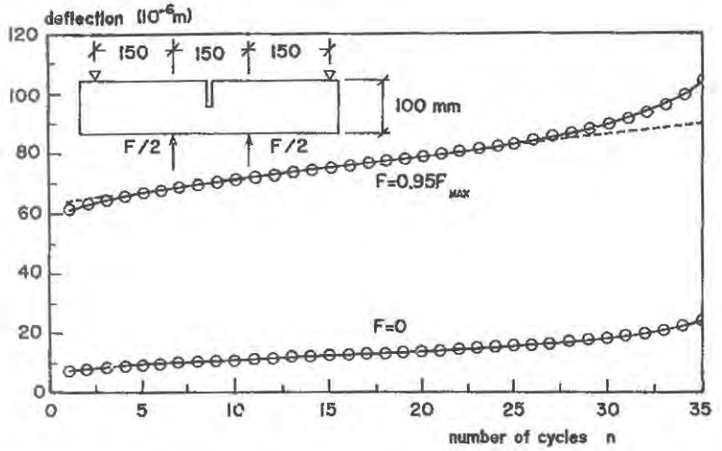

Fig. 2 Deflection as a function of number of cycles [8]

Expressions for the damage parameter D have been proposed by Zhang, et al. [9] for concrete beams loaded cyclically. Fracture mechanics concepts were used and a threshold parameter based on opening mode stress intensity, ΔK_{th} identified below which the elastic modulus E_d remains constant. For $\Delta K > \Delta K_{th}$, E_d decreases linearly with load cycle--according to their data--until a value of $N = N_L$. After this, E_d decreases non-linearly. The limit of linear response is denoted E_{dL}. Using K_{Icd} as the dynamic, mode I fracture toughness of concrete and $R = K_{min}/K_{max}$ (= 0.2 in the study), the variation of $\bar{E}_d$ (≈ 1-D) with N is given as

$$\frac{d\bar{E}_d}{dN} = \frac{\alpha(\Delta K - \Delta K_{th})^n}{K_{Icd}(1-R) - \Delta K} = f(\Delta K) \qquad (2)$$

and

$$N_f = \frac{1}{f(\Delta K)}(\bar{E}_{dL} - 1) \qquad (3)$$

is the fatigue life. The terms α, n are empirical constants.

FRACTURE MECHANICS

An approach commonly used for metals relates crack growth with number of cycles according to the so-called Paris' Law [10]:

$$da/dN = C(\Delta K)^m \qquad (4)$$

where C, m are experimental constants and K is the stress intensity factor. In the logarithmic form the resulting data should plot as a straight line. The difficulties implementing this approach are: measurement of crack length a; calculation of K = K(P, a, geometry); calculation of da/dN and ΔK. Inherent to this are the questions of the influence of process zone and validity of LEFM. These of course, are the same problems encountered in the static case which have been addressed extensively in the past few years and-in the writer's opinion - have been resolved.

The research presented by Baluch, et al. [11] describes a compliance-calibration technique using cracked specimens with the crack length measurement based on surface observations. Work by Swartz and Refai [12] indicates this approach will be approximately valid for determining Δa if the process zone is fully developed and if a is less than about 70% of the beam depth. Alternatively, an effective crack length could be used as proposed by Jenq and Shah[13].

Using this approach to determine da/dN and ΔK, results from ref. 11 are presented in Fig. 3a for three different stress ratios R. The straight lines were fitted to data values and all have about the same slope m. Similar work by Perdikaris and Calomino [14] is presented in Fig. 3b along with the data values which show the scatter. Their values of a, K were based on notched beam compliance calibration and LEFM.

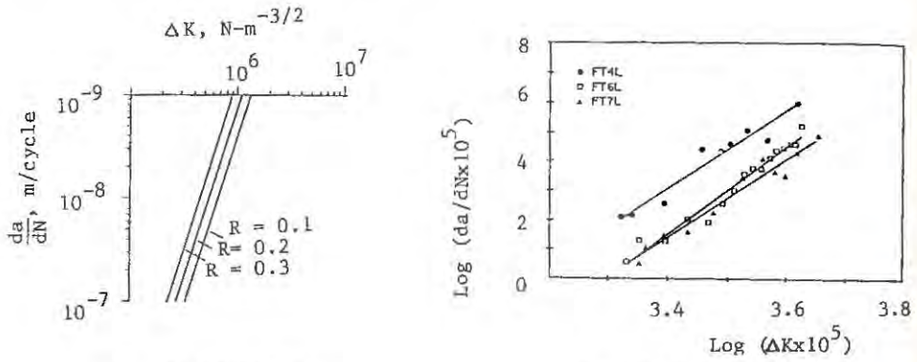

a. reference 11. b. reference 14.

Fig. 3. Crack growth da/dN versus ΔK [11,14].

Although the data in Fig. 3b appear to be fitted fairly well by the straight lines, the authors state that the error in crack growth rate or life expectancy could be as high as 100%.

Work by Bazant and Xu [15], which exploited the principle of the size effect law, resulted in a modified-or generalized, size-adjusted Paris' law:

$$\frac{\Delta a}{\Delta N} = C\left(\frac{\Delta K_I}{K_{Ic}}\right)^n \qquad (5)$$

where K_{Ic} is a size-dependent fracture toughness given by

$$K_{Ic} = K_{If}\left(\frac{\beta}{1+\beta}\right)^{\frac{1}{2}} \qquad (6)$$

In this K_{If} is the fracture toughness of an infinitely-large beam and $\beta = d/d_o$ where d is the beam depth and d_o is an empirical constant. The parameter β is called the brittleness number. Of interest, is that it was determined that d_o is not constant but depends ΔK_I. Also see Oh [3] for a related observation on the relative dispersion about the mean.

Swartz, et al. [16] tested beams in bending using two sizes and two mix designs. The crack lengths were determined using compliance calibration [16, 17]. The fatigue loading was done using CMOD strain control and was stopped at N = 1 x 10^6 cycles. A typical group of data plots is shown in Fig. 4.

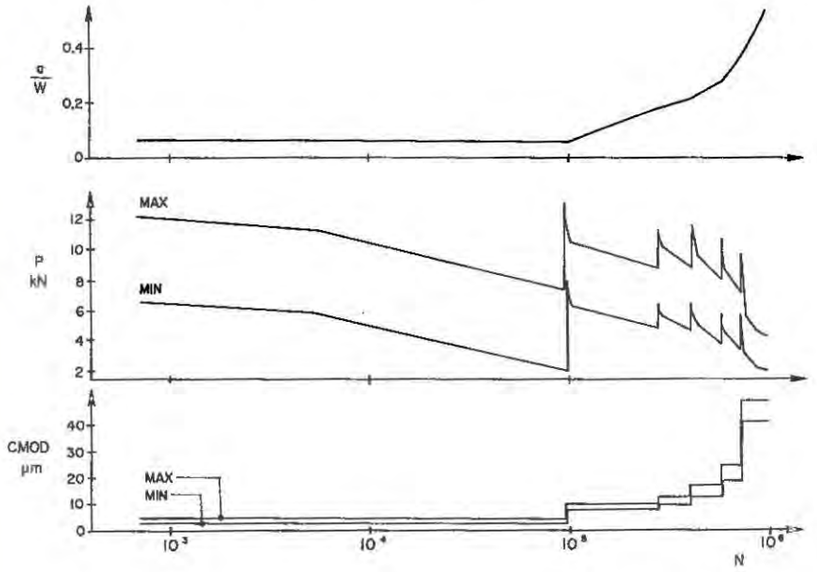

Fig. 4. Fatigue crack growth-displacement control [16].

The objective was to grow true fatigue cracks of different lengths but with about the same elapsed time (1 x 10^6/4 Hz = .25 x 10^6s). After cracking, the beams were loaded to failure and P-CMOD plotted. In each case a companion beam was cracked such that the slope of the ascending P-CMOD curve matched that of the fatigued beam. Then this was also loaded to failure. In both cases, K_{Ic} was computed using P_{max} and LEFM with the crack length corresponding to the slope of the ascending curve.

The results of these tests are presented in Table 1. Based on the compliance-calibration method of crack measurement, K_{Ic} (fatigue)/ K_{Ic} (static) = 0.90, CV = 6%. Corresponding results were obtained from the Jenq/Shah method[13].

Table 1. Stress intensity factors at unstable crack growth-fatigue and static precracking

W [1] mm	Load[2] Type	f'_c MPa	P_m kN	$\frac{a_s}{W}$ [3]	K^s_{Ic} kN-m$^{-3/2}$	$\frac{a}{W}$ [4]	K_{Ic} kN-m$^{-3/2}$	$\frac{F}{S}$
102	F3	48.9	4.54	.352	1192	.195	769	.84
102	S3	48.9	4.94	.297	1116	.245	916	
102	F3	54.2	1.92	.525	740	.510	727	.93
102	S3	54.2	2.02	.527	780	.520	782	
102	F3	51.7	2.06	.605	1117	.612	1102	.86
102	S3	51.7	2.31	.605	1252	.618	1276	
203	F3	22.5	12.37	.072	595	.160	842	.83
203	S3	23.4	13.71	.065	642	.180	1016	
203	F3	24.8	5.70	.350	631	.490	880	
203	S3	24.8	5.83	.350	646	.515	972	.91
203	F3	26.0	4.91	.380	590	.580	1032	
203	F3	52.7	11.35	.230	902	.374	1263	.95
203	S3	52.7	10.24	.290	963	.438	1329	
203	F3	53.1	3.90	.590	857	.740	1670	
203	S3	53.1	4.05	.760	1710	.742	1752	.95
203	F3	53.2	1.07	.770	1110	.830	779	

[1] For W = 102 mm, B = 76 mm, S = 381 mm. For W = 203 mm, B = 102 mm, S = 610 mm.
[2] F = fatigue precracking, S = static precracking, 3 = TPB.
[3] Method of Jenq and Shah [13]
[4] Compliance Calibration [17]

REINFORCED CONCRETE BEAMS

The term "reinforced concrete" (R/C) implies here the use of conventional rebars or prestressed, steel cable or bars. Previous work done on R/C beams subjected to long term (high N) fatigue loadings is described in reference 1. In general, fatigue failures in such members are due to reinforcement debonding or rupture. For post-tensioned, prestressed beams fatigue failure may occur at the anchorages. It is mentioned that in a properly designed unbonded, prestressed concrete beam for which precompression is such that the section will remain uncracked during its service load cycle, the consequences of fatigue have not been a major factor in design. However, a conceivable failure mechanisms could occur by a fatigue crack starting initially in a tensile region and extending through the compression zone.

Two small beam models were tested by Swartz and Noory [18] with the geometry and reinforcing shown in Fig. 5. The reinforcement consisted of smooth bars anchored at the beam ends to steel plates.

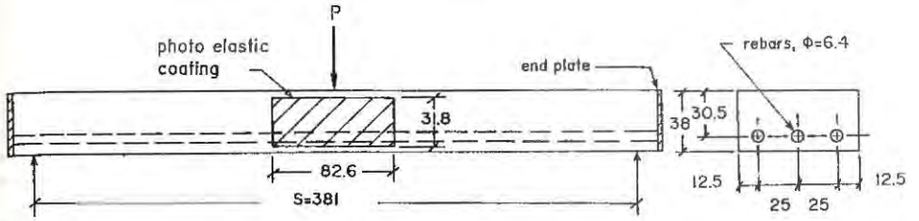

Fig. 5. Model beam with end-anchored reinforcement (after ref. 18).

Cracks were monitored using a photoelastic coating bonded to the beam surface at midspan as shown. Prior to starting fatigue testing the beam was loaded to its computed service level and cracks were induced in the central portion. Following this the beam was loaded in fatigue at 4 Hz with P_{max} = 3.56 kN, P_{min} = 2.67 kN (R = 0.75). The crack growth versus load cycles is shown in Table 2.

Table 2. Crack size versus number of cycles.

N x 10^3	$\frac{\text{Crack Depth}}{\text{Beam Depth}}$	% Change in Crack Width
0	0.232	--
25	0.344	5
850	0.376	11
1174	0.400	74
4300	0.600	137

The primary mode of failure was by penetration of a flexural crack completely through the compressed region after which the load was carried solely by the reinforcement. This induced a yield mechanism in the steel bars. The fatigue lives for the two beams were 4.83 x 10^6 cycles and 17.68 x 10^6 cycles.

This model study revealed that (1) it is possible for flexural cracks to propagate through the concrete matrix due to fatigue in a mode which is not normally considered in design and (2) serviceability requirements in terms of crack widths need to be considered with respect to fatigue loads.

CONCLUSIONS

From the survey of work presented here the following conclusions may be made.

1. Fracture mechanics approaches are indeed a useful way to model fatigue crack growth. The work in references 7 and 8 using the fictitious crack concept along with observed uniaxial cyclic behavior appears to be particularly promising. The approach using Paris' law [10] also appears to be valid if auxiliary techniques are employed to determine a, K_{Ic} (eg. refs. 12, 13, 15 and others) to account for the presence of a process zone and size effect.

2. Future work on testing plain concrete in bending to determine fatigue damage behavior and life should incorporate the concepts presented here.

3. Extension of this work to reinforced concrete should be done with particular emphasis on very lightly reinforced beams, over- reinforced beams and post-tensioned (unbonded) beams.

REFERENCES

1. Shah, S. P. ed. Fatigue of Concrete Structures, ACI SP-75, American Concrete Institute, Detroit, 1982.

2. Cornelissen, H.A.W., State of the art report on fatigue of plain concrete. Stevin Report 5-86-3, Delft University of Technology, 1986.

3. Oh, B.H., Fatigue-life distributions of concrete for various stress levels. ACI Mater. Jnl., 1991, 88, 122-8.

4. Barson, J.M. and Rolfe, S.T. Fracture and Fatigue Control in Structures, 2nd ed., Prentice-Hall, Inc., Englewood Cliffs, NJ, 1987.

5. Alliche, A. and François, D., Fatigue damage of concrete. In Fracture of Concrete and Rock, eds. S.P. Shah and S.E. Swartz, Springer-Verlag, New York, 1989, pp. 88-95.

6. Gylltoft, K., Fracture mechanics models for fatigue in concrete structures. PhD Thesis, Lulea University of Technology, 1983.

7. Hordijk, D.A., Local approach to fatigue of concrete. PhD Thesis, Delft University of Technology, 1991.

8. Hordijk, D.A. and Reinhardt, H.W., Growth of discrete cracks in concrete under fatigue loading. In Toughening Mechanisms in Quasi-Brittle Materials, ed. S.P. Shah, Kluwer Academic Publishers, Dordrecht, 1991, pp. 541-54.

9. Zhang, Binsheng, Zhu, Zhaohong, Wu, Keru, Fatigue rupture of plain concrete analyzed by fracture mechanics. In Fracture of Concrete and Rock, eds. S.P. Shah and S.E. Swartz, Springer-Verlag, New York, 1989, pp. 58-63.

10. Paris, P.C. and Erdogan, F., A critical analysis of crack propagation laws. Transactions of ASME, Journal of Basic Engineering, 1963, 85, pp. 528-34.

11. Baluch, M.A., Qureshy, A.B. and Azad, A.K., Fracture crack propagation in plain concrete. In Fracture of Concrete and Rock, eds., S.P. Shah and S.E. Swartz, Springer-Verlag, New York, 1989, pp. 80-7.

12. Swartz, S.E. and Refai, T.M.E., Cracked surface revealed by dye and its utility in determining fracture parameters. In Fracture Toughness and Fracture Energy-Test Methods for Concrete and Rock, eds. H. Mihashi, H. Takahashi and F.H. Wittmann, A.A. Balkema, Rotterdam, 1989, pp. 509-20.

13. Jenq, Y.S. and Shah, S.P., Two-parameter fracture model for concrete. J. of Eng. Mech., ASCE, 1985, 111, 10, 1227-41.

14. Perdikaris, P.C. and Calomino, A.M., Kinetics of crack growth in plain concrete. In Fracture of Concrete and Rock, eds. S.P. Shah and S.E. Swartz, Springer-Verlag, New York, 1989, pp. 64-9.

15. Bažant, Z.P. and Xu, K., Size effect in fatigue fracture of concrete. ACI Mater. Jnl., 1991, 88, 390-99.

16. Swartz, Stuart E., Huang, Chen-Ming James and Hu, Kuo-Kuang, Crack growth and fracture in plain concrete--static versus fatigue loading. ACI SP-75, ed. S.P. Shah, American Concrete Institute, Detroit, 1982, pp. 47-69.

17. Swartz, Stuart E., Hu, Kuo-Kuang and Jones, Gary L., Compliance monitoring of crack growth in concrete. Eng. Mech. Div., ASCE, 1978, 104, EM4, 789-800.

18. Swartz, S.E. and Noory, A.K., Photoelastic coatings to monitor crack growth in concrete. Exp. Tech., 1981, 5, 3, 2-3.

MATERIAL MODEL FOR HIGH STRENGTH CONCRETE EXPOSED TO CYCLIC LOADING

Terje Kanstad and Gordana Petkovic
Div. of Concrete Structures, The Norwegian Institute of Technology
SINTEF FCB, Research Institute for Cement and Concrete
Trondheim, Norway

ABSTRACT

Strain measurements performed as a part of an extensive experimental investigation of the behaviour of high strength concrete exposed to cyclic loading are here used in an attempt to develop a material model that can suit an arbitrary loading combination. The description of strain development is performed by applying the principles used in modelling of static time dependent deformations. The creep law given in CEB Model Code 1990 (MC 90) is used as a starting point, and the additional deformation due to cyclic load is expressed as a cyclic creep term. Based on the test results, we found an expression for this term dependent on the modulus of elasticity, the stress amplitude, the mean stress and the time under load. In this paper a tentative version of the material model and comparisons between the model and some of the experimental results are presented.

INTRODUCTION

The experimental basis used in the development of the model to be presented belongs to an investigation of the fatigue properties of high strength concrete performed at SINTEF FCB.

One can generally say that the capacity of concrete in cases of cyclic loading to failure in compression it quite well known. The tests were performed with three concrete qualities, but it was found that the fatigue life was independent of the concrete quality if expressed relatively to the compressive strength. S-N curves were, therefore, established on the basis of all qualities together. The design rules developed from these tests [4] have entered the draft of the 1990 CEB Model Code.

The extensive measurements of strain performed in these tests were a crucial supplement to the fatigue life registration under various

loading levels and have in each step been an important guideline for establishing further research plans. The strain measurements have enabled the calculation of the strain rate, volumetric strain, modulus of elasticity, and Poisson's ratio. In this way, the test results contribute to extending knowledge from the fatigue capacity of concrete on to the performance of concrete under cyclic loads below the "endurance limit", to combinations of cyclic and longterm static loading, etc.

The experimental programme was later on extended to investigating fatigue properties under loading with stress gradients, and on to combinations of cyclic and static loading. In this stage, the application of the model is still limited to cases of centric constant amplitude cyclic loading.

EXPERIMENTAL PROGRAMME

The experimental basis used for the development of the model described here is limited to centrically tested specimens of ND95 concrete [4,5]. The loading combinations applied are summarized in Fig 1, where S_m is the mean stress and ΔS is the stress amplitude, both expressed relatively to the compressive strength of the concrete. An asterisk denotes specimens failing in fatigue. The age at loading, absolute compressive strength, and the modulus of elasticity have varied somewhat, and have in the average been: 83.2 MPa, 33785 MPa, and 145 days, respectively.

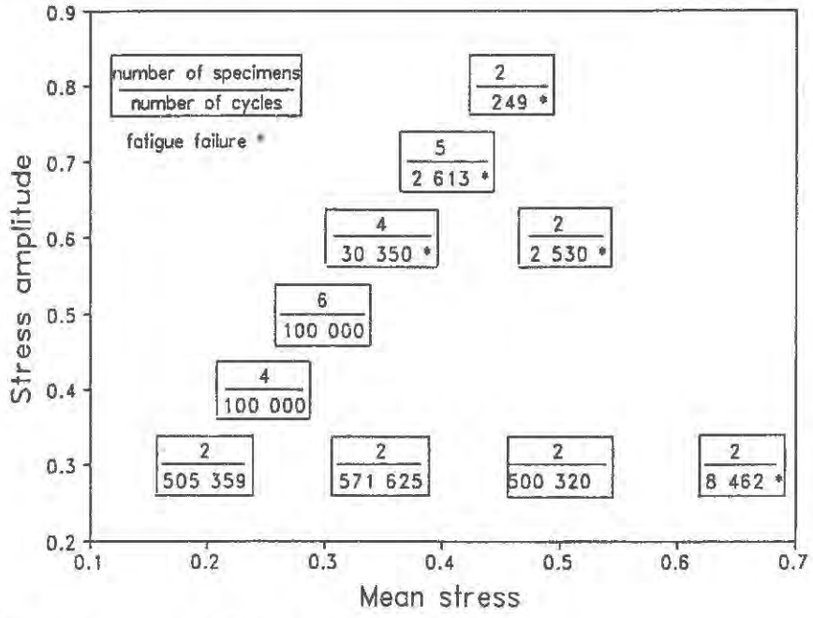

Fig 1. Overview of the testing programme

MATERIAL MODEL

The total stress dependent deformation is chosen to be described by means of three different terms: shorttime deformation, static creep and additional cyclic creep. At low stress levels we assumed that the stress dependent deformation is proportional to the mean stress. In the experiment, only strain at maximum and minimum load was measured. The experimental value of the strain at mean stress was, therefore, calculated as the average of the strains measured at the maximum and minimum stress levels.

The longtime material model presented in the 1990 CEB Model Code (MC90) [3] was chosen as the basis for the model. Static creep tests within the previously mentioned high strength concrete investigations [6] have shown that MC90 gives a reasonably good description of the static creep of these concrete qualities. The compliance function and the total stress dependent strain is defined as:

$$J(t,t') = \frac{1}{E_c(t')} + \frac{\varphi_c(t,t')}{E_c(28d)} + \frac{\varphi_{cc}(t,t')}{E_c(28d)}$$

$$\varepsilon(t) = J(t,t') \cdot \sigma_{mean}(t')$$

In these expressions $\phi_c(t,t')$ is the static creep ratio as defined in [3], $\phi_{cc}(t,t')$ the cyclic creep ratio, t' the concrete age at loading and t the actual time. The cyclic creep ratio is defined as:

$$\phi_{cc}(t,t') = \beta(t')\ \beta(f_{cm})\ \beta(S_m)\ \beta(\Delta)\ \phi_{cc1}\ \beta(N,\omega)$$

In this expression f_{cm} is the average compressive cylinder strength at 28 days, S_m the ratio between the mean stress and the concrete strength at the start of testing, Δ the relative stress amplitude, N the number of load cycles and ω the frequency ($N=(t-t')\omega$). So far we have only considered one concrete quality (ND95) and specimens tested at later concrete ages (90-270 days), so these effects are included simply by using the same functions as for static creep in MC 90.

The product of the parameters, $\beta(S_m)$, $\beta(\Delta)$ and ϕ_{cc1} was first adjusted to the experimental results of each test specimen individually. The following time function gave good agreement with the experimental strain development:

$$\beta(N,\omega) = N^n - 1 = ((t-t')\ 86400\ \omega)^n - 1 \quad \text{with} \quad n = 0.022$$

(t-t') is the time under load (days), ω the frequency (s^{-1}), and 86400 is the number of seconds in a day. In their general material models, both Bazant and Panula [2] and Whaley and Neville [1] used the same time function for both static and cyclic creep. We found it convenient to use two different time functions. After some considerations we also chose to use one time function for both the first and second stage of the strain development. Fig 2a shows the different terms in the compliance function for one of the test specimens with stresses below the endurance limit.

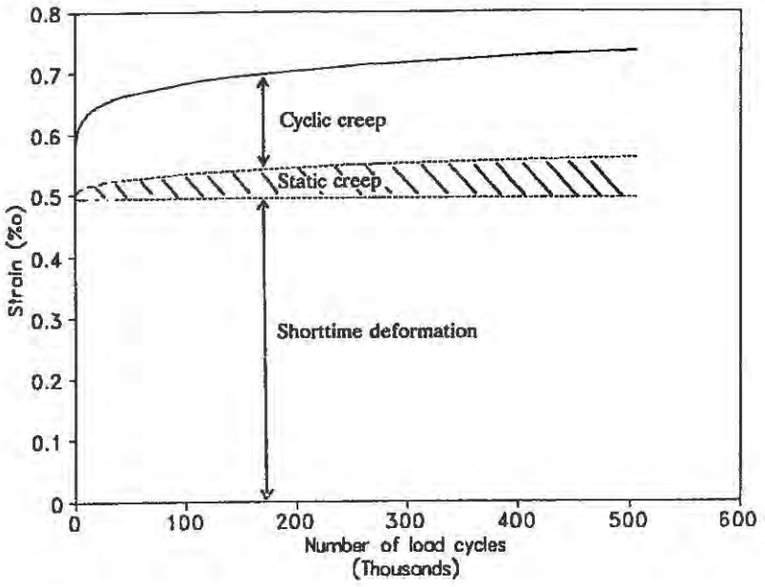

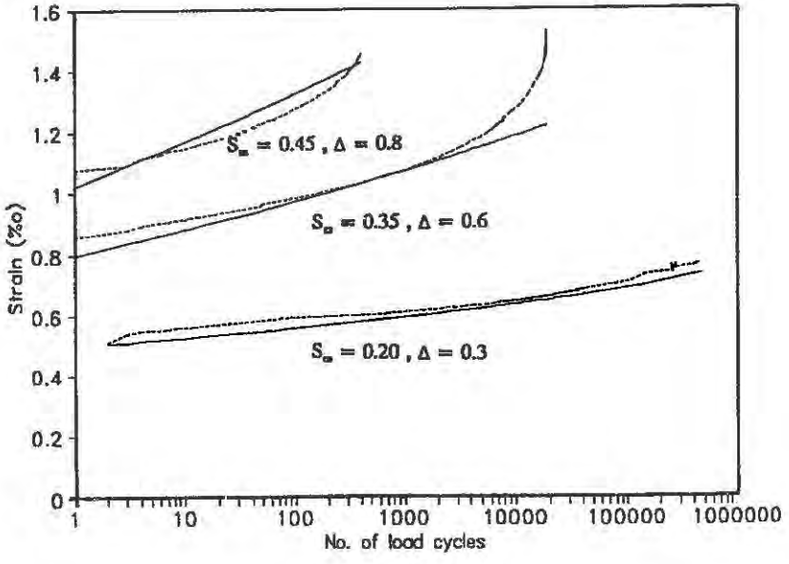

Figure 2.a)Calculated strain development for a specimen with mean stress level S_m=0.2, and stress amplitude Δ=0.3, and frequency $\omega=s^{-1}$.
b)Comparison between experimental behaviour and the general model for three specimens.

We assumed that the cyclic creep ratio was independent on the mean stress for mean stresses below 40% of the strength. The effect of the stress amplitude was found to be best described by the simple function:

$$\beta(\Delta) = \Delta^n , \qquad n=1.0$$

Finally the parameter ϕ_{cc1} was, by minimizing the sum of the squares of the deviations between model and experimental results, determined to be 1.39. The dependence of the mean stress level was less pronounced than for normal strength concretes [1,2], and the following function was found to give good agreement with the experimental behaviour:

$$\beta(S_m) = 1 + 10.5\ (S_m - 0.4)^2$$

The general expression for the cyclic creep term is then written as:

$$\phi_{cc}(t,t') = 1.39\ \beta(t')\ \beta(f_{cm})\ (1+10.5(S_m-0.4)^2)\ \Delta\ (N^n-1)$$

A comparison between the general expression for the cyclic creep ratio (the product $\beta(S_m)\ \beta(\Delta)\ \phi_{cc1}$), and the ratio which gave best agreement with the particular specimens, shows that most of the results lie within the limits of ±20%. Fig 2b compares the experimental behaviour and the results of the application of the model for three of the specimens. It can be seen that the general agreement is good.

SUMMARY AND CONCLUSIONS

For the understanding of fatigue behaviour of concrete before failure, the effect of low stress levels, of static preloading etc., the knowledge about the failure capacity of concrete under cyclic loading in compression must be completed by good descriptions of the strain development under varying loading conditions. The proposed model is the first step towards developing a general model.

The proposed model expresses the additional cyclic creep deformation as a function of the modulus of elasticity, the stress amplitude, the mean stress and the time under load. The model is generally in good agreement with experimental behaviour.

REFERENCES

1. Whaley, C.P., and Neville, A.M., Non-elastic deformation of concrete under cyclic compression. Magazine of Concrete Research, 1973, 25, No. 84, pp. 145-54.

2. Bazant, Z.P. and Panula, L.:, Practical prediction of timedependent deformations of concrete, Part V and VI, Materials and Structures (RILEM, Paris), 1979, 12, No. 69, pp. 169-83.

3. CEB-FIP Model Code 1990, Comite Euro-International du Beton, September, 1988.

4. Petkovic, G., Lenschow, R., Stemland, H., and Rosseland, S.: "Fatigue of high strength concrete", The Second International Symposium on High Strength Concrete, Berkeley, May 1990, ACI Publication SP-121

5. SINTEF, High strength concrete, phase 2&3, Unpublished test results.

6. Bjerkeli, L., Tomaszewicz, A., and Jensen, J.J.: "Deformation properties and ductility of high strength concrete", The Second International Symposium on High Strength Concrete, Berkeley, May 1990, ACI Publication SP-121

ACKNOWLEDGEMENTS

The work described is a part of a joint research program on High Strength Concrete, sponsored by The Royal Norwegian Council for Scientific and Industrial Research (NTNF) and the industry participants: Norwegian Contractors A/S, Norsk Hydro A/S, Saga Petroleum a.s., Statoil, A/S Norske Shell, Mobil Exploration Norway Inc., Conoco Norway Inc., Esso Norge A/S, Norwegian Petroleum Directorate, Norwegian Public Road Administration.

STIFFNESS DEGRADATION OF TENSION SOFTENING BEHAVIOR IN CONCRETE

N. Nomura and H. Mihashi
Faculty of Engineering, Tohoku University, Sendai 980, Japan.

ABSTRACT

The degrading stiffness and local fracture energy of concrete with normal, middle and high strength have been studied by using compact tension tests under a cyclic loading. The compliance of higher strength concrete increases with the advance of fictitious crack. The local fracture energy defined by the fictitious crack advance is possible to represent the properties of fracture process zone, which is attributed to concrete strength.

INTRODUCTION

There has been only limited studies concerning direct tensile tests to measure the stiffness degradation in tension softening behavior of concrete. Hordijk [1] has summarized the tests and crack cyclic models from the point of fatigue approach. The fracture mechanics approach based on the tension softening model appeals to numerical analysis such as finite element method to solve cracking behavior in a concrete structure. The tension softening model with degrading stiffness would be even more important for the analysis of structure under cyclic loading. On the other hand, the unloading and reloading procedure in a loading program has been used for fracture energy tests to observe the local fracture energy [2]. In this case the concept of degrading stiffness is replaced by the concept of local energy dissipation. This approach is practically useful to examine the properties of fracture process zone (f.p.z.) and tension softening behavior.

The main objective of the work reported here is to apply the method to evaluate the local fracture energy by using the cyclic loading tests in the fracture energy test in order to reveal the f.p.z. in the tension softening behavior of concrete with different strength.

EXPERIMENTAL PROCEDURE

Compact tension tests with cyclic loading in the post-peak region were performed (Fig.1).

The height, width and thickness of the specimens were 400, 480 and 120 mm, respectively. An initial notch length (a_0) was 200 mm. Triangular grooves of 10 mm depth were formed on both sides of the specimen, then the actual ligament thickness was 100 mm. Three grades of concrete mixes were designed to investigate the influence of the concrete strength on the stiffness degradation and the local fracture energy. The mix proportions and mechanical properties are given in Table 1.

TABLE 1
Mix proportion (per m^3)

series	d_{max} (mm)	W/C (kg)	W/(C+Si) (kg)	W (kg)	C (kg)	Sand (kg)	Gravel (kg)	Silica-fume(kg)	Superpl. (cc/CW)	Comp.Str. (MPa)	Tens.Str. (MPa)
H	5	0.25	0.20	111	444	721	1006	111	57.0	105.9	6.08
M	5	0.47	0.40	160	340	721	1006	60	28.0	58.8	3.82
L	5	0.65	0.65	227	349	721	1006	0	0.0	20.9	2.35

The deformation was measured at a crack mouth opening displacement (MOD) with a clip gauge. Although the MOD does not mean strictly a load-point displacement, there is no significant difference among them according to a preliminary numerical analysis. Three specimens were tested for each series, and the number of load-displacement curve with better unloading path were two, three and two for the L, M and H series, respectively. A typical load-displacement curve for M series is shown in Fig.2.

ANALYTICAL PROCEDURE

From the experimental load-displacement curves with unloading paths, stiffness degradation can be determined in terms of compliance which is a function of the displacement. The incremental energy dissipation can be calculated as an area surrounded by the load-displacement cycle. Consequently, if it is possible to measure crack advance in each cycle, the local fracture energy (g_f) can be assessed. The essential crack surface in

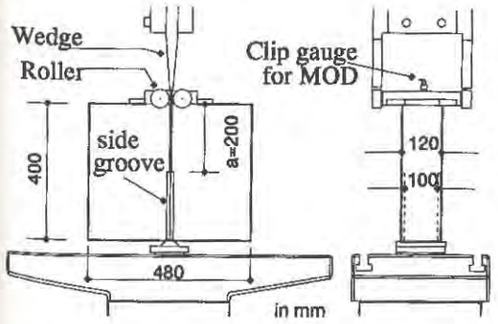

Figure 1. Specimen and loading set-up.

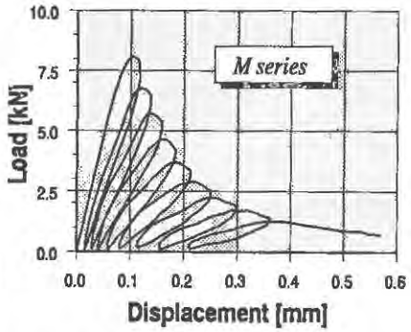

Figure 2. Example of load displacement curve.

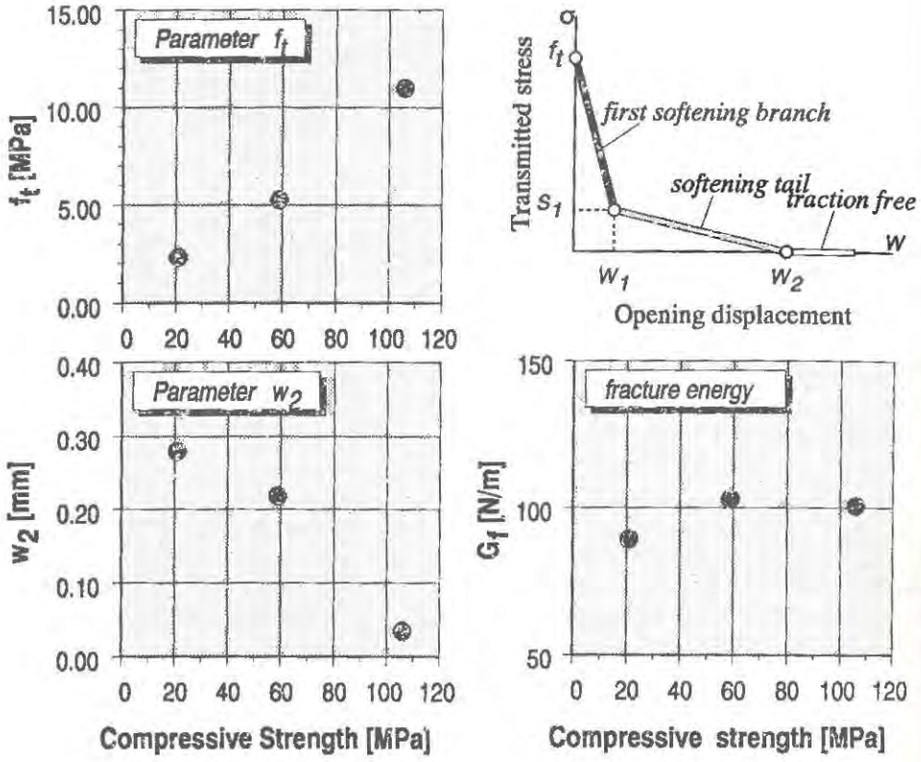

Figure 3. (a) Tension softening model, (b) Estimated fracture energy, (c) and (d) Estimated model parameters, f_t and s_1.

concrete, however, cannot be measured experimentally because of the smeared micro crack around the crack tip. In this report two methods were applied to define the crack advance:
(1) equivalent crack length : If the material is assumed to be linear elastic, a compliance–crack length relation can be calculated analytically and/or numerically. From this so–called compliance–method the equivalent crack length can be obtained so that the measured compliance corresponds to the calculated compliance–crack length relation. In the present study, the relation was determined by using a finite element analysis.
(2) fictitious crack length : A numerical load–displacement curve can be simulated by means of the fictitious crack model when an appropriate tension softening property for the material being tested is given. Since a certain position in the curve corresponds to a softening phase in the ligament (see. Fig.7), a fictitious crack advance can be defined so that the position in the experimental curve, where unloading begins, coincides with the simulated curve. The tension softening model used in the simulation was bilinear model (Fig.3(a)), and the model parameters were determined by optimizing the experimental load–displacement envelope curve based on the least square method [3].

RESULTS AND DISCUSSION

The fracture energy (G_f), and two of the parameters in the tension softening model, estimated by using averaged load–displacement curves in the optimizing procedure are shown in Fig.3 (b), (c) and (d). The results consistent with the previous work[4].

Fig. 4 shows the relation between the fictitious crack advance and the compliance normalized by an initial compliance. The degradation of stiffness after peak load decreases according to the progress of f.p.z. whose length is represented in terms of the fictitious crack advance. The higher the strength of material, the shorter the fictitious crack advance; in other words, if the fictitious crack advance is the same, the degradation of stiffness is marked in the higher strength concrete.

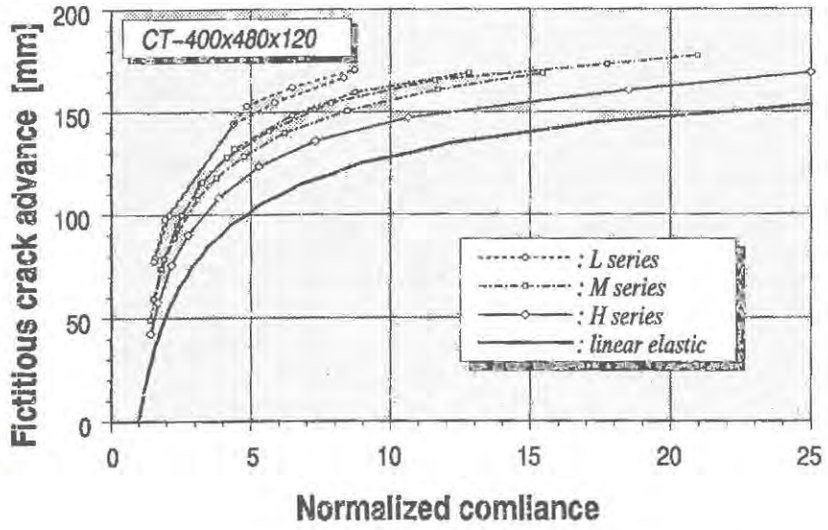

Figure 4. Relation between fictitious crack advance ($a_{fic.}$) and normalized compliance.

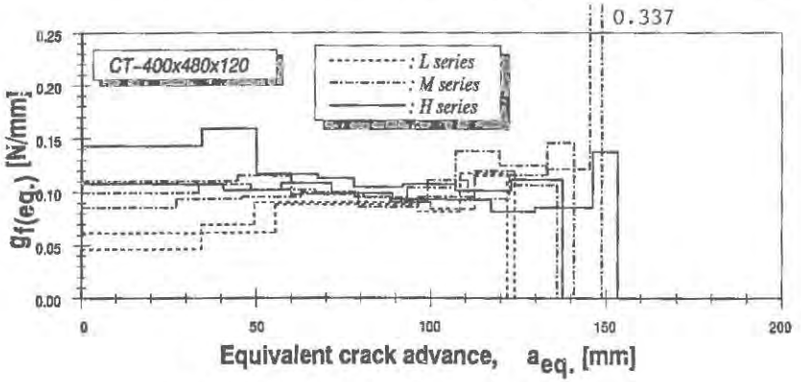

Figure 5. Local fracture energy, $g_{f(eq.)}$

The two kinds of local fracture energy, $g_{f(eq.)}$ and $g_{f(fic.)}$, during the crack advance is shown in Fig.5 and Fig.6. The $g_{f(eq.)}$ is defined using the equivalent crack advance ($a_{eq.}$) and $g_{f(fic.)}$, using the fictitious crack advance ($a_{fic.}$). It is considered that comparing to the $g_{f(eq.)}$ the $g_{f(fic.)}$ can provide obvious information about the local energy dissipation and the influence of material strength on that. The $g_{f(fic.)}$ is not constant during the $a_{fic.}$ advance. It increases with advance of the $a_{fic.}$. While in the weakest concrete $g_{f(fic.)}$ markedly rises up, the $g_{f(fic.)}$ in the high strength concrete becomes constant during the a_{fic} advance.

Fig. 7 demonstrates that the difference in the material strength exerts a great influence on the progress of the f.p.z. The hatches that indicate the softening phase correspond to those in Fig.3 (a). At lower load level after peak load, stress transmission caused by the softening tail remains in the lower strength concrete. On the other hand the stress transmission does not go on continuously in the case of high strength concrete. These are explained by considering the narrower width of f.p.z. in higher strength concrete [5] together with the correlation between the f.p.z. and the tension softening behavior [6]. The softening tail is attributed to the bridging mechanism, which is reduced in high strength concrete because the macro crack surface tends to proceed through aggregates.

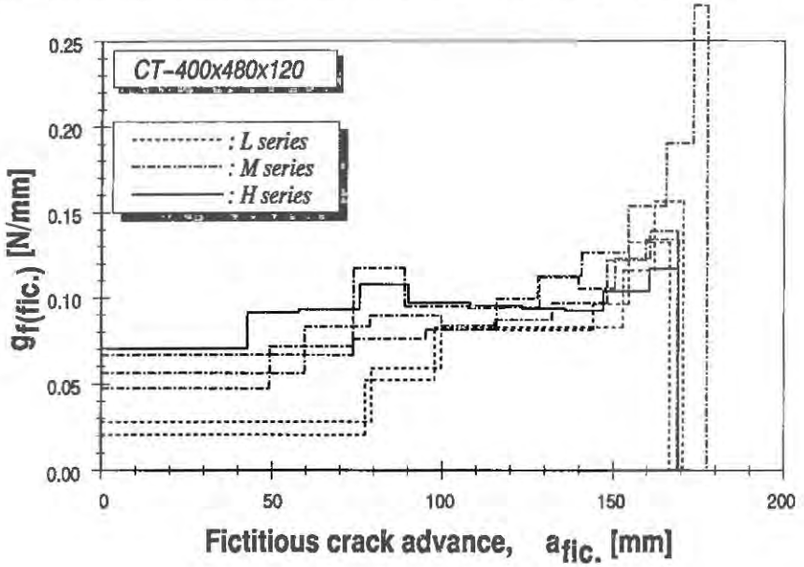

Figure 6. Local fracture energy, $g_{f(fic.)}$

CONCLUSION

The CT specimens with different strength were subjected to the cyclic loading to evaluate the stiffness degradation and the local fracture energy (g_f). The $g_{f(fic.)}$ defined by fictitious crack advance capable of providing reliable information concerning the fracture process zone are discussed. Based on the $g_{f(fic.)}$ and the numerical work, suggestions are made for the probable mechanism in f.p.z.

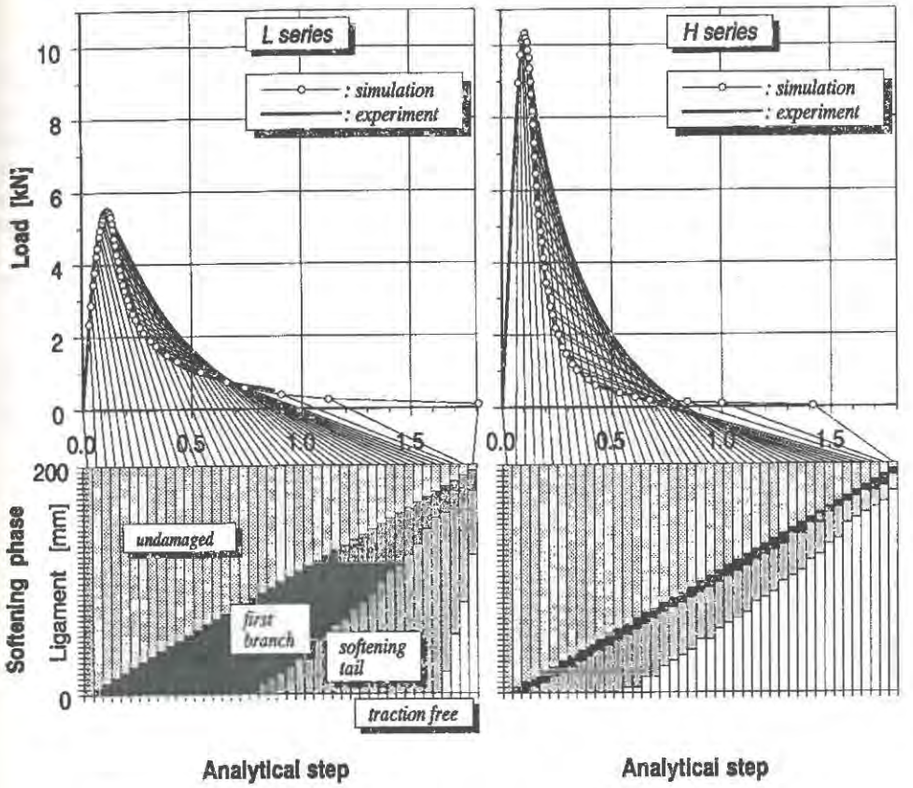

Figure 7 Simulated sotening phase for normal and high strength concrete.

ACKNOWLEDGEMENT

Partial financial support under Makita Scholarship Foundation is gratefully acknowledged.

REFERENCES

1. Hordijk, D.A., Doctoral Thesis, Technische Universiteit Delft, 1991.
2. Brameshuber, W. and Hilsdorf, H.K., Engrg. Frac. Mech., 1990, **35**, pp.95–106.
3. Roelfstra, P.E. and Wittmann, F.H., Frac. Toughness and Frac. Energy of Concr. ,(ed. F.H.Wittmann), Elsevier, 1986, pp.163–175.
4. Mihashi, H., Nomura, N. and Izumi, M., Intrn. Confr. on Recent Development on the Frac. of Concr. and Rock, 1989, pp.503–512,
5. Mihashi, H., Nomura, N. and Izumi, M., Proc. of the Imtrn. RILEM/ESIS Confr., (ed. J.G.M. van Mier, etc.), 1991, **1**, pp.441–456.
6. Nomura, N., Mihashi, H. and Izumi, M., Cem. and Concr. Res., 1991, **21**, pp.545–550.

TIME-DEPENDENT FRACTURE OF CONCRETE: TESTING AND MODELLING

FANPING ZHOU AND ARNE HILLERBORG
Division of Building Materials
Lund Institute of Technology
221 00 Lund, Sweden

ABSTRACT

A study of time-dependent fracture behaviour of concrete is presented. In order to investigate the time-dependency of the σ-w curve, a series of tensile relaxation tests on notched cylinders was carried out. Based on the results of the tests, a time-dependent crack model is proposed. In this model, an incremental σ-w relation based on a modified Maxwell chain is introduced for the fracture process zone. The model has been implemented in a finite element program and applied to predicting crack growth and failure in notched concrete beams subjected to sustained loading. The load-CMOD, CMOD-time, crack growth and stress-failure lifetime relations have been simulated. It seems that the theoretical simulations agree reasonably well with experimental results.

INTRODUCTION

Tensile cracking is a contributing factor to long-term deformations of concrete structures. Therefore, crack models including strain softening have been incorporated in creep and shrinkage analyses (e.g. Bazant et al. [1]). Hillerborg [2] accounted for the creep effect by assuming that only modulus of elasticity E depends on time, as $E=E^0/(1+\phi(t))$, where $\phi(t)$ is creep factor, and f_t and G_F are time-independent. He estimated the long-term strength of a structure from the structural strength and brittleness number (d/l_{ch}) relation evaluated by means of the Fictitious Crack Model (FCM). In those models, however, time-dependency is not taken into account in the fracture process zone.

In order to gain some insight into effects of time on the softening behaviour, a series of tensile relaxation tests on notched cylinders was carried out. Based on the experimental observation, a crack model is proposed. The application of the model to creep fracture of notched beams will be presented briefly. Further details can be found in the thesis by Zhou [3].

TENSILE RELAXATION TESTS

The cylinders are 60 mm in height and 64 mm in diameter. An encircling notch was introduced in each cylinder. The fracture cross-section is 40 mm in diameter. In all the tests wet specimens were used. The water-cement ratio is 0.55 and 28-day compressive strength is 38 MPa. The tests were carried out under deformation control in a MTS-810 testing machine, and a special arrangement [4] was used to assume stable direct tensile tests.

In each test, when the load had passed the ultimate value, the deformation was held constant somewhere, and the load relaxation was registered. Then the deformation continued to increase.

A typical test is shown in Figure 1. The stress relaxes very rapidly at first and then slows down during the holding period. When the deformation is increased again, the load increases at first until the static softening curve is reached and then decreases according to the curve. The static curve does not seem to be affected.

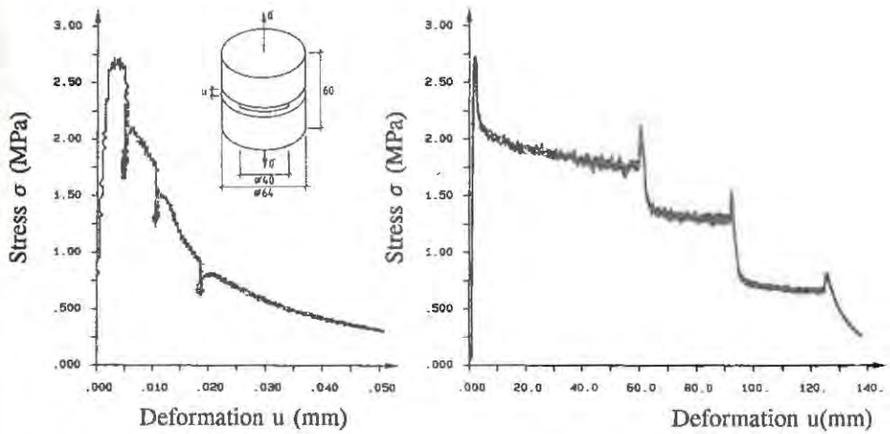

(a) Stress-deformation curve (b) Stress-time curve

Figure 1. A typical tensile relaxation test. The holding period of time at σ=2.65, 1,75 and 0.9 MPa are about 60, 30 and 30 minutes respectively.

THE PROPOSED MODEL

The proposed model can be regarded as a modified Maxwell chain incorporated with the static softening envelope (the σ-w curve) as a criterion, similar to a plasticity criterion.

The time-dependent σ-w relation may be expressed by the following incremental law:

$$d\sigma = d\sigma^R + d\sigma^I \qquad (1)$$

where $d\sigma^R$ and $d\sigma^I$ are stress changes due to relaxation and deformation increment dw

respectively during time increment dt.

The stress relaxation within time increment dt is assumed to be given by

$$d\sigma^R=(\sigma_i-\alpha\sigma_i^0)(\exp(-dt/\tau)-1) \tag{2}$$

where α is a constant, σ^0_i is the stress corresponding to w_i in the static σ-w curve, and τ is relaxation time.

The stress change $d\sigma^I$ is proposed as:

$$\begin{aligned} d\sigma^I&=F*(w_{i+1}-w_i) && w_{i+1}\le w_B \\ d\sigma^I&=F*(w_B-w_i)+F^0*(w_{i+1}-w_B) && w_{i+1}>w_B \end{aligned} \tag{3}$$

where

$$\begin{aligned} F &= F_{AB}(1+\exp(-dt/\tau))/2 \\ F_{AB}&=\frac{\sigma_A}{w_i}=\frac{\sigma_i+d\sigma^R}{w_i} \\ F^0 &=\frac{\partial\sigma^0}{\partial w}(w_B) \end{aligned} \tag{4}$$

and $\sigma^0(w)$ represents the static σ-w curve.

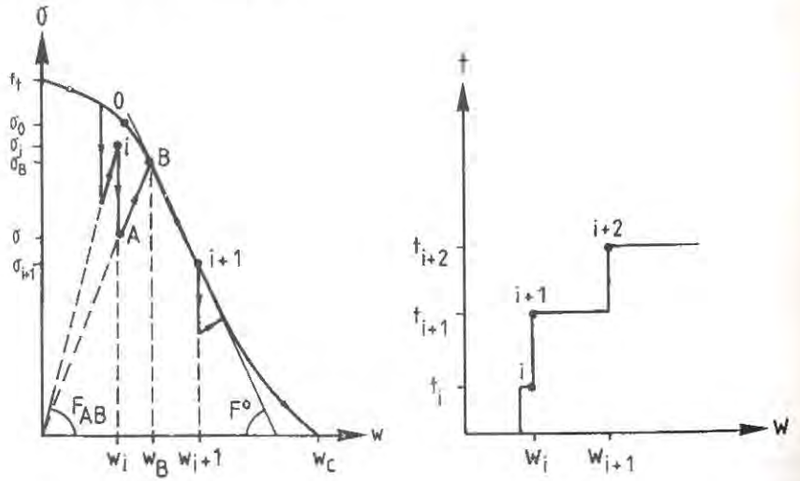

Figure 2. Schematic illustration of the proposed model.

According to this model, the σ-w curve depends on the deformation rate. The stress-transferring capacity in the fracture process zone decreases as the rate becomes slower.

CREEP FRACTURE ANALYSIS OF NOTCHED BEAMS

The proposed model was applied to analyzing crack growth and failure in plain concrete beams subjected to sustained loading. A number of tests was performed to verify the theoretical analysis. The dimensions of the beams are shown in Figure 3. The material properties used in the numerical analysis were: tensile strength f_t=2.8 MPa, modulus of elasticity E=36 GPa, fracture energy G_F=82 Nm/m², relaxation time τ=25 s, α=0.7.

The following computation procedures are carried out in each numerical simulation. First, a static FCM calculation is performed until the prescribed sustained load is reached. Then creep fracture analysis starts. In each time increment, relaxation stresses according to Equation 2 are evaluated in the fracture zone and a pseudo load calculated from the stresses is imposed on the beam, and deformation increments can be calculated. The calculation continues up to the failure point, where no equilibrium can be maintained in the sustained load. In a test the specimen will fail. In numerical analysis it is possible to carry out a static calculation until the load is about zero, if the deformation is controlled instead of the load.

Figure 3 shows the theoretical Load-CMOD curves both in static and sustained loads. In sustained loads the failure will occur when CMOD approaches the point in the descending part of the static Load-CMOD curve. In other words, the descending part of the static Load-CMOD curve serves as a failure criterion for creep fracture. Note that the curves are not smooth because a coarse mesh was chosen in the fracture zone (10 FCM element in a 50 mm long zone).

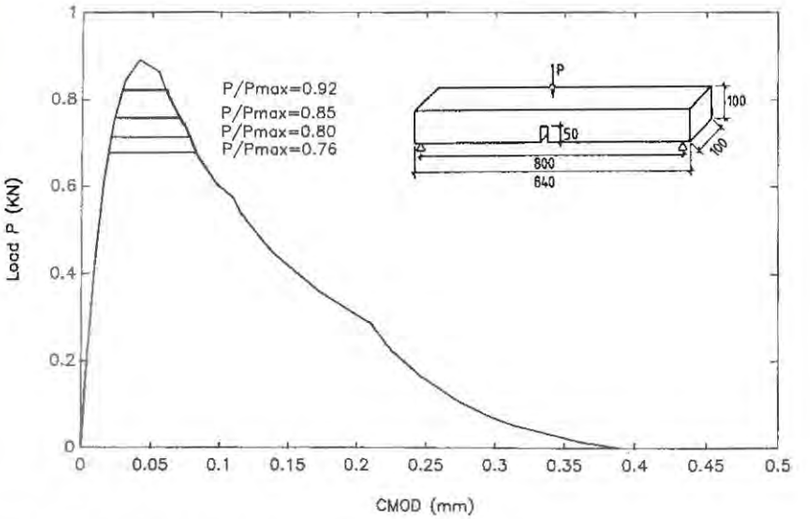

Figure 3. Theoretical Load-CMOD curves in static and sustained bending loads.

The simulated CMOD-time curve is compared with the experimental result in Figure 4. The creep curve seems to be simulated reasonably well. In Figure 5, the propagation of the fictitious crack tip is plotted.

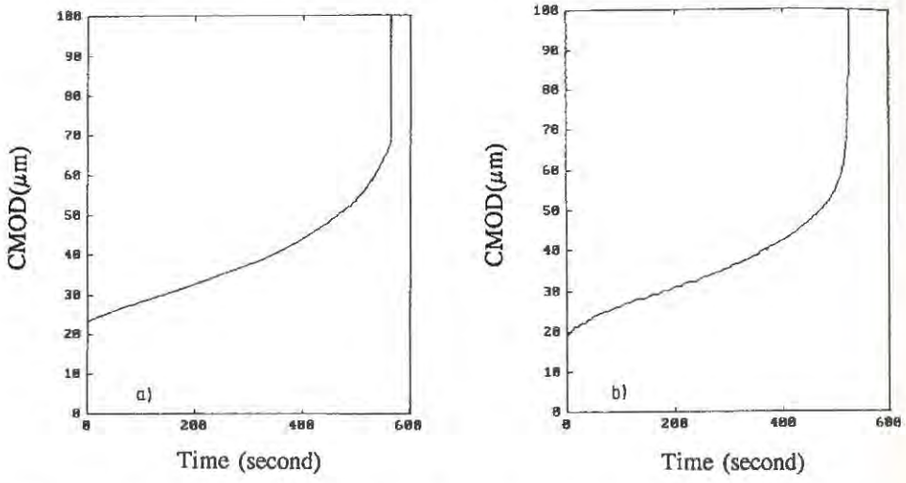

Figure 4. Theoretical (a) and experimental (b) creep curves in sustained bending on notched beams. The sustained load level $\sigma_{net}/f_{net}=0.85$, notch ratio $a_0/h=0.5$.

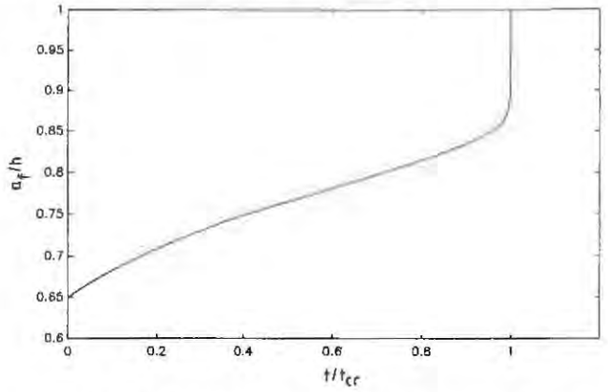

Figure 5. Propagation of the fracture process zone in a sustained bending. The sustained load level σ_{net}/f_{net} = 0.80, notch ratio $a_0/h=0.5$, a_f=total crack length, h=height.

The failure lifetime is plotted with the stress-strength level in a double logarithm in Figure 6. The lifetime increases with decreasing stress-strength level.

A theoretical analysis of size effects on creep fracture behaviour has also be made. For small beams the failure lifetime is solely determined by stress-strength level. For larger beams the failure lifetime also depends on the size.

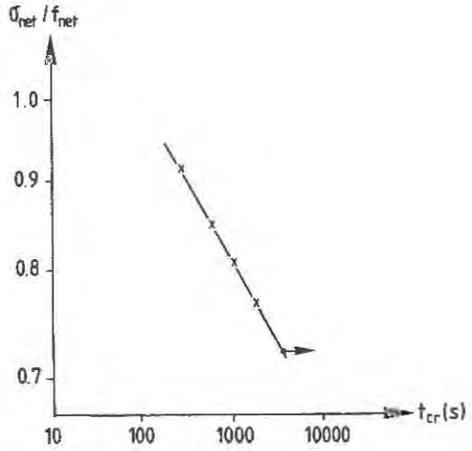

Figure 6. Theoretical stress-failure lifetime curve in sustained bending.

CONCLUSIONS

From the analysis presented above, the following conclusions may be drawn:

(1) The proposed model seems to be able to predict crack growth and fracture in plain concrete members subjected to sustained loading.

(2) Concerning the creep curve, the numerical result seems to resemble the experimental curve. The propagation of the fracture process zone in a beam in sustained loading can be numerically simulated.

(3) The theoretical analysis predicts that the descending part of static load-CMOD curve serves as a criterion for creep fracture.

(4) Size effect on creep fracture is indicated according to the model; the failure lifetime is longer for larger specimens even in the same stress-strength level.

REFERENCES

1. Bazant, Z.P. & Chern, J.-C., Strain softening with creep and exponential algorithm. J. Eng. Mesh. Div., ASCE, 1985, 111, pp.391-415.

2. Hillerborg, A., Reliance upon concrete tensile strength. In Structural Concrete. IABSE Colloquium, Stuttgart 1991, pp. 589-604.

3. Zhou, F.P., Time-dependent crack growth and fracture in concrete. Doctoral Thesis (in preparation), Div. of Building Materials, Lund Institute of Technology, Sweden.

4. Hassanzadeh, M., Hillerborg, A. & Zhou, F.P., Tests of material properties in mixed mode I and II. In Fracture of Concrete and Rock, proceedings of SEM-RILEM Int. Conf., Houston, June 1987, eds. S.P. Shah and S.E. Swartz, Springer-Verlag, NY(1989), pp. 353-358.

SIMULATION OF CYCLING BOND-SLIP BEHAVIOR

Joško Ožbolt and Rolf Eligehausen
Institut für Werkstoffe im Bauwesen, Stuttgart University, Germany.

ABSTRACT

In the present paper results of a numerical analysis for a deformed steel bar embedded in a concrete cylinder and pulled out by monotonic and cyclic loading are shown and discussed. The analysis is performed by the use of axisymmetric finite elements and an improved 3D general microplane model for concrete. Instead of the classical interface element approach, a more general approach with spatial discretization modeling the ribs of a deformed steel bar is employed. The pull-out failure mechanism is analyzed. Comparison between numerical results and test results indicate good agreement. The present approach is able to correctly predict the monotonic as well as cyclic behavior including friction and degradation of pull-out resistance due to the previous damage.

INTRODUCTION

In several experimental investigations the behavior of deformed bars under cycling excitations has been studied [1]. It has been found, that reversed cycling causes a degradation of the bond resistance and significant pinching. Some explanation for this behavior has been offered. However, the reason of the bond degradation and the development of cracks in the concrete during reversed cycling loading have not been fully understood. In recently published numerical studies of the bond-slip behavior, the analysis is usually carried out by the use of macroscopic bond-slip relations that is implemented in the finite element code employing interface elements (e.g. [2]). However, in order to better understand the mechanism of the bond-slip behavior in monotonic and cyclic loading it is necessary to perform spatial finite element discretization with an exact modeling of the ribs of the deformed steel bar. In the analysis a realistic material model must be used that is able to describe the behavior of concrete in complicated stress-strain states where large compressive, tensile and shear stresses are present in a small volume of the material. Therefore, in the present study a nonlinear finite element analysis of a deformed steel bar embedded

in a concrete cylinder and loaded by monotonic and cyclic loading has been performed which fulfils the above requirements.

MATERIAL MODEL AND FINITE ELEMENT ANALYSIS

Material Model

In the present study the general three-dimensional microplane model for concrete is used. In the microplane model the material properties are characterized separately on planes of various orientations within the material, called microplanes, on which there are only a few stress and strain components and no tensorial invariance requirements need to be observed. The tensorial invariance restrictions are satisfied automatically since the microplanes to some extent directly simulate the response on various weak planes in the material (interparticle contact planes, interfaces, planes of microcracks, etc.). The constitutive properties are entirely characterized by a relation between the stress and strain components on each microplane, both normal and shear directions. The model and its implementation into a 3D finite element code is described in [3] and [4]. In that version of the microplane model microplane shear stress-strain relations are the same and mutually independent for positive and negative shear deformations. This is sufficient in the case of monotonic loading. However, from the bond cycling experimental evidence [1], it is well known that a loading in one direction causing damage introduces a stiffness and strength degradation in the opposite loading direction. Due to this the microplane shear stress-strain law is here modified in a way that the microplane shear stiffness is multiplied by the damage function:

$$\omega = exp[-1.2(E/E_0)^{1.1}] \tag{1}$$

where E represents accumulated microplane shear energy dissipation and E_0 is a constant representing the area under the monotonic (undamaged) microplane shear stress-strain curve. Eq. 1 has been proposed in [1] and is based on a large number of cyclic bond test data. Except this improvement the basic microplane cyclic rules, in normal and shear directions, are the same as shown in [4].

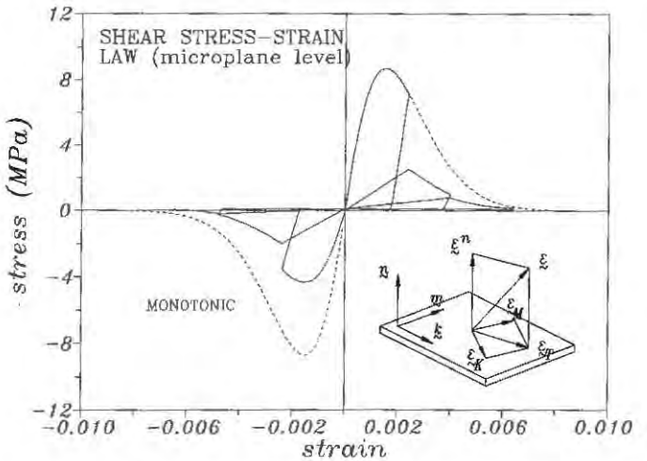

Figure 1. Shear stress-strain law on the microplane level

Using the shear stress-strain law introduced in [4] and the shear damage function (Eq. 1) a typical shear stress-strain relation on the microplane level is plotted in Fig. 1. The macroscopical shear response of the microplane model is shown in Fig. 2 where only one axisymmetric finite element is loaded by displacement control between two (positive and negative) displacement limits. As can be seen from Fig. 2, the shear resistance is decreasing with increasing number of cycles.

Note that according to Fig. 1 the shear strength at large deformations should tend to zero. This corresponds to a shear response on the microplane under the assumption that the normal stress on the microplane is zero. However, generally normal stresses are present and in the microplane model [4] the interaction between shear and normal (compressive) stresses is taken into account, i.e. with increasing normal compressive stresses the shear resistance is increasing.

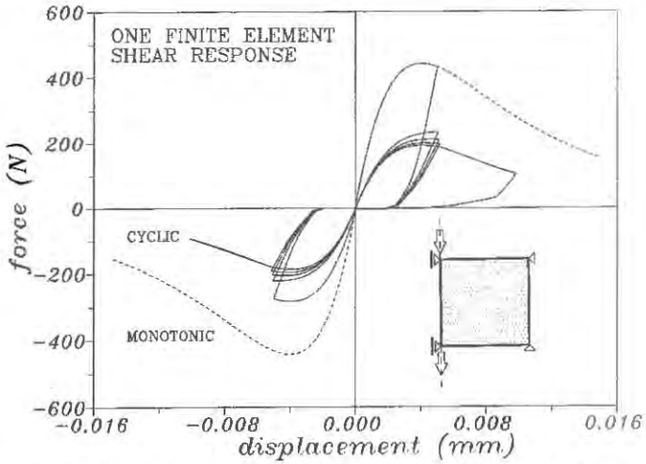

Figure 2. Shear stress-strain law on the level of one finite element

Finite Element Analysis

The geometry of the specimen employed in the present example is based on the geometry of the test specimen that has been used in [4]. The diameter of the concrete cylinder is 200 mm and the length 189 mm. The diameter of the deformed steel bar is d =25.2 mm, the height of the ribs a= 1.7 mm, the rib distance c= 13.4 mm and the embedment length l =5d. In order to avoid vertical splitting, reinforcement has been introduced as lateral confinement. The specimen is designed such that the failure is due to pull-out rather than yielding of the steel bar or splitting of the concrete. For comparison a specimen without confining reinforcement was also analyzed. The geometry (one half) and the axisymmetric finite element mesh are shown in Fig. 3. As can be seen from Fig. 3 the shape of the deformed steel bar is exactly modeled and displacement compatibility between ribs and concrete is assumed. In the analysis axisymmetric four node finite elements with four integration points are used.

The basic material parameters, Young's modulus and Poisson's ratio, are taken as E= 25000 MPa and ν= 0.18. The microplane model material parameters [4] are chosen such that the tensile and compressive concrete strength are f_t= 1.9 MPa and f_c= 28.0 MPa.

The behavior of the steel bar is assumed to be linear elastic. The analysis is based on the local continuum approach.

The specimen is loaded (monotonic and cyclic) by controlling the displacement at the top of the steel bar. The bottom or the upper side of the concrete cylinder are supported as in the test depending on the pull-out direction such that the support reactions are compressive forces. As a consequence the boundary conditions are not fixed during the cyclic analysis. In the analysis the loading type (monotonic and cyclic), the amount of confining reinforcement (none or strong) and the peak values of slip between reversed cycling were varied.

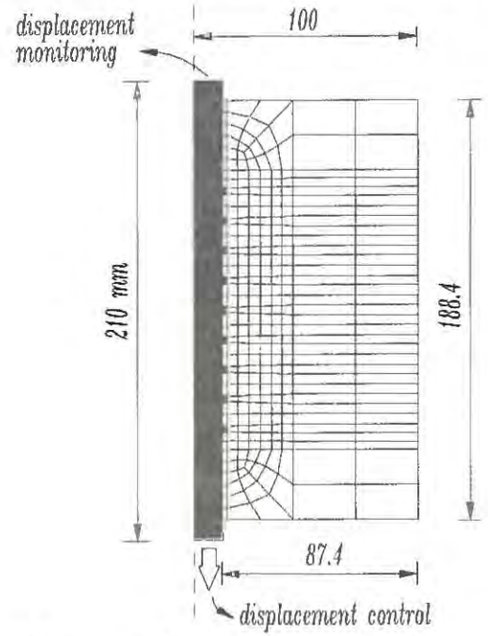

Figure 3. Geometry of the specimen and finite element mesh

RESULTS OF THE ANALYSIS

In Fig. 4 load-displacement curves for monotonic and cycling loading are plotted. The displacement is monitored at the unloaded end of the steel bar. Cyclic loading is performed by controlling the displacement (slip) at one side of the bar between two fixed and equal positive and negative values. The chosen value is slightly larger than the displacement at peak load under monotonic loading.

The shape of the load-displacement curve for monotonic loading as well as the value of the peak load (bond strength $\tau \sim 15$ N/mm^2) is in good agreement with experimental observations [1]. However, the total displacement at peak load is much smaller than measured in tests. There are several reasons for this such as: (a) The problem of an exact modeling of the concrete behavior for a stress-strain state with large volume dilatancy and high axial and lateral compression and shear stresses in a small concrete volume under the ribs, (b) while in the analysis geometrical linearity (small deformations and small

displacements) was assumed – in reality large deformations occur and (c) axisymmetric approximation of the problem.

Fig. 4 clearly indicates a decrease of the pull-out capacity as well as significant decrease of the shear stiffness with an increase of the number of cycles. As shown in [1] this is a consequence of accumulated damage. When increasing the slip to large values, the bond resistance is about constant. That is due to the fact that in the material model the interaction between normal and shear stresses, as mentioned above, is introduced on the microplane level. As a consequence, the macroscopical response at large shear deformations yields a residual force that represents friction. In the present example the friction is activated since strong lateral confinement prevents volume dilatancy in radial direction and causes compression stresses in the damage zone. Fig. 4 shows that the frictional resistance is decreased by cycling loading. Except for the magnitude of the slip, the calculated cyclic bond behavior agrees rather well with the behavior found in experiments [1].

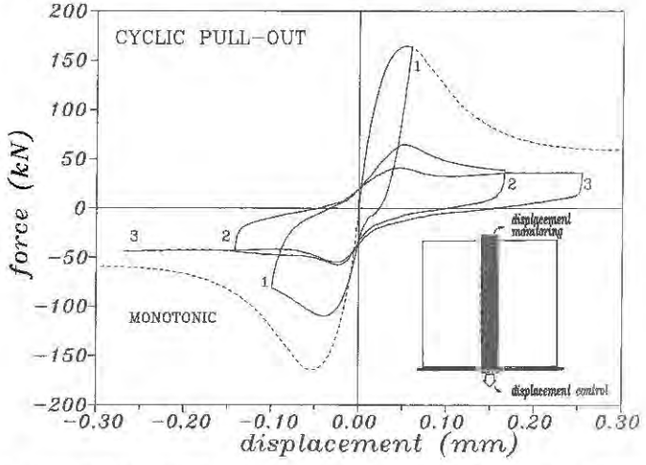

Figure 4. Pull-out load-slip relationship obtained in the finite element analysis

In order to understand the failure mechanism the stress-strain states under the bar ribs are analyzed at different load stages. Here, only a brief description of the mechanism is given.

At monotonic loading the nonlinearity starts at approx. 30% of the peak load caused by bond cracks that initiate at the ribs and propagate at an angle of approx. 65^0 measured from the bar axis. The next nonlinearity appears at approx. 60% of the peak load caused by splitting cracks which activate the reinforcement. As a consequence of the lateral confinement a further load increase is possible and significant compression stresses are developed under the ribs in axial and radial direction causing large displacements and a significant non-linear behavior. Failure is caused by shear cracks in the concrete under the ribs. Peak load, displacement at peak load as well as descending part of the load-displacement curve, for the same specimen geometry, strongly depend on the lateral confinement.

In the case of reversed cycling loading basically the same mechanism is active except

that the pull-out capacity in the reverced direction is reduced due to accumulated damage that was introduced in the concrete volume under the ribs during loading in the first direction. If cyclic loading is done between slips smaller than the peak value under monotonic loading, no significant damage is introduced in the concrete and the bond resistance is not much reduced by a few cycles. However, unloading from about peak load or after the peak has been passed causes a larger drop of the bond resistance in the reversed direction since a relatively large volume of the concrete under the ribs has been damaged. In this case only a few cycles cause complete damage reducing the pull-out resistance to friction only.

CONCLUSIONS

1. Comparison between experimental results and the results of the numerical analysis indicate that the present approach, based on the microplane model for concrete and the exact modeling of the shape of deformed reinforcing bars can in principle predict the behavior and the failure mechanism under monotonic and reversed cyclic loading in spite of the complicated stress-strain situations in the concrete close to the ribs (high compression and large volume dilatancy, large tensile and shear deformations). However, the computed slip values at peak load are much smaller than obtained in tests.

2. Bond failure in confined concrete specimen is due to the shear failure of the concrete under the ribs. In monotonic loading most of the nonlinearity up to peak load is due to concrete compression and shear deformations under the bar ribs. Reversed cyclic loading significantly decreases the shear capacity if first unloading is done from a bond stress that is larger than about 60 to 80 % of the monotonic bond strength or from the softening range. The numerical analysis indicates that the pull-out response strongly depends on the lateral confinement.

3. Further 3D finite element analyses are needed in order to investigate the influence of lateral confinement as well as the influence of the loading history and different geometrical shapes on the bond failure mechanism.

REFERENCES

1. Eligehausen, R., Popov, E.P. and Bertero, V.V., Local bond stress-slip relationships of deformed bars under generalized excitations. Report No. UCB/EERC-83/23, Earthquake Engineering Research Center, College of Engineering, University of California, Berkeley, California, October, 1983.

2. Rots, J.G., Computational modeling of concrete fracture. Dissertation, Civil Engineering Department of Delft University of Technology, september, 1988.

3. Bažant, Z.P., and Ožbolt, J., Nonlocal microplane model for fracture, damage, and size effect in structures. Journal of Engineering Mechanics, ASCE, 1990, 116(**11**), 2485-2504.

4. Ožbolt, J. and Bažant, Z.P., General microplane model for concrete. Journal of Engineering Mechanics, ASCE, 1992, in press.

R-CURVE MODELING OF RATE EFFECT IN STATIC FRACTURE AND ITS INTERFERENCE WITH SIZE EFFECT

ZDENĚK P. BAŽANT AND MILAN JIRÁSEK
Department of Civil Engineering, Northwestern University
Evanston, Illinois 60208, USA

ABSTRACT

The equivalent linear elastic fracture model based on an R-curve is generalized to describe both the rate effect and size effect. The crack propagation velocity is assumed to depend on the ratio of the stress intensity factor to its critical value from the R-curve, or on the difference of the stress intensity factor from this critical value. These dependencies can be assumed as power functions with an exponent much larger than 1. The shape of the R-curve is determined as the envelope of the fracture equilibrium curves corresponding to the maximum load values for geometrically similar specimens of different sizes. The creep in the bulk of a concrete specimen must be taken into account in the case of static loading, which is done by replacing the elastic constants with a linear viscoelastic operator in time. The model fits the existing data on concrete (as well as rock) reasonably well. It shows not only the effects of size and rate, but also, for concrete, an increase of brittleness with a decrease of loading rate, manifested as a shift of the maximum load points in the size effect plot toward linear elastic fracture mechanics (LEFM).

INTRODUCTION AND BASIC RELATIONS

The effect of loading rate on concrete strength and fracture properties has been studied intensely (e.g., [1]–[11]), however, only in the context of dynamic fracture. The problem is equally interesting for static fracture with loading durations ranging from 1 s to many years. The question is whether the trends known in dynamic fracture continue, and a further unknown is the effect of creep, which may be expected to be pronounced and must obviously be taken into account. A complicating feature for concrete is that the fracture model must be nonlinear and must reflect the experimentally observed size

effect, which exists at widely different rates of loading but differs from one loading rate magnitude to another. Experimental results of increasing scope have been obtained ([12]–[17]). The basic idea of generalizing the R-curve approach to take into account the size effect and rate effect including creep, was briefly outlined in ([14],[15]). The purpose of this paper is to refine this formulation and present results showing that it can indeed describe the experimentally observed behavior.

To analyze the response of specimens under a controlled rate r of the crack mouth opening displacement (CMOD) Δ, one needs the following relations from linear elastic fracture mechanics (LEFM): $\Delta = P\delta(\alpha)/Eb, K = Pk(\alpha)/b\sqrt{d}$, in which P = applied load, E = elastic modulus, b = specimen thickness, d = characteristic dimension (taken here as the beam depth), $\alpha = a/d, a$ = crack length and δ, k = functions that are known from LEFM. The classical rate-independent R-curve concept of fracture propagation is based on the assumption that the critical energy release rate R depends on the crack propagation length $c = a - a_0$, where a_0 = initial crack (notch) length. The corresponding critical stress intensity factor is $K_R(c) = \sqrt{ER(c)}$.

It has been shown that the R-curve can be completely determined from the size effect on the measured maximum loads of geometrically similar specimens of different sizes. The procedure given in ([18],[19]) yields a function ρ such that $R(c) = G_f\rho(c/c_f), K_R(c) = K_f\sqrt{\rho(c/c_f)}$, where G_f, K_f and c_f is fracture energy, fracture toughness and effective process zone length for an infinitely large specimen, which are geometry (shape) independent constants.

EQUATIONS MODELING THE RATE EFFECT

One process causing the rate effect is the fact that the crack growth rate is always finite and depends on the stress intensity factor K, as may be justified by considering the rate process theory for interatomic or intermolecular bond ruptures based on the concept of activation energy and Maxwell-Boltzmann distribution of thermal energies. Such considerations suggest that the crack growth rate should be expressed as $\dot{a} = \kappa_0 K^n \exp(-Q/RT)$, in which κ_0, n = constants, Q = activation energy, R = gas constant and T = absolute temperature. Since we do not study the temperature effect, this reduces to $\dot{a} = \kappa_0 K^n$. This relation may be applicable only to materials with a very small fracture process zone, and must therefore be generalized, which can be done using the R-curve concept. The following generalizations seem plausible:

$$\dot{a} = \kappa(K/K_R)^n \tag{1}$$

$$\dot{a} = \kappa[(K - K_R)/K_f]^n \quad (\text{for} K \geq K_R) \tag{2}$$

$$\dot{a} = \kappa[(K/K_R)^n - k_1]^q \quad (\text{for}(K/K_R)^n \geq k_1) \tag{3}$$

in which κ, n, q and k_1 are constants to be found empirically. So far only (1) and (2) have been explored and a study of (3) is planned.

Replacing the elastic modulus E with a corresponding compliance operator for creep, the CMOD is expressed as

$$\Delta(t) = b^{-1} \int_{t_0}^{t} J(t,t')\, d[P(t')\delta(t')] \tag{4}$$

in which t = current time, t_0 = time at the first loading and $J(t,t')$ = compliance function for creep in the bulk of the specimen, which is well known.

One very interesting observation from testing of the size effect in concrete at various rates ([12],[13],[16]) is that, in the plot of the logarithm of nominal stress versus log d, the response shifts to the right (i.e. toward the LEFM) as loading rate is getting slower. This suggests that c_f should decrease with a decreasing rate of loading, which must be described in terms of $\dot{a}$ because the material properties cannot directly depend on the loading rate. Therefore, it has been further assumed that

$$c_f = c_{f0}(\dot{a}/\dot{a}_0)^{1/m}, \tag{5}$$

in which $\dot{a}_0$ is a constant chosen for convenience and c_{f0}, m are constants to be determined empirically. This effect is, however, not seen in the tests of limestone [20], which is probably related to the fact that limestone does not exhibit creep.

The problem can be reduced to the solution of the following two coupled nonlinear integral and differential equations:

$$\dot{\alpha}(t) = d^{-1} f[b^{-1} d^{-1/2} P(t) k(\alpha(t)),\ K_f \sqrt{\rho(\alpha - \alpha_0) d / c_f}\,], \tag{6}$$

$$\int_{t_0}^{t} J(t,t')\, d[P(t')\delta(t')] = br(t - t_0), \tag{7}$$

which are to be solved for the proper initial conditions. The solution has been carried out numerically in small time steps. The values of material parameters $\kappa, n, K_f, c_{f0}, m$ have been varied in a trial and error fashion and ultimately optimized. Fig.1a shows the best fit of experimental data for limestone reported in [20], which has been obtained using the rate equation (2) with $\kappa = 60.14\,\mathrm{m\,s^{-1}}$, $n = 6$, $K_f = 818.5\,\mathrm{kN\,m^{-3/2}}$ and a constant value of $c_f = 6.4\,\mathrm{mm}$. As one can see, reasonably good fits can be obtained, which validates the present formulation.

To model the rate and size effect for concrete as reported in [16] (Fig.1b), the rate equation (1) has been used with $\kappa = 8 \cdot 10^{-6}\,\mathrm{m\,s^{-1}}$, $n = 29$ and $K_f = 900\,\mathrm{kN\,m^{-3/2}}$. The parameter c_f has been allowed to vary with varying crack propagation rate according to (5) with $c_{f0} = 14\,\mathrm{mm}$, $\dot{a}_0 = 0.01\,\mathrm{m\,s^{-1}}$, $m = 17$, in order to get a shift of the size effect plot towards LEFM for slow loading rates (Fig.2b). However, the experimentally observed shift of brittleness (Fig.2a) seems to be too strong to be exactly reproduced by the present numerical model. A further experimental study on the physical nature of this interesting phenomenon is needed.

It may be concluded that the R-curve concept, if generalized for the crack propagation rate effect and creep in the specimen bulk, can give a good description of both the observed size effects and rate effects in concrete (as well as limestone). It is a simple model of this complex phenomenon, which would lend itself easily to practical applications.

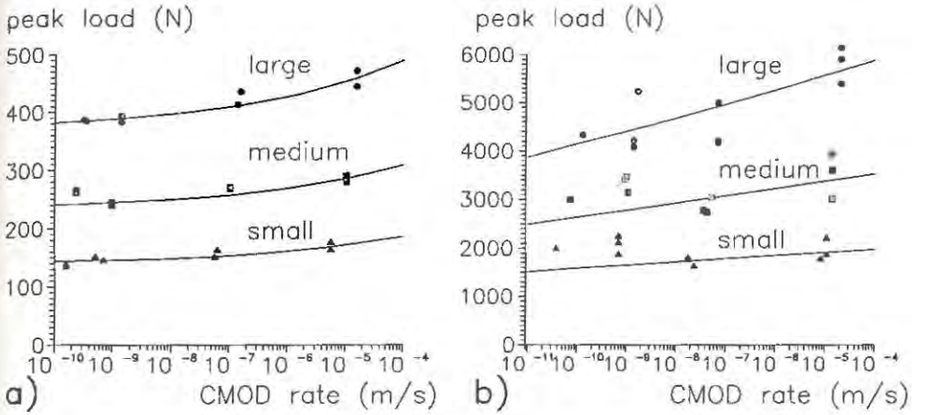

Figure 1: Rate effect for a) limestone, b) concrete.

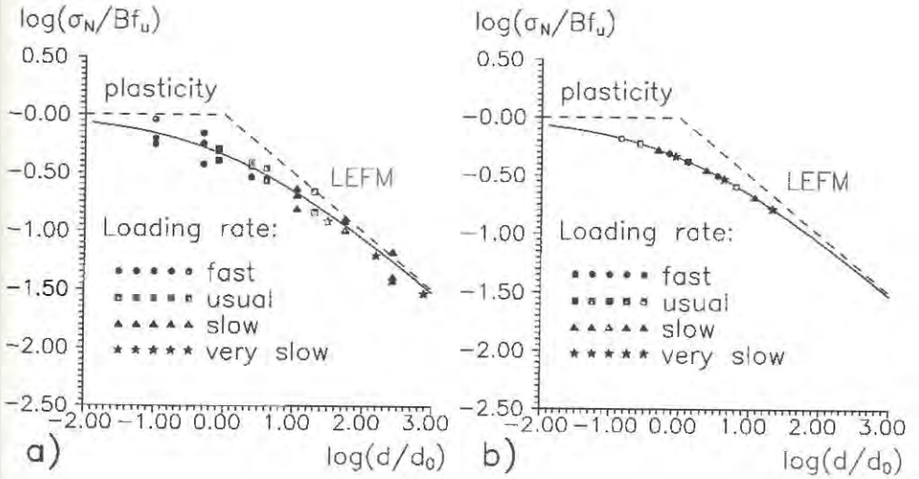

Figure 2: Size effect for concrete: a) experiments, b) theory.

AKNOWLEDGMENT.—Partial financial support obtained for the writing of this paper under AFOSR Grant 912-0140 to Northwestern University is gratefully acknowledged.

REFERENCES

1. Darwin, D., and Attiogbe, E. K., Effects of loading rate on cracking of cement paste in compression. In *Cement Based Composites: Strain Rate Effects on Fracture*, eds. S. Mindess and S. P. Shah, Materials Research Society, Pittsburgh, 1986, pp. 167-180.
2. Hughes, B. P., and Watson, A. J., Compressive strength and ultimate strain of concrete under impact loading. *Mag. Concr. Res.*, 1978, 30, 189-199.
3. Harsh, S., Shen, Z. and Darwin, D., Strain-rate sensitive behavior of cement paste and mortar in compression. *ACI Mater. J.*, 1990, 87, 508-516.
4. Liu, Z.-G., Swartz, S. E., Hu, K. K. and Kan, Y.-C., Time-dependent response and fracture of plain concrete beams. In *Fracture of Concrete and Rock: Recent Developments*, eds. S. P. Shah, S. E. Swartz and B. Barr, Elsevier Applied Science, London, 1989, pp. 577-586.
5. Mindess, S., Rate of loading effects on the fracture of cementitious materials. In *Application of Fracture Mechanics to Cementitious Composites*, ed. S. P. Shah, Martinus Nijhoff Publ., Dordrecht, 1985, pp. 617-638.
6. Reinhardt, H. W., Tensile fracture of concrete at high rates of loading. In *Application of Fracture Mechanics to Cementitious Composites*, ed. S. P. Shah, Martinus Nijhoff Publ., Dordrecht, 1985, pp. 559-592.
7. Reinhardt, H. W., Strain rate effects on the tensile strength of concrete as predicted by thermodynamic and fracture mechanics models. In *Cement-Based Composites: Strain Rate Effects on Fracture*, eds. S. Mindess and S. P. Shah, Materials Research Society, Pittsburgh, 1986, 1-14.
8. Ross, C. A. and Kuennen, S. T., Fracture of concrete at high strain-rates. In *Fracture of Concrete and Rock: Recent Developments*, eds. S. P.Shah, S. E. Swartz and B. Barr, Elsevier Applied Science, London, 1989, pp. 152-161.
9. Shah, S. P. and Chandra, S., Fracture of concrete subjected to cyclic and sustained loading. *ACI J.*, 1970, 67, 816-825.
10. Wittmann, F. H., Influence of Time on Crack Formation and Failure of Concrete. In *Application of Fracture Mechanics to Cementitious Composites*, ed. S. P. Shah, Martinus Nijhoff Publ., Dordrecht, 1985, pp. 593-616.
11. Wittmann, F. H. and Zaitsev, Y., Behavior of hardened cement paste and concrete under high sustained load. In: *Mechanical Behavior of Materials*, Proc. of 1971 Int. Conf., Soc. of Mat. Sci., Japan, 1972, 84-95.
12. Bažant Z. P. and Gettu, R., Determination of nonlinear fracture characteristics and time dependence from size effect. In *Fracture of Concrete and Rock: Recent Developments*, eds. S. P.Shah, S. E. Swartz and B. Barr, Elsevier Applied Science, London, 1989, pp. 152-161.
13. Bažant, Z. P. and Gettu, R., Size effect in concrete structures and influence of loading rates. In *Serviceability and Durability of Construction Materials*, ed. B. A. Suprenant, ASCE, Denver, 1990, pp. 1113–1123.
14. Bažant, Z. P., Rate effect, size effect and nonlocal concepts for fracture of concrete and other quasi-brittle materials. In *Toughening Mechanisms in Quasi-brittle Materials*, ed. S. P. Shah, Kluwer Academic Publ., Netherlands, 1990, pp. 131–153.
15. Bažant, Z. P., Size effects on fracture and localization: aperçu of recent advances and their extension to simultaneous fatigue and rate sensitivity. In *Fracture Processes in Concrete, Rock and Ceramics*, ed. J.G.M. van Mier, Noordwijk, Netherlands, 1991.

16. Bažant, Z. P. and Gettu, R., Rate effects and load relaxation in static fracture of concrete. *ACI J.*, to appear.
17. Bažant, Z. P., He S., Plesha, M. E., Gettu, R. and Rowlands, R. E., Rate and size effects in concrete fracture: implications for dams. In *Proc. Int. Conf. on Dam Fracture*, ed. V. Saouma, Univ. of Colorado, Boulder, 1991, pp. 413-425.
18. Bažant, Z. P. and Kazemi, M. T., Determination of fracture energy, process zone length and brittleness number from size effect, with application to rock and concrete. *Int. J. of Fracture*, 1990, 44, 111-131.
19. Bažant, Gettu, R. and Kazemi, M.T., Identification of nonlinear fracture properties from size-effect tests and structural analysis based on geometry-dependent R-curves. *International Journal of Rock Mechanics and Mining Sciences*, 1991, 28, 43-51.
20. Bažant, Z. P. and Gettu, R., Effect of loading rate on static fracture of limestone. Submitted for publication.

A FRACTURE MECHANICS APPROACH TO FATIGUE OF PLAIN CONCRETE

DIRK A. HORDIJK
TNO Building and Construction Research
Lange Kleiweg 5, NL-2288 GH Rijswijk, The Netherlands

HANS W. REINHARDT
Institute for Engineering Materials, Stuttgart University
Pfaffenwaldring 4, D-7000 Stuttgart 80, Germany

ABSTRACT

In order to better understand the behaviour of concrete and concrete structures, nonlinear fracture mechanics is more and more being applied. In this paper it is used to learn more about the possible cause and mechanism of fatigue of concrete. With a description of the post-peak cyclic behaviour of concrete, crack growth in a four-point bending specimen under repeated loading was studied. A multi-layer model was applied for the numerical analyses. The results, like cyclic creep curves and S-N curves, showed good resemblance with results that are usually found in fatigue experiments. So far only low cycle high amplitude fatigue could be studied.

INTRODUCTION

In order to design safe structures, its behaviour under different types of loading should be known. For several structures repeated or fatigue loading is one of these loading types. With the increasing slenderness of concrete structures fatigue becomes more important. The knowledge about the fatigue behaviour of concrete is so far mainly limited to empirical relations, like S-N curves. There is almost no information about the cause and mechanism of fatigue of plain concrete.

The fatigue analyses in the Codes are generally based on Miner's Rule. In reality, however, fatigue of concrete deals with growing of cracks. Therefore, applying fracture mechanics looks to be the obvious means for studying concrete fatigue behaviour in more detail. Crack propagation laws based on linear elastic fracture mechanics (LEFM) are commonly applied for metals and ceramics (for instance the law by Paris and Erdogan [1]). Although, it should be remarked that these crack propagation rules are also empirical. The parameters must be obtained from experimental findings.

For normal-sized concrete structures it has been demonstrated that LEFM is not applicable. Therefore the Paris-Erdogan law is in general not valid for concrete. Bazant and Xu [2] came up with a size-adjusted Paris-Erdogan law by combining it with the size effect law, proposed by Bazant.

In this study crack growth in plain concrete is studied by first describing the behaviour in front of a crack tip and then performing numerical analyses. The basic idea was previously presented [3] and will briefly be shown here. In this paper the principal results that were obtained with a simple numerical model will be presented. For more details about the analyses, the reader is referred to [4].

MODEL

Starting point in the model is the post-peak tensile behaviour of concrete. From experiments it is known that after an unloading-reloading cycle in the post-peak region, the maximum attainable stress will not be the same as the stress at which the envelope curve was left (see Fig. 1a). This behaviour may be explained by the damage that takes place during the loading cycle.

If in a concrete structure there exists a so-called softening zone in front of a crack tip, then the above described material behaviour will result in a stress-redistribution after a loading cycle (Fig. 1b). As a result, the length of the softening zone (or crack) will increase with the number of load cycles.

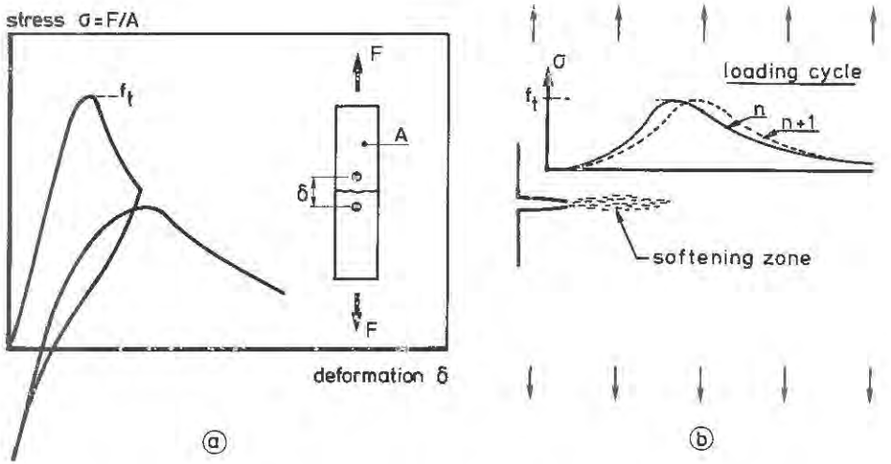

Figure 1 Post peak cyclic tensile behaviour of concrete (a) and stress redistribution after a loading cycle (b).

For studying crack growth, it is now only required to implement the post-peak cyclic tensile behaviour in a numerical programme and to simulate the behaviour of a structure under repeated loading.

Continuous-function model

Based on deformation-controlled uniaxial tensile tests a complete constitutive model for the stress-crack opening relation of concrete (continuous-function model or CFM) was previously proposed [4]. It should be remarked that so far damage is only included in loops that return to a crack opening that is larger than the crack opening at the envelope curve where the loop started. In reality damage will also occur in the so-called "inner loops".

Multi-layer model

For studying the crack growth, a four-point notched bending specimen was chosen. A number of preliminary analyses were performed with the DIANA FE-code [3]. Since the analyses were quite time consuming and fracture only occurs in a small zone, while the rest of the specimen behaves in a linear elastic way, it was chosen to apply a very simple numerical model (called: "multi-layer model").

A fictive part of the beam, encompassing the fracture zone, is replaced by springs, representing the behaviour of small-layers (Fig. 2).

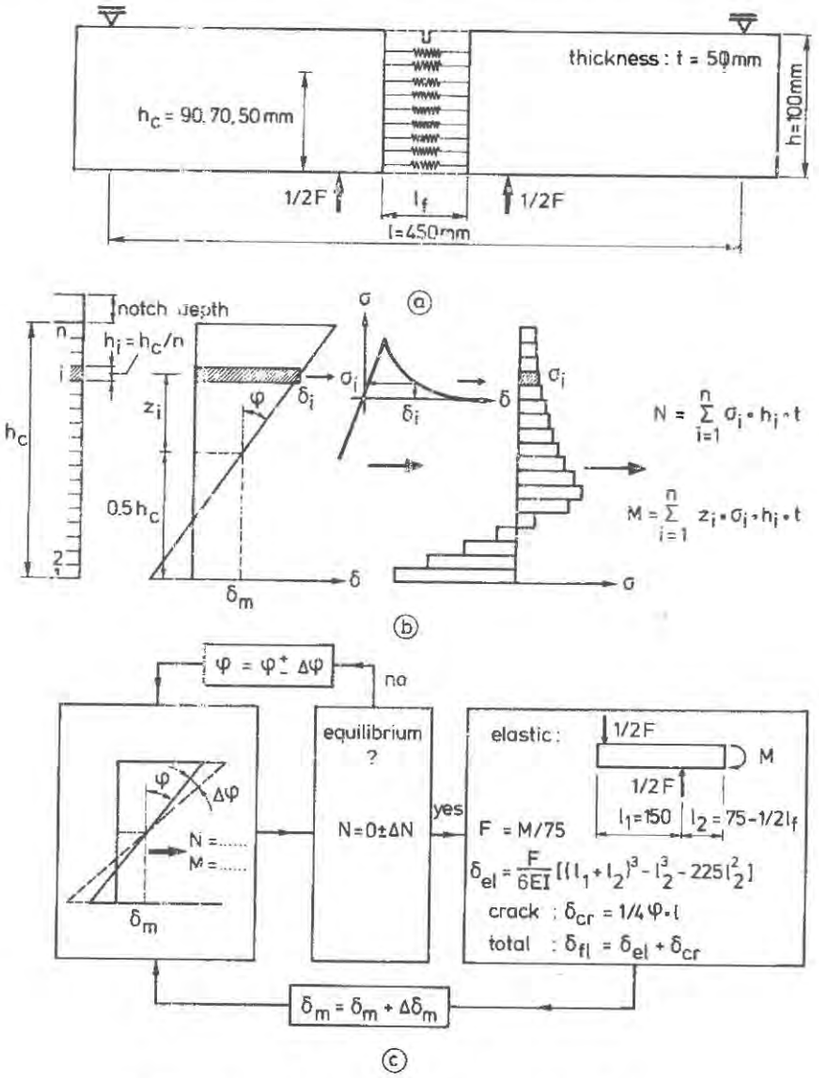

Figure 2. Principles of the multi-layer model

For simplicity, "fracture zone" will also be used to describe this part of the beam. The load-deformation (or stress-deformation) characteristic of the springs is determined by the combination of the stress-crack opening relation (CFM) and the elastic deformation over the arbitrarily chosen length of the fracture zone l_f. The main characteristic of the model is that for a deformation distribution of the fracture zone, the corresponding resulting force N and moment M are calculated (Fig. 2b). When equilibrium is found (N=0), then the internal moment M can be used to calculate the corresponding external load F and the deflection.

The results of the model are affected by the value that is chosen for the length of the fracture zone. Nevertheless, it has been demonstrated that results of FE analyses can very well be approximated and that the model is very suitable for studying phenomena [4].

ANALYSES

With the multi-layer model a number of analyses where performed. First some characteristic results of a single analysis will be shown, whereafter the results of a number of analyses will be presented in a S-N diagram. The dimensions of the beam can be obtained from Fig. 2a. The applied notch depth h_c was 50 mm. For all the analyses the material parameters were: tensile strength is 3 MPa, Young's modulus is 38000 MPa and fracture energy is 125 J/m². l_f was taken equal to 35 mm.

Results of a specific analysis

For the structure under investigation a value of 1403.6 N was found for the peak load. For the fatigue analysis that will be discussed, a relative upper load level of 0.94 and a lower load level equal to zero was chosen. It appeared that 146 loops could be performed before the descending branch of the static test was reached. Since the analysis is performed in a deformation-controlled manner, the last loop that could be performed is directly followed by the descending branch. Three loops (1, 100 and 146 respectively) are plotted in Fig. 3.

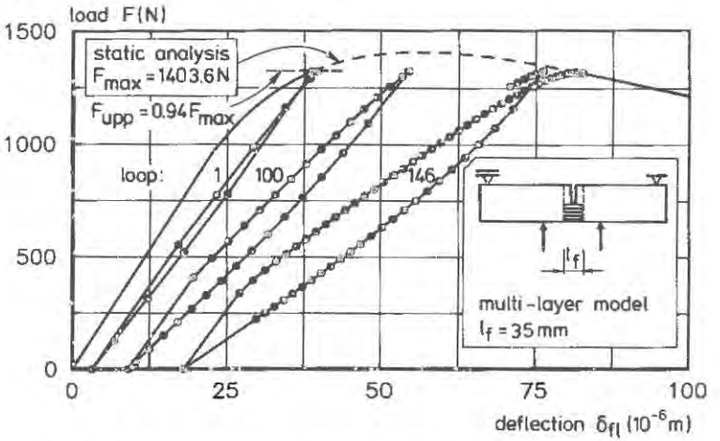

Figure 3. Load-deflection relations obtained with the multi-layer model.

The development of two different parameters versus the number of cycles is plotted in Fig. 4. It is very interesting to see that in these

curves three different stages can be observed, which is similar to results that are usually found in fatigue experiments (see among others [5]).

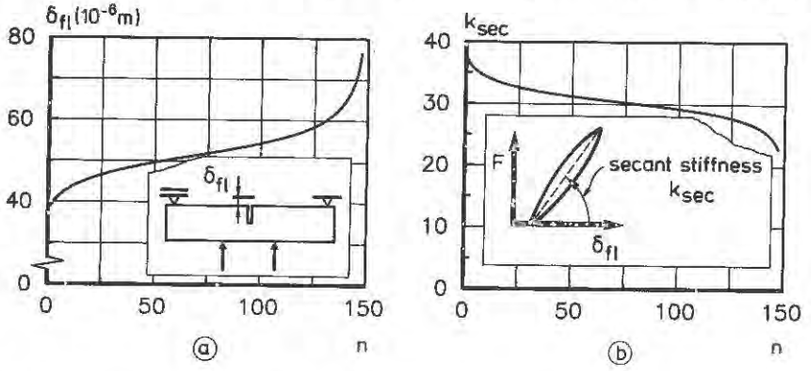

Figure 4. The variation of the deflection (a) and the secant stiffness (b) in relation to the number of cycles.

Fatigue analyses with different load levels
A number of analyses were performed with different upper and lower load levels. The results of these analyses, plotted in S-N curves, can be seen in Fig. 5.

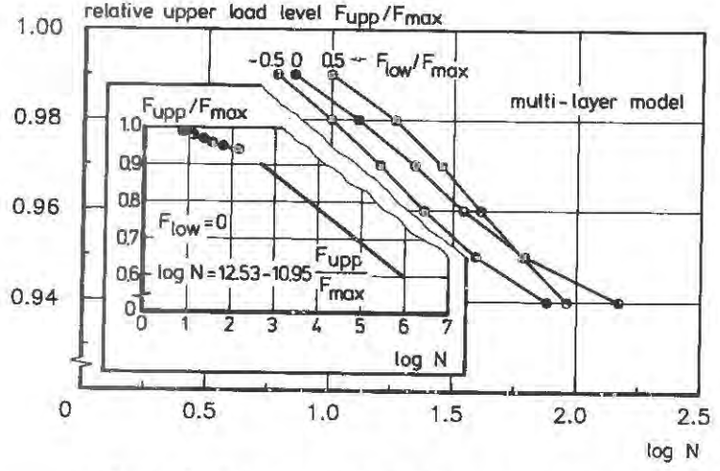

Figure 5. Fatigue results plotted as S-N curves.

First a remark will be made about inner loops. For most of the analyses the crack opening increased in every loop for every layer in the softening zone. For the smaller upper load levels inner loops were encountered. The occurrence of inner loops, in which damage is not taken into account in the continuous-function model, is probably the reason why analyses with smaller upper load levels could not be performed. In fact, after a number of load cycles in such analyses, all the layers in the

softening zone are in inner loops, which means that there will no longer be a stress redistribution after a loading cycle.

Due to the fact that the results obtained with the multi-layer model depend on the chosen value for l_f (see [4]), a direct comparison with experimental results is not possible. Despite it, see the inset in Fig. 5 for an illustration of the relation between the obtained results and experimental results. The straight line represents a regression equation of the S-N curve for flexural tension in the case of a zero lower load level [5]. The first noteworthy aspect of the obtained results is that the number of cycles plotted on a semi-logarithmic scale is almost linear, as usually observed in fatigue tests. Also the fact that the number of cycles decreases for a decreasing lower stress level corresponds with experimental results [5]. This, however, is not true for the relative upper load levels equal to 0.94 and 0.95 and the relative lower load levels equal to 0.5 and 0. The reason for this peculiar result is explained in [4].

CONCLUDING REMARKS

From the analyses the following main conclusions can be drawn:
- The multi-layer model is a suitable tool for a qualitative study of crack growth in a four-point bending specimen under repeated loading.
- In general, there is a similarity between the results of the fatigue analyses and results of fatigue experiments.
- With the CFM, only the "fatigue behaviour" for very high upper load levels could be investigated so far. For a further study of fatigue along the lines of the approach presented in this paper, it will be necessary to also incorporate damage effects in inner loops.

Finally, it can be remarked that damage, so far is only considered to be the result of a loading cycle, while time effects are totally ignored. In reality, of course, time effects will always play a role. For sustained loading tests, time effects are even the only contribution to crack growth. To the author's opinion a similar approach can be applied to study crack growth under sustained loading. In this respect, it can be mentioned that the load (or average stress) also decreases, when the deformation in the post-peak part of a deformation-controlled tensile test is kept constant. If then, after some time, the deformation is increased again, the envelope curve curve is also reached at a lower stress level.

REFERENCES

1. Paris, P.C. and Erdogan, F., A critical analysis of crack propagation laws. J. of Basic Engineering, Trans. ASME, Series D 85, pp. 528-534.

2. Bazant, Z.P. and Xu, K., Size effect in fatigue of concrete. ACI Materials Journal 4, 1991, pp. 390-398.

3 Hordijk, D.A. and Reinhardt, H.W., Growth of discrete cracks in concrete under fatigue loading. In Toughening Mechanisms in Quasi-Brittle Materials, ed. S.P. Shah, NATO ASI Series E: Applied Sciences - Vol. 195, Kluwer Acad. Publ., Dordrecht, 1991, pp. 541-554.

4. Hordijk, D.A., Local approach to fatigue of concrete. Doctoral Thesis, Delft University of Technology, Delft, 1991, 210 pp.

5. Cornelissen, H.A.W., Fatigue failure of concrete in tension. Heron 29(4), 1984, 68 pp.

A STUDY ON FATIGUE LIFE OF REINFORCED CONCRETE BEAM WITH MULTIPLE TENSION REINFORCING BARS

Nobuyuki MATSUMOTO
Chief Researcher / Concrete Structure Laboratory
Railway Technical Research Institute
2-8-38 Hikari-cho, Kokubunji-city, Tokyo, JAPAN

ABSTRACT

This paper presents an outline of fatigue tests of reinforced concrete rectangular beams with multiple tension reinforcing bars (rebars), and describes an attempt to predict the fatigue process of the rebars in beams by a statistical simulation in which fracture mechanics is applied. The proposed simulation models can successfully predict the statistical characteristics of fatigue lives of beams with multiple rebars.

INTRODUCTION

Since the early stage of the development of current bar deformations, studies on the fatigue strength of rebars have been extensively conducted. Some equations for the evaluation of rebar's fatigue strength have been adopted in design codes of several nations. These equations are mainly determined based on test results of independent rebars or beams with one or two rebars installed. However, many tensile rebars are placed in actual reinforced concrete railway bridges, so it is an interesting subject whether the bridge fatigue life is different from the fatigue lives of independent rebars and beams with one or two rebars installed or not.

In this research, the experimental and statistical assessment of the fatigue process and the distribution characteristics of fatigue lives of beams with multiple tension rebars is carried out. The fatigue process of rebars is assumed as the phenomenon of a system of parallel failure series and the linear fracture mechanics is applied to a statistical simulation analysis.

TEST METHOD AND RESULT

Fatigue tests consist of two kinds of S–N tests. In *Phase–I* of the test, "fatigue test in air," a tension fatigue test in air using 25 rebars was carried out. The fatigue strength and the distribution of fatigue life of the bars were obtained. In *Phase–II* of the test, four beam specimens, which use rebars cut from the same lot as the bars used in the fatigue test in air, were subjected to repeated loadings. Each rebar's fatigue life in a beam is measured. The properties of the rebars are shown in Table 1.

Fatigue Test in Air (Phase–I)

Test method: The *Phase–I* test was conducted at 5 different levels of stress range using the specimen with anchorages at both ends as shown in Fig. 1. The sample size for one level of stress range is 5. The loading waveform is sinusoidal and the frequency is 10 Hz.

Table 1 Rebar Properties

Manufacturer	Bar Size	Yield Point σ_y (kgf/cm²)	Tensile strength σ_u (kgf/cm²)	Elongation ϵ (%)	Chemical Contents in percent (from Mill Sheet)				
					C	*Si*	*Mn*	*P*	*S*
Tokyo Tekko Co., Ltd.	D16	4,159	6,143	20	0.27	0.23	0.80	0.036	0.033

Test result: The test result is shown in Fig. 2. The runout cycle was set at five million or more. The stress ranges are computed using the magnitude of the loading forces and the nominal cross-sectional area of the bars.

Fatigue life and its distribution: The S–N curve (50 % cumulative destruction probability) obtained by the method of least squares using only the failed data (n=17) is given as follows:

$$\log N = 20.13 - 4.188 \cdot \log S_r \quad \ldots (1)$$

In order to test the distribution characteristics of fatigue life from the test result, it was evaluated on a probability graph paper of the normal distribution using the *Mean rank method* of order statistics. As the sample size in each stress range is small, the residuals e_i are computed using all the failed data $N_{i(exp)}$ and mean fatigue life $N_{(cal)}$ for each stress range obtained from Eq. 1.

$$e_i = \log N_{i(exp)} - \log N_{(cal)} \quad \ldots (2)$$

The relation between e_i and cumulative probability P_e can be regarded to make a straight line, so that e_i and the logarithm of the distribution of fatigue life can be assumed to make a normal distribution. From this result, the standard deviation σ_l is obtained as 0.105 from the unbiased variance of population.

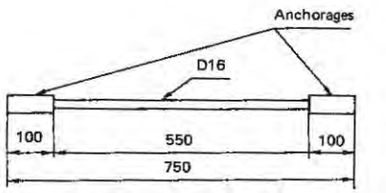

Fig. 1 Specimen for fatigue test in air (unit: mm)

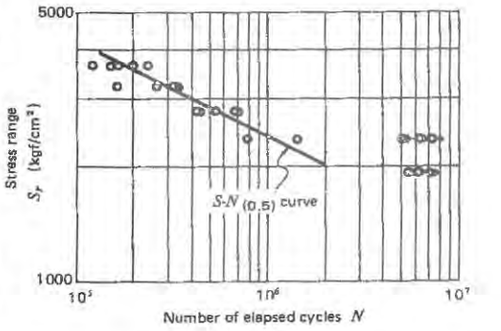

Fig. 2 S–N relation obtained from fatigue test in air

Beam Fatigue Test (Phase–II)

Test method: Beam fatigue tests were conducted using wide-width rectangular beams which have the specific dimensions as shown in Fig. 3. The tension rebars were arranged in one row. The compressive strength of concrete at the age of 28 days is 362 kgf/cm². The loading amplitude is kept constant throughout a test. However, it is varied for each specimen. The measurement was done dynamically once in a thousand cycles of loading. The number of failed cycles of each rebar was detected using a logic circuit which monitored the connecting condition of each rebar. The waveform was sinusoidal and the frequency was 3 Hz.

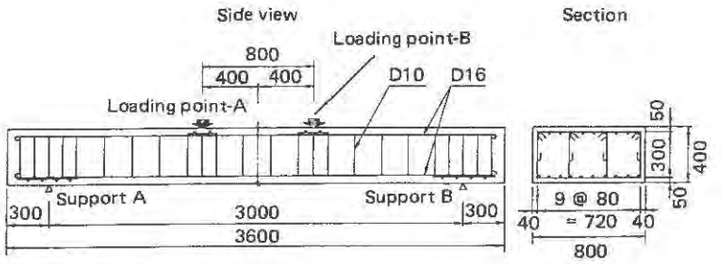

Fig. 3 Specimen for beam fatigue test (unit: mm)

Test result: An outline of the test result is shown in Table 2. Rebar stress was computed using the strain obtained with wire strain gages and *Young's modulus* of the rebars E=2.1·10^{6}kgf/cm^2. The fatigue process of the rebars is such that the weakest bar fails approximately at 60 % of the beam fatigue life N_f and the next weakest bar keeps the redundancy up to approximately 80 % of N_f. After this, it was observed that the bars failed one by one from approximately 90 % of N_f, and finally exhausted the beam fatigue life when half the embedded rebars failed by fatigue.

Table 2 Results of Beam Fatigue Test

No.	Load (t)		Bar stress (kgf/cm^2)			Weakest bar failure	Beam fatigue life
	P_{max}	P_{min}	σ_{max}	σ_{min}	S_r	N_i	N_j
1	37.0	3.0	3734	869	3337	1.63 X 10^5	2.59 X 10^5
2	35.0	3.0	3156	827	2691	2.48 X 10^5	4.19 X 10^5
3	28.0	3.0	2642	794	2122	7.47 X 10^5	1.394 X 10^6
4	25.0	3.0	2274	752	1734	6.74 X 10^6	8.710 X 10^6

Values of bar stress in the table are obtained at the initial stage

STATISTICAL SIMULATION AND DISCUSSION

In order to predict the fatigue process of the rebars in the beam, a combination of two numerical models is proposed here. The first model is a "basic model" where *Paris' law* is directly applied on each rebar. The other model is a "successive failure model" representing the parallel failure series. A statistical simulation applying these models, which may be regarded as equivalent to the fatigue test of p beams with n rebars in each beam, was performed using the *Monte–Carlo method*. The distribution characteristics of fatigue life and the "number–effect" on the beam with multiple rebars are discussed here.

Proposal of Numerical Models

Basic model: The fatigue process model for each rebar is set such that it originally contains an initial crack and its fatigue life is governed only by the fatigue crack propagation behavior of the crack. The fatigue crack propagation behavior is assumed to be governed by *Paris' law* and the criterion of bar failure is assumed to depend on the value of fracture toughness of the material. Therefore, fatigue crack growth rate per cycle of loading da/dN is denoted by the following equation.

$$da/dN = C \cdot (\Delta K)^m \qquad \ldots (3) \qquad \Delta K = S_r \cdot \sqrt{\pi a} \cdot F \qquad \ldots (4)$$

where, a: crack size, N: number of cycles, ΔK: fluctuation of stress intensity factor, C,m: constants depending on material, S_r: stress range, F: a parameter depending on the crack geometry and its position.

Then the fatigue life of a rebar N can be derived by integrating Eq. 3 and substituting a_i for the initial crack size and a_f for the critical crack size under the condition that $m \neq 2$.

$$N = \frac{1}{C \cdot (F \cdot S_r \cdot \sqrt{\pi})^m \cdot (m/2-1)} \times \left(\frac{1}{a_i^{m/2-1}} - \frac{1}{a_f^{m/2-1}} \right) \qquad \ldots (5)$$

Moreover, taking pseudo initial crack size a_i^* (=$1/a_i^{m/2-1}$), pseudo critical crack size a_f^* (=$1/a_f^{m/2-1}$) and A^*=$C \cdot (F \cdot S_r \cdot \sqrt{\pi})^m \cdot (m/2-1)$, Eq. 5 is simplified as follows:

$$N = (a_i^* - a_f^*) / A^* \qquad \ldots (6)$$

Successive failure numerical model: The successive failure model to represent the fatigue process of rebars in a beam is based on the following assumptions.

Assumption 1: A beam includes n rebars which follow the rule of the basic model. The order of failure of rebars is governed only by the initial crack sizes and their order is already known as follows.

$$a_{i(1)} > a_{i(2)} > \cdots > a_{i(k)} > \cdots > a_{i(n)} \qquad \ldots (7)$$

Assumption 2: The stress condition of each rebar is uniform. The failed bar stress redistributes equally to that of the unfailed rebars. So the stress amplitude $S_{r(k)}$ of each bar before the k–th bar's failure changes uniformly as follows. The calculation is continued even in the case when S_r becomes greater than σ_y.

Assumption 3: If the crack length $a_{(k)}$ of the $(k+1)$–th bar at the time when k–th bar failed is greater than the critical crack size $a_{f(k+1)}$ which corresponds to $S_{r(k+1)}$, $N_{(k+1)} \equiv 0$.

From a recurrence formula obtained by Eq. 6 expressing $A^*_{(k)}$ for A^* which corresponds to $S_{r(k)}$, $N_{(k)}$ is derived as follows.

$$N_{(k)} = [a_i^*{}_{(k)} - a_f^*{}_{(k)} - \{a_i^*{}_{(k-1)} - a_f^*{}_{(k-1)}\}] / A^*{}_{(k)} \qquad \ldots (8)$$

where $a_i^*{}_{(0)} - a_f^*{}_{(0)} \equiv 0$

Therefore the beam fatigue life is given by $N_f = \Sigma N_{(k)}$.

Initial crack size: In order to conduct the numerically simulated beam fatigue test in which the sample size of beams is p and the number of rebars in a beam is n, p groups of initial cracks consisting of n sets of initial cracks in a group were prepared as the input data. Therefore, taking $a_i^*{}_{(k\,j)}$ as the pseudo initial crack of the rebar k in the beam j, it is obtained from Eq. 9. The $N_{(RND)}$ in the equation is generated by the *Box and Muller method* using the statistical characteristics that the logarithm of fatigue life of rebars (*Phase–I*) follows a normal distribution (μ,σ_f). Normal random numbers of p groups of n sets are generated. Here, $N_{(RND)}$ is only treated as a variation and all of the other parameters are treated as deterministic. The value of parameters is shown in Table 3.

Table 3 Parameters Used in *Monte–Carlo* Simulation

Parameter	Value	Remarks
σ	0.105	σ_f from fatigue test in air
μ	5.693	From Eq.1 with S_r = 2,800
S_r	2,800 (kgf/cm^2)	Stress range (effect of mean stress is eliminated)
m	4.188	From fatigue test in air
F	0.8775	Correction for crack position (surface) F_1 = 1.12 Correction for crack configuration (crack length/half crack width = 0.5) F_2 = 0.7835 $F = F_1 \cdot F_2$
C	4.749 X 10^{-19}	Coefficient
n	10	Number of bars in a beam
p	10,000	Sample size

$$a_i^*{}_{(k\,j)} = N_{(RND)} \cdot A^* + a_f^* \qquad \ldots (9)$$

Critical crack size: The critical crack size a_f was obtained from Eq. 10 which gave the fracture toughness of the material, K_{Ic}. The value of fracture toughness K_{Ic} was computed using the minimum value of the *Charpy V-notch test* of *S25C-steel* (60 J/cm²), which has approximately the same carbon content as rebar, shown in *Fatigue Data Sheet*[1] and using the formula which was proposed by *Barsom et al.*[2] as shown in Eq. 11.

$$K_{Ic} = S_r \cdot \sqrt{\pi a_f} \cdot F' \quad \ldots (10)$$

$$K_{Ic}^2 / E = B \cdot CVN \quad \ldots (11)$$

where, F': parameter $F \cdot F_3$, $F_3 = \sqrt{sec(\pi a/W)}$ considering the size effect, W: width of specimen, CVN: energy absorption (kgf · cm), B:coefficient (=0.1603).

Simulated Fatigue Process and Distribution Characteristics of Fatigue Life

The distribution characteristic of rebars' fatigue lives in beams obtained from the simulation is presented for the case that the number of rebars in a beam n is 10; the sample size p is 10,000; and the stress range S_r is equal to 2,800 kgf/cm² as follows.

Distribution of the weakest bar's fatigue life: The fatigue life of the weakest rebar in beam $log\ N_{(1)}$ is obtained at the time when the rebar which has initial crack size $a_{i(1)}$ reaches the critical crack size and is shown in Fig. 4. The shape of distribution is similar to that of normal distribution but with a slight skewness to the right side. Assuming its shape as the normal distribution, the mean value, standard deviation and the maximum value of the probability density function were computed as 5.53, 0.062 and 0.40 respectively. Comparing the fatigue life of a rebar itself, a lower mean value of life and a reduction of variance are observed.

To evaluate the obtained values, they were compared with *the distribution of extremes*. Using the *Phase-I* test result for the original distribution and setting the number of sets in a group at 10, the maximum value of the probability density function of extremes became 0.36 at the variable x=5.54. The shape of the distribution of extremes is known to be similar to that of normal distribution having a skewness to the right side, so these two

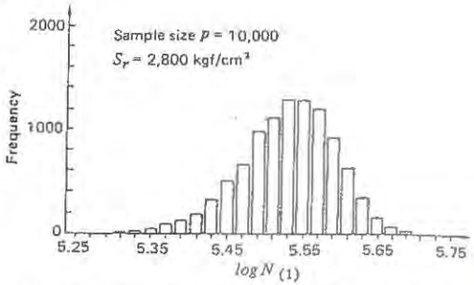

Fig. 4 Distribution of fatigue life of the weakest rebar obtained from simulation

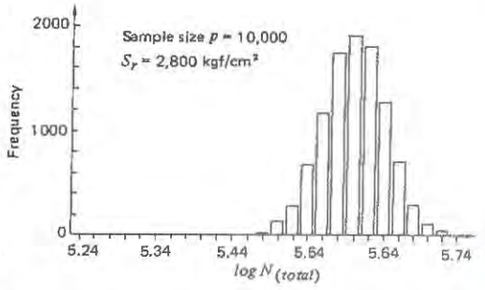

Fig. 5 Distribution of beam fatigue life obtained from simulation

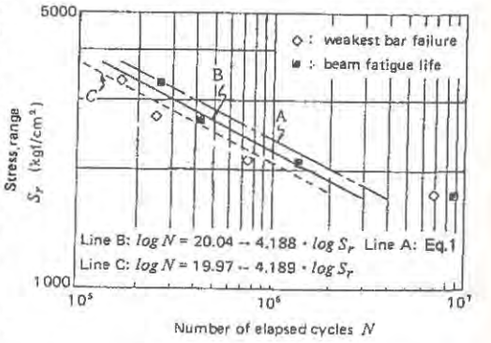

Fig. 6 Comparison with beam fatigue test

distributions seemed very close to each other and the appropriateness of the simulation may be verified.

Fatigue life of k-th failed rebar and its distribution: The mean value of the k-th failed rebar $log\ \Sigma N_{(k)}$, the range of standard deviations σ and the maximum and minimum values are computed. Differences in fatigue life up to the fifth bar's failure are observed, but little redundancy in life is seen after that. The standard deviation of each distribution tends to become gradually smaller and the distribution of fatigue life tends to converge to a symmetrical distribution.

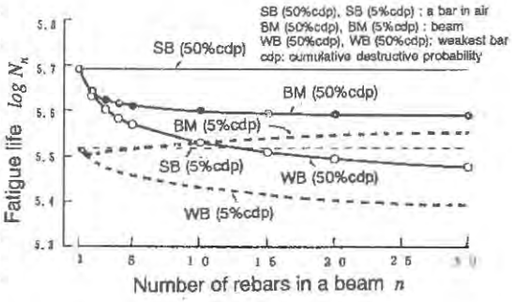

Fig. 7 Number effect on fatigue life

Distribution of the beam fatigue life: The frequency distribution of beam fatigue life, which is obtained as the fatigue life of the tenth rebar $log\ \Sigma N_{(10)}$ is shown in Fig. 5. The *Chi-square test* suggests that this distribution may be viewed as a normal distribution under the condition of the significant level of 5 %. The mean value and standard deviation are computed as 5.60 and 0.042 respectively. As compared with the *Phase-I* test result, a lower mean value of life and a reduction of variance are also observed.

Comparison of Fatigue Lives and Number Effect

S-N relation: The fatigue lives of the weakest rebar and the beam obtained from the test and the simulation on S-N diagram are shown in Fig. 6. The S-N curves of simulation are computed using mean fatigue lives corresponding to several stress ranges. The lines B and C in the figure present the simulated fatigue lives of the weakest rebar and the beam fatigue life respectively. The fatigue life of a beam with 10 rebars can be said to be shorter than that of a bar in air (shown as line A) excepting a very long fatigue life.

Number-effect: Taking S_r = 2,800 kgf/cm² as an example, the fatigue life of beam with n rebars N_n is shown in Fig. 7. The mean beam fatigue life, and the mean and 5 % cumulative destruction probability fatigue lives of the weakest rebar become shorter with an increase in the number of rebars in a beam. The 5 % cumulative destruction probability life of the beam, however, is found almost the same as that of a bar in air because the variance of beam fatigue life reduces with the number of rebars.

CONCLUSIONS

In order to understand the characteristics of fatigue life of a reinforced concrete beam with multiple tension rebars, a series of fatigue tests are conducted and a statistical numerical simulation is proposed and calculated. The knowledge obtained through this study is summarized as follows:

(1) The fatigue life of a reinforced concrete beam with multiple tension rebars is generally shorter than that of a bar tested in air. It is confirmed that there is some remaining life from the time of the weakest rebar failure to the beam fatigue life.

(2) The fatigue process of rebars in a beam can be traced by a numerical simulation model applying *Paris' law* of linear fracture mechanics. Through a statistical simulation, the general statistical characteristics of the fatigue life of rebars in a beam, and the number-effect on the fatigue life are obtained.

REFERENCES

[1] National Research Institute for Metals: *NRIM Fatigue Data Sheet No.1 Data Sheets on fatigue Properties of S25C (0.25C) Steel for Machine Structural Use*, 1978 (in Japanese).

[2] Rolfe,S.T. and Barsom,J.M.: *Fracture and Fatigue Control in Structures*, Prentice-Hall Inc., New Jersey, 1977.

Chapter 11

Environmental Effects (Temperature, Shrinkage, Corrosion)

Principal Lecture

DRYING SHRINKAGE EIGENSTRESSES AND STRUCTURAL SIZE-EFFECT

J. PLANAS and M. ELICES
Depto. de Ciencia de Materiales, Universidad Politécnica de Madrid.
ETS de Ingenieros de Caminos, Ciudad Universitaria s/n, 28040 Madrid, Spain.

ABSTRACT

This paper presents the first results of a research aimed at understanding the modifications of the behaviour of concrete structures due to shrinkage, most specially its influence on the structural strength. After defining the phenomenological framework and identifying the essential parameters, a simplified method to describe the eigenstress fields is presented and discussed and the numerical procedure, based on a cohesive crack model, is outlined. The effect of the shrinkage is numerically investigated for three point bent unnotched beams and three different softening curves. The results show that the effect of the shrinkage first increases as drying deepens, but then goes through a maximum and decreases again. This behaviour leads to the existence of upper bound and a lower bound curves for the strength. It is also shown that a Bazant size effect curve may describe very well the "average shrinkage" behaviour lying midway between the lower and upper bound curves. Finally, it is shown that the size effect curves for different softenings may be brought to lie on a "master" curve by defining an equivalent linear softening.

INTRODUCTION

Size effect in concrete structures plays a paramount role in the interpretation of laboratory experiments and in their extrapolation to full scale structures.

The size effect analyses performed to date are mostly devoted to laboratory situations, where the shrinkage eigenstresses are minimised. In practice, however, shrinkage eigenstresses may influence the size effect very much, as shown experimentally by Petersson [1].

This was theoretically analyzed by Hillerborg and co-workers for three point bending of unnotched specimens [1] and for tensile specimens [2] for a particular assumption regarding the distribution of shrinkage eigenstresses.

In their analyses, the shrinkage field was assumed to have a parabolic shape varying proportionally to size. As pointed out by Hillerborg and Petersson [1], this corresponds approximately to considering drying times proportional to the square of the structure dimension, i.e: specimens of differing sizes are tested at different times.

The aim of this paper is to present the first results regarding the modification of the size effect when the drying time is taken as an independent variable. To be specific, three point bending of an unnotched specimen subjected to symmetric in-plane drying is considered.

The parameters involved in the problem are first analyzed to show that shrinkage influences the size effect mainly through two parameters: a drying penetration length, which is proportional to the square root of drying time, and a shrinkage eigenstress intensity.

A simplified analysis of the linearized diffusion equation is next introduced to obtain approximate eigenstrain distributions, from which closed form expressions for the shrinkage eigenstresses are obtained which are the input for a numeric procedure conceptually equivalent to—although computationally different from— that used by Hillerborg's group.

Results for influence of the shrinkage penetration depth, the shrinkage severity and the kind of softening displayed by the material are presented and discussed. It is found that upper bound and lower bound curves exist for the strength, the upper bound corresponding to shrinkage free structures and the lower bound to the eigenstress distribution considered by Hillerborg and co-workers.

Moreover, it is shown that an expression of the type of Bazant's size effect law describes very well the average size effect lying midway between the upper and lower bound curves.

Finally, the influence of the shape of the softening curve of the material on the results is expounded, which shows that the softening shape does appreciably modify the strength, but also that the various size effect curves may be brought to fuse into a single master curve corresponding to an equivalent linear softening.

PHENOMENOLOGICAL FRAMEWORK

The strength of a structure depends on its size, shape and on the material properties. When dealing with size effect, we assume that the shape is fixed, so that the specimens are geometrically similar, and define the size by means of some relevant structural dimension, such as beam depth, which we denote as D.

When fracture of the material is described by a cohesive crack (or fictitious crack according to Hillerborg's denomination), the relevant material properties are the elastic parameters E and ν, the tensile strength f_t and the fracture energy G_F, together with the shape of the softening function relating the cohesive stresses to the crack opening. For a fixed softening shape, the material properties combine into a *characteristic size*, defined by Hillerborg as

$$\ell_{ch} = \frac{E\, G_F}{f_t^2} \tag{1}$$

Hillerborg was the first to realize that for these materials the structural strength must depend on the size through a function of the form

$$\sigma_{Nmax} = f_t\, F\left(\frac{D}{\ell_{ch}}\right) \tag{2}$$

where F(•) is a dimensionless function and σ_N is some nominal stress, proportional to P/BD where P is the load, D is the size and B the specimen thickness.

The above equation refers to proportional or uniparametric loadings. When non-proportional loadings are considered, as in the case of thermal or shrinkage eigenstrains, Eq. (2) must be generalized, having in mind that, in principle, the failure condition is history-dependent.

To be specific, we consider processes where drying shrinkage starts after nearly complete hardening and takes place under zero external load for a time *t*, after which a short term proportional loading is applied up to complete failure. The generalization of Eq. (2) must take into account the shrinkage eigenstrain field.

This field will depend on the detailed boundary conditions for drying, which in any practical case may be hard to establish, but which may be roughly characterized by an eigenstrain at the exposed surfaces ε_{s0} corresponding to the average hygral conditions. This eigenstrain may be converted to an eigenstress by writing

$$\sigma_{s0} \sim E\, \varepsilon_{s0} \tag{3}$$

and σ_{s0} may be used as a measure of the intensity of the shrinkage at the surface. However, within the structure, the moisture content — hence the eigenstrains and the eigenstresses— will depend on time and water diffusivity. These may be combined —as shown in the next section— to give a shrinkage penetration depth defined as

$$\ell_s \sim \sqrt{\alpha\, t} \tag{4}$$

where α stands for an average diffusivity.

When these new parameters are taken into account, the generalization of Eq. (2) turns out to be, from dimensional analysis considerations:

$$\sigma_{Nmax} = f_t\, \Phi\left(\frac{D}{\ell_{ch}},\ \frac{\ell_s}{\ell_{ch}},\ \frac{\sigma_{s0}}{f_t}\right) \tag{5}$$

where the second and third arguments are obviously size independent and act as parameters when, as seems logical, the effect of size is analyzed for fixed moisture boundary conditions (fixed σ_{s0}) and at a given age at loading (fixed ℓ_s).

Of course, the above phenomenological formulation gives only a very simplified picture of the actual behaviour of concrete. In particular, ageing and creep are altogether ignored, and the modulus of deformation and diffusivity appearing in Eqs. (3) and (4) must be understood to be effective or time-averaged values. However, it is expected that for not too young concrete, this approach is enough to give a good idea of the influence of shrinkage on size effect.

A SIMPLIFIED APPROACH TO SHRINKAGE EIGENSTRAINS

A detailed analysis of the shrinkage strains in concrete requires non-linear formulations and detailed specifications of the boundary conditions. However, when one looks only for trends, a linearization of the equations may be performed following, for example, that by Bazant and Raftshol [3]. After this linearization, the classical diffusion equation is obtained, which in the uniaxial case reads:

$$\frac{\partial \varepsilon_s}{\partial t} = \alpha \frac{\partial^2 \varepsilon_s}{\partial x^2} \tag{6}$$

where α is an average diffusivity which for an ordinary concrete is of the order of 10 mm^2/day.

The boundary condition at the exposed surfaces is controlled by a surface resistance which depends essentially on the air flow conditions, and according to [3] is negligible for any practical specimen size, so that the shrinkage at the surface is, on average, constant, and equal to ε_{s0}, known from the average environmental conditions.

Although the solution of Eq. (6) is analytically obtainable as a series expansion, there is no point in using such a complicated method after all the previous simplifications. Henceforth, we use the parabolic profiles shown in Fig. 1a and 1b for a symmetrically dried strip (or wall) of thickness *D*.

The parameters ℓ_s and β are obtained by imposing that the diffusion Eq. (6) be satisfied on average. The result is

$$\ell_s = \sqrt{12\alpha t} \tag{7}$$

$$\beta = e^{0.25 - \frac{12\alpha t}{D^2}} = e^{0.25 - \frac{\ell_s^2}{D^2}} \tag{8}$$

From now on, the shrinkage penetration length ℓ_s is used as the evolution parameter instead of time, and the shrinkage eigenstrains are written as

$$\varepsilon_s = \varepsilon_{s0}\,\psi(x) \tag{9}$$

where the dimensionless function ψ takes the form, over half the strip thickness,

$$\psi(x) = \begin{cases} \left(1-\dfrac{x}{\ell_s}\right)^2 & \text{for } x \le \ell_s \le \dfrac{D}{2} \\ 0 & \text{for } \ell_s \le x \le \dfrac{D}{2} \\ 1-\beta\left(1-\dfrac{2x}{D}\right)^2 & \text{for } \dfrac{D}{2} \le \ell_s \end{cases} \tag{10}$$

and is symmetric over the other half.

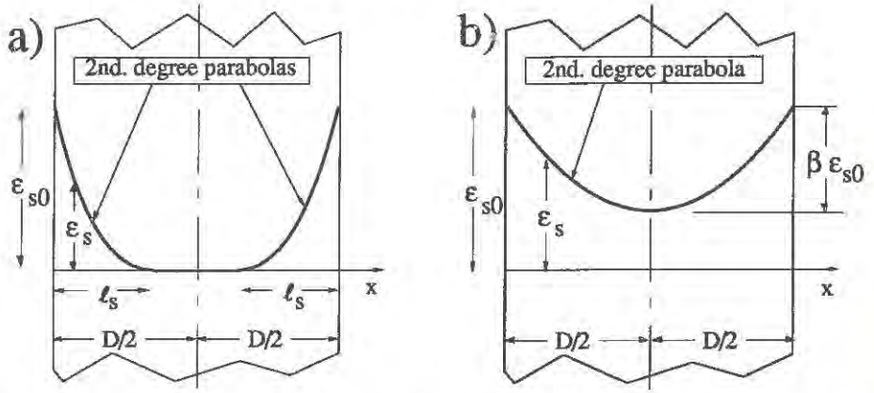

Figure 1. Approximate eigenstrain profiles in a strip. a) Shrinkage penetration less than half the strip depth. b) Shrinkage penetration deeper than half the strip depth.

SHRINKAGE EIGENSTRESSES

Assuming that the strip is long enough to neglect end effects, the shrinkage eigenstresses are obtained by setting that the cross sections remain plane and parallel in absence of external loads, and that the resultant force over a cross-section is zero.

The result (well known in the field of thermal stresses) is readily obtained as

$$\sigma_s(x) = \sigma_{s0}\left[\psi(x)-\langle\psi\rangle\right] \tag{10}$$

where $\langle\psi\rangle$ denotes the average value of $\psi(x)$ over a cross-section, and the eigenstress intensity σ_{s0} is approximately given by

$$\sigma_{s0} = E_{eff}\,\varepsilon_{s0} \tag{11}$$

where E_{eff} is some effective modulus adequately defined to include creep.

The above equation delivers the stresses appearing on a load free specimen which remains elastic throughout the drying process. In reality, drying eigenstrains may easily be high enough to provoke cracking. To be consistent with the cohesive crack model, cracking at a given point must start as soon as the tensile strength is reached. Hence, to avoid cracking due to shrinkage alone for any size, one must have

$$\sigma_{s0} \le f_t \tag{12}$$

which, following the analysis in [3] is always violated in dry environments. Indeed, taking ε_{s0} in the range 0.0004-0.0011, $E_{eff} \approx 20$ GPa and $f_t \approx 3$ MPa, one gets values for σ_{s0} always greater than 2.5 f_t, and as high as 7.3 f_t. In this paper we limit ourselves to the analysis of small intensity shrinkage satisfying condition (12). This decision is not arbitrary, and deserves justification.

The ultimate reason for this self-limitation is that to deal with high intensity shrinkage cases, one has to introduce non-linearities during the shrinkage process which require further assumptions relative to material behaviour. And the importance of these assumptions is difficult to ascertain at first glance. Indeed, a possible approximation, discussed in a forthcoming paper, is to assume distributed cracking during the shrinkage process and the first stages of loading, followed by a simplified bifurcation analysis to detect crack localization, and posterior single crack analysis with eigenstresses coming from shrinkage, but also from the distributed inelastic strains.

The essential result is that the eigenstresses induced by the inelastic strains are mostly controlled by the unloading-reloading behaviour of the material. That this is so may be easily understood by realizing that during the first stage of shrinkage, where the eigenstrain profile is as in Fig. 1a, the microcracks tend to open, while for longer times where the stage shown in Fig. 1b has been reached, these microcracks tend to close. Moreover, at initial loading these microcracks will be again driven open, and as soon as the fracture localizes in a single crack, there will be an unloading of the material surrounding the main crack, and the microcracks will tend to close again. If one further takes into account that the bifurcation condition depends on the unloading stiffness, and that detailed unloading-reloading behaviour is poorly known, avoiding the introduction of such behaviour seems a logical restriction.

NUMERICAL PROCEDURES

The numerical solution conceptually follows the procedure used by Petersson [1]. It is assumed that in the bent beam depicted in Fig. 2, a single crack develops across the central section, while the bulk of the beam remains linear elastic.

As pointed out by Gustafsson [2], this is a fiction, because at the early stages of cohesive crack growth, the tensile strength is necessarily exceeded at points in the bulk, which is contrary to the basic assumptions of the cohesive crack model. This means that some distributed cracking must take place around the main crack at the early stages of loading, and —as previously discussed for high intensity shrinkage— a rigorous analysis would require introducing the unloading-reloading behaviour of the material and considering bifurcation from more or less distributed cracking to growth of a single crack.

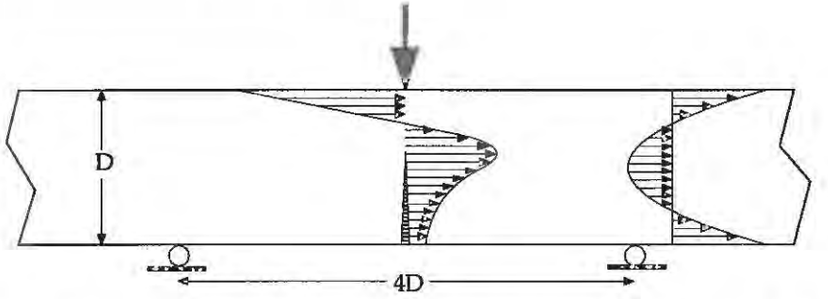

Figure 2. Assumed failure mode: a single cohesive crack develops across the central section.

These delicate points are considered in a forthcoming paper. At present we use the simplification of Hillerborg, Petersson and Gustafsson, which assumes that even if some secondary cracking occurs at the initial stages, the peak load is not much affected by it.

This formulation has the enormous advantage that it reduces the problem to a boundary integral equation, with fewer degrees of freedom than any global finite element or finite difference approximation, which permits a large parametric analysis of the problem at a reasonable cost, yet capturing the trend and order of magnitude of the shrinkage effects.

Just to give the reader an idea of the task at hand, to obtain the results included in this paper the fracture of 2976 beams has been simulated on a personal computer. These results may now be taken as a first approximation and a much more selective analysis may be performed to search for the influence of distributed cracking.

Regarding the characteristics of the computer programme, the only relevant aspect is that 100 equal elements are situated on the central cross-section. This means that the resolution in the description of stress distributions is 0.01 of the beam depth.

This limits the use of the program in the large size range since the fracture process zone at peak load must be several elements wide if it is to be described with reasonable accuracy. Results are consistent up to beam depths of about 8 times the characteristic material size. For a normal concrete with $\ell_{ch} \approx$ 250-300 mm, this turns out to be, about 2 m., a depth which is enough for most practical purposes.

NUMERICAL RESEARCH

The numerical research consisted in simulating fracture of three point bent beams of depths in the range $0.01\ell_{ch}$ to $8\ell_{ch}$, with shrinkage penetration depth ranging from $0.005\ell_{ch}$ to $5\ell_{ch}$. The shrinkage intensity was held equal to the upper limit defined by Eq. (12), i.e.: $\sigma_{s0} = f_t$.

Three kinds of softening were considered: *linear softening* , *quasi-exponential softening* and *extra-long tail softening*. The latter corresponds to a new equation that fits very well the direct tension experimental results of Rokugo *et al.* [4, 5]. The dimensionless representation of the three softening curves is given in Fig. 3. and their analytical equations in the Appendix.

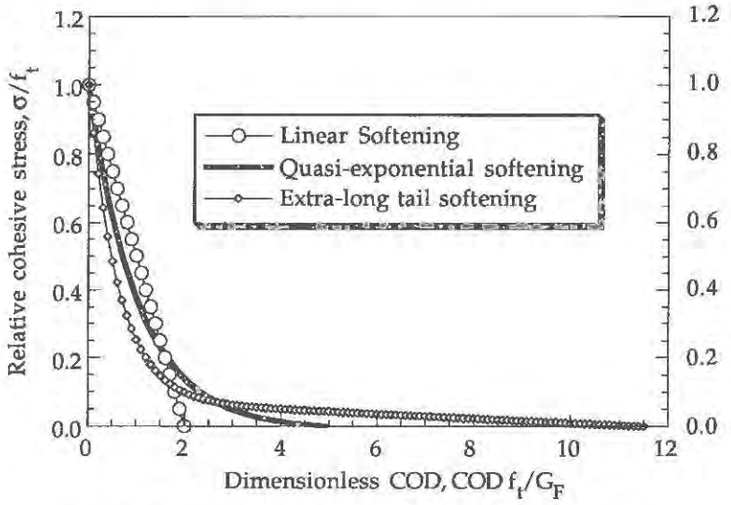

Figure 3. Softening curves considered in the simulations.

THE INFLUENCE OF THE SHRINKAGE PENETRATION DEPTH ON THE FLEXURAL STRENGTH

The quasi-exponential softening has been taken as the reference for the analysis of the effect of ℓ_s on the rupture modulus. The size effect curves for a number of shrinkage penetration depths (same drying time) are shown in a semi-logarithmic plot in Fig. 4.

This figure shows that the effect of the shrinkage increases with size for a given shrinkage depth ℓ_s, but is not monotonic for a given size. It rather evolves as shown in Fig. 5 which is a cross-plot of the results which demonstrates that the shrinkage detrimental effect vanishes at the beginning, then increases, goes through a maximum and decreases asymptotically to zero.

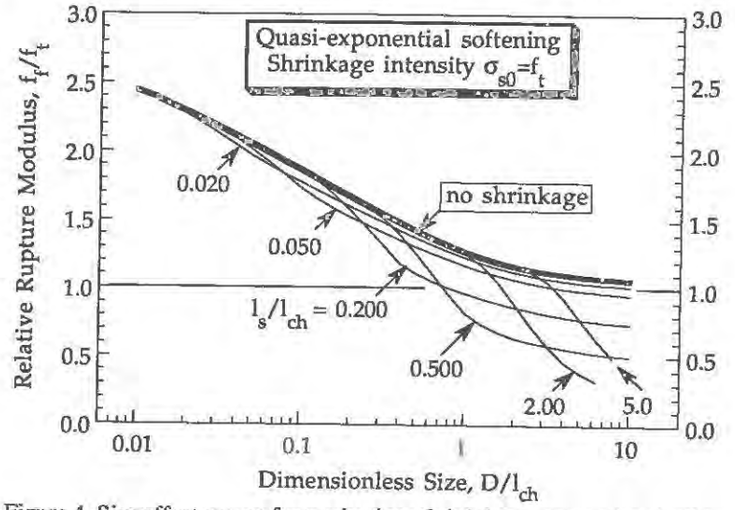

Figure 4. Size effect curves for a selection of shrinkage penetration depths.

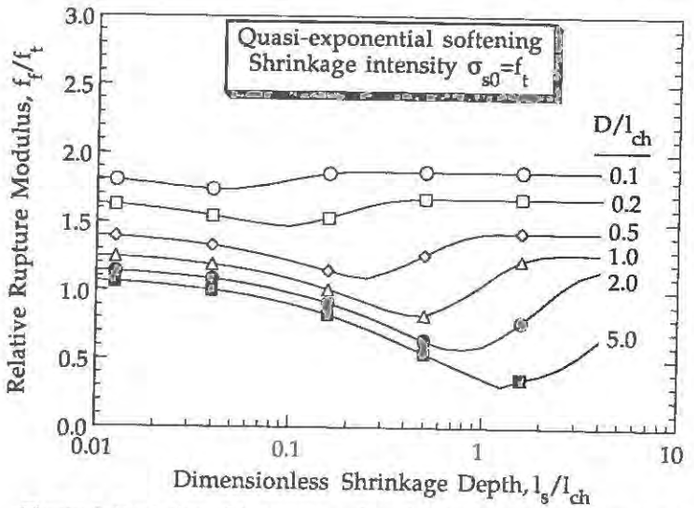

Figure 5. Evolution of beam strength with shrinkage penetration depth

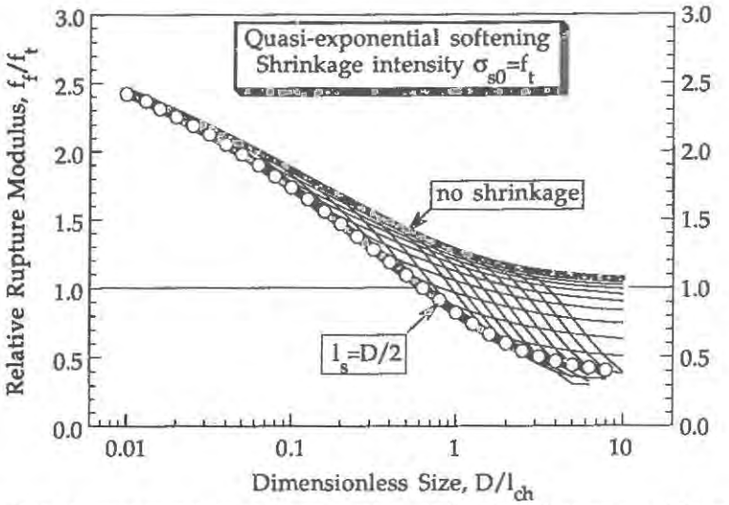

Figure 6. Plot showing that there exists an envelope of the size effect curves giving a lower bound for the strength. It coincides within numerical accuracy with the curve for $l_s = D/2$

This is so because of our simplifying assumptions, which imply that the eigenstresses for a completely dried strip (infinite ℓ_s) are zero.When all possible shrinkage depths are considered, the size effect curves scan a wedge-shaped band with well defined upper and lower bounds for the strength. The upper bound is the shrinkage-free size effect curve (or zero shrinkage penetration). The lower bound is the envelope of the size effect curves for all ℓ_s which may be guessed in Fig. 4, and is clearly shown in Fig. 6.

As shown by the thick curve with open symbols, the lower bound curve closely corresponds to situations where ℓ_s = D/2, which correspond to parabolic eigenstrain distributions. Interestingly, this corresponds to the case analyzed by Hillerborg, Petersson and Gustafsson.[1, 2].

BAZANT'S SIZE EFFECT CURVE

Bazant's size effect law [6] may be written as

$$\sigma_{Nmax} = \frac{1}{\sqrt{a + b\,D}} \tag{13}$$

where σ_{Nmax} is a nominal strength, D is the specimen size and a and b are experimentally determined constants. This equation may be rewritten in a number of ways to obtain linear plots. One of them, suggested by the authors to keep the large size range within focus, is to express it as

$$\frac{1}{\sigma_{Nmax}^2\, D} = b + a\frac{1}{D} \tag{14}$$

and plot the left hand member versus the inverse of the size.

In our case, we take the rupture modulus as the conventional strength of the three point beam and the beam depth as the size, and write Bazant's size effect in dimensionless form as

$$\left(\frac{f_t}{f_f}\right)^2 \frac{\ell_{ch}}{D} = b^* + a^* \frac{\ell_{ch}}{D} \tag{15}$$

where f_f is the rupture modulus and a* and b* are dimensionless experimental constants.

Plotting the left hand member of (15) versus ℓ_{ch}/D, Fig. 6 is transformed into Fig. 7 which shows that the wedge shaped region of the logarithmic plot in Fig. 6 now becomes a band with upper and lower bounds nearly parallel except for very large sizes.

If, furthermore, one focuses on the laboratory experimental range for ordinary concrete with ℓ_{ch}≈300 mm, and beam depths ranging from 50 mm to 500 mm, one obtains the plot in Fig. 8, where it is clear that an equation of Bazant's type describes very well the average between the upper and the lower curves.

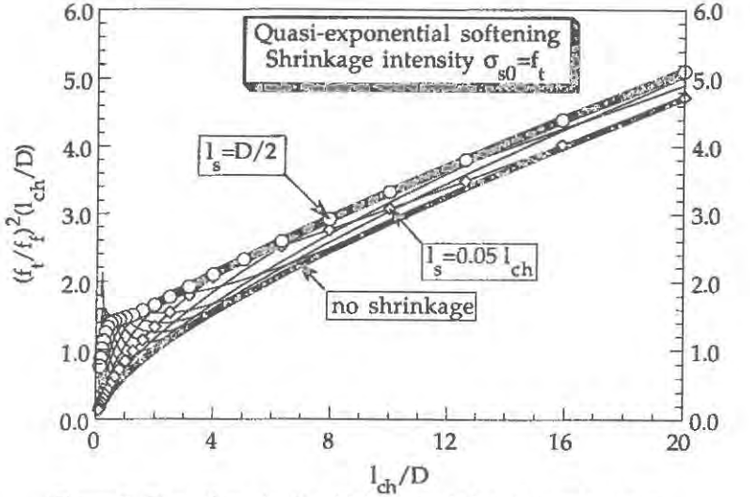

Figure 7. Size effect plot in which Bazant's law is a straight line.

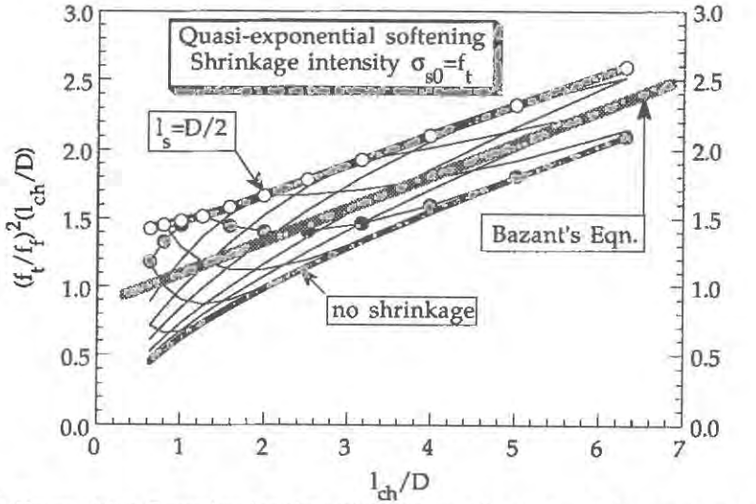

Figure 8. Zoom of Fig. 7 restricted to sizes within the usual experimental range for concrete specimens (beams 50 to 500 mm in depth)

EFFECT OF THE SHAPE OF THE SOFTENING CURVES

The upper and lower envelopes for the three kinds of softening functions previously introduced (Fig. 3) are depicted in Fig. 9. Obviously, there is a dependence on the type of softening, the strength being lower the longer the tail. However, the trends are very similar.

Close examination of Fig. 9 shows that the curves differ just by a horizontal shift. Since horizontal scale is logarithmic, this implies that they differ just by a change of the scale of sizes. Indeed, the results for long tailed curves are shifted on top of the curves for linear softening, as shown in Fig. 10 if one uses a smaller *ad hoc* effective fracture energy which we call the *linear equivalent fracture energy*, G_F^{le}, which is less than the true fracture energy of the material.

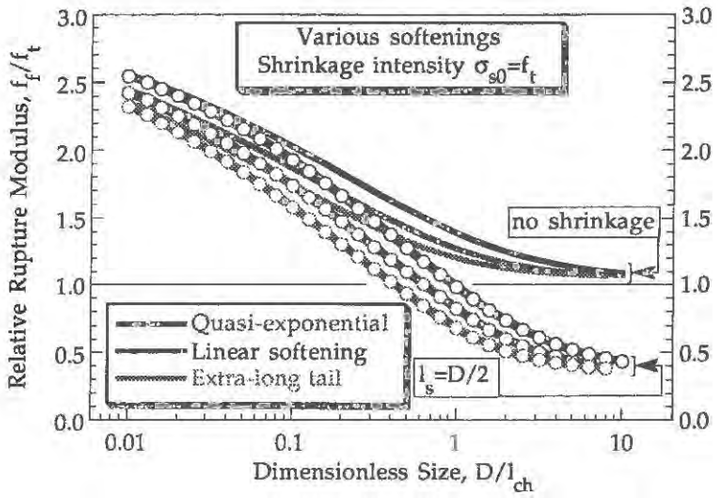

Figure 9. Upper and lower bound size effect curves for the softening curves in Fig. 4.

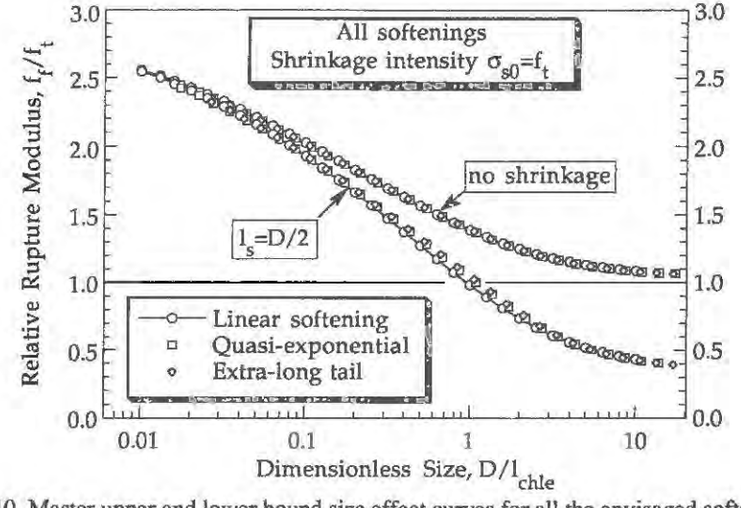

Figure 10. Master upper and lower bound size effect curves for all the envisaged softenings. ℓ_{chle} is the linear equivalent characteristic size obtained using relationships (16) and (17)

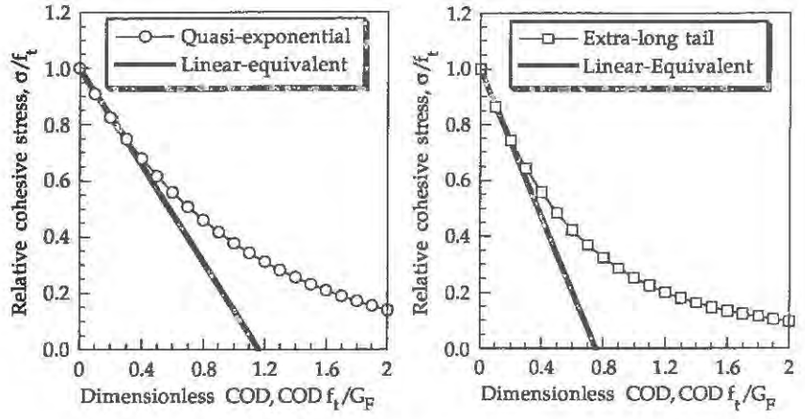

Figure 11. True softening curves and their linear equivalent softenings derived from the scale shift to reduce Fig. 9 to Fig. 10. They happen to coincide with the tangent approximations.

The linear effective fracture energy for the softenings here analyzed are

$$G_F^{le} = 0.581\, G_F \qquad \text{for quasi-exponential softening} \tag{16}$$

$$G_F^{le} = 0.377\, G_F \qquad \text{for extra-long tailed softening} \tag{17}$$

This scale shift means that only the initial portion of the softening curve matters as long as the peak load is concerned, so that the actual material behaves as an equivalent one with linear softening as depicted in Fig. 11. The slopes of the straight lines in this figure were derived from relations (16) and (17), hence from the scale shift in Fig. 9. They happen to be tangent to the "true" softening curves.

As will be discussed thoroughly in a forthcoming paper [5], the use of the tangent approach is valid only for small specimen *intrinsic* sizes, and, as shown in [7], the intrinsic size of an unnotched specimen is zero, whatever the physical size. That is why in our problem this approximation holds.

CONCLUSIONS

1. The shrinkage influences the size effect mainly through two parameters: a drying penetration length, which is proportional to the square root of drying time, and a shrinkage eigenstress intensity.

2. Upper bound and lower bound curves exist for the strength, the upper bound corresponding to shrinkage free structures and the lower bound to the eigenstress distribution considered by Hillerborg and co-workers.

3 An expression of the type of Bazant's size effect law describes very well the average size effect lying midway between the upper and lower bound curves.

4. The shape of the softening curve appreciably modifies the strength.But the various size effect curves may be brought to fuse into a single master curve corresponding to an *equivalent linear softening*.

ACKNOWLEDGEMENTS

The authors gratefully acknowledge financial support for this research provided by the Comisión Interministerial de Ciencia y Tecnología CICYT, Spain, under grant PB90-0276.

REFERENCES

1. Petersson, P. E., Crack Growth and Development of Fracture Zones in Plain Concrete and Similar Materials. Lund Institute of Technology Report TVBM-1006, 1981.

2. Gustafsson, P. J., Fracture Mechanics Studies of Non-Yielding Materials Like Concrete: Modelling of Tensile Fracture and Applied Strength Analyses. Report TVBM-1007, Division of Building Materials, Lund Institute of Technology, Lund, Sweden, 1985.

3. Bazant, Z. P., and Raftshol, W. J., Effect of Cracking in Drying and Shrinkage Specimens, *Cement and Concrete Research*, 1982, **12**, 209-226.

4. Rokugo, K., Iwasa, M., Suzuki, T., and Koyanagi, W., Testing Methods to Determine Tensile Strain Softening Curve and Fracture Energy of Concrete. *In Fracture Toughness and Fracture Energy*, Mihashi *et al.* (Eds.), Balkema, Rotterdam, 1989, pp. 153-163.

5. Planas, J.,Guinea, G. V. and Elices, M., Long-tailed softening curves for concrete and structural response, submitted to *2nd International Conference on Fracture and Damage of Concrete and Rock*, Vienna, November 9-13, 1992.

6 Bazant, Z.P., Size Effect in Blunt Fracture: Concrete, Rock, Metals. *J. Eng. Mech., ASCE*, 1984, **110**, 518-538.

7. Planas, J. and Elices, M., "Anomalous structural size effect in cohesive materials like concrete", in *Serviceability and Durability of Construction Materials, Vol. 2*, B. A. Suprenant, Ed., American Society of Civil Engineers, New York, 1990, pp. 1345-1356.

APPENDIX

The equations of the softening curves, with the crack opening denoted as w, are the following

Linear softening:

$$\frac{\sigma}{f_t} = \begin{cases} 1 - \dfrac{w f_t}{2G_F} & \text{for } w \le \dfrac{2G_F}{f_t} \\ 0 & \text{for } w \ge \dfrac{2G_F}{f_t} \end{cases}$$

Quasi-exponential Softening:

$$\frac{\sigma}{f_t} = \begin{cases} (1+c_1)\, e^{-c_2 \frac{w f_t}{G_F}} - c_1 & \text{for } w \le \dfrac{5G_F}{f_t} \\ 0 & \text{for } w \ge \dfrac{5G_F}{f_t} \end{cases}$$

with $c_1 = 8.290\ 10^{-3}$ and $c_2 = 9.602\ 10^{-1}$

Extra-long tailed Softening:

$$\frac{\sigma}{f_t} = \begin{cases} c_1 - c_3 \dfrac{w f_t}{G_F} + (1-c_1)\, e^{-c_2 \frac{w f_t}{G_F}} & \text{for } w \le \dfrac{11.5G_F}{f_t} \\ 0 & \text{for } w \ge \dfrac{11.5G_F}{f_t} \end{cases}$$

with $c_1 = 7.503\ 10^{-2}$, $c_2 = 1.614$ and $c_3 = 6.516\ 10^{-3}$

Invited Paper

FRACTURE MECHANICS APPLICATIONS IN THE ANALYSIS OF CONCRETE REPAIR AND PROTECTION SYSTEMS

H.K. Hilsdorf, M. Günter, P. Haardt
Universität Karlsruhe
Institut für Massivbau und Baustofftechnologie
Kaiserstr. 12, 7500 Karlsruhe

Abstract

Concrete overlays are used frequently for the repair of damaged concrete surfaces. Based on a fracture mechanics analysis it can be shown that such systems may fail due to shrinkage of the overlay or due to a temperature shock by delamination of the overlay. Starting from a free boundary a fracture zone and subsequently a crack form in the substrate-overlay interface.

In cases where thin polymer coatings are applied to a concrete surface the coating may fail due to the formation of blisters in the coating which may be caused by stress concentrations due to osmotic or capillary pressure. Using a so-called blister-test the resistance of a polymer coating against blister growth on a concrete substrate can be expressed in terms of fracture mechanics parameters.

1. THE PROBLEM

The repair of concrete surfaces which had been damaged due to various external or internal actions by comparatively thick concrete overlays as well as the prevention of such damage by the application of protective coatings today is one of the standard tasks of concrete construction. Nevertheless, no objective design rules based on analytical considerations exist for such systems. Thus, it is not surprising that failures of some systems e.g. delamination of concrete overlays or the formation of blisters in polymer coatings often occur requiring the repair of repair systems.

In the following some results of analytical and experimental studies presently being carried out at the University of Karlsruhe are reported. The objective of these studies is the

development of design rules for concrete repair and protection systems resulting in specific requirements with regard to the required properties of overlay or coating material for a given concrete substrate.

2. CONCRETE AND MORTAR OVERLAYS

Overlays with a thickness ranging from about 5 mm to 50 mm generally are made using hydraulic cements as a binder (CC). To improve the properties of such materials often polymers are added (PCC), and in special cases only polymers are used as a binder (PC). These materials vary widely with regard to their mechanical properties, in particular tensile and bond strength, modulus of elasticity as well as shrinkage and creep characteristics. In order to be effective such repair materials have to form a well bonded overlay free of cracks which protects the concrete substrate against the penetration of water, aggressive solutions or gas.

2.1 Actions and Stress States

If concrete or mortar overlays are applied to an old concrete substrate internal stresses and stresses due to restraint are generated in the system due to moisture loss and shrinkage of the repair material and due to seasonal temperature changes. Of particular significance are the stresses caused by rapid cooling of a concrete surface previously warmed by sunshine e.g. due to rain during a thunderstorm. In Fig. 1 the corresponding stresses are shown schematically for materials with linear elastic properties: restraint of shrinkage and thermal strains result in tensile stresses σ_x in the x-direction which are almost constant throughout the length of the member. In the interface between substrate and overlay shear stresses τ_{xy} as well as normal stresses σ_y are developed. At the free boundaries of the system (x = 0) the tensile stresses σ_y reach a maximum value. Superimposed are internal stresses due to the non-uniform shrinkage of the overlay.

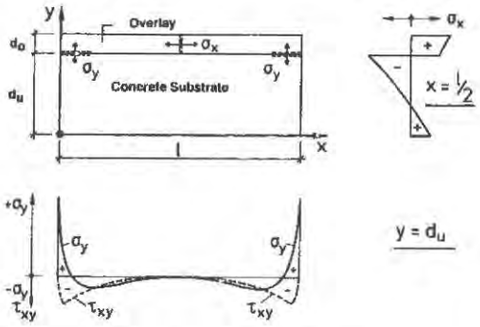

Fig. 1 Stresses due to restraint in a concrete repair system.

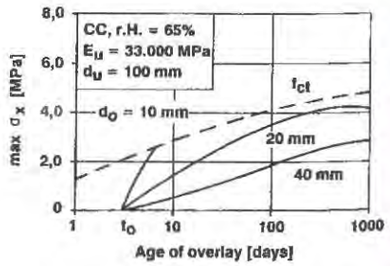

Fig. 2 Max. stress σ_x in a concrete overlay (CC) due to shrinkage of the overlay.

Whereas a uniaxial tensile stress σ_y acts at the free ends of the system a biaxial state of stress exists in the transition zone. The direction of principal stresses rotates towards the x-axis, and a state of uniaxial tension occurs beyond the transition zone whose length corresponds roughly to 4 · d_o where d_o = thicknesss of overlay.

Repair systems may be damaged by cracks in the y-direction if the stress σ_x in the overlay exceeds the tensile strength of the overlay material. Fig. 2 shows the result of a FE-analysis of a concrete repair system taking into account the effects of creep. The development of the maximum tensile stress at the free surface is given for concrete overlays of various thickness d_o due to shrinkage of the overlay in a constant environment of 20°C and 65 % r.H. Whereas in thin overlays max σ_x exceeds the tensile strength, f_{cto}, of the overlay after a few days of drying no cracks are expected in the thicker layers because of their slower rates of drying and the reduction of residual stresses due to creep.

Repair systems may fail if the stresses σ_y exceed limiting values. Then delamination of the overlay occurs starting at the free boundaries, x = 0. It can be shown by numerical analysis that the theoretical stresses max σ_y exceed the tensile strength of the overlay material or of the concrete substrate as well as the bond strength between both components particularly for the case of thermal shock by a factor of 2 or more if linear stress-strain relations for concrete in tension are used in the analysis [1]. This would result in complete delamination of the overlay.

2.2 Numerical Analysis

A realistic analysis of a concrete repair system particularly of the delamination process requires the use of constitutive relations which take into account the strain softening behavior of cementitious materials subjected to tensile stresses. Therefore, the application of fracture mechanics concepts appeared to be the most rational approach. Taking into account the stress states described in the previous section a mixed Mode I and Mode II fracture process should occur at the free ends of the system. In addition, the different fracture properties of the concrete substrate, the overlay material and of the transition zone between both should be considered. The material characteristics needed to take these parameters into account are not available and are very difficult to determine experimentally. Therefore, for the analysis only a Mode I fracture occuring in the concrete substrate was considered. This appeared to be an acceptable approximation since at the free boundary (x = 0) a Mode I condition prevails. Experimental results as well as practical experience also showed that delamination of overlays generally occurs due to lack of cohesion in the top layer of the substrate rather than by insufficient adhesion of the repair material to the substrate. Therefore, in the analysis the constitutive relations for the substrate concrete subjected to uniaxial tension was used to model fracture and delamination of the concrete in the transition zone.

The analysis is based on the fictitious crack model by

Petersson and Hillerborg [2] as modified by Curbach for a FE-analysis [3]. Curbach developed a rheological model for the stress-strain characteristics of concrete subjected to uniaxial tension in which the transmission of tensile stresses across a crack is controlled by friction elements whose properties follow a Weibull distribution. Values for the tensile strength of the concrete, f_{ct}, modulus of elasticity, E_c, and fracture energy, G_F, were taken from the relations given in the new CEB-FIP Model Code MC 90 [4]. Acc. to [4] fracture energy may be estimated from eq. 1:

$$G_F = G_{Fo} \, (f_c/f_{co})^{0.7} \qquad (1)$$

where G_F = fracture energy [Nm/m^2]; f_c = concrete compressive strength [MPa]; f_{co} = 10 MPa; G_{Fo} = base value of fracture energy which depends on the maximum aggregate size of the concrete. The analysis has been carried out for min. G_{Fo} = 20 Nm/m^2 and max. G_{Fo} = 40 Nm/m^2. Fig. 3 shows the stress-strain and the stress-crack opening relations used in the analysis for concrete grades C6, C20 and C40 corresponding to a weak, medium and high strength concrete substrate.

In Fig. 4 the distribution of tensile stresses σ_y in the transition zone ($y = d_u$) caused by thermal shock is given for different maximum tensile stresses σ_x in the overlay. The concrete substrate has a tensile strength f_{ct} = 1.56 MPa corresponding to a concrete grade C 20. For a maximum tensile stress in the overlay, σ_x = 1.0 MPa, the stress max σ_y at the boundary ($x = 0$) is equal to the tensile strength of the substrate, f_{ct}. Though a crack between substrate and overlay is initiated delamination does not as yet occur. Since the crack can transmit stresses max σ_x may increase further for a given value of max σ_y resulting in gradual crack propagation. The location at which max σ_y occurs moves along the x-axis towards the interior of the system, and a fracture zone of reduced tensile strength is developed. As soon as max σ_x reaches a limiting value equilibrium is no longer possible and rapid crack propagation corresponding to delamination occurs.

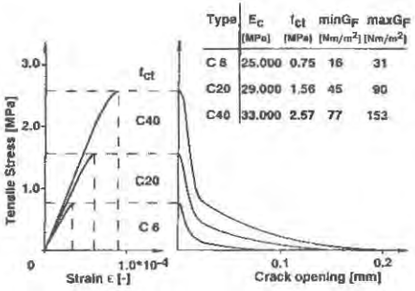

Fig. 3 Stress-strain and stress-crack opening relations for concrete in tension.

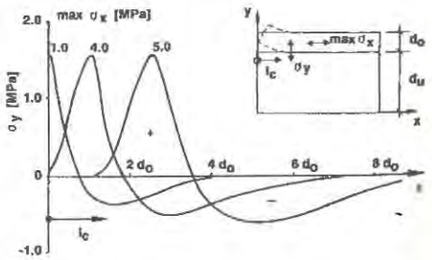

Fig. 4 Stresses in the transition zone ($y=d_u$) for different tensile stresses max σ_x in the overlay.

In Fig. 5 the length of the fracture zone i.e. the distance between the location of max σ_y from the free boundary, $x = 0$, expressed as a fraction of the thickness of the overlay, d_o, is given as a function of the maximum tensile stress max σ_x which is developed in the overlay. The vertical dashed lines give the limiting values of max σ_x for which unstable crack growth occurs. As the tensile strength of the substrate, f_{ct}, increases also the critical residual stress max σ_x* for which delamination occurs increases. This also follows from Fig. 6 where the tensile strength of the substrate, f_{ct}, which is required to take up a certain maximum value of the residual stress max σ_x* is given both for max. and min. values of fracture energy. For a given tensile strength f_{ct} the stress max σ_x* increases as the fracture energy G_F increases.

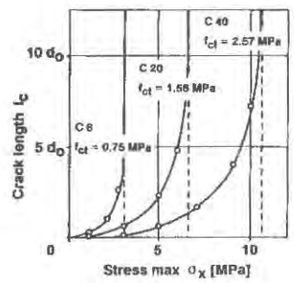

Fig. 5 Crack length l_c as a function of max σ_x for different substrate concrete grades.

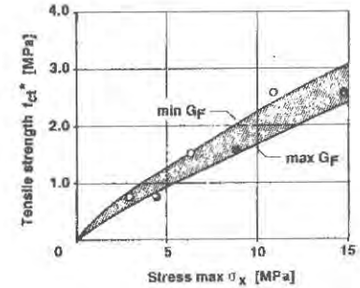

Fig. 6 Required tensile strength of substrate $f_{c,t}^*$ as a function of restraining stress max σ_x.

The development of a fracture zone could also be observed experimentally both in the laboratory and on site [1], [5]. It was particularly pronounced where overlays with a high tensile strength resulting in high values of max σ_x had been used.

2.3 Design Considerations

The actual values of max σ_x may be estimated from empirical relations which have been deduced from the numerical analysis and which give max σ_x as a function of thickness of the overlay as well as of modulus of elasticity, coefficient of thermal expansion, shrinkage and creep properties of the overlay [1]. From this the required tensile strength or the pull-off tensile strength of the concrete substrate f_{ct} prior to application of the overlay may be calculated. Limiting values may also be estimated from the following consideration: The maximum of the residual stress max σ_x is given by the tensile strength of the overlay material, f_{cto}. Therefore,

$$\max \sigma_x \leq f_{cto} \qquad (2)$$

From Fig. 6 the following correlation between the critical stress max σ_x^* corresponding to the required tensile strength of the concrete substrate, f_{ct}, and max σ_x may be deduced (eq. 3).

$$\min f_{ct} = b \cdot [\max \sigma_x/\sigma_{xo}]^{0.7} \qquad (3)$$

where σ_{xo} = 1 MPa. The coefficient b [MPa] depends on the characteristic length l_{ch} ($l_{ch} = E_c G_F / f_{ct}^2$) and may be estimated from eq. 4

$$b = \frac{f_{ctbo}}{(l_{ch}/l_{ch,o})^{1/3}} \qquad (4)$$

where $l_{ch,o}$ = 38,2 mm and f_{ctbo} = 1 MPa.

If the tensile strength of the concrete substrate is low an overlay material with a low tensile strength f_{cto}, generally associated with a low modulus of elasticity has to be chosen. From this we may draw the general conclusion that the overlay material should not be stronger or stiffer than the substrate.

For overlays with hydraulic cements (CC and PCC) with a tensile strength in the range of $3 < f_{cto} < 6$ MPa a tensile strength of the substrate $0.8 < f_{ct} < 1.5$ MPa is sufficient. Where polymer concrete (PC) is used as an overlay material values of $2 < f_{ct} < 3$ MPa are needed in order to prevent delamination. This requirement often cannot be met by a previously damaged concrete substrate, so that a different overlay material should be chosen.

3. POLYMER COATINGS

Polymer coatings generally with a thickness not exceeding 5 mm are used to protect concrete repair systems to ensure sufficient corrosion protection of the reinforcement in cases where the concrete cover is insufficient or for the protection of the entire concrete structure in cases of severe exposure conditions such as chemical attack. Therefore, suitable coating materials generally have a very low permeability with respect to fluids or gases.

3.1 Actions and Stress States

Because of their small thickness significant delamination of polymer coatings due to residual shrinkage and temperature stresses as described for the concrete or mortar overlays is rare. However, polymer coatings may be subjected to fluid or gas pressure caused by various mechanisms. Osmotic pressures are generated within the polymer coating or at the interface between coating and concrete substrate if the coating or the interface contain hydrophile substances. Capillary vapor pressures acting on the coating may be caused by a temperature increase of the concrete e.g. due to exposure to direct sunshine or by the take-up of water of the concrete substrate. These mechanisms and the corresponding pressures acting on a polymer coating have been studied experimentally [6]. The capillary pressures generally do

not exceed about 0.3 N/mm². Osmotic pressures depend primarily on the concentration and type of hydrophile substances as well as on the rigidity of the polymer coating. Fig. 7 shows the development of osmotic pressures with time both for a rigid and for a flexible polymer coating. For a flexible coating osmotic pressures up to 0.05 N/mm² have been observed. For rigid coatings pressures up to 16 N/mm² may occur.

One of the most significant aspects in the "design" of polymer coatings is that local defects in the coating-substrate interface e.g. due to foreign particles, grease etc. are inevitable. Stress concentrations at such defects caused by osmotic or capillary pressures lead to the development of local blisters and in extreme cases to delamination of the polymer coating.

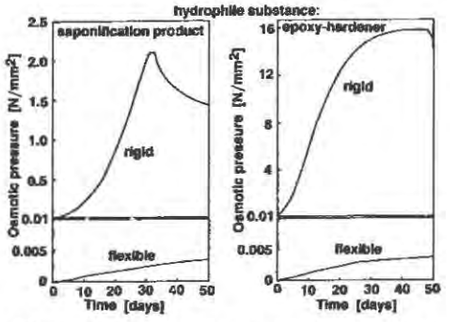

Fig. 7 Osmotic pressure acting on polymer coatings on a concrete substrate.

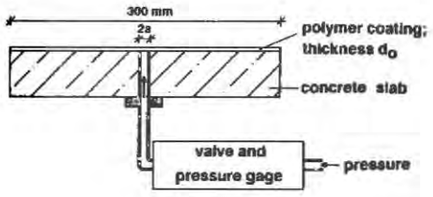

Fig. 8 The blister test.

3.2 Experiments

Because of the significant role of local defects in failures of polymer coatings fracture mechanics concepts also have been applied to estimate the resistance of such coatings to internal pressure [6]. For this a test method, generally referred to as blister test [7], has been used and developed further, c.f. Fig. 8. A polymer coating is applied to a concrete specimen. In the center of the specimen a circular defect, diameter 2a, is generated which corresponds to the nucleus of a blister. Pressure can be applied to the defect by means of a pump and a tubing which penetrates the concrete specimen. The pressure p at which growth of the blister occurs can be determined by visual inspection. Presently, only translucent polymer coatings can be tested. The method will be developed further to estimate the diameter of the blister from the curvature of the surface of the blister in the polymer coating. In Fig. 9 the critical pressure p which causes blister growth is given for different temperatures at testing as a function of the blister radius, a. As the radius, a, increases the critical pressure p decreases. An increase of temperature results in a significant reduction of the critical pressure for a given blister radius.

3.3 Fracture Mechanics Evaluation

For the preliminary evaluation of the experimental data an approach described in [8] has been used. The principle assumption is that similar to cohesive fracture also adhesive fracture can be described in general terms acc. to eq. 5:

$$p^2_{crit} = f(d_o/a)\ (\frac{E \cdot G_{ca}}{a}) \qquad (5)$$

where p_{crit} = critical pressure [N/mm²]; d_o = thickness of coating [mm]; a = radius of blister [mm]; E = modulus of elasticity of the polymer coating [N/mm²]; G_{ca} = fracture energy for adhesive fracture [N/mm]. Setting $E \cdot G_{ca} = K_{ca}^2$ the parameter $f(d_o/a)$ may be expressed by eq. 6

$$f(d_o/a) = \frac{p^2_{crit} \cdot a}{K^2_{ca}} \qquad (6)$$

In [8] values for $f(d_o/a)$ have been determined from FE-analysis assuming linear-elastic material properties.

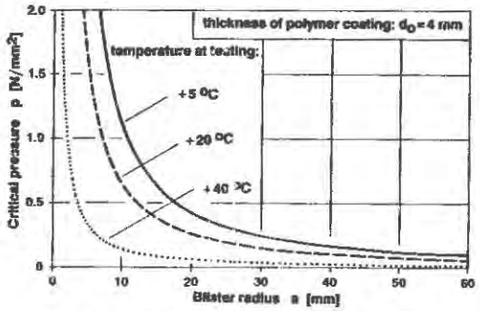

Fig. 9 Results of blister tests.

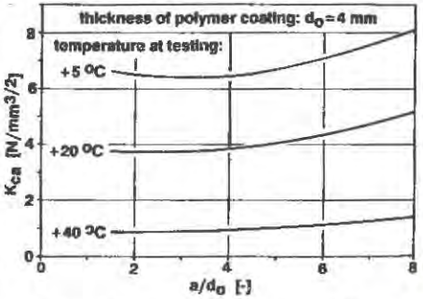

Fig. 10 Values of K_{ca} determined from the experimental data given in Fig. 9.

For the experimental data given in Fig. 9 values of K_{ca} have been calculated using the FE-solution presented in [8]. They are shown in Fig. 10. From this it follows that K_{ca} may be assumed to be constant only for small values of a/d_o. It increases as a/d_o increases. This may be due to a transition from Mode I to Mode II fracture as a/d_o increases i.e. as the polymer coating becomes more flexible. Further analysis and model development is needed in which also more realistic material parameters of the coating and of the substrate-coating interface are taken into account.

Nevertheless, these preliminary tests and their evaluation showed that the blister test is a promising approach to "design" polymer coatings taking into account the size of initial defects, the pressure to be expected under realistic conditions as well as the adhesive fracture energy which will depend not

only on the polymer coating but also on the surface preparation of the concrete substrate.

4. REFERENCES

1. Haardt, P., Zementgebundene und kunststoffvergütete Beschichtungen auf Beton. Dissertation, Universität Karlsruhe, 1991.

2. Hillerborg, A., Analysis of one single crack. In Report to RILEM Committee TC50-FMC, 1981.

3. Curbach, M., Festigkeitssteigerung von Beton bei hohen Belastungsgeschwindigkeiten. Dissertation, Universität Karlsruhe, 1987.

4. CEB-FIP Model Code 1990, First Draft. In CEB, Bulletin d'Information, No. 195, Paris, 1990.

5. Haardt, P., Hilsdorf, H.K., Einfluß von Haftbrücken auf die Haltbarkeit von Ausbesserungen mit Zementmörtel (Feldversuche). Final Report, Institut für Massivbau und Baustofftechnologie, Universität Karlsruhe, 1988.

6. Günter, M., Beanspruchung und Beanspruchbarkeit des Verbundes zwischen Polymerbeschichtungen und Beton. Dissertation, Universität Karlsruhe (in preparation).

7. Williams, M.L., The continuum interpretation for fracture and adhesion. In Journal of Applied Polymer Science, 1969, Vol. 13, pp. 29-40.

8. Bennet, S.J., Devries, K.L. and Willams, M.L., Adhesive fracture mechanics. In International Journal of Fracture, 1974, Vol. 10, pp. 33-43.

CRACK FORMATION DUE TO HYGRAL GRADIENTS

A.M. ALVAREDO and F.H. WITTMANN
Institute for Building Materials, ETH Zürich
ETH-Hönggerberg, 8093 Zürich, Switzerland

Abstract

Water transport in concrete is analysed by means of the theory of diffusion. The dependence of the diffusion coefficient on water content is taken into consideration. The resulting nonlinear problem is solved numerically. Next, a stress analysis is carried out in which a smeared crack formulation with strain-softening is employed to predict cracking. In order to induce strain localisation a statistical distribution of the fracture energy and the tensile strength is introduced. The conditions for the formation of real cracks and for the stability of crack propagation are discussed.

INTRODUCTION

If realistic hygral properties are available it is possible to calculate the humidity distribution within concrete elements for the complete drying history. Subsequently, a stress analysis allowing for crack formation can be carried out for different degrees of external restraint. In this way multiple predictions concerning the evolution of cracking can be made: Do softening zones and/or real cracks appear? If they do, when? How does the final crack pattern look like? Does cracking proceed in a stable way?

The analysis described in this brief presentation is based on a number of simplifications but it is nevertheless believed that the obtained results point out correctly the most salient features of crack formation due to hygral gradients. The employed methodology can be extended to the study of cracking due to thermal or to superimposed hygral and thermal gradients.

MATHEMATICAL MODEL AND NUMERICAL IMPLEMENTATION

As first step in the calculations, the humidity distribution in the specimen under study must be calculated. Non-linear diffusion theory is employed for this purpose, in which the relative humidity gradient, ∇h, acts as driving force. The governing equation reads

$$\dot{h} - \nabla\,[D(h)\,\nabla h] = 0 \tag{1}$$

In Eq. (1) it has been assumed that neither sinks nor sources are present. The function $D(h)$ represents the dependence of the diffusion coefficient on the relative humidity, which is strongly linked with the pore size distribution of the material.

Convective boundary conditions are prescribed at the surface of the specimen in contact with the air. The corresponding expression is

$$q = H(h_s - h_a) \tag{2}$$

where q is the humidity flux, H the film coefficient, h_s the unknown surface humidity and h_a the air relative humidity.

With respect to the stress analysis, a blunt crack model [1] with bilinear softening [2] is used to predict crack formation. The softening moduli are adapted to the spatial discretisation in the usual way. Regarding the unloading strategy, it is assumed that 30% of the attained crack strain remains as irrecoverable deformation at zero stress. The influence of the relative humidity on the mechanical properties has been neglected. Furthermore, no time-dependent deformations have been taken into account in the analysis.

A statistical (normal) distribution of the fracture energy G_F and of the tensile strength f_t is assumed. For the former a standard deviation of 20% and for the latter a standard deviation of 10% have been considered. This is in fair agreement with experimental findings. The local distribution of the material properties makes any further assumption on strain localisation superfluous.

The inevitable failure of the calculations to converge is interpreted as unstable material response, i.e. as unstable crack formation. In this case an a priori crack is introduced at the location where instability took place.

MATERIAL PARAMETERS

The humidity distributions have been calculated for two different cementitious materials: normal concrete and autoclaved aerated concrete (AAC). The relationship between the diffusion coefficient D and the water content w is reported in [3] and [4]. With the aim to obtain the variation of D with relative humidity, use must be made of the corresponding

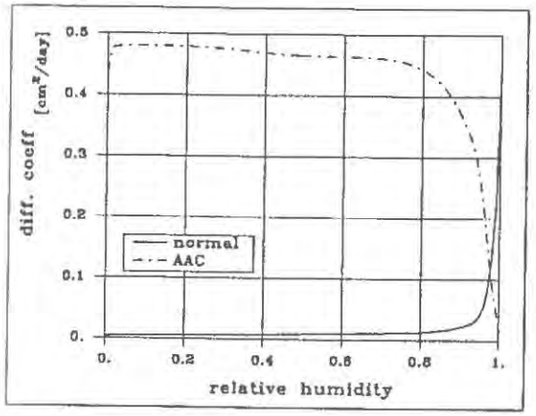

Figure 1: Diffusion coefficient as function of relative humidity for normal and autoclaved aerated concrete.

sorption isotherms [5], [6]. The obtained D vs. h relationships are illustrated in Fig. 1. A film coefficient (see Eq. (2)) $H = 0.5$ cm/day was used for both materials.

Shrinkage strains are assumed to be proportional to the humidity change

$$\epsilon_{sh} = \alpha_{sh} \cdot \Delta h \tag{3}$$

in which the strain-free state corresponds to saturation. For normal concrete the adopted shrinkage coefficient is $\alpha_{sh} = 1.4 \cdot 10^{-3}$ while for AAC the employed value is $\alpha_{sh} = 0.58 \cdot 10^{-3}$ [6].

The mechanical behaviour of normal concrete is described by $E = 40000$ MPa and $\nu = 0.2$. The mean values of the tensile strength and the fracture energy are $\bar{f}_t = 4$ MPa and $\overline{G}_F = 100$ N/m, respectively. The bilinear softening diagram proposed in [2] is used. For AAC the following values have been considered [7]: $E = 2060$ MPa and $f_t = 0.55$ MPa.

RESULTS

Moisture distribution

Calculations were carried out for a 400 mm deep specimen under one-dimensional flow. One side is in contact with air at $h_a = 0.6$ while the three remaining sides are sealed. The humidity distributions for normal concrete and AAC after 1 month, 1, 5, and 10 years of drying are presented in Figs. 2.a) and 2.b).

Stress development in AAC

The dimensions of the finite element mesh in Fig. 3.a). are 400x100x100 mm. As support

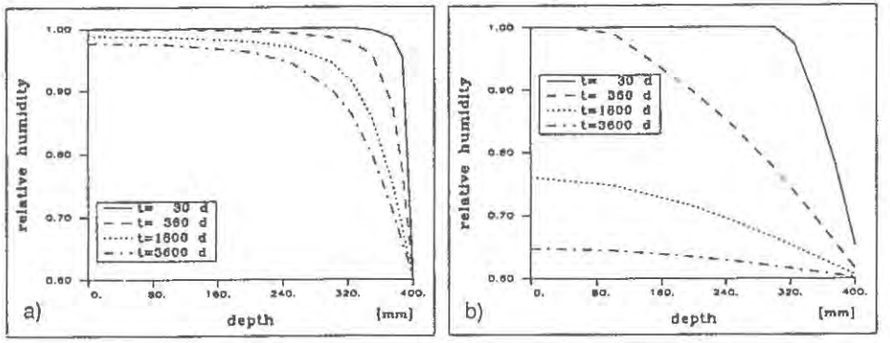

Figure 2: Humidity distributions after 1 month, 1, 5 and 10 years of drying: a) normal concrete; b) autoclaved aerated concrete.

conditions, the displacements perpendicular to the sealed sides have been suppressed. Consequently, the stress distributions shown in Fig. 3.b) correspond to full external restraint conditions. It can be seen that for the assumed hygral boundary conditions and after 10 years of drying, the tensile stresses do not reach the tensile strength. Therefore, no fracture process zones develop.

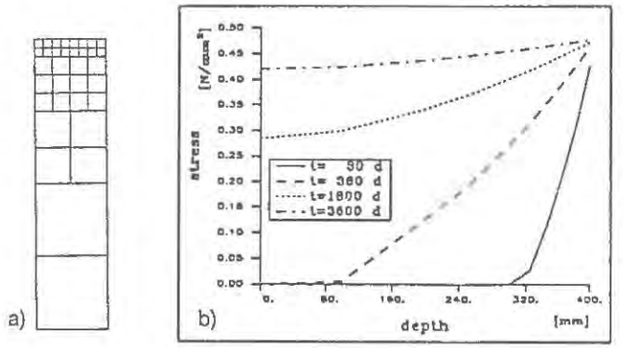

Figure 3: Stress development in AAC: a) finite element mesh; b) stress distribution.

Stress development in normal concrete

Fully restrained element: In Figs. 4.a) and b) the computed crack patterns after 1 and 5 years of drying are shown for a concrete element exposed to $h_a = 0.8$. All of the formed cracks are within the softening range, i.e. no real cracks appeared. This state can be denoted as latent instability.

The crack patterns depicted in Figs. 4.c), d), e) and f) were calculated for $h_a = 0.6$.

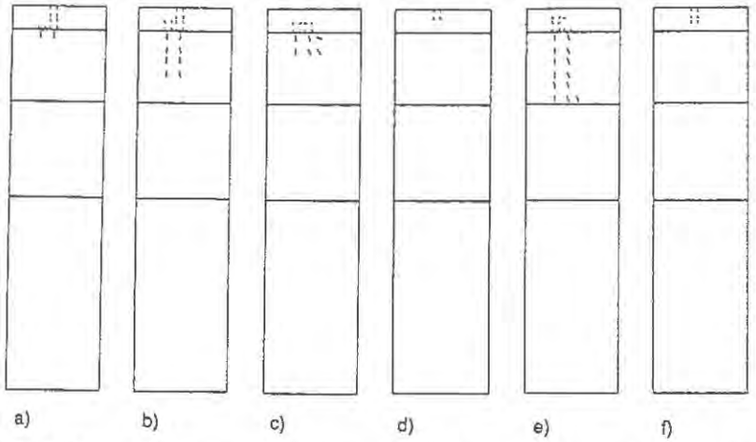

Figure 4: Crack formation under full external restraint: a) softening cracks after 1 year at $h_a = 0.8$; b) softening cracks after 5 years at $h_a = 0.8$; c) softening cracks after 1 year at $h_a = 0.6$; d) real cracks after 1 year at $h_a = 0.6$; e) softening cracks after 5 years at $h_a = 0.6$; f) real cracks after 5 years at $h_a = 0.6$.

Figs. 4.c) and e) show the active (i.e. still opening) softening cracks after 1 and 5 years of drying while in Figs. 4.d) and f) the corresponding real cracks are indicated. In this case crack formation proceeds in a stable way.

Eigenstresses in elements of different length: A 1 m long, 400 mm high and 100 mm thick concrete block in contact with air at $h_a = 0.6$ on its top side was analysed. The calculations were performed on half of the specimen (see Fig. 5). Symmetry support

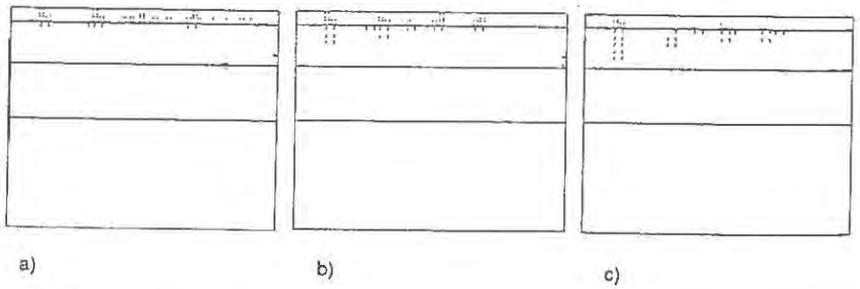

Figure 5: Softening cracks in half of a 1 m long, 400 mm high and 100 mm thick concrete block: a) after 1 year of drying; b) after 2 years of drying; c) after 5 years of drying.

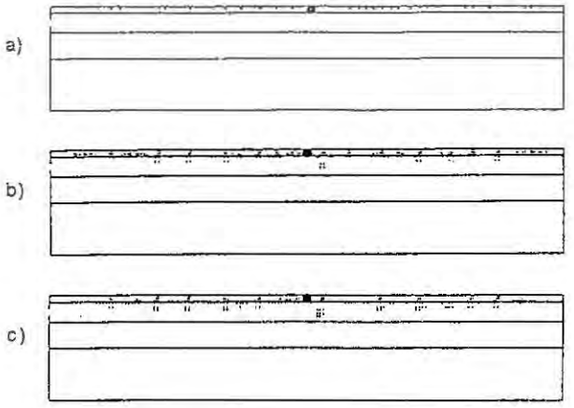

Figure 6: Softening cracks in a 2 m long, 400 mm high and 100 mm thick concrete block with an a priori crack (indicated by the circle): a) after 1 week of drying; b) after 1 year of drying; c) after 2 years of drying.

conditions were imposed at the left side; the vertical displacement of the bottom side was suppressed. The active softening cracks formed after 1, 2 and 5 years of drying can be seen in Figs. 5.a), b) and c), respectively. No real cracks appeared.

Next, a 2 m-long specimen was subject to the same hygral boundary conditions. Shortly after 300 days of drying the calculations failed to converge. This was interpreted as unstable crack propagation, i.e. as structural snap-back. By defining $E \simeq 0$ for three elements an a priori crack was determined at the location where instability took place (see Fig. 6). The analysis was repeated and convergence was achieved throughout the whole calculated drying history. The active softening cracks after 1 week, 1 and 2 years of drying are presented in Figs. 6.a), b) and c).

DISCUSSION AND CONCLUSIONS

When analysing cracking due to gradients, three types of situations must be distinguished: the formation of softening cracks, the stable propagation of real cracks and unstable crack propagation. Depending on the specimen dimensions (size effect), on the hygral boundary conditions (relative humidity) and on the mechanical boundary conditions (degree of restraint), one of these types of cracking will develop.

Softening cracks appear in unrestrained specimens not exceeding a certain critical dimension or in restrained specimens subject to mild hygral boundary conditions. Stable real crack formation takes place in small elements under full restraint or in unrestrained

specimens smaller than a critical dimension if drying is severe. Unstable real cracks form in specimens larger than a critical dimension under hygral conditions severe enough.

For the development of softening cracks and stable real cracks the full fracture energy of the material must be supplied. Fracture process zones can be considered to be latent instabilities. These latent instabilities will be activated if a specimen is large enough. The critical widening of the fracture process zone at which unstable crack formation takes place depends essentially on the shape of the strain softening diagram. Once the latent instability is activated further crack propagation is independent of the remaining fracture energy.

REFERENCES

1. Bazant, Z.P. and Oh, B.H., Crack band theory for fracture of concrete. Mat. et Constr., Vol. 16, No. 93, 1983, 155-177.
2. Petersson, P.E., Crack growth and development of fracture zones in plain concrete and similar materials. Report TVBM-1006, Lund (Sweden), 1981.
3. Wittmann, X.H., Sadouki, H. and Wittmann, F.H., Numerical evaluation of drying test data. Trans. 10th Intern. Conf. on Struct. Behaviour in Reactor Technology (SMiRT), Anaheim (USA), Vol. H, 1989, 71-79.
4. Wittmann, X.H., Sadouki, H. and Wittmann, F.H., Hygral drying of autoclaved aerated concrete. Int. Report, Inst. for Building Materials, ETH-Zürich (Switzerland), 1992.
5. Ferraris, C.F., Mecanismes du retrait de la pâte du cinent durcie. Thèse No. 621, EPF-Lausanne (Switzerland), 1986.
6. Houst, Y., Alou, F. and Wittmann, F.H., Influence of moisture content on the mechanical properties of autoclaved aerated concrete. In Autoclaved Aerated Concrete, Moisture and Properties, ed. F.H. Wittmann, Elsevier, London, 1983, 219-234.
7. Brühwiler, E., Wang, J. and Wittmann, F.H., Fracture of AAC as influenced by specimen dimension and moisture. J. Mat. Civil Engng., Vol. 2, No. 3, 1990, 136-146.

ANALYSIS OF SHRINKAGE CRACKS IN CONCRETE BY FICTITIOUS CRACK MODEL

HIROSHI AKITA
Professor/ Department of Civil Engineering
Tohoku Institute of Technology
3-16, Matsugaoka, Taihakuku, Sendai, 982, Japan

TADASHI FUJIWARA
Professor/ Department of Civil Engineering
Iwate University
3-5, Ueda 4, Morioka, 020, Japan

YOSHIO OZAKA
Professor/ Department of Civil Engineering
Tohoku University
Aoba, Aramaki, Aobaku, Sendai, 980, Japan

ABSTRACT

In order to study the shrinkage cracks in concrete, an experiment using a prismatic specimen and a numerical calculation using fictitious crack model were performed. As the crack mouth opening displacements obtained from the calculation are under 6μm, it can be difficult to find such cracks by using a glass of 10 magnifications. In fact, no crack could be seen by the glass in the specimen during the first 3 days, but some crack patterns were found just after the specimen was wiped with wet cloths. These patterns are considered to be the mouths of fracture process zones.

INTRODUCTION

It has great concern when and how shrinkage cracks initiate and grow in concrete due to drying. In this experiment, 10×10×40cm prismatic specimen was dried under the constant conditions of 20℃ and 60% relative humidity, and the initiation and growth of the cracks were observed. The behavior of the cracks was also investigated by numerical analysis using the fictitious crack model proposed by Hillerborg et al[1]. In the analysis, shrinkage strains were estimated by the water contents calculated from the non-linear diffusion equation[2], and by the relation of strain to water contents obtained from another experiment.

NUMERICAL MODEL

In this analysis, it is assumed that shrinkage strains vary only in one direction, Y axis, and that they are uniform in X and Z directions. Therefore, two-dimensional finite element model can be adopted as shown in Fig. 1. However , because the condition is neither plain stress nor plain strain, three displacements are considered at each nodal point, and the displacements in Z direction are supposed to be equal at every nodal point. Assuming that fictitious cracks locate at equal distances, the half portion between two cracks is necessary for the numerical model.

The crack spacing of the model was determined to be so large as the surface stresses did not exceed tensile strength. After a few trials, the crack spacing of 8 mm with a side crack in the center was obtained.

The water cement ratio of the specimen is 50%, and the mechanical properties for the analysis are Young's modulus of 24.4 GPa, Poisson's ratio of 0.21 and tensile strength of 3.23 MPa. In this analysis, Young's modulus is selected to be 64% of test value, considering the non-linear characteristics in the neighbor of tensile strength. The bilinear model was adopted as the tension softening curve based on the experimental data from Uchida et al[3].

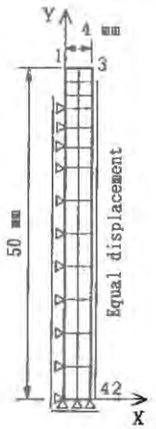

Figure 1. Finite element mesh.

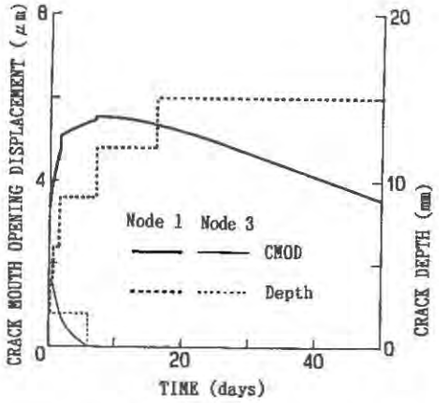

Figure 2. Histories of crack mouth opening displacements and crack depths for 50 days.

NUMERICAL RESULTS

The histories of fictitious crack depths and of crack mouth opening displacements are shown in Fig. 2. It must be noted that the results are concerned only with fictitious cracks, not real cracks. The opening displacement of the main crack reaches maximum value of 5.5 μm at drying periods of 7 days, after which it decreases gradually. The decrease in the

opening displacement seems to be caused by the change of specimen's water content gradually approaches to uniformity while drying progresses. The depth of the main crack reaches 15 mm 50 days later. On the contrary, the side crack does not grow over 2 mm of depth and closes after drying 6 days.

Fig. 3 shows the histories for one day, clearly illustrating the initial stage of drying. Fig. 4 illustrates that the main crack and the side crack grow together at first, but side crack closes when the main crack grows larger. The relation between the both cracks is similar to that of microcracks in fracture process zone.

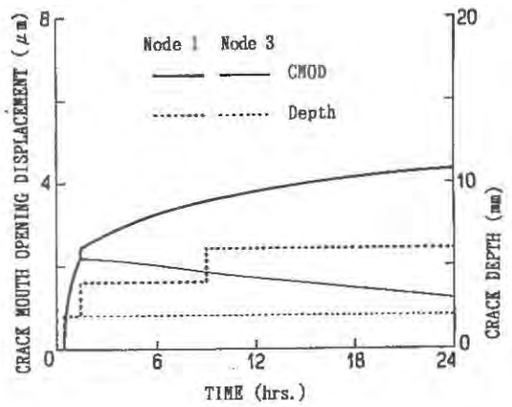

Figure 3. Histories of crack mouth opening displacements and crack depth for 1 day.

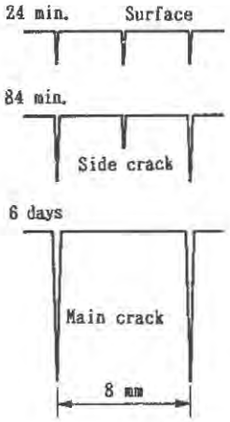

Figure 4. Growth of cracks.

EXPERIMENTAL RESULTS

Fig. 5 shows the crack patterns obtained by wiping the specimen with wet clothes after drying one day. Clear patterns can be seen, but no crack could be found by using a glass of 10 magnifications. Fig. 3 shows that the crack mouth opening displacement is about 4 μm at that time.

After drying the specimen for 3 days, the crack patterns in Fig. 6 were obtained by painting black ink on the specimen and wiping it away immediately. The patterns are more clear and thin than those in Fig. 5. It is considered that the patterns in Fig. 6 indicate slightly developed cracks because of the penetration of ink, and those in Fig. 5 indicate fracture process zones because of the penetration of water. In addition, the crack spacings appear to be nearly 8 mm in Fig. 6.

CONCLUSION

A numerical analysis using fictitious crack model and an experiment using prismatic specimen were performed. The following conclusions were developed from the results.

1. Crack spacing was determined to be 8 mm from the calculation, assuming that surface stress did not exceed tensile strength. The same crack spacing also could be seen in the experiment.
2. Crack mouth opening displacement reaches the maximum value of 5.5 μm 7 days later, after which it decreases gradually.
3. Main crack depth reaches 15 mm after drying 50 days.
4. Side crack does not grow over 2 mm of depth, and closes after 6 days.
5. If cracks of 5 μm opening displacement can be observed by a glass, it might be found after drying 2 days. But, no crack could be observed during the 3 days the specimen dried.
6. The mouth of fracture process zone can be observed by a simple method of wiping the specimen with wet clothes.

REFERENCES

1. Hillerborg, A., Modeer, M. and Petersson, P.E., Analysis of crack formation and crack growth in concrete by means of fracture mechanics and finite elements, Cement and Concrete Research, 1976, 6, 773-782.
2. Akita, H., Fujiwara, T. and Ozaka, Y., Water movement within mortar due to drying and wetting, Proc. JSCE, 1990, 420, 61-69.
3. Uchida, Y., Rokugo, K. and Koyanagi, W., Determination of tension softening diagrams of concrete by means of bending tests, Proc. JSCE, 1991, 426, 203-212.

Figure 5. Crack patterns after drying 1 day.

Figure 6. Crack patterns after drying 3 days.

CRACKING AND DAMAGE IN CONCRETE DUE TO NONUNIFORM SHRINKAGE

TATSUYA TSUBAKI, MONOJ K. DAS and KAZUSHIGE SHITABA
Department of Civil Engineering
Yokohama National University
Hodogaya-Ku, Yokohama, Japan 240

ABSTRACT

The effect of the nonuniform drying shrinkage on the deformational behavior of concrete is investigated by the finite element analysis with concrete elements. A concrete element is a kind of complex element made up of a number of finite elements to represent the inhomogeneous internal structure of concrete. From the numerical simulation for a number of model concrete specimens subjected to drying, the distributions of moisture and cracking are obtained. Then, the amount of cracks which indicates the damage of concrete is statistically analyzed.

INTRODUCTION

Concrete structures are exposed to various drying conditions immediately after the removal of the form. The shrinkage of concrete due to such a drying condition causes a nonuniform stress distribution inside concrete and, subsequently, cracking. Such cracking leads to reduction of the strength and the stiffness of concrete. Therefore, cracking and damage due to drying shrinkage are important factors from a viewpoint of design of concrete structures.

In this study, cracking and damage of concrete due to drying are investigated by using an analytical method with the use of the finite element method. Concrete is considered as a heterogeneous material made up of coarse aggregates and mortar (cf. Fig.1(a)). Such a composite material with a random internal structure would be modeled efficiently by using the concrete element concept [1–3]. A concrete element is a kind of complex element made up of three domains, i.e., a coarse aggregate, mortar and the interface between them (cf. Fig.1(b)). The shrinkage strain of concrete due to drying is calculated by the nonlinear diffusion analysis for the moisture movement in concrete, and it is used in the nonlinear stress analysis.

Numerical simulations are carried out to get the crack distributions. These results are used to estimate the influence of drying on the mechanical behavior of concrete. The damage of concrete is also evaluated from the result of the stress analysis.

METHOD OF ANALYSIS

In this study, concrete is modeled as an inhomogeneous material made up of coarse aggregates, mortar and the interface domain between them. Although there are several methods to deal with concrete as such a composite material [4], the method using concrete elements is employed in this study because of its computational efficiency. The analysis in this study is two-dimensional. Decomposing the overall stiffness equation for a concrete element into two parts related to the external and internal nodes, the incremental stiffness equation for a concrete element becomes as follows, assuming that external loads are not applied to the internal nodes.

$$\overline{\boldsymbol{K}}\,\mathrm{d}\boldsymbol{U}_{\mathrm{E}} = \mathrm{d}\overline{\boldsymbol{F}} \tag{1}$$

$$\overline{\boldsymbol{K}} = \boldsymbol{K}_{\mathrm{EE}} - \boldsymbol{K}_{\mathrm{EI}}\boldsymbol{K}_{\mathrm{II}}^{-1}\boldsymbol{K}_{\mathrm{IE}} \tag{2}$$

$$\mathrm{d}\overline{\boldsymbol{F}} = \mathrm{d}\boldsymbol{F}_{\mathrm{E}} + \mathrm{d}\boldsymbol{F}''_{\mathrm{E}} - \boldsymbol{K}_{\mathrm{EI}}\boldsymbol{K}_{\mathrm{II}}^{-1}\mathrm{d}\boldsymbol{F}''_{\mathrm{I}} \tag{3}$$

$$\mathrm{d}\boldsymbol{U}_{\mathrm{I}} = \boldsymbol{K}_{\mathrm{II}}^{-1}(\mathrm{d}\boldsymbol{F}''_{\mathrm{I}} - \boldsymbol{K}_{\mathrm{IE}}\mathrm{d}\boldsymbol{U}_{\mathrm{E}}) \tag{4}$$

where $\boldsymbol{K}$,$\boldsymbol{U}$,$\boldsymbol{F}$ and $\boldsymbol{F}''$ respectively stand for the element stiffness matrix of each component finite element, the displacement vector, the load vector, and the equivalent load vector due to various inelastic strains, etc. $\boldsymbol{F}''$ can take into account the effects of the nonlinear material properties of each component material such as visco-plastic behavior,

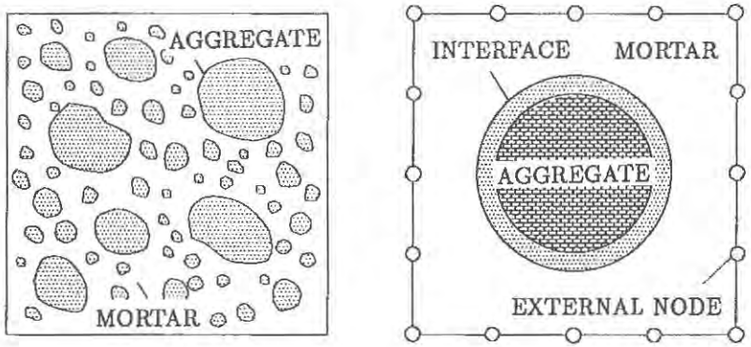

Figure 1. Modeling of concrete:

(a) Internal structure of concrete;
(b) Concept of concrete element.

creep, shrinkage, and cracking. Subscripts E and I stand for the quantities related to the external and internal nodes of a concrete element, respectively. Eq.(4) is used to calculate the displacements of the internal nodes using the displacements of the external nodes.

An example of the concrete element used in this study is shown in Fig.2(a). In this study, 8-node isoparametric elements are used for the internal elements of a concrete element. Each concrete element has 16 external nodes, 77 internal nodes and 28 internal elements. Since Eq.(1) is related to 16 external nodes only, it is clear that the size of the stiffness matrix is significantly reduced by the elimination of the degrees of freedom of the internal nodes. The shape of a concrete element is assumed to be square. The ratios between the diameter of an aggregate (D) and the side length of a concrete element (L) are 0.3, 0.5, 0.7 and 0.9. The thickness of the interface is 1/100 of the side length of a concrete element.

The analysis is decomposed into two parts, i.e., the analysis of moisture diffusion and the analysis of drying shrinkage. In this study, it is assumed that the moisture diffusion in concrete due to drying is expressed by the nonlinear diffusion equation. It is also assumed that the humidity-dependence of the diffusivity of the mortar is expressed by a trilinear relationship (cf. Fig.2(b)), considering the equation proposed by Bazant [5]. The moisture diffusivity of the aggregate is assumed to be negligible.

In the analysis of drying shrinkage, it is assumed that the unrestrained incremental shrinkage of mortar is linearly proportional to the incremental change of humidity and the proportional constant is $\kappa = 1.6 \times 10^{-3}$ [6,7]. This unrestrained shrinkage is converted into the equivalent nodal force to be used in Eq.(3). The mortar is assumed to crack when the tensile stress exceeds its tensile strength. The crack is modeled by the smeared crack model. The crack direction is perpendicular to the principal tensile stress and the tensile stress is released at once.

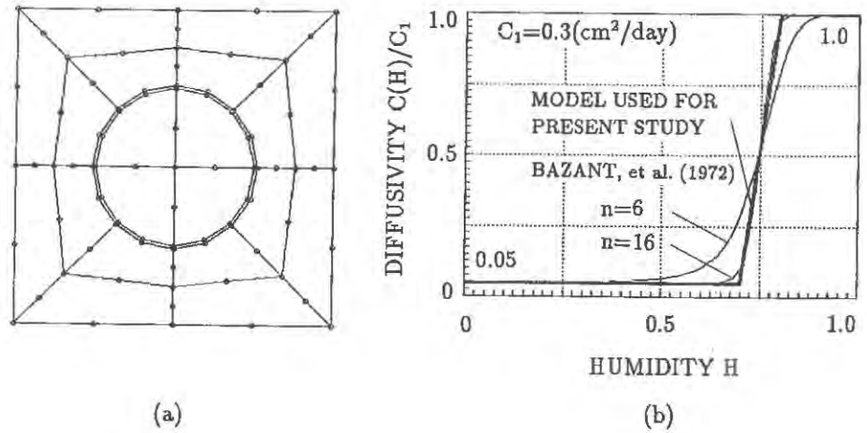

Figure 2. Analysis model of concrete specimen:

(a) Element discretization of concrete element (D/L=0.5);
(b) Model of humidity–dependence of diffusivity.

NUMERICAL SIMULATION AND DISCUSSION

The concrete specimen analyzed in this study is a rectangle (10 cm × 30 cm). The specimen is discretized by concrete elements with side length of 2.5 cm. An example of element discretization is shown in Fig.3. In this example, 48 concrete elements are used. The number of external nodes is 401 and that of the total nodes is 4097. Four types of concrete elements with different ratios of D/L are used in equal numbers and they are arranged randomly by using uniform random numbers. In this analysis, 30 model concrete specimens are analyzed for the moisture diffusion and the drying shrinkage. For the sake of simplicity, it is assumed that the interface has the same material properties as the mortar.

For the analysis of the moisture diffusion, it is assumed that the initial humidity in concrete is 100% and the ambient humidity is 70%. Fig.4 shows the humidity distribution for drying time $t\text{-}t_0 = 10$ days. It is observed that the humidity distribution is inhomogeneous due to the effect of random spatial distribution of coarse aggregates.

For the analysis of the drying shrinkage, it is assumed that the elastic modulus and the Poisson's ratio are 19.6 (GPa), 0.2 for the mortar and the interface, and 196 (GPa), 0.2 for the aggregate. Fig.5 shows the deformation of a concrete specimen due to drying shrinkage ($t\text{-}t_0 = 10$ days). Nonuniform deformation is observed because of the random-

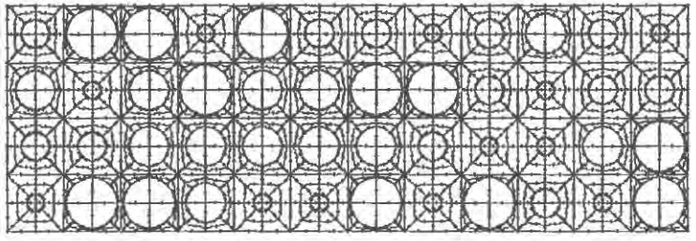

Figure 3. Element discretization of concrete specimen.

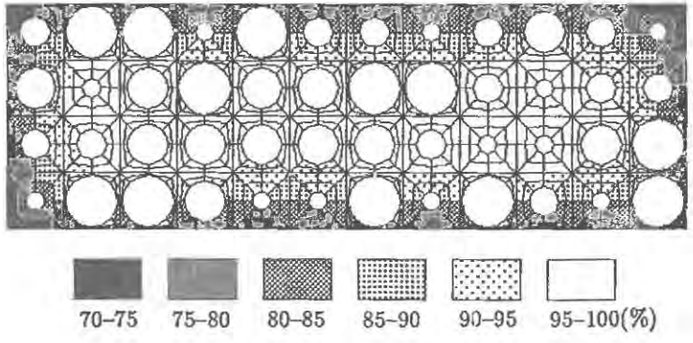

Figure 4. Humidity distribution in concrete.

ness of the internal structure of concrete. The pattern of the cracking corresponding to the deformation in Fig.5 is shown in Fig.6. The cracks are mainly located near the surface where the tensile stress becomes large because of drying shrinkage. However, cracks are also observed in the central portion because of the nonuniform stress distribution. The measure of the damage of the concrete specimen due to nonuniform shrinkage may be defined in various ways [8]. In this study, the effect of cracking on the mechanical proper-

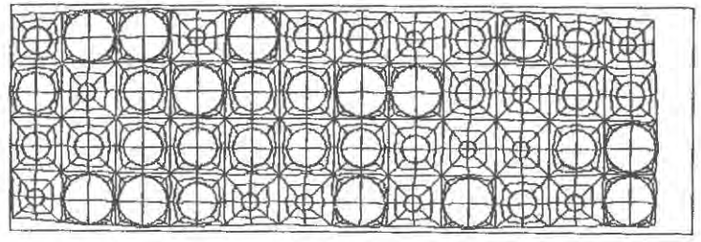

Figure 5. Deformation of concrete specimen due to drying shrinkage.

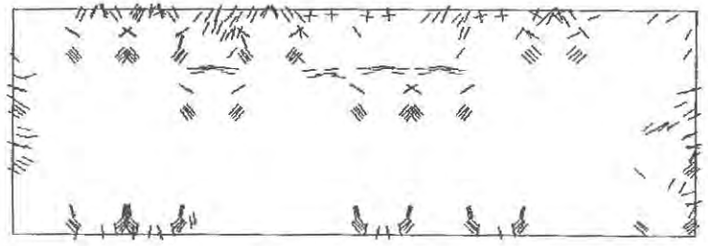

Figure 6. Cracking of concrete specimen due to drying shrinkage.

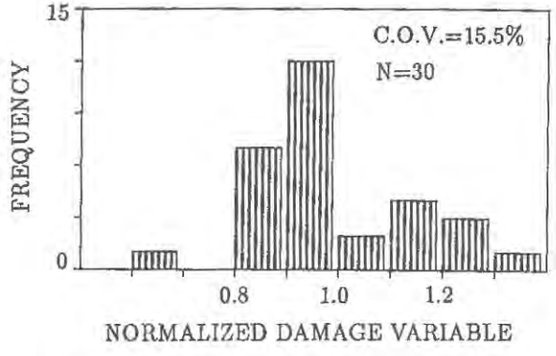

Figure 7. Variation of damage variable.

ties in the longitudinal direction is measured by the total cracked area projected on the transverse axis. Fig.7 shows the statistical variation of the damage variable thus defined. The coefficient of variation for 30 model concrete specimens is 15.5% which is larger than those of the water loss or the shrinkage [1–3].

CONCLUSIONS

The moisture diffusion and the drying shrinkage of a model concrete specimen are investigated by the finite element analysis with the use of concrete elements. It becomes clear that the inhomogeneous moisture distribution and the deformation of concrete due to drying are obtained efficiently. The damage due to tensile cracking is also discussed statistically.

REFERENCES

1. Tsubaki, T., Shitaba, K. and Das, M.K., Numerical simulation of the deformation and stresses of concrete due to drying. Trans. of the Japan Concrete Institute, Vol.13, 1991.
2. Tsubaki, T., Das, M.K. and Shitaba, K., Numerical simulation to analyze statistical variation of creep of concrete. Trans. of the 11th Int. Conf. on Struct. Mech. in Reactor Tech., Vol.H, H07/5, 1991, pp.175-180.
3. Tsubaki, T., Deformation of concrete due to drying. Proc., ASCE Engineering Mechanics Specialty Conference, Vol.2, 1991, pp.1149-1153.
4. Roelfstra, P.E., Sadouki, H. and Wittmann, F.H., Le beton numerique. Materials and Structures, Vol.18, 1985, pp.327-336.
5. Bazant, Z.P. and Najjar, L.J., Nonlinear water diffusion in nonsaturated concrete. Materials and Structures, Vol.5, 1972, pp.3-20.
6. Neville, A.M., Properties of Concrete, 3rd Ed., Pitman, London, 1981.
7. Wittmann, F.H., Deformation of concrete at variable moisture content. Chap.19, Mechanics of Geomaterials, ed. Z.P. Bazant, Wiley, 1985, pp.425-459.
8. Krajcinovic, D., Damage mechanics. Mechanics of Materials, Vol.8, 1989, pp.117-197.

SIMULATION OF THERMAL CRACKS OF MASS CONCRETE IN STAGE CONSTRUCTION

Chen Li-hong Fu Zuo-xin

Department of Mechanics, Hohai University,

Nanjing, 210024, P. R. China

ABSTRACT

The fictitious crack model has been developed to simulate the thermal crack of mass concrete in stage construction. The constitutive relation in fracture zone under sustained loading is obtained from the softening surface in the $\sigma-w-t$ space which is based on tensile strength f_t and fracture energy G_F of concrete at different ages. The test series to determine fracture energy G_F at early ages have been done. The analysis shows that the ability of concrete against cracking may be improved by softening and the possibility of fracture has been over estimated by ordinary analysis methods.

INTRODUCTION

The thermal crack of mass concrete depends on the history of temperature and creep. Generally a large concrete structure is made up of many concrete lifts

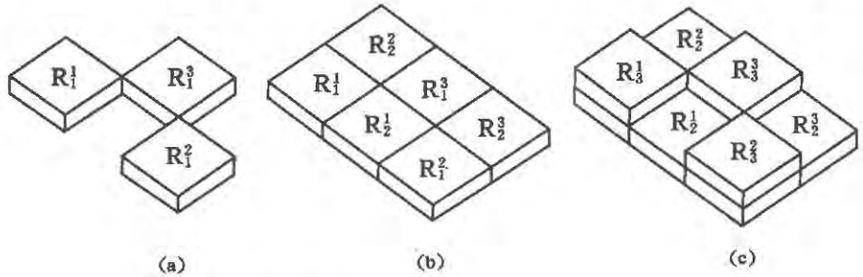

Figure 1. Mass concrete in stage construction

which are poured in batches (Figure 1.). A three-dimensional FEM program with the automatic generation function of mesh and boundary condition messages has been designed to simulate the transient temperature, creep and stress fields of large concrete structures in construction and operational periods. The thermal crack can then be simulated.

SOFTENING SURFACE AND ITS TEST DETERMINATION

As the thermal crack of mass concrete is caused by the sustained effects of the changes of temperature, the $\sigma-w$ curve [1] is no longer suitable for the fracture zone and the time effect must be taken into consideration. In order to consider both effects of softening and creep in fracture zone, the total additional deformation w_T is divided into two parts:

$$w_T = w_a + w_b \tag{1}$$

In which w_a ia the additional deformation caused by microcracking, w_b is the creep deformation caused by the other reasons, such as the removal of adsorbed water etc.. Under sustained loading, the relation between stress and deformation within the fracture zone, i. e. $\sigma-w_T(t)$ is the curve in the three dimensional space of $\sigma-w-t$ (Figure 2.), it can be called softening trace. Because of the softening trace relating with the rate of loading , it is very difficult to determine it by test directly; while the fracture energy G_F under the short-term loading can be determined easily at present and there is also a standard to follow. Therefore, through a appropriate assumption we can obtain $\sigma-w$ (t) curve based on the fracture eneygy G_F:

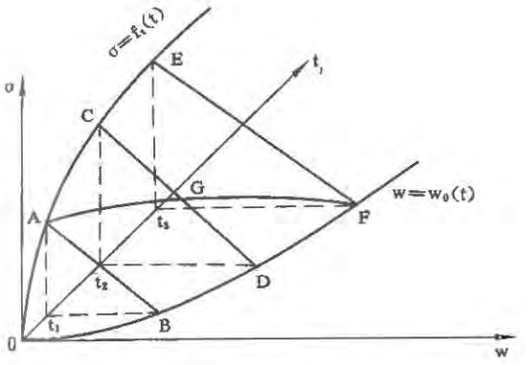

Figure 2. Softening surface in the $\sigma-w-t$ space

We assume that the shape of $\sigma-w$ curve under the short-term load is a straight line (or a bilinear), a series of curves on the planes perpendicular to the axis t are obtained from the $G_F(t)$ (Figure 2.). Connecting these curves, a surface in the three dimensional space of $\sigma-w-t$ is formed, we call it softening

surface. Because the softening surface is based on the short-term tests, the additional deformation w in the space $\sigma-w-t$ is w_a in Eq. (1)rather than w_T; therefore, real softening trace is in the outside of the softening surface and the softening surface is the lower boundary surface of all the possible softening traces. If we assume that the softening trace under sustained load is on the softening surface, then the softening ability of concrete can be taken into account in the lowest degree and the $\sigma-w(t)$ curve for fracture zone can be obtained from the equation of softening surface. For the assumption of straight line, there is

$$\begin{aligned} \sigma(t) &= f_t(t) - \frac{f_t^2(t)}{2G_F(t)}w(t) && (w(t) \leqslant 2G_F(t)/f_t(t)) \\ \sigma(t) &= 0 && (w(t) > 2G_F(t)/f_t(t)) \end{aligned} \tag{2}$$

Where $f_t(t)$ and $G_F(t)$ are tensile strength and fracture energy at different ages. They can be determined by tests. The similar Eqs. for bilinear assumption can be obtained in the same way. Table 1 gives the results of our tests [2]. There are more than 8 specimen in each age-group.

TABLE 1
G_F at early ages (N/m)

age (day)	7	14	21	28
Mean value	59.59	89.22	104.16	126.45
Standard deviation	16.64	17.99	23.09	15.42

In stage construction of mass concrete, the main loads are gravity and changes of temperature, there is no high compressive stress and the principal stress direction does not change appreciably, so the properties of fracture zone is independent of the type of stress field [1]. This means that Eq. (2) can be directly applied to the analysis of three dimensional problems.

THE SIMULATION OF THERMAL CRACK

Based on the simulation of transient temperature, creep and strass fields of mass concrete in stage construction, the fictitious crack model can be applied to analyze crack formation and crack growth in each time step, in which $\sigma-w$ curve is replaced by softening surface. At any time, every node of finite elements is in one of three states: (1) continuous; (2) softening; (3) crack. Once a node is in softening state, the node will be separated into two nodes. Between these two nodes, a tensile force is introduced, corresponding to the stress σ where σ varies with w according to the equation of softening surface. So the equations for incremental displacement fields are nonlinear after softening occurred, the iteration is needed in each time step.

We have used this method to analyze a practical problem: four concrete lifts on a rock (Figure 3). Observation data showed that no crack was found in this structure. Using numerical analysis, when maximum stress criterion was used

without consideration of softening, a vertical crack in 4-lifts formed; once the softening surface was taken into account, the distribution of tensile stress along the vertical direction tended to be uniform and the crack did not formed, only some nodes were in the state of softening.

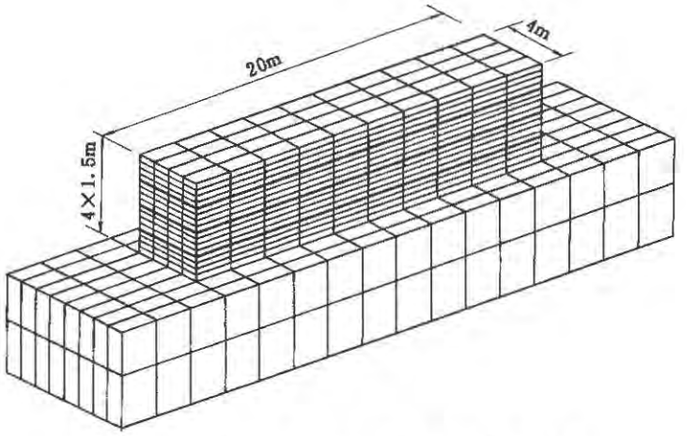

Figure 3. Four concrete lifts on the rock

CONCLUSIONS

1. The fictitious crack model can be developed to simulate the thermal crack of mass concrete in stage construction when the curve $\sigma - w$ is replaced by the softening surface in the $\sigma - w - t$ space.

2. The ability of concrete against cracking may be improved by softening and the possibility of fracture has been over estimated by ordinary analysis methods. Therefore it is possible to simplify the temperature control measures during construction which are used commonly and costly at present.

REFERENCES

1. Hillerborg, A. , Numerical methods to simulate softening and fracture of concrete. In Fracture Mechanies of Concrete, ed. G. C. Sih, Martinus Nijhoff Publishers, Dordrecht, 1985, pp. 141-170.

2. Chen, Li-hong, Analysis of the creep and fracture of concrete dams during construction with the consideration of softening. Ph. D Dissertation, Department of Mechanics, Hohai University, Nanjing, P. R. China, August, 1989.

Characteristics of Fracture Responses of Rate-dependent and Temperature-Sensitive Materials like Asphalt Concrete

Yeou-Shang Jenq and Pei Liu
Department of Civil Engineering
The Ohio State University
Columbus, Ohio 43210, USA

ABSTRACT

Effects of temperature and loading rate on fracture responses of asphalt concrete, which is a rate-dependent and temperature-sensitive material, are examined in the present study. Indirect tensile strength tests and notched half-disk tests were performed to evaluate temperature and rate effects on the material responses. Marshall tablets which were produced using the same mixing condition and compaction effort were used in all the tests. Fracture parameters such as critical stress intensity factor, fracture energy, and indirect tensile strength were found to be highly dependent on the applied loading rate and the testing temperature. The conceptual idea of using a viscous cohesive crack model to simulate the effect of temperature and loading rate on the progressive crack development and deformation characteristics of asphalt concrete is also discussed.

INTRODUCTION

Asphalt concrete is made of two major phases of materials: asphalt cement and mineral aggregates. Asphalt cement is mainly derived from the residues of petroleum crude during refining process and has a very complex polymeric structure. At low temperature (e.g., below "glass temperature", it should be noted that asphalt cement does not have a well defined glass temperature), the cement will behave like glass, and the fracture response can be described as brittle or quasi-brittle. However, as the temperature increases, asphalt cement starts to flow like a viscous liquid and is very sensitive to the loading rate. As a result, the overall response of asphalt concrete is dominated by the behavior of asphalt cement, since aggregates, in general, are not very sensitive to the service temperature and loading rate. Studies on applications of fracture mechanics to asphalt concrete have been very limited [1-3] and the applicability of fracture mechanics concepts to asphalt concrete is still under debate among the researchers. This may be due to the fact that the fracture response as well as the deformation process of asphalt concrete is highly sensitive to the applied loading rate and temperature. Past attempts in using a single parameter approach (such as critical stress intensity factor or critical J-integral) [1-2] to characterize fracture resistance of asphalt concrete did not seem to yield promising results. In order to properly model the fracture response of asphalt concrete, basic information regarding the progressive crack development and deformation characteristics under different temperatures and loading rates is needed. It is hoped that by better understanding the mechanisms that govern the fracture response and deformation process, one can develop a better mathematical model to capture the effects of loading rate and temperature on the material behavior of

asphalt concrete.

EXPERIMENTAL PROGRAM

Marshall disk samples with 4" diameter (D) and 2.5" thickness (T) were prepared using Marshall compaction hammer at a mixing temperature of 305°F. AC-20 graded asphalt cement and aggregates with gradation meeting Ohio Department of Transportation 404 specification were used. The asphalt content is 5.5%, which was determined from Marshall mix design method. These samples were used in the indirect tensile test and the notched-half disk test. All the samples were tested in an environmental chamber using a 20 Kip close-loop controlled MTS testing system. The load-point displacement was used as the feedback signal to control the loading rate. The loading rates used in the present program are: 0.03 inch/min, 0.3 inch/min, and 1.5 inch/min and the testing temperatures are: 32°F, 73°F, and 104°F. All the samples were conditioned at the testing temperature for 10 hours before the test. Three samples were evaluated for each loading ate and testing temperature.

Three-point bend notched half-disk test (Fig. 1) was used to evaluate the fracture response. One of the advantages of using the half-disk sample is that the samples can be directly produced by cutting the Marshall disks so that materials with the same mix proportion and compaction effort are used throughout the testing program. In addition to the quasi-static tests, some notched samples were also subjected to constant loads to evaluate the creep effect.

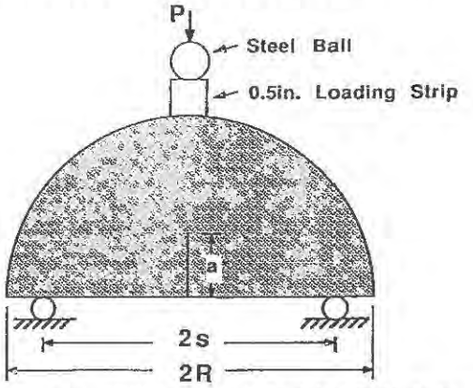

Figure 1. Three point bend notched half-disk test

EXPERIMENTAL RESULTS

Figure 2 shows the typical results of load-displacement curves of indirect tensile tests obtained at a loading rate of 0.03 inch/min. From the initial compliance, the modulus of elasticity can be calculated using the equation derived from finite elements analysis. The indirect tensile strength (f_{ts}) can be calculated from the measured peak load (P_{max}) and is equal to $2*P_{max}/(\pi DT)$. Based on work-of-fracture concept, the fracture energy (G_{fs}) associated with the indirect tensile test can be calculated from the area under the load-displacement curve divided by the cross section area (DxT). The experimental results are listed in Table 1. It can be noted that modulus of elasticity, fracture energy, and indirect tensile strength are highly dependent on the testing temperature and loading rate. In general, higher loading rate and lower testing temperature yielded higher fracture energy, modulus of elasticity, and indirect tensile strength. For the same loading rate, the indirect tensile strengths at 32°F are more than three times of those derived at room temperature (i.e. 73oF). Furthermore, for the same testing temperature, the effect of loading rate on the modulus of elasticity and indirect tensile strength are far significant than those

observed in portland cement concrete. This is also true for 32°F temperature, at which the material is believed to be very brittle. Similar trend is also observed for the fracture energy. However, it should be noted that due to the unique feature of indirect tensile test, some additional energies such as crushing at the loading points and energy for formation of multiple cracks are included in the calculation of fracture energy. As a result, care should be exercised in the interpretation and application of fracture energy derived from indirect tensile test.

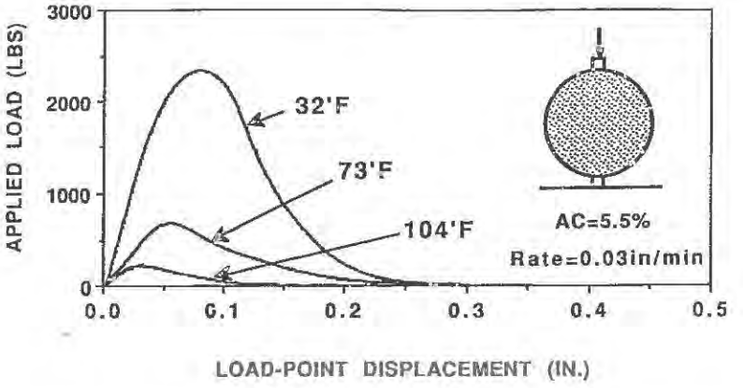

Figure 2. Typical load-displacement results of indirect tensile test

TABLE 1. EXPERIMENTAL RESULTS OF INDIRECT TENSILE TESTS

Temp. (°F)	Loading rate (inch/min)	Fracture energy, G_{Fs} (lb/in)	Indirect tensile strength (psi)	Modulus of Elasticity, E (psi)
32	0.03 0.3 0.15	29.977 39.956 34.081	163.893 339.76 403.48	69727.69 106370. 143039.
73	0.03 0.3 1.5	7.255 12.896 21.23	40.32 75.56 119.09	19845.9 34458. 53921.2
104	0.03 0.3 1.5	1.434 3.353 5.675	14.183 23.718 37.24	13917.0 16497.39 28830.

Figure 3 shows the typical load-displacement curves of notched disk samples tested at 73°F with a loading rate of 0.03 inch/min. The modulus of elasticity can be determined from the measured initial compliance. The critical stress intensity factor (K_{ic}) without nonlinear correction can be calculated from the measured peak load (P_{max}) and the original notch-radius ratio (a/R) as:

$$K_{ic} = P_{max}\sqrt{\pi a}F(a/R)/(2RT) \qquad (1)$$

in which a=initial notch length, R=radius of the sample, and F(a/R) = shape correction factor = $3.19578+17.7159(a/R)-79.1527(a/R)^2+143.801(a/R)^3-60.833(a/R)^4$. The shape correction factor was derived from finite elements analysis and was found to be comparable with the results reported by other researchers [4].

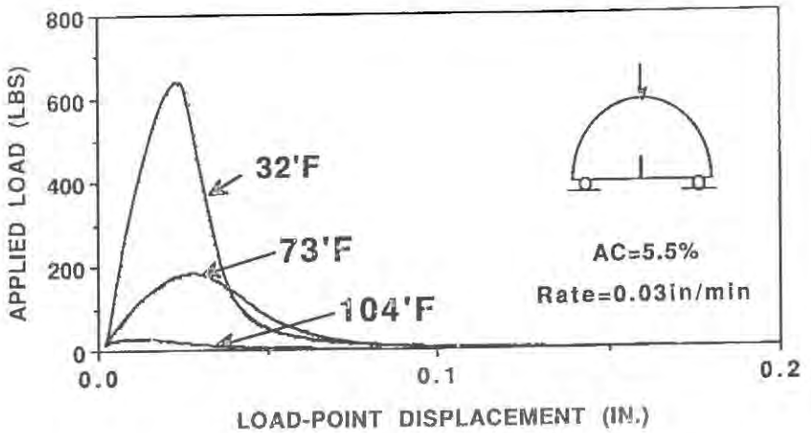

Figure 3. Typical load-displacement curves of three-point bend notched half disk tests

Table 2. EXPERIMENTAL RESULTS OF NOTCHED HALF-DISK TESTS

Temp. (°F)	loading rate (inch/min)	Fracture energy, G_F (lbs/in)	Critical stress intensity factor, K_{Ic} (psi$\sqrt{in}$)	Modulus of Elasticity, E (psi)
32	0.03	5.222	419.15	92422.3
	0.3	3.419	517.76	127125.
	1.5	3.342	547.695	153320.
73	0.03	1.878	101.925	28305.
	0.3	4.11	248.723	95985.
	1.5	6.46	396.424	135976.
104	0.03	0.27	18.999	5554.
	0.3	0.893	49.177	31348.
	1.5	1.802	99.294	49072.

The fracture energy (G_F) associated with the notched half-disk test can be calculated as:

$$G_F = \text{area under the load-displacement curve}/(T(R-a)) \quad (2)$$

Results obtained from the quasi-static fracture tests are listed in Table 2. The effects of loading rate and temperature on the critical stress intensity factor and modulus of elasticity are similar to those observed in the indirect tensile tests, i.e., at a lower temperature or a higher loading rate the values of K_{Ic} and E will be higher. Depending on the testing conditions, these increase can be several folds. Interestingly, the G_F values at 32°F were found to be lower than those obtained at 73°F, except for loading rate at 0.03 inch/min, which is different from that observed in the indirect tensile tests. The reason for this phenomenon is still not very clear. It is, however, believed that coupling effects of temperature and loading rate on the brittleness and viscous energy dissipation may play an important role on this seemingly contradictory observation. Note that fracture energy obtained using indirect tensile tests is about three to ten times higher than that determined using notched half-disk tests for reasons discussed earlier.

Constant loads were also applied to evaluate the time need to achieve creep failure. Four different constant loads were applied to the notched-disk samples. Figure 4 listed the displacement-time relationship obtained at different loading levels. It is very obvious that viscous flow has a significant contribution to the final failure of asphaltic materials.

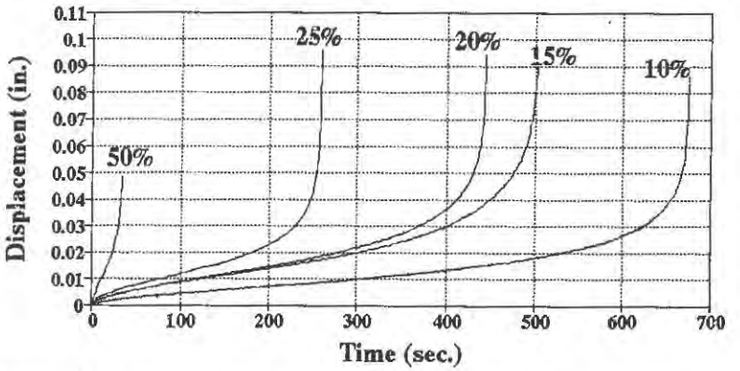

Figure 4. Typical displacement-time histories of creep tests

MATHEMATICAL MODELING

Since rutting (or permanent deformation) and cracking are the two major distress modes in asphalt concrete pavements, a sound mathematical model is needed to simulate not only the fracture resistance but also the deformation characteristics of asphaltic mix. A line crack approach similar to Dougdale-Barenblatt type of cohesive crack model [5-9] seems to be a good choice in terms of simulating the deformation characteristics and progressive crack development of asphalt concrete. Jenq and Perng [5] has extended the cohesive crack model originally proposed by Hillerborg et al [6] using phenomenonlogical approach to simulate the temperature effect. The associated viscous behavior was lumped into the line crack, i.e. assuming that the non-critical zone is linear elastic. Although progressive crack development at different temperatures can be properly simulated, this model, however, can not be used to predict the associated time-dependent deformation and creep failure.

A more reasonable model is the viscous cohesive crack model proposed by Schapery [7-9]. In the model, materials outside the fracture zone were assumed to be linear viscoelastic. Furthermore, the cohesive zone is assumed to be governed by the fracture zone length and is independent of the Young's modulus and Poisson's ratio so that the extended correspondence principle can be used for a moving boundary problem. To apply this model to a finite geometry and to simulating the experimentally observed load-

displacement curve, however, does not seem to be very straight forward. First, the solution process for a finite geometry is more complicated than that of an infinite domain. Furthermore, if one assumes that the cohesive crack zone is governed by the stress-separation curve, then the extended correspondence principle may not be directly applicable to obtain the associated viscoelastic solution, even if the elastic solution is known. A special technique using principle of superposition may be necessary to obtain the associated viscoelastic solution. Second, determination of material properties such as fracture energy, indirect tensile strength, modulus of elasticity, and shape of stress-separation curve is becoming more difficult. As discussed earlier, work-of-fracture concept is used to determine the fracture energy. This means that energy dissipation due to viscous deformation, which is rate-dependent and temperature dependent, is also included as part of the fracture energy. Therefore, to determine the true fracture energy, one needs to assess the quantity of the associated viscous energy dissipation. Furthermore, as indicated earlier, the indirect tensile strength and the modulus of elasticity were very sensitive to the applied loading rate. However, the stress rate in the notched sample is difficult to quantify due to the stress concentration effect. Therefore, correlation of different loading rates among different tests has to be established first if one wants to use this model to predict the observed load-displacement curve of the notched specimens. Issues related with the proposed viscous cohesive crack model will be discussed in more detail at the conference.

ACKNOWLEDGEMENTS

The authors appreciated partial support provided by the Ohio Department of Transportation to the present project.

REFERENCES

1. Karakouzian, M,, A Simplified Method for Material Testing and Design of Pavement Systems. Ph.D. Dissertation, The Ohio State University, Columbus, Ohio, 1978.
2. Dongre, R., Sharma, M. G., and Anderson, D. A., Development of Fracture Criterion for Asphalt Mixes at Low Temperature. Transportation Research Records, to appear.
3. Perng, J. D., Analysis of Crack Propagation in Asphalt Concrete Using A Cohesive Crack Model. M.S Thesis, The Ohio State University, Columbus, Ohio, 1989.
4. Chong, K. P., Kuruppu, M. D., and Kuszmaul, J. S., Fracture Toughness Determination of Rocks with Core-Based Specimens. Fracture of Concrete and Rock, edited by S. P. Shah and S. E. Swartz, 1987, 9-21.
5. Jenq, Y. S., and Perng, J. D., Analysis of Crack Propagation in Asphalt Concrete Using A Cohesive Crack Model. Transportation Research Records, 199, to appear.
6. Hillerborg, A., Modeer, M., and Petersson, P. E., Analysis of Crack Formation and Crack Growth in Concrete by Means of Fracture Mechanics and Finite Elements. Cement and Concrete Research, 1976, 6, 773-782.
7. Schapery, R. A., A Theory of Crack Initiation and Growth in Viscoelastic Media I. Theoretical Development. International Journal of Fracture, 1975,11, 141-1259.
8. Schapery, R. A., A Theory of Crack Initiation and Growth in Viscoelastic Media II. Approximate Method of Analysis. International Journal of Fracture, 1975,11, 369-388.
9. Schapery, R. A., A Theory of Crack Initiation and Growth in Viscoelastic Media III. Analysis of Continuous Growth. International Journal of Fracture, 1975,11, 549-562.

Damage of Concrete under Combined Influence of Loading and Corrosion - A Test Method

Matthias M. Middel

Concrete as a building material is not resistant in all media. Especially in industrial areas we can see the bearing of air and soil pollution on concrete buildings. The destruction of concrete, especially the cement paste, due to chemical effects is summarized with the term concrete corrosion. When we talk about concrete corrosion we have to distinguish between dissolving corrosion, where diffusing elements, for example acids, destroy the compounds of the cement paste, and expansive corrosion, where diffusing elements, for example sulphates, react with the cement paste by building new compounds with higher local requirements as the origin elements, so that the cement paste may burst.

Both types of corrosion - dissolving and expansive corrosion - result in a change of concrete structure, especially the micro-structure. In addition resulting hollows are often classified as pores, but there are also new formed microcracks.

These microcracks superpose with microcracks caused by to external load, or those microcracks which also exist without external load. Both types of microcracks - those due to corrosive effects and those due to load - influence each other, when a corrosive stressed concrete solid is loaded.

With regard to the experimental method of measuring, we must differentiate undirected microcracks which occur at a very low level of stress from directed microcracks

which occur by microcrack-accumulation at a stress of about 70 % of the strength. While undirected microcracks have to be determined by accustical measurement in a very simple way, directed microcracks have to be determined with the aid of energetical criterias and fracture mechanical attempt. These experiments need a high-precise measurement for uniaxial tensile loaded, specimens to determine the unloading branch of the stress-strain curve.

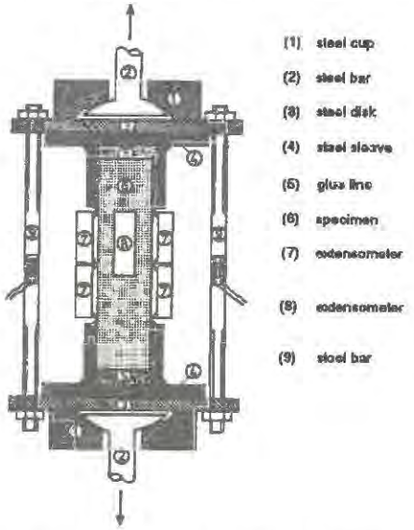

Fig. 1: Measuring device [1]

To compare the effects of different corrosive media it is necessary to put the specimens into the same state of structure. This is possible by the testing device shown in Fig. 1, which has been developed at the University of Bochum to carry out uniaxial tensile tests. This testing device, which is described in [1], [2] and [3], permits stressing the specimens up to the point, where microcrack-accumulation starts and to stop the loading, before microcracking becomes critical. This is the case before strength is reached. Thus, all specimens are put into the same state of structure which makes them comparable. The pre-cracked specimens are stored in corrosive media, water and air. Half of these specimens are stressed by a uniaxial tensile load, which runs up to about 60 % of the stress which implicated microcrack-accumulation; the other half is unloaded. After defined periods of time the specimens will be tested with the above mentioned Bochum testing device. With these tests, all mechanical and fracture mechanical values like strength,

Young's modulus and fracture energy are measured. The corrosive effects of different media on the structure of concrete, especially the cement paste, are demonstrated by means of a comparison of the measured stress-strain curves of the loaded and unloaded and the specimens which are stored in corrosive media, water or in air.

These variations are time-dependent. A testing device for uniaxial long-term tensile stressing of specimens has been developed at the University of Bochum. This device is shown in Fig. 2.

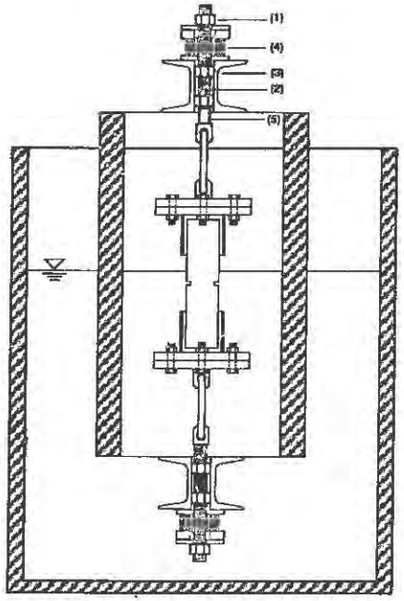

Fig. 2: Long-term testing device

The pre-cracked specimens, either notched or unnotched, are stressed by tightening the nuts (1) and stretching the threaded bars (2), which are supported by the steelen crossmembers (3). Before the threaded bars are stretched by tightening the nuts the stacks of plate springs (4) will be compressed. To define and control the stress of the specimens an extensometer (5) is attached to the threaded bars, stress-strain relationship of which has been determined before. The force in the bars is the same as in the specimen. The deformation of the extensometer is controlled continuously. The creeping and relaxation of the specimens is compensated by the plate springs which are much softer than the other aggregates of the testing

device. Owing to this process the force and the stress in the specimen remains constant all over the testing time.

Comparing tests with missing plate springs are suitable for determining creep curves of uniaxial tensile loaded concrete specimens.

Conclusions

Up to the present time variations of concrete structure due to load effects have been described in combination with those due to corrosive effects.

Indicator for these variations are mainly mechanical values, which have been determined as an average of a large number of either loaded or corrosive stressed specimens. At Bochum University a test method and testing device has been developed to separate these effects by determining variation of mechanical values under combined influence of loading and corrosion. Particular attention will be given to the investigation of long-term effects.

References

[1] Schorn, H.; Berger-Böcker, T., "Test Method for Determining Process Zone Position and Fracture Energy of Concrete," Experimental Techniques, 29-33 (June 1989)

[2] Budnik, J., "Fracture and Deformation Behaviour of Uniaxial Loaded Polymer Modified and Fibre Reinforced Concrete (in German)," PhD thesis, University of Bochum (1985)

[3] Middel, M., "Experimentelle Bestimmung von lastabhängigen Mikrorißbildungen und Rißöffnungsenergien," 25. Forschungskolloquium des Deutschen Ausschuß für Stahlbeton, 209-217 (October 1991)

THE NONMECHANICAL LOADING FRACTURE AND CONTROLLING IN CONCRETE PAVEMENTS

Luo-Yu Xu, Yong-Qi Li*, Qing-Lin Sha* and Bing-Xian Yang**
Structural Strength Division, Jinan R & D Center for Composite Structure
P.O.Box 302, Jinan, Shandong Province, 250023, P.R.China
* Highway Research Institute of the Ministry of Transportation, Beijing, China
** Beijing University of Aeronautics and Astronautics, Beijing, China

ABSTRACT

An expressway and some highways were monitored for long time to summarize characteristics of cracking. Tests were conducted to explore the influence factors such as structures and materials of pavements. An important observed feature of transverse cracking is it'll form a final regular cracking state giving equivalent crack spacing. A hypothesis of section contraction in overlay is presented and the finite element method is used to calculate the temperature stress field. Results show that stress concentration exists at the free-edge of overlay under low temperature contraction and the good bonding action between subgrade and overlay may reduce the stress concentration. The shear-lag model of two-layer system is used to explain the final regular cracking state and gives good agreement with experimental results. Study shows that increasing the thickness or the elastic modulus of pavements and decreasing the elastic modulus of base, especially increasing the crack depth in base will decrease the regular transverse crack spacing. Longitudinal cracking in the center of road is also regarded to be caused by the same mechanism of transverse cracking. Its onset depends on the relative magnitude of the width of road and the regular transverse crack spacing. To prevent transverse cracking in rigid pavements, the spacings of joints should be less than the regular transverse crack spacing.

INTRODUCTION

Cracking in concrete pavements is the main failure mode for pavements. Both in flexible or rigid pavement, cracking seems to be impossible to prevent after several years' service. Hence, fracture controlling should be focused on the late onset and the few number of cracks. Mechanical load is important definitely for cracking, however, even in the footpath there exists a lot of cracks, nonmechanical loading fracture is a kind of wider failure mode. The main cracking manner is transverse cracking. Most current view of points are that those cracks are caused mainly by the

enviromental effect, for instance, the low temperature[1–2]. Those transverse cracks often have a great number, and cause the vibration of vehicles, and poor duriablity of road. Repairing those cracks is very costly. So the study of fracture controlling is necessary.

EXPERIMENTAL STUDY

Typical crack spectrum in asphalt pavement has been shown in Fig.1. Crack forms are mainly transverse cracks, some longitudinal cracks and local multiple cracks[1]. The feature of cracking can be summed up as follows: 1) The direction of transverse crack is perpendicular to the road direction, even in circular road. 2) Transverse crack often st ms from the edge of road, propagates to the center of road, but not all the transverse cracks can run through the whole width of road. 3) Most of the man–made defects such as check well or drail well become the origins of transverse cracks. 4) The transverse crack will approach a regular distributive state after several years' service, i.e., most of the crack spacings are the same value about 5–10 m. Similar phenomenon has been found in the "Characteristic Damage State" of transverse cracking in composite laminates[3–4]. 5) In the narrow or the low traffic loading road, transverse cracking is the main cracking manner. For the wide or the heavy traffic loading road, longitudinal cracking often appears in two different positions. One type of cracking lies in the center of road, another type is located in the center of lane (Fig.1). For the onset and growth of transverse cracks,most current viewpoints are that they stem from subgrade and reflect into overlay to form cracks called "reflective cracks". We tested in a highway with the same subgrade and different overlay. After one winter,the crack ratio (total crack length / area) for the thick (20cm) overlay was 0.1m / m^2,about a half of the thin (4cm) overlay. The main cracks in thin overlay may be regarded as the "reflective cracks" from subgrade. However, that transverse crack stems from overlay and propagates into subgrade is possible completely. Since different temperatures exist in overlay and subgrade, overlay has the bigger tensile stress than subgrade during low temperature contraction, so crack in overlay is possible to onset at first. Hence, drilling tests on overlay cracks were performed in an expressway and some highways. Results showed that all kinds of cracks with different opening widths, subgrade may have cracks or not and the opening width decreased from overlay to subgrade. Those show that crack may propagate from overlay to subgrade[2]. On the properties of asphalt,thin asphalt can be used to reduce the crack ratio. Three kinds of asphalts were used in the overlays of a highway in Shanxi Province. From the first winter to the third winter, the crack ratios (m / 1000m^2) for different asphalt overlays are: 1.from 292 to 1354 for DLY–60; 2.from 109 to 475 for SLY–100; 3.from 58 to 228 for DSY–60. The DSY–60 is the thinnest asphalt among three kinds of asphalt. In order to distinguish the crack forms in flexible and half–rigid subgrades, two sections with different subgrades and the same overlay were built in an expressway. After one winter, transverse crack spacings were 93.2m (flexible subgrade) and 85.4m (half–rigid subgrade), special difference on cracking form hasn't been observed. Crack growth in a highway was monitored for 24 times from 1980 to 1982 and shown in Fig.2. Crack initiated during the first winter and grew even in summer and its growth had a three–stage mode just like the growth of transverse crack in composite laminate[4]. The crack spacing increased very slowly at first, then a rapid increase was noticed. Finally, crack spacing seemed to tend to a limit value called "saturate crack spacing", crack spacings were approximately equal.

SECTION CONTRACTION ANALYSIS

Because a lot of defects exist in pavements and they may become the symmetry axex of contraction at low temperature and there exists the final regular transverse cracking state, the hypothesis of section contraction is used to analyze the stress field of pavement befoe cracking[5]. This model is shown in Fig.1,where m–n are the cracking positions,their displacements are assumed to be zero at low temperature contraction. In order to simulate the bonding action between overlay and subgrade,the bottom displacements of overlay are reduced gradually and included in the displacement field by means of the technique of boundary element. The distribution of temperature in overlay T(z) is assumed to be linear along the direction of thickness. The overlay is divided into 2–3 layers in finite element analysis. Stress in overlay can be given by the linear thermal–elastic constitutive relation

$$\sigma_i = E_{ij}(\varepsilon_j - \alpha_j \Delta T) \qquad (1)$$

Typical result is shown in Fig.3 describing the distribution of normal stress in the edge of road along the direction of

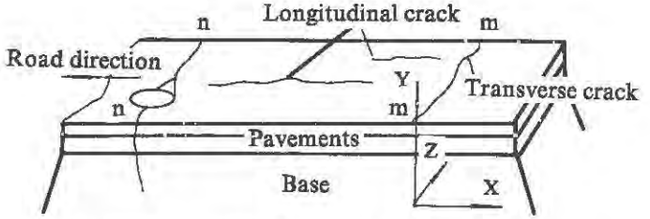

Fig.1. Typical cracking forms of concrete pavement

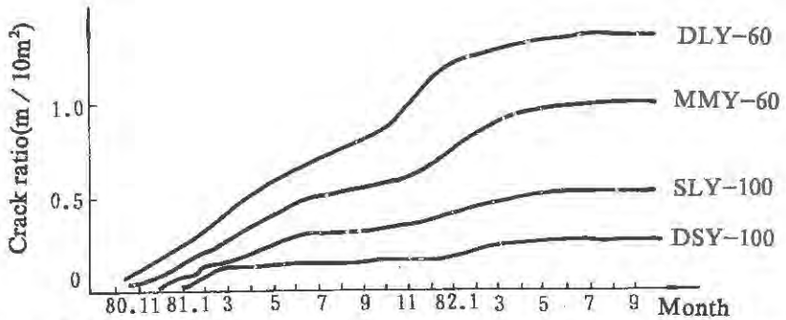

Fig.2. Growth of crack ratio versus every month for different asphalts in a highway

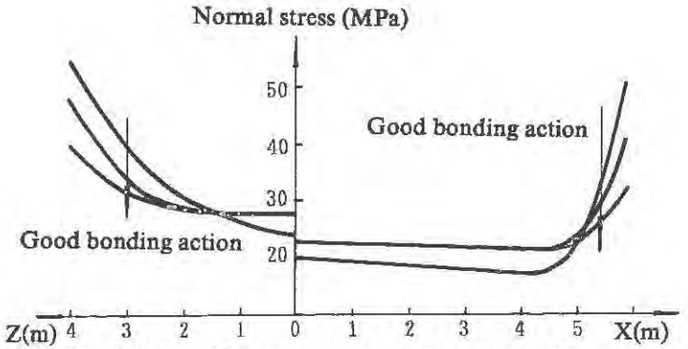

Fig.3. Stress distribution of the section contraction position (m–m) by F.E.M.

road. Stress concentraction exists in the position of section contraction where the crack may be induced. Fig.3 also gives the trend of normal stress in the position of the section contraction (along the transverse direction of the road). Higher tensile stress also exists at the edge of overlay and it agrees with the observed feature that transverse crack often initiates from the edge of road. Analysis shows that good bonding action between overlay and subgrade may reduce the stress concentration both at the edge of road and the position of section contraction.

SHEAR LAG ANALYSIS

According to the general principles of pavement design, the stiffness and strength are designed to degrade from overlay to base[1]. Hence, whatever crack initiates in overlay or subgrade,it will propagate into base finally. The contraction of pavements can be divided into two kinds,i.e.,chemical contraction and physical contraction. The former means that the volume of products is less than that of reactants after the mixture of concrete. After the mixed concrete is laid in pavements,contraction will tend to a small value rapidly. Physical contraction refers to dry contraction and temperature contraction. When the concrete is in service,moisture content evaporates gradually from surface to interior so dry contraction occurs. The temperature contraction comes from the cyclic temperature of everyday and four seasons, especially in winter or night, temperature in pavements is lower than that in base. Because of the different contraction properties of base and pavements,the contraction of pavements is prevented by base, tensile stress occurs in pavements as the result. Two-layer system for pavement analysis is used to study this problem[1]. At a given time, the average tensile stress in pavements caused by the total effect of contractions can be expressed by:$\sigma_s = \sigma_s^e + \sigma_s^t$ Where σ_s^e is the constant tensile stress caused by other contractions, mainly the chemical and dry contractions and σ_s^t is the cyclic stress caused by the temperature contraction. So the crack growth in pavement is a failure process caused by tension-tension fatigue. When temperature drops suddenly,an overload will occur in pavements then transverse cracking will appear because of the low tensile strength of concrete. Considering that the main direction of pavement contraction is in longitudinal direction,we establish a plane stress model of two-layer system on cracked pavements without traffic loading shown in Fig.1. The average stress of pavements in longitudinal direction satisfying equilibrium equations and boundary condictions is given by a shear lag analysis[4]

$$\sigma_s = \sigma_s^0(1 - e^{-kx}(kx + 1)) \tag{2}$$

where σ_s^0 is the stress in pavements at far position from transverse crack,$k$is the shear lag parameter

$$k = \sqrt{\frac{3}{2(1+\mu)}\left(\frac{1}{b^2} + \frac{E_b}{abE_s}\right)} \tag{3}$$

where μ is the poisson's ratio,E_s,$E_b$are elastic modulus of pavements and base respectively,a is the total thickness of pavements and $b$is the crack depth in base. The pavements consist of many layers so the average modulus of pavements can be expressed by the rule of mixtures,i.e.,$E_s = \sum E_i a_i / a$ $b$is difficult to detect and can be derived from

$$W_s = \frac{6\sigma_s^0}{k}\left(\frac{1}{E_s} - \frac{a}{bE_b}\right) \tag{4}$$

where W_s is the maximum opening width of crack in overlay in winter when σ_s^0 is given the value of tensile strength of pavements. As soon as the transverse cracking occurs, a shear-lag zone forms beside the transverse crack because of the shear stress between pavements and base. So normal stress varies from zero to a finite value from cracking position to far position. Only after several years,transverse crack is possible to form in the shear-lag zone. So the transverse crack spacing will be given an approximately equal value finally. The value L_{CDS} can be given by

$$1 - e^{-kx}(kx + 1) \leqslant 1 - \varepsilon, \varepsilon \leqslant 0.1 \tag{5}$$

Fig.4 (a)(b) gives the crack distributions and the predicted saturate crack spacings. The rule of crack distribution can be described as follows: the peak is small and the span is large at the first stage, gradually, the peak becomes higher and the span becomes narrow,i.e.,crack spacing tends to a limit value called "saturate crack spacing". This value is about 7-10m for general highways[1]. To verify the reliablity of the present model,calculation on varying parameters was conducted and shown in Fig.5 and 6. Predicted value of saturate crack spacing approaches the experimental value when design parameters are in permitting values. Certainly,more other condictions should be taken into account[6].

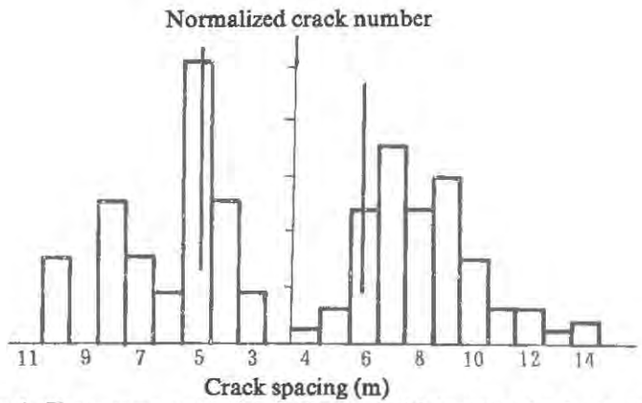

Fig.4. Transverse crack distributions of a highway and a footpath, —predictled saturate crack spacing

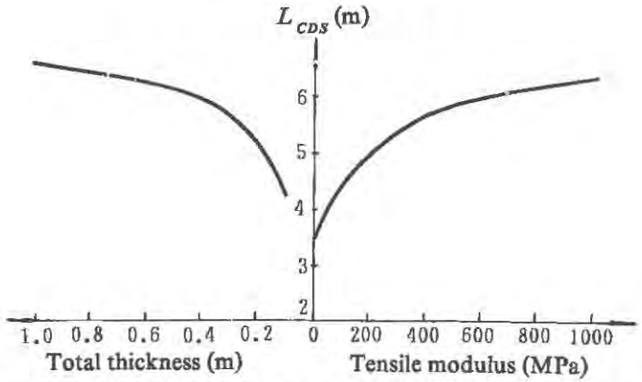

Fig.5. Saturate transverse crack spacing versus parameters of pavements

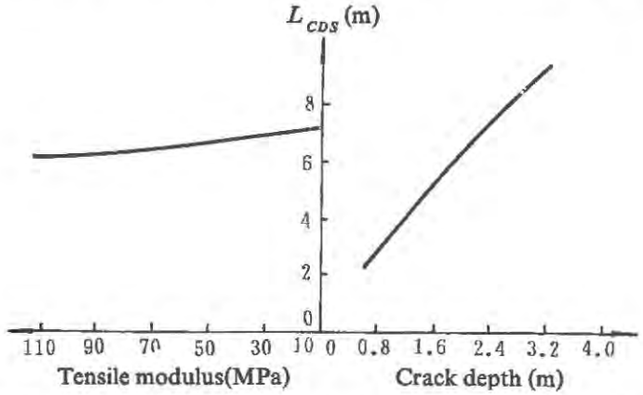

Fig.6. Saturate transverse crack spacing versus parameters of base

When the transverse crack grows especially its saturate crack spacing approaches the width of road, the longitudinal crack will initiate in the center of road from the same shear–lag mechanism of transverse crack but it's under a plane strain analysis state. So the onset condiction for this kind of longitudinal cracks caused by nonmechanical loading is $W > L_{CDS}$. We observe these cracks often appear in the road whose width W is bigger than 5m. Another kind of longitudinal cracks in the center of lane may be regarded to be caused by the traffic (mechanical) loading. For the rigid pavements with cement overlay, joints are used to prevent transverse cracks. The spacing of joints should be less than the saturate transverse crack spacing of rigid pavements,i.e., $L_f < L_{CDS}$. If the cement overlay is paved continuously without joints,L_{CDS} can be measured from the final saturate spacing after several years' service. Preliminary describtion of shear–lag zone in cracked rigid pavements has been reported[7].

CONCLUSIONS

1.The nonmechanical loading crack in concrete pavements may be regarded as the tension–tension fatigue crack from the total effects of various kinds of contraction.

2.Transverse cracks often stem from the edge of road and the serious defects. Finite element analysis shows higher tensile stress exists at the edge of road and good bonding action may reduce the stress concentration in overlay.

3.One observed feature of transverse cracks is that they may form a regular state giving equal crack spacing after long time. This saturate crack spacing can be predicted by the present shear–lag model.

4.The main manner of fracture controlling is by reducing the saturate spacing of transverse cracks. It may be realized by increasing the total thickness or the elastic modulus of pavements and reducing the elastic modulus of base,especially increasing the crack depth in base.

5.Longitudinal cracks in concrete pavements can be divided into two kinds. One kind in the center of road is regarded to be caused by the same mechanism of nonmechanical loading fracture as transverse crack. Its condiction for onset depends on the relative magnitude of the width of road and the final saturate spacing of transverse crack.

6.To prevent the onset of transverse cracking in rigid pavements,the spacing of joint should be less than the measured saturate spacing of transverse crack in the same pavements without joints.

REFERENCES

1.E.J.Yoder and M.W.Witczak,Principles of Pavement Design,2nd ed.,John Wiley and Sons,Inc., New York, (1975), pp.391–399.

2.Q.L.Sha, "On the Cracks in Asphalt Pavement with Half–Rigid Subgrade", Report, Highway Research Institute of the Ministry ofTransportation, Beijing, China,(1989),(In Chinese).

3.K.L.Reifsnider et.al., in Z.Hashin and C.T.Herakovich,ed., Mechanics of Composite Materials:Recent Advances, Pergamon Press,New York,(1982),pp.399–420.

4.L.Y.Xu et.al.,"An Analogous Investigation on Transverse Cracking in Composite Laminate and Concrete Pavement", Proceedings of the 8th Inter. Conf. on Composite Materials,27–F,Published by SAPME,USA,(1991).

5.Y.Q.Li,"Stress Analysis on Low Temperature Cracking in Asphalt Overlay and the Study on Direct Tensile Creep Test", Report,Highway Research Institute of the Ministry of Transportation, Beijing, China,(1988),(In Chinese).

6.B.E.Ruth et.al., Proceedings of AAPT,Missouri,USA,(1982),pp.53–103.

7.B.F.McCullough in A.F.Stock ed.,Concrete Pavements, Eleservier Ltd.,London,(1988),pp.279–318.

INDEX OF CONTRIBUTORS